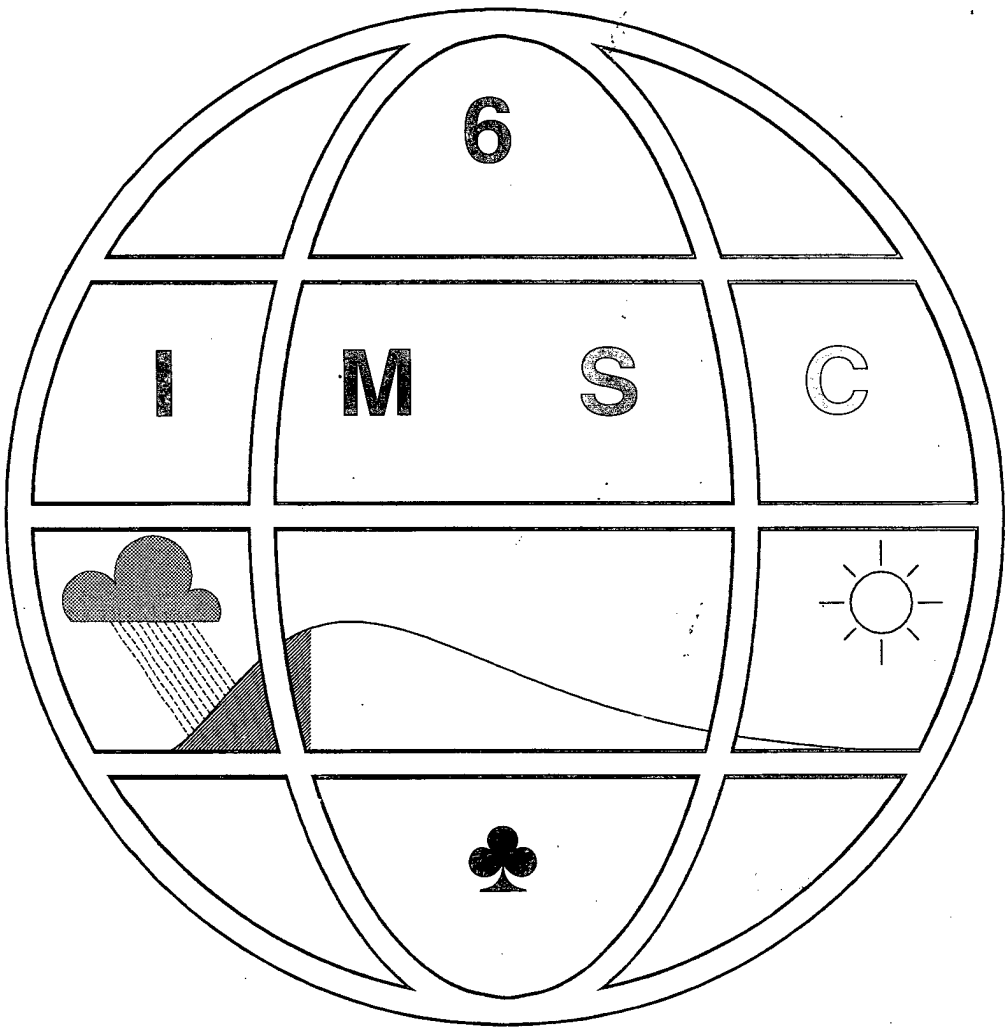
Coláiste na hOllscoile
Gaillimh
Éire

University College
Galway
Ireland

6th International Meeting
on
Statistical Climatology



19 - 23 June, 1995

Galway, Ireland

6th International Meeting
on
Statistical Climatology

19-23 June, 1995

University College, Galway
IRELAND

Organiser

The Steering Committee
for
International Meetings on Statistical Climatology

Cosponsors

All-Ireland Committee on Statistics
American Meteorological Society (Committee on Probability and Statistics)
European Union
Irish Meteorological Service
University College Galway
World Meteorological Organisation

1995.9.

Steering Committee
International Meetings on Statistical Climatology

Francis Zwiers (Chair - Canadian Climate Centre)
George Gruza (Institute for Global Climate and Ecology - Russia)
Allan Murphy (Prediction Evaluation Systems - USA)
Neville Nicholls (Bureau of Meteorology Research Center - Australia)
Ignacio Rodriguez-Iturbe (Instituto International de Estudios Avanzados -Venezuela)
Shyamvir Singh (Indian Institute of Tropical Meteorology)
Raymond Sneyers (Royal Meteorological Institute of Belgium)

Program Committee
6th International Meeting on Statistcal Climatology

Iognáid Ó Muircheartaigh (Chair - University College Galway, Ireland)
Peter Guttorp (University of Washington, USA)
John Haslett (University of Dublin, Ireland)
Tom Karl (NCDC, USA)
Peter Lamb (University of Oklahoma, USA)
Robert Livezey (CPC, USA)
Roland Madden (NCAR, USA)
Allan Murphy (Evaluation and Prediction Systems, USA)
John Petkau (University of British Columbia, Canada)
Johanthan Tawn (University of Lancaster, UK)
Jean Thiebaux (NSF, USA)
Hans von Storch (Max Planck Institute for Meteorology, Germany)
Grace Wahba (University of Wisconsin, USA)
Dan Wilks (Cornell University, USA)
Francis Zwiers (Canadian Climate Center)

The papers printed in this volume are presented in the order in which they are to be presented in the scientific program of the Meeting. These consist of all papers which were accepted for presentation at 6IMSC, and which were received in time for inclusion in the volume, and at least one of the authors of which had registered to participate in 6IMSC at the time of going to press. Where a paper was not received in time, and an abstract of the paper was available, the abstract was included in the volume.

Preface

Fearaimid Céad Míle Fáilte romhaimh go léir go dtí an Cómhdháil seo. It is indeed a pleasure to welcome you all to this sixth in the series of International Meetings on Statistical Climatology, a series that has now grown to the extent that upwards of 200 participants are expected to attend 6IMSC. The geographical dispersion (we have participants from over 30 countries), and the wide variety of disciplines represented in this volume, indicate the dynamism and energy which has emerged from these International Meetings.

The underlying rationale of the sequence of meetings is that statistics is an essential part of climatology, and that the development and application of powerful statistical methodologies have a very important role to play in searching for and achieving a deeper and fuller understanding of our climate and its mechanisms. The small Steering Committee which has overseen the evolution of this series of International Meetings has been the common thread between all the meetings, which while similar in general thrust, have each had their own special emphasis.

There are many people and organisations who have contributed to the preparations for and the presentation of this Meeting. It would be invidious, and indeed impractical, for me to enumerate the many people who should be thanked. I deeply appreciate the assistance which I have received from many sources, and the very positive and tolerant attitude which has been the hallmark of almost all my interactions with the many who either are here at the meeting, or who would like to have come, but for various reasons could not. I feel there are a number of groups and organisations whom I must specifically single out for thanks. The Meeting would not take place without the existence of, and the active encouragement of, both the Steering Committee and the Program Committee; the quality of the meeting is the best thanks I can offer to them. The several financial backers whom we have managed to attract have made it possible to cover many of our administrative costs, and also (and this aspect has always been an important part of all IMSC meetings) to offer assistance to keynote speakers and to participants from developing countries. Those financial backers included, in alphabetical order, the All-Ireland Statistics Committee, the European Union, the Irish Meteorological Service and the World Meteorological Organisation. Next I would like to offer a special word of thanks to the staff of the Computer Services department in UCG for their invaluable assistance in dealing with electronic transmission of papers in various states of encoding, compression, and impenetrability to the non-expert. Not only was the assistance of the highest technical standard, it was provided in a most co-operative and positive manner. Ms. Anne Duggan, of UCG's Conference Office, provided professional advice on all aspects of conference management; this was much appreciated. Finally, I would like to thank my wife and family who provided tremendous support during the long period of preparation for the meeting.

I trust that the Meeting will be professionally rewarding to you all, and it is my earnest wish that you enjoy your visit to our country to the full.

Iognáid Ó Muircheartaigh



Program Chair

6th INTERNATIONAL MEETING ON STATISTICAL CLIMATOLOGY

Invited and Contributed Papers

Sixth International Meeting on Statistical Climatology

Scientific Program / Table of Contents

Monday June 19

(0830) Official Opening by Dr. Colm Ó hEocha, President, University College, Galway

(0840-1000) Session 1: Climate Change Detection I

DETECTING AND ATTRIBUTING AN ANTHROPOGENIC INFLUENCE ON CLIMATE. B. Santer[1], P.D. Jones[2], K.E. Taylor[1], T.M.L. Wigley[3], J.E. Penner[1], U. Cubasch[4]. [1]Lawrence Livermoree National Laaboratory, USA. [2]University of East Anglia, ENGLAND. [3]National Center for Atmospheric Research, USA. [4]Deutsches Klimarechenzentrum, GERMANY 1

CLIMATE CHANGE DETECTION, OBSERVATIONAL AND STATISTICAL CHALLENGES. C.F. Ropelewski. National Weather Service/NOAA, USA 5

STRUCTURAL TIME SERIES MODELS AND THE KALMAN FILTER: APPLICATIONS IN CLIMATOLOGY. H. Visser. KEMA, THE NETHERLANDS 7

(1030-1200) Session 2: Climate Change Detection II

DETECTING HUMAN INFLUENCE ON CLIMATE WITH AN OPTIMAL FINGERPRINT METHOD. G. Hegerl. MPInstitut fur Meteorologie, GERMANY 11

DETECTING CLIMATE CHANGE IN PROGRESS. T. Brown, Uwe Radok. University of Colorado, USA 13

A BAYESIAN APPROACH TO DETECTING CLIMATE CHANGE. B. Cairns. Colombia University, USA 17

TREND AND DRIFT IN CLIMATOLOGICAL TIME SERIES. A. Dempster, Chuanhai Liu. Harvard University, USA 21

PRACTICE OF CLIMATE CHANGE DETECTION IN THE CASE OF A SPECIAL ALTERNATIVE TO RANDOMNESS. M. Vandiepenbeeck. Institut Royal Meteorologique de Belgique, BELGIUM 25

OPTIMAL ESTIMATION OF THE SPHERICAL HARMONIC COMPONENTS OF THE SURFACE AIR TEMPERATURE. S.S. Shen[1], Gerald. R. North[2], Kwang-Y. Kim[2]. [1]University of Alberta, CANADA. [2]Texas A&M University, USA 29

(1330-1530) Session 3: Downscaling I

NEEDS FOR DOWNSCALING: APPLICATIONS AND EXAMPLES. B.C. Hewitson. University of Cape Town, SOUTH AFRICA 33

STATISTICAL-DYNAMICAL DOWNSCALING OF GLOBAL CLIMATE SIMULATIONS. U. Fuentes, V. Sept, D. Heimann, R. Sausen. Institut fur Physik der Atmosphare, GERMANY 37

LINKS BETWEEN LOCAL DAILY SURFACE TEMPERATURES AND CONTINTENTAL-SCALE CIRCULATION PATTERNS. R. Huth, Jiri Novotny. Institute of Atmospheric Physics, CZECH REPUBLIC 41

A STATISTICAL DOWNSCALING OF OBSERVED AND OF CLIMATE MODEL LARGE SCALE FLOW INTO LOCAL NEAR SURFACE WIND. E. Kaas, T. Lee. Danish Meteorological Institute, DENMARK 45

ESTIMATING SURFACE CLIMATIC VARIABLES FROM FREE-ATMOSPHERE QUANTITIES. I. Matyasovszky, Istvan Bogardi. University of Nebraska, USA 49

INFLUENCE OF CLIMATE VARIATION ON AQUATIC ECOSYTEMS. S. Guess. MP Institut fur Meteorlogie, GERMANY

(1330-1530) Session 4: Forecasts and forecast verification

STATISTICAL MODELS IN FORECAST VERIFICATION: METHODOLOGICAL FOUNDATIONS AND PRACTICAL APPLICATIONS. A.H. Murphy[1], Daniel S. Wilks[2]. [1]Prediction and Evaluation Systems, USA. [2]Cornell University, USA 53

DYNAMICAL ENSEMBLE ONE-MONTH FORECAST EXPERIMENTS WITH THE JMA GLOBAL PREDICTION MODEL. K. Takano, S. Maeda, S. Yamada, T. Kudoh, T. Tsuyiki. Japan Meteorological Agency, JAPAN 57

SPECIFICATION OF MONTHLY MEAN 700 MB HEIGHTS FROM SURFACE DATE. W.H. Klein, Y.Dai. University of Maryland, USA 61

COMPARISON OF GAUSSIAN SHIFT AND GAUSSIAN HYBRID MODELS FOR DECISION MAKING WITH THE NWS LONG LEAD TEMPERATURE FORECASTS. R.L. Lehman. National Meteorological Center, USA 65

STATISTICAL CLIMATOLOGY OF ICING EVENTS AND FORECASTS OVER THE CONTINENTAL UNITED STATES1. B.G. Brown. National Center for Atmospheric Research, USA 69

ERROR ANALYSIS OF MONTHLY FIRE WEATHER FORECASTS. F.M. Fujioka. Department of Agriculture, USA 73

FORECASTING PROBABILITY OF LOCAL SEVERE STORMS USING SINGLE STATION DATA. J.K. Sahu, S.V. Singh. Indian Institute of Tropical Meteorology, INDIA 75

(1600-1800) Session 5: Climate Variations

THE NORTH ATLANTIC STORM TRACK AND CLIMATE VARIABILITY. J.C. Rogers. Ohio State University, USA 79

DEVELOPMENT IN OCCURRENCE AND STRENGTH OF SEVERE WINDS OVER THE NORTHEAST ATLANTIC DURING THE PAST 100 YEARS. T. Schmith. Danish Meteorolgical Institute, DENMARK 83

OBJECTIVE DIVIDING PATTERNS FOR CLIMATIC DROUGHT/FLOOD OF EASTERN CHINA IN RECENT 30 YEARS BY CHEBYSHEV QUADRATURE POLYNOMIALS. J. Shen[1], Dong Xiaomin[2]. [1]Iowa State University, USA. [2]Jiangsu Institute of Climate Application, P.R. CHINA 87

SINGULAR VALUE DECOMPOSITION OF INTERACTION AMONG ATMOSPHERIC CIRCULATION, SST AND SEA ICE DURING WINTER. F. Zhifang. Chengdu Institute of Meteorology, P.R.CHINA 91

AN EXTENDED EMPIRICAL FUNCTION ANALYSIS OF MODES OF MID-LATITUDE DECADAL VARIABILITY IN A COUPLED ATMOSPHERE-OCEAN MODEL. C. Frankignoul, E. Zorita. Universite Pierre et Marie Curie, FRANCE 95

VARIABILITY IN "INDICATIONS OF SPRING": AN ANALYSIS OF SPECIES RESPONSE TO CLIMATE OVER TWO CENTURIES USING THE MARSHAM FAMILY DATA. T.H. Sparks, P.D. Carey. NERC Institute of Terrestrial Ecology, UK 99

LOW FREQUENCY VARIATIONS OF POLAR SEA-ICE EXTENT AND RELATED ATMOSPHERIC VARIABLES IN THE NORTH ATLANTIC REGION - PART I, STATISTICAL ASPECTS. P. Frich. Danish Meteorological Institute, DENMARK 103

NON-LINEAR EFFECTS IN INTERANNUAL VARIABILITY OF SPATIAL STATISTICS FOR THE NORTHERN HEMISPHERE TEMPERATURE. G. Alekseev, P.N. Svyashchennikov. The Arctic and Antarctic Research Institute, RUSSIA 107

(1600-1800) Session 6: Pattern Analysis Methods

A MULTIVARIATE STATISTICAL METHOD FOR COMPARISON OF LOW FREQUENCY MODES OF VARIABILITY IN NMC ANALYSES TO THOSE GENERATED FROM THE ECHAM2 GCM. M.B. Richman. University of Oklahoma, USA 111

TOWARDS THE DEVELOPMENT OF PIP MODEL FOR ATMOSPHERIC DATA. U. Achatz, G. Schmitz. Univeritat Rostock, GERMANY 115

AN EFFICIENT DESCRIPTION OF LARGE-SCALE ATMOSPHERIC FLOW USING PRINCIPAL INTERACTION PATTERNS. F. Kwasniok. Max-Planck-Institut fur Meteorologie, GERMANY 119

SENSITIVITY TEST OF POP SYSTEM MATRICES - SPECTRAL PORTRAITS OF A NONSYMMETRIC MATRIX. Y. Zhang, Valentin Dymnikow, John M. Wallace. University of Washington, USA 123

NORMALISATION CONSTRAINTS IN ROTATED PRINCIPAL COMPONENT ANALYSIS: ILLUSTRATIONS IN CLIMATOLOGY. I.T. Jolliffe, Barry Law. University of Aberdeen, SCOTLAND 127

ROBUSTNESS OF LOW-FREQUENCY CIRCULATION PATTERNS DERIVED FROM UNROTATED AND ROTATED PRINCIPAL COMPONENT ANALYSES. X. Cheng, Gregor Nitsche and John M. Wallace. University of Washington, USA 131

EFFICIENT PREDICTION OF COVARIANCES USING SINGULAR VECTORS. M. Ehrendorfer[1], Joseph J. Tribia[2]. [1]University of Vienna, AUSTRIA. [2]National Center for Atmospheric Research, USA 135

TWO METHODS TO DESCRIBE THE STATISTICAL QUALITY OF PATTERNS PRODUCED BY CLUSTER ANALYSIS PROCEDURES. F.-W Gerstengarbe, Peter C. Werner. Potsdam Institute for Climate Impact Research, GERMANY 139

Tuesday, June 20

(0830-1000) Session 7: Design and Analysis

INTER-COMPARISON OF SIMULATED POTENTIAL PREDICATABILITY IN SEVERAL AMIP EXPERIMENTS. F.W. Zwiers. Canadian Centre for Climate Modelling and Analysis, CANADA 143

MULTIPLE SIMULATIONS AND OCEAN MODEL TESTING. C. Frankignoul. Univesite Pierre et Marie Curie, FRANCE 147

NONLINEAR PRINCIPAL COMPONENT ANALYSIS OF CLIMATE DATA. S. Sengupta, J. Boyle. Lawrence Livermore National Laboratory, USA 149

(0830-1000) Session 8: Methods I

PCA-BASED CLASSIFICATION OF CIRCULATION AND WEATHER PATTERNS: SOME METHODOLOGICAL CONSIDERATIONS. R. Huth. Institute of Atmospheric Physics, CZECH REPUBLIC 155

USING STATE-SPACE STATISTICAL MODELS TO DESCRIBE RECENT TRENDS IN THE SPATIAL STURCTURE OF THE CALIFORNIA CURRENT SYSTEM. R. Mendelssohn, Franklin B. Schwing. Pacific Fisheries Enviromental Group, USA 159

VALIDATION OF THE SMALL-SCAEL PERFORMANCE OF A CLIMATE MODEL BY ANALYSING THE CONSISTENCY OF LARGE-SCALE AND SMALL-SCALE CLIMATE. U. Burkhardt. Universtat Munchen, GERMANY 163

SINGLULAR-VALUE-DECOMPOSITION TECHNIQUE FOR MULTIVARIATE MODELING OF HYDROLOGIC TIME SERIES. C. Chaleeraktrakoon, Van-Thanh-Van Nguyen. McGill University, CANADA 167

SIGNIFICANT HARMONICS IN PARAMETERS THAT REPRESENT THE SEASONAL PROCESS. J.V.A. Revfeim. Wellington, NEW ZEALAND 171

PROBABLE INFERENCE OF SIMPLE MODELS FOR UNCERTAIN QUANTITIES. V. Solana, Alberto Solana-Ortega. CSIC, SPAIN 175

(1030-1200) Session 9: Climate Variability

CLIMATE SIGNAL AND WEATHER NOISE. C.E. Leith. Lawrence Livermore National Laboratory, USA 179

ON THE REDDEST ATMOSPHERIC MODES GENERATED BY A COUPLED ATMOSPHERE-OCEAN GENERAL CIRCULATION MODEL. J-S. von Storch. MP Innstitut fur Meteorologie, GERMANY 183

ANALYSIS OF LOW-FREQUENCY CLIMATE VARIATIONS USING HISTORICAL ATMOSPHERIC DATA. J. Hurrell, Harry van Loon. National Center for Atmospheric Research, USA 185

(1330-1530) Session 10: Downscaling III:

Downscaling III: APPLICATIONS TO ECOSYSTEM MODELLING. D. Gyalistras, A. Fischlin. Swiss Federal Institute of Technology, SWITZERLAND 189

THE USE OF WEATHER TYPES FOR GCM DOWNSCALING. D. Conway, P. Jones. University of East Anglia, UK 193

ON RELATIONSHIP BETWEEN THE PRECIPITATION OF THE NORTHWEST MOROCCO AND THE 700 HPA HEIGHT IN WINTER. A. Belaassal, A. Douguedroit. University of Aix-Marseille, FRANCE 197

STATISTICAL GENERATION OF SURFACE AIR TEMPERATURE FOR THE CENTRAL USA USING A GENERAL CIRCULATION MEDEL SIMULATION. D.R. Easterling. NOAA/NESDIS/NCDC, USA 201

DOWNSCALING DAILY TEMPERATURE DATA FROM GCMS: AN EXAMPLE FROM THE MEDITERRANEAN BASIN. J. Palutikof[1], J.A. Winkler[2], J.A. Andresen[2], C.M. Goodess[1]. [1]University of East Anglia, ENGLAND. [2]Michigan State University, USA 203

DOWNSCALING INDIAN MONSOON RAINFALL FROM THE SIMULATIONS OF THE ECHAMT21 COUPLED OCEAN-ATMOSPHERE MODEL. S.V. Singh[1], H.V. Storch[2]. [1]Indian Institute of Tropical Meteorology, INDIA. [2]Max Planck Institute for Meteorology, GERMANY 207

(1330-1530) Session 11: Change and Variations I

A CHANGE IN THE ANNUAL CYCLE ON THE SOUTHERN HEMISPHERE AND ITS POSSIBLE IMPLICATION FOR THE ANTARCTIC OZONE IN SPRING. H. van Loon[1], K. Tourpali[1], J.W. Hurrell[2]. [1]National Center for Atmospheric Research, USA. [2]Aristotle University of Thessaloniki, GREECE 211

THE VARIABILITY OF CIRCULATION PATTERNS AT 500 HPA LEVEL OVER EUROPE. J. Wibig. University of Lodz, POLAND 215

VARIATIONS OF ATMOSPHERIC CIRCULATION AND CLIMATE CHANGE. G. Gruza, E.Ya. Rankova. Institute for Global Climate and Ecology, RUSSIA 219

CLIMATE VARIATIONS OVER THE FORMER USSR IN RECENT DECADES. V.N. Razuvaev, O.N. Buiygina, E.G. Apasova, L.G. Korulina, R.A. Martuganov. World Data Centre, RUSSIA 223

VECTOR OF GEOSTROPHIC WIND IN THE NORTH ATLANTIC REGION AS AN INDEX OF LOCAL ATMOSPHERIC SUB-CIRCULATION. M. Mietus. Institute of Meteorology and Water Management, POLAND 227

VARIATIONS OF THE ATMOSPHERIC CENTERS OF ACTION IN THE NORTHERN HEMISPHERE AND THEIR ASSOCIATIONS WITH THE CLIMATE CHANGE IN CHINA. Q.Y. Zhang, Shao Wu Wang, Wei Chyung Wang. Chinese Acadamy of Sciences, P.R. CHINA 231

TEMPERATURE CHANGES IN ATMOSPHERE: STRONG SIGNAL ON GLOBAL COOLING IN LOWER STRATOSPHERE. R. Reitenbach, Alexander M. Sterin. World Data Centre, RUSSIA 235

EFFECTS OF SOLAR-IRRADIANCE VARIATIONS ON THE HYDROCLIMATOLOGY OF SELECTED REGIONS WITHIN THE UNITED STATES. C.A.. Perry. U.S. Geological Survey, USA 239

(1600-1800) Session 12: Change and Variations II

SELF-SIMILARITIES, LINKS, AND WARMING TRENDS OF GLOBAL CLIMATE DYNAMICS; THEIR DETECTIONS AND PREDICTIONS. D.M. Sonechkin. Hydrometeorological Research Centre of Russia, RUSSIA 243

TREND AND CORRELATION ANALYSIS 1961-1990 OF EUROPEAN SURFACE AND RAWINSONDE DATA. J. Rapp, C.-D. Schonwiese. University of Frankfurt, GERMANY 247

ASYMMETRIC CHANGE IN MAXIMUM AND MINIMUM TEMPERATURES IN BEIJING SINCE 1940. Zhuang Xie[1], Hong-xing Cao[2]. [1]Beijing Meteorological Bureau, P.R. CHINA. [2]Chinese Academy of Meteorological Sciences, P.R. CHINA 253

GREENHOUSE STATISTICS - A TIME SERIES ANALYSIS OF THE RELATIONSHIP BETWEEN THE GLOBAL MEAN TEMPERATURE AND THE ATMOSPHERIC CARBON EIOXIDE. R. Tol, Aart F. de Vos. Vrije Universiteit, THE NETHERLANDS 257

A STATISTICAL ANALYSIS OF EXTERNAL CLIMATE FORCING USING SSA, NONPARAMETRIC CORRELATION AND NEURAL NETWORKS. M. Denhard, C.-D. Schonwiese. J.W. Goethe University, GERMANY 259

FLUCTUATIONS AND TRENDS OF TEMPERATURE EXTREMES IN SOUTHERN PANNONIAN LOWLAND. M. Gajic-Capka, K. Zaninovic. Meteorological and Hydrological Service, CROATIA 263

THE TEMPERATURE CHANGE AT TAIPEI BASIN. H.Y. Tseng. Air Navigation & Weather Services, TAIWAN 267

ESTIMATION OF AGREEMENT AND DISAGREEMENT IN THE INTERANNUAL VARIABILITY OF AIR TEMPERATURE IN HIGH, TEMPERATE AND LOW LATITUDES OF THE NORTHERN HEMISPHERE. G. Alekseev, P.N. Svyashcnennikov, N.W. Harlanenkova. The Arctic and Antarctic Research Institute, RUSSIA 271

(1600-1800) Session 13: Analysis of Extremes

CYCLES AND TRENDS IN TIME SERIES OF CANADIAN RAINFALL EXTREMES. B. Hogg. Climate Research - AES, CANADA 275

PROBABILISTIC DURATIONS OF AGRICULTURAL DROUGHT IN BANGLADESH DURING THE PRE-MONSOON SEASON. R. Ahmed. University of Wisconsin, USA 279

PROBABILITY MODELS AND DESIGN VALUES OF EXTREME RAINFALL OVER CHINA ON VARIOUS TIME SCALES. X. Wang, Joao Corte-Real, Xuebin Zhang. University of Lisbon, PORTUGAL 283

STATISTICAL-DYNAMICAL ANALYSIS OF EXTREME EVENTS IN TUSCANY (ITALY): DROUGHT AND ANNUAL MAXIMUM DAILY RAINFALL. SPATIAL DISTRIBUTION AND FORECASTING. F. Meneguzzo[1], M. Niccolai[2], N. Musetti[2], F. Tampucci[2]. [1]Academia dei Georgofili, ITALY. [2]A.R.S.I.A.- Regione Toscana, ITALY 291

CHANGES IN FLOOD FREQUENCIES IN SOUTH AFRICA. S.J. Mason, G.M. Mimmack. University of Witwatersrand, SOUTH AFRICA 295

THE INFLUENCE OF THE EXTREMAL INDEX ON THE ESTIMATION OF RETURN PERIODS OF HIGH LEVELS. I. Gomes. University of Lisbon, Portugal 299

STORM CONDITIONS OVER THE NORTH SEA: A HISTORICAL PERSPECTIVE AND IMPLICATIONS FOR THE 21ST CENTURY. T. Holt. University of East Anglia, ENGLAND 303

VARIABILITY IN DAILY MINIMUM AND EXTREME TEMPERATURES FOR THE NIAGARA REGION. A.B. Shaw. Brock University, CANADA 307

Wednesday, June 21

(0830-1000) Session 14: Short term forecasting

OPERATIONAL MULTI-SEASON OUTLOOKS OF SEASONAL MEAN TEMPERATURE AND PRECIPITATION. E. O'Lenic. Climate Prediction Center, USA 311

CURRENT DEVELOPMENTS IN STATISTICAL SEASONAL RAINFALL PREDICTION IN AUSTRALIA. W. Drosdowsky. Bureau of Meteorology Research Centre, AUSTRALIA 315

SEASONAL FORECASTING OF TROPICAL RAINFALL. N. Ward[1], C. Mutai[2], I. Mohammed[3], A. Colman[1]. [1]UK Meteorological Office, UK. [2]Drought Monitoring Centre, KENYA. [3]African Centre of Meteorological Applications for Development, NIGER 319

(1030-1230) Session 15: Downscaling III

DOWNCALING OF LARGE-SCALE GCM OUTPUT TO REGIONAL RAINFALL IN AUSTRALIA USING RECURSIVE PARTITIONING. R. Schnur, Dennis P. Lettenmaier. University of Washington, USA 323

STATISTICAL DOWNSCALING OF WINTER MONTHLY MEAN NORTH ATLANTIC SEA-LEVEL PRESSURE TO SEA-LEVEL ANOMALIES IN THE BALTIC SEA. H. Heyen[1], Eduardo Zorita[2], Hans von Storch[1]. [1]MP Institut fur Meteorologie, GERMANY. [2]Universite Pierre et Marie Curie, FRANCE. 327

A SPACE-TIME DOWNSCALING APPROACH IN TERMS OF PATTERNS RECOGNITION AND STOCHASTIC GENERATION. XIA Jun. Wuhan University of Hydraulic and Electric Engineering, CHINA 331

DOWNSCALING TECHNIQUES FOR SNOWFALL PREDICTION IN GLOBAL CHANGE STUDIES. D.L. McGinnis. University of Colorado, USA 335

A TWO-STEP METHOD TO TRANSFORM CLIMATE MODEL OUTPUTS INTO REGIONAL AND LOCAL WEATHER ELEMENTS. W. Enke, A. Spekat. Free University of Berlin, GERMANY 339

A COMPARATIVE ANALYSIS OF PRINCIPAL COMPONENT ANALYSIS AND BISERIAL CORRELATION TECHNIQUE TO SPECIFY PRECIPITATION. N.E. Ruiz, Walter M. Vargas. 343

DOWNSCALING GCM INFORMATION TO REGIONAL SCALE: A NON-PARAMETRIC MULTIVARIATE REGRESSION APPROACH. J. Corte-Real, X. Zhang, X. Wang. University of Lisbon, Portugal 347

(1030-1230) Session 16: Precipitation and its Climatology

INTRA-SEASONAL OSCILLATIONS AND ASSOCIATED SPATIAL-TEMPORAL STRUCTURES OF PRECIPITATION OVER CHINA. X. Wang, Joao Corte-Real, Xuebin Zhang. University of Lisbon, PORTUGAL 351

THE BREAKPOINT REPRESENTATION OF RAINFALL. J. Sansom. National Institute of Water and Atmospheric Research, NEW ZEALAND 355

CHANGES OF PRECIPITATION CHARACTERISTICS IN FINLAND. R. Heino. Finnish Meteorological Institute. FINLAND 359

FRACTAL PROPERTIES OF PRECIPITATION IN SPAIN. J.J. Onate. Universidad Autonoma de Madrid, SPAIN 363

RAINFALL DISTRIBUTION IN THE GISBORNE REGION, NEW ZEALAND, IN DIFFERENT SYNOPTIC SITUATIONS. G. Daw. Meteorological Service of New Zealand, NEW ZEALAND 367

ON THE CONNECTION OF PRECIPITATION SYSTEMS WITH SPATIAL CORRELATION FIELDS IN THE PROVINCE OF ENTRE RIOS. D. Barrera. Universidad de Buenos Aires, ARGENTINA 371

METHODOLOGIC ASPECTS OF EVALUATING THE CORRELATION FIELD OF PRECIPITATION IN MESOSCALE FROM PLUVIOMETRIC DATA. D. Barrera. Universidad de Buenos Aires, ARGENTINA 375

DAILY ALPINE PRECIPITATION AND RELATION TO THE SYNOPTIC SCALE FLOW - A PRINCIPAL COMPONENT AND SINGULAR DECOMPOSITION APPROACH. M. Widmann, D. Bresch, C. Frei, C. Schar. Atmospheric Physics ETH, SWITZERLAND 381

Thursday, June 22

(0830-1000) Session 17: Interpolation and Analysis I

USING EOF ANALYSIS TO CREATE A NEW GISST DATA SET. N. Rayner, M.N. Ward,C.K. Folland, D.E. Parker. 385

RECONSTRUCTION OF GLOBAL SST USING EOF ANALYSIS AND COADS DATA T. Smith, R.W. Reynolds, R.E. Livezey. National Meteorological Center, USA 387

SMOOTHING SPLINE ANOVA AND THE SPATIO-TEMPORAL ANALYSIS OF CLIMATE DATA. G. Wahba. University of Wisconsin, USA 391

APPLICATION OF STATISTICAL OBJECTIVE ANALYSIS TO RAINFALL FIELDS FROM A CONVENTIONAL MESO-NETWORK: COMPARISON WITH THE EMPIRICAL WEIGHING SCHEME. D. Barrera, Adriana B. Basualdo. Universidad de Buenos Aires, ARGENTINA 393

EFFECTS OF NETWORK DESIGN ON ESTIMATION OF PRECIPITATION. H. Kutiel[1], P.A. Kay[2], L. Dickey[2]. [1]University of Haifa, ISRAEL. [2]University of Waterloo, CANADA 397

INTERMITTENT CLOUD STRUCTURE AND RADIATION. R. Cahalan. NASA, USA. 401

(0830-1000) Session 18: Mechanisms I

DETECTION OF STRONG-ENSO FORCED SIGNALS IN THE NORTHERN EXTRATROPICS. R.E. Livezey, M. Masutani, Ming Ji, H. Rui, A. Leetma, A. Kumar. NOAA, USA 403

STATISTICAL-DYNAMICAL ANALYSIS OF MULTIPLE DECADAL LONG ATMOSPHERIC SIMULATIONS USING THE ECHAM3 MODEL UNDER GISST FORCING. U. Roemer[1], A. Hense[1], C.K. Folland[2]. [1]Universtat Bonn, GERMANY. [2]Hadley Center for Climate Prediction and Research, USA 405

EXTERNAL AND INTERNAL SEASONAL VARIABILITY SIMULATED WITH THE LMD AGCM DURING THE NORTHERN HEMISPHERE WINTER. C. Dichampt, S. Parey, J.Y. Caneill. EDF/DER, FRANCE 409

STATISTICAL ANLAYSIS OF RELATIONSHIP BETWEEN TRANSIENT EDDY SENSIBLE AND LATENT HEAT FLUXES IN THE SOUTHERN HEMISHPERE. M. Raphael. University of California, UCLA, USA 411

STUDY OF OCEAN-ATMOSPHERE INTERACTION USING A MARKOV CHAIN MODEL. C. Mares, C. Mares, Mihaela Mihailescu. National Institute of Meteorology and Hydrology, ROMANIA 415

CLOUD COVER AND TYPE OVER THE FORMER USSR, 1936-83; TRENDS DERIVED FROM THE RIHMI-WDC 223-STATION 6- AND 3-HOURLY METEOROLOGICAL DATABASE. D. Kaiser[1], V. N. Razuvaev[2]. [1]Oak Ridge National Laboratory, USA. [2]World Data Centre, RUSSIA 419

(1030-1200) Session 19: Spatial Statistics

SPACE-TIME COVARIANCE MODELLING. W. Meiring, Peter Guttorp and Paul D. Sampson. University of Washington, USA 423

LINEAR MODELS FOR SPATIAL OR TEMPORAL MULTIVARIATE DATA. H. Wackernagel, Michel Grzebyk. Ecole des Mines de Paris, FRANCE 427

SPATIAL-TEMPORAL RAINFALL PROCESSES: STOCHASTIC MODELS AND DATA ANALYSIS. R. Chandler, V. Isham, A. Kakou, P. Northrop. University College London, ENGLAND 431

(1330-1530) Session 20: Homogeneous Time Series

ON THE DEVELOPMENT AND USE OF HOMOGENIZED CLIMATE DATA SETS. D.R. Easterling, T. Karl, T.C. Peterson. NOAA/NESDIS/NCDC, USA 435

HOMOGENEITY TESTING, MUTLIPLE BREAKS AND TRENDS. H. Alexandersson. Swedish Meteorological and Hydrological Institute, SWEDEN 439

ADJUSTMENT OF APPARENT CHANGES IN VARIABILITY OF TEMPERATURE TIME SERIES. H. Tuomenvirta[1], Hans Alexandersson[2]. [1]Finnish Meteorological Institute, FINLAND. [2]Swedish Meteorolgical and Hydrological Institute, SWEDEN 443

CORRECTING MEAN ANNUAL MAXIMA FOR DATA DISCRETIZATION. I.W. Dwyer, D.W. Reed. Institute of Hydrology, UK 447

LONG TIME SERIES OF TEMPERATURE IN NORWAY. P.O. Nordli. Norwegian Meteorolgical Institute, NORWAY 451

ANALYSIS OF ANNUAL RAINFALL SERIES IN IVORY COAST IN ORDER TO DETECT CLIMATIC VARATIONS. H. Lubes[1], J.E. Paturel[2], E. Servat[2], J.M. Masson[3], B. Kouame[2]. [1]ORSTOM, FRANCE. [2]ORSTOM, IVORY COAST. [3]Universite Montpellier, FRANCE 455

TRENDS OF MAXIMUM AND MINIMUM TEMPERATURES IN NORTHERN SOUTH AMERICA (VENEZUELA AND COLOMBIA) DURING THE PERIOD 1918-1990. HOMOGENEITY TEST. R.A. Quintana-Gomez. Universidad Nacional Experimental de Los Llanos "Ezequiel Zamora", VENEZUELA 459

CHANGES IN THE WINTER PRECIPITATION IN ROMANIA INDUCED BY CHANGES IN THE LARGE SCALE CIRCULATION. A. Busuioc. National Institute of Meteorology and Hydrology, ROMANIA 463

(1330-1530) Session 21: Seasonal Climate Forecasts

AN EMPIRICAL ATMOSPHERIC MODEL FOR USE IN FORECASTS OF THE COUPLED ATMOSPHERE/OCEAN SYSTEM. G. Branstator[1], Sue Ellen Haupt[2]. [1]National Center for Atmospheric Research, USA. [2]University of Colorado, USA 467

PREDICTABILITY LIMISTS OF ENSO; THE ROLE OF STOCHASTIC FORCING. C. Eckert, Mojib Latif. Max-Planck-Institute for Meteorology, GERMANY 471

THE POTENTIAL FOR LONG-RANGE PREDICTION OF PRECIPITATION OVER INDIA FOR THE MONSOON SEASON: AN ANALYSIS OF VARIANCE APPROACH. D. Shea[1], N.A. Sontakke[2], Roland Madden[1], Richard W. Katz[1]. [1]National Center for Atmospheric Research, USA. [2]Indian Institute for Tropical Meteorology, INDIA 475

PREDICTING SOUTH AFRICAN SEASON RAINFALL BY MEANS OF CANONICAL CORRELATION ANALYSIS. W.A. Landman. South African Weather Bureau, SOUTH AFRICA 479

GLOBAL SEA SURFACE TEMPERATURE VARIABILITY ASSOCIATED WITH WEST AFRICAN RAINFALL ANOMALY TYPES. APPLICATION TO SEASON FORECAST OF SAHEL AND GUINEA COAST RAINFALL. S. Janicot[1], B. Fontaine[2], V. Moron[3]. [1]CNRS, Palaiseu, FRANCE. [2]CNRS, Universite de Bourgogne, FRANCE. [3]Universite de Bourgogne, FRANCE 483

THE USE OF EQUATORIAL INDICES FOR WINTER CLIMATE PREDICTION IN THE YUKON. E. Taylor. Enviroment Canada, CANADA 487

THE APPLICATION OF SINGULAR VALUE DECOMPOSITION ANALYSIS IN THE PREDICTION OF SEASONAL RAINFALL. X. Jiongguang, Qin Bingbing.

30-DAY MEAN PREDICTION OF A DYNAMIC-STOCHASTIC MODEL. W. Jiang[1], William Gutowski, Jr.[2]. [1]Iowa State University, USA. [2]Chinese Academy of Meteorological Science, P.R. CHINA 493

(1600-1800) Session 22: Change and Variations III

WEAKLY QUADRATIC STRUCTURE OF THE SPECTRUM OF ATMOSPHERIC PRESSURE VARIATIONS ON TIME SCALES OF MONTHS TO SEVERAL YEARS. S. Hameed, R.G. Currie. State University of New York, USA 497

CLIMATOLOGY OF THE CYCLONE IN GLOBAL ATMOSPHERE. V.E. Lagun. The Arctic & Antarctic Res. Ins., RUSSIA 501

VARIATIONS IN ANTICYCLONICITY ACROSS THE EASTERN AUSTRALASIAN REGION FOR THE 29-YEAR PERIOD (1965 - 1993). R. Leighton, H. Nowak. Bureau of Meteorology, AUSTRALIA 503

ON THE EFFECTS OF NONLINEARITY ON THE VARIABILITY OF LONG CLIMATIC RECORDS. J.A. Garcia-Miguel, F. Valero, J.F. Gonzalez, F.J. Doblas. Universidad Complutense, SPAIN 507

CLIMATOLOGICAL VARIABILITY IN REGIONAL AIR POLLUTION. J.D. Shannon[1], Edward C. Trexler, Jr.[2] [1]Argonne National Laboratory, USA. [2]U.S. Department of Energy, USA 511

GLOBAL AND LOCAL CLIMATIC CHANGES IN THE WEST AFRICAN UPWELLING ECOSYSTEMS. C. Roy, M.-H. Durand. 515

MODELLING CURRENT AND FUTURE DISTRIBUTIONS OF NATIVE SPECIES. T.H. Sparks, T.W. Parr, S.M. Wright. NERC Institute of Terrastrial Ecology, UK 517

INTERANNUAL AND INTERDECADAL VARIABILITY IN A FIEXD-SST, PERPETUAL JANUARY GCM RUN. G. Nitsche, J.M. Wallace. University of Washington, USA 521

(1600-1800) Session 23: Methods II

CAVEATS IN THE APPLICATION OF STATISTICAL ANALYSIS IN CLIMATE RESEARCH. H. von Storch. MP Institut fuer Meteorologie, GERMANY 525

MIXTURES OF STOCHASTIC PROCESSES: APPLICATION TO GENERATION OF CLIMATE CHANGE SCENARIOS. R. Katz. National Center for Atmospheric Research, USA 527

A NEW METHODOLOGY FOR INVESTIGATING LONG RANGE PREDICTABILITY. R. Jones, R. Madden, D. J. Shea. National Center for Atmospheric Research, USA 531

MULTIVARIATE TESTS FOR COMPARISON OF TEMPORAL VARIABILITY IN OBSERVED AND SIMULATED CLIMATES. J. Beersma, T.A. Buishand. Royal Netherlands Meteorological Institute, THE NETHERLANDS 535

ENTROPY ESTIMATION OF JOINT DISTRIBUTIONS. N.C. Lind. University of Victoria and University of Waterloo, CANADA 539

THE ASYMPTOTIC BEHAVIOUS OF THE MAXIMUM OF A RANDOM SAMPLE SUBJECT TO TRENDS IN LOCATION AND SCALE. C.S. Withers. The New Zealand Institute for Industrial Research and Development, NEW ZEALAND 543

CLIMATE INSTABILITY DETERMINATION. DISCUSSION OF METHOD AND EXAMPLES. R. Sneyers. Royal Meteorological Institute, BELGIUM 547

A BAYESIAN APPROACH TO MODELLING SPATIAL-TEMPORAL PRECIPITATION DATA. R. Smith[1], P.J. Robinson[2]. [1]University of Cambridge, U.K. [2]University of North Carolina, USA 551

Friday, June 23

(0830-1000) Session 24: Interpolation and Analysis II

OPTIMUM AVERAGING OF INCOMPLETE CLIMATOLOGICAL DATA. B. Kusserow, Andreas Hense. Universtat Bonn, GERMANY 555

FINE-MESH ANALYSES OF THE MONTHLY MEAN TEMPERATURE AND PRECIPITATION FIELDS OVER FINLAND. J. Helminen. Finnish Meteorological Institute, FINLAND 559

OJECTIVE ANALYSIS USING A HIERARCHY OF CLIMATE FEATURES. A.R. Boehm. Hughes STX Corporation, USA 563

SPATIAL INTERPOLATION OF RAINFALL STATISTICS AT DIFFERENT TIME SCALES. L. Guenni. Universidad Simon Bolivar, VENEZUELA 567

CORRECTION OF SOLID PRECIPITATION. H. Madsen. The Danish Meteorological Institute, DENMARK 571

DETERMINATION OF DROUGHT/FLOOD INDEX BY STATISTICS AND ITS APPLICATION TO EASTERN CHINA. J. Shen[1], Dong Xaomin[2]. [1]Iowa State University, USA. [2]Jiangsu Institute of Climate Application, P.R. CHINA 575

(0830-1000) Session 25: Change and Variations IV

ON THE STATISTICAL SIGNIFICANCE OF "OPTIMAL CLIMATE NORMALS". D.S. Wilks. Cornell University, USA 575

DIVERGENT INFLUENCES IN INTRASEASONAL TELECONNECTIONS: AN OBSERVATIONAL STUDY USING ISCCP CLOUD STATE AND ECMWF WIND STATE DATA. S. Mauget. University of California, USA 583

PREFERRED CLIMATE PATTERSN IN THE UNITED STATES ASSOCIATED WITH CATEGORIZED EL NINO / SOUTHERN OSCILLATION (ENSO) EVENTS. W. Presnell. National Weather Service, USA 587

LONG-TERM ANOMALIES AND TRENDS IN THE MID-TROPOSPHERE OF THE NORTHERN HEMISPHERE. I.I. Zveryaev, O.A. Razoryonova. P.P. Shirshov Institute of Oceanology, RUSSIA 591

MONTHLY MEAN PRECIPITATION AND TEMPERATURE OVER THE UNITED STATES - EOF ANALYSIS. R. Cahalan. NASA, USA 595

LONG TERM VARIABILITY OF INTENSITY AND FREQUENCY OF INDIAN MONSOON RAINFALL. A. Kulkarni, S.V. Singh. Institute of Tropical Meteorology, INDIA 597

(1030-1200) Session 26: Chaos

ENSEMBLE PREDICTIONS AND CHAOTIC SYSTEMS. L. Smith. University of Oxford, ENGLAND 599

TESTING (AND I MEAN TESTING) FOR THE PRESENCE OF CHAOS. R. Wolff. University of Glasgow, SCOTLAND 603

(1330-1530) Session 27: Mechanisms II

CLIMATE VARIABILITY UNDER CLEAR SKIES: APPLICATIONS FOR THE CLOUD AND SNOW COVER FEEDBACK PROBLEMS. P. Groisman[1], Pan-Mao Zhai[2]. [1]University of Massachusetts, USA. [2]National Climate Center, P.R. CHINA 605

ON TEMPORAL VARIABILITY OF THE ZONAL AND GLOBAL AVERAGE RADIATION AND CLOUDINESS. O. Karner. IAAP, Toravere, ESTONIA 609

THE RELATIONSHIP BEWTEEN THE DRAG COEFFICIENT AND THE EXTENT OF WHTIECAPPING, AS INFERRED FROM OBSERVATIONS MADE IN THE NORTHEAST PACIFIC OCEAN. E.C. Monahan[1], I.G. Ó Muircheartaigh[2], W. Wang[1], Q. Wang[1]. University of Connecticut, USA. University College, Galway, IRELAND 613

USE OF CLIMATIC DATA IN MATHEMATICAL MODELS APPLIED TO AGRICULTURE IN NORTHERN IRELAND. D.S. Lennox, E.A. Goodall, R.V. Smith. Department of Agriculture, NORTHERN IRELAND 617

SPECTRAL ESTIMATES OF THE SURFACE PRESSURE FLUCTUATIONS ASSOCIATED WITH THE "BORA" WIND RECORDED IN UDINE AND TRIESTE. M. Ceschia, G. Job. University of Udine, ITALY 621

THE ASSESSMENT OF THE WATER REGIME FOR RAINFED AGRICULTURE IN AREAS OF SEASONAL RAINFALL IN VENEZUELA. M. Puche[1], J.L.L. Morison[2]. [1]Universidad Central De Venezuela, VENEZUELA. [2]University of Essex, U.K. 625

(1330-1530) Session 28: Data, models and impacts

GENERAL PROBLEMS OF THE ESTIMATION OF INHOMOGENEITIES, A CONDITIONAL MAXIMUM LIKELIHOOD DECISION. T. Szentimrey. Hungarian Meteorological Service, HUNGARY 629

RESPONSE OF THE INTENSITY OF SUBTROPICAL HIGH IN THE NORTHERN HEMISPHERE TO SOLAR ACTIVITY. X. Qun, Yan Qiuming. Jiangsu Meteorological Institute, CHINA. Jiangsu Meteorological Observatory, CHINA 633

EFFECTS OF THE CONTINTENTAL SHELF ON MONTHLY SPATIAL DIFFERENCES IN AIR AND SEA TEMPERATURES. S.A. Hsu. Louisiana State University, USA 637

CHARACTERISTIC FREQUENCY DISTRIBUTIONS OF REMOTE-SENSED, GROUND-TRUTH, AND MODELED SURFACE WINDS. E. Bauer. Universitat Hamburg, GERMANY 641

ROBUST ESTIMATES OF LOCATION AND SCALE PARAMETERS IN CLIMATOLOGICAL ANALYSIS OF RADIOSONDE DATA. A. Sterin. World Data Center, RUSSIA 645

PATTERNS AND CHANGES IN PRECIPATIATION AND STREAMWATER CHEMISTRY OVER TEN YEARS FROM PLYNLIMON, WALES. T.H. Sparks, B. Reynolds. NERC Institute of Terrastrial Ecology, UK. 649

1530 Official closing of 6IMSC

DETECTING AND ATTRIBUTING AN ANTHROPOGENIC INFLUENCE ON CLIMATE

Benjamin D. Santer[1], Philip D. Jones[2], Karl E. Taylor[1,3], Tom M. L. Wigley[4], Joyce E. Penner[3] and Ulrich Cubasch[5]

1. PCMDI, Lawrence Livermore National Laboratory, USA
2. Climatic Research Unit, University of East Anglia, UK
3. Global Climate Research Division, Lawrence Livermore National Laboratory, USA
4. National Center for Atmospheric Research, Boulder, USA
5. Deutsches Klimarechenzentrum, Hamburg, Germany

ABSTRACT

We use a pattern correlation statistic, R(t), to compare the observed pattern of temperature change with that predicted by the equilibrium model results with carbon dioxide and sulphate aerosols forcing. Our results indicate that in JJA and SON the pattern of changes is showing similarities with the observations. We assess the significance of the trends in R(t), using the century-long control integrations of two coupled ocean atmosphere GCMs. Although results are robust to both model integrations there are doubts whether such models adequately represent the full range of natural variability on the century timescale when compared with paleoclimatic data.

1. INTRODUCTION

Most previous greenhouse gas (GHG) detection studies employing the so-called 'fingerprint' strategy introduced by Madden and Ramanathan (1980) have used some form of pattern correlation statistic to compare the pattern of a model-predicted GHG signal with the time history of observed patterns of near-surface temperature changes (e.g. Barnett, 1986; Barnett and Schlesinger, 1987; Santer et al., 1993). The signal pattern in such studies is usually taken from an equilibrium CO_2-doubling experiment, or towards the end of an experiment with a time-dependent GHG increase at a point where the response pattern is relatively stationary.

The strategy in this method is to search for a long- term, positive trend in the pattern correlation statistic, which would indicate an increasing expression of the GHG signal in the observations. Previous fingerprint studies have employed either uncentered statistics, in which the searched-for signal consists of both a pattern and the global-mean change (e.g. Barnett and Schlesinger, 1987; Hegerl et al., 1995), and/or uncentred statistics, in which the global-mean change is removed and the signal is simply a spatial anomaly pattern (Santer et al., 1993). Hegerl et al., (1995) show that the global mean change is an important component of a GHG signal. A large body of earlier work has also shown that observed changes in global-mean annually-averaged near-surface air temperature are significant relative to various statistical and model-based estimates of natural variability noise (e.g. Wigley and Raper, 1990, 1991, 1992; Stouffer et al., 1994).

The studies cited above suggest that we might attach high confidence to the statement that the observed changes in global-mean temperature over the past century are significant relative to current 'best estimates' of the magnitude of natural variability noise. However, the same investigations do not allow one to attach high confidence to the statement that the observed changes are solely attributable to anthropogenic influences. Model experiments recently performed by Taylor and Penner (1994; henceforth TP), however, may help to clarify whether the detection and attribution of an anthropogenic effect on climate can be facilitated by incorporating the climatic effects of anthropogenic sulphate aerosols. Sulphate aerosols arise from the SO_2 emitted by fossil fuel combustion, industrial activities, and biomass burning. Such aerosols are likely to have caused some degree of regional-scale cooling (Wigley, 1989), both directly through clear-sky radiative forcing (reflection of incident solar radiation) and indirectly due to changes in cloud brightness (Taylor and Penner, 1994; Charlson and Wigley, 1994).

The TP integrations used an atmospheric general circulation model (AGCM) coupled to a tropospheric chemistry model to investigate the climate response to forcing by anthropogenic sulphate aerosols and CO_2. Four integrations were performed: a control run with no anthropogenic sulphate aerosols and nominal pre-industrial CO_2 concentrations, a 'sulphate only' experiment with present-day sulphur emissions, a 'CO_2-only' experiment with near-current atmospheric CO_2 concentrations, and a 'combined forcing' experiment with present-day sulphur emissions and CO_2 levels. The experiments indicated that the sulphate-induced cooling pattern was very different from the inverse of the pattern of greenhouse warming. More importantly, the response pattern in the combined forcing experiment was generally dissimilar to the response patterns in the sulphate-only and CO_2-only experiments. These results strongly indicate that the combination of sulphate and CO2 forcing yields a signal pattern substantially different from the greenhouse warming pattern typically produced by AGCMs coupled to mixed-layer oceans (Schlesinger and Mitchell, 1987) or fully-coupled A/OGCMs (Meehl et al., 1993).

2. PATTERN SIMILARITY STATISTIC

Details of the statistics are given in Santer et al. (1995a). We summarise the statistics used here. We first compute seasonal and annual mean temperature

changes in the TP control run and response experiments. In each of the three TP response experiments (S, C, and SC), the temperature change signal is defined as

$$\Delta M(x) = \overline{M_{EXP}}(x) - \overline{M_{CTL}}(x) \qquad (1)$$

where M denotes model data, with the subscripts EXP and CTL identifying output from one of the TP response experiments and control integration, respectively. The index x is a discrete variable running over space (grid points), with $x = 1,...,n$. The overbars in $M_{EXP}(x)$ and $M_{CTL}(x)$ indicate time averages, here computed using 20-year samples of experiment and control data.

The observed data, $D(x,t)$, consist of monthly-mean, land-based surface air temperature and sea-surface temperatures from the combined land-ocean data set described by Jones et al. (1991), (see also Jones and Briffa, 1992, and Parker et al., 1994), spanning the interval 1854-1993. The data are in the form of anomalies relative to the mean over 1950-79. Observed data were processed in the following way. We first define a temporally-smoothed reference state $\overline{D_1}(x)$ centred on the year t_0 as

$$\overline{D_1}(x) = \sum_{v=-q}^{+q} D(x, t_o + v) W(v) \qquad (2)$$

where $W(v)$ are the normalised symmetric weights for a p-term Gaussian filter centred at t_0 (with $p = 2q + 1$; we use $p = 13$ in the study here producing an approximate decadal filter. We then define anomalies relative to $\overline{D_1}(x)$ by

$$\Delta D(x,t) = \overline{D_2}(x,t) - \overline{D_1}(x) \qquad (3)$$

The index t denotes the centre year of an interval of length p over which the observed data are filtered. Thus

$$\overline{D_2}(x,t) = \sum_{v=-q}^{+q} D(x, t+v) W(v) \qquad (4)$$

where $q = (p-1)/2$. We use $t = 1910, 1911,...,1993$, so that the filtered anomalies cover the 84-year period 1910-1993, while the data used in the filtering extend from 1904-1999. Filter weights are set to zero if data are missing. Since data are not available for 1994-1999, we assigned a missing value code for all post-1993 data. We then stipulated that a filtered mean can only be computed if a critical fraction of the sum of the Gaussian filter weights (W_{crit}) is exceeded at any grid-point over any p-year period. Here $W_{crit} = 0.6$, which allows us to calculate filtered means for 1993.

For a given response experiment and a given season, we now have a single pattern characterising the model temperature signal, $\Delta M(x)$, and a series of time-evolving patterns characterising observed temperature changes, $\Delta D(x,t)$.

Two different types of measure have been used previously to compare the spatial fields $\Delta M(x)$ and $\Delta D(x,t)$: centred statistics (with the spatial means removed), such as $R(t)$, and uncentred statistics, such as $C(t)$. These are defined by

$$R(t) = \left[\sum_{x=1}^{n} \left(\Delta D(x,t) - \widehat{\Delta D(t)} \right) \left(\Delta M(x) - \widehat{\Delta M} \right) \right] / \left[n s_D(t) s_M \right] \qquad (5)$$

where

$$s_D^2(t) = \sum_{x=1}^{n} \left[\Delta D(x,t) - \widehat{\Delta D(t)} \right]^2 / (n-1) \qquad (6)$$

is the spatial variance (with s^2_M defined similarly), and the ^ in (5) and (6) indicates a spatial average, and

$$C(t) = \left[\sum_{x=1}^{n} \Delta D(x,t) \Delta M(x) \right] / \left[\sum_{x=1}^{n} \Delta M(x)^2 \right] \qquad (7)$$

$R(t)$ is simply a spatial anomaly correlation with the statistic centred about the spatial means of the observed and simulated fields. $C(t)$ is the statistic originally defined and used by Barnett and Schlesinger (1987). Further discussion of $R(t)$ and $C(t)$ is given in Santer et al., (1995a).

3. PATTERN SIMILARITY RESULTS

The $R(t)$ time series of the combined forcing experiment shows large positive trends sustained over the last 40-60 years of the observed record. The result is most pronounced in JJA and SON but is still present in the annual as well. These results suggest that the inclusion of forcing by both CO_2 and anthropogenic sulphate aerosols enables one to obtain a better fit between observed variations in near-surface temperature and a model-predicted temperature response pattern.

4. SIGNIFICANCE OF THE $R(t)$ TRENDS

In the previous section we showed that for certain seasons, the $R(t)$ time series for surface temperature signals from the TP experiment with combined CO_2 and sulphate aerosol forcing show large, positive linear trends over the last 40-60 years. Such trends are qualitatively consistent with the hypothesis that sulphate aerosol-induced cooling could have obscured an enhanced greenhouse effect warming signal. But are these trends statistically significant? This is a difficult question to answer. In order to make meaningful statements about trend significance, we need information about the characteristics of 'unforced' $R(t)$

trends due solely to the effects of internally-generated natural variability on decadal-to-century timescales.

The observational data are probably contaminated by anthropogenic influences. In this study, we employ model-generated noise data. In the model world, we can examine output from experiments with no external forcing in order to estimate the magnitude and spatial properties of natural variability noise. Near surface temperatures data were taken from a 600-year control integration with the Hamburg A/OGCM, and a 1,000-year integration of the GFDL coupled model. These experiments are referred to below as HAMCTL and GFDLCTL, respectively.

In order to determine the significance of the $R(t)$ trends, we need first to establish the sampling distributions of trends in these statistics in the absence of external forcing. The method we use is similar to that employed by Santer et al., (1995b). We treat HAMCTL and GFDLCTL in the same way that we treated the observed near-surface temperature data, and first define anomalies relative to some reference state of the control run

$$\Delta N(x,t) = \overline{N_2}(x,t) - \overline{N_1}(x) \qquad (8)$$

where N denotes noise data from either HAMCTL or GFDLCTL and the reference state $N_1(x)$ is the time-average over the entire control run. As in equation (4), data in $N_2(x,t)$ were smoothed with a 13-term Gaussian filter, and the index t denotes the centre year of an interval of length p (= 13). The HAMCTL and GFDLCTL anomalies were then interpolated to the observed data grid, and model data points outside of the observed region were excluded from the analysis. We then substituted $\Delta N(x,t)$, ΔN, etc. for the corresponding observed terms in equations (5-7), and computed pattern correlation time series in the absence of external forcing.

Using these distributions, $R(t)$ trends for the SC signal are significant for trend lengths of 50 years in JJA and SON. This result does not depend on the model used to define natural variability noise, at least not for the two control runs examined here. It indicates that, in these seasons, there is an evolving expression of the SC signal pattern in the observed data, independent of any trend in global-mean temperature.

5. CONCLUSIONS

Our results indicate that in summer (JJA) and autumn (SON), the pattern of near-surface temperature change in response to combined sulphate aerosol and CO_2 forcing shows increasing similarity with observed changes over the last 50 years. The results from the individual CO_2-only and sulphate-only experiments suggest that at least some of this increasing spatial congruence is attributable to areas where the real world has cooled.

In the absence of reliable information on the magnitude and spatial characteristics of long timescale natural variability in the real world, we use data from multi-centennial control integrations performed with two different coupled atmosphere-ocean models to estimate the sampling distributions of trends in $R(t)$ on timescales of 10-50 years. For the combined CO_2/sulphate aerosol experiment, the 50-year $R(t)$ trends for the JJA and SON signals are significant relative to the trends obtained in the absence of external forcing. Results are robust in that they do not depend on the choice of control run used to estimate natural variability noise properties. The $R(t)$ trends for the CO_2-only signal are not significant in any season.

The caveats regarding the signals and natural variability noise which form the basis of this study are numerous. Most important is that GCMs of this kind at present probably underestimate natural variability by a factor of at least two when compared to syntheses of long paleoclimatic time series (Bradley and Jones, 1993; Barnett et al., 1995). Nevertheless, we have provided first evidence that both the large scale (global-mean) and smaller scale (spatial anomalies about the global mean) components of a combined CO_2/anthropogenic sulphate aerosol signal are identifiable in the observed near-surface air temperature data. If the coupled model noise estimates used here are realistic, we can be highly confident that the anthropogenic signal we have identified is distinctly different from natural variability noise. The fact that we have been able to detect the detailed spatial signature in response to combined CO_2 and sulphate aerosol forcing, but not in response to CO_2 forcing alone, suggests that some of the regional scale background noise (against which we are trying to detect a CO_2-only signal) is in fact part of the signal of a sulphate aerosol effect on climate. The large effect of sulphate aerosols found in this study demonstrates the importance of their inclusion in experiments designed to simulate past and future climate change.

REFERENCES

Barnett TP, 1986: Detection of changes in global tropospheric temperature field induced by greenhouse gases. *J Geophys Res* **91**, 6659-6667

Barnett TP, and Schlesinger ME, 1987: Detecting changes in global climate induced by greenhouse gases. *J Geophys Res* **92**, 14772-14780

Barnett TP, Santer BD, Jones PD, Bradley RS and Briffa KR, 1995: Estimates of low frequency natural variability in near-surface air temperature. *Science* (submitted)

Bradley RS and Jones PD, 1993: 'Little Ice Age' summer temperature variations: their nature and relevance to recent global warming trends. The *Holocene* **3**, 367-376

Charlson RJ and Wigley TML, 1994: Sulfate aerosol and climate change. *Sci Amer* **270**, 48-57.

Hegerl GC, von Storch H, Hasselmann K, Santer BD, Cubasch U, Jones PD, 1995: Detecting Anthropogenic climate change with an optimal fingerprint method. *J Climate* (in press)

Jones PD and Briffa KR, 1992: Global surface air temperature variations during the twentieth century: part 1, spatial, temporal and seasonal details. *The Holocene* **2**, 165-179

Jones PD, Wigley TML and Farmer G, 1991: Changes in hemispheric and regional temperatures 1851 to 1988 over land and marine areas. In Schlesinger ME (ed.) *Greenhouse gas induced climate change: a critical appraisal of simulations and observations.* Elsevier, Amsterdam, 153-172.

Madden RA and Ramanathan V, 1980: Detecting climate change due to increasing carbon dioxide. *Science* **209**, 763-768

Parker DE, Jones PD, Folland CK and Bevan A, 1994: Interdecadal changes of surface temperature since the late nineteenth century. *J Geophys. Res* **99**, 14373-14399

Santer BD, Wigley TML and Jones PD, 1993: Correlation methods in fingerprint detection studies. *Clim Dyn* **8**, 265-276

Santer BD, Taylor KE, Wigley TML, Penner JE, Jones PD and Cubasch U, 1995a: Towards the detection and attribution of an anthropogenic effect on climate. *Climate Dynamics* (in press)

Santer BD, Mikolajewicz U, Brüggemann W, Cubasch U Hasselmann K, Höck H, Maier-Reimer E and Wigley TML, 1995b: Estimates of detection period and detection time for ocean greenhouse warming signals. *J Geophys Res* (in press)

Schlesinger ME, Mitchell JFB, 1987: Climate model simulations of the equilibrium climatic response to increased carbon dioxide. *Rev of Geophys* **25**, 760-798

Stouffer RJ, Manabe S and Vinnikov K Ya, 1994: Model assessment of the role of natural variability in recent global warming. *Nature* **367**, 634-636

Taylor KE and Penner JE, 1994: Response of the climate system to atmospheric aerosols and greenhouse gases. *Nature* **369**, 734-737

Wigley TML, 1989: Possible climate change due to SO_2-derived cloud condensation nuclei. *Nature* **339**, 365-367

Wigley TML and Raper SCB, 1990: Natural variability of the climate system and detection of the greenhouse effect. *Nature* **344**, 324-327

Wigley TML and Raper SCB, 1991: Internally-generated natural variability of global mean temperatures. In Schlesinger ME (ed.). *Greenhouse gas induced climatic change: a critical appraisal of simulations and observations.* Elsevier, Amsterdam, 471-482

Wigley, TML and Raper, SCB, 1992: Implications of revised IPCC emissions scenarios. *Nature* **357**, 293-300.

ACKNOWLEDGEMENTS

Work at Lawrence Livermore National Laboratory was performed under the auspices of the U.S. Dept. of Energy, Environmental Sciences Division, under contract W-7405-ENG-48. Support for JEP was provided by the CHAMMP program; TMLW and PDJ were supported by the U.S. Dept. of Energy, Environmental Sciences Division, under grant no. DE-FG02-86ER60397. The EPRI MECCA Program supplied the computer time necessary to extend the TP integrations. The authors are grateful to Eduardo Zorita and Jin-Song Xu for supplying results from the 600-year HAMCTL integration. Ron Stouffer and Tom Delworth kindly supplied data from the 1,000-year GFDLCTL integretaion.

CORRESPONDING AUTHOR

P.D. Jones
Climatic Research Unit,
University of East Anglia,
Norwich,
NR4 7TJ, UK.

Tel.: +1603 592090
Fax: + 1603 507784
e-mail: p.jones@uea.ac.uk

Climate Change Detection, Observational and Statistical Challenges

Chester F. Ropelewski

Climate Analyis Center/NMC
National Weather Service/NOAA
Washington, DC, 20233 USA

The detection of climate change and, more importantly, the attribution of any perceived climate change to a specific cause severely tests the limits of the observational system as well as our abilities to assess the significance any perceived changes.

The importance of routine weather observations for climate has been recognized through the establishment of the Global Climate Observing System (GCOS) project and, within the WMO, the Climate Change Detection Project. Among the challenges for climate change detection are development of methods to harness current weather observations for climate change studies. Another challenge is development of new statistical methods to relate the current measurements to past observations. In particular, the longest climate observations are station measurements, while the newest tools for climate observations include global gridded analyses from satellites and from numerical-model-based data assimilation systems.

Given that it is unlikely that significant new sources of past station observations will be uncovered, the development of techniques to use relatively short term (20-40 years) of gridded global data in conjunction with the longer station data (100-150 years) sets becomes of paramount importance. These issues are discussed and examples presented.

STRUCTURAL TIME SERIES MODELS AND THE KALMAN FILTER: APPLICATIONS IN CLIMATOLOGY

Hans Visser

KEMA, Arnhem, The Netherlands

ABSTRACT

The detection of trends and coherence within climatological data has become an important topic in the discussion on climate change due to the enhanced greenhouse effect. Therefore, powerful mathematical tools are needed. A structural time series model is proposed with which a stochastic trend, a deterministic trend and regression coefficients can be estimated simultaneously. The stochastic trend component is described using the class of ARIMA models. The regression coefficients corresponding with the explanatory variables may in principle be time-dependent, although they can also be forced to be constant. The mathematical technique used to estimate this trend-regression model is the Kalman filter. Examples of trend-regression estimation are given using two temperatures series: the De Bilt series, a station in the Netherlands (1706-1990), and the Central England temperature data set (1772-1992).

1 INTRODUCTION

The detection of trends in climatological data has become crucial in the discussion on climate change due to the enhanced greenhouse effect. The detection problem was described in detail by Wigley and Barnett (1990) in the IPCC report. They state that, in order to prove the existence of global warming due to greenhouse gases, we should be able, first, to determine the natural variability of the climatic variables, and, secondly, to link the observed spatial variations in the climate system to the predictions of general circulation models (GCMs) for various emission scenarios. If global warming reaches a sufficiently high level, we shall eventually be able to claim detection, simply because there will be no other possible explanation (the argument of "unprecedented change").

Recently much attention has been paid to the detection of trends in climatic series. Especially the issue whether the undeniably increasing trends in annual mean temperatures can be described by a deterministic trend model, possibly in combination with a stochastic model, receives much attention (Galbraith and Green 1992; Bloomfield and Nychka 1992; Bloomfield 1992; Woodward and Gray 1993; Richards 1993). In addition to these trend analyses, the relations between climatic series and exogenous forcing factors such as greenhouse gases are studied using linear multiple regression models (Schönwiese 1991, 1992; Richards 1993, and the references therein). In view of the increasing amount of research in this field the purpose of this paper is to provide a general model that deals with trend estimation and regression simultaneously. This approach may result in avoiding certain pitfalls. Quantities of e.g. volcanic dust can considerably muddle the trend estimation in global temperatures. Because large eruptions cool the climate, although only for a couple of years, possible greenhouse warming can be underestimated if trends and regression are performed separately.

Regression models with time-varying parameters, with or without a trend component, may be viewed as submodels from the class of *structural time series models*. The theory thereof was developed in the 1980s in the field of econometrics (e.g. Pagan 1980 and Chow 1984). An extensive treatment can be found in the work of Andrew C. Harvey (1989).

A structural model partitionates the series of interest as a sum of unobserved components. These may be a trend, a regression model, a cyclic component and a random error term. By writing structural time series models into the so-called state-space form, one may apply the Kalman filter. This filter was designed by R.E. Kalman in the 1960s in the field of control theory and it has been applied in many fields of research since then. The filter is attractive because it yields the minimum mean square estimator of the state vector as well as the possibility to estimate unknown noise variances by optimization of the likelihood function.

The mathematical treatment of the Kalman filter is straightforward but rather complicated, and therefore not easily accessible to practitioners. This characteristic of the filter may explain the lack of applications of regression models with time-varying parameters. A few examples are given in the field of economics, e.g. Newbold and Bos (1985), Harvey and Durbin (1986) and Dagum, Quenneville and Sutradhar (1992). A recent example in air pollution research is Ruijgrok and Römer (1993) and in tree-ring analysis LeBlanc (1993) and Visser and Molenaar (1992). A complete description of the Kalman filter, tailored to the applications used here is given by Visser (1995). A textbook on the Kalman filter is Brown and Hwang (1992).

2 MATHEMATICAL FORMULATION

A model is introduced from the class of structural time series models. It allows for the simultaneous estimation of a stochastic trend, a deterministic trend, and the regression coefficients of exogenous forcing factors :

$$y_t = \mu_t + \delta_{1,t}\, x_{1,t} + \ldots + \delta_{k,t}\, x_{k,t} + \xi_t\,, \quad t=1,\ldots,N \qquad (1)$$

Here, y_t represents the variable to be explained, e.g. annual mean temperature. The stochastic trend is described by an ARIMA(p,d,q) model and described in Section 2b. The factor ξ_t represents a zero-mean white noise process. The variables $x_{i,t}$ may be used in two ways. First, they may represent explanatory variables such as CO_2 concentrations, volcanic dust and lagged versions thereof. Temperature predictions from GCMs may also act as such. Secondly, the $x_{i,t}$ may stand for a deterministic trend function, i.e. a function of time t. The notations for the deterministic trend and the regression variables are kept the same in the model in order to emphasize that these components are treated completely similarly. The $\delta_{1,t},\ldots,\delta_{k,t}$ are regression coefficients. They can be kept constant, but in general they may vary over time. The trend-regression model (1) is denoted by TR(p,d,q,k), where p,d and q refer to the specific ARIMA model for μ_t

and k refers to the number of explanatory variables.

ARIMA models are widely applied in time-series analysis (Box and Jenkins, 1976; Kendall and Ord, 1990). The ARIMA(p,d,q) model requires the trend μ_t to satisfy the equation

$$(1 - \phi_1 B - .. - \phi_p B^p)\nabla^d \mu_t = (1 - \theta_1 B - .. - \theta_q B^q)\epsilon_t \quad (2)$$

where B is the backshift operator, i.e. $B\mu_t = \mu_{t-1}$, ∇ is the backward difference operator, i.e. $\nabla = 1 - B$, and ϵ_t is a white noise process with constant variance σ_ϵ^2.

In the simplest case, i.e. p=d=q=0, μ_t is a white noise process. More complex correlation structures between trend values at successive times are found when p and/or q > 0. The integration part ∇^d allows the trend to be non-stationary.

As for the stochastic behaviour of the regression coefficients, we use the random walk scheme:

$$\delta_{i,t} = \delta_{i,t-1} + \epsilon_{i,t} \quad , i=1,...,m, \quad t=1,...,N \quad (3)$$

with $\varepsilon_{i,t}$ representing a random noise process with constant variance $\sigma_{\varepsilon,i}^2$. The flexibilities of the μ_t and $\delta_{i,t}$ series, generated by models (2) and (3), respectively, are determined by the variances of the noise processes σ_ϵ^2 and $\sigma_{\varepsilon,i}^2$, i=1,...,k. These variances may be chosen by hand or estimated by maximum likelihood optimization (Visser, 1995).

Examples will be given of the TR(0,1,0,1) model:

$$y_t = \delta_{0,t} + \delta_{1,t} x_{1,t} + \xi_t, \; t=1,....,N \quad (4)$$

Here, a random walk model for the trend is combined with a single regression term in which the weighting factor δ may vary over time. It should be noted that model (4) is reduced to the well-known single regression model

$$y_t = \delta_0 + \delta_1 x_{1,t} + \xi_t, \; t=1,....,N \quad (5)$$

if the noise processes σ_ϵ^2 and $\sigma_{\varepsilon,1}^2$ are set to zero. Also, the estimates for both δs are equal, because the Kalman filter is based on least squares optimization.

A more elaborate description of structural time series in the context of climatological data sets can be found in Visser and Molenaar (1995).

3 EXAMPLES

Two examples are given using model (4). The model is applied to temperature series at De Bilt (monthly and annual data over 1706-1994) and the Central England temperature (CET) series (monthly data over 1723-1992).

The remarkably long temperature record at De Bilt is a compilation of 6 stations (Labrijn 1945). From 1706 to 1734 stations at Delft and Rijnsburg were used. The records of Zwanenburg, 1735-1800 and 1811-1848, completed with data from Haarlem for 1801-1810, were corrected for De Bilt. For the period 1849-1897 data from Utrecht - at that period the main observatory of the Royal Netherlands Meteorological Institute (KNMI) - were used and finally, from 1898 on, when this station moved to De Bilt, the period 1898-1992 is covered. A thorough analysis of homogeneity is given by Engelen and Geurts (1985). The De Bilt series has been used in a number of publications, e.g. Vannitsem and Nicolis (1991). A detailed description of the CET series (daily data) is given by Parker, Legg and Folland (1992).

Schuurmans (1980) compared the De Bilt series with the CET series to test for homogeneity. He found a good correspondence (correlation) between the two series. A disadvantage of correlations is, however, that it gives a statistic which is constant for the whole sampling period. Model (4) can be used to test the hypothesis of constant coherence (correlation) over time. As an example, model (4) is applied to winter temperatures of De Bilt (DJF) over the period 1723-1992 (y_t). Explanatory variable (x_t) is the winter temperature of Central England. It should be noted that the period 1706-1722 may not be used here because the CET series was adjusted using the De Bilt series for that specific period.

To estimate model (4), maximum likelihood has been used to find the unknown variances. For the seek of simplicity, the CET series was standardized to unit variance and zero mean. It appears that both variances equal zero and model (4) is reduced to model (5). This means that the correspondence between both temperature series is indeed stable over time, leading to the model

$$T_{DeBilt} = 2.05\ (\pm 0.18) + 1.64\ (\pm 0.28) * T_{CentralEngland} \quad (6)$$

In brackets the 95% confidence limits are given. The variance of $T_{De\ Bilt}$ is reduced from 3.23 °C² to 0.66 °C² by adding the regressor. This is a variance reduction of 80%. It can be shown that the quotient of both variances equals R^2, thus $R^2 = 0.80$. The results are shown in Figure 1.

The residuals or innovations should be tested for independence, homogeneity of variance and normality. All these requirements are fulfilled here.

A second example deals with persistence in monthly mean air temperatures. Persistence can be seen as a lazy man's forecast for the next month, using the correlation between sucessive months. Dool and Nap (1981) calculated for the De Bilt series the correlation between 12-month-successions. Highest correlations are found for February-March and August-September, with R= 0.40. Lowest correlations are found for April-May and October-November, with R≈ 0.0. They conclude that besides a background persistence caused by the large-scale atmospheric circulation, there is a strong persistence directly controlled by the North Sea, which has a large gradient in the coastal area. The variations of persistence throughout the year can be qualitatively explained by considering (1) the persistence of the sea surface temperature anomaly, (2) the stability of the atmospheric boundary layer over sea and (3) the stability of the atmospheric boundary layer over land.

It is interesting to verify if the correlation between successive months is stable over time. In other words, is persistence time-invariant? Again, model (4) is applied. As an example the months March (x_t) and April (y_t) have been chosen, while x_t has been standardized to unit variance and zero mean. It appears that the trend is constant ($\sigma_\epsilon^2 = 0.0$) and that the regression coefficient δ_1 varies over time ($\sigma_{\varepsilon,1}^2 = 0.00018$).

The estimates are shown in Figure 2. Figure 2A shows the monthly temperatures of April (1706-1994), the trend (8.14 °C) and the full regression model. Figure 2B shows $\delta_{1,t}$ with 95% confidence intervals. Interesting is that the value steadily decreases from 0.5 during the period 1706-1750 to 0.2 in 1995. If these values are divided by the standard deviation of April temperatures (1.44 °C), the regression coefficient may be interpreted as a time-varying correlation coefficient ρ_t. In this particular example R_t steadily decreases from 0.35 during 1706-1750 to 0.14 in 1994. The constant value given by Dool and Nap is 0.20 (estimated for the period 1949-1975).

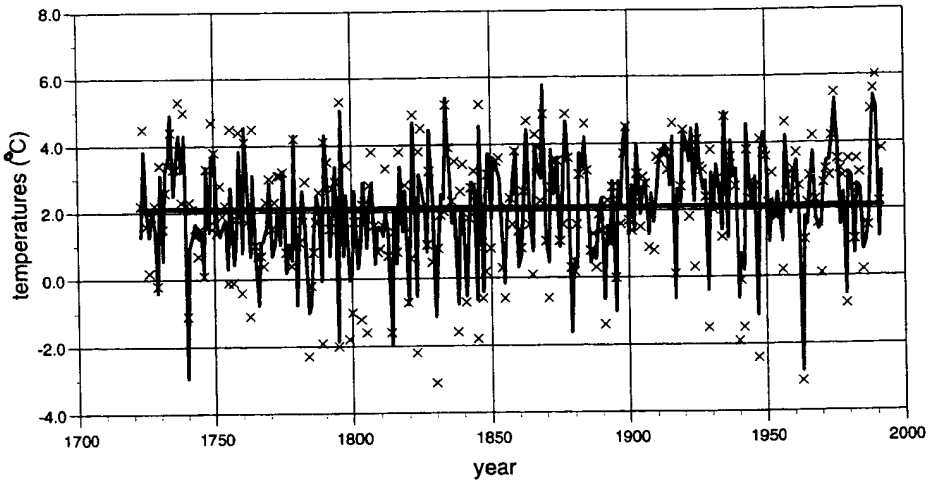


Figure 1 Winter temperatures De Bilt over the period 1723-1992 (x), the trend and the trend plus influence of Central England winter temperatures (solid lines). The estimates are from the structural time series model (4), which is reduced to the single regression model (5).

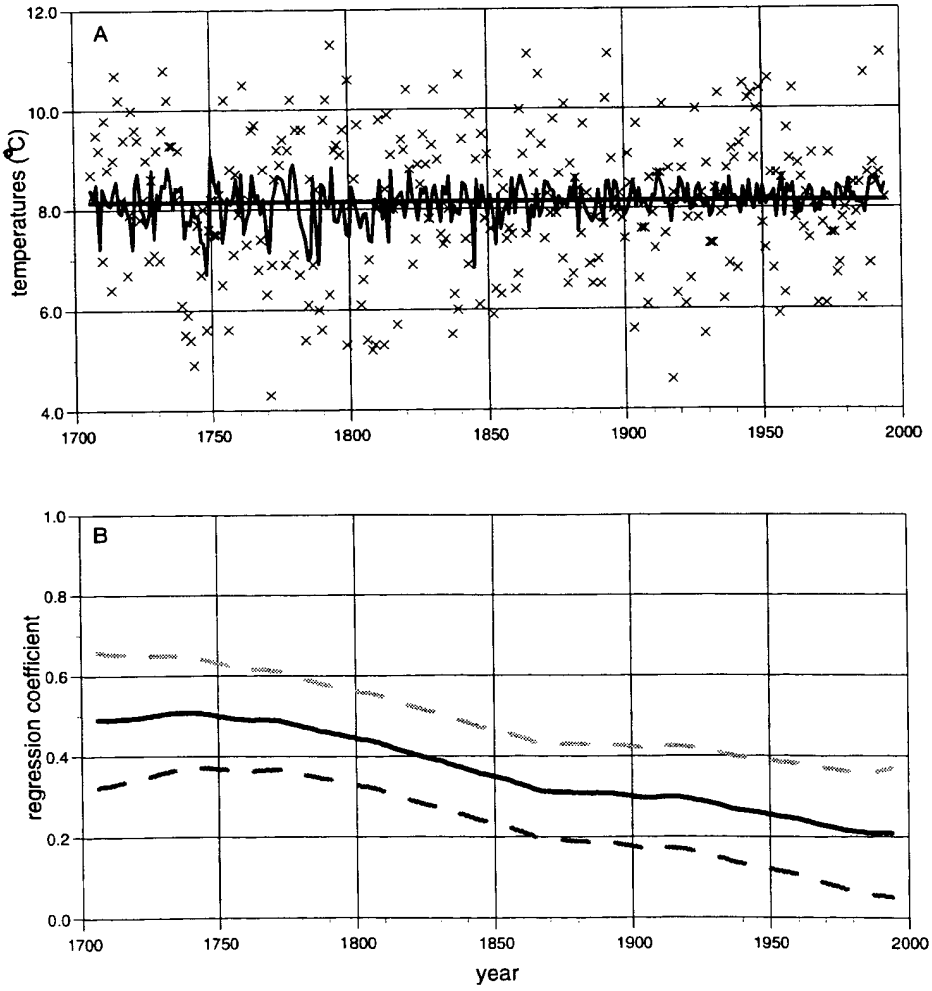


Figure 2 April temperatures of De Bilt over the period 1706-1994 (x), the trend and the trend plus influence of March temperatures (solid lines) (A). The estimates are from the structural model (4). The time-varying regression coeffient is shown in (B).

4 EVALUATION

The examples above and those given by Visser (1994) and Visser and Molenaar (1995) illustrate that structural time series models, in combination with the Kalman filter, yield a useful set of models for data analysis. If this class of models is compared with a well-known time series technique such as ARIMA transfer function modelling, a number of advantages arise: (1) trends, cyclic components and the influence of exogeneous variables can be given separately, (2) there is no limit to the number of exogenous variables, (3) regression variables may show time-varying behaviour and (4) missing values are handled easily. In fact, ARIMA models may be viewed as *submodels* from the class of structural time series models. This is also true for many other time series models, i.e the linear regression model with a polynomial trend part. Therefore, it may be concluded that structural time series models will become a powerful tool in the near future.

REFERENCES

Chow, C.C., 1984, "Random and changing coefficient models"' *Handbook of Econometrics*, Vol II, eds. Z. Griliches and M.D. Intriligator, Elsevier, pp. 1214-1245.

Dagum, E.B., Quenneville, B. and Sutradhar B., 1992, "Trading-day variations multiple regression models with random parameters", *Int. Stat. Rev.*, 60(1), pp. 57-73.

Bloomfield, P, 1992, "Trends in global temperature", *Climatic Change*, 21, pp. 1-16.

Bloomfield, P., and Nychka, D., 1992, "Climate spectra and detecting climate change", *Climatic Change*, 21, pp. 275-287.

Box, G.E.P. and Jenkins, G.M., 1976, "Time series analysis: forecasting and control", *Holden-Day*.

Brown, R. and Hwang, P.Y.C., 1992. Introduction to random signals and applied Kalman filtering. Wiley & Sons.

Dool, H.M. van den, and Nap, J.L., 1981, "An explanation of persistence in monthly mean temperatures in the Netherlands", Tellus, 33, pp. 123-131.

Engelen, A.F.V. v. and H.A.M. Geurts, 1985. Nicolaus Cruquius (1678-1754) and his meteorological observations. *KNMI Publication* 165-IV.

Galbraith, J.W., and Green, C., 1992. "Inference about trends in global temperature data", *Climatic Change*, 22, pp. 209-221.

Harvey, A.C., 1989, "Forecasting, structural time series models and the Kalman filter", *Cambridge University Press.*

Kendall, Sir M. and Ord, J.K., 1990, "Time series", *Edward Arnold, Mill Road.*

Labrijn, A., 1945, "The climate of the Netherlands during the past two and a half centuries", *KNMI Mededelingen en Verhandelingen*, No. 49.

LeBlanc, D.C., 1993, "Temporal and spatial variation of oak growth-climate relationships along a pollution gradient in the midwestern United States", *Can. J. For. Res.*, 23, pp. 772-782.

Newbold, P. and Bos, T., 1985, "Stochastic parameter regression models", *Sage Publications, Inc.*

Pagan, A., 1980, "Some identification and estimation results for regression models with stochastically varying coefficients", *J. of Econometrics*, 13, pp. 341-363.

Parker, D.E., Legg, T.P., and Folland, C.K., 1992, "A new daily Central England temperature series, 1772-1991", *Int. J. of Clim.*, 12, pp. 317-342

Richards, G.R., 1993, "Change in global temperature: a statistical analysis", *J. of Climate*, 6, pp. 546-559.

Ruijgrok, W. and Römer, F.G., 1993, "Aspects of wet, acidifying deposition in Arnhem: source regions, correlations and trends", *Atm. Environm.*, 27A (5), pp. 637-653.

Schönwiese, C.D., 1991, "Multivariate statistical assessments of greenhouse-gas-induced-climatic change and comparison with results from general circulation models", *Greenhouse-gas-induced climatic change : a critical appraisal of simulations and observations*, M.E. Schlesinger, Ed., Elsevier Sci. Publ., pp. 483-503.

Schönwiese, C.D., 1992, "Observational signs of greenhouse-gas-induced climate change, with special reference to northern latitudes", *J. Atm. Terr. Physics*, 54, pp. 1101-1106.

Schuurmans, C.J.E., 1980, "Central England and De Bilt series. Climatic variations and variability. *Climatic variations and variability*, J. Berger, Ed., Reidel Dordrecht, pp. 271-285.

Vannitsem, S. and Nicolis, C., 1991, "Detecting climatic transitions: statistical and dynamical aspects", *Beitr. Phys. Atmosph.*, 64, pp. 245-254.

Visser, H. and J. Molenaar, 1992, "Estimating trends and stochastic response functions in dendro-ecology with an application to fir decline. *Forest Science*, 38, pp. 221-234.

Visser, H. and Molenaar J., 1995, "Trend estimation and regression analysis in climatological time series: an application of structural time series models and the Kalman filter", *J. of Climate*, 8(5), pp. 969-979.

Visser, H., 1995, "Regression models with time-varying parameters: applications in the environmental sciences", *Ph. D. Thesis*, Univ. of Amsterdam.

Wigley, T.M.L. and Barnett, T.P., 1990, "Detection of the greenhouse effect in the observations", *Climate change, the IPCC Scientific Assessment*, J.T. Houghton, G.J. Jenkins and J.J. Ephraums, Eds., Cambridge University Press, pp. 245-255.

Woodward, W.A., and Gray, H.L., 1993, "Global warming and the problem of testing for trend in time series data", *J. of Climate*, 6, pp. 953-962.

ACKNOWLEDGEMENTS

The author wishes to thank A.F.V. van Engelen (KNMI) for the temperture data of De Bilt and Prof. J.G. de Gooijer (University of Amsterdam) for discussions on the Kalman filter. This research was funded by the Dutch Electricity Production Companies.

CORRESPONDING AUTHOR

Dr. H. Visser
KEMA Environmental Services, P.O. Box 9035
6800 ET Arnhem, The Netherlands
E-mail: visser@mta6.kema.nl

DETECTING HUMAN INFLUENCE ON CLIMATE USING OPTIMAL FINGERPRINTS

Gabriele C. Hegerl,
MPI für Meteorologie, Hamburg

Model results suggest that the present observed climate is influenced by anthropogenic greenhouse gas forcing and anthropogenic aerosol forcing. This can be verified by attempting to locate the signature of both forcings in the observations, e.g. of near surface temperature (Jones and Briffa, 1992). A new model simulation forced with observed greenhouse gas and aerosol forcings from 1880 to 1985 and a scenario of the development of anthropogenic forcing thereafter has been used to define the expected spatial pattern of temperature trends. The signal of climate change in this simulation is represented by the first EOF of the model output. This fingerprint is optimized statistically by weighting the original model-predicted pattern towards low-noise directions (Hasselmann, 1993). The noise estimate used for the optimization is derived from a 1000 y integration with the coupled OAGCM ECHAM/LSG.

The observed climate change is compared with this fingerprint by a scalar product, leading to a univariate "detection variable". When the detection variable is computed for running multi-decadal trends from the observations, the amplitude of the signal can be estimated. The same exercise can be done for transient model simulations forced with greenhouse gas and aerosol estimates since early industrialized time. Thus, the evolution of the climate response to greenhouse gas and aerosol forcing can be compared between observations and climate models.

In order to decide if climate has changed significantly by the anthropogenic forcing, the statistics of the detection variable is estimated by calculating the detection variable with natural variability patterns. These are extracted from the control runs of several coupled ocean-atmosphere models (ECHAM2/OPYC and the 1000 year GFDL simulation) and additionally from long-time observations. Additionally, the model variability can be compared to paleo data variability. The resulting estimate of climate noise is far from perfect, but it is qualitatively the best we can presently offer.

The results indicate that the recent temperature trends deviate from model internal and also from observed variability, i.e. they represent a significant climate change. This result holds under the caveat that the "natural" variability of climate is represented correctly by the model and observation data. Projecting the observations and model data synchronously onto a purely greenhouse gas induced model signal and onto the combined signal including the response to the aerosol forcing leads to the conclusion that at present both signals cannot be separated due to climate noise. Additionally, other possible reasons of the climate change, e. g. interactions of natural and anthropogenic forcing mechanisms with climate, which are not contained in the variability data, need to be systematically excluded. Further information is expected from a seasonal analysis of the data and a better representation of the time-evolution of the climate change signal.

References:

Cubasch U., G. C. Hegerl, A. Hellbach, H. Höck, U. Mikolajewicz, B. D. Santer and R. Voss (1994 b): A Climate change simulation starting at an early time of industrialization, accepted by **'Climate Dynamics'**.

Hasselmann K. (1993): Optimal fingerprints for the detection of time dependent Climate Change. **J. of Climate, Vol. 6, No. 10,** October 1993.

Jones P. D. and K. R. Briffa (1992): Global surface air temperature variations during the twentieth century: Part 1, spatial, temporal and seasonal details. **The Holocene 2**, 2, pp. 165-179.

DETECTING CLIMATE CHANGE IN PROGRESS

Timothy J. Brown and Uwe Radok

CIRES, University of Colorado, Boulder, Colorado, USA

ABSTRACT

A "consistency index (CI)" is proposed to measure whether or not the statistical parameters of a developing time series remain valid after one or more new values have been added to the existing "base" data. A substantial parameter change is signaled by a rapid or abrupt CI decrease which persists for different lengths of the base data set. The same index can also be used to search for changes in climatic series resulting from station moves or altered observational routines. The use of the index is illustrated with two sets of recent global mean temperatures, and with mean temperatures recorded before and after an airport station move.

1 INTRODUCTION

Many climate series resemble a sequence of short segments, representing "regimes" with descriptive parameters that can change from regime to regime. Examples include circulation patterns (Toth, 1992) and hydrological quantities exhibiting the "Hurst effect" (Klemes, 1974, Mesa and Poveda, 1993). When new values are added to such a series, the immediate question arises whether or not they have substantially changed the previously existing regime parameters, such as the mean, variance, or trend. The "consistency index (CI)", derived in the next section, is designed to answer that question.

2 THEORY

Consider a series of m observations x_i, i = 1,2,...m, for which further j observations (j = 1,2...m+j) become available. For a parameter θ, the first m values yield an optimum ("maximum likelihood") parameter estimate θ_m, and the additional observations $m+j$ introduce a new parameter estimate, θ_{m+j}. Let $\Pr(x_i, \theta)$ be the probability of obtaining an individual x_i, then the "likelihood" $L(n;\theta)$ of n observations is given by

$$L(n,\theta) = \Pr(x_1,\theta)\cdot\Pr(x_2,\theta)\cdot\ldots\cdot\Pr(x_n,\theta). \quad (1)$$

With $n = m$ or $m+j$ and $\theta = \theta_m$ or θ_{m+j}, there are four different likelihoods: $L(m;\theta_m)$, = L_1; $L(m+j;\theta_{m+j})$ = L_2; $L(m+j;\theta_m)$, = L_3; and $L(m;\theta_{m+j}) = L_4$. With their maximum likelihood estimates of the parameter θ, the likelihoods L_1 and L_2 will tend to be somewhat larger than the likelihoods L_3 and L_4, even when no appreciable change has been introduced by augmenting the original "base" data sample. A measure of the consistency of the parameter estimate θ_{m+j} with that found for the base sample θ_m is provided by the likelihood ratio $\varepsilon = L_4/(L_1+L_4)$. The corresponding likelihood ratio for the optimum estimate, θ_m, is $L_1/(L_1+L_4) = 1-\varepsilon$. Analogous ratios for the augmented sample of $m+j$ values are $L_3/(L_2+L_3) = \eta$ and $L_2/(L_2+L_3) = 1-\eta$.

A combined measure of the consistency which the two parameter estimates have for both the original and the augmented samples is provided by a further likelihood ratio,

$$Q = \frac{L_1 L_2}{L_3 L_4} = \frac{(1-\varepsilon)(1-\eta)}{\varepsilon\eta} = \frac{(1-(\varepsilon+\eta)+\varepsilon\eta)}{\varepsilon\eta}. \quad (2)$$

In order to obtain a single index, we write the second form of Q in equation (2) as

$$Q = \frac{(1-\gamma)^2}{\gamma^2}. \quad (3)$$

Solving (3) for γ then yields the "consistency index (CI)",

$$\gamma = \frac{1}{(1+\sqrt{Q})}. \quad (4)$$

Its value lies between the arithmetic and geometric averages of ε and η, as can be demonstrated by alternatively substituting those averages for ε and η in the last form of Q in equation (2).

As new values are added to the base sample, and without a regime change in the parameters, Q starts from near 1, and the CI decreases slowly from 0.5, as the parameter θ_{m+j}, with increasing sample size, moves closer to its population value. The two estimates then are consistently valid for both the original and the augmented data samples. Across the beginning or end of a regime the two parameter estimates become substantially different, creating a rapid CI decrease as the base sample is augmented.

CI formulae have been derived for small

samples from Poisson, Chi-square, and Gaussian distributions, and for regression coefficients measuring linear or exponential trends. They have been presented in a NASA project report (Radok and Brown, 1993) together with "Sequitor", a Fortran code for their evaluation. For Gaussian samples, with means $\bar{x}_m$ and x_{m+j} and estimates s_m^* and s_{m+j}^* of the population variance σ^2,

$$Q = \exp\left[j \log_e \frac{s_m}{s_{m+j}} + \frac{s_{m+j}^2 - s_m^2}{2}\left(\frac{m+j-1}{s_m^2} - \frac{m-1}{s_{m+j}^2} \right) + \frac{(\bar{x}_{m+j} - \bar{x}_m)^2}{2}\left(\frac{m+j}{s_m^2} + \frac{m}{s_{m+j}^2} \right) \right]. \quad (5)$$

This formula has provided the CI values for the examples presented in the next section.

3 EXAMPLES

Two examples illustrate a situation commonly encountered with climatic time series: recent data resemble a state of "statistical control" (Shewart, 1939), with quasi-steady mean and variance, but the newest observation appears to be anomalous. Progressive CI values for this and subsequent observations, using the immediately preceding data as base, then provide a quantitative test of whether a regime change is, or is not, in progress.

Anomalies of annual mean temperature reported by Angell and Korshover (1987) for a global network of radiosonde stations are shown in Figure 1. For the present purpose, the series has been terminated in 1977 when temperature rises were recorded at the surface and in the lower stratosphere (the layer between 300-100 mb) after three successive years of decreasing temperatures. Was this the start of a return to warmer conditions?

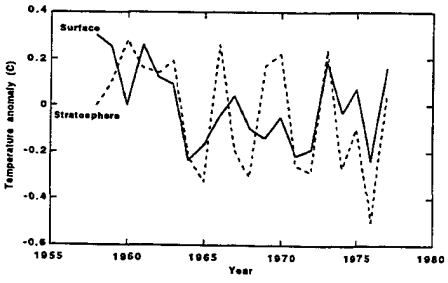


Figure 1. Annual mean temperature anomalies reported for 1958-1977 by a global net of radiosonde stations (from Angell and Korshover, 1987).

Epstein (1982) tested this possibility with Gaussian likelihood ratios assuming several different forms of change. By contrast, those of the consistency index CI, calculated with the preceding five anomalies (1972-1976) as base and shown in Figure 2, used only each new anomaly as it became available. The successive real-time CIs would have pointed to a warmer regime developing at the surface, but not in the lower stratosphere.

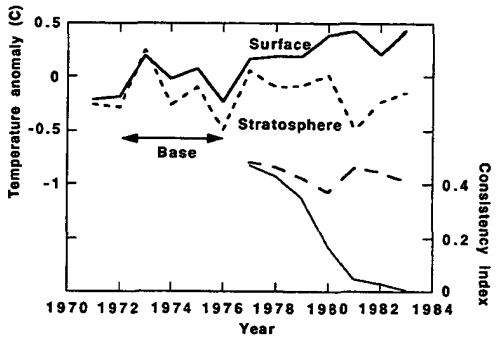


Figure 2. As in Figure 1, except anomalies since 1971, and consistency indices using the data for 1972-1976 as base sample.

The second example illustrates how the CI can be used to detect inhomogeneities in a climate series, caused by a station move or by a change in observational routine. Such discontinuities resemble sudden regime changes, or appear as outliers if the change was of short duration. A case in point is provided by the San Francisco, California, National Weather Service airport station, which is known to have been moved further inland during the 1940s. By reducing the number of maritime air incursions experienced at the new site, this should have raised the mean monthly temperatures, especially for the summer season.

Figure 3 shows the mean summer temperatures for the years 1933 through 1956. The CI calculations in this case started with a moving ten-year base period, advancing by two-year increments. For each of the first three bases, the gradual CI decline changed to a rapid drop with the 1948 temperature. This drop vanished as soon as the moving ten-year base reached and included the 1948 temperature itself. The station move in fact took place that year (Jon Eischeid, pers. comm.).

4 CONCLUSION

Likelihoods computed for an existing sample, and for the same data augmented by one or more values, show quantitatively whether a regime change is in progress. The consistency index (CI), moreover, has been defined by likelihood *ratios* which are less sensitive to the distribution shape assumed for their calculation than are the likelihoods themselves. The CI is an *exploratory* tool (cf. Flueck and Brown, 1993) defined even when a short "controlled" data sequence and one or several new observations constitute the entire information available.

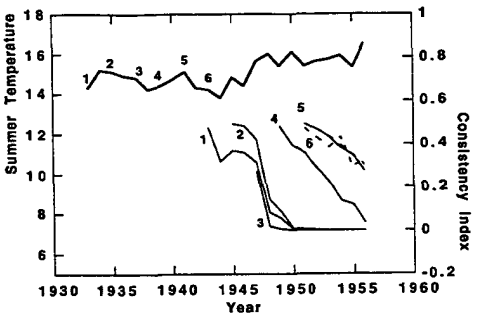


Figure 3. Summer mean temperatures recorded at the San Francisco International Airport. The numbers show the starting years of a moving base that ends the year before the start of the CI profile with the same number.

ACKNOWLEDGMENTS

This work has been made possible by NASA Grant NAGW-2706 to the second author. Partial support for the first author was provided by NOAA's Climate and Global Change Program.

CORRESPONDING AUTHOR

Dr. Timothy J. Brown
Western Regional Climate Center
Desert Research Institute
P.O. Box 60220
Reno, Nevada, 89506-0220, USA

References

Angell, J.K., and J. Korshover, 1987: *Annual and seasonal global temperature anomalies in the troposphere and lower stratosphere, 1958-summer 1986.* Report NDP-008/R1, Carbon Dioxide Information Analysis Center, Oak Ridge National Laboratory, Oak Ridge, TN.

Epstein, E.S., 1982: Detecting climate change. *J. Appl. Meteor.*, **2**, 1172-1182.

Flueck, J.A., and T.J. Brown, 1993: Criteria and methods for performing and evaluating solar weather studies. *J. Climate*, **6**, 373-385.

Klemes, V., 1974: The Hurst phenomenon - a puzzle? *Water Resour. Res.*, **10**(4), 675-688.

Mesa, O.J., and G. Poveda, 1993: The Hurst effect: the Scale of Fluctuations approach. *Water Resour. Res.*, **29**(12), 3995-4002.

Radok, U., and T.J. Brown, 1993: Inverse sequential procedures for the monitoring of time series. Progress Report # 3 on NASA Grant NAGW-2706.

Shewhart, W.A., 1939: *Statistical method from the viewpoint of quality control.* U.S. Department of Agriculture, Washington, D.C., 155 pp.

Toth, Z.,1992: Quasi-stationary and transient periods in the northern hemisphere circulation series. *J. Climate*, **5**, 1235-1247.

A Bayesian Approach to Detecting Climate Change

Brian Cairns

Columbia University, New York, USA

ABSTRACT

One problem that is sometimes encountered when attempting to estimate whether climate change can be detected is accounting in a rigorous way for prior information about the way we expect the climate to change. We analyze a regression model of climate change in which we include the type of prior information that might be provided by a GCM. Simple analytic results are obtained for the distributional properties of the regression model and we find that maximizing the expected forecast skill is a reasonable criteria for model selection. This method for including prior information can readily be extended to more general climate change detection models

1. INTRODUCTION

To detect climate change one must identify the climate change signal that one wishes to detect, estimate the statistical properties of the natural climatic variability and then determine an optimal method for detecting the signal in the noise (Hasselman 1993). Given that one can accurately characterize the signal and the noise, the detection problem is well posed and can readily be solved (Wainstein and Zubakov 1962). The principal problem of course is that the signal of climate change and the noise in the observed climate system are not readily distinguishable.

In order to address this problem one would expect to use climate models as a means to estimate climate change signals. Global warming is the principal predicted response of climate models to the anthropogenic release of CO2, although the magnitude is uncertain and only certain aspects of change appear to be common to most models. Thus our knowledge of global warming does not constitute a definitive statement about its magnitude and global distribution, but probabilistic statements regarding our degree of certainty about certain aspects of climate change. This knowledge should evidently be incorporated into any detection strategy since any failure to observe a signal about which we are reasonably certain should constitute a more considerable blow to our estimate of climate change than failure to detect a signal which is only apparent in a few climate models.

The method for incorporating such uncertainty into a statistical detection theory is provided within the formalism of Bayesian statistics (Epstein 1985). A Bayesian approach to statistical inference about climate change was initiated by Solow (1988). Here we extend the elegant analysis given there, to include the maximum entropy formalism as a method for specifying the prior probability distribution which is most consistent with the prior information. We also eliminate (cf. Janes 1983) the difficulty encountered with uninformative prior distributions (Solow 1988, Leamer 1978), which allows us to recover the classical results exactly in the case where there is no prior information. The Bayesian estimator of a linear climate change vector can be readily interpreted, as being a weighted sum of the change estimated from the data and the prior (model) prediction of change, with the variability of the estimator being inflated by the amount of disagreement between the estimate and the prior prediction of change. This agrees with a common sense view of the situation, in that, if our prediction of change disagrees with the observed data, then we are less certain about the validity of our prediction.

With regard to the significance of detection of climate change, one encounters the classical statistical problem that if enough signals are included in a definition of climate change then some of them may well be detected as changing, simply by chance. This problem can be eliminated by analyzing the Bayesian estimate of forecast skill of the specified climate change signals and then retaining only those signals which maximize the forecast skill. For the case of a time series the maximization of forecast skill can be shown to be asymptotically the same as minimization of final prediction error, or minimization of Akaike's information criteria (Akaike 1974). In the following section we define the problem that is addressed and briefly derive a number of results that may help to eliminate some of the confusion regarding the validity and use of Bayesian methods. We then present some results related to the use of the method in the analysis of temperature time series. Future work will apply the formalism to the analysis of climate change caused by the eruption of Mount Pinatubo, through the use of an ensemble of model runs of the Goddard Institute for Space Studies ICP model.

2. ANALYSIS METHOD

There has been an extensive debate about the validity of Bayesian methods, which

we won't enter into here. It will merely suffice to note that whenever the discussion is couched in terms of quantitative results the Bayesian approach cannot be faulted and moreover has, in most cases, the considerable virtue of simplicity when compared with classical methods. We will show that the Bayesian approach provides useful information about the forecast skill, contrary to the conclusions others have drawn (Hasselman and Barnett). Indeed, because Bayesian methods provide distributional results, we can not only show that maximizing the expected forecast skill is a useful method of model selection, but also provide confidence intervals for the forecast skill. For the convenience of the reader the notation used here is similar to that used by Solow (1988) and Priestley (1981). In what follows we will extend the approach presented by Solow (1988) to include the maximum entropy method as an objective means for incorporating prior information and eliminate the problems encountered therein with non-informative prior distributions. We will not discuss the simplicity and power of hypothesis testing that is provided by Bayesian methods since detailed discussions of theses issues have been given elsewhere (Janes 1983, Solow 1988).

In the following discussion we will consider a time series T_i which can be modeled in the following form,

$$\hat{T}_i = \sum_{j=1}^{d} X_{ij}^{c} a_j \qquad (1)$$

$$\hat{\mathbf{T}} = \mathbf{X}^{c}\mathbf{a}$$

where we have written this expression both explicitly and in the matrix notation that we will use henceforth. We will bear in mind that the time-series that we wish to analyze using this methodology are geophysical time series such as tropospheric temperatures, sea-level pressure fields, or surface-air temperatures, for which prior information may be obtained from GCM simulations. The matrix $\mathbf{X}^{c}$ represents a d-dimensional regression model of a time series that depends parametrically on c, for example a two phase regression model, and the regression coefficients of the model are given by the d-dimensional vector **a**.

From the Bayesian viewpoint we may regard the parameter c, the vector **a** and the variability of the time series σ^2 as unknown random variables. The posterior distributions of these variables, conditional on the variability of the observed time-series, can then be readily derived using Bayes theorem. This requires that the prior distributions of these variables are specified or, if we have no information about their value, that we use the correct non-informative prior distributions.

There are two posterior probabilities that are of interest, one being the distribution of c which tells us about the form of our time series model and the other being the distribution of **a**, which tells us about the significance of the model (Priestley 1981). The posterior distribution of c is given by the expression,

$$p(c/T) \propto \int p(T/c,\mathbf{a},\sigma^2)\pi(\mathbf{a},\sigma^2/c)\pi(c)\,d\mathbf{a}\,d\sigma \qquad (2)$$

where the constant of proportionality in eq.(2) can be evaluated from the constraint that the total probability be unity and the posterior distribution of **a** is given by the formula

$$p(\mathbf{a}/T) \propto \int p(T/c,\mathbf{a},\sigma^2)\pi(\mathbf{a},\sigma^2/c)\pi(c)\,dc\,d\sigma \qquad (3)$$

There are therefore two probabilistic structures that we must define. The posterior probability of the time-series T_i and the prior probability distribution of the model, which can be related to the prior probability of this time-series. For the sake of simplicity we will assume that the residuals of the model fit to the time-series are Gaussian distributed and uncorrelated, so that the posterior probability distribution of the time-series T_i is given by the usual expression,

$$p(T/\mathbf{a},\sigma,c) \propto \sigma^{-n} e^{\left\{[\mathbf{a}-\mathbf{a}_e).\mathbf{M}.(\mathbf{a}-\mathbf{a}_e)+RSS_e\right]/2\sigma^2\}} \qquad (4)$$

where **M** is defined to be

$$\mathbf{M} = \left(\mathbf{X}^{c}\right)^{T}\mathbf{X}^{c} \qquad (5)$$

and RSS_e is the residual sum of squares from fitting the model with a maximum likelihood estimate of **a** given by $\mathbf{a}_e$.

The prior probability structure of the model has usually been dealt with by using a conveniently simple (and intuitively appealing) prior probability, the normal gamma distribution. This model has been introduced in an ad hoc manner, though it has an entirely reasonable form, rather than through any rigorous derivation that would relate the prior probability distribution to the actual prior information. The most useful way of specifying a prior probability distribution is the principal of maximum entropy which provides a simple and rigorously justifiable means for assigning the probability structure of the model. Indeed, given any testable prior information, the probability distribution which maximizes the entropy is numerically identical with the frequency distribution which can be realized in the greatest number of ways.

The entropy of a discrete distribution is defined to be

$$H = -\sum_{i=1}^{n} p_i \log p_i \qquad (6)$$

where the probabilities $p_i=p(T_i)$.are to be determined under certain constraints. We assume for convenience that these constraints are in the form of the mean values of several functions $f_k(T_i)$, though this is in no way necessary for the application of the maximum entropy method. The entropy must therefore be maximized subject to the constraints

$$\sum_{i=1}^{n} p_i = 1$$
$$\sum_{i=1}^{n} p_i f_k(T_i) = F_k \quad (7)$$

where the F_k are the observed mean values of the functions $f_k(T_i)$. The well known solution to this problem is

$$p_i = \frac{\exp\left[\lambda_1 f_1(T_i)+\ldots+\lambda_k f_k(T_i)\right]}{Z(\lambda_1 \ldots \lambda_k)} \quad (8)$$

with the partition function

$$Z(\lambda_1 \ldots \lambda_k) = \sum_{i=1}^{n} \exp\left[\lambda_1 f_1(T_i)+\ldots+\lambda_k f_k(T_i)\right] \quad (9)$$

in which the real coefficients λ_k are to be determined from the constraints (7), which reduces to the relations

$$F_k = \frac{\partial \log\left[Z(\lambda_1 \ldots \lambda_k)\right]}{\partial \lambda_k} \quad (10)$$

Thus any prior information about the time-series T_i can readily be incorporated into its prior probability distribution. From the form of eq.(8) we can see that the normal-gamma distribution will be the prior probability distribution if the prior information that we have is in the form of means and variances of a prior time-series, provided perhaps by some stochastic, or general circulation model of the earth's tropospheric, or surface air temperature. The appropriate form of the normal-gamma distribution for such prior information is

$$\pi(\mathbf{a}, \sigma / c) \propto \sigma^{-(v+1)} e^{\left\{\left[\mathbf{a}-\mathbf{a}_p\right).\mathbf{N}.(\mathbf{a}-\mathbf{a}_p)+RSS_p\right]/2\sigma^2\}} \quad (11)$$

where v is the length of the prior time-series, $\mathbf{a}_p$ are the estimates of **a** obtained from this prior time-series and **N** is the similar to **M**, except that the regression model $\mathbf{X}^c$ is for a time series of length v. The residual sum of squares of the fit to the prior data is RSS_p. The extra factor of σ^{-1} in this definition comes from the imposition of a group invariance constraint (Wigner 1959) on the prior probability distribution, aswell as the mean value and normalization constraints in eq.(7). That is we know that the variance is a scale parameter, not a location parameter. The use of this prior distribution incorporates all the available information and ensures that when no prior information about mean values [cf. eq.(7)] is available viz., **N**=0,v=0 the appropriate non-informative priors are obtained.

In writing the expressions for the posterior probability distributions a number of definitions will prove useful. The Bayesian estimate of **a**, $\mathbf{a}_B$, is

$$\mathbf{a}_B = (\mathbf{N}+\mathbf{M})^{-1}(\mathbf{N}\mathbf{a}_p + \mathbf{M}\mathbf{a}_e) \quad (12)$$

which weights the estimates of **a** from prior and current data according to the length of the record and the form of the model $\mathbf{X}_C$. The residual sum of squares of the Bayesian estimate of **a**, RSS_B, is also a weighted sum of the variance estimates from the prior and current data, but can also be inflated by any disagreement between the two estimates of **a** viz.,

$$RSS_B = RSS_p + RSS_e + (\mathbf{a}_e - \mathbf{a}_p).\mathbf{C}.(\mathbf{a}_e - \mathbf{a}_p) \quad (13)$$

where

$$\mathbf{B} = \mathbf{N}+\mathbf{M}$$
$$\mathbf{C} = \mathbf{N}\mathbf{B}^{-1}\mathbf{M} \quad (14)$$

and n'=n+v is the effective number of degrees of freedom from both prior and current data. Using these definitions the posterior probability of the parameter c is given by the expression

$$p(c / T) \propto (RSS_B)^{-[(n'-d)/2]}\pi(c) \quad (15)$$

This expression can be recognized as a generalization of the classical likelihood ratio approach (Epstein 1982), which also includes prior information. Rather than stating the posterior probability distribution of **a** we will give the posterior probability of the errors in modeling the time series T_i as a function of **a**. This distribution is of more interest than the distribution of **a** itself, since it is related to the question of forecast and artificial skill. If we define a function x

$$x = (\mathbf{a}-\mathbf{a}_B).\mathbf{B}.(\mathbf{a}-\mathbf{a}_B) \quad (16)$$

then x/RSS_B is F-distributed with d and n'-d degrees of freedom. This result reduces to the usual form for the distribution of model coefficients when N=0,v=0 (Priestley 1981). In the limit of large n the F distribution can be approximated by a chi-squared distribution with d degrees of freedom (Box and Jenkins 1970) which is the more frequently used form (Hasselman and Barnett, Hasselman).

This result is useful when we consider forecast and hindcast skill. The hindcast skill of a model, S_H, is defined to be

$$S_H = 1 - \frac{RSS_e}{\sum_{i=1}^{n} T_i^2} \quad (17)$$

Evidently the residual sum of squares of any model fit to data is an underestimate of the actual noise in the data since any noise that projects onto the model will be erroneously estimated as being part of the model rather than

noise. Therefore, the hindcast estimate of skill is doubly biased when applied to forecasting, first by the error in the estimate of model parameters and second by the underestimate of the noise in the signal. In the case of non-informative priors (v=0,N=0) the forecast skill is given by the simple expression

$$S_F(\mathbf{a}) = 1 - \frac{RSS_e + 2(\mathbf{a}-\mathbf{a}_e).\mathbf{M}.(\mathbf{a}-\mathbf{a}_e)}{\sum_{i=1}^{n} T_i^2} \quad (18)$$

for which we have already obtained the posterior probability distribution. The formula for the expected value of the forecast skill is therefore

$$\langle S_F \rangle_a = S_H - 2(1-S_H)\frac{d}{n-d} \quad (19)$$

where we have averaged the forecast skill over the posterior distribution of model coefficients **a**. This expression reduces to the usual form when there is negligible hindcast skill (Davis 1976, Barnett and Hasselman 1979). The form of this expression for the expected forecast skill is such that as the number of model coefficients, d, increases the forecast skill increases as the hindcast skill increases. This effect will eventually saturate, after which point the forecast skill will decrease as d increases. This behavior is the same as that found in other model selection criteria and indeed in the limit of large n, we can show that maximizing the expected forecast skill is the same as minimizing the final prediction error, or Akaike's information criteria (Priestley 1981).

3. CONCLUSIONS

A Bayesian approach to statistical inference about climate change has been presented. This approach provides a method for incorporating prior information into the analysis of climate change, while yielding the correct classical results when no prior information is available. The principal of maximum entropy is used to provide a simple and rigorous means for specifying prior probability distributions. Intuitively satisfying results, such as the inflation of variance in the estimate of a change when our prior information disagrees with the data can be precisely quantified. We have also shown that this method allows issues of model significance to be easily addressed in the context of whether the model maximizes the expected forecast skill (a desirable property). Since Bayesian methods provide distributional results we can also give confidence intervals for the forecast skill that may be of particular importance for climate prediction.

ACKNOWLEDGEMENTS

The author wishes to thank Dr. Barbara E. Carlson for suggesting the topic of this research and Dr. William S. Russell for reading and commenting on an early draft of this paper. This work was supported by the Department of Energy Interagency Agreement under the Atmospheric Radiation Measurement Program

REFERENCES

Akaike, H., 1974: A new look at the statistical model identification. IEEETrans.Autom.Control, **AC-19**, 716-723.

Barnett,T.P. and Hasselman,K., 1979: Techniques of linear prediction, with application to oceanic and atmospheric fields in the tropical Pacific. Revs.Geophys.Space Sci., **17**, 949-968.

Box, G.E.P. and Jenkins, G.M. 1970: Time series analysis, forecasting and control. (Holden-Day, San Francisco).

Davis, R.E., 1976: Predictability of sea-surface temperature and sea-level pressure anomalies over the North Pacific ocean. J.Phys.Oceanogr., **6**, 249-266.

Epstein, E.S., 1985: Statistical inference and prediction in climatology: Bayesian approach. American Meteorological Society, Boston.

Epstein, E.S., 1982: Detecting climate change. J.Appl.Met., **21**, 1172-1182.

Hasselman,K., 1993: Optimal fingerprints for the detection of time-dependent climate change. J.Clim. **6**, 1957-1971.

E.T. Janes, 1983: Papers on probability, statistics and statistical physics. ed. Rosenkrantz, R.D.(D.Reidel, London, England).

Leamer, E.E., 1978: Specification Searches. Wiley and Sons.

Solow, A.R. 1988: A Bayesian approach to statistical inference about climate change. J.Clim., **1**, 512-521.

Wainstein, W.M. and Zubakov, V.D., 1962: Extraction of signals from noise. R.A.Silverman trans., (Prentice-Hall, New York).

Wigner, E.P., 1959: Group Theory. New York Academic Press.

Trend and Drift in Climatological Time Series

Arthur P. Dempster and Chuanhai Liu

Department of Statistics, Harvard University

ABSTRACT

We specify models and illustrate Bayesian analysis on a familiar global annual average temperature series to assess two assumed components, one a linear trend and other a stochastic "long memory" drift. The stochastic component is allowed to be stationary or nonstationary, as controlled by an exponent parameter in the spectral density. One indicator of a tendency to nonstationarity is that the phases of the discrete Fourier transform become nonuniform. We explain the nonuniformity, and illustrate on real and simulated data. We also apply "singular spectrum analysis" to simulated data, and show that periodicities not in the model nor replicated in repeated simulations generally result.

1. INTRODUCTION

Trend signifies a smooth monotone progression across an observation period, whereas drift implies a random appearance with several or many upward and downward segments of varying lengths. Given formal representations of both components, each with unknown parameters to be estimated from the data, we can in effect separate trend and drift by computing Bayesian posteriors for the parameters of each. We illustrate below on a familiar global annual average temperature series, where we represent trend by a straight line, and drift by a red noise Gaussian process whose log-log spectral density over the range of frequencies resolved by the data is approximately linear with slope $-d$.

The problem we address is similar to that of Bloomfield (1992), Bloomfield and Nychka (1992), and Smith (1993) in that they also use linear trends and long memory models. We present different statistical techniques, relying on Bayesian inference in our basic approach to parametric models, and describing and evaluating diagnostic data analysis procedures that look at phases of the discrete Fourier transform (DFT) and principal components of a truncated sample autocorrelation matrix (called singular spectrum analysis or SSA in the climatological literature).

Another difference is that we allow the parameter range of d to exceed unity, implying stochastic nonstationarity. In earlier studies, it seemed plausible to restrict attention to $d < 1$ on the grounds that natural variability should not have the long run infinite variance that goes with nonstationarity. On reconsideration, however, there is no reason that $d > 1$ should not be plausible on a frequency range down to below the low frequency limit resolved by the data, while stationarity is maintained on scales of several centuries and longer. Moreover, it was already clear from earlier comments in Dempster and Hwang (1992) that, unlike the sampling theory of traditional statistics, in Bayesian analysis there is a smooth transition across $d = 1$, as illustrated below.

We give a few details of our stochastic models in Section 2 and the results of a Bayesian analysis in Section 3. We discuss and illustrate the "phase banding" phenomenon that accompanies nonstationarity in Section 4, and venture some analysis and criticism of SSA in Section 5.

2. MODELS

The essential feature of the long-memory stochastic models is a spectral density function that takes the form

$$f_X(\omega) \sim \tau^2 |\omega|^{-d}. \qquad (1)$$

in the limit near $\omega = 0$, and in practice approximately takes this form over the full range of frequencies. Note here that the parameter τ^2 is a scale parameter that controls the variability of the process, but has a different relation to variance σ^2 for different d. We argue that τ is the natural measure of scale to use for d in the neighborhood of 1. In fact, the traditional concepts of mean μ and variance σ^2 become meaningless as d crosses 1, and they should be avoided as potentially misleading for an interval of $d < 1$ because they become unstable and infinite, respectively, as $d \to 1$.

There are two families of long memory processes in common use in the statistical professions, namely, the fractional differencing models of Hosking (1981) derived from the ARMA modelling tradition of applied statistics, and the earlier more mathematically elegant fractional Gaussian noise (fGn) models of Mandelbrot and Van Ness (1968). See the review of Beran (1992) for more details. We have used the latter models for 15 years, and use them here to take advantage of software developed over a long period. We believe the choice has little effect on results.

In order to extend the fGn models to $d \geq 1$ we take

the standard formula

$$R_X(t) = \frac{\sigma^2}{2}\left(|t+1|^{1+d} - 2|t|^{1+d} + |t-1|^{1+d}\right), \tag{2}$$

for the autocovariance of the fGn process $\{X_t : t = 0, \pm 1, \pm 2, ...\}$ with $-1 < d < 1$ from Mandelbrot and van Ness (1968) and derive the autocovariance function of $Y_t = X_t - X_{t-1}$ to have the form

$$R_Y(t) = \frac{\gamma^2}{2}\left(-|t+2|^{1+d} + 4|t+1|^{1+d} - 6|t|^{1+d} + 4|t-1|^{1+d} - |t-2|^{1+d}\right). \tag{3}$$

which can be shown to be a valid autocovariance for a stationary process on $-1 < d < 3$. It can also be shown that the nonstationary process defined from (3) up to an arbitrary location has a meaningful spectral density satisfying (1) where

$$\tau^2 = -\frac{\gamma^2}{8\pi(2^{d-1}-1)}\Gamma(2+d)\sin\left(\frac{(1+d)\pi}{2}\right) \tag{4}$$

for $1 \leq d < 3$.

3. BAYESIAN INFERENCE

The extended fGn stochastic model defined above for $-1 < d < 3$ permits standard Bayesian calculations to be performed on the differenced data. In practice, such Bayesian analyses could be made more realistic by developing genuine prior distributions for the two parameters of the stochastic models, and for the slope of the linear trend line, but for illustrative purposes we limit ourselves to conventional uniform priors for $\ln \tau$, the exponent d, and the slope of the trend. Figures 1, 2, and 3 show plots of the basic marginal posterior densities computed from a basic X_t time series of estimated global annual average temperatures of length 129 (data for 1861 — 1989 obtained from Peter Bloomfield). The plots indicate clearly that the data show positive posterior probability of nonstationary drift ($d \geq 1$). Also, agreeing with Bloomfield (1992), there appears to be no reasonable doubt that the trend has positive slope.

All statistical analyses come with warning labels attached regarding the assumptions made. Our Bayesian analyses are of course model- dependent. Our judgment is that the models are plausible, and that sensitivity analyses would not upset major conclusions. For example, plausible changes in the mathematical form of the trend are unlikely to have a major effect. Adding a white noise term to the model should make the posterior densities of d wider, but not change the conclusion that nonstationarity should be considered a definite possibility. Sensitivity analyses can be provided for a later publication.

4. PHASE BANDING UNDER NONSTATIONARITY

Part of the folklore of parameter estimation from

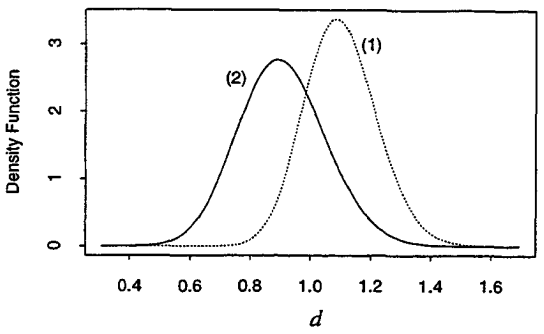


Figure 1: The posterior density of d for 2 cases (1) assuming trend slope $b = 0$, and (2) averaging over the posterior of a nonzero slope b.

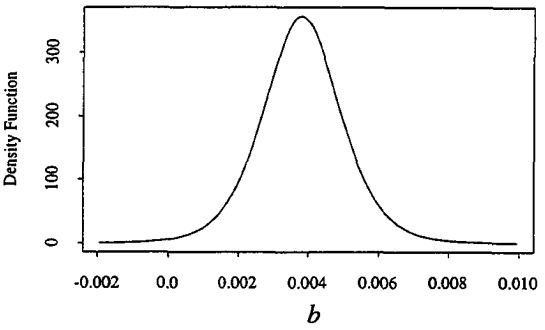


Figure 2: The posterior density of the trend slope b.

a stationary Gaussian time series is that the periodogram values at the Fourier frequencies are approximately sufficient for the second order parameters (variance and autocovariances). The argument is that the data are equivalent to the discrete Fourier transform whose amplitudes are the periodogram ordinates, while the phases are approximately independently uniform and independent of the amplitudes which in turn have sampling distributions that are approximately independent chi-squares. It has been known for some time that the independence of the periodogram ordinates breaks down at the lowest frequencies under stationary long memory conditions. See Beran (1992) and Hurvich and Beltrao (1992).

Our observation is that the pathologies of the discrete Fourier transform become more pronounced in the region of nonstationarity. In particular, the phases at the Fourier frequencies begin to deviate from their uniform distribution as d increases. It turns out that the nonuniformity has approximately the same character across the full frequency range with the result that phase plots tend to show a

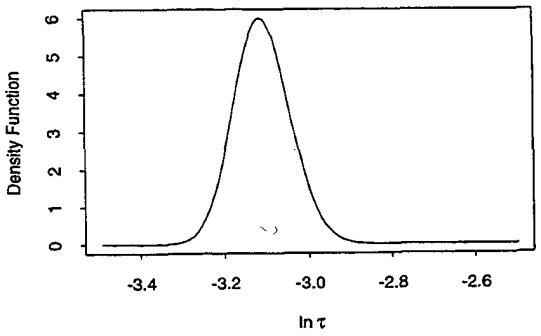


Figure 3: The posterior density of $\ln \tau$.

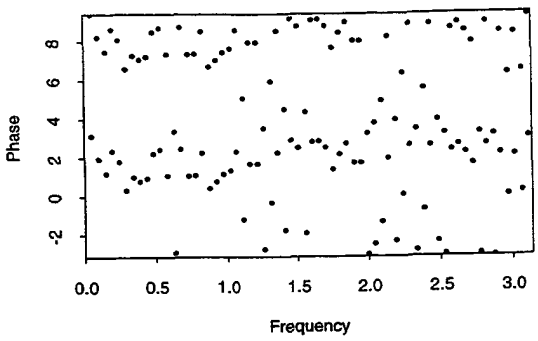


Figure 5: The phases of the discrete Fourier transformation of the simulated series shown in Figure 6.

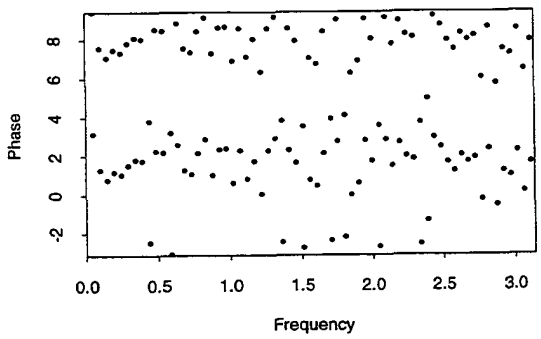


Figure 4: The phases of the discrete Fourier transformation of the temperature series.

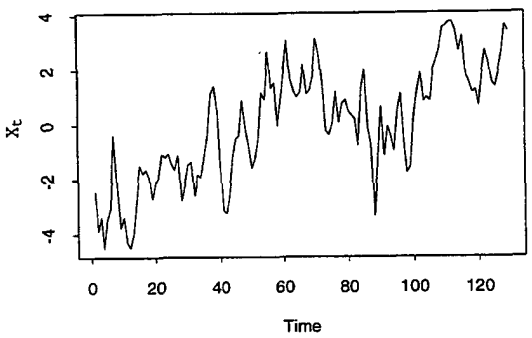


Figure 6: A simulated series of length 129 with $b = 0$ and $d = 1.1$.

banding effect that becomes increasingly strong as d increases. One consequence of this is that the periodogram is no longer a sufficient statistics, and statistical estimation of d needs inputs from amplitude and phase (as a Bayesian analysis automatically does).

Phase banding is illustrated in Figure 4 for the global temperature series analyzed above, and in Figure 5 for a simulated series with $d = 1.1$ as shown in Figure 6.

The phase-banding phenomenon can be understood theoretically by considering the cosine and sine coefficients of the time-centered DFT. At each Fourier frequency, the data-determined cosine coefficient loads only on the cosine coefficients of the Cramer representation of underlying stochastic process with the same time origin, and similarly for the data-determined sine coefficient loading on the theoretical sine coefficients. Hence the cos and sin coefficients from the data have independent Gaussian zero mean distributions, but the ratio of their variances deviates markedly from the white noise case where they are equal. These ratios are exhibited for the extended fGn models and time series of length 129 in Figure 7. A ratio of 1 implies a uniform distribution of phase angles, but as the ratio declines the distribution of phases becomes more clustered, as shown in the densities plotted in Figure 8.

5. SINGULAR SPECTRUM ANALYSIS

Climatologists have developed a form of spectral analysis based on the statistical technique of principal components analysis applied to a sample-based autocovariance matrix. See for example Vautard, Yiou, and Ghil (1992). SSA is an appealing idea because spectral analysis is formally equivalent to a principal components analysis applied to the underlying stationary process, i.e., an infinite time series. Theoretical statisticians have not studied the method, as far as we are aware, but it seems likely that the method can successfully identify trends, or periodic/quasi-periodic phenomena, or indeed any prominent patterns that explain a considerable fraction of raw variance in an observed record.

There is a concern, however, that the method may mislead by pointing to patterns that are no more than random consequences of mixtures of long-

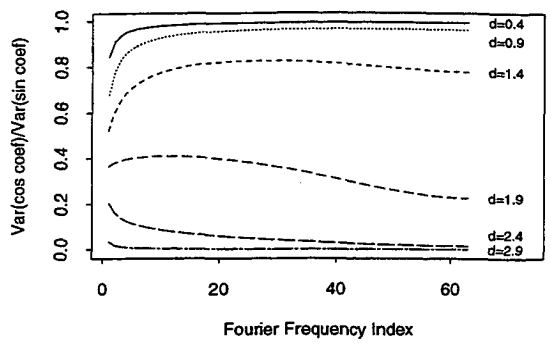


Figure 7: The ratios of variances of sine and cosine coefficients of fGn series of length 129.

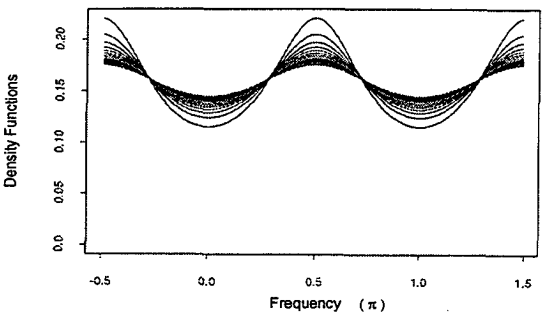


Figure 8: The marginal distributions of the phases of the discrete Fourier transformation for fGn series of length 128 with $d = 1.4$ and $b = 0$.

range cycles such as those generating long-memory processes. One warning signal is that the very concepts of variance and associated autocovariances become increasingly meaningless as d increases, and hence the sample versions of these quantities become a dubious heuristic foundation for statistical analysis. We have seen several papers using the SSA toolkit to identify oscillations and/or trends in the global temperature time series (Ghil and Vautard, 1991 and Schlesinger and Ramankutty, 1994). The correspondence in Nature of 8 Dec 1994 did not resolve the issue, because AR processes themselves can approximate real quasi-periodic phenomena. We therefore applied SSA to several series of length 129 simulated from fGn processes that are known not to have any periodic or quasi- periodic long-run features. Typically, the largest eigenvalues have associated eigenvectors that suggest long swings or multidecadal periodicities. Yet subsequent simulations of the same processes suggest quite different patterns. Due to space restrictions these plots are not shown here.

REFERENCES

Beran, J., 1992, "Long-Range Dependence" (with comments), Statistical Science, Volume 7, pp. 404-427.

Bloomfield, P., 1992, "Trends in Global Temperature", Climatic Change, Volume 21, pp. 1-16.

Bloomfield, P. and Nychka, N., 1992, "Climate Spectra and Detecting Climate Change", Climatic Change, Volume 21, pp. 275-287.

Dempster, A. P. and Hwang, J-S., 1992, "Comment: Short-Range Consequences of Long-Range Dependence", Statistical Science, Volume 7, pp. 416-420.

Ghil, M. and Vautard, R., 1991, "Interdecadal Oscillations and the Warming Trend in Global Temperature Time Series", Nature, Volume 350, pp. 324-327.

Hosking, J. R. M., 1981, "Fractional Differencing", Biometrika, Volume 68, pp. 165-176.

Hurvich, C. M. and Beltrao, K. I. (1992), "Asymptotics for the low- frequency ordinates of the periodogram of a long-memory time series", Journal of Time Series Analysis, Volume 14, pp. 455-472.

Mandelbrot, B. B. and van Ness, J. W., 1968, "Fractional Brownian Motions, Fractional Noises and Applications". SIAM Review, Volume 10, pp. 422-437.

Schlesinger, M. E. and Ramankutty, N., 1994, "An oscillation in the global climate system of period 65-70 years", Nature, Volume 367, pp. 723-726. (See also related correspondence, Nature, Volume 372 pp. 507-509.)

Smith R. L., 1993, "Long-Range Dependence and Global Warming", Statistics for the Environment (ed. Barnett, V. and Turkman, K. F., pub. J. Wiley) pp.141-161.

Vautard, R., Yiou, P. and Ghil, M. 1992, "Singular-Spectrum Analysis: A Toolkit for Short, Noisy, Chaotic Signals", Physica D, Volume 58, pp. 95-126.

ACKNOWLEDGEMENTS

Dempster is a part-time member of the Statistics Project in the Climate Analysis Section at NCAR, and acknowledges helpful discussions at NCAR. Dempster's research at Harvard is supported by NSF grant DMS-9404396 and Liu's research by NSF grant SES 92-07456. Computing for Section 5 was carried out by Igor Perisic.

CORRESPONDING AUTHOR

Professor Arthur P. Dempster
Department of Statistics
Harvard University
Cambridge, MA 02138 USA

PRACTICE OF CLIMATE CHANGE DETECTION IN THE CASE OF A SPECIAL ALTERNATIVE TO RANDOMNESS.

M. Vandiepenbeeck

Institut Royal Météorologique de Belgique

ABSTRACT

The study of climate change puts forward the necessity of analysing the internal structure of chronological series. Two tests are used in conjunction to explain the behaviour of the time series : the test of Pettitt (1979) and the test of Mann-Kendall (1945) in its progressive form as recalled in Sneyers (1992). These two tests have been used among others by Sneyers, Böhm and Vanitsem (1992) and Demarée (1990).

After a summary of the theory of these tests, we examine their application on synthetic series in order to study their behaviour in well known situations.

The initial series is a random one generated by a statistical program. Other series are issued from this initial series in order to simulate different changes that we can find in climatological series.

These series are submitted to the two tests. In the case where the test of Pettitt gives one or two significant values, we cut up the total series into two or three subseries limited by the significant values. We resubmit these subseries to the tests of Pettitt and Mann as far as we don't find more significant values. A graphic investigation allows to find the stable parts, the abrupt changes or the trends.

A real climatological series will be finally considered as a concrete example of the method.

1. Introduction

Studies on climate change put forward the necessity of having climatological series without heterogeneities. Thus the first work is detecting the changes into the series and, with station history, determining the different heterogeneities and their characteristics; in this way reconstruction of homogeneous series is made possible.

The heterogeneities in a series may have an abrupt (change of site, of instrumentation, ...) or a progressive (change in the environment of the station, urbanisation, ...) character.

The aim of this paper is to give a tool for detecting the different changes inside series. To verify the simple randomness of the series, we use two tests :

a) randomness against serial correlation (Wald-Wolfowitz, 1943),

b) randomness against trend or abrupt change (Mann, 1945 ; Pettitt, 1979).

2. Test of simple randomness

2.1. Independence of the elements of a climatological series

To verity the independence of the elements of a climatological series, we use a non parametric test against the serial correlation (Wald-Wolfowitz, 1943; Sneyers, 1975). If we have a series x_i , $i = 1, 2, ..., n$, going over from x_i to x_i' such that $\sum_{i=1}^{n} x'_i = 0$, the statistic of the test is

$$R = \sum_{i=1}^{n} x'_i \, x'_{i+1}$$

with $x'_{n+1} = x'_1$.

Under the null hypothesis of randomness, the distribution of the statistic R is approximately normal for large values of n .

Mean and variance of R are respectively

$$E(R) = - S_2/(n-1) \text{ and } \quad \text{var } R = S_2^2/(n-1)$$

where $S_2 = \sum_{i=1}^{n} (x_i')^2$.

It follows that the autocorrelation coefficient

$$r = R/S_2$$

has respectively mean and variance

$$E(r) = -1/(n-1) \quad \text{and} \quad \text{var } (r) = 1/(n-1)$$

This statistic is one developed by Anderson (1942).

2.2. Stability of the distribution of the elements of the series

To determine the stability of these elements, the two most appropriate non parametric tests : the Mann-Kendall test (Sneyers, 1975) and the Pettitt test (Demarée, 1990).

2.2.1. Mann test

This test, introduced by Mann (1945), is based on the Kendall rank correlation statistic (Kendall, 1938).

If, for each element x_i (i = 1, 2, ..., n) of the series, n_i is the number of smaller preceding ones the trend statistic is the quantity

$$t = \sum_{i=1}^{n} n_i$$

which, under the null hypothesis of randomness, provided $n_j \geq 10$, has practically a normal distribution with mean and variance

$E(t) = n(n-1)/4$ and $\text{var } t = n(n-1)(2n+5)/72$

The standardized statistic of the test is then

$$u(t) = [t - E(t)] \sqrt{\text{var } t}$$

If we determine the value α_1 of the probability determined from a standard normal distribution table, such that $\alpha_1 = P(|u| > |u(t)|)$, the null hypothesis is accepted or rejected at the critical level α_0 depending on whether $\alpha_1 > \alpha_0$ or $\alpha_1 < \alpha_0$. It is in his onward and backward form (Sneyers, 1975) that the Mann test appears to be especially useful. In particular, the graphical presentation of the test allows to have an idea on the internal structure of the series.

2.2.2. The Pettitt test

A particular form of instability of a series is characterised by abrupt changes. This can be put forward with the help of the Pettitt test (1979) (Snijders, 1983; Demarée, 1990; Vanitsem and Demarée, 1991; Coops, 1992).
If x_i , i = 1, 2, ..., n, are the elements of a time series, for i=t, Pettitt test statistic is

$$u_{tn} = 2 W_t - t(n+1)$$

with $W_t = \sum_{j=1}^{t} R_j$, R_j being the rank of the element x_j in the series ranked in increasing order.
Under the null hypothesis of randomness, the distribution of W_t has normally mean and variance

$$E(W_t) = \frac{t(n+1)}{2}$$

and

$$\text{var } (W_t) = \frac{t(n-6)(n+1)}{12}$$

The probability associated to the extreme value U_E of the statistic u_{tn} is for a one sided test given by

$$P(U < -|U_E|) = P(U > |U_E|) = \exp [-6 * (U_E)^2 / (n^3+n^2)]$$

When comparing the different u_{tn} for t =1,2,...,n , for the extreme values of u_{tn}, the critical value at the level $\alpha = 0.05$ is given by

$$U_c = \sqrt{(n^3+n^2) * \lg 0.05 / (-6)}$$

When $|U_E| > U_c$ the corresponding t is the estimation of an existing change point. The change-point is increasing or decreasing whether $U_E < 0$ or $U_E > 0$.
The application of the Pettitt test to the two subseries defined by the estimated point t allows to verify their own stability.

3. Use of the test

The study of the stability of a chronological series is realised by the application of the Pettitt test and the Mann test. In the case of one or two significant values of the Pettitt test statistic, the Pettitt test is applied again to each of the two or three subseries defined by the estimated change-points. To visualise the result of the statistical analysis, three graphs are realised:

(1) the first one gives the deviations of the elements of the series to its general average,
(2) the second one gives the values of the Pettitt test statistics as well for the total series as for the subseries,
(3) the last one gives the values u(t) and u'(t) of the Mann test statistics for respectively its onward and backward application.

These will allows a good visualisation of the internal structure which can be present in the time series.

4. Application of the test on synthetic series

The two tests have been jointly applied on different synthetic series the behaviour of which is well defined. Exception made of the random series, all the other tested series show a significant serial correlation. The first one is a simple random one built with a function of a package. It is composed by 50 different elements the values of which are calculated from 0 to 20. This initial series has also been used as random component for the other ones.

4.1. Simple random series

In this case, the two tests give no significant values. The curves of $u(t)$ and $u'(t)$ are mixed up.

4.2. Series with an abrupt change in the middle
In the case of such a series, the Pettitt statistic has a negative extreme value for an increasing abrupt change and a positive one for a decreasing one. The Pettitt

test applied to the two subseries shows no significant value. The position t of the extreme value corresponds at the change. If the change occurs after the value i in a series of n values, the extreme is placed in i . The series $u(i)$ of the onward application of the Mann test shows stability up to i=t and increasing (or decreasing) values of $u(i)$ for i>t. Similarly the series $u'(i)$ of the backward application shows stability from i=n to t+1 and increasing (or decreasing) values for i<t+1.

4.3. Series showing an abrupt change after the first third of the series
This case presents the same characteristic as the preceding one. The point of the change is correctly situated.

4.4. Series showing two opposite abrupt changes
The Pettitt test gives two significant values at the two change-points. The application of this test to the three subseries limited by the change-points gives no more any significant value for the Mann test, the onward curve shows a stable series up to the first change, and the same is found for the backward curve from the second change to the end of the series. In this case the Pettitt test and the Mann test show that the middle series is also stable.

4.5. Series showing two successive abrupt changes
The Pettitt curve shows anything particular : between the two changes, it shows a plateau more or less stable. The extreme value is situated in the middle of this plateau. The Pettitt test applied to the two subseries gives significant value at the two change-points. The onward Mann curve shows a stable subseries up to the first change-point and the backward curve a stable subseries from the second change-point and the end of the series.
Applying Mann and Pettitt tests to each of the three subseries conclude to their stability.

4.6. Series showing an increasing part between two stable ones
Pettitt test gives a significant value in the middle of the series, whereas the Mann test has the same characteristics as the precedent case. As the stable parts given by the Mann test coincide with these given by the Pettitt test, we must investigate the behaviour of the central part of the series.

4.7. Increasing series
If the case of an increasing series, the Pettitt test provides a significant value in its middle, the curve having a more parabolic form. The Mann test shows no stable part. The graph of the deviation of the mean shows a trend. We must then determine the parameters of the linear regression and determine their significant character.

4.8. Series showing a stable part followed by an increasing one
The Pettitt test shows a significant value in its middle. The curve has not a V form but a parabola one. The Mann test shows a stable part in its onward part but no stability appears in its backward one. On the basis of the result of the Mann test the series is divided into two subseries and the Pettitt test is applied again on these two subseries. The second part show the same behaviour as 4.7.

4.9. Series showing an increasing (decreasing) part followed by a decreasing (increasing) one
The Pettitt test may show no, one or two significant values. The ones which are not significant, have a near critical value. The Pettitt curve has a sinusoidal form. The extreme values of Pettitt curve are situated in the middle of the increasing and decreasing parts. The Mann test shows no stable part and no significant value at the end of the series, but well inside the series.
In no case neither the Mann nor the Pettitt test give the correct solution of the actual evolution. However advantage may be taken from the graph of the deviations of the mean which suggests an increasing (linear) trend followed by a decreasing one. Estimation by least squares remains a possibility for determining an acceptable solution.

5. Application of the method on a climatological series
In order to give a practical application of this method, the series of the annual averages of air temperature at Brussels-Uccle has been considered. Its last study (Sneyers et all, 1989) concluded to a stable part between 1833 and 1910, a progressive one between 1910 an 1933 and finally a stable part between 1934 and 1988. The present application has been made with data extended to 1994.
The application of Pettitt gives a stable part up to 1909. The investigation of the backward curve of the Mann test shows a discontinuity in 1987.
In order to investigate more carefully the period 1910 to 1994, the complete methodology has been applied to this series. Pettitt curve appears to be similarly to that found for a series having two change in the same way (4.5.). The two changes are situated in 1942 for the first one and 1987 for

the second one. Moreover the subseries 1833-1909, 1910-1942, 1943-1987, 1988-1994 are random. The mean of each subseries are respectively 8.8, 9.5, 9.7 and 10.7. The difference of the two subseries 1910-1942 and 1943-1987 seems to be less important but a Student test after normality verification of the subseries shows that the difference between the two means is significant at level 0.05. The same verification applied to the two subseries 1943-1987 and 1988-1994 has the same conclusion.

6. Conclusion

This method will permit to study long time series in the aim either to find the heterogeneities, or, in the case of a homogeneous series, to find the climate changes. We can moreover distinguish between several behaviours that can be present in climatological series.

References

Anderson, R.L., 1942 : Distribution of the serial correlation coefficient. Ann. Math. Statist., 13, 1.

Coops A.J.,1992 : Analysis of temperature series in Europe in relation to the detection of enhanced greenhouse effect., Theor. Appl. Climatol. 46, 86-98.

Demarée, G., 1990 : Did au abrupt global climate warming occur in the 1920 ? - In : Contribution à l'étude des changements de climat - Inst. Roy. Météorol. de Belgique, Publ. Série A, 124, 80 p.

Kendall, M.G., 1938 : A new measure of rank correlation. Biometrika, 30, 81-93.Wald, A. and Walfowitz, J., 1943 : An exact test for randomness in the non parametric case based on serial correlation. Ann. Math. Statist. 14, 378-388.

Mann, H.B., 1945 : Non parametric test against trend. Econometrika, 13, 245-259.

Pettitt, A.N., 1979 : A non parametric approach to the change-point problem. Appl. Statis., 28, 126-135.

Sneyers, R., 1975 : Sur l'analyse statistique des séries d'observations. Note Techn. 143, Organisation Météorologique Mondiale, Genève, 192 p.

Sneyers, R., Vandiepenbeeck, M., Van Lierde, R. and Demarée, G., 1989 : Climatic changes in Belgium appearing from the homogenized series of observations made in Brussel-Uccle (1833-1988). In : Contribution à l'étude des changements de climat - Inst. Roy. Météorol. de Belgique, Publ. Série A, n° 124, 80 p.

Sneyers, R, 1992 : Use and misuse of statistical methods for the detection of climate. Preprint, American Meteorological Society, 12th Conference on probability and statistics in the Atmospheric Sciences, 22-26 June 1992, Toronto Canada, pp J76-J81.

Snijders, T.A.B., 1983 : A study of the variability in space and time of Upper Volta rainfall., Meteorological Meeting on Statistical Climatology, sep 26-30, 1983, Lisboa, Portugal.

Vanitsem S. and Demarée G., 1991 : Détection et modélisation des sécheresses au Sahel. Proposition d'une méthodologie., Hydrol. continent., vol. 6, n° 2, 155-171.

Wald, A. And Wolfowitz, J., 1943 : An exact test for randomness in the non parametric case based on serial correlation. Ann. Math. Statist., 14, 378-388.

CORRESPONDING AUTHOR

M. Vandiepenbeeck,
Institut Royal Météorologique
Av Circulaire, 3
B - 1180 Bruxelles, Belgium

Optimal Estimation of the Spherical Harmonic Components of the Surface Air Temperature

Samuel S. Shen
University of Alberta, Edmonton, CANADA T6G 2G1

Gerald R. North and Kwang-Y. Kim
Texas A&M University, College Station, TX 77843, U.S.A.

ABSTRACT

This paper provides a method to calculate the mean squared error (MSE) when estimating the spherical harmonic components of the surface air temperature field by a network of N stations. The MSE is minimized by choosing an optimal weight for each station. Based upon the homogeneous noise forced linear energy balance model, we conclude that: with about 60 reasonably positioned stations for sampling the spherical harmonic components T_{00}, T_{10} and T_{11}, one can get the sampling error below 10% when the optimal weights are applied.

1 INTRODUCTION

The field of surface air temperature anomalies is not distributed uniformly. The global average explains only the lowest mode of the climate variations. To explain hemispherical and regional climate variations, it is necessary to describe the features of smaller length scales of the temperature anomaly field. A systematic way to delineate this uneven distribution is to use spherical harmonics, i.e., to express the temperature anomaly field in terms of the series sum of spherical harmonic functions. While the zeroth order spherical harmonic component corresponds to the global mean temperature, the higher order components consist of contributions from finer scale climate variations.

It is obvious that accurate estimation of the higher order spherical components is essential to evaluate regional climate variation. To appraise the accuracy of a scheme computing regional averages and variances of temperature anomalies from observational data, one necessarily needs to estimate the sampling error. The purpose of this paper is to provide a method of calculating such an error when estimating various orders of spherical harmonic components from measurement data. A distinguishing feature of the paper is its use of optimal weights, which can substantially reduce the sampling error computed from the use of uniform weights (Shen, et al., 1994).

We regard Earth as a perfect sphere of unit radius. Let the surface air temperature field be denoted by $T(\hat{\mathbf{n}})$, where $\hat{\mathbf{n}} = (\cos\phi\cos\theta, \cos\phi\sin\theta, \sin\phi)$ is unit vector pointing from the sphere's center to the point in question, and ϕ and θ are latitude and longitude respectively. The function $T(\hat{\mathbf{n}})$ can be expanded into spherical harmonics Y_{lm}:

$$T(\hat{\mathbf{n}}) = \sum_{l=0}^{\infty} \sum_{m=-l}^{l} T_{lm} Y_{lm}(\hat{\mathbf{n}}). \tag{1}$$

The spherical harmonic components T_{lm} are determined by

$$T_{lm} = \int_{4\pi} d\Omega\, T(\hat{\mathbf{n}}) Y^*_{lm}(\hat{\mathbf{n}}), \tag{2}$$

where Y^*_{lm} is the complex conjugate of Y_{lm}.

The global average temperature is reflected in the amplitude of the zeroth order spherical harmonic. The relationship between the zeroth order spherical harmonic component T_{00} and the global average $\bar{T}$ is

$$T_{00} = \frac{1}{\sqrt{4\pi}} \int_{4\pi} d\Omega\, T(\hat{\mathbf{n}}) = \sqrt{4\pi}\bar{T}, \tag{3}$$

where the global average is given by

$$\bar{T} = \frac{1}{4\pi} \int_{4\pi} d\Omega\, T(\hat{\mathbf{n}}). \tag{4}$$

2 THE FORMULATION OF MSE

The homogeneity assumption leads to

$$\langle T(\hat{\mathbf{n}}) T(\hat{\mathbf{n}}') \rangle = \sigma^2\, \rho(\hat{\mathbf{n}} \cdot \hat{\mathbf{n}}'), \tag{5}$$

$$\sigma^2 = \langle T^2(\hat{\mathbf{n}}) \rangle = \text{constant variance}, \tag{6}$$

where $\langle \cdot \rangle$ denotes the ensemble average.

An important consequence of the homogeneity assumption is that the spectra of the covariance field consist only of the coefficients of the Fourier-Legendre series of the function $\rho(x)$:

$$\rho_n = \frac{1}{2} \int_{-1}^{1} dx\, \rho(x) P_n(x), \quad (n = 0, 1, 2, 3, \cdots). \tag{7}$$

Correspondingly, the correlation function ρ is expressed in a series sum of Legendre polynomials:

$$\rho(x) = \sum_{n=0}^{\infty} (2n+1)\, \rho_n\, P_n(x). \tag{8}$$

For real climate, the temperature field is not homogeneous. Consequently, the spectra are not merely the Fourier-Legendre coefficients ρ_n and EOFs should be used, as remarked earlier in section 1. However, at very low frequencies, experience with models suggests that the homogeneity assumption applies at least qualitatively.

We use the data from N stations at points $\hat{\mathbf{n}}_1$, $\hat{\mathbf{n}}_2$, $\cdots$, $\hat{\mathbf{n}}_N$ to estimate the spherical harmonic component T_{lm} defined by (2). The linear estimator is

$$\hat{T}_{lm} = \sum_{j=1}^{N} w_j^{(lm)} T(\hat{\mathbf{n}}_j) Y_{lm}^*(\hat{\mathbf{n}}_j), \tag{9}$$

where $T(\hat{\mathbf{n}})$ is the anomaly field and $w_j^{(lm)}$ $(j = 1, 2, \cdots, N)$ are the real-valued weights and satisfy the no-bias condition

$$\sum_{j=1}^{N} w_j^{(lm)} = 4\pi. \tag{10}$$

The MSE for estimating T_{lm} is

$$\epsilon_{(lm)}^2 = \langle |T_{lm} - \hat{T}_{lm}|^2 \rangle. \tag{11}$$

Using estimation (9) and formula (2), further expansion of the last formula results in

$$\begin{aligned}
\epsilon_{(lm)}^2 &= \langle T_{lm} T_{lm}^* \rangle - 2\Re\left(\langle T_{lm} \hat{T}_{lm}^* \rangle\right) + \langle \hat{T}_{lm} \hat{T}_{lm}^* \rangle \\
&= \sigma^2 \Big[\int_{4\pi} d\Omega \int_{4\pi} d\Omega' \, \rho(\hat{\mathbf{n}} \cdot \hat{\mathbf{n}}') \, Y_{lm}^*(\hat{\mathbf{n}}) Y_{lm}(\hat{\mathbf{n}}') \\
&\quad - 2\Re\Big(\sum_{j=1}^{N} w_j^{(lm)} Y_{lm}(\hat{\mathbf{n}}_j) \int_{4\pi} d\Omega \, \rho(\hat{\mathbf{n}} \cdot \hat{\mathbf{n}}_j) \, Y_{lm}^*(\hat{\mathbf{n}}) \Big) \\
&\quad + \sum_{i,j=1}^{N} w_i^{(lm)} w_j^{(lm)} \rho(\hat{\mathbf{n}}_i \cdot \hat{\mathbf{n}}_j) \, Y_{lm}^*(\hat{\mathbf{n}}_i) Y_{lm}(\hat{\mathbf{n}}_j) \Big],
\end{aligned} \tag{12}$$

where $\Re(\cdot)$ denotes the real part.

The addition theorem and the orthogonality property of spherical harmonics are useful for us to simplify the expression for MSE (12) (Arfken, 1985):

$$P_n(\hat{\mathbf{n}} \cdot \hat{\mathbf{n}}') = \frac{4\pi}{2n+1} \sum_{k=-n}^{n} Y_{nk}(\hat{\mathbf{n}}) Y_{nk}^*(\hat{\mathbf{n}}'), \tag{13}$$

$$\int_{4\pi} d\Omega \, Y_{lm}(\hat{\mathbf{n}}) Y_{nk}^*(\hat{\mathbf{n}}) = \delta_{ln}\delta_{mk}, \tag{14}$$

where δ is the Kronecker delta. Then the expression (12) can be reduced to

$$\begin{aligned}
\frac{\epsilon_{(lm)}^2}{4\pi\sigma^2} &= \sum_{n=0}^{\infty} (2n+1)\rho_n \frac{1}{4\pi} \sum_{i,j=1}^{N} w_i^{(lm)} w_j^{(lm)} \\
&\quad \times P_n(\hat{\mathbf{n}}_i \cdot \hat{\mathbf{n}}_j) Y_{lm}^*(\hat{\mathbf{n}}_i) Y_{lm}(\hat{\mathbf{n}}_j) \\
&\quad + \rho_l \left(1 - 2 \sum_{j=1}^{N} w_j^{(lm)} |Y_{lm}(\hat{\mathbf{n}}_j)|^2 \right).
\end{aligned} \tag{15}$$

Thus, the sampling error is explicitly expressed in terms of a series sum of spectral components whose coefficients are functions of the positions and weights of the stations. And the spectra ρ_n $(n = 0, 1, 2, \cdots)$ can be obtained from either the observation data or a climate model (GCM or simple models). For the simple noise forced linear energy balance model, the detailed calculations of the spectra are given in section 4.

3 RANDOM DISTRIBUTION OF STATIONS

Historically, the positions of the measurement stations were not planned. Instead, they were irregularly distributed over the earth surface, mostly on land. Let us consider the case that the stations are randomly distributed. The simplest possible case is the uniform distribution of the stations, and these stations are independent. Namely, the probability distribution function $\wp(\hat{\mathbf{n}}_1, \hat{\mathbf{n}}_2, \cdots, \hat{\mathbf{n}}_N)$ has the following properties:

$$\wp(\hat{\mathbf{n}}_1, \hat{\mathbf{n}}_2, \cdots, \hat{\mathbf{n}}_N) = \wp(\hat{\mathbf{n}}_1)\wp(\hat{\mathbf{n}}_2) \cdots \wp(\hat{\mathbf{n}}_N) \tag{16}$$

$$\wp(\hat{\mathbf{n}}_j) = \frac{1}{4\pi} \quad (j = 1, 2, \cdots, N). \tag{17}$$

Since $\hat{\mathbf{n}}_1$, $\hat{\mathbf{n}}_2$, $\cdots$, $\hat{\mathbf{n}}_N$ are random variables, the MSE given by the formula for fixed station positions is a function of these variables, $\epsilon_{(lm)}^2(\hat{\mathbf{n}}_1, \hat{\mathbf{n}}_2, \cdots, \hat{\mathbf{n}}_N)$. We are now interested in the expectation value $E_{(lm)}^2$ of $\epsilon_{(lm)}^2(\hat{\mathbf{n}}_1, \hat{\mathbf{n}}_2, \cdots, \hat{\mathbf{n}}_N)$:

$$\begin{aligned}
E_{(lm)}^2 &= \int d\Omega_1 \cdots \int d\Omega_N \, \epsilon_{(lm)}^2(\hat{\mathbf{n}}_1, \cdots, \hat{\mathbf{n}}_N) \\
&\quad \times \wp(\hat{\mathbf{n}}_1, \cdots, \hat{\mathbf{n}}_N).
\end{aligned} \tag{18}$$

From (15) with uniform weighting, after some algebraic manipulations, one can obtain

$$\frac{E_{(lm)}^2}{4\pi\sigma^2} = \frac{1 - \rho_l}{N} \tag{19}$$

4 THE EBM SPECTRA

In the above two sections, MSE formulas for both N fixed stations and N randomly and uniformly distributed stations are obtained. Yet, in order to get numerical output, one has to know the values of ρ_n, which can be found by using either a climate model or real data. Here we consider the case of climate model which is a time independent white noise forced linear energy balance model given by

$$-\lambda_0^2 \nabla^2 T(\hat{\mathbf{n}}) + T(\hat{\mathbf{n}}) = F(\hat{\mathbf{n}}) \tag{20}$$

The spherical harmonic expansion for $F(\hat{\mathbf{n}})$ is

$$F(\hat{\mathbf{n}}) = \sum_{l=0}^{\infty} \sum_{m=-l}^{l} F_{lm} Y_{lm}(\hat{\mathbf{n}}). \tag{21}$$

The white noise forcing yields that

$$\langle F_{lm} F_{l'm'}^* \rangle = \sigma_F^2 \delta_{ll'} \delta_{mm'} \tag{22}$$

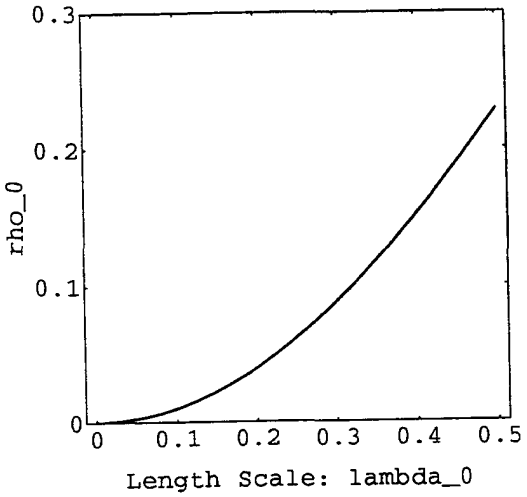


Figure 1: The relationship between the length scale λ_0 and the zeroth order Fourier-Legendre coefficient ρ_0 of the correlation function $\rho(x)$.

Then we can derive that

$$\rho_n = \frac{\sigma_F^2/4\pi\sigma^2}{[1+\lambda_0^2 n(n+1)]^2}, \quad n = 0, 1, \cdots, \tag{23}$$

$$\frac{\sigma_F^2}{4\pi\sigma^2} = \frac{1}{\sum_{n=0}^{\infty} \frac{2n+1}{[1+\lambda_0^2 n(n+1)]^2}}. \tag{24}$$

Hence $\rho_0 = \sigma_F^2/4\pi\sigma^2$ is only a function of the length scale λ_0. The larger the λ_0 is, the more variance is explained by the spectral component ρ_0. Fig. 1 shows the relationship between ρ_0 and λ_0, which, of course, is a monotonically increasing function. The value of λ_0 is determined by the length scale of the anomaly field. For the annual mean field, EBM length scale is about 2000 km (Kim and North, 1991; Hansen and Lebedeff, 1987). If we take the radius of the earth to be 6367 km, λ_0 takes the value: $2000/6367 = 0.3141$. The corresponding ρ_0 is 0.0954. Thus, the zeroth order spectral component ρ_0 explains about 10% of the low frequency point variance of the surface air temperature.

To evaluate the effectiveness of a network, it is common to use either a variance signal-noise ratio or percentage of total variance explained by sampling error variance which are defined respectively by:

$$\Lambda_{(lm)}^{[N]} = \frac{\langle |T_{lm}|^2 \rangle}{\langle |\hat{T}_{lm} - T_{lm}|^2 \rangle} = \frac{\sigma_{(lm)}^2}{\epsilon_{(lm)}^2}, \tag{25}$$

$$V_{(lm)}^{[N]} = \frac{\epsilon_{(lm)}^2}{\epsilon_{(lm)}^2 + \sigma_{(lm)}^2} \times 100\%. \tag{26}$$

5 COMPUTATION OF OPTIMAL WEIGHTS

In the discussion of section 2, we took all the weights to be equal. Obviously, we do not have to choose this method. For a given network of stations, it is clear that the best way is to choose the values of the weights in such a way that the sampling error becomes minimum. These weights are called the optimal weights. Therefore, we are going to minimize $\epsilon_{(lm)}^2$ determined by (15) under the no-bias condition (10). The Lagarange function is

$$J[w_1^{(lm)}, w_2^{(lm)}, \cdots, w_N^{(lm)}] = \epsilon_{(lm)}^2/\sigma_{(lm)}^2 + 2\Lambda \left(4\pi - \sum_{i=1}^{N} w_i^{(lm)}\right), \tag{27}$$

where Λ is the Lagarange multiplier. Then the conditions

$$\frac{\partial J}{\partial w_j^{(lm)}} = 0, \quad (j = 1, 2, \cdots, N) \tag{28}$$

and the no-bias condition result in the following linear equations:

$$\sum_{i=1}^{N} w_i^{(lm)} \left[\sum_{n=0}^{\infty} (2n+1)\rho_n P_n(\hat{\mathbf{n}}_i \cdot \hat{\mathbf{n}}_j)\right] \times \Re\left(Y_{lm}^*(\hat{\mathbf{n}}_i) Y_{lm}(\hat{\mathbf{n}}_j)\right) - \Lambda = 4\pi\rho_l |Y_{lm}(\hat{\mathbf{n}}_j)|^2, \quad (j = 1, 2, \cdots, N), \tag{29}$$

$$\sum_{i=1}^{N} w_i^{(lm)} = 4\pi. \tag{30}$$

Hence, for a given network of stations, one can solve the above $N+1$ linear equations to find the optimal weights $w_1^{(lm)}, w_2^{(lm)}, \cdots, w_N^{(lm)}$, and Λ. With these optimal weights, one can use formula (15) to find the minimum sampling error.

6 NUMERICAL EXAMPLES

With the development of physical intuition and mathematical formulation so far, we proceed to networks of many stations. It appears that it is not possible to find an analytic expression for the sum of the infinite series (15), when there are many stations, even for uniform weighting. Therefore, we carried out numerical computations. The numerical results for both the optimal weights and the uniform weights are included in Table 1. In this numerical test, we considered four different networks. Caution needs to be taken to avoid the stations located on the node lines of the spherical harmonic functions Y_{lm}'s, since on the node lines the spherical harmonic functions Y_{lm} vanish and hence the linear equations (29) and (30) do not have a unique solution. For instance, we do not put stations on the equator or poles.

Net I consists of four rings of six stations at latitudes: 50°S, 15°S, 15°N, and 50°N and longitudes: 150°W, 90°W, 30°W, 30°E, 90°E, and 150°E. Net II consists of eight rings of eight stations and it equally partitions the latitude-longitude map. The first column of stations are on the 157.5°W longitude line. Net III has 62 stations. It is the commonly referred Angell-Korshover network determined by WMO in

Table 1. Percentage sampling error (V) and signal-to-noise ratio (Λ) in estimating the first ten spherical harmonic components using four different networks. Listed are two sets of experiments with optimal weighting scheme and uniform weighting scheme (in parenthesis), respectively.

	Net I N=24	Net II N=64	AK Net N=62	Net IV N=210
$V_{(00)}$	10 (10)	3.0 (15)	4.0 (11)	0.3 (13)
$\Lambda_{(00)}$	8.7 (8.7)	32 (5.9)	24 (8.1)	347 (6.6)
$V_{(10)}$	13 (15)	2.3 (36)	5.0 (23)	0.2 (35)
$\Lambda_{(10)}$	6.5 (5.9)	43 (1.8)	19 (3.4)	439 (1.9)
$V_{(11)}$	15 (15)	5.2 (9.3)	5.8 (10)	0.5 (7.0)
$\Lambda_{(11)}$	5.7 (5.5)	18 (9.7)	16 (8.7)	185 (13)
$V_{(20)}$	27 (27)	5.0 (64)	7.7 (39)	0.6 (63)
$\Lambda_{(20)}$	2.7 (2.7)	19 (0.6)	12 (1.5)	172 (0.6)
$V_{(21)}$	18 (24)	5.6 (7.1)	9.8 (18)	0.6 (3.4)
$\Lambda_{(21)}$	4.5 (3.2)	17 (13)	9.2 (4.5)	160 (29)
$V_{(22)}$	25 (30)	11 (14)	10 (17)	1.1 (8.8)
$\Lambda_{(22)}$	2.9 (2.4)	8.2 (6.3)	8.8 (5.0)	88 (10)
$V_{(30)}$	43 (45)	9.1 (79)	11 (53)	1.0 (79)
$\Lambda_{(30)}$	1.3 (1.2)	9.9 (0.3)	8.4 (0.9)	96 (0.3)
$V_{(31)}$	36 (42)	9.4 (20)	17 (37)	1.1 (14)
$\Lambda_{(31)}$	1.8 (1.4)	9.6 (4.0)	4.9 (1.7)	92 (6.1)
$V_{(32)}$	37 (39)	12 (13)	16 (24)	1.4 (4.8)
$\Lambda_{(32)}$	1.7 (1.6)	7.0 (6.8)	5.3 (3.1)	68 (20)
$V_{(33)}$	40 (55)	22 (22)	18 (29)	2.5 (10)
$\Lambda_{(33)}$	1.5 (0.8)	3.6 (3.5)	4.6 (2.4)	39 (8.8)

1958 (Trenberth and Olson, 1992), with the station on the south pole excluded. Net IV is a $24° \times 12°$ network. The first column of the stations are on the 168°W longitude line. This dense network is designed to estimate the higher order spherical harmonic components. It even samples T_{54} with less than 10% error when the optimal weights are applied.

Table 1 includes the results of the percentage sampling errors and the signal-noise ratios of the first 10 modes for the above four networks. In order to expose the advantage of the optimal weighting scheme, we list the uniform weighting results in parenthesis for comparison. Net I is sparse. The correlation between each pair of stations is small. Hence the optimal weights are pretty close to the optimal weights, and the optimal weighting results are close to the uniform weighting results as shown in the first column of the table. Net II and AK Net are dense enough to show the effectiveness of the optimal weights for reducing the sampling error. The effect of the optimal weighting is more dramatical for the more dense network, Net IV, which can sample the first ten modes with almost no error if the measured data are processed by the optimal weighting scheme.

ACKNOWLEDGEMENTS

The authors gratefully acknowledge support from a grant from the US Department of Energy "Quantitative Links" program. Shen wishes to thank the Environment Canada for a subvention grant by the Atmospheric Environment Service.

REFERENCES

Arfken, G., 1985, "Mathematical Methods for Physics", 3rd ed., Academic Press, San Diego, 985 pp.

Hansen, J., and S. Lebedeff, 1987, "Global trends of measured surface air temperature", *J. Geophys. Res.*, **92**, 13345–13372.

Kim, K.-Y., and G. R. North, 1991, "Surface temperature fluctuations in a stochastic climate model", *J. Geophys. Res.*, **96**, 18573–18580.

Shen, S. S., G. R. North, and K.-Y. Kim, 1994, "Spectral approach to optimal estimation of the global average temperature", *J. Climate*, **7**, 1999–2007.

Trenberth, K. E., and J. G. Olson, 1992, "Representativeness of a 63-station network for depicting climate changes", *Greenhouse-Gas-Induced Climatic Change: A Critical Appraisal of Simulations and Observations*, M. E. Schlesinger, Ed., Elsevier, 249–259.

CORRESPONDING AUTHOR

Samuel S. Shen
Department of Mathematical Sciences
University of Alberta
Edmonton, CANADA T6G 2G1

THE DEVELOPMENT OF CLIMATE DOWNSCALING: TECHNIQUES AND APPLICATIONS

B.C. Hewitson

University of Cape Town, South Africa

ABSTRACT

Downscaling, or translation across scales, attempts to determine local and regional scale parameters in terms of larger scale atmospheric forcing. This concept has direct application in the light of global change and the current need for more detailed temporal and spatial information which General Circulation Models (GCMs), the primary global change tool, have not been able to meet.

Two general categories exist for downscaling techniques, nested models and empirical transfer functions. While nested models are possibly the best long term option this approach is still in develpoment whereas empirical relationships offer a more immediate short term solution. An application to regional climate change scenarios in Africa demonstrate the effectiveness of the technique.

1 INTRODUCTION

The explicit use of the term 'downscaling' in climatological applications has only recently come into wide spread use. Nonetheless, in concept the application of downscaling has been with us for many years in the form of techniques to translate across spatial scales, such as from the synoptic to the regional and local scales. In this context many examples of 'downscaling' may be found in the literature from the early 1970's onward. A significant portion of these applications fall under the class of methodologies often called 'synoptic climatology'. This has the explicit objective of relating local and regional parameters to synoptic forcing and is usually in terms of the synoptic scale circulation, or more explicitly, daily circulation *types*.

While such empirical techniques have been used successfully in many diverse applications, they all suffer in one degree or another from generalizing the atmospheric forcing. For example, many techniques use some form of circulation pattern classification to create weather types. The underlying assumption here is that similar weather patterns produce similar regional climatic conditions. Although in general this may be true, for example, cold fronts produce cold frontal conditions, nonetheless cold fronts may differ substantially from one to another. The over-generalizing of the circulation into a finite range of types thus looses power to distinguish finer detail.

Notwithstanding the fundamental difficulties in even the actual typing or classification procedure, attempts have been made to circumvent the problem of an over-generalized relationship by using such solutions as a stochastic model to describe the link between weather patterns and local climate (e.g.: Bardossy, 1994). These approaches, although a significant improvement, still have at their core a generalizing of the weather patterns into a finite number of types.

An alternative path pursued in downscaling has been to generalize along another dimension, that of time. In this case one looks for relationships between the mean state of the atmosphere and the mean response at, say, seasonal time scales. This approach can be informative and has special application in seasonal forecasting. However, in applications where information on finer temporal scales is desired there remains a difficulty.

Given that the state of the atmosphere is a continuously changing function and not a finite set of discrete states, it would seem desirable to develop methodologies that relate a variable of interest at the local scale to the atmospheric forcing in a similar continuous manner. Two approaches are possible, to downscale with the use of a dynamic model 'nested' within the coarser resolution large scale circulation fields, or alternatively to derive quantitative continuous functions between circulation state and ones variable of interest.

2 GLOBAL CHANGE & DOWNSCALING

Global change reseaqrch has proved to be a major incentive in the development of downscaling techniques. In global change research the primary tool of investigation is the GCM, unfortunately GCMs have finite resolutions which are relatively coarse. This grid resolution, a *minimum scale*, is furthermore the scale at which GCMs are the most inaccurate and is substantially removed from the relative *skillful scale* of the model (von Storch et al., 1993). In many cases the skillful scale of the GCM may only be realized when taken over a number of grid cells (Grotch and MacCracken, 1991). Here downscaling would seem to offer an especially useful service to attain more detailed regional information from the GCM.

Nonetheless, while downscaling in concept is a suitable solution, in global change impacts research what is most often needed is precisely the detail missed by the more traditional empirical downscaling techniques. For example, while GCM accuracy decreases as spatial scales become finer, in hydrological applications one usually needs *increasing* detail as spatial scales become finer -- such as increasing detail at catchment basin scale on individual rainfall events to determine runoff and storage. It is in response to this need that downscaling methodologies need to be improved.

In particular, it is with regard to precipitation that detailed downscaling is needed. Flood, drought, storage and resources depend on knowledge of the frequency, timing, persistence, and intensity of precipitation. Conversely, while one of the major financial inputs to global change research is in the development of GCMs, it is precipitation that is most often the poorly simulated parameter. GCMs do, however, produce reasonable simulations of the synoptic scale circulation, and it is this fact that can be explicitly exploited by downscaling.

3 NESTED MODEL DOWNSCALING

Perhaps the most fruitful long term avenue of downscaling research is that of nested models. The typical application in this case is to drive a regional dynamic model at mesoscale or finer resolutions with the synoptic and larger scale information from a GCM (e.g.: Giorgi and Mearns, 1991). In such applications detailed information at spatial scales down to 20 km may be achieved, and at temporal scales of hours or less.

However, such models are computationally demanding and are thus not an easily accessible research avenue. Furthermore, there are still difficulties to be overcome in the interface between the GCM and the nested model. For example, how to relate the coarse resolution grid cell data of the GCM (often below the GCM skill scale) to boundary conditions for the far finer scale nested model. Nonetheless, in terms of meeting the long term needs this technique is likely to be the best solution and needs to be encouraged.

To date nearly all nested model applications have been in the northern hemisphere western nations. However, in order to meet the needs of global change impacts research in the developing nations (which are at the same time the nations most vulnerable to global change) one must in the short term turn to other methods.

4 EMPIRICAL DOWNSCALING

In the alternative approach of empirical downscaling one seeks to derive quantitative relations between circulation and local climate in some form of $y = f(x)$. In this case the relationship is derived based on observational data sets and then used with GCM circulation data to generate local scale information *consistent* with the synoptic scale forcing. The approach hinges on three basic premises:

- that the local scale parameter is dominantly a function of synoptic forcing,
- that the GCM circulation used to drive the derived relationship is valid at the synoptic scale,
- that the relationship derived using observed data remains valid under a $2xCO_2$ atmosphere.

The first premise is implicitly tested in the derivation of a relationship while the second is the subject of much ongoing research and has a number of procedures to draw on (e.g.: Hewitson and Crane, 1992) and will not be discussed in detail here. The third premise, that the relationship holds under a $2xCO_2$ atmosphere is the most difficult to justify. However, given that basic dynamics are not about to be transformed, it would seem a reasonable assumption. The major caveat in

this regard is in the case of precipitation where if the atmospheric water vapour content were to be dramatically altered the relationship may significantly change. Nevertheless, if the primary atmospheric response will be in terms of changes of persistence, intensity, and frequency of synoptic circulation events (as seems likely), then the third premise may be accepted, at least in the interim.

A important additional benefit of downscaling in GCMs is one of GCM validation. Through the application of transfer functions (derived off observed data) to GCM data one implicitly tests the internal cross-scale consistency of the GCM. Particular products that may be derived are for example, information on the seasonal timing of synoptic forcing, intraseasonal variability, and data consistent with the circulation for variables that may then be compared to the data produced by the GCM itself.

A number of applications have been undertaken with empirical downscaling (e.g.: von Storch, 1992; Hewitson and Crane, 1992), and the results appear promising. The remainder of this paper will thus focus on an implementation of regional precipitation downscaling from GCMs.

5 PRECIPITATION DOWNSCALING

In downscaling a number of choices may be made about the spatial and temporal scales to be used. In terms of deriving a relationship of the form $y = f(x)$, the atmosphere forms the independent variable whose scale needs to be large enough to capture the synoptic forcing features which are represented by the GCM. However, in the case of the independent variable, in this example precipitation, one can choose to work on a wide range of scales from, say, the catchment basin scale, up to perhaps the scale of the GCM grid cell. Similarly, one may choose to use temporal scales ranging from daily to seasonal. Obviously the finer the spatial or temporal scales the more local effects will be an influence and the less clear will be the synoptic forcing.

In this example a relatively coarse spatial scale of 2.5° is selected for a first look at regional climates, and a temporal scale of intraseasonal variation using 15-day smoothed data. The region for analysis is southern Africa, of particular interest due to it's high variability of precipitation, shortage of water resources, vulnerability to climate change, and sharp topographic and climatic boundaries. The rainfall over the region includes both convective rainfall as well rain from mid-latitude cyclones. The observed data used for deriving the downscaling relationships precipitation data, Sea Level Pressure (SLP) fields, and 500hPa fields from the GSFC assimilation of global observed data. The GCM data are from the Genesis GCM, a derivative of the NCAR CCM incorporating a 2° x 2° land surface model and multilayer soil and ice models.

The methodology employed is as follows:

- validation of the GCM circulation fields using Principal Components Analysis (PCA).
- derivation of downscaling functions for each 0.5° grid location using Artificial Neural Nets (ANNs).
- Validation of the derived relationships by generating regional precipitation from the observed circulation and comparing with the observed precipitation.
- Deriving regional precipitation from the GCM control simulation circulation data and comparing with observed precipitation -- a GCM validation procedure.
- Deriving regional precipitation from the $2xCO_2$ simulation circulation. This is then differenced from precipitation derived off the control simulation circulation to generate regional climate change scenarios consistent with changes in synoptic forcing under a doubled CO_2 atmosphere.

The procedures used demonstrate that accurate relationships may be derived between the synoptic scale forcing and the regional precipitation. In particular the phase of precipitation events are well captured in both convective and mid-latitude regimes, as well as the seasonal boundaries and intra-seasonal variations. Precipitation derived from the GCM control simulation circulation demonstrates that the synoptic forcing of the GCM is substantially correct with some regional error. Of perhaps more significance is that the circulation derived precipitation indicates a particular problem with the timing of the seasonal boundaries in the model. Application of the $2xCO_2$ simulation circulation generates regional climate change scenarios which indicate primarily a drying in

the eastern portion of the summer rainfall region with an extension of the summer rains southward, and beginning earlier in the season.

6 CONCLUSIONS

Downscaling, while implicitly present in many applications in the past, has developed to address the needs of the climate change research issues. In particular methodologies are developing that allows the derivation of information at scales finer than both GCM skill resolution and GCM physical resolution. While nested model techniques are likely to provide the best downscaling information in the long term, immediate needs may be addressed satisfactorily with empirical methods.

References

Bardossy A., 1994, "Downscaling from GCMs to local climate through stochastic linkages", in Climate Change, Uncertainty, and Decision-Making (G. Paoli, ed.), University of Waterloo, 29-45.

Grotch S.L., MacCracken, M.C., 1991, "The use of general circulation models to predict regional climatic change, J. Climate, 4:286-303.

Giorgi F., Mearns L.O., 1991, "Approaches to simulation of regional climate change: A review", Reviews of Geophysics, 29: 191-216

Hewitson B.C., Crane R.G., 1992, "Regional-scale climate prediction from the GISS GCM", Palaeogeography, Palaeoclimatology, Palaeoecology (Global and Planetary Change Section), 97: 249-267.

von Storch H., Zorita E., Cubasch U., 1992, "Downscaling of global climate change estimates to regional scales: An application to Iberian rainfall in wintertime", J. of Climate, 1993, 6: 1161-1171.

ACKNOWLEDGMENTS

The Earth System Science Center at the Penn State University and the Water Research Commission of south Africa are gratefully acknowledged for their assistance.

CORRESPONDING AUTHOR

Dr. B.C. Hewitson
Dept. Environmental and Geographical Science
University of Cape Town
Private Bag
Rondebosch 7700
SOUTH AFRICA

Statistical-dynamical downscaling of global climate simulations

Ursula Fuentes,Vladimir Sept, Dietrich Heimann, Robert Sausen
DLR,Institut für Physik der Atmosphäre

ABSTRACT

A statistical-dynamical downscaling procedure for global climate simulations is presented. The method is based on a separation of large-scale atmospheric fields into several classes of weather situations. For each of the classes one mesoscale simulation is performed, so that the regional climate is given by the mesoscale model output distributions, weighted with the frequencies of the classes corresponding to the global climate. The procedure is applied to the Alpine region. First results of the verification of the regionalization method are shown. Verification is based on an application of the downscaling method to global ECMWF analysis data and subsequent comparison of the regional model results with local SYNOP station observations.

INTRODUCTION

The spatial resolution of global circulation models (GCM) used for climate simulation is limited to the order of some 500 km. Hence present GCM's are inadequate to represent the mesoscale modifications of large-scale flow fields, especially in a mountainous region like the Alpine one. The flow over mountains, effects as valley wind systems or land-sea breezes are characteristic climatic features of a size which is far beyond the resolution of current GCMs.

Several alternative methods are presently discussed in order to incorporate regional scale phenomena into climate simulation Giorgi,Mearns (1991).

The statistical-empirical methods use regional and global observations and derive statistical relations between regional-scale anomalies and corresponding anomalies on a scale large enough to be resolved by GCMs. The dynamical or nesting method provides a regional fine mesh model being embedded in a global model for a certain region. It is time dependently driven by the global model, so that its computational expense is large. The nesting method is therefore mainly applied to short periods (some months).

The statistical-dynamical downscaling method presented here also uses regional model simulations, but it requires significantly less computer resources than the nesting method without being restricted to short periods. This approach links global and regional model simulations using statistics about large-scale weather situations. The regional model is operated once for each weather situation without being permanently forced by the global model. This method can be applied to climatologically relevant multi-year periods.

A general assumption of this approach is that the climate of a given region (e.g. the Alpine region) is characterized by the frequency distribution of large-scale weather situations: In a changed climate the frequencies of the large-scale events might be altered, but their characteristics are assumed to remain unchanged.

THE DOWNSCALING PROCEDURE

The procedure consists of the following steps (Frey-Buness 1993, Frey-Buness et al. 1995):

1. Each day of a multi-year time series of global simulations (horizontal resolution: 250 to 500 km) is classified into one of about 100 large scale weather situations characteristic for the regional model domain. Presently, classification is based on season, 850 hPa geostrophic wind direction and -speed and on the type of precipitation (stratiform or convective precipitation). Alternative classification schemes based on cluster analysis are in preparation.

2. Regional model simulations are carried out once for each weather class, being initialized with the vertical profiles of geostrophic wind, temperature and humidity corresponding to this class. The regional model calculates the deviations from the basic state (defined by the initial profiles) due to the impact of the internal topography. The simulations are performed with a three-dimensional hydrostatic mesoscale model

which has been sucessfully applied to process studies over the Alpine region with respect to the interaction of fronts and orography (Heimann 1990,1992). The model domain covers the greater Alpine region (1000 x 800 km^2) with a horizontal resolution of 20 km.

3. The mesoscale model output is weighted with the frequency distribution of the classes to give the mesoscale climate (two dimensional fields of frequency distributions of climatological parameters like temperature, wind, precipitation).

Possible results are fine mesh disributions of the probability of regional events and other climatological characteristics like mean values, variances, and extremes.

More formally, let Φ_i and $P(\Phi_i|C)$ with $i = 1 \ldots N$ denote large-scale weather situations and the conditional probabilities for the ocurrance of these situations in a given climate C. In general, $P(\Phi_i|C)$ will be different for different climates C.

In step 1 of our procedure $P(\Phi_i|C)$ is estimated by the relative frequency at which the weather situation Φ_i occurs in a given set of observed or simulated large-scale data which is representative for the climate C.

Next we consider regional events ψ_j with $j = 1 \ldots n$, e.g. a local temperature within a certain range, or the occurance of a thunderstorm.The set $\{\psi_j; j = 1 \ldots n\}$ should be a complete coverage of the type of regional event.

In step 2 we perform one regional-model integration over a sufficiently long simulation time for each weather class Φ_i. We then estimate the conditional probability $P(\psi_j|\Phi_i)$ for the occurance of the regional event ψ_j unter the condition that the large-scale class is Φ_i by the relative frequency of the event ψ_j in the output of the model run forced by Φ_i.

The result of the downscaling procedure is the conditional probability $P(\psi_j|C)$ that the event ψ_j is found in the climate C. It is given by:

$$P(\psi_j|C) = \sum_{i=1}^{N} P(\Phi_i|C) \times P(\psi_j|\Phi_i).$$

VERIFICATION

Any downscaling procedure transmits uncertainties of the global climate simulation to the regional scale. Therefore, the verification of the procedure itself must be based on "perfect" large scale data.

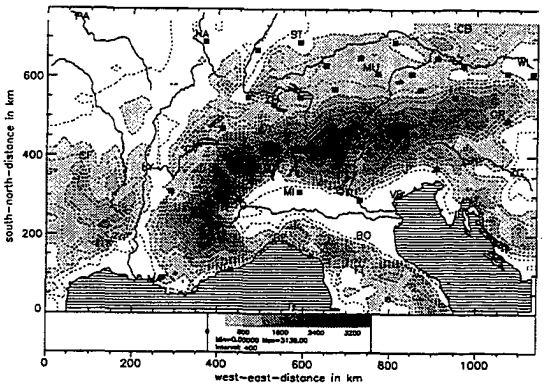


Figure 1: Regional model domain showing the orography, major rivers and places. Also shown: The location of the 30 stations (black boxes).

A set of 10 years (1981 - 1990) of daily (00 UTC) homogenized ECMWF-analysis data on a Gaussian grid of T42-resolution (which is the same horizontal resolution as that of globale climate simulations to which the downscaling is being applied) serves as input to the regionalization method, whereas the output is compared with SYNOP-data from 30 stations (from the same 10 years period) located throughout the regional model domain (see Fig. 1)

Classification

To obtain the weather classes, the ten year time series of ECMWF analysis data was devided on a daily basis into two seasons (winter/summer) and three large-scale precipitation types for each season (dry,convective,stratiform). Thus, situations which admit radiation induced diurnal variations are distinguished from situations with overcast sky and stratiform precipitation. In addition, situations which favour convective precipitation are taken into account seperately.

Dry days were distinguished from days with convective or stratiform precipitation according to the station data, because (in contrast to GCM-simulation results) the ECMWF analysis data do not include precipitation data.

Each of these weather groups was further subdivided according to the geostrophic wind speed and direction at 850 hPa as derived from geopotential at 3 x 4 grid meshes which cover an area almost identical to the regional model domain. Large scale wind direction has been chosen as classification criterion since the orographic impact of irregularly shaped mountains strongly depends on flow direction.

Thus about 50 weather classes for each season were defined. For each of these classes the corresponding frequency and the mean vertical profiles of temperature, geostrophic wind and

humidity with which the regional model simulations are initialized, were computed.

Regional Model Simulations

For the classes which belong to the dry weather groups the regional model simulations extend over a full daily cycle in order to enable the development of thermal circulations. The classes representing large scale precipitation situations, that is overcast sky, agree with regional simulations that end up with a quasi-constant precipitation rate in a stationary flow field after only eight hours of temporal integration.

The precipitation in the regional model is triggered by the prescription of an appropriate supra-scale lifting. This method is, of course, not able to provide absolute amounts of precipitation but allows to determine the regional pattern of the precipitation rate.

The regional model output (two-dimensional fields of distribution of temperature, pressure, wind and precipitation) is stored in hourly intervals, after a spin-up time of four hours, so that 24 values of one regional event are available for the dry weather classes and 5 for the other ones.

As an example for the modification of the prescribed basic state by the regional topography, figure 2 shows the regional frequency distributions of the surface wind direction for the winter half year.

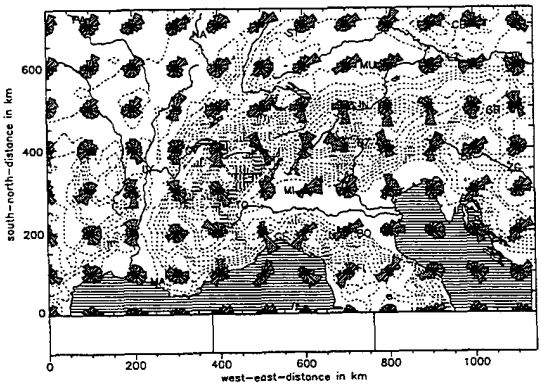


Figure 2: Regional distribution of the wind direction at 10m AGL for winter half year. The frequencies of the sectors are proportional to the length of the area of the beams.

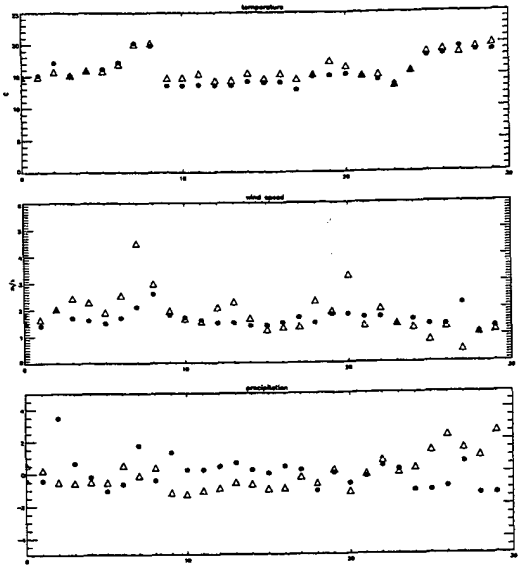


Figure 3: Mean values of temperature, wind speed and precipitation at the location of the thirty stations for summer half year. Precipitation values are standardized. Dots: model data, triangles: observations.

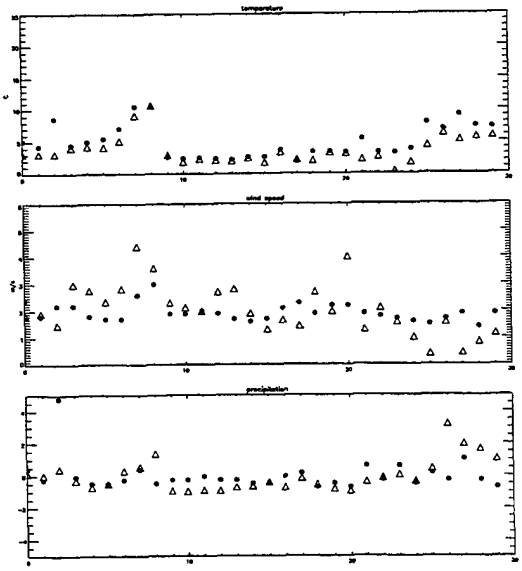


Figure 4: Mean values of temperature, wind speed and precipitation at the location of the thirty stations for winter half year.

Comparison with Observations

For the comparison of the downscaling results with observations at 30 locations throughout the model domain, daily values of temperature, pressure, wind and precipitation 8 times a day for the same ten years period used for classification of ECMWF-analysis data are statistically evaluated corresponding to the statistical evaluation of model results.

Daily values being available, the verification can be performed e.g. for each precipitation type weather group or even for single weather classes seperately.

RESULTS OF VERIFICATION

We discuss here only results for the regional distribution of mean values of temperature, wind speed and precipitation as well as of the distribution of wind direction. Other parameters like variances or extreme values are considered in a later study.

The agreement betwen model results and observations is generally quite good for temperature and wind speed fields (see figures 3,4). Absolute values as well as the regional distribution are fairly well reproduced. The quality of agreement varies between the different weather types (not shown), because the model runs differ concerning inclusion of parametrizations and length of simulations. For some weather groups, a systematic error in temperature was found, the regional distribution being in agreement with observations. For these cases, the temperature profile used to initialize model runs and derived from ECMWF analysis data showed the same systematic error when compared to the corresponding station data for the same time of the day. Thus, one reason for deviations between the model results and observations can be that the "perfect" large scale input data are not totally "perfect".

The results for precipitation, which in fact is a much more critical parameter in models than e.g. temperature, are not as satisfacting. In winter, some features of the regional distribution can be reproduced. (See figure 4.). As noted above, the absolute amounts of precipitation in the model output have no meaning, so that only standardized values are compared, that is, the regional distribution of precipitation rates.

As to the regional frequency distribution of the wind direction (see figure 2), the pointwise comparison of model data with observations does not yield a good agreement (not shown). Nevertheless, one has to bear in mind that wind direction strongly depends on local features on a scale which is not resolved by the model, so that one cannot expect good results from a pointwise verification of this parameter.

OUTLOOK

After being verified, the statistical-dynamical regionalization method will be applied to a control scenario (present day climate) as well as to a climate change scenario simulation (transiently increasing CO_2 concentration) with the coupled atmosphere/ocean model ECHAM/OPYC. A climate change is supposed to lead to a change in the frequency distribution of weather classes, so that the expected regional climate change can be estimated by comparing the regional climate patterns obtained by comparing the mesoscale model results, weighted with the corresponding frequency distributions of weather types.

REFERENCES

- Frey-Buness A., 1993, "Ein statistisch-dynamisches Verfahren zur Regionalisierung globaler Klimasimulationen", DLR-Forschungsbericht DLR-FB 93-47.
- Frey-Buness A., Heimann D., Sausen R.,1995, "A statistical-dynamical downscaling procedure for global climate simulations", Theor. Appl. Climatol. 50, 117-131.
- Giorgi, F., Mearns, L.O., 1991, "Approaches to the simulation of regional climate change: A review", Rev. of Geophys 29, 191 - 216.
- Heimann, D., 1990, "Three-Dimensional Modeling of Cold Fronts Approaching the Alps Including Latent Heat Effects", Meteor. Atmosph. Phys. 42, 197-219.
- Heimann, D., 1992, "Three-Dimensional Modeling of Cold Fronts Interacting with Northern Alpine Foehn", Meteor. Atmosph. Phys. 48, 139-163.

CORRESPONDING AUTHOR

Ursula Fuentes
DLR
Institut für Physik der Atmosphäre
Postfach 1116
82230 Wessling
Germany
e-mail: Ursula.Fuentes@dlr.de

LINKS BETWEEN LOCAL DAILY SURFACE TEMPERATURES AND CONTINENTAL-SCALE CIRCULATION PATTERNS

Radan Huth, Jiří Novotný

Institute of Atmospheric Physics, Praha, Czech Republic

Abstract

Daily surface temperatures in the Czech Republic and Slovakia are most strongly influenced by the intensity of the NAO low-frequency pattern (explaining almost 35% of the total variance). The influence of EU1 and EU2 patterns is also significant though weaker. Synoptic-frequency patterns (with periods between 2.5 and 6 days) do not affect surface temperatures at all. Temperature distributions under different circulation types well differ from one another. Long-lasting events of cold circulation types are shown to be connected with considerable cooling.

1. Introduction

General Circulation Models (GCMs) are still unable to provide regional and local details necessary for many kinds of climate studies. One of possible methods to determine such details, consisting in deriving statistical relationships between large-scale fields and climate features on regional and local scales, is frequently referred to as climate downscaling (Giorgi and Mearns 1991). Particularly, recent attempts have been made to determine daily local surface temperature from mid-tropospheric (500 or 700 hPa) large-scale geopotential height data (Hewitson 1994).

This contribution deals with one aspect of the downscaling problem, viz. with regional variations of links between continental-scale circulation over Europe and local daily temperatures in the Czech Republic and Slovakia during winter.

2. Data

2.1. Circulation

The circulation data are ECMWF analyses of 500 hPa heights at 00 UTC over most of Europe and adjacent part of the Atlantic Ocean (for the area covered see figures) given in a 5 x 7.5° grid. Ten winters (DJF) are available: 1983/84 to 1992/93. The circulation on each day is characterized by circulation types and low- and synoptic-frequency circulation modes.

Five circulation types were determined using the obliquely rotated principal component analysis (PCA) in a T-mode so that each day is classified with just one type (cf. Huth 1993). Mean maps of each type are shown in Fig.1.

Low- and synoptic- frequency variations were extracted by the pointwise application of Blackmon's (1976) filters. The low-pass (bandpass) filter retains periods over 10 (2.5 to 6) days. Circulation modes were uncovered by means of obliquely rotated PCA in an S-mode in both frequency bands. Four low-frequency patterns, corresponding in turn to EU1, NAO, EA and EU2 patterns according to Barnston and Livezey's (1987) nomenclature, are presented in Fig.2. Six synoptic-frequency patterns were uncovered over the region in question (not shown). For more details see Huth (1994).

2.2. Temperature

Daily mean temperatures are taken at six measuring sites whose locations are shown in Fig.3 together with their respective altitudes. Data were available for the same period as for circulation at Milešovka and Kopisty; the series at the other four sites (Teplice, Hradec Králové, Čáslav, Hurbanovo) terminate at the end of 1990.

3. Results

3.1. Low-frequency modes

The links between the low-frequency circulation patterns and local temperatures have been expressed in terms of correlation coefficients between the PC-scores (i.e., intensity of patterns) and daily mean temperatures. Correlations for the period of 1983-1990 are given in Tab.1. Apparently, the influence of circulation on local temperature is stronger at a mountain station (Milešovka) than nearby valley stations (Teplice or Kopisty - not shown).

Tab.1 Correlation coefficients (x100) between low-frequency oscillations and daily mean temperatures, 1983-90 (MIL = Milešovka, TEP = Teplice, HK = Hradec Králové, CAS = Čáslav , HUR = Hurbanovo).

	MIL	TEP	HK	CAS	HUR
EU1	-30.2	-26.6	-22.1	-25.6	-17.7
NAO	58.9	56.3	59.7	57.5	49.9
EA	18.3	14.9	24.6	27.7	15.1
EU2	-29.4	-17.9	-40.4	-37.3	-43.8

Over the whole area studied, the influence of the NAO pattern is most strongly pronounced: The link between NAO and temperature is weakest at Hurbanovo; at the other sites, NAO itself accounts for almost 35% of the total variance of mean temperature. Positive correlations indicate that high-amplitude NAO events are accompanied by the above-normal temperatures, which is an expected consequence of a warm air inflow from southwest.

The patterns EU1 and EU2 are negatively correlated with temperature: their negative phases are connected with the inflow of oceanic air from northwest (west) into the area of interest. Their influence is however less important and more regionally dependent: Correlation with temperature tends to weaken (strengthen) eastwards for EU1 (EU2). Intensity of the EA pattern affects the temperatures in the Czech Republic and Slovakia only marginally. This could be well anticipated since its centres of action are located far from the Central Europe.

3.2. Synoptic-frequency modes

The influence of the intensity of synoptic-frequency patterns on mean temperature is insignificant at all stations. For an illustration, corresponding correlation coefficients for Milešovka are shown in Tab.2. At any station, correlations with any mode do not exceed 0.18. Therefore, synoptic-frequency variability seems to play a negligible role in controlling surface temperature.

Tab.2 As in Tab.1 except for synoptic-frequency variability and Milešovka only.

1	9.3
2	-1.4
3	-8.0
4	-5.6
5	-14.6
6	3.0

Tab.3 Temperature statistics conditioned on circulation types: mean anomaly from the local winter mean (top), standard deviation (middle), difference between 'middle' day and total mean temperatures (bottom - for explanation see the text).

type	MIL	TEP	HK	CAS	HUR
1	-7.9	-8.9	-8.4	-7.4	-6.2
2	0.9	1.0	0.1	0.7	-0.5
3	1.8	1.4	2.5	2.9	2.5
4	-3.4	-3.2	-4.2	-3.7	-3.4
5	-1.0	-0.5	-0.4	-0.4	-0.5
1	5.1	4.3	5.8	5.8	5.1
2	4.2	4.8	4.2	4.6	3.9
3	3.9	5.0	3.9	4.0	4.0
4	6.0	6.0	6.0	7.0	6.0
5	3.0	4.6	3.8	3.8	3.7
1	-4.7	-4.2	-5.0	-5.1	-4.5
2	-0.3	-0.3	-0.5	-0.5	-0.4
3	0.1	0.2	0.2	0.2	0.6
4	-3.4	-2.0	-2.0	-2.2	-1.6
5	0.3	-0.6	0.6	0.4	0.9

3.3. Circulation types

Table 3 contains basic characteristics of temperature distributions within circulation types at the five stations: mean anomaly from the local winter mean (top) and standard deviation (middle). Clearly, the types differ considerably in mean temperature. The type 1 with a blocking anticyclone over the Norwegian Sea is the coldest one whereas zonal type 3 is warmest at all sites. The mean anomaly of the coldest type is most negative at the valley station of Teplice and seems to decrease eastwards. The temperatures are most variable under type 4 whereas the least variability is generally connected with type 5.

Tab.4 Kolmogorov-Smirnov statistic for difference between temperature distributions under individual circulation types, Milešovka

	1	2	3	4
2	3.02			
3	3.60	1.41		
4	1.54	3.00	3.98	
5	2.93	2.38	3.11	2.57

Whether the temperature distributions differ among the types was determined by Kolmogorov-Smirnov test. The values of test statistic for each pair of types are shown in Tab.4 for Milešovka. The hypothesis that the two distributions are equal is rejected at the 99% significance level for values exceeding 1.63. The temperature distributions appear to differ significantly for all pairs of types except for 2/3 and 1/4. Results for other stations are similar. Therefore we can claim that the objectively determined circulation types provide a good stratification of temperature events.

It is possible that the temperature within a type can also be affected by the duration of the event (the event is defined as an uninterrupted sequence of days classified with one type, preceded and succeeded by another type), the position of the day within the event (if the day is first, last, or in the middle of the event), and the circulation type on the preceding day.

Mean temperatures for 'middle' days (all days of an event except for the first and last ones) were determined for each type. Differences between 'middle' and total means are shown in the bottom part of Tab.3, indicating that the onset and breakdown of cold types 1 and 4 is considerably warmer than their 'middle' days. Duration of events of other types does not seem to have a pronounced effect on temperatures.

The dependence of temperature at Milešovka on a preceding type is manifested in Tab.5 where ten winters (1983-93) were included. Naturally, if a cold (warm) type precedes, temperature tends to be lower (higher). No considerable difference among stations was found in this respect.

Tab.5 Mean temperature at Milešovka under type T preceded by type P, 1983-93. Number of days denoted by n.

T	P	n	
1	1	19	-12.1
1	2	2	-11.6
1	4	1	-9.7
1	5	4	-6.1
2	1	2	-8.9
2	2	257	-2.7
2	3	21	-0.6
2	4	18	-2.6
2	5	21	-2.7
3	1	2	-5.6
3	2	31	-0.7
3	3	267	-1.0
3	4	6	-1.4
3	5	5	-1.9
4	1	3	-9.8
4	2	15	-1.2
4	3	7	-0.7
4	4	80	-7.4
4	5	6	-6.6
5	2	17	-3.6
5	3	15	-3.2
5	4	6	-7.0
5	5	85	-4.2

4. Conclusions

Local surface daily mean temperatures in the Czech Republic and Slovakia are shown to be influenced by the low-frequency modes of variability (with periods over 10 days retained). The influence is strongest of the NAO pattern whose intensity explains about 35% of the total temperature variance at all Czech stations. The contribution of EU1 and EU2 patterns is also significant though considerably weaker. The EA pattern does not have any significant effect on temperatures in the area of interest.

Synoptic-frequency variability (with periods between 2.5 and 6 days) has no pronounced effect on local temperatures: correlations between

the ntensity of synoptic-frequency modes and temperatures do not exceed 0.18.

There is a significant difference between almost all pairs of temperature distributions under different circulation types. For the two cold circulation types, a pronounced dependence of temperatures on the duration of events was found: The first and last days are warmer than the rest of the event.

Although circulation is a significant contributor to surface temperature variability, the circulation itself does not seem to provide information sufficient for reliable estimates of local daily temperatures. This finding is of considerable importance for attempts at assessing future local climates (under enhanced greenhouse effect) from large-scale outputs from general circulation models.

Acknowledgements

This study was supported by the Grant Agency of the Czech Republic under contract 205/93/0294. Thanks are due to Mrs. E.Lhotková for her technical assistance.

References

Barnston,A.G., Livezey,R.E. (1987): Classification, seasonality and persistence of low-frequency atmospheric circulation patterns. Mon.Wea.Rev. 115, 1083-1126

Blackmon,M.L. (1976): A climatological spectral study of the 500 mb geopotential height of the Northern Hemisphere. J.Atmos. Sci. 33, 1607-1623

Giorgi,F., Mearns,L.O. (1991): Approaches to the simulation of regional climate change: A review. Rev.Geophys. 29, 191-216

Hewitson,B. (1994): Regional climates in the GISS general circulation model: Surface air temperature. J.Climate 7, 283-303

Huth,R. (1993): An example of using obliquely rotated principal components to detect circulation types over Europe. Meteorol. Zeitschrift, N.F. 2, 285-293

Huth,R. (1994): On the ability (or inability?) of GCMs to reproduce continental-scale circulation. In: Contemporary Climatology, R.Brázdil and M.Kolář, Eds., Masaryk University, Brno, 255-260

Corresponding address

Dr. Radan Huth
Institute of Atmospheric Physics
Boční II 1401
CZ - 141 31 Praha 4
Czech Republic

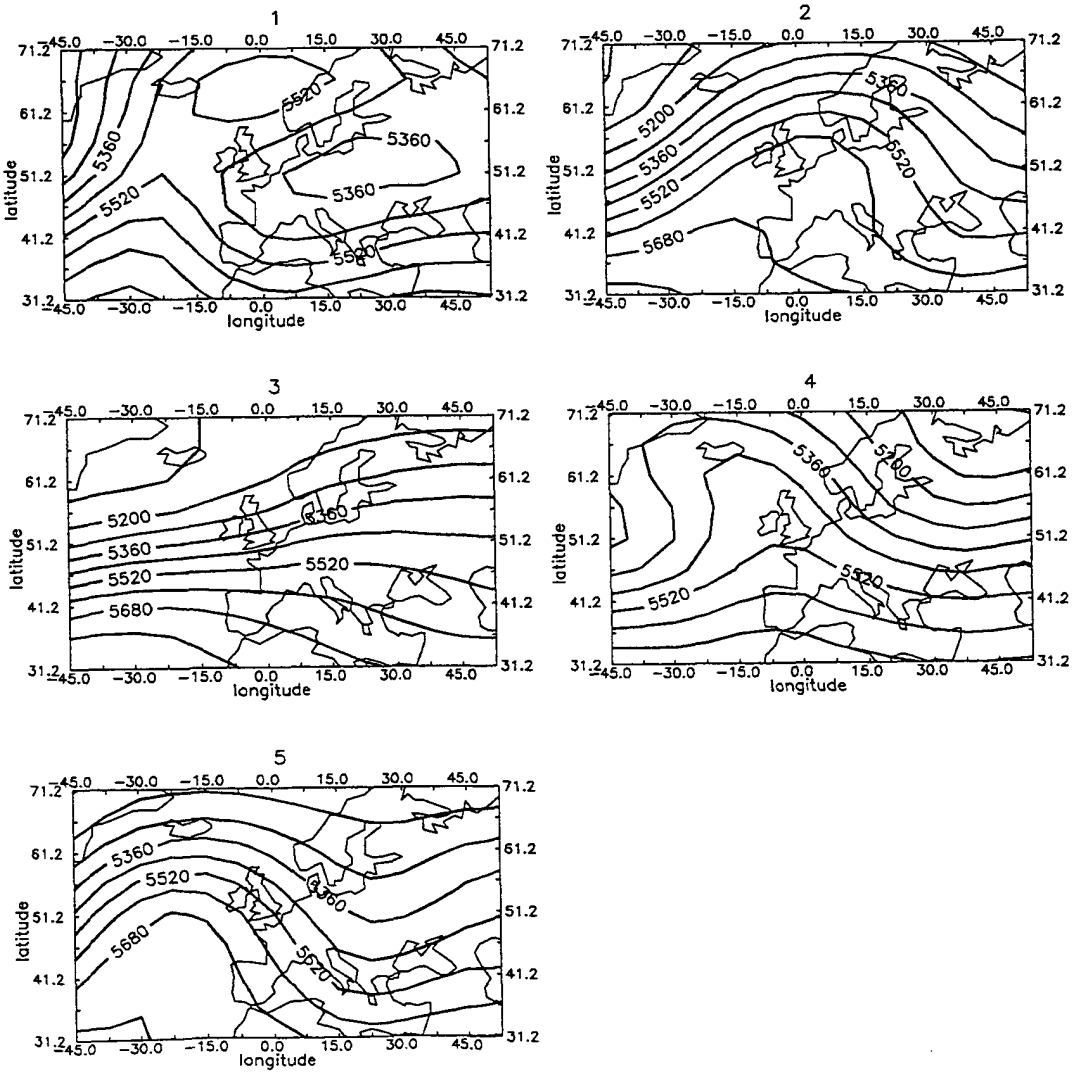


Fig.1 Mean 500 hPa geopotential for the five circulation types.

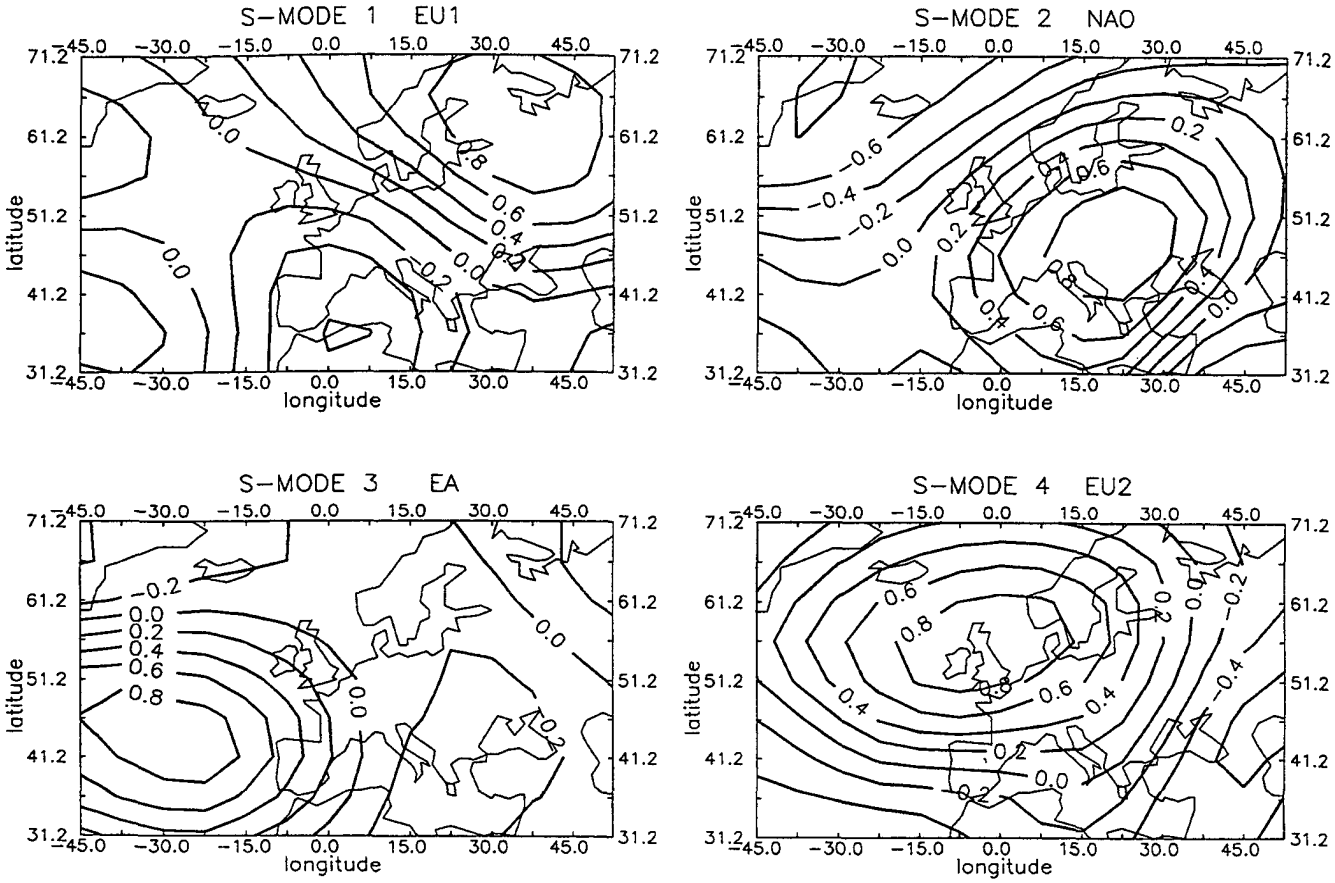


Fig.2 Low-frequency oscillation patterns.

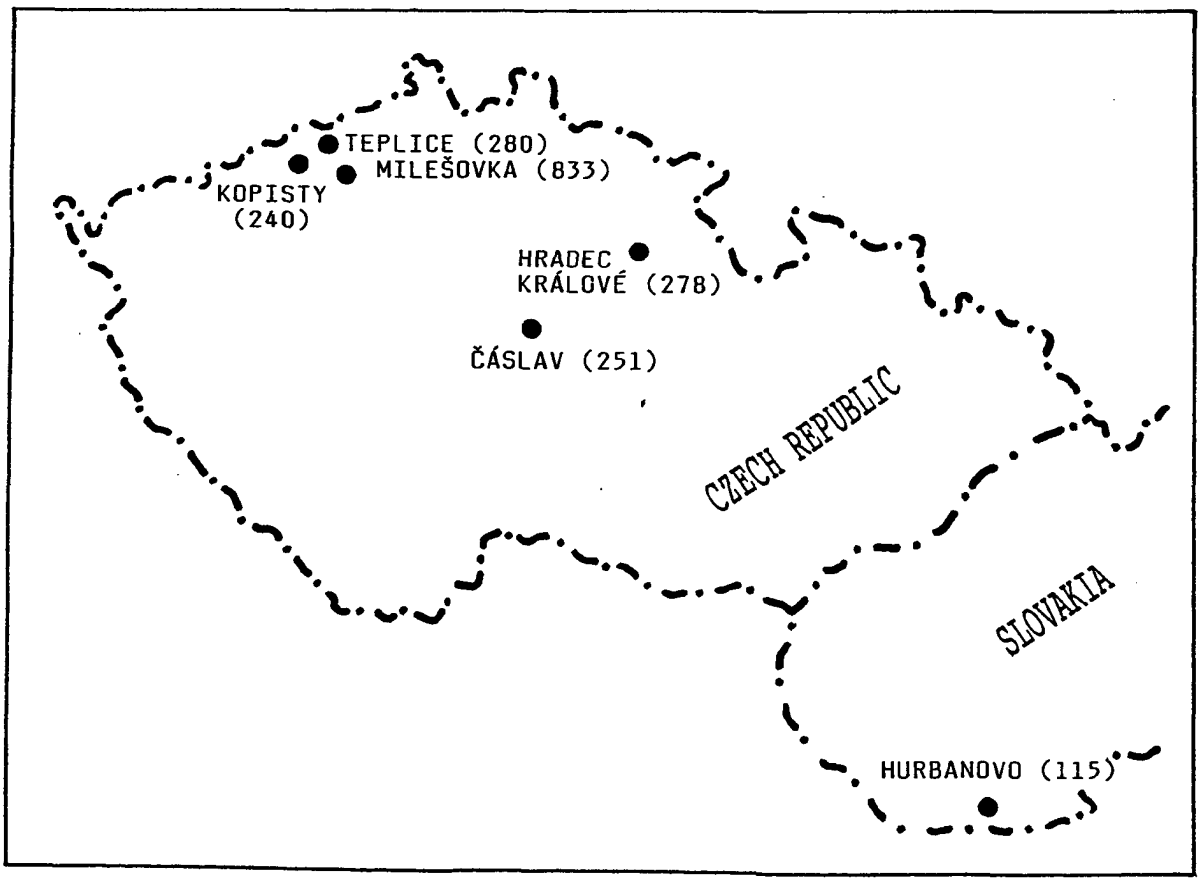


Fig.3 Six stations discussed in the study. Their respective altitudes are given in parenthesis.

A Statistical Downscaling of Observed and of Climate Model Larg Flow into Local Near Surface Wind

E. Kaas and T. Lee

Danish Meteorological Institute, Copenhagen Denmark

ABSTRACT

A regression model (RM) has been used to downscale large scale atmospheric flow into near surface windiness in winter. The predictors of the RM are projections onto the dominating patterns of the large scale flow over the North Atlantic region, in this study represented by quantities as monthly mean of mean sea level (MSL) pressure and 500 hPa height fields. The predictands (windiness) are chosen as monthly means of the wind speed squared, since this variable is a fairly good estimator of strong winds. Furthermore, it can be represented reasonably well by the regression model using independent data. The predictor variables observed in the period 1901-1960 and simulated in a transient climate model experimented with steadily increasing levels of atmospheric CO_2 are downscaled using the RM trained on observed data 1961-1987.

1. INTRODUCTION

This paper presents some preliminary results from the WASA (Waves and Storms in the North Atlantic) project and aims at investigating 1) the windiness in the past and 2) if any trends in the observed windiness are consistent with changes that might be a consequence of the increasing levels of (future) greenhouse gases.

Concerning the first goal, it is noted that observed wind data prior to approximately 1950-60 are based on subjective estimates and must be considered not usable for detecting rather small trends. For this reason indirect estimates of the windiness based on (presumably) more homogenous data as MSL pressure will generally be used in WASA. In the present study a statistical downscaling model (briefly described in section 3) is used to investigate to what extend gridded monthly mean MSL pressure data can be used as a valuable predictor of the "monthly mean windiness" at 10 observation stations in the North Atlantic region.

Next, in section 4, the downscaling model is used to create a synthetic time series of windiness in the period 1901-1960 for those stations which can be reproduced with reasonable accuracy on independently observed data in the training period (1961-1987). Estimates of future windiness are obtained by downscaling the large scale flow generated in a climate model exposed to steadily increased concentrations of greenhouse gases. This downscaling is based on predictors which reflect not only monthly mean flow but also temperature of the lower troposphere, since the perturbed climate model flow to be downscaled is characterized mainly by anomalous high temperatures while only small anomalies are seen in the mean (barotropic) flow. This part of the work is described in section 5.

All data used in the study are described in section 2 while a discussion of the results can be found in section 6.

2. DATA

The observed predictand variable used to train the RM is monthly mean of wind speed squared (w) in winter (Dec., Jan, Feb.) at the 10 synop stations shown in Fig. 1. These data cover the period 1961-1987, i.e. a total of 81 winter months. The variable w is a simple proxy for windiness.

Observed monthly mean MSL pressure fields on a grid covering the area shown in Fig. 1 are used to train the RM in the period 1961-1987, while observed MSL pressure fields (1901-1960) are used as predictor in the RM to obtain a synthetic time series of windiness in the period 1901-1960. The data are analyses from the National Meteorological Center (NMC), US.

To downscale the large scale flow generated in a climate model, both lower tropospheric mean flow ((500 hPa height +1000 hPa height)/2) *and* lower tropospheric temperature ((500 hPa height -1000 hPa height)/2) is used. The observed data used to train the RM, again covering the period 1961-1987, are extracted from NMC analyses. The climate model flow data cover model years 71-100 of the control and IPCC (1992) scenario A experiment with the ECHAM-1 climate model described in Cubasch et al. (1992).

All predictors used in the study are compressed via packing in Empirical Orthogonal Functions (EOFs). The yearly cycle has been removed from the observed

predictors and predictands before they are used as input to the RM.

3. THE REGRESSION MODEL (RM)

A multiple linear regression model is under development within the WASA project. The predictors used in the model for the actual applications were described in section 2. A cross validation is used to determine the most skillful predictors. However, for the downscaling of the scenario A climate model output a predictor reflecting the long term mean difference between the scenario A experiment and the corresponding control experiment is always forced to be included as predictor to ensure a correct downscaling of the large scale, long term mean flow difference between the two climate model experiments. A double cross validation technique (Michalsen, 1987) is applied to estimate the RM-performance on independent data. It is as a rough approximation assumed that the relationship between predictors and windiness remains the same in the prediction period (1901-1987 or the climate model data). This assumption is anticipated rather uncertain for the scenario A data.

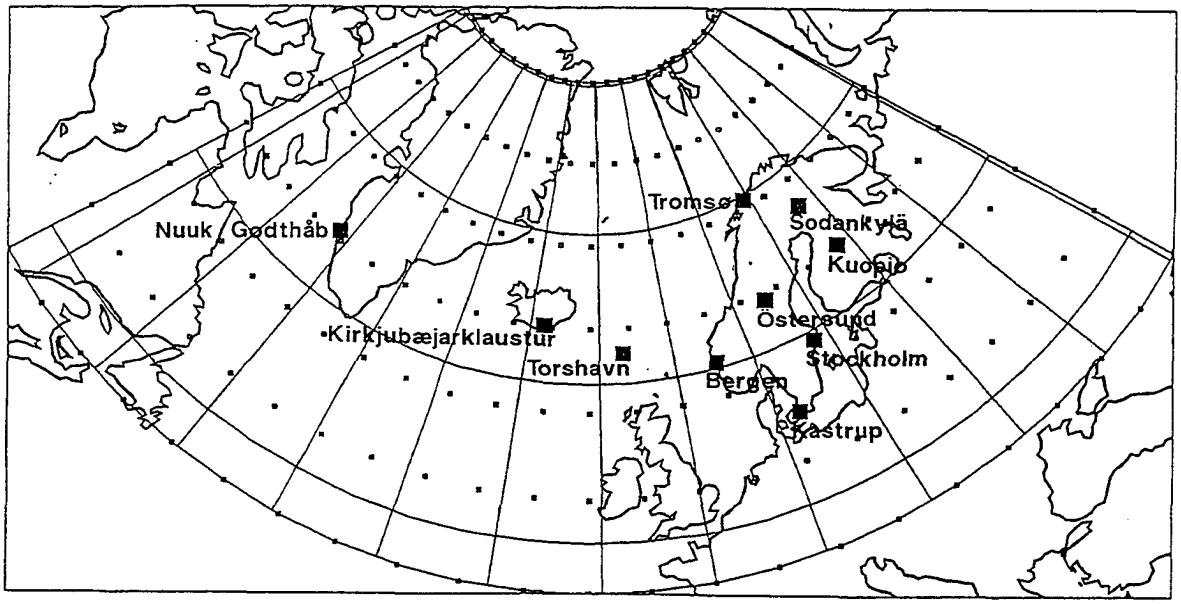


Fig. 1. Location of the 10 synop stations used in the study and the grid points representing the large scale flow fields.

4. WIND CLIMATE 1901-1961

Calculated from data in the training period, the regression coefficients are used to downscale the MSL-pressure patterns 1901-1960. Table 1 shows (as indicated) the long term mean of w observed 1961-1987 ($=w_2$), the skill of the RM (independent correlation *CI* based on double cross validation) and w_2 minus the average in the period 1901-1950 ($=w_1$). It is seen that *CI* for several of the 10 stations is very low (but positive). Only stations with *CI* above .6 (anticipated) can be assumed predicted reasonably well. Taking into account the fact that only a fraction of the variability in w can be estimated from monthly mean MSL pressure data it can be concluded from the table that only very small changes, if any, are predicted with the RM in the present century.

STATION	w_2	CI	w_2- w_1
Tromsø	24.2	0.60	-0.92
Bergen	32.8	0.61	-3.63
Östersund	18.0	0.53	-1.61
Stockholm	18.2	0.54	-0.85
Sodankylä	11.3	0.64	-1.24
Kuopio	16.3	0.60	-1.13
Kirkjubæjarklaustur	28.1	0.54	1.86
Nuuk/Godthåb	67.8	0.23	0.83
Thorshavn	62.5	0.47	-2.76
Kastrup	48.2	0.13	-1.73

Table 1. See text for further explanation.

5. DOWNSCALING CLIMATE MODEL GENERATED FLOW

Calculated from data in the training period the regression coefficients are used to downscale the flow generated in the scenario A experiment with the ECHAM-1 model. The scenario A predictors are calculated as anomalies from the long term mean of the corresponding control experiment in order to eliminate the systematic errors in the climate model. The results are presented in table 2, which shows the long term mean of the observed windiness, w_2 (identical to table 1) the skill (*CI*) of the RM, (but now with different predictors than in table 1), and the average of w in the 30 scenario A model years ($=w_A$) minus w_2 (= control simulation value)

STATION	w_2	CI	$w_A - w_2$
Tromsø	24.2	0.57	11.5
Bergen	32.8	0.61	17.6
Östersund	18.0	0.56	9.8
Stockholm	18.2	0.57	3.1
Sodankylä	11.3	0.59	9.0
Kuopio	16.3	0.51	7.5
Kirkjubæjarklaustur	28.1	0.32	-3.9
Nuuk/Godthåb	67.8	0.24	8.4
Thorshavn	62.5	0.50	15.5
Kastrup	48.2	0.33	-5.5

Table 2. See text for further explanation.

We can see that these values generally are above zero indicating higher winds in the scenario A case. A Monte Carlo technique reflecting the uncertainties in the regression coefficients gives that these results are significant at the 99% percent level for stations 1,2,3,5 and 9. Since the main difference between scenario A and control is a heating of the troposphere the results in the last column show - in an indirect way - that when the observed troposphere is anomalous warm the tendency for high observed winds must similarly be high - otherwise the results would not positive.

6. DISCUSSION

The results presented in this extended abstract should be considered preliminary, particularly concerning the historical estimates for the early part of the 20th century. The gridded NMC analyses have not been corrected for inhomogeneities in the underlying observations, and possibly even more important, the number of observations actually entering the analyses have increased dramatically during the period. The use of wind-predictors assumed to be homogenous will be continued throughout the WASA project. In the future applications of the RM the predictors will be daily MSL pressure at a series of stations currently being digitized and homogenized. It is also planned to test if the inclusion of temperature information (as a measure of baroclinicity) will improve the performance of the regression model. This information may be either SST's or temperature measured at the array of WASA stations.

Concerning downscaling of climate model generated flow, we note, that one has to be very cautious about the use of statistical relationships (reflecting atmospheric variability under present day conditions) to estimate the impact of increased CO_2 concentrations. In this study we have found that when the observed atmosphere is warm over long time (a month) and on a large scale, there is a tendency for higher winds than when it is cold. It is this relationship which gives the high scenario A winds in table 2. But we have no guarantee that the reason for a warm troposphere is the same in the observed climate and in the CO_2 perturbed climate. In the scenario A case it is actually a different level of the radiation balance in the atmosphere which causes the high temperatures, whereas the reason for high monthly mean temperature anomalies in the observations usually is anomalous advection of warm air. One could easily immagine advection of warm air being part of a large scale flow system that is more baroclinic unstable than a large scale flow system heated more uniformly by a modified radiation balance. A physically more correct downscaling is obtained by performing so called time slice experiments with high resolution climate models. In fact such an experiment with a newer version of the ECHAM model run at horizontal resolution T106 do not show an increase in the storminess as indicated by our results. This will be further discusssed during the oral presentation.

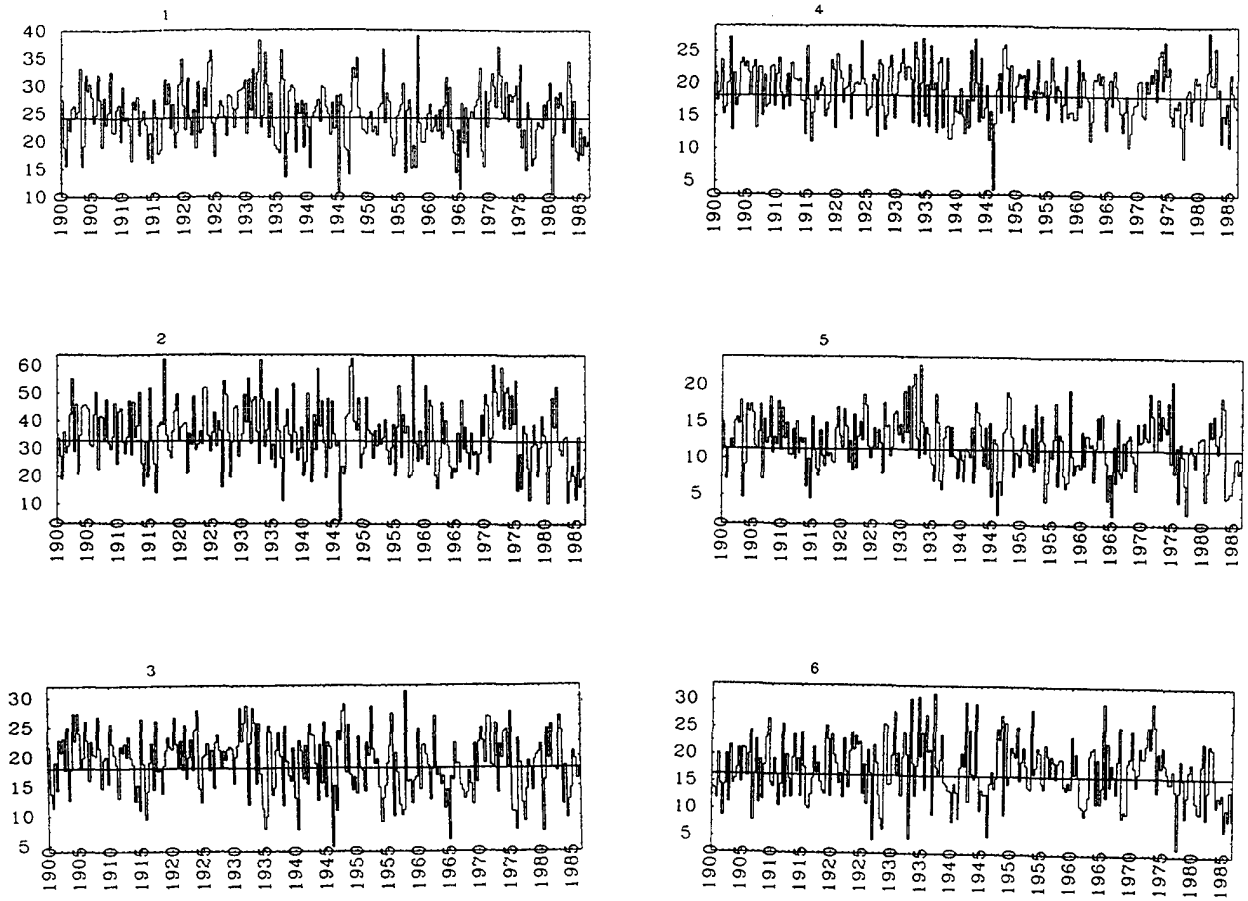


Fig. 2 Time series of downscaled w (1901-1987) at 6 selected stations (numbers indicated) with reasonably high values of *CI*. Solid horizontal line indicates w_2. See text for further explanation.

REFERENCES

Cubasch, U., K. Hasselmann, H. Höck, E. Maier-Reimer, U. Mikolajewicz, B.D. Santer and R. Sausen, 1992: Time-dependent greenhouse warming computations with a coupled ocean-atmosphere model. Clim. Dyn., 8, 55-69.

IPCC, Supplementary Report, 1992: Climate Change. J.T. Houghton, B.A. Callander and S.K. Varney (Eds.), Camb. Univ. Press, p 200.

Michaelsen, J., 1987: Cross-validation in statistical climate forecast models. J. Clim and Appl. Meteor., 26, 1589-1600.

ESTIMATING PROBABILITY DISTRIBUTION OF SURFACE CLIMATIC VARIABLES FROM FREE-ATMOSPHERE QUANTITIES

Istvan Matyasovszky
Civil Engineering Department, University of Nebraska-Lincoln
on leave from
Department of Meteorology, Eotvos Lorand University, Budapest, Hungary
Istvan Bogardi
Civil Engineering Department, University of Nebraska-Lincoln

ABSTRACT

A methodology is presented for estimating the probability distribution of climate variables conditioned on other variables (predictor variables) using kernel techniques. A simulation experiment performed with a two-dimensional normal variable shows a considerable reduction of the bias of the estimate as compared to the kernel estimate without involving the predictor variables. The method is applied to the daily precipitation amount when the large-scale surface of the 500 hPa geopotential height is incorporated as a variable influencing precipitation. The estimated probability distribution function fits the empirical distribution.

1 INTRODUCTION

The purpose of this paper is to develop a methodology for estimating the probability distribution of local surface climate variables using large-scale free-atmosphere quantities. This is a basic element of our ultimate purpose, namely, to estimate local surface climate under a possible global climate change induced by increasing concentration of atmospheric greenhouse gases. The space-time variability of climate variables will be described by a stochastic model conditioned on daily geopotential height surfaces of air pressure levels defining atmospheric circulation.

Three-dimensional numerical General Circulation Models (GCMs) simulate basic mechanisms of the climate system with a horizontal resolution of hundreds of kilometers. Many impacts of global climate change, however, act on smaller spatial scales; therefore, a methodology is necessary to distribute large-scale climate changes to smaller scales. This procedure is called downscaling.

Semiempirical techniques representing a frequently used type of downscaling approaches generally include the classification of daily circulation patterns (CPs) (Bardossy and Plate, 1992; Wilson et al., 1992). Circulation patterns are characterized by the spatial distribution of sea level air pressure or of some low or middle tropospheric pressure heights. Statistical properties of local climatic variables are conditioned on a set of CP types and the effect of global climate change is estimated throughout changes in the frequency and duration of CP types generated by GCMs. However, predictions based on changes in frequency and duration of CP types must be treated with caution. An important question is the sensitivity of results on classification schemes and number of CP types (Yarnal, 1993). The choice of the technique for classifying CP is subjective and the number of types is a trade-off between two problems, namely, how strongly one type differs from another and how the CPs are similar within their types. The greatest concern is, however, that GCMs under $1xCO_2$ control run may fail to reproduce the observed CP type characteristics, so there are not smaller differences between the observed and the $1xCO_2$ characteristics than the difference between the $1xCO_2$ and $2xCO_2$ characteristics (Matyasovszky et al., 1993).

Let $\mathbf{X}$ be a p-dimensional random vector representing the geopotential height surfaces over an area and let Y be a surface climate variable at a given location. Y is a scalar variable, but the method can be extended for vector variables. Using the CP type approach, the probability distribution function F(y) of Y can be expressed as:

$$F(y) = \sum_{i=1}^{I} p_i F_i(y) \qquad (1)$$

where p_i denotes the occurrence probability of type i, and $F_i(y)$ is the probability distribution function of Y conditioned on type i. Note that Eq.(1) can be considered as a discretized version of

$$F(y) = \int F_{\mathbf{x}}(y) g(\mathbf{x}) d\mathbf{x} \qquad (2)$$

where $F_{\mathbf{x}}(y)$ is the conditional probability distribution function of Y under $\mathbf{X}=\mathbf{x}$, and $g(\mathbf{x})$ is the probability density function of $\mathbf{X}$. Given the hypothesis that $F_{\mathbf{x}}(y)$ will stay invariant under changing global climate, a new distribution of Y reflecting climate change can be estimated with Eq.(2) using a modified $g(\mathbf{x})$ obtained from a GCM. Elementary consideration of probability theory shows that using an observed time series $\mathbf{x}(1),..., \mathbf{x}(n)$. Eq.(2) can be approximated by

$$F(y) = \sum_{j=1}^{n} F_{\mathbf{x}=\mathbf{x}(j)}(y) \qquad (3)$$

Thus, if an estimator for $F_{\mathbf{x}}(y)$ is available from the observed data set, the distribution function of Y under a new climate can be estimated with Eq.(3) by means of substituting the data set $\mathbf{x}(j)$, $j=1,..,n$ by a sequence of GCM-generated free-atmosphere variables. The problem of estimating F(y) via conditional distributions is due to the high dimensionality of $\mathbf{X}$. In the paper the well-developed kernel density estimator is modified for distribution functions and applied to the distribution Eq.(3). The reason of applying distribution and not density functions is that daily precipitation, one of the most important climate elements, has temporal intermittence, therefore, has no density function. The methodology is first illustrated with a simulation experiment for a two-dimensional Gaussian variable using the density function, then applied for an observed daily precipitation data series in Nebraska, representing midwest conditions in USA.

2 PROBABILITY DENSITY ESTIMATION BY KERNELS VIA CONDITIONAL DENSITIES

Given a sample y(1),..., y(n) of Y the classical kernel density estimator (Parzen, 1962; Rosenblatt, 1956) is defined as:

$$\hat{f}(y) = \frac{1}{n}\sum_{i=1}^{n}\frac{1}{b}k\left(\frac{y-y(i)}{b}\right) \qquad (4)$$

where k(s) is a so-called kernel function satisfying certain properties to provide an appropriate estimate of f(y). The bandwidth b tends to zero as n tends to infinity. The kernel function can be chosen as a density function because it is required to integrate to unity. A more general class of k(s) with support [-1,1] is called kernel of order q if the condition

$$\int_{-1}^{1} k(s)s^{j}ds = \begin{cases} 1, & j=0, \\ 0, & 0<j<q \end{cases} \qquad (5)$$

is satisfied. Note that a density symmetric of zero is a second order kernel. Eq.(4) provides an asymptotically unbiased and consistent estimate of f(y) and the asymptotic mean square error (MSE) of the kernel estimate (4) is

$$MSE(y) = \left(B\frac{h^{q}}{q!}f^{(q)}(y)\right)^{2} + V\frac{f(y)}{nb} \qquad (6)$$

where

$$B = \int_{-1}^{1} k(s)s^{q}ds\ ,\quad V = \int_{-1}^{1} k^{2}(s)ds \qquad (7)$$

and $f^{(q)}$ is the qth derivative of f which is assumed to be finite. The first term in Eq.(6) represents the square of the bias, while the second term corresponds to the variance of the estimator in Eq.(4). The dependence of the MSE on the density and its qth derivative, the kernel, and the bandwidth is clearly shown by Eqs.(6)-(7). The bias is higher in areas where $f^{(q)}(y)$ is higher, and the variance is higher where f(y) is large. The bias term penalizes oversmoothing and the variance term penalizes undersmoothing; thus an optimal b that recognizes this trade-off must exist. The optimal b minimizing MSE at a point y, however, cannot be determined in practice because it requires the knowledge of f(y). A possibility for estimating the bandwidth is to use a least square cross-validation technique suggested by Rudemo (1982).

Several simulation and real data studies suggest that a small variability in q does not considerably affect the resulting density. Generally, a relatively small value of q, i.e. q=2, can be chosen. The choice of kernels is based on asymptotic properties Eqs.(6)-(7). Kernels minimizing the asymptotic variance can be found in Gasser et al. (1985). Muller (1984) discussed a more general class of kernel functions which minimizes the variance of the μth ($\mu \geq 0$) derivative of the kernel estimate. The above kernels, however, may be used just in the case when f is defined on the interval $(-\infty,\infty)$, unless the kernels are modified near the endpoints. Gasser and Muller (1979) defined boundary kernels with asymmetric support satisfying moment conditions necessary to maintain the order of unbiasedness in boundary intervals. Minimum variance kernels were derived by Gasser et al. (1985). Muller (1991) has developed a very general formulation to have kernels for any y and for any q. His kernel for q=2, $\mu=1$ is used in this paper.

For multivariate densities there are several possibilities to define the bandwidth. The simplest choice is just one bandwidth, i.e. the amount of smoothing is the same in every direction. An obvious extension is to use different bandwidths for each of the coordinate directions. One can have, however, a bandwidth matrix that permits smoothing in orientation different from those of the coordinate directions. For normal distributions these three approaches become equivalent after using a coordinate transformation with the help of covariance matrices (using principal components). The use of this latter technique for other distributions is studied in Wand and Jones (1993).

The conditional density $f_x(y)$ can be calculated using the joint probability density of (X, Y) and probability density of X. Let, for simplicity, X be a one-dimensional variable. The conditional estimator for f(y) corresponding to the distribution function in Eq.(3) is therefore

$$\hat{f}(y) = \frac{1}{n}\sum_{j}\frac{\frac{1}{b}\sum_{i}k\left(\frac{y-y(i)}{bd_y}\right)k\left(\frac{x(j)-x(i)}{bd_x}\right)}{\sum_{i}k\left(\frac{x(j)-x(i)}{bd_x}\right)} \qquad (8)$$

where d_x and d_y denote the corresponding standard deviations. In order to study the basic properties of estimator Eq.(8), two standard normal variables were considered with a correlation r=0.6 between them. A sample of size n=200 was simulated and the bandwidth was estimated by a cross-validation technique. This procedure was repeated 100 times. Mean and standard deviation obtained from this simulation were compared to the mean and standard deviation calculated from a similar simulation using the direct estimator Eq.(4). Typical behavior, over estimation at flat regions and under estimation at peak of the density, can be seen in Fig. 1. However, performance of the conditional estimator seems substantially better. Indeed, the difference between the two curves is statistically significant even at 99.9% significance level. There is no clear tendency concerning standard deviations. Statistical tests do not detect

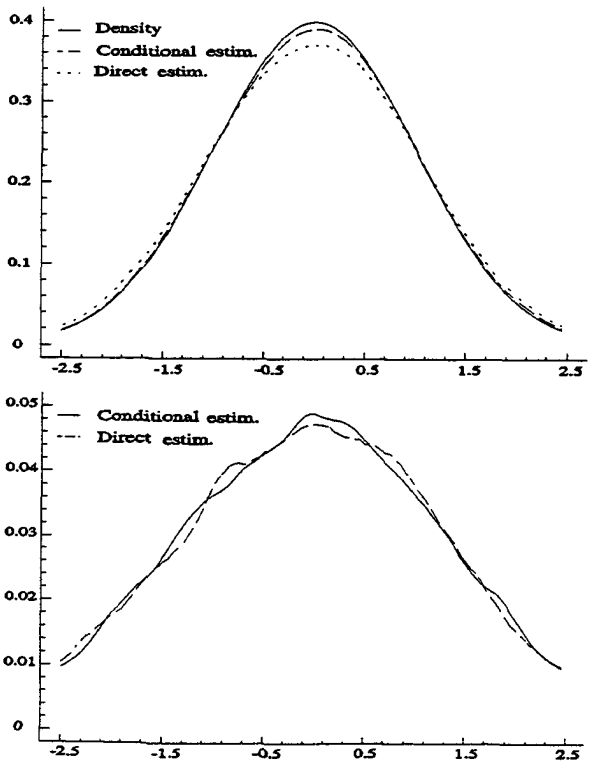


Figure 1. Comparison of direct and conditional kernel estimates for mean (top) and standard deviation (bottom) of 100 simulations

differences between them, however, the conditional estimation curve is considerably smoother. Similar experiments with other values of correlation were also performed. The advantage of the conditional estimator disappeared when using a low correlation (r=0.2) and no considerable better result was obtained as compared to the case r=0.6 when a high correlation (r=0.9) was chosen.

3 PROBABILITY DISTRIBUTION ESTIMATION BY KERNELS VIA CONDITIONAL DISTRIBUTIONS

The kernel estimator for distribution functions corresponding to the kernel density estimator Eq.(4) is defined as:

$$\hat{F}(y) = \frac{1}{n}\sum_{i=1}^{n} K\left(\frac{y-y(i)}{b}\right) \qquad (9)$$

where $K(z)=\int_{-\infty}^{z} k(s)ds$. The conditional estimator for F(y):

$$\hat{F}(y) = \frac{1}{n}\sum_{j} \frac{\sum_{i} K\left(\frac{y-y(i)}{bd_y}\right)\prod_{u} k\left(\frac{w_u(j)-w_u(i)}{b\lambda_u^{1/2}}\right)}{\sum_{i}\prod_{u} k\left(\frac{w_u(j)-w_u(i)}{b\lambda_u^{1/2}}\right)} \qquad (10)$$

where $w_u(i)$ is the ith observation for the uth principal component of the vector **X** and λ_u is variance of the uth principal component. Note that geopotential heights can be considered as normally distributed variables, so the above use of principal components in Eq.(10) delivers an optimal bandwidth specification for the joint distribution of geopotential variables.

To apply the above estimator, a 10-year (1963-1972) series of daily precipitation amounts in Seward, Nebraska, representing midwest conditions in USA, is examined in summer. The application uses solely the 500 hPa geopotential height field as free-atmosphere variable **X** at 40 points on a diamond grid covering the sector 25^0-60^0 N, 80^0-125^0.

Fig. 2 shows the empirical and the conditional kernel estimate of the probability distribution function. To reproduce the probability of daily precipitation event and the quickly increasing values of the distribution function at small precipitation amounts the first term of the numerator in Eq.(10) is slightly modified. A very small value of b was chosen at the zero precipitation amount. For larger amounts (>4 mm) a cross-validation technique was used to estimate the bandwidth, while within the interval (0, 4) mm the bandwidth was changed linearly. The resulted smooth estimate fits very well the empirical distribution.

At this stage of methodological development the computation requires excessive CPU time for long time series. Note that CPU time for calculating F(y) (Eq.10) is proportional to n^2 and for a cross-validation technique necessary to estimate the bandwidth, it is proportional to n^3. Computation is even more time consuming in higher dimensions.

4 CONCLUSION

A methodology has been developed for estimating the probability distribution of climate variables conditioned on other

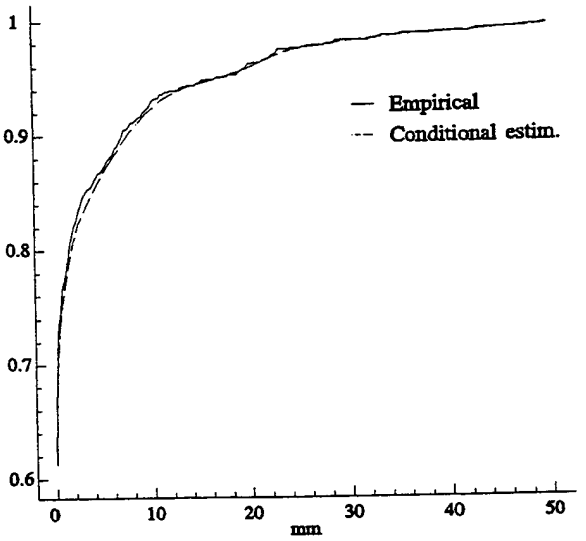


Figure 2. Empirical and conditional kernel estimate of the probability distribution function of daily precipitation amount in Seward

variables (predictor variables) using kernel techniques. In order to study basic theoretical properties of this technique, a simulation experiment was performed with a two-dimensional normal variable.

The most important finding is that the bias of this estimator is smaller than the bias of the direct kernel technique. A possible explanation of the bias reduction can be summarized as follows. The kernel estimator Eq.(4) is formed by a superposition of densities concentrated around the sample elements y_i. These densities are, however, somewhat artificially introduced due to choosing a kernel. When using the conditional estimator for the density of Y, the superposing densities are the conditional densities of Y. This seems a more "natural" choice, although conditional densities are estimated by the kernel technique. In this case, the location of superposing densities is determined by the observations of the predictor variable and the nature of relationship between Y and the predictor variable. The weaker the relationship, the smaller the difference between the conditional densities. In the independent case the conditional densities correspond just to the density and no bias reduction can be obtained.

An application to daily precipitation with geopotential data as vector predictor variable gave encouraging results. However, computation is quite time consuming in higher dimensions.

References

Bardossy, A., and Plate, E., 1992, "Space-time model for daily rainfall using atmospheric circulation patterns", Water Resour. Res., 28, 1247-1260.

Gasser, T., and Muller, H.G., 1979, "Kernel estimation of regression functions", Lecture Notes in Mathematics, 757, 23-68.

Gasser, T., Muller, H.G., and Mammitzch, V., 1985, "Kernels for Nonparametric Curve Estimation", Q. J. R. Statist. Soc. B., 47, 238-252.

Matyasovszky, I., I. Bogardi, A. Bardossy, and Duckstein, L., 1993, "Space-Time Precipitation Reflecting Climate Change", Hydrol. Sci. J., 38, 539-558.

Muller, H.G., 1984, "Smooth optimum kernel estimates of densities, regression curves and modes", The Annals of Statistics, 12, 766-774.

Muller, H.G., 1991, "Smooth optimum kernel estimators near endpoints", Biometrika, 78, 521-530.

Parzen, E., 1962, "On the estimation of probability density function and mode", Ann. Math. Statist., 33, 1065-1076.

Rosenblatt, M., 1956, "On some nonparametric estimates of a density function", Ann. Math. Statist., 27, 832-837.

Rudemo, M., 1982, "Empirical choice of histograms and kernel density estimators", Scand. J. Stat., 9, 65-78.

Wand, M.P., and Jones, M.C., 1993, "Comparison of Smoothing Parametrizations in Bivariate Kernel Density Estimation", J. Amer. Stat. Assoc., 88, 520-528.

Wilson, L.L., Lettenmaier, D.P., and Skyllingstad, E.,1992, "A Hierarchical Stochastic Model of Large Scale Atmospheric Circulation Patterns and Multiple Station Daily Precipitation", J. Geoph. Res., 97(D3), 2791-2809.

Yarnal, B., 1993, "Synoptic Climatology in Environmental Analysis" Studies in Climatology Series, Belhaven Press London and CRC Press.

ACKNOWLEDGEMENTS

Research leading to this paper has been partly supported by grants from the U.S. National Science Foundation, EAR-9205717, and the Great Plains Regional Center of the National Institute for Global Environmental Change. The additional support of the Center for Infrastructure Research of the University of Nebraska is also acknowledged.

ON THE USE OF STATISTICAL MODELS IN FORECAST VERIFICATION

Allan H. Murphy
Prediction and Evaluation Systems
Corvallis, Oregon, U.S.A.

Daniel S. Wilks
Cornell University
Ithaca, New York, U.S.A.

ABSTRACT

Traditional practices in forecast verification (i.e., calculating one or two measures of overall performance for a particular set of data) generally do not respect the dimensionality of the underlying verification problems and frequently overlook the effects of sampling variability on the results. Statistical modeling of the empirical joint, conditional, and/or marginal distributions of forecasts and observations represents a conceptually sound means of reducing both dimensionality and sampling variability. Recent studies that have employed parametric statistical models to describe various aspects of forecast quality are reviewed. Some initial results of a study in which regression analyses and beta distributions are used to model the quality of precipitation probability forecasts will be reported.

1 INTRODUCTION

The practice of forecast verification generally consists of calculating one or two measures of overall forecasting performance based on a particular sample of data. Yet, the fact that method A's forecasts are more accurate or more skillful than method B's forecasts is no guarantee that all aspects of A's performance are superior to all aspects of B's performance. It is relatively easy to show that traditional measures-oriented practices are frequently inadequate to demonstrate unambiguous superiority (i.e., superiority in all aspects of quality and in value), even in simple verification problems such as situations involving categorical forecasts of dichotomous variables. Clearly, if such practices are inadequate in these situations, then they are inadequate in most if not all situations involving categorical forecasts of polychotomous variables or probabilistic forecasts.

The joint distribution of forecasts and observations has been shown to provide the basis for a sound approach to verification problems (Murphy and Winkler 1987). Under certain assumptions (see Section 2), this distribution contains all of the information relevant to the assessment of forecast quality and its various aspects. A basic concept within this distributions-oriented approach is the concept of the *dimensionality* of verification problems (Murphy 1991). In this context, dimensionality refers to the number of parameters (e.g., joint, conditional, and/or marginal probabilities) that must be specified in order to reconstruct the underlying empirical joint distribution. Consideration of traditional practices from the perspective of the distributions - oriented approach reveals that evaluation methods associated with these practices generally fail to respect the dimensionality of verification problems. As a result, traditional practices frequently overlook important aspects of quality, thereby producing potentially misleading results regarding absolute or relative forecasting performance.

When the distributions-oriented approach to verification problems is applied to empirical joint relative frequencies of forecasts and observations (and/or to the associated conditional and marginal relative frequencies), the dimensionality of these problems can be quite large (see Section 2). A complete description of forecast quality under these conditions may require the determination of a relatively large number of parameters. This fact alone is sufficient to deter the use of sound approaches that respect - or more nearly respect - the underlying dimensionality of verification problems.

Parametric statistical models of the joint, conditional, and/or marginal distributions appear to offer a possible means of describing forecast quality in a reasonably complete yet parametrically economical manner (see Murphy 1991, p. 1597). The purposes of this paper are to describe the motivation and background for the application of statistical models to this problem and to report some results of a study undertaken to evaluate and compare the quality of precipitation probability forecasts using parametric statistical models. Section 2 describes deficiencies in current practices with respect to two issues; namely, the dimensionality of verification problems and the sampling variability of verification results. Previous studies in which aspects of forecast quality have been modeled using parametric statistical models are reviewed in Section 3. Section 4 briefly outlines a study in which models based on regression analyses and beta distributions will be fit to empirical distributions involving precipitation probability forecasts and the matching observations, and in which the parameters of these models will then be used to evaluate and compare these forecasts.

2 CURRENT PRACTICES: SOME PROBLEMS

As noted in Section 1, current practices in forecast verification generally involve calculating one or two measures of overall performance for a verification data sample (VDS) consisting of matched pairs of forecasts and observations. Although this approach may be adequate to identify gross features of forecasting performance, such as overall accuracy or skill, it is inadequate in at least two important ways. First, current practices generally fail to respect the underlying dimensionality of verification problems. As a result,

verification studies frequently overlook important aspects of forecasting performance and thereby produce potentially misleading results concerning the quality of alternative forecasting methods or models. Second, current practices usually ignore the problem of sampling variability. As a consequence, it may be difficult to judge to what extent the results of a specific verification study are representative of the results that would have been obtained if the study had been based on another VDS.

Under the assumption that a VDS represents a stationary bivariate time series consisting of independent pairs of forecasts (f) and observations (x), the empirical joint relative frequencies of f and x can be used to estimate the joint distribution of forecasts and observations. This joint distribution, denoted here by p(f,x), contains all of the information in the VDS relevant to the assessment of forecast quality and its various aspects. Moreover, it is possible to factor p(f,x) into conditional and marginal distributions in two ways:

$$p(f,x) = \begin{cases} p(x|f)p(f), & (1a) \\ p(f|x)p(x), & (1b) \end{cases}$$

where p(x|f) represents the conditional distributions of the observations given the forecasts, p(f|x) represents the conditional distributions of the forecasts given the observations, p(f) represents the marginal distribution of the forecasts, and p(x) represents the marginal distribution of the observations. In brief, these factorizations reveal that forecast quality can be fully described by specifying p(f,x), p(x|f) and p(f), or p(f|x) and p(x).

From the perspective of the VDS, the dimensionality of a verification problem can be defined as the number of joint relative frequencies that must be specified in order to recover the underlying empirical joint distribution. (Equivalent definitions of dimensionality can be formulated in terms of conditional and/or marginal relative frequencies.) Since these joint relative frequencies must sum to one, the dimensionality (d) can be defined as

$$d = n(f)n(x) - 1, \quad (2)$$

where n(f) and n(x) are the number of distinct forecasts and observations, respectively. That is, it takes a minimum of d independent parameters (e.g., joint relative frequencies) to specify fully the joint distribution p(f,x).

The dimensionality of some common verification problems involving categorical or probabilistic forecasts is indicated in Table 1. Note that d = 3 in the simplest problem, which involves categorical forecasts and dichotomous observations. In this problem, three joint relative frequencies must be specified in order to determine p(f,x). [Alternatively, p(f,x) could be determined from two conditional relative frequencies and a marginal relative frequency, or from three verification measures such as the fraction correct (FC), the probability of detection (POD), and the false alarm ratio (FAR).] Clearly, verification problems involving categorical forecasts with more than two possible forecasts and observations, or problems involving probabilistic forecasts, are of considerably greater dimensionality.

The contents of Table 1 indicate that one or two measures of overall performance are inadequate to fully reconstruct the underlying joint distribution in almost all verification problems. Thus, a verification study based on such an approach necessarily overlooks potentially important aspects of forecast quality. Viewed from this perspective, it is evident that sound approaches to forecast verification problems - that is, approaches that respect the underlying dimensionality of these problems - necessarily suffer from the "curse of dimensionality." That is, such studies generally require the determination of a relatively large number of parameters. Clearly, it would be desirable to find a conceptually sound way to reduce the dimensionality of verification problems and yet retain the important characteristics of forecasting performance reflected in the underlying empirical joint distribution.

Table 1. Dimensionality of common verification problems involving (a) categorical forecasts and (b) probabilistic forecasts, when the underlying distributions are modeled in terms of empirical joint, conditional, and/or marginal relative frequencies of forecasts and observations.

Number of forecasts n(f)	Number of observations n(x)	Dimensionality d
(a) Categorical forecasts		
2	2	3
3	3	8
5	5	24
10	10	99
20	20	399
*(b) Probabilistic forecasts**		
11	2	21
66	3	197
286	4	1143

*The number of distinct probabilistic forecasts is based on the assumption that eleven, uniformly-spaced probability values (i.e., 0, 0.1, 0.2, ..., 1) are available.

Although the problem of sampling variability - and its effects on the results of verification studies and the interpretation of these results - may not be as serious as the problem of dimensionality, complete reliance on the results obtained on the basis of a particular VDS is seldom warranted, unless the sample size is very large (and otherwise representative). Of course, it is possible to estimate the effects of sampling variability on these results by means of various well-known procedures of statistical inference, including modern computer-intensive methods such as resampling. Alternatively, it may be possible to reduce the effects of sampling variability by modeling - and thereby smoothing - the

underlying empirical distributions of forecasts and/or observations derived from the VDS. In this latter approach, which is explored here, it is essential that the modeled distributions retain the important features of the underlying empirical distributions.

3 STATISTICAL MODELS OF FORECAST QUALITY

As indicated in Section 1, modeling the joint, conditional, and/or marginal distributions of the forecasts and observations using parametric statistical models appears to offer a potentially effective and efficient means of reducing the dimensionality of verification problems. (The *empirical* joint, conditional, and/or marginal relative frequencies constitute a primitive statistical model of relatively high dimensionality.) If such models can provide a good fit to the underlying empirical distributions based on the VDS, then they may also provide a means of reducing the effects of sampling variability.

Perhaps the first application of parametric statistical models to characterize forecast quality was Anders Ångström's use of the Gaussian distribution to model the errors in temperature forecasts about 75 years ago (see Liljas and Murphy 1994). More recently, these models have been introduced in decision-analytic studies of the use and value of forecasts, in studies concerned with calibrating and/or combining forecasts, in studies involving the sufficiency relation and its application, and in studies exploring the use of signal-detection-theory concepts and methods in forecast verification. Some basic information related to the variables involved, the distributions for which statistical models were formulated, and the particular form of these parametric models is presented in Table 2.

In the case of decision-analytic studies, parametric statistical models have been introduced as a convenient means of describing - and assessing the economic value of - forecasts of "current" quality (or one or more of its aspects). These models also facilitate the assessment of the value of potential improvements in forecasting performance by allowing such improvements to be accommodated through changes in the values of model parameters. For example, Katz et al. (1982) fit Gaussian models to conditional distributions of temperature observations given temperature forecasts [i.e., p(x|f)], in the context of their study of the value of minimum temperature forecasts to orchardists concerned with protecting their fruit crops against frost. Wilks and Murphy (1986) used a simplified version of a bivariate Gaussian model to fit marginal distributions to transformed, long-range temperature and precipitation forecasts [i.e., p(f)], in the context of a study of the joint value of these forecasts in a choice-of-crop problem. In decision-analytic studies involving precipitation probability forecasts (e.g., Wilks 1991; Wilks et al. 1993), beta distributions (hereafter "beta models") were used to fit the marginal distributions of the forecasts [i.e., p(f)]. Under the assumption of well-calibrated probabilistic forecasts [i.e., p(x|f) = f for all f], these marginal distributions fully describe forecast quality.

Parametric statistical models of aspects of forecast quality have been used in studies related to calibrating and/or combining of forecasts (or forecast information). For example, Clemen and Winkler (1987) used a Gaussian log-odds model to fit the conditional distributions of precipitation probability forecasts given the observations [i.e., p(f|x)]. In a combining study of a different type, Wilks and Shen (1991) used beta models to fit conditional relative-humidity-duration events given relative humidity and temperature forecasts [i.e., p(x|f)].

Some studies involving the sufficiency relation also have utilized parametric statistical models of aspects of forecast quality. For example, Krzysztofowicz and Long (1991) used beta models to fit the empirical conditional distributions of precipitation probability forecasts given the observations [i.e., p(f|x)]. In a subsequent study aimed at developing a universal measure of forecasting performance for comparative verification, Krzysztofowicz (1992) fit Gaussian models to transformed forecasts given observations [i.e., p(f|x)] and applied this measure to forecasts of runoff volume.

Table 2. Some studies in which aspects of forecast quality, as embodied in joint, conditional, and/or marginal distributions of forecasts and observations, were described using parametric statistical models.

Author(s)(Year)	Variable(s)	Distribution
(a) Decision-analytic studies		
Katz et al.(1982)	T	p(x|f)-Gaussian
Wilks/Murphy(1986)	T(tr.), P(tr.)	p(f)-Gaussian
Wilks(1991)	PP	p(f)-beta
Wilks et al.(1993)	PP	p(f)-beta
(b) Calibrating-combining studies		
Clemen/Winkler(1987)	PP(tr.)	p(f)-Gaussian
Wilks/Shen(1991)	RH(duration)	p(x|f)-beta
(c) Sufficiency studies		
Krzy./Long(1991)	PP	p(f|x)-beta
Krzy.(1992)	RV(tr.)	p(f|x)-Gaussian
(d) Signal-detection-theory study		
Mason(1982)	PP(tr.)	p(f|x)-Gaussian

Key: Krzy. = Krzysztofowicz; T = temperature, P = precipitation, PP = precipitation probability, RH = relative humidity, RV = runoff volume; tr. = transformed.

Finally, parametric statistical models of aspects of forecast quality have been used in conjunction with the signal-detection-theory approach to verification problems (e.g., Mason 1982). Specifically, this approach involves fitting standard Gaussian models to transformations of the probabilities associated with the conditional distributions of the forecasts given the observations [i.e., p(f|x)].

In summary, the studies briefly reviewed here - and identified in Table 2 - indicate that some experience has been gained in fitting various parametric statistical models to the empirical distributions underlying common verification problems. With regard to dimensionality, these models have reduced what in most

cases were problems of relatively high dimensionality to problems involving at most a handful of parameters. However, it should be noted that the objectives of the decision-analytic and calibrating-combining studies were neither absolute nor comparative verification, as these processes or practices are usually defined. Only the sufficiency and signal-detection-theory studies possess goals similar to the underlying objectives of this study; namely, to use parametric statistical models as a means of describing and comparing aspects of forecast quality in a conceptually sound yet parsimonious manner. Moreover, these latter two types of studies have frequently involved assumptions or restrictions that limit their usefulness as guides to the application of parametric statistical models to forecast verification (e.g., the assumption of well-calibrated forecasts, the restriction to dichotomous events).

4 REGRESSION MODELS, BETA MODELS, AND POP FORECASTS

The basic goals of this study of the use of parametric statistical models in forecast verification can be summarized as follows: (1) to model the empirical joint, conditional, and/or marginal distributions of forecasts and observations faithfully and thereby reduce both the dimensionality of the underlying verification problems and the effects of sampling variability on the results; and (2) to use the parameters of the modeled distributions to describe and compare forecast quality in a relatively low-dimensional - and less noisy - framework.

In the study to be reported here, parametric statistical models will be fit to empirical distributions involving probability of precipitation (PoP) forecasts produced by both numerical-statistical models and National Weather Service forecasters for selected locations in the U.S. Specifically, the study will consist of fitting regression models to the conditional distributions of the observations given the PoP forecasts [i.e., p(x|f)] [recall that $p(x|f) = E(x|f)$, the conditional mean of a dichotomous variable (x), in the case of PoP forecasts] and fitting beta distributions to the marginal distributions of the PoP forecasts [i.e., p(f)]. In the case of the regression models, the use of transformations of the conditional relative frequencies (e.g., log odds) may facilitate the model fitting process. Careful evaluation of the correspondence between the empirical and modeled distributions will be an important feature of the model fitting process. If successful, this process will reduce the dimensionality of the underlying verification problems from $d = 21$ ($= 11x2 - 1$) to $d = 4$ (2 parameters each, in the cases of the regression and beta models). Manipulation of these parameters is expected to make it possible to interpret the results in terms of familiar aspects of forecast quality. Results of an initial assessment of this model-based approach to absolute and comparative forecast verification will be reported at 6IMSC.

REFERENCES

Clemen, R.T., and R.L. Winkler, 1987: Calibrating and combining precipitation probability forecasts. *Probability and Bayesian Statistics* (R. Viertl, Editor). London, U.K., Plenum, pp. 97-110.

Katz, R.W., A.H. Murphy, and R.L. Winkler, 1982: Assessing the value of frost forecasts to orchardists: A dynamic decision-making approach. *Journal of Applied Meteorology*, **21**, 518-531.

Krzysztofowicz, R., 1992: Bayesian correlation score: A utilitarian measure of forecast skill. *Monthly Weather Review*, **120**, 208-219.

Krzysztofowicz, R., and D. Long, 1991: Beta likelihood models of probabilistic forecasts. *International Journal of Forecasting*, **7**, 47-55.

Liljas, E., and A.H. Murphy, 1994: Anders Ångström and his early papers on probability forecasting and the use/value of weather forecasts. *Bulletin of the American Meteorological Society*, **75**, 1227-1236.

Mason, I.B., 1982: A model for assessment of weather forecasts. *Australian Meteorological Magazine*, **30**, 291-303.

Murphy, A.H., 1991: Forecast verification: Its complexity and dimensionality. *Monthly Weather Review*, **119**, 1590-1601.

Murphy, A.H., and R.L. Winkler, 1987: A general framework for forecast verification. *Monthly Weather Review*, **115**, 1330-1338.

Wilks, D.S., 1991: Representing serial correlation of meteorological events and forecasts in dynamic decision-analytic models. *Monthly Weather Review*, **119**, 1640-1662.

Wilks, D.S., and A.H. Murphy, 1986: A decision-analytic study of the joint value of seasonal precipitation and temperature forecasts in a choice-of-crop problem. *Atmosphere-Ocean*, **24**, 353-368.

Wilks, D.S., R.E. Pitt, and G.W. Fick, 1993: Modeling optimal alfalfa harvest scheduling using short-range weather forecasts. *Agricultural Systems*, **42**, 277-305.

Wilks, D.S., and K.W. Shen, 1991: Threshold relative humidity duration forecasts for plant disease prediction. *Journal of Applied Meteorology*, **30**, 463-477.

CORRESPONDING AUTHOR

Dr. Allan H. Murphy
Prediction and Evaluation Systems
3115 NW McKinley Drive
Corvallis, Oregon 97330-1139, U.S.A.
(Telephone: 503-754-7424, Telefax: 503-737-2540,
E-mail: murphya@ucs.orst.edu)

Dynamical Ensemble One-month Forecast Experiments with the JMA Global Prediction Model

Kiyoharu Takano, Syuhei Maeda, Shingo Yamada, Tatsuya Kudoh
Long-range Forecast Division, JMA

and

Tadashi Tsuyuki
Numerical Prediction Division, JMA

Abstract

Ensemble one month forecast experiments using the JMA operational global spectral model with the lagged average forecast (LAF) and the dynamically optimal perturbation (DOP) method were carried out. The experiments show that the ensemble mean improves the forecast skill and the thirty day mean fields have almost enough quality to be used for one month forecast practically at least in winter. We also found good correlation between the forecast skill and the spread in the ten day mean fields of DOP experiment at least for the first 20 days.

1. Introduction

Japan Meteorological Agency (JMA) is going to start operational dynamical one-month forecast from the FY 1996. In a dynamical one month forecast, we must take chaotic character of atmosphere into account (Lorenz 1965). In other words, prediction of forecast skill or probabilistic forecast is essential. Therefore we have carried out some kinds of ensemble forecast experiment.

2. The model

The model used in our experiments is T63 version of an operational JMA global spectral model (JMA.GSM8911). It has 21 vertical levels based on a hybrid vertical coordinate, with the top at 10 hPa.

3. The LAF experiment

We carried out 20 cases of one-month ensemble forecast in winter (Yamada et al. 1991) and 16 cases in summer with lagged average forecast (LAF) method. Each ensemble forecast consists of 9(5) samples in winter (summer) whose initial conditions are derived from consecutive operational global analyses 12 hours apart.

The skills of ensemble mean forecast are better than those of single operational dynamical forecast (ODF). The average anomaly correlation coefficient of ensemble forecasts in winter for the 30 day mean 500 hPa geopotential height in the Northern Hemisphere is 0.56 if independent systematic errors are removed (Table 1.) This skill is almost enough to be used for practical one month forecast. The skill of summer experiments is not so good as of winter. The average anomaly correlation coefficient for summer experiment is 0.5 if independent systematic errors are removed. For ten day mean 500 hPa field of winter experiment, the improvements of ensemble mean score comparing with ODF are not evident for the first ten days of forecasting time but evident after first ten days (Fig.1).

For prediction of forecast skill, the (inverse) correlation between the forecast skill and the spread of individual single forecasts in an ensemble are important. However we did not find the correlation between the skill and the spread in the LAF experiment.

4. The DOP experiment.

To improve the correlation between the forecast skill and the spread, we adapted the dynamically optimal perturbation (DOP) method (Mureau et al. 1992). The optimal modes (singular vectors) are calculated using T21L2 hemispheric model and optimized over 48 hours. The greatest ten growing modes are linearly superposed to avoid localization of perturbations and used as perturbations to an initial condition.

We have carried out two kinds of experiment. One is 10 case wintertime ensemble forecasts with three samples whose initially added perturbation amplitudes are 1 m/s in terms of horizontal velocity (D1 experiment) and the other is 19 cases with five samples whose perturbation amplitudes are 2 m/s (D2 experiment).

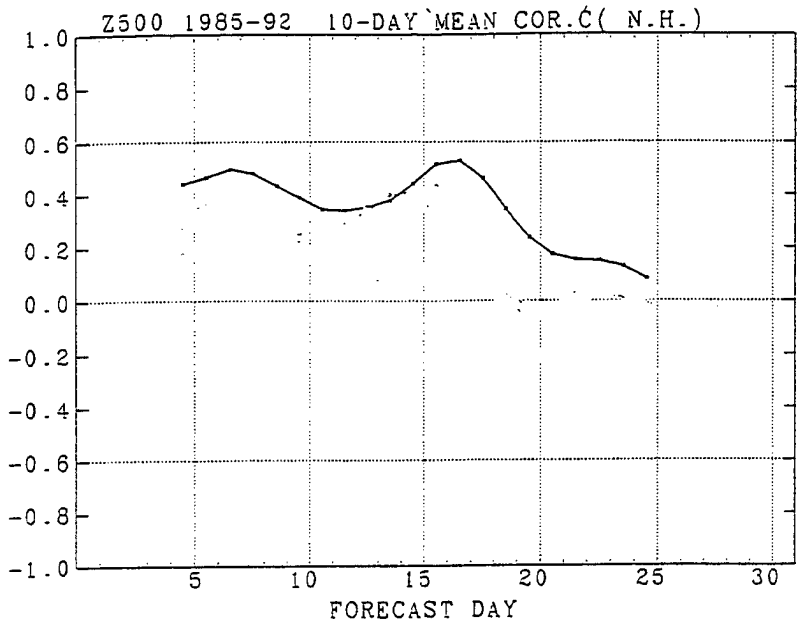


Figure 3. The correlation coefficients between skill and spread for **10 day mean** 500 hPa geopotential height in the Northern Hemisphere with DOP method (initial perturbation amplitudes are **2 m/s**). The measure of skill and spread is anomaly correlation.

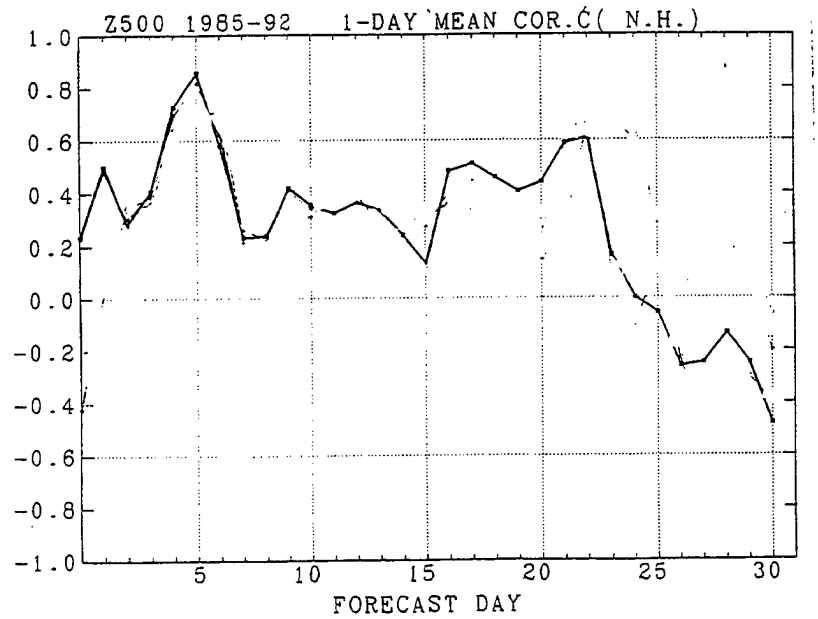


Figure 4. The correlation coefficients between skill and spread for **daily** 500 hPa geopotential height in the Northern Hemisphere with DOP method (initial perturbation amplitudes are **1 m/s**). The measure of skill and spread is anomaly correlation.

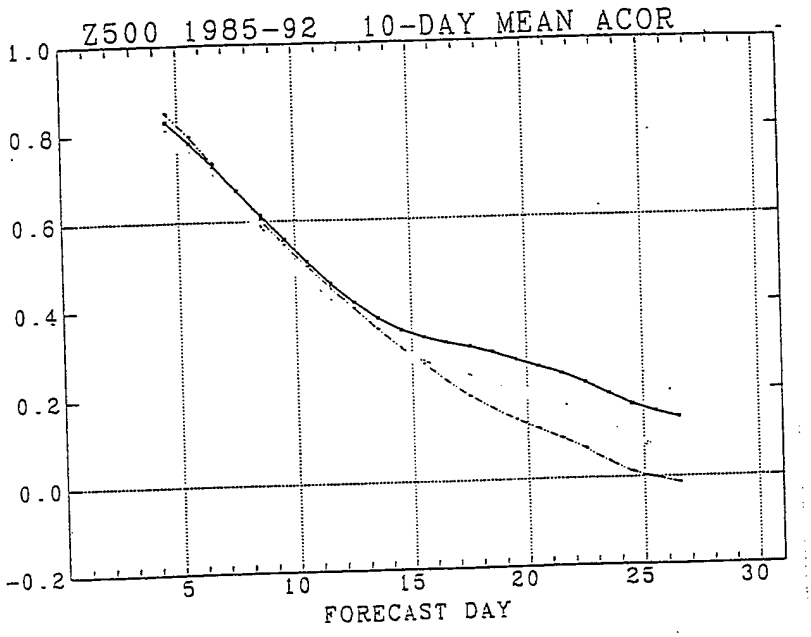


Figure 1. 20 case average anomaly correlation coefficients for 10 day mean 500 hPa geopotential height in the Northern Hemisphere (winter cases). Ensemble mean with **LAF** method (solid line) and ODF (dashed line with two dots).

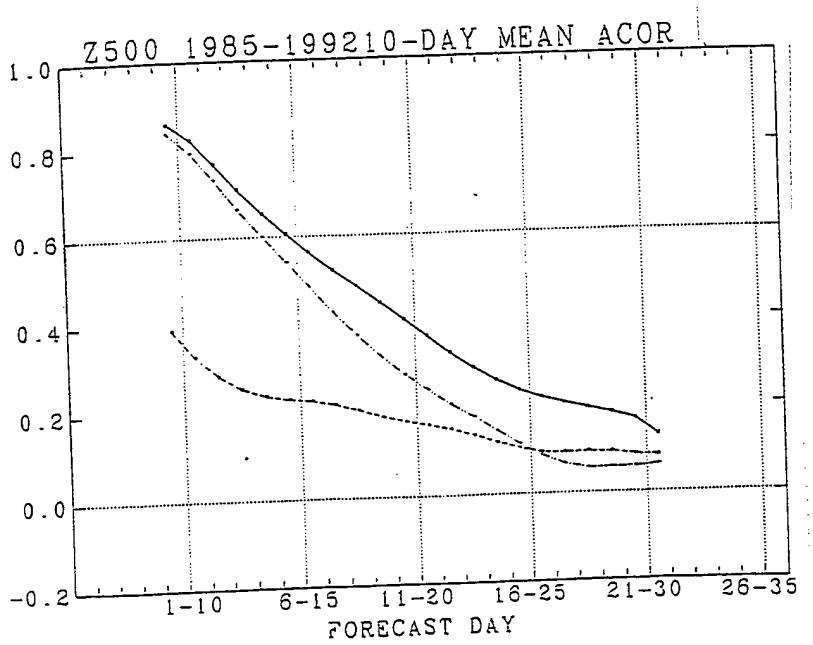


Figure 2. 19 case average anomaly correlation coefficients for 10 day mean 500 hPa geopotential height in the Northern Hemisphere (winter cases). Ensembles mean with **DOP** method (solid line), ODF (dashed line with two dots) and persistency forecast (dashed line).

In both experiments with the DOP method, ensemble mean skills are improved compared with the experiment with the LAF method especially for the first 10 days (Table 1.,Fig.2). This is because in the DOP method we need not to use older initial conditions as in the LAF method.

For the ten day mean field, good skill–spread correlation is found in D2 experiment but not in D1 experiment. On the other hand, for daily field, better skill–spread correlation is found in D1 experiment than in D2 experiment. These facts suggest that 2 m/s amplitude is more appropriate for spread–skill correlation of low frequency variations but for that of high frequency (synoptic scale) variations 1 m/s amplitudes are more appropriate. The reasons why the skill–spread correlation depends on the initial perturbation amplitude are not clear but incompleteness of the numerical model or analyses may be able to explain some parts of those.

5. Conclusions

In our experiment, we showed that average score of ensemble mean skill is almost enough so that we may use 30 day mean fields for one month forecast. For ten day mean field, although average score is enough to be used practically only for the first ten days, we found good skill–spread correlation at least for the first twenty days. Therefore we can expect prediction of forecast skill at least for the first twenty days. If we can use more samples to a ensemble, the probabilistic forecasts will be possible.

Our experiments shown above are restricted mainly for winter season. Evidently the experiments for other seasons are necessary and are now on under way.

Reference:

Lorenz, E.N. 1965 "A study of the predictability of a 28–variable atmospheric model" Tellus,17,321–333.

Mureau, R, F. Molteni and T.N. Palmer 1992, "Ensemble prediction using dynamically–conditioned perturbations", ECMWF Workshop Proceedings "New development in predictability 13–15 November 1991" PP.143–174

Yamada, S., S. Maeda, T. Kudo, T. Iwasaki, and T. Tsuyuki. 1991, "Dynamical one–month forecast experiments with the JMA global prediction model" J. Meteor. Soc. Japan, 69 153–159

O D F	ENSEMBLE MEAN (LAF)	ENSEMBLE MEAN (DOP Amp=2m/s)
0.49 (0.47)	0.58 (0.56)	(0.59)

Table 1. Average anomaly correlation coefficients for 30 day mean (day 0–29) 500 hPa geopotential height in the Northern Hemisphere (winter cases). The upper row shows 20 case averages. The lower row (within brackets) shows 19 case average (same cases with DOP experiment).

SPECIFICATION OF MONTHLY MEAN 700MB HEIGHTS FROM SURFACE DATA

W. H. Klein and Y. Dai

University of Maryland, College Park, Maryland

ABSTRACT

This paper develops an objective method of computing monthly mean 700mb height anomalies (H) at 108 grid points (70°-20°N and 180°-10°W) for a 40-year period (1951-1990) from concurrent anomalies of monthly mean sea level pressure (P), at the same points used for H, and monthly mean surface air temperature (T) averaged over 112 areas in North America. We applied a forward stepwise program to derive linear multiple regression equations that explained 81% of the variance of H by means of only 3.5 variables, averaged over all months and grid points. The stability of these equations held up well on six years of independent data (1947-1950 and 1991-1992)) in terms of explained variance, root-mean-square error and the spatial anomaly correlation coefficient. We conclude that it is feasible to reconstruct maps of H for the first half of the 20th century from P and T only.

1 INTRODUCTION

A reliable archive of hemispheric upper air maps for studies of climate and climate change is not available prior to 1947. In order to fill this gap, we developed an objective method of computing monthly mean 700mb height anomalies (H) from surface data only by reversing the customary technique of specifying surface weather elements (such as temperature, precipitation, dew point and wind speed) from concurrent values of H (Klein and Whistler, 1991). Here we specified H at 108 grid points in the western half of the Northern Hemisphere on a 10° latitude/longitude grid from 70° - 20°N and 180° - 10°W for the 40-year period: 1951 - 1990. Our potential predictors were simultaneous monthly mean anomalies of sea level pressure (P) at the same 108 points used for H, surface air temperatures (T) averaged over 68 climate divisions (CDs) in the contiguous United States, as well as over 44 boxes (5° latitude by 5° longitude) in the remainder of land areas, and precipitation amounts at the same 68 CDs used for T (precipitation at the 44 grid boxes was not available). Fig. 1 shows the location of the 68 CDs (data obtained from the National Climate Data Center in Asheville, N.C.) (Cayan et al., 1986) and the 44 temperature boxes (data obtained from the University of East Anglia in England) (Parker et al., 1994).

We used a forward stepwise regression procedure (screening) to derive linear multiple regression (specification) equations for H for each month and each grid point. We increased our sample size from 40 to 120 by pooling data for the target month with its two adjacent months. For example, the equations for March were derived from data for February, March and April. We used an automatic cut-off procedure based on various probability levels to produce equations with 3 to 5 variables on average (more on the continent and less in the oceans).

2 DERIVATION

We first tested our predictor fields one at a time. The P field reduced the unexplained variance (RV) of H by about 74%, averaged over all months and points. The corresponding statistics for T and precipitation were 45% and 27%, respectively. Screening of P produced higher RV over the oceans than over the land, but screening of T gave the opposite pattern. Screening of P and T simultaneously increased the RV by about 10% overall and as much as 30% over the interior of North America. However, the improvement in RV produced by adding precipitation as a potential predictor was negligible (less than 0.5% overall).

As a result of these and other experiments, we derived final specification equations for H based only on P and T. Sample equations are illustrated in Table 1. The first is for a point just south of Iceland during the winter months. Here only two variables were selected: the local P which explained 95% of the variance of H, and P at a point 10° to the east, which added 2%. The second equation is for a point near the center of the United States during summer, where five variables made a significant contribution to the RV. Three of these (the 1st, 4th and 5th) were T terms, while only two were P (including a point in northwest Canada). The contrast between these two equations shows that the lower troposphere is usually equivalent barotropic in the oceans (especially the east-central part), but baroclinic over the continents (especially in the interior).

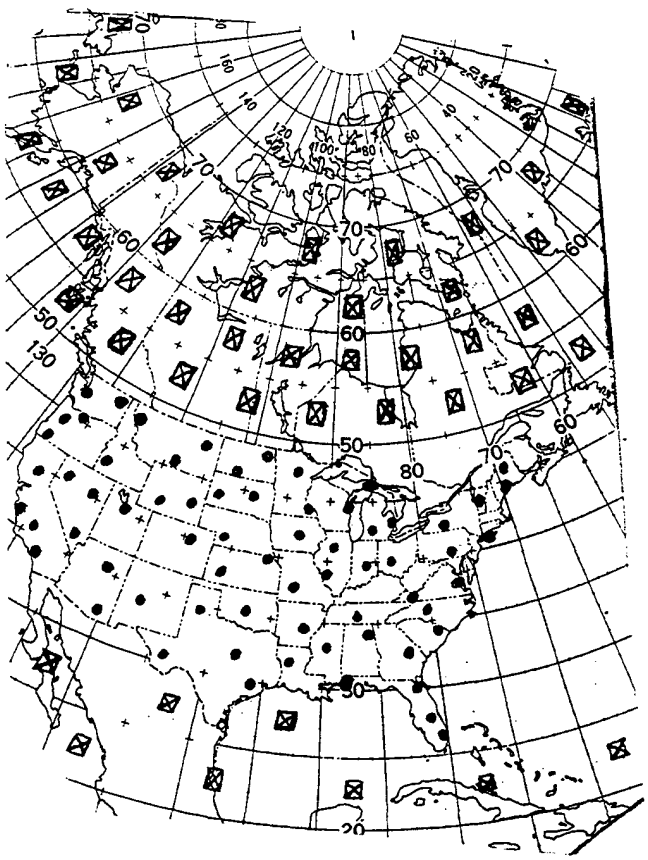


Figure 1. Locations of temperature potential predictors.

For all months and grid points, the specification equations yielded an RV of 81% by means of just 3.5 variables. The annual cycle of RV on a hemispheric basis (Fig. 2) ranged from 87% in winter to 74% in summer, while the number of variables varied from 3.9 in winter to 3.2 in summer. On a latitudinal basis (Fig. 3), the RV was uniformly poor at 20°N but very good (about 90%) from 40°N to 70°N. When latitude and season were combined, the mean RV varied from 96% at 50°N in January to 33% at 20°N in July. Like most features of the general circulation, belts of maximum and minimum were farthest north in summer and fall, but farthest south in winter and spring.

Table 1. Sample multiple regression statistics obtained by screening monthly mean 700mb height anomalies from 1951 to 1990 as a function of the concurrent anomaly fields of monthly mean sea level pressure (P) and surface air temperature (T). The significance level at which a predictor variable was accepted in an equation (cutoff criterion) was 0.03 % applied to the reduction of variance (RV) added at each step.

Step	Predictor	Location	Added RV(%)	Cumulative RV(%)	Coefficient in Final Equation
		a) 60°N, 20°W during December, January and February:			
1	SLP	60°N, 20°W	95.40	95.40	5.961
2	SLP	60°N, 10°W	1.90	97.30	3.221
		b) 40°N, 100°W during June, July and August:			
1	SAT	42°N, 105°W	50.85	50.85	6.082
2	SLP	30°N100°W	18.70	69.55	5.439
3	SLP	60°N,130°W	5.00	74.55	2.024
4	SAT	29°N,95°W	2.66	77.21	5.487
5	SAT	53°N,103°W	4.33	81.54	2.850

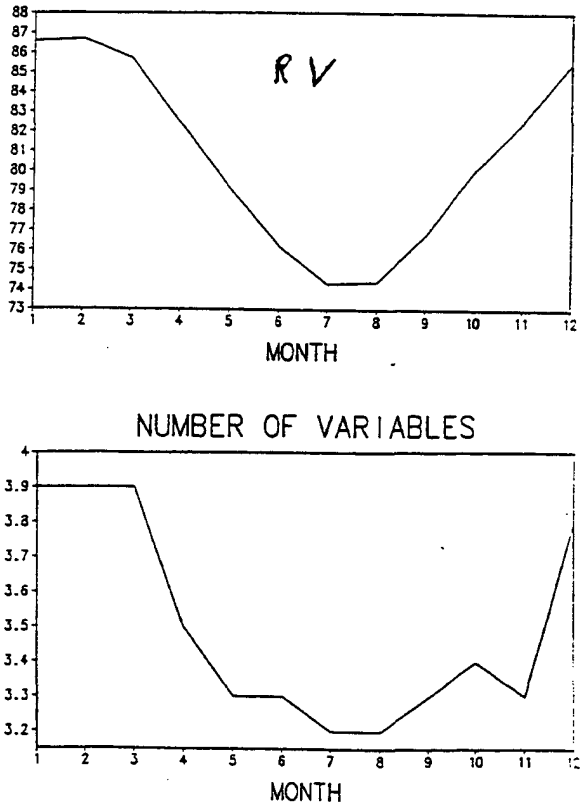


Figure 2. Annual cycle of reduction of variance and number of variables selected in the specification equations.

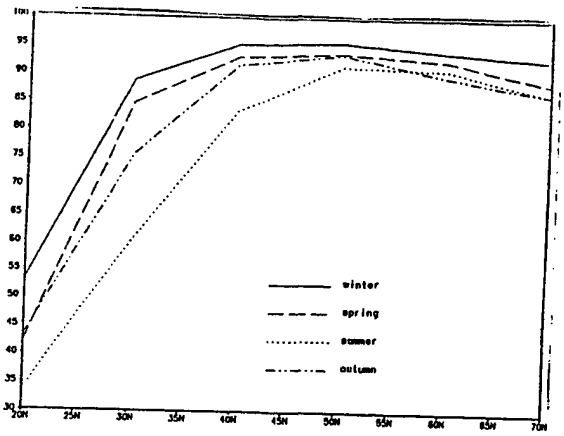


Figure 3. Reduction of variance of H as a function of latitude and season.

3 TEST RESULTS

The stability of the specification equations held up well on six years of independent data (1947-1950 and 1991-1992). Three verification statistics were computed. The first was identical to the RV used for the dependent data, but for a smaller sample (6 years instead of 40) (Table 2). The shrinkage in RV expected in going from dependent to independent data was only 2.8% overall, with best results in winter and poorest in summer. The shrinkage was least at 50°N and greatest at 20°N. The geographical pattern of RV on the independent data closely resembled that on the dependent data.

Table 2. Mean temporal values of RV (%) for specified monthly mean 700 mb height anomalies at 108 points in the western hemisphere (20°-70°N) for independent data (1947-1950 and 1991-1992) and dependent data (1951-1990).

Month	Independent Data	Dependent Data	Shrinkage (D-I)
January	86.7	86.6	-0.1
April	81.2	82.4	1.2
July	67.0	74.3	7.3
October	77.2	80.0	2.8
Mean	78.0	80.8	2.8

The second verification statistic was identical to the first, but for the root-mean-square error (RMSE) (Table 3). For all months and grid points, the mean RSME of the specification equations was only 2.7m, with a small range from 3m in winter to 2.4 m in summer. By comparison, the RMSE obtained by assuming the 40-year normal (1951-1990) averaged 8.0m or 67% greater. On a latitudinal basis, the improvement of specification over normal ranged from 7.9m at 60°N to 0.7m at 20°N.

Table 3. Root mean square errors (meters) in the western hemisphere (20°-70°N) for specified and normal (40 yr. mean) 700 mb height fields during 72 independent months of 6 test years (1947-1950 and 1991-1992).

Season	Months	Specified Heights	Normal Heights	Difference (N-S)
Winter	Dec., Jan., Feb.	3.0	11.0	8.0
Spring	Mar. Apr. May	2.6	8.0	5.4
Summer	June, July, Aug.	2.4	5.4	3.0
Autumn	Sept., Oct., Nov.	2.6	7.4	4.8
Year	All 12 months	2.65	7.95	5.30

Table 4. Spatial correlation coefficients for the western hemisphere (20°-70°N) between specified and observed monthly mean 700mb height anomaly fields during 72 independent months of 6 test years (1947-1950 and 1991-1992).

Season	Months	Mean R(%)	Range of R(%)
Winter	Dec., Jan., Feb.	96.0	93-98
Spring	Mar., Apr., May	93.2	83-97
Summer	June, July, Aug.	90.7	81-95
Autumn	Sept., Oct., Nov.	92.9	87-96
Year	All 12 months	93.2	81-98

The third verification statistic was the spatial anomaly correlation coefficient (R) (Table 4). It was computed by comparing the specified (reconstructed) with the observed values of H at each grid point for each map of the 72 test months (6 years x 12 months). The values of R averaged 0.93 for all 72 maps, with maximum of 0.96 during the winter months and minimum of 0.91 in summer. Examples of the best and worst individual reconstructions are illustrated in Fig. 4. The specified and observed maps are so similar that it is hard to tell one group from the other. We therefore believe that it is feasible to reconstruct maps of H from surface data only.

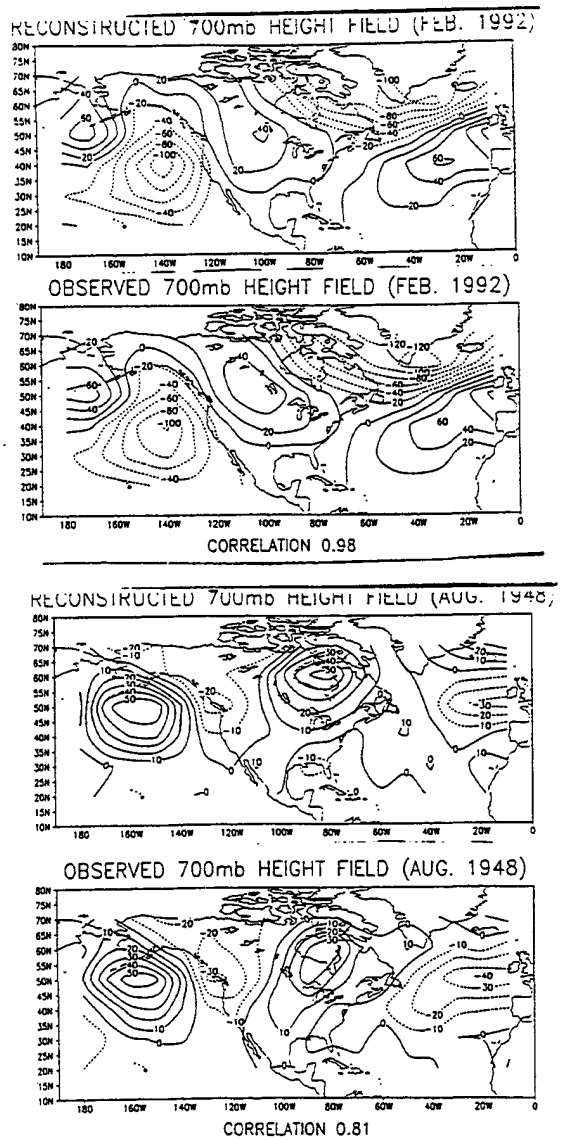


Figure 4. Reconstructed and observed height anomalies with correlations of 0.98 & 0.81.

4 CONCLUSION

Our recommendations for further research are to: 1) Rederive the specification equations by using the T data in 5° boxes that go back to the 19th century, instead of the CD data over the contiguous United States which began in 1931. 2) Screen the field of sea surface temperature as a possible source of improved specification, especially at low latitudes. 3) Derive specification equations for the eastern hemisphere. 4) Apply the above equations to reconstruct maps of H covering most of the Northern Hemisphere and going back to 1899, the year the Historical Map Series began.

References

Cayan, D. R., C. F. Ropelewski and T. R. Karl, 1986: An Atlas of United States Monthly and Seasonal Temperature Anomalies: December 1930-November 1984. United States Climate Program Office, Dep't. of Commerce, Washington, DC 244 pages.

Klein,W. H. and B. T. Whistler, 1991: Specification of monthly mean anomalies of fire-weather elements in the United States. *Agricul. Forest Meteor.*, 56, 145-172.

Parker, D. E., P. D. Jones, C. K. Folland and A. Bevan, 1994: Interdecadal changes of surface temperature since the late nineteenth century. *J. Geophys. Res.*, 99, 14373-14399.

ACKNOWLEDGMENTS

This research was suggested by Huug van den Dool of the U. S. Climate Prediction Center and John Knox of the Canadian Climate Centre. Valuable help was received from Tony Barnston and Jil Huang of the Climate Prediction Center, as well as Alan Robock and Jianping Mao of the University of Maryland.

CORRESPONDING AUTHOR

Doctor William H. Klein,
Department of Meteorology,
Cooperative Institute for Climate Studies
University of Maryland,
College Park, MD 20742, USA.

Comparison of Gaussian Shift and Gaussian Hybrid Models for Decision Making with the NWS Long Lead Temperature Forecasts

Richard L. Lehman
National Meteorological Center
National Weather Service, Washington, DC 20233

Abstract
The new Long Lead (LL) Temperature Forecasts issued by the Climate Prediction Center(CPC) consist of three types, each based on a Gaussian model of a climatological distribution of seasonal average temperature values. Competing Gaussian Shift and Gaussian Hybrid models for decision making based on the LL forecasts have been advanced, posing the problem of which is the better model to use. This paper develops exact values for the parameters of the decision models for the three types of forecast, and presents data showing that each forecast set of Gaussian Shift models better approximates the given Gaussian climatology than each competing set of Gaussian Hybrid models. The latter are shown to have too much density near the mode and too little in the tails. Based on its better consistency with climatology, we conclude that the Gaussian Shift is the better model for decision making.

1. Introduction.

The new Long Lead (LL) Temperature Forecasts consist of probability statements that modify the densities in three defined categories in the Gaussian model of the climatological distribution of seasonal average temperature . The categories consist of the central 1/3 of the distribution and the two equal tails, each with 1/3 of the distribution. In a standardized normal distribution the category boundaries are at -.4307 and +.4307, equally distant from zero, the mean value. At a given station, the boundaries are at $\mu \pm .4307\sigma$, where μ is the mean value and σ^2 the variance of the observed climatological distribution of temperature (T) values at the station. We consider below only the standardized form of the station variable $t = (T - \mu)/\sigma$.

There are three types of LL temperature forecast, Below(B) , Near(N), and Above(A) normal, each given in terms of specific changes in the three categories(O'Lenic, 1994), as in the following examples. An N-type forecast with a 10% chance of occurrence (N10) implies a .1 increase in the central category and a .05 decrease in the upper and lower tail categories. The N10 forecast increases the chances that the unknown outcome will fall in the central category and reduces chances that it will fall in the tails. The forecast changes the probabilities from 1/3,1/3,1/3 to .283,.433,.283. An A forecast with 10% chance of occurrence(A10) implies a categorical change to .233, 1/3, .433, that is the .1 increase in the upper, or A category is at the expense of the lower, or B category, the central category remaining unchanged. Similarly a B5 forecast implies a change to .383, 1/3, .283. Thus only N-type forecasts change the central category. Ignoring rounding of the last digits, the sum of the categories is one: there is always a 100% chance that a future outcome will fall into one of the three categories.

Lehman (1987a), and Briggs and Wilks (1994) have developed Gaussian decision making models that can convert the categorical information in NWS LL forecasts into probability distributions describing the forecast-contingent variables. But the two models interpret the categorical information differently and provide different probability distributions for the same LL forecast. The objective of this paper is to provide data that help answer the question: Which is the better model to use? We propose here to answer the question by use of a constraint that applies to all forecast models: consistency with climatology. The suite of distributions associated with the better decision model should have densities that *in weighted sum* better approximate the climatological distribution of the forecast variable.

In order to measure model consistency with climatology, we must be able to specify the parameters of the density functions provided by the two models. We begin by describing how the two models interpret the LL forecast categorical information, and how the parameters in the two models are found.

2. The Gaussian Shift Model for Decision Making.

The Gaussian Shift (GS) model decomposes the forecast temperature variable into three complete Gaussian distributions, supposing that each monthly A-type shifted forecast distribution at a site will be 'balanced' on average over time by an equal and opposite B-type forecast distribution, and a hidden, zero mean distribution, Lehman (1987b). The three distributions are identical, differing only in the location parameter, which is determined by the forecast categorical anomaly (the difference from the climatologically expected 1/3). The common variance of

the three distributions is determined by use of the shift w, *or change in the mean of a Gaussian distribution*, in the direction that gives the increased probability in the tail favored by the forecast f, and fab, the fraction of the A- and B-type forecasts at a site. For the pre-1995 monthly forecasts, fab was taken to be .6, and the variance $c^2 = 1 - .6w^2$, where w = Inv(G(x-w)) - Inv(G(x)). Inv(G(x)) is the inverse of the gaussian function G(x)= 1/3, i.e. x = -.4307, and Inv(G(x-w)) is the inverse of G(x-w) = 1/3 + .01f. f is the forecast percent change in the chance of outcomes in the preferred tail: for example, in an A10 forecast f=10, and w=0.263.

For the new LL forecasts, the GS model makes fab a parameter, allowing it to change with season and location, thus the variance $c^2 = 1 - (fab)w^2$. The hidden zero mean distribution is explicitly recognized as an N-type Gaussian forecast distribution with variance c^2. In theory fab can take on any value between 0 and 1, but until experience dictates otherwise, a value of .7 seems reasonable for most sites, suggesting that on average 30% of the forecasts at the site will be of the N-type. The GS forecast-contingent, compressed set of distributions used for decision making are rescaled to unit variance by shifting the mean of the A- and B-types from zero by $\pm cw$, and using $t = [T - (\mu \pm \sigma w)]/c\sigma$. G(t) then gives the GS model probability, given the forecast f, that an unknown temperature outcome of interest will fall at or below T. For an N-type forecast f, G(t) is also used but with $t = (T - \mu)/c\sigma$.

3. The Gaussian Hybrid Model for Decision Making.

Briggs and Wilks (1994) have advanced a Monte Carlo - derived version of a Gaussian Hybrid model that determines the mean and variance of the hybrid distribution composed of the sum of the forecast-weighted Gaussian categorical fragments. The mean and variance values so obtained are proposed **for direct use as** the parameters of a Gaussian forecast-conditional distribution to be used in decision making. The Monte Carlo estimates of the mean values of the hybrid distributions is excellent, but since the estimates of variances differ somewhat from the theoretically correct results given below, the comparisons that follow make use of the theoretical rather than the estimated parameters for the Gaussian Hybrid suite of models.

a. Expressions for the Mean Value of Gaussian Hybrid Model distributions

We begin by finding τ, the mean value of the standard Gaussian distribution, truncated at x, the value of t at the boundary of the lower category. This may be obtained from $\tau F(x) = \int(-\infty,x)\{tf(t)\}dt$, = -f(x), or τ = -f(x)/F(x) (see, e.g. Cramér, 1946). Here we use $\int(-\infty,x)\{\}dt$ to denote the integral of the quantity brackets over the limits given in the parenthesis. f(x) and F(x) are the Gaussian density and distribution functions, respectively. At x = -.4307, f(x) = .3636, F(x) = 1/3, and τ = -1.0908. By symmetry, the mean of the central category is zero, and the mean of the upper category is $-\tau$.

The separate contribution of each category to the total Gaussian distribution is

$$\text{mean} = \tau F(x) + \int(x,-x)\{tf(t)\}dt - \tau F(x), \quad (1)$$

where F(x) is the size of the categories, or
mean = -1.0908(1/3) + 0 + 1.0908(1/3) = 0, when f=0 and F(x)=1/3.

Thus the mean of the overall distribution is the sum of the means of the independent categories, weighted by the size of each category. We use this result to find a simple expression for the mean of any A or B LL temperature forecast f, where f = % change in chance of occurrence of an outcome in the forecast-preferred category.

The hybrid distribution mean for the B forecast = $\tau(1/3+f/100)-\tau(1/3-f/100) = .02\tau f = -.021816f$. By symmetry, the mean for the A forecast = .021816f, and the mean for the N forecast = 0.

b. Expressions for the Variance of Gaussian Hybrid Model distributions

We begin by finding Vx the variance of a standard Gaussian distribution, truncated at x. This may be obtained from $Vx = (1 + x\tau)$, in Lehman (1987b). With x = -.4307, Vx = 1.4698, and F(x)Vx = .4899.

Now $F(x)Vx = \int(-\infty,x)\{t^2f(t)\}dt$ is the contribution of the lower category to the variance of the total Gaussian distribution, which is one. Since the upper category is symmetrical to the lower, its contribution to the total variance is also F(x)Vx, hence the contribution of the second, or central category $F(x)Vc=\int(x,-x)\{t^2f(t)\}dt$ is by default 1-2F(x)Vx or .0201, with Vc = .0603.

Thus the separate contribution to each category to the total Gaussian distribution variance is

$$\text{variance} = VxF(x) + VcF(x) + VxF(x), \quad (2)$$

where F(x) is the size of the categories, or
variance=.4899 + .0201 + .4899, when f=0 and F(x)= 1/3.

For N forecasts, the size of the lower and upper categories is the same (1/3-f/200). We thus have the rule, with the same notation as that for the means,

model variance for N forecasts =

$2Vx(1/3 + f/200) + Vc(1/3 + f/100)$, (3)
or $1 - .014095f$.

In order to find the variance for B forecasts, we evaluate separately the contribution from each category, recalling the rule that for the distribution of any variable Z, $Var(Z + k) = Var(Z) + k^2$, when k is a constant. Now Vx is the variance of the first category about an external mean value zero. Thus the variance of the first category about its own mean τ is given by $V_\tau = Vx - \tau^2$, and the variance of the first category *about mb, the mean of the hybrid distribution(B forecasts),* $Vb1 = V_\tau + (\tau - mb)^2$. Substituting terms, $Vb1 = Vx - 2\tau mb + mb^2$. In a similar manner the variance of the third category *about mb* is $Vb3 = Vx + 2\tau mb + mb^2$, and the variance of the central category *about mb*, $Vb2 = Vc + mb^2$.

Collecting terms and applying the forecast changes to the categories, we obtain:

model variance for B forecasts = $Vb1(1/3+f/100)+Vb2(1/3)+Vb3(1/3-f/100) = 1-mb^2 = 1-(.02\tau f)^2 = 1-.0004759f^2$ (4)

By symmetry, (4) is also the hybrid distribution variance for A forecasts.

4. Results and Conclusion

Table 1 shows how the parameters for the Gaussian Shift and Gaussian Hybrid decision models differ: the means in the Hybrid model distributions for A- and B-type forecasts are smaller than those in the Shift model, while the variances, especially in the distributions for N-type forecasts, are larger. Table 2 compares the models in their consistency with climatology. It is readily apparent that the Hybrid models assign too much density near the mode, and too little near the tails, while the Shift model provides reasonably good consistency for any forecast These model differences arise from the differences in the model parameters just discussed. We conclude on the basis of consistency with climatology that the Gaussian Shift model is the better one for decision making.

References.

W. M. Briggs and D. S. Wilks, November 1994, Estimating monthly and seasonal distributions for temperature and precipitation using the new CPC long-range forecasts, Dept. Soil, Crop, and Atmospheric Sciences, Cornell Univ., Ithaca, NY 14583.

H. Cramér, 1946, *Mathematical Methods of Statistics*, Princeton Univ. Press, 248pp.

R. L. Lehman, 1987a, A model for decision making based on NWS monthly temperature outlooks, *J. Clim. Appl. Meteor.* 26, 263-274.

R. L. Lehman, 1987b, Probability distributions of monthly degree day variables at U. S. Stations, *J. Clim. Appl. Meteor.* 26, 329-340.

E. A. O'Lenic, 1994, Operational long-lead forecasts for the climate outlook, Draft Technical Procedures Bulletin, NOAA/NWS/CPC.

Table 1. Comparison of Parameters for Gaussian Shift (GS) and Gaussian Hybrid (GH) Decision Making Models Related to LL Temperature Forecasts

	B-forecast means				B-forecast std.devs				N-forecast std.devs		
f	μ0gs	μgs	μgh	μmc*	σ0gs	σgs	σgh	σmc*	σgs	σgh	σmc*
0	0.000	-0.000	0.000	0.000	1.000	1.000	1.000	1.000	1.000	1.000	1.000
1	-0.027	-0.027	-0.022	-0.022	1.000	1.000	1.000	1.000	1.000	0.992	0.993
2	-0.054	-0.054	-0.044	-0.044	0.999	0.999	0.999	0.999	0.999	0.984	0.986
3	-0.081	-0.081	-0.065	-0.066	0.997	0.998	0.998	0.998	0.998	0.976	0.979
4	-0.107	-0.107	-0.087	-0.087	0.994	0.996	0.996	0.996	0.996	0.968	0.971
5	-0.133	-0.133	-0.109	-0.109	0.991	0.994	0.994	0.993	0.994	0.961	0.964
6	-0.158	-0.159	-0.131	-0.131	0.987	0.991	0.991	0.990	0.991	0.953	0.957
7	-0.183	-0.184	-0.153	-0.153	0.983	0.988	0.988	0.987	0.988	0.945	0.949
8	-0.207	-0.209	-0.175	-0.175	0.977	0.985	0.985	0.983	0.985	0.937	0.942
9	-0.231	-0.233	-0.196	-0.197	0.971	0.981	0.981	0.978	0.981	0.929	0.934
10	-0.254	-0.257	-0.218	-0.219	0.965	0.977	0.976	0.973	0.977	0.921	0.927
11	-0.276	-0.280	-0.240	-0.240	0.958	0.972	0.971	0.967	0.972	0.913	0.919
12	-0.298	-0.303	-0.262	-0.262	0.950	0.967	0.965	0.961	0.967	0.905	0.912
13	-0.319	-0.325	-0.284	-0.284	0.941	0.961	0.959	0.954	0.961	0.897	0.904
14	-0.339	-0.347	-0.305	-0.306	0.931	0.955	0.952	0.947	0.955	0.889	0.896
15	-0.358	-0.369	-0.327	-0.328	0.921	0.948	0.945	0.939	0.948	0.882	0.888
16	-0.377	-0.390	-0.349	-0.350	0.910	0.941	0.937	0.931	0.941	0.874	0.880
17	-0.395	-0.410	-0.371	-0.372	0.898	0.934	0.929	0.922	0.934	0.866	0.872
18	-0.411	-0.429	-0.393	-0.393	0.886	0.925	0.920	0.912	0.925	0.858	0.864
19	-0.427	-0.449	-0.415	-0.415	0.872	0.917	0.910	0.902	0.917	0.850	0.856
20	-0.441	-0.467	-0.436	-0.437	0.858	0.908	0.900	0.892	0.908	0.842	0.847

* Data based on Monte Carlo results of Briggs and Wilks, 1994.
μ0gs and σ0gs are values for areas where few if any N forecasts will be made.
μgs and σgs are values for areas where 1/3 of the forecasts will be N type.

Table 2. Comparing Gaussian Shift (GS) and Gaussian Hybrid (GH) Decision Making Models for Consistency with Climatology: 70% AB Forecasts*

	GS	GH	GS	GH	GS	GH	GS	GH	GS	GH
f	Σf(0)	Σf(0)	Σf(½)	Σf(½)	Σf(1)	Σf(1)	Σf(1½)	Σf(1½)	Σf(2)	Σf(2)
0	0.399	0.399	0.352	0.352	0.242	0.242	0.130	0.130	0.054	0.054
1	0.399	0.399	0.352	0.352	0.242	0.241	0.130	0.129	0.054	0.054
2	0.399	0.399	0.352	0.352	0.242	0.241	0.130	0.128	0.054	0.053
3	0.399	0.399	0.352	0.352	0.242	0.241	0.130	0.128	0.054	0.053
4	0.399	0.399	0.352	0.352	0.242	0.240	0.130	0.127	0.054	0.052
5	0.399	0.400	0.352	0.352	0.242	0.240	0.130	0.127	0.054	0.052
6	0.399	0.400	0.352	0.352	0.242	0.239	0.130	0.126	0.054	0.051
7	0.399	0.400	0.352	0.352	0.242	0.239	0.130	0.125	0.054	0.051
8	0.399	0.401	0.352	0.352	0.242	0.239	0.130	0.125	0.054	0.051
9	0.398	0.401	0.352	0.352	0.242	0.238	0.130	0.124	0.054	0.050
10	0.398	0.402	0.352	0.353	0.242	0.238	0.130	0.124	0.054	0.050
11	0.398	0.403	0.352	0.353	0.242	0.238	0.130	0.123	0.054	0.049
12	0.398	0.404	0.351	0.353	0.242	0.237	0.130	0.123	0.054	0.049
13	0.398	0.405	0.351	0.354	0.242	0.237	0.130	0.122	0.054	0.048
14	0.397	0.406	0.351	0.355	0.242	0.237	0.130	0.121	0.054	0.048
15	0.397	0.407	0.351	0.355	0.242	0.237	0.130	0.121	0.055	0.047
16	0.397	0.408	0.351	0.356	0.243	0.237	0.131	0.120	0.055	0.047
17	0.396	0.410	0.351	0.357	0.243	0.237	0.131	0.120	0.055	0.046
18	0.395	0.411	0.350	0.358	0.243	0.237	0.131	0.119	0.055	0.046
19	0.395	0.413	0.350	0.359	0.243	0.237	0.132	0.118	0.055	0.045
20	0.394	0.415	0.350	0.361	0.243	0.237	0.132	0.118	0.055	0.044

*for each forecast f the densities for A-, B- and N-type forecasts for each decision model are summed at half-integral t values. The A- and B-types are weighted by .35, and the N-type by .30. The closer to the f=0 climatology value, the more consistent is the model.

STATISTICAL CLIMATOLOGY OF ICING EVENTS AND FORECASTS OVER THE CONTINENTAL UNITED STATES

Barbara G. Brown

National Center for Atmospheric Research
Boulder, Colorado, U.S.A.

ABSTRACT

In-flight icing remains a significant aviation hazard. Icing regions currently are identified using reports from pilots ("PIREPs"), but a climatology of icing events does not exist. Because PIREPs are not systematic in time or space, they represent a difficult dataset for use in building a climatology. A regression-based methodology (utilizing climatological and other information about city regions) to standardize icing frequency estimates is developed and applied to five years of PIREP data. The climatological icing estimates are compared to frequencies associated with icing forecasts for one year.

1 INTRODUCTION

In-flight icing poses a significant hazard to aircraft, as witnessed by the crash of a commuter airplane near Chicago last fall. This crash had a major impact on commuter airline safety regulations in the U.S., which resulted in economic and other impacts on the airline industry.

The ability to forecast the occurrence of icing events has been the subject of much research in recent years (Rasmussen et al., 1992; Schultz and Politovich, 1992; Thompson et al., 1995). This research has focused on the development of algorithms that can be applied to the output of national- or regional-scale numerical weather prediction models. Currently these algorithms are rather unsophisticated, being based simply on whether atmospheric conditions meet specified temperature and humidity criteria.

A reliable national climatology of icing conditions would be beneficial both for estimating economic and other impacts of new safety regulations and for evaluating the quality of new forecasting systems. Observations of icing are based on reports from pilots (termed "pilot reports" or PIREPs). These reports form a rather unusual dataset on which to base a climatology in that they are not recorded systematically in time or space. In fact, for most locations, PIREPs are sporadic in both time and space. However, previous research has shown that PIREPs are nearly systematic in certain locations, such as around large cities where icing conditions are more consistently reported due to higher volumes of air traffic (Brown et al., 1993).

Climatological characteristics of observed and forecast icing conditions in the United States are described in this paper. The observed climatology, based on PIREPs collected over a 5-year period, is smoothed and extended using a regression model based on more standard climatological and population information. This climatology is compared to a summary of experimental icing forecasts for one year.

2 DATA

PIREPs provide information about numerous weather conditions observed by pilots (e.g., cloud cover, turbulence, freezing level), including icing. In the U.S., pilots voluntarily issue PIREPs by voice, sometimes at the request of an air-traffic controller. The reports are manually entered into a computer as part of the air traffic control system.

PIREPs of icing indicate both the severity and type of icing. Severity is coded on a scale from "Trace" to "Extreme," with several levels (e.g., "Light," "Moderate," and "Severe") inbetween. Types of icing include Rime, Clear, and Mixed. Clear ice is the least common type, but perhaps the most dangerous in terms of its impact on aircraft performance (e.g., Politovich, 1993). PIREPs also may be negative, indicating that no icing was observed. However, negative reports are relatively rare.

Due to the voluntary nature of PIREPs, they are biased both in time and space. For example, few PIREPs are recorded at night. Moreover, large regions of the U.S. (e.g., Nevada) have very few reports, as illustrated in Figure 1.

The entire icing PIREP dataset includes reports recorded in February and March, 1990-1994. PIREPs within 80-km regions around 56 U.S. cities were selected for development of the icing climatology. The cities were chosen primarily to provide good coverage of the continental U.S. They include numerous very large cities (e.g., New York, Chicago) as well as a number of very small cities (e.g., several small cities in Montana). Although large cities have greater air traffic and thus more opportunities for pilot reports, many parts of the U.S. (particularly the West) have few large cities. The entire PIREP dataset includes about 58,000 reports; 33 percent of these reports were located in the 56 city regions.

In addition to the PIREPs, basic climatological normal information was obtained for February and March for each city. The climatological variables include average temperature (T), average dew point (T_d), number of rainy days per month (N_r), and percent sunshine (%Sun). Latitude (Lat) and longitude (Lon) were included as factors that might relate to the spatial distribution of PIREPs.

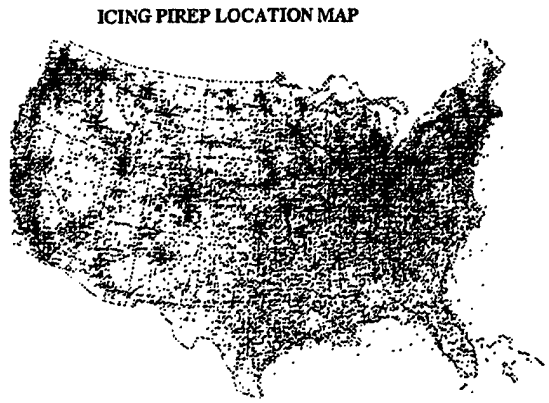


Figure 1. Locations of all icing PIREPs, February and March, 1990-1994.

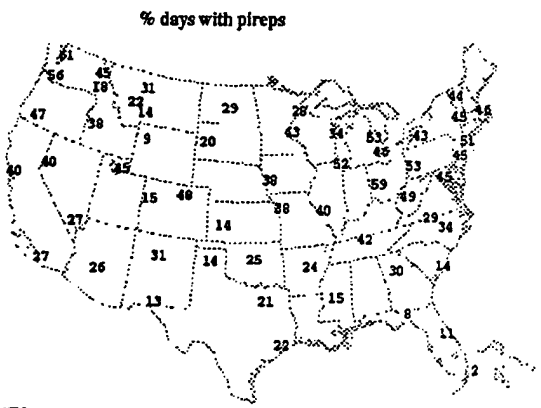


Figure 2. Percent of days with PIREPs in selected city regions (PCDAYS), February and March, 1990-1994.

Because PIREPs are dependent on the availability of aircraft to provide them, two variables that would be expected to be related to aircraft availability were also included in the study: (a) city population (Pop) and (b) aircraft departures (Dep). The Dep values represent the number of departures of commercial aircraft and do not include flights made by private pilots.

3 PERCENT OF DAYS WITH ICING

PIREPs at the individual cities can be summarized in a number of ways to obtain various measures of icing threat. For example, the average number of PIREPs per year could be estimated. A relevant characteristic for benefit studies, as well as for the evaluation of icing prediction algorithms, is *icing frequency*, which can be estimated by the *proportion of days with reported icing*.

Figure 2 shows for each city region the percentage of the total number of days (295) with at least one report of icing of any severity (PCDAYS). The values on the map are largest in highly populated regions of the eastern and far-western U.S. and smallest in the far South. PCDAYS values in the less densely populated regions of the western U.S. (e.g., Wyoming, Montana, Idaho) seem unexpectedly small compared to the values for their more populated neighbors. We speculate that the bulk of these differences do not result from real differences in the frequency of icing conditions between the neighboring regions, but are primarily related to variations in the amount of air traffic. Specifically, if aircraft are not available to report icing conditions, it is not possible to determine whether or not the conditions existed.

4 REGRESSION MODEL

Correlations shown in Table 1 indicate that PCDAYS is well correlated with a number of factors, including Lat, ln(Dep) and ln(Pop). Note that because PCDAYS is a proportion, the arcsine transformation* was applied (Neter et al., 1983, p. 138). Dep and Pop were transformed with the natural logarithm because distributions of the untransformed values were highly skewed, with a few very large values. Strong relationships with climatological variables such as N_r, T, and %Sun are also indicated by the correlations.

Multiple regression analyses suggest that a linear equation, with Lat, ln(Pop), N_r, and $T\text{-}T_d$ as predictors, provides a good model for transformed PCDAYS. The adjusted R^2 value obtained with this model was 0.70. Evaluations of the residuals indicated no apparent problems with the final model formulation.

TABLE 1. Correlations of transformed PCDAYS with various climate and city descriptor variables.

Variable	Correlation	P-Value
Latitude	0.52	0.00
Longitude	0.09	0.53
ln(Dep)	0.37	0.00
ln(Pop)	0.36	0.01
T	-0.41	0.00
T_d	-0.27	0.05
$T\text{-}T_d$	-0.35	0.01
N_r	0.60	0.00
%Sun	-0.59	0.00

While ln(Dep) was expected to be an important predictor of PCDAYS, it was found to be a less useful predictor than ln(Pop) in the complete model. This result may be due to the fact that only commercial aircraft were included in the departure counts, and small planes generally are more affected by icing than are larger commercial aircraft. Specifically, Pop may provide a better index of general aviation activity than Dep.

The regression model can be used to re-estimate PCDAYS for all of the cities, using the same value of Pop for each city. The resulting estimates should be free of most differences that are simply due to variations in population, and by extension, variations in aircraft availability. Of course, other reporting biases (e.g., if pilots in the East feel more obligated to report than pilots in the West) will not be eliminated by this approach.

Selection of an appropriate Pop value to use in the estimates is not straightforward. What value would represent observation of all icing events? Use of

*Transformed PCDAYS $= 2\arcsin\sqrt{\frac{PCDAYS}{100}}$

the maximum Pop might imply over-observation and could lead to rather extreme estimates. Several Pop values were selected for this initial analysis, based on the quantiles of the distribution of Pop. Figures 3 and 4 show the resulting estimates of PCDAYS based on the median and 0.90th quantile values of the Pop distribution (276,667 and 1,110,549, respectively). In summary, these specific Pop values were used for each city, along with each city's "true" values of Lat, N_r, and $T\text{-}T_d$, to create the new estimates of PCDAYS shown in Figures 3 and 4.

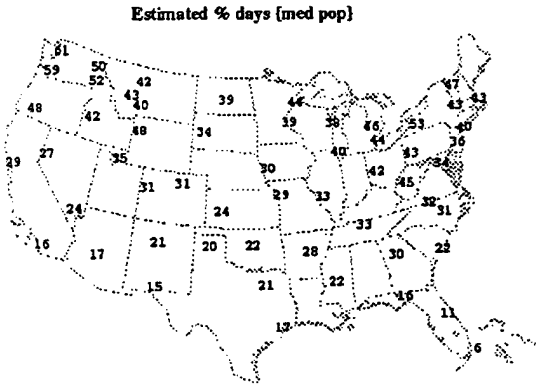


Figure 3. Estimated PCDAYS, using median city population.

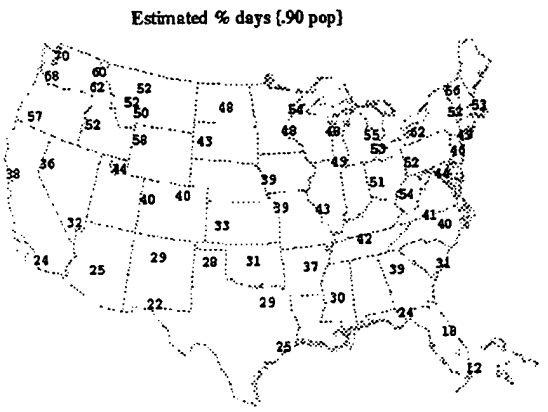


Figure 4. Estimated PCDAYS, using 0.90th quantile of Pop distribution.

The numbers in Figures 3 and 4 are smoother in appearance than the values presented in Figure 2. For many cities, the differences between Figure 2 and Figures 3 and 4 are rather small. In other cases, the differences are substantial. For example, for the cities in Idaho, Montana, and Wyoming, the median and 0.90th Pop regression estimates of PCDAYS are much larger than the observed values.

Figures 3 and 4 suggest that the Northwest, Great Lakes region, and far Northeast regions have the greatest icing threat. These regions also stand out in the map of observed PCDAYS (Figure 2). Results of the regression approach also suggest that regions in Idaho, Montana, Wyoming, and North and South Dakota have a fairly high icing threat.

5 COMPARISON TO MODEL-BASED FORECASTS

Figures 5 and 6 present estimates of PCDAYS based on application of an icing algorithm to numerical weather prediction model output from the Mesoscale Analysis and Prediction System (MAPS) modeling system, for February and March of a single year (1994). MAPS, a modeling system developed by NOAA's Forecast Systems Laboratory, is run operationally by the U.S. National Center for Environmental Prediction (formerly NMC) as the Rapid Update Cycle. The version of MAPS utilized here has a 60-km nominal horizontal spacing, with a hybrid vertical coordinate, which provides 25 vertical levels (Benjamin et al., 1991).

The icing algorithm used for these analyses is the so-called RAP algorithm, which is under development by NCAR's Research Applications Program (Thompson et al., 1995). The version of the algorithm applied here includes four categories of icing, including "stable," "unstable," "freezing drizzle," and "freezing rain." Temperature and relative humidity (RH) criteria applied in the stable icing category are $-16\ C < T < 0\ C$ and $RH > 63\%$. The results shown in Figures 5 and 6 are based on the combination of all four categories, with the algorithm applied to all 25 levels of model data at the horizontal grid point closest to the city.

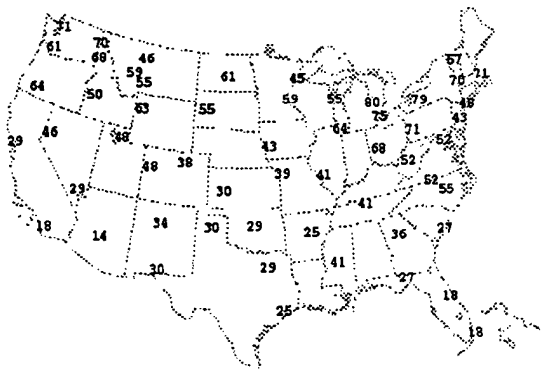


Figure 5. RAP algorithm PCDAYS estimates, February and March 1994, with MAPS model 0-hr forecasts issued at 0000 UTC.

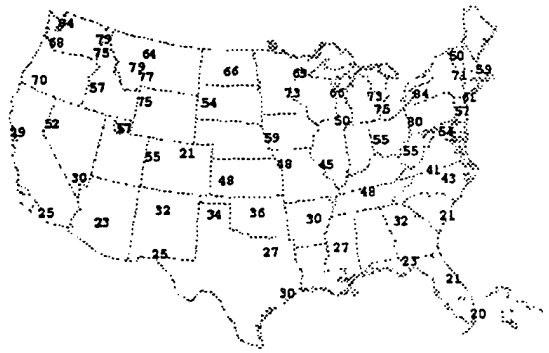


Figure 6. As in Figure 5, for 6-hr forecasts issued at 1200 UTC.

The results in Figures 5 and 6 are for two different combinations of forecast issue and lead time. These results indicate that the algorithm generally predicted icing more frequently than the climatological value observed or estimated using the median Pop. The model values for the 0-hr lead time, 0000 UTC issue time are fairly similar to the 0.90th Pop regression estimates, but the 6-hr lead time, 1200 UTC issue time values are larger than those estimated with the 0.90th Pop regression equation. These results suggest overforecasting by the algorithm, particularly for the 1200 UTC 6-hr forecasts. It's important to note that the differences may be due, at least in part, to year-to-year variations in PCDAYS. However, as shown in Figure 7, the observed PCDAYS values for 1994 were actually somewhat *smaller* overall than the values for the other years.

6 CONCLUSION

This study has suggested one approach that may be taken to standardize climatological estimates, controlling for the availability of data. Further analysis of the data is required to determine appropriate interpretations and uses of the results of this application to PIREP data. Further extensions, using additional data would also be valuable. In particular, it would be desirable to find variables that provide a better indication of aircraft availability. The number of private pilots or general aviation operations at particular airports would be helpful for this purpose, but such data are difficult to obtain.

In addition, it would be useful to develop regression models for the individual monthly PCDAYS values, utilizing actual climatological measurements rather than climate normals. As can be seen in Figure 7, the values of PCDAYS vary from year to year, and it would be useful to be able to standardize the actual values. Other measures of icing threat (e.g.,% days with clear icing) should also be investigated, and comparisons should be made with a climatology of operational icing forecasts (i.e., in the U.S., "AIRMETs").

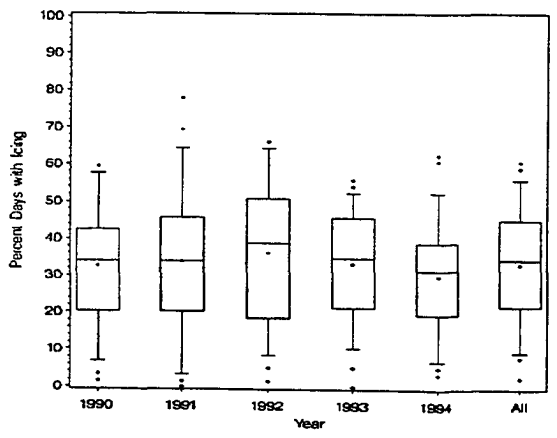


Figure 7. Box plots of yearly and 5-year observed PCDAYS for 56 U.S. cities.

ACKNOWLEDGMENTS

This research is sponsored by the U.S. National Science Foundation through an Interagency Agreement in response to requirements and funding by the U.S. Federal Aviation Administration's Aviation Weather Development Program. The views expressed are those of the authors and do not necessarily represent the official policy or position of the U.S. Government.

Frank McDonough contributed a great deal to this study, through development and analysis of the PIREP and climatology datasets. His assistance is deeply appreciated. Randy Bullock's timely contributions to the analyses were also very helpful and are greatly appreciated.

REFERENCES

Benjamin, S.G., K.A. Brewster, R.L. Brummer, B.F. Jewett, T.W. Schlatter, T.L. Smith, and P.A. Stamus, 1991, "An Isentropic Three-Hourly Data Assimilation System Using ACARS Aircraft Observations", *Monthly Weather Review*, 119, 888-906.

Brown, B.G., T.L. Fowler, B.C. Bernstein, and G.S. Forbes, 1993, "Use of Pilot Reports for Verification of Aircraft Icing Diagnoses and Forecasts", *Preprints, Fifth International Conference on Aviation Weather Systems*, (Vienna, VA, 2-6 August), American Meteorological Society, Boston, 277-281.

Neter, J., W. Wasserman, and M.H. Kutner, 1983, "Applied Linear Regression Models", Richard D. Irwin, Inc., 547 pp.

Politovich, M.K., 1993, "Aircraft Icing: Meteorological Effects on Aircraft Performance", *Preprints, Fifth International Conference on Aviation Weather Systems*, (Vienna, VA, 2-6 August), American Meteorological Society, Boston, 435-439.

Rasmussen, R., M. Politovich, J. Marwitz, W. Sand, J. McGinley, J. Smart, R. Pielke, S. Rutledge, D. Wesley, G. Stossmeister, B. Bernstein, K. Elmore, N. Powell, E. Westwater, B. Boba Stankov, and D. Burrows, 1992, "Winter Icing and Storms Project (WISP)", *Bulletin of the American Meteorological Society*, 73, 951-974.

Schultz, P., and M.K. Politovich, 1992, "Toward the Improvement of Aircraft Icing Forecasts for the Continental United States", *Weather and Forecasting*, 7, 492-500.

Thompson G., R.T. Bruintjes, and B.G. Brown, 1995, "A comprehensive icing prediction and evaluation program", *Preprints, Sixth Conference on Aviation Weather Systems*, (Dallas, 15-20 January), American Meteorological Society, Boston.

CORRESPONDING AUTHOR

Barbara G. Brown
Research Applications Program
National Center for Atmospheric Research
PO Box 3000
Boulder CO 80307 USA

ERROR ANALYSIS OF MONTHLY FIRE WEATHER FORECASTS

Francis M. Fujioka
Pacific Southwest Research Station Forest Service,
US Department of Agriculture
4955 Canyon Crest Drive Riverside,California 92507 USA

Forecasts of monthly mean afternoon dry-bulb and dew point temperatures and wind speed have been issued for the conterminous USA since 1990. These forecasts are designed to support wildfire management planning activities in natural resource agencies. Statistical analysis showed that wildfire activity correlates higher with a function of the forecast variables than with the variables themselves. A decision model was constructed to optimize dispatching strategies given the uncertainties in the forecasts. This study examines the errors in the temperature and dew point forecasts, and the effects of the error in specified decision scenarios.

Forecasting Probability of Local Severe Storms Using Single Station Data

Flt Lt J K Sahu & Dr. S.V.Singh

Indian Institute of Tropical Meteorology ,Pune-411008 ,India

ABSTRACT

A Probability Forecast for Local Severe Storms have been attempted following a statistical approach. Forecast has been evolved on a single station basis. A radius of 100 k.m. around a station has been considered as the forecasting region. In this work six stations over North West of India (NWI) have been identified for the development of the probability equations for the pre-monsoon season (April to July). These stations are Srinagar (SRN),Patiala(PTL), Delhi(DLH) , Gwalior (GWL), Jodhpur (JDP) and Ahemadabad (AHM) . Data for a period of 1981 to 1988 have been utilised for this purpose. Various observed and derived dynamical parameters as well as thermodynamic derived parameters and various stability indices have been considered as the independent variables. Multiple linear regression equations have been developed using the Stepwise regression procedure. Five years data sample have been considered for developing the equation and another three years data have been used as the test sample. Two forecast equations have been developed based on the 00 and 12 GMT data set. The performance of these probability forecasts have been compared to the result obtained on basis of the persistence / climatology . It is found that the true skill score obtained is significantly higher compared to the persistence forecast.

1.Introduction

Forecasting of the occurrence of thunderstorm and their intensity has always been a difficult task due to their complex nature and small spatial-temporal scale. Statistical prediction has been used for forecasting thunderstorm for many years.Reap & Foster (1979) had developed a Model Output Statistics(MOS),eg. Glahn & Lowry (1972) based thunderstorm outlook guidance. Charba(1979) combined LFM forecast (6,9,12 and 18 hr) with the surface and Radar observation to prepare a t'storm outlook forecast. McNaulty (1984) used a multiple discriminant analysis (MDA) approach to evolve single station forecasting equations. Miller and Lang(1991) had used a generalised markov model (GEM) procedur to obtain 1-6 hr probability forecast.Most of these methods have used either the Manually Digitised Data(MDR) or the lightning data ,reap (1993), as the predictand to represent the occurrence of Local Severe Storm (LSS). In absence of operational numerical model forecast as well as MDR data ,most of the works on thunderstorm forecasting over Indian region however have been related to development of synoptic models. The Occurrences of thunderstorms have also been related with synoptic and other parameters through scatter diagrams. Various static stability indices are examined and the regions of occurrence and non-occurrence are demarcated on the scatter diagrams. (Subramanium and jain ,1966 ; Kumar,1977 and many others). However the experience has suggested that not only local but also the synoptic scale features influence the occurrence and nature of the thunderstorms.In this work an attempt has been made to develop regression equations by making use of the surface meteorological observations and some dynamical parameters computed utilizing the aerological data. Two sets of equations have been developed using the 00 and 12 UTC data separately.For the 00 UTC data set ,the forecasts are made and validated with next 24 hours weather ,where as for the 12 UTC data set the forecast and validation period is only 12 hours.as the data sample is not very large ,we have used only one equation for all the four months (April to July).

2. Data and Methodology

The six hourly Synoptic observation data of 24 observatories, hourly METARs of six air fields and aerological data (00 and 12 UTC) data of 13 stations for April- July of 1981 to 1988 forms the basic meteorological data used in this study. All the data have been subjected to extensive quality control check to filter out and/or to correct the erroneous data,e.g. Gandin et.al.(1988,1993) . As we are interested in a local weather activities like thunderstorm, the low and middle atmosphere has great significance. For developing the forecasting equations ,We have thus excluded for those days for which aerological data was not available at least upto a minimum level of 500 hpa level. The aerological data are then subjected to quality control check using the algorithm developed by Sahu (1995).The missing data for intermediate level have been interpolated using Cubic Spline method and the data have been substituted after a hydrostatic check.An automated thermodynamic analysis package has been developed based on the basic algorithm given by Doswell et.al.(1982). A total number of 41 thermodynamic parameters have been computed using this package.(For details ,please see Sahu (1995)) .The Convective Available Potential Energy (CAPE) and Convective Inhibition Energy (CINE) have been computed using the algorithm suggested by William & Renno (1993) and Doswell et.al , (1994). Besides the observed parameters ,various derived parameters such as relative vorticity ,horizontal divergence ,vertical velocity ,moisture divergence and moisture ,Vorticity and temperature advection are computed using the daily twice Radio-Sonde and Rawin Wind data of the selected 13 stations. These dynamical parameters are developed for all the six airfields under study.These parameters are computed using a least square solution of a quadratic surface,fitted through these stations eg. Krishnamurthy (1986) . Because of the error due to the uncertainties of the method, the calculated divergence fails to satisfy the dine's compensation , i.e the vertical integration of the divergence will not be identically zero . To cater for this error O'Brien's correction has been adopted (O'Brien 1970 and Chein & Smith 1973). At this stage the top of the atmosphere layer is considered at 100 hPa , the vertical velocity at both top and bottom of the atmosphere has been considered to be zero . The temperature flux of U,V components and speed at various levels are also used as a potential predictors.All these above predictors are computed for these six stations, Srinagar (34.0 ^{o} north ,74.8 ^{o} east ;SRN) , Patiala (30.0 north 76.5 east),Delhi (28.5 ^{o} north ,77.0 ^{o} east ;DLH) ,Gwalior (26.2 north 78.2 east

;GWL),Jodhpur (26.3 north 73.0 east ;JDP) ,Ahemadabad (23.1. north 72.6 east ;AHM).

3. Regression Analysis :

Multiple linear regression equations for all the six stations are developed separately for both morning as well as for evening time.We carried out the screening analysis on a set of total 128 predictors given in table 1. The screening procedure begins by selecting the individual independent variable which is maximally correlated with the predictand. The correlation coefficient squared gives the proportion of variance explained by the predictors. At subsequent steps ,the variable added to the equation is the one which increases the percent of variance explained by a minimum of 1 percent. The independent variables are entered in a stepwise manner based on the F-Value criteria. We have restricted the entry of new variable by F-Test (5 % significant level) or if a maximum of 12 predictors have already entered to limit the entry of a spurious predictors.

List of the Predictors:(Table 1) :

001 SURFACE PRESSURE
002 SURFACE TEMPERATURE
003 SURFACE DEW POINT
004 SURFACE GPM HEIGHT
005 SURFACE WIND DIRECTION
006 SURFACE RELATIVE HUMIDITY
007 SURFACE POTENTIAL TEMPERATURE
008 SURFACE EQU.POTENTIAL TEMPERATURE
009 850 HPA-TEMPERATURE
010 850 HPA-DEW POINT
011 850 HPA-WIND DIRECTION
012 850 HPA-GPM HEIGHT
013 850 HPA-HUMIDITY
014 850 HPA-POT.TEMP
015 850 HPA-EQU.POT.TEMP
016 700 HPA-TEMPERATURE
017 700 HPA-DEW POINT
018 700 HPA-GPM HEIGHT
019 700 HPA-WIND DIRECTION
020 700 HPA-HUMIDITY
021 700 HPA-POT.TEMP
022 700 HPA-EQU.POT.TEMP
023 500 HPA-TEMPERATURE
024 500 HPA-DEW POINT
025 500 HPA-GPM HEIGHT
026 500 HPA-WIND DIRECTION
027 DIVERGENCE AT 850 HPA
028 DIVERGENCE AT 750 HPA
029 DIVERGENCE AT 550 HPA
030 DIVERGENCE AT 250 HPA
031 VORTICITY AT 850 HPA
032 VORTICITY AT 750 HPA
033 VORTICITY AT 550 HPA
034 VORTICITY AT 250 HPA
035 OMEGA AT 800 HPA
036 OMEGA AT 700 HPA
037 OMEGA AT 500 HPA
038 OMEGA AT 200 HPA
039 TOTAL MOISTURE DIVERGENCE
040 500 HPA-HUMIDITY
041 500 HPA-POT.TEMP
042 500 HPA-EQU.POT.TEMP
043 300 HPA-TEMPERATURE
044 300 HPA-DEW POINT
045 300 HPA-GPM HEIGHT
046 300 HPA-HUMIDITY
047 300 HPA-WIND DIRECTION
048 300 HPA-POT.TEMP
049 300 HPA-EQU.POT.TEMP
050 24 HR-SURFACE-PRESSURE CHANGE
051 24 HR-SURFACE- TEMPERATURE CHANGE
052 24 HR-SURFACE-DEW POINT CHANGE
053 24 HR-850 HPA- TEMPERATURE CHANGE
054 24 HR-850 HPA-DEW POINT CHANGE
055 24 HR-700 HPA- TEMPERATURE CHANGE
056 24 HR-700 HPA-DEW POINT CHANGE
057 24 HR-500 HPA- TEMPERATURE CHANGE
058 24 HR-500 HPA-DEW POINT CHANGE
059 (SFC-700)THETA-E
060 (SFC-500)THETA-E
061 CONVECTIVE INSTABILITY OF REAP
062 DRY STATIC ENERGY INDEX
063 MOIST STATIC ENERGY INDEX
064 VIRTUAL DRY STATIC ENERGY INDEX
065 LIQUID STATIC ENERGY INDEX
066 SATURATED MOIST STATIC ENERGY INDEX
067 MEAN RELATIVE HUMIDITY (SURFACE-700 HPA
068 BOUNDARY LAYER POTENTIAL TEMPERATURE
069 BOUNDARY LAYER EQU. POT. TEMPERATURE
070 TEMPERATURE LAPSE RATE (850 TO 500 HPA)
071 THICKNESS BETWEEN 850 TO 500 HPA
072 THETA-E LAPSE RATE : SURFACE TO 700 HPA
073 TEMPERATURE FLUX OF U-COMPONENT AT SURFACE
074 TEMPERATURE FLUX OF V-COMPONENT AT SURFACE
075 TEMPERATURE FLUX OF SPEED AT SURFACE
076 TEMPERATURE FLUX OF U-COMPONENT AT 850 HPA
077 TEMPERATURE FLUX OF V-COMPONENT AT 850 HPA
078 TEMPERATURE FLUX OF SPEED AT 850 HPA
079 TEMPERATURE FLUX OF U-COMPONENT AT 700 HPA
080 TEMPERATURE FLUX OF V-COMPONENT AT 700 HPA
081 TEMPERATURE FLUX OF SPEED AT 700 HPA
082 TEMPERATURE FLUX OF U-COMPONENT AT 500 HPA
083 TEMPERATURE FLUX OF V-COMPONENT AT 500 HPA
084 TEMPERATURE FLUX OF SPEED AT 500 HPA
085 THERMAL WIND BETWEEN 850-500(ADVECTION)
086 THERMAL WIND BETWEEN 1000-850(ADVECTION)
087 FREEZING LEVEL HEIGHT IN METERS
088 SURFACE WET BULB TEMPERATURE
089 WET BULB TEMPERATURE AT 850 HPA
090 WET BULB TEMPERATURE AT 700 HPA
091 WET BULB TEMPERATURE AT 500 HPA
092 MEAN WET BULB TEMPERATURE OF BOUNDARY LEVEL
093 DIFFERENCE BETWEEN SURFACE AND 700 HPA
094 MAXIMUM VELOCITY
095 WET BULB ZERO HEIGHT
096 POSITIVE PART OF ENERGY
097 NEGATIVE PART OF ENERGY
098 AVERAGE MIXING RATIO IN LOWEST 100 HPA
099 LIFTING INDEX
100 GEORGE'S INDEX
101 SHOWALTER'S INDEX
102 NET WIND SHEA UPTO 6 K.M.
103 ENERGY INDEX
104 VECTOR PRODUCT SHEAR UPTP 5000 FT
105 VECTOR PRODUCT SHEAR BET. 5000 & 10000 FT
106 VECTOR PRODUCT SHEAR BET. 10000 & 15000 FT
107 SPEED SHEAR UPTO 5000 FT
108 SPEED SHEAR BET. 5000 & 10,000 FT
109 SPEED SHEAR BET. 10,000 & 15,000 FT
110 NET U-COMPONENT UPTO 5000 FT
111 NET U-COMPONENT BET. 5000 & 10,000 FT
112 NET U-COMPONENT BET. 10,000 & 15,000 FT
113 NET V-COMPONENT UPTO 5000 FT
114 NET V-COMPONENT BET. 5000 & 10,000 FT
115 NET V-COMPONENT BET. 10,000 & 15,000 FT
116 MODIFIED CHARBA'S INDEX
117 CONVECTIVE TEMPERATURE IN CENTIGRADE
118 LIFTING CONDENSATION LEVEL
119 CONVECTIVE CONDENSATION LEVEL
120 MEAN THETA-W BET. 850 & 300 HPA
121 CROSS TOTAL INDEX
122 VERTICAL TOTAL INDEX
123 TOTAL TOTAL INDEX
124 MODIFIED TOTAL TOTAL INDEX
125 RACKCLIFFE'S INDEX
126 POTENTIAL WET BULB INDEX
127 MODIFIED JEFFERSON'S INDEX
128 CONTINUITY FACTOR

4. Regression equations developed

On basis of the regression analysis ,the following equations have been developed. The predictors assigned in these regression equations have been used as per the order shown in table (1).The data set used here was not initialised and as we define the Y value to a maximum of 1.0 only ,the regression coefficients have been considered upto six digits after decimal .As discussed earlier ,the regression equatios are developed for both the 00 and 12 UTC data set.

Jodhpur :00 UTC Forecast

Y =0.275174+ 0.244698A128+ 0.003185A67+ 0.000095A38+ 0.002516A86+ 0.000035A80+ 0.000353A47+ 0.000165A31-

0.025377A53+ 0.004164A63+ 0.01323A57+ 0.001763A40

Jodhpur 12 UTC Forecast
Y= -0.41489+ 0.312777A128+ 0.003538A52- 0.020636A51- 0.000265A35+ .00819A123+ .000038A83+ 0.011515A53+ 0.000859A85+ 0.000811A120-0.001510A94-0.00867A56

Patiala 00 UTC Forecast
Y=7.10042+ 0.0266A114 +0.14285A128 -0.00022A36 - 0.00115A25 +0.01101A56 +0.00116A85 -0.00018A34 +0.00745A24 +0.00003A83

Patiala 12 UTC Forecast
Y=0.053089+ 0.2467A128 +0.00154A96 +0.00783A102 - 0.01744A51 +0.0041A85 -0.00114A120 +0.00811A43

Gwalior 00 UTC Forecast
Y=-1.2012+0.19394A128 -0.00059A26 -0.00086A120 - 0.0268A53 +0.02213A57 +0.01945A124 +0.00534A6 - 0.01304A113 +0.01175A55 +0.00973A117

Gwalior 12 UTC Forecast
Y=0.9682+0.02219A2 +0.16988A128 +0.01265A124 - 0.01758A51 -0.01092A111 -0.00185A41- 0.01972A53 +0.0173A57

Ahmedabad 00 UTC Forecast
Y= -3.17842+0.006322A40+0.187238A128 + 0.000203A32 - 0.000426A19 +0.00036A11 +0.000026A83 +0.000210A29 - 0.009885A24 +0.008798A41

Ahmedabad 12 UTC Forecast
Y=0.25835+ 0.27353A128 +0.001387A20 +0.00007A83 +0.002507A58 +0.005472A73 -0.000053A79 -0.000062A15 +0.003571A80 +0.000045A77 -0.000058A36 +0.000096A11 - 0.000952A12

Delhi 00 UTC Forecast
Y=0.48721+0.25199A1+0.01234A2+0.00008A3+0.00004A4 - 0.02582A5 +0.0041A6 +0.00238A7 +0.00061A8

Delhi 12 UTC Forecast
Y=1.349670+0.00913A1+ 0.25218A2 -0.01989A3 -0.06349A4 - 0.01971A5 +0.00567A6 -0.00228A7 +0.01047A8 -0.017740A9 +0.01618A10 +0.00004A11 -0.00004A12

Srinagar 00 UTC Forecast
Y=8.951040 +0.004810A1 +0.14426A2 +0.00007A3 +0.02059A4 -0.010720A5 -0.02337 A6 +0.015200A7 -0.026A8 +0.11134A9 +0.00208A10

Srinagar 12 UTC Forecast
Y=10.4845+0.3598A1 -0.3116A2 +0.12552A3 +0.0001A4 - 0.03418A5 +0.106720A6 +0.01341A7 +0.00004A8

5. Verification of forecast equations :

The above equations are tried to forecast the occurrence of thunderstorm in terms of probability forecast. A cut off value for Y is fixed and if the forecast probability exceed that cut-off value , a thunderstorm is then forecasted to occur , Otherwise forecast for non-occurrence is made . The forecast is then compared with the actual weather and a contingency table is prepared . The contigency table is shown in table 3 and on that basis the various assessement scores are determined.The selection of the cut-off value for Y has been based on the BIAS value. We have tried to keep BIAS close to 1 as a value greater than zero indicate an overfitting of the equation.Table (4) gives the cut-off value for Y assigned and corresponding BIAS score.

Table (3) :
Forecast conditions :

STNS	BIAS 00 UTC	BIAS 12 UTC	CUT OFF VALUE
DLH	1.196	1.126	0.45
JDP	1.125	0.976	0.40
PTL	1.042	1.096	0.45
GWL	1.257	1.00	0.50
AHM	1.037	1.115	0.42
SRN	1.167	1.082	0.55

Various skill scores have been computed using the three years test data (1982,86,88).These skill scores have been computed using the relations as shown earlier on basis of a 2 by 2 contingency table.The skill scores have been computed for both 00 as well as 12 UTC and are shown in subsequent tables.Various notations of skill scores and probability forecasts notations are used such as Probability of detection (POD) ,False alarm rate (FAR),Miss rate (MR) ,Correct non occurrence (CNO) , Critical success index (CSI) ,True skill score (TSS) ,Percent correct (PC) and BIAS.

Table 4(a) : Skill Score for Patiala

	00 UTC Persis.	00 UTC Forecast	12 UTC Persis.	12 UTC Forecast
POD	.526	.621	.538	.635
FAR	.495	.422	.451	.421
MR	.474	.379	.462	.365
CNO	.779	.806	.784	.775
CSI	.347	.428	.373	.434
TSS	.306	.427	.322	.409
HSS	.302	.419	.324	.399

Table 4(b) : Skill Score for Delhi

	00 UTC Persis.	00 UTC Forecast	12 UTC Persis.	00 UTC Forecast
POD	.490	.725	.505	.709
FAR	.510	.393	.505	.371
MR	.510	.275	.495	.291
CNO	.794	.810	.791	.830
CSI	.325	.493	.333	.500
TSS	.285	.536	.296	.539
HSS	.285	.506	.290	.519

Table 4(c) : Skill Score for Gwalior

	00UTC Persis.	00 UTC Forecast	12 UTC Persis.	12 UTC Forecast
POD	.229	.657	.226	.710
FAR	.733	.477	.767	.290
MR	.771	.343	.774	.290
CNO	.912	.916	.909	.965
CSI	.140	.411	.130	.550
TSS	.141	.573	.135	.674
HSS	.150	.516	.137	.674

Table 4(d) : Skill Score for Ahmedabad

	00 UTC Persis.	00 UTC Forecast	12 UTC Persis.	12 UTC Forecast
POD	.296	.593	.269	.577
FAR	.667	.429	.731	.483
MR	.704	.407	.731	.423
CNO	.938	.953	.934	.952
CSI	.186	.410	.156	.375
TSS	.234	.546	.204	.529

HSS	.247	.537	.204	.502

Table 4(e) : Skill Score for Jodhpur

	00 UTC Persis.	00 UTC Forecast	12 UTC Persis.	12 UTC Forecast
POD	.587	.750	.578	.614
FAR	.412	.333	.415	.370
MR	.412	.250	.422	.386
CNO	.860	.873	.853	.870
CSI	.416	.545	.410	.451
TSS	.448	.623	.431	.485
HSS	.448	.598	.433	.488

Table 4(f) : Skill Score for Srinagar

	00 UTC Persis.	00 UTC Forecast	12 UTC Persis.	12 UTC Forecast
POD	.631	.821	.624	.882
FAR	.361	.296	.376	.185
MR	.369	.179	.376	.180
CNO	.878	.882	.873	.933
CSI	.465	.611	.453	.735
TSS	.509	.703	.497	.815
HSS	.511	.667	.497	.793

6. Conclusion

In the present study , an attempt has been made to test ,how a statistical model could be used for a discreete weather phenomenon like a thunderstorm .The inclusion of various dunamical parameters has been aimed at explaining the effect of large scale features. Examination of the predictors entered in the regression equations for all the six stations shows the importance of persistence in the forecasting problem. This is understood for this region as undoubtadly the synoptic disturbances and availability of low level moisture play a leading role for convective activities.The list of predictors also extend to a total number of 64 predictors (!) for these six stations .Many predictors are choosen for once only. It is quite surprising to find that widely used stability indices are rarely choosen in the regression equations (their relative chances have increased for 1200 UTC). We attributed this information that the forecasted stability indices could be a better forecasting tool.It is also believed that the probability forecast model developed in the present study could be improved further in forecasting the convective activities by the possible inclusion of various forecasted meteorological parameters from a large scale numerical prediction model. In the present restricted condition ,it can be argued that these sets of 12 equations can be usefull to improve the operational forecasting efficiency.

References

Charba J.P. , 1977 : Operational system for predicting thunderstorm 2-6 hour in advance ,NOAA Tech memo ,NWS ,TDL -64 ,24 pp

Chien H ,P.J. Smith ,1973 : On the estimation of kinematic parameters in the atmosphere from radio-sonde wind data , Mon. Wea. Rev. ,101,252-261

Doswell C.A. III ,Erik N.Rasmussen (1994) : The effect of neglecting the virtual temperature correction on CAPE calculations ,Weather & Forecasting ,9,4,625-629

Doswell C.A. III ,J.T.Schaefer, D.W.McCann, T.W. Schlatter & H.B.Wobus ,1982 : Thermodynamic Analysis Procedure at the National Severe Storm Forecasting Centre ,Pre-Ptints ,9th Conf. report on Weather Forecasting and Analysis ,304-309 ,Amer. Meteo. Soc. <boston ,Mass

Gandin L.S. ,1988 : Complex quality control check of meteorological observations , Mon. Wea. Rev. ,116,1138-56

Glahn H.R and D.A.lowry ,1972 :The Use of Model Output Statistics (MOS) in Objective Weather forecasting ,Jour .of Appl. Met ,11,1203-11

Krishnamurthy T.N. ,1986 : Workbook on numerical weather prediction for the tropics for the training of Class I and Class II meteorological personnel ,WMO ,No 669 ,33-44

Kumar S ;1972 :Forecasting Pre-Monsoon thunderstorm/ dust storm ,I.J.M.G ,23,45-50

Lee R.R ,Jeffrey Passner ,1993 : The development of TIPS : An expert system to forecast thunderstorm Occurrence , Weather and Forecasting ,8,271-280

Gandin L.S. ,1993 : Complex quality control of meteorological observations ,Mon. Wea. Review ,116,1138-1156

McNaulty R.P., 1984 : A statistical approach to short term thunderstorm outlooks ,Jour. of Appl. Meteo. ,20,765-771

Miller R.G. ,Joseph Lang ,1991 : verification of 1-6 hour statistical weather forecasts ,TDL ,91-1 ,51 pp

O'Brien J.J ,1970 : Alternative solutions to the classical vertical velocity problem , Jour. of Appl. meteor ,9,197-203

Pepler R.A & P.J. Lamb , 1988 : Estimation of Large Scale Vertical motion over the central United States for Summer ,Mon. Wea. Review ,116,3,622-635

Reap R.M. and D.S.Foster , 1979 : Automated 12-36 hour probability forecasts of thunderstorms and Severe Local Storms ,Jour. of Appl. Meteor. ,18,1304-1315

Reap R.M , 1993 : The Use of Lightning data to detect thunderstorm near surface reporting stations , Mon. Wea. rev , 2,464-469

Sahu J.K ,1995 : Various Implications of Automated Thermodynamic Analysis Procedure ,Accepted for Publication in VATAVARAN.

Subramanium D.V and P.S Jain ,1966 :Stability index and area forecasting of Thunderstorms, Preprints ,12th Conf. Radar Met ,norman ,Amer. Meteor. Soc ,156-159

William G.C. & Lev S. Gandin (1990) : Comprehensive hydrostatic quality control at National Meteorological Centre ,Mon. Wea. Review ,118,2752-67

Williams E and Nilton Renno ,1993 :An analysis of the Conditional Instability of the Tropical Atmosphere ,Mon. Wea .Rev ,121,21-36

CORRESPONDING AUTHOR

Flt Lt J K Sahu
Indian Institute of Tropical Meteorology
NCL Post Office
Pune- 411008
(INDIA)

The North Atlantic Storm Track and Regional Climate Variability

Jeffrey C. Rogers

The Ohio State University, Columbus, Ohio USA

ABSTRACT

The primary mode of sea level storm track variability in the northern Atlantic is examined. It exhibits large variability in synoptic activity northeast of Iceland toward the Norwegian and Barents Seas. The strength of northeastern Atlantic cyclone activity is positively correlated to the severity of winters in Greenland, northern Europe and Siberia. Two modes of sea level pressure circulation are associated with relatively mild winter months in northern Europe. One is characterized by strong cyclones in the northeastern Atlantic while the other is associated with southeasterly flow around anticyclones in eastern Europe. The relationship between the storm track and Atlantic teleconnection patterns is also examined.

INTRODUCTION

The association is examined between temporal and spatial variations in the main winter North Atlantic storm track and the longer-term climatic variability over northern Europe. Characteristics of the main storm track are determined using gridded once-daily December, January and February sea level pressures for 1899-1992. The pressures are high-pass filtered to emphasize 2 - 8 day periods. Monthly root-mean squares (rms) of the daily high-pass filtered data are obtained. These show the spatial areas of largest pressure variability on synoptic time scales and represent a proxy of the monthly mean storm track. Rotated principal component analysis is performed on the monthly rms fields, determining (1) the principal spatial pattern of rms variability, and (2) a time series index of the strength of the storm track represented by the principal component.

2 THE STORM TRACK PATTERN AND TELECONNECTIONS

The primary principal component of the monthly rms fields is a dipole pattern exhibiting highest variability in an area extending from Iceland northeastward toward the Norwegian and Barents Seas and northern Europe (Fig. 1). A secondary center of opposite sign lies west of Portugal. Monthly mean sea level pressures are partly the product of the recurring tracks of moving high-frequency weather systems and are used in Figs. 2-4 in lieu of trajectory plots to display the monthly spatial paths of the cyclones and anticyclones.

When the monthly storm track index is most negative (Fig. 2), the Icelandic low and Azores high are weak and centered over the central Atlantic. The main cyclone track extends toward the east-southeast and Mediterranean basin, represented by a trough over that area. The southern dipole near Portugal in Fig. 1 then exhibits relatively large monthly rms values (> 3 hPa).

When the storm track index is most positive (Fig. 3), the subpolar low is very deep and extends far to the northeast into the Barents Sea, essentially as a Norwegian Sea low. Relatively high monthly rms pressures occur in this area (>6 hPa). The Azores high is very strong and is also displaced far to the northeast, compared to its position in Fig. 2.

The mean sea level pressure differences between Figs. 2 and 3 (Fig. 4) form a dipole with centers east of the Bay of Biscay and over the extreme northern Atlantic and Norwegian Sea. Both dipole centers have maximum differences in excess of absolute 16 hPa, and they coincide spatially with the dipole centers in Fig. 1.

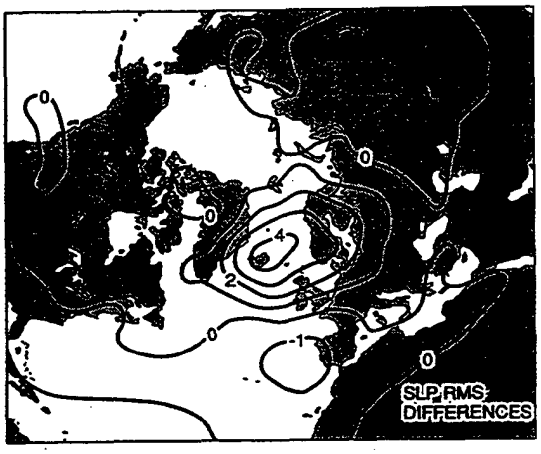


Figure 1. A representation of the first principal component of proxy storm track variability, showing the mean differences in root-mean-square pressures (in hPa) between 32 months with highest positive and 27 months with lowest negative component scores.

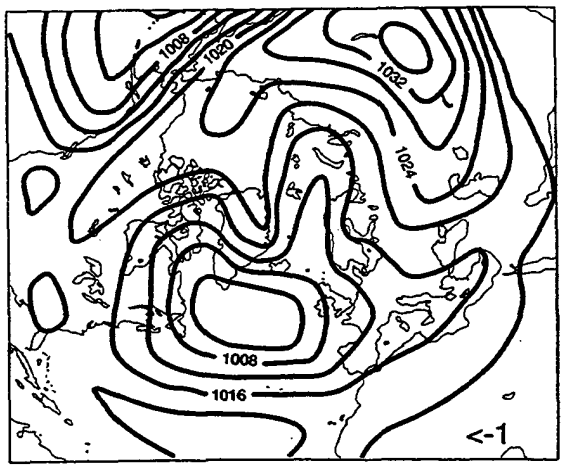


Figure 2. The mean sea level pressures (hPa) during the set of months when the storm track index reaches its lowest negative values.

The passages of deep cyclones and strong anticyclones may only partly explain the pressure distributions of Figs. 2 and 3. There is also a contribution from the background low-frequency pressure field that

prevails during a given month. Fig. 5 further elaborates upon features of the day-to-day pressure variability, using data for grid point 65N, 20W (over Iceland), where some of the largest rms variability is observed (Fig. 1). Frequency distributions of raw daily pressures (Figs. 5a and 5b) have nearly the same range of values in positive and negative storm track index months. However, the negative (lowest) index months (Fig. 5b) have a higher frequency of pressures between 1015-1025 hPa and far fewer pressures under 995 hPa compared to the positive cases (Fig. 5a). The daily (24 hour) *absolute* pressure change during these sets of months only exceeds 20 hPa between 20 pairs of days in negative storm track index months (Fig. 5d) while the same is true between 203 pairs of days (21% of the full set) in the positive months (Fig. 5c).

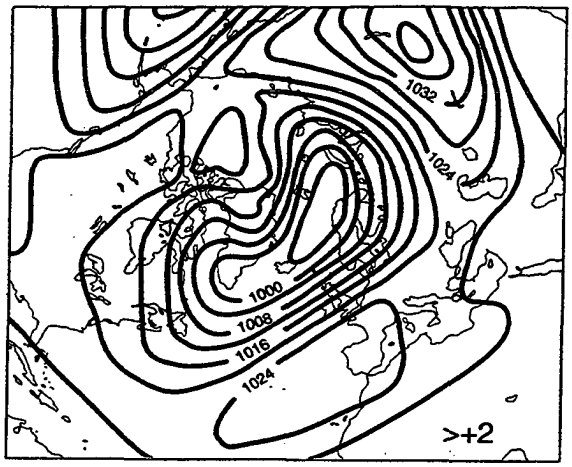


Figure 3. Same as Fig. 2 but for the highest positive index values.

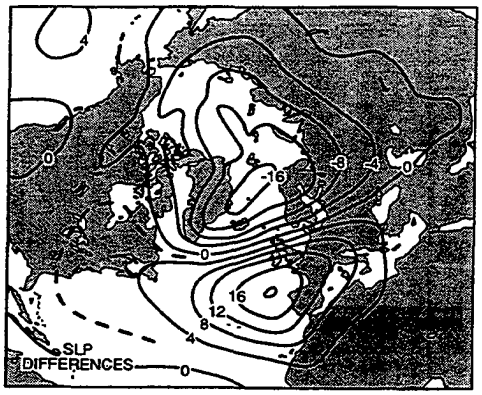


Figure 4. The net mean pressure differences (hPa) between the most positive (Fig. 3) minus the lowest negative (Fig. 2) storm track index cases.

Rogers (1990) identified four sea level pressure low-frequency teleconnection patterns, named primarily after their centers of action: (1) the NAO; (2) the Southern Europe/Northeastern Atlantic (SENA) pattern, (3) the East Atlantic (EA) pattern, and (4) and the Scandinavian (SCAN) pattern. Each of the four teleconnections have winter season time series that are correlated to the winter mean storm track index with coefficients between r = + 0.45 to r = + 0.55 (n=86). The storm track pattern and its index is therefore not *solely* linked to the NAO, the most well-known regional teleconnection. Other evidence that this is so include the facts that (1) the time series of the storm track index exhibits random fluctuations about its mean during the twentieth century (not shown here), whereas the NAO has large trends and interdecadal variability (Rogers, 1984), and (2) because Fig. 4 arguably is not the spatial pressure distribution typically associated with the NAO, the centers being shifted too far to the north and east. Each of the low-frequency teleconnections, other than the NAO, has one extreme mode in which the subtropical high is shifted unusually far to the east or northeast of its mean position while concurrently the mean subpolar low is very deep and extended far into the northeastern Atlantic. This pattern appears most noticeably in Fig. 3. The teleconnection modes where this occurs are the negative modes of EA and SCAN and the positive mode of SENA [see Rogers (1990), his Figure 7]. The SENA pattern is a dipole with centers displaced about 50° of longitude east of those of the NAO, over southern Europe and the extreme northeastern Atlantic [see Rogers (1990), his Fig. 4].

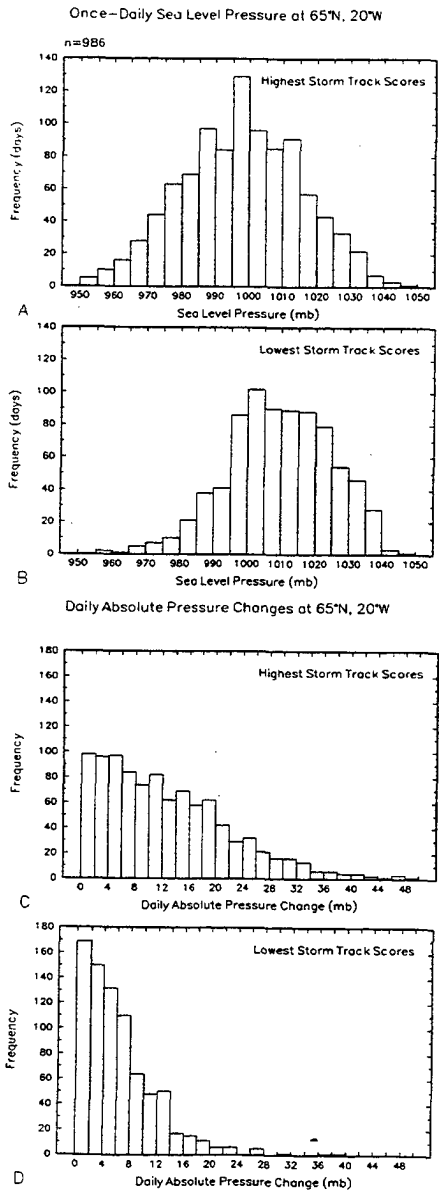


Figure 5. Frequency of raw daily pressures during (a) 32 months with the highest storm track index values and (b) 27 months with the lowest index values. The frequency of daily absolute pressure changes occurring between days in these months are also shown for (c) highest index months and (d) lowest index months.

3 THE STORM TRACK AND CLIMATE

The storm track index is highly correlated (Fig. 6) to winter air temperatures over Greenland, northern Africa, and in a broad area extending from Ireland, eastward across Europe and into Siberia. The seesaw in winter air temperatures between Greenland and northern Europe (van Loon and Rogers, 1978) can be identified in the correlations of Fig. 6. Rogers and Mosley-Thompson (1995) have examined the winter climate variability in Siberia associated with Atlantic cyclones traversing the Barents and Kara Seas.

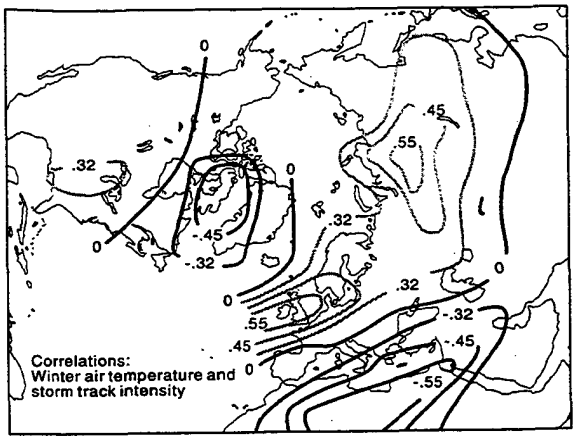


Figure 6. Coefficients of correlation between winter mean values of the storm track index and gridded land air temperatures. Lighter (darker) lines are positive (negative) coefficients. Coefficients of absolute r = 0.32 (r = 0.55) are statistically significant at the 95% (99.9%) confidence interval (n=90).

Twentieth century winter months were identified when extremes occurred in air temperature seesaw between Greenland and northern Europe. During months when the "Greenland Above" seesaw mode occurs (Fig. 7 - top) the storm track index values are almost always negative, associated with the build-up of polar high pressure over Europe (Fig. 2) and a weak Icelandic low located south of the southern tip of Greenland. During the months when the Greenland Below (GB) mode of the seesaw occurs (northern Europe has a mild winter month) the storm track index values are negative almost as frequently as they are positive (Fig. 7 -bottom) - exhibiting a somewhat bimodal frequency distribution.

The composite mean sea level pressure is shown for GB months when the storm track index is negative (Fig. 8) and GB months when the storm track index is positive (Fig. 9). In both sets of months there is a deep low near Iceland, suggesting considerable cyclone activity in the region. However, in the negative index cases (Fig. 8) the Siberian high is farther west and the isobars of the Icelandic low turn northward, paralleling the Scandinavian coast. The pressure pattern in Fig. 8 most nearly resembles that of the NAO and it is *not* a strongly maritime flow. The mean flow prevailing in Fig. 8 over northern Europe is from the southeast, from lower latitudes over the continent.

In the positive index cases (Fig. 9), a strong secondary center of the subpolar low lies in the Norwegian Sea and deep cyclones enter the Barents Sea. The flow over Europe in Fig. 9 is clearly maritime. The northeastward extended subpolar low and Azores high resembles the pressure pattern for SENA (see also Fig. 3). The time series of both SENA and the NAO are significantly correlated to the winter air temperature seesaw (Rogers 1990).

The mean sea level pressure differences (Fig. 10), obtained by subtracting Fig. 8 from Fig. 9, exhibit a dipole pattern with centers near Ireland and over eastern Europe. The eastern European pressure anomaly in Fig. 10 is positive (anomalous high pressure) in the "GB

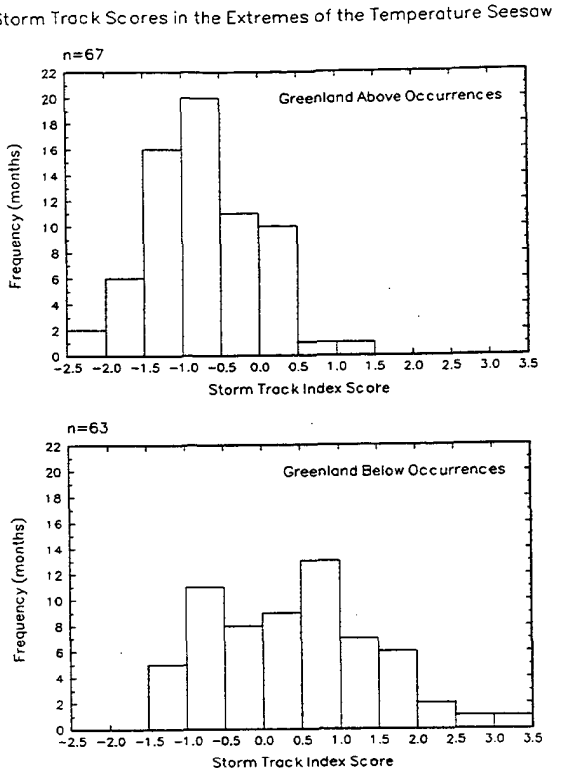


Figure 7. Frequency (in months) of monthly storm track index values during Greenland Above (top) and Greenland Below (bottom) occurrences since 1899 - the extremes of the Greenland/Northern Europe air temperature seesaw.

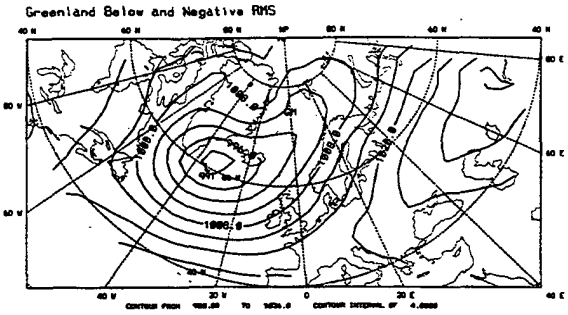


Figure 8. Mean sea level pressure (hPa) during winter months when Greenland Below events occur and the storm track index is negative.

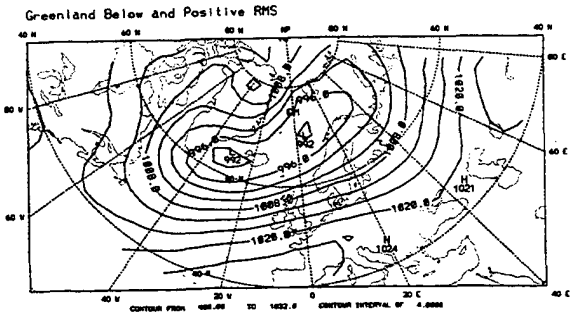


Figure 9. Same as Fig. 8 but for Greenland Below events and the storm track index is positive.

and negative" cases of Fig. 8, producing a net southeasterly flow into northern Europe and helping build the westward extension of the Siberian anticyclone (Fig. 8). The eastern European pressure anomaly is negative in the months comprising Fig. 9, and a strong maritime westerly flow occurs into the continent.

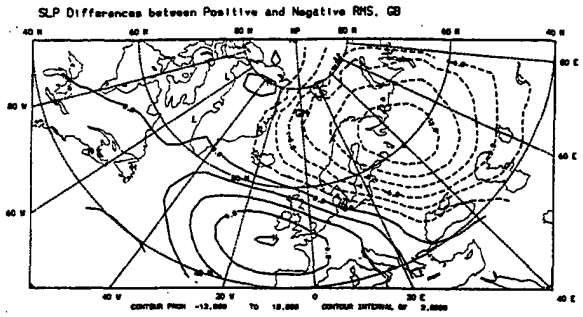


Figure 10. Net mean sea level pressure differences (hPa) for Greenland Below events with the storm track index positive (Fig. 9) minus negative (Fig. 8).

4 SUMMARY

Statistical analysis of monthly mean rms fields of high-pass (2 - 8 day period) sea level pressures has been performed. Comparison of the results to low frequency pressure teleconnection patterns offers new insights into the Atlantic circulation variability both in regard to regional teleconnections and to the winter air temperature seesaw. The storm track pattern exhibits highest variability in the extreme northeastern Atlantic, representing an enhancement of the storm track into the Arctic (Norwegian and Barents Sea area). The primary principal component of storm track variability cannot clearly be linked to any single low-frequency sea level pressure teleconnection pattern. This precludes a major association with the NAO, with its centers over the central Atlantic and the Denmark Strait, and at least by visual inspection draws more attention to the SENA, SCAN and EA patterns, each of which exhibits a mode in which both the subpolar low and Azores high are extended far to the east or northeast of their normal position.

When data are stratified by air temperatures, using the winter air temperature seesaw, a similar picture emerges. The GB seesaw mode, when northern Europe has mild winter months, can occur in conjunction with two separate sea level circulation regimes. In one (much like SENA or SCAN) a strong maritime flow prevails into Europe as cyclones penetrate far to the northeast of Iceland and into the Barents Sea. In the other, (the NAO) cyclones are confined more toward Iceland and a prevailing southeast flow occurs around anticyclones passing over eastern Europe.

This study shows that the climate of Europe cannot be evaluated solely in terms of the NAO and it suggests that the Atlantic pressure field might be thought of as exhibiting an interannual northeast/southwest swaying of the key pressure centers, incorporating more than one teleconnection in the process. Further evaluation of the northeastward extension of the subpolar low is warranted (the "Norwegian Sea" low) as is analysis of the synoptic dynamics of the deep cyclones entering the Arctic Ocean.

ACKNOWLEDGMENTS

John Nagy, of the Byrd Polar Research Center, and Chung-Chieh Wang, Atmospheric Science Program at The Ohio State University, assisted in producing the diagrams. This work is supported by the NOAA Office of Global Programs - Atlantic Climate Change Program under grant number NA36GP0236.

REFERENCES

Rogers, J.C., 1984, "The Association between the North Atlantic Oscillation and the Southern Oscillation in the Northern Hemisphere", *Mon. Wea. Rev.*, 112, 1999-2015.

Rogers, J.C., 1990, "Patterns of low-frequency monthly sea level pressure variability (1899-1986) and associated wave cyclone frequencies", *J. Climate*, 3, 1364-1379.

Rogers, J.C., and E. Mosley-Thompson, 1995, "Atlantic Arctic wave cyclones and the mild Siberian winters of the 1980s", *Geophysical Research Letters*, in press.

van Loon, H. and J.C. Rogers, 1978, "The Seesaw in Winter Temperatures Between Greenland and Northern Europe. Part I: General Description", *Mon. Wea. Rev.*, 106, 296-310.

CORRESPONDING AUTHOR

Prof. Jeffrey C. Rogers
Department of Geography
1036 Derby Hall
The Ohio State University
Columbus, Ohio 43210-1361 USA
Internet: jcrogers@magnus.acs.ohio-state.edu
Phone: 614-292-0148 fax: 292-6213

OCCURRENCE OF SEVERE WINDS IN DENMARK DURING THE PAST 100 YEARS.

T. Schmith

Danish Meteorological Institute, Copenhagen, Denmark.

ABSTRACT

Pressure records of three daily readings back to 1875 form the basis of a geostrophic wind calculation representing the Danish area. The pressure time series have been statistically tested for inhomogeneities and necessary adjustments performed, before the geostrophic wind has been calculated. All severe winds so calculated have been checked against weathermaps.

On basis of the time series of geostrophic winds annual statistics are calculated with emphasis on severe winds. While the annual resultant mean wind has increased since mid-1970'es, maximum annual geostrophic wind and number of storm days per year exhibits a maximum in the twenties but show no overall trend since 1880. Furthermore we find no relationship between the annual resultant and maximum wind speed.

1. INTRODUCTION

Wind can in principle be estimated by three different methods, namely:

- visually, by inspecting the movement of a streamer or the state of sea.
- by measuring by means of an anemometer or other instrument.
- by calculating geostrophic wind from pressure observations.

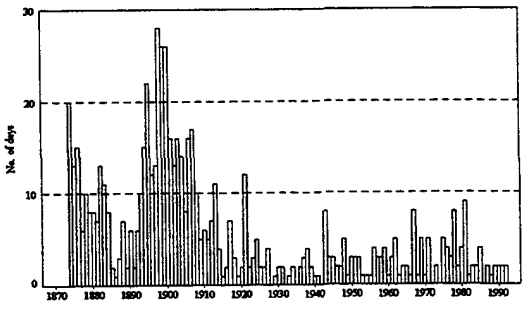


Figure 1. Number of days per year at climatic station Vestervig where the wind force exceeds 9 bf.

In fig. 1 is shown an example of a visually estimated wind series, namely for the climatic station Vestervig (see fig. 2). The figure shows the number of days per year, with wind force exceeding 9 bf. Several suspicious features are noticed. For instance, we wouldn't believe the rather sudden decrease around 1900-1910 to be real, but rather due to a change of observer, movement of station or the like. In other words the time series of winds from that station is most likely inhomogeneous.

Regarding measured winds, these too can be suspected to be inhomogeneous due to change of instrument, growing up of neighbouring trees etc. Apart from that anemometers were introduced during the 1950'es giving time series of only 40 years or so.

Many investigations concerning storm frequency uses weather maps, which can be said to combine the three different method of wind estimation. These investigations, however, suffer from several drawbacks, possibly making them inhomogeneous. Firstly, the number of stations has increased during the past 100 years and the probability of observing a high wind in a specified area has therefore increased "artificially". In particular over the sea the number of weather-observing ships have increased. Secondly, after the introduction of numerical models, there is a tendency to analyse stronger gradients in areas where no observations are present. Also introduction of weather satellites might have "increased" the number of lows.

All in all we therefore see an advantage in using geostrophic wind calculated from pressure records from *fixed* stations throughout the whole period of investigation. Therefore, this method is used in the work here reported.

2. DATA

Pressure observations from three climatic stations is used, namely Fanø, Vestervig and Sandvig. These three stations are situated in SW-, NW- and

E-Denmark respectively (see fig. 2) and have a station elevation not exceeding 100 m.

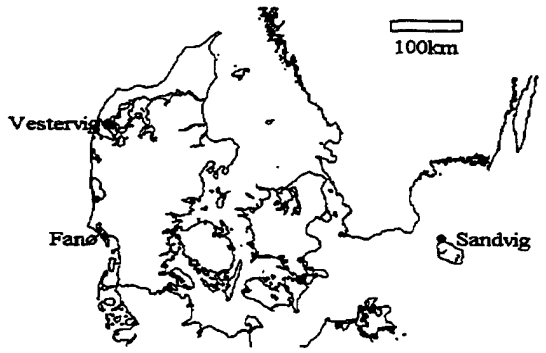


Figure 2. Map showing situation of climatic stations used.

All three stations have been operated almost unbroken since approximately 1875 with three daily observation hours, namely 0700, 1300 and 2000 utc. For observing the pressure, mercury barometers, each having a unique instrument number, have been used. The barometer reading was, once observed, written on a 'climatic list' together with a reading of the barometer temperature, and other observed climatic elements.

Every fortnight the climatic lists were sent to the Meteorological Institute for further processing. The barometer readings were corrected for index error, temperature and (from 1893 onwards) gravity, see WMO (1983). These corrections were done by means of a correction table for each individual barometer, and it is therefore important, that the individual observers refers to the correct instrument number on their climatic lists. The corrected station pressure and other observed elements have been published once a year in "Meteorologisk Årbog" (Meteorological Yearbook) by the Danish Meteorological Institute (DMI). Recently pressure and air temperature data have been put into digital form, and is now stored in the DMI climatological database.

In 1987 the barometers were withdrawn from all Danish climatic stations, and it has therefore been necessary to continue the record with observations from neighbouring synoptic stations.

3. STATION HISTORY

The history of the three stations have been investigated by a historian. By looking through the relevant archives it was possible, partly to clarify movement of stations and change of observer, barometer height over MSL, barometer number and type etc. On the other hand holes in the filed material concerning the stations were found. All material so revealed was put in to structured form as metadata and stored in the DMI climatological database.

4. REDUCTION TO MEAN SEA LEVEL

Combining the law for hydrostatic pressure and the equation of state it is easy to arrive at the following reduction formula to calculate the MSL pressure p_0 from the station pressure p_s (valid for low-level stations only):

$$p_0 = p_s\left(1+\frac{g}{R}\frac{h}{T_s}\right) \qquad (1)$$

where g and R are the gravity and gas constant for atmospheric air respectively, h the station height, and T_s the air temperature in K observed at the station. This reduction procedure follows closely WMO (1983), and was applied to the three records of station pressure to get the corresponding three series of MSL pressure.

5. HOMOGENEITY TEST

A homogeneity test similar to Alexandersson (1986) was performed on each of the three annual mean MSL pressure series. However, instead of forming a ratio series, we form a series $\{q_n\}$ of *differences* between the annual mean pressures of the test station p_n^{test} and the reference station(s) p_n^{ref} by

$$q_n = \left(p_n^{test} - \overline{p}^{test}\right) - \sum_{ref}\left(p_n^{ref} - \overline{p}^{ref}\right) \qquad (2)$$

Now, broadly speaking, if for some year N the series $\{q_n\}$ has different mean values $\overline{q}_{before} = \overline{q_n}|_{n<N}$ and $\overline{q}_{after} = \overline{q_n}|_{n>N}$ for $n<N$ and $n>N$ respectively, then the test series has a break at year N provided the reference series is homogeneous. For details we refer to Alexandersson (1986).

When performing the homogeneity test a certain level of statistical significance must be chosen. We accept the detection of a break if *either* the break is significant at the 5% level *or* the break is significant at the 10% and supported by some event recorded in the metadata, e.g. renewal of

barometer. When a break in a series has been accepted, we assume that the series is correct after the break, and therefore all pressure values before the break are adjusted by adding $\bar{q}_{after} - \bar{q}_{before}$.

Of course, we don't know, whether the reference series really are homogeneous. So when a break is detected, it could as well be one of them being inhomogeneous. Therefore the each reference series is removed successively, and the test quantities recalculated. If the break becomes insignficant by removing one particular reference series, that series is most likely inhomogeneous. By proceeding along these guidelines it is possible to adjust all series and thereby make them homogeneous. The adjustment constants applied is usually below 0.5hPa.

6. CALCULATION OF GEOSTROPHIC WIND

Each triple of MSL pressure from the three stations determines unique constants a, b and c in a polynomium of the form

$$p = ax + by + c = ar\lambda\cos\varphi + br\varphi + c \quad (3)$$

where λ and φ are longitude and latitude respectively. From that we calculate the geostrophic wind components u_g and v_g as

$$u_g = -\frac{1}{\rho f}\frac{\partial p}{\partial y} = -\frac{b}{\rho f} \quad (4)$$

and

$$v_g = \frac{1}{\rho f}\frac{\partial p}{\partial x} = \frac{a}{\rho f} \quad (5)$$

where ρ is the density of air and f the Coriolis parameter. We thus arrive at a time series of approximately 100 years of three daily geostrophic wind s.

7. QUALITY CHECK

As the aim of the project is to evaluate severe winds, all geostrophic winds exceeding 40m/s were examined more closely. This limit corresponds according to Luthardt&Hasse (1981) to a surface (10m) wind under neutral conditions of 25m/s. These cases were checked against weather maps and other sources to verify, whether severe winds really were likely. In some cases erroneous pressure values were found, often it was a nx5mmHg misreading. These pressure values were corrected and geostrophic wind recalculated.

8. RESULTS

The annual resultant (vector mean) geostrophic wind is calculated and shown in fig. 3

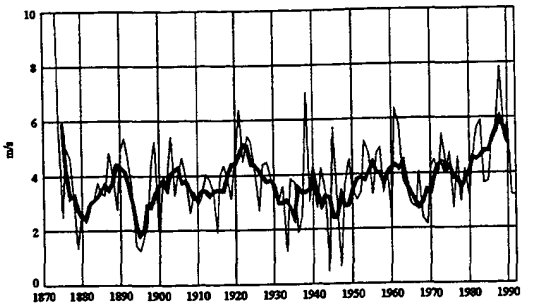


Figure 3. Annual resultant geostrophic wind in Denmark (Thick curve: 5-year running mean).

Oscillations with a period of 2-3 years are seen. Applying a 5-year running mean the trend and longer periods reveal more clearly. In particular we note an increase since around 1975.

Turning now to annual maximum of geostrophic wind shown in fig. 4 we see a quite different picture, namely no increase since around 1975 but rather a small decrease. We also note a period around 1920-1930 with enhanced annual maximum winds.

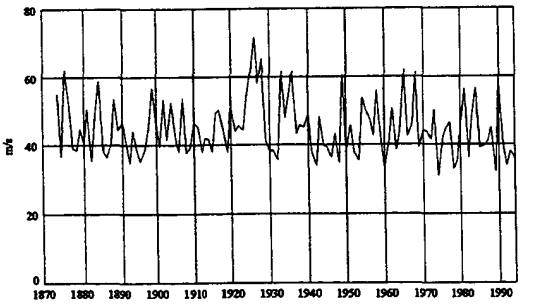


Figure 4. Annual maximum geostrophic wind in Denmark.

We now want to compare the annual resultant and maximum geostrophic wind for each year and show a scatterplot in fig. 5 We see, that the two quantities are not correlated at all. The correlation coefficient amounts to 0.11.

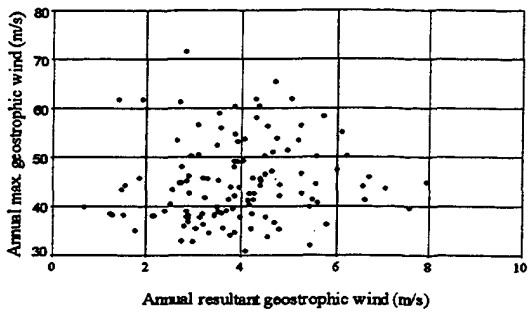


Figure 5. Scatterplot of annual resultant geostrophic wind and maximum geostrophic wind.

Finally we present in fig. 6 a diagram showing the number of days with storm (geostrophic wind exceeding 40m/s) for each year. Like in fig. 4, we see no overall trend. We also notice a similar increase in number of storm days in the period around 1920-1930.

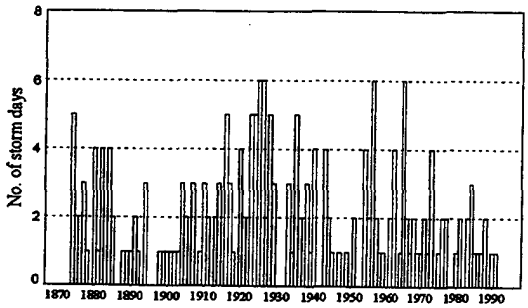


Figure 6. Number of days with storm (geostrophic wind exceeding 40m/s) for each year.

9. LIMITATIONS OF METHOD

The most important drawback of the method is, that pressure gradients with a smaller scale than the distance between the stations are not resolved. In particular, intense storms passing across central Denmark might not be resolved at all. By utilising more stations covering a wider area, we might be able to catch these storms better.

Regarding the optimal distance between the stations very little has been said so far. Intuitively we can say, that if the distance is to small the noise becomes significant, while if the distance is to big, we can't resolve the pressure gradients.

If we follow WMO (1983) and put the standard error of the pressure measurement equal to 0.3hPa, we get a standard error on the pressure *difference* of approxemately 0.4hPa. Putting the pressure difference itself to 4hPa and the station difference to 100km, corresponding approximately to Vestervig-Fanø, we get from (4) a geostrophic wind of 25m/s. We thus conclude, that geostrophic wind of storm force are determined with a standard error of 10% or less.

10. FUTURE PLANS

It is the intention, eventually to carry out similar storm statistics for a number of triangles covering Northeast Atlantic and Northwest Europe. Thereby we hope to clarify the whole pattern of severe storms in the entire area and its possible changes during the past 100 years.

REFERENCES:

Alexandersson, H., 1986, "A homogeneity test applied to precipitation data", Journal of Climatology, vol. 6, p. 661-675.

H. Luthardt and L. Hasse, 1981, "On the relationship between surface and geostrophic wind in the region of the German Bight", Contributions to Atmospheric Physics, vol. 54 No. 2, p. 222-237.

WMO, 1983, "Guide to meteorological instruments and methods of observation", 5th ed., Geneva.

ACKNOWLEDGEMENTS

This study was funded by the European Commission (DG XII), Environment programme, under contract EV5V - CT94-0506: "The impact of storms on waves and surges: Changing climate in the past 100 years and perspectives for the future".

CORRESPONDING AUTHOR

Torben Schmith,
Danish Meteorological Institute,
Database Department,
Lyngbyvej 100,
DK-2100 Copenhagen Ø,
DENMARK.

Telephone: +45 39 15 75 97
Telefax: +45 39 15 75 98
E-mail: tsc@dmi.min.dk

OBJECTIVE DIVIDING PATTERNS FOR CLIMATIC DROUGHT/FLOOD OF EASTERN CHINA IN RECENT 30 YEARS BY CHEBYSHEV QUADRATURE POLYNOMIALS

Jinmei Shen

Department of Geo. & Atmospheric Sciences, Iowa State University, 3010 Agronomy Hall, Ames, Iowa 50011, USA

Xiaomin Dong

Jiangsu Institute of Climate Application, Nanjing 210009, PRC

ABSTRACT Based on the drought/flood index $I_{i,k,l}$ for every station in the eastern China for every dekad and every year, the two-dimensional spatial distribution of $I_{i,k,l}$ is expanded by using Chebyshev quadrature polynomials. According to the contribution amount R_{pq} of Chebyshev quadrature polynomial coefficients for every order to the expanded field, the corresponding coefficients A_{pq} are adopted to diagnose the climatic drought/flood distribution features, and the classification effects with clear climatic signification, geometric figure and analytical form are obtained .

1. INTRODUCTION

Drought/flood is one of the most severe natural calamity in the eastern China. Its occurrence and variation play an important effect on the products of agriculture and industry as well as economic construction. More and more cares about drought/flood disasters have been taken by the government officials and meteorologists. It is necessary to study and analyze its characteristics of distribution, the mechanism of formation and the variation laws.

2. METHODOLOGY

In this paper, based on our previous work on calculating the drought/flood index $I_{i,k,l}$ for every station (i=1-60) in the eastern China for every dekad (k=1-36) and every year (l=1-30, 1961-1990) after the "Bhalme and Mooley" method was improved (Shen and Dong, 1991), the two-dimensional spatial distribution of $I_{i,k,l}$ is expanded by means of Chebyshev quadrature polynomials (Zhou, 1990).

From above 60 stations, we chose 28 stations (in x direction j_1=1-4, in y direction j_2=1-7) according to their geographical locations. The Chebyshev quadrature polynomial coefficients A_{pq} and the corresponding contribution amount R_{pq} are determined by the following equations.

$$
\begin{aligned}
I_{i,k,l}(j_1 j_2) &= \sum_{p=0}^{p_0}\sum_{q=0}^{q_0} A_{pq}\varphi_p(j_1)\psi_q(j_2) \\
A_{pq} &= \frac{\sum_{j_2=1}^{J_{20}}\sum_{j_1=1}^{J_{10}} I_{i,k,l}(j_1 j_2)\varphi_p(j_1)\psi_q(j_2)}{\sum_{j_2=1}^{J_{20}}\sum_{j_1=1}^{J_{10}} \varphi_p^2(j_1)\psi_q^2(j_2)} \\
R_{pq} &= \frac{A_{pq}^2\sum_{j_2=1}^{J_{20}}\sum_{j_1=1}^{J_{10}} \varphi_p^2(j_1)\psi_q^2(j_2)}{\sum_{j_2=1}^{J_{20}}\sum_{j_1=1}^{J_{10}} [I_{i,k,l}(j_1 j_2) - A_{00}]^2}
\end{aligned}
\qquad (1)
$$

where p_0=3, q_0=6, J_{10}=4 and J_{20}=7. Chebyshev quadrature polynomials $\phi_p(j_1)$ and $\psi_q(j_2)$ are computed as follows:

$$
\begin{aligned}
\varphi_{p+1}(j_1) &= \varphi_1(j_1)\varphi_p(j_1) - \frac{p^2(J_{10}^2 - p^2)}{4(4p^2-1)}\varphi_{p-1}(j_1) \\
\varphi_0(j_1) &= 1 \\
\varphi_1(j_1) &= j_1 - \frac{J_{10}+1}{2}
\end{aligned}
\qquad (2)
$$

$$\psi_{q+1}(j_2)=\psi_1(j_2)\psi_q(j_2)-\frac{q^2(J_{20}^2-q^2)}{4(4q^2-1)}\psi_{q-1}(j_2)$$
$$\psi_0(j_2)=1 \qquad (3)$$
$$\psi_1(j_2)=j_2-\frac{J_{20}+1}{2}$$

By using above equations (1)-(3), we computed Chebyshev quadrature polynomial coefficients A_{pq} and their corresponding contribution amount R_{pq} of the expanded field of $I_{i,k,l}$ for every dekad and every year. According to the contribution amount R_{pq} (p=0-3, q=0-6) of Chebyshev quadrature polynomial coefficients for every order to the expanded field, the corresponding coefficients A_{pq} are adopted to diagnose the distribution features of the climatic drought/flood, and the classification effects with clear climatic signification, geometric figure and analytical form are obtained.

3. RESULTS

a. General mean characteristics of climatic droughts/floods extent in the eastern China

Table 1. General mean level of distribution of droughts/floods in the Eastern China during 30 years (1961-90)

Season	A_{00}	Extent and grade of drought/flood	number of year
winter	≥1.00	mild flood	1
		moderate flood	1
		severe flood	2
		extreme flood	2
	[-0.99,0.99]	normal	10
	≤-1.00	mild drought	14
spring	≥1.00	flood	7
	[-0.99,0.99]	normal	12
	≤-1.00	mild drought	11
summer	≥1.00	flood	7
	[-0.99,0.99]	normal	15
	≤-1.00	mild drought	8
autumn	≥1.00	flood	10
	[-0.99,0.99]	normal	7
	≤-1.00	mild drought	13

The Chebyshev coefficient A_{00} accounts for the general mean level of the drought/flood extent for every season in eastern China, as shown in Table 1.

IN SPRING: During 30 years from 1961 to 1990, the majority are "near normal" and "mild drought". However, "moderate drought" and "severe flood" may also exist.

IN SUMMER: The ratio of the "near normal" years to the whole 30 years is 0.5, the other years alter in "drought" and "flood" vary fast, and are uncertain.

IN AUTUMN: During 30 years, both "drought" years and "flood" years obviously exist, yet the "near normal" years are less.

IN WINTER: In the 30-year period, the majority of these years are "normal" and "mild drought", and the minority are "flood" which are almost the serious flood.

b. Distribution characteristics of climatic droughts/floods extent for every season in the eastern China

According to the contribution amount R_{pq} and the corresponding coefficient A_{pq}, the drought/flood distribution features may be divided into 5 patterns in winter and spring, into 6 patterns in summer and autumn. The elementary characteristics of these patterns can be concluded as follows:

TYPE 1. The isolines of $I_{i,k,l}$ show the longitudinal distribution, $I_{i,k,l}$ decreases or increases linearly from the east to the west; when $A_{10}>0$, the west of the eastern China is drought and the east is flood (or near normal), when $A_{10}<0$, the west is flood (or mild drought) and the east is severe drought. A_{10} accounts for the east-westward distribution feature of climatic drought/flood in the eastern China.

TYPE 2. The isolines of $I_{i,k,l}$ show the south-northward parabola distribution, and the more the contribution of A_{02}, the larger the degree of bumps and holes in the parabola curve. When $A_{02}<0$ (or $A_{02}>0$), both the end of the south and the north of the eastern China are flood (or drought), then the middle is drought (or flood).

TYPE 3. The isolines of $I_{i,k,l}$ show the latitudinal distribution, $I_{i,k,l}$ decreases or increases linearly from the south to the north; When $A_{01}>0$ and $A_{10}>0$ (or $A_{01}<0$ and $A_{10}<0$), the north (or the northwest) is drought (or flood) and the south (or the southeast) is flood (or drought); When $A_{01}>0$ and $A_{10}<0$ (or $A_{01}<0$ and $A_{10}>0$), the north (or northeast) is drought (or flood) and the south (or southwest) drought(or flood). A_{01} presents another main south-northward distribution features of climatic drought/flood in the eastern China.

TYPE 4. The isolines of $I_{i,k,l}$ show the cubic curve distribution from north to south; When $A_{03}<0$, there are two alteration of drought/flood from the north to the south, i.e., the mild drought in the north (or northwest) -- drought -- normal -- drought in the south or drought in the north -- normal -- drought -- normal; or drought in the north -- flood -- normal -- flood in

TABLE 2. Objective dividing patterns of climatic drought/flood distribution in Spring

Dividing patterns by A_{00}			Dividing patterns by A_{00} and A_{pq} and R_{pq}		
A_{00} Feature	Years	Type	Parameter	$I_{i,k,l}$ distribution	Drought/flood feature
≤-1.00	1966,68	I	$R_{10} \geq 0.227$	Longitudinal, linear	$A_{10} < 0$ (>0) HD (LD) in the east and LD (HD) in the west
(11 years)	1984	II	$R_{02} \geq 0.256$	North-South parabola	$A_{20} > 0$ (<0) HD (LD) in the mid but LD (HD) in the other
	1976,78	III	$R_{01} \geq 0.349$	Latitudinal, linear	$A_{01} < 0, A_{10} < 0$: LD in the northwest, HD in the southeast
	86,89	III	Same as above		$A_{01} > 0, A_{10} > 0$: drought in the north, flood in the south
Drought	1970,72	IV	$R_{03} \geq 0.140$	North-South cubic curve	$A_{03} < 0$ from north to south: LD→D→Normal→D
	1971,83	V	R_{pq} small	irregular	unsteady and irregular drought/flood distribution
[-0.99,0.99]	1962,87	I	Same as above Type I		$A_{10} > 0$ drought in the west, flood in the east
	1961,65	III	Same as above Type III		$A_{01} > 0, A_{10} < 0$: D in the north, F in the south
	73,80	III			$A_{01} < 0, A_{10} > 0$: F in the north, D in the south
	81,85	III			$A_{01} > 0, A_{10} > 0$: D in the northwest, F in the southeast
(12 years)	1963,75,90	IV	Same as above Type IV		$A_{03} < 0$(>0), North→South(South→North):Normal→D→Normal→D
Normal	1982	V	Same as above Type V		Same as above Type V
≥1.00	1964,68	II	Same as above Type II		$A_{02} < 0$ F in the mid, LF in the other
	77	II			$A_{02} > 0$ D in the mid, F in the other
	1966,74	III	Same as above Type III		$A_{01} > 0, A_{10} < 0$ F in the south, D in the north; $A_{01} < 0, A_{10} < 0$(opposite)
(7 years)	1967	IV	Same as above Type IV		$A_{03} > 0$ North→South: LF→F→LD→F
Flood	1979	V	Same as above Type V		Same as above Type V

Note: F and D stand for flood and drought; L and H stand for light and heavy.

TABLE 3. Objective dividing patterns of climatic drought/flood distribution in Summer

Dividing patterns by A_{00}			Dividing patterns by A_{00} and A_{pq} and R_{pq}		
A_{00} Feature	Years	Type	Parameter	$I_{i,k,l}$ distribution	Drought/flood feature
[-0.99,0.99]	1985	I	$R_{10} \geq 0.188$	Longitudinal, linear	$A_{10} > 0$ F in the east, D in the west
(15 years)	1968,76	II	$R_{02} \geq 0.148$	North-South parabola	$A_{20} < 0$ F in the mid but D in the other
	79,84	II			$A_{20} > 0$ D in the mid but Normal in the other
	1961,71	III	$R_{01} \geq 0.400$	Latitudinal, linear	$A_{01} < 0, A_{10} < 0$:Normal in the nort, D in the south; $A_{01} > 0, A_{10} > 0$:
	77,83	III			F in the north, D in the south; $A_{01} > 0, A_{10} > 0$:D in the north
Normal	1986	IV	$R_{03} \geq 0.161$	North-South cubic curve	$A_{03} > 0$ from north to south: D→F→Normal→F
	1963,73,75,89	V	R_{pq} small	irregular	unsteady and irregular drought/flood distribution
	1967	VI	$(R_{11}+R_{33}) \geq 0.36$	Saddle field	$A_{11} > 0, A_{33} > 0$: F in NW and SE, D in NE and SW
≤1.00	1964,88	I	Same as above Type I		$A_{10} < 0$ D in the west, HD in the east
(8 years)	1966	II	Same as above Type II		$A_{02} > 0$ D in the mid, LD in the other
Normal	1978	III	Same as above Type III		$A_{01} < 0, A_{10} < 0$: Normal in the north, D in the south
	1970,74,82,90	V	Same as above Type V		Same as above Type V
≥1.00	1965,80,81	II	Same as above Type II		$A_{02} < 0$ F in the mid, LF in the other
(7 years)	1969,87	III	Same as above Type III		$A_{01} > 0$, $A_{10} > 0$ F in the south, D in the north
Flood	1962,72	V	Same as above Type V		Same as above Type V

the south; When $A_{03} > 0$, the mild flood in the north -- flood-- mild drought -- flood in the south, or drought in the north -- flood -- normal -- flood in the south.

TYPE 5. The isolines of $I_{i,k,l}$ show saddle-like field distribution; When $A_{11} > 0$ and $A_{22} > 0$ and $A_{33} > 0$ (or $A_{11} < 0$), the southeast and the northwest are drought (or flood), then the southwest and the northeast flood (or drought).

TYPE 6. This is the overlapping of several order curves, whose corresponding contribution amount R_{pq} of Chebyshev coefficients A_{pq} are all small. Under the circumstance, the contour lines of $I_{i,k,l}$ are irregular, always change in both the longitudinal and the latitudinal distribution forms, and drought and flood alter rapidly in each station (or each county, or each city).

Tables 2-5 list the characteristics of climate drought/flood distribution and objective dividing patterns in the four seasons in the eastern China.

4. CONCLUSION

The distribution characteristics of climatic drought/flood for four seasons in the eastern China

TABLE 4. Objective dividing patterns of climatic drought/flood distribution in Autumn

Dividing patterns by A_{00}			Dividing patterns by A_{00} and A_{pq} and R_{pq}		
A_{00} Feature	Years	Type	Parameter	$I_{i,k,l}$ distribution	Drought/flood feature
≤-1.00	1966,76	II	$R_{02} \geq 0.214$ ($R_{10} < 0.37$)	North-South parabola	$A_{20} < 0$ (> 0) F (D) in the mid but D (LD) in the other
(13 years)	1967,79	III	$R_{01} \geq 0.416$	Latitudinal, linear	$A_{01} < 0, A_{10} < 0$: Normal or D in the north, HD in the south
	82,88	III	Same as above		$A_{01} > 0, A_{10} > 0$: HD in the north, LH in the south
Drought	1963,78	IV	$R_{03} \geq 0.234$	North-South cubic curve	$A_{03} > 0$ from north to south: D→Normal→D→Normal
1970,86,87,89,90		V	R_{pq} small	irregular	unsteady and irregular drought/flood distribution
[-0.99,0.99]	1964,72,73	II	Same as above Type II		$A_{02} > 0$ D in the mid, LD or F in the other
(7 years)	1965,69	III	Same as above Type III		$A_{01} > 0, A_{10} > 0$: D in the north, F in the south
Normal	1977	V	Same as above Type V		Same as above Type V
	1968	VI	$R_{11} > 0.289$	Saddle field	$A_{11} > 0$ F in NW and SE, D in SW and NE
≥1.00	1974	I	$R_{10} \geq 0.373$	Longitudinal, linear	$A_{10} < 0$ D in the east and F in the west
1975,81,84		II	Same as above Type II		$A_{02} < 0$ F in the mid, LF in the other
(10 years)	1961,62	III	Same as above Type III		$A_{01} > 0, A_{10} > 0$ F in the south, D in the north; $A_{01} < 0, A_{10} < 0$ (opposite)
	80,83	III			$A_{01} > 0$, $A_{10} < 0$ D in the south, Normal in the north
Flood	1971,85	VI	Same as above Type VI		$A_{11} > 0, A_{22} > 0$ D in NW and SE, Normal in NE and SW

TABLE 5. Objective dividing patterns of climatic drought/flood distribution in Winter

Dividing patterns by A_{00}			Dividing patterns by A_{00} and A_{pq} and R_{pq}		
A_{00} Feature	Years	Type	Parameter	$I_{i,k,l}$ distribution	Drought/flood feature
[-0.99,0.99]	1972,88	I	$R_{10} \geq 0.400$	Longitudinal, linear	$A_{10} > 0$ F in the east, D in the west
(10 years)	1966,75	II	$R_{02} \geq 0.11$ ($R_{02} + R_{03} \geq 0.4$)	North-South parabola	$A_{20} < 0$ F in the mid but D in the other
1964,69,85		III	$R_{01} \geq 0.68$	Latitudinal, linear	$A_{01} < 0$: D in the nort, F in the south; $A_{01} > 0$ (opposite)
Normal	1967,90	V	R_{pq} small	irregular	unsteady and irregular drought/flood distribution
	1983	VI	$R_{11} \geq 0.3$	Saddle field	$A_{11} < 0$ D in NW and SE, F in NE and SW
≤1.00 (14 years)	1981,82	I	Same as above Type I		$A_{02} > 0$ D in the mid, LD in the other
1962,63,65,68,71,74,76,79,84,86		III	Same as above Type III		$A_{01} < 0, A_{10} < 0$: D in the south, LD in the north,
Drought	1970,78	V	Same as above Type V		Same as above Type V
≥1.00 (6 years)	1973,87	II	Same as above Type II		$A_{02} < 0$ F in the mid, LF in the other
Flood	1961,80,77,89	III	Same as above Type III		$A_{01} > 0$, $A_{10} > 0$ F in the south, D in the north

during recent 30 years can be concluded the following:

IN SPRING: The linear south-northward distribution pattern is dominate, the cubic curve distribution pattern takes the second place. For the other patterns their occurrence probabilities are equivalent. Those show that there are some differences of drought /flood in both the south-north and the west-east, but the alternation between the south and the north is more obvious.

IN SUMMER: The unsteady distribution pattern takes the first place, the linear south-northward distribution and parabola distribution takes second place. It indicates that the drought/flood distribution in summer is in disorder, and shows nonuniform and unsteady characteristics, that is consistence with the changeable climate in summer in the eastern China.

IN AUTUMN: The drought/flood distribution shows different from that in summer with nonuniform and unsteady characteristics but analogous to that in spring, the south-northward linear distribution takes first place, both the south-northward cubic curves and unsteady distributions take important place. There are less east-westward differences in the drought/flood.

IN WINTER: The linear distribution form the south to the north is dominant, the parabola distribution takes the second place, and the drought/flood difference from the south to the north exists obviously. However, the difference from the west to the east is not obvious.

REFERENCE

Shen, J. and X. Dong, 1991, An improvement of "BM" method and its application to analyses of Drought/Flood in Jiangsu Province, Chinese *Journal of Meteorology*, Vol.17, No.11, pp. 12-18.

Zhou, J., 1990, *Chebyshev quadrature polynomial and its application on the meteorology*, Chinese Meteorological Press, pp.180.

CORRESPONDING AUTHOR: Jinmei Shen, Department of Geological and Atmospheric Sciences, Iowa State University
3010 Agronomy Hall, Ames, Iowa 50011, USA
E-mail: jinmei@iastate.edu Fax: (515) 294-3163 Tel: 294-4758

SINGULAR VALUE DECOMPOSITION OF INTERACTION AMONG ATMOSPHERIC CIRCULATION, SST AND SEA-ICE DURING WINTER

Fang Zhifang

Chengdu Institute of Meteorology, Chengdu, Sichuan 610041, P.R.China

ABSTRACT

The sea-ice concentration and SST in the North Pacific sectors, 500hPa height, sea-level pressure and 1000-500 hpa thickness of monthly mean data are examined for the period 1972-1989, with emphasis on the winter season.

The relationship among the large-scale patterns of atmospheric variability , sea-ice and SST variability are investigated, making use of the Singular Value Decomposition (SVD) of the temporal covariance matrix. The analysis is conducted for the Pacific sectors. The strongest sea-ice pattern is composed of a dipole with opposing centers of action in Bering sea and the Sea of Okhotsk. Its temporal Variability is strongly coupled to the atmospheric West Pacific pattern (WP). The relationship between the two patterns is strongest with the atmosphere leading the sea-ice by one month. The WP pattern also force on the Kuroshio SST of lagging one month.

The relationship among the fields are indicative of local forcing of sea-ice and SST in most regions, with wind stress and thermodynamic fluxes at air-sea interface both contribution.

1 INTRODUCTION

The role of sea-ice and ocean in the climate system involves the feedback by way of thermodynamic fluxes and dynamic process at air-sea interface. The interactions among sea-ice, ocean and the atmospheric circulation have obviously seasonal variability with the solar radiation. During wintertime the solar radiation is very weak in high latitudes, while the atmospheric circulation is stronger both in geostrophic wind and thermal advection. Therefore the atmospheric forcing play a dominant role.

Rogers and Van Loon (1979) used the sea-ice severity through summer in Davis Strait, springtime icebergs near Newfoundland, and the wintertime maximum ice extent in Baltic sea as sea-ice indices. They indicated that the GB pattern in winter (Greenland below normal temperature and anomalously deep Icelandic low in sea level pressure (SLP)) is associated with heavy-ice conditions through summer in the Davis Strait, with more springtime icebergs near Newfoundland, and with light ice conditions in Baltic Sea in winter.

Fang and wallace (1994), Based on sea-ice concentration, 500hPa height, Sea-level pressure and 1000-500 hPa thickness at 7 day interval data from 1972-1989, indicated that there exists the connection between sea-ice pattern in the Atlantic and atmospheric NAO (North Atlantic Oscillation) pattern in the North Hemisphere, and pointed out that the relationship between the two patterns is strongest with the atmosphere leading the sea-ice by two weeks.

The large scale air-sea interaction plays a crucial role in the climate system. Lau N. C. (1988) indicated that the West Pacific pattern (WP) and the west Atlantic Pattern (WP) can effect on the mix layer SST in the ocean, and SST lagging the atmosphere.

This paper emphasized the Pacific sector in North Hemisphere. The sea-ice concentration and SST, 500 hPa height and sea level pressure (SLP) on monthly time scales are examined for the period 1972-1989 with emphasis on winter season. The relationship among large scale pattern of the atmospheric variability , sea-ice and SST in Kuroshio are investigated, making use Singular Value Decomposition (SVD) of the temporal covariance matrix and correlation fields.

2 DATA

The analysis described in this paper is based on two data sets: monthly sa-ice concentration data and monthly mean atmospheric 500 hPa height, Sea-level pressure fields.

The sea-ice data are the archives on a $2^{\circ}*2^{\circ}$ grid toward polar at Pacific sector, 90 E-90 W. The data compiled by NSIDC of U.S.A. in 1991, that call the Sea Ice Data in Digital Form (SIGRID). The record encompasses the period from January 1972 to December 1989 for 18 years.

The SST data in Pacific sector are the archives on $4^{\circ}*6^{\circ}$ grid, 2°-58° N and 120°E-180°-90° W over the North Pacific area. The data compiled by NCAR of U.S.A., it call COADS data. The record are same period as sea-ice data.

The atmospheric Data used in this study are for the same period of record as sea-ice data. The data consist of the NMC operational analyses of daily 500 hPa height and sea-level pressure on the 1977-point octagonal grids, superimposed on a polar stereographic projection of the Northern Hemisphere, extending to 20° N. The monthly means are condensed from the full NMC grids to 445-point grids, using a Gaussian interpolation scheme to avoid aliasing.

3 SEA-ICE CLIMATOLOGY

Using the EOF method, we analyse the sea-ice distribution in Pacific sector during wintertime (January, February and March). We chose the three months, because the months have largest sea-ice concentration for all year and these months belong the winter time. The horizontal structure of the leading EOF of sea-ice concentration over the Pacific sector during the there months is shown in Fig.1.

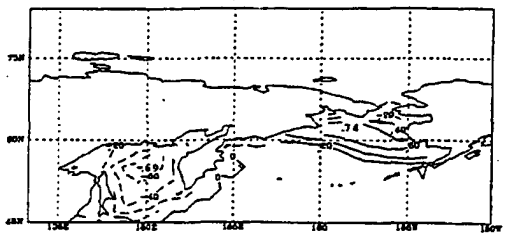


Figure 1. Horizontal structure of leading EOF of the sea-ice concentration during winter time (J. F. M.) for the Pacific Sector. The contours show the temporal correlation between the time series of the expansion coefficient of EOF and sea-ice concentration at each grid point, contour interval 0.2.

This mode of variability dominated by out-of-phase between sea-ice fluctuations in the Sea of Okhotsk and the Bering Sea. The weight for the leading mode is 35%. It can be assumed that a large ice area in Sea of Okhotsk has a company filed with a small sea-ice extent in Bering Sea. The pattern often appear in wintertime.

4 THE ATMOSPHERIC CIRCULATION FORCING ON THE SAE-ICE DISTRIBUTION.

Table 1. The leading SVD statistics for the leading mode in SVD expansion between the sea-ice concentration over the Pacific sector in J.F.M and 500 hPa and SLP in leading or lagging months.

lag	500 hPa		SLP	
	SCF(%)	r	SCF(%)	r
-2	37	0.54	32	0.52
-1	39	0.59	47	0.56
0	42	0.62	43	0.61
1	49	0.73	51	0.73
2	40	0.56	43	0.59
3	38	0.56	34	0.54

The relationship between fluctuations in wintertime sea-ice concentration (J.F.M.) over the north Pacific and the hemispheric 500 hPa height, Sea level pressure were explored, making use the SVD method. In order to show for the strongest relationship, not only in the simultaneous correlation, but in the one field lagging by some time interval to the another, the analysis was performed for a sequence of different lag interval, ranging from -2 months to 3 months, where negative values denote sea-ice leading 500 hPa or SLP, and the positive values denote sea-ice lagging 500 hPa or SLP. The statistics of the leading modes derived from these calculations are summarized in Table 1. The SVD method was been described by Bretherton, Smith and Wallace at 1992.

SCF is the squared covariance fraction between the two field explained by the leading mode, r is the correlation coefficient between the both time series of the expansion coefficients for the leading mode. In table 1, these indicators in 500 hPa and SLP reach their peak value with sea-ice lagging the atmospheric variability by one month.

Fig. 2 shown the leading SVD results. The heterogeneous correlation pattern for sea-ice lagging 500 hPa by one month, shown in Fig. 2a. is virtually identical to the pattern for the leading EOF, shown in Fig.1. The correlation 500 hPa height pattern, shown in Fig. 2b, resembles the West Pacific Pattern (WP). Wallace and Gutzler (1981) had paid particular attention to the statistical significance of the height distributions at 500 hPa level and SLP in North Hemisphere. The corresponding SLP pattern, shown in Fig. 2c, also resembles the WP pattern.

It means that if there exists a WP pattern in 500 hPa or SLP, then the next month the sea-ice often have the distribution, which is similar with Fig.1.

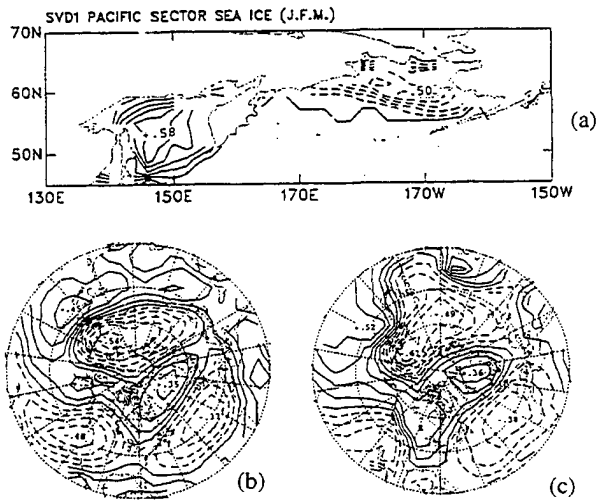


Figure 2. The leading SVD results for the sea-ice lagging 500 hPa by one month. The heterogeneous correlation pattern for (a) sea-ice concentration over the Pacific sector, (b) 500 hPa height, (c) correlation coefficient between the time series of the expansion coefficient of sea-ice concentration in the leading SVD and leading SLP by one month.

5 THE ATMOSPHERIC CIRCULATION FORCING ON THE KUROSHIO SST

We use the Kuroshio SST index, Based on the average of the SST in 20-45 N, 120-170 E during January, February and

March. The relations between the Kuroshio SST index and the North hemispheric 500 hPa height and SLP were investigated, making use the correlation field.

We use same idea in section 4. The analysis was performed for the ranging from -2 months to 3 months, where negative value denoted SST leading 500 hPa or SLP, and positive value denoted the SST lagging 500 hPa or SLP.

These calculations are summarized in Table 2. All of these correlation coefficients in 500 hPa and SLP reach their peak value with the Kuroshio SST lagging the atmospheric variables by one month.

Table 2. The correlation coefficients between the time series of the Kuroshio SST index (J.F.M.) and 500 hPa and SLP. The lag time as Table 1, but the negative means the SST leading atmosphere.

lag	500 hPa		SLP	
	South r	North r	South r	North r
-2	No WP		No WP	
-1	0.38	-0.38	0.36	-0.41
0	0.50	-0.35	0.43	-0.36
1	0.77	-0.46	0.69	-0.47
2	0.57	-0.36	0.66	-0.20
-3	No WP		No WP	

Note: the South r means the correlation coefficients between the Kuroshio SST index and atmospheric point at 30 N, 150 E, the North r means at 60 N, 150 E, and the No WP means there is not WP pattern in the correlation field map.

Fig. 3 shown the correlation fields for the Kuroshio SST lagging 500 hPa and SLP by one month. The corresponding 500 hPa height pattern, shown in Fig. 3a, resembles with the WP pattern, and identical to the Fig. 2b. The corresponding SLP pattern (Fig. 3b) is very similar with Fig. 2c. As the results, when the anomalies of 500 hPa and SLP in North Hemisphere appeared the WP pattern, The atmospheric circulation influence on the SST Kuroshio and sea-ice distribution in the Pacific sector.

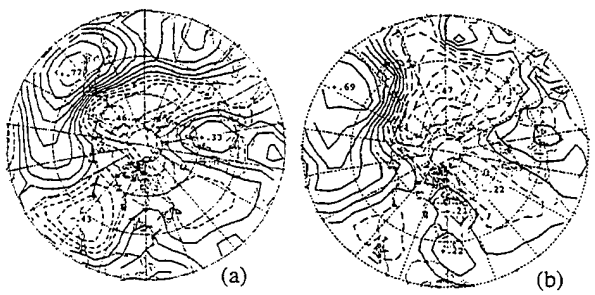


Figure 3. The correlation coefficient fields between the Kuroshio SST index (J.F.M.) and (a) 500 hPa, (b) SLP during December, January and February.

6 THE WINTER MONSOON INFLUENCE ON THE SEA-ICE AND SST

We use the composite maps of 500 hPa and SLP for clearly showing different winter monsoon systems in some special months.

The six months composite map, based on the six highest months of the time series of the expansion coefficients from leading SVD in the section 2, was shown in Fig. 4. There exists a polar vortex near 120-140°E in 500 hPa (Fig. 4a), therefore the north part of East Asia trough is stronger than normal, and the storm track propagates to rather north of its climatic mean position. In SLP field (Fig. 4b), the Mongolia High and the Aleutian Low are weaker than normal, it is a weaker winter monsoon situation. The northerly wind covering the sea of Okhotsk replaces the normal north easterly wind, which would be conducible to the advance of the ice edge. The south-east wind covers the Bering sea, which would be presume the resulting in a reduced southward transportation of sea-ice. The northerly wind over the Pacific of east Japan is weaker than normal, and would be resulting in the positive anomalies SST in the Kuroshio area.

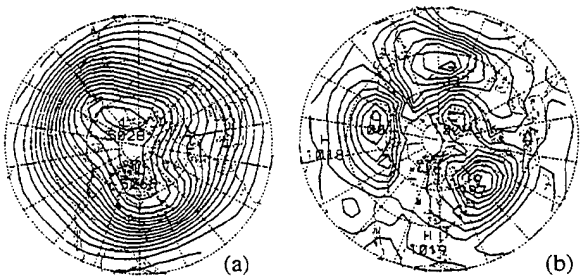


Figure 4. Composite maps, based on the six highest months of the time series of leading SVD for (a) 500 hPa, (b) SLP.

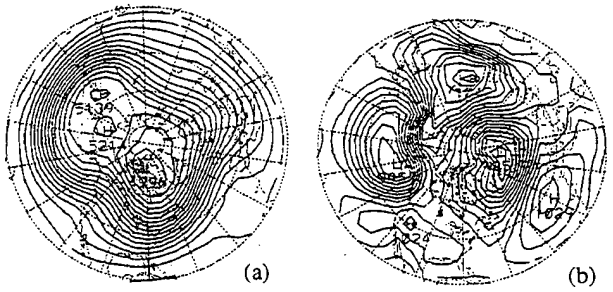


Figure 5. composite maps, as Fig. 4, but for the six lowest months. (a) 500 hPa and (b) SLP.

Fig. 5 is composite maps, based on the six lowest months. There exists a cut-off Low in 140 E and a cut-off high in 175 E in 500 hPa, which just located over the sea of Okhotsk and the Kamchatka peninsula, the storm track is south of normal, shown in Fig. 5 a. In SLP field (Fig. 5b), the Mongolia High and the Aleutian Low are stronger than climatic mean, it is a

stronger East Asia winter monsoon situation. Therefore the wind field is different with the six highest months, shown in Fig. 4, it should change the sea-ice distribution over the North Pacific and the Kuroshio SST. In the case, the wind direction will cause the Okhotsk sea-ice reduced and the Bering sea-ice advanced to southward. The northerly wind in Pacific near east of Japan is stronger than normal, therefore the negative anomalies SST appear in the Kuroshio area.

7 SUMMARY

From the foregoing analysis, the study suggests that :
In Pacific sector, the strongest sea-ice pattern is composed of a dipole with opposing centers of action in Bering sea and Sea of Okhotsk. Its temporal variability is strongly coupled to the atmospheric West Pacific pattern (WP). The relationship between the two pattern is strongest with atmosphere leading the sea-ice by one month. The atmospheric WP pattern also force on the Kuroshio SST of lagging one month.

ACKNOWLEDGMENTS

The authors wish to thank Xinhua Cheng and Yuan Zhang, who provided the atmospheric data and advised and assisted in setting up the analysis. John M. Wallace and Iwasaka Naoto, who provided helpful comments and encouragement. The author received the financil assistance from the National Science Foundation of China.

REFERENCES

Bretherton, C.S., C.Smith and J.M.Wallace, 1992, An intercomparision of methods for finding coupled patterns in climate data. J. Climate, 5, 541-560.

Fang Z.-F., and J.M.Wallace, 1994, Arctic sea-ice on a time-scale of weeks and its relation to atmospheric forcing. J. Climate, 7, 3245-3263.

Lau N.-C., 1988, Variability of the observed midlatitude storm tracks in relation to low-frequency changes in the circulation pattern, J. Atmos.Sci., 45, 2718-2743.

Rogers, J.C. and H.Von Loon, 1979, The seesaw in winter temperatures between Greenland and northern Europe, Part 2: some oceanic and atmospheric effects in middle and high latitudes, Mon. Wea. Rev.,107, 509-519.

Wallace, J.M., and D. S. Gutzler, 1981, Teleconnection in the geopotential height field during the northern hemisphere winter. Mon. Wea. Rev., 109, 784-812.

AN EXTENDED EMPIRICAL ORTHOGONAL FUNCTION ANALYSIS OF MODES OF MID-LATITUDE DECADAL VARIABILITY IN A COUPLED ATMOSPHERE-OCEAN MODEL

Claude Frankignoul and Eduardo Zorita

Laboratoire d' Océanographie Dynamique et de Climatologie,Université Pierre et Marie Curie, Paris, France.

ABSTRACT

Two oscillatory modes of variability in the North Atlantic sector with a period of about 20 and 10 years respectively have been identified by Extended Empirical Orthogonal Function analysis in a 325-year integration of a coupled OAGCM. The 20-year mode is driven by the atmosphere through air-sea fluxes and Ekman pumping. It seems to be remotely forced by climate anomalies in the North Pacific. The 10-year mode primarily arises from the retarded response of the subtropical gyre to windstress anomalies, which in turn changes the heat transport by the ocean and probably influences the atmospheric circulation.

1. INTRODUCTION

There is growing observational evidence that the climate system is able to support modes of oscillation in the decadal frequency range, and that the ocean has an important role, but different mechanisms of variability have been suggested for the Atlantic and for the Pacific sectors.

In the Pacific, the role played by ENSO and its teleconnection with the extratropical atmospheric circulation has been underlined in the observations. Trenberth and Hurrel (1993) have shown that the Pacific-North-American (PNA) pattern, which is in part remotely forced by ENSO, also varies on the decadal scale, and they suggested that it was due to a positive feedback between the PNA and extratropical SST anomalies, the atmospheric circulation anomalies influencing the ocean currents in a way that enhances the SST anomalies. This could amplify the ENSO forcing in the decadal range. Based on the results of an shorter experiment with the higher-resolution ECHO coupled GCM, Latif and Barnett (1994) suggested that a substantial interdecadal variability results from the unstable air-sea interaction between the subtropical gyre and the atmosphere in the North Pacific: an anomalously strong subtropical gyre causes higher SSTs at mid-latitudes, which in turn give rise to a weaker Aleutian Low. The associated wind-stress anomalies weaken the subtropical gyre after a certain lag and the cycle repeats with the reversed sign. A mode with an apparently similar mechanism has been also found in the North Pacific in a coupled integration of the ECHAM1-LSG model (Robertson, 1995).

In the Atlantic, observational studies have stressed the mid and high latitude air-sea interactions and the role of the meridional overturning and the deep-water formation (see Gordon and Zebiak (1992) for a short review). In a long integration of the Geophysical Fluid Dynamic Laboratory (GFDL) low-resolution ocean-atmosphere GCM, Delworth et al (1993) found that the interaction between the thermohaline circulation and the gyre circulation could generate oscillations in the 50-year time scale. The mechanisms involved in this phenomenon were chained in the following way: a weaker than normal thermohaline circulation would produce colder water temperatures in the upper ocean layers at mid latitudes, which in turn would be associated with a cyclonic circulation anomaly. This circulation would enhance the advection of more saline waters to the sinking region in the North Atlantic, thereby strengthening the thermohaline circulation. Then the cycle continues with reversed sign.

So far, the modes of interdecadal variability appear to be somewhat different in the various coupled models, and they may differ in the Atlantic and Pacific basins. Delworth et al.'s (1993) mode in the North Atlantic actively involves the thermohaline circulation, while the Pacific modes described by von Storch (1994) and Latif and Barnett (1994) primarily involve the coupling between the atmosphere, the oceanic mixed-layer and the gyre circulation. It is therefore of interest to analyse the results of a different coupled OACGM integration to ascertain which mechanism may be common to other models.

2. MODEL DESCRIPTION.

A more detailed description of the coupled model has been provided by Cubasch et al (1992). The coupled GCM used in this study was developed at the Max-Planck-Institut für Meteorologie in Hamburg. The atmospheric component is the ECHAM1-T21 model, which is a version of the ECMWF atmospheric GCM modified for climate studies. It is a spectral model with a equivalent horizontal resolution of about 5.6 x 5.6 degrees and 19 vertical levels. The ocean component is represented by the Large-Scale-Geostrophic (LSG) model . In the present run, it has an effective resolution of about 4 x 4 degrees and 11 vertical levels. In this model, the non-linear advection of momentum is neglected and the velocity field calculated diagnostically from the density. The models are coupled synchronously, with a large flux correction to avoid climate drift.

The results presented here are based on the first 325 years of an extended integration whose main features have been described by von Storch (1994). The North Atlantic domain between 5° N and 75° N and 90° W and 20° E will be the focus of our analysis The long-term mean sea level pressure (SLP) is rather realistic, although there are some discrepancies with the observations, mainly a poor simulation of the Icelandic low. The mean sea surface temperature (SST) and sea surface salinity (SSS) compare well with observations, as expected from the strong flux correction. The mean geostrophic stream function for the 450 m level is shifted too far south in the model, with a corresponding southward extension of the subpolar gyre.

3. STATISTICAL TECHNIQUE

The analysis heavily relies on using extended empirical orthogonal function (EEOF) technique (Weare and Nasstrom, 1982), which is a classical EOF analysis where time is considered as additional dimension: at each time t, the fields are considered simultaneously at time t, t + 1, t + 2, ..., M -1, so that the temporal evolution during M time steps become part of the mode structure. Just as EOFs identifies the dominant coherent spatial structures of variability, the EEOFs identify the main patterns that are coherent in space *and* time: they consist of a spatial pattern for each of the M time slices. If an quasi-oscillating structure were present in the data, it would yield a pair of eigenvectors explaining a similar amount of variance and with the same dominant frequency, and the spatial structures would be dephased by a quarter of the dominant period. Note that such quasi-oscillation will be represented here by the sum of both eigenvectors, rather than by the two separately. See Kousky and Kayano (1994) for recent applications of EEOF analysis, and Vautard et al (1992) for a more theoretical discussion of its one-dimensional analogue, known as Singular Spectrum Analysis.

The value of M is not fixed "a priori", but has to be adjusted. It should be large enough to encompass all the stages of the oscillating structures, and additionally to increase the signal to noise ratio, but small enough to retain sufficient independent degrees of freedom in the time series. A practical problem is that by augmenting the original field in the time dimension, one would soon have to work with prohibitively large dimensions. This is overcome by first reducing the spatial dimension with an EOF analysis where only the leading modes are retained.

4. EEOF ANALYSIS.

Three fields were selected for the Extended EOF analysis: annual means of the sea level pressure (SLP), sea surface temperature (SST) and the temperature at 450 m depth. Two modes of decadal variability with periods of about 20 years and 10 years, respectively, were identified and are described below.

a. The 20-year mode

The evolution of the SLP field may be described as a well developed pattern of positive SLP anomalies in the mid-Atlantic centered at about 50° N, flanked by negative SLP anomalies over Iceland-Greenland and in the subtropical Atlantic. The positive SLP anomalies seem to migrate northwards and be replaced by SLP anomalies of the reversed sign coming from the south. The SST evolution is characterised by positive SST anomalies off the American coast centered at about 40° N, that slowly wander northwards up to the coast of Newfoundland while decaying and being replaced by similar anomalies of the reversed sign. Also noteworthy is the presence of weaker anomalies of the opposite sign in the eastern side of the basin. The SST anomalies evolve in phase with the SLP variations. The evolution of the 450 m potential temperature anomalies is somewhat more complicated. Initially the North Atlantic is dominated by a dipole-like structure with opposite anomalies separated roughly by the 30° N parallel. The structure reaches its maximum amplitude about three years later than the SLP, and then begins to weaken while rotating clockwise. The amplitude of these anomalies are small, however, as expected from the small amount of variance explained by the EEOF pair: for SLP, they are of the order of tenths of hP, and for SST, of a few tenths of °K.

To understand the physics of this quasi-oscillatory behaviour, regression patterns between the time series associated with the pair of EEOFs eigenvectors and other variables have been calculated. Again, only the sum of both regression patterns is shown in each case. The pattern evolution of the geostrophic stream function at 450 m depth primarily reflects a variation in the strength of the subtropical and subpolar gyres, with a lag of about 2-3 years with respect to the SLP anomalies. The salinity anomalies at 450 m displays an evolution that is very similar to that of the 450 m potential temperature anomalies and they have the same sign. Note that temperature and salinity anomalies of the same sign have opposing effects on density, but that the temperature effect is dominant in this case. The velocities in the first oceanic layer closely follow the Ekman forcing, with convergence under high pressure cells and divergence under low pressure. The associated rainfall patterns are very patchy and do not show any discernible structure. Finally, the vertical velocity anomalies evolve in phase with the SLP anomalies, also reaching their maximum amplitude in phase with the SLP, and showing a very patchy pattern when the SLP anomalies are weakest. Positive (upward) vertical velocity anomalies occur under negative SLP anomalies, and vice versa. This suggests a direct link with the Ekman pumping.

The SST anomalies evolve in phase with the SLP anomalies and their patterns are consistent with the forcing of the oceanic surface variables by the overlaying atmosphere, as observed at shorter time scales. Sea surface temperatures are colder (warmer) than normal in areas where the air is advected by the anomalous wind from colder (warmer) regions, as found also by other authors, both at interannual time scales and at decadal time scales. Also, stronger (weaker) westerlies should be associated with an enhanced (reduced) mechanical mixing with lower ocean layers, contributing to the SST cooling (warming). Furthermore, the surface horizontal velocities, convergent under high pressure regions and divergent under low air pressure, are in agreement with the expected oceanic mixed-layer response, resulting in the observed Ekman pumping.

The sign of the stream function anomalies at 450 m depth suggest that the strength of the subtropical gyre is driven by the geostrophic winds over the mid-Atlantic. The lag between gyre intensity and wind forcing is consistent with the adjustment time of the mid-latitude ocean .

The temperature at 450 m depth is approximately in phase with the stream function, as expected from geostrophic equilibrium, with higher temperatures (lower densities) associated with anticyclonic circulation anomalies, and lower temperatures associated with cyclonic circulation anomalies. Furthermore, when the vertical velocity anomalies get weaker the temperature anomalies stop growing and begin to rotate clockwise, advected by the mean gyral currents.

The physical interpretation of this mode can therefore be summarized as follows:

- The evolution of the ocean surface variables (SST, surface velocities) suggests that the atmospheric forcing is important for the surface anomalies, even at these time scales, consistent with the findings of other authors .

•The wind stress drives the intensity of the subtropical gyre. The adjustment time seems to be about 2-3 years. The temperature and salinity anomalies associated to this 20-year mode are mainly affected by the vertical advection, driven by Ekman pumping. In the stages of the oscillation when the atmospheric anomalies are weak the effects of the advection by the mean gyre are also observed.

Thus, the 20-year mode appears to be primarily driven by the atmosphere, but the origin of these atmospheric circulation anomalies could not be traced back to any oceanic forcing in the Atlantic. Therefore, a remote forcing hypothesis has been tested by constructing an index based on the ocean temperature anomalies associated with the Atlantic 20-year mode and the lagged regression with the atmospheric stream function at 950 mb has been calculated. The regression coefficients are only statistically significant in the Pacific and Atlantic oceans at mid-latitudes. The behaviour of the regression pattern is clearly temporally asymmetric. The atmospheric stream function anomalies in the Atlantic attain their highest amplitude one year preceding the Atlantic temperature anomalies and vanish when they lag the temperature anomalies, indicating again the atmospheric forcing in the Atlantic sector. In the Pacific sector the anomalies in the atmospheric stream function precede the atmospheric anomalies in the Atlantic by about 2-3 years. This behaviour has been also tested with data of the full 1200-year integration and it remains essentially stable, only the lag between the Pacific and the Atlantic sector seems to be somewhat shorter. It suggests that the ultimate forcing of the 20-y mode in the Atlantic Ocean may be of Pacific origin. Indeed, Robertson (1995) has recently analysed air-sea interactions in the North Pacific in the same experiment as in the present paper and he reports the existence of a mode of variability with a dominant period of about 18 years, which is probably a part of the 20-year mode identified by von Storch (1994) in the whole Pacific basin. However, the mechanism by which the cross-basin forcing may effectively occur remains to be investigated, which will probably require an ACGM experiment forced by North Pacific SST anomalies.

b. The 10-year mode.

The EEOF analysis of the SLP, SST and the 450 m temperature fields yields another pair of eigenvectors that also have an oscillatory character, but a shorter period of about 10 years. This mode explains a smaller amount of variance, but when the EEOF analysis is repeated with the 150 m temperature, instead of the 450-m temperature, this higher frequency mode becomes more energetic than the 20-year period mode. This mode is therefore more surface-trapped. Therefore, the SLP, SST and the temperature at 150 m depth anomalies associated with this pair of EEOF eigenvectors will be described. The SLP anomalies evolve from a dipole pattern with centers of action located at 30^0 N and 50^0 N, which become progressively weaker and move northward, and are replaced by anomalies of the opposite sign after half a cycle. In turn, SST anomalies of one sign dominate the mid-Atlantic and are flanked by anomalies of the opposite sign in the Northeast and in the subtropical Western Atlantic. These subtropical anomalies seem to grow in extension in the following years until they cover most of the basin after half a cycle. The temperature at 150 m depth is also caracterized in the first time slice by a dipole pattern with anomalies of opposite signs separated at about 30^0 N. This structure weakens and begins to rotate clockwise giving rise after about five years to a dipole pattern of the opposite sign.

As for the previous mode, the evolution of other variables associated to this mode has been calculated to gain a better understanding of the physics involved. In the first time stages of the oscillation there is an anomalous cyclonic circulation at 150 meter depth in the subtropical Atlantic and anticyclonic anomalies located further north. This pattern gets weaker and eventually anticyclonic anomalies begin to develop at mid-latitudes. They also fade away afterwards, completing one cycle after about 10 years.

The oscillatory behaviour of the SST anomalies through the 10-year cycle seems to lag the SLP anomalies by about one year, which would be consistent again with an atmospheric origin of the SST anomalies. However, in this mode the spatial structures of the SLP and SST anomalies suggest that the atmospheric anomalies are not the sole origin of the SST anomalies and that the advection by ocean currents is more important than in the 20-year mode. In some stages of the cycle one finds higher SSTs at mid-latitudes associated with weaker than normal zonal winds, which is consistent with a heat-flux forcing of the SSTs driven by the atmosphere, but simultaneously negative SST anomalies appear and grow in the West Atlantic at lower latitudes, when the atmospheric circulation anomalies are becoming weaker. In these time stages the intensity of the oceanic subtropical gyre at 150 m depth is weaker, as a result of the weaker zonal winds at midlatitudes the previous years. This should cause the observed decrease in water temperatures in the western Atlantic. If the response of the atmosphere to these lower temperatures consists of lower SLP at midlatitudes, thereby strengthening the wind forcirng of the gyre, the cycle can coontinue with the reversed sign. This atmospheric response, however, should be ascertain with a stand-alone ACGM experiment.

5. AIR-SEA FEEDBACK AT DIFFERENT TIME SCALES.

In this work, only yearly averaged data have been considered. However, a brief discussion on the differences in the air-sea interactions at short and longer time scales may help undestand the results on the decadal variability. On the monthly to yearly time scale, the modelled air-sea interactions are realistic, showing a primarily passive response of the ocean: sea surface temperature anomalies arise in response to the short time scale variability of the atmospheric forcing and the heat flux strongly contributes to the SST damping, as predicted by the theory of the stochastic climate models (Frankignoul, 1985). The antisymmetric form of the lagged-correlation function between the SST and heat flux anomalies, with maximum values attained when the heat flux anomalies lead the SST anomalies by one month, is characteristic of a negative feedback between both, i.e. the atmosphere circulation adjusts in a way that tends to oppose the SST anomalies. A positive feedback would have resulted in a more or less symmetric lagged-

correlation function with no zero-crossing and maximum values at zero lag (Frankignoul, 1985). These results are also valid for time series describing the evolution of spatial patterns, such as the leading principal components of the SST and heat flux fields.

Using these concepts one may look for the existence of feedback between the SST anomalies and the atmospheric circulation anomalies associated with each one of these two decadal modes. For this purpose, for each of them, the SST anomaly pattern with largest amplitude and the associated heat flux pattern have been projected onto the monthly mean anomalies to obtain the time series that describe their time evolution. Then, the lagged correlation function between the time series has been calculated. The lagged-correlation functions have the same sign at postive and negative lags, although the correlation diminishes much more rapidly when the heat flux lags the SST. This may indicate that although there is no clear positive feedback between SST and heat flux anomalies, the atmospheric adjustement to these particular SST anomaly patterns is such that, on the whole, the heat-flux remains neutral, in contrast to the behaviour of the leading spatial structures at monthly time scales, for instance EOFs. This is an important point since a strong negative feedback would be related to a short anomaly life-time and be incompatible with a decadal time scale.

REFERENCES

Cubasch U., K. Hasselmann, H. Hoeck, E. Maier-Reimer, and U. Mikolaewicz, 1992: Time dependent greenhouse warming computation with a coupled ocean-atmosphere model. Climate Dynamics 8, 55-69.

Delworth, T., S. Manabe, and R. Stouffer, 1993: Interdecadal variability of the thermohaline circulation in a coupled ocean-atmosphere model. J. Climate 6, 1993-2011.

Frankignoul, C., 1985: Sea surface temperature anomalies, planetary waves and air-sea feedback in the middle latitudes. Rev. of Geophys. 23, 357-390.

Gordon, A.L., and S.E. Zebiak, 1992: Climate variability and the Atlantic Ocean. EOS Transactions, 73, 161-165.

Kousky, V., and M.T. Kayano, 1994: Principal modes of outgoing longwave radiation and 250-mb circulation for the South American sector. J. Climate 7, 1131-1143.

Latif, M. and T.P. Barnett, 1994: Causes of decadal climate variability in the North Pacific/North American sector. Max-Planck-Institut für Meteorologie Report No. 141, Hamburg, Germany, 17 pp.

Robertson, A.W., 1995: Interdecadal variability over the North Pacific in a coupled ocean-atmosphere general circulation model. Submitted to Climate Dynamics.

Trenberth, K.E, and J. Hurrell, 1993: Decadal atmosphere-ocean variations in the Pacific. Climate Dynamics 9, 303-319.

Vautard, R., P. Yiou, and M. Ghil, 1992: Singular spectrum analysis: a toolkit for short noisy chaotic signals. Physica D58, 95-126.

von Storch, J., 1994: Interdecadal variability in a global coupled model. Tellus, 46A, 419.

Weare, B.C., and J.S. Nasstrom, 1982: Examples of extended empirical function analysis. Mon. Wea. Rev. 110,481-485.

ACKNOWLEDGEMENTS. The results of the coupled GCM integration were kindly made available to us by J. von Storch from the Max-Planck-Institut für Meteorologie, Hamburg.

CORRESPONDING AUTHOR

Eduardo Zorita
LODYC
4, Place Jussieu, tour 14
75005, Paris, France.

VARIABILITY IN "INDICATIONS OF SPRING": AN ANALYSIS OF SPECIES RESPONSE TO CLIMATE OVER TWO CENTURIES USING THE MARSHAM FAMILY DATA

T.H. Sparks & P.D. Carey

NERC Institute of Terrestrial Ecology, Monks Wood, UK.

ABSTRACT

This paper compares plant records from the unique Marsham family phenological records with Manley's Central England temperature data. Early spring temperatures had a considerable influence on the date on which a number of plants came into leaf or flowered. Over and above the temperature influences some species exhibited trends over time which could not be explained by the data in our possession. The relationships established with these historical data have been used to predict how global warming might change our perception of spring. We predict, for the species examined, that leafing will occur two to three weeks earlier.

1 INTRODUCTION

There is an increasing demand to predict the consequences of climate warming on native flora and fauna. Studies of the response of species to climate usually involve just a small run of years or are a "snapshot" based on a large number of sites with varying climate. The former case suffers from low replication and in the latter case apparent response may be confounded with factors such as geology, habitat and land-use. We believe that confidence in the predictions of species performance in a changed climate can be gained by studies of historical data.

2 DATA

The collection of phenological data has been a popular pastime for several centuries and from 1875 until 1948 the Royal Meteorological Society (RMS) collated and reported extensive observations from throughout the British Isles (Clarke, 1936). In 1926, a paper in the Quarterly Journal of the RMS (Margary, 1926) reported the rediscovery of a unique set of phenological records dating back to 1736 which had been kept by five generations of the same family. Records of the first dates of 27 indications of spring had been taken in the Marsham family estates, a few miles to the north of Norwich, UK. We have extended that data set to include all additional published data (1926-1947) to create a series of two centuries of data collected in the same locality in Norfolk. There are, inevitably, some gaps in the record, particularly from 1811-1834. Whilst we have access to other contemporary records which we believe could fill and extend this record, this work is not sufficiently advanced to report here. The originator of these indications of spring, Robert Marsham FRS (1708-1797), was a dedicated arboriculturalist; undertaking a range of tree experiments from an early age and recording growth of these trees throughout his lifetime. His contemporaries included Parson Woodforde (at nearby Weston Longville) and Gilbert White (with whom Marsham corresponded; Marsham & Bell, 1876).

For reasons of brevity only the 17 plant records (Table 1) are discussed here, further details appear in Sparks & Carey (1995).

Table 1. The 17 Plant Records, Numbers of Recorded Years, Mean Date of Record, and Extreme Dates.

Flowering Records			
Snowdrop	168	Jan 17	(Dec 14 - Mar 13)
Wood anemone	143	Mar 25	(Feb 13 - Apr 25)
Hawthorn	165	May 11	(Apr 15 - Jun 9)
Turnip	140	Apr 8	(Dec 25 - May 16)
Leafing Records			
Hawthorn	174	Mar 10	(Jan 19 - Apr 26)
Sycamore	164	Apr 2	(Jan 29 - May 4)
Birch	164	Apr 5	(Mar 2 - May 7)
Elm (common)	137	Apr 4	(Feb 9 - May 7)
Mountain ash	154	Apr 6	(Mar 5 - May 2)
Oak	167	Apr 24	(Mar 25 - May 20)
Beech	167	Apr 21	(Mar 15 - May 12)
Horse Chestnut	162	Apr 4	(Mar 3 - May 2)
Sweet Chestnut	144	Apr 19	(Mar 15 - May 18)
Hornbeam	149	Apr 8	(Feb 8 - May 7)
Ash	147	Apr 29	(Mar 27 - May 27)
Lime	156	Apr 13	(Mar 4 - May 12)
Maple	104	Apr 19	(Mar 12 - May 20)

In attempting to relate these data to contemporary climate data the choice is somewhat limited. To cover the length of the Marsham series, the Central England monthly temperature data of Manley

(1974) and the annual rainfall data of Craddock (1976) have been used. Manley's temperature data have been shown to correlate well with those of Edinburgh (Duncan, 1991) and we would expect a similar, or better, level of agreement with Norfolk temperatures.

3 ANALYSIS

Data were analysed using stepwise regression techniques, with 15 possible explanatory variables. These variables were the temperature data for each of the 12 months preceding mean collection date, rainfall of the recorded and preceding years and a year index (1=1700) to examine for unexplained trends over time. To retain parsimony, a 1% significance cut off was adopted when adding variables to the models. Data were examined for significant autocorrelation prior to analysis and the residuals from the regression models were similarly examined. A first order autoregressive term was included in the final regression models where appropriate.

4 RESULTS

Trends in time were apparent for many species both before and after eliminating temperature effects, for example results suggested that the wood anemone (Figure 1) was flowering earlier and the hornbeam (Figure 2) was leafing later. Negative correlations with early spring weather emphasised the strong relationship between climatic conditions and performance of natural flora, for example hawthorn (Figure 3) and mountain ash (Figure 4). Conversely, in the multiple regression models, autumn temperatures tended to be positively associated with appearance dates. However, autumn temperatures were less influential than spring temperatures. There was little evidence of rainfall effects, but this may be because of the crude nature of the available rainfall data. Models achieved satisfying levels of significance with R^2 terms between 26% and 73%.

These models gave us the opportunity to suggest how climate change might affect the observed species. Estimates based upon a typical climate change scenario (Houghton *et al.*, 1992): 3.5°C increase in December to February temperatures, 3°C increase in all other monthly temperatures and a 10% increase in precipitation, are given in Table 2. Species ranged in their response but trees were generally predicted to come into leaf two to three weeks earlier. These estimates are in accord with those from other studies (Margary, 1926; Fitter et al., 1995) and those of oak agree with results from temperature controlled experiments being undertaken at ITE Bangor (A. Buse, personal communication). These predictions may have to be tempered by the unexplained trends over time (Table 2). In the case of oak and beech the net effect will be exaggerated (by perhaps an additional three days over the next century), whilst the predictions may be reduced by three to seven days over a similar time scale for species such as birch and horse chestnut.

Table 2. The Predicted Effect of the Climate Change Detailed in the Text on the Appearance Dates of the 17 Plant Records, and Residual *per annum* Trends Unaccounted for by Temperature (. = no significant trend).

Flowering Records		
Snowdrop	-25	.
Wood anemone	-23	-0.064
Hawthorn	-20	.
Turnip	-24	+0.165
Leafing Records		
Hawthorn	-18	.
Sycamore	-21	.
Birch	-13	+0.074
Elm (common)	-21	+0.066
Mountain ash	-20	+0.032
Oak	-22	-0.032
Beech	-15	-0.029
Horse Chestnut	-13	+0.032
Sweet Chestnut	-19	.
Hornbeam	-18	+0.074
Ash	-20	.
Lime	-24	.
Maple	-15	.

4 DISCUSSION

Phenological data have received much criticism in the past. It is argued that the recording of first dates can be seriously influenced by a rogue event or individual. First date data are strictly left-censored; the actual date being no later than that recorded. This situation is likely to be more serious for fauna, when individuals may be present for several days before being observed or heard. However, first dates require relatively little effort to record, and, if their limitations are recognised, provide valuable information, especially if extensive in numbers of years or geographical location. Our analysis explored the former case.

We can not explain the reasons for trends in appearance dates after eliminating temperature effects. The use of more localised temperature and other weather data (e.g. from Norwich) would be more satisfactory, but this does not exist over the full time scale of the Marsham record. Examination of Manley's data suggests a tendency for warming of the winter months and it may be that the pattern

in Norfolk doesn't mirror the changes taking place in 'Central England'. There has certainly been environmental change in this corner of Norfolk with a greater emphasis on arable production and a reduction in lowland heath. Consequent changes to land drainage may have affected the performance of the examined species. All these remarks are conjecture; we would welcome the opportunity to establish the true causes.

If climate change brings forward the appearance of plant species then what are the implications? We, or rather our descendants, will perceive spring as occurring some two to three weeks earlier. We can not tell from the Marsham data whether the time distribution of leafing will remain stable, but earlier, or whether the leafing period will be extended at both ends of the growing season. Other data in our possession may be able to answer this question, but, at the current time, await analysis. Plants making an earlier appearance may be able to acquire a competitive advantage over other species. There is concern that vernal species (such as bluebell and wood anemone) that flower on woodland floors before the canopy trees leaf and exclude daylight may be affected by a disturbance of the *status quo*. However our predictions suggest that the wood anemone will make a sufficiently early appearance to match changes in canopy trees. Climate change may result in a greater photosynthetic period which may lead to greater seed production and increased growth if trees are not limited by other factors such as water availability. Any lengthened growing season could result in a change to the geographical distribution of our native plant species as formerly marginal areas become suitable for plant establishment.

What is apparent is that historic data sets such as the one described here can provide very useful information to help us suggest ways in which climate change may affect the distribution and nature of plant communities. A large amount of such data exists in published material and we believe an even larger quantity exists unpublished in the notebooks of dedicated naturalists throughout the UK. Perhaps the time is right to campaign for the reinstatement of a co-ordinated national phenological body?

References

Clarke, J.E. (1936). The history of British phenology. *Quarterly Journal of the Royal Meteorological Society*, **62**, 19-23.

Craddock, J.M. (1976). Annual rainfall in England since 1725. *Quarterly Journal of the Royal Meteorological Society*, **102**, 823-840.

Duncan, K. (1991). A comparison of the temperature records of Edinburgh and central England. *Weather*, **46**, 169-173.

Fitter, A.H., Fitter, R.S.R, Harris, I.T.B. & Williamson, M.H. (1995). Relationships between first flowering date and temperature in the flora of a locality in central England. *Functional Ecology*, **9**, 55-60.

Houghton, J.T., Callander, B.A. & Varney, S.K. (eds)(1992). *Climate Change 1992: the Supplementary Report to the IPCC Scientific Assessment*. Cambridge University Press, Cambridge, pp 1-22.

Margary, I.D. (1926). The Marsham phenological record in Norfolk, 1736-1925, and some others. *Quarterly Journal of the Royal Meteorological Society*, **52**, 27-54.

Marsham, H.P. & Bell, - (1876). The correspondence of Robert Marsham of Stratton-Strawless, in the County on Norfolk, Esquire and Fellow of the Royal Society; and The Reverend Gilbert White, of Selborne, in the County of Southampton, Master of Arts and Fellow of Oriel College in the University of Oxford. 1790-1793. *Transactions of the Norfolk and Norwich Naturalists' Society*, **2**, 133-195.

Manley, G. (1974). Central England temperatures: monthly means 1659 to 1973. *Quarterly Journal of the Royal Meteorological Society*, **100**, 389-405.

Sparks, T.H. & Carey, P.D. (1995). The responses of species to climate over two centuries: An analysis of the Marsham phenological record, 1736-1947. *Journal of Ecology*, **83**, 321-329.

ACKNOWLEDGEMENTS

We are indebted to the Marsham family for their enthusiasm and commitment to natural history through many generations. This work was supported by the NERC's TIGER (Terrestrial Initiative in Global Environment Research) programme.

CORRESPONDING AUTHOR

T H Sparks
ITE Monks Wood
Abbots Ripton
Huntingdon
Cambs PE17 2LS
UK

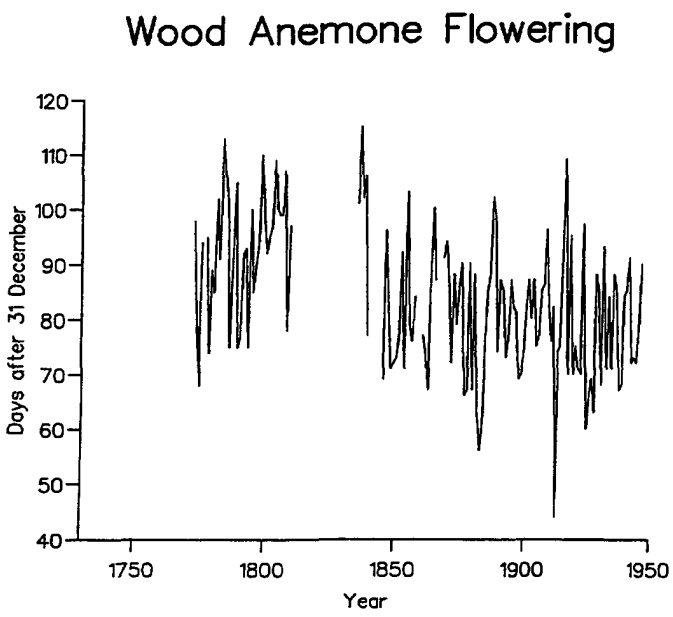


Figure 1

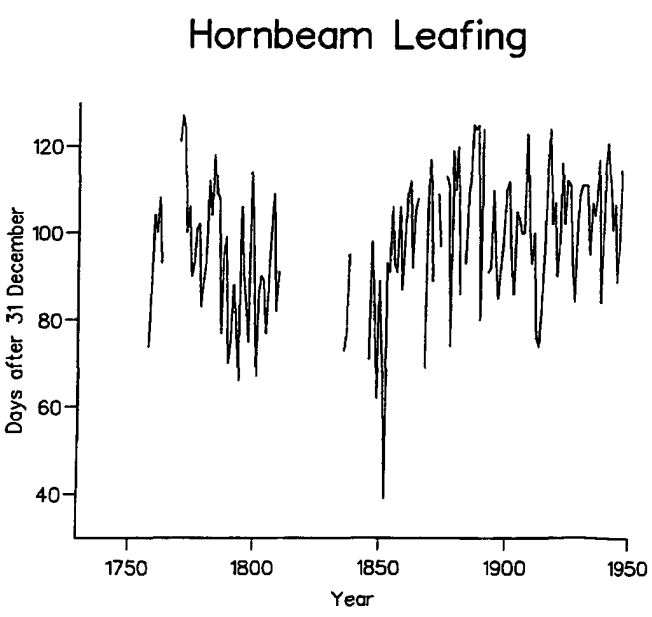


Figure 2

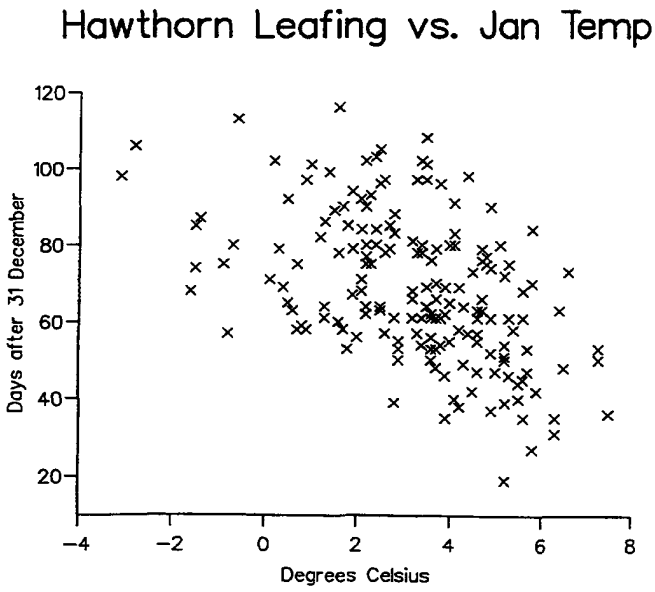


Figure 3

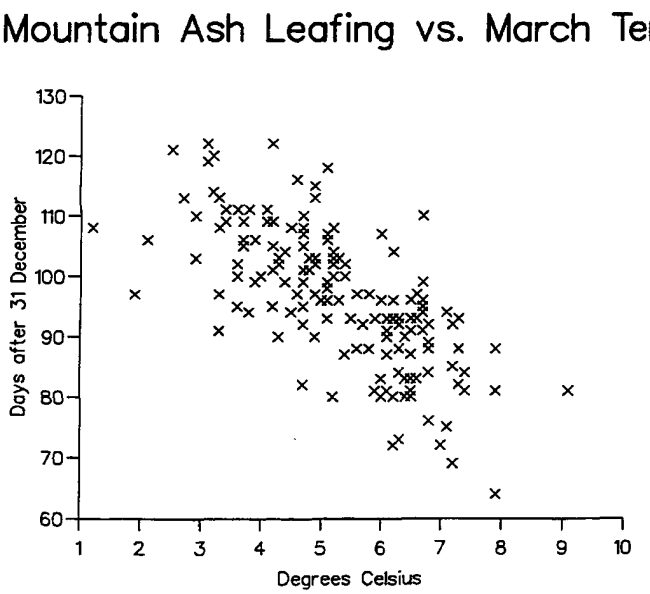


Figure 4

LOW FREQUENCY VARIATIONS OF POLAR SEA-ICE EXTENT IN THE NORTHWEST ATLANTIC REGION - PART I, STATISTICAL ASPECTS

P. Frich

Danish Meteorological Institute, Copenhagen, Denmark

ABSTRACT

A new index of sea-ice extent has recently been extracted from the archives of the Danish Meteorological Institute. The extent of Polar sea-ice Northwest of Kap Farvel has been determined for each summer since 1820. The 175 year long record is compared with the Icelandic Ice Severity index, and the two series seem to complement each other. It was not possible to correlate the new sea-ice index with selected atmospheric variables, which indicate that the index may represent the variability of the ocean circulation in the north-western parts of the North Atlantic Ocean.

INTRODUCTION

"Storis" is the Danish expression for polar sea-ice which originates in the polar basin. This multi-annual pack-ice forms in the Arctic Ocean and neighbouring seas. It is transported southwards by the East Greenland Current in a characteristic annual pulsation. The polar sea-ice normally reaches Kap Farvel around New Year and during spring the ice advances north-westwards following the West Greenland Current. The maximum extent of Storis (heavy Polar sea-ice) off West Greenland is normally reached during early summer.

Based on a vast number of ice observations from ships and shore stations (e.g. Speerschneider, 1931), later on supplied with flight reconnaissance and satellite observations, the maximum extent of polar sea-ice off West Greenland has been determined for each summer since 1820. The methods of deriving this series has been described in Fabricius et al. (in press). The resultant time series shows large inter-annual fluctuations as well as multi-annual to centennial variations.

Another time series, the so-called "Icelandic Ice Severity index", is also analysed with respect to low frequency variations. This index, as first described by Thoroddsen (1884), and later modified by Koch (1945), was treated by Lamb and Mörth (1978) and Kelly et al., (1987) and fairly convincing statistical relations with various circulation parameters were presented. The Iceland Ice-severity index is presently being revised, and recent updates have been published by Ogilvie (1984 and 1992).

The presence of Polar sea-ice has a major impact on the temperature and other weather conditions on shore. Normally, the Polar sea-ice is accompanied by cold waters and the frequency of fog is closely related to cold water and the stabilising influence of Storis. In years of heavy sea-ice off the coast, the coastal stations have lower spring and summer temperature than stations which escape the cooling effect of icy waters.

The Polar sea-ice indices are valuable indicators of many atmospheric and oceanographic processes, which are active in the north-western part of the North Atlantic Ocean. During the last few years a number of studies have shown that sea-ice-, salinity- and sea surface temperature anomalies in the Northwest Atlantic area may hold the key to many coupled atmospheric and oceanographic processes. In particular, the low frequency variations have attracted considerable interest from a wide range of research groups recently. A wide number of both empirical and modelling studies have all helped to throw new light on the complicated processes taking place in the waters and air masses around the Greenland Sea.

The two Polar sea-ice indices have one thing in common, which is that they hardly show up in any of the existing grid sea-ice datasets. Another aspect is of course that they represent a marginal feature of the Polar sea-ice system. In this respect they are interesting in a discussion of climatic change.

RESULTS

The place names cited in the text and figures are shown in fig. 1. The main results are shown in figures 2-5. It was decided to keep the original code numbers referring to each place name along the West coast of Greenland. Further details are given in Fabricius et al. (in press) and Frydendahl et al. (in prep.)

The extent of Storis exhibits both long-term and short-term variations with an absolute maximum around the turn of the century and minima around the middle of the centuries. In 1896 and 1898, the Polar sea-ice reached far north of its normal position. During August 1898 a thin patch of Storis even reached as far north as Aasiaat/Egedesminde (89). During no single one of these 175 years, have all of the months from May to August been ice-free. Amongst the 4 summer months, August is the month with the highest frequency of completely ice-free waters off the west coast of Greenland.

The same stability is not always present in the Icelandic Ice Severity index, which occasionally contains several consecutive years without ice anywhere near Iceland. This instability hampers a rigorous statistical analysis of the coherence between this index and the Storis-index. Figure 3 shows the Iceland Ice Severity index over the period 1820 to 1985.

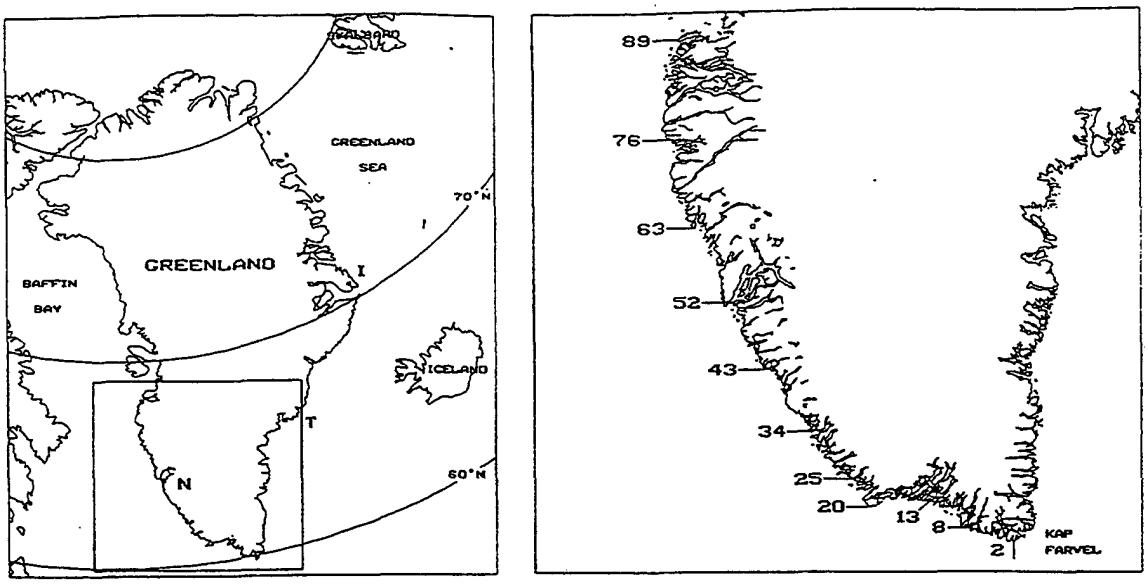


Figure 1 Map with place names cited in text and numerical representation of northernmost position of Storis. Letters N (Nuuk/Godthåb), I (Ittoqortomiit/ Scoresbysund and T (Tasiilaq/Ammassalik).

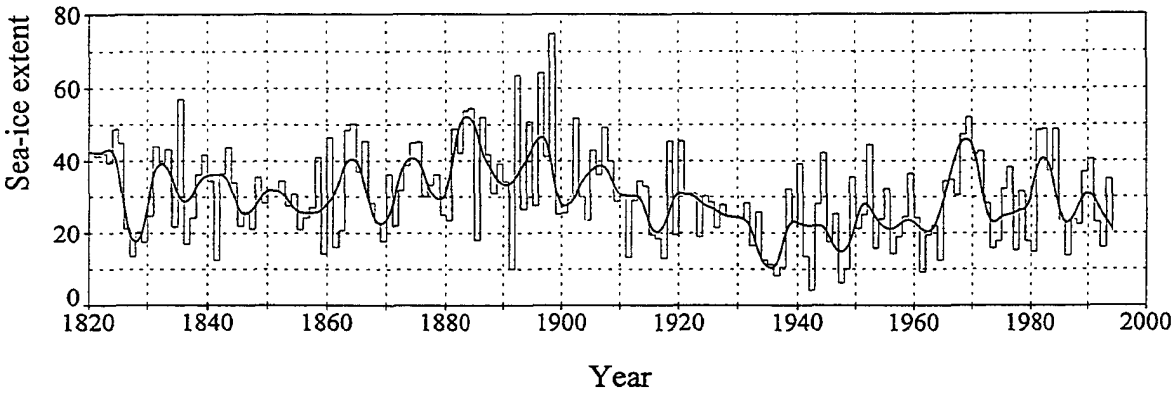


Figure 2 Storis extent NW of Kap Farvel 1820-1994. Code numbers refer to fig. 1. The thin line is mean extent during summer (May, June, July and August). The thick line represents the T4253H smoothing, as defined by Velleman and Hoaglin (1988).

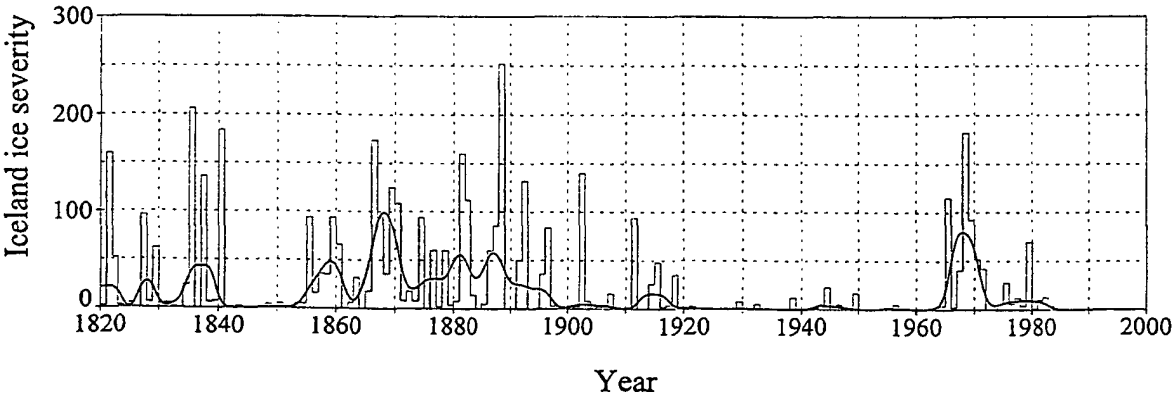


Figure 3 The Icelandic Ice Severity index, which is the number of weeks with Polar sea-ice near Iceland multiplied by the number of areas. The values have been read from figures 115 and 116 in Koch (1945). Updates since 1940 were kindly provided by Trausti Jónsson, Vedurstofan Islands.

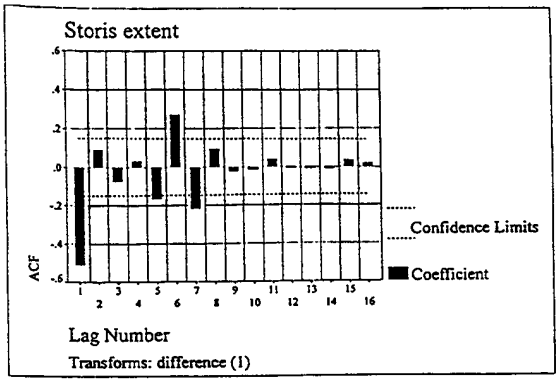


Figure 4 Auto correlation function (ACF) of Storis extent NW of Kap Farvel (after Frydendahl et al., in prep.).

The auto correlation function of summer (MJJA) mean values have been plotted in fig. 4. About 50 percent of the detrended variance in the series is explained by the negative lag 1 auto correlation. This means, that the mean Storis extent of the present year, in 50 percent of the cases will explain the mean extent during next year. The other significant lag is related to the 6 year periodicity.

The spectral density plot is another way of illustrating the lower frequency variations in Storis extent, as shown in fig. 5.

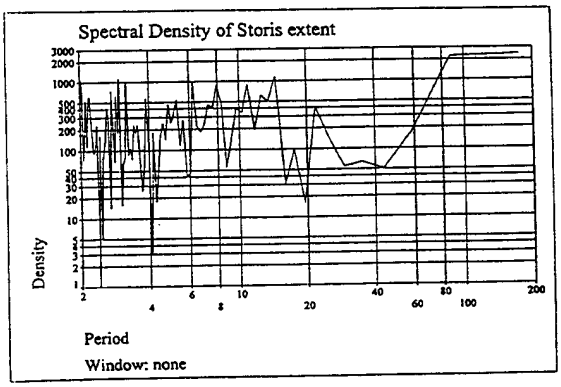


Figure 5 The spectral density of Storis extent NW of Kap Farvel over the period 1820 to 1994. (After Frydendahl et al., in prep.)

It was the attempt of this study to link the Storis index with selected atmospheric variables. This exercise has however been without positive results. Seasonal and annual mean pressure differences between Tasiilak/Ammassalik on the East coast of Greenland and Stykkisholmur in Iceland did not reveal any statistical significant coherence with the various sea-ice indices. Neither did the pressure series analysed alone give any indication that the wind conditions in Denmark Strait was responsible for the low frequency variations in sea-ice extent along the SW coast of Greenland.

DISCUSSION

In a study similar to the present one, Hill and Jones (1990) extracted a time series of ice extent off Newfoundland from the period 1860 to 1988. Several statistical significant correlation patterns were established, but the time series had to be divided in order to reach statistical significant results.

Sear (1988) made a summary table of observed low frequency variations in various polar sea-ice indices. The most conspicuous cycle was related to a quasi 3 year signal in many of the analysed sea-ice indices. He also noted a significant out of phase relationship between sea-ice extent in the Barents Sea and southern Greenland Sea. Gloersen (1995) detected a 4 year so-called El Ninó/ Southern Oscillation (ENSO) signal in several sea-ice series from the Northern North Atlantic. This study was however hampered by the short length of the satellite series (9 years). Using a Discrete Fourier Transform technique, Mysak et al. (1990) discovered a 5 year cycle in gridded sea-ice data from the Greenland and Labrador sea areas.

The fairly robust auto correlation patterns found in this study, centred around 6 years, may indicate an oscillation in the coupled ocean-atmosphere system of the same periodicity. The 6 year periodicity is however not present in all sub-periods of the most recent 175 years, so despite the statistical significance, it can only be concluded, that the sea-ice series from Iceland and south-western Greenland contains primarily some long-term variability (80-90 years) and some higher frequency oscillations which are linked to either some kind of internal variability in the ocean, or a kind of feedback system involving both the ocean and the atmosphere.

Previous studies have indicated that there might be a connection between the 9-17 year solar cycles and the extent of Polar sea-ice. By applying a 3 year moving average, Vibe (1967) argued that there was an apparent 10-12 year periodicity in the Storis series he used. Similar conclusions were reached by applying a 5 year weighted moving average to the Newfoundland Ice extent series (Hill and Jones, 1992).

It is interesting to note, that the 6 year periodicity is flanked by negative auto correlations at lag 5 and 7, which is in line with the highly significant lag 1 auto correlation. The use of any kind of moving average will remove the 6 year cycle from the plotted data. Applying more complicated filters like the T4253H smoothing (Velleman and Hoaglin, 1981) will do the same, so we may conclude that the apparent 10-12 year periodicity in many of the sea-ice series is an artefact, which is due the use of a filter with a band with of 2-6 year.

As long as the physical mechanism behind the 6 year cycle is poorly known, it is advisable to include also other oceanographic and atmospheric variables in any seasonal forecasting efforts. It is encouraging that Hurrell and van Loon (1994) have recently observed a similar periodicity in the so-called North Atlantic Oscillation index (NAO). If the low frequency variations in sea-ice extent to some extent reflects or controls the atmospheric circulation over the North Atlantic ocean, we may have discovered a mechanism which can explain some of the long-term changes in the climate system. The results of Rogers (1985) and Schlesinger and Ramankutty (1994) both point to the important role played by long-term changes in the North Atlantic Ocean with respect to the Global Climate.

The new index of Polar sea-ice extent off Southwest Greenland can be used for a number of studies concerned with changes in sea currents, including salinity anomalies. Future studies will also include a more thorough analysis of the coherence between the Polar sea-ice extent and the local climate around the coasts of Greenland.

REFERENCES

Chapman, W.L., W.J. Welch, K.P. Bowman, J. Sacks and J.E. Walsh, 1994: Arctic sea-ice variability: Model sensitivities and a multidecadal simulation. *J. Geophys. Res.*, 99, C1, 919-935.

D'Arrigo, R.D., E.R. Cook, G.C. Jacoby and K.R. Briffa, 1993: NAO and sea surface temperature signatures in tree-ring records from the North Atlantic sector. *Quaternary Science Reviews*, 12, 431-440.

Delworth, T., S. Manabe and R.J. Stouffer, 1993: Interdecadal variations of the thermohaline circulation in a coupled ocean-atmosphere model. *J. Climate*, 6, 1993-2011.

Fabricius, J.F., K. Frydendahl and P. Frich, (in press): Polar Sea Ice off West Greenland - A Review. *Proceedings of the 14th International Offshore Mechanics and Arctic Engineering Conference*, (ASME Paper No. OMAE-95-227) Copenhagen Denmark, June 18-22, 1995. 7 pp.

Frydendahl, K., J.S. Fabricius and P. Frich, (in prep.): Polar sea-ice variations off West Greenland 1820-1994. *DMI Scientific Report 95-xx*. The Danish Meteorological Institute, Copenhagen, Denmark.

Gloersen, P., 1995: Modulation of hemispheric sea-ice cover by ENSO events. *Nature*, 373, 503-506.

Hill, B.T. and S.J. Jones, 1990: The Newfoundland ice extent and the solar cycle from 1860 to 1988. *J. Geophys. Res.*, 95, C4, 5385-5394.

Hurrell, J.W. and H. van Loon, 1994: Analysis of low-frequency climate variations over the North Atlantic using historical atmospheric data. *Climate Diagnostics*, 6 pp.

Kelly, P.M., C.M. Goodess, and B.S.G. Cherry, 1987: The interpretation of the Icelandic sea ice record. *J. Geophys. Res.*, 92, C10, 10,835-10,843.

Koch, L., 1945: The East Greenland ice. *Meddelelser om Grønland*, 130 (3), 1-375.

Lamb, H.H. and H.T. Mörth, 1978: Arctic ice, atmospheric circulation and world climate. *Geogr. J.*, 144, 1-22.

Mysak, L.A., D.K. Manak and R.F. Marsden, 1990: Sea-ice anomalies observed in the Greenland and Labrador seas during 1901-1984 and their relation to an interdecadal Arctic climate cycle. *Climate Dynamics*, 5, 111-133.

Mysak, L.A. and S.B. Power, 1992: Sea-ice anomalies in the western Arctic and Greenland-Iceland Sea and their relation to an interdecadal climate cycle. *Climatological Bulletin* 26(3), 147-176.

Ogilvie, A.J.E., 1984: The past climate and sea-ice record from Iceland, Part 1: data to A.D. 1780. *Climatic Change*, 6, 131-152.

Ogilvie, A.J.E., 1992: Documentary evidence for changes in the climate of Iceland, A.D. 1500 to 1800. Page 92-117 in Bradley, R.S. and P.D. Jones (eds): *Climate since A.D. 1500*. Routledge, London and New York.

Rogers, J.C., 1985: Atmospheric circulation changes associated with the warming over the northern north Atlantic in the 1920s. *J. Clim. Appl. Meteor.*, 24, 1303-1310.

Schlesinger, M.E. and N. Ramankutty, 1994: An oscillation in the global climate system of period 65-70 years. *Nature*, 367, 723-726.

Sear, C.B., 1988: An index of sea ice variations in the Nordic seas. *J. Climatology*, 8, 339-355.

Speerschneider, C.I.H., 1931: The state of the ice in Davis Strait. *Medd., Danish Meteorol. Inst.*, 8, 1-53 Copenhagen.

Thoroddsen,Th., 1884: Den grönlandske drivisen vid Island (The Greenlandic drift ice at Iceland). *Ymer*, 145-160.

Velleman, P.F. and D.C. Hoaglin, 1981: *Applications, basics and computing of exploratory data analysis*. Boston: Duxbury Press.

Vibe, C., 1967: Arctic animals in relation to climatic fluctuations. *Meddelelser om Grønland*, 170, 5, 1-227.

ACKNOWLEDGMENTS

This study was supported through the project: North Atlantic Climatological Dataset (NACD) by the Nordic Council of Ministers (FS/ULF 93-001) and the European Commission (EV5V CT93-0277). The financial contribution from these institutions is appreciated. I also thank my good colleague, Trausti Jónsson, from Vedurstofan Islands, for providing updates of the Icelandic Ice Severity index.

CORRESPONDING AUTHOR

Povl Frich
Danish Meteorological Institute
Lyngbyvej 100, DK-2100 Copenhagen Ø

NON-LINEAR EFFECTS IN THE INTERANNUAL VARIABILITY OF AIR TEMPERATURE OVER THE NORTHERN HEMISPHERE

G.V. Alekseev , P.N. Svyashchennikov

The Arctic and Antarctic Research Institute, St. Petersburg, Russia

ABSTRACT

A dependence of second moments of the field of mean monthly air temperature in the Northern Hemisphere on an averaging of initial data is investigated. It has been found out that with an increase of a spatial averaging the variability of mean values diminishes more slowly, than as it follows from the central limit theorem. Between spatial mean temperature values and mean deviation squares there is a strong negative correlation for the winter month. One of the causes of the observed features of temperature field statistics is a non-linear character of the dependence both between the outgoing long-wave radiation and the temperature, which increases the heat losses from the atmosphere at a greater spatial non-uniformity of the temperature field.

INTRODUCTION

The statistical studies of the climate variability widely employ the methods of mathematical statistics and the theory of random stationary processes. However, the climatic system of the Earth differs from the ideal models of the corresponding mathematical theories. So, estimates of the climate characteristics by the observation data do not wholly correspond to model idea of the nature of the stochastic variability. The main reasons for this disagreement are related to the nonclosedness of climatic system or some of its parts and to the effect of the internal interactions in the system on the climate variability. Examples of such disparity for the variability estimates of the temperature climate characteristics and their possible causes are considered below.

DATA AND METHODS

Data on mean monthly air temperature near the Earth's surface in the Northern Hemisphere for 1891-1993 were used. They are represented by gridded values every 10 degrees of longitude and 5 degrees of latitude. There were calculated: spatial mean temperature values at latitudinal circles and in different latitudinal zones; mean square deviations (MSD) for the temperature changes in each grid point, for the changes in spatial means; characteristics of a spatial nonhomogenity of the temperature fields in the form of mean squares of deviations from corresponding spatial means. The mean square deviations at different averaged initial data and correlations between the fluctuations of the means and mean square deviations from them were estimated.

RESULTS

The comparisons of the estimates of mean square deviations (MSD) of temperature calculated at separate points of the latitudinal circle and MSD of mean latitudinal temperature for January and July show (Table I) that in high and midlatitudes the MSD excess over mean zonal temperature values in January relatively July is greater than a similar excess for the point estimates. At latitudes south of 35 N a winter increase in the variability of temperature values at points exceeds an increase in the variability of mean latitudinal values.

The calculations of an equivalent number of independent observations $n_e = (\langle\sigma\rangle / \sigma_{\langle T\rangle})^2$, where $\langle\sigma\rangle$ - mean value of MSD at the points of the latitudinal circle $\sigma_{\langle T\rangle}$ - the MSD value for mean zonal temperature at a given latitude (Table 2), present lower

Table 1

MSD ratios in January and July calculated for temperature values at each point of the latitudinal circle *) (1) and for its mean latitudinal values (2).

	NORTHERN LATITUDE											
	80	75	70	65	60	55	50	45	40	35	30	25
(1)	3.15	2.51	2.20	2.88	2.85	2.49	2.02	1.75	1.50	1.30	1.28	1.24
(2)	3.14	2.67	2.94	3.07	3.17	3.46	3.76	2.34	2.03	1.44	0.93	0.85

*) the MSD values are averaged over the latitudinal circle.

Table 2

Estimates of an equivalent number of independent values (n_e)for mean latitudinal values of surface air temperature

	NORTHERN LATITUDE											
	80	75	70	65	60	55	50	45	40	35	30	25
January-February	2.62	4.15	5.05	5.65	6.45	6.85	5.64	6.56	7.78	7.00	10.78	10.60
July-August	2.66	5.41	9.60	7.98	10.78	12.71	12.56	10.52	11.06	7.09	4.66	4.46

effectiveness of spatial averaging of January temperatures as compared with July in high and midlatitudes. In lower latitudes this ratio is opposite .

The variability of mean air temperature at increased averaging area decreases, however, its MSD decreases slower, than the MSD estimates of the means obtained under the assumption that fluctuations of mean latitudinal temperature values are random and independent (Table 3).

Significant interannual fluctuations of mean temperature of different latitudinal zones in the colder half of a year are negatively correlated with the characteristics of a spatial inhomogeneity of the temperature fields (Table 4). And the correlation increases with an increase in the spatial averaging area. Here D_φ - mean square deviation of mean zonal temperatures from a mean value over the whole of the area. D_λ - MSD of temperature values at the points of the latitudinal circle from its mean zonal value averaged for the entire area, $D = (D_\varphi^2 + D_\lambda^2)^{1/2}$ The correlation also increases with the increasing deviations in mean temperature of the areas under consideration from their mean multiyear values.

DISCUSSION

It is seen that the statistics under consideration have a significant spatial and seasonal non-uniformity which contradicts the hypothesis of the sampling variability (Leung and North, 1991). The main causes for a winter increase in the variability of spatial mean values of mean monthly temperature and their correlations with spatial inhomogeneity of its fields are related to the variations in heat influxes from the ocean in winter due to the atmospheric circulation fluctuations, to an increase in spatial scales and amplitudes of atmospheric disturbances during the colder half of the year and to advective-radiation fluctuations of mean air temperature (Alekseev, Podgorny, 1991; Alekseev, 1994).

An approximate estimate of mean air temperature deviation at an increase or a decrease in atmospheric circulation in winter is equal to

$$\langle T \rangle_a' = a'(T_0 - T_k)(1-\beta)$$

where a'-an increase (decrease) of advective transfer normalized to the atmospheric volume; T_0, T_k - air temperature over the ocean and the continent; β - a ratio of integral heat capacities of the atmosphere and the upper ocean layer. A close relation between the winter anomalies in mean air temperature and circulation fluctuations is confirmed by the comparisons of a spatial distribution of anomalies of mean January temperature for the January months with positive and negative anomalies of mean air temperature near the surface. During warm Januaries over the Northern Hemisphere the positive temperature anomalies are located in the climatic centers of cold and negative one - in centers of heat. For cold Januaries the situation is reverse. The west-eastern transport in the atmosphere of high and midlatitudes is enhanced at positive mean temperature anomalies and at negative - attenuated.

The estimates of the correlation radius of mean monthly air temperature fields in temperate latitudes for January and July indicate (Gruza, Reitenbah., 1982) the excess of January values by 1.3 times on the average. According to Table 2, such ratio is estimated to be within 1.6-2.2, thus, also confirming the presence of other components in the mean temperature variability, than sampling variability.

The third component in the variability of mean temperature is related to a non-linear temperature dependency of outgoing longwave radiation. Due to this dependency at the changes in advective heat transfer between the "warm" and "cold" parts, an advective-radiation change in mean temperature occurs in the climatic system that is approximately equal to $\langle T \rangle_r' = \frac{a'}{2}\left[b_2^{-1} - b_1^{-1}\right]$, where $b_1 = 4\delta T_1^3, b_2 = 4\delta T_2^3, \delta$ - the integral longwave atmospheric transparency, T_1, T_2 -mean temperatures of the "warm" and "cold" parts. Since $T_1 > T_2$, $b_2 > b_1$

Table 3

Estimates of MSD of mean January temperature in different latitudinal zones of the Northern Hemisphere (1) and MSD calculated by assuming the fluctuations of mean latitudinal temperatures to be random and independent (2)

Estimate of MSD	AVERAGING AREA FROM 90 N UP TO						
	75 N	65 N	55 N	45 N	35 N	25 N	15 N
(1)	1.93	1.39	1.10	0.87	0.63	0.48	0.40
(2)	1.45	0.65	0.42	0.26	0.15	0.09	0.06

Table 4

Correlation coefficients between the characteristics of spatial non-uniformity (D) and spatial mean values of mean monthly air temperature fields in the region 85-25 N.

	MONTHS											
	1	2	3	4	5	6	7	8	9	10	11	12
D_φ	-0.58	-0.46	-0.55	-0.69	-0.49	-0.27	-0.12	-0.21	-0.32	-0.68	-0.58	-0.57
D_λ	-0.53	-0.59	-0.44	-0.12	-0.12	0.06	-0.05	0.04	0.09	-0.32	-0.40	-0.52
D	-0.70	-0.57	-0.63	-0.67	-0.49	-0.22	-0.11	-0.21	-0.29	-0.70	-0.65	-0.71

,then the sign depends on the sign of the deviation of the advective heat influx (a') from the "warm" to the "colder" area of the atmosphere. The temperature contrasts in high and temperate latitudes are large in winter. That is why, the contribution of $\langle T \rangle'_r$ to the mean temperature variability can be noticeable in this season.

CONCLUSIONS

1. An increase in the variability of mean latitudinal and mean values of mean monthly temperature by latitudinal zones in winter for high and midlatitudes of the Northern Hemisphere exceeds an increase in the sampling variability of the corresponding statistics.

2. Estimates of an equivalent number of independent values show a large increase in the correlation radius in the fields of mean monthly temperature in winter, as compared with the estimates on the basis of observation data.

3. Strong negative correlations between the fluctuations of mean temperature of high and midlatitudes and the characteristics of spatial inhomogeneities of the temperature fields in winter are observed.

4. At latitudes south of 35 N there is a summer increase in the variability of mean latitudinal values, while the variability of values at some points remains to be larger in winter.

5. The variability in mean temperature at an increase in the averaging area decreases slower than according to the hypothesis of the sampling variability of mean values.

6. The causes for the deviations in the obtained estimates of the variability and correlations for spatial mean monthly temperature values from the hypothesis of sampling fluctuations are related to the contributions from the additional variability sources of the means, such as the changes in the intensity of winter heat fluxes from the ocean to the atmosphere and advective-radiation fluctuations of mean temperature due to the changes in winter temperature contrasts in high and midlatitudes.

ACKNOWLEDGEMENTS

The research described in this publication was made possible on part by Grant N NSF300 from International Science Foundation and Russian Government.

REFERENCES

1. Alekseev G.V., 1994, "The influence of Polar Oceans on Interannual climate variations". In: O.M. Johannessen, R.D. Mucnch,J.E. Overland (Editors), "The Polar oceans and their role in shaping of global environment. Geophysical Monograph, 85, p.327-336.

2. Alekseev G.V., Podgorny I.A., 1991 "Advective-radiation fluctuations of the climate in the atmosphere- land- ocean system", Izv. Acad. Sci. USSR, Physics of the atmosphere and ocean, vol.37, p.1120-1130.

3. Gruza G.V., Reitenbah R.G., 1982, "Statistic and analysis of the hydrometeorological data" (in Russian), Gidrometeoizdat,Leningrad, 216 p.

4. Leung L.Y. and North G.R., 1991, "Atmospherics variability on a Zonally symmetric land Planet, Journ. of Climate, N 4, pp.753-765.

CORRESPONDING AUTHOR

Dr. G.V.Alekseev.
Arctic and Antarctic Research Institute,
St.-Petersburg, RUSSIA.

A Multivariate Statistical Method for Comparison of Low Frequency Modes of Variability in NMC Analyses to Those Generated from the ECHAM2 GCM

Michael B. Richman
School of Meteorology and
Cooperative Institute for Mesoscale Meteorological Studies
Norman, OK 73019-0626

I. Introduction

In recent years, global climate models (GCMs) have become the preferred tool for controlled analysis of climate variability. A prerequisite for the successful application of GCMs in this setting is the determination of the accuracy of the model in replicating the observed climate. In the present analysis, one such GCM, the European Center-Hamburg (ECHAM) model developed by the Max Planck Institut für Meteorologie, will be examined for the validity of its low frequency variability.

II. Data and Methodology

Observed geopotential height data for 700 and 200 hPa were obtained from the NCAR NMC gridpoint data set. These twice daily data were drawn for 1970-1988 for 3954 gridpoints on the NMC octagonal grid (1977 points per level). Missing and bad data were temporally interpolated. Seasonality was removed by subtracting the daily mean value from each 12 hour observation. A Lanczos low pass filter with 121 weights was applied to eliminate high frequency variability of <7 days. The data were then separated into 4 seasonal sets corresponding to traditional meteorological seasons. Model data were first interpolated onto the NMC octagonal grid and processed identically to the observed data.

Multivariate analysis of the observed and ECHAM2 model data included an eigenanalysis of the observed data to isolate the low frequency variability. The leading 15 winter (14 summer) modes were retained as signal explaining 61.4% of the total geopotential variance (47.1% summer). Orthogonally rotated principal components (RPC) were used to isolate modes of variability and also served as the targeted values to be searched for in the ECHAM2 model subspace (Fig. 1). The technique used to match the observations to the model was orthogonal Procrustes Target Analysis (PTA). It involved minimizing the trace of the discrepancies between the model and observational PC subspaces under the constraint of orthogonality. Full derivation of the technique is given in Richman (1994).

III. Results

Only a single result will be shown in detail. A complete summary of the effects of applying PTA to the subspace spanned by the ECHAM model as well as full results are shown in Richman (1994).

North Atlantic Oscillation (NAO) [Summer]

This mode of observed variability in the NMC data (Fig. 2a) was characterized at 700 hPa by a ridge over Greenland and a zonally extensive trough from the East Coast of the United States eastward to northern Europe. This had a nearly perfect match to Barnston and Livezey (1987) NAO mode for June, July, and August. The 200 hPa counterpart (Fig. 2e) showed some baroclinic tilt with increasing height. The magnitude of the Varimax rotated PC loadings did not decrease with height substantially, suggesting that the mode was well established in both the lower and upper troposphere. When the Varimax rotated PC analysis was applied directly to the output of the ECHAM2 GCM, the closest matching mode had a correlation (congruence) coefficient of 0.51 (0.50) for a shared variance of 26 percent. Such a low value manifested itself in a pattern illustrating little correspondence to the NAO at 700 hPa (Fig. 2b) or at 200 hPa (Fig. 2f). The model pattern shifted the ridge over northwestern Canada. When PTA was applied, the match between the observations and model increased to a correlation (congruence) of 0.72 (0.71) for a variance overlap of 51.8 percent. This is close to a doubling from the Varimax model results and suggests that a NAO-like mode was buried in the model subspace and Varimax could not uncover it. The 700 hPa portion of the mode (Fig. 2c) depicts a strong ridge over Baffin Bay and a trough over the Atlantic from the United States coastline across most of the central North Atlantic Ocean. The European center was not as strong as the observed mode. The discrepancy fields (Fig. 2d and 2h) highlight the difference over Europe.

The time series for the NAO mode for the observed data (Fig. 3a) indicated an upward trend with time. Neither the interannual variability of the Varimax rotated mode (Fig. 3b) or the PTA model mode (Fig. 3c) had much in common. The intraseasonal variability, of the observed data, as depicted by spectral analysis of each year (averaged over the 19 summers) showed spectral peaks at 18 and 22 days with a secondary one at 45 days for the observed data (Fig. 3d). The Varimax rotated PC model data spectra had a small peak at 9.5 days and at large one at 22 to 30 days (Fig. 3e). Correlations of these spectra from 7 to 90 days yielded a value of 0.67. The PTA model spectra has a 10 day peak and a 22-30 day peak (Fig. 3f). The model-observation spectral correlation increased only slightly to 0.73 after PTA was applied. Hence, the spatial match improved dramatically whereas the temporal matches improved only slightly.

IV. *Summary*

The advantages of application of PTA to model data with the observed modes serving as the target can be seen in the example provided. For all summer and winter modes, the percent variance overlap between observation and ECHAM2 model modes without and with PTA. The mean match over all RPC's retained comparing matched Varimax RPCs was 41% (winter) and 23% (summer), which increased to 60.8% (winter) and 41% (summer), after application of PTA. These values suggest that the PTA technique has versatility and utility in uncovering modes of variability embedded within the model subspace. It also suggests that the ECHAM2 model performs quite admirably in isolating similar low frequency modes to those observed (Table I).

Acknowledgments: ECHAM2 model data were kindly provided by Dr. Hans von Storch of Max Planck Institut für Meteorologie. This work was performed as a portion of the author's Ph.D. thesis. Computational support was provided by the National Center for Supercomputing applications CRAY Y-MP and CM-5 as well as the CRAY C-90 at Pittsburgh Supercomputing Center. The research was partially supported by NSF Grant ATM 92-96119 and U.S.E.P.A. Cooperative Agreement CR 819646-01-0.

References

Barnston, A.G. and R.E. Livezey, 1987: Classification, seasonality and persistence of low frequency atmospheric circulation patterns. *Mon. Wea. Rev., 115,* 1083-1126.

Richman, M.B., 1994: On the use of multivariate statistics to validate global climate models. Unpublished Ph.D. thesis, University of Illinois, 321 pp.

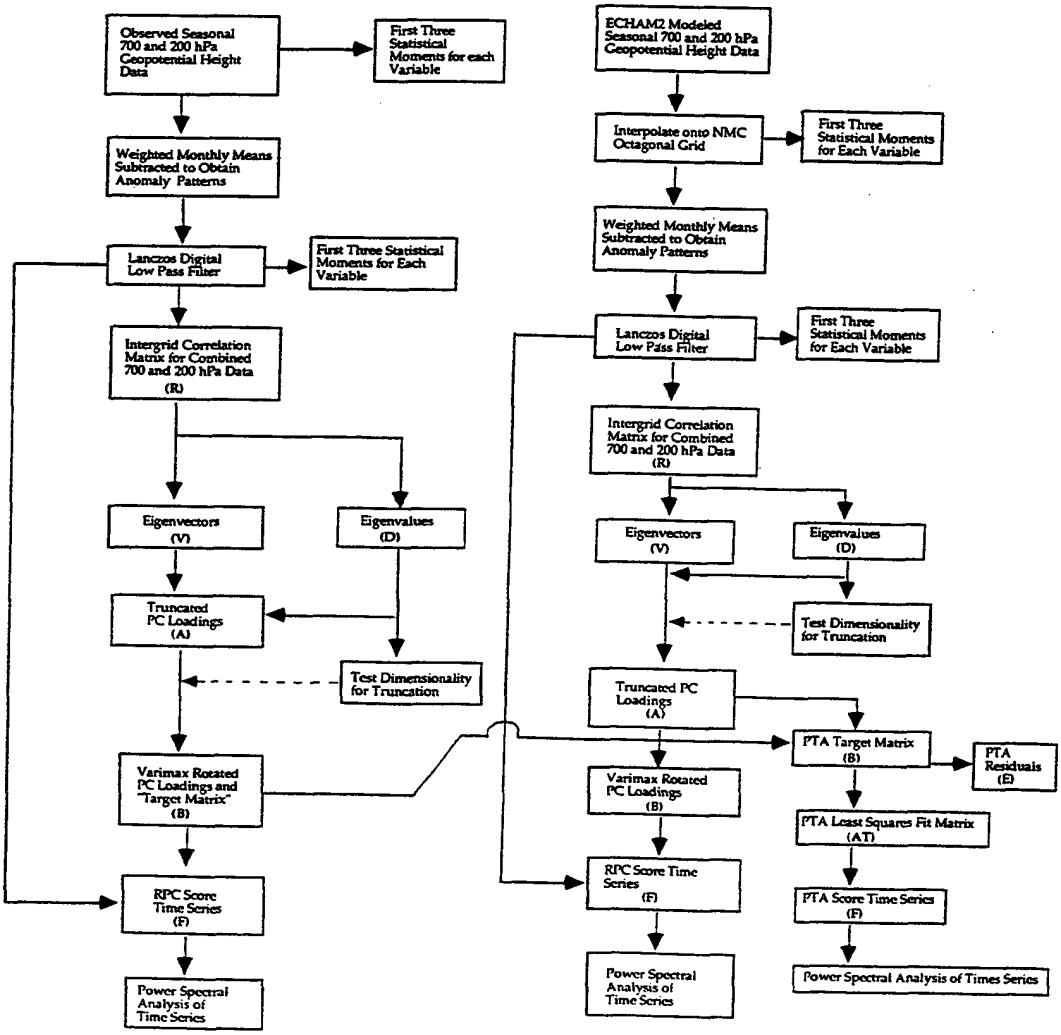


Fig. 1: Schematic flowchart of univariate and multivariate analyses.

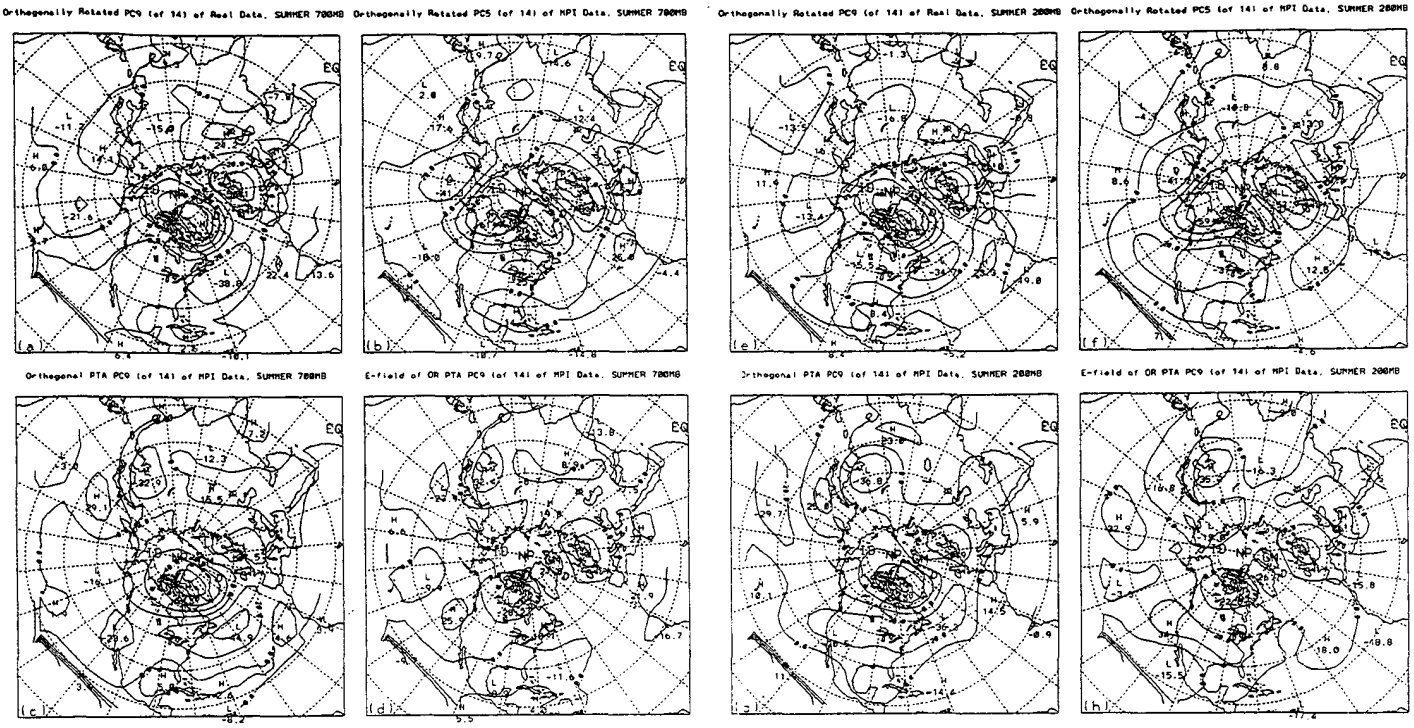


Fig. 2: Summer eigenanalysis for North Atlantic Oscillation mode of hybrid 700/200 hPa geopotential height. Panel a is the 700 hPa Varimax observations RPC loadings ("B"), panel b is the 700 hPa Varimax ECHAM2 RPC loadings, panel C is the 700 hPa PTA fit matrix coefficients ("AT"), and panel d 700 hPa is the discrepancies ("E"). Panels e-h are the same as panels a-d for 200 hPa.

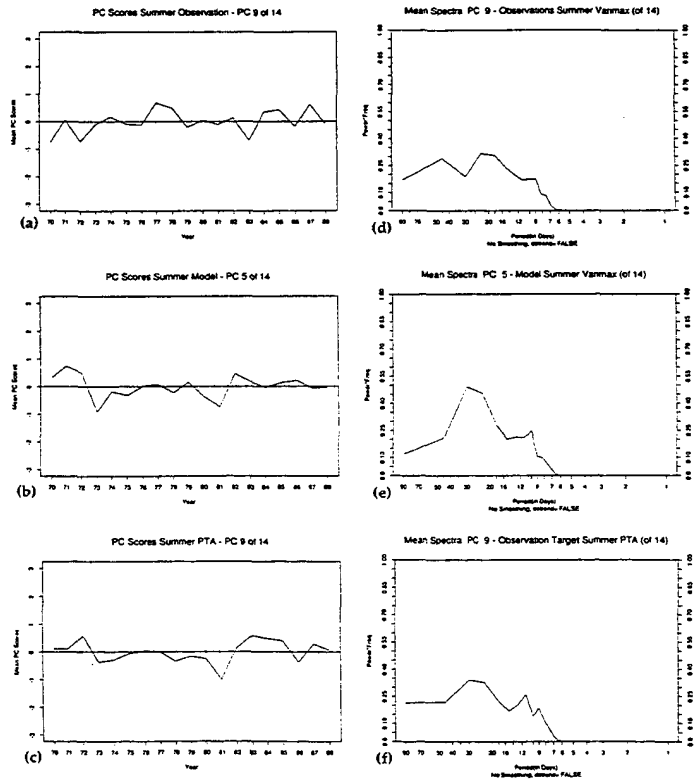


Fig. 3: Time series analysis for summers of 1970-1988 for North Atlantic Oscillation hybrid mode of 700/200 hPa height. Panels a-c are interannual variability of Varimax observed, Varimax model and PTA model, respectively. Panels d-f are the intraseasonal spectra for the same 3 analyses.

Table I. Overview of Low-Frequency Mode of Variation Matches from Observation to GCM

Mode[1] Name	Winter Observational PC Number	Winter Observation/ Model RPC % Variance Overlap	Winter Observation/ Model PTA % Variance Overlap	Summer Observational PC Number	Summer Observation/ Model RPC % Variance Overlap	Summer Observation/ Model PTA % Variance Overlap
Subtropical Zonal Pattern[2,3]	1	74	77	1; 14	79; 34	81; 66
Eastern Atlantic Pattern[2]	2	48	61	5; 12	31; 34	40; 53
Tropical Northern Hemisphere	3	59	72	—	—	—
North American Pattern[4]	4	28	62	—	—	—
Trans-Asian Pattern[4]	5	25	46	—	—	—
Asian Summer Pattern	6	62	61	4	32	56
Pacific North American	7	67	76	—	—	—
North Pacific Pattern	8	36	69	—	—	—
North Atlantic Oscillation	9	36	71	9	26	52
Wave Train Pattern[2,4]	10	18	50	7; 10; 11	8; 3; 5	22; 11; 11
Mediterranean Pattern[4]	11	42	58	—	—	—
Eastern Pacific Pattern	12	48	81	—	—	—
Eurasian Type 1 Pattern	13	38	59	13	9	25
West Pacific Oscillation	14	25	34	8	21	55
Northern Asian Pattern	15	35	38	6	12	35
Asian Monsoon Pattern[4]	—	—	—	2	42	61
Pacific Transition Pattern	—	—	—	3	26	58

[1] Name matched to Barnston and Livezey (1987) unless noted.
[2] Pattern had two or more subtypes in summer.
[3] Also Tropical Wide Pattern.
[4] Did not match to any Barnston and Livezey pattern.

Towards the Development of a PIP Model for Atmospheric Data

U. Achatz and G. Schmitz

Institut für Atmosphärenphysik an der Universität Rostock, Kühlungsborn, F.R.G.

ABSTRACT

A Principal Interaction Pattern (PIP) analysis aims at finding basic patterns in data of a complex dynamical system which are able to describe the dynamic behavior of this system on the basis of a suitably chosen model for the interaction of these patterns with each other at the best possible accuracy. Because of the large freedom in choosing a useful PIP model such an analysis has only recently been done. On the basis of first successful analyses we present a general method for developing PIP models using accepted dynamical equations. The usefulness of the method is demonstrated by a PIP analysis of multiple baroclinic wave life cycles in a T42 quasigeostrophic two-layer model. The extracted PIPs are compared to EOFs and superiority of PIP models over EOF models is shown. Some preliminary results on role of the PIPs in the life cycles are given.

1 INTRODUCTION

Over the decades there has been a continuous effort in analyzing and simulating atmospheric dynamics on the basis of a limited number of elementary patterns. The development of a suitable method for identifying such structures is still a major problem. Several powerful tools have already been successfully used. Point-correlation maps of atmospheric data have proven very useful for the identification of major hemispheric-scale horizontal flow patterns as the Pacific/North American (PNA) and North Atlantic Oscillation (NAO) patterns (Wallace and Gutzler, 1981). Frederiksen (1982, 1983) examined the most unstable normal modes of a quasigeostrophic two-layer model with orography and nonzonal forcing. He was able to associate these as well to elementary processes like cyclogenesis and on-set of blocking as to the above mentioned teleconnection patterns. Simmons et al. (1983) could show that teleconnection patterns can already be identified among the normal modes of a similarly forced barotropic model. Another interesting approach is EOF analysis. Rhinne and Karhilla (1975) and Schubert (1985, 1986) have investigated dynamical interactions between EOFs determined from atmospheric observations. They could show that a few dominant EOFs are able to describe the predominant part of the observed tendencies at a quality comparable to grid point or spectral models with much larger numbers of degrees of freedom.

Further progress in this line is to be achieved by a direct utilization of observed dynamics in the form of measured tendencies. This is the aim of a Principal Interaction Pattern (PIP) analysis (Hasselmann, 1988). It aims at finding a limited number of structures in the seemingly very complicated dynamics that are time-independent up to their amplitudes and phases. These vary according to nonlinear equations determining the interaction between the different structures. By minimizing a suitably chosen error function both these structures and their interaction coefficients are determined simultaneously. Useful results have already been achieved by a similar identification of patterns with a predominantly linear behavior, so-called Principal Oscillation Patterns (POP). Among numerous examples an interesting work is the one by Schnur et al. (1993) where POPs have been identified in atmospheric data resembling baroclinic waves in their respective growth and decay phases. Because of the linearity, however, this approach is not well able to guide our understanding about the interaction of the identified structures with each other. Additionally, a POP analysis is not designed for an identification of a reduced number of patterns on which an atmospheric model can be built. A nonlinear PIP model could be the basis for an analysis satisfying this need. Indeed, in a first investigation it has been shown by Achatz et al. (1995, hereafter ASG) that multiple baroclinic wave life cycles in a quasigeostrophic two-layer model at R15 spectral truncation can be quite satisfyingly simulated using three wave patterns as identified by a suitably chosen PIP analysis. On the ground of this work we propose here a general method for the development of PIP models on the basis of accepted dynamical equations. The usefulness of the method is further investigated by PIP analyses of more complex synthetic data sets than formerly used, namely baroclinic wave life cycles in a T42 quasigeostrophic two-layer model.

In section 2 a short description of the two-layer model is given. Section 3 outlines the PIP analysis in general and describes our method for designing PIP models for various synthetic and observed data sets. Section 4 gives a comparison of the performance of the identified PIPs in simulating the analyzed data with analogous EOF-based integrations, gives a short description of the most prominent PIPs and shows what is to be learned about complex dynamical processes by using PIPs.

2 THE TWO-LAYER MODEL

The data used in this work for a PIP analysis were obtained by numerical integration of the tendency equations of a standard quasigeostrophic two-layer model on the sphere. Surface friction and Newtonian cooling have been included. Furthermore we have incorporated forcing terms which make a chosen zonal wind configuration a stationary solution of the system.

For the determination of the synthetic data set all variables are represented by a truncated expansion in terms of equatorially antisymmetric spherical harmonics (yielding equatorially symmetric velocity fields). For details see ASG.

3 PRINCIPAL INTERACTION PATTERNS

PIP Analysis

The general idea of a PIP analysis (Hasselmann, 1988) is the following: Let us assume that we have a dynamical system which can be described at any moment by a complex state vector $\vec{\Phi}(t)$. Its time development shall be given by a set of first order differential equations

$$\frac{d}{dt}\vec{\Phi} = \hat{F}(\vec{\Phi}, t) \tag{1}$$

where $\hat{F}$ may depend nonlinearly on $\vec{\Phi}$. For such a system a PIP analysis tries to find a limited number of patterns $\hat{p}_\nu$ which in combination give an optimal representation of the complete state vector at any time such that the residual error

$$\hat{p}(t) = \vec{\Phi}(t) - \sum_\nu a_\nu(t)\,\hat{p}_\nu \tag{2}$$

becomes as small as possible. The only time dependence is in the $a_\nu(t)$. Assuming the patterns $\hat{p}_\nu$ to be known their coefficients can be determined for any time by projecting all $\hat{p}_\nu$ simultaneously onto the data:

$$a_\nu = \sum_\mu \left(N^{-1}\right)_{\nu\mu} \sum_i \overline{p_{i\mu}}\,\Phi_i \tag{3}$$

where i is the index of the state space spanned by the system and the matrix N is given by

$$N_{\nu\mu} = \sum_i \overline{p_{i\nu}} p_{i\mu} \quad (4)$$

The overbar denotes complex conjugation. The dynamical aspect of the method enters with a second step which makes PIPs so interesting for the reduction of complex dynamical systems. The evolution of the PIP coefficients is postulated to follow a set of nonlinear equations - the PIP model -

$$\frac{da_\nu}{dt} = G_\nu(\hat{a}, \alpha_1, ..., \alpha_q) \quad (5)$$

with a number of parameters α_q which might be connected to the patterns by some boundary conditions. The determination of these and of the patterns is then done by minimization of the error

$$\varepsilon(\alpha_1, ..., \alpha_q, \hat{p}_1, ..., \hat{p}_M) = \sum_t \left| \dot{\hat{\Phi}} - \dot{\hat{\Phi}} \right|^2 \quad (6)$$

where the sum is over all times at which data from a time series for $\hat{\Phi}$ exist, and

$$\dot{\hat{\Phi}} = \sum_\nu G_\nu(\hat{a}, \alpha_1, ..., \alpha_q)\, \hat{p}_\nu \quad (7)$$

is the tendency of the approximated state vector.

PIP Models in General

How would a PIP model for data from a general circulation model or atmospheric observations look like? Restricting ourselves to dynamical aspects state space is e.g. spanned by all spectral coefficients of streamfunction, velocity potential and potential temperature at all pressure levels, and surface pressure. In most cases it will suffice to consider a suitably chosen subspace, e.g. spectral coefficients at some spectral truncation or the dominant Principal Components of streamfunction and potential temperature at a few levels. We assume that for this subspace a model exists which describes the relevant dynamics at some accuracy. Keeping within the framework of the so far chosen example this could be a quasi-geostrophic multi-layer model or the projection of this on the dominant EOFs. The tendency equations of this model shall be given by

$$\dot{\hat{\Phi}}_M = \hat{H}\left(\hat{\Phi}, \alpha_1, ..., \alpha_q, t\right) \quad (8)$$

so that

$$\dot{\hat{\Phi}} = \dot{\hat{\Phi}}_M + \hat{\xi} \quad (9)$$

with a not too large residual error $\hat{\xi}$. The parameters α_q denote external parameters as diabatic parameters, mean static stability, etc. For extracting from this a PIP model we insert the expansion

$$\hat{\Phi} = \sum_\nu a_\nu \hat{p}_\nu \quad (10)$$

into (8) and (9), combine the resulting equations under neglect of $\hat{\xi}$, and arrive at

$$\dot{a}_\nu = G_\nu(\hat{a}, \alpha_1, ..., \alpha_q, t)\big|_{\hat{p}} \quad (11)$$

where

$$G_\nu(\hat{a}, \alpha_q, t)\big|_{\hat{p}} = \left(N^{-1}\right)_{\nu\mu} \sum_i \bar{p}_{i\mu} H_i\left(\sum_\nu a_\nu \hat{p}_\nu, \alpha_q, t\right) \quad (12)$$

and the index $\hat{p}$ indicates evaluation of the specified function using a given set of PIP vectors. The error function to be minimized is then given by

$$\varepsilon(\alpha_1, ..., \alpha_q, \hat{p}_1, ..., \hat{p}_M, t) = \sum_t \left| \dot{\hat{\Phi}} - \sum_\nu G_\nu(\hat{a}, \alpha_q, t)\big|_{\hat{p}} \hat{p}_\nu \right|^2 \quad (13)$$

The a_ν are to be calculated via (3). If good knowledge about some external parameters exist these might be kept fixed during the optimization. One great advantage of PIP analysis is, however, that all external parameters can also be determined by the optimization.

A PIP Model for a Quasigeostrophic Two-Layer Model

In the case of two-layer model data state space is spanned by all spherical harmonic coefficients of the two streamfunctions which are possibly nonzero and for which the zonal wave number is non-negative. In the case of equatorially symmetric baroclinic wave life cycles starting with a single normal mode at a given zonal wave number on a zonally symmetric wind our state space is reduced to coefficients with odd meridional wave numbers describing the zonal wind, the wave and all its upper harmonics in zonal wave number.

In order to make the following development more clear we decompose the full state space into two subspaces. One of them comprises all zonally symmetric components forming a vector $\hat{z}$. In principle the other contains all wave coefficients (zonal wave number $m \neq 0$). In practice it proves to be useful not to consider the full wave subspace but only the leading PCs corresponding to the dominant complex EOFs of full wave subspace[1]. These will in the following be lined up in the vector $\hat{w}$. Thus we can formally write

$$\hat{\Phi} = \begin{pmatrix} \hat{z} \\ \hat{w} \end{pmatrix}. \quad (14)$$

For reasons of simplicity all PIPs are assumed to be an element of one of these two subspaces.

For the moment, simplifications of the zonally symmetric part are not sought so that we suppose that there are as many zonally symmetric PIPs as there are dimensions for them. They are taken to be the set of natural unit vectors of this space, i.e. each of them corresponds to one zonal spherical harmonic coefficient of one of the streamfunctions, i.e they are defined by

$$\vec{p}_\nu = \begin{pmatrix} \vec{e}_\nu \\ \hat{0} \end{pmatrix} \quad (15)$$

where $\vec{e}_\nu$ is the νth unit vector of the zonally symmetric subspace. Their coefficients are then given by

$$a_\nu = z_\nu \quad (16)$$

The PIPs we are really looking for are the prominent ones existing in the wave subspace, i.e.

$$\vec{p}_\nu = \begin{pmatrix} \hat{0} \\ \vec{q}_\nu \end{pmatrix} \quad (17)$$

The evolution equations describing their development by interaction with each other and the zonal wind can be derived by the above described method via projection onto the dynamics of our two-layer with the result:

$$\dot{z}_i = \sum_j A_{ij}(z_j - Z_j) + \sum_{\nu,\mu} \alpha_{i\nu\mu} a_\nu \overline{a_\mu} \quad (18)$$

and

$$\dot{a}_\nu = \sum_\mu \omega_{\nu\mu} a_\mu + \sum_{j,\mu} \beta_{\nu\mu j} a_\mu z_j + \sum_{\mu,\rho} \left(\varepsilon_{\nu\mu\rho} a_\mu a_\rho + \varphi_{\nu\mu\rho} a_\mu \overline{a_\rho} + \iota_{\nu\mu\rho} \overline{a_\mu}\, \overline{a_\rho} \right) \quad (19)$$

All tensor coefficients are unique functions of the PIP vectors $\hat{q}_\nu$ and the interaction coefficients of the two-layer model.The Z_j denote a forced zonally symmetric stationary zonal solution They assume the role of the α_i not connected to the patterns by boundary conditions.

4 PIPS IN MULTIPLE BAROCLINIC WAVE LIFE CYCLES

In ASG it has been demonstrated that for fairly typical values of surface friction ($0.25\,d^{-1}$) and thermal damping ($0.1\,d^{-1}$) three patterns are sufficient for a reasonable simulation of multiple baroclinic wave life cycles with a basic zonal wave number 6 in an R15 version of our two-layer model. One is virtually identical with the most unstable normal mode of the forced stationary state, the second describes momentum transport on the southern jet flank, the third on the northern flank. Conspicuous was also the special ability of the latter to simulate jet steepening on the northern flank by a change of the direction of momentum transport from northwards to southwards near the flank and to mimic the enstrophy cascade in the decay of eddy energy in the late phase of a life cycle. It should also be noted that direct interactions between PIPs

1. This kind of prefiltering is also employed by Kwasniok (1995, private communication) in PIP analyses of different data sets.

seemed to be of negligible importance. Major questions arising from these results are:

- How much does this picture depend on the spectral truncation and horizontal diffusion of the model?
- Can more be learned in a higher resolution model about the specific way enstrophy takes as it cascades down to smaller scales?

A further question of interest is how much we gain by performing PIP analysis in comparison to the numerically much easier obtained EOF models.

In an attempt to answer these questions we have performed a PIP analysis of multiple baroclinic wave life cycles in a version of the two-layer model with a much better horizontal resolution (T42) which also made it possible to use a horizontal diffusion three times smaller than in the previous work ($1.0 \cdot 10^{-6} a^4/d$). Forcing was once more towards a zonally symmetric jet with $u_3 = 20.0 \sin^2 2\varphi$ m/s in the upper layer and no wind in the lower layer. The time series is 1500 d long. Days 300 - 600 were used for the analysis (data taken once every day). A basis of the 30 leading complex EOFs was used in order to extract 15 PIPs from the time series. The original wave space has 126 complex degrees of freedom.

Comparison between PIP and EOF models

PIP analyses are computationally rather expensive. The identification of leading EOFs is a much faster procedure. It has been shown by several authors (Rhinne and Karhilla, 1975, Selten, 1993) a useful reduction of the number of degrees of freedom of a complex system can also be obtained by projecting its dynamics onto a sufficient number of leading EOFs. For an investigation wether PIP models can be even superior to thus derived EOF models we have projected day 300 onto either the 15 leading EOFs or our 15 PIPs and integrated the corresponding EOF or PIP model from there up to day 1500. Figure 1 shows the resulting time dependence of the eddy kinetic energy (K_E). The PIP model is at least qualitatively able to simulate the maximum amplitude oscillation of the original life cycles. The EOF model is able to give a good simulation of the first few life cycles but later on approaches a quasi equilibrium which is quite different from the time dependence of the original data. Thus only the PIP model is able to give a reasonable simulation of the long-time variability in our data. The orientation of PIP analysis at the observed dynamics seems to give a definite improvement over a variance oriented EOF analysis. This is further confirmed by a comparison of the time averaged zonal mean zonal wind (figure 2) and zonal mean eddy momentum and temperature fluxes of the two model runs (not shown). PIPs give systematically better results.

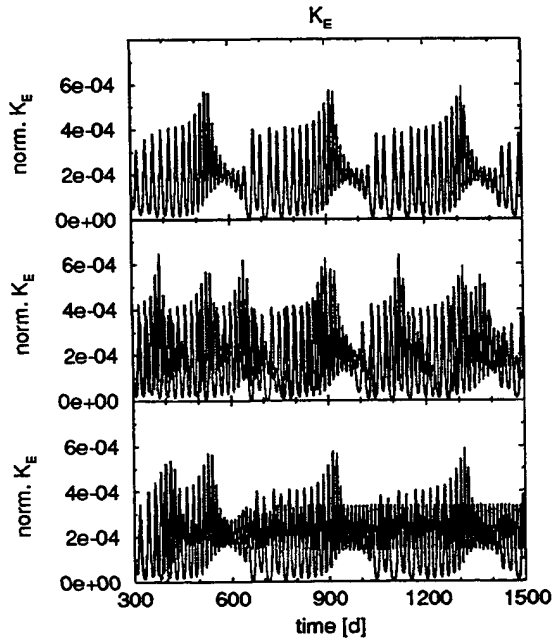


Figure 1. Time dependence of the eddy kinetic energy between day 300 and 1500 in the analyzed time series (top and dotted line in the middle and bottom graphs), a 15 PIP simulation (middle) and a 15 EOF simulation (bottom).

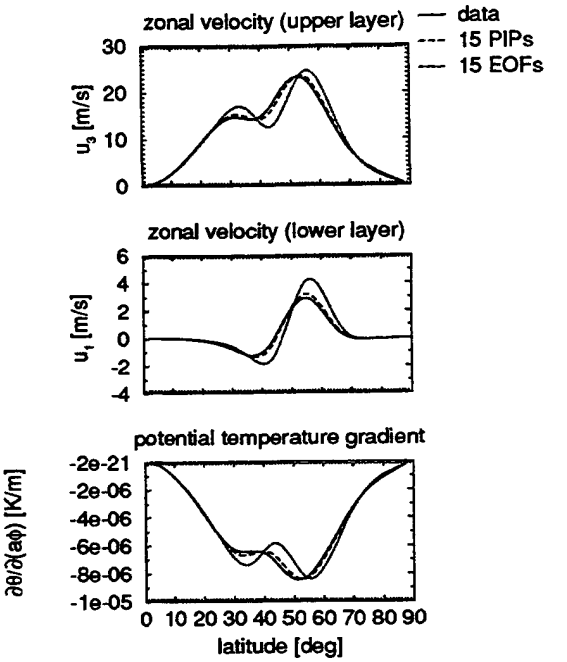


Figure 2. Comparison between the time averaged zonal mean wind in the 15 PIP and 15 EOF integrations shown in fig. 1.

Life Cycle Dynamics in the PIP Picture

The error function used for the PIP analysis is invariant under general basis transformations in PIP subspace, i.e.

$$\tilde{q}_{i\nu} = \sum_{\mu} H_{\nu\mu} q_{i\mu} \qquad (20)$$

with a nonsingular matrix H (Kwasniok, private communication). We have therefore chosen the normal modes of the linearized PIP model with respect to the forced stationary zonally symmetric state as basis vectors of PIP subspace. With this choice, after numbering the patterns according to their statistical importance for a description of the tendencies in our data between day 300 and 1500 (not explained here in detail) also in the T42 case PIP 1 is the most unstable normal mode of the PIP model, followed by a pattern simulating momentum transport on the northern jet flank (PIP 2) and another pattern which is affecting the zonal wind most effectively on its southern flank via momentum transport (PIP 3). The relevant zonal mean eddy transport terms of these together with the four following patterns are displayed in figure 3.

Now, however, as an according test has shown, a satisfying simulation is not possible any more on the basis of just these three patterns. The following PIPs are also indispensable. A rise and fall in the importance of specific patterns in the different typical phases of the long-time behavior can be identified. On the other hand, some patterns never really dominate. Nonetheless, model integrations using only the dominant patterns do not give satisfying results. Thus, the higher resolution and smaller horizontal resolution of the model than in the one used in ASG leads to a much more detailed enstrophy cascade which can only be described at the necessary completeness by inclusion of all patterns. For conciseness the specific role of these cannot be discussed here in detail. Only the most important aspects will be summarized.

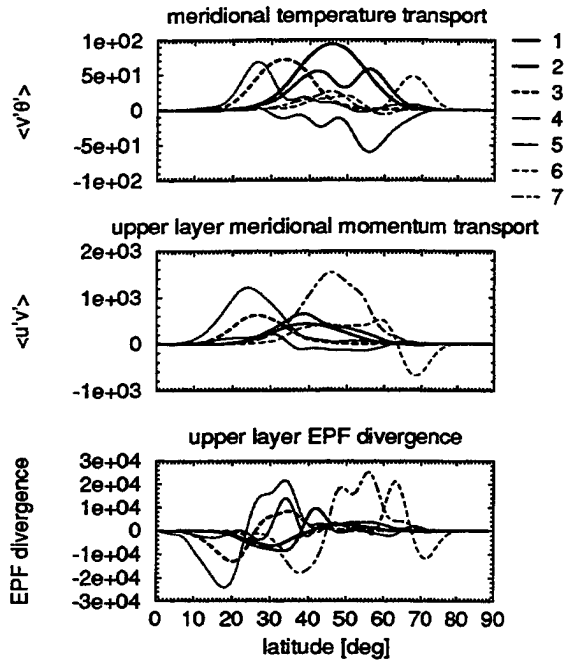


Figure 3. Zonal mean upper layer momentum transport, potential temperature transport and upper layer Eliassen-Palm flux divergence as parameterized by the seven leading PIPs in arbitrary units.

- Among the patterns with a predominant zonal wave number 6 there is another one (PIP 5) which resembles PIP 3 in that it is mainly transporting momentum on the southern jet flank. It has, however a markedly more small-scaled structure than PIP 3 (measured in terms of the average total wave number of the pattern's total energy spectrum) and lies more to the south. During each life cycle both patterns rise and fall in amplitude parallel to the overall eddy activity, however PIP 5 reaches its maximum amplitude at later times. It therefore seems to be a natural follower of PIP 3 in the enstrophy cascade on the southern jet flank.
- There are three major wave 6 patterns acting on the northern jet flank: PIPs 2, 6 and 7. PIP 6, and even more PIP 7, are more small-scaled than PIP 2. Both are also even more concentrated on the northern flank. Whereas PIP 7 seems to be especially effective in transporting momentum northwards, PIP 6 now is the pattern which is responsible for southwardly directed momentum transport on the northmost flank of the jet. Both patterns appear systematically later in a life cycle than PIP 2. Summarizing this and the previous point on both jet flanks a much more detailed enstrophy cascade becomes visible in T42 life cycles at weaker horizontal resolution than in the ASG case.
- The cascade on the northern flank seems to have a key role in the long-time oscillation (modulation) of the maximum amplitudes in the life cycles. With growing eddy activity zonal available energy decays from life cycle to life cycle. In a modulation decay phase the reverse happens. It can be shown that in this decay phase the ability of the waves to act onto the zonal wind is systematically weakened. Much more eddy energy is lost via dissipation. This is conspicuously associated by a diminished role of PIP 7. It is much less important for the simulation in comparison to PIP 5 and 6 than in the modulation growth phases. The weakened role of this pattern seems to contribute to the strong decay of eddy energy and a weakened eddy influence on the zonal mean wind in the modulation decay phase so that the zonally symmetric stationary state can be reestablished much better by forcing and dissipation. This partially confirms the picture of the role of eddy dissipation in the reestablishment of consecutive life cycles as given by ASG.

References

Achatz, U., G. Schmitz, and K.-M. Greisiger, 1995: Principal Interaction Patterns in baroclinic wave life cycles. *J. Atmos. Sci,* in press

Frederiksen, J.S., 1982: A unified three-dimensional instability theory of the onset of blocking and cyclogenesis. *J. Atmos. Sci,* **39,** 969-982

Frederiksen, J.S., 1983: A unified three-dimensional instability theory of the onset of blocking and cyclogenesis. Part II: Teleconnection patterns. *J. Atmos. Sci,* **40,** 2593-2609

Hasselmann, K., 1988: PIPs and POPs: The reduction of complex dynamical systems using principal interaction and oscillation patterns. *J. Geophys. Res.,* **93,** 11015-11021

Rhinne, J., and V. Karhilla, 1975: A spectral barotropic model in horizontal empirical orthogonal functions. *Quart. J. Roy. Meteor. Soc.,* **101,** 365-382

Schnur, R., G. Schmitz, N. Grieger, and H. v. Storch, 1993: Normal modes of the atmosphere as estimated by Principal Oscillation Patterns and derived from quasigeostrophic theory. *J. Atmos. Sci,* **50,** 2386-2400

Schubert, S. D., 1985: A statistical-dynamical study of empirically determined modes of atmospheric variability. *J. Atmos. Sci,* **42,** 3-17

Schubert, S. D., 1986: The structure, energetics and evolution of the dominant frequency-dependent three-dimensional atmospheric modes. *J. Atmos. Sci,* **43,** 1210-1237

Selten, F. M., 1993: Toward an optimal description of atmospheric flow. *J. Atmos. Sci,* **50,** 861-877

Simmons, A. J., J. M. Wallace, and G. W. Branstator: Barotropic wave propagation and instability, and atmospheric teleconnection patterns. *J. Atmos. Sci.,* **40,** 1363-1392

Wallace, J. M., and D. S. Gutzler, 1981: Teleconnections in the geopotential height field during the Northern Hemisphere winter. *Mon. Wea. Rev.,* **109,** 784-812

CORRESPONDING AUTHOR

U. Achatz
Institut für Atmosphärenphysik an der Universität Rostock
Schloßstr. 4-6
18221 Kühlungsborn
F. R. G.

AN EFFICIENT DESCRIPTION OF LARGE-SCALE ATMOSPHERIC FLOW USING PRINCIPAL INTERACTION PATTERNS

Frank Kwasniok
Max-Planck-Institut für Meteorologie, Hamburg, Germany

ABSTRACT

A method of constructing low-dimensional nonlinear models capturing the main features of complex dynamical systems with many degrees of freedom is described. The system is projected onto a linear subspace spanned by only a few characteristic spatial structures called Principal Interaction Patterns (PIPs). The expansion coefficients are assumed to be governed by a nonlinear dynamical system. The optimal low-dimensional model is determined by identifying spatial modes and interaction coefficients describing their time evolution simultaneously according to a nonlinear variational principle.

The algorithm is applied to a barotropic spectral model. The truncated models based on Principal Interaction Patterns are compared to those using Empirical Orthogonal Functions (EOFs) as basis functions. A PIP-model using 12 patterns is capable of capturing the long-term behaviour of the complete system monitored by second-order statistics, while in the case of EOFs 17 modes are necessary.

1 INTRODUCTION

In various fields of research such as fluid dynamics, atmospheric science and other physical subjects there occur complex dynamical systems with many degrees of freedom. Frequently a model is formulated in terms of partial differential equations (PDEs) from which a system of ordinary differential equations (ODEs) is derived via a Galerkin procedure using eigenfunctions of some linear differential operator, commonly Fourier modes, as basis functions. Despite the complexity the dynamics of such systems are often confined to attractor sets of a dimension much smaller than the dimension of phase space. Coherent structures emerge; the dynamical behaviour of the system (or at least of an important part of the system representing e. g. a particular physical phenomenon one focuses on) seems to be dominated by the interaction among relatively few characteristic spatial patterns; i. e. the system is in fact in some sense low-dimensional. Hence the construction of minimal models capturing the principal properties of the complete system is an interesting task in such cases. Reduced models especially may be a helpful tool to understand the system, e. g. to gain insight in the physical driving mechanisms of particular phenomena occuring in the system. The Fourier modes in principle allow for a complete description of the time evolution, but this description cannot be expected to be very efficient as to the number of functions involved since Fourier modes are completely general and do not take advantage of information about the particular system under consideration at all. This leads to the idea that a description in terms of characteristic patterns may be more adequate when searching for a minimal model.

How to identify such patterns is far from clear. Modes obtained from an Empirical Orthogonal Function analysis are an obvious candidate on intuitive grounds. They can be calculated quite easily as solutions of an eigenvalue problem involving second-order correlation tensors of the dynamical variables. Empirical Orthogonal Functions (EOFs) provide an optimal representation of a multivariate dynamical field in a mean least-squares sense using a given number of modes. But they a priori do not contain any information about the time evolution or the dynamical structure of the system. Of course the modes obtained from an EOF-analysis can be used and have been used (e. g. Selten (1993, 1995)) to build a low-dimensional model, but they are not optimized for this purpose.

In the present paper modes which are optimal with respect to the time evolution are calculated to construct reduced models. They are obtained from a nonlinear minimization procedure based on a dynamical optimality criterion involving higher-order correlation tensors of both the state variables and their time derivatives. The method takes into account spatial as well as temporal features of the dynamical system by identifying spatial modes and interaction coefficients describing their time evolution simultaneously, in contrast to EOF-analysis which concentrates solely on spatial properties of the system and does not deal with mode interaction.

Achatz et al. (1995) applied the concept of Principal Interaction Patterns successfully to the description and analysis of the periodic time evolution of baroclinic wave life cycles.

The present study starts out from a chaotic barotropic spectral atmospheric model. The question is addressed to what extent a system with relatively few degrees of freedom using optimized basis functions succeeds in capturing the essential dynamical behaviour of the full system. The paper is organized as follows: In section 2 the methodology is outlined in general. Then the barotropic model used as an example to test and study the method is introduced. The Galerkin procedure to derive reduced systems from this equation is described. Then the main results are presented in section 5. Some emphasis is put on the comparison with reduced models based on EOFs. The paper is concluded in section 6.

2 METHODOLOGY

The algorithm follows a general concept proposed by Hasselmann (1988) which is slightly modified in this study. Consider a nonlinear autonomous dynamical system of first order in N-dimensional phase space :

$$\dot{\Phi} = F(\Phi) \qquad \Phi = (\Phi_1, \cdots, \Phi_N) \qquad (1)$$

N may be quite large $(10^2 - 10^5)$; e. g. think of a system of differential equations originating from a partial differential equation via a Galerkin procedure (cf. section 4.1). The high-dimensional dynamical field $\Phi(t)$ is projected onto a limited number of time-independent spatial modes which will be called Principal Interaction Patterns (PIPs):

$$\Phi(t) = \sum_{i=1}^{L} z_i(t)\, p_i + \rho \qquad L << N \qquad (2)$$

ρ denotes the vector of the residual error. In matrix notation eq. (2) reads

$$\Phi = Pz + \rho \qquad (3)$$

where P is the $(N \times L)$-matrix with the PIPs as its columns. The time dependence is suppressed in the notation from now on. For a given set of patterns the vector of expansion coefficients z at each time is defined by requiring that the error in the representation of the state vector

$$\mathrm{Err} = (\Phi - Pz)^t M (\Phi - Pz) \qquad (4)$$

measured in some metric M be minimized. This constitutes a linear least-squares problem which can be solved uniquely using the Moore-Penrose generalized inverse of P with respect to M

$$z = P^+\Phi = (P^tMP)^{-1}P^tM\Phi \qquad (5)$$

or in other terms

$$z = P^{*t}M\Phi \qquad (6)$$

with P^* being the $(N \times L)$-matrix of adjoint patterns

$$P^* = P(P^tMP)^{-1} \qquad (7)$$

defined as the set of vectors p_i^* which lie in the linear subspace spanned by the PIPs and which are orthonormal to them with respect to the metric M :

$$p_i^{*t} M p_j = \delta_{ij} \qquad (8)$$

The dynamics of the time-dependent coefficients z are assumed to be governed by an autonomous system of L first-order differential equations

$$\dot{z} = G(z;\tau) \qquad (9)$$

depending on a set of adjustable parameters $\tau = (\tau_1, \cdots, \tau_r)$. The dynamical system is specified as a member of a model class suitably chosen based on some physical knowledge or reasoning about the character of the system to model. The optimal set of patterns and the optimal parameters are determined simultaneously by minimizing the error in the derivative of the PIP-coefficients between the reduced system and the entire system in a mean least-squares sense :

$$Q(P,\tau) = \overline{\left(G - P^+\dot{\Phi}\right)^t \tilde{M} \left(G - P^+\dot{\Phi}\right)} = \mathrm{Min.} \qquad (10)$$

The overbar denotes ensemble averaging which is equivalent to time averaging if ergodicity is assumed. In practice it will be replaced by a sum over a discrete and finite time series. The metric $\tilde{M}$ may be chosen as the inverse of the covariance matrix of the derivatives of the PIP-amplitudes to guarantee equal weighting of all modes :

$$\tilde{M} = (P^+ \Pi P^{+t})^{-1} = P^tMP(P^tM\Pi MP)^{-1}P^tMP \qquad (11)$$

Π is the covariance matrix of the derivatives of the full system:

$$\Pi_{ij} = \overline{\dot{\Phi}_i \dot{\Phi}_j} \qquad (12)$$

In principle the parameters τ are independent variables in the minimization problem. However, in this study as a first step they will be (mainly) connected to the patterns by a projection procedure (cf. section 4.2). Eq. (10) in general (if G is nonlinear) poses a high-dimensional nonlinear minimization problem which has to be solved numerically by iterative techniques.

3 THE BAROTROPIC MODEL

In this study a vertically homogeneous layer of incompressible fluid over topography on the rotating sphere is considered. If the approximations of shallowness and quasigeostrophy are applied the flow can be described by a streamfunction $\Phi(\lambda,\mu)$ which obeys the non-divergent barotropic quasigeostrophic potential vorticity equation :

$$\frac{\partial}{\partial t}\Delta\Psi + \mathcal{J}(\Psi, \Delta\Psi + f + h) = -\kappa_1\Delta\Psi - \kappa_2\Delta^4\Psi + \Delta\tilde{\Psi} \qquad (13)$$

λ and $\mu = \sin\theta$ denote the longitudinal and latitudinal coordinates on the sphere, respectively. Δ and $\mathcal{J}$ stand for the Laplacian and the Jacobian operator, respectively. $f = 2\mu$ is the Coriolis parameter. h represents an effective topography. The linear damping represents surface friction; κ_1 is assigned a value corresponding to a damping time scale of 15 days. The scale selective horizontal diffusion term parametrizes the effect of eddies on very small non-resolved spatial scales onto the resolved scales. The coefficient κ_2 is set to a value representing a damping time scale of 3 days in the smallest spatial scale (wavenumber 21). $\tilde{\Psi}$ is a constant forcing streamfunction which can be interpreted as thermal forcing owing to solar radiation and is specified from a 500hPa streamfunction analysis data set in a way that the system has a realistic mean state and a variance pattern similar to that of 10 days running mean streamfunction fields. The Rossby radius of deformation is set to infinity in this study (rigid lid approximation). Eq. (13) has been nondimensionalized using the radius of the earth as unit of length and the inverse of the angular velocity of the earth as unit of time. The barotropic vorticity equation may be regarded as the crudest model of large-scale atmospheric dynamics.

4 DERIVATION OF TRUNCATED MODELS

4.1 Spectral Basis

The streamfunction, the topography and the forcing are expanded into a triangularly truncated series of spherical harmonics. The vorticity equation is considered on the Northern hemisphere. Hence only modes with odd parity are used in the expansion. This corresponds to the boundary condition $v = 0$ at the equator (no flow across the equator). For the streamfunction the expansion reads :

$$\Psi(\lambda,\mu,t) = \sum \Psi_\alpha(t)\, Y_\alpha(\lambda,\mu) \qquad (14)$$

Y_α denote the spherical harmonics. The index $\alpha = (n,m)$ covers both wavenumbers. In this study the expansion is truncated at wavenumber $n_{\max} = 21$. This yields a linear subspace spanned by $N = 231$ real modes. The usual Fourier-Galerkin procedure then yields a forced, dissipative system with quadratic nonlinearity for the expansion coefficients :

$$\dot{\Psi}_\alpha = \frac{1}{2}\sum_{\beta,\gamma} A^{\rm sh}_{\alpha\beta\gamma}\Psi_\beta\Psi_\gamma + \sum_\beta B^{\rm sh}_{\alpha\beta}\Psi_\beta + C^{\rm sh}_\alpha \qquad (15)$$

The superscript sh signifies that the quantities refer to spherical harmonics.

4.2 Principal Interaction Patterns

Now we consider an L-dimensional subspace spanned by the Principal Interaction Patterns. It is convenient to separate the flow into the mean flow and the anomalies. The streamfunction anomalies are expanded into a series of PIPs :

$$\Psi = \overline{\Psi} + \sum_{i=1}^{L} z_i\, p_i \qquad (16)$$

A reduced model is then defined by a projection of eq.(13) onto PIP-space. This yields a system of ordinary differential equations for the PIP-amplitudes z defined according to eqs. (5) and (6) of the form

$$\dot{z}_i^{\rm pip} = G_i = \frac{1}{2}\sum_{j,k=1}^{L} A_{ijk} z_j z_k + \sum_{j=1}^{L} B_{ij} z_j + C_i \qquad (17)$$

where the coefficients are given by

$$C_i = <p_i^*, M\left(\tilde{\Psi} - \Delta^{-1}\mathcal{J}(\overline{\Psi}, \Delta\overline{\Psi} + f + h) - \kappa_1\overline{\Psi} - \kappa_2\Delta^3\overline{\Psi}\right)> \qquad (18)$$

$$B_{ij} = -<p_i^*, M\left(\Delta^{-1}\left[\mathcal{J}(\overline{\Psi}, \Delta p_j) + \mathcal{J}(p_j, \Delta\overline{\Psi} + f + h)\right] + \kappa_1 p_j + \kappa_2\Delta^3 p_j\right)> \qquad (19)$$

$$A_{ijk} = -<p_i^*, M\Delta^{-1}\left[\mathcal{J}(p_j, \Delta p_k) + \mathcal{J}(p_k, \Delta p_j)\right]> . \qquad (20)$$

$< \cdots, \cdots >$ signifies the canonical scalar product. $\dot{z}^{\rm pip}$ denotes the tendencies of the PIP-amplitudes as given by the truncated model in contradistinction from the exact tendencies $\dot{z} = P^+\dot{\Psi}$.

The elements of the tensors A, B and C form the set of parameters τ. Hence the parameters in this case are connected to the patterns rather than determined independently from them.

In the present calculations the metric $M = -\Delta$, the turbulent kinetic energy metric, is used.

Note that eqs. (16)-(20) are completely general; they hold for any L-dimensional subspace spanned by L arbitrary linearly independent modes. The optimal subspace in the sense of the variational principle expressed in eq.(10) is now determined via a nonlinear numerical minimization procedure using data from a long-term integration of the complete system (eq.(15)).

4.3 Uniqueness of the PIP-model

It is evident that the Principal Interaction Patterns are only determined to within a linear transformation. Consider an arbitrary regular linear transformation R and a matrix of patterns P. The transformed set of patterns is then $P' = PR$, the corresponding vector of expansion coefficients is $z' = R^{-1}z$. The interaction coefficients C, B and A are transformed according to the rules for tensors of first, second and third order, respectively. The error function Q is invariant under this transformation : $Q(P') = Q(P)$

To eliminate this gauge freedom one has to refer to some normal form for the matrix of patterns. One possibility to do so is to impose the constraints that the patterns be orthogonal with respect to M, that their amplitudes be uncorrelated with the patterns ordered by descending mean squared amplitude and that the coefficients C_i be always positive.

4.4 Reduction of Dimension Using EOFs

The projection procedure is carried out in two steps. In order to reduce the number of variables in the minimization procedure the Principal Interaction Patterns are assumed to lie in the S-dimensional subspace spanned by the leading S EOFs ($L \leq S \leq N$) :

$$p_i = \sum_{j=1}^{S} \hat{P}_{ji}\, e_j \qquad (21)$$

5 RESULTS

Minimizations of the error function Q have been carried out for increasing numbers of patterns and different numbers of retained EOFs. They are based on a data sample of 10000 points; i. e. the time average in the variational principle is taken as a time average over this data set. In all cases the minimization starts out from the first L EOFs taken as a first guess for the patterns. It turned out to be sufficient to search for the PIPs in the subspace of the leading 60 EOFs; no substantial improvement could be obtained by inclusion of higher modes.

5.1 Long-term behaviour

12 patterns turned out to be the minimum number of degrees of freedom to reproduce the first and second moments in PIP-space quite faithfully. Long-term integrations of the reduced models show that they tend to have systematically too much variance (and also too much energy and enstrophy). This is due to the fact that the horizontal diffusion term which removes energy from the tail of the spectrum is not captured very well by the PIP-model since it affects mainly the modes of high wavenumbers whereas the PIPs are concentrated on the long and medium waves (large-scale patterns). This difficulty may be solved by introducing an additional linear damping in the evolution equations for the PIP-amplitudes to parametrize the mean effect of the unresolved modes on the resolved PIP-modes in analogy to the additional diffusion term incorporated in the spectral model. In the present framework this can be done by calculating the elements of B as independent variables according to the variational principle simultaneously with the patterns instead of determining them via eq. (19). Fig. 1 shows the energy spectrum obtained from a long-term integration of a PIP-model

using 12 modes with additional damping. The energy spectrum in PIP-space is reproduced almost perfectly.

With truncated models based on EOFs it was not possible to reproduce the energy spectrum with less than 17 modes.

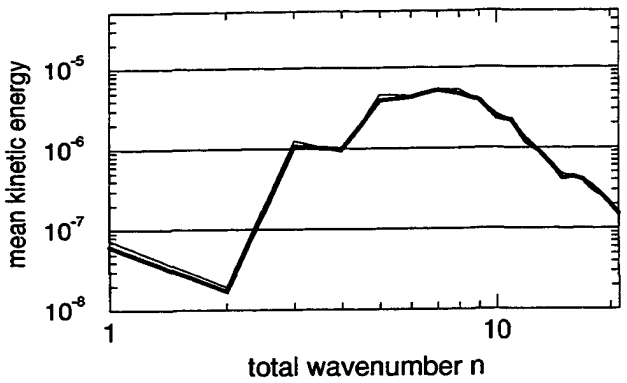


Figure 1. Mean turbulent kinetic energy as obtained from the full model (thin line) and the reduced model (thick line)

5.2 Local properties

Fig. 2 shows the correlation between the tendencies of the PIP-amplitudes given by the truncated model and those given by the full model separately for each pattern (solid line) and the corresponding values for an EOF-model (dotted line) both using 12 modes. The PIP-model provides a considerable improvement on the EOF-model.

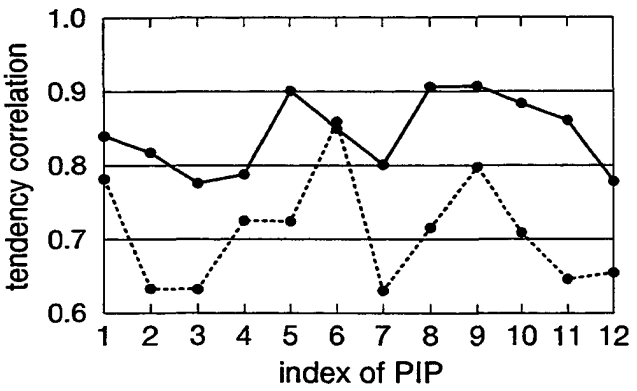


Figure 2. Correlation between tendencies of pattern amplitudes given by the full model and the reduced model

5.3 Prediction experiments

Now the ability of the truncated model to predict the time evolution of the PIP-amplitudes for a finite time is investigated. Starting out from an initial anomaly field projected onto PIP-space the PIP-model and the complete model are integrated in time. The forecast periods are different from the data sample used to determine the PIPs. The quality of the forecasts as a function of the prediction time is measured by the mean anomaly correlation (Fig. 3, thick line). The persistence forecast simply reflecting the autocorrelation of the PIP-amplitudes is considered as a trivial control forecast (thin line). The PIP-forecasts with 12 patterns have considerable skill.

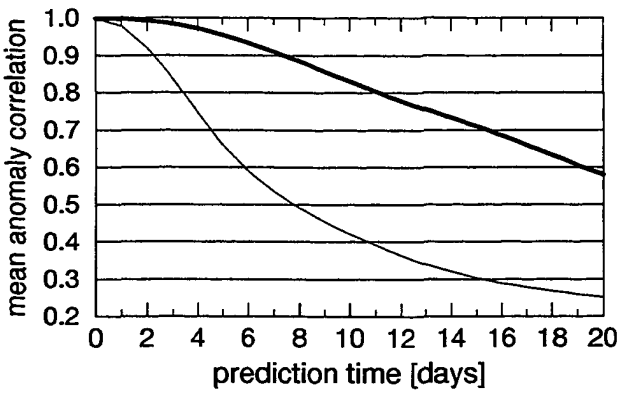


Figure 3. Mean anomaly correlation skill of the PIP-model in predicting the PIP-amplitudes

6 CONCLUSIONS

An algorithm for constructing optimal low-dimensional models of complex dynamical systems has been described. An optimal linear subspace spanned by a few characteristic spatial patterns and the coefficients of a dynamical system describing the time evolution of these modes are determined simultaneously according to a variational principle. The method involves higher-order correlation tensors of the variables and their time derivatives and leads to a nonlinear minimization problem in contrast to e. g. EOF-analysis which is based on second-order statistics and leads to an eigenvalue problem. In an application to a two-dimensional fluid system the EOFs turn out to be already a rather good approximation to the optimal modes, but the PIPs provide a considerable improvement, a PIP-model with 12 modes being approximately as good as an EOF-model with 17 patterns as to both global behaviour monitored by second-order statistics and short time prediction skill.

REFERENCES

Achatz, U., Schmitz, G., Greisiger, K.-M., 1995, "Principal Interaction Patterns in Baroclinic Wave Life Cycles", J. Atmos. Sci. (in press)

Hasselmann, K., 1988, "PIPs and POPs: The Reduction of Complex Dynamical Systems Using Principal Interaction and Oscillation Patterns", J. Geophys. Res. 93, 11015-11021

Selten, F. M., 1993, "Toward an Optimal Description of Atmospheric Flow", J. Atmos. Sci. 50, 861-877

Selten, F. M., 1995, "An Efficient Description of the Dynamics of Barotropic Flow", J. Atmos. Sci. (in press)

A more extensive paper on this work entitled "The Reduction of Complex Dynamical Systems Using Principal Interaction Patterns" is available as an MPI-report and can be ordered by the author.

CORRESPONDING AUTHOR

Frank Kwasniok
Max-Planck-Institut für Meteorologie
Bundesstr. 55
20146 Hamburg, Germany
Fax : + 49 40 / 41173298 , Email : kwasniok@dkrz.d400.de

SENSITIVITY TEST OF POP SYSTEM MATRICES - SPECTRAL PORTRAITS OF A NONSYMMETRIC MATRIX

Yuan Zhang, Valentin Dymnikov and John M. Wallace

University of Washington, Seattle, Washington, USA

ABSTRACT

By using the POP (propagating oscillation pattern) system matrices as examples, this study introduces the concept of spectral portraits of a nonsymmetric matrix. This study also provides an analytical formula to estimate the system error of a POP system matrix due to the inversion of an covariance matrix. By comparing the spectral portraits and the system errors, this study demonstrates the possible way to test the sensitivity of the POP analysis.

1 INTRODUCTION

This study introduces a new methodology for examining the sensitivity of a nonsymmetric linear system.

North et al. (1982) discussed the disturbance of a covariance matrix due to sampling errors. They pointed out that, in practice, when we estimate a covariance matrix from samples, what we really obtain (C_0') is the unknown real covariance C_0 plus a disturbance $\delta(C_0)$ (i.e., $C_0' = C_0 + \delta(C_0)$). This disturbance can be due to many different factors, in their case, they discussed the role of sampling errors. To obtain a robust eigensolution, the disturbance has to be small relative to C_0 (i.e., $\|\delta(C_0)\| \le \varepsilon \|C_0\|$, where ε represents a small number). For a symmetric matrix, the eigenspace consists of a complete set of orthogonal vectors, and an analytic formula to estimate the size of the sampling error for each eigenvector can be obtained (North et al., 1982). For a given sample, the spacing between two eigenvalues determines the stability of the eigenanalysis. When two eigenvalues are too close, their error bars due to sampling errors will overlap. This means that the linear system is 'effectively' degenerate in the sense that the eigenvectors can be different from one sample to the other.

The problem of the disturbance of a linear system matrix that North et al. (1982) discussed is a general problem of any matrix analysis technique, including not only symmetric but also nonsymmetric matrices like the system operator of POP (Propagating Oscillation Pattern) analysis.

POP analysis is a well-established method for finding propagating modes in geophysical fields (Hasselmann, 1988; v. Storch et al., 1988). Let $x(t)$ represent a n-dimensional stochastic process (for practical purposes, the original process is usually reduced to the subspace of leading Empirical Orthogonal Functions or EOFs). The evolution of the vector x can be represented as a first order multivariate Markov process: $(x(t+1) = Ax(t) + r(t+1))$, where $r(t)$ is the noise forcing which is, in general, nonwhite, non-Gaussian, and with zero mean. It can be shown that in order to minimize $\langle r^2 \rangle$, A has to be chosen as $A = C_1 \cdot C_0^{-1}$, where C_1 denotes the lag-1 covariance matrix of $x(t)$ and C_0 the lag-0 covariance matrix. To find the POPs is equivalent to solving the eigenproblems of A and defining the temporal variation of each POP.

The usefulness of POP analysis has been demonstrated in the forecasting of ENSO (El Nino / Southern Oscillation) (Xu and v. Storch, 1990). It seems to yield satisfactory results when the signals under investigation have quasi-periodic behavior, such as the equatorial quasi-biennial oscillation and, to a lesser extent, ENSO (Xu and v. Storch, 1990; Xu, 1992). However, when trying to apply POP analysis to find the lagged connection between tropical sea surface temperature and extratropical atmospheric circulation, we found it to be quite sensitive to the number of EOF modes retained in calculation. Even the leading modes can appear very different when different number of EOF modes are retained for the POP analysis.

Like in EOF analysis, any estimated POP system matrix A' is the sum of an unbiased system matrix A and a disturbance $\delta(A)$. Here the disturbance is not only due to sampling errors, but also due to truncation errors and errors related to inverting a covariance matrix. Eigenvalues and eigenvectors for a nonsymmetric matrix can be either real or complex, and the eigenvectors are not necessarily orthonormal, so that the rule of thumb derived in North et al. (1982) is not suitable here. Hence, a closer investigation of the sensitivity of this analytic tool will provide us with a better understanding of this statistical method.

2 DEFINITION OF A SPECTRAL PORTRAIT OF A LINEAR SYSTEM y=Ax

The spectral portraits of a matrix A for a given A, A, are neighborhoods around each eigenvalue of A in the complex plane and are defined as follows: $\lambda_i \in A_\varepsilon$, if there exists a matrix disturbance $\delta(A)$ ($\|\delta(A)\| \le \varepsilon \|A\|$), which satisfies

$$\det[\lambda_\varepsilon I - (A + \delta A)] = 0 \qquad (1)$$

or equivalently (as proved by Godunov et al., 1990), if

$$\frac{\sigma_{min}(A - \lambda_\varepsilon I)}{\sigma_{max}(A)} \le \varepsilon \qquad (2)$$

σ_{min} and σ_{max} represent the smallest and largest singular values of the respective matrices, and I is the identity matrix.

For each eigenvalue, the maximum disturbance that can be imposed without its spectral portraits touching those of other eigenvalues is called 'tolerance' of this eigenvalue. Different eigenvalues may have different tolerances. By comparing the spectral portraits of two different matrices, or just comparing their tolerances, we can compare their sensitivities. Furthermore, if we can estimate the system error and then compare it with the tolerances of the system matrix, we can determine whether or not the system matrix is effectively stable or effectively degenerate.

3 SYSTEM ERRORS OF THE POP SYSTEM MATRIX

As discussed earlier, the POP system matrix is given by

$$A = C_1 \cdot C_0^{-1}, \qquad (3)$$

where $$C_{1ij} = \langle x_i(t+1) x_j(t) \rangle \qquad (4)$$

and $$C_{0ij} = \langle x_i(t) x_j(t) \rangle \qquad (5)$$

The error in the estimate of A due to errors in estimation of C_0 and C_1 is given by

$$\delta A \cong C_1 \cdot \delta(C_0^{-1}) + \delta(C_1) \cdot C_0^{-1} \qquad (6)$$

so that $$\|\delta A\| \le \|C_1 \cdot \delta(C_0^{-1})\| + \|\delta(C_1) \cdot C_0^{-1}\| \qquad (7)$$

Here, we mainly consider the disturbance due to the first term on

the right hand side of (7), since we believe that the inversion of the covariance matrix C_0 is the main contribution to δA.
Therefore

$$\|\delta A\| \le \|C_1\| \cdot \|\delta(C_0^{-1})\| \qquad (8)$$

Now C_0 is a diagonal matrix and $C_{0ii} = \lambda_i$. λ_i represents the i^{th} diagonal element or i^{th} eigenvalue of C_0, therefore,

$$\|\delta(C_{0ii}^{-1})\| = \left\|\delta\left(\frac{1}{\lambda_i}\right)\right\| = \left\|\frac{\delta\lambda_i}{\lambda_i^2}\right\| \le \left\|\frac{1}{\lambda_i}\right\| \cdot \left\|\frac{\delta\lambda_i}{\lambda_i}\right\|, \text{ where}$$

$$\left\|\frac{1}{\lambda_i}\right\| \le \frac{1}{\lambda_{min}}$$

Here, $\lambda_{min} = \lambda_{min}(C_0)$, the smallest eigenvalue or the smallest diagonal element of C_0.
By applying the approach of North et al. (1982) ($\delta\lambda_\alpha / \lambda_\alpha \approx (2/N)^{1/2}$), N is the number of temporal degrees of freedom in the sample, which represents the part of error that can be attributed to sampling fluctuations). We obtain

$$\|\delta(C_0^{-1})\| \le \left(\frac{2}{N}\right)^{\frac{1}{2}} \cdot \frac{1}{\lambda_{min}} \qquad (9)$$

Furthermore, equation (3) is equivalent to $C_1 = A \cdot C_0$, therefore, $\|C_1\| \le \|A\| \cdot \|C_0\|$, or

$$\|A\| \ge \frac{\|C_1\|}{\|C_0\|} \qquad (10)$$

By applying (8), (9) and (10), we can obtain the relative error due to the disturbance of inversion of the covariance matrix:

$$\frac{\|\delta A\|}{\|A\|} \le \frac{(\frac{2}{N})^{\frac{1}{2}} \cdot \frac{1}{\lambda_{min}} \cdot \|C_1\|}{\|A\|} \le \frac{(\frac{2}{N})^{\frac{1}{2}} \cdot \frac{1}{\lambda_{min}} \cdot \|C_1\| \cdot \|C_0\|}{\|C_1\|} \cdot$$

$$= \left(\frac{2}{N}\right)^{\frac{1}{2}} \cdot \frac{\lambda_{max}}{\lambda_{min}} \sim \varepsilon$$

Hence, we obtain the following rule of thumb for the disturbance amplitude of POP analysis due to the first term of (7) on the right hand side.

$$\varepsilon = \left(\frac{2}{N}\right)^{\frac{1}{2}} \cdot cond(C_0) \qquad (11)$$

where $cond(C_0) = \frac{\lambda_{max}}{\lambda_{min}}$, the condition number of C_0

Hereafter, we will refer to ε obtained from (11) simply as the POP system error. The system error estimated by this formula is consistent with equation (8) in that the system error includes two parts: one is the sampling error, which is represented as $(2/N)^{1/2}$, the other is the error related to the inversion of the covariance matrix C_0, which is represented as the condition number of C_0. In the next section, we will show some examples that EOF truncation error can lead to a large $cond(C_0)$, and hence to a large system error.

4 EXAMPLES

Example 1: An idealized propagating signal and a Monte Carlo experiment

As we mentioned earlier, POP analysis is generally successful at capturing periodic signals. As a first example, we therefore generated a 24-by-24 dimensional covariance matrix from a process that contains an idealized propagating signal. This process is represented by the equation

$$y(t) = \cos[(\omega_1 t - \frac{\pi}{6})x] \qquad (12).$$

Applying EOF analysis to the 24-by-24 covariance matrix, we keep PCs for the first 2 leading EOFs to form a 2-by-2 POP system matrix. POP analysis captures the propagating mode well in terms of the amplitude and frequency of the signal (not shown). The two eigenvalues are presented as two dots in Fig. 1a. All the contours surrounding the two eigenvalues in Fig. 1a together constitute the spectral portraits of the system matrix. The area enclosed by each contour in the figure represents all the possible values that one or both eigenvalues can take under the specified amount of disturbance (here, 20%, 50%, 75% and 120%, respectively). The tolerance for both eigenvalues is between 75% and 80%. At a disturbance of 75% the eigenvalues are still well separated. When the disturbance increases to 80% (not shown), the corresponding spectral portraits start to merge. This merging or mixing represents the mixing of the eigenvalues and eigenvectors, and hence means that the system matrix is degenerate at a disturbance somewhere between 75% and 80%.
o test our results, we performed a Monte Carlo experiment. We randomly added disturbance matrices to the system matrix under the condition that the norm of the disturbance does not exceed 50% of the norm of the matrix. All the eigenvalues for the disturbed system matrix are plotted in Fig. 1b. It is evident that all the eigenvalues for the disturbance matrices fall within the expected neighborhoods.

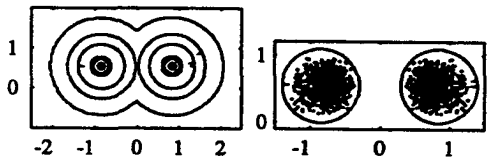


Figure 1: (a) Spectral portraits of POP system matrix as applied to an idealized propagating signal. The disturbances applied to the system are 20%, 50%, 75% and 120%. The 20% contour is thickened. (b) Eigenvalues of the system matrix subject to a random disturbance whose norm is less than 50% of that of the original matrix.

Example 2: An idealized propagating signal and a standing wave

As in Example 1, we generated a 24-by-24 dimensional covariance matrix from a process that contains one propagating mode and one standing mode. This process is represented by the equation

$$y(t) = \cos[(\omega_1 t - \frac{\pi}{6})x] + \sin(\frac{\pi}{6}x)\cos(\omega_2 t). \quad (13)$$

Applying EOF analysis to the 24-by-24 covariance matrix, we keep the first three PCs to form a 3-by-3 POP system matrix. The three eigenvalues are presented as three dots in Fig. 2. As in Example 1, POP analysis captures the propagating mode well in terms of its amplitude and frequency, but it recovers only to about 70% in terms of the amplitude of the standing wave. In this case (Fig. 2), the tolerance for all three eigenvalues is between 20% and 30%, which is much lower than in the previous example. Hence, the system tends to be less stable when a non-propagating signal is mixed in with the data.

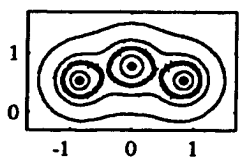


Figure 2: As Fig. 1a, but for a system with an idealized propagating mode and a standing mode. The disturbances applied to the system are 10%, 20%, 30% and 50%. The 20% contour is thickened.

Example 3: The Quasi-biennial Oscillation

As presented in Xu and v. Storch (1990), POP analysis can successfully capture the biennial oscillation signal. Here, we want to investigate the sensitivity of the corresponding POP system matrix.

The dataset we used here consists of 38 years (1956-1993) of monthly zonal wind at equatorial stations Canton Island, Gan and Singapore measured at the levels of 70, 50, 40, 30, 20, 15 and 10 mb. We applied EOF analysis to this dataset. The two leading modes explain 99.6% of the total variance. The third mode only explains 0.2% of the total variance, and so we consider it to be noise. We performed POP analyses by first retaining PCs for the first two leading EOF modes, then for the first three, to see how the sensitivity of the POP system matrix changes. Fig. 3a shows the spectral portraits of the POP system matrix under the disturbances of 5%, 15% and 20%. It shows that the tolerance of the disturbance for the system matrix is between 15% and 20% (the 15% curve is thickened). The system error is about 11%, which is smaller than the tolerance of the disturbances, hence the POP system matrix is stable.

We then form the POP system matrix by retaining PCs of the first three EOF modes, which is equivalent to adding some noise to the system. The spectral portraits of the system matrix under the disturbances of 5%, 10% and 20% (the 10% contour is thickened) after adding in the third mode are shown in Fig. 3b. Apparently, even though the leading modes change very little, the tolerance of the disturbance drops to some value between 10% and 5%. Apparently, this decrease in the stability of the system matrix is due to the EOF truncation error. Furthermore, the system error increases significantly from 11% to 125% due to the error in the inversion of the covariance matrix which is related to truncation problems (the condition number increases from 1.6 to 18.7) when the third mode is retained. Therefore, the system error exceeds the tolerance of the disturbance, and the system is unstable.

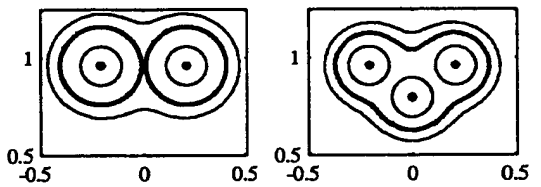


Figure 3: (a) As Fig. 1a, but using real QBO data with 2 EOF modes. The disturbances are 5%, 15% and 25%. The 15% contour is thickened. (b) Same as (a), but with 3 EOF modes. The disturbances are 5%, 10% and 20%. The 10% contour is thickened.

Example 4: Capturing the ENSO signal from Tropical SST and Southern Hemispheric SLP

Xu and v. Storch (1992) showed that POP analysis can well capture the ENSO process when the process is presented by Southern Hemisphere SLP anomalies. Here, we will also analyze ENSO, but first by using an SST anomaly field. We retained three and five EOF modes, respectively, to form two different POP system matrices in order to further examine the effect of EOF truncation. Fig. 4a shows the spectral portraits of the system matrix when three EOF modes are retained. The tolerance of the disturbances for this system matrix lies between 3% and 5%, which is considerably lower than for the QBO. In other words, this system matrix is much more sensitive than that of the QBO. The system error estimated by using equation (10) is 1.15, which is significantly larger than the tolerance. Hence, the system is unstable. It is worth noting that the first mode of the system is a standing mode, and the second and third modes shown as a pair of propagating modes do not have the same frequency as ENSO modes would have. Hence we did not capture any propagating ENSO mode by applying POP analysis to monthly SST data. This strong sensitivity can be further demonstrated by Fig. 4b, which shows the spectral portraits of the POP system matrix for five EOF modes under disturbances of 2%, 5%, 7% and 10%. The tolerance is about 2%, but the system error is much larger (180%). The lack of robustness of this POP system matrix hints at the possibility that when POP analysis is applied to a physical process which is not quasi- periodic, this method might tend to be more sensitive or less effective.

For the same analysis, we also calculated the spectral portraits of POP matrices formed from monthly SLP anomalies (not shown). When only two EOF modes were retained, we obtained a stable system. However, the corresponding period and damping time indicate that this pair of modes does not represent ENSO. Spectral portraits of the POP matrix with 9 EOFs as presented in Xu and van Storch (1992) were also examined. From the temporal variation of the time coefficient and the spatial patterns, we know that mode 5 and mode 6 are Southern Oscillation patterns. However, this system is very unstable, which means that we might not be able to capture the same mode in another sample.

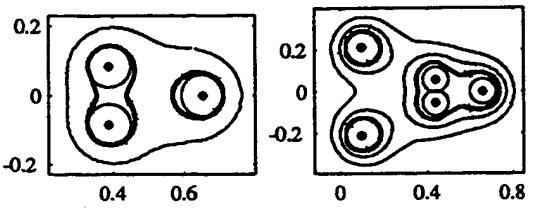


Figure 4: Spectral portraits of the POP system matrix based on PCs of tropical SST anomalies. (a) Retaining three modes, for disturbances of 3%, 5% and 10%; (b) retaining five modes, for disturbances of 2%, 5%, 7% and 10%. The 5% contours are thickened in both figures.

5 SUMMARY AND CONCLUSION

The examples shown above introduce the concept of spectral portraits of nonsymmetric matrices, and illustrate the use of spectral portraits in examining the sensitivity and stability of a matrix. Example 3 stresses an important issue concerning POP analysis: its sensitivity to the EOF truncation error and to the inversion of the covariance matrix. Adding minor EOF modes can change the POP system from a stable linear system to an unstable one. Example 4 demonstrates that when a system does not contain a well-defined propagating mode, the POP system matrix can be rather sensitive. The tolerance value for the disturbances of the POP system matrix due to the inversion of the covariance matrix provides a crude indication of the robustness of a POP system matrix. We have shown that, in practice, POP analysis system matrices can be ill-conditioned not only because of the inversion of a system matrix, but also because of the sampling error associated with limited data records.

Examining spectral portraits of a matrix is a simple and practical way of assessing the robustness of a linear system, and can be generally applied to any type of matrix analysis technique. The sensitivity test for POP system matrices discussed here is just one example. However, it is important to examine the sensitivity of a linear system matrix before attaching a physical interpretation to the results.

REFERENCES

Godunov, S. K., O. P. Kiriljuk, and W. I. Kostin, 1990: Spectral portraits of matrices. Preprint #3, Inst. of Math., Acad. Sci. USSR, Novosibrisk.

Xu, J.-S., 1990: Analysis and prediction of the El Nino Southern Oscillation phenomenon using Principal Oscillation Pattern Analysis. Examensarbeiten 4, Max-Planck-Institute fur Meteorologie, 95 pp.

_____, 1992: On the relationship between the stratospheric QBO and the tropospheric SO. J. Atmos. Sci., 49, 725-734.

_____, and H. von Storch, 1990: Predicting the state of the

Southern Oscillation using principal oscillation pattern analysis. J. Climate. 3, 1316-1329.

ACKNOWLEDGMENTS
We are thankful to Hans von Storch and Gregor Nitsche for their helpful comments.

CORRESPONDING AUTHOR
Yuan Zhang
JISAO
University of Washington
Box 354235
Seattle, WA 98195-4235
USA
email: zhang@atmos.washington.edu

NORMALISATION CONSTRAINTS IN ROTATED PRINCIPAL COMPONENT ANALYSIS: ILLUSTRATIONS IN CLIMATOLOGY

Ian T. Jolliffe and Barry Law

University of Aberdeen, Scotland

ABSTRACT

Principal components are widely used in climatology to reduce the dimensionality of large data sets. To simplify interpretation, the principal components are often rotated. Various normalisations are possible for the loadings of principal components. The implications of the choice of normalisation for the properties of the rotated components are not widely appreciated. This paper discusses these implications, and illustrates them using two examples.

1 INTRODUCTION

Principal components, also known as empirical orthogonal functions (EOFs), are in widespread use as a dimension-reducing tool in climatology. It is common practice to rotate some of these components in order to provide a simplified interpretation. The merits of rotation, in general, and of different types of rotation, have been widely debated - see, for example, Richman (1986), Jolliffe (1987). In this paper we restrict attention to orthogonal rotation of principal components, which has been used almost as a routine procedure in many applications.

Principal components are linear combinations of the originally measured variables, and they have the unique property of being uncorrelated with each other, and having vectors of loadings on the original variables which are pairwise orthogonal. Each component thus represents a 'separate' source of variability, and it is a common misconception that rotated components, which are also linear combinations of the original variables, will have the same property. In fact, it is impossible to simultaneously achieve both uncorrelated components and orthogonal loadings with the standard definition of orthogonal rotation.

Principal components may have their loadings normalised in a number of different ways. It turns out that whether or not either of the two properties of uncorrelated components or orthogonal loadings is retained after rotation depends on the normalisation chosen before rotation. In Section 2 we define three possible normalisations and discuss their properties. The use of the three normalisations, and their implications in terms of correlation and non-orthogonality for rotated components, is illustrated for two examples in Section 3. The paper concludes with a brief discussion of related topics such as factor analysis, and the interpretation of rotated components.

2 THE NORMALISATIONS

Suppose that $\mathbf{x}$ is a vector of p measured variables, typically the measurements of a meteorological variable at p grid points. The kth principal component may be denoted by $z_k = \mathbf{a}'_k\mathbf{x}$, where $\mathbf{a}_k$ is the vector of coefficients or loadings which defines the component. In many standard statistical packages which treat principal component analysis as a special case of factor analysis, $\mathbf{a}_k$ is normalised so that

$$\mathbf{a}'_k\mathbf{a}_k = \ell_k, \qquad (1)$$

where ℓ_k is the eigenvalue associated with $\mathbf{a}_k$, and is the variance of z_k when $\mathbf{a}'_k\mathbf{a}_k = 1$. With this normalization the elements of $\mathbf{a}_k$ can be interpreted as correlations between z_k and each of the original variables, assuming, as is often the case, that the variables in $\mathbf{x}$ have been standardised to have unit variance. A second commonly used normalisation for $\mathbf{a}_k$ is

$$\mathbf{a}'_k\mathbf{a}_k = 1. \qquad (2)$$

This normalization arises naturally in the derivation of principal components, and has the property of preserving distances.

A less common, but nevertheless useful, normalisation, is given by

$$\mathbf{a}'_k\mathbf{a}_k = \ell_k^{-1}. \qquad (3)$$

With this normalization the variances of all the components are the same (unity), which is appropriate if it is required that all the components should have equal importance.

Suppose that **A** is a $(p \times q)$ matrix, whose columns are vectors $\mathbf{a}_k$ of loadings associated with a subset of q components which are to be rotated. If $\mathbf{Z} = \mathbf{XA}$, then the ith row of **Z** consists of the values of the q selected components for the ith observation (the principal component scores or amplitudes). Rotating the q PCs is achieved by postmultiplying **A** by a $(q \times q)$ matrix **T** to obtain rotated loadings $\mathbf{B} = \mathbf{AT}$. For orthogonal rotation, **T** is an orthogonal matrix. Note that rotation is done with respect to the loadings, rather than the observations. It can be shown (Jolliffe, 1995) that whereas the original principal components have orthogonal loadings and uncorrelated scores, the rotated components using normalisation equation (1) possess neither of these desirable properties. The rotated components obtained from the normalisation in equation (2) have orthogonal loadings, but their scores are correlated. To achieve uncorrelated scores it is necessary to use the normalisation given by equation (3), but in this case the rotated loadings are not orthogonal.

3 EXAMPLES

Mediterranean Sea-Surface Temperatures

These data were analysed by Bartzokas et al. (1994) and consist of 43 years (1946-1988) of mean monthly sea-surface temperature (SST) in 16 5° latitude by 5° longitude grid boxes covering most of the Mediterranean. Separate analyses were done for different seasons, and for illustration we present results for spring, defined here as March, April, May. In a principal component analysis of these data, based on the correlation matrix, the first three components account for 83.5% of the variation in the 16 original variables. Loadings for these three components are given in Table 1, together with three sets of rotated loadings obtained from using the three normalisation constraints defined in Section 2 together with the varimax rotation criterion. It should be noted that in order to aid comparisons between the different sets of loadings, all have been renormalised for display purposes, using equation (2).

It can be seen from Table 1 that the results for the first three rotated components using normalisation (1), which correspond to those of Bartzokas et al. (1994), give large loadings to variables 11-16 (the Eastern Mediterranean), variables 5-11 (Central Mediterranean) and variables 1-5 (Western Mediterranean) respectively. All the loadings are positive, and so clearly not orthogonal. In addition there are large correlations between rotated component scores, with values between 0·78 and 0·93. These rotated components are certainly not measuring separate sources of variation.

For the normalisation (2) a similar pattern of loadings (in a different order) is evident, but there are two advantages over the more usual normalisation (1). First, the loadings are orthogonal, and second they appear to be simpler in structure. This latter suggestion is borne out by the value of the varimax criterion which at -8·10 is better for normalisation (2) than the value (-5·56) for normalisation (1). However, correlation between the rotated component scores remains high (0·40 to 0·65).

To remove correlation between rotated component scores we need to use normalisation (3). This is done by keeping large positive loadings for the same areas as in normalisation (2), but introducing some negative loadings, hence giving contrasts with other areas. The pattern of loadings is less simple than for normalisation (2), but the value of the varimax criterion (-6·08) is better than that for normalisation (1).

Table 1

Loadings for the Spring Principal Components

Unrotated						Rotated					
Normalisation (2)			Normalisation (1)			Normalisation (2)			Normalisation (3)		
-0.176	0.358	0.449	0.034	0.044	0.479	0.573	-0.179	0.013	-0.441	0.059	0.555
-0.234	0.275	0.223	0.097	0.171	0.404	0.423	0.017	0.031	-0.204	0.005	0.414
-0.220	0.367	0.321	0.052	0.138	0.477	0.533	-0.051	-0.009	-0.308	-0.010	0.525
-0.267	0.179	0.012	0.147	0.268	0.308	0.259	0.184	0.048	0.017	-0.039	0.259
-0.272	0.292	-0.027	0.092	0.313	0.366	0.320	0.237	-0.041	0.048	-0.144	0.336
-0.269	0.106	-0.314	0.145	0.391	0.167	0.036	0.425	-0.010	0.345	-0.178	0.061
-0.277	0.185	-0.286	0.117	0.402	0.227	0.109	0.422	-0.051	0.312	-0.217	0.139
-0.180	0.204	-0.371	0.014	0.356	0.138	0.030	0.432	-0.154	0.378	-0.312	0.076
-0.289	-0.058	-0.274	0.247	0.358	0.101	-0.047	0.378	0.131	0.321	-0.025	-0.044
-0.241	-0.110	-0.340	0.222	0.332	0.014	-0.141	0.391	0.114	0.382	-0.042	-0.134
-0.291	-0.178	0.002	0.338	0.220	0.118	0.018	0.144	0.308	0.059	0.225	-0.017
-0.261	-0.243	0.101	0.356	0.138	0.089	0.011	0.038	0.369	-0.037	0.323	-0.038
-0.243	-0.287	0.152	0.367	0.091	0.066	-0.001	-0.021	0.405	-0.087	0.381	-0.059
-0.264	-0.315	0.111	0.394	0.122	0.053	-0.032	0.019	0.424	-0.042	0.383	-0.090
-0.229	-0.294	0.243	0.369	0.040	0.080	0.036	-0.100	0.432	-0.178	0.435	-0.031
-0.254	-0.288	0.177	0.380	0.091	0.082	0.018	-0.034	0.421	-0.111	0.400	-0.044

Monthly mean sea level pressure

This data set consists of January mean sea level pressure at 328 grid points covering the Northern Hemisphere. The period of study is 1950-1984, so the 328 variables are measured at 35 time points. In a principal component analysis based on the correlation matrix, the first ten components account for 84·5% of the total variation. Rotating these 10 components, using the varimax criterion and the three normalisation constraints described in Section 2 produces some remarkable results. Figure 1 illustrates a sample of these results. Here we adopt the usual convention of displaying loadings in map form - this was not done for the first example because there were so few variables.

The first point to make about the maps of loadings is that it is very easy to find matching triples of maps from the three normalisations. Figure 1 displays three of these triples.

The second point is, that despite the visual similarity between maps of a triple, their properties can be quite different. In terms of overall simplicity, as measured by the varimax criterion, the ordering is the same as for the first example - normalisation (2) is much better (-108·22) than normalisation (3) (-96·38), which in turn is slightly better than normalisation (1) (-95·24).

To investigate the properties of the different solutions, consider the two triples {(1),2}, {(2),9}, {(3),8} and {(1),8}, {(2),6}, {(3),1}, where $\{(i), j\}$ denotes the jth rotated component using normalisation (i). Within each triple, the patterns on the three maps look very similar, and different from other triples. However, whereas {(3),8} and {(3),1} necessarily produce uncorrelated components, the correlation between {(1),2} and {(1),8} is -0·81, and that between {(2),6} and {(2),9} is -0·42. It is surprising that apparently small differences in map patterns can change correlations quite drastically.

4 DISCUSSION

The choice of normalisation constraints has important consequences for the properties of rotated principal components. There is little to recommend the most common normalisation (1). Normalisation (2) often gives simpler structure, and has orthogonal loadings. If it is required that the rotated components represent separate sources of variation, in the sense of having uncorrelated scores, then normalisation (3) is needed. It should be noted, however, that if rotation is restricted to subsets of components whose eigenvalues are similar, as recommended by Jolliffe (1989), then there will be little difference between the results obtained from the three normalisations.

The discussion above has been in terms of rotated principal components, rather than factor analysis which is different (see, for example, Jolliffe, 1986, Chapter 7). In fact, some software will produce 'rotated components' with loadings normalised according to (1), but with uncorrelated scores. This is achieved because a factor analysis model is being used and the scores are 'estimated' using a method which is equivalent to using loadings with normalisation (3). There is nothing wrong with this if factor analysis, rather than rotated principal component analysis, is the chosen approach, but it can then be misleading to present loadings normalised using (1) as a way of interpreting the factors in terms of the original variables.

Interpretation of principal components is, an any case, a trickier exercise than is often realised (see Cadima and Jolliffe, 1995) and similar considerations will arise in interpreting rotated principal components or factors.

References

Bartzokas, A., Metaxas, D.A. and Ganas, I.S., 1994, "Spatial and temporal sea-surface temperature covariances in the Mediterranean", Int. J. Climatology, Volume 14, pp.201-213.

Cadima, J.F.C.L. and Jolliffe, I.T., 1995, "Loadings and correlations in the interpretation of principal components". To appear in J. Appl. Statistics.

Jolliffe, I.T., 1986, "Principal component analysis", Springer-Verlag.

Jolliffe, I.T., 1987, "Rotation of principal components: some comments", Int. J. Climatology, Volume 7, pp.507-510.

Jolliffe, I.T., 1989, "Rotation of ill-defined principal components", Appl. Statistics, Volume 38, 139-147.

Jolliffe, I.T., 1995, "Rotation of principal components: choice of normalization constraints", J. Appl. Statistics, Volume 22, pp.29-35.

Richman, M.B., 1986, "Rotation of principal components", Int. J. Climatology, Volume 6, pp.293-335.

ACKNOWLEDGEMENTS

We are grateful to Dr Bartzokas and his colleagues, and to the UK Meteorological Office for permission to use the data sets. Discussions with Neil Ward were also very helpful. Barry Law is supported by an EPSRC CASE Studentship, in collaboration with the UK Meteorological Office.

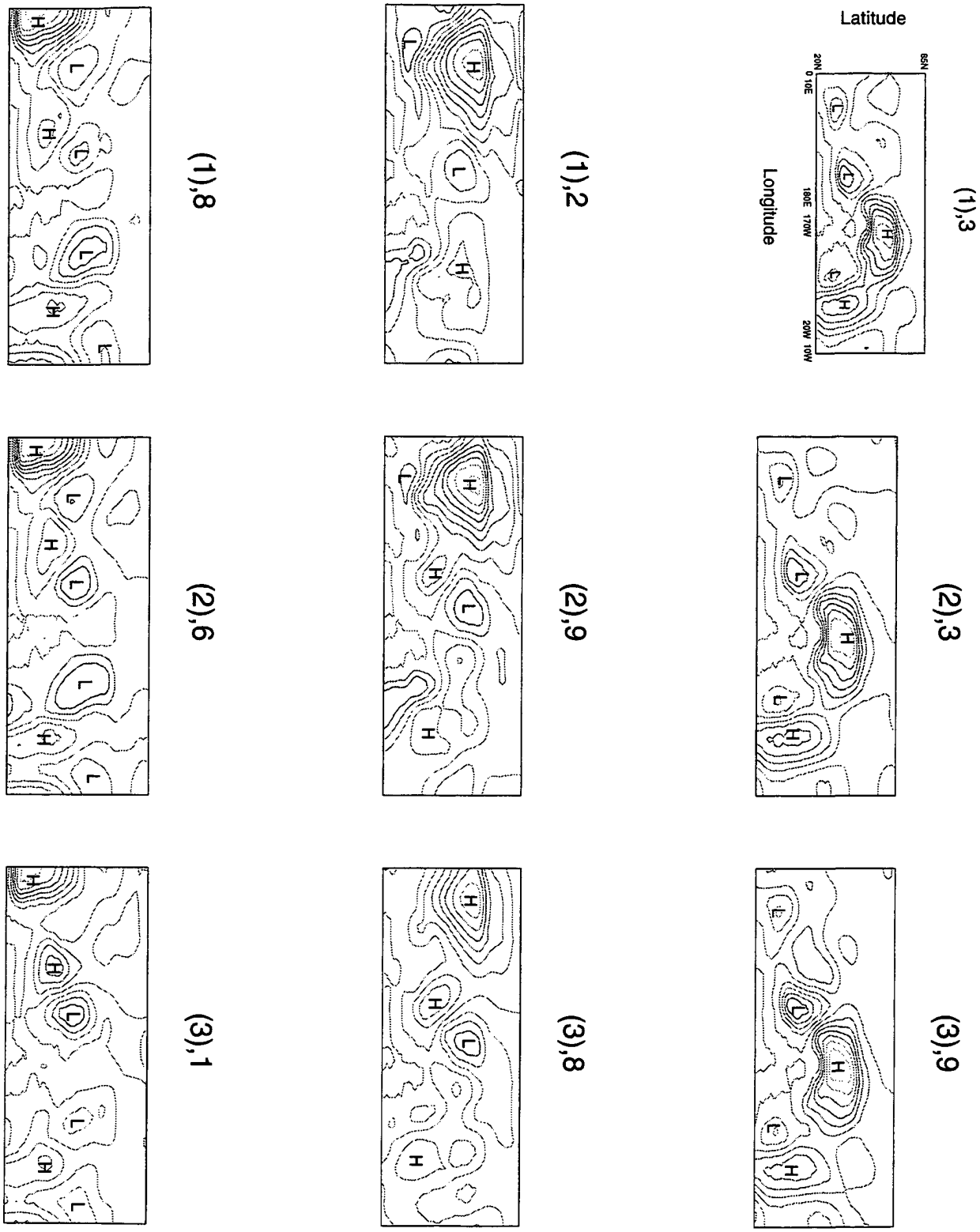


Figure 1 Rotated component loadings for mean sea level pressure. $(i)j$ denotes the jth rotated component using normalisation i.

ROBUSTNESS OF LOW-FREQUENCY CIRCULATION PATTERNS DERIVED FROM EOF AND ROTATED EOF ANALYSES

Xinhua Cheng, Gregor Nitsche, and John M. Wallace

Department of Atmospheric Sciences, University of Washington, Seattle, Washington

ABSTRACT

The robustness of low-frequency circulation patterns defined by unrotated and rotated empirical orthogonal functions are compared based on the Northern Hemisphere low-pass-filtered wintertime 500-hPa height field. The Pacific/North American pattern and the North Atlantic Oscillation are the most prominent modes of low-frequency variability in the data. The reproducibility of the spatial patterns derived from EOF and rotated EOF analysis is assessed by repeating the analysis on subsets of the data. The results indicate that rotated spatial patterns are less sensitive to sampling fluctuations than their unrotated counterparts.

1 INTRODUCTION

Since empirical orthogonal function (EOF) and rotated EOF (REOF) analyses are performed on datasets consisting of finite numbers of samples, the results are bound to suffer from sampling fluctuations. North et al. (1982) showed that spatial patterns of unrotated eigenvectors are subject to large sampling variability when the corresponding eigenvalues are not well separated from one another. Richman (1986) compared the robustness of unrotated and rotated solutions based on randomly generated synthetic datasets, and concluded that the rotated solutions are statistically more robust than their unrotated counterparts. Many studies of low-frequency variability have relied mainly upon REOF analysis. The purpose of this study is to provide a graphic example of the ambiguity in the definition of EOFs whose eigenvalues are not sufficiently well separated, and the greater robustness of the corresponding REOFs.

2 DATA

Our dataset consists of the Northern Hemisphere 10-day low-pass-filtered 500-hPa height anomalies, derived from the National Meteorological Center (NMC) final analyses from January 1946 through February 1989. Maps at 5-day intervals are selected from the low-pass-filtered anomaly field for each winter (December–February), which are then transformed from the 1977-point NMC full grid to a 445-point half resolution grid that covers the Northern Hemisphere north of 20°N.

Corresponding author address: Dr. Xinhua Cheng, Northwest Research Associates, Bellevue, Washington, USA.

The number of independent samples in the dataset is estimated by computing autocorrelations of the daily unfiltered anomaly time series (within the same winter) at each grid point. The one-day lag autocorrelation averaged over the hemisphere and over all the winters is ~0.72. Modeling the unfiltered data as a first order Markov process, we estimate the number of independent samples in the 10-day low-pass-filtered data conservatively as 300 based on the relationship between the filtered and unfiltered time series derived by Munk (1960).

3 RESULT

Figure 1 shows the spatial patterns of the first two EOFs. These two patterns contain elements of the Pacific/North American (PNA) pattern documented by Wallace and Gutzler (1981) and the North Atlantic Oscillation (NAO) identified by Walker and Bliss (1932). Spatial patterns of the higher EOF modes (not shown) tend to be more hemispheric in extent and progressively smaller in horizontal scale.

According to the formula derived by North et al. (1982), it is evident that only the first EOF mode is distinct from the subsequent modes. Even for the first mode, the separation is only two standard deviations (i.e., significant at the 95% level). If the interannual variability had been taken into account in estimating the number of independent samples through the use of a more involved statistical model, the statistical significance of the separation between the first two EOFs would have been even less.

To test the statistical robustness of the leading EOFs, we made repeated applications of the EOF analysis to subsets of the 10-day low-pass-filtered 500-hPa height field and examined how well the leading EOFs of the total record can be reproduced. A total of 50 subsets were generated for the analysis by collecting maps belonging to 22 randomly selected winters from the 44 winters in the original record. For convenience, we will refer to the EOFs based on the original record as the master EOFs and to the EOFs derived from the subsets as the perturbed EOFs.

Figure 2 illustrates how well the two leading master EOFs are reproduced in the subsets. The x and y axes in Fig. 2a point to the respective directions of the master EOFs 1 and 2, which together define a two-dimensional (2D) space. The points in the figure correspond to the projections of the first two perturbed EOFs in the 2D space: the

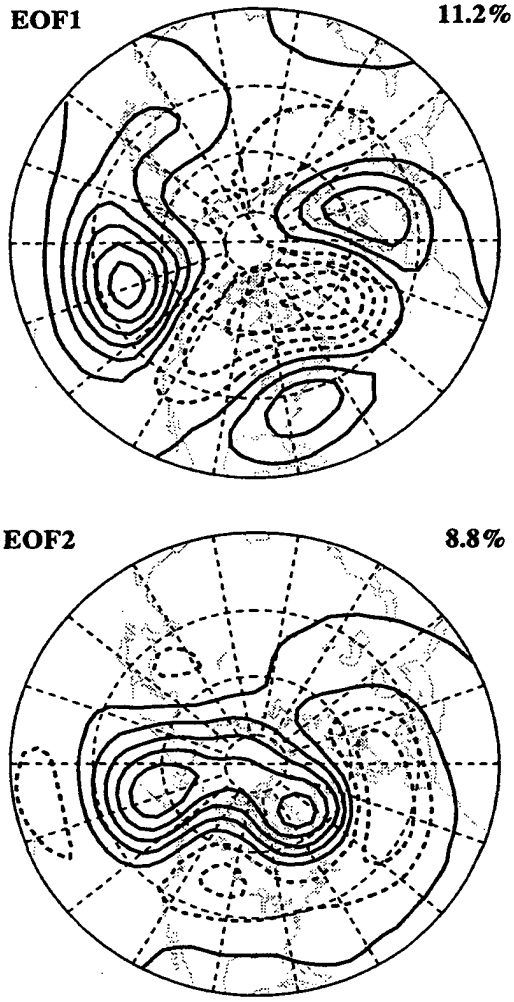


Figure 1. Spatial patterns of the two leading EOFs of the temporal covariance matrix of the 10-day low-pass-filtered 500-hPa height anomalies, scaled by the square root of the corresponding eigenvalue. Contour interval 20 m; negative contours are dashed. The percentage at the top right corner of each panel refers to the fraction of the hemispherically integrated variance explained by the mode.

asterisks denote the perturbed EOF1s and the crosses the perturbed EOF2s. All EOFs are scaled as unit vectors. Hence, coordinates of the points along the x and y axes can be interpreted as the correlation coefficient between the perturbed EOFs and the corresponding master EOFs. Because the number of independent samples in the subsets is about half that in the original record, we expect some mixing to occur between the two leading perturbed EOFs.

It is evident that the perturbed EOF1s (asterisks) in Fig. 2a tend to line up along a segment of a unit circle centered on the origin. The scatter of the asterisks along the unit circle in the y direction indicates that in the sampling fluctuations the

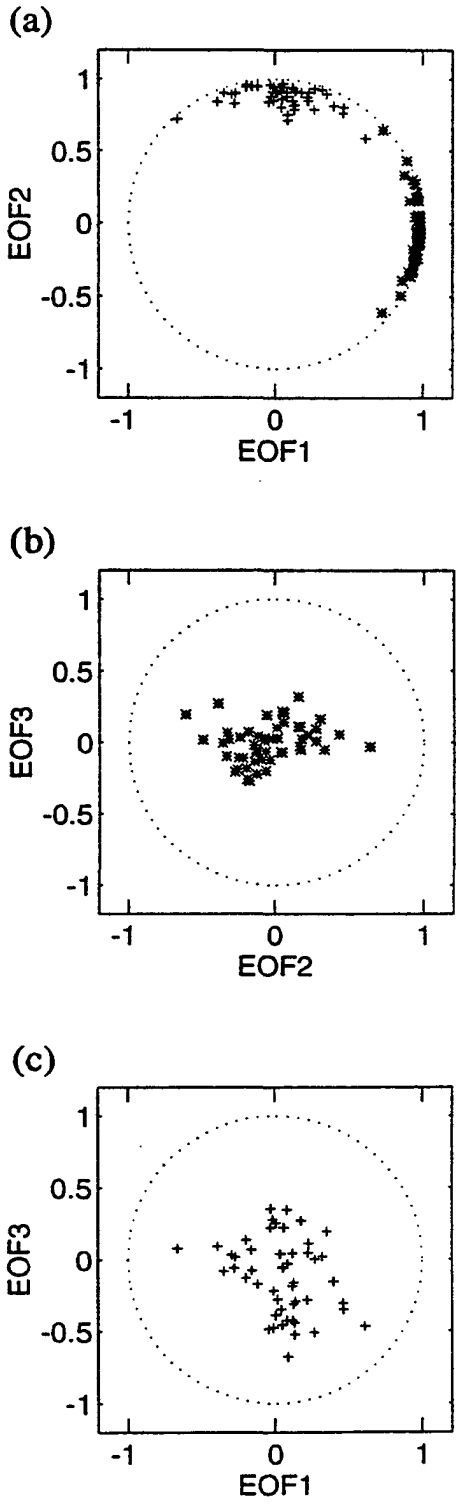


Figure 2. Projections of the two leading perturbed EOFs (asterisks for EOF1 and crosses for EOF2) based on randomly selected halves from the original data set onto the planes defined by the three leading EOFs based on the covariance matrix of the unperturbed 10-day low-pass-filtered 500-hPa height field. All the EOFs are scaled as unit vectors. The circle is centered at the origin and has unit radius.

EOF1s are primarily mixed with the master EOF2: the larger the projection on EOF2, the smaller the projection on EOF1. The mixing between EOFs 1 and 2 is also revealed in Fig. 2b, in which the perturbed EOF1s project more strongly upon master EOF2 than on master EOF3. The perturbed EOF2s (crosses) in Fig. 2a show a similar tendency to lie along the unit circle but some of them lie inside it, indicating that the perturbed EOF2s are mixed not only with the master EOF1 but also with higher EOF modes. It is evident from Fig. 2c that the perturbed EOF2s (crosses) project equally strongly onto the master EOF1 and EOF3 axes.

We applied varimax rotation to the 15 leading EOFs derived from the original data set. Figure 3 shows that the two leading REOFs correspond to the PNA pattern and the NAO, respectively. Both exhibit larger amplitudes over their principal centers of action than the leading EOFs in Fig. 1. These results are in agreement with early studies (i.e., Barnston and Livezey 1987; O'Lenic and Livezey 1988; and Kushnir and Wallace 1989) concerning the physical interpretation of the low-frequency circulation patterns despite differences in analysis procedures.

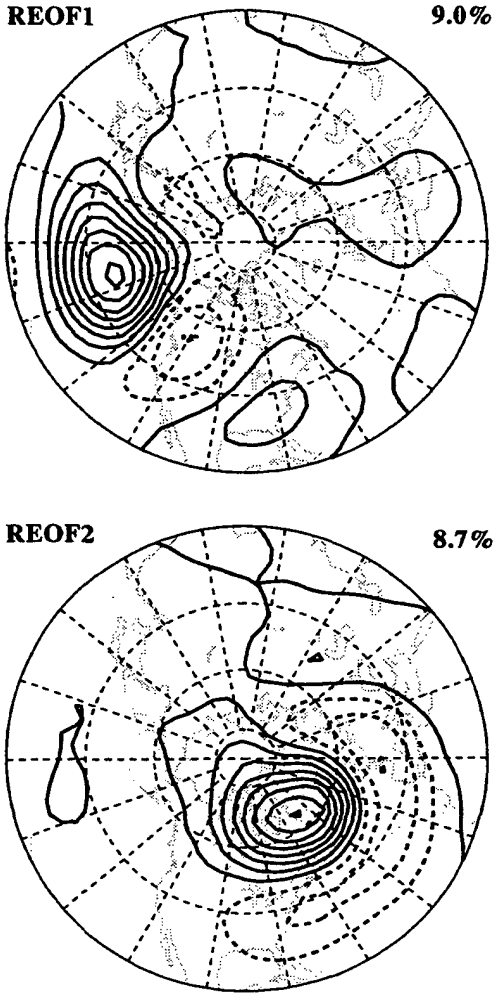


Figure 3. As in Figure 1 but for the two leading REOFs.

To evaluate the robustness of the REOFs, the 50 sets of the perturbed EOFs were also subjected to varimax rotation, retaining the 15 leading EOFs in each run. As with the unrotated EOFs, we will refer to the REOFs based on the original data as the master REOFs and to the REOFs derived from the subsets as the perturbed REOFs. The results are shown in Fig. 4, in which the x and y axes point to the respective directions of the master REOFs 1 and 2. The axes are drawn to be perpendicular to each other for purposes of presentation. Again, asterisks represent projections of the perturbed REOF1s and crosses the perturbed REOF2s. In comparison to Fig. 2a, it is evident that the points of the perturbed REOF1s and REOF2s are much more concentrated in the directions of the master REOF1 and 2 than the unrotated ones upon which they are based, indicating that little mixing occurs between them.

The uniqueness of the individual REOFs derives from the fact that they represent circulation anomalies in different regions of the hemisphere. The points corresponding to the perturbed REOFs are located inside the unit circle, suggesting that they may mix with REOFs other than 1 and 2. In this case, mixing is most likely to occur among the patterns whose primary centers of action are located in the same geographic regions. We examined the 2D planes defined by the master REOFs whose centers of action are in the same geographic regions as those of the two leading REOFs and found that the projections of the perturbed REOF1s and REOF2s onto the planes (not shown) are much smaller than those in Figs 2b and 2c (i.e., the points are clustered much closer to the origin).

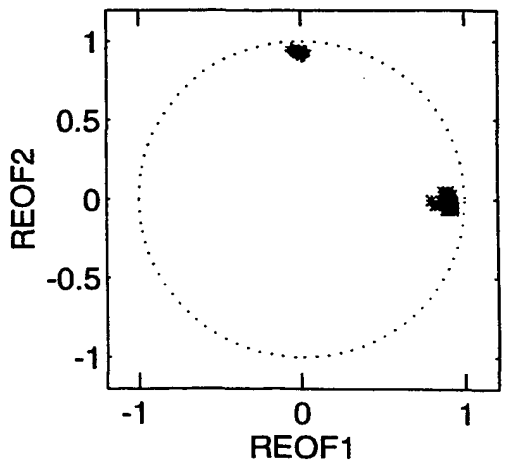


Figure 4. Projections of the two leading REOF's (asterisks for REOF1 and crosses for REOF2) derived from the perturbed EOF's onto the planes defined by the two leading REOF's of the unperturbed 10-day low-pass-filtered 500-hPa height field.

To test whether the two leading EOFs behave any differently from subsequent EOFs, we conducted the following two experiments on synthetic datasets. In the first experiment, the aforementioned robustness test was applied to a dataset constructed by removing the EOF1 component from the original record. Results of the analysis (not shown) indicate that mixing occurs in the same sense as in the case of the original data. Namely, the leading EOF tends to mix with the second EOF, which also mixes with the third EOF and so on, and the amount of mixing increases for the higher EOF modes whose eigenvalues lie closer to one another.

In the second experiment, a synthetic dataset was constructed by increasing the amount of variance associated with the EOF3 to the level of EOF2 in the original record simply by rescaling the corresponding time series of expansion coefficients. Note that the spatial patterns of the EOFs and REOFs of the synthetic dataset are identical to their counterparts based on the original record except for a slight difference in the fractional variance explained by each mode. The results concerning the robustness of the spatial patterns of EOFs 1 and 2 are shown in Fig. 5, in which the x and y axes are parallel to the respective master EOFs 2 and 3. Because the EOFs 2 and 3 form a degenerate multiplet in the synthetic dataset, the perturbed EOF1s (asterisks) are mixed with both the master EOFs 2 and 3 while the perturbed EOF2s (crosses) appear as linear combinations of the master EOFs 2 and 3. Upon varimax rotation of the perturbed EOFs based on the synthetic data, the master EOFs can be reproduced just as well as those based on the original data shown in Fig. 5, indicating the effectiveness of rotation in isolating real physical structures in the data even when the unrotated eigenvectors are completely degenerate.

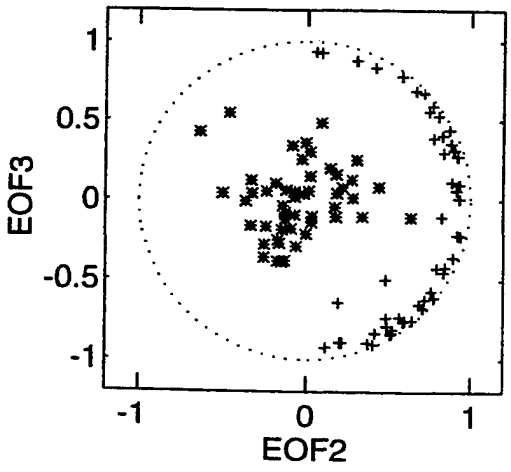


Figure 5. As in Fig. 2a but for the analysis based on the temporal covariance matrix of a synthetic dataset constructed by increasing the amount of variance explained by EOF3 to the level of that explained by EOF2 in the unperturbed 10-day low-pass-filtered 500-hPa height field.

4 REFERENCES

Barnston A., and R. E. Livezey, 1987, "Classification, seasonality and persistence of low-frequency circulation patterns", Mon. Wea. Rev., 115, 1083-1126.

Kushnir, Y., and J.M. Wallace, 1989, "Low-frequency variability in the Northern Hemisphere winter: geographical distribution, structure and time-scale dependence", J. Atmos. Sci., 46, 3122-3142.

Munk, W. H., 1960, "Smoothing and persistence", J. Meteor., 17, 92-93.

North, G. R., T. L. Bell, R. F. Cahalan and F. J. Moeng, 1982, "Sampling errors in the estimation of empirical orthogonal functions", Mom. Wea. Rev., 110, 699-706.

O'Lenic, E. A., and R. E. Livezey, 1988, "Practical considerations in the use of rotated principal component analysis (RPCA) in diagnostic studies of upper-air height fields", Mon. Wea. Rev., 116, 1682-1689.

Richman, M. B., 1986, "Rotation of principal components", J. Climatol., 6, 293-335.

Walker, J.M., and E.M. Bliss, 1932, "World Weather V", Mem. Roy. Meteor. Soc. 4, 53-84.

Wallace, J. M., and D. S. Gutzler, 1981: Teleconnections in the geopotential height field during Northern Hemisphere winter. Mon. Wea. Rev., 109, 784-812.

EFFICIENT PREDICTION OF COVARIANCES USING SINGULAR VECTORS

Martin Ehrendorfer[1] and Joseph J. Tribbia[2]

[1]Institute for Meteorology and Geophysics
University of Vienna, A-1190 Vienna, Austria

[2]National Center for Atmospheric Research
Boulder, Colorado 80307, USA

1. INTRODUCTION

The importance of quantitatively assessing the uncertainty of meteorological forecasts has been recognized since the very early days of weather forecasting. This assessment of uncertainty has recently attracted considerable attention in the context of efforts directed towards the direct prediction of the uncertainty of forecasts made with dynamical numerical weather prediction (NWP) models. The uncertainty of forecasts made with NWP models arises from uncertainty caused through two distinct error sources; namely, from errors in the specification of the initial model state, as well as from imperfections in the model formulation.

Neglecting for the moment the latter source of uncertainty, it is, in principle, for a given NWP model possible to predict the evolution of initial state uncertainty that is (ideally) described in terms of a probability density function (pdf) ρ_0. One possible strategy, also called the Monte Carlo method, consists of generating an initial ensemble through (random) sampling from ρ_0, and evolving each of the resulting initial states by the model. As the sample size is increased, reliable estimates of (moments of) the time–evolved pdf ρ_t may be computed by appropriately averaging over the individual ensemble members. This approach accounts for the initial state uncertainty insofar as each of the initial states selected is a likely candidate for the initial model state, consistent with the accuracy of the available analysis.

The Monte Carlo method, as described above (originally proposed by Leith 1974), while being cheaper than solving the relevant stochastic–dynamic equations (first posed in a meteorological context by Epstein 1969), or even the relevant Liouville equation, is still prohibitively expensive in the context of state-of-the-art operational NWP models, due to the large dimension of their associated phase space. Ongoing efforts at operational centers (e.g., European Centre for Medium–Range Weather Forecasts (ECMWF); see Molteni et al. 1995) are therefore concentrating on the design of sampling strategies that allow one to gain information about the evolution of ρ_0 even in the case when the sample size is restricted to be small (when compared to the dimension of the model phase space). Such techniques based partly on the concept of directions of most rapid error growth, as described by singular vectors (SVs), are collectively referred to here as ensemble prediction methods.

In the design of ensemble prediction methods the goal of primary interest is the prediction of the accuracy (or skill) of a single (control) forecast. This goal is considerably more difficult to achieve than the prediction of the evolution of ρ_0 both conceptually and practically. The additional difficulty of this question arises from the fact that (i) there does not exist a necessarily simple relationship between ρ_t and the accuracy of the control forecast, and that (ii) model errors presumably play an important role.

In the present paper the main emphasis will be on the design of ensemble prediction methods in the absence of model formulation errors. In this context, it is particularly emphasized that it is important to define the specific objective that is desired to be achieved by a particular ensemble prediction method. Here we concentrate on a method that is closely related to the approach taken at ECMWF, called here the SV–method. It is shown that – under certain assumptions, most notably the assumption of tangent–linear error evolution – the SV–method is optimal for the reconstruction of the (tangent–linearly approximated) forecast error covariance matrix $\hat{\mathbf{S}}_t$ (i.e., the dispersion matrix of the time–evolved pdf ρ_t). The optimality of this method arises from the fact that the (tangent–linearly) time–evolved SVs of the resolvent of a given tangent–linear model constitute – appropriately scaled – the orthogonal eigenvectors of $\hat{\mathbf{S}}_t$. This result, in turn, allows the most efficient reconstruction of $\hat{\mathbf{S}}_t$, given a pre–specified number of permissible model integrations.

2. FORMULATION OF THE PROBLEM

Consider the representation of any given NWP model through the following vector–valued mapping N_t between the state of the model at two different times:

$$X_t = N_t(X_0), \tag{1}$$

where X_t (X_0, respectively) represents the model state at time t (at the initial time, respectively). Eq. (1) can be considered as the solution (in discrete form) of the continuous model equations. Taking into account uncertainty in the initial state requires that X_0 be regarded as a random variable. At the same time, it is assumed that each realization of that random variable is transported in time through (1). Ideally, initial state uncertainty is described through the initial pdf ρ_0; however, in the absence of sufficient information, one might be content with a specification of mean– and (co)variance–structure of X_0 in the form:

$$E(X_0) = X_0^c \qquad D(X_0) = \mathbf{V}. \tag{2}$$

The expectation operator E of any function G of the model state X_τ at any time τ is defined as integral over the phase space Ω utilizing the time–evolved pdf ρ_τ:

$$E[G(X_\tau)] \equiv \int_\Omega G(X_\tau)\rho_\tau(X_\tau)dX_\tau. \tag{3}$$

In (2) it is assumed that the mean of X_0 is given by X_0^c which may be taken as the actual analysed state of the atmosphere, the subscript c standing for *control*. Similarly, the variance/covariance structure is prescribed as the positive–definite matrix $\mathbf{V}$ with the definition of the dispersion operator D as:

$$D(X_\tau) \equiv E\Big[\Big(X_\tau - E(X_\tau)\Big)\Big(X_\tau - E(X_\tau)\Big)^T\Big], \quad (4)$$

where the superscript T denotes the transpose.

The problem considered in the remainder of this paper may now be posed as follows: given a model of the form (1), and X_0^c and $\mathbf{V}$, describe a method for optimal prediction of the time–evolved covariance matrix $\mathbf{S}_t$ defined as:

$$\mathbf{S}_t \equiv D(X_t). \quad (5)$$

3. COVARIANCE PREDICTION WITH SVs

It is obvious that the above problem above may be approached by either the Monte Carlo method or through integration of the stochastic–dynamic equations. These methods seem, of course, to be the only viable approaches when significant nonlinearities are present in (1). Below the problem is addressed for the situation where a tangent–linear error evolution is appropriate.

In the situation where the tangent–linear approximation is valid, the evolution of deviations from a reference state (denoted by an overbar) is governed by:

$$Z_t \equiv X_t - \bar{X}_t \simeq \mathbf{R}_t(X_0 - \bar{X}_0) = \mathbf{R}_t Z_0, \quad (6)$$

where $\mathbf{R}_t$ represents the linearization of N_t at $\bar{X}_t$. The tangent–linear approximation seems to be a realistic assumption even for state–of–the–art NWP models for $t \sim 24$ hours and correspondingly small initial errors Z_0 (see, e.g., Lacarra and Talagrand 1988). Assuming the validity of (6), and:

$$\bar{X}_0 = X_0^c \quad (7)$$

it can be shown that $\mathbf{S}_t$ as defined in (5) can be approximated as:

$$\hat{\mathbf{S}}_t = \mathbf{R}_t \mathbf{V} \mathbf{R}_t^T = (\mathbf{R}_t \mathbf{V}^{1/2})(\mathbf{R}_t \mathbf{V}^{1/2})^T, \quad (8)$$

where $\hat{\mathbf{S}}_t$ denotes the tangent–linear approximation of $\mathbf{S}_t$ (the second equality will be used below). Thus, in the tangent–linear framework the initial covariance matrix $\mathbf{V}$ evolves into $\hat{\mathbf{S}}_t$ as given above. This result has been stated in slightly different form by Houtekamer (1993).

Certain ensemble prediction methods that are currently under investigation rely on an initial ensemble generated from so–called fastest–growing perturbations, or SVs (e.g., Buizza et al. 1993, Ehrendorfer and Errico 1995). It is pointed out below that this SV–method allows an optimal reconstruction of $\hat{\mathbf{S}}_t$ (if certain requirements are met).

The SVs are defined here as the structures Y maximizing the non–negative cost function:

$$J(Y) = (\mathbf{R}_t Y)^T (\mathbf{R}_t Y), \quad (9)$$

subject to the normalizing constraint:

$$Y^T \mathbf{V}^{-1} Y = 1. \quad (10)$$

The solution to this maximization problem is obtained from the solution of the symmetric eigenproblem:

$$(\mathbf{R}_t \mathbf{V}^{1/2})^T (\mathbf{R}_t \mathbf{V}^{1/2}) \hat{Y} = \lambda \hat{Y}, \quad (11)$$

with $\hat{Y}^T \hat{Y} = 1$ and:

$$Y = \mathbf{V}^{1/2} \hat{Y}. \quad (12)$$

Rewriting (11) in the matrix form:

$$(\mathbf{R}_t \mathbf{V}^{1/2})^T (\mathbf{R}_t \mathbf{V}^{1/2}) = \hat{\mathbf{Y}} \mathbf{\Lambda} \hat{\mathbf{Y}}^T \quad (13)$$

shows that $\hat{\mathbf{Y}}$ provides an orthonormal decomposition of $(\mathbf{R}_t \mathbf{V}^{1/2})^T (\mathbf{R}_t \mathbf{V}^{1/2})$. Clearly, from the close relationship between this matrix and $\hat{\mathbf{S}}_t$ (see (8)), this decomposition can be used to find the eigenstructure of $\hat{\mathbf{S}}_t$ in the form:

$$\hat{\mathbf{S}}_t = \mathbf{\Pi} \mathbf{\Lambda} \mathbf{\Pi}^T, \quad (14)$$

where the orthonormal eigenvectors $\mathbf{\Pi}$ are given by:

$$\mathbf{\Pi} = (\mathbf{R}_t \mathbf{V}^{1/2}) \hat{\mathbf{Y}} \mathbf{\Lambda}^{-1/2}. \quad (15)$$

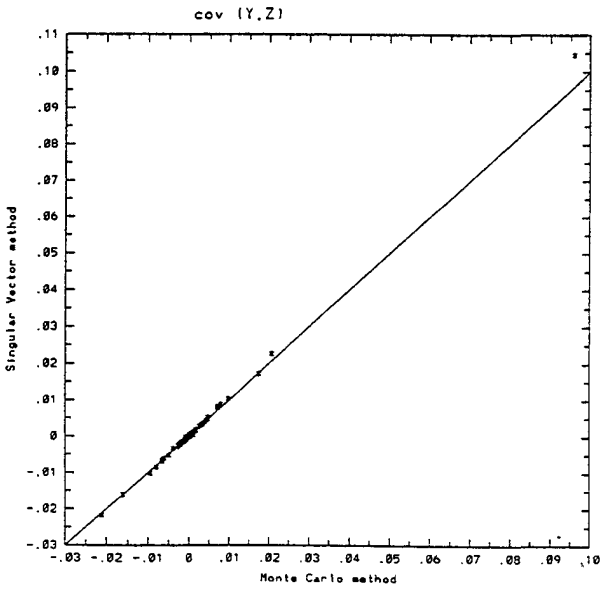


Fig. 1. Scattergram of cov(Y, Z) determined by Monte Carlo method (abscissa; 10^5 integrations) and by SV–method (ordinate, 1 tangent–linear integration).

This result shows that the time–evolved SVs are (up to the scalings in (15)) the eigenvectors of the tangent–linearly approximated covariance matrix of the model state X_t at time t. Due to the maximum–variance property of the eigenvectors of a covariance matrix, this result implies that $\hat{\mathbf{S}}_t$ can – for a given number of tangent–linear integrations (say, k) – be most efficiently approximated by the first k time–evolved SVs. In view of this property, the SV–method represents an optimal strategy for the problem of section 2. It seems important to emphasize in this context that the SVs do not in any sense sample extremes of the pdf (as is sometimes remarked), but rather account for a maximum possible (if reconstruction is restricted to k vectors) fraction of variance at time t.

4. ILLUSTRATION FOR A LORENZ SYSTEM

The approximation of the time–evolved covariance structure along the lines outlined above is illustrated here for the three–dimensional dynamical system presented by Lorenz (1984) as the simplest prototype of the atmospheric general circulation. The length of time–integration chosen here is such that the tangent–linear error evolution is a good approximation for the perturbations relevant here (see below); this time is referred to here as t_1 (2 non–dimensional time units). The model's free parameters are chosen such that it shows chaotic behavior; however, this irregularity does not play a significant role in the present context.

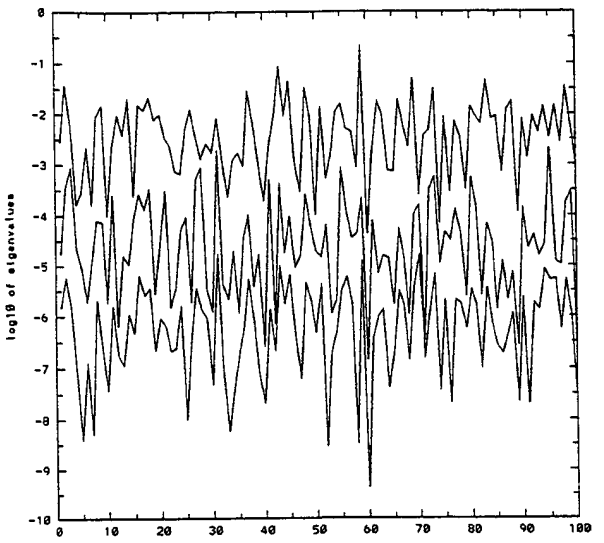


Fig. 2. The three eigenvalues appearing in (13) on a logarithmic scale for each of the 100 repetitions of the basic experiment.

The basic experiment consists of determining the time–evolved covariance matrix $\mathbf{S}_{t_1}$ in two ways. The first way consists of a simple Monte Carlo integration (ensemble size of 10^5) of the full nonlinear equations, with random sampling from the initial pdf (see below) for the specification of the initial conditions. The second way consists of computing $\hat{\mathbf{S}}_{t_1}$ as described in section 3; in the results shown here only $k = 1$ eigenvectors were used for the reconstruction. The initial pdf is taken as Gaussian, with diagonal $\mathbf{V}$ (entry of $\sigma^2 = 0.01^2$) and specified mean (see below). From the agreement of these two independently determined covariance matrices, the goodness of the approximation through the SV–method may be assessed, taking the Monte Carlo results as reference.

This basic experiment has been repeated one hundred times; the only difference between these repetitions (cases) concerns the mean of initial pdf (in each repetition the mean is taken as realization of a standard–normal random variable). Through this design the dependence of the properties of the SV–method on the position on the attractor can be investigated.

Figure 1 summarizes the results for one entry of $\mathbf{S}_{t_1}$, namely cov(Y, Z) (in this context, Y and Z denote the second and third component of the state vector). Apparently, the covariances determined by the SV–method are very close to their true (Monte Carlo) values. Such close correspondence depends crucially on the validity of the tangent–linear assumption which enters the derivation in section 3 at the very beginning. However, it is further of interest to note that reconstruction of the covariance matrix with only one eigenvector already leads to this remarkable agreement. It is also clear from this picture that in this situation the number of Monte Carlo integrations (10^5) is sufficient for very reliable determination of the covariances. The agreement between other entries of S (not shown) is in some cases slightly less satisfactory; reconstruction with $k = 2$ leads to improvement.

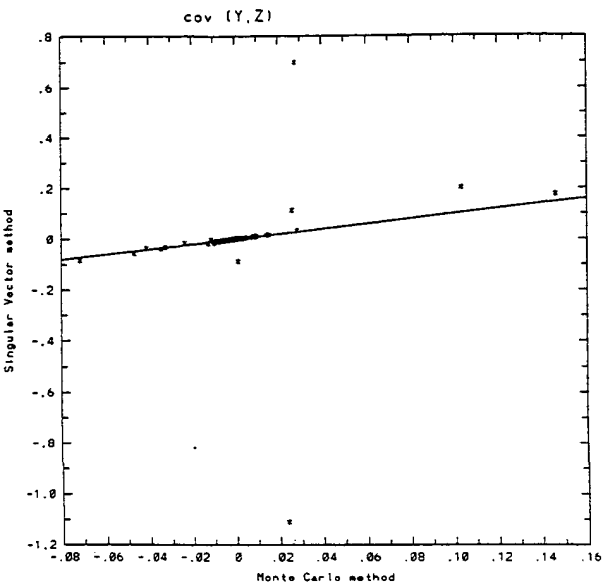


Fig. 3. As in Fig. 1, except for $2t_1$.

It is of interest to study the eigenvalues appearing in (13) for each of the 100 cases summarized in Fig. 1, because these eigenvalues are sometimes used as a surrogate for the predictablity of a specific (flow) situation. Note that in the present context these eigenvalues cannot, without further computation, be interpreted as growth rates due to the different choices for the norm in the cost function (9) and constraint (10). Each curve in Fig. 2 represents one eigenvalue (as a function of case number). In most cases the first and second eigenvalue are separated by several orders of magnitude. In some cases, however, these two eigenvalues are separated by less than a factor of ten (e.g., case 3). It turns out that in these cases it becomes necessary to use $k = 2$ for satisfactory reconstruction of *all* entries of S (see above).

For a given perturbation size (determined typically by the entries of $\mathbf{V}$), the tangent–linear approximation becomes increasingly less accurate, as the integration time t increases.

This fact leads, in turn, to the question to what extent the method investigated above can yield useful results beyond the tangent–linear regime, as nonlinear effects become important. Clearly, the answer will, at least partially, depend upon the model used.

In the present context, Fig. 3 shows a scattergram of $\mathrm{cov}(Y, Z)$ obtained in a manner completely analogous to the computations leading to Fig. 1, with the notable exception that the time of integration has been extended to $2t_1$. The approximation of $\mathbf{S}_t$ through the SV–method is not nearly as good as before. The primary reason must be that the tangent–linear approximation is no longer valid to the same degree of accuracy as before. Using $k = 2$ instead of $k = 1$ does not lead to an improvement.

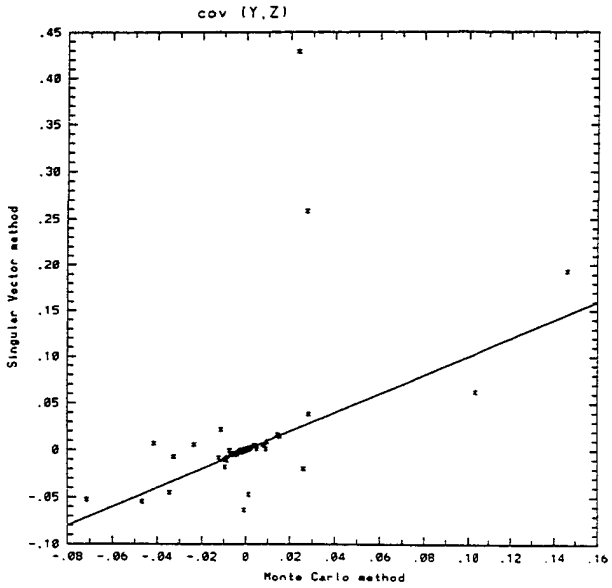


Fig. 4. As in Fig. 1, except for $2t_1$, and modified (nonlinear) SV–method.

Instead of performing tangent–linear computations up to $2t_1$, an empirical extension of the SV–method has been investigated (similar to the one used at ECMWF). Specifically, SVs were computed by optimizing up to time t_1. These SVs were then evolved nonlinearly up to time $2t_1$. Clearly, one is faced here with the problem of scaling the perturbations to be added to the control (basic) state X_0^c. In the present context, the scaling is done in the exact same manner as in the tangent–linear computations, namely such that the difference of time–evolved perturbed state and the time–evolved unperturbed state equals the corresponding column of $\mathbf{\Pi}\mathbf{\Lambda}^{1/2}$ (see (14)).

Results obtained with this modified nonlinear SV–method are shown in Fig. 4. It is evident that the modified SV–method gives a better approximation to the Monte Carlo covariance estimates than the unmodified (tangent–linear) method. However, the overall agreement is still poor. It is noted specifically that the overall range of $\mathrm{cov}(Y, Z)$ (on the ordinate) is smaller in Fig. 4 than in Fig. 3, indicating that including the effect of nonlinearities gives a better representation of the correct magnitude. This result also shows that the role of nonlinearities is not necessarily to lead to more rapid growth of second moments.

5. CONCLUDING REMARKS

It has been shown that the eigenvectors of the forecast error covariance matrix can – in a tangent–linear context – be computed as the solution of a specific optimization/maximization problem, sometimes referred to as optimal growth problem. It is of importance to note that the initial covariance structure enters this maximization problem through the constraint (10). The relevant discussion clearly shows the properties of this so–called SV–method. This method performs very well in a tangent–linear context. It has been pointed out that the optimality properties of this method do not immediately carry over to the nonlinear regime, even for the low–dimensional Lorenz model considered. It is necessary to investigate more carefully the preliminary results presented here. One relevant point concerns the scaling of perturbations in the nonlinear modified SV–method. Another point that needs to be addressed is the performance of this method within more realistic models. Finally, this method needs to be studied not only in a perfect–model context (as done here), but also in the presence of model errors. Theoretical extensions to include simple noise representations, as well as projection operators seem easily possible. Relevant studies are underway.

Acknowledgment. The National Center for Atmospheric Research is sponsored by the National Science Foundation.

REFERENCES

Buizza, R., J. Tribbia, F. Molteni, and T. Palmer, 1993: Computation of optimal unstable structures for a numerical weather prediction model. *Tellus*, **45 A**, 388-407.

Ehrendorfer, M., and R.M. Errico, 1995: Mesoscale predictability and the spectrum of optimal perturbations. *J. Atmos. Sci.*, in press.

Epstein, E.S., 1969: Stochastic dynamic prediction. *Tellus*, **21**, 739-759.

Houtekamer, P.L., 1993: Global and local skill forecasts. *Mon. Wea. Rev.*, **121**, 1834-1846.

Lacarra, J.-F., and O. Talagrand, 1988: Short-range evolution of small perturbations in a barotropic model. *Tellus*, **40A**, 81-95.

Leith, C.E., 1974: Theoretical skill of Monte Carlo forecasts. *Mon. Wea. Rev.*, **102**, 409-418.

Lorenz, E.N., 1984: Irregularity: a fundamental property of the atmosphere. *Tellus*, **36A**, 98-110.

Molteni, F., R. Buizza, T.N. Palmer, and T. Petroliagis, 1994: The ECMWF ensemble prediction system: methodology and validation. Submitted to *Q. J. R. Meteorol. Soc.*

TWO METHODS TO DESCRIBE THE STATISTICAL QUALITY OF CLUSTER ANALYSIS PATTERNS

F.-W. Gerstengarbe and P. C. Werner

Potsdam Institute for Climate Impact Research, Potsdam, Germany.

ABSTRACT

Two statistical methods are presented which on the one hand enable to define more precisely the structure within a cluster and on the other hand to assess the quality of separation between the clusters. An example shows the applicability of the suggested methodology.

1 INTRODUCTION

Multivariate statistical procedures are the presently most developed methods to describe complex correlations. They enable to evaluate several coherent parameters on a distribution-free basis and to identify patterns. Among the different multivariate procedures, cluster analysis is playing an important role. This is due to its transparency and multifarious ways to be applied. However, there are three characteristics that restrict the application of cluster analysis:

1. Cluster analysis includes a series of analysis methods from which the most effective one has to be selected.
2. Although cluster analysis can relate certain parameter combinations to certain clusters, a graduation of parameter combinations within the cluster is not possible.
3. There has not yet been a statistical test which allows to assess the quality of clustering.

At the moment, there is no general solution approach for the first restricting characteristics. For the second and the third problem, a new method will be suggested. Without restricting generality, this solution will be represented by using the non -hierarchic minimal distance procedure.

2 METHODOLOGY

In cluster analysis, the multivariate correlation between defined parameters p_{ij} $(j = 1,n)$ is produced by each element e_i

$$e_i = f(p_{i1}, \ldots, p_{in}) \quad . \tag{1}$$

Using the non-hierarchic procedures (Steinhausen, Langer, 1977), the initial partition has to be determined. That means that the existing elements e_i will be equally distributed on a given number k of clusters:

$$\begin{aligned} &e_1, \ldots, e_L \ni c_1 \\ &e_{L+1}, \ldots, e_{2L} \ni c_2 \\ &\cdot \qquad\qquad \cdot \\ &\cdot \qquad\qquad \cdot \\ &\cdot \qquad\qquad \cdot \\ &e_{(k-1)L+1}, \ldots, e_{kL} \ni c_k \end{aligned} \tag{2}$$

For each of these clusters a mean group centroid $\bar{e}_k$ will now be calculated as follows:

$$\bar{e}_k = \frac{1}{L} \sum_{i=(k-1)L+1}^{kL} e_i \tag{3}$$

Thus, there is a group centroid for each cluster which is defined by the mean values of the elements describing the parameters in this cluster.

By means of the euclidic distance, the following target function can now be defined for each grouping step g:

$$z(g) = \sum_{m=1}^{k} \sum_{i \in m} |e_i - \bar{e}_m|^2 \tag{4}$$

A grouping step can be understood as the shifting of the elements e_i into the cluster with the nearest centroid $\bar{e}_k$ considering the euclidic distance. The aim of this procedure is to minimize the target function $z\ (g)$:

$$z(g) \vee g \rightarrow \min \tag{5}$$

The target function reaches a local minimum if two successive grouping steps are equal. In this case, the iteration procedure will be interrupted, i.e., that the optimum classification as to the given number of clusters has been obtained. The cluster analysis has been completed. On the one hand, a statement regarding the quality of the separation of the clusters is still missing, on the other hand, the question of how far the elements e_i within a cluster can be grouped has still to be clarified.

The latter question can for instance be answered as follows: If the location of the group centroid $\bar{e}_k$ is defined as the coordinate origin of a n-dimensional space within a cluster, then for each e_i within this cluster the parameters p_j $(j = 1,\ldots,n)$ can be defined as vectors with the coordinate origin $\bar{e}_k$. If furthermore one of the parameters p_j is defined as a reference value, the vectors of all other parameters can be projected to the vector of the reference parameter. The sum of the vector projections which can be derived from that is a measurement for the location of an element within the cluster.

The clusters can be separated from each other by using another multivariate procedure (e.g., discrimination analysis, hotelling-t-test, etc.).

Both solutions, to describe either the internal cluster structure or the cluster separation, are combined with a number of disadvantages which should not be neglected as there are for instance:

- the relatively high number of calculations.
- the necessity of normal distribution (discrimancy analysis).
- the restriction of the statistical result of the methods with small random samples.
- the non-existing independence from the cluster analysis.

Thus, we are looking for a method that considerably eliminates these disadvantages. A suggestion to solve these problems is presented in the following. Starting point for these considerations are n-grouped samples for the parameters $p_{i1}, \ldots, p_{in}$ for $i = 1, \ldots, kL$. A grouped sample with kL should be defined as a real random vector $(p_1, \ldots, p_{kL})$ whose uth component p_u $(u = 1,2,\ldots, kL)$ for each possible concrete sample $([p_{11}, \ldots, p_{kL1}], \ldots, [p_{1n}, \ldots, p_{kLn}])$ within the basic samples is accepting the uth value $p(s_u)$ of the tupel $([p_{11}, \ldots, p_{kL1}], \ldots, [p_{1n}, \ldots, p_{kLn}])$ grouped according to $p\ (s_1) < p(s_2) < \ldots < p(s_{kL})$. In the next step the non-grouped sample values of the parameters are related to the ranks estimated from the grouped samples. That

means that (1) turns over to

$$e_i = h(R_{i1}, \ldots, R_{in}) \tag{6}$$

with

$R_i \Rightarrow$ rank of $p(s)$.

Then the ranks R_i are summed up with a weight for each element e_i. A weighting has to be done in order to consider a possible dependence of the parameters among each other. The basis for the weighting is the correlation coefficient describing the interrelation between the parameters which can easily be determined by the distribution-free four-fold-test (Taubenheim 1969):

$$r = \sin(q \cdot 0.5\Pi) \tag{7}$$

with

$q = 1 - 4a/n$

q = ratio of quadrants

a = number of values in the 1st quadrant

The weights w_j $(j = 2, \ldots, n)$ shall have the following characteristics:

- The weight for the rank of each parameter should show a value of at least 1/n, since each parameter p_j provides information for the cluster analysis even though the absolute value of the correlation coefficient r between the reference parameter p_1 and the appropriate parameter p_j is 1.
- The weight w_1 for the reference parameter p_1 is always 1 according to definition.
- The weight w_j for such a parameter p_j which has no correlation with the reference parameter p_1 shall also be equal 1.
- Since negative and positive correlations are treated equally, the sign of the correlation coefficient has to be considered for calculating the weights.

Thus, the weights can be calculated as follows:

$$w_j = \frac{n - (n - 1)\,|r_j|}{n}\, sign(r_j) \quad j = 2, \ldots, n \tag{8}$$

The rank sum RS_i for the ith element e_i can therefore be described as:

$$RS_i = \sum_{j=1}^{n} w_j p_{ij} \quad i = 1, \ldots, kL \tag{9}$$

If ranks R_i as described above are again calculated for the rank sums RS_i and these are related to the respective elements of the individual clusters, one receives an ordered series of elements within the clusters. This series of elements represents the respective internal structure of the cluster. Only in case of an absolute separation of the clusters, the ranks of the elements represent in each individual cluster an uninterrupted series of positive increasing/decreasing whole numbers. Usually, a certain number of elements will not be found in the respective cluster according to the rank sum grouping. There will be so-called "overlaps". These "overlaps" can serve as a starting point to answer the before-mentioned question as to the quality of cluster separation. The basic idea is the following:

After clustering, each cluster has a certain number of elements which can differ from cluster to cluster. The elements can be found in a n-dimensional parameter space.

That means that the number of "overlaps" between two clusters is defined as

$$U_{a,b} = \sum_{i_1=1}^{L_a} \sum_{i_2=1}^{L_b} \sum_{j=1}^{n} u_{i_1, i_2, j} \qquad \begin{matrix} a = 1, \ldots, k-1 \\ b = 2, \ldots, k \end{matrix} \tag{10}$$

with

$$u_{i_1, i_2, j} = \begin{cases} 1 & p_{i_2, j} > p_{i_1, j} \\ 0 & p_{i_2, j} \le p_{i_1, j} \end{cases} \tag{11}$$

under the precondition that

$$\bar{e}_1 > \bar{e}_2 > \ldots > \bar{e}_k \tag{12}$$

There is an absolute separation for $U = 0$. The maximum possible number of "overlaps" is determined by

$$U_{max} = n(L_a L_b - 1)\,. \tag{13}$$

Using this previous knowledge, the quality of cluster separation can statistically be determined in the following steps:

1. Calculation of the mean number of maximum possible or actually existing "overlaps" for all cluster combinations.
2. Testing if the calculated mean values have the same basis (Student's test). If the zero hypothesis, saying that the mean values have the same basic sample, is not rejected, a statistically-based separation of the clusters among each other will not be possible.
   Otherwise, it can be proceeded as follows:
3. For each actual number of overlaps among the clusters, a corresponding ratio number related to the maximum possible number of "overlaps" is determined:

$$\nu_{a,b} = \frac{U_{a,b}}{U_{a,b\,max}} \tag{14}$$

4. Calculation of the mean value $\bar{\nu}$ over all $\nu_{a,b}$.
5. Due to paragraph 2, it has to be valid for all $\nu_{a,b} < \bar{\nu}$ that its separation regarding the clusters is statistically significant. This is not valid for all $\nu_{a,b} > \bar{\nu}$.
6. Testing of the frequency of occurrence $U_{a,b}$ against the mean frequency of occurrence $\bar{U}$ of "overlaps" by means of an adjusted χ^2-test:

$$\chi^2 = \frac{(U_{a,b} - \bar{U})^2 * (2U_{a,b\,max} - 1)}{(U_{a,b} + U_{a,b\,max}) * (2U_{a,b\,max} - U_{a,b} - \bar{U})} \tag{15}$$

   with the degree of freedom

$$fg = 1\,.$$

7. The evidence of the test is the following:

If the calculated χ^2 value is above a given significance value, the frequency of "overlaps" above the mean value is significantly deviating from it. That means that the separation between the clusters is statistically not safe. Otherwise the separation is statistically safe. The following example shall now demonstrate that the suggested method is a practicable way to better represent the internal structure of the clusters and to statistically save the quality of separation of the clusters among each other.

3 EXAMPLE

The temperature conditions of the summers at a defined location are the object of investigation. The series of measurement of daily mean as well as daily maximum values of the air temperature of the weather station Potsdam for a period of 101 years are available as a data basis. In a previous investigation (Gerstengarbe, Werner 1992), it could be demonstrated that on the basis of the two given meteorological values five parameters $(n = 5)$ are necessary in order to characterize the element summer. In that case, the optimum number or clusters was $k = 9$. The number of elements kL is equal to the number of years available (101). After clustering, the mean group centroids $\bar{e}_k$ are calculated for each cluster in accordance to (3). The results are mentioned in table 1.

Simultaneously with the clustering, the rank sum analysis will be carried out according to the equations (6) - (9). If the calculated clusters are ordered according to the condition (12) and

the elements within the clusters according to the ranks R of the rank sums RS, one receives the results mentioned in table 2.

Regarding the results in table 2, one can see that there are several "overlaps" between the individual clusters (see line of ranks). Thus, it is necessary to examine the quality of cluster separation.

For this reason, the actual number of "overlaps" between the clusters has to be determined according to the equations (10) and (11) (see table 3).

The number of maximum possible "overlaps" [calculated by (13)] is mentioned in table 4. Comparing the mean number of occurred and possible "overlaps" by means of the Student's test, one can see that at a calculated test value of $t = 8.21$ the mean "overlaps" do not have the same basis (error probability ($\leq$ 1 per cent). Thus, the investigation according to the given methodology can be continued (see 2. - 7.). Due to the χ^2-values calculated by (15), a test statement for the investigated case can be formulated . Table 5 includes the necessary values.

It shows that the neighbouring clusters are not to be separated statistically significant (exception: cluster 7/8). As to non-separation, the same statement can be made for the cluster combinations 2/5 and 3/5. That means that further statistical investigations of the clusters among each other are only useful for those combinations for which a significant separation has been proved.

Since in the present case mostly the neighbouring clusters are "overlapped", it is possible to have a better separation by reducing the number of clusters. Changing from 9 to 5 clusters, for instance, reduces the number of significant overlaps to 2! However, it has to be noted that the stricter separation between the clusters leads to a greater fuzzy within the clusters.

The decision to neglect a certain fuzzy depends upon the respective task. With this methodology the user is able to answer cluster-analytic questions more precisely than before.

References

Gerstengarbe, F.-W. and Werner, P.C., 1992, "The Time Structure of Extreme Summers in Central Europe between 1901 and 1980", Meterorol. Z., N. F. 1, pp. 285-289.

Steinhausen, D. and Langer, K., 1977, "Clusteranalyse", Berlin, New York: Walter de Gruyter, 206 p.

Taubenheim, J., 1969, "Statistische Auswertung geophysikalischer und meteorologischer Daten", Leipzig: Akademische Verlagsgesellschaft Geest & Portig, 386 p.

CORRESPONDING AUTHOR
Dr. F.-W. Gerstengarbe and Dr. P. C. Werner,
Potsdam Institute for Climate Impact Research,
P.O. Box 601203, 14412 Potsdam, Germany
E-mail: gerstengarbe@pik-potsdam.de

Cluster	1	2	3	4	5	6	7	8	9
$\bar{e}_k$	12.168	5.374	1.502	1.198	0.271	-2.257	-2.695	-5.431	-6.043

Table 1. Values of the mean group centroids

Cluster	1		2		3		4		5		6		7		8		9	
	a	R	a	R	a	R	a	R	a	R	a	R	a	R	a	R	a	R
1	1947	1	1983	4	1938	24	1949	29	1943	28	1919	50	1967	54	1984	86	1898	76
2	1992	2	1982	5	1986	27	1901	32	1900	35	1931	60	1933	55	1977	87	1993	78
3	1911	3	1917	6	1895	30	1914	37	1945	44	1979	63	1955	59	1894	90	1918	82
4			1975	7	1939	31	1906	40	1904	45	1981	64	1988	61	1974	92	1899	83
5			1976	8	1970	33			1966	46	1941	66	1940	65	1980	93	1923	85
6			1934	9	1951	34			1908	47	1928	68	1897	67	1987	95	1903	88
7			1959	10	1968	36			1915	48	1961	69	1924	72	1962	101	1926	89
8			1989	11	1991	38			1942	49	1920	70	1927	77			1913	91
9			1921	12	1925	39			1936	51	1910	71	1958	80			1907	94
10			1944	13	1990	41			1930	52	1978	73	1896	81			1956	96
11			1964	14	1946	42			1893	53	1960	74	1912	84			1965	97
12			1932	15	1905	43			1952	56	1922	75					1916	98
13			1963	16					1957	57	1954	79					1902	99
14			1937	17					1985	58							1909	100
15			1971	18					1972	62								
16			1969	19														
17			1929	20														
18			1973	21														
19			1953	22														
20			1948	23														
21			1935	25														
22			1950	26														
R	1-3		4-26		24-43		29-40		28-62		50-79		54-84		86-101		76-100	

Table 2. Results of the ordered cluster rank sum analysis

Cluster	1	2	3	4	5	6	7	8	9
1		23	2		2				
2			120	28	93	18		1	
3				113	253	79	7	2	9
4					105	31	17	5	3
5						127	130	3	17
6							317	52	82
7								79	90
8									210
9									

Table 3. Number of real appeared "overlaps"

Cluster	1	2	3	4	5	6	7	8	9
1		325	505	565	790	985	1150	1255	1465
2			1495	1995	3870	5495	6870	7745	9495
3				735	3510	5915	7950	9245	11835
4					3070	5735	7990	9425	12295
5						3635	6715	8675	12595
6							3790	6205	11035
7								2795	8395
8									6085
9									

Table 4. Number of possible "overlaps"

Cluster	1	2	3	4	5	6	7	8	9
1		1							
2			1		5				
3				1	1				
4					1				
5						1			
6							1		
7									
8									1
9									

Table 5. Error probability for the significant difference between the frequency of occurrence of "overlaps" of the clusters among each other

Inter-comparison of Simulated Potential Predictability in Several AMIP Experiments

Francis W. Zwiers
Canadian Centre for Climate Modelling and Analysis
Victoria, Canada

1 Introduction

A *potential predictability* calculation is a one-way time-domain analysis of variance (ANOVA) (see, for example, Madden, 1976 or Zwiers, 1987) in which the inter-annual variability of a seasonal or monthly mean is compared to the variation in this mean which is induced by daily weather noise. The inter-annual variance is thought to contain potentially predictable contributions from both external and internal sources. On the other hand, the component of inter-annual variance which is weather noise induced in not likely to be predictable on seasonal or longer time scales.

The data used in a potential predictability calculation are typically adjusted prior to analysis by subtracting an estimate of the annual cycle. This step is required to insure that daily variations within seasons are roughly stationary (in the statistical sense).

Inter-annual variance is estimated from the adjusted data in the usual way.

An independent estimate of the contribution to this variance which comes from weather noise is computed by assuming (i) that within season variations behave as white noise at low frequencies; and (ii) that the stochastic character of the weather noise is independent of the seasonal mean state. With these assumptions and the further assumption that between season variations are independent of each other, it can be demonstrated that the inter-annual variance of the seasonal mean contains contributions from external boundary forcing, internal sources of low frequency variation, and weather-noise. Thus F-ratios comparing the inter-annual variance with the induced weather noise variance are computed to ascertain whether the contributions from external and internal sources are significant. F-ratios significantly greater than one imply the presence of long time scale variations in the climate system which are potentially predictable.

In most cases only a single realization of an observed or simulated climate is available with the consequence that the potentially predictable contributions from external and internal sources are confounded. When multiple runs of the same model are available, or when runs from a number of similar models are available, it may be possible to further partition variability according to source.

For example, the CCC GCMII (McFarlane, et al., 1992; Boer, et al., 1992) has been used to generate 6 AMIP simulations (see Gates, 1992, for a description of the AMIP project) from 6 different sets of initial conditions. Each integration experienced the same observed evolution of sea surface temperatures and sea ice boundaries. These 6 integrations can be viewed as 6 independent realizations of the same simulated climate. Under these circumstances one can conduct a 2-way time-domain ANOVA and obtain estimates of the contribution to total inter-annual variance which arises from the initial conditions, the external boundary forcing, internal low-frequency sources, and weather noise. It is possible to test null hypotheses that (i) variation induced by varying initial conditions amongst the 6 runs is not potentially predictable; (ii) variation induced by the varying boundary conditions is not potentially predictable; and (iii) that there is no potentially predictable contribution to the inter-annual variance of seasonal means which arises from slowly varying internal sources (such as the atmosphere's internal dynamics or land surface processes).

The remainder of this short note discusses such potential predictability calculations made with (i) "observations" (1979-1988 NMC analyses of 500 mb geopotential); and (ii) the CCC GCMII ensemble of AMIP simulations (forced with observed 1979-88 SSTs and sea-ice extent). Similar calculations have been performed using the AMIP simulations provided by all 30 modelling groups participating

in AMIP. Methodological details are described in Zwiers (1995) and Storch and Zwiers (1995).

2 The Inter-annual Variance of 500 mb Geopotential

Figure 1: *Zonally averaged inter-annual variance of DJF mean 500 mb geopotential computed from 1979-88 NMC analyses.*

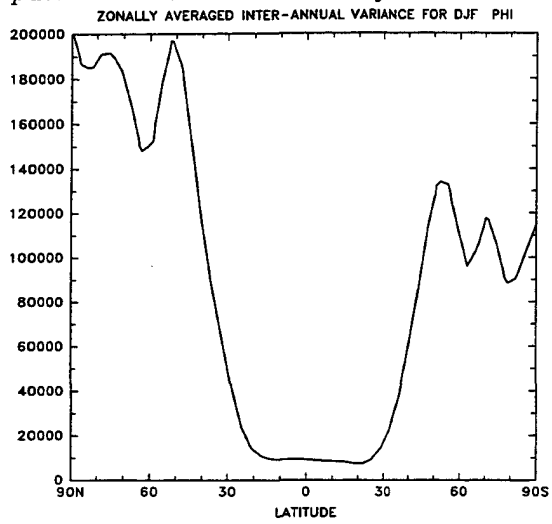


Figure 2: *As Fig. 1, except for DJF mean 500 mb geopotential simulated in the ensemble of 6 CCC GCMII AMIP runs.*

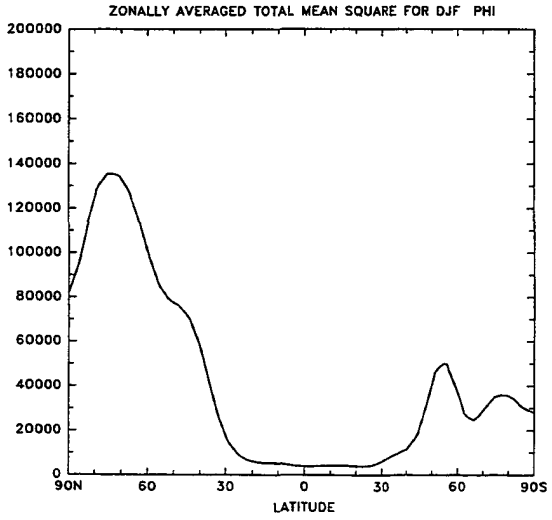


Figure 1 displays the zonally averaged inter-annual variance of DJF mean 500 mb geopotential as computed from 1979-88 NMC analyses. Note the peak at the north pole (which may be due to sampling variability), a peak at about 75° N which is due to variation over Greenland, and a third peak at about 42° N which reflects the mid-latitude NH storm tracks. Note also the broad tropical trough with variances less than $10^4 g^2 m^2$. The latter represents primarily low-frequency variations in the temperature of the troposphere.

Figure 2 displays the zonally averaged inter-annual variance of DJF mean 500 mb geopotential aggregated across the 6 CCC GCMII AMIP simulations. Note that only about 50% of the observed variance is simulated. The peak at the North Pole is not present in the simulations, the peak at 75° N which is associated with variation over Greenland is present (but not large enough), while the peak associated with northern mid latitude storm tracks is entirely absent. Centers of variation which are associate with these storm tracks are present in the simulated climate but are much weaker than observed. Variation in the tropics is also only about 50% of that which is observed despite the imposition of the observed SSTs at the lower boundary.

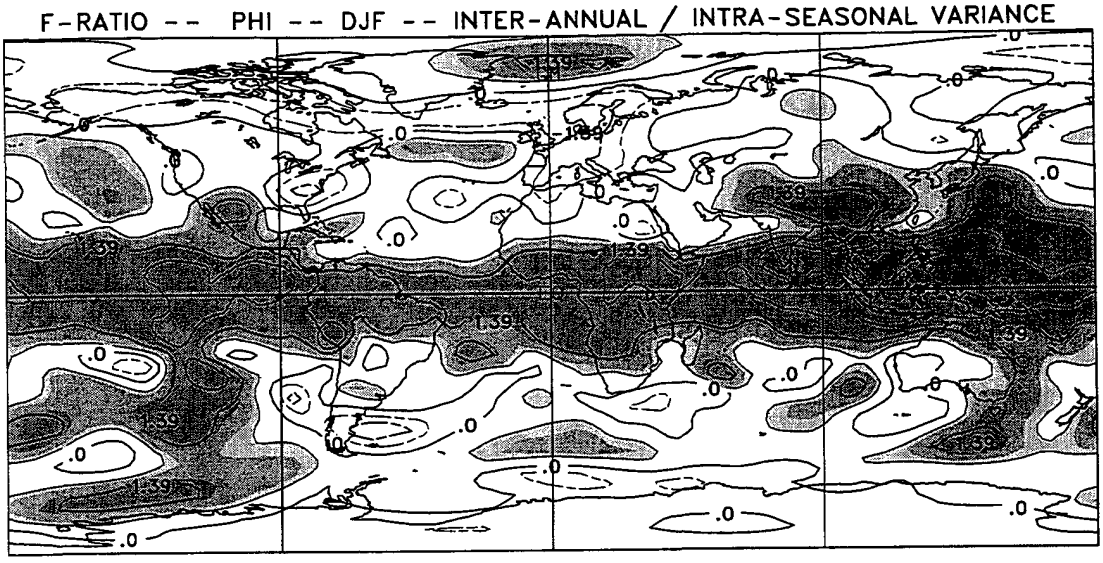
Underestimation of the inter-annual variability of geopotential is a common problem shared by many of the models participating in the AMIP project. Preliminary analysis of the AMIP simulations suggests that the amount of inter-annual variability which a model simulates may be related to its vertical resolution (with higher resolution models simulating more variance). However, because higher resolution models also tend to be the more modern models participating in AMIP, the apparent relationship between resolution and inter-annual variance may be due to evolutionary changes in models other than increased vertical resolution.

3 Potential Predictability

Figure 3 displays locations at which the inter-annual variance of the observed 500 mb geopotential is significantly greater than the variance induced by weather noise alone. Significantly large F-ratios occur over approximately 51% of the globe. They can be seen in a broad tropical band which presumably reflects slow variations in SST in the tropics. Also, note the significant F-ratios in the north-east Pacific, over the southwestern US and Mexico, over China, and a suggestion that variations in the SPCZ are potentially predictable.

These findings are in general agreement with those of Madden (1976) who used 1899-1972 NH MSLP station data, but are somewhat at

Figure 3: *The natural logarithm of the ratio of the inter-annual variance of DJF mean 500 mb geopotential to the weather-noise induced variance of DJF mean 500 mb geopotential (see Zwiers, 1987 for details). The light, medium and dark shading indicate F-ratios which are significantly greater than one at the 10%. 5% and 1.25% significance levels respectively. The contour interval is ln(2).*



odds with those of Trenberth (1985) who used 1972-80 ECMWF analyses and found significantly large F ratios over Antarctica as well as in the tropics.

Results obtained from the various AMIP simulations are generally similar to those displayed above. Despite the fact that the amount of inter-annual variance simulated by models participating in AMIP ranges between approximately 20% and 150% of that which is observed, most models simulate a reasonable balance between inter-annual variance and weather noise. The structure of the F-ratio fields corresponding to Figure 3 which are computed from the AMIP simulations is generally similar to that which is observed, and significant ratios general cover about the same proportion of the globe.

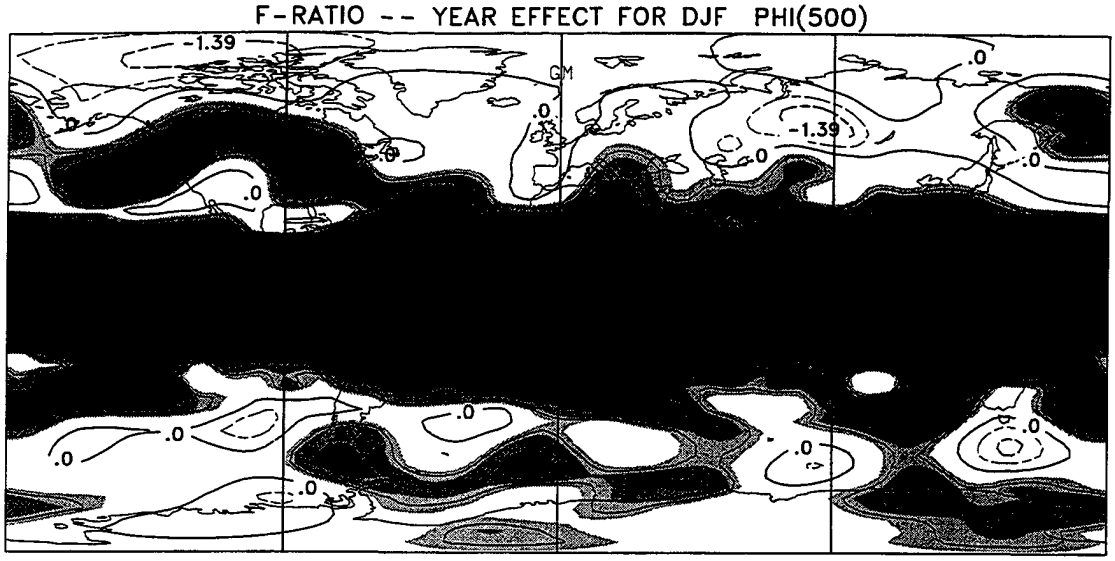
Note that the PNA is not readily apparent in Figure 3 even though the AMIP period includes two warm ENSO events (1982/3 and 1986/7). Our AMIP experience suggests that this is due to two kinds of sampling problems. First, this analysis is not specifically designed to isolate the ENSO signal. Secondly, the analysis is applied to a single 10-year record. The use of a longer record, or multiple realizations, would increase the sensitivity of the F-test to relatively weak signal-to-noise ratios.

Application of the 2-way ANOVA to the CCC GCMII ensemble of simulations reveals that there are no significant contributions to the total simulated inter-annual variability of 500 mb height from either the initial conditions or from sources internal to the model. However there are significant contributions from boundary forcing. When the 2-way ANOVA computation is repeated with 850 mb temperature and 1000 mb geopotential we find strong contributions from boundary forcing and weak evidence that slow land surface variations (which are internal to the model) have a local potentially predictable effect over tropical land masses.

Figure 4 displays the result of the test for potential predictability from external sources in 500 mb geopotential climate of CCC GCMII. The general structure of this field of test statistics and the magnitude of the statistics is quite similar to that computed from observations in the extratropics. The F-ratios in the tropics are larger than in the observations mainly because the experimental design and analysis technique allow us to separate the SST/sea-ice signal from other sources of variability and because the larger volume of data has increased the sensitivity of the F-test. A band of large F-ratios can be seen stretching across North America in Figure 4 which is at least somewhat suggestive of the PNA.

The F-ratios displayed in Figure 4 are easily re-expressed as a signal-to-noise ratio. When

Figure 4: *As Fig. 2, except the F-ratio is computed as the ratio of the "year" component of the simulated DJF 500 mb geopotential inter-annual variance to the "internal-sources" component (see Storch and Zwiers, 1995) . This F-ratio tests the null hypothesis that potential predictability* does not *arise from either external (boundary) forcing.*



this is done we see that the prescribed SST and sea-ice conditions explain 20% t0 40% of the simulated inter-annual variance in the North American region of large F-ratios (not shown). This suggests that there is potential for useful dynamical forecasts of mean DJF conditions if good global SST and sea-ice extent forecasts can be made one or two seasons in advance. This potential is partially confirmed when realizations of the simulated climate are verified against each other. This is done by assuming that most of the useful forecast skill on seasonal time scales can be realized from correctly forecasting boundary conditions one or more seasons in advance. With this assumption correlation skill scores can be computed by treating pairs of realizations in the ensemble of 6 simulations as forecast/verification pairs. Large correlation skill scores are found to correspond to large F-ratios in Figure 4. Similar skills are also diagnosed when the simulations are verified against observations.

Similar results to those displayed in Figure 4 are obtained when the 2-way ANOVA is repeated with a selection of AMIP simulations from a number of models rather than an ensemble of simulations from a single model. Interestingly, the PNA signal is more apparent in the consensus SST/sea-ice signal derived from these diverse simulations than it is in any single simulation or in the CCC GCMII ensemble.

References

[1] G.J. Boer, N.A. McFarlane, and M. La zãre. Greenhouse Gas-induced Climate Change Simulated with the CCC Second-Generation General Circulation Model. *J. Climate*, 5:1045–1077, 1992.

[2] W.L. Gates. AMIP: The Atmospheric Model Intercomparison Project, 1992. PCMDI Report No. 7.

[3] R. A. Madden. Estimates of the natural variability of time averaged sea level pressure. *Mon. Wea. Rev.*, 104:942–952, 1976.

[4] N.A. McFarlane, G.J. Boer, J.-P. Blanchet, and M. Lazare. The Canadian Climate Centre Second Generation General Circulation Model and its Equilibrium Climate. *J. Climate*, 5:1013–1044, 1992.

[5] K. E. Trenberth. Potential predictability of geopotential heights over the southern hemisphere. *Mon. Wea. Rev.*, 113:54–64, 1985.

[6] F. W. Zwiers. A potential predictability study conducted with an atmospheric general circulation model. *Mon. Wea. Rev.*, 115:2957–2974, 1987.

[7] F.W. Zwiers. Sources of interannual variability in an ensemble of AMIP simulations. *In preparation*, 1995.

Multiple simulations and ocean model testing

Claude Frankignoul

Laboratoire d'Océanographie Dynamique et de Climatologie, case 100
Université Pierre et Marie Curie, 4 place Jussieu, 75005 Paris

A difficulty in ocean model testing is that the ocean is primarily forced by the atmosphere, but the atmospheric forcing is poorly known, in particular in the tropics and at very high latitudes, where the synoptic global analysis are inaccurate and marine observations sparse. The bulk formulae used to estimate the air-sea fluxes are also uncertain, ocean precipitation is barely known, and the oceanic initial conditions are little documented at best. Thus, even the predictions of a perfect ocean model would not be consistent with the observations, and there is a need to distinguish between model inadequacies and data uncertainties. To do so, a multivariate model testing procedure has been developed, which compares the main space and time structures of the model-observation differences to their expected errors. To represent the effect of the atmospheric forcing uncertainties, a number of independent simulations must be performed, and their dispersion taken into account. The observational errors must also be carefully quantified.

Two different ways have been used to produce the required multiple simulations. To test model ability at simulating the variability of the thermocline depth in the tropical Atlantic, Monte Carlo techniques have been used to construct several different wind stress fields consistent with the ship report statistics and our limited knowledge of the drag coefficient. The fields, considered as equally plausible, were used to force several tropical ocean models, which could then be tested and intercompared. The construction of the various forcing fields was fastidious and would be more difficult in the tropical Pacific, where the wind data base is more limited. Thus, a different strategy was chosen for a recent intercomparison project for the latter ocean: both the observationally based FSU wind stress product and forcing fields derived from AMIP-like runs with atmospheric general circulation models (AGCMs) were used to simulate the effects of the forcing uncertainties. The AGCM fields may biased to a varying extent, however, so that it is misleading to consider the different simulations as equally plausible. Thus, both ensemble simulations and a comparison with individual runs have been used in the model intercomparison.

Nonlinear Principal Component Analysis of Climate Data

Sailes Sengupta and James Boyle

Program for Climate Model Diagnosis and Intercomparison
Lawrence Livermore National Laboratory, Livermore CA USA

Introduction

A Principal Component Analysis (PCA) is concerned with the understanding of the covariance structure through a few 'significant' linear combinations of the original variables, the motivations being twofold. First, it enables us to compress data significantly when in presence of correlated variables. Secondly, it allows us to attempt understanding the physical meaning of the data.While in the engineering sciences, the primary motivation is the first one, in the geophysical sciences, it is particularly important to discern any physical information content that may be present in the extracted principal components (Preisendorfer, 1988). Given a space-time data set {X(s,t), s=1,2,..., m; t=1,2,...,n}, the spatio-temporal behavior of the physical field X can be decomposed into an uncorrelated set of m time series or n spatial fields depending on the PCA mode.If we drop the requirement of uncorrelatedness and allow nonlinear functions of the original variables we can gain significantly in terms of data compression. Furthermore, the lack of uncorrelatedness per se, may not necessarily preclude us from trying to understand the physical meanings of the fields or time series derived using a nonlinear mode of analysis. We can, in fact, by using an auto-associative neural network perform in a nonlinear fashion a task equivalent to the extraction of principal components.Such a task has been termed 'nonlinear principal component analysis (NLPCA)' by some authors (Cramer, 1991). This paper deals with a geophysical data set, that of precipitation over the North American continent during the decade 1979 - 1988. In choosing this data set, we anticipated an NLPCA applied to this data set may provide additional insight into the physical process. The data set is described in the next section. Neural Networks used in this paper is described in the following section . The final section presents some results and conclusions.

Data

The data used in this study consists of precipitation observations gridded to a 4degree by 5 degree latitude, longitude lattice. The observations are from surface stations over land and satellite MSU estimates, Spencer(1993), over the oceans. The bulk of the analysis grid used here is over the United States where the observational network provides reliable precipitation fields. the data are monthly averages for the 120 months from January 1979 to December 1988. The 120 month mean was subtracted from each gridpoint to form the deviations. The seasonal cycle was retained since it was of interest to compare how well the GCMs simulated this cycle. The data comprised a matrix of 120 time points at 95 space points. Figure 3 shows the

spatial coverage of the data.

Artifical Neural Network

Connection with Principal Componet Analysis (PCA)

PCA is an essential technique in data compression, feature extraction, compact coding and computational efficiency.In the context of climatological data analysis the constraints and interdependency of spatio-temporal data can be identified and redundancy eliminated by the use of PCA. For example, the use of PCA is commonplace in climatological literature (Preisendorfer, 1988) and MPEG Video Compression is based on the same principle (LeGall, 1991).Briefly speaking, if x is a centered n-dimensional vector, PCA extracts p (<=n) linear combinations W x of the components of x where W is a p x n matrix of weiights subject to the constraints that (a) the variance of each linear combination appearing as elements of W x is maximized and (b) the extracted linear combinations are mutually orthogonal.In practice one solves the eigensystem for the sample covariance matrix say, C with the resulting p dominant eigenvectors representing the principal vectors. Several workers in the Neural Network community have related (Bourlard and Kamp, 1987;Baldi and Hornik, 1989; Sirat, 1991, Oja, 1992) multilinear perceptron learning by back propagation algorithm with principal components extraction in classical statistics. Becker (1991) gives a comprehensive survey relating PCA models to unsupervised learning neural networks. While neural networks can derive the principal components, the self-organizing rules of PCA perform very poorly when outliers are present. Xu and Yuille (1995) discusses the problem and present robust self-organizing rules of PCA extraction based on statistical physics approach. In suggesting a transition from linear to 'nonlinear' principal components (sometimes called 'principal manifolds'), Demers and Cottrell (1992) argues that PCA finds an optimal linear subspace on which one projects the data with minimum loss of information (in the sense of 'explained' variance in the data). However, if the data lie on a nonlinear submanifold of the feature space, then the number of dominant PCs will overestimate the dimensionality. Take for example data from a sampled from a 3-d helix. The covariance will have a full rank (=3) with 3 distinct eigenvaue/eigenvector pairs leading to 3 distinct principal components. However, the intrinsic dimensionality of any 3-d curve such as a helix is one since it can ordinarily be parametrized by a single parameter.Furthermore, as has been observed by other authors (Kramer, 1991; Oja, 1991; Usui, Nakauchi and Nakano, 1991 and Demers and Cottrell, 1992), the addition of hidden layers between the inputs and the representation layer as well as between the representation and the output layer provide a network which is capable of learning nonlinear representation also.In the process, one achieves what may be termed a nonlinear analogue of PCA.In the following we present the sketch of such a network.(Fig.) The network consists of five layers which are fully interconnected. In addition to the input and output layers which are identical since the network is made to be auto-associative, we have a central representation layer (where the principal manifolds or nlpcs are generated as outputs) and two identical layers placed on the two sides of the representation layer.These last two layers as described above are called the encoding and decoding layer respectively. The training algorithm which is essen-

tially adjustment of the connection weights to minimize the vector difference between the target and the network output is based on the back propagation of error algorithm.(Rumelhart and McClelland, 1986)

Network Architecture

Although there are no specific guidelines for the choice of the number of nodes in the encoding and the decoding layer, Kramer (1991) provides bounds based on the principle that the number of weights in the network should be a fraction of the number of constarints imposed by the data set. A few simplifying assumptions then lead to the constraints

$$M1 + M2 << n,\ M1 > f \text{ and } M2 > f$$

where M1, M2 are respectively the sizes of the encoding and the decoding layers and n is the size of the training set.

In determining the size of the representation layer three different approaches have been indicated in the literature. Demers and Cottrell (1992) suggest a 'pruning' method based on successive elimination of representation nodes by penalizing variances. This results in encodings of minimum dimensionality with respect to allowable reconstruction error. Kramer (1991) on the other hand introduces a sequential determination of the nlpcs one at a time similar in spirit to its linear counterpart, namely the PCA extraction algorithm. Applied in this context, it amounts to using in a recursive manner the same network in fig. except with a single node in the representation layer and in each recursion feeding the residual matrix obtained from the previous stage as the I/O pair. The residual matrix is simply the error matrix obtained by subtracting the output of the trained network from the input. The procedure stops when either a desired number of nlpcs have been extracted or a desired level of accuracy has been attained in the residual matrix.In yet a third method, instead of a sequential procedure, we may simply decide to use a fixed number p say, of nodes in the representation layer and extract the p nlpcs. This will however preclude any ranking of these nlpcs. In our work, we have used the last two methods only.

Analysis

The PC analysis used the standard routine, PRINC from IMSL (1994) to compute the principal components from the covariance matrix computed from the data consisting of the 120 time points at 95 space points.
The same data were used as input to the neural net described above.

Results:

The results will focus on the first components of each method since these represent the seasonal cycle and allow a fairly direct interpretation in the limited space available in this paper. Figure 3 shows the projection of the first nlpc onto the data. This spatial distribution allows for some physical insight into the components. The projection for the first PC was very similar overall, with some differences in detail. From the times series in Figs. 4 and 5. it can be seen that these first components are a representation of the seasonal cycle. Figure 3 clearly shows the characteristic west and east coast wintertime maxima in precipitation due to cyclonic storms, while the mid-continent has a summertime maximum which is attributable to convective, severe storms.
Both the PC and nlpc techniques capture the bulk of the seasonal oscillla-

tion but the nlpc displays a somewhat sharper distinction and transition from the winter to summer precipitation regimes. This is shown in the spectra of Figs. 6 and 7. The PC analysis has a significant contribution from the second PC at 12 months (1/12 = 0.083) while the nlpc has virtually all the seasonal contribution in the leading component. The extra freedom allowed by the non-linearity permits this more distinct characterization. This property would be of use when the comparisons are made with GCM output. The proper simulation of the seasonal cycle is an essential benchmark for a acceptable integration.
On the other hand, the close resemblance of the analogous PC figure(not shown)to Fig. 3 indicates that the linear PC does capture the essence of the spatial distribution and might well be adequate for most purposes.

References:

Baldi Pierre and Kurt Hornik, 'Neural Networks and Principal Component Analysis: Learning ffrom Examples Without Local Minima,' Neural Networks, Vol 2, pp 53-58, 1989

Becker, S., 'Unsupervised Learning Procedures for Neural Networks,' International JOurnal of Neural Systems, 2, 17-33, 1991.

Bourlard, H and Y. Kamp, 'Auto-association by Multi-Layer Perceptron and Singular Value Decomposition,' Biological Cybernetics, 59, 291-294, 1988.

DeMers, David and Garrison Cottrell, ' Non-Linear Dimensionality Reduction,' in Advances in Neural Processing Systems 5, eds Hansen et al.Morgan Kaufmann, 1992.

Kramer, Mark A., 'Nonlinear Principal Comp[onent Analysis Using Autoassociative Neural Networks,' AIChE Journal, vol 37, No. 2, 1991.

LeGall, D., MPEG: A Video Compression Standard for Multimedia Applications,' Communications of the ACM, 34, 46-58, 1991.

Oja, Erkki, 'Principal Components, Minor Components, and Linear Neural Networks,' Neural Networks, Vol 5. pp 927-935, 1992.

Preisendorfer, R W, 'Principal Component Analysis in Meteorology and Oceanography,' Developments in Atmospheric Science 17, 425pp., Elsevier, Amsterdam, 1988.

Rumelhart, D. and James McClelland, Parallel Distributed Processing: Explorations in the Microstructure of Cognition, Vol 1, MIT Pr., Cambridge, MA 547 pp., 1986

Sirat, J. A., ' A Fast Neural Algorithm for Principal Component Analysis and Singular Value Decomposition,' International Journal of Neural Systems, 2, 147-155, 1991.

Xu, Lei and Alan Yuille, 'Robust Principal Component Analysis by Self-Organizing Rules Based on Statistical Physics Approach,' IEEE Trans. Neural Networks, Vol.6, No. 1, 131-143, 1995.

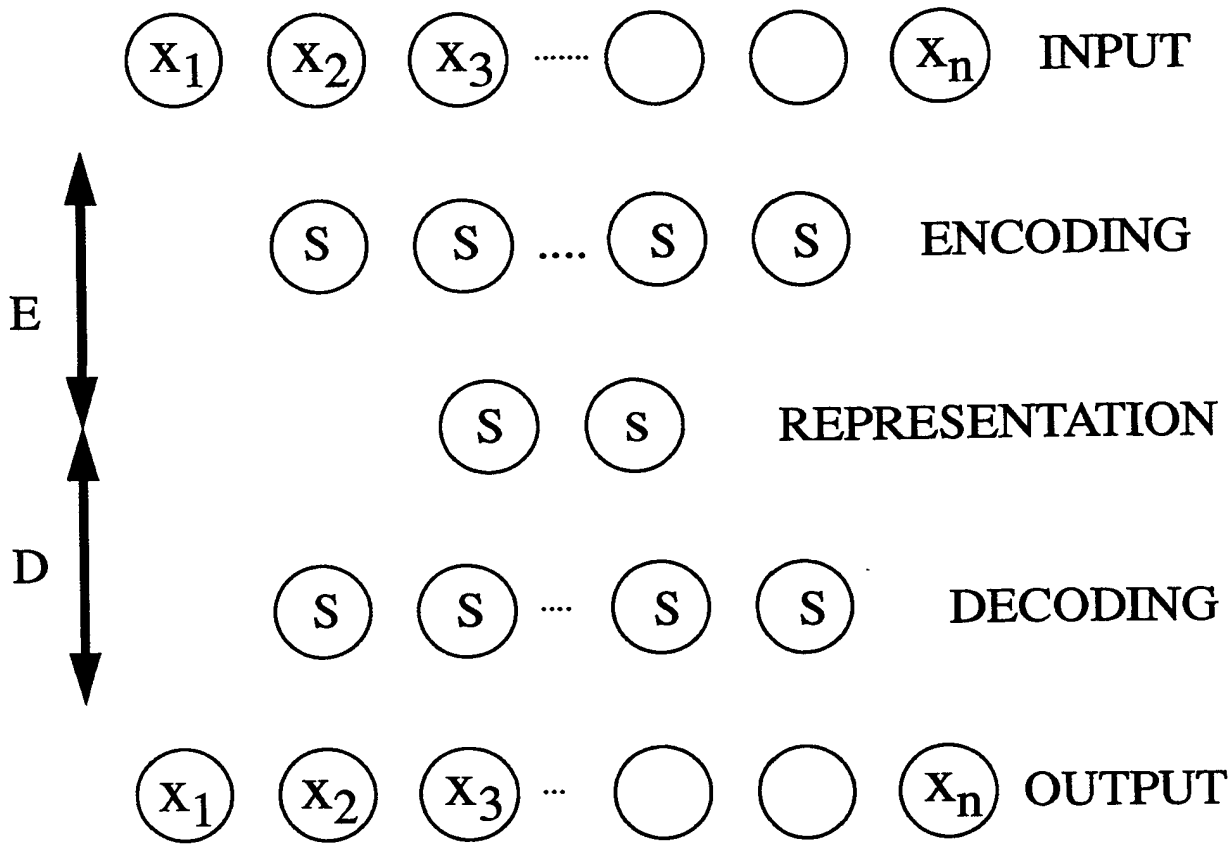


Figure 1. A fully interconnected (connections not shown) auto-associative neural network architecture. Showing from top to bottom: the input layer, encoding layer, the representation layer (with two nlpc nodes), the decoding and output layers.

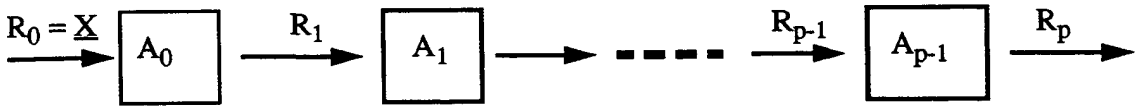


Figure 2. Sequential selection of non-linear principal components showing a sequence of p auto-associative networks $A_0, A_1, ...A_{p-1}$ with each A_i configured like A in Fig. 1 (except with a single node in each representation layer). The I/O pair within each A_i during training are the successive residuals $R_0, R_1, ...R_{p-1}$ with the original data matrix in R_0.

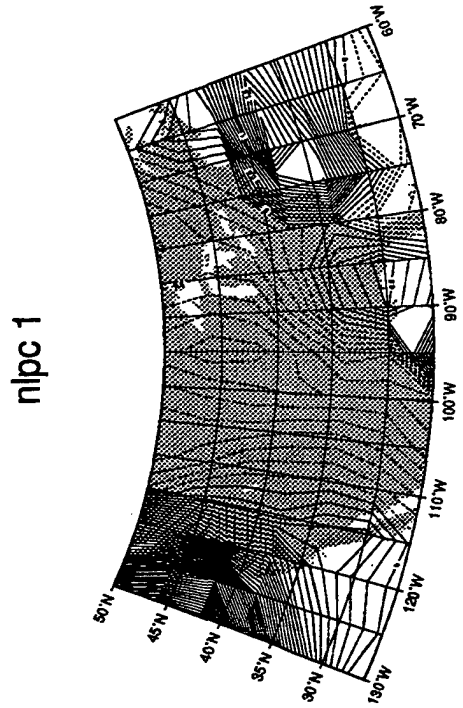


Figure 3. Projection of the first nlpc. The data is the observed precipitation. The analysis grid is a 4 x 5 latitude longitude grid over the US. Dashed lines indicate negative deviations, solid lines positive deviations.

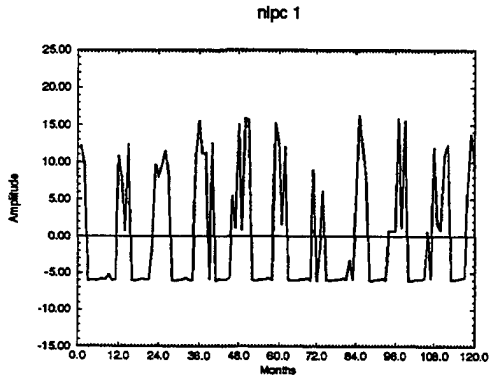


Figure 4. First nlpc of precipitation data.

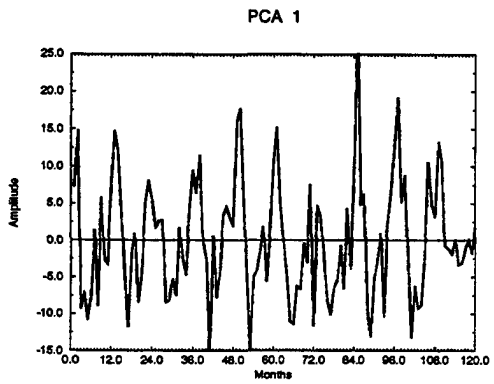


Figure 5. First PC of precipitation data.

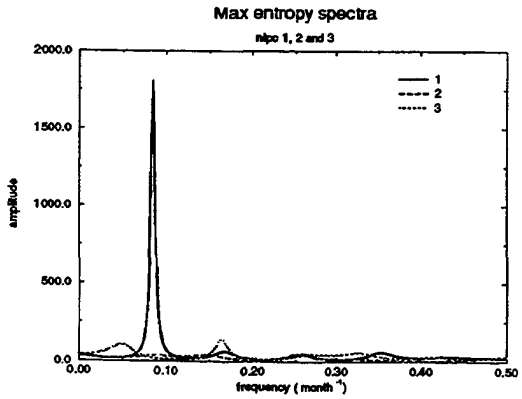


Figure 6. Spectra of first nlpc using maximum entropy estimation.

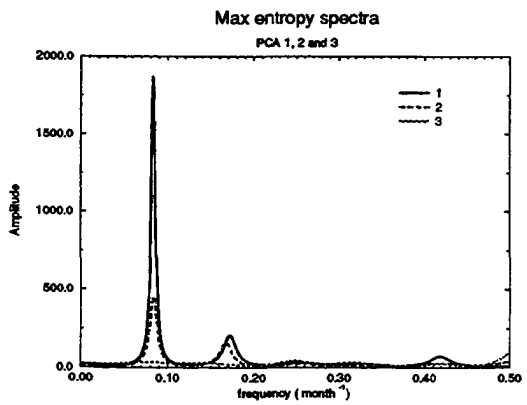


Figure 7. Spectra of first PC using maximum entropy estimation.

PCA-BASED CLASSIFICATION OF CIRCULATION AND WEATHER PATTERNS: SOME METHODOLOGICAL CONSIDERATIONS

Radan Huth

Institute of Atmospheric Physics, Praha, Czech Republic

Abstract

Three variants of input data (raw, anomalies, normalized anomalies) and similarity matrix (correlation, covariance, congruence) have been compared as to their applicability to classification of circulation and weather by the principal component analysis. Synthetic data have been analyzed for that purpose. Correlation matrix applied to raw data complies with synoptic ideas on the circulation classification best. PCA did not prove to be a good tool for weather classification.

1. Introduction

One of possible applications of Principal Component Analysis (PCA), first suggested by Richman (1981), is the classification of circulation patterns. It has recently been shown that the PCA must be obliquely rotated and used in a T-mode for this purpose, i.e. the geopotential height (or sea level pressure) being fixed entity, the time realizations are regarded as variables and grid point values as observations (Compagnucci and Ruiz 1992, Huth 1993, 1995).

Since there is an apparent analogy between the classification of circulation patterns and that of local weather, one may expect the PCA to be suitable to the weather classification, too. Such an analysis should apparently be performed in an O-mode, which consists in keeping the spatial index constant (data from one station only are analyzed), with time points (daily measurements) considered as variables and meteorological quantities (e.g. temperature, humidity, cloudiness, wind speed etc.) as their realizations. [For definitions of the modes of PCA refer to Richman (1986)].

The idea of using the obliquely rotated T-mode (O-mode) PCA for classification purposes is simple: Each daily pattern is classified with the type for which it has the highest loading (in the absolute sense). Therefore, we can potentially have twice as many classes as retained principal components (PCs): high positive and high negative loadings can define two opposite types for each PC. Loadings are rescaled eigenvectors of a similarity matrix. To make rotation possible, loadings are normalized so as the sums of squares in each row of the loading matrix equal one.

2. Objective of the study

This contribution concerns the effect on PCA's proficiency in the circulation and weather classification of 1) normalization of rows in a T-mode (O-mode) input data matrix and 2) the choice of similarity matrix. Three forms of input matrices are discussed here: raw (without any normalization; denoted as R), anomalies (respective means are subtracted from rows of the data matrix; A), and normalized anomalies (after subtracting mean, each row is further divided by its standard deviation; N). Three possible similarity matrices are examined: correlation (R), covariance (V), and congruence (G) [for a discussion on this subject, see Drosdowsky (1993)]. Two-letter reference is used to denote the nine possible combinations - e.g. AV denotes analysis of covariance matrix computed from anomalies.

For the purpose of this study, synthetic data are used. Its objective is to assess PCA's ability to classify circulation and weather, not to carry out some classification. Since this ability can be deduced directly from unrotated solutions, no rotation has been performed.

3. Classification of circulation

3.1. Data. The synthetic data simulate the 500 hPa height patterns in the European / North Atlantic region. They are given in a 5 x 7.5° grid (13x9 = 117 grid points). 45 different patterns were created according to the following definition:
Here, ϕ and λ denote latitude and longitude, respectively. All possible

$$z = B(50 - \varphi - A \sin \tfrac{\lambda}{14.3} \cos \tfrac{\varphi - 50}{20}) + 540 + C$$

combinations of the following values of constants A, B, C were used: A (amplitude of the anomaly) = -40, -20, 0, 20, 40; B (intensity of the gradient) = 0.5, 1., 1.5; C (additive constant) = -10, 0, 10. The cases are numbered 1 to 15 for C = 0; 1- to 15- for C = -10; and 1+ to 15+ for C = 10. Selected patterns are mapped in Fig.1; Fig.2 shows corresponding anomalies.

To enable pattern 8 (time mean) and patterns 8- and 8+ to be classified when A and N data are used (for discussion see below), random errors with zero mean and standard deviation of 0.1 were added to the three raw patterns at all grid points.

3.2. Results. The loadings for PCs with eigenvalues explaining more than 0.1% of the total variance are presented in Tab.1 for selected patterns. Percentages of variance explained are also included there. Some of the conclusions drawn from Tab.1 are listed in the following.

1. Variant RG is useless for classification purposes as only one significant eigenvalue results from it.

2. All the three variants based on normalized anomalies as well as variant AG make distinction between patterns only differing in their spatial means (i.e. in an additive constant) (cf. 6 and 6-). This should be considered undesirable because of a clear contradiction to the synoptic experience: there is no reason for the fields with identical synoptic features to be treated as different. Therefore, the further discussion is limited to the remaining four variants (RR, RV, AR, AV) that do not take into account differences in spatial means.

3. There appear to be problems with the mean pattern (8) and its "added" and "subtracted" versions (8+ and 8-) if respective means are subtracted from the data. The truly mean pattern would be unclassifiable since its anomalies at all grid points and, consequently, also its loadings on all PCs would necessarily be zero. Nevertheless, the situation simulated here (very small random errors added to the three patterns in question - see above) is more realistic: the exactly mean pattern hardly ever appears in the nature. If a covariance matrix is applied the loadings of the very-close-to-mean pattern (and its two counterparts differing in spatial mean) remain very small, not allowing its classification after the rotation. On the other hand, the correlation matrix handles the anomalies regardless of their amplitude. This causes an overestimation of the negligible anomalies of the three patterns which, because of their independence on each other and on the "real" large-scale ones, form three additional seemingly significant PCs.

4. The patterns with anomalies differing only in their magnitude (6 and 7; 9 and 10) are treated as identical if the anomalies are used as an input matrix.

5. The classifications based on the raw data do not distinguish between the patterns differing in the gradient (1 and 6; 3, 8 and 13; 5 and 10).

6. There is no noticeable distinction between the outputs from correlation and covariances matrices (apart from the mean pattern discussed above). The normalization of the loading matrix, necessary to make a subsequent rotation possible, sweeps out the differences between the respective pairs of original eigenvectors.

7. Excluding the singular case of the mean pattern from considerations, only two principal components appear to be significant, i.e., all the discussed patterns lie on a two-dimensional plane. This means that, regardless of the variety of the patterns formed according to the above equation, a subsequent rotation would be able to identify only two distinct types (or four if we count also negative ones). This limitation is a clear consequence of the linearity of the PCA.

3.3. Synoptic interpretation. The applicability of individual variants of input data and similarity matrices to the circulation classification should be evaluated in accordance with the synoptic experience. One aspect of it has already been discussed: to distinguish otherwise identical patterns, differing only in their spatial means, seems to be meaningless.

Most synoptic-climatological applications require all the patterns to be classified. In such a case, AV variant should not be used since it does not allow the classification of similar-to-mean patterns.

Other demands on a classification may depend on its purpose. Frequently, more emphasis is put on the location and shapes of synoptic disturbances (troughs and ridges), which control the weather through the origin and properties of advected air masses, rather than on the intensity of air flow, which affects air mass properties to a much lesser extent. Following this assumption, classifications based on anomalies appear to be inferior since they treat anomalies with the same location and shapes but various amplitudes as identical. This means that they may not distinguish between a slightly disturbed zonal (near-to-normal) flow and a fully developed ridge-trough pattern (cf. patterns 6 and 7). On the other hand, methods based on raw data do not take gradients into account (cf. patterns 1 and 6), which in view of the above assumption is not a disadvantage.

The linear nature of the PCA poses clear limitations on its use for clasification purposes. If more than two distinct clusters of patterns lie in one plane defined by two PCs (i.e., are approximately linearly dependent), the PCA fails to identify them. The key question is whether real circulation patterns manifest such a behaviour. The answer to it goes beyond this contribution; hopefully, it will read "not".

4. Classification of weather

"Weather" on each day is characterized by six quantities: three values of temperature and of humidity. Several combinations of daily mean and diurnal course for both quantities result in 62 cases, some of which are listed in Tab.2. Table 2 also includes mean values of the six quantities. Note that case 61 (62) has anomalies ten times smaller than case 60 (1).

Percentage of variance explained and PC loadings on selected cases for PCs with non-zero eigenvalues are presented in Tab.3. Since PC loadings resulting from correlation and covariance matrices differ no more than marginally again, Tab.3 includes only variants based on correlation and congruence matrices. The results confirm the expectations that if quantities with different location and scale parameters are treated simultaneously serious problems can appear, leading to meaningless results.

Variants RR and AR produce several pairs of cases with identical loadings, e.g. 1/14, 2/15, 4/17, 43/56, although their "weather" is totally different.

Other variants except for RG fail to distinguish between cases whose anomalies are multiples of each other, i.e. near-normal days with small say negative anomalies of all variables may not be distinguished from anomalously cold and dry days: cf. pairs of cases 60/61 and 1/62.

For the above reasons, the only possible candidate for providing a meaningful classification is variant RG, i.e. congruence matrix applied to the raw data, which treats all the days in a different way. However, the apparent dominance of the first PC (resulting from highly different variances of the input quantities) does not allow a meaningful classification since the rotation would lead to an extreme obliquity between rotated factors. This could be circumvented by scaling the original variables to have comparable variances (not shown). Nevertheless, the obvious dependence of potential classification on scaling factors is discouraging.

5. Conclusions

The main findings concerning circulation classification by PCA can be summarized as follows:

- correlation and covariance matrices yield very close solutions;
- problems with the mean pattern arise when anomalies are used as an input;
- common synoptic ideas are best complied with if correlation matrix is applied to raw input data;
- the linearity of PCA does not make it possible to identify more than two (approximately) linearly dependent clusters of data; nevertheless, it is not clear whether this can cause problems when analyzing real data.

On the other hand, the PCA is hardly applicable to weather classification. The only possibility seems to be using congruence matrix based on variables rescaled so as to have comparable variances.

Acknowledgements

This study was supported by the Grant Agency of the Czech Republic under contract 205/93/0294.

References

Compagnucci,R.H., Ruiz,N.E. (1992): On the interpretation of principal component analysis as applied to meteorological data. In: Proc. 5th Int. Meeting on Stat. Climatol., Toronto, 241-244

Drosdowsky,W. (1993): An analysis of Australian rainfall anomalies: 1950-1987. I: Spatial patterns. Int.J.Climatol. 13, 1-30

Huth,R. (1993): An example of using obliquely rotated principal components to detect circulation types over Europe. Met. Zeitschrift, N.F. 2, 285-293

Huth,R. (1995): Properties of the circulation classification scheme based on the rotated principal component analysis. Met.Atmos.Phys. (in press)

Richman,M.B. (1981): Obliquely rotated principal components: An improved meteorological map typing technique? J.Appl.Met. 20, 1145-1159

Richman,M.B. (1986): Rotation of principal components. J. Climatol. 6, 293-335

Corresponding address

Dr. Radan Huth
Institute of Atmospheric Physics
Boční II 1401
CZ - 141 31 Praha 4
Czech Republic

Tab.1 Percentage of variance explained (top) and loadings of selected circulation patterns on PCs explaining more than 0.1% of total variance.

PC	RR		RV		RG	AR					AV		AG				NR				NV			NG			
	1	2	1	2	1	1	2	3	4	5	1	2	1	2	3	4	1	2	3	4	1	2	3	1	2	3	4
	52.9	47.1	59.9	40.1	99.9	66.9	26.6	2.4	2.2	1.9	91.3	8.7	54.1	27.5	16.2	2.2	55.0	29.3	13.6	2.2	76.5	17.2	6.3	42.8	34.9	20.1	2.2
1	.50	.87	.87	.50	1.00	.86	.50	.00	-.01	-.01	.87	.50	.87	-.00	.50	.01	.75	.66	-.00	-.00	.75	.66	-.00	.75	.00	-.66	-.01
3	1.0	.00	.00	1.0	1.00	-.00	1.0	.01	-.00	-.02	-.00	1.0	-.00	-.00	1.00	.02	.00	1.0	-.00	-.00	.00	1.0	.00	.00	-.00	-1.0	-.00
5	.50	-.87	-.87	.50	1.00	-.87	.50	.00	.00	-.01	-.87	.50	-.87	-.00	.50	.01	-.75	.66	.00	.00	-.75	.66	.00	-.75	-.00	-.66	.00
6	.50	.87	.87	.50	.999	1.0	.00	-.00	-.01	.00	1.0	.00	1.0	-.00	.00	-.00	1.0	-.00	-.00	-.00	1.0	.00	.00	1.0	.00	.00	-.01
7	.76	.65	.65	.76	1.00	1.0	.00	-.00	-.01	.00	1.0	.00	1.0	-.00	.00	-.00	1.0	-.00	-.00	-.00	1.0	.00	.00	1.0	.00	.00	-.00
8	1.0	.00	.00	1.0	1.00	-.03	.10	.80	.20	.56	-.03	.10	-.03	-.14	.11	-.98	-.10	-.02	-.12	-.99	-.09	-.02	-.10	-.10	.01	.02	-.99
9	.76	-.65	-.65	.76	1.00	-1.0	-.00	.00	.01	-.00	-1.0	-.00	-1.0	.00	-.00	.00	-1.0	.00	.00	.00	-1.0	.00	.00	-1.0	-.00	-.00	.00
10	.50	-.87	-.87	.50	.999	-1.0	-.00	.00	.01	-.00	-1.0	-.00	-1.0	.00	-.00	.00	-1.0	.00	.00	.00	-1.0	.00	.00	-1.0	-.00	-.00	.01
13	1.0	.00	.00	1.0	1.00	.00	-1.0	-.01	.00	.02	.00	-1.0	.00	.00	-1.0	-.02	-.00	-1.0	.00	.00	.00	-1.0	.00	-.00	.00	1.0	.00
6-	.50	.87	.87	.50	.999	1.0	.00	-.00	-.01	.00	1.0	.00	.91	.41	.00	-.01	.97	-.00	.26	-.01	.97	.00	.26	.82	.57	.00	-.00
8-	1.0	.00	.00	1.0	1.00	.11	-.23	.64	.00	-.72	.10	-.22	.00	1.0	.00	-.01	.00	.00	1.0	-.02	.00	.00	1.0	-.00	1.0	-.00	.00
8+	1.0	.00	-.00	1.0	1.00	.17	.01	-.17	.96	-.12	.16	.01	-.00	-1.0	-.00	.01	-.00	-.00	-1.0	.02	.00	.00	-1.0	.00	-1.0	.00	-.00

Tab.2 Selected cases of synthetic weather data.

No.	T7	T14	T21	RH7	RH14	RH21
mean	-8	-2	-5	85	65	75
1	-16	-14	-15	80	50	65
2	-16	-14	-15	90	60	75
3	-16	-14	-15	100	70	85
4	-16	-14	-15	70	60	65
5	-16	-14	-15	80	70	75
6	-16	-14	-15	90	80	85
13	-6	-4	-5	80	50	65
14	-6	-4	-5	90	60	75
15	-6	-4	-5	100	70	85
16	-6	-4	-5	70	60	65
17	-6	-4	-5	80	70	75
18	-6	-4	-5	90	80	85
43	-10	0	-5	80	50	65
44	-10	0	-5	90	60	75
45	-10	0	-5	100	70	85
46	-10	0	-5	70	60	65
47	-10	0	-5	80	70	75
48	-10	0	-5	90	80	85
55	0	10	5	80	50	65
56	0	10	5	90	60	75
57	0	10	5	100	70	85
58	0	10	5	70	60	65
59	0	10	5	80	70	75
60	0	10	5	90	80	85
61	-7.2	-3.2	-4.0	85.5	66.5	76.0
62	-8.8	-3.2	-6.0	84.5	63.5	74.0

Tab.3 Percentage of variance explained (top) and loadings of selected weather cases on PCs with non-zero eigenvalues.

PC	RR			RG				AR			AG				NR				NG			
	1	2	3	1	2	3	4	1	2	3	1	2	3	4	1	2	3	4	1	2	3	4
	99.37	.54	.09	98.79	.86	.30	.05	51.5	41.8	6.6	42.3	35.5	19.2	3.1	55.2	34.6	9.4	.8	43.4	37.5	15.1	4.1
1	-.997	.068	.030	-.985	.157	.073	.021	.00	.94	.34	.82	.51	-.24	.10	.40	.81	.39	-.16	.89	.39	.21	-.11
2	-.999	.045	.032	-.990	.129	.050	.023	.85	.49	.18	.22	.90	-.34	.14	.92	.36	.18	-.03	.92	-.24	.27	-.14
3	-.999	.026	.033	-.993	.107	.032	.024	.96	.28	.10	-.50	.82	-.27	.11	.98	.19	.10	.01	.58	-.77	.23	-.12
4	-.997	-.073	.028	-.986	.159	-.047	.020	-.00	-.92	.40	.80	.50	.31	.10	.33	-.81	.46	-.18	.88	.39	-.26	-.11
5	-.996	-.081	.029	-.990	.130	-.055	.021	.85	-.49	.21	.19	.88	.40	.15	.88	-.42	.21	-.04	.91	-.25	-.31	-.15
6	-.996	-.088	.030	-.992	.107	-.062	.022	.95	-.27	.12	-.51	.80	.28	.11	.95	-.27	.12	.00	.57	-.78	-.23	-.12
13	-.995	.097	.029	-.997	.010	.076	.021	-.85	.50	.18	.90	-.19	-.35	.14	-.83	.51	.23	-.04	.25	.89	.34	-.18
14	-.997	.068	.030	-.998	.000	.052	.023	.00	.94	.34	.03	.03	-.93	.37	.05	.90	.42	.02	.02	.01	.89	-.46
15	-.999	.045	.032	-.999	-.008	.034	.024	.85	.49	.18	-.88	.22	-.40	.15	.87	.43	.21	.07	-.23	-.88	.37	-.19
16	-.998	-.063	.026	-.999	.010	-.047	.020	-.85	-.48	.21	.88	-.22	.39	.15	-.87	-.41	.27	-.06	.23	.88	-.37	-.18
17	-.997	-.073	.028	-.998	-.000	-.055	.021	-.00	-.92	.40	-.03	-.02	.93	.38	-.04	-.87	.50	.00	-.02	-.01	-.88	-.47
18	-.996	-.081	.029	-.998	-.008	-.061	.022	.85	-.49	.21	-.90	.20	.35	.16	.83	-.49	.25	.06	-.24	-.89	-.33	-.19
43	-.995	.098	-.035	-.997	.010	.077	-.028	-.85	.49	-.21	.90	-.20	-.35	-.16	-.83	.49	-.25	-.06	.24	.89	.33	.19
44	-.997	.068	-.026	-.998	.000	.053	-.020	.00	.92	-.40	.03	.02	-.93	-.38	.04	.87	-.50	-.00	.02	.01	.88	.47
45	-.999	.045	-.019	-.999	-.008	.034	-.014	.85	.48	-.21	-.88	.22	-.39	-.15	.87	.41	-.27	.06	-.23	-.88	.37	.18
46	-.997	-.062	-.040	-.998	.010	-.046	-.030	-.85	-.49	-.18	.88	-.22	.40	-.15	-.87	-.43	-.21	-.07	.23	.88	-.37	.19
47	-.997	-.072	-.030	-.998	-.000	-.054	-.022	-.00	-.94	-.34	-.03	-.03	.93	-.37	-.05	-.90	-.42	-.02	-.02	-.01	-.89	.46
48	-.997	-.080	-.022	-.998	-.008	-.061	-.016	.85	-.50	-.18	-.90	.19	.35	-.14	.83	-.51	-.23	.04	-.25	-.89	-.34	.18
55	-.990	.136	-.047	-.987	-.140	.078	-.028	-.95	.27	-.12	.51	-.80	-.28	-.11	-.95	.27	-.12	-.00	-.57	.78	.23	.12
56	-.995	.098	-.035	-.990	-.131	.054	-.021	-.85	.49	-.21	-.19	-.88	-.40	-.15	-.88	.42	-.21	.04	-.91	.25	.31	.15
57	-.997	.068	-.026	-.992	-.124	.035	-.015	.00	.92	-.40	-.80	-.50	-.31	-.10	-.33	.81	-.46	.18	-.88	-.39	.26	.11
58	-.997	-.048	-.053	-.988	-.143	-.044	-.031	-.96	-.28	-.10	.50	-.82	.27	-.11	-.98	-.19	-.10	-.01	-.58	.77	-.23	.12
59	-.997	-.062	-.040	-.989	-.133	-.053	-.022	-.85	-.49	-.18	-.22	-.90	.34	-.14	-.92	-.36	-.18	.03	-.92	.24	-.27	.14
60	-.997	-.072	-.030	-.990	-.125	-.060	-.016	-.00	-.94	-.34	-.82	-.51	.24	-.10	-.40	-.81	-.39	.16	-.89	-.39	-.21	.11
61	-1.00	-.009	-.002	-1.00	-.014	-.007	-.002	-.01	-.94	-.34	-.82	-.52	.24	-.10	-.40	-.81	-.39	.16	-.89	-.39	-.21	.11
62	-1.00	.005	.004	-1.00	.014	.006	.002	.01	.94	.34	.82	.52	-.24	.10	.40	.81	.39	-.16	.89	.39	.21	-.11

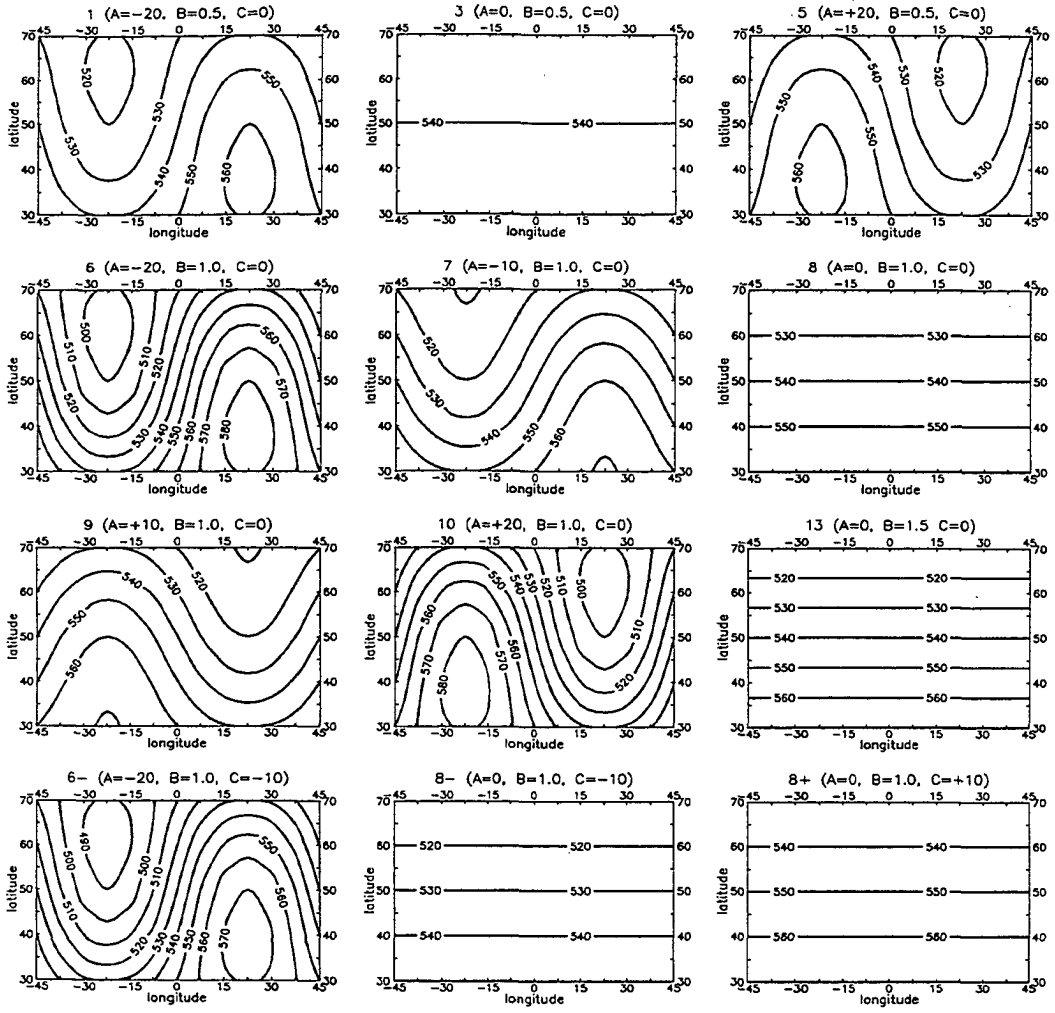


Fig.1 Selected circulation patterns.

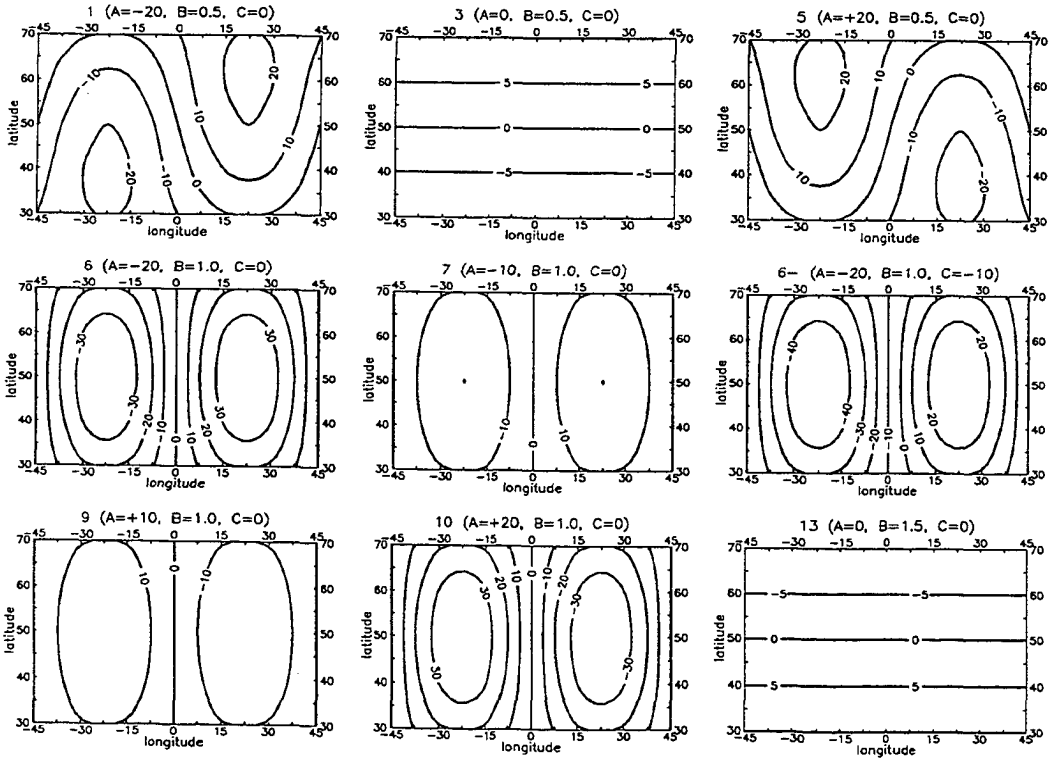


Fig.2 Anomaly fields.

USING STATE-SPACE STATISTICAL MODELS TO DESCRIBE RECENT TRENDS IN THE SPATIAL STRUCTURE OF THE CALIFORNIA CURRENT SYSTEM

Roy Mendelssohn and Franklin B. Schwing

Pacifc Fisheries Environmental Group
Pacific Grove, California, USA

ABSTRACT
A state-space decompostion of time-series into a non-linear, non-parametric trend, a non-stationary seasonal component and an autoregressive component are used to study changes in the Californai Current System. The changes in SST and wind stress are shown to be non-homogeneous over the reason. The hypothesis of Bakun of increased coastal upwelling is also examined.

1 INTRODUCTION

State-space statistical models are applied to long environmental time series of wind stress, sea surface temperature (SST), salinity and sea level from the California Current System (CCS) off the west coast of North America. The models estimate a non-parametric trend, a non-stationary and non-deterministic seasonal signal as well as an autoregressive term. The univariate models can be extended to non-gaussian dynamics that better model sharp changes in the dynamics, as well as to a multivariate factor model that tests for common components in the trends and the seasonal signals. We provide an overview of the state-space method, and use the model's results to describe temporal and spatial variability of the California Current System (CCS) over the last several decades. The results demonstrate that the CCS cannot be treated as a spatially homogeneous system when evaluating climate trends, nor can these trends be assumed to be regular in time.

2 STATE-SPACE DECOMPOSITION OF A TIME SERIES

A simple starting point for modeling an observed time series y_t such that the series can exhibit some of the more complex behavior of the previous section is to assume that the observed series is additively composed of independent components:

$$y_t = T_t + S_t + I_t + e_t, \quad t = 1,T \tag{1}$$

where T_t is the unobserved time-dependent mean-level (trend) at time *t*, S_t is the seasonal component at time *t*, I_t is the irregular term (stationary but autocorrelated) at time *t*, and e_t is the stationary, uncorrelated component at time *t*, which here can be viewed as "observation" or "measurement" error.

The model (Equation 1) states mathematically the assumed form of the observed time series, but leaves open the question of the form of each component and how to estimate the component series from the observed data. The components could be modeled parametrically - the trend by a polynomial of a given order, the seasonal by harmonics, for example, but this approach is very limited in handling series with the types of dynamics discussed above. Ideally the components would be defined as flexibly as possible while allowing the model to be estimated. One way to achieve this is to put a constraint on the "smoothness" (in this case through time) of the component. In the case of continuous functions of time, this implies constraining the derivatives of the function to be estimated. When time is discrete, the equivalent would be to put a smoothness constraint on the differences of the components, or other relevant linear combinations through time.

The use of such piecewise continuous "smoothing splines" to estimate unobserved components dates back to Thiele (1880, see Lauritzen 1981), and in the more modern era to a paper by Whittaker (1923). Shiller (1973) modeled the distributed lag (impulse response) relationship between the input and output of a time series under difference equation "smoothness" constraints on the distributed lags. He termed these constraints "smoothness priors", but did not offer an objective method of choosing the smoothing parameter. Akaike (1980) developed a Bayesian interpretation of the model and used maximum likelihood to estimate the smoothness parameter. Brotherton and Gersch (1981) showed how the Kalman filter and maximum likelihood could be used to solve the smoothing problem. Kitagawa and Gersch (1984,1985,1988), in a series of papers, extended the Kalman filter-maximum likelihood approach to a variety of nonstationary problems, and Harvey (1989) developed similar models under the title "structural time series models".

3 SMOOTHNESS PRIORS TIME-SERIES MODELING

How a smoothness constraint can allow for both a flexible and for a well-defined model can be most clearly understood in terms of estimating a "smooth" but unknown function which has been observed with "noise", that is data of the form

$$y_t = f_t + e_t, \quad t = 1,T \tag{2}$$

where the y_t are the observed data, f_t is an unknown smooth function and e_t are independent gaussian errors. In this model there is no seasonal component and no autoregressive component. The aim is to nonparametrically estimate a functional form (in this case a trend in time) that is obscured by the independent noise component. Whittaker (1923) suggested that the solution should balance fidelity to the data with fidelity to a constraint on the smoothness of the unknown function f_t:

$$\sum_{t=1}^{T}(y_t - f_t)^2 + \mu^2 \sum_{t=1}^{T}(\nabla^k f_t)^2. \tag{3}$$

Equation (3) is equivalent to solving the least-squares problem subject to a constraint on the differences of the

unknown function, using Lagrangean multipliers .The first term in Equation (3) is the usual sum-of-squares criterion, while the second term constrains the *k*-th order finite differences of the unknown function (the discrete equivalent of splines where the *k*-th order derivatives are constrained). The two parts are balanced by the "smoothness parameter" μ^2. As μ^2 goes to zero, the smoothness constraint disappears, and the estimate of the unknown function exactly interpolates the data. As μ^2 approaches infinity, the sum-of-squares term becomes negligible, and the solution is the appropriate *k*-th order polynomial of time (e.g. linear for *k=1*, quadratic for *k=2* etc.)

Equation (2) leaves unanswered the crucial question of how to estimate the smoothness parameter μ^2. Akaike (1980) gave the problem a Bayesian interpretation. He viewed the constraint as a stochastic, zero mean difference equation, that is

$$\nabla^k f_t \sim N(0, \sigma^2) \tag{4}$$

where the notation $N(0, \sigma^2)$ denotes a normal random variate with mean zero and variance σ^2, and where $\sigma^2 = 1/\mu^2$ (which can be interpreted as a signal-to-noise-ratio), is a hyperparameter that can be estimated using maximum likelihood methods. (That for a fixed value of μ^2 the Bayesian model is equivalent to Equation (3) see the references cited above). Akaike termed this a "smoothness prior", because the smoothness constraint is given an a prior distribution and is then estimated by likelihood methods.

The "local trend" fit by the smoothness priors approach can be shown to be a linear smoother - for a given value of the smoothness parameter the estimate of the unknown function at any time period is linear in the data, that is it can be calculated as a weighted linear combination of the observed time series. This estimate differs from a running mean, for example, which is also a linear smoother, in that the window used to smooth the data can vary as can the weights (see Hastie and Tibshirani 1990). Though the smoothing spline fit by this model is more complex than a running mean, the basic idea is the same - estimate the unobserved component by a linear smoother. We will return to this idea in order to model the seasonal component.

The smoothness prior approach can be used to model the seasonal component either by constraining the seasonal running sum as:

$$\sum_{i=0}^{p-1} S_{t-i} \sim N(0,\sigma_S^2) \tag{5}$$

or by constraining the seasonal differences:

$$S_t - S_{t-p} \sim N(0,\sigma_s^2). \tag{6}$$

The stationary irregular term is modeled as a q-th order autoregression:

$$I_t = \sum_{i=1}^{q} \phi_i I_{t-i} + e_t \tag{7a}$$

$$e_t \sim N(0,\sigma_I^2). \tag{7b}$$

The entire model can be put into a state-space format, and the hyperparameters estimated by maximum likelihood using a combination of Kalman filtering and smoothing and the EM algorithm (details can be found in Schwing and Mendelssohn 1995). The minimum mean square error estimates of the components are obtained from the Kalman smoother calculated with the hyperparameters equal to their maximum likelihood estimates. By appropriate adjustment of the state-space model, multiple series can be modeled and tested for common trends (up to an affine transformation), common seasonals or common AR components. The state-space formulation also allows for the inclusion of measurement error or for reconciling several sources of the data.

4 TRENDS IN THE CALIFORNIA CURRENT SYSTEM

The staet-space decomposition was applied to long environmental time series of wind stress, SST, salinity and sea-level from both coastal and oceanic locations in the CCS. SST trends are visually more correlated on the interannual (1-5 year) scale than wind stress (Figure 1-2). Major El Niños (1957, 1983) and a well-documented "regime shift" about 1976 dominate the SST trends series, particularly south of 38°N, but are not apparent in the wind trends. Instead their variance is seen in the wind AR series, presumably because of their rapid atmospheric response. SST also shows decadal-scale periods of warm and cool anomalies that extend through the entire CCS. Wind stress anomalies are less extensive and uncorrelated with SST, suggesting that decadal-scale SST variability in the CCS is controlled by the large-scale pressure and wind fields, rather than local wind forcing.

The CCS appears to be divided into three regions - one south of roughly 38°N, one north of 42°N, and a transition zone. Wind stress in the southern region was equatorward and became increasingly equatorward over time in a relatively monotonic pattern; SST decreased consistently with latitude. Stress was maximum off 32-38°N, the area of greatest interannual variation. The northern region featured a mean poleward stress that increased over time, and spatially uniform SST. While SST trends at all coastal sites display significant warming patterns, SST in the CCS shows a warming tendency south of 36°N and cooling north of 36°N. During the period of study (1946-90), the transition zone expanded southward. Moreover, during the course of the record, the transition zone shifted from a wind (SST) pattern similar to the northern region to one consistent with the southern region, but shifted from being characterized by the southern to northern region SST patterns.

The estimated seasonal components are examined for patterns consistent with increasing coastal upwelling during April-July. We test the hypothesis of Bakun (1990) that equatorward wind stress, hence upwelling, has been increasing in Eastern Boundary Current (EBC) systems over the past several decades, presumably in response to a pattern of long-term global warming.

Over the CCS region 30-40°N, where coastal upwelling is a dominant process in spring-summer, April-July equatorward wind stress and salinity display a highly significant (>.99) linearly increasing tendency over time, while SST and sea level decrease significantly, in agreement with increased upwelling (Figure 3). The four parameters are significantly correlated in a manner consistent with greater upwelling as well. The gains (relative rates of change) between these parameters also

are reasonable when compared to the expected physical balances between wind forcing, sea level set-down and isopycnal displacement in EBC systems.

This relationship does not occur at lower and higher latitudes within the CCS, presumably because coastal upwelling is a less important process in these areas. A key to identifying these patterns has been the ability to remove the long-term non-linear trend, using the state-space models, which mask the effect of increased upwelling in the observations.

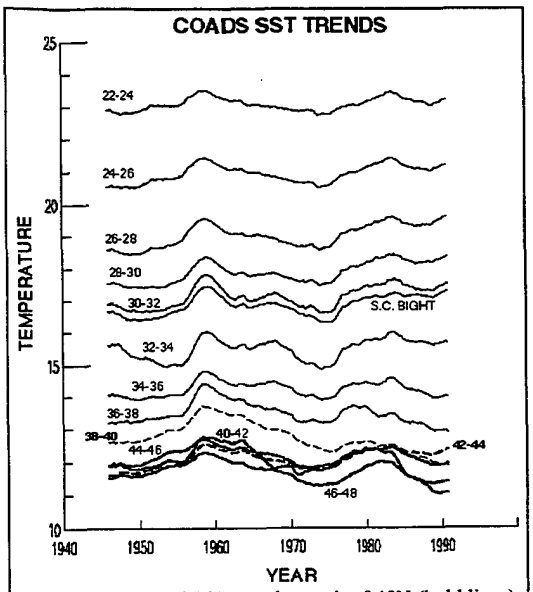


Figure 1. Estimated SST trends, north of 40N (bold lines), 38-40N (fine lines) and 42-44N (bold broken lines).

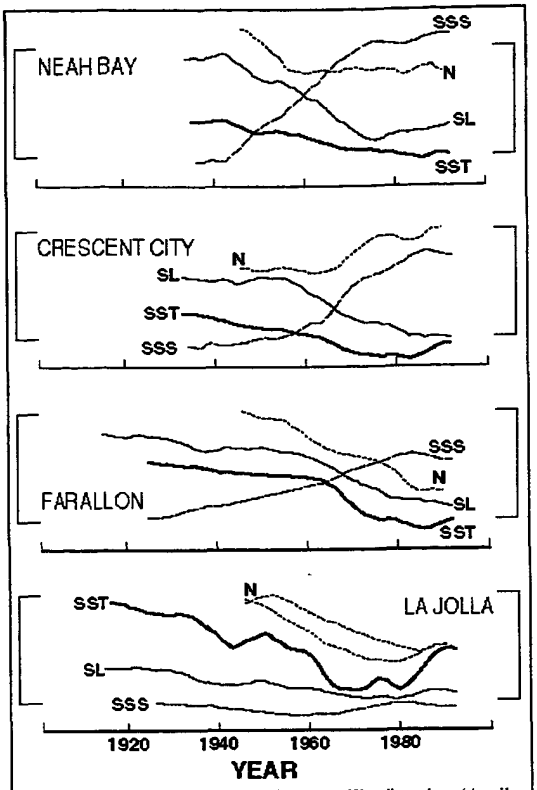


Figure 3. Time series plots of ``upwelling" series (April--Julyaverages from seasonal model components) for shore SST (bold solid lines), sea level (SL, light solid lines), surface salinity (SSS, bold dashed lines), and COADS poleward wind stress (light dotted lines).

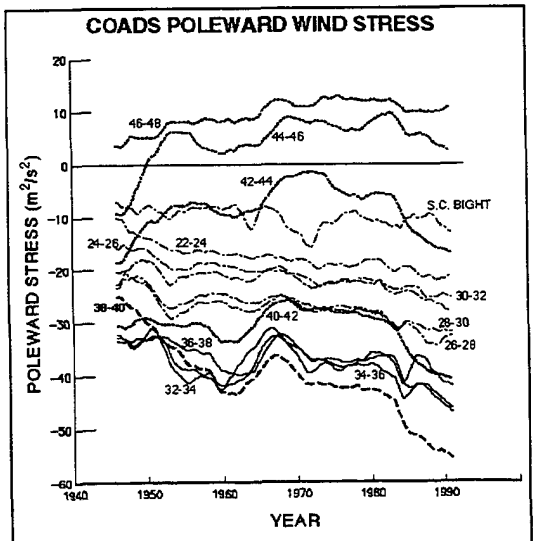


Figure 2. Estimated poleward pseudo-wind stress trends for 22-32N (dashed-dotted lines), 32-40N (solid lines), 38-40N (bold dashed lines), and 40-48N (bold dotted lines).

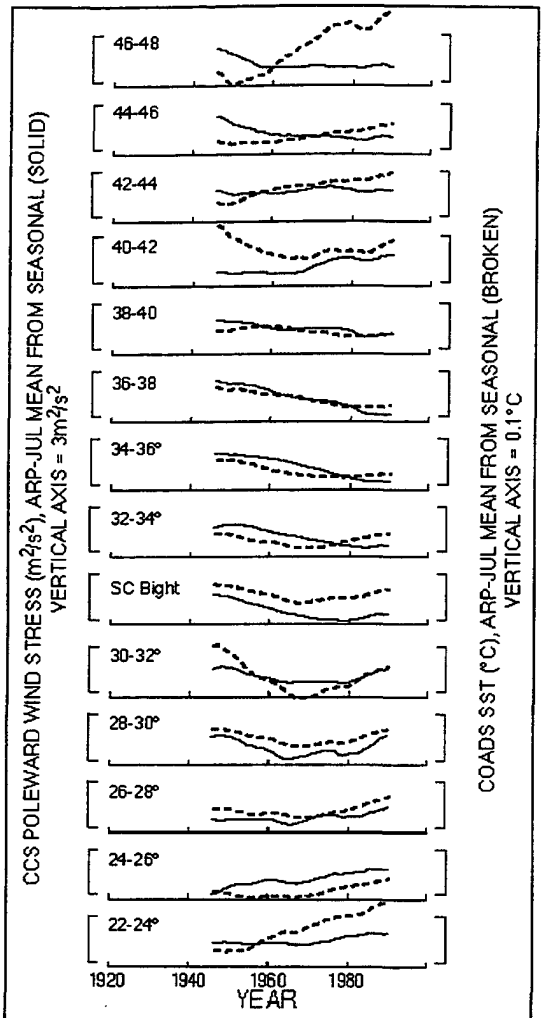


Figure 4. Time series plots of ``upwelling" series (April--July averages from seasonal model components) for poleward wind stress (solid lines) and SST (dashed lines), for COADS boxes.

5 REFERENCES

Akaike, H., 1980, Likelihood and the Bayes procedure, in *Bayesian Statistics*, edited by J.M. Bernardo, M.H. DeGroot, D.V. Lindley and A.F.M. Smith,pp 143-166, University Press, Valencia.

Bakun, A., 1990, Global climate change and intensification of coastal ocean upwelling, *Science 247*, 198-201.

Brotherton, T. and W. Gersch, 1981, A data analytic approach to the smoothing problem and some of its variation,. *Proceedings of the 20th IEEE Conference on Decision and Control*, 1061-1069.

Harvey, A.C., 1989, *Forecasting, Structural Time Series Models and the Kalman Filter*, 554 pp., Cambridge University Press, Cambridge.

Hastie, T.J. and R. J Tibshirani, 1990, *Generalized Additive Models*, 335 pp., Chapman and Hall,, London.

Kitagawa, G. and W. Gersch, 1984, A smooothness priors - state space modeling of time series with trend and seasonality, *J. Am. Statist. Assoc. 79*, 378-389.

Kitagawa, G. and W. Gersch, 1985, A smoothness priors time varying AR coefficient modeling of nonstationary time series, *IEEE Trans. on Auto. Control AC-30*, 48-56.

Kitagawa, G. and W. Gersch, 1988, Smoothness priors in time series, in *Bayesian Analysis of Time Series and Dynamic Models*, edited by J. Spall, Marcel Dekker, N.Y.

Lauritzen, S.L., 1981, Time series analysis in 1880: A discussion of contributions made by T.N. Thiele, *Int. Statist. Review 49*, 319-331.

Schwing, F. B. and R. Mendelssohn, 1995, Increased Coastal Upwelling in the California Current System, *Submitted for Publication.*

Shiller, R., 1973, A distributed lag estimator derived from smoothness priors, *Econometrica 41*, 775-778.

Whittaker, E.T., 1923, On a New Method of Graduation, *Proc. Edinborough Math. Assoc 78*, 81-89.

CORRESPONDING AUTHOR

Dr. Roy Mendelssohn
Pacific Fisheries Environmental Group
1352 Lighthouse Avenue
Pacific Grove, CA 93950-2097
USA.

Validation of the small-scale performance of a climate model by analysing the consistency of large-scale and small-scale climate

Ulrike Burkhardt

Institut für Meteorologie, Universität München, Germany

ABSTRACT

A canonical correlation analysis is used to study the simulation of the monthly mean relationships between small-scale precipitation patterns near the Alps and lage-scale flow patterns by the ECHAM climate model. Three simulations of the present day climate by the ECHAM general circulation model with varying resolution and model physics are analysed. Though little progress can be seen in simulating the mean precipitation over Europe, CCA reveals a much more realistic relationship between the rainfall field and the large-scale circulation in the simulations of later model versions.

1 INTRODUCTION

General circulation models (GCMs) are widely used for climate change experiments. Such experiments provide information about climate change on the large-scale, since the GCMs are assumed to be able to simulate the global-scale climate in a realistic way. However, for climate impact studies, it is usually the regional climate that is needed. Therefore a big effort is also being made towards improving the simulation of small-scale features by these models. Nevertheless, the models are not yet able to provide useful information on scales of just a few gridpoints (Grotch and MacCracken, 1991). The main problem is the coarse resolution and, consequently, the treatment of subgrid-scale processes. Such processes are represented by parametrizations which are often scale-dependent and therefore tuned to a particular resolution (Boer and Lazare, 1988). Therefore the consistency of the performance of a model may vary depending on the large-scale physics, the parameterizations or the resolution. In this paper a test is proposed to identify whether or not the small-scale field of a variable is consistent with the large-scale dynamics. The test consists of identifying relationships between the large-scale circulation and the small-scale field of a variable in the simulations. These simulated relationships are then compared to those relationships found in observational data.

The focus of this paper is on winter precipitation in the Alpine region. Three simulations of the present day climate by the ECHAM general circulation model with varying resolution and model physics are analysed. A canonical correlation analysis is used to study the simulation of the relationship between small-scale precipitation patterns near the Alps and large-scale flow patterns in the ECHAM climate model. The analysis is performed on a monthly-mean time scale for the winter months of the ECHAM1/T21, ECHAM3/T21 (improved model physics) and ECHAM3/T42 (increased resolution) simulations. The patterns obtained are compared with an identical analysis of observational data.

2 DATA AND METHODS

The observational data used are monthly mean values of precipitation and 500 hPa geopotential height for the winter months (DJF). They comprise of the NMC analysis of geopotential heights and precipitation data from 16 stations (from the WMSC and EMSD data sets) located in the region of the Alps of the years 1951-1984. The ECHAM model data, precipitation and geopotential height data, consist of 30-year simulations of the present day climate by the ECHAM1/T21, ECHAM3/T21 and ECHAM3/T42 model versions. A review of these model versions is given by Roeckner et al. (1992).

A canonical correlation analysis (CCA) is used for investigating the relationships between the regional pattern of precipitation near the Alps and the large-scale flow pattern at 500 hPa. This method is described in detail by Preisendorfer (1988). CCA was applied after filtering the dataset by EOF analysis following Barnett and Preisendorfer (1987). The significance of the canonical correlation was tested using a Monte-Carlo method (Metz, 1991).

3 RESULTS

CCA was applied to the large-scale geopotential field at 500 hPa and the precipitation field over the Alps. The precipitation field consisted of station measurements in the case of observational data and, otherwise, of model output at a few gridpoints in the area of the 'model-Alps'. The previous filtering of the data retained about 80% of the respective data fields.

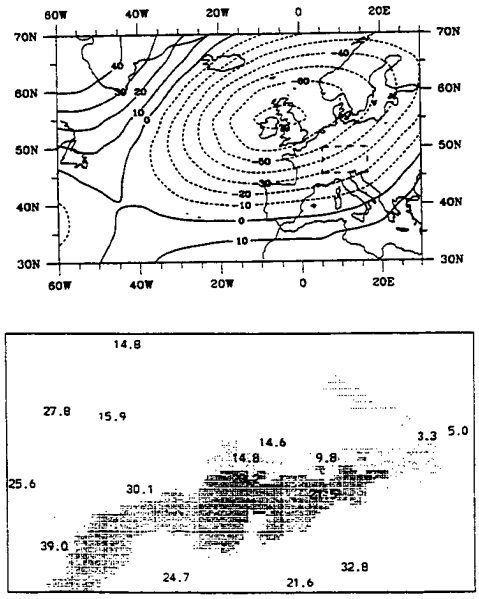


Figure 1: First canonical correlation patterns of the observational data a) geopotential height of the 500 hPa field (in gpm) and b) precipitation pattern (in mm/month) at 16 stations in the Alpine region. Shading denotes where orographic height exceeds 600 m, with an increment between levels of 400 m. The box in the geopotential height pattern indicates the area shown in b).

When applying the analysis to observational data, two statistically significant pairs of patterns are obtained. The first pair of patterns (fig. 1) consists of enhanced westerlies over Europe being connected with more precipitation in the area of the Alps whereas a reduced zonal flow is connected with less precipitation. This is probably due to greater storm activity over central Europe in the case of enhanced flow. The canonical correlation of these patterns is .83.

The second pair of patterns (fig. 2) displays an anomalous cross Alpine flow. This pattern is associated with more precipitation on the windward side and less precipitation on the lee-side of the Alps. The canonical correlation of the patterns is .74.

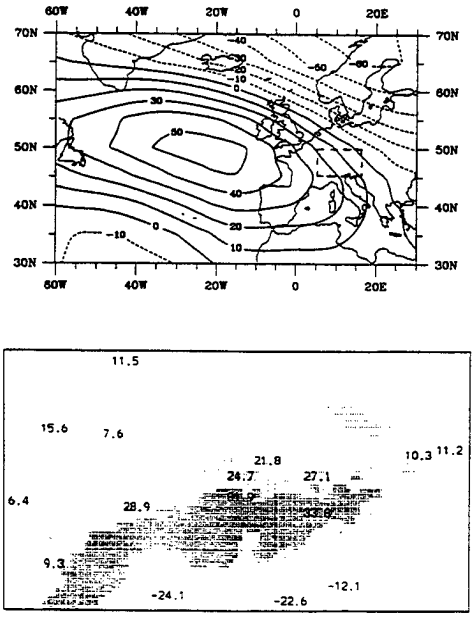


Figure 2: As in figure 1 but for the second canonical correlation patterns of the observational data.

A canonical correlation analysis was then applied to the output of the three ECHAM model versions. In the ECHAM1/T21 output canonical correlations between the rainfall field and the large-scale circulation were much smaller though significant. Furthermore the obtained patterns didn't show any resemblance with those of the observational data.

Applying CCA to the simulations of the ECHAM3/T21 version, a pair of patterns (fig. 3) is obtained which is comparable to the second canonical correlation patterns of the observational data. A westerly anomaly over the Atlantic and an anomalous northwesterly

flow over central Europe is connected with positive precipitation anomalies on the northern side and negative on the southern side of the Alps. The canonical correlation is .78.

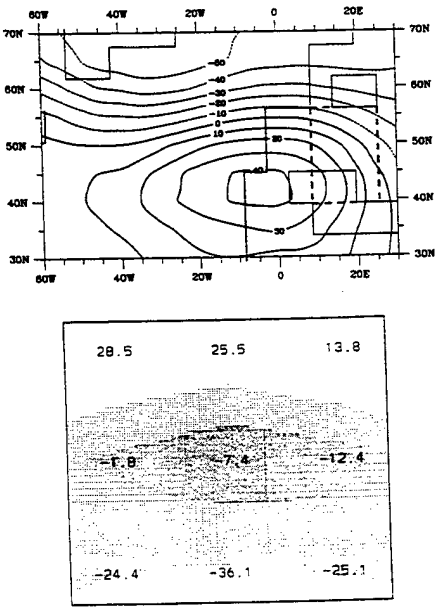


Figure 3: Canonical correlation patterns of the ECHAM3/T21 model a) geopotential height of the 500 hPa field (in gpm) and coast line of the T21 model and b) precipitation anomalies (in mm/month). Shading denotes where orographic height exceeds 600 m, with an increment between levels of 200 m. The box in the geopotential height pattern indicates the area shown in b).

The analysis of the ECHAM3/T42 model data produces two pairs of patterns, which resemble those found in the observations. One of the pairs of patterns (not shown) is very similar to the canonical correlation patterns of the ECHAM3/T21 output and has a canonical correlation of .86. The other pair of patterns (fig. 4) shows an anomalous northwesterly flow. This flow is connected with positive rainfall anomalies at each grid point. The canonical correlation is .88. These patterns resemble the first pair of patterns of the observational data.

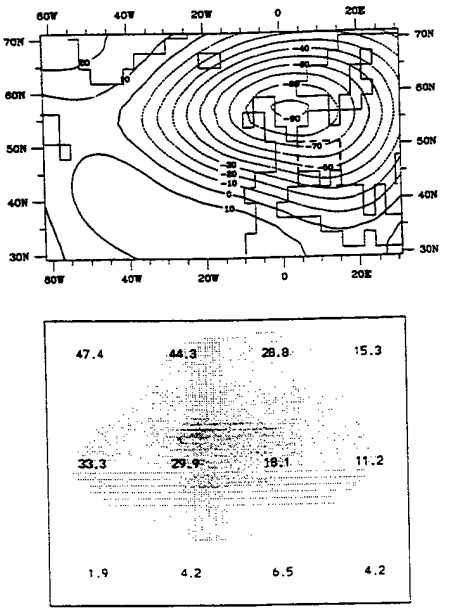


Figure 4: First canonical correlation patterns of the ECHAM3/T42 model a) geopotential height of the 500 hPa field (in gpm) and coast line of the T42 model and b) precipitation anomalies (in mm/month). Shading denotes where orographic height exceeds 600 m, with an increment between levels of 200 m. The box in the geopotential height pattern indicates the area shown in b).

4 CONCLUSION

The coarse structures of the observed relationships seem to be well simulated by the ECHAM3/T42 model version despite the simple shape of the 'model-Alps', while the results for the ECHAM1/T21 and ECHAM3/T21 are not as good. This is not only due to the increased resolution but also to the improved model physics, since one of the relationships at least has been found in the ECHAM3/T21 simulation, but not in that of the earlier ECHAM1/T21 model version.

Although the simulation of the wintertime mean precipitation field over Europe is not improved by the later model versions, the above analysis shows a marked improvement in the simulation of the relationship between precipitation and large-scale weather patterns. This means that the slightly better simulation of the monthly-mean precipitation in southern Europe by the T21 model versions might be due to a compensation of different errors in this area.

Although there is some progress detectable in the simulation of precipitation at small scales there is still a need of 'downscaling' of the

model output since even the smallest scale of the GCMs is still too large for climate impact studies.

References

Barnett, T. and R.Preisendorfer, 1987: Origins and levels of monthly and seasonal forecasts skill for United States surface air temperatures determined by canonical correlation analysis. *Mon. Wea. Rev.*, **115**, 1825-1850.

Boer, G.J. and M. Lazare, 1988: Some results concerning the effect of horizontal resolution and gravity wave drag on simulated climate. *J. Climate*, **1**, 789-906.

Grotch, S.L. and M.C. MacCracken, 1991: The use of general circulation models to predict regional climatic change. *J. Climate*, **4**, 286-303.

Metz, W., 1991: Optimal relationship of large-scale flow patterns and the barotropic feedback due to high-frequency eddies. *J. Atmos. Sci.*, **48**, 1141-1159.

Preisendorfer, R.W., 1988: *Principle Componenet Analysis in Meteorology and Oceanography, Developments in Atmospheric Science,* **17**, Elsevier, 425 pp.

Roeckner, E., K. Arpe, L. Bengtsson, S. Brinkop, L. Dümenil, M. Esch, E. Kirk, F. Lunkeit, M. Ponater, B. Rockel, R. Sausen, U. Schlese, S. Schubert and M. Windelband, 1992: Simulation of the present.-day climate with the ECHAM model: Impact of model physics and resolution. *Max Planck Institut für Meteorologie, Report 93*, 172 pp.

ACKNOWLEDGEMENTS

Financial support by *BayFORKLIM* is gratefully acknowledged as well as helpful comments from J. Egger, W. Metz and E. Zorita.

Ulrike Burkhardt
Institut für Meteorologie
Universität München
Theresienstr. 37
80333 München
Germany

SINGULAR-VALUE-DECOMPOSITION TECHNIQUE FOR MULTIVARIATE MODELING OF HYDROLOGIC TIME SERIES

Chavalit Chaleeraktrakoon and Van-Thanh-Van Nguyen
Department of Civil Engineering and Applied Mechanics
McGill University
Montreal, Quebec, Canada H3A 2K6

ABSTRACT: The objective of the present study is to propose a stochastic approach for multisite flow simulation. The suggested simulation scheme is based on the combination of the singular-value-decomposition (SVD) technique and AR(1) process. It has been shown that the SVD technique is efficient for computing the standardized principal components of a correlated flow matrix. The proposed method has been tested using monthly net-basin-supply (NBS) of Great Lakes water-resource system. Results have indicated that the suggested simulation scheme can describe adequately the basic statistical properties (e.g., mean, standard deviation, and lag-zero cross-correlation) of the historic flow data at various aggregation time scales.

1. INTRODUCTION

Simulation study of a water resource system against many samples of synthetic streamflows is fundamental to successful planning and design of the system. Various stochastic models have been proposed to generate such flow samples. In particular, multivariate AR and ARMA models (e.g., Salas et al., 1985; Haltiner and Salas, 1988) are usually suggested. Generally, these models can preserve the mean, standard deviation, and first few orders of serial correlations and cross-correlations of historic flow data used. The models, however, do not reproduce the historic statistics at higher aggregation time scales. For instance, if the multivariate ARMA model is applied to historic monthly flows, the basic properties of the monthly data will be preserved but the historic statistics at successive seasonal and annual time scales will not be reproduced.

A possible solution is to use disaggregation models (e.g., Valencia and Schaake, 1973; Mejia and Rousselle, 1976). The models describe the historic properties at various time intervals. Unfortunately, they are not suitable for multisite streamflow generation because the number of parameters may exceed easily the number of available flow data. This limitation can be solved by using condensed disaggregation models (e.g., Grygier and Stedinger, 1988; Santos and Salas, 1992). The condensed disaggregation models generally reproduce the basic statistical properties of historic flows at the two time scales used. However, the historic properties at intermediate time intervals are not reproduced. For example, if the condensed model is applied to disaggregate monthly flows from an annual flow generated using the ARMA model, the historic monthly and annual statistics will be preserved while the observed statistics at successive aggregation levels (bi-monthly, tri-monthly, quaterly, and semi-annual time scales) will not be reproduced.

The objective of the present study is therefore to propose a simulation procedure that can be used to generate synthetic streamflows at different locations concurrently. The proposed simulation scheme is the combination of the singular-value-decomposition (SVD) technique (e.g., Jöreskog et al., 1976) and AR(1) process. Results of an illustrative application using monthly net-basin-supply (NBS) of Great Lakes water-resource system have demonstrated that the stochastic procedure can preserve adequately the historic statistics at all successive aggregation levels.

2. PROPOSED SIMULATION SCHEME

Let p be the number of flow records in years, n be the number of sites, ω be the number of seasons, and $\bar{Q} = [\bar{Q}_{\nu,\tau}]$ be a matrix of streamflows with zero means where $\nu = 1, ..., p$; and $\tau = 1, ..., n\omega$. Now, the $p \times n\vartheta$ matrix of zero-mean flows at a upper time scale is denoted by $\bar{S} = [\bar{S}_{\nu,\tau}]$ in which ϑ is the number of seasons for the aggregate flows. These flow matrices are linearly related as

$$\bar{S}_\nu = \bar{Q}_\nu L \tag{1}$$

where $\bar{Q}_\nu$ is the $1 \times n\omega$ row vector of $\bar{Q}$, $\bar{S}_\nu$ is the

$1 \times n\vartheta$ row vector of $\tilde{S}$, and L is the $n\omega \times n\vartheta$ coefficient matrix. Depending on the definition of L, the matrix $\tilde{S}$ can be flows at any successive aggregation level of $\tilde{Q}$. It follows from eqn. (1) that

$$E[\tilde{S}_\nu] = E[\tilde{Q}_\nu]L \quad (2)$$

and

$$E[\tilde{S}_\nu^T \tilde{S}_\nu] = L^T E[\tilde{Q}_\nu^T \tilde{Q}_\nu]L \quad (3)$$

That is, the mean vector $E[\tilde{S}_\nu]$, and variance-covariance matrix $E[\tilde{S}_\nu^T \tilde{S}_\nu]$ of $\tilde{S}$ can be given through the corresponding statistics of $\tilde{Q}$.

In the following, a description of the proposed streamflow simulation procedure is presented. The procedure will start with normalizing the matrix Q of historic flow data if the flow data at each site and in each season are non-gaussian distributed. The normalized flow $Y_{\nu,\tau}$ is computed using logarithmic transformation as (Loucks et al., 1981):

$$Y_{\nu,\tau} = \ln(Q_{\nu,\tau} - a_\tau) \quad (4)$$

in which a_τ is the location parameter of a three-parameter lognormal distribution. Next, the transformed flow matrix Y of dimensions $p \times n\omega$ is standardized. Then, the SVD, a decomposition for a rectangular matrix, is applied to the standardized matrix $\tilde{Y}$. For $p > n\omega$, the decomposition computes the $n\omega \times n\omega$ lag-zero correlation matrix M_0 of Y. Now, the $r \times r$ diagonal matrix of positive eigenvalues Ω (r is the rank of $\tilde{Y}$), and the $n\omega \times r$ associated eigenvector matrix Ψ are estimated based on M_0. The eigenvector matrix Ψ has orthonormal columns and rows ($\Psi^T\Psi = I_r$ and $\Psi\Psi^T = I_{n\omega}$ where I_r and $I_{n\omega}$ are identity matrices of orders r and $n\omega$). The next step is to compute the $p \times r$ matrix W of standardized principal components as

$$W = \tilde{Y}\Psi\Omega^{-0.5} \quad (5)$$

This principal component matrix has orthogonal columns, $W^TW = (p - 1)I_r$.

In practice, the flow data matrix may have $n\omega > p$. Hence, the SVD estimates the $p \times p$ matrix $N = (p - 1)^{-1}\tilde{Y}\tilde{Y}^T$. Then, the $r \times r$ diagonal matrix of non-negative eigenvalues Ω and $p \times r$ matrix of associated eigenvectors Γ of N are computed. The following step is to determine the eigenvector matrix Ψ by

$$\Psi = (p - 1)^{-0.5}\tilde{Y}^T\Gamma\Omega^{-0.5} \quad (6)$$

Next, the principal component matrix W is computed as

$$W = (p - 1)^{0.5}\Gamma \quad (7)$$

Noted that the SVD is efficient for computing the principal component matrix W. It can be estimated based on M_0 or N whichever is smaller in dimensions. Further, the SVD assures that the lag-zero correlation matrix M_0 is preserved through Ψ and Ω as shown in the following equation:

$$M_0 = \Psi\Omega\Psi^T \quad (8)$$

If the correlations between flows of two successive years are important, an AR(1) process is fitted to each standardized principal component W_j as

$$W_{\nu,j} = \phi_1 W_{\nu-1,j} + U_{\nu,j} \quad (9)$$

in which ϕ_1 is the parameter and $U_{\nu,j}$ is the residual with zero mean and σ variance. The parameter ϕ_1 and residual variance σ are estimated by

$$\phi_1 = \rho_1 \quad (10)$$

and

$$\sigma = 1 - \phi_1^2 \quad (11)$$

where ρ_1 is lag-one autocorrelation of W_j.

3. APPLICATION

The proposed simulation procedure has been applied to monthly NBS of Lake Michigan-Huron, Lake Superior, Lake Erie, and Lake Ontario in Great Lakes water-resource system. The common record period is 90 years (1900-1989).

One-hundred synthetic samples of the monthly NBS data with the same size as that of the historic data were generated. The performance of the suggested simulation scheme for preserving the historic basic statistics (e.g., mean, standard deviation, and lag-zero cross-correlation) at aggregate annual time scale was tested.

Fig. 1 shows the box plot (Tukey, 1977) of ratio of generated to historic annual statistics (normalized statistics). It is readily seen that the proposed simulation scheme can reproduce the historic annual mean, standard deviation, and lag-zero cross-correlation quite well. The historic statistics (e.g., the ratio = 1) contain in the one-standard-deviation interval.

4. CONCLUSIONS

This paper presents a stochastic procedure for multisite streamflow simulation. The proposed simulation scheme consists of the SVD technique and AR(1) process. The SVD technique is shown to be efficient for transforming correlated flow variables into its uncorrelated principal components. A numerical application using monthly NBS of Great Lakes water-resource system was illustrated. Results have demonstrated that the proposed simulation scheme can reproduce accurately the basic statistics such as mean, standard deviation, and lag-zero cross-correlation of historic data at various aggregation time scales.

5. REFERENCES

Grygier, J. C., and Stedinger, J. R. (1988). "Condensed disaggregation procedures and conservation corrections for stochastic hydrology." *Water Resour. Res.*, 24(10), 1574-1584.

Haltiner, J. P., and Salas, J. D. (1988). "Development and testing of a multivariate, seasonal ARMA(1,1) model." *J. Hydrol.*, 104, 247-272.

Jöreskog, K. G., Klovan, J. E., and Reyment, R. A. (1976). *Geological factor Analysis*, Elsevier Scientific Pub. Co., N.Y.

Loucks, D. P., Stedinger, J. R., and Haith, D. A. (1981). *Water resource system planning and analysis*, Prentice-Hall, Englewood Cliffs, N.J.

Mejia, J. M., and Rousselle, J. (1976). "Disaggregation models in hydrology revisited." *Water Resour. Res.*, 12(2), 185-186.

Salas, J. D., Tabios III, G. Q., and Bartolini, P. (1985). "Approaches to multivariate modeling of water resources time series." in: *Special AWRA Monograph on Time Series Analysis*, edited by K. W. Hipel, Water Resources Bulletin, 21(4), 683-708.

Santos, E. G., and Salas, J. D. (1992). "Stepwise disaggregation scheme for synthetic hydrology." *J. Hydraul. Engrg.*, ASCE, 118(5), 765-784.

Tukey, J. W. (1977). *Exploratory data analysis*, Addison-Wesley, Reading, Mass.

Valencia, D. R., and Schaake, J. C. (1973). "Disaggregation processes in stochastic hydrology." *Water Resour. Res.*, 9(3), 580-585.

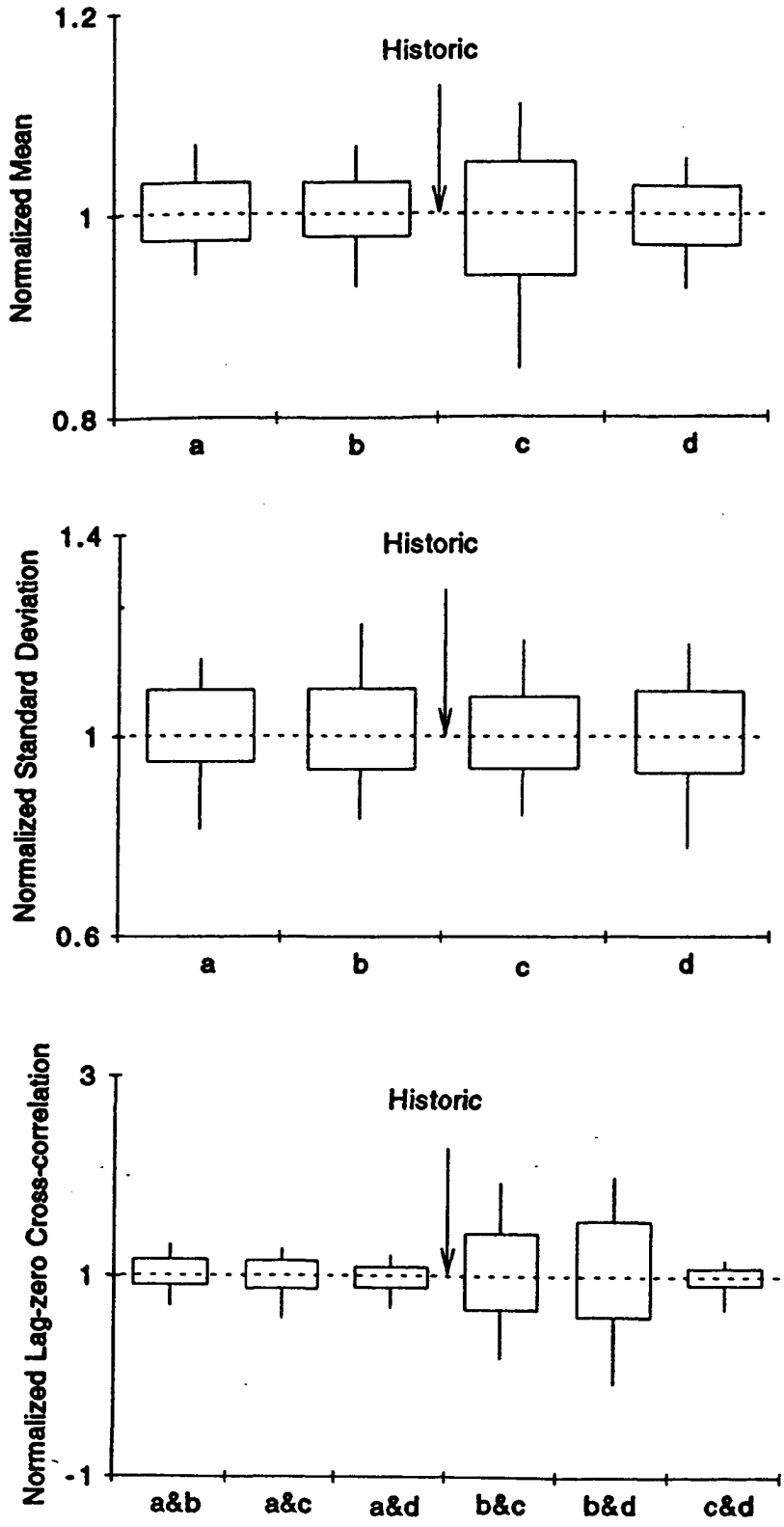


Figure 1. Box plots of normalized annual statistics; a: Lake Michigan-Huron, b: Lake Superior, c: Lake Erie, and d: Lake Ontario

SIGNIFICANT HARMONICS IN DISTRIBUTION PARAMETERS OF THE SEASONAL PROCESS

K.J.A. Revfeim

278 Cockayne Road, Wellington, New Zealand

ABSTRACT

A Fourier series is often fitted to monthly mean data with the objective of getting a smoothed annual process and employing fewer than 12 parameters. The same procedure applies to data for any sub-interval of the year and a decision has to be made on how many harmonics are significant. The basis of a statistical 'stopping rule' is given by joint fitting to all sub-interval data of a statistical distribution whose parameters have a Fourier form. This method given previously for total and extreme rainfall distributions is applied to temperature data assuming an underlying approximate Gaussian distribution.

1 INTRODUCTION

Seasonal patterns in various elements are commonly represented by means for sub-intervals of the year, usually months. With a sufficiently long period of observations the sub-intervals could be just one day but 'noise' in the pattern and the difficulty in tabulation leave only three practical choices of months (12 'equal' intervals), decads (36 'equal' intervals derived from days 1-10, 11-20,21-28/29/30/31 in each month), or pentads (73 genuinely equal 5-day intervals ignoring 29 February). A more complete description of the seasonal pattern is given by sample characteristics (mean, variance or other parameters of element-specific statistical distributions) in each of the 12, 36, or 73 subintervals.

To reduce the possibly large number of parameters, yet give an adequate representation, an accepted method of smoothing the sample characteristics is to fit a harmonic model to each parameter separately. The maximum number of harmonics that can be used is half the number of sub-intervals (6 for months, 18 for decads, 36 for pentads) so, for monthly data in particular, unless 4 or fewer harmonics are used there is very little advantage in the harmonic representation. On the other hand it may be difficult to establish the statistical significance of more than 1 or 2 harmonics even though the data fit appears reasonable. Of course this begs the question whether sine/cosine functions are the best periodic building blocks of an alternate representation.

For each characteristic of the data harmonics can be added successively to test in various ways how well the truncated harmonic forms fit the sample values. Taking the truncated harmonic forms to be the *true* population mean/variance, and assuming sample means to be normally distributed, Epstein (1991) produced standardised sampling values separately for means (t-distribution) and variances (F-distribution). Epstein then used the frequencies of these standardised sampling values, in each decile of their respective sample distribution, to assess the best fit and establish an optimum number of harmonics. The average value of the chi-square statistic of the decile frequencies over 198 US stations was not a strong discriminator. However total frequencies in each decile (over all stations) showed that 3 harmonics best fitted the 17 year record of that particular set of station mean temperatures. A separate analysis of variances, about the *true* 3 harmonic means, showed 2 harmonics best fitted 90% of the 198 stations.

For an assumed distribution $f(x_{ij}, \Theta_j)$, $i = 1....n(\text{years}), j = 1...s(\text{sub}-\text{intervals})$ of sub-interval data $\{x_{ij}\}$ the parameters Θ (not necessarily mean/variance, although these will be functions of parameters) can be taken as varying seasonally in harmonic form

$$\theta_j = t_0 + \sum_{k=1}^{[s/2]} t_k \cos(2\pi jk/s + p_k) \qquad (1)$$

Harmonic parameters $\{t_k, p_k\}$ can be estimated by maximum likelihood (ML) and the benefits of each additional harmonic (or subset of harmonics) can be tested for statistical significance by -2Δ log-likelihood which is assumed to have approximate chi-square distribution. The notable differences from the procedure used by Epstein are that all parameters are estimated jointly, and the number of statistically significant harmonics for an individual station record is readily established.

The same method was used for monthly data with 2-parameter extreme and total rainfall distributions (Revfeim, 1982 a,b). Besides the log-likelihood testing for additional harmonics one can apply t-tests as to whether individual harmonic amplitudes are

significantly greater than zero.

2 EXAMPLES

We assume a Gaussian distribution for mean temperatures

$$f(x) = (2\sigma^2)^{-1/2} \exp\{-(x-\mu)^2/2\sigma^2\}$$

where μ and σ^2 have the harmonic form (1).

In joint ML estimation there is an inherent assumption of independence of deviations about the mean seasonal pattern. Obviously there will be a degree of dependence in 5-day mean temperatures with cold/warm spells bridging successive pentads, although monthly means will dilute dependence. However the ML procedure is considered robust enough to give reasonable parameter estimates despite some dependence. It is a small detraction from the benefits of joint parameter estimation and resultant significance-testing/harmonic-fitting decisions.

Pentad temperature data for New York (NY No. 14732), Boise (Idaho No. 24131) and Tallahassee (Florida No. 93805) were kindly provided by Dr Epstein covering the period October 1973 to December 1990 (5,5 and 34 pentads respectively excluded due to missing/dubious values for individual days). All data were given in degrees Fahrenheit and because this is a model fitting exercise, not a climate description, conversion to degrees Celcius was considered unnecessary.

A first pass fitting of mean/variance is equivalent to an exact fit (maximum log-likelihood $\hat{L}$) with 146 harmonic parameters. Fitting just 2 parameters μ_0, σ_0^2 (i.e. ignoring seasonality) gives the lower bound of log-likelihood L_0 from which the space available for harmonic seasonal parameters $L_0 - \hat{L}$ is measured.

The procedure used was to add harmonics to *both* mean and variance testing that the increment in log-likelihood (approx. chi-square with 4 d.o.f.) was significant at the prescribed level. The 'stopping rule' was based on non-significance of the next attempted harmonic fit and in the residual parameter space. Naturally for these mid-latitude sites the first harmonic is expected to be dominant and the point of interest is how many additional harmonics are significant. Table 1 shows the 3 or 4 harmonic fit to the three stations including the likelihood space available and utilised by added harmonics.

Fitting harmonics for New York and Boise was straightforward but Tallahassee was notable for the inability to jointly fit the first harmonic alone. This was primarily due to the steep fall and rise shape in seasonal variance and Table 2 shows a pseudo monthly pattern (73rd pentad ignored) of means and variances for Tallahassee. Starting the fitting procedure with two harmonics overcame the problem.

3 DISCUSSION

Pentad temperatures give sufficient smoothing on daily data to allow estimation of harmonic components of distribution parameters for as short a record as 5 years. However compared with a longer record the less well defined seasonal pattern in mean and variability leads to fewer harmonics established as being significant. Estimated coefficients for New York pentad temperatures are shown (first harmonic only) in Table 3 revealing the consistency of consecutive 6 year periods with approximate $\sqrt{3}$ enhancement of s.e.'s compared with the full 18 year record parameter estimates in Table 1.

Fitting harmonics to monthly mean temperatures provides a subtle tool for checking data quality since joint fitting of parameters can fail to demonstrate significance in the expected pattern of variances. This may be found for one station whereas adjacent stations do show the dominant outcome of low variability at high mean temperatures and high variability at low mean temperatures.

Joint ML estimation of seasonally varying parameters in harmonic form of element distributions is a straightforward procedure. This method appears to have advantages over calculation of harmonic coefficients separately. The latter requires the assumption that some truncated harmonic form is the *true* mean for higher order statistics and provides no quick tests of significance for harmonic amplitudes.

References

Epstein, E.S., 1991, "Determining the optimum number of harmonics to represent normals based on multiyear data", J. Climate, 4, 1047-1051.

Revfeim, K.J.A., 1982a, Comments "On the study of a probability distribution for precipitation totals", J. Appl. Meteor., 21, 1942-1945.

——, 1982b, "Seasonal patterns in extreme 1-hour rainfalls", Water Resour. Res., 18, 1741-1744.

Table 1: Likelihood space for seasonal parameters, harmonic increments, and parameter estimates for pentad mean temperatures 1973-90 at New York, Boise and Tallahassee.

	$L_0 - \hat{L}$	H_1	H_2	H_3	H_4		mean(se)	H	amp(se)	t-stat	phase(se)
New York	1607.7	1502.7	9.9	15.8	-	μ	54.4(0.2)	1	22.7(0.3)	105.2	-156(0)
								2	0.6(0.3)	2.6	-173(11)
								3	0.9(0.2)	4.2	-101(7)
						σ^2	26.9(1.2)	1	16.2(1.8)	9.0	+23(3)
								2	4.5(1.6)	2.8	+53(11)
								3	2.9(1.4)	2.1	+84(14)
Boise	1355.0	1158.8	80.4	43.0	10.4	μ	50.6(0.2)	1	21.8(0.3)	76.9	-162(0)
								2	3.1(0.3)	12.5	+125(2)
								3	1.8(0.3)	7.2	-157(4)
								4	0.8(0.3)	3.3	+160(9)
						σ^2	42.3(1.9)	1	26.4(3.3)	8.0	+13(2)
								2	20.4(2.7)	7.4	+1(3)
								3	16.4(2.5)	6.6	+38(4)
								4	4.6(2.1)	2.2	+25(13)
Tallahassee	1411.4	-	1317.9	10.6	14.9	μ	66.9(1.5)	1	16.0(0.2)	74.3	-159(0)
								2	1.5(0.2)	7.4	+167(4)
								3	0.3(0.2)	1.2	+136(22)
								3	0.3(0.2)	1.2	+136(22)
						σ^2	27.1(1.4)	1	28.6(2.1)	13.4	+12(2)
								2	3.5(1.7)	2.1	+6(17)
								3	3.2(1.7)	1.9	+166(17)
								4	2.0(1.0)	2.0	+155(14)

Table 2: Seasonal pattern of temperature means/vces for Tallahassee.

Pentads	1-3	4-7	etc									
Mean	49.7	52.7	60.7	65.6	73.1	79.2	81.3	81.1	78.9	68.6	61.4	52.6
Vce	37.0	12.4	8.5	2.5	2.5	1.2	1.0	0.6	1.7	10.6	10.9	14.6

Table 3: Likelihood space for seasonal parameters, harmonic increments, and first harmonic parameter estimates for pentad mean temperatures at New York.

Period	$L_0 - \hat{L}$	H_1	H_2	H_3	H_4		mean(se)	H	amp(se)	t-stat	phase(se)
1973-78	521.5	435.6	-	-	μ	54.4(0.3)		1	22.0(0.4)	62.8	-157(0)
					σ^2	26.3(1.7)		1	15.4(2.2)	7.0	+25(4)
1979-84	631.0	525.2	19.9	15.2	μ	53.9(0.3)		1	23.3(0.4)	61.9	-155(0)
					σ^2	26.6(2.0)		1	18.9(3.3)	5.7	+28(3)
1985-90	620.5	534.6	5.3	-	μ	54.8(0.2)		1	22.5(0.3)	65.5	-156(0)
					σ^2	24.6(1.8)		1	13.0(2.6)	4.9	+4(5)

PROBABLE INFERENCE OF SIMPLE MODELS FOR UNCERTAIN QUANTITIES

Vicente SOLANA and Alberto SOLANA-ORTEGA
Instituto de Matemáticas y Física Fundamental, CSIC, Madrid, Spain

ABSTRACT

Data based inference of simple physical models for a set of observable uncertain quantities regarding other unobserved quantities is formulated in a plausible logical language. The Relative Entropy procedure employing logical probabilities is extended to this modelling at several inference levels. It is applied to an example of regional flood analysis.

1. INTRODUCTION

This paper studies the following question: Given the different sets of data associated to several observable uncertain quantities corresponding to the same physical magnitude, how can we select a simple physical model for these quantities by making use of probable inference based only on the available data?

It is of the greatest importance in regional analysis in climatology and related fields. Usually, frequentist modelling only considers the statistical dependence between the observed uncertain quantities. However, physical modelling should also involve the use of models with some kind of functional dependence of the observed quantities with regard to unobserved uncertain quantities.

Here, it will be examined the class of homogeneous models, in which the set of observed uncertain quantities, corresponding to the observed data at different locations, are assumed to have the same type of simple functional dependence on each hidden quantity.

Some particular applications of the homogeneous class of models in regional flood analysis were already presented, based on the flood index method using L-moments (Hosking 1988,93). This method suggests the possibility of some type of intersite dependence between the uncertain quantities but does not clearly formulate any model which takes into account a function dependence of the observed quantities on the unobserved ones. Besides, it is developed in a statistical frequentist framework where numerous difficulties at all inference levels exist (Ashkar et al. 1994, Solana 1995b)

Instead of statistical methods we need probable inference methods which are formulated in a plausible logical language using logical probabilities. In addition to Bayesian methods, a new Entropy probable inference procedure that also employs logical probabilities has been proposed for data based uncertain quantities modelling (Solana and Lind 1993). When using fractile probability constraints to encode data it was named the Relative Entropy method with Fractile constraints, or the REF method for short. Between these methods, Entropy inference exhibits greater logical consistency than Bayesian inference (Solana 1991,95a).

In Section (2) the inference problem is described in a plausible language. Next, the REF method is applied at the successive inference levels in Section (3). An example illustrates in Section (4) an application to regional modelling of annual maximum floods of a set of unregulated rivers.

2. INFERENCE FOR A FAMILY OF SCALAR UNCERTAIN QUANTITIES

Let $\{\mathrm{X}_k\}$, $k = 1,2,..,m$, be a set of real-valued scalar observed uncertain quantities, defined, respectively, on the given domains $\{\mathrm{E}_{(\mathrm{X}_k)}\}$. Let $\{(\mathrm{x}_k)_i\}$, $i = 1,2,...n$, be the set of observational data associated to each quantity X_k. Every observational data $(\mathrm{x}_k)_i$ corresponds to a "precise" numerical real value assigned to an observation of X_k. The quality of the observation measurements is not considered in this simple problem.

Let X_k be a future observation of X_k and denote by x_k any possible value of X_k, $x_k \in \mathrm{E}_{(\mathrm{X}_k)}$. Note that the future observation is written in italics to distinguish it from the uncertain quantity.

Physical modelling consists in the inference of models comprising some kind of functional dependence of the quantities X_k, with regard to unobserved uncertain quantities. This paper examines the class of function models in which the set of uncertain quantities $\{\mathrm{X}_k\}$, corresponding to the same physical magnitude associated to observational data at different locations, are assumed simply dependent on the hidden uncertain quantities $\{\mathrm{Z}_k\}$, $k = 1,2,...,m$, likely related to another physical magnitude. Such a dependence is here symbolically represented by the functions $h_k[.]$ given as

$$\mathrm{X}_k = h_k\left[\mathrm{Z}_k,\ \{(a_k)_j\}\right], k \in 1,2,...,m\ , \qquad (1)$$

where $\{(a_k)_j\}$, $j = 1,2,...,s$, denotes the parameter vector of each type of function.

$\{\mathrm{Z}_k\}$, $k \in N$, is, then, the set of real-valued scalar unobserved uncertain quantities to which the observed quantities $\{\mathrm{X}_k\}$are functionally related. They are correspondingly defined on the domains $\{\mathrm{E}_{(\mathrm{Z}_k)}\}$. Let Z_k be a future observation of Z_k and denote by z_k any possible value of Z_k , $z_k \in \mathrm{E}_{(\mathrm{Z}_k)}$.

The function $h_k[.]$ applies to the possible values of future observations of X_k and Z_k. For the sake of simplicity we restrict our analysis to the class of monotonic homogeneous models having the same type of functional dependence on each hidden quantity Z_k, though different parameter vectors for each observed uncertain quantity. Since $\{\mathrm{Z}_k\}$, $k \in N$,are unobserved quantities, the only available data that will be used to make probable inference are $\{(\mathrm{x}_k)_i\}$. They may be

identically expressed as the transformed data$\{(z_k)_i\}$ by using the same transformation functions $h_k[.]$.

2.1 PLAUSIBLE LOGIC LANGUAGE

Let $\mathcal{L}$ be the language system of sentential plausible logic in which the inference problem is formulated. It includes two classes of sentences:

- The class of atomic sentences formed by only one variable and one predicate(well formed formula sentences), related to future observations of the uncertain quantities. They are:

  -For the observed quantities $\{X_k\}$: both the sentences $X_k \leq x_k$, which stands for "the next observation X_k is less than or equal to x_k ", and the evidential context sentence denoted by e_{x_k} that stands for "the next observation X_k is contained within the domain $E_{(X_k)}$".

  -For the unobserved quantities $\{Z_k\}$: $Z_k \leq z_k$, which stands for "the next observation Z_k is less than or equal to z_k" , and the evidential context sentence denoted by e_{z_k} that stands for "the next observation Z_k is contained within the domain $E_{(Z_k)}$ ".

- The class of evidential sentences of observational data. They are the sentences denoted by D_{x_k} that stand for "the observed data are the numerical values $\{(x_k)_i\}$ ".

The plausible logic system also contains the logical products and sums of pairs of well formed sentences. In this paper the symbol "(,)" employed with sentences means the logical product of sentences. The logical product operation is here extended to the joint evidences for this inference problem formed as the pairs of the evidential sentences represented by (D_{x_k}, e_{x_k}) and (D_{z_k}, e_{z_k}), associated, respectively, to the uncertain quantities X_k and Z_k, which cannot be reduced to simple sentences.

The plausible logic system also contains the following elements:

- The truth contents of the sentence $X_k \leq x_k$ with regard to the true evidence e_{x_k} and the joint evidences (D_{x_k}, e_{x_k}), which are defined by the logical products $(X_k \leq x_k, e_{x_k})$ and $(X_k \leq x_k, e_{x_k}, D_{x_k})$, respectively.

- The truth contents of the sentence $Z_k \leq z_k$ with regard to the true evidence e_{z_k} and the joint evidences (D_{x_k}, e_{z_k}), which are defined by the corresponding logical products $(Z_k \leq z_k, e_{z_k})$ and $(Z_k \leq z_k, e_{z_k}, D_{x_k})$.

- The plausibilities or "certainty degrees" for the inferred sentence $X_k \leq x_k$ on the given evidences e_{x_k} and (D_{x_k}, e_{x_k}), which, respectively, are represented by $X_k \leq x_k \mid e_{x_k}$ and $X_k \leq x_k \mid (D_{x_k}, e_{x_k})$. The plausibility $X_k \leq x_k \mid e_{x_k}$ is the relative amount of the truth content $(X_k \leq x_k, e_{x_k})$ on the evidence e_{x_k}. Likewise, the plausibility $X_k \leq x_k \mid (D_{x_k}, e_{x_k})$ is the relative amount of the truth content $(X_k \leq x_k, e_{x_k}, D_{x_k})$ on the true joint evidences (D_{x_k}, e_{x_k}).

- The plausibilities for the inferred sentence $Z_k \leq z_k$ on the given evidences e_{z_k} and (D_{x_k}, e_{z_k}), which, respectively, are represented by $Z_k \leq z_k \mid e_{z_k}$ and $Z_k \leq z_k \mid (D_{x_k}, e_{z_k})$. The plausibility $Z_k \leq z_k \mid e_{z_k}$ is the relative amount of the truth content $(Z_k \leq z_k, e_{z_k})$ on the evidence e_{z_k}. Likewise, the plausibility $Z_k \leq z_k \mid (D_{x_k}, e_{z_k})$ is the relative amount of the truth content $(Z_k \leq z_k, e_{z_k}, D_{x_k})$ on the true joint evidences (D_{x_k}, e_{z_k}).

The truth contents and their relative amounts can be explained as a specific semantics by using ranges of sentences (Solana 1992).

2.2 LOGICAL PROBABILITIES

Logical probabilities are the numerical values assigned to plausibilities. For the sentence $X_k \leq x_k$, they are the real values, scaled from 0 to 1, assigned to the plausibilities $X_k \leq x_k \mid e_{x_k}$ and $X_k \leq x_k \mid (D_{x_k}, e_{x_k})$, which, therefore, are always conditioned either on the context evidence e_{x_k} or on the joint evidences (D_{x_k}, e_{x_k}). These logical probabilities can be written as the two following monotonic probability distribution functions:

- The "reference" probability distribution function $P(x_k \mid e_{x_k})$, which defines the numerical probability initially assigned as a reference model for the plausibility $X_k \leq x_k \mid e_{x_k}$, as a function of any possible value x_k :

$$P(x_k \mid e_{x_k}) = \Pr[X_k \leq x_k \mid e_{x_k}]. \qquad (2)$$

- The "inferred" probability distribution function $Q(x_k \mid D_{x_k}, e_{x_k})$, which defines the numerical probability assigned to the plausibility $X_k \leq x_k \mid (D_{x_k}, e_{x_k})$ as a function of x_k :

$$Q(x_k \mid D_{x_k}, e_{x_k}) = \Pr[X_k \leq x_k \mid (D_{x_k}, e_{x_k})]. \qquad (3)$$

Analogously, it is possible to define the logical probabilities for the sentence $Z_k \leq z_k$, by assigning the real values, scaled from 0 to 1, to the plausibilities $Z_k \leq z_k \mid e_{z_k}$ and $Z_k \leq z_k \mid (D_{x_k}, e_{z_k})$. They can be written as $P(Z_k \mid e_{z_k})$ and $Q(Z_k \mid D_{x_k}, e_{z_k})$, the "reference" and the "inferred" distribution functions for the unobserved uncertain quantity Z_k, defined as above.

The homogeneous model is defined by the functions (1) that relate the uncertain quantities $\{X_k\}$ and $\{Z_k\}$. Physically, it expresses a causality relationship between the unobserved quantities and the observed ones. For example in the case of severe storms and floods. Thus, it makes sense to formulate the logical inference problem starting with a reference probability distribution function for the hidden quantities which "generate" the others.

The set of uncertain quantities $\{Z_k\}$ can be described by a reference joint probability distribution function. A candidate reference probability distribution $P(\mathbf{z} \mid \mathbf{e_z})$, as a function of $\mathbf{z} = (z_1, z_2, ..., z_m)$ given the evidences $\mathbf{e_z} =$

$(e_{z_1}, e_{z_2}, ..., e_{z_m})$, may be any appropriate mathematical function, monotonic and scaled from 0 to 1 , which represents an arbitrary measure of the certainty degrees for the logical product of the sentences $Z_k \leq z_k, k = 1,2,...,m$, on the logical product of the evidence contexts $\{e_{z_k}\}$. It will be assumed that it factorizes:

$$P(\mathbf{z} \mid \mathbf{e_z}) = P(z_1 \mid e_{z_1}) P(z_2 \mid e_{z_2}) ... P(z_m \mid e_{z_m}). \quad (4)$$

This means that the hidden uncertain quantities are statistically independent. Since we are investigating simple models, another assumption will be that factors are identically distributed such that $P(z_1 \mid e_{z_1}) = P(z_2 \mid e_{z_2}) = ... = P(z_m \mid e_{z_m})$.

2.3 INFERENCE LEVELS

The data based inference problem for several uncertain quantities involves some different probability assignments which are referred to as inference levels.

The first inference level deals with the assignment of an inferred distribution $Q(\mathbf{z} \mid (\mathbf{D_z}, \mathbf{e_z}))$ given a specific $P(\mathbf{z} \mid \mathbf{e_z})$ and the sets of data $\mathbf{D_z} = (D_{z_1}, D_{z_2}, ..., D_{z_m})$ on the given domains $\{E_{(Z_k)}\}$. The inference procedure in this level may be formulated explicitly as the symbolic operator g[.] , such that (Solana 1995b)

$$Q(\mathbf{z} \mid (\mathbf{D_z}, \mathbf{e_z})) = g\left[P(\mathbf{z} \mid \mathbf{e_z}), (\mathbf{D_z}, \mathbf{e_z})\right]. \quad (5)$$

At the second inference level a reference distribution is chosen from a space of candidate reference distributions, which contains different types of distributions.

Finally, at the third level, the procedure selects a simple model from a space of candidate models.

3. REF INFERENCE PROCEDURE

The Relative Entropy method with Fractile constraints, or REF method for short, is a new version of the Entropy methods using logical probabilities, developed in (Solana and Lind 1993). The method extends the Entropy formalism by Jaynes with two important advances: First by encoding the information of each given dataset $D_{z_k} = \{(z_k)_i\}, i \in N$ as the fractile constraint pairs $\{(z_k)_i, i/(n_k+1)\}$ such that probabilities $i/(n_k+1)$ are assigned to the data points $(z_k)_i$, and, second, by double extremization of the relative entropy functional

$$S\left[p, q\right] = S\left[p(\mathbf{z} \mid \mathbf{e_z}), q(\mathbf{z} \mid (\mathbf{D_z}, \mathbf{e_z}))\right] =$$

$$= \int_{E_1} \int_{E_2} ... \int_{E_m} d\mathbf{z}\; q(\mathbf{z} \mid (\mathbf{D_z}, \mathbf{e_z}))\; \log \frac{q(\mathbf{z} \mid (\mathbf{D_z}, \mathbf{e_z}))}{p(\mathbf{z} \mid \mathbf{e_z})}, \quad (6)$$

with $\mathbf{z} = (z_1, z_2, ..., z_m)$, $\mathbf{e_z} = (e_{z_1}, e_{z_2}, ..., e_{z_m})$ and $(\mathbf{D_z}, \mathbf{e_z}) = ((D_{z_1}, e_{z_1}), (D_{z_2}, e_{z_2}), ...(D_{z_m}, e_{z_m}))$, where $p(\mathbf{z} \mid \mathbf{e_z}) = \Pr\left[\mathbf{z} \leq \mathbf{Z} \leq \mathbf{z}+d\mathbf{z} \mid \mathbf{e_z}\right]$ and $q(\mathbf{z} \mid (\mathbf{D_z}, \mathbf{e_z})) = \Pr\left[\mathbf{z} \leq \mathbf{Z} \leq \mathbf{z}+d\mathbf{z} \mid (\mathbf{D_z}, \mathbf{e_z})\right]$ are the density functions.

The REF method applies to the inference levels in Section (2.3). In the first place, given the probability density $p(\mathbf{z} \mid \mathbf{e_z})$, the REF method assigns the inferred distribution $q(\mathbf{z} \mid (\mathbf{D_z}, \mathbf{e_z}))$, subjected to the fractile constraints. This assignation is symbolically represented by the expression

$$q(\mathbf{z} \mid (\mathbf{D_z}, \mathbf{e_z})) = \arg\min_{(q_A)} S[(p_A, q_A),$$

$$\text{such that } Q_A\left((z_k)_i \mid (\mathbf{D_z}, \mathbf{e_z})\right) = \frac{i_k}{n_k+1}, \forall i_k \in N]. \quad (7)$$

To make data based inference with logical probabilities a space of candidate reference probability distributions for the unobserved quantities is required. The method chooses a reference distribution from such a space. The following expression represents this step

$$p(\mathbf{z} \mid \mathbf{e_z}) = \arg\min_{E(p)} [\min_{(p_A)} [\min_{(q_A)} [S(p_A, q_A),$$

$$\text{such that } Q_A\left((z_k)_i \mid (\mathbf{D_z}, \mathbf{e_z})\right) = \frac{i_k}{n_k+1}, \forall i_k \in N]],$$

$$\min_{(p_B)} [\min_{(q_B)} [S(p_B, q_B),$$

$$\text{such that } Q_B\left((z_k)_i \mid (\mathbf{D_z}, \mathbf{e_z})\right) = \frac{i_k}{n_k+1}, \forall i_k \in N]], ...], \quad (8)$$

being $E_p = \{E_{p_A} \cup E_{p_B} \cup ...\}$ the space of candidate reference distributions.

Finally, there is the need to select a model from E_m, a space of candidate models which must contain, at least, one model of the homogeneous class and the independence model, which imposes no functional dependence between the observed and the unobserved uncertain quantities. The selection procedure can be expressed symbolically as

$$m = \arg\min_{E(m)} [\min_{E(p)} [\min_{(p_A)} [\min_{(q_A)} [S(p_A, q_A),$$

$$\text{such that } Q_A\left((z_k)_i \mid (\mathbf{D_z}, \mathbf{e_z})\right) = \frac{i_k}{n_k+1}, \forall i_k \in N],$$

$$\min_{(p_B)} [\min_{(q_B)} [S(p_B, q_B),$$

$$\text{such that } Q_B\left((z_k)_i \mid (\mathbf{D_z}, \mathbf{e_z})\right) = \frac{i_k}{n_k+1}, \forall i_k \in N]], ...]. \quad (9)$$

4. EXAMPLE

An application of probable inference of simple models for uncertain quantities is shown in the case of regional analysis of annual maximum discharges of a set of unregulated rivers in the Bay of Biscay watershed of the Iberian Peninsula, by employing the daily maximum flow series in a station for each river. The data are 21 years (1971-1991) of observations of the annual maximum discharges (in m^3/s) of the rivers Asón, Cares, Deba and Oria.

The REF method is applied to the set of uncertain annual maximum discharges. It allows the selection of a model from a space of candidate models which includes a linear homogeneous model and the independence model. It also makes possible to choose a reference distribution for the set of hidden quantities from a space of candidate reference distributions, which includes: normal, gamma, Cauchy, lognormal and Gumbel two parameters probability distributions. The results are summarized in Tables 1 and 2.

Table 1. Reference Distribution Selection for linear models for uncertain quantities

distribution type	mean-value	standard deviation	relative entropy
Normal	2.95	1.70	3.5655
Gamma *	1.03	1.15	2.6165
Cauchy	-	-	3.3180
LogNormal	8.65	8.96	2.6948
Gumbel	5.14	2.72	2.9639

The inference procedure indicates that, for the given sets of data, the linear homogeneous model extremizes the relative entropy, when the Gamma distribution is chosen as the reference distribution for the unobserved uncertain quantities. Figure 1 represents the inferred distributions for the observed quantities related to the selected reference Gamma for distribution and homogeneous linear model.

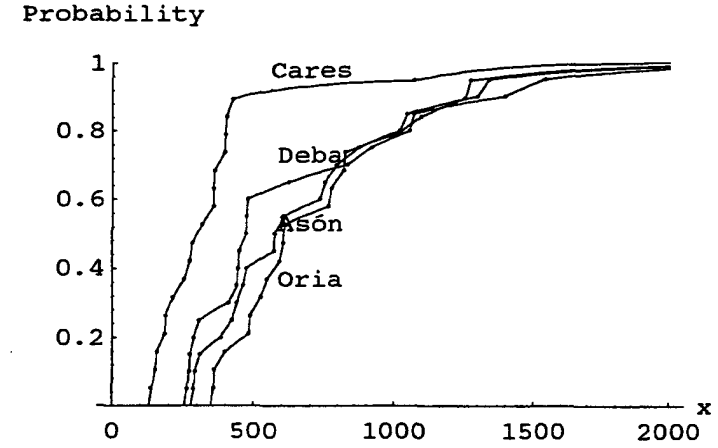


Fig1. Observations and inferred distributions for the four rivers.

For the Asón river, observations encoded as fractile constraints and inferred distributions for the observed quantities, corresponding to different candidate reference distribution types, are represented in Figure 2, where the selected Gamma distribution tail is drawn in a gross line.

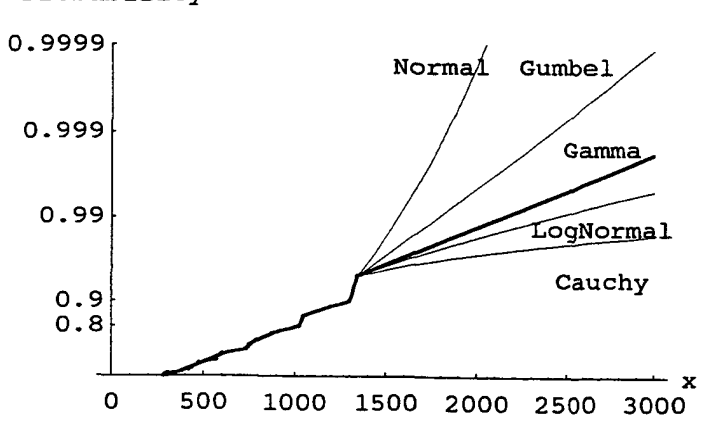


Fig2. Observations and Tail distributions for Asón river.

Table 2. Selected Model for the Gamma regional reference distribution

rivers	homogeneous linear models
Asón	$X_1 = 277.6 + 407.9\ Z_1$
Cares	$X_2 = 131.0 + 213.6\ Z_2$
Deba	$X_3 = 255.2 + 400.7\ Z_3$
Oria	$X_4 = 349.6 + 377.7\ Z_4$

5. CONCLUSIONS

1. Physical modelling involves the inference of models in which the observed uncertain quantities are functionally dependent on some unobserved uncertain quantities. Entropy methods developed as probable inference methods in a logical probability framework are suitable for this modelling.

2. The Relative Entropy method with Fractile constraints provides a logical procedure for selecting simple functional models, as well as reference and inferred probability distributions for a set of observed uncertain quantities related to the same physical magnitude.

REFERENCES

Ashkar, F. et al., 1994, "A Perspective on the Annual Maximum Flood Approach to Flood Frequency Analysis", Stochastic and Stat.Methods in Hydrology and Environmental Engineering, Vol. 1, 3-14. Kluwer.

Carnap, R., 1950, "Logical Foundations of Probability", University of Chicago Press, Chicago.

Hosking, J.M.R. and Wallis, J.R., 1988, "The Effect of Intersite Dependence on Regional Flood Frequency Analysis", Water Resources Research, Vol. 24 (4), 588-600.

Hosking, J.R.M. and Wallis, J.R., 1993, "Some Statistics Useful in Regional Frequency Analysis", Water Resources Research,Vol.29 (2), 271-281.

Solana, V., 1991, "Consistency Principle for Data Based Probabilistic Inference", in Maximum Entropy and Bayesian Methods, Fougere P.F. (ed), Fund. Theories of Physics, Vol. 50, 41-52, Kluwer.

Solana, V., 1992, "Linking the Plausible and Demonstrative Inferences", in Maximum Entropy and Bayesian Methods, Smith, C.R. et al. (eds.), Fund. Theories of Physics, Vol. 50, 41-52, Kluwer.

Solana, V.and Lind, N.C., 1993, "Relative Entropy Method Using Tail Fractiles", Reliability Engineering and System Safety, Vol. 40, 61-67.

Solana, V., 1995a,"Entropy versus Bayesian Inference.Why Bayesian Inference for an Uncertain Quantity Fails",13th.Workshop on Maximum Entropy and Bayesian Methods, University of California, Sta. Barbara (to appear).

Solana, V., 1995b, "Consistent Tail Modelling for Uncertain Quantities" (to appear).

ACKNOWLEDGEMENTS

The work here reported received finantial support from DGICYT of Spain as the research project PB 93-0177.

CLIMATE SIGNAL AND WEATHER NOISE

C. E. Leith

Lawrence Livermore National Laboratory
Livermore CA USA

ABSTRACT
A signal of small climate change in either the real atmosphere or a numerical simulation of it tends to be obscured by chaotic weather fluctuations. Time-lagged covariances of such weather processes are used to estimate the sampling errors of time average estimates of climate parameters. Climate sensitivity to changing external influences may also be estimated using the fluctuation dissipation relation of statistical mechanics. Answers to many climate questions could be provided by a realistic stochastic model of weather and climate.

1 INTRODUCTION

In any discussion of weather and climate it is, first of all, important to distinguish clearly the meaning of these terms. Climate is usually considered to be in some sense the average weather. Here averages will be considered to be taken over a hypothetical ensemble of earths with specified external influences, but each with its own evolving weather patterns. If the external influences are fixed except for a specified annual cycle, then the resulting climate is expected to be fixed or stationary except for an induced annual cycle. As has been said "Climate is what you expect, weather is what you get." Thus the climate is the hypothetical probability distribution from which weather samples are drawn to produce weather statistics.

There is much current interest in the possibility that the underlying climate probability distribution is changing owing to changes in external influences such as changes in concentrations of greenhouse gases that change the radiative properties of the atmosphere or changes in land surface features that change the thermal properties of the earth's surface. Numerical simulations of the climate system that generate artificial but realistic evolving weather patterns are used to predict the climatic consequences of artificially imposed changes in external influences. Or the real weather records are examined in a search for real climate changes induced by observed real changes in external influences.

Whether examining real or simulated weather records for evidence of a change in the climate there is obviously a sampling problem of distinguishing the signal of climate change from the noise of weather statistics. Enough is known about the time-lagged covariance of weather processes to estimate the magnitude of the weather noise. In the next Section such estimates will be reviewed.

The observed time-lagged covariance of weather processes can also be used to estimate the sensitivity of climate response without the use of numerical simulations but by making use of the fluctuation dissipation relation of statistical mechanics. This relation, as will be discussed in Section 3, is not strictly valid for the climate system and must be treated as an approximation.

The weather sampling problem could, of course, be avoided if one were to construct true climate models that deal directly with the probabilistic properties of the climate system rather than to require sampling from a weather model. Such an approach has been taken with moderate success in

the devising of stochastic models of turbulence, a far simpler problem. In Section 4 is described a crude stochastic model of the global atmosphere that captures enough of the observed space and time statistics of the weather to provide encouragement that such an approach may be feasible.

2 WEATHER NOISE

Sampling errors associated with a finite time average estimate of any weather variable depend on the time-lagged covariance of the random process given by the time series of observations of that variable. The point is, of course, that successive observations are not independent and their dependence must be taken into account. In application to climate mean statistics this problem has been discussed in detail by Leith (1973) and by Jones (1975). But a rough engineering estimate can be made from the concept of effective time between independent samples defined as

$$S = \int R(t)\, dt \qquad (1)$$

where R(t) is the time-lagged correlation.

For a finite time average based on an averaging interval T, one finds an effective number of independent samples as

$$N = T/S \qquad (2)$$

The sampling error variance of the estimate of the mean is reduced then by a factor N from the variance of the original time series.

Since S is observed to be of the order of a week for weather variables, it is to be expected, for example, that there will be sizable fluctuations in seasonal average temperatures from year to year based solely on sampling fluctuations with N=13 even with no change in the underlying climate probabilities.

This is weather noise, and it tends to obscure the estimation of climate probabilities whether from the real atmosphere or from numerical model of it.

Spatial averaging does not help much since spatial correlation lengths are of the order of a megameter, and this is typically greater than the size of regional climate domains of interest.

3 CLIMATE SIGNAL

The key problem in climate system modeling is the detection of a change in the underlying climate probabilities in response to changing influences, especially those induced by human activities, such as CO_2 concentration in the atmosphere, or land surface properties.

For the climate system, consider the symbolic evolution equation

$$dx/dt = Q(x) + f(t) \qquad (3)$$

where x is a state vector for the system, Q(x) represents complicated nonlinear internal dynamical processes and f is a vector of external forcing influences. We assume that there exists a stationary base climate for which

$$\langle dx/dt \rangle = d\langle x \rangle/dt = 0 \qquad (4)$$

where $\langle\ \rangle$ indicates the population expectation. Without loss of generality we assume for the base climate that $\langle x \rangle = 0$, so that x represents anomalies from the base climate mean.

The simplest question that can be asked about the climate system is its sensitivity as given by the infinitesimal response of $\langle x \rangle$ to an infinitesimal change in f, i.e., the linear probabilistic response of the mean climate.

We look then for the Greens matrix function G(t) such that

$$\delta\langle x \rangle(t) = \int G(t-s)\delta f(s) ds \qquad (5)$$

Note that an impulsive $\delta f(0) = f\delta(0)$ introduced at time t = 0 will induce a jump in $\langle x \rangle = 0$ to $\langle x \rangle(0+)$ which relaxes back to the base state by the relation

$$\langle x \rangle(t) = G(t)\langle x \rangle(0+) \qquad (6)$$

The state vector x may, in a typical numerical model of the atmosphere, have of order a million components. The corresponding Greens matrix provides the linear response of any one component to a perturbation in any other. The determination of all of the matrix elements of G is therefore an overwhelming task by the usual method of making long integrations with numerical models.

In practice, instead of perturbing each component separately, a collective perturbation is introduced such as of sea surface temperature over a domain or of perturbed heating induced by a change in CO_2 concentration in the global atmosphere.

An interesting alternative (Leith, 1975; Bell, 1980) is provided by the fluctuation dissipation relation of statistical physics which states simply that

$$G(\tau) = R(\tau) \text{ for } \tau \geq 0 \qquad (7)$$

where $R(\tau) = C(0)^{-1}C(\tau)$ is the multivariate time-lagged regression matrix for the system, $C(\tau) = \langle x(t)x^*(t+\tau)\rangle$ being the time-lagged covariance matrix.

Although the fluctuation dissipation relation can be proved as a theorem for statistical mechanical systems in thermodynamical equilibrium, the climate system is not one of these, and the relation must be taken as an approximation.

It is not yet clear whether such an approximation, based after all on properties of the real atmosphere, is better or worse than that of devising a numerical model of the atmosphere.

In any case, as a part of the validation of any such model, it seems desirable to check that $R(\tau)$ for the model agrees with $R(\tau)$ as observed in the atmosphere, for otherwise it is unlikely that the important Greens matrix, $G(\tau)$, of the model would agree with that of the real atmosphere.

Remember that the dimension of the regression matrix R is great enough to describe the spatial as well as the temporal statistical properties of the atmospheric climate system.

4 STOCHASTIC CLIMATE MODEL

It is tempting to try to devise a stochastic atmospheric climate model of the Langevin type, i.e., with random white forcing and specified damping, that mimics all first and second moments as observed in the real atmosphere. The fluctuation dissipation relation would be built into such a model which would thus provide an estimate of climate sensitivity. The feasibility of doing so is suggested by the success of a first crude step in which the atmosphere is treated as a homogeneous, isotropic, two-dimensional turbulent fluid with an eddy mixing of potential vorticity.

Define the potential vorticity as

$$q = \Delta\psi - \lambda^2\psi \qquad (8)$$

where Δ is the Laplacian operator, ψ is the stream function and λ is a deformation wavenumber. Eddy diffusion dynamics for the model is given by

$$\partial q/\partial t = D\Delta q - \alpha q + w \qquad (9)$$

where D is an eddy diffusion coefficient, α an eddy damping rate and w is space- and time-white noise forcing. For a particular wavenumber, k, Eqns. (8) and (9) may be written as

$$q_k = -(k^2 + \lambda^2)\psi_k \qquad (10)$$

$$\partial q_k/\partial t = -(Dk^2 + \alpha)q_k + w_k \qquad (11)$$

The stochastic differential equation (11) of Langevin type generates stationary statistics with variance Q_k of q_k given by

$$Q_k = A/(2(\alpha + Dk^2)) = (A/2D)/(k^2 + \mu^2) \qquad (12)$$

In order to maintain parsimony of parameters it has been found adequate to set

$$\mu^2 = D\alpha = \lambda^2 \qquad (13)$$

The stream function variance, Ψ_k, for wavenumber k is then given by

$$\Psi_k = (A/2D)/(k^2 + \lambda^2)^3 \qquad (14)$$

where A is a constant, and the two-dimensional velocity variance is given by

$$U(k) = k^2\Psi_k \approx k^2/(k^2 + \lambda^2)^3 \qquad (15)$$

The isotropic energy spectrum has the shape

$$E(k) \approx kU(k) \approx k^3/(k^2 + \lambda^2)^3 \qquad (16)$$

For $x = k/\lambda$, one finds

$$E(k) \approx f(x) = 8(x + x^{-1})^{-3} \qquad (17)$$

which has a maximum at x = 1. The transient energy spectrum for the global atmosphere is observed to have a maximum at planetary wavenumber $k = \lambda = 8$, and for such a choice of λ Eqn. (16) provides a fair fit.

Consider next the temporal statistics, in particular, the time-lagged height-height correlation. In this model this is proportional to

$$\begin{aligned} &\pi\int k\Psi(k)\ \mathrm{Exp}[-(\alpha+Dk^2)\tau]\ dk \\ &= \pi\int k\Psi(k)\ \mathrm{Exp}[-\alpha(1+k^2/\lambda^2)\tau]\ dk \\ &\approx \int(1+k^2/\lambda^2)^{-3} \\ &\qquad \mathrm{Exp}[-\alpha(1+k^2/\lambda^2)\tau]\ kdk \\ &\approx \int s^{-3}\ \mathrm{Exp}[-\alpha\tau s]\ ds = E_3(\alpha\tau) \qquad (18) \end{aligned}$$

With suitable normalization, we find

$$R(\tau) = 2E_3(\alpha\tau) \qquad (19)$$

in terms of the exponential integral, E_3. A good fit to the observed height-height correlation is obtained by choosing the parameter $\alpha = 0.187$ /day.

Note that the parameter λ is chosen to fit spatial statistics and independently α is chosen to fit temporal statistics. Note also that in this model the amplitude of the variance depends only on the specified strength of the white-noise forcing.

It is clear that such a model is only a starting point for the development of models that take into account the observed three-dimensional mean flow and the inhomogeneous nature of the real climate system.

References

Bell, T.L., 1980, "Climate Sensitivity from Fluctuation Dissipation: Some Simple Model Tests", Journal of the Atmospheric Sciences, vol. 37, pp. 1700-1707.

Jones, R.H., 1975, "Estimating the Variance of Time Averages", Journal of Applied Meteorology, vol. 14, pp. 159-163.

Leith, C.E., 1973, "The Standard Error of Time-Average Estimates of Climatic Means", Journal of Applied Meteorology, vol. 12, pp. 1066-1069.

_____, 1975, "Climate Response and Fluctuation Dissipation", Journal of the Atmospheric Sciences, vol. 32, pp. 2022-2026.

ACKNOWLEDGMENT

This work was supported by the U.S. Department of Energy through its Contract No. W-7405-ENG-48 with the Lawrence Livermore National Laboratory.

CORRESPONDING AUTHOR
Dr. C. E. Leith
Lawrence Livermore National Laboratory, L-256
Livermore, CA 94550 USA

On the reddest atmospheric modes generated by a coupled atmosphere-ocean general circulation model

Jin-Song von Storch
Max Planck Institute for Meteorology, Germany

Low frequency variations can never exist in isolation. In order to understand the dynamics which produce these variations, we need also to consider the effect of the short-term motions on the low frequency motions. This idea was proposed and described by Hasselmann (1976) in the concept of stochastic climate model. Following this concept, the low-frequency variability might be explained simply as the integral response of the slowly varying parts of the system to internal random forcing by the always present short-term fluctuations. The resulting low-frequency variations would have a random walk character, as indicated by the redness of the spectra. The challenge is not to find the positive feedback mechanisms which enhance the small disturbances, but to identify the negative feedbacks that must be present to balance the continual generation of low-frequency fluctuations by the short-term forcings. The 1000-year simulation performed by the coupled ECHAM1/LSG model in Hamburg provides the opportunity to test the concept of stochastic climate model for the atmospheric low-frequency variations.

The redness of the atmospheric motions generated by the ECHAM1/LSG model is studied systematically by using the decorrelation time T_0 as a simple measure for the memory time scale. T_0 is calculated for both grid point time series and for coefficients of large scale patterns. Different variables are considered. It turns out that there are two modes in the model atmosphere which have a memory of about a few months. These two modes have the reddest spectra and display large spatial scale and strong zonal symmetry. A spectral analysis shows that the first long-memory mode which is related to the variations of tropical winds varies coherently with the global relative angular momentum on long time scales and the second long-memory mode which is related to a dipole wind structure in the Southern Hemispheric mid- and highlatitudes varies coherently with the global omega angular momentum on long time scales. A potential predictability analysis indicates that the Southern Hemispheric mode is generated by an internal dynamical process which is able to operate on time scales of about a few month, or even a year.

According to the concept of the stochastic climate model, the dynamical process of the reddest modes must present a negative feedback mechanism. A detailed scaling analysis of the equations of motions suggests that for the Southern Hemispheric mode, the negative feedback is simply a compensation of the boundary convergence which is caused by the surface stress and the interior convergence which is caused by the drain of momentum by small-scale motions. Such a balance is possible to exist over long time period in the presence of short-term random forcings. The dynamics of the tropical mode is the damped persistence due to the drain of momentum by small-scale motions. A consideration of global angular momentum which is the overall constraint for motions on all possible scales suggests that small-scale motions must drain momentum from large-scale motions. To conclude, the low-frequency motions can not exist without the short-term motions and vice versa.

Decadal trends in the North Atlantic Oscillation and relationships to regional temperature and precipitation

James W. Hurrell and Harry van Loon

National Center for Atmospheric Research, Boulder, CO, USA 80307

ABSTRACT

Analyses of historical and proxy data have shown that relatively rapid and large climate changes have occurred in the past over the North Atlantic. These fluctuations can be related to a major source of both interannual and low-frequency variability: the North Atlantic Oscillation (NAO). Low-frequency changes in surface variables such as temperature and precipitation are directly related to changes in the oscillation. Over the past decade during winter, the NAO has remained in one extreme phase. This has contributed to significant decadal regional anomalies such as the recent wintertime warmth observed across Europe and dry conditions over much of southern Europe and the Mediterranean.

1 INTRODUCTION

Much attention has been given to the possibility that human activities might be responsible for significant changes in the climate. It is also clear, however, that the natural variability of the climate system is large, and perhaps even large enough to overwhelm climate change signals resulting from anthropogenic forcing. The purpose of this paper is to analyze low-frequency climate variations in winter over the North Atlantic to show how regional changes and trends in variables such as surface temperature and precipitation are strongly tied to changes in the atmospheric circulation. Variations in local surface temperatures on interannual and longer time scales are not uniform, but occur in distinctive large-scale patterns. An example is the surface temperature and sea surface temperature (SST) anomalies for the period 1977-1993 (Fig. 1), expressed as departures from the 1951-1980 means and averaged over the four winter months December–March. The large warm wintertime anomalies over the middle and high latitude continents resemble the results obtained by some coupled atmosphere–ocean models forced with steadily increasing atmospheric greenhouse gases (IPCC 1992), and evidence suggests that the recent warming may be related to increasing tropical ocean temperatures that have led to an enhancement of the tropical hydrologic cycle (Kumar et al. 1994; Graham 1995). What is clear is that there have been significant decade-long changes in the atmospheric circulation that have contributed substantially to the regional warming, and these changes complicate the interpretation of the climate system response to increased greenhouse gas forcing.

2 RESULTS

a Large-scale observed trends

The very large North Pacific basin temperature anomalies, with warming along the west coast of North America and Alaska and cooling in the central North Pacific, have been linked to a substantial decadal change in the atmospheric circulation that corresponded to a deeper and eastward-shifted Aleutian low pressure system during winter (Fig. 1). It has been hypothesized that the Pacific decadal timescale variation has its origin in the tropics (Trenberth and Hurrell 1994), and several modeling studies have confirmed that North Pacific atmospheric circulation changes are largely controlled by anomalous tropical SST forcing (Chen et al. 1992; Graham 1994). Decadal changes in the wintertime atmospheric circulation over the North Atlantic, however, do not appear to be as strongly influenced by tropical Pacific SST variability (Kumar et al. 1994). The

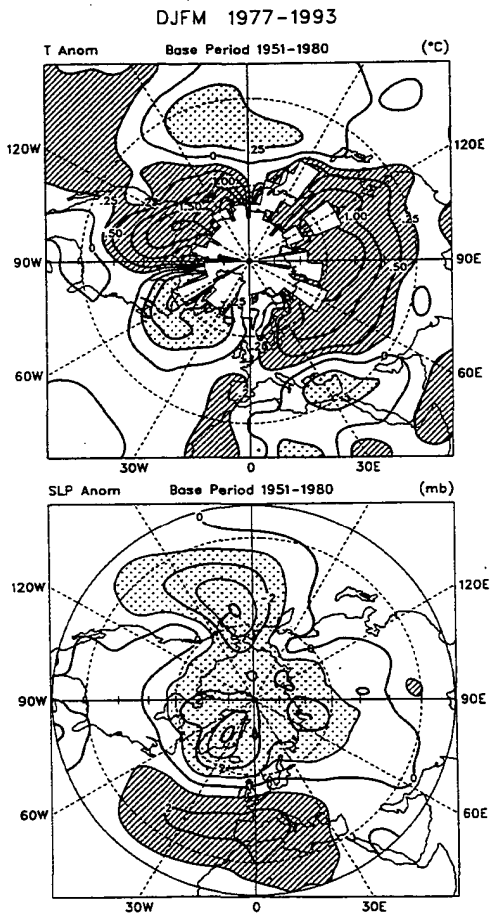


Figure 1. Average surface temperature and SST anomalies (top) and SLP anomalies (bottom). Negative (positive) anomalies are stippled (hatched).

anomalous coldness over the past decade near Greenland and the eastern Mediterranean, and the very warm conditions over Scandinavia, northern Europe, the former Soviet Union and much of central Asia (Fig. 1) are more strongly linked to the recent behavior of the North Atlantic Oscillation (NAO), which is a meridional oscillation in atmospheric mass with centers of action near the Icelandic low and the Azores high (e.g., van Loon and Rogers 1978).

An index of the NAO, defined as the difference between the normalized mean winter (December-March) sea level pressure (SLP) anomalies at Lisbon, Portugal and Stykkisholmur, Iceland reveals the variability of the oscillation since 1864 (Fig. 2). In addition to a large amount of interannual variability, there have been several periods when anomalous circulation patterns persisted over many winters. A sharp phase reversal has occurred over the past 30 years from very low index values in the 1960s to unprecedented strongly-positive NAO index values since 1980, with higher-than-normal pressures south of 55° N and a broad region of anomalously low pressure across the Arctic (Fig. 1).

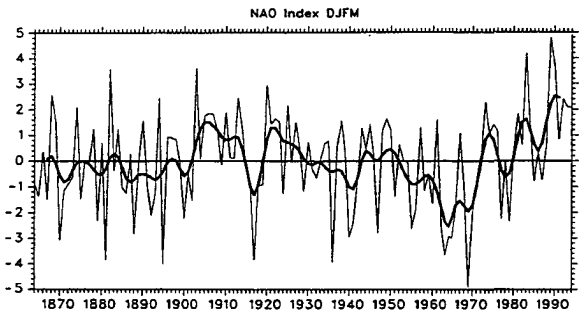


Figure 2. Winter index of the NAO. The heavy solid line represents the meridional pressure gradient smoothed with a low pass filter to remove fluctuations with periods less than 4 years.

To more objectively isolate the important coupled modes of variability between the SLP and surface temperature and SST fields, singular value decomposition (SVD) analysis was applied to the temporal covariance matrix between a 95-winter (1899-1993) dataset consisting of unnormalized seasonal mean SLP anomalies and concurrent SST and surface land temperature anomalies. The first set of singular vectors correspond to the NAO and explain nearly 75% of the total squared covariance. The homogeneous and heterogeneous correlation maps show the relationships between the expansion coefficients of the first SLP vector and the surface temperature and SLP fields (Fig. 3). The first SVD mode confirms that Lisbon and Stykkisholmur are near the main opposite centers of the NAO teleconnections. The correlation coefficient between the expansion coefficients of the first SLP vector and the NAO time series (Fig. 2) is 0.91 from 1899-1993. The similarity between the heterogeneous correlation map and the decadal anomalies over the North Atlantic and surrounding landmasses (Fig. 1) is striking and suggests that the recent temperature anomalies over these regions are strongly related to the persistent and exceptionally strong positive phase of the NAO index since the early 1980s.

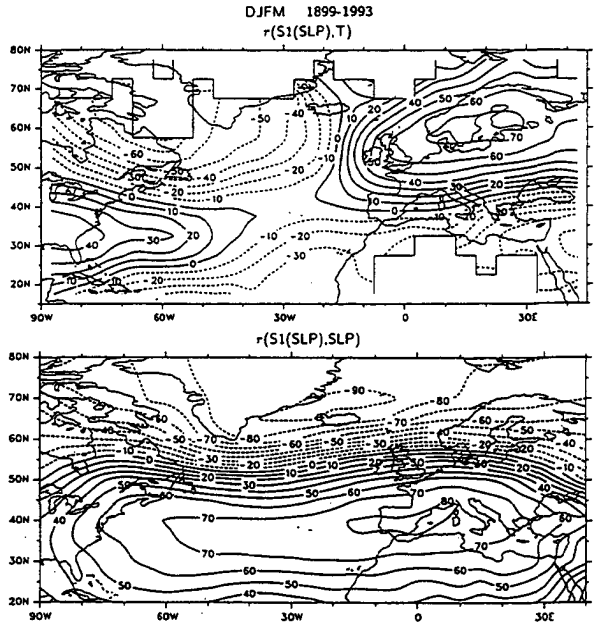


Figure 3. Geographical patterns of the temporal correlation coefficients (%) between the expansion coefficients of the first SLP vector and surface temperature and SST anomalies (top), and SLP anomalies (bottom). Negative correlations are dashed.

b Time scales

To explore which time scales contribute most to the correlations in Fig. 3, the relationship between the NAO index and winter temperatures over northern Europe is examined as a function of frequency. Figure 4 shows the power spectrum of the winter mean NAO index for the 130 years 1864–1993 (Fig. 2). The spectrum is scaled so that the sum of the spectral estimates is the same as the variance of the NAO time series. Also shown is the corresponding red noise spectrum with the same lag one autocorrelation coefficient and the 5% and 95% confidence limits. The spectrum reveals significant variance at biennial periods, a deficit in power at 3 to 5 year periods, and enhanced power at 6 to 10 year periods. The power at the lowest frequencies reflects the trends evident in Fig. 2. The time evolution of these signals is shown in Fig. 4 as a contour plot of the power spectra computed from running 60 year intervals beginning with the time period 1864–1923 and ending with the series from 1934–1993. It is clear that much of the variance at biennial periods comes from early in the record, while the enhanced variability between 6 and 10 years is most pronounced over the latter portion of the time series. The tendency for the NAO power spectrum to become redder with time is indicated by the lag one autocorrelations also presented Fig. 4.

Figure 5 presents the power spectrum of winter temperature anomalies from Copenhagen, Denmark for the period 1864–1993. The spectrum is very similar in character to that shown in Fig. 4 for the NAO index. The power spectra of Copenhagen temperatures are dominated by variations at biennial periods early in the record, and this frequency band accounts for a significant percentage of the total variance throughout much of the record. The variance at 6 to 10 years periods is

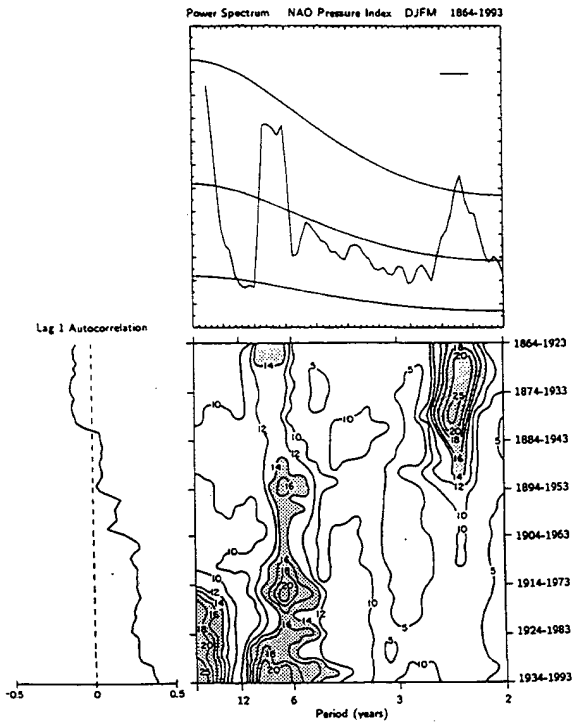


Figure 4. Power spectra of NAO index for 1864-1993 (top) and running 60-year intervals (bottom). Variances greater than 0.14 mb^2 frequency^{-1} are shaded in the lower panel. Also shown is the lag one autocorrelation coefficient for each 60 year interval.

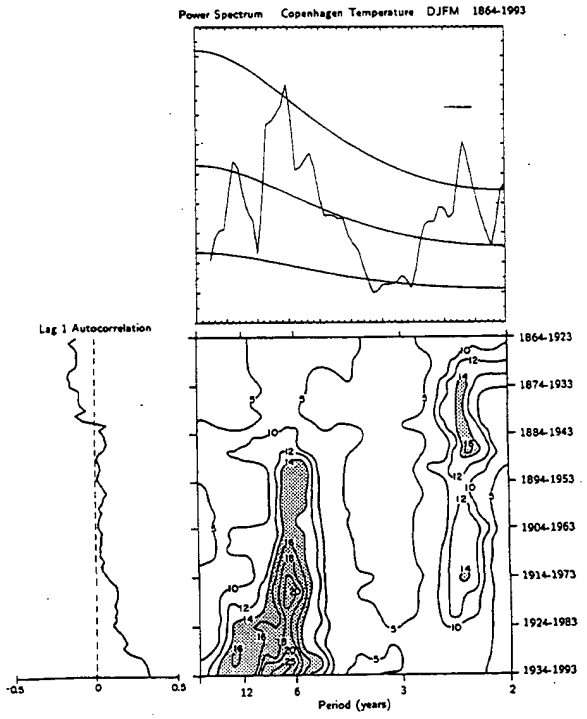


Figure 5. As in Fig. 4 but for Copenhagen temperature anomalies. Variances greater than 0.14° C^2 frequency^{-1} are shaded in the lower panel.

enhanced later in the data record and accounts for the largest percentage of the total variance over the last several 60 year periods. The spectra in Figs. 4 and 5 suggest a strong relationship between the NAO index and temperatures over northern Europe, but one that has changed over time. This nonstationary behavior is documented in Fig. 6, which shows the coherence squared between the NAO and temperature anomalies at Copenhagen as a function of time and frequency. The high correlations evident in Fig. 3 over northern Europe result from coherent fluctuations at biennial periods early in the data records and lower-frequency fluctuations at 6 to 10 year periods later on.

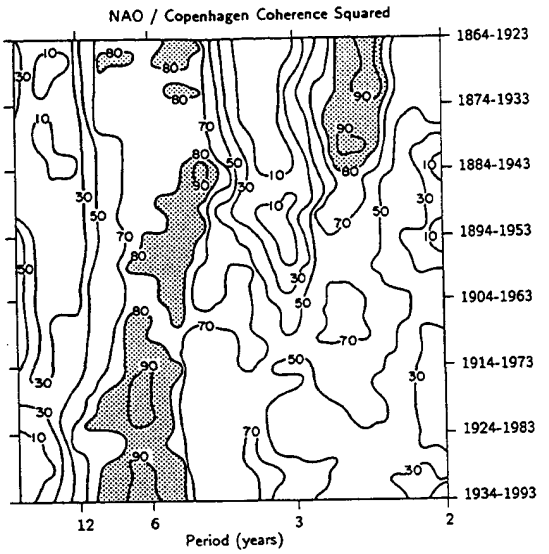


Figure 6. Coherence squared (× 100) between the NAO index and Copenhagen temperature anomalies for over running 60 year intervals. Values greater than 80 are shaded

c The atmospheric moisture budget

Changes in the mean circulation patterns over the North Atlantic are accompanied by pronounced shifts in the storm tracks and associated synoptic eddy activity (Hurrell 1995). The associated changes in the transport and convergence of atmospheric moisture can be directly tied to changes in regional precipitation. The global analyses produced by the European Centre for Medium Range Weather Forecasts are used to evaluate the large-scale moisture budget and highlight differences between winters composited during high NAO index years and low NAO index years. Evaporation (E) exceeds precipitation (P) over much of Greenland (Fig. 7) during high NAO winters, especially in the south where changes are on the order of 1 mm day^{-1}. When viewed with the low-frequency changes evident in the NAO index (Fig. 2), these results are consistent with observational and modeling evidence of a declining precipitation rate over much of the Greenland Ice Sheet over the past two decades (Bromwich et al. 1993). Drier conditions during high NAO index winters are implied over much of central and southern Europe and the Mediterranean, while enhanced moisture flux convergence is indicated from Iceland through Scandinavia. Indeed, over much of the past decade wetter-than-normal conditions have been observed over northern Europe and Scandinavia, while wintertime droughts have afflicted much of southern Europe and the Mediterranean (e.g., NOAA 1991).

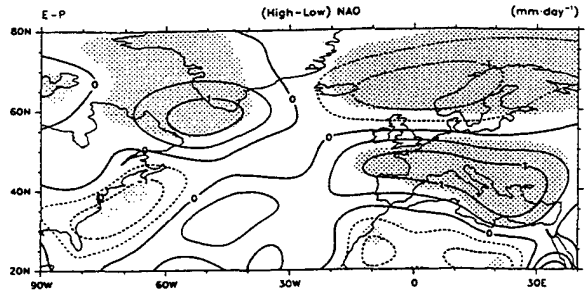


Figure 7. Composited E−P for high minus low NAO index winters. The contour interval is 0.5 mm day^{-1}, and the stippling indicates values significantly different from zero at the 5% level using a t-test.

3 CONCLUSIONS

The above analysis of changes in surface pressures, temperatures and other measures of the atmospheric circulation reveals coherent coupled variations on long-time scales that are especially important regionally. Evidence for large and rapid fluctuations in the climate of the Atlantic abound in historical and proxy records. Recent analyses of Greenland ice-core data, for instance, reveal abrupt changes in the climate of the North Atlantic at decadal time scales that may be related to fluctuations in the NAO (Barlow et al. 1993). Prolonged periods with anomalous atmospheric circulation patterns, such as those associated with the NAO (Fig. 2), may affect the rate of deep water formation in the North Atlantic by altering the amount of heat extracted from the ocean by the atmosphere and the fresh water input to the ocean through changes in $E - P$, melting of sea ice and continental runoff. Significant thermal variability on decadal time scales has been observed at depth in the ocean (Levitus et al. 1994), so that it is likely that there have been changes in the ocean thermohaline circulation similar to those simulated by models (e.g., Delworth et al. 1993).

The large warm wintertime anomalies over the middle and high latitude continents over the past decade (Fig. 1) resemble the results obtained by some coupled atmosphere–ocean models forced with steadily increasing atmospheric greenhouse gases; however, it is also clear that there have been significant decade-long changes in the atmospheric circulation that have contributed substantially to the regional warming. Decadal variability in the NAO has become especially pronounced since about 1950 (Fig. 2), but the causes for such variability in the Atlantic are not clear. The relationship of the NAO to other distinctive modes of decadal oceanic and atmospheric variability in the Atlantic (e.g., Deser and Blackmon 1993; Kushnir 1994), and the links to coherent variations in tropical Atlantic SSTs need to be examined further. More attention should be given to evaluating how well state-of-the-art general circulation models simulate the NAO, or how the NAO might change with changes in greenhouse-gas forcing.

REFERENCES

Barlow, L. K., J. W. C. White, R. G. Barry, J. C. Rogers, and P. M. Grootes, 1993: The North Atlantic Oscillation signature in deuterium and deuterium excess signals in the Greenland Ice Sheet Project 2 ice core, 1840-1970. *Geophys. Res. Lett.*, **20**, 2901–2904.

Bromwich, D. H., F. M. Robasky, R. A. Keen, and J. F. Bolzan, 1993: Modeled variations of precipitation over the Greenland ice sheet. *J. Climate*, **6**, 1253–1268.

Chen, T.-C., H. van Loon, K.-D. Wu, and M.-C. Yen, 1992: Changes in the atmospheric circulation over the North Pacific-North America area since 1950. *J. Meteor. Soc. Japan*, **70**, 1137–1146.

Delworth, T., S. Manabe, R. J. Stouffer, 1993: Interdecadal variations of the thermohaline circulation in a coupled ocean-atmosphere model. *J. Climate*, **6**, 1993–2011.

Deser, C., and M. L. Blackmon, 1993: Surface climate variations over the North Atlantic Ocean during winter: 1900–1989. *J. Climate*, **6**, 1743–1753.

Graham, N. E., 1994: Decadal-scale climate variability in the tropical and North Pacific during the 1970s and 1980s: observations and model results. *Clim. Dyn.*, **6**, 135–162.

Graham, N. E., 1995: Simulation of recent global temperature trends. *Science*, **267**, 666–671.

Hurrell, J. W., 1995: Transient eddy forcing of the rotational flow during northern winter: *J. Atmos. Sci.*, in press.

IPCC, 1992: *Climate Change 1992: The Supplementary Report to the IPCC Scientific Assessment*, J. T. Houghton, B. A. Callander, and S.K. Varney, Eds. Cambridge University Press, 200 pp.

Kumar, A., A. Leetmaa, and M. Ji, 1994: Simulations of atmospheric variability induced by sea surface temperatures and implications for global warming. *Science*, **266**, 632–634.

Kushnir, Y., 1994: Interdecadal variations in North Atlantic sea surface temperature and associated atmospheric conditions. *J. Climate*, **7**, 141–157.

Levitus, S., J. I. Antonov, and T. P. Boyer, 1994: Interannual variability of temperature at a depth of 125 meters in the North Atlantic Ocean. *Science*, **266**, 96–99.

NOAA, 1991: Climate Assessment: A Decadal Review 1981-1990, 109 pp.

Trenberth, K. E., and J. W. Hurrell, 1994: Decadal atmosphere-ocean variations in the Pacific. *Clim. Dyn.*, **9**, 303–319.

van Loon, H., and J. C. Rogers, 1978: The seesaw in winter temperatures between Greenland and Northern Europe. Pt. I. General description. *Mon. Wea. Rev.*, **106**, 296–310.

Downscaling III: Applications to Ecosystems Modeling

Dimitrios Gyalistras & Andreas Fischlin

Institute of Terrestrial Ecology, Swiss Federal Institute of Technology, Zurich, Switzerland

ABSTRACT

We discuss the potentials and limitations of statistical downscaling (DS) when dealing with terrestrial ecosystems studies in complex terrains, by providing examples based on a linear DS technique and the dynamic forest gap model ForClim. We show that DS is essential to assess regional ecosystem responses to global climate change in a sensible manner. However, for several applications DS needs to be complemented by additional techniques such as spatial interpolation, stochastic weather generation, the parameterization of regional climate responses as a function of atmospheric greenhouse-gas concentrations, and the estimation of the uncertainties that occur within or between future climate scenarios.

1 INTRODUCTION

Ecosystem modelers who wish to study possible regional impacts of climate change have particularly demanding requirements for climate scenarios. Typically needed are application-specific combinations of several meteorological variables, which must be provided with high spatial detail (10^0-10^1 km), and at a hourly to seasonal resolution of the annual cycle. Further, in some cases the scenarios must cover regions of several 10^2-10^3 km^2, or they must be provided for time spans of several decades or even centuries (cf. Gyalistras *et al.* 1994, 1995).

In the last years a series of techniques to statistically downscale large-scale climate changes as simulated by General Circulation Models (GCMs) to the regional scale have become available (see reviews in this volume). Here we discuss advantages and limitations of such downscaling (DS) approaches when dealing with the climate scenario requirements of ecosystem studies.

For illustration we provide examples using a DS technique which predicts local climate anomalies from large-scale monthly mean sea-level pressure and near-surface temperature anomaly fields based on Canonical Correlation Analysis (von Storch *et al.* 1993, Gyalistras *et al.* 1994). We discuss results from application of this technique to climate change experiments with the Hamburg MPI ECHAM1/LSG GCM (Cubasch *et al.* 1992, 1994) and the Canadian Climate Centre (CCC) GCMII (Boer *et al.* 1992).

On the ecosystem side we consider the dynamic forest ecosystem model ForClim (Bugmann 1994, Fischlin *et al.* 1995a), which simulates site-specific tree species compositions in function of a location's climate (Fig. 1). The climatic input requirements of ForClim (see below) are representative for several ecosystem applications, and, typically, more stringent than the input needs of empirical vegetation-climate relationships.

2 SPATIAL ASPECTS

Resolution

DS is in principle applicable to any location at which meteorological measurements are available, and thus enables to study ecosystems at a very high spatial resolution. Further it allows to coherently adjust climate parameters between different locations under a given large-scale climate change, thus reinforcing the consistency of the scenarios at the regional scale.

Fig. 1 compares the responses of ForClim at the case study location of Bever (1712 m.a.s.l., 9.9 °E, 46.6 °N, Upper Engadine valley) in the Swiss Alps under two climate change scenarios constructed with and without DS. The climatic inputs required by ForClim are the expected values, variances, and covariances of mean temperatures and precipitation totals for every month of the year, which are used to stochastically generate an annual weather cycle for every simulation year. In the first scenario (left panel) the monthly expected values for temperature and precipitation were modified based on DS. In the second scenario (right panel) the required inputs were from GCM-simulated average monthly changes from three gridpoints in the vicinity of the Alps. In both cases the monthly variances and covariances were held constant at present values.

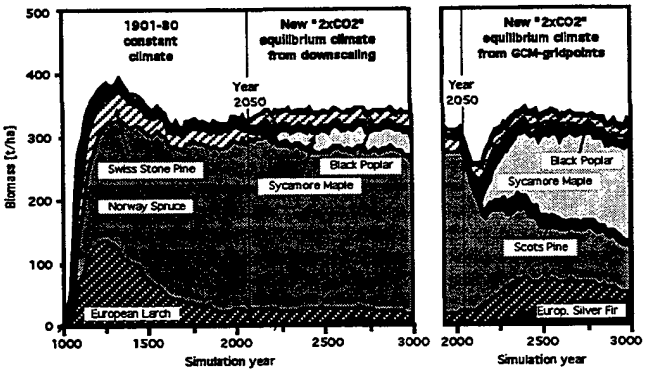


Figure 1. Comparison of average tree species compositions simulated by ForClim (Bugmann 1994, Fischlin *et al.* 1995a) at the site Bever (1712 m.a.s.l., Swiss Alps) for present climate, and under two climate scenarios derived with (left panel) and without (right panel) downscaling from a "2xCO_2"-experiment with the ECHAM1 GCM (Cubasch *et al.* 1992). All data are averages from 200 independent stochastic forest simulation runs.

It can be seen that ForClim's behaviour is sensitive to the method by which the scenario was constructed. Under the DS scenario only minor changes in the tree species composition occur. In the case of the gridpoint scenario, which specifies larger temperature and precipitation changes than the DS scenario (cf. Gyalistras *et al.* 1994), the model projects a partial forest breakdown, which is followed by significant changes in the tree species composition.

Since DS is the climatologically more consistent procedure, we concluded that the simpler gridpoint-based method yields misleading results – at least in a topographically complex region such as the Alps.

Spatially Extended Scenarios

The locations of interest to ecologists rarely coincide with climatological stations. For example, Bever is located at the valley floor, whereas most forests in the vicinity of this station grow on the surrounding slopes.

Consequently, the forest simulated at Bever contains a large fraction of Norway Spruce (Fig. 1), and the model can not reproduce the dominance of European Larch, which is actually found on the much warmer, south-facing slopes (Bugmann & Fischlin 1994, Bugmann 1994). Hence the point estimates available from measurements or downscaled climate scenarios need to be extended by means of an appropriate procedure into space.

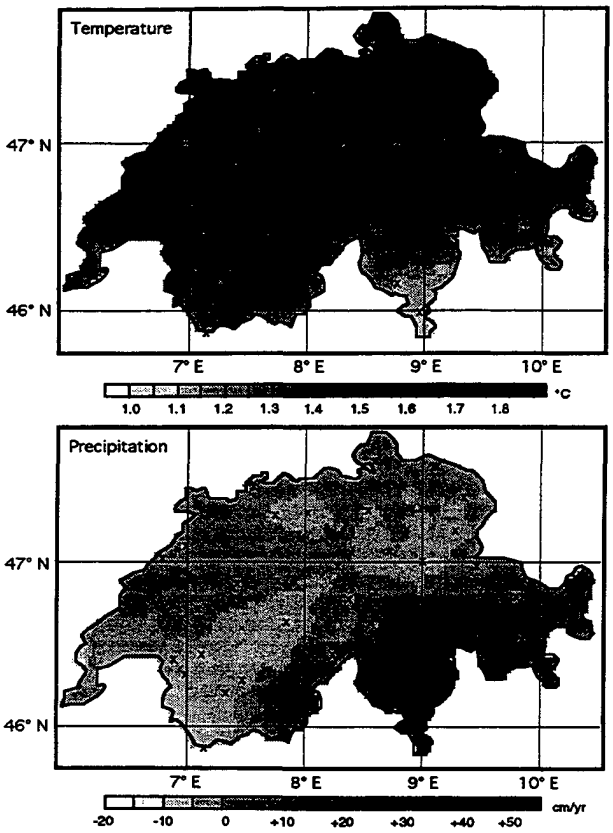


Figure 2. Interpolated maps of changes in annual mean temperature (*top*) and precipitation (*bottom*) in the Swiss region as downscaled (Gyalistras *et al.* 1994, Gyalistras 1940, Gyalistras & Fischlin 1995b) from a "2xCO_2" simulation with the ECHAM1 GCM (Cubasch *et al.* 1992). Dots signify the 40 long-term climatological stations at which monthly temperature and precipitation changes from downscaling were available. For interpolation 68 additional stations with at least 20 yr of data available were used (not shown). The main ridge of the Alps crosses Switzerland between 46 and 47 °N in a W/SW-E/NE direction.

A procedure which combines DS with spatial interpolation was proposed by Gyalistras & Fischlin (1995a). First, the baseline (present) climate at any location of interest is estimated from the application of empirical altitude-climate dependencies, plus an inverse-distance weighted mean of altitude-detrended measurements from adjacent climatological stations. DS is carried out at all nearby stations where at least 50 years of data are available ("base" stations), and the downscaled anomalies are then interpolated by means of linear regressions to all remaining "secondary" stations. Finally inverse-distance weighted means are again used to estimate the climate anomalies at the interpolation site from all surrounding base and secondary stations.

This method was applied to a "2xCO2" experiment with the ECHAM1 GCM to construct on a 2.5 km x 2.5 km latitude-longitude grid maps of changes in annual mean temperature and total precipitation for the Swiss region. The maps provide spatial details (Fig. 2) which are at present not available from simulations with regional climate models. Their salient feature is a strong N-S gradient, which is caused by different patterns of change at the northern vs. the southern slope of the Alps (cf. Gyalistras *et al.* 1994, 1995).

Crossvalidation experiments with ForClim showed that for the simulation of present tree species compositions the interpolation of monthly long-term mean temperature and precipitation in several cases falls short of the required precision. However, if a few years of measurements are available to improve the estimation of the baseline climate, the accuracy of the interpolated anomalies is in most cases sufficient to project scenarios of future forest responses (Gyalistras & Fischlin 1995a).

3 TEMPORAL ASPECTS

Resolution

Two basic approaches can be envisaged to construct scenarios with the high temporal resolution required by various ecosystem studies.

The first is to apply DS directly at the required, e.g. daily, temporal resolution. The advantage of this approach is that it uses directly the physically-based simulation of weather patterns by GCMs (e.g. Bardossy & Plate 1992, Zorita *et al.* 1995). However, at the same time it requires a sufficiently realistic performance of the climate models at this high temporal resolution, as well as the analysis of very large GCM-generated data sets.

The second approach is to use DS to adjust only the parameters of a stochastic weather generator. The latter can then be used to produce synthetic time series of weather variables at the required temporal resolution (e.g. Wilks 1992). In addition to DS-based adjustments the advantages of this approach are: (i) it can provide a large number of weather realizations, (ii) it allows to perform extensive sensitivity studies based on arbitrary adjustments of the weather generator parameters, and (iii) it relies upon commonly available (i.e. monthly) GCM-outputs. The main drawback is that the weather process is described by statistical approximations which may not necessarily hold under a changed climate.

Ecosystem modelers often need to explore in a flexible manner the relevance of different climate respectively weather parameters, as well as a wide range of possible climate changes. This is an additional reason to favour the weather generator approach.

Transient and Long-term Scenarios

The exploration of transient and/or long-term ecosystem responses (e.g. Fig. 1) by means of DS is at present limited by the fact that the currently available time-dependent GCM-simulations cover only a small sample of scenarios for future greenhouse-gas (GHG) concentrations, or cover only a relatively short future time period.

One possibility to improve this situation is to apply DS to a time-dependent GCM-experiment, and then parameterize the local climate change as a function of the GHGs used to force the GCM.

Fig. 3 shows an example of this technique for July mean temperature at Bever. First we downscaled year-to-year temperature anomalies from a transient (simulation years 1935-2084) experiment with the ECHAM1 GCM. Then we applied a 15-yr running mean filter to remove high-frequency variability, and fitted a linear response model $\Delta T_{k+1} = \lambda C_k + \alpha T_k$ to the smoothed temperature anomalies ΔT (cf. Hegerl *et al.* 1994). Here k is the simulation year; λ=0.212 and α=-0.91 are constants deter-

mined by means of a least-square fit; $C_k = \ln(GHG_k / GHG_o)$ is the forcing term, where GHG_k is the 15-year mean GHG forcing in the year k expressed in CO_2 concentration equivalents; and finally GHG_o is the preindustrial GHG-concentration (278 ppmv).

Such a model can be used to estimate the time-dependent shift in the expected value of the local climate variable in response to an arbitrary GHG- forcing. For example in Fig. 3 we constructed a "stabilization" scenario by rescaling the IPCC "S 550" scenario (Houghton *et al.* 1995) to account for all GHGs in addition to CO_2.

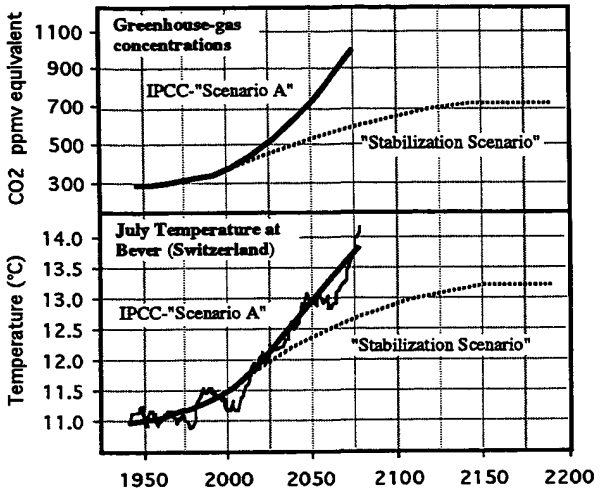


Figure 3. Use of downscaling to construct transient, long-term climate scenarios under arbitrary assumptions on future atmospheric greenhouse-gas concentrations. *Top*: prescribed profiles of equivalent CO_2 concentrations. *Bottom*: thin line: 15 year running mean of July mean temperature at Bever (1712 m.a.s.l., Swiss Alps), derived by downscaling from a transient IPCC "Scenario A" experiment with the ECHAM1 GCM (Cubasch *et al.* 1994); thick line: fitted linear response model; dotted line: application of the linear response model.

Moreover an arbitrary number of interannual monthly weather courses can be generated by assuming that the local variable is e.g. normally distributed with a time-dependent expected-value, and a constant variance (same as present). This approach can easily be extended to several local variables and more sophisticated time series models.

4 UNCERTAINTIES

Uncertainties Within Scenarios

A particularly attractive feature of DS with regard to ecosystem applications is that it can be flexibly applied to any regional climate variable of interest. However, the reliability of the empirical link between large-scale and local climate critically depends on the season, location, and the variables considered (Gyalistras *et al.* 1994). Unfortunately, the performance of DS deteriorates for several ecologically important variables such as summertime precipitation or winds.

One resort is to try to improve the performance of present DS procedures. However, the accurracy of DS can be expected to be always be limited due to (i) physical reasons, e.g. due to the occurrence of more erratic precipitation in summer, (ii) the sampling variability which enters the estimation of the statistical DS model, and, in some cases, (iii) the need to extrapolate climate changes beyond the range of the data which were available to fit the model.

A second possibility is to quantify the uncertainties in the downscaled climate scenarios, and then explore their effect on the ecosystem models (e.g. Bugmann & Fischlin 1994).

For instance, Gyalistras (1994) used a "bootstrap" technique (Efron 1979) to estimate uncertainty intervals for downscaled changes in monthly mean temperature and total precipitation at 22 Swiss locations. For each month and location N=800 different DS models to N data sets, each consisting of 57 large-scale and local data pairs, were fitted separately. The data pairs were sampled at random (with replacement) from a 57-year observational data base. The intervals obtained from application of the DS models to four different GCM-experiments are shown in Fig. 4.

These intervals account for sampling variability in the definition of present climate and for parameter uncertainty of the DS models. Certainly, they are only valid under the assumptions that (i) regional climate variations can be described as a sum of a "signal", which is forced by the large-scale component, plus a "residual variability", (ii) the "signal" is captured correctly, and (iii) the statistical properties of the "residuals" remain unchanged under a changing climate. The last point implies corresponding assumptions on the constancy of e.g. regional climate forcings or feedback mechanisms which are not resolved by the driving GCMs.

Uncertainties Between Scenarios

The complexity of ecosystem models often prevents a systematic assessment of possible ecosystem responses. An important application of DS is thus to generate at relatively small expenses a wide range of sensible working points for sensitivity and impact studies.

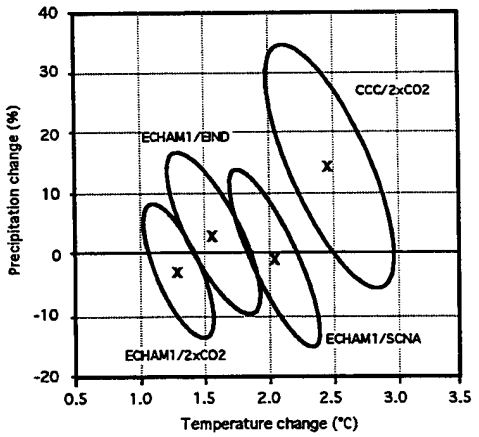


Figure 4. Comparison of changes in annually and regionally averaged temperature and precipitation for the Swiss region as downscaled from experiments with the ECHAM1 GCM (Cubash *et al.* 1992, 1994) and the CCC GCMII (Boer *et al.* 1992). 2xCO2: changes under an equilibrium CO_2-doubling; EIND, SCNA: changes for the decade 2075-84 under the transient "IPCC Scenario A" for greenhouse-gas concentrations; the GCM integrations started at 1935 (EIND) resp. 1985 (SCNA). Crosses denote best estimates, ellipses empirical 90% intervals of changes obtained from a bootstrap-procedure involving 800 downscaling models fitted separately for each month of the year and each of the 22 Swiss locations considered. After Gyalistras (1994).

This is again illustrated in Fig. 4. The overall range covered by the different scenarios reflects the different climate sensitivities of the ECHAM1 and the CCC GCMs, which respond to a CO2-doubling with a global

mean temperature increase of 1.7 °C and 3.5 °C, respectively. The relatively modest regional temperature increase under the ECHAM1 EIND-experiment is because the GCM projects a cooling over the North Atlantic, which is more pronounced in the EIND- as compared to the SCNA-experiment.

Recent investigations on the role of these uncertainties for forest responses as projected by ForClim demonstrated that the sensitivity of the forest model was largest at sites close to the precipitation and temperature determined timberlines. At these locations climate scenario uncertainties in the order of ±1 °C for temperature and ±15% for precipitation already affect forest compositions significantly (Bugmann 1994, Fischlin *et al.* 1995a,b).

These results underpinn the importance to explore a wide range of scenarios, respectively the regional uncertainties resulting from inter-GCM variability. At present, this can only be accomplished by downscaling.

5 CONCLUSIONS

Statistical downscaling is a flexible and economic method to construct regionally consistent climate scenarios as required by ecosystem studies. However, many ecological modeling applications need a downscaling complemented by additional methods, such as spatial interpolation and stochastic weather generation, in order to make best use of existing theory and data.

ACKNOWLEDGEMENTS

This research was financed by the Swiss National Science Foundation, grants no 5001-036812 and 5001-35172 (Swiss Priority Programme Environment).

REFERENCES

Bardossy, A., Plate, E.J., 1992, "Space-time model for daily rainfall using atmospheric circulation patterns", Wat. Resour. Res., **28**(5): 1247-1259.

Boer, G.J., McFarlane, N.A., Lazare, M., 1992, "Greenhouse gas-induced climate change simulated with the CCC second-generation general circulation model", J. Climate **5**: 1045-1077.

Bugmann, H., 1994, "On the ecology of mountainous forests in a changing climate: a simulation study", Dissertation No. 10638, Swiss Federal Institute of Technology, Zürich, 258p.

Bugmann, H. & Fischlin, A., 1994, "Comparing the behaviour of mountainous forest succession models in a changing climate". In: Beniston, M. (ed.), "Mountain Environments in Changing Climates", London, Routledge Publishing Co., p237-255.

Cubasch, U., Hasselmann, K., Höck, H., Maier-Reimer, E., Mikolajewicz U., Santer, B.D., Sausen, R., 1992, "Time-dependent greenhouse warming computations with a coupled ocean-atmosphere model", Clim. Dyn. **8**: 55-69.

Cubasch, U., Hegerl, G. C., Hellbach, A., Höck, H., Mikolajewicz, U., Santer, B.D., Voss, R., 1994, "A climate change simulation starting at an early time of industrialization", MPI Report No. 124, Max-Planck-Institut für Meteorologie, Hamburg, 33p.

Efron, B., 1979, "Bootstrap methods: another look at the Jacknife", The Annals of Statistics, **7**: 1-26.

Fischlin, A., Bugmann, H. & Gyalistras, D., 1995a, "Sensitivity of a forest ecosystem model to climate parametrization schemes", Environ. Pollut., **87**(3): 267-282.

Fischlin, A., Lischke, H., Bugmann, H., 1995b, "The fate of forests in a changing climate: model validation and simulation results from the Alps". In: Cebon, P., Dahinden, U., Davies, H.C., Imboden, D., & Jäger. C., "Climate and environment in the Alpine region", in review.

Gyalistras, D. & Fischlin, A., 1995a, "Derivation of climate change scenarios for mountainous ecosystems: a GCM-based method and the case study of Valais, Switzerland", Systems Ecology Report Nr. 22, Swiss Federal Institute of Technology, ETH Zurich.

Gyalistras, D. & Fischlin, A., 1995b, "Experience with the derivation of climatic change scenarios in the Alpine region". In: "Proceedings of a workshop on regional climate change in Central-East Europe", Budapest, Hungary, Nov. 28-30, 1994, Eotvos Lorand Univ., Budapest (in press).

Gyalistras, D., 1994, "Case studies in bioclimatic scenario derivation", Report Nr. 2 to the Swiss National Science Foundation, Systems Ecology, Swiss Federal Institute of Technology, ETH Zurich, 8p.

Gyalistras, D., von Storch, H., Fischlin, A. & Beniston, M., 1994, "Linking GCM-simulated climatic changes to ecosystem models: case studies of statistical downscaling in the Alps", Clim. Res., **4**(3): 167-189.

Gyalistras, D., Schär, C., Davies, H.C., Wanner, H., 1995, "Future alpine climate". In: Cebon, P., Dahinden, U., Davies, H.C., Imboden, D., & Jäger. C., "Climate and environment in the Alpine region", in review.

Hegerl, G. C., von Storch, H., Hasselmann, K., Santer, B.D., Cubasch, U., Jones, P.D., 1994, "Detecting anthropogenic climate change with an optimal finger-print method", MPI Report No. 142, Max-Planck-Institut für Meteorologie, Hamburg, 59p.

Houghton, J.T., Meira Filho, L.G., Bruce, J., Hoesung Lee, Callander, B.A., Haites, E., Harris, N., Maskell, K., 1995, "Climate change 1994: radiative forcing of climate change", Cambridge Univ. Press, Cambridge, 339p.

von Storch, H., Zorita, E., Cubasch, U., 1993, "Downscaling of global climate change estimates to regional scales: an applicaton to Iberian rainfall in wintertime", J. Climate, **6**: 1161-1171.

Wilks, D.S., 1992, "Adapting stochastic weather generation algorithms for climate change studies", Clim. Change, **22**: 67-84.

Zorita, E., Hughes, J. P., Lettemaier, D.P, von Storch, H., 1995, "Stochastic characterization of regional circulation patterns for climate model diagnosis and estimation of local precipitation", J. Climate **8** (in press).

CORRESPONDING AUTHOR

Dimitrios Gyalistras
Institute of Terrestrial Ecology
Swiss Federal Institute of Technology (ETHZ)
Grabenstr. 3, CH-8952 Schlieren
SWITZERLAND.

THE USE OF WEATHER TYPES FOR GCM DOWNSCALING

P.D. Jones and D. Conway

Climatic Research Unit, University of East Anglia, Norwich, NR4 7TJ, UK.

ABSTRACT

A variety of different methods have been proposed for downscaling large scale GCM output to the time and space scales required for climate impact studies. Using weather types to achieve this goal provides greater understanding of the problems that are involved compared to the many 'black box' techniques that have been proposed. Analyses using Lamb weather types, with observed data and GCM control run output over the British Isles, indicate that models neither produce the correct seasonal cycles for the three main weather types (westerly, cyclonic and anticyclonic days) nor similar internal relationships between the types and surface weather. Both failures have implications for scenario development. A weather type method is described for generating daily rainfall series based on the statistical characteristics of weather types and the daily rainfall associated with them.

1. INTRODUCTION

Various techniques have been proposed for circulation (or weather) typing (Yarnal, 1993). Many schemes, such as the Grosswetterlagen (Hess and Brezowsky, 1977) or Lamb Weather Types (Lamb, 1972), have been used at the regional scale by synoptic climatologists for decades (see review by Yarnal, 1993). Some research is now addressing the issue of automated (hence, more objective) schemes based on synoptic/meteorological typing for selected regions; for example by criteria classes (Jones et al., 1993) or by fuzzy rules (Bàrdossy, 1994). In addition to the synoptic or meteorological approach, a range of objective pattern typing schemes that use correlation-based pattern recognition (Kirchofer, 1973), principal components (White et al., 1991) and compositing (Moses et al., 1987) have been proposed. The compositing approach to circulation typing has potential for extreme event analysis, by determining the circulation characteristics for days of certain extreme events only.

All the circulation classification techniques mentioned above and others may be applied to General Circulation Model (GCM) control run integrations as a way of assessing model performance (Hewitson and Crane, 1992 and Hulme et al., 1993). There are advantages in assessing GCM simulations of atmospheric variability via circulation classification. Circulation is the fundamental control for surface weather, and the use of a surface variable (pressure) which may be regarded as representative of the free atmosphere has advantages. Although some aspects of climate variability since 1881 have been studied on the hemispheric scale (Trenberth, 1995) and the regional scale (von Storch et al., 1993b) (with considerable amounts of decade-to-decade variability observed), the ability of very long (~1000-year) GCM control runs to simulate this variability has only just begun to be investigated (von Storch, 1994). There is some evidence that, for surface temperature, the variability of long GCM control runs from the Max-Planck Institut für Meteorologie and Geophysical Fluid Dynamics Laboratory is less than observed on time scales beyond 50 years (Barnett et al., 1995 and Santer et al., 1995). This might be expected since the GCMs do not incorporate variations due to solar activity, volcanoes or ocean circulation changes, such as the El Nino/Southern Oscillation (ENSO), which are important on these time scales.

It is generally accepted that neither the current nor the next generation of GCMs will have the required spatial or temporal resolutions to allow direct assessments of the impacts of future climatic change (Carter et al., 1994). A number of methods have been proposed to link the relatively coarse-scale GCM output with the finer scale required for realistic impact assessments. The methods, which have all been termed *downscaling*, fall broadly into three categories:

- *Statistical linkages* between the large "planetary GCM scales" and the local "weather-scales". Various approaches have been developed to cope with what has been known as the climate inversion problem (Kim et al., 1984) or the sub-grid scale problem (Wigley et al., 1990).
- *Physically-based empirical linkages* between the same two scales using weather or circulation classifications to define the large scale. This technique has a large literature (Barry and Perry, 1973; Yarnal, 1993) but has only recently been applied to the downscaling problem (Hay et al., 1992; Wilson et al., 1992; Zorita et al., 1992; Hughes et al., 1993; Wilby, 1994).
- *Nesting* a much finer grid scale, more detailed, model for a limited area within a GCM (Higher Resolution Limited Area Modelling - HIRLAM; see Giorgi et al., 1990; 1992; Jones et al., 1995).

Nesting a HIRLAM within a GCM can produce dramatic improvements in detail in model simulations. Partly because of the much-improved geography and orography, the mean precipitation fields are more realistic (Giorgi et al., 1990; 1992; Jones et al., 1995). In many respects, the models are performing the same downscaling as the other techniques, by using the physics of the model.

With infinite computing resources nesting would be the ideal approach, with the required resolution being modelled at the global scale. As such resources are many decades away, the size of the limited area, the degree of improvement to the model physics, and many other issues, influence the results.

The circulation-type based approach to downscaling is both the subject of this paper and a relatively new example of the second kind of approach, which stresses the importance of physically-based relationships between climate on a large scale and weather on the local scale. These relationships will be controlled, to a large extent, by geography and orography. Local precipitation is partly controlled by the large scale variability of circulation defined by both surface pressure (Zorita et al., 1992; von Storch et al., 1993a), and free atmosphere variations such as 500 hPa heights (Wigley et al., 1990). Techniques such as multiple regression, canonical correlation analysis, and related methods, have been proposed to produce the statistical linkages. The

ultimate application to scenario generation depends on relationships between the large and small scale being stable through time, both in the past and in the future. Relationships founded on sensible physical linkages should better cope with future changes, but the no-analogue possibility should be countenanced. In some recent GCM perturbed run experiments, for example, it appears that increased precipitation was the result of fewer but wetter rain days rather than an increase in the number of rain days (Gregory and Mitchell, 1995).

2. LAMB WEATHER TYPES (LWTs)

The subjective weather typing (WT) scheme developed by Lamb (1972) can be objectively simulated using daily grid point pressure data using the relatively coarse 5° latitude by 10° longitude dataset (Jones et al., 1993). Agreement between the two schemes is good on the monthly scale for both directional and synoptic types over the 1881 to 1990 period. Comparison of the correlations between the types and England and Wales precipitation and Central England temperatures indicates negligible differences between the two schemes. Jones et al. (1993) show that the weather types can explain about 70-80% of seasonal variability of precipitation totals. This may be improved still further by the incorporation of additional information on the number of weather fronts over the region (Wilby, 1995 and Wilby et al., 1995).

The objective scheme has been applied, using the same grid point pressure dataset, to the Iberian Peninsula and northern Italy and Switzerland. Exactly the same wind flow characteristics were used, the only difference being a looser criterion for the definition of an unclassifiable day. Both regions show no marked trends in weather types over the whole length of record, although there are numerous multi-decadal trends.

The criteria may not be the most suitable for classifying circulation patterns over Portugal and Italy. We have therefore compared the results of the objective WT classification for Italy (OITWT) with a published subjective classification scheme for the Abruzzo region (SITWT). The scheme was devised by Mariani et al. (1995) and classifies daily weather types from the 850 hpa daily maps into 16 different types, defined *a priori*. Days were classified for a five year reference period between 1983 and 1987. This period is very short, but intercomparisons of this kind are important to assess the usefulness of objective typing.

The monthly totals of each SITWT were correlated with the OITWT for the five year period. Table 1 lists the results. A is negatively and C is positively correlated with SITWT 1 (low pressure), respectively, and A and C are correlated with SITWTs 9 and 11 (both high pressure types) in opposite directions. The most common SITWTs are 1 and 8-12. SITWT 8 (high pressure) has strong negative correlation with C and W. Table 1 shows the percentage of overall precipitation associated with each SITWT (%P) SITWTs 10 and 12 (low pressure types) are not strongly correlated with any OITWTs, however, these types do not produce much precipitation.

For the most common SITWTs, the objective scheme classifies the atmospheric circulation along similar lines. But, as might be expected, for the less frequent types the objective scheme, which has fewer WTs and is not regionally specific, does not produce similar results.

	% F	% P	A	C	N	E	S	W
% F			27.9	11.3	11.4	21.3	10.8	9.6
1	23	20	**-0.44**	**0.64**	-	*-0.27*	-	**0.35**
2	5	17	-	-	**0.42**	-	-	-
3	1	3	*-0.25*	*0.26*	-	-	-	-
4	5	10	-	-	-	*0.32*	*-0.28*	-
5	5	8	-	**0.38**	*-0.29*	-	**0.39**	*0.29*
6	2	10	-	-	**-0.33**	-	-	-
7	5	1	*0.27*	-	-	*-0.27*	-	-
8	13	4	*0.31*	**-0.54**	-	-	-	**-0.39**
9	8	2	**0.55**	**-0.36**	-	-	-	-
10	8	8	-	-	*0.30*	-	-	-
11	7	5	**0.50**	**-0.48**	-	-	-	-
12	6	1	-	-	-	-	-	-
13	1	1	-	-	-	-	-	-
14	1	1	-	-	-	-	*0.29*	**0.36**
15	3	6	**-0.43**	*0.29*	0.05	**0.40**	-	-
16	2	7	-	-	-	**0.37**	-	*-0.27*
IU	3	*	-	-	-	-	-	-

Table 1: Correlation between the main Italian weather types classified using the objective WT scheme over Italy (OITWT) and the manual subjective classification scheme for Italy developed by Mariani et al. (1995) (SITWT). Correlation coefficients are based on monthly frequencies (F) of each weather type, six types for the objective WT scheme are shown and 17 types for the manual scheme (IU=Unclassified). The overall percentage frequency (%F) and percentage precipitation (%P) associated with each WT are also shown. Period for analysis is 1983-1987, 60 months. * = missing data, 5% level of significance in italics, 1% level of significance in bold.

3. THE USE OF WEATHER TYPES FOR WEATHER GENERATION

Traditional weather generators all possess a similar structure. Precipitation is considered to be the primary variable. Depending on whether the day is wet or dry, other meteorological variables are determined by regression relationships, maintaining the cross- and auto-correlations between and within each of the variables. The realism of the procedure rests primarily on the method of precipitation generation (Hutchinson, 1986). An alternative to the generation of wet and dry sequences is to use weather types, either those generated by observed data (see section 4) or using weather types derived from GCM output. The sequences of wet and dry days will be incorporated in the weather types. Generating weather at neighbouring stations should be simpler with weather types because the interstation correlations are an inherent property of the types. More parameters of a generator may be required as each of the basic weather types necessitates a different distribution to determine the precipitation amount on wet days. Figure 1 shows an example of such distributions, seasonally for cyclonic WTs, using precipitation data for Durham

in the UK (1932-1990). The length of the LWT and daily rainfall series in the UK means that the consistency of the relationships between the large and small scale can be tested in different epochs of the observations. Current work is attempting to relate these distributions to additional information incorporated in the objective weather types such as the strength of the flow and vorticity over the region. These variables may improve the distributions fitted in a similar way to how the incorporation of weather fronts improved the relationships between types and precipitation totals (Wilby, 1994).

4. APPLICATIONS TO GCMs - SOME CONCLUDING REMARKS

All the ideas and techniques described in this paper may be theoretically applied to GCM data, providing the weather typing scheme is objective with certain decision rules. Application of the LWTs to GCM control run integrations shows that the monthly counts of weather types differ somewhat from reality (Hulme et al., 1993). Furthermore the relationships in the GCMs between the weather types and surface weather differ from those evident in reality. This is a serious impediment to the use of weather types for GCM downscaling. It should not be considered as a drawback, however. Indeed, the lack of similarity between reality and the GCM is more apparent when weather types are used, whereas these differences may be hidden in the mathematical detail of techniques such as canonical correlation analysis.

The development of downscaling methods is a response to the need for the appropriate spatial and temporal scale data for climate impact assessment studies. Many applications require sequences of future weather for design purposes. Without climate change these would come from long observational series or synthetically generated weather series when records were short. GCMs are the best tool for incorporating the effects of climate change through transient integrations including the effects of increasing levels of greenhouse gases and sulphate aerosols. Transient scenarios for the future, however, will have the climate changing by a sufficient amount on the decadal timescale to violate the stationarity constraints recognised for designs. GCMs cannot be run for specific design criteria. Therefore there will be a need for weather type generation to produce long sequences with the characteristics of a future time period suitable for design purposes.

REFERENCES

Bárdossy, A., 1994: Downscaling from GCMs to local climate through stochastic linkages. In: G. Paoli (ed.) *Climate Change, Uncertainty and Decision Making*, Institute for Risk Research, Waterloo, pp. 33-46.

Barnett, T.P., Santer, B.D., Jones, P.D., Bradley, R.S. and Briffa, K.R., 1995: Estimates of low frequency natural variability in near-surface air temperature. *Science* (submitted).

Barry, R.G. and Perry, A.H., 1973: *Synoptic Climatology*. Methuen, London.

Carter, T.R., Parry, M.L., Harasawa, H. and Nishioka, S., 1994: *IPCC Technical Guidelines for Assessing Climate Change Impacts and Adaptations*. IPCC Special Report to Working Group II of IPCC, 59pp.

Giorgi, F., Marinucci, M.R. and Visconti, G., 1990: Use of a limited area model nested in a general circulation model for regional climate simulation over Europe. *Journal of Geophysical Research* **95**, 18413-18431.

Giorgi, F., Marinucci, M.R. and Visconti, G., 1992: A $2xCO_2$ climate change scenario over Europe generated using a limited area model nested in a general circulation model. 2. climate change scenario. *Journal of Geophysical Research* **97**, 10011-10028.

Gregory, J.M. and Mitchell, J.F.B., 1995: Simulation of daily variability of surface temperature and precipitation over Europe in the current and $2xCO_2$ climates using the UKMO high-resolution climate model. *Quarterly Journal of the Royal Meteorological Society*, in press.

Hay, L.E., McCabe, G.J., Wolock, D.M. and Ayers, M.A., 1992: Use of weather types to disaggregate general circulation model predictions. *Journal of Geophysical Research* **97**, 2781-2790.

Hess, P. and Brezowsky, H., 1977: Katalog der Grosswetterlagen Europas (1881-1976). *Berichte des Deutschen Wetterdienst*, Bd. **15**. Selbstverlag des Deutschen Wetterdienstes, Offenbach am Main.

Hewitson, B. and Crane, R.G., 1992: Regional climates in the GISS global circulation model: synoptic-scale circulation. *Journal of Climate* **5**, 1002-1011.

Hughes, J.P., Lettenmaier, D.P. and Guttorp, P., 1993: A stochastic approach for assessing the effect of changes in synoptic circulation patterns on gauge precipitation. *Water Resources Research* **29**, 3303-3315.

Hulme, M., Briffa, K.R., Jones, P.D. and Senior, C.A., 1993: Validation of GCM control simulations using indices of daily airflow types over the British Isles. *Climate Dynamics* **9**, 95-105.

Hutchinson, M.F., 1986: Methods of generation of weather sequences. In (A.H. Bunting ed.) *Agricultural Environments*. C.A.B. International, Wallingford, 149-157.

Jones, P.D., Hulme, M. and Briffa, K.R., 1993: A comparison of Lamb circulation types with an objective classification scheme. *International Journal of Climatology* **13**, 655-663.

Jones, R.G., Murphy, J.M. and Noguer, M., 1995: Simulation of climate change over Europe using a nested regional climate model. Part 1: Assessment of control climate, including sensitivity to location of lateral boundaries. *Quarterly Journal of the Royal Meteorological Society*, in press.

Kim. J-W., Chang, J-T., Baker, N.L., Wilks, D.S. and Gates, W.L., 1984: The statistical problem of climate inversion: determination of the relationship between local and large-scale climate. *Monthly Weather Review* **112**, 2069-2077.

Kirchofer, W., 1973: Classification of European 500 mb patterns. Arbeitsbericht der Schweizerischen Meteorologischen Zentralanstalt Nr. 43, Geneva.

Lamb, H.H., 1972: British Isles weather types and a register of daily sequence of circulation patterns, 1861-1971. *Geophysical Memoir* **116**, HMSO, London, 85pp.

Mariani, L., V., Menichini V. and Minardi G.P., 1995: Frequency of weather types and climatic risk of extreme rainfall and thermal events. *International Journal of Climatology*, in press.

Moses, T., Kiladis, G.N., Diaz, H.F. and Barry, R.G., 1987: Characteristics and frequency of reversals in the mean sea level pressure in the North Atlantic sector and their relationship to long-term temperature trends. *Journal of Climatology* **7**, 13-30.

Santer, B.D., Taylor, K.E., Penner, J.E., Wigley, T.M.L., Jones, P.D. and Cubasch, U., 1995: Towards the detection and attribution of an anthropogenic effect on climate. *Climate Dynamics*, in press.

Trenberth, K.E., 1995: Atmospheric circulation climate changes. *Climatic Change*, in press.

von Storch, J., 1994: Interdecadal variability in a global coupled model. *Tellus* **46A**, 419-432.

von Storch, H., Zorita, E. and Cubasch, U., 1993a: Downscaling of global climate change estimates to regional scales: an application to Iberian rainfall in wintertime. *Journal of Climate* **6**, 1161-1171.

von Storch, H., Guddal, J., Iden, K.A., Jonsson, T., Perlwitz, J., Reistad, M., de Ronde, J., Schmidt, H. and Zorita, E., 1993b: Changing statistics of

storms in the North Atlantic. Max-Planck Institut für Meteorologie Report No. 116, Hamburg, 19pp.

White, D., Richman, M. and Yarnal, B., 1991: Climate regionalization and rotation of principal components. *International Journal of Climatology* **11**, 1-25.

Wigley, T.M.L., Jones, P.D., Briffa, K.R. and Smith, G., 1990: Obtaining sub-grid-scale information from coarse-resolution general circulation model output. *Journal of Geophysical Research* **95**, 1943-1953.

Wilby, R.L., 1994: Stochastic weather type simulation for regional climate change impact assessment. *Water Resources Research* **30**, 3395-3453.

Wilby, R.L., 1995: Simulation of precipitation by weather pattern and frontal analysis. *J. of Hydrology*, in press.

Wilby, R.L., Barnsley, N. and O'Hare, G., 1995: Rainfall variability associated with Lamb weather types: the case for incorporating weather fronts. *International Journal of Climatology*, in press.

Wilson, L.L., Lettenmaier, D.P. and Skyllingstad., E., 1992: A hierarchical stochastic model of large-scale atmospheric circulation patterns and multiple station daily precipitation. *Journal of Geophysical Research* **97**, 2791-2809.

Yarnal, B., 1993: *Synoptic Climatology in Environmental Analysis*. Belhaven Press, London, 195pp.

Zorita, E., Kharin, V. and von Storch, H., 1992: The atmospheric circulation and sea surface temperature in the North Atlantic area in winter: their interaction and relevance for Iberian precipitation. *Journal of Climate* **5**, 1097-1108.

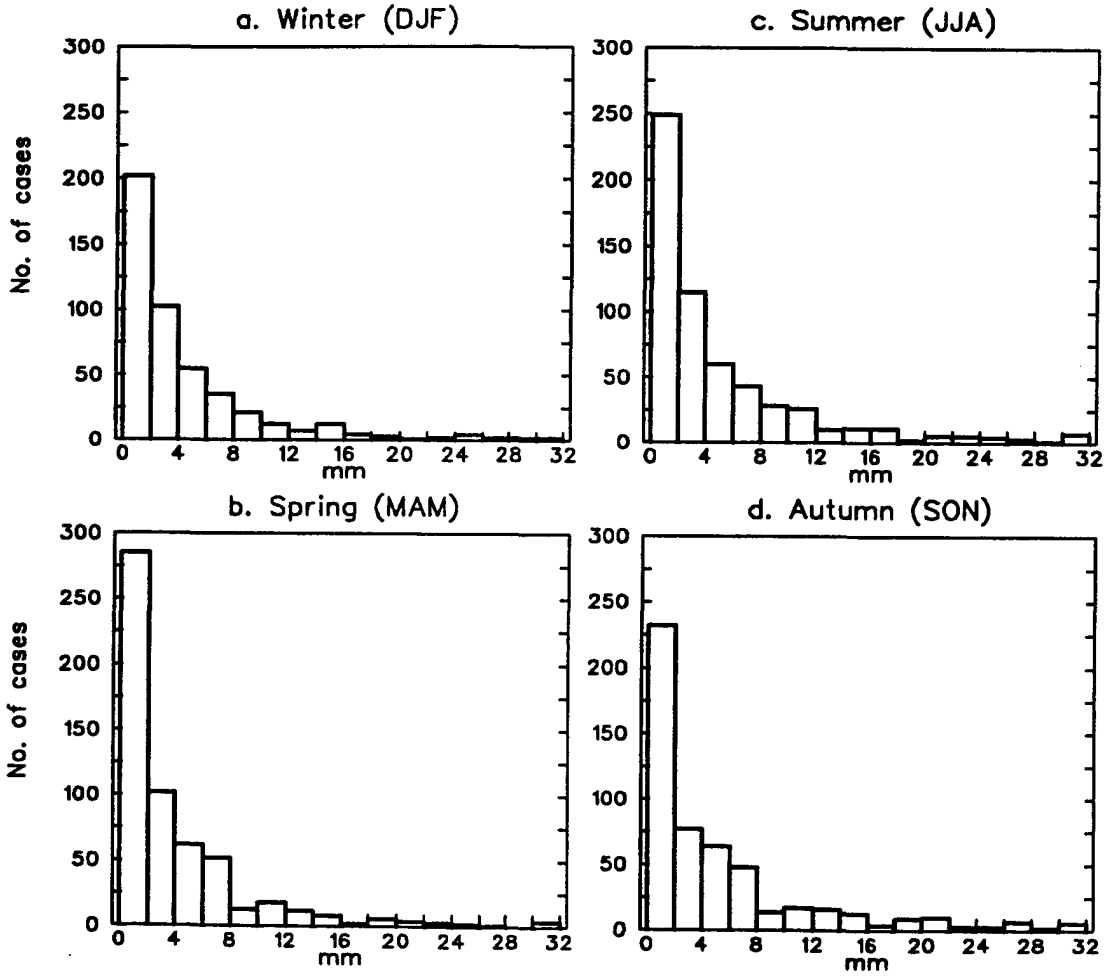
ACKNOWLEDGEMENTS

This research was supported by the European Community Environment Research Programme (contract: EV5V-CT-94-0510, Climatology and Natural Hazards).

CORRESPONDING AUTHOR

P.D. Jones
Climatic Research Unit,
University of East Anglia,
Norwich,
NR4 7TJ, UK.

Tel.: +1603 592090
Fax: + 1603 507784
e-mail: p.jones@uea.ac.uk



	Winter (DJF)	Spring (MAM)	Summer (JJA)	Autumn (SON)
C days as % of total	11.0	13.0	13.8	12.0
Mean rain depth (mm)	4.4	4.0	5.2	5.6
% of C days wet	79.4	81.2	77.5	81.8

Figure 1: Frequency distributions of raindays (>0.1mm, 2mm bins) with cyclonic weather types by season. Durham (UK) daily rainfall data, 1932-1990

ON RELATIONSHIP BETWEEN THE PRECIPITATION OF THE NORTH-WEST MOROCCO AND THE 700 HPA HEIGHT IN WINTER

A. Belaassal and A. Douguédroit

Institute of Geography, The University of Aix-Marseille I, Aix-en-Provence, France

ABSTRACT

The ten-day winter anomalies of the 700 hPa geopotential height of the ECMWF dataset have been studied. A Varimax principal component analysis has allowed to determine 16 low frequency circulation patterns including 2 unknown before : the North East Atlantic Oscillation (NEAO) dipole and the Africa Mediterranean (AM). The relations studied between all the patterns and the winter precipitation of the north-west Morocco display that only 3 patterns play an important part in the variability of the precipitation : the NEAO, the AM and the EA (East Atlantic). Unlike what is usually written, the part of the North Atlantic Oscillation (NAO) is very small.

1 - INTRODUCTION

Up to now the study of the relationship between the Morocco precipitation and the atmospheric circulation has been mostly based on synoptic weather maps to determine and classify weather types. Studies on precipitation predictor in Morocco and even North Africa related with the atmospheric circulation are very scare : Lamb and Peppler (1987), Delannoy (1988) for Morocco and Clinet and Douguédroit (1992) for North Africa.

Here we intend to determine the 700 hPa geopotential height patterns which play an important part in the low frequency variability of the north-west Morocco precipitation and could be used later on for their prediction. Some patterns well known at that height field are found again (Barnston and Livezey 1987, Clinet 1990, Clinet and Martin 1992). But the novelty of the study lies in the emergence of two unknown patterns that we named North East Atlantic Oscillation (NEAO) and Africa Mediterranean (AM).

2 - STUDY FRAMEWORK

The ten-day average pressure heights of the three adjacent winter months (from December to February) for 10 years (1980 - 1989) have been used. They have been calculated using the ECMWF dataset of Reading (UK). The 380 point grid is the same as the one used by Barnston and Livezey (1987). The low frequency patterns have been determined by computing the 10 day anomalies with a rotated principal component analysis (Varimax type). 16 components have been retained by a scree test and several trials. Each pattern has an associated temporal index.

The study of the precipitation is based on the synoptic meteorological stations which are reliable. It is restricted to the densest part of the network, the north-west Morocco (Fig. 1) whose unity has been demonstrated before (Delannoy and Douguédroit 1983, 1984). It includes 16 stations from Tangiers to Agadir whose daily precipitation have been aggregated in ten-day totals.

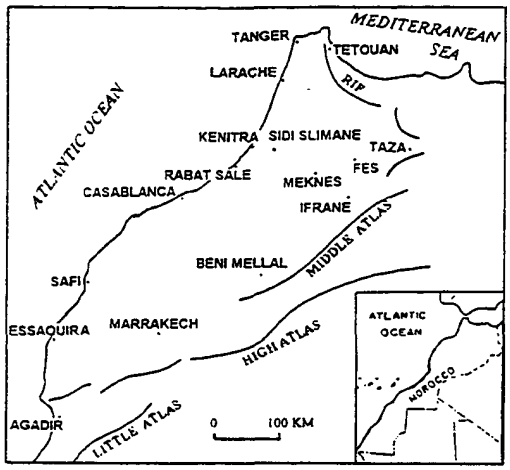


Fig. 1 : Location of the Moroccan stations

After, linear correlations between the precipitation of the 16 stations and the temporal index of each of the 16 rotated components have been calculated. 4 patterns with significant correlations according to the Bravais-Pearson test have been only retained here. Each individual pattern is physically realizable (Barnston and Livezey 1987).

The diagnostics of their physical interpretation is conducted by two types of composite analyses applied to the five extreme negative (positive) values of the temporal index of each of the 4 retained patterns : on anomalies and on raw values.

3 - THE PATTERNS SIGNIFICANT FOR THE MOROCCAN PRECIPITATION

The 16 patterns resulting from the Varimax rotation applied to the 90 ten-day anomalies (1980 - 1989) of the 700 hPa geopotential height in winter represent 82 % of total variance. The 4 patterns well correlated with the Moroccan precipitation are the first (8,2 % of explained variance), the 9th (4,5 %), the 13th (4 %) and the 16 th (3 %).

The first pattern corresponds with the North Atlantic Oscillation (NAO). It is a dipole characterized by a strong positive centre on Greenland and a wide negative strip in the south at about 50° long. (non represented). It is regarded as an indicator of the westerlies circulation on the North Atlantic ocean (Rogers, 1984).It has been

described in the first analyses of the low frequency patterns of the 700 hPa geopotential (see Barnston and Livezey, 1987). It is the same for the 13th component which corresponds with the East Atlantic - EA (non represented). The EA is a dipole with a positive centre off the Moroccan coast and a negative one north of the British Islands.

On the contrary, the components 9 and 16 cause low frequency patterns unknown up to now appear : the North East Atlantic Oscillation (NEAO) and the Africa Mediterranean (AM). The first one is a north-south dipole with a negative centre north of the British Islands and a positive one off the Moroccan coast (Fig. 2). It is located at about longitude 0° - 10° W close to the east of the NAO (50° W). The centres of both patterns have opposite signs at the same latitudes.

The AM is characterized by a positive cell over North Africa and the Western Mediterranean sea (Fig. 3). It is located east of the positive centre of the NEAO with a centre in Libya, at longitude 10° E (Belaassal and Douguédroit, 1995).

The reasons explaining that those two patterns have not been determined in the previous analyses on the 700 hPa geopotential height lie in the dataset used. These analyses were based on the twice-daily data of the Northern Hemisphere 700 mb height from the NMC series (Barnston and Livezey, 1987) and from the French Hemis dataset (Clinet, 1990, Clinet and Martin, 1992). The previous authors have demonstrated that a bias exists over North Africa in the 700 hPa height field that they used. Such a bias very likely explains why the NEAO and the AM patterns are missing in the previous analyses. It appears as if it has been removed in the European dataset.

4 - RELATIONSHIP BETWEEN THE MOROCCAN PRECIPITATION AND THE LOW FREQUENCY PATTERNS AT 700 HPA HEIGHT

Only 4 low frequency atmospheric circulation patterns are significantly correlated in winter with the north-west Morocco precipitation.

The correlations between the NAO and the Morocco precipitation are poor. The only significant one at the 10% level concerns Tangiers (0.18). This can be explained by the physical meaning of the NAO in the atmospheric circulation at 700 hPa .The composite analysis based on the 5 positive extreme anomalies found in its associated temporal index displays a pressure increase on Greenland and a lowering pressure of the negative strip over the Atlantic (not represented). The map of the average height field obtained with the 5 retained cases displays a blocking. It slightly carries off towards the south the westerlies. They can only concern the far north of Morocco. So the NAO does not play an important part in the explanation of the winter precipitation of Morocco.

The low level of correlation found in this study between the Moroccan precipitation and the NAO pattern appears as a surprise as several authors have previously demonstrated such a relation. Lamb and Peppler (1987) after Walker (1924) and Rogers (1984) have displayed relations between the variability of the precipitation in Morocco and the NAO oscillation represented by an index consisting in the pressure difference between Iceland and the Azores Island. In fact, they confuse two patterns the NAO and the NEAO which they did not know that it exists.

The relations between the north-west Morocco precipitation and the 700 hPa geopotential height are the highest in winter with the NEAO. Except in the far north, they represent around 25 % of explained variance for the precipitation of all the stations. The NEAO is a basic pattern of the low frequency circulation in Morocco (Tabl 1).

	NEA	EA	AM
TANGIERS	- 0.39	- 0.36	
TETOUAN	- 0.53		
LARACHE	- 0.36	- 0.43	
KENITRA	- 0.46		
SIDI SLIMANE	- 0.45	- 0.30	- 0.21
RABAT SALE	- 0.46	- 0.25	
CASABLANCA	- 0.52	- 0.27	
SAFI	- 0.55		
ESSAOUIRA	- 0.48		
AGADIR	- 0.49		
TAZA	- 0.46		- 0.22
FES SAIS	- 0.34	- 0.34	- 0.25
MEKNES	- 0.39	- 0.36	- 0.21
IFRANE	- 0.38	- 0.32	- 0.27
BENI MELLAL	- 0.50		- 0.21
MARRAKECH	- 0.49		

Table 1 : Correlations between north-west Morocco precipitation and 3 low patterns of the 700 hPa geopotential height (all the correlations are significant at the 98% level except the four lowest AM ones).

The NEAO temporal index is negatively correlated with the precipitation of all the stations of the North-West Morocco. The highest values concern the stations along the coast south of Larache and in the inner south. The composite average of the NEAO five negative extreme anomalies of the temporal index displays a pressure increase in the north centre of the pattern and a decrease in the south one (Fig. 4). In the map of the corresponding 700 hPa field , there is a diffluence of the westerlies with a southern branch over North Africa (Fig. 5). The composite average of the five positive extreme NEAO anomalies corresponds with values opposed to the previous one. The subtropical high moves towards the north tooking the westerlies off in the same direction (not represented). There is no rain in Morocco.

The NEAO consist of two centres at the same latitude of the NAO's one but situated at the east of them, at about the prime meridian longitude. This location corresponds with the so-called NAO dipole index, mentionned previously. The explanation lies, of course, in the ignorance of the NEAO up to now. Apart from the difference in pattern, our results confirm the teleconnections previously defined.

The EA pattern is less correlated with the winter precipitation in Morocco than the NEAO except for the stations located on the north and central coast south of Safi (Tab 1). The composite analysis of the 5 extreme negative anomalies displays an important pressure decrease on the east Atlantic and a slight increase on the subtropical Atlantic centre of the dipole (not represented). Such anomalies cause a small sliding, towards the south, of the westerlies which only bring

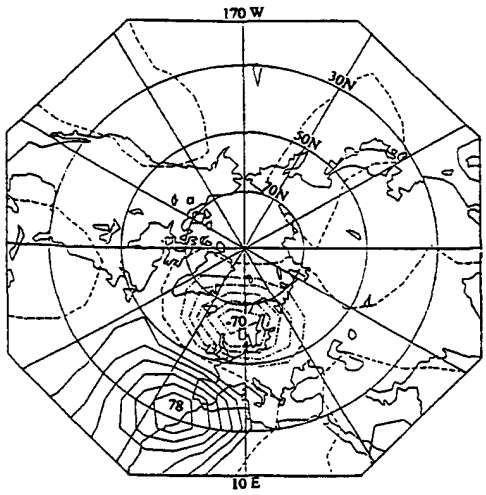


Fig. 2 : NEAO pattern (only significant correlations are represented). Solid line : positive correlations. Dashed line : negative correlations

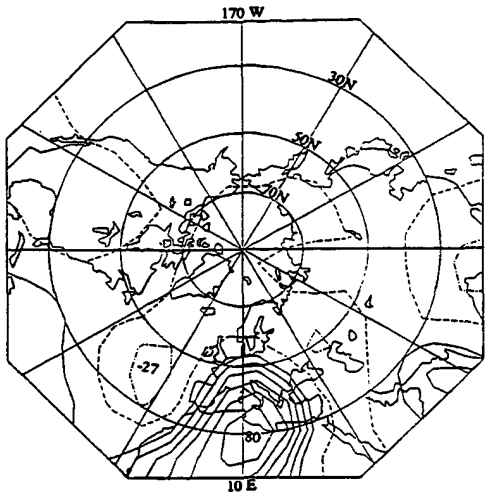


Fig. 3 : Same as Fig. 2 except AM (Africa Mediterranean)

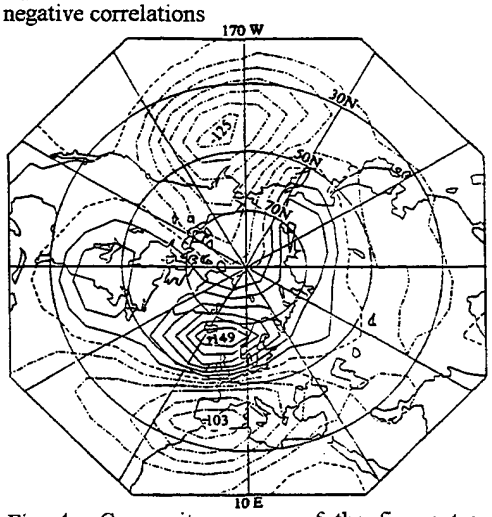


Fig. 4 : Composite average of the five extreme negative anomalies of the NEAO temporal index. Solid and dashed lines : positive and negative anomalies.

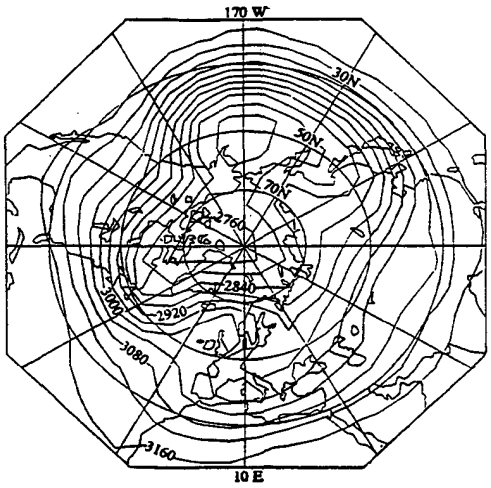


Fig. 5 : Composite average of altitude of the 700hPa height for the 5 extreme negative anomalies of the NEAO temporal index.

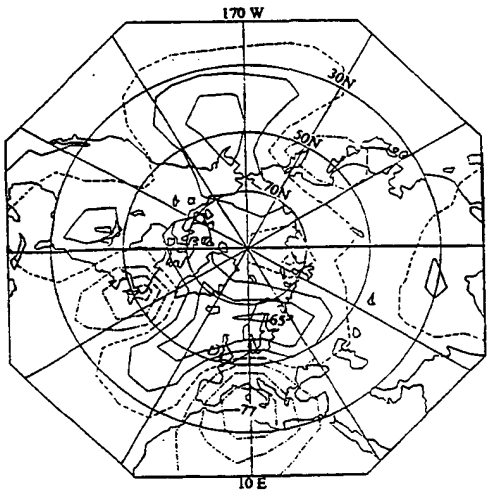


Fig. 6 : Same as Fig. 4 except AM

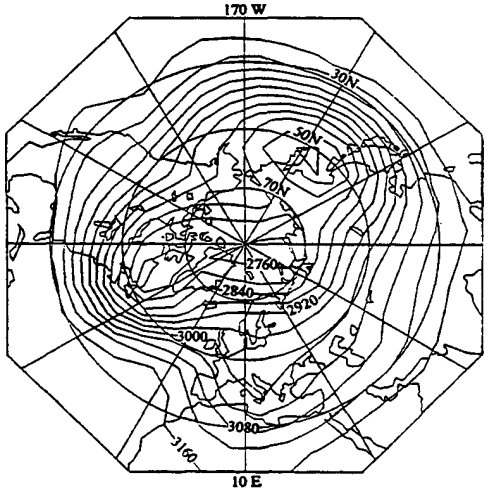


Fig. 7 : Same as Fig. 4 except AM

rain in North Morocco. The explained variance of the total precipitation is about 10 % (Tab 1). The composite analysis of the 5 extreme positive anomalies shows values with a sign opposite of the previous case. It induces a high and no rain on Morocco (not represented).
The correlations between the AM pattern and the Morocco precipitation are limited to the stations located in central Morocco(Tab. 1). The extreme negative anomalies are linked with a general pressure decrease of the pattern (Fig. 6). It provokes a north-west flow on the north centre (Fig. 7). This explains between 4 and 8 % of variance of the winter precipitation.

5 - CONCLUSION

Two new low frequency atmospheric circulation patterns, the NEAO (North East Atlantic Oscillation) and the AM (Africa Mediterranean) have been determined at the 700 hPa geopotential height taken from the ECMWF dataset. The first is situated on the East Atlantic, at the same latitude than the NAO but on the east side of it and the second on North Africa and on the west Mediterranean Sea. The first corresponds with the location of the index which has been considered as representative of the NAO and correlated with the Moroccan precipitation. A bias existing in the datasets previously used to determine the low frequency circulation patterns explains the confusion between the two patterns, the NAO and the NEAO.
Only three low frequency patterns are well correlated with the winter Moroccan precipitation : the NEAO, the EA(East Atlantic) and the AM.
Composite analyses carried on the 5 extreme positive and negative anomalies of the corresponding temporal index of each pattern allows to diagnose the explanation of such relationship. It lies in the location of the westerlies according to the pressure differences induced by the patterns. Rain in Morocco supposes high pressure making the westerlies slip at the Moroccan latitudes.

REFERENCES

Barnston A.G., Livezey R.E., 1987, « Classification seasonality and persistance of low frequency atmospheric circulation patterns », Mon. Wea. Revue, volume 115, pp. 1088 - 1126.

Belaassal A., Douguédroit A., 1995, « Teleconnections between the winter precipitation in Morocco and the low frequency circulation patterns of the 700 hPa height », in Atmospherics Physics and Dynamics in the Analysis and Prognosis of Precipitation Fields, Roma, 15 - 18 Nov. 1994 (in press).

Clinet S., 1990, « Variabilité du champs de pression hémisphérique nord extratropical - analyse des géopotentiels décadaires et mensuels à 700 et 500 hPa », Doctorat, Grenoble, 381 p. + annexes.

Clinet S. and Martin S., 1992, « 700 hPa Geopotential Height Anomalies from a Statistical Analysis of the French Hemis Data Set », Intern J. of Climatol. volume 12, 3, pp. 229 - 256.

Delannoy H., 1988, « Précipitations saisonnières du Maroc cisatlasique et téléconnexions dans la circulation atmosphérique », Bull. Assoc. Géogr. Franç., volume 5, pp. 393 - 406.

Delannoy H. , Douguédroit A, 1983, « A propos des précipitations dans le Sud Ouest européen et le Maghreb occidental », Météorologie, volume 34, pp. 169 - 181.

Delannoy H. , Douguédroit A., 1984, « Les variations des précipitations printanières dans le Sud Ouest européen et le Maghreb occidental (1916 - 1965) », Rev. Géogr. Est, volume 1, pp. 47 - 63.

Lamb P.J. and Peppler R.A., 1987, « North Atlantic Oscillation : Concept and Application », J. of Climate, volume 68, 10, pp. 1218 - 1225.

Rogers J.C.,1984, « The association between the North Atlantic Oscillation and the Southern Oscillation in the Northern Hemisphere », Mon. Wea. Revue, volume 112, pp. 1995 - 2015.

Walker G.T., 1924, « Correlation in seasonal variation of weather », Mem. Indian. Dep., volume 24, pp. 275 - 332.

CORRESPONDING AUTHOR
Professor A. Douguédroit
Institut de Géographie
Université d'Aix-Marseille I
29, Avenue Robert Schuman
13621 Aix-en-Provence Cedex 1, FRANCE

Statistical Generation of Surface Air Temperature for the Central USA Using a General Circulation Model Simulation

David R. Easterling

Global Climate Laboratory
NOAA/NESDIS/NCDC
Federal Building
Asheville, NC 28801 USA

ABSTRACT.
Free atmosphere variables for eleven gridpoints over the Central USA from both control and transient simulations from the GFDL General Circulation Model were used with thirty years of nearby station data to generate surface air temperatures. The free atmosphere variables were subjected to a rotated principal components analysis and used in an inflated regression analysis to generate surface air temperature for each location. The statistically generated temperatures are then compared with those produced in the model simulation. Results indicate that the statistically generated surface air temperatures show less warming in the transient simulation than the temperatures produced by the model.

1. INTRODUCTION.
One of the major problems of using General Circulation Model (GCM) simulations for examining potential climate change is that it is difficult to extend the results of these coarse resolution models to local changes in climate. One approach to providing estimates of local climate simulation of surface variables using GCM output is to perform a statistical downscaling. Karl, et al. (1990) introduced a downscaling approach using a combination of rotated principal components analysis (RPCA), canonical correlation analysis (CCA), and inflated multiple regression (IMR) which has the potential for providing site specific climate change scenarios. For this paper a similar approach is taken to generate monthly surface air temperature for a series of locations in the Central USA using both the results of GCM simulations and observing station data.

2. METHODS.
The GCM simulations used for this paper were from the Geophysical Fluid Dynamics Laboratory (GFDL) model as described in Manabe, et al. (1991) and Manabe, et al. (1992). Two simulations were used; a 100 year control simulation where atmospheric carbon dioxide was held constant, and a 100 year transient simulation where carbon dioxide was increased 1% each year above the previous year's level. Eleven grid points (Fig. 1) and eleven nearby observing stations were selected to represent the Central USA. Free atmosphere variables from both the model simulations and observing stations were used. The free atmosphere variables used were: surface pressure, relative humidity, temperature, geopotential heights, and the U and V wind components at 500 hPa. Data from the observing stations were used to develop the relationship between the free atmosphere variables and surface temperature at each station using a RPCA and IMR. In developing the regression equations for surface air temperature at each station typically about 70% of the variance in surface air temperature was explained indicating that the variables used were fairly robust indicators of monthly mean surface temperatures. The same free atmosphere variables for each corresponding gridpoint from the GCM simulation were also subjected to a RPCA. In both RPCAs only the first two principal components were kept, which accounted for approximately 70% of the variance. The results from the RPCA for the model simulations at each gridpoint were then used with the IMR coefficients from the nearby station to generate surface temperatures. This was done on a month by month basis.

3. RESULTS.
The results shown are area-averaged temperatures (averaged over all eleven gridpoints) for the annual and seasonal for both the statistically-generated and model simulated temperatures. A comparison of the annual and seasonal averaged temperatures for the transient GCM simulation are shown in Table 1. The linear trend for the model simulated annual surface temperatures show a strong warming over the 100 years of the simulation with a linear trend of 5°C/100 yrs.

However the statistically-generated annual surface temperatures show less warming with a 100 year trend of 4°C. For the winter season the results from the model simulated temperatures show less warming over the 100 years than the statistically-generated temperatures. In spring, the trends are nearly identical. However, in both the summer and fall seasons the warming as simulated by the model is considerably more than that shown by the statistically-generated temperatures.

Karl, et al. (1990) have shown that this type of statistical-generation of surface temperatures using GCM simulations can reproduce quite well the statistical distributions of observed local surface temperature and precipitation. Preliminary results shown here indicate that this type of methodology can be used to provide alternative estimates of surface variables and their trends for enhanced CO_2 GCM simulations.

Season	Model Trend (per 100 yrs)	Statistical Trend (per 100 yrs)
Annual	5.0 C	4.0 C
Winter	4.5 C	5.9 C
Spring	4.3 C	4.4 C
Summer	6.1 C	3.0 C
Fall	5.0 C	3.3 C

Table 1. Results for each season and annual. Model are the slopes for the model simulated time series, and Statistical are the slopes for the statistically-generated time series.

4. REFERENCES.

Karl, T.R., W-C. Wang, M.E. Schlesinger, R.W. Knight, and D. Portman, 1990: A method of relating General Circulation Model simulated climate to the observed local climate. Part I: seasonal statistics., *J. Climate*, V. 3, 1053-1079.

Manabe, S., R.J. Stouffer, M.J. Spelman, and K. Bryan, 1991: Transient response of a coupled ocean-atmosphere model to gradual changes of atmospheric CO2. Part I: annual mean response, *J. Climate*, V. 4, 785-818.

Manabe, S., M.J. Spelman, and R.J. Stouffer, 1992: Transient response of a coupled ocean-atmosphere model to gradual changes of atmospheric CO2. Part II: seasonal response. *J. Climate*, V. 5, 105-126.

ACKNOWLEDGEMENTS: Partial support for this work was provided to the National Climatic Data Center by the U.S. Department of Energy through Interagency Agreement: DE-AI05-90ER60952.

CORRESPONDING AUTHOR
Dr. David R. Easterling
Global Climate Laboratory
National Climatic Data Center
Federal Building
151 Patton Avenue
Asheville, NC 28801
USA
deasterl@ncdc.noaa.gov

DOWNSCALING DAILY TEMPERATURE DATA FROM GCMS: AN EXAMPLE FROM THE MEDITERRANEAN BASIN

J.P. Palutikof*, J.A. Winkler**, J.A. Andresen** and C.M. Goodess*

*Climatic Research Unit, University of East Anglia, Norwich, UK
**Department of Geography, Michigan State University, East Lansing, MI, USA

ABSTRACT

Daily temperature time series from a GCM are compared with observations from a site in Spain. The model data does not adequately simulate observations at this scale. A method to generate more realistic daily time series from model data is presented, and the results analysed with respect to changes in the occurrence of extreme events due to global warming.

1. INTRODUCTION

It is likely that the principal impacts of global warming will be due to changes in the frequency and severity of extreme climatic events. Yet scenarios of future climate generally consider changes in the mean value of some climate variable, usually temperature or precipitation. A reason for this is that the commonest approach to scenario construction is to start with the results from General Circulation Models (GCMs), which cannot adequately simulate climate at the daily scale.

Here, we examine the ability of one GCM to simulate daily time series of maximum and minimum temperature. A method is then demonstrated to generate realistic time series for maximum and minimum temperature from GCM output The results are analysed for changes in extreme events due to global warming. This method is heavily influenced by the approach of Karl et al. (1990) which in turn is influenced by Perfect Prog algorithms. Essentially, regression equations are developed which relate free atmosphere variables (the predictors), such as sea level pressure, to surface variables (the predictands), such as temperature and precipitation. The method is based on the hypothesis that free-atmosphere variables are better simulated by GCMs than the surface variables.

2. THE DATA

Alcantarilla, in south-eastern Spain (38°N, 1.2°W), was selected for analysis because it has a long and reliable temperature record.

The required free-atmosphere data sets were obtained from the twice-daily (0000 UTC and 1200 UTC) gridded National Meteorologial Center operational analyses for the Northern Hemisphere, available on CDROM from the National Center for Atmospheric Research, Boulder, CO. The grid consists of equally-spaced points on a polar stereographic projection with a horizontal resolution of approximately 380 km. Using a 16-point Bessel scheme, data for sea level pressure (SLP) and the height of the 500hPa surface (z500) were interpolated to the site of Alcantarilla.

The Canadian Climate Centre retained ten years of daily data from the control and perturbed climate simulation by their second-generation model (McFarlane et al., 1992) for a European and a North American window. The spatial resolution of the model grid is 3.71° latitude approximately over the two windows by 3.75° longitude. The model experiment was performed in equilibrium mode. The daily data from the $1xCO_2$ and $2xCO_2$ model runs were interpolated to the site of Alcantarilla, again using a 16-point scheme, and time series for maximum and minimum temperature (tmax and tmin), SLP and z500 were extracted.

3. DATA COMPARISON

Table 1 compares summary statistics for seasonal and annual tmax and tmin calculated from observations for 1975-84 and from $1xCO_2$ model data. Modelled maximum temperatures are too low, minimum temperatures too high. In consequence, daily mean temperatures are well-simulated: the annual mean temperature is 17.6°C for 1975-84, and 17.3°C for $1xCO_2$. Standard deviations in winter are far too small, although in the other three seasons they are

CORRESPONDING AUTHOR:
Dr. J.P. Palutikof
Climatic Research Unit
University of East Anglia
Norwich NR4 7TJ, UK

Table 1 Summary temperature statistics for 1975-84 observations and model control run.

	Maximum (°C)		Minimum (°C)	
	Mean	S.D.	Mean	S.D.
Annual				
1975-84	24.3	6.8	11.2	6.0
Control	20.9	7.3	13.6	5.9
Winter				
1975-84	17.3	3.6	5.1	3.8
Control	12.5	1.7	7.7	1.3
Spring				
1975-84	22.4	4.1	9.3	3.5
Control	18.2	3.7	10.8	3.2
Summer				
1974-84	32.1	3.5	18.0	2.7
Control	29.7	3.1	21.0	2.9
Autumn				
1975-84	25.2	5.3	12.3	4.7
Control	23.0	5.3	14.7	4.4

well-modelled. The cause of the low standard deviations in winter is clearly shown by Fig. 1. For each day, the highest and lowest of the ten values (in this case, for tmin) are plotted. There is a clear threshold, at around 5°C, below which temperatures do not fall in winter, and which is responsible for the low winter standard deviation in the modelled data. Further investigation of grid-point data has shown that the true threshold is at 0°C, and that the higher threshold at Alcantarilla is an artefact of the interpolation from the 16 model grid points.

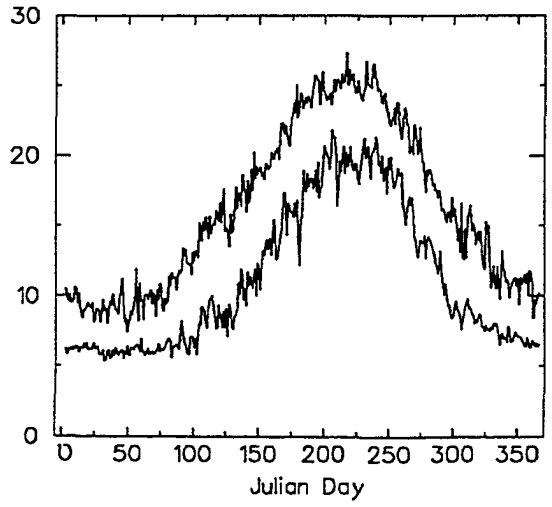


Figure 1 Extreme high and low daily tmin (°C) from the model control run.

4. TRANSFER FUNCTION DEVELOPMENT

Data from 1975-84 were used for transfer function development. Standardized anomalies were used as variables in the regression equations where possible, to avoid the problem of applying the regression equations outside the development range. This was considered a particular risk for the $2xCO_2$ model data sets. Four equations were calculated, using stepwise regression, one for each season.

a) The predictand

Tmax/tmin cannot be expressed as straightforward standardized anomalies, because we do not know the true mean and standard deviations of the modelled series Taking this approach, it would be impossible to reconstruct absolute time series from the transfer function predictions. We therefore expressed the predictand as the standardized distance from the mean daily temperature, as described below.

It was found by inspection of the control-run data that monthly averages of the mean temperature (tmax+tmin/2) are well-simulated, but that the standard deviations are too low. Thus, each daily value in the observed series was adjusted, such that the standard deviations of the observed and $1xCO_2$ series matched:

$$tmean_{adj} = \overline{tmean} + \left(\frac{tmean - \overline{tmean}}{\sigma_{obs}} \right) \sigma_{ccc} \qquad ...1$$

where $tmean$ is the mean temperature for that day, $\overline{tmean}$ is the average mean temperature for the month, σ_{obs} and σ_{ccc} are the standard deviations of the observed and control run mean temperatures for that month, respectively.

The dependent variable in the calibration and validation stages, when observed values are being used, is then, for each day, and for tmin:

$$tpred = \frac{t\,\mathrm{min} - tmean_{adj}}{\sigma_{tmeanadj}} \qquad ...2$$

where $\sigma_{tmeanadj}$ is the standard deviation, for each month, of $tmean_{adj}$. When the regression equations are used for predictive purposes, with predictor variables drawn from model output, the dependent variable is simply:

$$tpred = \frac{t\,\mathrm{min} - tmean}{\sigma_{mean}} \qquad ...3$$

This specification ensures that a time series of actual tmax/tmin can be reconstructed from the predicted variable.

b) The predictor variables

The predictor variables were selected by stepwise regression analysis from the following set for 0000 and 1200 UTC, extracted from the NMC CD-ROM:

i. SLP at Alcantarilla; north-south and east-west pressure gradient; backward and forward 24-hour pressure tendency (from 0000 UTC values).
ii. 1000-500 hPa thickness at Alcantarilla; N-S and E-W gradient, backwards and forwards 24-hour tendencies.

These variables were expressed as standardized anomalies from the monthly mean. Originally, predictors derived from the 500hPa geopotential height were also included. However, we found that the resulting regression equations performed poorly at the validation stage, possibly because of duplication of information between the thickness and height variables. When 500hPa-height variables were excluded, the regression equations stabilized.

Sine and cosine of Julian day were included. The final predictor variable is the standardized anomaly of the adjusted (as shown by Equation 1) mean temperature. The stepwise regression was therefore performed using a possible 19 predictors.

Table 2 Summary temperature statistics for observations (Obs.) and transfer function-generated series (TFG) for 1965-74

	Maximum (°C)			Minimum (°C)		
	Mean	S.D.	R^2	Mean	S.D.	R^2
Winter						
Obs.	16.7	3.4		4.5	3.6	
TFG	16.4	3.4	0.74	4.2	3.5	0.74
Spring						
Obs.	22.5	4.8		9.0	3.8	
TFG	22.4	4.1	0.83	9.2	3.9	0.76
Summer						
Obs.	31.7	3.6		18.0	2.7	
TFG	31.7	3.4	0.85	18.0	3.0	0.77
Autumn						
Obs.	24.4	5.3		12.5	4.7	
TFG	25.1	5.6	0.90	11.8	4.3	0.86

Table 3 Summary statistics for TFG tmax and tmin using $1xCO_2$ (Control) output and $2xCO_2$ (Pert.) output for initialization.

	Maximum (°C)		Minimum (°C)	
	Mean	S.D.	Mean	S.D.
Winter				
Control	16.2	2.9	4.1	4.7
Pert.	20.2	3.2	5.9	5.5
Spring				
Control	21.1	3.8	7.9	4.2
Pert.	26.3	4.9	11.1	4.6
Summer				
Control	32.3	3.4	18.4	3.5
Pert.	37.2	3.1	23.5	3.6
Autumn				
Control.	25.3	5.4	12.4	5.1
Pert.	28.9	5.3	17.2	5.4

5. VALIDATION

The regression equations were tested on an independent data set for 1965-74. The performance is shown in Table 2, where R^2 is calculated between the observed and transfer function-generated (TFG) series. It can be seen that the transfer functions perform well on the independent data set.

6. APPLICATION

Control-run data from the Canadian Climate Centre GCM were inserted in the regression equations. The results are shown in Table 3, and can be compared with Table 1 to demonstrate the improvement achieved. Two problems were noted with respect to the raw control-run data shown in Table 1:

i. low winter standard deviations. The standard deviations of control tmax and tmin (1.7°C and 1.3°C respectively) have increased to 2.9°C and 4.7°C, compared to 3.6°C and 3.8°C observed.
ii. mean tmax too cool, mean tmin too warm. The differences, 1975-84 observations minus TGF control-run temperatures, are (in °C):

	tmax	tmin
Winter	1.1	1.0
Spring	1.3	1.4
Autumn	-0.2	-0.4
Winter	-0.1	-0.1

Table 3 also shows the results from initialization of the regression equations with $2xCO_2$ data. The differences, $2xCO_2$ minus $1xCO_2$, for the raw model data and for the TFG data are shown in Table 4. For tmax, the TFG mean change is greater in three seasons (winter, spring and

autumn), and lower in summer, than the change indicated by the raw model data. The annual change is only slightly different, 4.4°C for TFG, 4.1°C for the raw model data. For tmin, the mean TFG change is smaller in winter and spring, and larger in summer and autumn, than the raw model change. The annual warming is 3.6°C for TFG, 3.7°C for the raw model data. There are some surprisingly large differences between the changes in variance indicated by the two data sets. For example, the raw data shows a very large change in the variance of autumn tmax, whereas a small decrease is suggested by the TFG data. The large spring increase in spring tmax variance in the TFG data is not repeated in the raw data.

Table 4 Changes (perturbed - control) for TFG-generated and raw tmax and tmin.

	Maximum (°C)		Minimum (°C)	
	Mean	S.D.	Mean	S.D
Winter				
Raw	3.7	-0.2	2.2	0.4
TFG	4.0	0.3	1.8	0.8
Spring				
Raw	4.7	0.4	3.6	0.7
TFG	5.2	1.1	3.2	0.2
Summer				
Raw	5.2	0.2	4.8	-0.3
TFG	4.9	-0.3	5.1	0.1
Autumn				
Raw	2.8	2.3	4.1	0.4
TFG	3.6	-0.1	4.8	0.3

7. EXTREME EVENTS

Four measures of temperature extremes have been calculated, as shown in Table 5. From tmax, the total number of days with temperatures equal to or above 35°C (NoHD) were found, and the number of degree days with a threshold temperature of 35°C (HDG). From tmin, we calculated the number of days with temperatures at or below freezing (NoFD) and the number of freezing degree days (FDG).

The TFG predictions for 1965-74 (TFG65) are slightly below the observed (Obs65), with the exception of NoFD. The raw model data (CCCcont) perform poorly in comparison to observations, with no days at or below freezing, and only nine days with tmax equal to or above 35°C. The TFG tmax time series initialized with $1xCO_2$ produces values for NoHD and HDG which are close to the observed. The tmin series perform less well, in particular overestimating NoFD. This suggests that there is still some threshold in this time series, at about 0°C, since FDG is close to the observed. Further investigation is required.

The perturbations in extremes due to $2xCO_2$ are greater in the TFG series than in the raw model data. The number of hot days increases in the TFG series by 70 days/year, compared to only 57 days/year in the model output. The number of HDG increases by 259 degree-days/year for TFG, compared to 186 degree-days/year for model output. The raw model data indicates no change in cold events. The TFG time series show a reduction of 10 days/year for NoFD, and 4 degree-days/year for FDG.

Table 5 Measures of temperature extremes, calculated from ten years of data.

	NoHD	HDG	NoFD	FDG
Obs65	167	292	145	115
TFG65	144	221	174	81
CCCcont	9	2	0	0
CCCpert	577	1859	0	0
Change	568	1857	0	0
TFGcont.	222	284	416	165
TFGpert	926	2869	320	126
Change	704	2585	-96	-39

ACKNOWLEDGEMENTS

This work was funded by the Commission of the European Communities (Contract No. EV5V-CT92-0164), the Midwestern Regional Center of the National Institute for Global Environmental Change, and the NATO Collaborative Research Grants Programme.

REFERENCES

Karl, T.R., W.-C. Wang, M.E. Schlesinger, R.W. Knight and D. Portman, 1990: A method of relating general circulation model simulated climate to the observed local climate. Part I: Seasonal statistics. *J. Climate*, **3**, 1053-1079.

McFarlane, N.A., G.J. Boer, J.-P. Blanchet and M. Lazare, 1992: The Canadian Climate Centre second generation general circulation model and its equilibrium climate. *J. Climate*, **5**, 1013-1044.

Downscaling Indian Monsoon Rainfall from the simulations of the ECHAMT21 coupled ocean-atmospheric model

S.V.Singh and H.V.Storch

1. Indian Institute of Tropical Meteorology, Pune
2. Max Planck Institute for Meteorology, Hamburg

ABSTRACT

We have examined the effect of increasing anthropogenic gases on the Indian monsoon rainfall in next 100 years by following an approach of statistical downscaling. The mean sea level pressure data of the Northern Hemisphere and rainfall data of 306 stations over India for a period of 1901-1984 are used to establish concurrent relationship between Indian rainfall and surface pressure field. Canonical correlation patterns between Eurasian pressure field and rainfall field over India are determined and used to project Indian monsoon rainfall for next 100 years by using the simulations of ECHAMT21-LSG coupled model made at MPI. A 6 to 8% of rise in rainfall by the time of doubling of CO2 is anticipated.

1. INTRODUCTION

Increasing green house gases will cause significant changes in the climate of the world in coming decades. Rising temperature in the present century are attributed to this anthropogenic effect by most scientists. According to some recent long simulations of climate, the observed change in temperature of above 0.5°/100 year during present century is unlikely to arise due to natural climate variability (Stouffer et al., 1993). Where there is agreement amongst the General circulation models and amongst observations about the anticipated climate change on global scale little can be inferred from the direct runs of the current low resolution models about the regional climates. Therefore, some other strategy is to be adopted to downscale the global scale simulations to the regional scale. This strategy forms focus of the Biospheric Aspects of the Hydrological cycle a core project of IGBP.

Normally two approaches have been persued; one by nesting a fine mesh model within the coarse model and the other by developing empirical relationship between large (near global) scale climatic features and the regional climate of interest. This latter approach is particularly suitable for the regional climates, like south Asian monsoon, which are not yet well simulated. We have followed this approach to project the changes in monsoon rainfall over India by using the ECHAMT21 coupled model runs made at Max Planck Institute Fur Meteorology, Hamburg. For projecting monsoon rainfall we closely follow the method of Storch et al. (1993) which employs the Technique of Canonical correlation for developing relationship between the global and regional climate. The approach followed and the results are briefly summarised in this paper.

2. DATA AND METHOD

For statistical downscaling, we require observed data of global scale meteorological fields and of the regional climate for establishing relationships. The simulated meteorological fields for future time are then used to project the regional climate in future. For establishing relationship between large scale circulation and regional scale climate, we need good quality observations of sufficient length, good enough to develope the relationship on one subset and validate it on another independent subset. From this consideration, the surface pressure is the obvious choice as uniform quality of observations of this parameter are available for long periods. It may be noted that this parameter may not be as well simulated

as an upper air circulation field by a GCM. Monthly mean sea level pressure data at 5° x 5° grid for the Northern Hemisphere were obtained for a period 1901-1984 from the National Meteorological Centre, USA. From this data a domain bounded between 20-60°N, 20-120°E is selected after examining the concurrent relationship between all India rainfall and the surface pressure fields (see below). This domain is large enough to contain several model grid points and at the same time small enough to exclude the areas of insignificant information. The processed monthly rainfall data of 306 stations uniformly spread over contiguous India are taken from Dr.B.Parthasarthy. Spatial averages for 45 2.5°Lat./Long. boxes are prepared from these data for contiguous India excluding the hilly regions of north and northeast India. For projection of climate we use central and Transient runs of low resolution (T21, grid distance ~ 5.6°Lat./Long.) ECHAM1-LSG coupled model. The transient model run begins from the preindustrial year 1935 and extends for 150 years. The first 50 years of the run are avoided due to the cold start problem of coupled models.

For downscaling, we have closely followed the approach of Storch et al. (1993). It consists of 3 essential steps, viz.,

(i) Validation of model simulations against obsevations in terms of mean fields, zonal structure, seasonal cycles, multivariate structure etc.

(ii) Development of relationship between large scale field and regional climate. For downscaling to be effective, there must exist relationship between the large scale circulation field and the local climate. The particular large scale field should be simulated with desired fidelity, and

(iii) Apply the relationship developed in (ii) above to the simulated data for future projection of climate. The multivariate tools of empirical orthogonal function analysis and the canonical correlation analysis are used in the above steps.

3. RESULTS

3.1 Validation

The ECHAM1 model shows satisfactory performance in terms of global climate, the mean fields and the annual cycle like other models of similar complexity (Gates et al., 1993). Lal et al. (1994) have examined the seasonal distribution of regional surface pressure, temperature, rainfall, upper level humidity, winds and monsoon onset and have found reasonable agreement with observations. Though the mean pressure and rain intensity are close to the observed values their spatial distributions are different. The lowest surface pressure is obtained over the Tibetan massif (around 34°N, 90°E) instead of over Arabia and high rainfall region is located along 17°N over the peninsula instead of over central India. Yet the spatio-temporal structure of the pressure and rainfall fields as represented by the empirical orthogonal functions show good resemblence, at least with regard to the first two most important EOF's. Similar observations can be made for the two canonical correlations between pressure and rainfall fields. We have found good agreement between multivariate structure of the simulated and the observed fields.

3.2 Relationship between observed pressure field and rainfall

For identifying the domain of pressure field concurrently related with Indian monsoon rainfall, we have correlated the all India rainfall with the northern hemispheric pressure field. Significant correlations almost over whole of the Eurasian continent west of India with highest values near Bombay (< -0.7) and north of Aral sea (< -0.6) are obtained. This pattern of correlation is stable over various subperiods. After examining this correlation field, we have selected an area bounded between 20°N-60°N and 20°-120°E for downscaling. The second step is to determine canonical correlation between this pressure field and the rainfall field represented by 45 grid boxes. For computations of canonical correlations we have first computed EOF's of both (pressure and rainfall)fields to filter some noise. The first canonical correlation pattern corresponding to the pressure field shows a pattern similar to the teleconnection between Indian monsoon rainfall and pressure field.

Similarly the corresponding rainfall patterns, show the features like those of the first EOF of rainfall. We have then computed the canonical correlation patterns

by using the data set for 1951-1984 and reconstructed the all India monsoon rainfall (average of 45 blocks) for the whole period 1901-84. The procedure reproduces the major rising and falling trends in rainfall satisfactorily with correlation coefficient between observed and reconstructed time series of 0.36. The canonical correlation analysis is again repeated by using the data for 1901-40 and the entire rainfall time series is again reconstructed with similar satisfaction. These results suggest that the large scale pressure fields over Eurasian region can be used to project the long term climate scale behaviour of Indian monsoon, satisfactorily.

3.3 Projection of Indian Rainfall in future

For projection of rainfall in future, we use the first canonical correlation pattern determined by using all 80 years of data. The pressure anomalies required for computation of covariance matrices are determined by subtracting the long term average of the control run from the transient run. The reconstructed rain amounts averaged for 45 blocks, show a rising trend in Indian rainfall which becomes more conspicuous when running average filters are applied. The rise in rainfall is of about 5 cm by the year 2030, around the time of doubling of CO2 after which it seems to have stabilised.

4. CONCLUSIONS

The following are the main conclusions of the present study.

(i) The Indian rainfall shows significant concurrent correlation with pressure field over much of Eurasia, particularly, over the area extending from Aral sea to the west coast of India.

(ii) The pressure distribution over the Asian region and the Indian monsoon rainfall show satisfactory relationship, particularly in terms of long period behaviour of Indian monsoon rainfall.

(iii) The ECHAM1-LSG coupled model simulates the leading multivariate functions of pressure and rainfall over India satisfactorily.

(iv) The increasing greenhouse gases will result in increase of 6 to 8% of monsoon rainfall by the time of doubling of CO2.

ACKNOWLEDGEMENTS

The work was done while the first author was visiting the MPI under EC fellowship.

REFERENCES

Gates, W.L., U.Cubash, G.A., Meehl, J.F.B. Mitchell, and R.J.Stouffer, 1993, An intercomparison of selected features of the control climates simulated by coupled Ocean-atmosphere General Circulation Models. WCRP-82, WMO/TD-No.574, pp.46.

Lal, M., U.Cubash and B.D.Santer, 1994, Effect of global warming on Indian monsoon simulated with a coupled ocean-atmosphere general circulation model, Current science, 66, 430-438.

Storch, H.V., E.Zorita and V.Cubash, 1993 : Downscaling of climate change estimates to regional scales : an application to Iberian rainfall in winter time. J.Climate 6, 1161-1171.

Stouffer, R.J., S Manabe and K.Ya Vinnikov, 1994, Model assessment of the role of natural variability in recent global warming, Nature, 367, 634.

CORRESPONDING AUTHOR

Dr. S.V.Singh
Forecasting Research Division
Indian Institute of Tropical Meteorology
NCL Post Office
Pune -411008
(INDIA)

A Change in the Annual Cycle on the Southern Hemisphere and its Possible Implication for the Antarctic Ozone in Spring

H. van Loon, K. Tourpali[1] and J. W. Hurrell

National Center for Atmospheric Research, Boulder, Colorado
[1]Aristotle University of Thessaloniki, Greece

ABSTRACT
The circulation in the troposphere of the Southern Hemisphere changed from the 1970s to the 1980s: the previously large semi-annual wave weakened or disappeared at middle latitudes, pressure fell at higher and rose at lower latitudes, the meridional and zonal components of the wind in the cyclonic vortex increased, and the westerly vortex remained strong into late spring. The changes happened as the ozone began to decline in spring in the antarctic, but the trend in the troposphere is present already in early winter. The change in the troposphere therefore was not caused by the decline in ozone during September-October, but it may be a necessary condition for the decline.

1 INTRODUCTION

Two papers (van Loon et al. 1993, Hurrell and van Loon 1994, hereafter HuvL) described a marked change in the annual cycle on the Southern Hemisphere which took place toward the end of the 1970s, from the ground to the middle stratosphere. The tropospheric change consisted of a modulation of the dominant second harmonic in the annual cycle in the sense that the second peak in the westerly vortex was delayed one month into late southern spring. The change occurred at the time when the stratospheric ozone began to decrease over Antarctica in spring. Here we add details which suggest a connection between the change in the troposphere and the decline of ozone in the antarctic, the former possibly being a necessary but not sufficient condition for the latter.

2 ANALYSIS AND DATA

The basis of our analyses are the monthly means of the operational daily maps of sea level pressure and 500-hPa height from the Australian Bureau of Meteorology, which are a much used source that has been described in several papers, many of them listed in van Loon et. al 1993 and HuvL. The maps of 0000 UTC are the most carefully analyzed ones; they begin with May of 1972. When reduced to monthly and seasonal means the data at these two levels have few flaws, in contrast to the other standard pressure levels (van Loon 1980).

The total ozone values were measured at the South Pole (Amundsen-Scott station) and at Syowa (69°S, 40°E) by Dobson ozone spectrophotometers. The data from the Total Ozone Mapping Spectrometer (TOMS) on the Nimbus 7 satellite are not available before 28 November 1978, that is, before the time when the change in the troposphere took place.

3 THE CHANGE FROM THE 1970s TO THE 1980s

The change from the 1970s to the 1980s consisted mainly of the suppression and local disappearance of the semi-annual oscillation (SAO) which earlier dominated the mean annual cycle south of the subtropical ridge (van Loon et al. 1993, HuvL). References to the literature about the SAO can be found in van Loon (1967, 1972). Especially important among these are references to Schwerdtfeger, who was able to document the existence of the SAO back to the middle of the 19th century by means of observations from sailing ships, and to Meinardus who observed it in the data from the German South Polar Expedition, 1901–1903. Hurrell and van Loon (1994) showed its continuous existence at Chatham Island (43°S, east of New Zealand) since observations began in 1930. The SAO is thus a well documented component of the annual cycle in middle and high south latitudes.

Analysis of gridpoint data from the decade which followed the Global Weather Experiment in 1979 showed the SAO as weak, or even gone, in middle latitudes over the South Pacific and the eastern half of the Indian Ocean (van Loon et al. 1993, HuvL). The SAO failed in the 1980s because its second pressure maximum at middle latitudes, in September-October, became a minimum, and its second minimum, in November-December, became a maximum, extending the peak strength of the westerly vortex into late southern spring. The change between the 1970s and 1980s was thus most pronounced during the second half of the year (HuvL).

The maps in Fig. 1 show the difference in the 500-hPa height, (1980–1990) minus (1972–1979), for June-July, July-August, August-September, and September-October. The same decadal difference in geopotential height and in sea level pressure is shown in HuvL for September-October and November-December. Because of the almost barotropic structure of the tropospheric mean maps of the Southern Hemisphere (van Loon and Jenne 1972; van Loon et al. 1973), the shape of the pattern is the same from sea level to the tropopause — as seen in the sea level pressure and 500-hPa changes in HuvL (Figs. 8 and 9).

In Fig. 1 the largest falls in the 500-hPa heights from the 1970s to the 1980s are in the Atlantic and Pacific

Oceans, and they remain there through the rest of the year (HuvL, Fig. 9). The pattern has a large three-wave component, and zonal harmonic wave 3's amplitude and share of the mean spatial variance therefore increased from the 1970s to the 1980s: at 55°S the wave's mean amplitude in September-October almost doubled from 22m in the 1970s to 42m in the 1980s, and its share of the mean spatial variance grew from 6% to 19%.

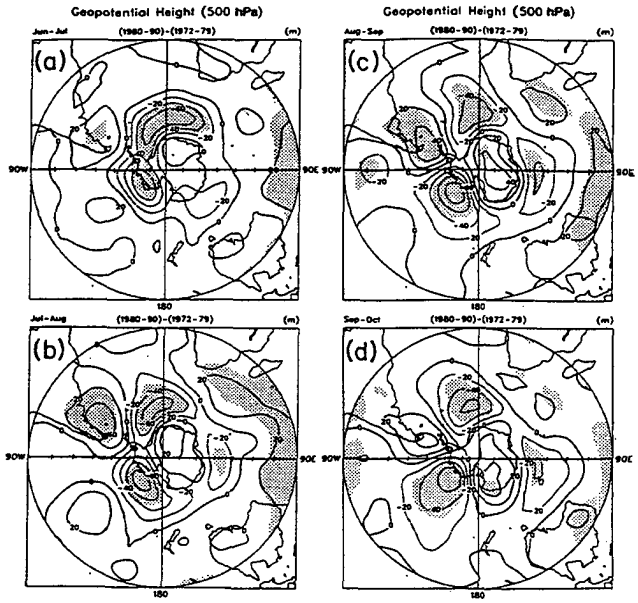


Figure 1. Difference in 500-hPa height (m); (1980–1990) minus (1972–1979); (a) June–July, (b) July–August, (c) August–September, (d) September-October. The shading indicates values significantly different from zero at the 5% level, using a Student t-test.

The meridional component of the mean circulation underwent its largest changes over the western hemisphere as shown, for example, for September-October at 55°S in Fig. 2. The 500-hPa height contrast between 70°W and 10°W (Fig. 2a) increased from an average of 20m in the 1970s to 135m in the 1980s; that is, the southerly flow between South America and the central Atlantic Ocean increased appreciably. And the contrast between 130°W and 70°W (Fig. 2b) fell from an average of 30m in the first decade to -55m in the second, so that the mean wind in the eastern Pacific changed from southerly to northerly. In both instances the meridional wind changed quite suddenly from one state to the other, 1979 being the last year of the first state.

Since the 500-hPa heights generally rose north of about 50°S and fell to the south (Fig.1), the *zonal* component of the wind strengthened between 40°S and 70°S (Fig. 3).

In summary: Both the meridional and the zonal component of the circulation in the troposphere increased in winter and spring from the 1970s to the 1980s. The increase in the zonal wind can be followed into the lower stratosphere, whereas the enhanced meridionality associated with the amplification of wave 3 is less obvious in the stratosphere (HuvL, Fig. 12). The changes in the circulation appear to be linked to an upward trend in the tropical sea surface temperature (HuvL; Komhyr et al. 1991; Kodera and Yamazaki 1989). The stronger zonal circulation in the troposphere, conspicuous already in early winter and lasting into late spring, strengthened the westerly vortex in the lower stratosphere in spring and suppressed meridional exchange, thus providing a necessary condition for the decline of ozone in spring (see e.g., Newman and Randel 1988; Kawahira and Hirooka 1992). The enhancement of wave 3 in the troposphere did not extend into the stratosphere, since waves smaller than wave 2 typically decay above the tropopause (see wave 3 in Fig. 4 of van Loon et al., 1973).

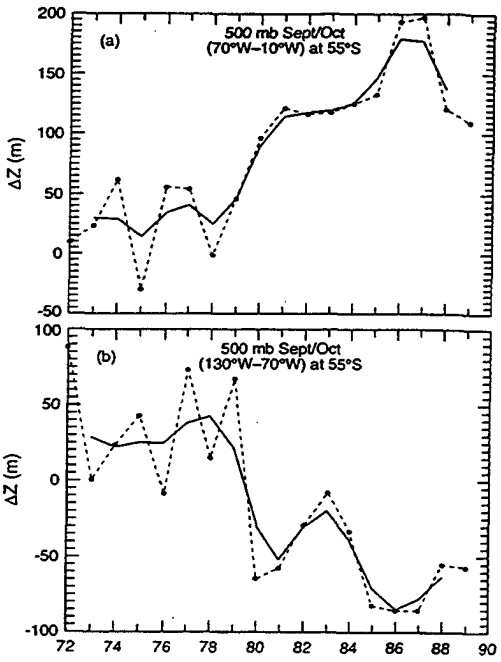


Figure 2. Time series at 55° of the difference (m) 70°W minus 10°W and 130°W minus 70°W. For September-October. The solid lines are three-year running means.

The most obvious changes in the atmosphere occurred in the subantarctic where the 500-hPa height and the sea level pressure fell substantially from the 1970s to the 1980s, especially in the South Pacific and Atlantic Oceans (Fig. 1, see also HuvL). We have chosen two areas near the strongest falls (70°S–75°S, 120°W–150°W; and 50°S–6°S, 0°–30°W), and correlated the two-month values of the average 500-hPa height in each area with the total ozone in the same months at Syowa and the South Pole. Since daylight is necessary for measuring the total ozone, only the months from September onwards are available at Syowa, and from October onwards at the South Pole. The correlation coefficients are shown in Table 1. The total ozone at both stations is well correlated with the 500-hPa heights in the Pacific area; in the Atlantic area the correlations are somewhat lower than in the Pacific.

The increased tropospheric circulation in the 1980s is thus related, *statistically*, to the loss of ozone. The ozone decline, however, takes place in spring, whereas

the tropospheric circulation change is found already in early winter (Figs. 1a,b and Fig. 3a).

The correlations in Table 1 suggest that from 25% to 50% of the interannual variance in the ozone is linked to the variance in the troposphere, but the comparatively large correlation coefficients are due mainly to changes at low frequencies in both quantities. This is obvious when one compares the three time series in Fig. 4. Sometimes the short term variations in 500-hPa height and ozone are in-phase and sometimes out-of-phase, so they add little or nothing to the correlation coefficients, whereas the trends are similar in both quanties.

Table 1. Mean 500 mb Height Correlation with Total Ozone

A. Pacific (70°S–75°S, 120°W–150°W)

	SYOWA		South Pole	
	n	r	n	r
Sep/Oct	17	0.57	–	–
Oct/Nov	17	0.69	16	0.53
Nov/Dec	17	0.69	15	0.60

B. Atlantic (50°S–65°S, 0–30°W)

	SYOWA		South Pole	
	n	r	n	r
Sep/Oct	17	0.57	–	–
Oct/Nov	17	0.43	16	0.59
Nov/Dec	17	0.49	15	0.35

One cannot expect the changes in ozone and 500-hPa heights to be in the same sense on all time scales — which would lead to a correlation coefficient near 1.0 — because of forcing which is characteristic of a single year. Such annually varying forcing is noise with respect to the trend; examples are the Quasi-Biennial Oscillation, the Southern Oscillation, or purely random variation.

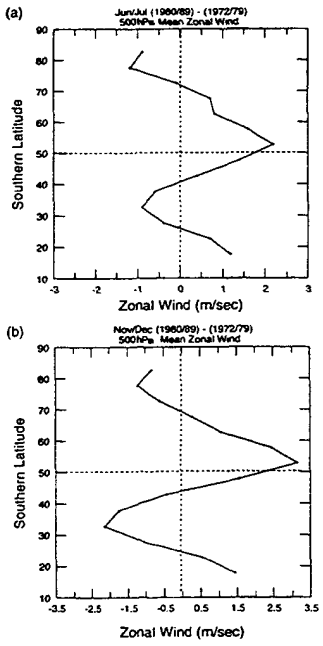


Figure 3. The difference in the zonally averaged, zonal geostrophic wind at 500hPa (m sec^{-1}) between 1980-1989 and 1972-1979. (a) June-July, (b) November-December.

CONCLUSION

The semi-annual oscillation that previously dominated the annual cycle in sea level pressure and tropospheric wind at the middle and high south latitudes was disturbed in the late 1970s. We have shown that, as part of the disturbance, the sea level pressure and tropospheric heights in the subantarctic were lower during winter and spring in the 1980s than in the preceding decade, the zonal circulation strengthened, and the planetary waves amplified in the troposphere.

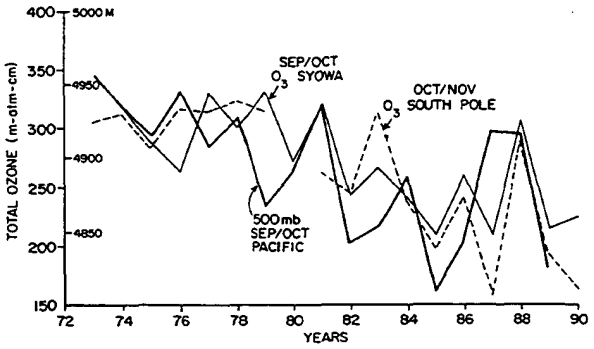


Figure 4. Time series of the mean 500-hPa height (m) for September-October in the area 70°S-75°S, 120°W-150°W (heavy solid line); of total ozone in September-October at Syowa, 69°S 40°E (thin solid line), in Dobson units; milli-atmo-cm; and the total ozone at the South Pole in October-November (dashed line).

Since the ozone decline in the antarctic spring began in the same years as the change in the annual cycle in the troposphere, it is possible that the two are related. Linear correlations between antarctic total ozone in spring and 500-hPa heights do show that as much as 25% to 50% of the interannual variance in the two are connected. The fairly large size of the correlations stem mostly from the fact that the ozone and the 500-hPa heights have similar trends. The tropospheric trend is, however, present in early and mid winter, whereas the loss of ozone, which creates the trend in the ozone, does not begin till spring. The decline in the ozone (the so-called ozone hole) therefore cannot have caused the trend in the troposphere. *The latter may, rather, be a necessary precursor of the former.*

Kodera and Yamazaki (1989) found that the variability in the structure of the planetary waves on the Southern Hemisphere could be related to variations in the tropical Pacific sea surface temperature; and HuvL showed that the changes in the SAO, which are associated with the trend in the troposphere, are linked to changes in the tropical sea surface temperature. Komhyr et al. (1991) have, in addition, demonstrated that the equatorial sea surface temperature in the Pacific Ocean in the southern winter is negatively correlated with antarctic ozone in spring. If these associations are not accidental, the antarctic ozone in spring is susceptible to changes in the troposphere and the tropical oceans.

References

Hurrell, J.W and van Loon, H., 1994, "A change in the atmospheric annual cycle of the Southern Hemisphere", Tellus, Volume 46A, pp. 325-338.

Kawahira, K. and T. Hirooka, 1992, "Variations of mean zonal winds relating to the ozone hole", Journal of Geophysical Research, Volume 97, pp. 10,157-10,163.

Kodera, K. and K. Yamazaki, 1989, "A possible influence of sea surface temperature variation on the recent development of ozone hole", Journal of the Meteorological Society of Japan, Volume 67, pp. 465-472.

Komhyr, W.D., S.J. Oltmans, R.D. Grass, R.K. Leonard, 1991, "Possible influence of long-term sea surface temperature anomalies in the tropical Pacific on global ozone", Canadian Journal of Physics, Volume 69, pp. 1093-1102.

Newman, P.A. and W.J. Randel, 1988, "Coherent ozone-dynamical changes during the southern hemisphere, 1979-1986", Journal of Geophysical Research, Volume 93, pp. 12,585-12,606.

van Loon, H., 1967, "The half-yearly oscillations in middle and high southern latitudes and the coreless winter", Journal of the Atmospheric Sciences, Volume 24, pp. 472-486.

van Loon, H., 1972, "Meteorology of the Southern Hemisphere", American Meteorological Society, (Boston, Mass.) Met .Monogr. Volume 13/35. pp. 25-100.

van Loon, H., 1980, "Transfer of sensible heat by transient eddies in the atmosphere on the Southern Hemisphere: An appraisal of the data before and during FGGE", Monthly Weather Review, Volume 11, 1774-1781.

van Loon, H. and R.L. Jenne, 1972, "The zonal harmonic standing waves in the Southern Hemisphere", Journal of Geophysical Research, Volume 77, pp. 992-1003.

van Loon, H., R.L. Jenne, K. Labitzke, 1973: "Zonal harmonic standing waves", Journal of Geophysical Research, Volume 78, pp. 4463-4471.

van Loon, H., J.W. Kidson, and A.B. Mullan, 1993, "Changes of the annual cycle in the Australian data set", Journal of Climate, Volume 6, pp. 1227-1231.

THE VARIABILITY OF CIRCULATION PATTERNS AT 500 HPA LEVEL OVER EUROPE

Joanna Wibig

Dept. of Meteorology and Climatology, University of Łódź, Poland

ABSTRACT

The field of mean monthly values of 500 hPa geopotential height over Europe has been analyzed. For each calendar month the significant principal components were found and subjected to a varimax rotation. The fields of correlation coefficients between rotated eigenvectors and original time series were interpret as patterns of geopotential field anomalies characteristic for appropriate calendar month. Then the variability in time of components were examined. The sisnificant tendencies were found only in months just before winter (in October and November) and near the end of winter (in February and March).

1 INTRODUCTION

Problem of contemporary climatic changes is one of the most interesting nowadays. A lot of authors try to find symptoms of global warming in records of mean global temperature, mean temperature of the Northern or Southern Hemispheres or temperature records from particular regions or stations (Jones at al , 1986a, 1986b; Schonwiese, 1983; Hansen and Lebedeff, 1987; Brazdil, 1988). But temperature is only one of the climatic elements and its distribution all over the world should be connected with global circulation. So it there are real changes of climate they should be also evident in changes of circulation patterns or their frequency. Bardossy and Caspary (1990) analyzed the variability of frequencies of European Atmospheric circulation types defined by Hess and Brezowsky, Kalnicky (1987) examined the frequencies of Dzerdzeevskij circulation groups for the Northern Hemisphere. There were also a lot of paper analysing the variability of circulation indices in different regions of Europe. Makrogiannis at al (1982) analyzed the zonal circulation index variability, Kożuchowski at al (1994) examined zonal and vorticity indices over Poland and the Southern Baltic Sea. This paper in an attempt of examinig the climate variability on the area of Europe analysing the variations of circulation patterns. The circulation is described by a few only variables – rotated principal components of 500 hPa level heights field.

2 DATA AND METHODS

The fields of mean monthly values of 500 hPa geopotential height defined in 80 points of geographical grid over Europe and the Northern Atlantic have been considered. The data cover the period 1951–1990. On that ground for each month of the year 80 time series were built, each of them describes the variability of 500 hPa height at a particular gridpoint. Then observations were normalized by subtracting the long term mean value for appropriate calendar month and dividing by the appropriate monthly standard deviation. The set of normalized 500 hPa height time series was then transformed into a new set of principal components. As the results three types of variables were obtained: the principal components, eigenvalues and the loadings. The principal components are the new normalized time series, the eigenvalues give the amounts of normalized variance explained by appropriate principal component, the loadings give the correlation coefficients between the principal component and the original time series of 500 hPa height (Horel, 1981).

The principal components allow to replace the huge original data set by a relatively few temporally uncorrelated components. Unfortunately there are also some disadvantages of this method. The first one is that the principal components depend on the domain used for calculations. The second that the principal component solution maximizes the sum of squared correlation coefficients. It means that many loadings have similar values and it is difficult to interpret the correlation coefficients between time series at different grid points. If two eigenvectors have high correlations with some time series it is possible that one of them indicate the positive correlation between these series while the second indicates the negative one.

To avoid these disadvantages the varimax rotation of principal component was applied. The varimax method maximizes the variance of the squared correlation coefficients between each of the rotated principal component and each of the original time series. In result each of the rotated principal components has high correlations with a few of original time series and a lot of correlations close to zero. Hence the rotation increase the discrimination among the loadings and make them easier to interpret, also the dependence of solution on the domain is much smaller (Ladd and Driscoll, 1980).

3. RESULTS AND CONCLUSIONS

For each month of the year a few significant principal components were chosen and rotated. The Kaiser's criterion was used (Kaiser, 1960), which involves retaining the components with eigenvalues greater than unity. A number of significant components varies from four in January and February to seven in April, June and July (Table 1). This number is generaly smaller in winter and greater in spring and summer. The significant components describe between 82.4 and 90.0 per cent of total variance of geopotential field. The appropriate values of explained variance for each calendar month are collected in Table 1. The values of variance described by particular rotated components for four selected months are presented in Table 2. The most important eigenvectors explain more than 25 per cent of total variance.

Table 1. A number of significant principal components and a percentage of explained variance in particular months of the year.

month	number of components	percentage of described variance
January	4	82.9
February	4	83.3
March	5	87.5
April	7	88.6
May	6	84.6
June	7	86.8
July	7	85.3
August	5	82.4
September	6	87.0
October	5	82.5
November	5	85.0
December	5	90.0

Table 2. The percentage of variance explained by rotated principal components for four selected months (the one for each season).

number of the mode	January	April	July	October
1	29.0	15.4	17.2	20.2
2	19.1	15.3	14.8	19.8
3	19.0	14.1	13.7	14.1
4	16.1	13.3	13.0	13.3
5		11.1	11.0	13.1
6		10.4	8.9	
7		9.1	8.5	

Then the fields of correlation coefficients were calculated. They can be interpreted as anomalies of geopotential field characteristic for appropriate month. The most important one, obtained in each calendar month as a first or second eigenvector presents the see – saw between Icelandic Low and Azorian High. Four such patterns, one for each season, are presented on Fig. 1, whereas Fig. 2 shows the other most frequent patterns. The geopotential height anomalies over the Northern Scandinavia appear in all months of the year. Fig. 2a shows the case from December. Anomalies over Mediterranean are stronger during warmer months a pattern from September is presented on Fig. 2b. Anomalies over Atlantic near 40N wander from east to west, pattern from February is shown on Fig. 2c. Characteristic is also the pattern with positive anomalies over East Europe and Atlantic and negative over West Europe. Usually the anomalies over East Europe are the strongest. The case from May can be seen on Fig. 2d. There are also some patterns characteristic only for one or a few months of the year.

Each component correlates markedly with geopotential field in limited area. Figure 3 presents the regions where one of the components explain at least 50 per cent of total variance of each of the original time series. It means that the absolute value of correlation coefficients are greater than 0.7. These regions for different components (modes) do not overlapp because the components are temporally independent. It may be assumed that the variability of component determine the variability of geopotential heights in appropriate regions.

All components show great year to year variability but the most interesting are variation of the trend nature. The regression analysis was used to all series of principal components. No significant tendencies were found in series from December, January, May and June. There are trends significant at 90 per cent level for April, July, August and September but only for last modes which explain the smallest part of variance (Table 3). Only in four months there are significant tendencies in modes which explain considerable part of variance. Two of them are from late fall – October and November , the other two from February and March. So the significant tendencies occur before the beginning and close to the end of winter season.

The strongest tendency occurs in March and concerns the first component which explain 26 per cent of geopotential field variance for this month. This component corresponds to Icelandic – Azorian see – saw. It is a decreasing tendency with slope –0.045 per year (it is a change of about one standard deviation in 22 years) and it explains 28 per cent of this mode variability. Figure 4 shows the time series of all modes in March. The other components also show some tendencies but they are not significant.

Fig. 5 shows the remaining components with significant tendencies. There are mode second from February, third from October and first from November. The spatial pattern corresponing to mode 2 from February is presented on Fig. 2c, this from October is very close to it. The pattern from November is connected with anomalies over the Northern Scandinavia (close to the one presented on Fig. 2a).

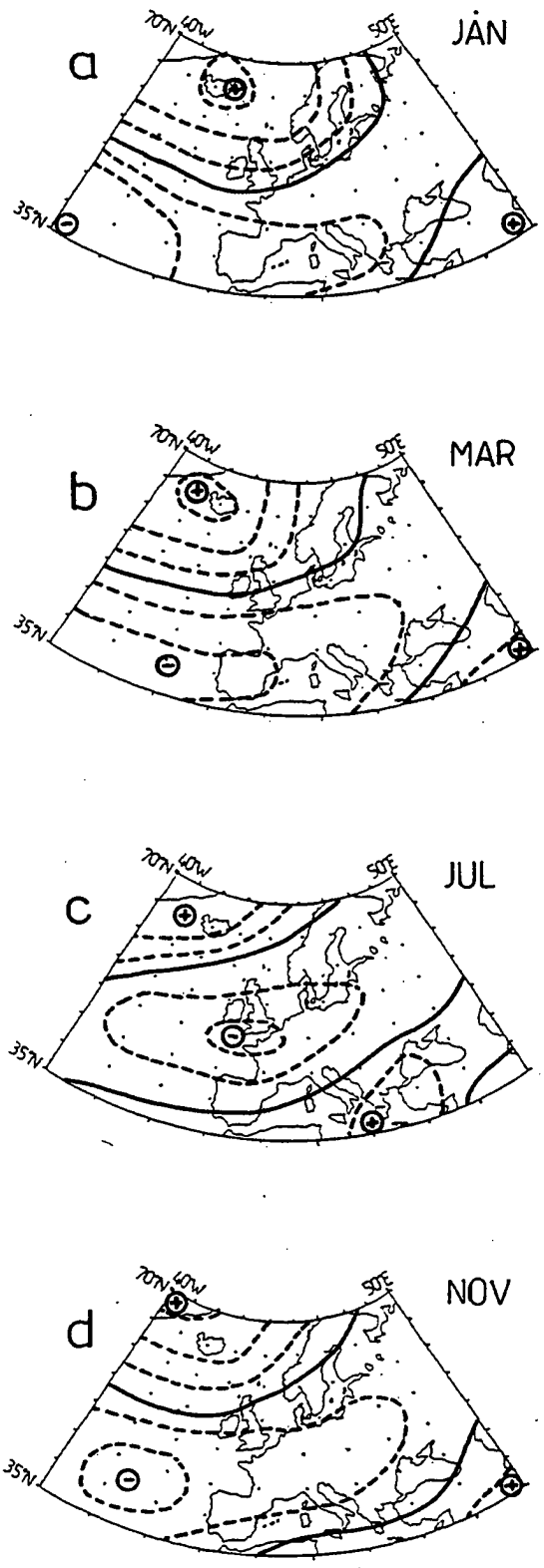
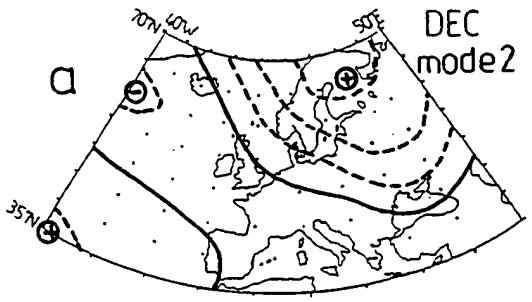
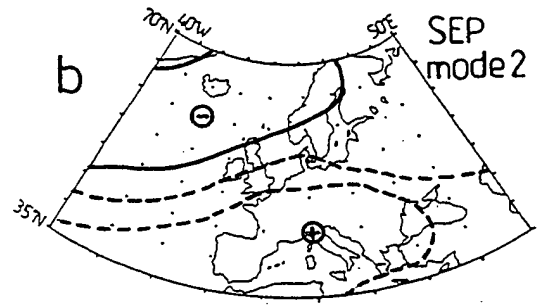
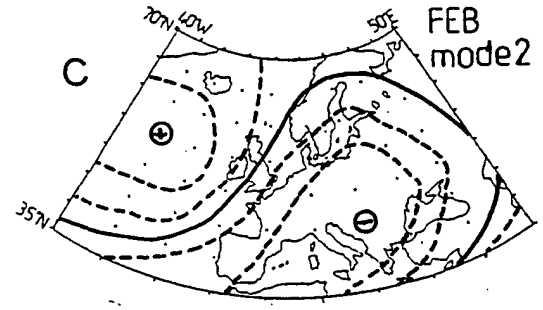


Fig. 1. The correlations between components and original time series presenting the see – saw patterns. Solid line indicates transition from positive to negative correlations. Dashed lines are isocorrelates with interval 0.3. The highest positive and negative correlations are marked by + and – respectively.







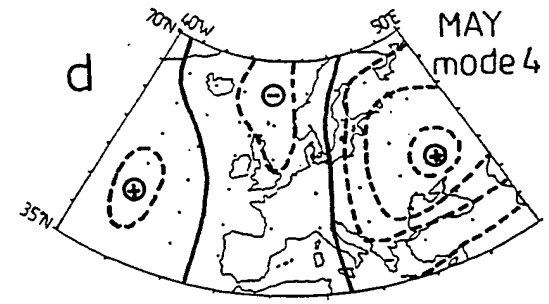
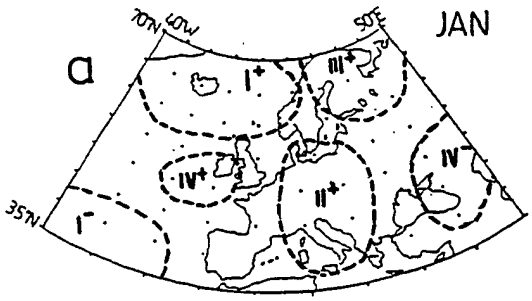
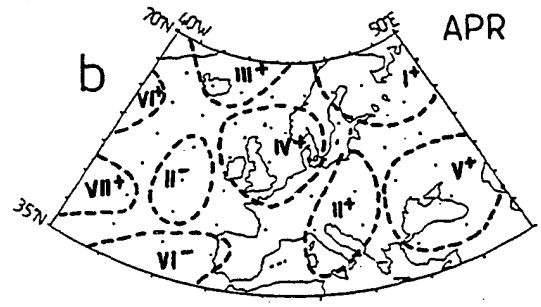
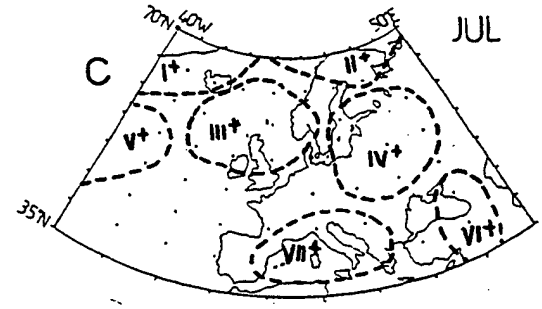


Fig. 2. The correlations between components and original time series presenting four from most characteristic patterns. Solid lines indicate transition from positive to negative correlations. Dashed lines are isocorrelates with interval 0.3. The highest positive and negative correlations are marked by + and – respectively.







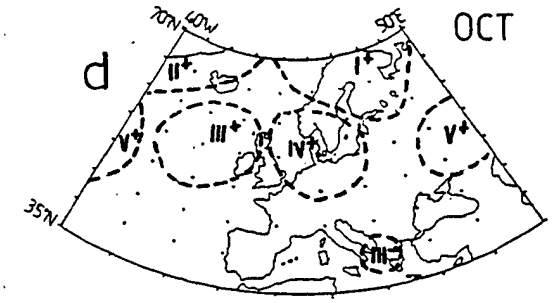


Fig. 3. Regions where the percentage of the local normalized variance explained by rotated principal components exceed 50 . The numer of the mode and the sign of correlation are marked.

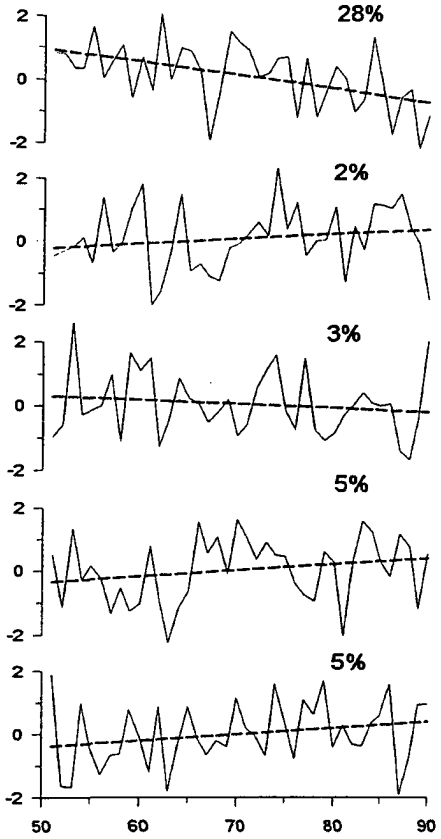


Fig. 4. The principal components for March (solid lines) and their trends (dashed lines). Percentages of variance described by trend are shown over and to the right of each series

Table 3. Features of time series of components with tendencies significant at 90 per cent level.

month and mode number	percentage of variance explained by the mode	percentage of the mode variance explained by regression
Feb. – 2	23	10
Mar. – 1	26	28
Apr. – 7	9	11
Jul. – 7	8	25
Aug. – 5	6	7
Scp. – 6	10	8
Oct. – 3	14	11
Nov. – 1	23	10

Decreasing tendency for the March component means that the strenght of the see – saw has generally weaken during last 40 year period in this month. The tendencies from February and October may be connected with weakening of Mediterranean Lows or on the contrary with intensifing of high pressure systems over South and Central Europe during these months. The decreasing tendency in the first mode from November may be connected with higher frequency of low pressure systems over the Northern Scandinavia.

It is worth to underline that the highest variability of circulation patterns concerns months close to winter season. It suggest that the lenght of winter season may constitute a clue point.

References

Bardossy, A., Caspary, H.J., 1990, "Detection of Climate Change in Europe by Analyzing European Circulation Patterns from 1881 to 1989", Theor.Appl. Climatol., Vol. 42, pp. 155–167.

Brazdil, R., 1988, " Air temperature variations in the CSSR with respect to air temperature changes on the Northern Hemisphere", Geogr. Cas., Vol. 40, pp.26–39.

Hansen, J., Lebedeff, S., 1987, "Global trends of measured surface temperature", J.Geophys. Res., Vol.92, pp.13.345–13.372.

Horel, J.D., 1981, "A rotated principal component analysis of the interannual variability of the Northern Hemisphere 500 mb height field", Mon.Wea.Rev., Vol.109, pp.2080–2092.

Jones, P.D., Raper, S.C.B., Bradley, R.S., Diaz, H.F., Kelly, P.M., Wigley, T.M.L., 1986a, "Northern Hemisphere surface air temperature variations: 1851–1984". J. Clim. Appl. Met., Vol.25,pp.161–179.

Jones, P.D., Raper, S.C.B., Bradley, R.S., Diaz, H.F., Kelly, P.M., Wigley, T.M.L., 1986b, "Southern Hemisphere surface air temperature variations: 1851–1984". J. Clim. Appl. Met., Vol.25, pp.1213–1230.

Kaiser, H.F., 1960, "The application of electronic computers to factor analysis", Education and Psychological Measurements, Vol. 20, pp. 141–151.

Kalnicky, R.A., 1987, "Seasons, Singularities, and Climate changes over the Midlatitudes of the Northern Hemisphere during 1899–1969, Jour. of Clim. and Appl. Met., Vol. 26, pp. 1496–1510.

Kożuchowski, K., Stolarczuk, A., Wibig, J., 1994, "Indices of the atmospheric circulation at the 500 hPa level over Poland and the Southern Baltic in the period of 1951–1990" in Climate in Poland and in the region of Baltic Sea versus global changes, pp. 105–122, Szczecin (in Polish).

Ladd, J.W., Driscoll, D.W., 1980, "A comparison of objective and subjective means of weather typing: An example from western Texas", J. Appl. Meteor., Vol.19, pp.691–704.

Makrogiannis, T.L., Bloutsos, A.A., Giles, B.D., 1982, "Zonal index and circulation change in the North Atlantic area, 1873–1972", Jour. of Clim., Vol. 2, pp. 159–169.

Schonwiese, Ch.–D.,1983, "Northern Hemisphere Temperature Statistics and Forcing. Part A: 1881–1980AD", Arch. Met. Geoph. Biocl., Ser.B, Vol 32 pp.337–360.

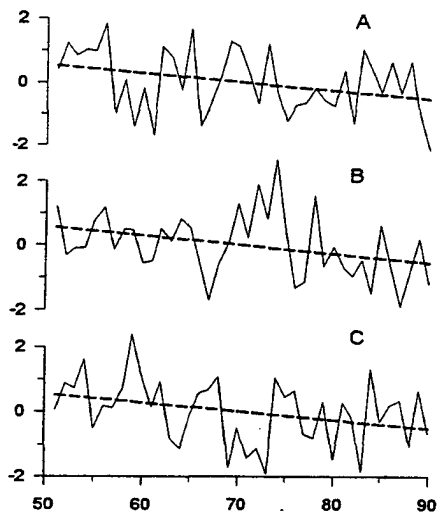


Fig. 5. The series for mode 2 from February (A), mode 3 from October (B) and mode 1 from November (C) (solid lines) and their trends (dashed lines).

Author's address: Dr Joanna Wibig
Department of Meteorology and Climatology
University of Lodz, POLAND
90–418, Łódź, Kościuszki 21

VARIATIONS OF ATMOSPHERIC CIRCULATION AND CLIMATE CHANGE

G.V. Gruza and E.Ya.Rankova

Institute for Global Climate and Ecology, Moscow, Russia

ABSTRACT

An attempt was made to perform an automated classification of synoptic situations. The final goal is to investigate possibilities to reconstruct large scale surface climate anomalies (in particular, these of air temperature and precipitation) on the base of regularities in circulation regimes alternation.

INTRODUCTION

Climate variability of atmospheric circulation and the role of circulation regimes alternation in the development of climatic anomalies were investigated in many aspects: Girs (1971); Dzerdzeevskiy (1975); Gruza, Rankova (1994,1995); IPCC (1990).

Synoptic (visual) typifications (Vangengeim (1952), Dzerdzeevskiy (1975)), and automated classifications (Barnston, Livezey (1987), Gruza, Rankov (1970), Cheng, Wallace (1993), Molteni et al. (1990)) both were widely used to analyze circulation regimes. The principal components, i.e. coefficients of dominant empirical orthogonal functions, became a practice to reduce analyzed space dimensionality (Molteni et al. (1990)).

As for circulation analysis, it is natural to use small-dimensional phase space including different circulation indices rather than station or gridded data. These are Blinova-Rossby zonal circulation index, Kats indices (meridional, zonal, total ones - for the whole hemisphere, and for the sectors), as well as "teleconnections", etc.

As an example of synoptic typification, let us consider the typification by M.Kh.Baydal (Figure 1). The 500-hPa height field is considered within the six sectors (Figure 1a), and each one is recognized in terms of 11 patterns (Figure 1b). These include zonal transport (0), and two sets: from trough to cyclone (from -1 to -5) and from ridge to anticyclone (from 1 to 5). The codes were chosen that they should characterize intensity of corresponding baric pattern or vorticity. Frequencies of the patterns are estimated for the season central months (Figure 1c) over all six sectors for the 1944-1993. One can conclude rather strong stability of the types distribution, as if the last practically does not depend on season. From the other hand, the form of the distribution is very close to normal. So, there is no reason to consider these types as clusters. They rather resemble to the discrete intervals of continuous variable, such as vorticity or temperature, etc. The same was concluded by Toth (1990).

DATA, METHODS, and RESULTS

To estimate a possibility to perform a simplified typification of 500-hPa height fields, we used wintertime data on location of the frontal zone axial isohypse of this. The isoline of 540 dam was chosen as this isohypse (after Khrabrov (1960)). So, 36-dimentional phase space was used, as including the closest to the Pole latitude of 540 dam isohypse (L540) on each of 36 meridians (0,10E,20E...).

Mean values and 10% and 90%-quantiles of L540 are shown (Figure 2, top) as functions of longitude. The skewness and kurtosis as well as the Kolmogorov's normality test are shown therein (bottom). It is noteworthy that the maximum deviation from normality occurs in the area of the troughs, while the maximum conformity with normal distribution is in the ridges locations.

The processes of circulation types alternation within Pacific-North-American and Atlantic-Eurasian sectors were found to be practically independent with each other. From the other hand, interlongitudinal correlation of L540 decreases up to zero as the longitudinal lag is as small as 40-50 deg.

Thus, typification should be performed within a limited longitudinal sector not exceeding 160-180 deg.

As the first explorative experiment, two automated classifications ("V-means" and "Random-3") were carried out by using the simplest cluster analysis algorithm within sector of 80W-100E which is concerned in Vangengeim's typification. First, the Vangengeim type means of L540 (Figure 3) were notified as starting centroids. The second classification was realized starting from three random realizations. In both cases three classes were obtained as a result of five iterations (their means are shown in Figure 4a,b). As one can see, rather similar centroids were obtained, and the types contingency was also strong enough. So, there is a reason to consider that the result of automated classification weakly depends on starting centroids, i.e. the process is approximately convergent and unambiguous.

To solve a question whether the 3-classes' typification is the final one, i.e. whether these 3 classes are really the clusters, the clustering procedure was repeated starting with 4 random dates ("Random-4"). Its centroids after five iterations are shown on Figure 4c. The four classes describe a more complicated patterns of 540 isohypse. None of centroids was kept in details, but a new class appears to be extracted from the previous first one.

The problem of comparison with different typifications quality is a difficult one.

The authors attempted to compare "V-means"-types with "Random-3". Daily data on the frontal zone latitude (used in cluster procedure), and surface air temperature at some stations of European Russia were used.

It was appeared that the visual typification did not take any advantage over automated one. Opposite, automated types (even being not the real clusters) have at least such advantage over visual ones that they were obtained using formal computer procedure. They are easy to be used, for example, in comparative analysis of the atmosphere behavior (in terms of circulation type frequency) on modelled and observed data to be aimed at a validation the GACMs. These are also useful for synoptic climatology and analysis of the climate changes reasons.

CONCLUSION

1. Synoptic (visual) typifications, being a useful instrument of atmospheric processes investigation, are the examples of successful grouping of observed situations. However, there are no reliable evidence that these patterns (groups, subspaces) represent clusters in any phase space.

2. Variance analysis of surface air temperature at some stations over European part of Russia showed the temperature is essentially depending on circulation patterns.

3. Statistical analysis of the frontal zone axial isohypse of 500 hPa heights over the Northern Hemisphere showed the automated classification should be carried out within some limited sector, not more than 160-180 deg.

4. Examples of automated classification, resembled to synoptic (visual) typifications, were obtained for Atlantic-Eurasian sector of the Northern Hemisphere extratropics.

REFERENCES

Barnston, A.G., and R.E. Livezey, 1987: Classification, seasonality and persistence of low-frequency atmospheric circulation patterns. - Mon. Wea. Rev., 115, 1083-1126.

Cheng, X., and J.M.Wallace, 1993: Cluster Analysis of the Northern Hemisphere Wintertime 500-hPa Height Field: Spatial Patterns. -J. Atmos. Sci., 50, 2674-2696.

Dzerdzeevskiy, B.L., 1975: General atmospheric circulation and climate. Selected proc., M., 286 pp.

Girs, A.A., 1971: Multiyear oscillations of atmospheric circulation and long-range hydrometeorologic forecasts. - L., Gidrometeoizdat, 280pp. (in Russian).

Gruza, G.V., E.Ya.Rankov, 1970: On principles of automated classification of meteorologic objects. - Meteorology and Hydrology, 2, 12-22 (in Russian).

Gruza, G.V., E.Ya.Rankova, 1994: Climate variability with emphasis on extreme climatic events and circulation/synoptic regimes.- Proceedings of the 18-th Annual Climate Diagnostics Workshop, CAC/NMC/NOAA, Boulder, CO, 98-101.

Gruza G.V., E.Ya.Rankova, 1995: Long-term trends in frequency and lifetime of circulation patterns in the Northern Hemisphere. - Proceedings of the 19-th Annual Climate Diagnostics Workshop.

Intergovernmental Panel of Climate Change (IPCC), 1990: Climate Change, The IPCC Scientific Assessment. J.T.Houghton, C.J.Jenkins, and J.J.Ephraums, Eds., Cambridge University Press, 365 pp.

Kimoto, M., and M.Ghil., 1993, a,b: Multiple flow regimes in the Northern Hemisphere winter. - Journal of the Atmospheric Sciences, 50, 2645-2673 (Part I), 2645-2673 (Part 2).

Khrabrov, Yu.B., 1960: Mean monthly air temperature formation, and its prediction. - Trudy CIP, 92 (in Russian).

Molteni,F., S.Tibaldi and T.N.Palmer, 1990a,b: Regimes in the wintertime circulation over northern extratropics. - Q.J.R. Meteorol. Soc., 116, 31-67 (Part I), 1263-1288 (Part 2).

Toth Z., 1990: Circulation Patterns in Phase Space: A Multinormal Distribution? - Mon.Wea.Rev.,119, 1501-1511.

Toth Z., 1993: Prefered and Unprefered Circulation Types in Northern Hemisphere Wintertime Phase Space. - J.Atmos.Sci., 50, 2868-2888.

Vangengeim, G.Ya., 1952: Principles of macrometeorological method of long-range meteorologic forecast for Arctic region. - Trudy AANII, 34 (in Russian).

Corresponding Author

Professor G.V. Gruza,
Institute for Global Climate and Ecology
20b Glebovskaya Str., Moscow 1107258, Russia

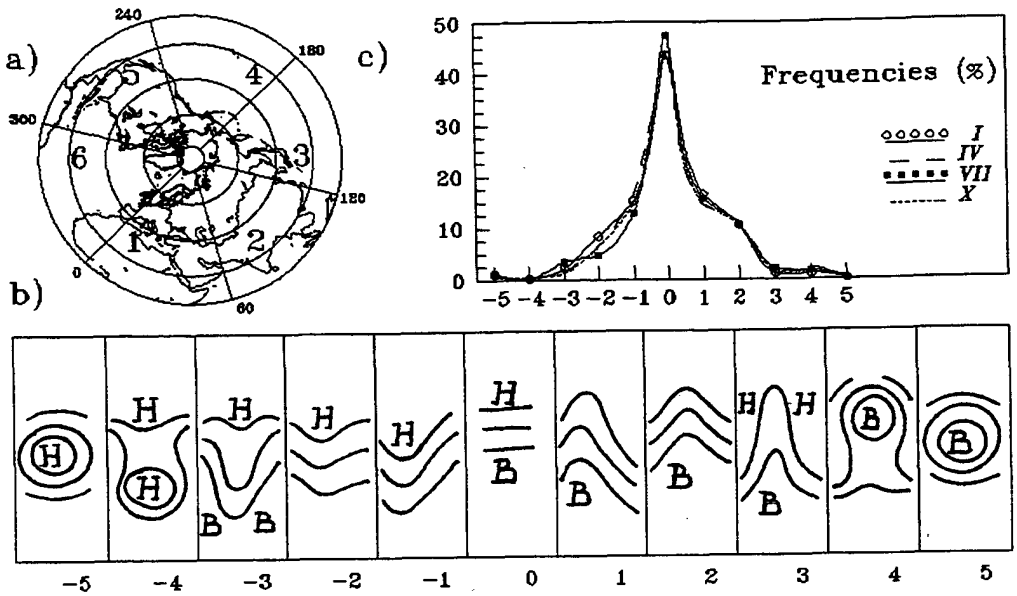


Figure 1. N.H.extratropic 500-hPa height field typification by Baydal: a) sectors wherein the type is recognized; b) 500-hPa height field patterns and their codes; c) frequencies of the circulation types (Jan.-Apr.-Jul.-Oct.)

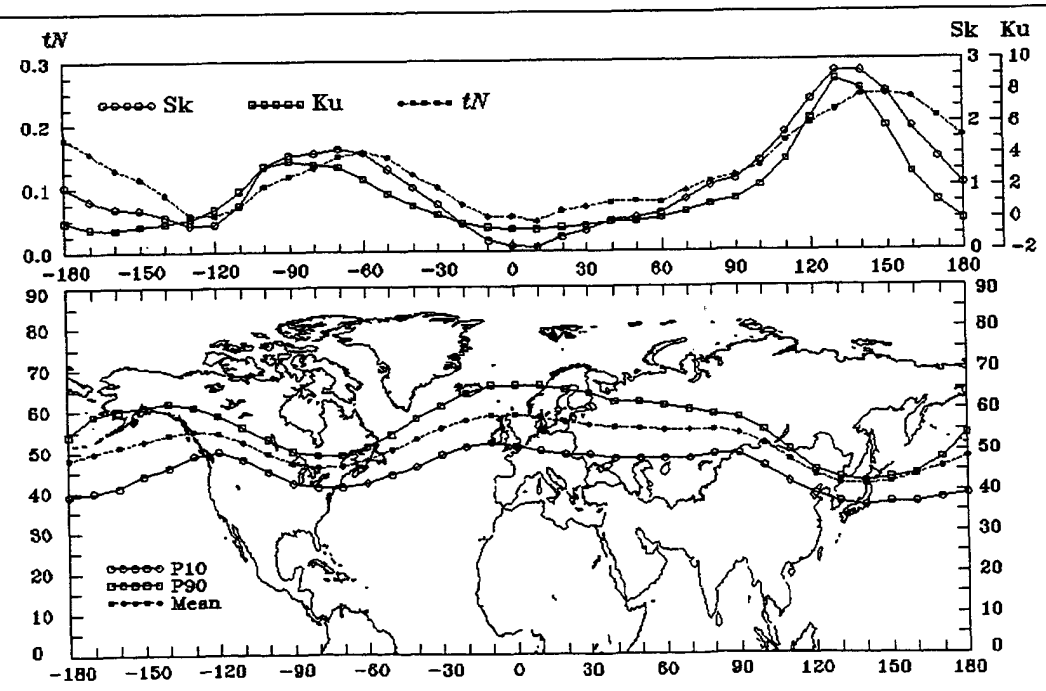


Figure 2. The wintertime 540 dam isohypse latitude statistics as functions of longitude (for 1951-1993). Top: skewness Sk, kurtosis Ku, and Kolmogorov test of normality tN. Bottom: means, and quantiles 10%, 90 %.

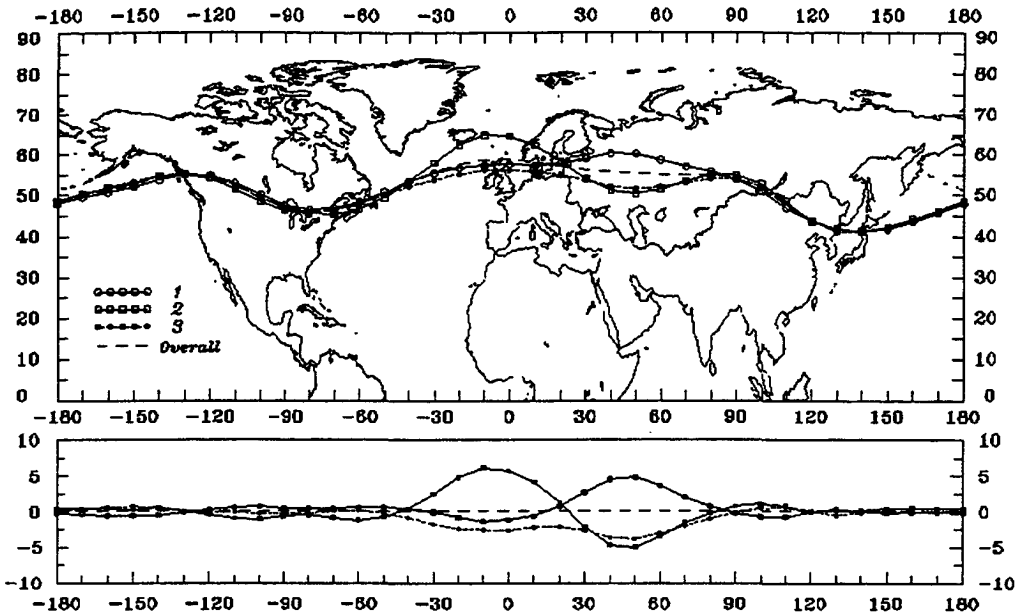


Figure 3. Mean values of the wintertime 540 dam isohypse latitudes corresponding to Vangengeim circulation forms and overall mean (top) and their anomalies (bottom) as functions of longitude, for 1951–1993

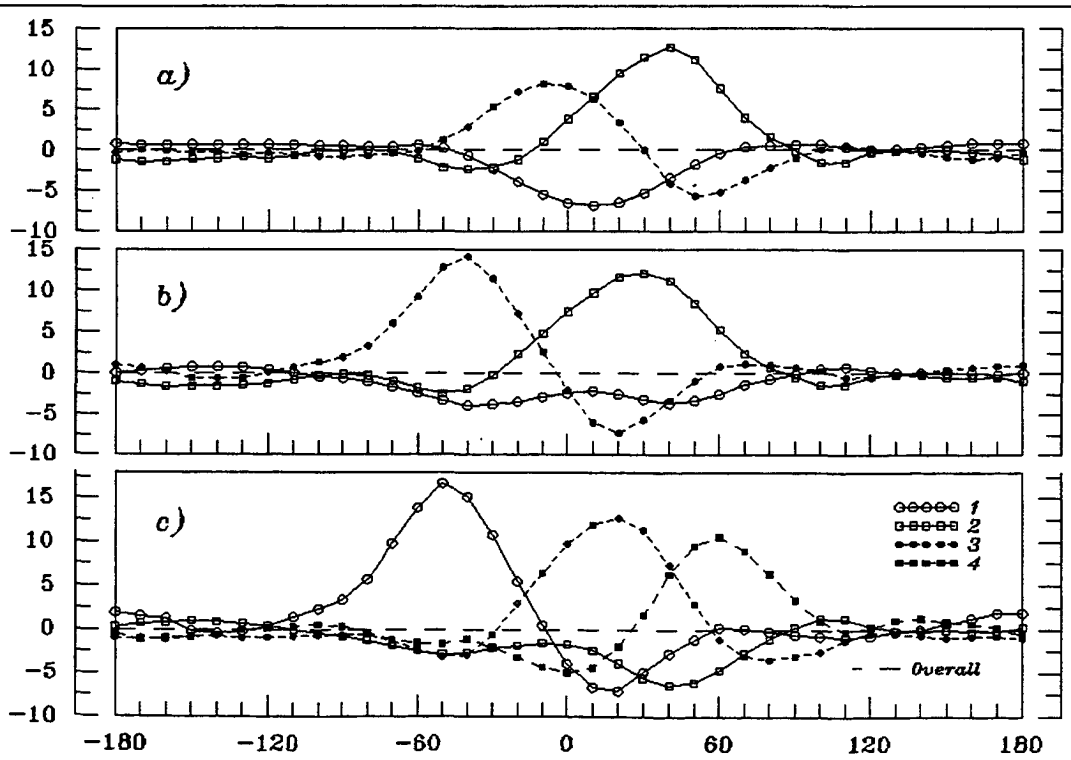


Figure 4. The wintertime 540 dam isohypse latitude mean anomalies (1951–1993, 80W–100E) corresponding to automated classifications starting with: a) Vangengeim types means; b) 3 random dates; c) 4 random dates.

CLIMATE VARIATIONS OVER THE FORMER USSR IN RECENT DECADES

V.N.Razuvaev, O.N.Bulygina, E.G.Apasova, L.G.Korulina, R.A.Martuganov

All-Russian Research Institute of Hydrometeorological Information-
World Data Centre
6, Korolyov str.,Obninsk, Kaluga reg.,249020 RUSSIA

ABSTRACT

The results of the former USSR climate variations study, based on the statistical analysis of surface air temperature, atmospheric pressure and sunshine duration time-series which were prepared in RIHMI-WDC, Obninsk, Russia in 1991-1994, are presented. The linear trend coefficients in these time-series were calculated for ten different parts of the USSR. Temperature rise in winter time has been found for the most part of the former USSR area. Analyses of correlation coefficients between temperature, atmospheric pressure and sunshine duration give an additional information about possible reasons of temperature increase in various parts of the USSR.

1 INTRODUCTION

The former USSR area represents about 16% of the Northern Hemisphere land mass and contents quite different climatic regions. A lack of computer-compatible high quality data sets on this territory prevented the climatologists from making the comprehensive assessment of climatic variability over this region assosiated with ovserved global warming. Over the past few years climatologists in RIHMI-WDC (Russia) have worked to build high-quality data sets which contain temperatures, atmospheric pressure, sunshine duration, water vapour pressure, precipitation for reasonably well-distributed across the country 243 stations.

An important aspect af any analysis of regional climate variability relates to the potential impact of atmospheric circulation and solar radiation on air temperature. In previous work (Bulygina et al.,1991) we have found that there is a positive tendency in air temperature change over the former USSR area in recent decades. In this work we are going to continue the investigation of main features of air temperature variations in the various climatic zones of the former USSR by using statistical approach to analysis of monthly mean temperature, atmospheric pressure and sunshine duration time-series.

2 DATA

To analyze regional climate variability, we used baseline datasets of monthly mean air temperatures, sea-level air pressure and sunshine duration which were built in the RIHMI-WDC in 1991-1993 for 200 stations uniformly distributed over the former USSR. Extreme air temperature data (minimum, maximum temperatures and diurnal temperature range) are also used in this study. Additional information on the station history (relocation, change of instruments and observation procedures) was used to check long-term time-series for a statistical inhomogeneity.

3 RESULTS

Air temperature is one of the major elements of the climate system and is the most popular indicator of climate variability. A tendency towards air temperature rise over the former USSR is well established. A linear trend coefficient in the one-hundred years time-series (1890-1990) of annual temperature anomalies averaged over the USSR area is 0.06°C/10yr. Warming is largely induced by temperature rise in a cold period (November-March); a linear trend coefficient in one-hundred series of seasonal anomalies was 0.10°C/10yr (Bulygina et al.,1991). The air temperature rise tendency derived from one hundred-year data is accounted for by a considerable warming in the past thirty years (1961-1990) (Belokrylova et al.,1991).

The former USSR area is extremely inhomogeneous in its natural conditions and this fact should be taken into account when analyzing regional climate variability. The regionalization of the USSR area was performed for the purpose of this study. As a bazis, we used the identification of homogeneous climatic zones made with regard to climatic features and local landscape that was suggested by B.P.Alisov (Alisov,1969).



Figure 1. Climate divisions used to calculate regional area-averaged (1 - West Arctic, 2 -East Arctic, 3 - North Pacific, 4 - East Europe, 5 - West Siberia, 6 - East Siberia, 7 - Kazakhstan and Northern Middle Asia, 8 - Far East, 9 - Caucasus and Southern Middle Asia, 10 - Altay Mountains).

Regional averages of temperature were calculated within various areas by arithmetic everages of each station's year-seasonal-month mean temperature anomaly. Anomalies were calculated from 1961-1990 mean air temperatures.Linear trend coefficients in the series of annual and seasonal anomalies are given in Table 1.

Table 1. Linear trend coefficients (°C/10yr) in the time-series of air temperature anomalies for various regions of the former USSR. A double underline represents trends significant at the 0.10 level and a single underline the 0.05 level.

REGION	YEAR	WARM SEASON	COLD SEASON
1	0.25	0.12	0.53
2	0.29	0.22	0.42
3	0.12	0.24	-0.02
4	0.11	-0.05	0.54
5	0.33	0.18	0.82
6	0.46	0.25	0.86
7	0.15	0.14	0.36
8	0.29	0.18	0.44
9	0.05	0.06	0.09
10	0.23	0.12	0.43

It is apparent from Table 1 that the rise of annual air temperature over the former USSR is largely attributed to temperature rises in Siberia and the Far East (regions 2,5,6,8). A maximum linear trend coefficient (β=0.46°C/10yr) is obtaned for the continental part of Eastern Siberia (region 6). A temperature rise is not so pronounced over the European territory (regions 1 and 4). In the cold time, a tendency towards air temperature rise is observed over most of the USSR. Linear trend coefficients in the continental regions of Siberia amount to 0.86°C/10yr. No significant temperature rise tendency was found in Kasakhstan and Middle Asia (region 7 and 9). In the warm period, temperature rise is only observed in Eastern Siberia and the Far East.

The first evidence that the warming over the USSR area in the recent few decades can be attributed to an increase of mean minimum air temperatures was obtained in 1991 (Karl et al.,1991). According to the subsequent analysis, this is also true for individual climatic regions. The recent data on the change of minimum (T_{min}), maximum (T_{max}) temperatures and diurnal temperature range (DTR) for the period 1951-1994 are given in Table 2.

A steady minimum temperature rise is found for most of climatic regions. Maximum temperatures do not change significantly in most of the regions except for the European territory (region 4) which experiences a noticeable rise in T_{max}. As is seen from Table 2, the diurnal temperature range decrease in the cold period is largely associated with a prevailing rise in minimum temperatures. The exception is region 3, where DTR decrease results from the maximum temperature decrease. It should be noted that a similar effect is observed for a number of stations on the Black Sea coast (Razuvaev et al.,1993).

Table 2. Linear trend coefficients (°C/10yr) over the period of record 1951-1994 in the time-series of anomalies of diurnal temperature range (DTR), minimum (T_{min}) and maximum (T_{max}) air temperatures in cold period (November-March) for various regions of the former USSR. A double underline represents trends significant at the 0.10 level and a single underline the 0.05 level.

REGION	DTR	Tmin	Tmax
1	-0.23	0.73	0.19
2	-0.14	0.71	0.45
3	-0.20	0.10	-0.93
4	-0.17	0.61	0.45
5	-0.21	0.84	0.73
6	-0.39	1.13	0.11
7	-0.26	0.44	0.77
8	-0.11	0.52	0.17
9	-0.40	0.28	0.01
10	-0.15	0.84	0.70

Table 3. Same as Table 2, except for the warm period (April-October).

REGION	DTR	Tmin	Tmax
1	0.01	0.07	0.09
2	-0.07	0.23	0.17
3	-0.02	0.30	0.28
4	-0.17	0.08	-0.09
5	-0.08	0.22	0.13
6	-0.22	0.40	0.17
7	-0.10	0.19	0.10
8	-0.13	0.25	0.12
9	-0.05	0.10	0.04
10	-0.11	0.18	0.07

Table 3 lists the data on the change of T_{min}, T_{max} and DTR for warm period (April-October). Unlike the cold time, a steady decrease of DTR (linear trend coefficients are significant on 5-10% level) is observed only for three climatic regions (4,6,8). Minimum temperature rise is observed in most of the regions, except for the European territory. However, the values of the linear trend coefficient are lower than those in the cold time. The changes in maximum temperatures are insignificant for most of the regions.

Air surface temperature, considered here as an indicator of climatic variation, is affected by two major characteristics of the climatic system state, i.e. atmospheric circulation and solar radiation. Of great interest in this context is to establish a possible relationship between temperature regime variability over the USSR and the changes in atmospheric circulation and solar radiation.

Until recently ,this study has been limited by the lack of appropriate data sets. Baseline data sets on air pressure and sunshine duration for 243 stations of the former USSR has been prepared in RIHMI-WDC in 1991-1994. An attempt is made in this study to analyze relationships between temperature variability and air pressure and sunshine duration. Atmospheric pressure and sunshine duration are considered here as parameters that characterize circulation and radiation factors affecting air temperature.

Let us consider variability of air pressure and sunshine duration in various climatic zones of the former USSR (Fig.1) in the cold period, which is characterized by the highest variability in air temperature. Long-term time-series of sunshine duration and sea - level air pressure anomalies averaged over the cold period (November - March) have been used for this purpose. The anomalies were calculated as deviations from long-term means for 1961 - 1990. Table 4 lists the linear trend coefficients in the time-series of seasonal anomalies for the period 1961 - 1993 for each region.

Table 4. Linear trend coefficients in the time-series of anomalies of atmospheric pressure, β_P(mb/10yr), and sunshine duration, β_S(hours/10yr) for cold period (November-March) over the period of records 1961-1993 in various regions of the former USSR. A double underline represents trends significant at the 0.10 level and a single underline the 0.05 level.

REGION	β_P	β_S
1	-1.91	-0.18
2	-1.16	-2.45
3	-0.08	2.41
4	-0.78	-3.20
5	-1.53	-2.53
6	-1.11	-1.26
7	-0.88	-8.05
8	0.10	-1.54
9	-3.21	-0.72
10	1.93	2.83

A tendency towards the air pressure decrease in the cold time is found in most of the regions, except for the Far East (region 8). It can be explained by the growing cyclonic activity in the recent decades over the former USSR area that was mentioned before (Nemirovsky et al.,1990). A reduced sunshine duration in the cold period is attributed to the growing of cloudiness in day time. An indication on increasing of cloudiness (at least in the day time) is rather interesting, because it is closely connected with possible explanation of asymmetric increase of minimum temperature in recent decades (Karl et al.,1993). It should be noted too, that decrease of sunshine duration and increase of cloudiness is in a good agreement with the conclusion about the intensification of cyclonic processes in this period of year. On the other hand it may be concluded that sunshine duration in winter periods of recent decades is strongly influenced by circulation pattern and hardly can be used for investigation of relationship between variations in surface air temperature and solar radiation. Some other parameters, such as total, direct and scattered solar radiation should be used for this purpose.

It can be seen from Tables 1 and 4 that rise of air temperature in winter period in the most climatic zones of the former USSR is accompanied by decreasing of atmospheric pressure (regions 1,2,4,5,6). A quantitative assessment of interrelation between these two meteorological parameters can be made on the bazis of correlation analysis. Table 5 lists the coefficients of linear correlation between anomalies of air temperature and sea-level atmospheric pressure in winter time for ten USSR regions, calculated for the period of record 1961-1993.

Table 5. The correlation coefficients between anomalies of atmospheric pressure (P) and anomalies of mean (T_{mean}), maximum (T_{max}) and minimum (T_{min}) temperatures for cold period (November-March) in various parts of the former USSR. A double underline represents correlation coefficients significant at the 0.10 level and a single underline the 0.05 level.

REGION	R(P,T)	R(P,T_{max})	R(P,T_{min})
1	-0.63	-0.75	-0.72
2	-0.38	-0.40	-0.36
3	-0.07	-0.08	-0.06
4	-0.73	-0.74	-0.69
5	-0.60	-0.62	-0.60
6	-0.61	-0.60	-0.62
7	-0.76	-0.74	-0.73
8	0.11	0.09	0.10
9	-0.33	-0.36	-0.31
10	-0.51	-0.52	-0.59

The resulting coefficients of correlation between air pressure and temperature characteristics indicate that a close relationship is found for contiguous parts of the former USSR (above mentioned regions 1,2,4,5,6). It confirmed the fact that contribution of the circulation factor to the temperature regime formation is considerable in these regions. Other factors to be established in further studies are likely to be determining in the temperature regime formation in regions 3 and 8 (North Pacific and Far East regions).

6 CONCLUSIONS

The spatial pattern of air-surface temperature variations over the former USSR in recent decades is rather non-uniform. Annual temperature increase is most pronounced in the central part (West Siberia). It was found too that the annual temperature increase in many regions is caused by temperature rise in winter time (November-March). There are some places where temperature increase has not been found (Kazakhstan and Middle Asia).

At present we lack an adequate understanding of the causes of different changes in temperature in various parts of the former USSR area, but there is some evidence to suggest that changes in atmospheric pressure plays a direct role. Decrease of atmospheric pressure is well expressed across much of the country and coefficients of linear correlation between air temperature and atmospheric

pressure are large and significant on 5-10% level for most of the regions (Table 5). Significant negative trends in sunshine duration time series and assosiated increasing in day-time cloud cover (Table 4) are in a close agreement with decreasing of atmospheric pressure and intencification of extra-tropical cyclonic activity in winter time. But in some regions (Far East, for example) other forcings must be operating to increase of air temperature. These results are important for a better understanding of how global warming may be related to change of regional climate. We are continuing to expand the climate variations study over the former USSR area and are beginning rigorous diagnoses of variations in mean daily temperature.

REFERENCIES

Bulygina,O.,N.Korshunova,V.Razuvaev,1991,"Temperature anomalies in cold periods on the USSR territory", Proceedings of the Sixteenth Annual Climate Diagnostics Workshop,28 October-01 November, Los Angeles, USA,pp.179-184.

Belokrylova,T.,O.Bulygina,V.Razuvaev,1991,"Temperature pattern variability on the USSR territory in 1931-1990",Ibid, pp.173-178.

Alisov,B.P.,1969,"Climate of the USSR"(Vyschaya shkola, Moscow), 104p.

Nemirovsky, A.V., V.T.Radyukhin,1990,"Characteristics of oceanic centers of action ot the atmosphere as indicators of regional climate fluctuations", Proceedings of the Fifteenth Annual Climate Diagnostics Workshop, 29 October-02 November,Asheville, USA, pp.202-206.

Karl,T.R., G.Kukla, V.N.Razuvaev, M.J.Changery, R.G.Quayle, R.R.Heim,Jr., D.R.Easterling, C.B.Fu, 1991,"Global warming: evidence for asymmetric diurnal temperature change", Geoph.Res.Let.,v.18,#12,pp.2253-2256.

Karl,T.R., P.D.Jones, R.W.Knight, G.Kukla, V.N.Razuvaev, K.P.Gallo, J.Lindseay, R.J.Charlson, T.C.Peterson, 1993, "Asymmetric trends of daily maximum and minimum temperature", Bul.Am.Met.Soc.,v.74,#.6,pp.1007-1023.

Razuvaev, V.N., E.G.Apasova, O.N.Bulygina, R.A.Martuganov, 1995, "Variations in the diurnal temperature range inthe European region of the former USSR during the cold season", Atmospheric Research (in press).

CORRESPONDING AUTHOR

Dr.V.N.Razuvaev
RIHMI - WDC
6, Korolyov str.,Obninsk,249020 Kaluga reg. RUSSIA

Vector of geostrophic wind over the North Atlantic region as an index of local atmospheric sub-circulation

Mirosław Miętus

Institute of Meteorology and Water Management, Maritime Branch, Poland

ABSTRACT

Daily air presure data from the years 1961-1990 of ten synoptic stations in the Northeast Atlantic region were used to calculate daily values of geostrophic wind, applying triangle technic. The results confirmed the general circulation pattern in the investigated region. Additionally long-term variation of mean speed was considered and a weak intensification tendency found.

INTRODUCTION

Depending on the area covered by a pressure system we speak about circulation of a given scale - global, regional or local. When air movement of a given scale is to be described, a suitable method must be sought for, which allows to stress the factors essential to the process. The understanding of deviations in air circulation over neighbouring areas is of great importance. For the purposes of this understanding a quantitative description is more advantageous than only a qualitative one.

DATA AND METHODS USED

To describe quantitatively air circulation over Northeast Atlantic daily surface pressure data from ten points, represented by meteorological stations, were used from the years 1961-1990. All series of pressure data have been homogenized according to Alexandersson (1986). These ten stations form a net of triangles (Fig.1) over which, using the method applied in (Miętus 1993, 1994), mean daily vector of geostrophic wind has been computed, both for each of the elementary triangles and for a greater one (constructed on the apexes represented by Reykjavik, Isfjord and Oslo). The computed wind vectors are fastened to the geometrical centres of individual triangles (sub-areas). Besides, a measure of air flow steadiness towards the mean direction was established, expressed in form of a ratio of the mean vector length to its scalar value.

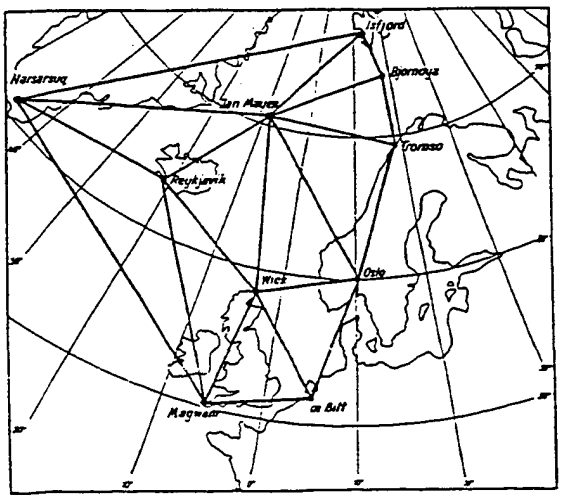


Fig.1. Stations and net of triangles used for calculation of mean wind vector in the northeastern part of North Atlantic.
Note: Isfjord stands for Isfjord Radio 1961-1969, Longyerbyen 1970-1976 and Svalbard Lufthavn 1997-1990.

RESULTS

Mean surface wind vector in the triangle Isfjord-Reykjavik-Oslo

One of the larger areas analysed was the triangle Reykjavik-Isfjord-Oslo, enclosing the northern, eastern and central parts of the whole area under consideration.

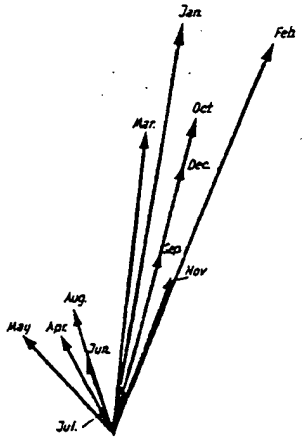


Fig.2. Mean monthly geostrophic wind vectors in the northern, central and eastern part of Northeastern Atlantic.

The general character of the air flow over this part of Northeastern Atlantic in the years 1961-1990 reveals a domination of southerly directions throughout the year, reaching its greatest intensity from September to March (Fig.2). In these months the values of mean monthly meridional component are closed between 1.3 ms^{-1} in November to 3.4 ms^{-1} in January, whereas mean monthly values of zonal component vary between 0.3 ms^{-1} in March to 1.3 ms^{-1} in February. In spring and summer the intensity of southerly air flow is much lower - between 0,2 ms^{-1} in July and 1.0 ms^{-1} in August. Furthermore, in these months the zonal component is negative (easterly winds from -0.1 ms^{-1} in July to -0.7 ms^{-1} in May).

Coefficients of steadiness for this area are comparatively high (>0.3, November excluded) in autumn and winter. In the rest of year these coefficients are smaller, to as low as 0.06 in July.

Predominance of directions from between SW and SE in this area is also confirmed by annual variation of mean monthly frequency distribiution of geostrophic wind direction there (Fig.3). The supremacy of these directions can be compared to a sort of "driving belt" of seasonally changing width and intensity of transmission. This belt is wider in the cool months, when also the rate of air transport towards north is more intensive (not less than 55 per cent).

Differentiation of geostrophic wind conditions in particular sub-areas

Spatial distribution of speed and direction of geostrophic wind over northeastern part of North Atlantic reveals considerable differentiation between particular, even adjacent, sub-areas (represented by triangles). It, however, confirms the classic distribution of atmospheric pressure systems

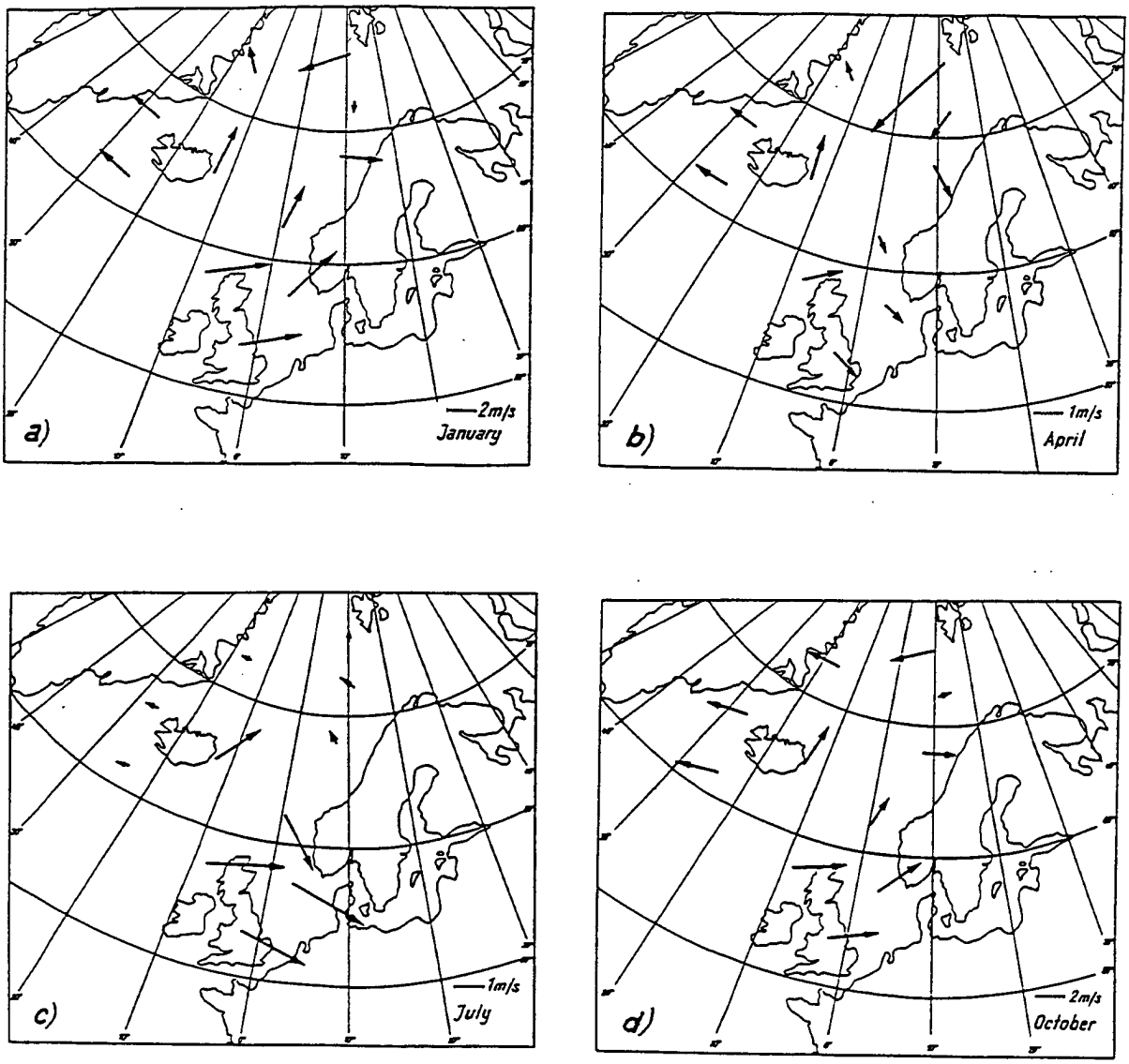


Fig.4. Mean monthly geostrophic wind vectors (1961-1990) for particular sub-areas of Northeastern Atlantic for January (a), April (b), July (c) and October (d). Note the different velocity scale in figs. (a) and (d) and figs. (b) and (c).

in this region (Fig.4). The wind vectors on the maps point to the climatological depressions or high pressure areas. Depending on the season the intensity of air mass flow increases or diminishes in particular sub-areas. In winter and autumn (Fig. 4a and 4d) the air flow - geostrophic wind speed is about 2-3 times more intensive than in the remaining seasons (Fig. 4b and 4c) over all sub-areas. An exception is the triangle Bjornoya - Isfjord - Jan Mayen, where also in spring (April, Fig. 4b) the northeasterly air flow is as intensive as in the preceding winter and autumn.

Of small differentiation (though not of small values) is the mean geostrophic wind over the southeastern sub-areas, where the zonal air flow is disturbed less (than over the northwestern sub-areas). This results in approximately similar vectors of mean geostrophic wind there. To these four triangles in autumn and winter join the areas north of them, with somewhat greater departures however.

The mean vectors in the sub-areas off Greenland have the greatest deviation from the conditions in neighbouring sub-areas. The explanation can be seen from the frequency distribution of wind direction (Fig.5a). Majority of winds blows there from two quite opposite sectors (due to the oscillating gyre of the Islandic low): from NE to E in more than 35 per cent and from SW to W in more than 40 per cent. As the northeasterly winds strike usualy stronger, the resulting vector is of easterly direction.

Frequency distribution of wind directions, in annual variation, over the sub-area Jan Mayen - Wick - Oslo is presented in Fig. 5b. Though it looks more "disordered" than that one for off Greenland, the air transport, beginning with August through December and January to May occurs there in more than 35 per cent by southeasterly to southwesterly winds. In summer the majority of directions (more than 55 per cent) is closed within NW and N.

The wind field presented in Fig. 4a-d and gained by computations is confirmed by data from shipborne observations (Isemer, Hasse, 1985), though these data cover the period 1941-1972, overlaping the years 1961-1990.

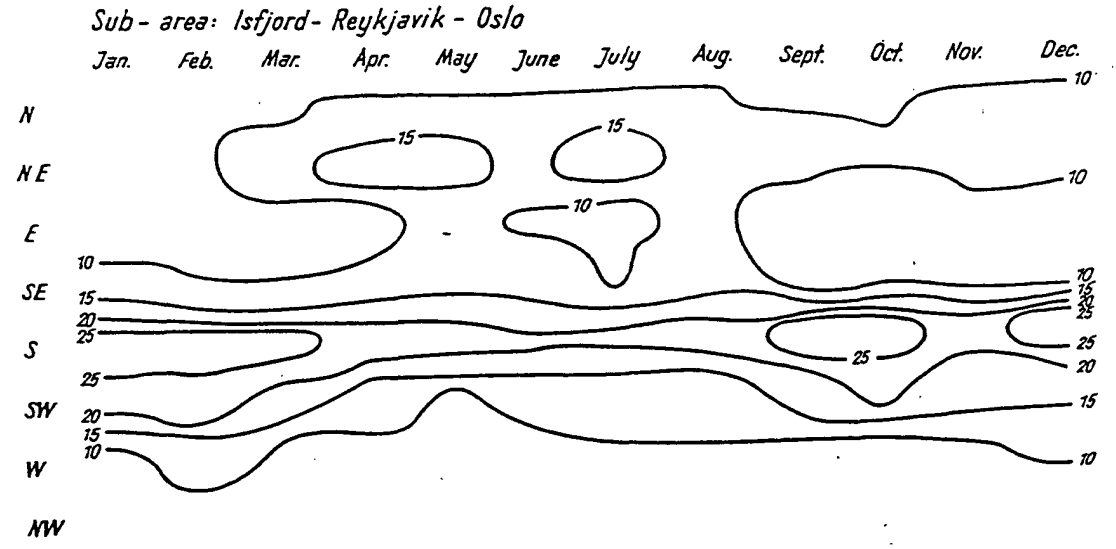


Fig.3. Annual variation of mean monthly frequency distribiution of geostrophic wind directions in the northern, eastern and central part of Northeastern Atlantic.

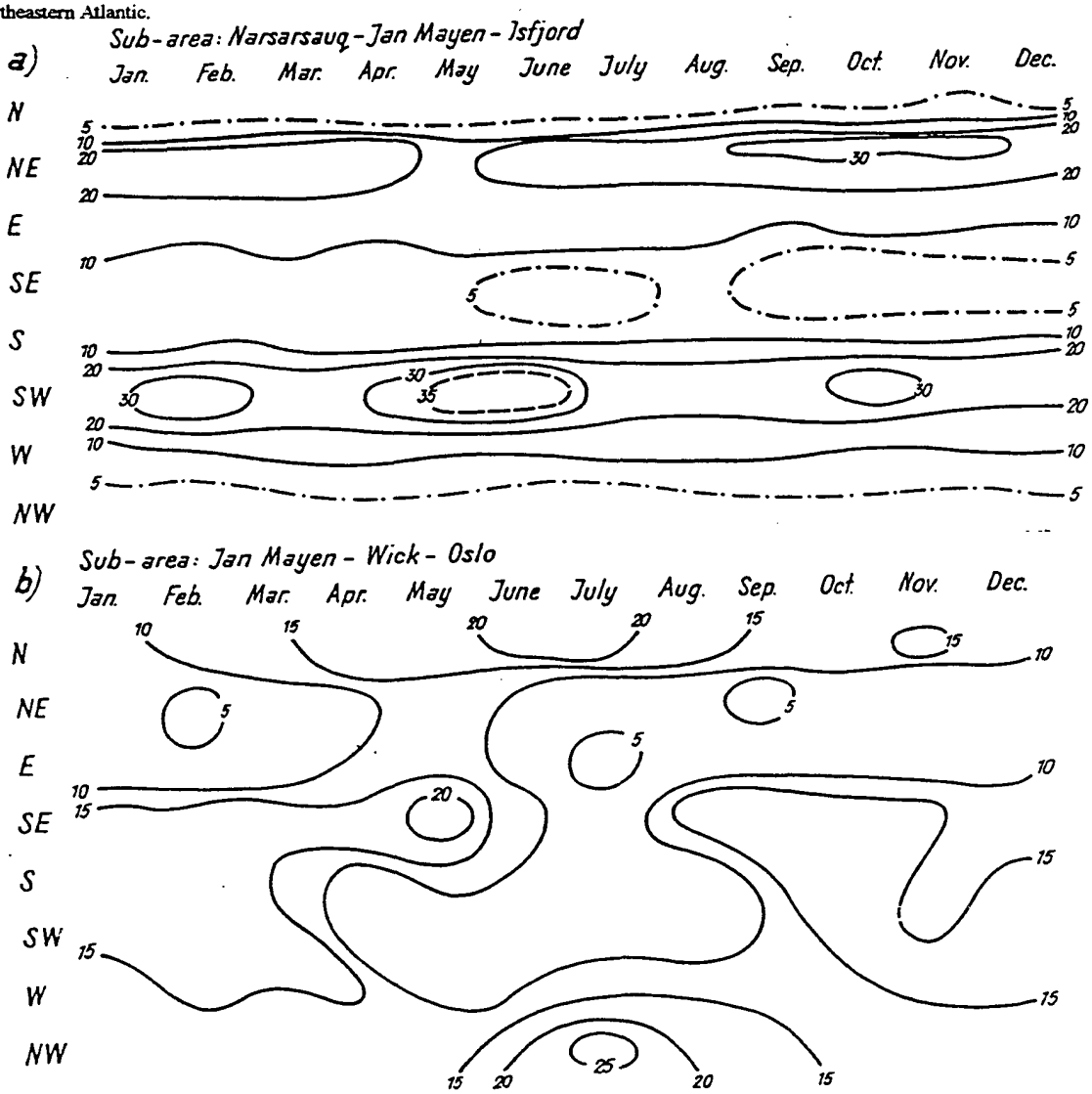


Fig.5. Annual variation of mean monthly frequency distribution of geostrophic wind direction in sub-area Narsarsauq-Jan Mayen-Isfjord (a) and Jan Mayen-Wick-Oslo (b).

Long-term variation

An overview through the 30-years-long series of computed geostrophic wind in particular sub-areas allows to conclude on a growing tendency of mean annual wind speeds.

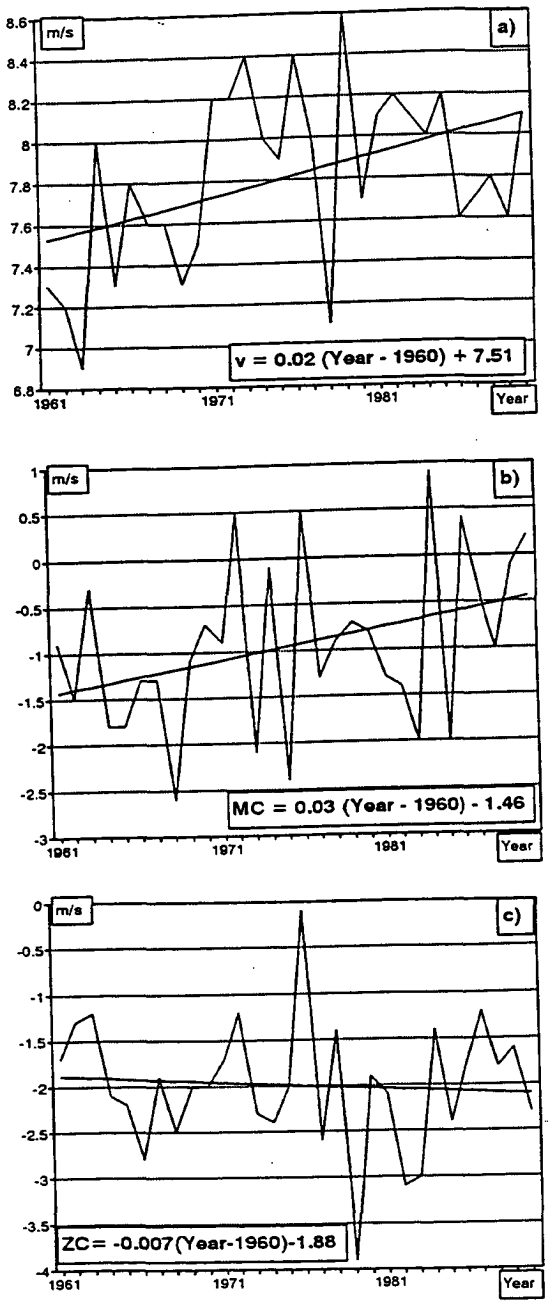


Fig.6. Variation of annual mean values of: geostrophic wind speed (a), meridional componet (b), zonal component (c), in the sub-area Jan Mayen-Isfjord-Bjornoya in the time 1961-1990.

The rate of growth is rather small, it nevertheless gives an increase of the mean wind speed by about 0.4 - 0.7 ms^{-1} in these 30 years in particular sub-areas. In one of the northern sub-areas, the triangle Jan Mayen - Isfjord - Bjornoya, rate of growth of mean wind speed amounts to 0.02 ms^{-1} per year, what gives 0.6 ms^{-1} in these 30 years (Fig.6a).

When meridional and zonal components of the geostrophic wind vector are considered, the relations are changing from sub-area to sub-area. Staying with the triangle Jan Mayen - Isfjord - Bjornoya we have to say that intensity of the northerly air flow (meridional northern component of geostrophic wind vector) diminished and in its place growth of intensity of the southerly air flow could be observed (Fig. 6b), by about 0.03 ms^{-1} per year. These values result from the domination of southerly air flow twice in the decade of nineteen seventies and four times in the eighties. Over the same sub-area zonal component (of negative sign) reveals a very slow growth of intensity of the easterly air flow (Fig.6c). During these 30 years no year could be observed there, in which westerly flow would be dominant. Scarcely an equilibrium was reached in 1976 between these two directions.

It must be stressed that a time span of 30 years is much too short to gain conclusions statistically significant and to set long-term trends. Therefore the results presented above are of limited extent and can only point out to some tendencies.

CONCLUSIONS

Areas remaining under influence of three prevailing wind systems could be distinguished

- southern and central part of the area under prevailing westerly and southwesterly winds
- northeastern part with evident influence of the northerly wind system
- northwestern part, off Greenland and Iceland, where the winds rotate around the gyre of Icelandic low

Limits of these areas are instable and shift depending on the season of the year.

Further, the known fact has been confirmed that over the North Atlantic region an intensive transport of air masses occurs, generally from southwest towards northeast.

Additional feature of this transport in the thirty years considered was a weak, nevertheless steady increase of the mean wind speed, differing somewhat from sub-area to sub-area.

REFERENCES

Alexandersson H., 1986, A homogeneity test applied to precipitation data, J. of Climatology 6, 661-675.

Isemer H-J., Hasse L., 1985, The Banker Climate Atlas of the North Atlantic Ocean, Volume 1: Observations, Springer-Verlag, Berlin, 220pp.

Miętus. M., 1993, "Some results of the WMO Project - Climate of the Baltic Sea Basin", Proceedings of the First Workshop on the Baltic Sea Ice Climate, (Tvarminne, Finland), Un. of Helsinki, Dept. of Geoph., Rep. Ser. in Geoph. No. 27, 73-86.

Miętus M., 1994, "Vector of geostrophic wind in the Baltic Sea region as an index of local circulation and its relationship to hydro-meteorological characteristics along the Polish coast", Proceedings of the European Workshop on Climate Variations (Majvik, Finland), SILMU, 3/94, 278-292.

ACKNOWLEDGEMENTS

The author expresses his sincere thanks to DMI, DNMI, DWD, KMI, KNMI, VI and UKMO for their kindness in delivering the data sets indispensable to perform these computations.

CORRESPONDING AUTHOR

Dr. Miroslaw Miętus
Institute of Meteorology and Water Management,
Maritime Branch,
Deptartment of Polar and Marine Meteorology and Climatology,
Waszyngtona 42, PL-81-342 Gdynia, POLAND

VARIATIONS OF THE ATMOSPHERIC CENTERS OF ACTION IN THE NORTHERN HEMISHERE AND THEIR ASSOCIATIONS WITH THE CLIMATE CHANGE IN CHINA

Qing Yun Zhang Shao Wu Wang*
Wei Chyung Wang**
Institute of Atmospheric Physics, Chinese Academy of Sciences
Beijing, 100029 China

ABSTRACT

Interannual variability of the atmospheric center of action (ACA) over the Northern Hemishere was examined. Six ACAs were identified in winter half year. (Oct. to Mar.) four in summer half year (Apr. to Sep.). Among them Indian Low showed the greatest month to month persistence. No significant correlation coefficient (CC) was found between the ACAs except between the Icelandic Low and the Atlantic High in winter half year. Aleutian Low in winter half year varies with the change of the phase of ENSO. Aleutain Low usually deepened in the El Nino episode, and was filled up in the La Nina episode. Temperature and precipitation in China closely relate to the change of the SLP at the key area.

1. INTRODUCTION

From the very early stage of the application of daily SLP map in the latter of nineteenth century, monthly mean SLP map had constructed for the Atlantic – European sector, and then for the Northern Hemisphere. A series of high pressure centers and depressions had been found on the maps, some of them occurred throughout a year, and some others appeared in winter or summer time only. The former or the latter was called as permanent or semi–permanent atmospheric center of action (Hildebrandson 1897).

Walker and Bliss (1932) synthesized three Oscillations: North Atlantic Oscillation (NAO), North Pacific Oscillation (NPO) and Southern Oscillation (SO) on the basis of correlation coefficients between the element at two single stations.

Bjerknes (1969) had initiated a new epoch in the climatological researches on the ACA. He successfully linked the SO to the El Nino event ENSO as a combined terminology was frequently used in the literature at present time. Numerous studies were carried out in examining the relationship between the variation of precipitation in tropical zones and SO (Rassmusson 1982, Rassmusson and wallace 1983, Ropelewski and Halpert 1987). All these studies detailed the connections between the Oscillations and the local climate, improved the understanding of the Oscillations and their Variability.

Recently a series of studies have been accomplished in simulation of the ACA and the three Oscillations by using of the GCM. NAO,NPO and SO were fairly simulated in application of GCM (Pittalwala and Hameed 1991, Hameed and Pittalwala 1991).

Present paper aims at providing an assessment on the interannual Variability of ACA, which is yet to be fairly undestood. At the same time, the interrelationship between the ACA and the influence of the ACA on the climate were examined based on the data set of 1951–1990. The anomalies of the intensity of ACA during 1951–1990 were studied in relation to the climate change over China. In present paper, twelve months were divided into two parts: winter half year and summer half year. The former start from October and ended in March. The latter consisted of six months from April to Septemper.

2. ATMOSPHERIC CENTER OF ACTION ON THE SEA LEVEL PRESSURE MAP

2.1 Definition of the Intensity of the Atmospheric Center of Action

Monthly mean sea level pressure (SLP) map shows explicitly the low and high pressure center, which was called as the atmospheric center of action (ACA). However, a definition of the intensity of the ACA remained obscure till recent time. Usually the central maximum or minmum of SLP in the center of a High or a Low was accepted as the intensity. But the maximum or minmum is often difficult to estimate exactly, especially in the early time, when the SLP observation was scarce and did not evenly distribute over the earth surface. The grid point data set of SLP improved greatly the availability of the information of pressure system, but it missed sometimes the real maximum or minimum of the central pressure. Now, the key step in the study was how to find the grid points which can be properly used to characteristic the ACA. Therefore, correlation coefficient (CC) between the SLP in the central point of a ACA

and the SLP elsewhere over the Northern Hemisphere was calculated. The grid on which maximum or minimum was found in a High or a Low on the normal monthly mean SLP map was used as the central point. Correlation map was found for each ACA. Then the six maps of each ACA for summer or winter half year were compared to each other and a common area was found, which consisted of twelve grid points. Therefore, the same area was used for one ACA in six months of winter or summer half year. A twelve point mean was taken to characterize the intensity of ACA. Six ACAs were found in the winter half year and four in summer half year. Winter half year: Siberian High, North American High, Aleutian Low, Icelandic Low, Pacific High and Atlantic High, Summer half year: Indian Low, North American Low, Pacific High and Atlantic High. All of the ACAs show at least one closed isobar on the SLP map except the North American Low, Which was usually expressed as a trough oriented from equatorial Low pressure zone to the subtropical latitudes.

Fig.1 shows the interannual Variation of the intensity of the ACA which was defined as the average of the SLP at twelve grid points. It indicated that the greater variance was found for the Icelandic Low, the Aleutian Low and Atlantic high that Looked stronger in winter since 1970's and for the Indian Low looked weaker in summer since the middle of 1960's.

2.2 Interrelation Between the Atmospheric Centers of Action

As indicated in the section 1, the studies on the ACA revealed a series of interrelation between the ACAs in the Northern Hemisphere, for example, NPO, NAO. It is of interest to examine the simultaneous relationship between the ACA based on the systematic data set. Table 1 and Table 2 give the CC between the intensity of the ACAs in January and July respectively. The only one significant of CC at 95% of the confidence level for a *posteriori* correlation was that between the Atlantic High and Icelandic Low.

Indeed, the Atlantic High negatively correlated to the Icelandic Low. However the pacific High was positively correlated to the Aleutian Low. It contradicts to the NPO, according to which the SLP should be low in the Aleutian Low when the SLP is high in the Pacific High, and vice versa. This contradiction probably associated with the difference of the region used to represent the high. The maximum contrast of SLP in the NPO (Rogers 1981) was found between the SLP in the Aleutian and in the central Pacific. The area used in present paper was located in the Eastern Pacific. It has been indicated that no significant CC was found between the NAO and NPO (Walker and Bliss 1932). The recent date shows also poor CC between the Icelandic Low and Aleutian Low, and between Atlantic High and Pacific High. (Table 1 and 2).Examination of the interrelation between the ACAs indicated that the ACAs seem varied independently each other except the Icelandic Low linked closely to the Atlantic High.

Table 1 Correlation Coefficient between the Atmospheric Centers of Action in January

	Sib.	Ame.	Ale.	Icela.	Pac.	Atl.
Siberian	1.00	0.14	−0.29	0.28	−0.41	−0.12
American		1.00	0.13	0.37	−0.30	−0.18
Aleutian			1.00	−0.12	0.31	0.02
Icelandic				1.00	−0.31	−0.69
Pacific					1.00	0.14
Atlantic						1.00

Tabel 2 Correlation Coefficient between the Atmospheric Centers of Action in July

	Ind.	Ame.	Pac.	Atl.
Indian	1.00	0.06	−0.03	−0.04
American		1.00	−0.01	0.12
Pacific			1.00	−0.01
Atlantic				1.00

3. RELATIONSHIP OF THE ATMOSHPERIC CENTER OF ACTION TO THE ENSO

The climate anomaly in Pacific Basin closely related to the ENSO. So, The relationship between the ACA and ENSO was examined.

The Aleutian Low in winter half year showed some relationship to the ENSO. The intensity of the Aleutian Low for nine El Nino events and nine La Nina events were outlined in Table 3. The ENSO events were identified according to the sea surface temperature in Eastern Equatorial Pacific (Zang and Wang). Table 3 shows that the Aleutian Low was stronger than the normal in the El Nino years (SLP decreased) and weaker in the La Nina years (SLP increased).

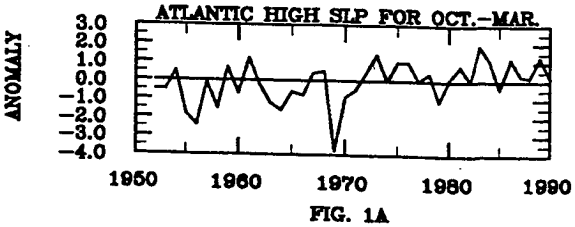


FIG. 1A

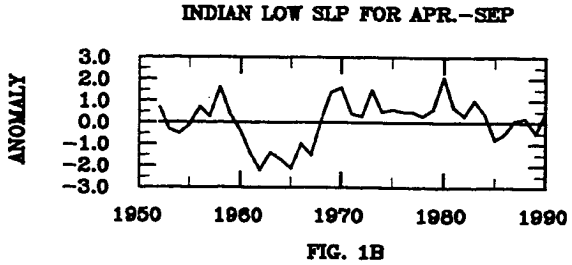


FIG. 1B

The Pacific High was stronger in the La Nina years and weaker in the El Nino years than the normal. Only the monthly mean for the two groups were given in Table 4. The predominance of negative anomaly in the El Nino events and positive anomaly in the La Nina events were exciting. Other ACAs did not show any significant relationship to the ENSO.

Table 3 Intensity of the Aleutian Low in relation to the ENSO in winter half year

El Nino	Oct.	Nov.	Dec.	Jan.	Feb.	Mar.	Mean
1957–58	−0.3	−5.4	4.7	−5.6	−2.4	2.5	−1.5
1963–64	0.6	2.3	−7.1	−2.6	−0.4	3.2	−0.7
1965–66	0.3	4.6	6.1	−5.3	4.7	3.6	2.3
1969–70	−2.9	0.1	−7.9	3.6	−7.1	−6.0	−3.4
1972–73	1.0	−2.7	4.4	4.2	0.5	−2.5	0.8
1976–77	−1.5	−4.6	−4.3	−10.6	−10.0	4.6	−4.4
1982–83	4.8	−2.7	−3.4	−3.4	−10.5	−8.2	−3.9
1986–87	−2.3	−0.2	−11.4	−4.4	−2.5	−3.2	−4.0
1987–88	−1.4	−0.9	0.4	−2.4	−5.9	0.7	−1.6
mean	−0.5	−1.1	−2.1	−2.9	−3.7	−0.6	−1.8
La Nina	Oct.	Nov.	Dec.	Jan.	Feb.	Mar.	Mean
1954–55	−3.5	−4.7	3.8	−2.5	10.4	6.6	1.7
1955–56	0.8	3.8	7.7	−10.4	5.0	1.2	4.8
1964–65	2.2	2.4	6.4	−1.9	1.8	−2.9	2.0
1970–71	2.4	6.2	4.2	10.1	0.6	0.6	4.0
1971–72	2.4	1.1	6.0	7.1	8.1	2.4	4.5
1973–74	2.7	5.8	−2.9	3.2	5.8	−3.7	1.8
1974–75	−3.1	−1.0	−2.6	5.7	1.8	3.0	0.6
1975–76	1.7	2.0	−1.2	−0.8	7.5	3.3	2.1
1988–89	−0.5	−1.4	−1.0	5.7	7.6	6.3	2.8
mean	0.6	1.6	2.3	4.5	5.4	1.9	2.7

Table 4 Intensity of the Pacific High in Relation to the ENSO

	Oct.	Nov.	Dec.	Jan.	Feb.	Mar.	Mean
El Nino	−0.7	−0.3	−0.1	−0.7	−0.6	0.0	−0.4
La Nina	0.5	0.2	1.1	1.6	1.8	0.3	0.9
	Apr.	May.	Jun.	Jul.	Aug.	Sep.	mean
El Nino	−0.8	−0.8	−1.0	0.1	−0.1	−1.4	−0.7
La Nina	0.2	0.3	−0.2	−0.4	0.3	0.6	0.2

4. IMPLICATION OF THE SLP ANOMALY AT KEY AREA TO THE CLIMATIC ANOMALY OVER CHINA

The number of 0.3 (or−0.3) or more correlation coefficient between the SLP of the every basic point and other point elsewhere in the Northern Hemisphere has been calculated. The maximum one of the Northern Hemisphere is at 60 ° N, 70 ° E in winter half year and at 50 ° N, 110 ° E in summer half year. Therefore the point of 60 ° N, 70 ° E and 50 ° N, 110 ° E were used in present paper as a key point in winter half year and summer half year respectively.

1980's was the warmest decade (Jones and Wigleg 1991). The Northern Hemispheric and Global mean surface temperature raised 0.23℃ and 0.21℃ respectively during the last two decades (Houghton et al 1992). Fig.2a showed the temperature change during 1951–1992 over the northern China. It can be seen that the temperature has increased since 1970. Fig.2b showed the SLP in Icelandic Low during 1951–1992. It is obvious that the SLP in the Icelandic Low has decreased since 1970, and that the change of SLP in the Icelandic Low wasopposite with the temperature over the northern China. January 1977 was the record broken cold month in China. The SLP at the key point (60N, 70E) was one of the maximum (14.5hpa) from 1951 to 1989 for all months in the winter half year. Another month with the SLP maximum of same value (14.5 hpa) was the January 1969 which was also well known as the severest month for the last a few decade (Wagner 1969), March 1990 was the warmest month for the last one hundred years or more (Jones and Wigley 1991). SLP at the key point in this month was −12.8hpa, the lowest value in the last forty years. It indicated that the SLP at the key point provided a good indicator which characteristics the climatic anomaly for the Northern Hemishpere. But, the reason of the decreasing or increasing of the SLP is yet to be understood.

The relationship between the SLP at key point (50 ° N, 110 ° E) and precipitation in Northern China have been studied. Fig.3 showed the SLP at key point (50 ° N, 110 ° E) and the rainfall over the Northern China during 1951–1992. It can be seen that the rainfall has decreased since 1965, and the change of rainfall was opposite with the change of SLP at the key point (50 ° N, 110 ° E). An abrupt change occurred in the middle of 1960's at key point (50 ° N, 110 ° E) in summer half year.

5. CONCLUSIONS

5.1 Six ACAs were found in the SLP map in winter half year (October to March); and four ACAs in the summer half year (April to Septemper). Twelve points mean of the SLP was used to characteristics the intensity of the ACA.

5.2 Greater interannual variability of the intensity of the ACA was found for the Icelandic Low, Atlantic high and the Aleutian Low in winter half year, and for Indian Low in summer half year.

5.3 No significant consistent correlation was found between the ACAs except the Icelandic Low and Atlantic High. Insignificant correlation coefficient between the Aleutian Low and the Icelandic Low, and between the Pacific High and Atlantic High proved again the independence of NPO to NAO.

5.4 Aleutian Low was usually deeper in an El Nino year than the normal, and weaker in a La Nina year in winter half year. Intensity of the Pacific High decreased in an El Nino year and increased in a La Nina year both in winter and in summer half year. The change of other ACAs seems independent to ENSO.

5.5 Key point was identified during winter half year at 60 ° N, 70 ° E and during summer half year at 50 ° N, 110 ° E. The change of at key point or in key area during 1951–1992 was in good accordance with the change of surface air temperature or rainfall over the Northern China.

References

Bjerknes, J., 1969: Atmospheric teleconnections from the tropical Pacific. Mon. Wea. Rev., 97, 163–172.

Hildebrandson, H. H., 1897: Quelquers recherches sur les entres d'action del' atmosphere. K. Svenska Vetens. – Akad. Handl., 29, 33 pp.

Houghton, J. T., et al. 1992: Climate change, The IPCC scientific Assessement, Cambridge, University press, pp. 365.

Jones, P. D., and T.W.L. Wighley., 1991: Recent global warmth during the 1980's and 1990. in proceedings of fifteen Annual climate Diagnostical Workshop. Oct. 29–Nov. 2, 1990, 344–349.

Pittalwala, I. I., and S. Hameed, 1991: Simulation of the North Atlantic Oscillation in a general circulation model. Geophys. Res. Lett., 18, 841–844.

Rassmusson, E. M., and T. H. Capenter, 1982: Variations in tropical sea surface temperature and surface wind field associated with the Sonthern Oscillation El Nino. Mon. Wea. Rev., 110, 354–384.

Rassmusson, E.M., and J. M. Wallace, 1983: Meteorological aspects of the El Nino/ Southern Oscillation. Science, 222, 1195–1202.

Rogers, J. C., 1981 The North Pacific Oscillation J. Climatal.,1, 39–57.

Ropelewski, C. F., and M.S. Halpert, 1987: Global and regional scale precipitation patterns associated with the El Nino/ Southern Oscillation. Mon, Wea, Rev., 115, 1606–1626.

Wagner, A. J., 1969: The weather and circulation of January 1969 continued strong high–latitude blocking and flood–producing rains in california Mon, Wea. Rev., 97, 351–358.

Walker, G. J., and E.W. Bliss, 1932: World Weather V, mem. Roy. Meteor. Soc., 4, 53–84.

Zang Hengfan and Wang Shaowu, 1984: Equatorial Eastern Pacific SST and the subtropical highs Acta Oceanologica Sinica, 3, 471–476.

CORRESPONDING AUTHOR

* Prof. Shao Wu Wang, The department of geophysics, Beijing University.

* * Dr. Wei Chyung Wang, Atmospheric Sciences Research Center, State University of New York, Albany, N.Y. 12205.

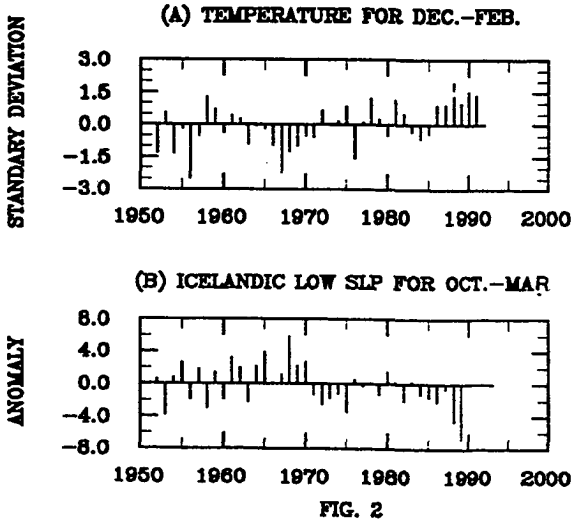


FIG. 2

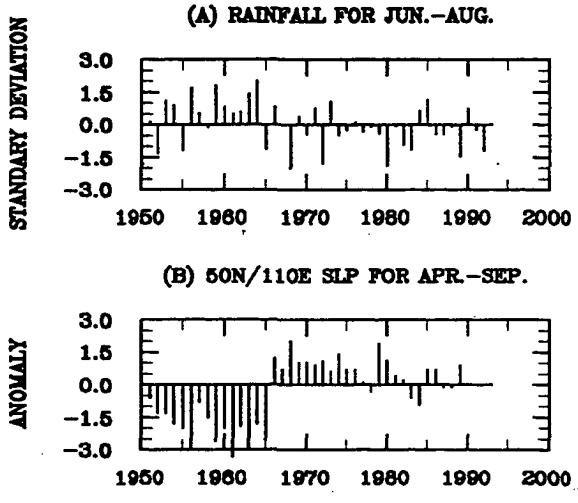


FIG. 3

TEMPERATURE CHANGES IN ATMOSPHERE: STRONG SIGNAL OF GLOBAL COOLING IN LOWER STRATOSPHERE

Rudolf H.Reitenbach, Alexander M.Sterin

All-Russian Research Institute for Hydrometeorological Information-World Data Center

6, Korolyov str., Obninsk, Kaluga Region, RUSSIA, 249020

ABSTRACT

The Upper - Air (U/A) temperature variations were estimated for various vertical layers and latitude zones. These estimates were based on processing data for about 800 radiosonde stations. For the base period (1961-1975) parameters of linear trends in U/A temperature were estimated. and R^2 value was considered for estimations of linear trend models in various vertical layers and latitude zones. High value of R^2 enabled to suggest strong signal on cooling in lower stratosphere.

Stratospheric cooling estimates for 1993-1994 were obtained both by linear trend model extrapolation and by processing the observational data for period 1993-1994. These estimates are shown to be close.

INTRODUCTION

In our previous publications (Reitenbach, Sterin, 1991, 1992) time series of monthly and seasonal temperature anomalies for various latitude zones and various atmospheric layers were studied. Linear trends were estimated for the period 1961-1975. In this study radiosonde data for global network of about 800 stations were used. Complex Quality Control (Alduchov, 1985) was applied to raw data first. A number of climatological processing procedures were applied to the data before the anomalies were estimated.

Currently several groups of scientists are working to update their time series for temperature anomalies by current data in quasi-operational regime. Their approaches are based on different data sources as well as on different methods of climatological processing. J.Angell (Angell, 1988) uses in his study radiosonde data for a limited baseline network of 63 stations over the world.

R.. Spencer and J. Christy (Spencer, Christy, 1993) use the data from NOAA's polar orbital satellites. Data from two different channels of Microwave Sounding Unit (MSU) enable them to estimate temperature anomalies in lower troposphere and in lower stratosphere.. These authors are operationally updating their time series from 1979.

D.Gaffen (Gaffen, 1994) noted that some previously computed temperature trends in atmosphere, especially estimates of stratospheric cooling, may be influenced by data inhomogeneities, and careful analysis of data homogeneity must precede any conclusion on temperature changes.

Beginning on January 1993 radiosonde data from global network are processed and archived at World Data Center, Obninsk, Russia. The processing of these data enables the authors of this paper to provide quasi-operational monitoring of temperature parameters for free atmosphere. For these goals authors use the same methods and statistical algorithms as they used to process the radiosonde data and to evaluate temperature time series for historical period (Reitenbach, Sterin, 1991).

In this paper time series of upper-air temperature anomalies will be considered for two periods: 1961-1975 (this period is taken as reference one and is used for calculating climatic normals), and 1993-1994.

DATA PROCESSING

Mean monthly values of temperature on standard levels are calculated for global network of about 800 radiosonde stations. Objective analysis of monthly statistics is performed to obtain the grid-point values from station-point values for each of the level and for each of the stations of global network. The algorithm of objective analysis is based on sequential corrections of grid-point values by station values. The use of primary grid-point field is necessary for this algorithm.

Each of corrections is based on local adaptive polynomial interpolation of primary grid-point values (for a limited amount of grid points close to station point), - into the station point. While the building of each polynom is based on Ordinary Linear Regression (OLR) least-square estimates, the choice of polynom's type is based on specific analysis of local discrepancies between real and interpolated values in station point. The detailed description of this interpolation algorithm is contained in (Reitenbach, Sterin, 1987).

Both the goal of radiosonde data processing and primary radiosonde data base are similar to those used by A.Oort, in particular, in his research of U/A temperature trends (Oort, Liu, 1993). But due to different approaches in grid-point field building, the estimates of temperature anomalies may differ, especially in the regions with sparse station network. In particular, our approach enables to exclude overestimated values of anomalies for such regions.

The further processing of grid-point data included vertical weighting of grid point temperature values to obtain layer values, anomaly calculations referred to base period 1961-1975, spatial horizontal generalization of grid-point values to obtain anomaly estimates for latitudes, latitude zones, hemispheres and Globe.

In (Reitenbach, Sterin, 1991) the comparison of temperature anomalies estimates obtained by authors, with those obtained by J. Angell and by A. Oort, is contained.

RESULTS AND DISCUSSION

Linear regression models were built on the base of monthly time series of temperature anomalies data for the period 1961- 1975. Data obtained by

authors of this paper at RIHMI-WDC (referred as Reitenbach & Sterin Data - RSD) were used for this goal.
The model built was of the simplest type:

$$DT=a+bn,$$

where **DT** - value of temperature anomaly,
n - ordinary number of month beginning from January 1961,
a and **b** - parameters of model estimated in standard way.
For comparison, similar estimates but based on seasonal temperature anomalies data for the same period, were made for Angell's data (referred as AD).
Tables 1 and 2 contain estimates of linear regression model parameters for RSD (Table 1) and AD (Table 2), for vertical layers 850-300 hPa (troposphere) and 100-50 hPa (lower stratosphere). The results are given for both Northern (NH) and Southern (SH) hemispheres as well as for the Globe (GL).

Table 1. Parameters of linear regression models for temperature anomalies, period 1961-1975, based on Reitenbach & Sterin Data (RSD):
b - linear trend angular coefficient for monthly temperature change, degrees C * 100/month;(values different from 0 with probability greater than .95, are marked by asterisk),
R^2- fraction of total variability explained by model

	Layer, hPa	b, °C*100	R^2
NH	850-300	-0.06	0.04
	100-50	-0.31*	0.36
SH	850-300	0.03	0.03
	100-50	-0.11*	0.11
GL	850-300	-0.02	0.01
	100-50	-0.22*	0.38

Table 2. As in Table 1, but based on Angell's Data (AD).

	Layer, hPa	b, °C*100	R^2
NH	850-300	-0.14*	0.08
	100-50	-0.04	0.00
SH	850-300	0.14*	0.07
	100-50	-0.70*	0.33
GL	850-300	0.00	0.00
	100-50	-0.13	0.02

The analysis based on data obtained at RIHMI (RSD, see Table 1) enables to detect lower stratosphere cooling for both hemispheres and for the Globe. At the same time the analysis based on J.Angell's data (AD, Table 2) enables to detect stratosphere cooling only in the Southern Hemisphere, but not in the Northern Hemisphere and not in the Globe
The monthly temperature anomalies for various vertical layers and for various latitude zones were estimated by authors for the period 1993-1994 (24 months total). The methods of processing and calculation for the period 1993-1994 were the same as for the period 1961-1975, which was considered in this research as the reference one. Time series of temperature anomalies for the period January 1993 - December 1994 are presented on Fig. 1, 2 and 3.
Note that lower stratospheric cooling is detected persistently during the 24 month period. At the same time, the relative warming in the Southern Hemisphere within January-March 1993 may be explained by volcanic eruption (Mt. Pinatubo in Summer 1991). The detected deviation is the final stage of this stratospheric warming.
Note that tropospheric temperature variations within 24 month period enable to detect warming, but this warming is essentially less evident than the stratospheric cooling.

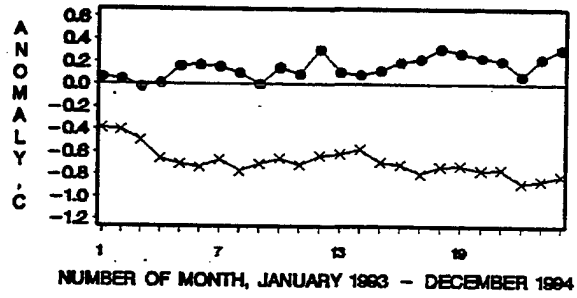


Fig. 1. Time series of temperature anomalies for the Globe:
solid dots - layer 850-300 hPa,
crosses - layer 100-50 hPa
Horizontal axis - ordinary number of month, from 1 to 24, period January 1993-December 1994.

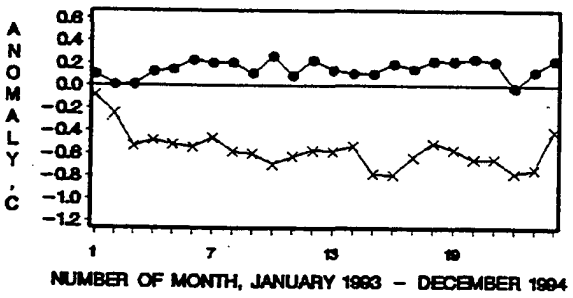


Fig. 2. As in Fig.1, but for the Southern Hemisphere

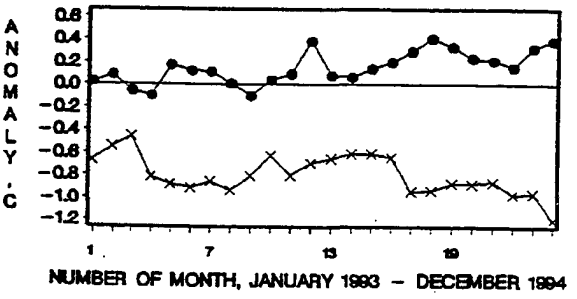


Fig.3. As in Fig.1, but for the Northern Hemisphere

To test the hypothesis whether the mean values of temperature anomalies in the two periods could be considered equal, Student's t-test was applied to

pairs of monthly anomalies data samples (for Globe, both Hemispheres as well as for 30-degree latitude zones) for the periods 1961-1975 and 1993-1994. The results for various zones for lower stratosphere are contained in Table 3. Similar estimates, but for troposphere, are contained in Table 4.

Note that for lower stratosphere (see Table 3) for each of zones studied, not depending on results of variance equality test applied, the tested hypothesis on equal mean values of temperature variations in lower stratosphere cannot be accepted with high probability. This enables to suppose that the signal of lower stratospheric cooling is strong enough.

Table 3. Testing the hypothesis that the mean anomalies of temperature in lower stratosphere (layer 100-50 hPa) are equal for two periods: 1961-1975 and 1993-1994, for various zones.

DT_{calc}- value of mean anomaly for 1993-1994 (the anomaly for period 1961-1975 is considered equal to zero);

Var(E/U) accepted with probability >.95 assumption on Equality (E) or Unequality (U) of variations in both data samples based on sample variations equality test;

t - value of t-statistic;

Prob >|t| - probability of a greater absolute value of t under the null hypothesis: means are equal.

Zone	DT_{calc}	Var (E/U)	t	Prob >|t|
Globe	-0.69	U	23.55	0.0001
South H	-0.57	E	13.52	<0.0001
North H	-0.80	U	19.16	0.0001
90-60S	-0.47	U	4.50	0.0001
60-30S	-0.28	U	7.70	0.0001
30S-0	-0.79	E	13.28	<0.0001
0-30N	-0.67	E	8.37	<0.0001
30-60N	-0.77	U	12.80	0.0001
60-90N	-1.28	U	5.17	0.0001

Table 4. As in Table 3, but for troposphere (layer 850-300 hPa)

Zone	DT_{calc}	Var (E/U)	t	Prob >|t|
Globe	0.15	E	-5.50	<0.0001
South H	0.15	U	-8.22	0.0001
North H	0.15	E	-4.02	0.0001
90-60S	-0.19	U	3.45	0.0009
60-30S	0.02	U	-0.89	0.3736
30S-0	0.32	U	-10.97	0.0001
0-30N	0.24	E	-4.83	<0.0001
30-60N	0.10	E	-1.74	0.0822
60-90N	-0.01	E	0.13	0.8910

As the results of Table 4 are analyzed, the values of tropospheric temperature anomalies are non-negative for all zones excluding the southern polar zone. The hypothesis on equal mean anomalies of tropospheric temperature for the studied two periods can be accepted with high probability (probability >.95) only in some latitude zones: 60-30S, 30-60N as well as in 60-90N zone. Concerning both hemispheres, Globe and other zones, we can suppose warming, that was, however, not so evident as cooling in lower stratosphere.

Based on the linear trend models built on data for the period 1961-1975, the estimates of lower stratospheric cooling in the period 1993-1994 were calculated. The calculations were done for vertical layer 100 - 50 hPa. Values of linear trend angular coefficients **b** were used for this goal. In parallel, the estimates of lower stratosphere temperature anomalies were estimated directly for the period January 1993 - December 1994 as means of 24 monthly anomaly values for this period.

Both results, extrapolated and calculated directly from data for this period, are contained in Table 5. The results are presented for those latitude zones, where the linear angular coefficients **b** are different from 0 with probability higher than .95.

Table 5. Estimates of temperature anomalies **DT** in the period January 1993 - December 1994 in the layer 100 - 50 hPa, for various latitude zones:

b - linear angular coefficient

DT_{ext}- as obtained from linear models (extrapolated)

DT_{calc}- as calculated from 24 monthly anomalies

Zone	b, °C*100/ month	DT_{ext}	DT_{calc}
Globe	-0.22	-0.69	-0.69
North H.	-0.31	-0.98	-0.80
South H	-0.11	-0.35	-0.57
30°S - 0°	-0.15	-0.48	-0.79
0° - 30°N	-0.26	-0.84	-0.67
30°N-60°N	-0.43	-1.38	-0.77

CONCLUSIONS

The stratospheric cooling in the last years was both detected from radiosonde data processed for global network and extrapolated from the model of linear trend based on data for period 1961-1975. As for the Globe the cooling in lower stratosphere was estimated to be close to -.69 deg. C per the period of 318 months (between the middle points of two periods January 1961-December 1975 and January 1993 - December 1994), the decadal cooling may be estimated as equal to -.26 deg.C per decade. Note that the kind of this signal on cooling in lower stratosphere is simple (this enables to obtain predicted anomaly estimates close to the observed ones), and the effect of this signal in various zones is not differing essentially.

The two possible factors that define this evident lower stratospheric cooling, are ozone depletion and carbon dioxide concentration increase. According to current publications, the layer of maximal ozone depletion in the lower stratosphere is just close to 100-50 hPa, i. e. to the layer, for which the temperature anomalies were used in this study. During the last 25 years the decrease of ozone content in this layer for middle latitudes is known to be estimated as 6% per decade.

The observed positive temperature anomalies in troposphere in 1993-1994 are believed to be defined by several factors. Among them: tropospheric warming due to greenhouse gas

effect, volcanic eruption effect, and current phase of ENSO phenomenon effect. Referring to (Christy and McNider, 1993), we shall note that model removal of volcanic eruption effect and ENSO effect enables to estimate tropospheric warming due to greenhouse gas effect with a decadal trend .09°C.
The authors believe that the estimated above stratospheric cooling is an objective. The inhomogeneities in data, which are believed to be serious factor for carefulness in any conclusions on temperature trends in atmosphere, in this situation are hardly able to finally change the conclusions on this stratospheric cooling.

REFERENCES

Alduchov, O. A., 1985, "Complex Quality Control of Geopotential and Temperature in Station Archives of Upper-Air Data". Proc. RIHMI-WDC, 115, pp. 34-63 (in Russian).

Angell, J. K., 1988, "Variations and Trends in Tropospheric and Stratospheric Global Temperatures, 1958-87". Journ. of Climate, vol.1 pp.1296-1313.

Christy, J. R., and R. T. McNider, 1993. "Detecting Global Atmospheric Warming Using a Precise, But Short (15 - Year), MSU Time Series". Proc. XVIII Annual Climate Diagnostics Workshop, NOAA/NWS, pp. 1 - 4.

Gaffen, D. J., 1994, "Temporal Inhomogeneities in Radiosonde Temperature Records", Journ. Geophys. Research, vol. 99 No. D2, pp.3667-3676.

Oort A.H., and Huanzhu Liu, 1993, "Upper-Air Temperature Trends over the Globe, 1958-1989". Journ. of Climate, vol.6 No. 2, pp.292-307.

Reitenbach, R. H., and A. M. Sterin, 1987, "The Free Atmosphere Climatological Characteristics Gridpoint Data Sets Creation Based on Objective Analysis". Proc. RIHMI-WDC, 135, pp. 3 - 45 (in Russian).

Reitenbach, R. H., and A. M. Sterin, 1991, "The Analysis of Free Atmosphere Temperature Seasonal Anomaly Series". Proc. XV Annual Climate Diagnostics Workshop. U.S. Dept. Commerce, NOAA, pp. 365-372.

Reitenbach, R. H., and A. M. Sterin, 1992, "Free Atmosphere Temperature Variations from Historical Radiosonde Data", Proc. of the International Symposium on the Little Ice Age Climate, Ed.: T.Mikami. Tokyo, Japan, pp. 266-274.

Reitenbach, R. H., and A. M. Sterin, 1994, "Temperature Variations in Troposphere and Lower Stratosphere in 1993 - 1994". Proc. XIX Climate Diagnostics Workshop

ACKNOWLEDGMENTS

This study was partially supported by Russian Fundamental Research Foundation (RFFI) grant 95-05-15267a.
The efforts of RIHMI Aerology Department's personnel in upper-air data processing are gratefully acknowledged.

CORRESPONDING AUTHOR

Dr. Rudolf Reitenbach,
Deputy Director
RIHMI-WDC
6, Korolyov str., Obninsk, Kaluga region, Russia, 249020
e-mail: reitenbach@storm.iasnet.com

ASSOCIATION BETWEEN SOLAR-IRRADIANCE VARIATIONS AND HYDROCLIMATOLOGY OF SELECTED REGIONS OF THE USA

Charles A. Perry
U.S. Geological Survey, Lawrence, Kansas, USA

ABSTRACT

Hydrologic time series can be indicators of climate trends and cyclic variations. Although the mechanisms of climatic trends and variations are not completely understood, extraterrestrial solar-irradiance variations may be associated with variations in regional hydroclimatology. A proposed mechanism responsible for the association involves three basic processes: varying amounts of solar energy are (1) absorbed by tropical oceans creating ocean temperature anomalies that (2) move with the ocean currents to locations where they can (3) alter regional atmospheric moisture and pressure patterns which affect regional precipitation and temperature and, consequently, the hydroclimatology of a region. Hydrologic time series in selected regions in the western two-thirds of the United States of America (USA) are shown to correlate with solar-irradiance variations lagged 4-5 years.

1. INTRODUCTION

Water availability is becoming a critical issue as supplies are pressured by an increasing world population; information on hydroclimatic trends and variations is important for wise management of water resources. Hydrologic information, such as streamflow peak discharges and annual flow volumes, lake levels, glacier volumes, and groundwater levels, provide convenient measures of regional climate. Whereas meteorologic data such as precipitation, temperature, radiation, and wind are usually point measurements, hydrologic information is the result of temporal and spatial integration of environmental factors that affect the accumulation of water.

Time series of hydrological data can provide much information on climate trends and variations, and possible forcing factors. For example, the floods in the upper Mississippi River Basin (upstream from the confluence of the Missouri and Mississippi Rivers) were of historic proportions in 1993. Peak discharges and annual flow volumes measured at many stream-gaging stations throughout the basin exceeded previously observed extremes. A peak flow of 30,590 cubic meters per second (m^3/s) occurred on the Mississippi River at St. Louis, Missouri, on August 1, 1993. Peak streamflow records show that the 1993 peak discharge was the largest since 1861 and has been exceeded only by an estimated discharge of 36,820 m^3/s for the historic flood of 1844. Discharge for the flood of 1903, 28,860 m^3/s, was only slightly less than that of 1993. Examination of volume data at the same location since continuous records began in 1934 reveal high volumes of runoff during 1993, 1983, 1973, and 1951. A pattern of major runoff years occurring approximately every 10, 20, 42, and 90 years emerges from this flow data and other flood data within the upper Mississippi River Basin.

Solar activity displays a cyclic pattern of increasing to a peak every 10-12 years. Other multiples of this cyclic pattern are seen in the 20- to 24-year Hale cycle, the 40- to 45-year Double-Hale cycle, and the 80- to 90-year Gleissberg cycle. The floods of 1993, 1983, 1973, 1951, and 1903 tend to follow this pattern. However, projections of solar-activity cycles for estimating future hydroclimatic events have been suspect because there has been no identified physical mechanism to explain the connection between activity on the Sun and regional hydroclimatic patterns on Earth.

Measurements of the Sun's total energy output (total solar irradiance) by Earth satellites show small changes in total energy that generally follow the solar-activity cycle and are providing new information on the controversial solar/climate relation. These variations have been shown to correlate significantly with regional precipitation in various locations in the USA (Perry, 1994). Association between solar-irradiance variations and the hydroclimatology of selected regions of the United States will be presented in this paper.

2. PROPOSED SOLAR/HYDROCLIMATE MECHANISM

The mechanism proposed for the coupling of solar-irradiance variations with regional hydroclimate consists of three main components. These are: (1) absorption of solar energy by the tropical oceans in a deep surface layer, (2) transport of that energy by major ocean currents of the Pacific Gyre, and (3) transfer of that energy by evaporation into atmospheric moisture and atmospheric pressure systems that can be advantageous for precipitation formation (Perry, 1994). The components are depicted in Figure 1.

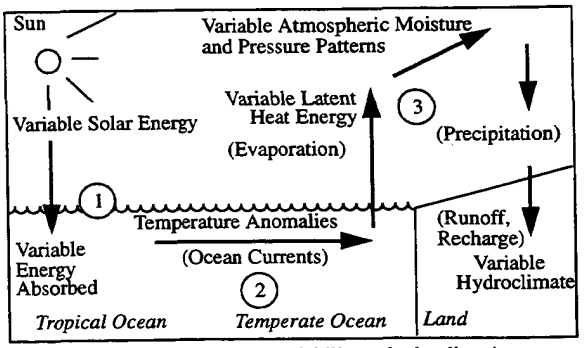


Figure 1. Pathway from solar variability to hydroclimatic variability

A. Absorption of Energy

Although sea surface temperatures (SST) show significant coupling with atmospheric components (Wallace et al. 1990), it is not the ocean's surface that stores the majority of the solar energy. The visible part of the solar spectrum contains about one-half of the total energy available from the Sun at the Earth's surface (Loiv, 1980), and those wavelengths penetrate well below the ocean's surface. Lewis et al. (1990) showed that solar radiation in visible frequencies, usually assumed to be absorbed at the sea surface, penetrates to a significant depth below the upper mixed layer of the ocean that interacts directly with the atmosphere. In clear water, the blue wavelengths, where the greatest amount of energy is available, penetrate the deepest, to nearly 100 meters (m). Energy injected into the ocean at this depth can be stored for a substantial period of time.

The transparency of the tropical oceans is dependent upon the amount of biogenic material, phytoplankton pigments, and degradation products that are present. In the Pacific Ocean, transparency increases from east to west, with the greatest penetration of solar energy occurring in the western tropical Pacific. This stored energy eventually returns to the ocean's surface to interact with the atmosphere as the general circulation of the Pacific Ocean transports water to the north and east toward North America (Figure 2).

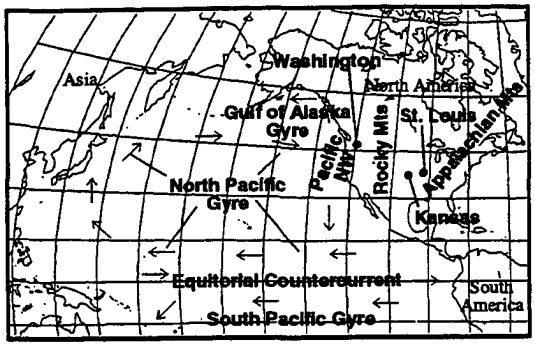


Figure 2. Location and features referred to in this paper

Other factors that affect the amount of solar energy absorbed by the oceans include latitude, season, sea-surface roughness, atmospheric particulates, and cloud conditions. All of these factors contribute in various degrees to the development of anomalous ocean temperatures. However, extraterrestrial solar-irradiance variations may be a significant factor.

B. Transportation of Ocean Temperature Anomalies

The North Pacific Ocean currents take approximately 4 years to move temperature anomalies from the western tropical Pacific to near North America (Favorite and McLain, 1973) In addition, the Equatorial Countercurrent flows eastward between the westward flowing currents of the North Pacific and South Pacific Gyres. Upon this countercurrent rides the elusive oceanic warming of El Nino and the oceanic cooling of La Nina. Another important minor circulation is the counterclockwise flow of the Gulf of Alaska Gyre. The North Pacific Gyre and its minor circulations are the conveyors of absorbed solar energy from the central and western tropical Pacific to locations north and east. If incoming solar energy varies on time scales of months to years, then different parts of the gyre will receive different amounts of solar energy as the water moves through the tropics. During a period of diminished irradiance, a part or pool of the tropical ocean would receive less energy and be anomalously cool, whereas increased irradiance would result in an anomalously warm pool. These pools of slightly warmer or cooler water would move around the Pacific Gyre like riders on a carousel.

C. Transfer of Energy to the Atmosphere

In the tropical Pacific Ocean, the net flux of energy is downward into the ocean, whereas at the higher latitudes this flux is upward. Energy is transferred from the ocean to the atmosphere primarily by evaporation. Evaporation from the surface of the ocean is a mechanism that could amplify the effect of solar-irradiance variations. The vapor pressure of water increases by approximately 7% for each 1 °C of increase in water temperature between 5 and 15 °C. Therefore, a 1 °C positive anomaly in SST could result in about a 7% increase in the amount of energy available to the atmosphere. Variations in the vapor pressure at the sea surface can significantly alter atmospheric moisture fields, from which further amplification of solar-irradiance variations can occur through dynamic atmospheric processes. Energy patterns in the upper atmosphere are responsible for the persistent upper air flow patterns that interact on a global scale. The strength, shape, and location of the jet stream and other motions of the atmosphere, which are critical factors in precipitation formation, are largely dependent upon the temperature patterns of the oceans.

3. SOLAR-IRRADIANCE VARIATIONS

Solar irradiance has been measured in space by sensors on several spacecraft including the Earth Radiation Budget Experiment (ERBE) on the Nimbus-7 satellite, the Active Cavity Radiometer (ACRIM I) that flew on the Solar Maximum Mission (SSM), and an ACRIM II that is presently aboard the Upper Atmospheric Research Satellite (UARS). In Figure 3, the Nimbus-7 data show a sinusoidal variation of more than 3 watts per square meter (W/m^2) over the 14-year period shown, with annual variations of more than 1 W/m^2. Presently (1995), these measurements account for more than 16 years of data. However, 16 years is a short time for comparison with climatic data. Fortunately, two solar-irradiance investigators have developed empirical models for estimating total solar irradiance before 1978 (Foukal and Lean, 1990).

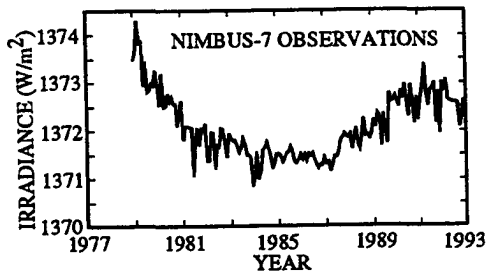


Figure 3. Total solar irradiance measured by NIMBUS-7, 1979-1993 (Kyle, written commun.)

One solar-irradiance model is based on changes in excess radiation from bright magnetic faculae (areas of higher irradiance on the Sun's disk) and on changes in reduced radiation from dark sunspots. Using this model, estimates of bright magnetic faculae were made back to 1954 using daily flux 10.7-centimeter (cm) wavelength (Lean and Foukal, 1988). Estimates of irradiance were later extended back to 1874 by Foukal and Lean (1990) in a second model using monthly means of the sunspot number in place of the 10.7-cm flux. Because the 10.7-cm flux was not measured before 1947, the 42-year period (1947-88) of monthly values of irradiance is assumed to have a greater reliability than the values for the period from 1874-1946. Irradiance values generated by the 1990 model are depicted in Figure 4.

This paper is based on the hypothesis that increases or decreases in solar irradiance have an effect on regional hydroclimate. Increased irradiance creates warmer pools of Pacific Ocean water that are transported to a location where increased evaporation leads to increased precipitation and ultimately increased terrestrial water. The opposite is hypothesized for decreasing irradiance. Because of the process of ocean temperature-anomaly formation, a time series of differences of average annual solar irradiance were determined (Figure 5), based on the model-generated values (Foukal and Lean, 1990.

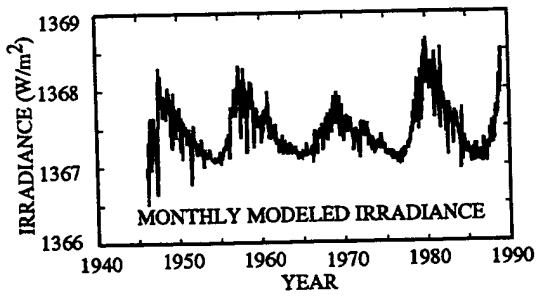


Figure 4. Monthly modeled irradiance, 1947-88 (Foukal and Lean, 1990)

To obtain a series of annual solar-irradiance values, a series of 13-month averages of monthly irradiance values centered on July were determined. An annual difference was computed by subtracting one year's average from the previous year's average.

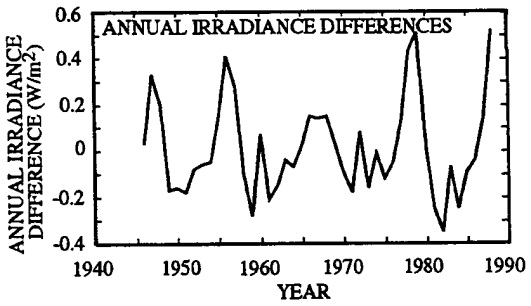


Figure 5. Annual difference in total solar irradiance 1947-88

4. IRRADIANCE VARIATIONS COMPARED WITH HYDROCLIMATOLOGIC TIME SERIES

Solar-irradiance variations and hydroclimatic time series in selected regions within the USA were correlated to test the proposed hypothesis that a solar/hydroclimate association exists. Examples of time series for precipitation, glacier mass, groundwater levels, and flow volumes of a major river basin were compared to a time series of solar-irradiance variations.

A. Precipitation

Regional annual average precipitation was the initial hydrologic variable compared to annual solar-irradiance variations (Perry, 1994). Correlations were performed at eight different lag times ranging from 0 to 7 years for the 344 meteorological regions in the USA. Correlation coefficients (R>0.4, significant at the 1% level) were obtained in several major sections of the country and at several different lag times. The highest correlations were obtained in the Pacific Northwest with a lag time of 4 years. This time coincides with the average time of travel of ocean water from the western tropical Pacific to the Gulf of Alaska (Perry, 1994). A comparison of 3-year moving averages of solar-irradiance variations lagged 4 years and precipitation in a meteorological region in the Pacific Northwest is shown in Figure 6.

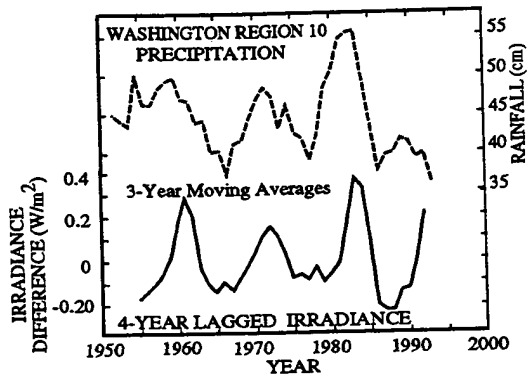


Figure 6. 3-year moving averages of Washington meteorological region 10 precipitation and solar-irradiance variations lagged 4 years

B. Glacier Mass Balance

The South Cascade Glacier in the State of Washington is also in the Pacific Northwest located approximately 400 kilometers (km) northwest of Washington meteorological region 10. Variations in the glacier's mass balance is a result of the interaction of precipitation, temperature, wind, humidity, and insolation on the snow and ice within a 6.12 square kilometer (km^2) basin ranging in elevation from 1,615 to 2,518 m (Krimmel, 1994). In Figure 7, a 3-year moving average for both the solar-irradiance variations lagged 4 years and the glacier mass balance (expressed as change in thickness) is depicted.

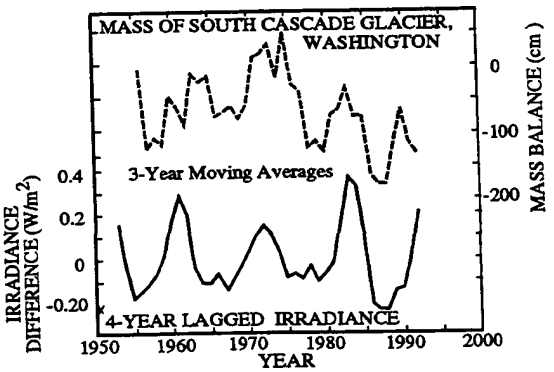


Figure 7. 3-year moving averages of the mass balance of the South Cascade Glacier and solar-irradiance variations lagged 4 years

C. Groundwater Levels

Groundwater levels are also responsive to variations in the hydroclimatology of a region. Water levels in an observation well located in a shallow aquifer in Osborne County, Kansas (central USA) shows some similarity at times with solar-irradiance values lagged 5 years (figure 8). Many other shallow wells in this area of the country show similar patterns. However, factors such groundwater pumpage, irrigation, and land use can complicate the response of groundwater levels to hydroclimatic variability.

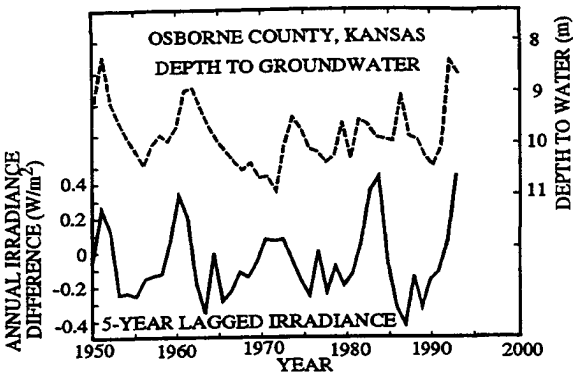


Figure 8. Groundwater levels in a shallow aquifer in Osborne County, Kansas, and solar-irradiance variations lagged 5 years

D. River Volume

The average annual flow of a river is the total volume of water produced by runoff and groundwater discharge and is an integration of many climatic as well as hydrologic factors over the river basin. The Mississippi River Basin measured at St. Louis, Missouri, encompasses slightly more than 2 million km^2, draining more than one-fourth of the area of the 48 contiguous United States. Figure 9 shows the annual average flow of the Mississippi River at St. Louis and annual solar-irradiance differences. The best correlation is obtained with a 5-year lag time. The correlation coefficient for these data is R=0.52, significant at the 1% level. An approximate 5-year lag is apparent for other basins and subbasins between the Rocky Mountains and the Appalachian Mountains, as opposed to the 4-year lag time observed in the Pacific Northwest. A possible explanation for the greater lag time may be in the more eastward location of the ocean temperature anomalies in the Pacific Ocean that affect atmospheric dynamics over the midsection of the United States than over the Pacific Northwest. An additional year may be needed to move the ocean temperature anomalies farther to this location.

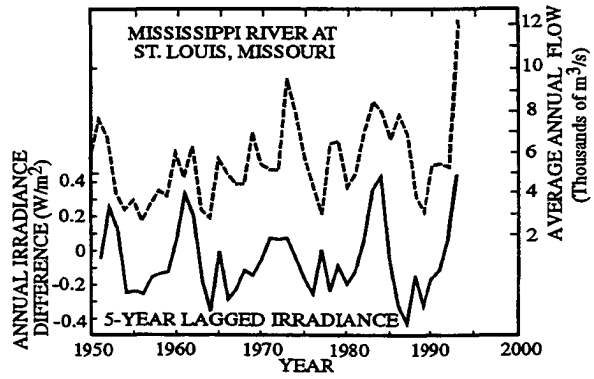


Figure 9. Average flow of the Mississippi River at St. Louis, Missouri, and solar-irradiance variations lagged 5 years

An intriguing observation of individual graphical correlations of annual solar-irradiance variations with annual precipitation and streamflow in the United States is an apparent change in effective lag times for a specific location. Prior to the mid-1970's, lag times were slightly less than lag times after the mid-1970's. This point in time coincides with an apparent shift in atmospheric pressure patterns and with an increase in global surface air temperatures recorded at land-based stations (Graham, 1995).

5. CONCLUSIONS

Comparison of hydroclimatologic times series from selected regions in the USA with variations in annual solar irradiance, provides apparent support for a solar/hydroclimate association. The mechanism for this association is thought to begin with variations in the amount of solar-irradiance energy absorbed by the tropical Pacific Ocean, which result in ocean temperature anomalies that are transported by major oceanic currents to locations where the process of evaporation transfers latent-energy variations to the atmosphere. Variations in atmospheric moisture and pressure patterns ultimately affect the amount of regional precipitation. Variations in precipitation, along with the effects of temperature, humidity, wind, and insolation, determine the long-term regional water budget and, therefore, the hydroclimate of a region.

There is a tendency for hydroclimatologic time series to lag solar-irradiance variations by 4 years in the Pacific Northwest and 5 years in the midsection of the United States. These lag times are similar to the traveltimes of water from the tropical Pacific Ocean to the Gulf of Alaska. Although variations in solar irradiance may be only one component of the complex process of precipitation formation, it is a component that could prove valuable in long-term hydrologic risk assessment due to the 4-5 year lag time between solar-irradiance input and the resultant response by a hydrologic basin.

REFERENCES

Favorite, Felix, and McLain, D. R., 1973, "Coherence in transpacific movements of positive and negative anomalies of sea surface temperature, 1953-60", Nature, Volume 244, pp. 139-143.

Foukal, P., and Lean, J., 1990, "An empirical model of total solar irradiance variation between 1874 and 1988", Science, Volume 247, pp. 556-559.

Graham, N.E., 1995, "Simulation of recent global temperature trends", Science, Volume 267, pp.666-671.

Krimmel, R.M., 1994, "Runoff, precipitation, mass balance, and ice velocity measurements at South Cascade Glacier, Washington, 1993 balance year", U.S. Geological Survey Water-Resources Investigations Report 94-4139, 35 p.

Kyle, H.L., (written commun.) NASA/GSFC, NSSDC, Greenbelt, Md.

Lean, J., and Foukal, P., 1988. "A model of solar luminosity modulation by magnetic activity between 1954 and 1984", Science, Volume 240, pp. 906-908.

Lewis, M.R., Carr, M., Feldman, G.C., Esaias, W., and McClain, C., 1990, "Influence of penetrating solar radiation on the heat budget of the equatorial Pacific Ocean", Nature, Volume 347, pp. 543-545.

Liov, K.N., 1980, "An introduction to atmospheric radiation", Academic Press, New York, 392 p.

Perry, C.A., 1994. "Solar-irradiance variations and regional precipitation fluctuations in the western USA, International Journal of Climatology, Volume 14, pp. 969-983.

Wallace, J.M., Smith, C. and Jiang, Q. 1990 "Spatial patterns of atmosphere-ocean interaction in the northern winter", Journal of Climate, Volume 3, pp. 990-998.

CORRESPONDING AUTHOR
Dr. Charles A. Perry
U.S. Geological Survey
4821 Quail Crest Place
Lawrence, Kansas 66049 USA

SELF-SIMILARITIES, LINKS, AND WARMING TRENDS OF GLOBAL CLIMATE DYNAMICS: THEIR DETECTIONS AND PREDICTIONS

D.M. Sonechkin

Hydrometeorological Research Centre of Russia, Moscow, Russia

ABSTRACT

Last years fractal self-similarities of nature draw increasing attention of meteorologists. We study such properties of extended meteorological data time series by means of multifractal techniques, in particular, by wavelet transform of time series of interest.

We conclude that among many climatic processes the Southern Oscillation is prominent. The process seems to be the conductor of a chronology of main epochs of the current climate: before 1900s, between 1900s and 1940s, and between 1940s and 1980s. Large oscillations of the surface air temperature, which are quantitatively different but qualitatively similar and coupled with the Southern Oscillation, exist in both Hemispheres. These oscillations are imposed on the single warming trend that was started from 1900s.

We speculate that the today's global warming will be checked during the XXth century end.

1. INTRODUCTION

Looking at the well-known time series of the global, Northern, and Southern Hemisphere surface air temperature almost all of us agree to some general warming is real. But, substance of the warming is rather vague. Our interest here is to find out the ingredients of the warming those suit to be predictable in the nearest future. To do it, we have used wavelet transform of the above time series.

The series may be modelled (see the pioneering works of Budyko (1949, 1969 etc)) by the heat balance equation. Because the heat balance value is a rather erratic quantity the balance equation needs to be a form of the so-called fractional Brownian motion (fBm) (Mandelbrot and Van Ness (1968)). It is very important, even if the balance value forms a statistically steady sequence the fBm (=air temperature dynamics) is always nonsteady, and so, the air temperature dynamics does not admit a Fourier spectrum in the usual sense. It is a reason of numerous misunderstandings those come across the meteorologists who use traditional statistical tools for the climate change studying. It needs to be noted that statistical properties of the balance value, like such properties of any fBm increment, only depend on the time period on which the value is calculated. If the period is changed by a positive factor, then the balance value needs to change (in a statistical sense) by the factor of a certain power. This property is known as self-affinity.

So, two features are to be taken into account when analysing the climate change problem: nonsteady, which necessitates some time dependent analysis, and self-affinity, which necessitates some scale dependent one. A new powerfull tool of the so-oriented analysis is wavelet transform (Combes et al (1989), Chui (1992), Datsenko and Sonechkin (1993)) of a time serie of interest.

2. WAVELET TRANSFORM OF THE SOI DYNAMICS

We have used continuous real wavelet transform with the well-known "Mexican hat" wavelet function to study SOI dynamics in very different time scales (Figure 1).

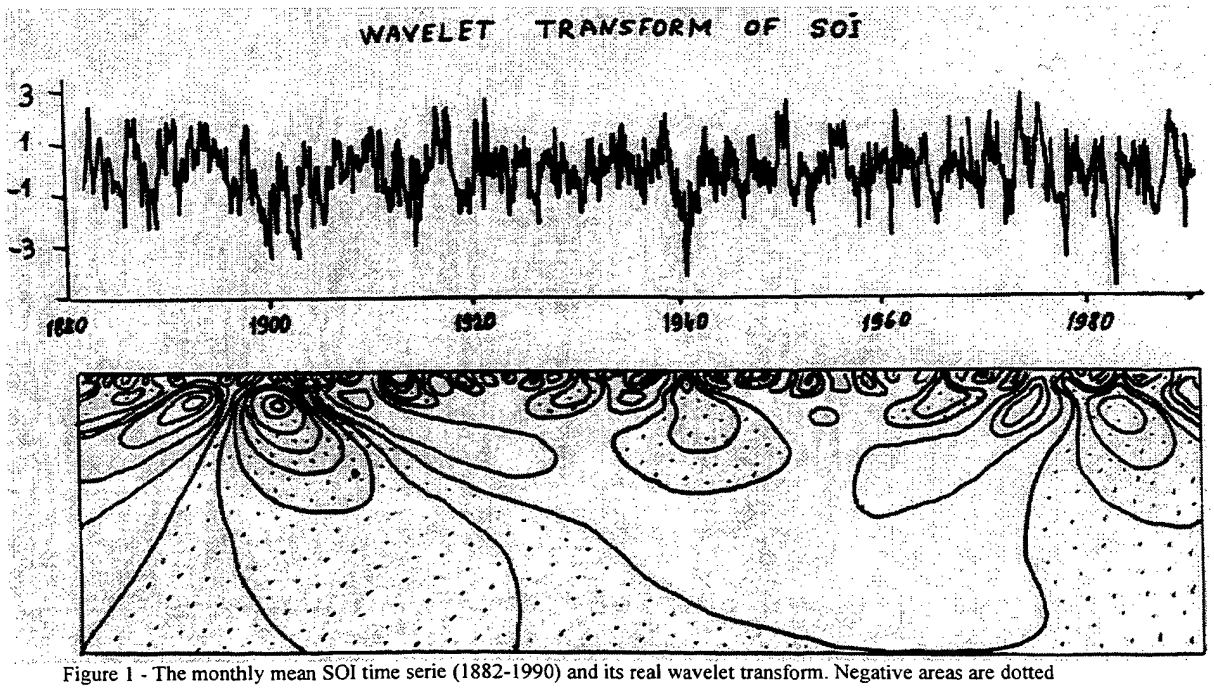


Figure 1 - The monthly mean SOI time serie (1882-1990) and its real wavelet transform. Negative areas are dotted

Our conclusion is that there exist three main self-similarly repeating epochs those boundaries are the strongest El-Nino events: 1898-1900, 1940-1941, and 1982-1983. A new epoch probably was started after 1983. This finding agrees well with a recurrence of "proxy evidenced" very strong ancient El-Ninos (1844-1846, 1790-1793, 1694-1695 etc). Each of these epochs may be redivided into shorter time periods those dynamics to be diminished copies of a main epoch. So, there exist rather high correlations between the SOI values of these periods on the condition that corresponding rescalings are fulfilled. Therefore, the SOI time serie displays some recurrences or approximative repeatings of itself as well. The phenomenon can be used to predict macro-scale features of SOI dynamics for a few decades ahead. More detailed predictions can be created by means of some few-component mappings for sequences of extrema (and corresponding time intervals between those) like the well-known in the dynamical systems theory circle- or annulus-mapping ontoitself.

3. WAVELET TRANSFORM OF THE AIR TEMPERATURE DYNAMICS

The next series of our scope are the global and both hemispherical surface air temperature ones. Their continuous real wavelet transform patterns of the time scales less 30-50 years are approximative negative copies of the corresponding SOI wavelet transform patterns (Figure 2). Three main edges of the temperature series are located near the same time moments as those of the above strongest El-Ninos: the XXth century beginning is an apparent start of a general warming, 1940s is a switch from the warming to a cooling (or stabilization within the Southern Hemisphere), 1980s is a warming restart.

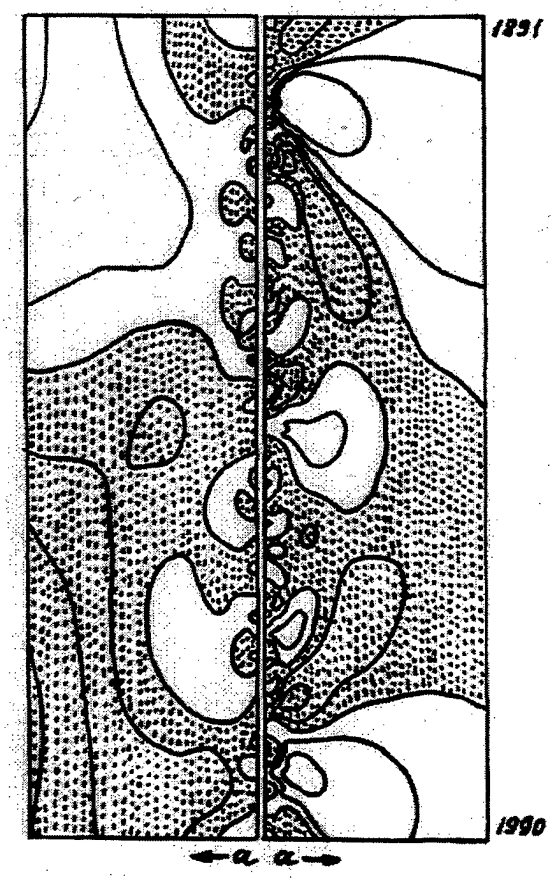


Figure 2. The comparison of the wavelet transforms of the SOI (right) and the global surface air temperature (left)

The above links between different wavelet transform patterns manifest complex couplings between different parts of the global climate system. In exeptional cases, the links are rather simple. An example is the correlation between the corresponding wavelet transform values of the Northern and Southern Hemispheres (Figure 3). In Figure 3 are compared the continuous wavelet transforms of the Northern and Southern Hemisphere surface air temperature time series from Jones et al (Trends'91). One can see that these wavelet transform patterns seem to be very similar. Almost each branch of the Northern Hemisphere pattern has a counterpart in the Southern Hemisphere one. Some of such pairs of the counterparts are almost synchronous in time. But, it is more often that there exists a certain vis-a-vis temporal lag of the counterparts. In order to estimate a quantitative manner such an interhemispherical coupling of the surface air temperature dynamics we calculated the correlation coefficients between the both hemispherical wavelet transform values of some selected time scales. The following sequence of the correlation coefficients were obtained: R(1)=0.63, R(2)=0.65, R(4)=0.71, R(8)=0.68, R(16)=0.74, R(32)=0.98, and R(64)=0.997, where the time scale (in years) are shown in brackets. As a result, we recognize that there exists one single linear warming trend of the both hemispherical air temperature dynamics of the scales up of a century. In order to extract the trend one needs to use the so-called discrete orthogonal wavelet transform of time series of interest. The transform consists in calculation of wavelet transform of a discrete set of its scale and position parameter values, and than in reconstruction of the primary serie taking into account only a limited range of the scales less a century. These inverse wavelet transforms of both Hemispheres are shown in Figures 4 and 5.

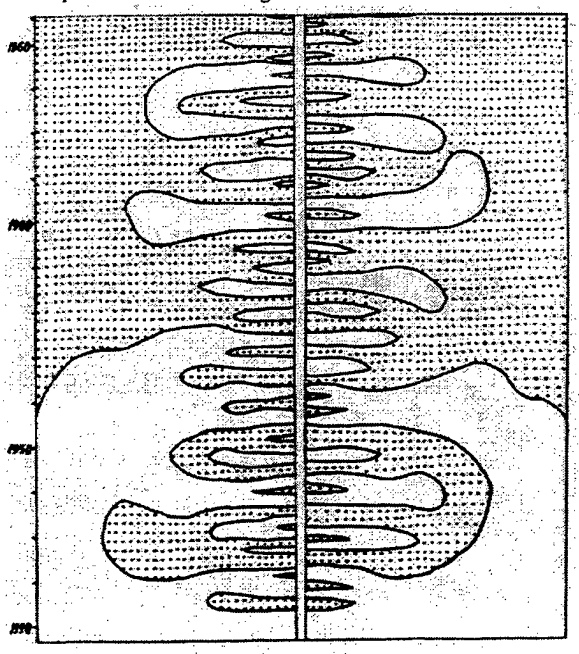


Figure 3. The comparison of the wavelet transforms of the Northern (left) and the Southern (right) surface air temperatures

One can see two different versions of the inverse wavelet transform together with the corresponding primary air temperature time series and two versions of residual trends which were revealed by means of subtractions of the reconstructed series from the primary ones.

Although the residual trends are aggrevated by observational and calculational noises of wavelet transforms and their inversions, one can easily recognize linear warming trends which started in the same time moment closes to 1900 in the both series.

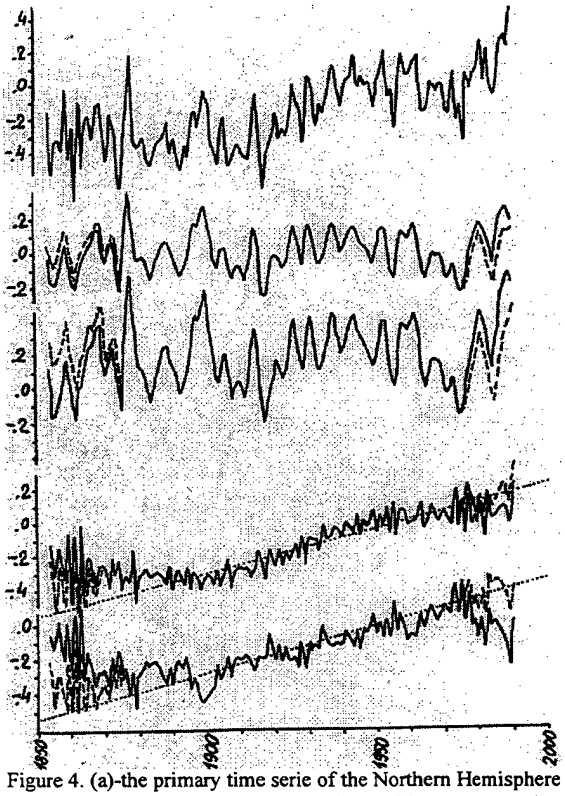


Figure 4. (a)-the primary time serie of the Northern Hemisphere surface air temperature, (b)-two versions of its reconstruction by an inverse wavelet transform, (c)-two versions of its low-pass residual. Estimations of the trend are shown by dotted lines

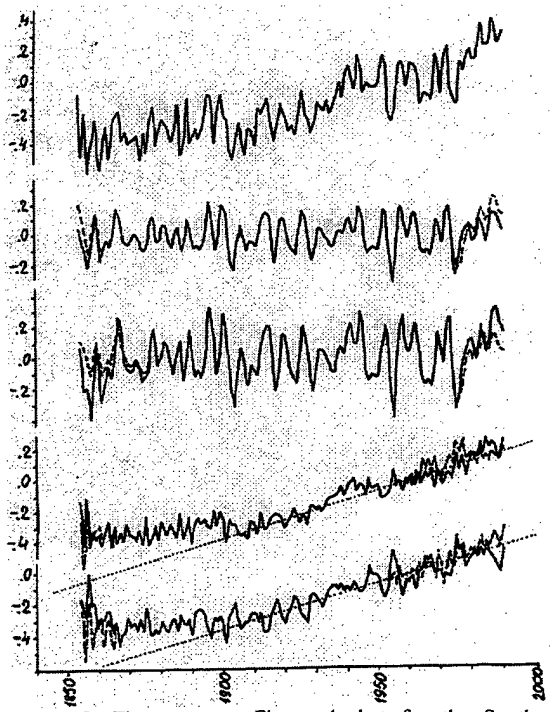


Figure 5. The same as Figure 4, but for the Southern Hemisphere

The rootmeansquare fits of the residual trends, which are necessary in order to eliminate the above noises, are shown by dotted lines. Bearing in mind the noisy magnitude, the distinction between the hemispherical trends is unessentional. Large statistically steady oscillations, which include within themselves all differences between the Northern and Southern Hemisphere temperature time series, are imposed on the trend. The contribution of the oscillations into the general warming is positive one during 1980-1990s. So, these (internally induced ?) oscillations determine the strong warming of the today's climate.

4. CONCLUSION

Our study of self-similar properties of extended meteorological data time series by means of their wavelet transform resulted in extractions main epochs and a single warming trend of the global climate system. The system appeares as an indissoluble whole in this study. Because of the reasons that main sources of the greenhouse gases situated in the Northern Hemisphere mainly, and, at the same time, we see the absence of any trend delay between the Hemispheres we voice our doubts respect to the greenhouse gas origin of the trend. Irrespective of the true origin of the trend, we believe that the trend will be preserved during the XXth century end, but , on the other hand, the contribution of the wavelet oscillations will become negative. So, we speculate that the warming will be checked in nearest future.

References

Budyko, M.I., 1949: The heat balance of the Northern Hemisphere, Trudy of the Main Geophysical Observatory (in russian), **18**, 5-22

Budyko, M.I., 1969: The effect of solar radiation variations on the climate of the Earth, Tellus, **21**, 611-619

Chui, C.K., 1992: An introduction to wavelets, Academic, Boston, 266 pp.

Combes, J.M., Grossmann, A. and Tchamitchian, Ph. (eds.), 1989: Wavelets, Springer, Berlin, 315 pp.

Datsenko, N.M. and Sonechkin, D.M., 1993: Wavelet analysis of time series and atmospheric dynamics, Applied Nonlinear Dynamics (in russian), **1**, 9-14

Mandelbrot, B.B. and J.W. Van Ness, 1968: Fractional Brownian motion, fractional noises and applications, SIAM Review, **10**, 422-437

CORRESPONDING AUTHOR

Professor Dmitry M. Sonechkin,
Hydrometeorological Research Centre of Russia,
Bolshoy Predtechensky lane, 9/13,
Moscow 123242, RUSSIA
E-mail: RUSGMC@GLAS.APC.ORG

TREND AND CORRELATION ANALYSIS 1961 - 1990 OF EUROPEAN SURFACE AND RAWINSONDE DATA

J. Rapp and C.-D. Schönwiese

University of Frankfurt a. M., Germany

ABSTRACT

On the base of a 72 stations European rawinsonde network covering the period 1961 - 1990 a trend analysis is performed where temperature and geopotential height are considered. Moreover, related surface temperature, pressure and precipitation data are analysed. The results are presented in two-dimensional trend charts for different levels and seasons and imply homogeneity tests, trend-to-noise ratios, as well as the non-parametric Mann-Kendall test. Finally, a correlation analysis reveals some relationships of the field characteristics of the different climatic variables.

1 DATA BASE AND METHOD OF ANALYSIS

In an earlier paper (Schönwiese et al., 1993, 1994) we analysed the linear trends 1891 - 1990 or 1961 - 1990, respectively, of the following European (15° W - 50° E, 35 - 72° N) monthly, seasonal, and annual surface climate variables: air temperature, air pressure, air humidity and precipitation. All these time series passed a system of homogeneity tests leading to a network of 117 stations (at the most) which seems to represent homogeneous or nearly - homogeneous records. Representativeness was checked by a station-to-station correlation analysis. Then, trend charts were evaluated using a 3° x 3° grid and the Kriging interpolation scheme (Brown and Eischeid, 1992). Finally, this two-dimensional field analysis was completed by the computation of trend-to noise ratios (using the standard deviation as a proxy of noise) and the confidence of the results was estimated using the Mann-Kendall test (Sneyers, 1990).

We now add a similar analysis of upper air data based on a 72 stations European rawinsonde network, consider temperature and geopotential height (850 - 30 hPa), and compare the related trend charts with those of the related surface data. Moreover, we look on variable-to-variable correlations. In the following, however, only a few results are summarised. For detailed reports see Bayer et al., 1994; Schönwiese et al., 1993 (in addition, Schönwiese et al., 1994; Meyhöfer et al., 1995).

2 SOME SELECTED TREND RESULTS

Similar to the secular period 1891 - 1990 (Schönwiese et al., 1993, 1994), also in 1961 - 1990 the prevailing surface air temperature feature is a pronounced winter warming, see Figure 1. However, this behaviour is not uniform in space, the maximum warming appears in Central and Eastern Europe, and there is also a cooling area existent (Northern Scandinavia). In summer, again warming is prevailing but less pronounced than in winter, and a relatively large area of SE Europe shows a cooling (spring and autumn not presented). As far as the upper air temperature is concerned, in Figure 2 the 500 hPa level is selected. Due to better representativeness (higher station-to-station correlations) the trend contour lines appear to be more smoothed. The qualitative result is again that a temperature rise prevails where a maximum warming (> 2 K) is indicated in the Mediterranean winter (secondary maximum in the Eastern European winter) whereas in summer the maximum warming (> 1 K) is found in the Atlantic sector (uncertain due to poor station coverage); note also a summer cooling in SE Europe (similar to the surface data).

The few selected temperature trend profiles shown in Fig. 3 confirm that in all seasons (with the uncertain exception of Kiev, autumn) all the troposphere has warmed within the recent decades and the stratosphere has cooled. Such a behaviour is roughly consistent with the climate change predictions due to the enhanced greenhouse effect (Hougthon et al., 1990, 1992). However, the regional characteristics which are unreliable in case of global climate model predictions differ from level to level and from season to season in the observations. Moreover, the confidence of the observed temperature trends is rather weak exceeding seldom a Mann-Kendall test value of 2 (corresponding to approximately < 5% error probability), see Figure 3. (In relation to Figure 2 the Atlantic region summer and Mediterranean winter warmings are confident at the 5% level).

In case of sea level pressure, see Figure 4, the predominant feature is an outstanding intensification of the zonal flow (decreasing pressure in the area of the Icelandic low pressure system, increasing Azores high pressure system) in winter within the recent decades (see also Flohn et al., 1990) which is evident also in the 500 hPa geopotential height, see Figure 5. In summer , the contrary is indicated (see again Figure 5, increasing pressure in the area of the Icelandic low pressure system) where generally the spatial patterns of the tropospheric geopotential height are quite similar to those of the sea level pressure.

Precipitation, see Figure 6 (surface data), has significantly decreased in the Mediterranean winter. In Central and NW Europe increasing winter and decreasing summer precipitation was observed within the recent decades.

3 A LOOK ON VARIABLE-TO-VARIABLE CORRELATIONS

The analysis of the correlation of the different climatic variables previously described in terms of trend charts shows some interesting results, especially in the middle troposphere. It seems that the geopotential height in 500 hPa is more correlated with precipitation, see Figure 7, than with sea level pressure, where maximum numbers of roughly r = - 0.6 arise (British Isles and Denmark in summer). The correlation between the geopotential height in 500 hPa or sea level pressure, respectively, and the air temperature (Figures not shown) reveals a different behaviour in Northern and Southern Europe. We have reason to believe that the typical maritime and continental conditions may be a cause of this behaviour.

4 CONCLUSIONS

Within the 1961 - 1990 (recent CLINO = climate normal) period European climate has changed in a rather complicated way so that the two-dimensional change patterns (trend field charts) differ from variable to variable, from level to level, and from season to season. Only a few of these trends exceed the 5% confidence level. Most important is a tropospheric warming, especially in winter, an intensification of the zonal flow (meridional pressure gradient) in winter, more dryness in the Mediterranean winter, and a tendency to drier Central/NW European summers, simultaneously to wetter winters in the same area. Although some of these trends are similar to

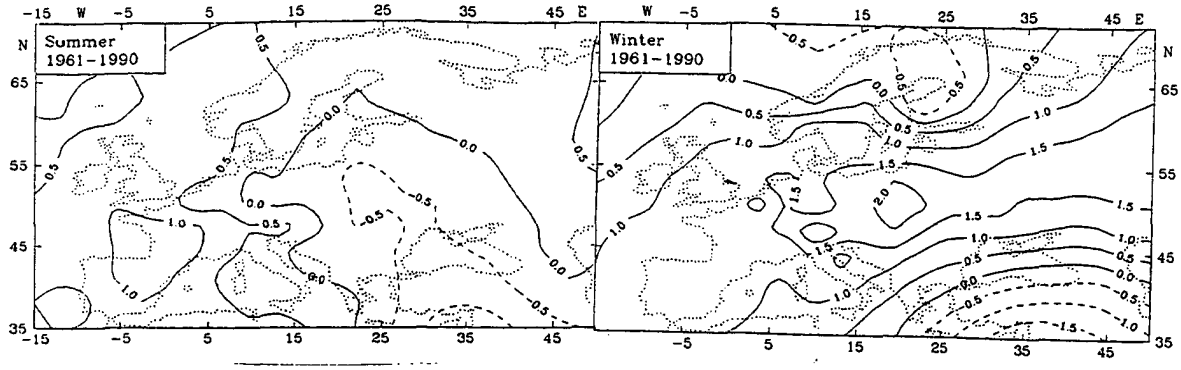


Figure 1a. Surface air temperature trends 1961 - 1990 in K, summer.

Figure 1b. Similar to Fig. 1a, but winter.

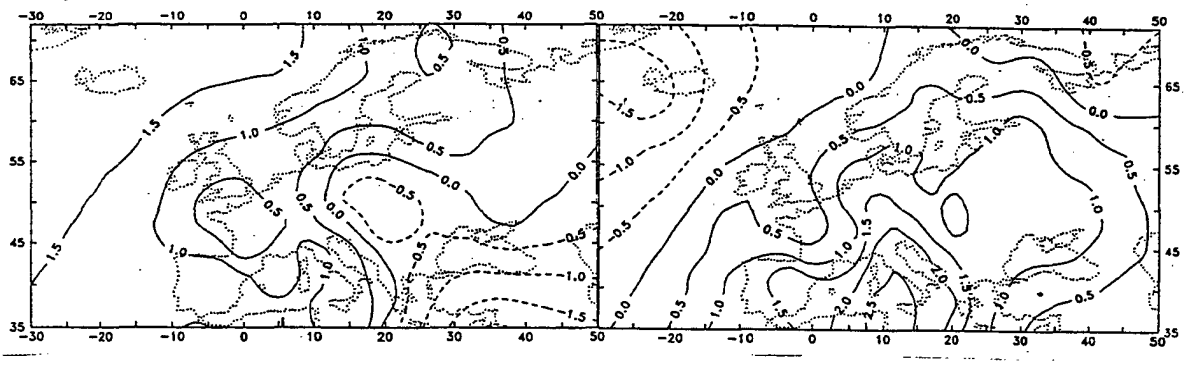


Figure 2a. 500 hPa temperature trends 1961 - 1990 in K, summer.

Figure 2b. Similar to Fig. 2a, but winter.

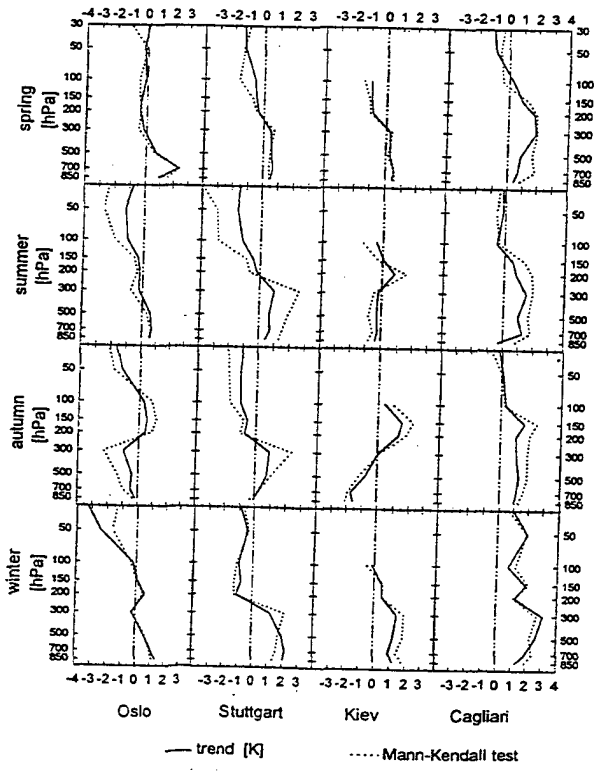


Figure 3. Temperature trend 1961 - 1990 profiles at selected stations, all seasons.

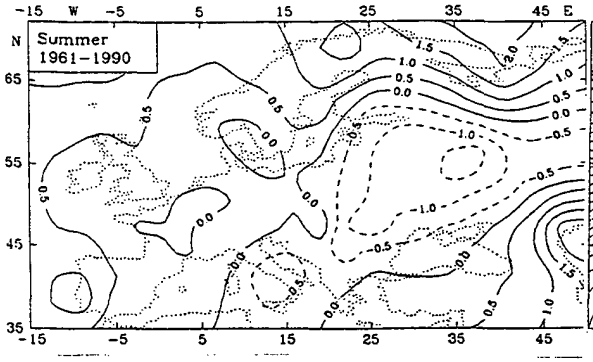


Figure 4a. Mean sea level air pressure trends 1961 - 1990 in hPa, summer.

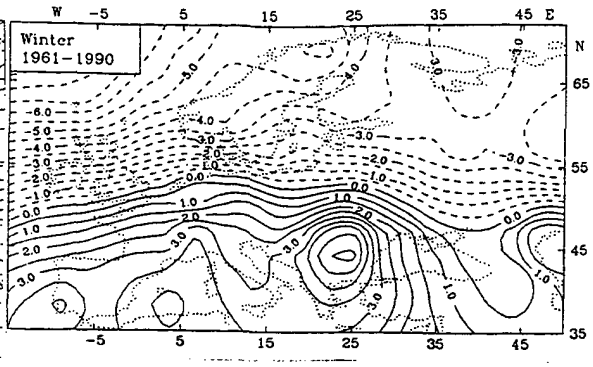


Figure 4b. Similar to Fig. 4a, but winter.

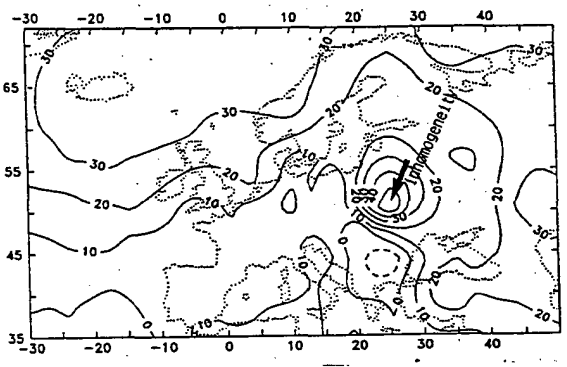


Figure 5a. 500 hPa geopotential height trends 1961 - 1990 in gpm, summer.

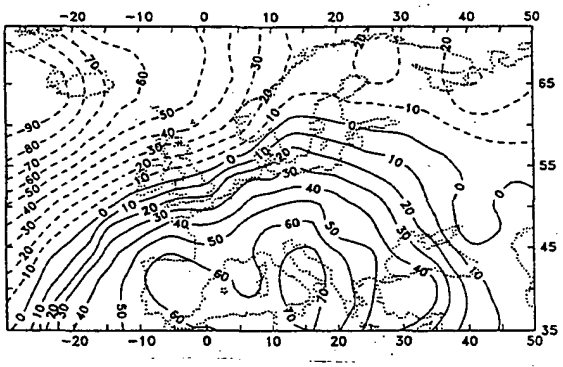


Figure 5b. Similar to Fig. 5a, but winter.

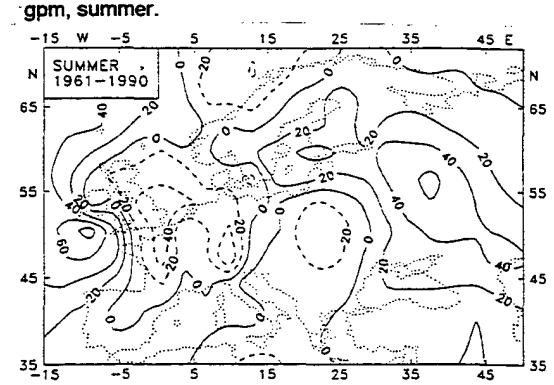


Figure 6a. Precipitation (surface) trends 1961 - 1990 in mm, summer.

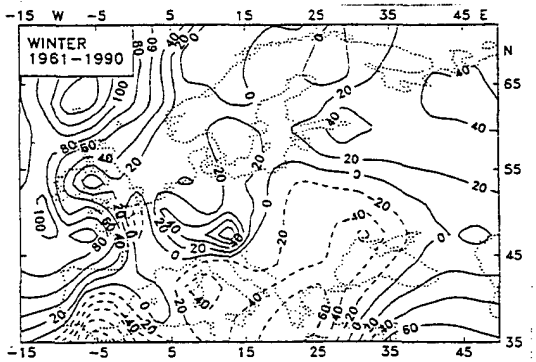


Figure 6b. Similar to Fig. 6a, but winter.

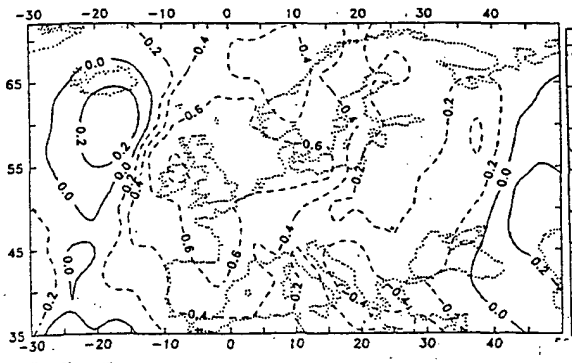


Figure 7a. Pearson correlation coefficients of 500 hPa geopotential height and (surface) precipitation 1961 - 1990, summer.

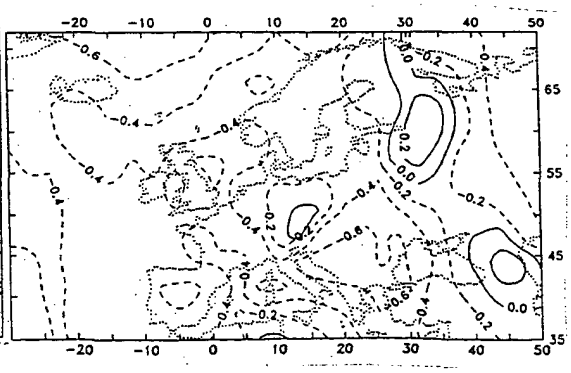


Figure 7b. Similar to Fig. 7a, but winter.

climate model predictions simulating the enhanced greenhouse effect, a causal interpretation is difficult. In this situation it is not clear whether these trends may continue or not because alternatively they may be an effect of relatively low-frequent natural fluctuations.

REFERENCES

Bayer, D., Denhard, M.,Meyhöfer, S., Rapp, J., Schönwiese, C.-D., 1994, „Trend- und multiple Signalanalyse globaler bzw. europäischer Klimavariationen", Report No. 98 Inst. Meteorol. Geophys. Univ. Frankfurt/M,172 pp.

Brown, T.J., Eischeid, J.K., 1992, „An examination of spatial statistical techniques for interpolation of gridded climate data", Joint Proc. Amer. Meteorol. Soc./Environment Canada, 12th Conf. Prob. Statis. Am. Sci./ 5th Internat. Meeting Statist. Climatol., Toronto, pp. 739 - 742.

Flohn, H., Kapala, A., Knoche, H.R., Mächel, H., 1990, „Recent changes of the tropical water and energy budget and of midlatitude circulations", Climate Dyn., Vol. 4, 237 - 252.

Hougthon, J.T., Jenkins, G.J., Ephraums, J.J., 1990, „Climate Change. The IPCC Scientific Assessment", Cambridge Univ. Press, Cambridge, 365 pp.; 1992, „Supplementary Report", 200 pp.

Meyhöfer, S., Rapp, J., Schönwiese, C.-D., 1995, „Observed three-dimensional climate trends in Europe 1961 - 1990", submitted to Meteorol. Z.

Schönwiese, C.-D., Rapp, J., Fuchs, T., Denhard, M., 1993, „Klimatrend-Atlas Europa 1891 - 1990, Report No. 20, Center Environm. Res. Univ. Frankfurt/M. 210 pp.(„Climate Trend Atlas Europe 1891 - 1990", engl. ed. in prep., Kluwer, Amsterdam).

Schönwiese, C.-D, Rapp, J., Fuchs, T., Denhard, M., 1994, „Observed climate trends in Europe 1891 - 1990", Meteorol. Z., N. F., Vol. 3, 22 - 28.

Sneyers, R., 1990, „On the Statistical Analysis of Series of Observations", WMO Publ. No. 415, Geneva, 192 pp.

ACKNOWLEDGEMENT

This study was partly supported by the German Climate Research Programme (BMBF, Project Numbers 07KFT16/5 and 07VKV01/1). This is gratefully acknowledged.

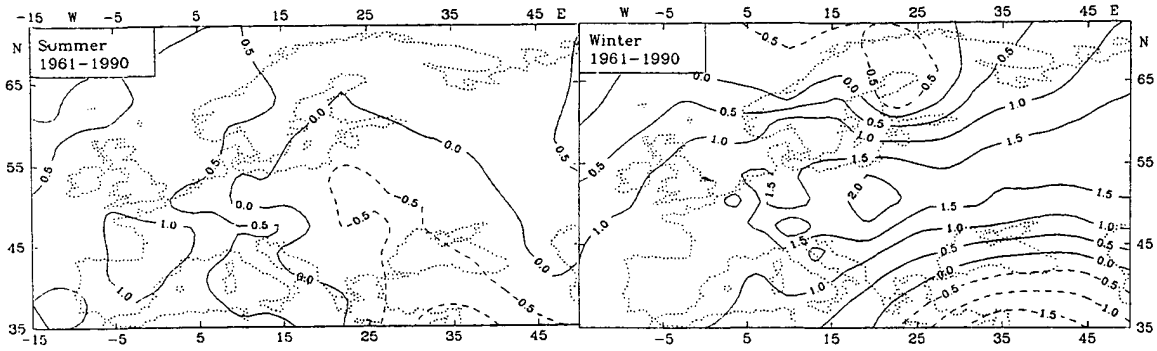


Figure 1a. Surface air temperature trends 1961 - 1990 in K, summer.

Figure 1b. Similar to Fig. 1a, but winter.

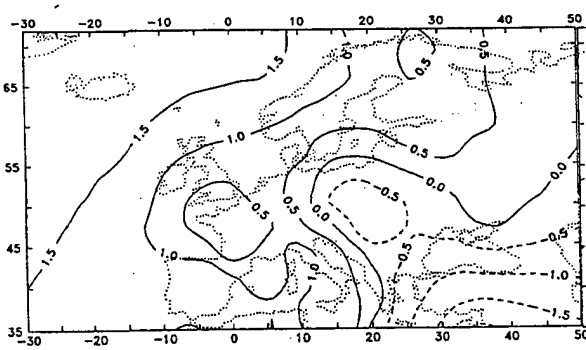


Figure 2a. 500 hPa temperature trends 1961 - 1990 in K, summer.

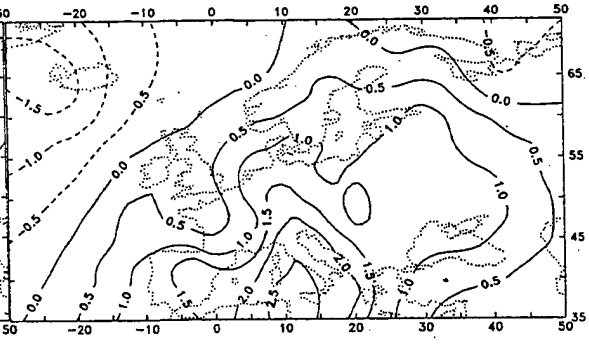


Figure 2b. Similar to Fig. 2a, but winter.

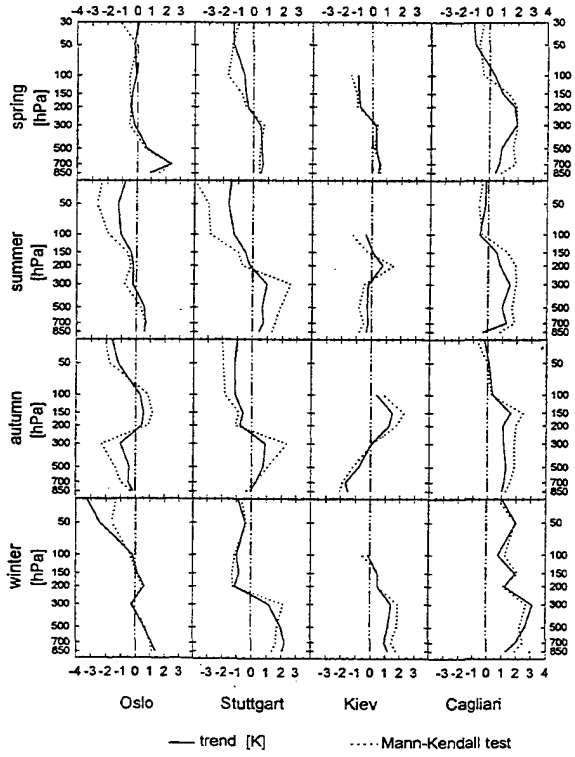


Figure 3. Temperature trend 1961 - 1990 profiles at selected stations, all seasons.

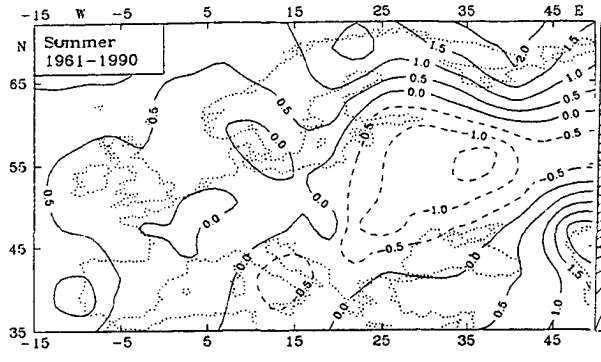


Figure 4a. Mean sea level air pressure trends 1961 - 1990 in hPa, summer.

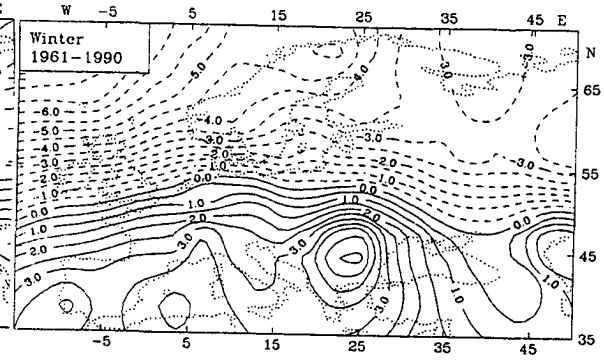


Figure 4b. Similar to Fig. 4a, but winter.

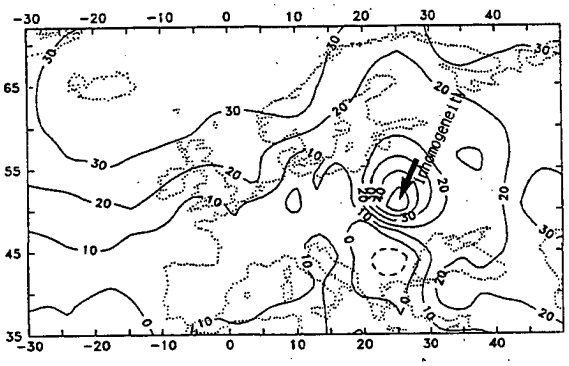


Figure 5a. 500 hPa geopotential height trends 1961 - 1990 in gpm, summer.

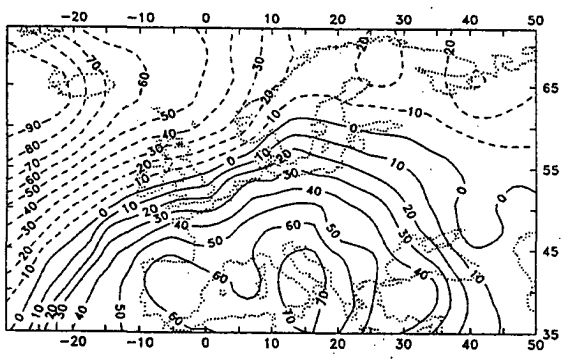


Figure 5b. Similar to Fig. 5a, but winter.

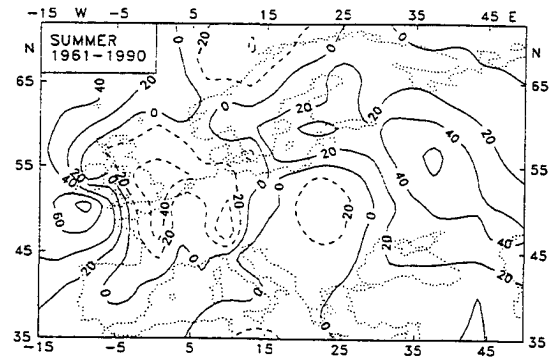


Figure 6a. Precipitation (surface) trends 1961 - 1990 in mm, summer.

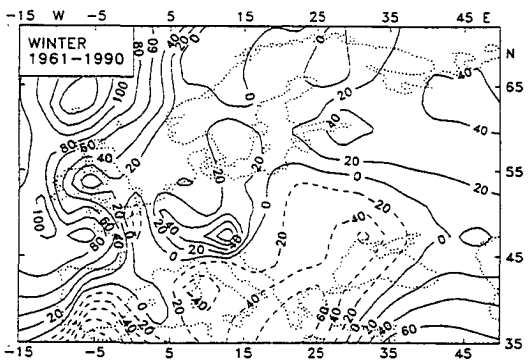


Figure 6b. Similar to Fig. 6a, but winter.

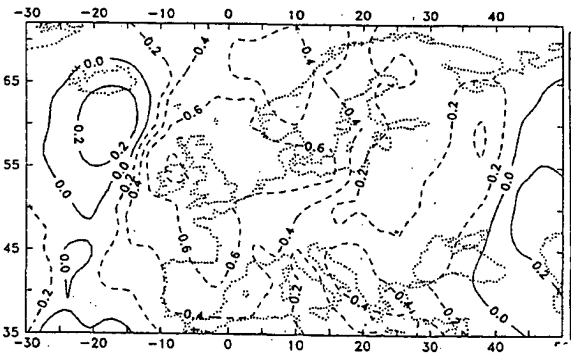


Figure 7a. Pearson correlation coefficients of 500 hPa geopotential height and (surface) precipitation 1961 - 1990, summer.

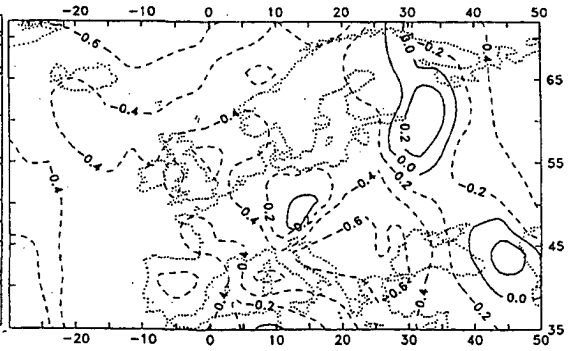


Figure 7b. Similar to Fig. 7a, but winter.

ASYMMETRIC CHANGE IN MAXIMUM AND MINIMUM TEMPERATURE IN BEIJING

Zhuang Xie
Beijing Meteorological Bureau, Beijing , China
Hong-Xing Cao
Chinese Academy of Meteorological Sciences, Beijing , China

ABSTRACT

Based on the observation data in Beijing since 1940, the general trend of daily maximum, minimum and mean temperature are studied in this paper. It is shown that the linear rate of increase in minimum temperature is 4.08 ° C/100yr, whereas the maximum temperature decreases with a linear rate of -0.245 ° C/100yr. Consequently, the diurnal temperature range(DTR) become smaller.

In addition, it is found that temperature warming in Beijing occurred mainly in daytime in1940s; but in the night in 1980s. Although the latter has been commonly admitted in the world, the former is discovered at first by us. The difference of temperature and diurnal temperature range between urban and suburban areas in Beijing are also analysed in this paper.

1 Introduction

Global warming has become an environmental problem that scientists and the public have concerned about. Recent research has clarified that global warming occurs mainly in the night, e.g. minimum temperature increases quicker than maximum one. The statistical research on 44 observational stations in China for the period of 1951-1988 revealed that the diurnal temperature range in winter and summer decreases with a rate of 3.0 ° C and 1.0 ° C respectively and the annual temperature range with a decreasing rate of 2.0 °C (Karl et al. 1993; IPCC, 1992), showing the existence of asymmetric trend in maximum and minimum temperature in China. This paper is devoted to study the asymmetric trend further by using the related data of Beijing since 1940. Studying the difference of temperature warming between the period from 1940s to 1980s and the early 1990s is of great significance for discovering climate warming in China, since there is a warmer period in 1940s.

Cao et al(1992) simulated the diurnal temperature range by using global climate model and radiation convective model. The result shows that 0.26 ° C decrease of DTR would be expected following a doubling of Carbon dioxide(CO_2). So the asymmetric changes in maximum and minimum temperature which has been found now may come from the increasing concentration of CO_2. Thus the international attention has focused on this problem.

2 Data and Data Processing

The mean monthly maximum and minimum temperature are derived from an average of the daily maximum and minimum temperature. The monthly and annual mean maximum, minimum and mean temperature are collected for 1940-1992 in Beijing. We take January to represent winter and July to represent summer.

3 The Asymmetric Trends of Monthly Maximum and Minimum Temperature

At first the regression is applied to find out the linear trend of temperatures. We set up a linear regressive model

$$X(t)= a_0+a_1 t$$

where X(t) indicates temperature, t indicates year, e.g. 1940, 1941,.....1992. a_0 is a constant. Coefficient a_1 indicates the linear trend of temperature. Meanwhile the correlation coefficients(CC) between the regressive fitting and the observed are calculated. All coefficients passed the statistical significance tests. And the results are showed in Table 1. $a_1>0$ means temperature increase. $a_1<0$ means temperature decrease The unit of a_1 is centigrade per year.

Table 1. Linear trends of temperature(Tem) and correlation coefficients(cc)

month (year)	Tem	Trend (a_1, °C/yr)	cc
January			
	min.	0.04080	0.4313
	max.	0.00736	0.0793
	mean	0.02960	0.3586
July			
	min	0.000566	0.1291
	max	-0.002450	-0.2533
	mean	-0.000755	-0.0962
year			
	min	0.03330	0.6361
	max	-0.00970	-0.1970
	mean	0.01150	0.2904

In order to obtain an intuitive impression of the yearly temperature change, the minimum temperature in January, maximum temperature in July and annual temperature and their linear trends are shown in Fig.1 and Fig .2.

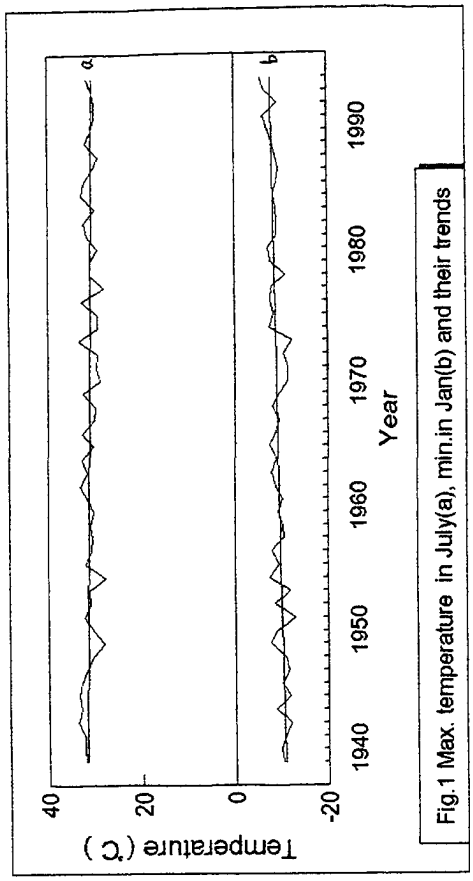


Fig.1 Max. temperature in July(a), min.in Jan(b) and their trends

The asymmetric trends of annual maximum and minimum temperature are demonstrated clearly. There are two features in Fig.1 and Fig.2. The first one is that whenever in January or in July all of the increasing rates of minimum temperature are much higher than that of maximum temperature. The former is 6 times higher than the latter in January; the former increases slightly and the latter decreases in July; annual and mean minimum temperature increase and annual maximum temperature decreases. The second feature is that temperature warming mainly occurs in winter, such as the increasing rate of minimum temperature in January is 72 times higher than that in July; maximum temperature increases in January ,but decreases in July. The increasing rate of mean temperature in winter(January) in Beijing is 0.296 ° C/10 yr, as well as in China(0.3 ° C/10 yr). However in summer(July) it is small than in China (-0.23 ° C/10 yr)(Tang et al, 1992). The increasing rate of annual mean temperature in Beijing is larger than that in China(0.4° C/100yr) (Lin et al, 1990) and in the world(0.3--0.6 ° C/100yr) as well. So Beijing is the strikingly warming area in China and the world.

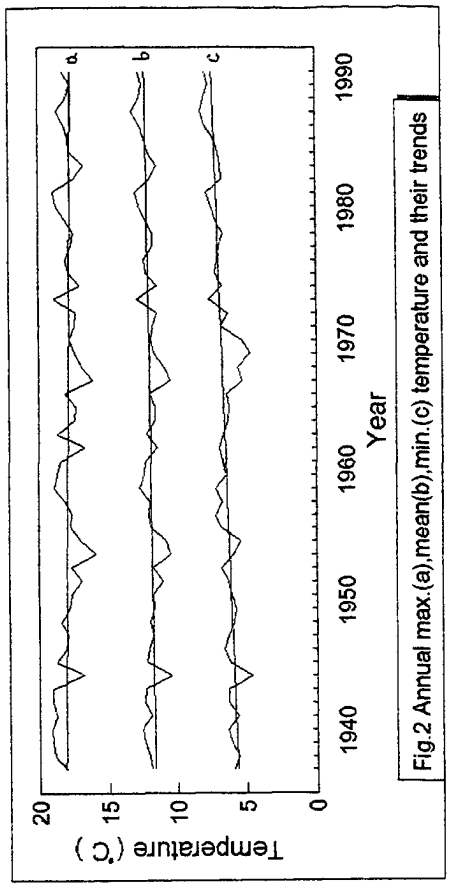


Fig.2 Annual max.(a),mean(b),min.(c) temperature and their trends

4 The Decade Change in temperature

4.1 The extreme temperature

The extreme minimum and maximum temperatures and the dates in which these temperature appeared for 5 decades during 1940-1989 and 1990-1993 are given in Table 2. From Table 2, the extreme minimum temperature went up from -19.5 ° C to -14.8 ° C. The extreme maximum temperature decreased from 42.6 ° C to 37.5 ° C. Since 1972 the maximum temperature did not reach 40 ° C, and the anomalous cold or hot days occurred rarely. It seems

Table 2. Annual extreme temperature (°C)

19-	Tmin	19-	Tmax	19-
40-49	-19.5	Jan. 47	42.6	June. 42
50-59	-22.8	Jan. 52	39.6	July. 52
60-69	-19.3	Feb..69	40.1	June. 61
70-79	-18.6	Jan. 72	40.3	June. 72
80-89	-15.5	Jan. 87	38.5	June. 86
90-93	-14.8	Jan. 90	37.5	July.90,92

that the climate in Beijing is coming to warming climate. These trend coincide with the linear trend mentioned above.

4.2 10-yr mean annual temperature for 1940-1989

Table 3 shows the average of temperature, DTR, ATR. The annual temperature variation range(ATR) is defined as the difference between the maximum temperature in July and the minimum temperature in January[ATR=T_7(max)=T_1(min)]. d_1 is the difference of 10-yr mean temperature between 1980s and 1940s [d_1=T(1980s)-T(1940s)]. d_2 is that between 1980s and 1960s. The features of 10-yr mean temperature is the same as the extreme temperature in Tab 2. Since T_7(max) decreased and T_1(min) increased since 1940s, ATR became smaller and DTR became smaller as well. What are found from Tab. 3 are shown as follows.

Table 3. 10-yr mean of annual temperatures for 1940-1989. d_1 stands for mean for 1980-89 minus mean for 1940-49.d_2 stands for mean for 1980-89 minus mean for 1960-69.

		1940-49	1950-60	1960-69
Jan.				
	min	-10.3	-9.7	-9.1
	mean	-4.7	-4.5	-4.2
	max	1.6	1.3	1.4
	DTR	11.9	11.0	10.5
July				
	min	21.7	21.4	21.7
	mean	26.5	25.7	26.3
	max	32.0	30.8	31.4
	DTR	10.3	9.4	9.7
Year				
	min	6.0	6.3	6.5
	mean	12.0	11.6	11.9
	max	18.5	17.4	17.8
	ATR	42.3	40.5	40.5

(Continue)

1970-79	1980-89	d_1	d_2	trend
-9.3	-8.4	1.9	0.7	up
-4.2	-3.7	1.0	0.5	up
1.5	1.6	0.0	0.2	steady
10.8	10.0	-1.9	-0.5	down
21.4	22.0	0.3	0.3	up
25.7	26.5	0.0	0.2	steady
30.5	31.2	-0.8	-0.2	down
9.1	9.2	-1.1	-0.5	down
6.4	7.3	1.3	0.8	up
11.9	12.4	0.4	0.5	up
17.6	18.0	-0.5	0.2	down
39.8	39.6	-2.7	-0.9	down

a. In January the mean and minimum temperature in 1940s were lower than in 1980s whereas the maximum temperature in 1940s was higher than in 1980s. In July the mean temperature in 1940s was equal to that in 1980s, the minimum temperature in 1940s was lower than in 1980s, whereas the maximum temperature in 1940s was higher than in 1980s(the highest one in five 10-yr value). The features of annual temperature are the same as that in January. All of these facts clarify that temperature warming in 1940s are mainly contributed by maximum temperature. especially in July. Whereas the higher minimum temperature is a contributing factor to climate warming in 1980s.

b. DTR and ATR is coming to decrease, the decreasing rate of DTR is 0.38 °c/10 yr in January, but 0.22 ° C/10 yr in July during 1940-1989.

c. The trend of temperature in Tab.3 is in agreement with the linear trend and extreme temperature trend.

5 The Difference of Temperature Warming Between 1940s and 1980s

There were three warm period, e.g. in 1920s (ΔT= 0.64 °C), 1940s(0.14 °C) and 1980s(0.46 ° C). The features of temperature in 1920s are the same as in 1940s(Xie et al, 1994).So a comparison of temperature in 1940s with that in 1980s is made merely. Based on three aspects mentioned above, namely the linear trend, the extreme and the 10-yr mean temperature trend, the difference of temperature in 1940s and 1980s is expounded. For further, the warmest years (1943,1989) in Beijing are selected from 1940s and 1980s respectively. Taking both as two center and going forward and backward two years respectively, the averaged temperatures for five years are calculated and given in Tab. 4.

Table 4 . The averaged temperature during 1941-1945 and 1987-1991

		1941-45	1987-91	difference
Jan.				
	min	-10.6	-7.5	-3.1
	mean	-4.7	-3.1	-1.6
	max	1.9	1.8	0.1
July				
	min	21.9	21.9	0 0
	mean	27.1	25.9	1.2
	max	33.0	30.5	2.5
year				
	min	6.0	7.8	-1.8
	mean	12.3	12.7	-0.4
	max	18.9	18.0	0.9

From Tab 4., the annual minimum temperature in 1941-1945 is much lower than that in 1987-1991 but

the annual maximum temperature is quite higher; characteristics of temperature in January or July are the same as the 10-yr mean temperatures. It reveals an important fact that the maximum temperature, e.g. warming in daytime cause the warmer period in 1940s but the temperature warming in the night in 1980s, e.g. minimum temperature warming cause the warmer period in 1980s and the early 1990s in Beijing. If this fact would be proved by temperature changes in other places, it is important for research in global warming. Since the physical factors which control temperature warming in daytime and in the night are different.

6 Urban Heat Island Effect(UHIE)

Beijing as a city has been expanded rapidly in recent years. Scientists have concerned about whether UHIE is a main factor to warming. The temperature difference between urban and suburban areas in Beijing are investigated. This difference is defined as UHIE commonly (Beijing Meteorological bureau, 1992). Let ΔT be the difference between the temperatures of Beijing and Miyun Country which located in northeast part of Beijing and d_3 be the difference between the ΔT in 1980s and in 1960s. d_3 is UHIE in Beijing. Tj, Tm means the temperature in Beijing, Miyun Country respectively. Then we have the Tab.5.

ΔT=Tj(Beijing)-Tm(Miyun)

ΔT(range)= ΔT(max)- ΔT(min)
=[Tj(max)-Tj(min)]-[Tm(max)-Tm(min)]

d_3= ΔT(1980s)- ΔT(1960s)
=[Tj(1980s)-Tm(1980s)]-[Tj(1960s)-Tm(1960s)]
=[Tj(1980s)-Tj(1960s)]-[Tm(1980s)-Tm(1960s)]

Table 5. Difference between monthly mean temperature in Beijing and County Miyun. T_1, T_7 stands for temperature in Jan., July, respectively. T_1 (range)=T_1 (max)-T_1 (mim). T_7 (range) is similar. d_3 is mean for 1980-1989 minus mean for 1960-69.

19-	60-69	70-79	80-89	trend	d3
ΔT_1 (min)	3.01	2.55	3.37	up	0.76
ΔT_1 (mean)	2.33	2.25	2.85	up	0.52
ΔT_1 (max)	0.92	0.68	1.02	up	0.10
ΔT_1 (range)	-2.09	-1.87	-2.75	down	-0.66
ΔT_7 (min)	0.22	0.45	1.27	up	1.05
ΔT_7 (mean)	0.18	0.19	0.92	up	0.74
ΔT_7 (max)	0.45	0.25	0.82	up	0.39
ΔT_7 (range)	0.23	-0.20	-0.43	down	-0.66

What we have found from Tab.5 are following:

a. All of the differences of minimum, maximum and mean temperature between urban and suburban areas have an increasing trend.
b. Whenever in January or July the temperature range have a decreasing trend.
c. The UHIE has become large. The highest one is 3.77℃ in winter(January) in 1980s.
d. The difference of UHIE between winter and summer is significant. All value of T_1 are larger than that of T_7.
e. The change in UHIE from 1960s to 1980s in July is higher than that in January.

Since the warming in winter is evident and the change of UHIE in summer is enormously in Beijing, so the change of UHIE does not match the warming trend from 1960s to 1980s (d_2). The conclusion that UHIE is not the main factor contributing to warming in Beijing has been deduced. So there are other factors, such as greenhouse effect and natural variability, contributing to climate warming.

7. References

Beijing Meteorological Bureau, Urban Climate in Beijing, China Meteorological Press, Beijing 1-8,1992

Cao H.-X., J.F.B.Mitchell and J.R.Lavary, Simulated diurnal range and variability of surface temperature in a global climate model for present and doubled CO_2 climates, J.Climate 5 920-934,1992.

International Panel on Climate Change (IPCC), Climate Change 1992, The Supplementary Report to IPCC Scientific Assessment, Cambridge University Press, 200pp.142-152,1992.

Karl T.R.et al., Asymmetric trend of daily maximum and minimum temperature, Bulletin of the American Meteorological Society, 74(6) 1007-1023,1993.

Xie et al, The change of temperature and precipitation in Beijing during last 100 years, Scientia Atmospheric Sinica 18(6),683-690,1994.

Corresponding Author
Professor Zhuang Xie
44 Zizhuyuanlu, 100081
Beijing, China

GREENHOUSE STATISTICS
A Time Series Analysis of the Relationship between the Global Mean Temperature and the Atmospheric Carbon Dioxide

Richard S.J. Tol, Aart F. de Vos
Vrije Universiteit, Amsterdam
The Netherlands

The debate on the enhanced greenhouse effect continues, confusing the climate change impact analysts and the decision makers. This paper attempts to quantify the uncertainties surrounding the temperature's response to increasing atmospheric concentrations of greenhouse gases and attempts to weigh the hypothesis that the observed warming is due to the long-term natural variability against the hypothesis that it is due to human influence.

We show, as others before have shown, that the global mean temperature and the atmospheric concentration of carbon dioxide do cointegrate, using observations over the period 1870-1991. This confirms the theoretical notion that the enhanced greenhouse effect is a plausible explanation for the observed global warming.

However, establishing cointegration does not discriminate between long term natural variability and anthropogenic influence. Long term natural variability is incorporated using linear time trends. Information from the distant past on the size of natural variability based on a 10,000 year record of temperature reconstructions is incorporated in a Bayesian fashion. Based on this, we conclude that the hypothesis that the observed temperature rise is not related to the enhanced greenhouse effect is rejected at the 99% significance level. The estimated parameter lies in the range of the IPCC.

Next the model is extended with sunspots, volcanic eruptions, and the Southern Oscillation to capture short term natural variability. The alternative hypothesis that changes in solar irradiance caused the observed warming is clearly rejected.

The interpretation of the estimated parameter is not straightforward. The atmospheric concentration of carbon dioxide is used as a proxy for a suite of human influences on the atmosphere and climate. Bayesian ways to separate out the influence of carbon dioxide are discussed. This is done by comparing our estimate of the composite effect to expert judgements of the size and sign of its elements.

A statistical analysis of external climate forcing using SSA, nonparametric correlation and neural networks

M. Denhard and C.-D. Schönwiese
J.W. Goethe University, Frankfurt, Germany

Abstract

SSA and nonparametric correlation are used to relate complex spectral features of climate forcing parameters to the observed global mean temperature. The eleven year solar cycle is found in the last 40 years starting in 1950.

Introduction

An appropriate statistical analysis of the climate system should take into account the internal dynamics in relation to the external forcing. Unfortunately, both the system variables and the external forcing parameters show a complex dynamical behaviour.

Multiple linear regression and filter technics are frequently used to evaluate the relation between the climate dynamics and the forcing. Cycle searching was not very successful in the past. This is due to the complex spectral features in observational data.

Singular spectrum analysis (SSA) and nonparametric correlations are used to relate the spectral characteristics of the forcing to the climate dynamics. Neural networks (see e.g. Widrow and Lehr 1990) are needed to approximate the unknown probabely non linear relations.

Selective Filter

Singular spectrum analysis gives adaptive spectral filters associated with the dominant oscillations of the system (e.g. Vautard and Ghil 1988). It uses delay coordinate embedding to construct the autocorrelation space of the time series. The dimension is determined by the number of delays and the structure depends on the delay time. Since the autocorrelation of a time series is related to the dynamical behaviour of the system, the autocorrelation space reveals information on the system dynamics and its spectral characteristic.

The autocorrelation space can be described by its principal axes. The coordinate transformation is performed by searching the eigenvalues and the eigenfunctions (EOF) of the associated covariance matrix. Finally, SSA provides an optimal description of the spectral characteristics of the time series.

Selecting a distinct subspace of the autocorrelation space reveals a simple way to achieve a spectral filter. In this case, only the spectral characteristics present in the subspace are used to reconstruct the analysed time series. The spectral features outside the subspace are supressed.

In this paper SSA will be used as a filtering tool. The task is to determine whether two different time series have similar spectral characteristics or not.

A forcing parameter (e.g. changes of the incoming solar radiation) and a system variable (e.g. the global mean temperature record) are analysed using SSA. Both autocorrelation spaces are compared by nonparametric correlation (Kendall's τ) of each principal component. This determines the correlated subspaces. The dimension of the autocorrelation space is changed until the subspace with maximum correlation is found. A reconstruction of the time series exclusively uses information from the determined subspaces. A selective filtering is achieved which includes the similar dynamics of the forcing parameter and the system variable.

The Data

These concepts are applied to the global mean temperature record from 1874 to 1991 (Jones, see NASA 1991). All observational data is from the GEDEX experiment (NASA 1991) exept when indicated. Forcing mechanisms considered are Greenhouse Gases (GHG), Volcanos (VI), Solar radiation (SOC) and the El Niño/Southern Oscillation phenomenon (ENSO). The solar radiation forcing is assumed to be related to the sunspot numbers (see Foukal and Lean 1990). The volcanic index uses the Volcanic Expolsivity Index (VEI) classification of the Smithonian Institution (Simkin and Siebert 1993).

Results

Figure 1 shows the forcing parameters and the filtered time series applying selective filters to the global mean temperature from 1874 to 1991. All forcings determine temperature signals. The GHG and the solar forcing are mainly related to the temperature trend. The eleven year solar cycle is not related to temperature variations while the ENSO phenomenon provides strong high frequency correlations. Volcanic forcing effects the temperature if strong eruptions are considered. The filtered volcanic time series, of course, does not describe the inclines of the signals correctly.

In Figure 2 a similar analysis is performed with changing periods of time. The examined time intervals always end in 1991 but the beginning ranges from 1874 to 1970. Two correlations are calculated. The first determine the correlation between both filtered time series (xf/yf, x = forcing, y = temperature) and the second correlates the the unfiltered forcing time series with the filtered temperature (xu/yf). A selective filter is accepted if the latter correlation is significant. A forcing time series consisting of random numbers always provide a variaty of spectral characteristics. A selective filter always will be quite successfull. But in this case the filtered spectral feature does not significantly correlate with the unfiltered time series.

Figure 2 shows the nonparametric correlation (in units of the standard deviation) of the filtered forcing time series and the filtered global mean temperature. A value of zero indicates that the correlation xu/yf is lower than 99% . Volcanic forcing includes only a small number of strong eruptions. Therefore, the selective filter is not very useful. Additionally, the estimation of the stratospheric aerosol content using the VEI classification contains many uncertainties because the VEI is not a direct measure of the ejected sulfur gases.

The ENSO phenomenon is always correlated to the global mean temperature. But the correlation decreases with the analysed period of time. Since GHG and solar forcing are related to the temperature trend very strong correlations are found for xf/yf. The most interesting features are the two distinct correlation levels for solar forcing. Figure 3 shows the filtered temperature signals in relation to the unfiltered forcing time series for both significance levels. It is obvious that the eleven year solar cycle is not present if the whole period from 1874 to 1991 is analysed. But the solar cycle is found in the last 40 years providing a separated significance level. The appearance of the solar cycle in the last decades may be due to:

1. increasing sunspot numbers since 1950 changing the amplitude of the solar cycle

2. changes in the radiation balance, e.g. increasing atmospheric content of greenhouse gases

This list may not be complete. In anyway, both suggestions require non linear relations. A power of two or higher is required to simulate the influence of an increasing solar cycle amplitude. If the appearance of the solar cycle is due to increasing greenhouse gases, mixed terms are needed. Non linear regression and neural networks can be used to evaluate this problem. But this is left to the presentation in Galway.

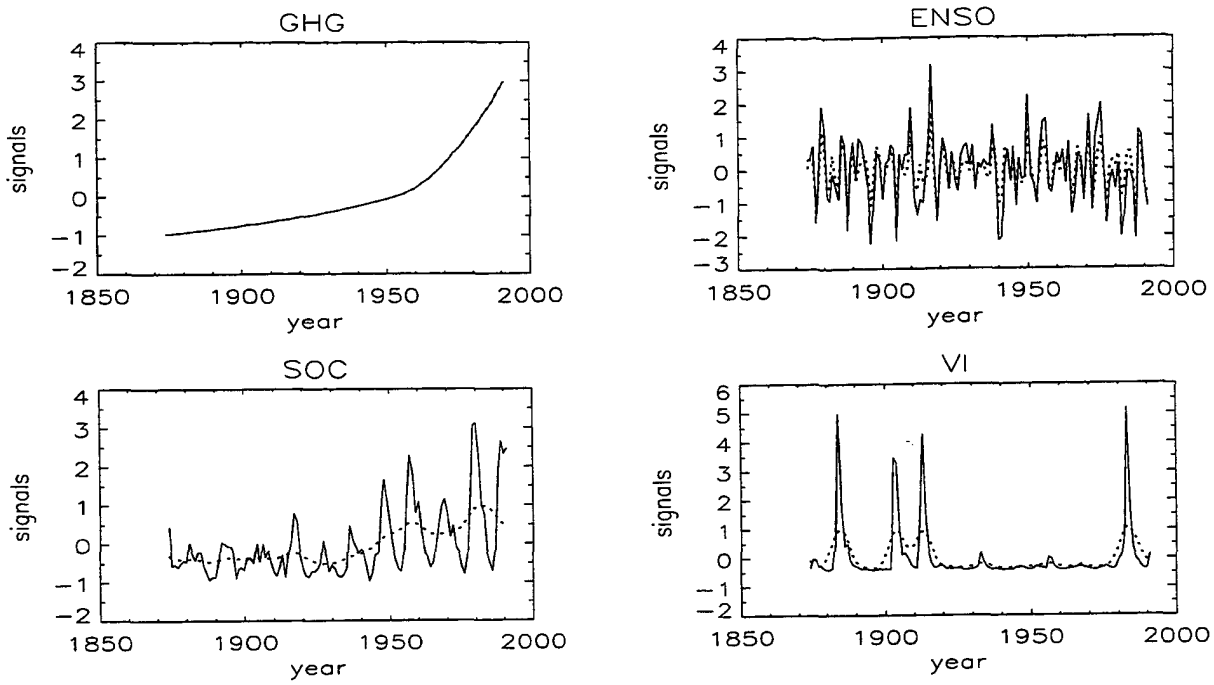


Figure 1: Selective filtered temperature signals related to the specified forcing. The dotted lines denote the filtered signals. The solid lines represent the forcings.

References

Foukal, P.V. & Lean, J. (1990): Science, 247, 556-558.
Kendall, M.G. (1970): Rank Correlation Methods, London: Griffin, Fourth Edition.
Mann, H.B. (1945): Nonparametric Test Against Trend, Econometrica, 13, 245-259.
NASA (1992): Greenhouse effect detection experiment GEDEX.
Simkin, T. & Siebert, L. (1993): personal comunication.
Vautard, R. & Ghil, M. (1989): Physica 35D, 395-424.
Widrow, B. & Lehr, M. A. (1990): 30 Years of Adaptive Neural Networks, Proc. IEEE, 78, 1415-1441.

Corresponding Authors

M. Denhard and C.-D. Schönwiese Institute for Meteorology and Geophysics,
P.O.Box 111932, D-60054 Frankfurt a.M., Germany

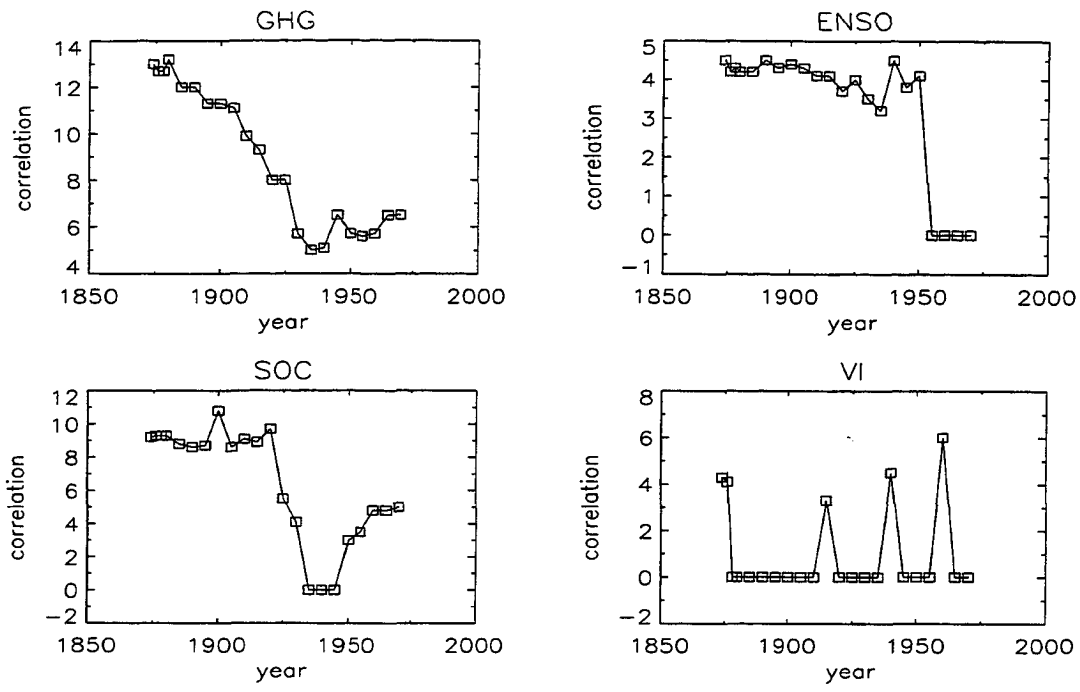


Figure 2: Nonparametric correlation, in units of the standard deviation, of the filtered forcing time series and the filtered global mean temperature (xf/yf). A value of zero indicates that the correlation between the unfiltered forcing time series and the filtered temperature signal (xu/yf) is lower than 99%.

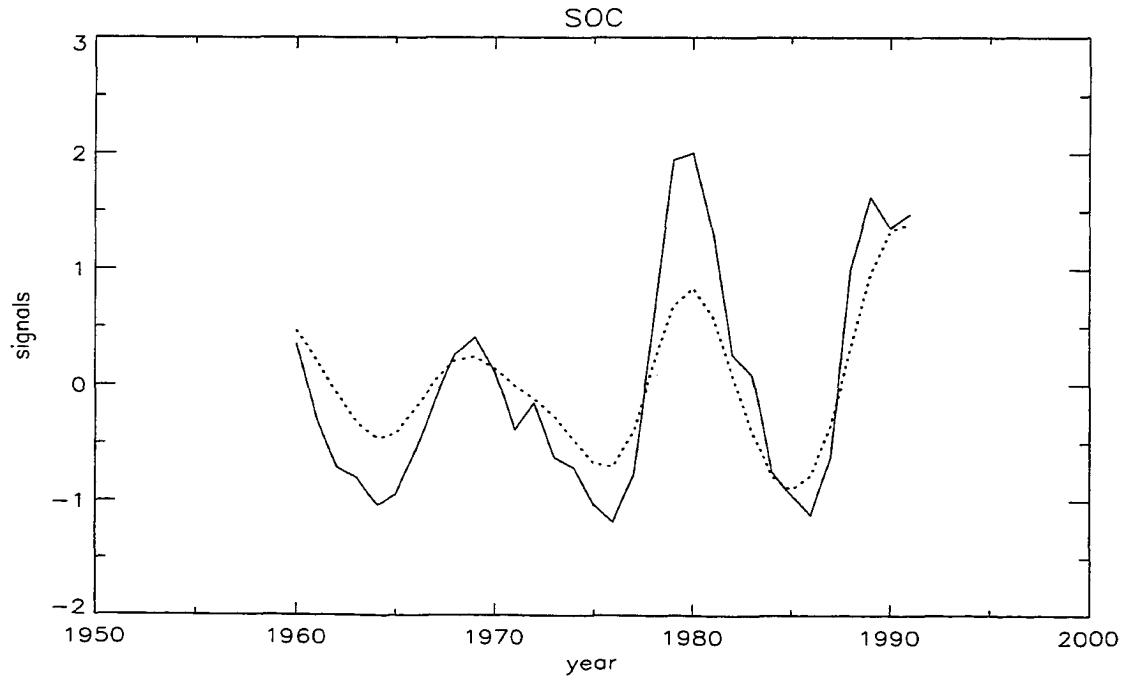


Figure 3: Selective filtered temperature signal related to the solar forcing (SOC). The dotted line denotes the filtered signal. The solid line represents the forcing.

FLUCTUATIONS AND TRENDS OF TEMPERATURE EXTREMES IN SOUTHERN PANNONIAN LOWLAND

Marjana Gajic-Capka, Ksenija Zaninovic

Meteorological and Hydrological Service, Zagreb, Croatia

ABSTRACT

The subject of global warming has initiated an investigation of time changes of mean extreme temperatures for Croatian lowland which has a great agricultural importance. The fluctuations and trends of seasonal and annual anomalies of mean maximum and minimum temperature and diurnal temperature range relative to the mean 1961-1990 have been determined. Short-term changes of areal and high elevated location data during the last 42 years (1951-1992) have been compared with the short- and long-term changes (1901-1992) at the two stations situated on the eastern and western edge of the observed region.

1 INTRODUCTION

In the framework of the climatic change investigation of extreme temperatures in central Europe there have been published some papers concerning the region of the Austrian, German and Swiss Alps (Stefanicki et al., 1994), Slovak Republic (Lapin, Fasko, 1994), Czech Republic (Brazdil et al., 1994), and Poland (Niedzwiedz, Ustrnul, 1994). The intention of our investigation is to fulfill the existing gaps of similar results in the very southern part of the Pannonian lowland. The comparison of the corresponding results of temperature changes for Croatia-lowland, central Europe and northern hemisphere (Karl, 1993) has to lead to the evaluation of the results on local, regional and global scale.

2 DATA AND METHOD

Seasonal and annual mean daily temperature maximum (TMAX), minimum (TMIN) and diurnal temperature range (DTR), i.e. the difference between TMAX and TMIN, have been calculated during the period 1951-1992.

Areal averages for the northern Croatia have been determined after the data series of 13 stations in this region. The reference period for calculating departures from the mean was 1961-1990. The same kind of data have been calculated for the mountain station Puntijarka situated at the western edge of this area at the elevation of 988 m a.s.l. and for the long-term date series (1901-1992) at Zagreb-Gric on the western and Osijek on the eastern edge of the observed area.

The time series analysis has been deduced by means of weighted 11-year moving average filter and linear trend tested for significance with the Mann-Kendall rank statistics.

3 RESULTS

a) Trend analysis

During the last forty years generally increasing annual trends are present in areal averages TMIN and TMAX. Concerning the seasons, increasing trends are indicated in spring and winter for both mean extreme temperatures and in summer for TMIN (0.10°C to 0.32°C per 10 years), and decreasing trends in autumn for both mean extreme temperatures and in summer for TMAX (0.03°C to 0.12°C per 10 years). Neither trend is statistically significant according to the Mann-Kendall rank statistics. These reflect in the very weak decrease in annual trend of DTR, with apparent weak decrease from spring to autumn, but with slight increase during winter (Table 1).

The results presented for high elevated station (Puntijarka) as well as for two lowland stations (Zagreb-Gric and Osijek) indicate some different results on the local scale.

At the mountain station DTR trend increases throughout the year, significantly in summer and for annual average, as a result of constant increase of TMAX and weaker increase or even decrease of TMIN. During the same short-term period, two

Table 1. Seasonal and annual trends (°C/10years) of mean maximum (TMAX), mean minimum (TMIN) and diurnal temperature range (DTR). Shading denotes trends significant at the 0.05 level.

CROATIA-LOWLAND (1951-1992)			
Seasons	TMAX	TMIN	DTR
SPRING	0.17	0.20	-0.03
SUMMER	-0.03	0.10	-0.13
AUTUMN	-0.12	-0.08	-0.05
WINTER	0.32	0.29	0.03
ANNUAL	0.06	0.11	-0.01

PUNTIJARKA (1951-1992)			
Seasons	TMAX	TMIN	DTR
SPRING	0.22	0.13	0.08
SUMMER	0.18	-0.03	0.21
AUTUMN	-0.00	-0.12	0.12
WINTER	0.22	0.22	0.01
ANNUAL	0.13	0.03	0.10

ZAGREB-GRIC (1951-1992)			
Seasons	TMAX	TMIN	DTR
SPRING	0.18	0.21	-0.02
SUMMER	-0.03	0.09	-0.12
AUTUMN	-0.07	-0.06	-0.01
WINTER	0.38	0.35	0.02
ANNUAL	0.09	0.13	-0.04

OSIJEK (1951-1992)			
Seasons	TMAX	TMIN	DTR
SPRING	0.24	0.01	0.24
SUMMER	-0.07	-0.16	0.09
AUTUMN	-0.04	-0.27	0.23
WINTER	0.29	-0.00	0.21
ANNUAL	0.08	-0.12	0.20

ZAGREB-GRIC (1901-1992)			
Seasons	TMAX	TMIN	DTR
SPRING	-0.01	0.07	-0.08
SUMMER	-0.09	0.09	-0.18
AUTUMN	0.04	0.08	-0.04
WINTER	0.03	0.08	-0.06
ANNUAL	-0.00	0.09	-0.09

OSIJEK (1901-1992)			
Seasons	TMAX	TMIN	DTR
SPRING	0.00	-0.05	0.05
SUMMER	-0.08	0.02	-0.10
AUTUMN	0.11	-0.04	0.16
WINTER	0.03	-0.07	0.08
ANNUAL	0.02	-0.03	0.05

lowland locations exhibit increase in TMAX in spring and winter, but decrease in summer and autumn. However, TMIN shows prevailing decrease in Osijek and at the same time increase in Zagreb, what led to the increasing trend of DTR in Osijek and decreasing trend in Zagreb.

As the interannual fluctuations strongly influence the calculation of short-term linear trends, the investigation of the long-term data series is necessary to identify climatic change.

During the present century, TMAX in Zagreb exhibits practically no trend, while TMIN increases significantly, resulting in significant decreasing trend of DTR. Furthermore, the decrease in DTR is significant in all seasons except in autumn, because of increase in TMIN throughout the year (significant in spring and summer), and slighter increase (during autumn and winter) or even decrease (in spring, and quite strong in summer) in TMAX. Osijek shows opposite annual trends in TMAX (slight increase) and TMIN (slight decrease) and therefore a slight increase in DTR. The same trend patterns appear during the year, except in summer.

b) Fluctuations

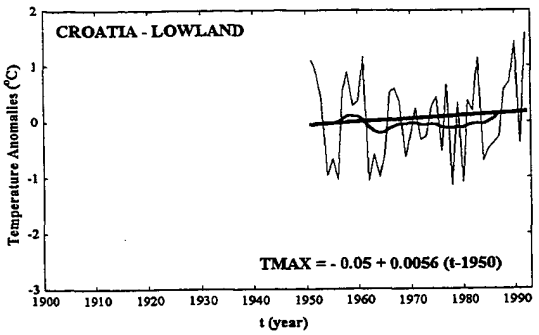
With regard to the short-term fluctuations, the general decrease in DTR is present in Zagreb from the beginning of the century. The exceptions are 1940s as part of dramatic increase in TMAX, and the period since mid 1970s until today due to faster increase in TMAX than in TMIN.

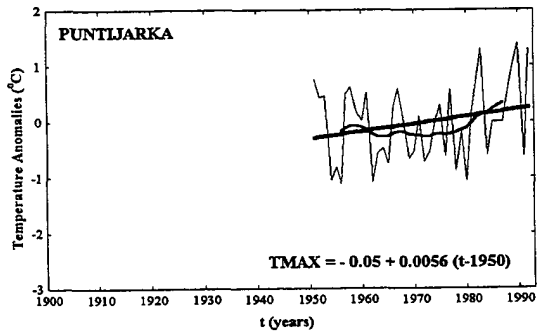
Since the beginning of this century until mid 1920s sharp decrease in DTR occurs in Osijek, which coincides with the substantial increase of TMIN. In the following years, smaller increasing and decreasing changes of DTR appear, with the increasing tendency of DTR and TMAX in the last decade.

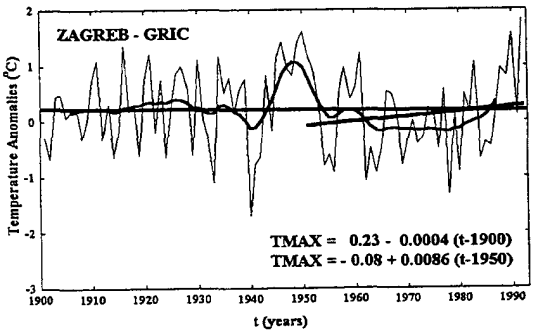
4 CONCLUSIONS

The obtained results of trend for the period 1951-1992 in the Croatian part of Pannonian lowland show practically identical tendency patterns of TMIN, TMAX and DTR for annual, spring, winter and summer values with the most central European countries as well as with northern hemisphere, while autumn trends agree with some neigbouring countries and with the average for the northern hemisphere. The mountain station reveals no diurnal asymmetry, similarly to the high-lying Alpine stations.

The long-term trend (1901-1992) in Zagreb has the same behaviour of TMIN, TMAX and DTR as the most long-term trends in central Europe.







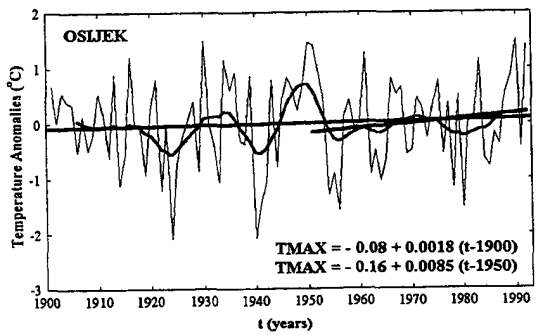
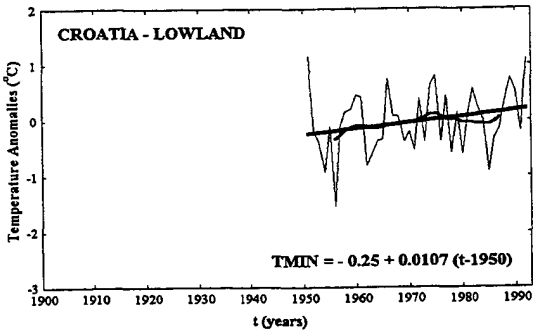
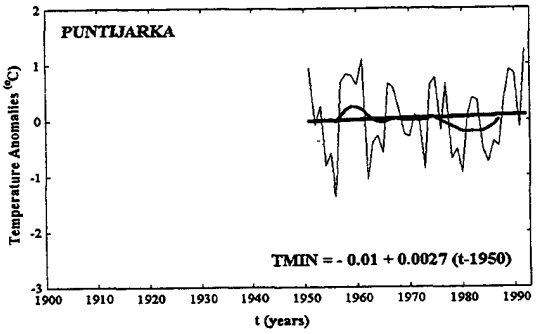
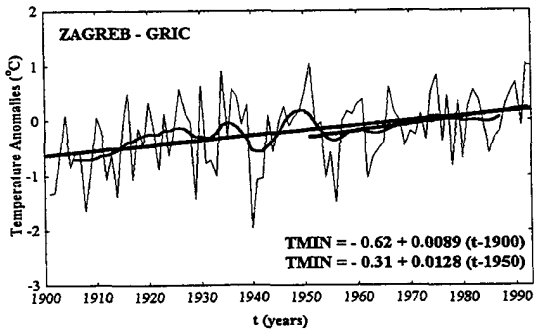


Figure 1. Variations of the mean maximum temperature (TMAX), 11-year weighted moving average series and linear trends during the period 1951-1992 and 1901-1992.







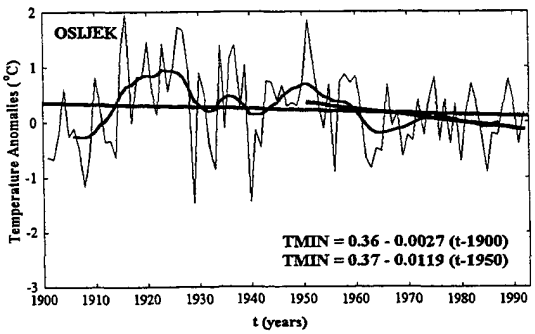


Figure 2. Variations of the mean minimum temperature (TMIN), 11-year weighted moving average series and linear trends during the period 1951-1992 and 1901-1992.

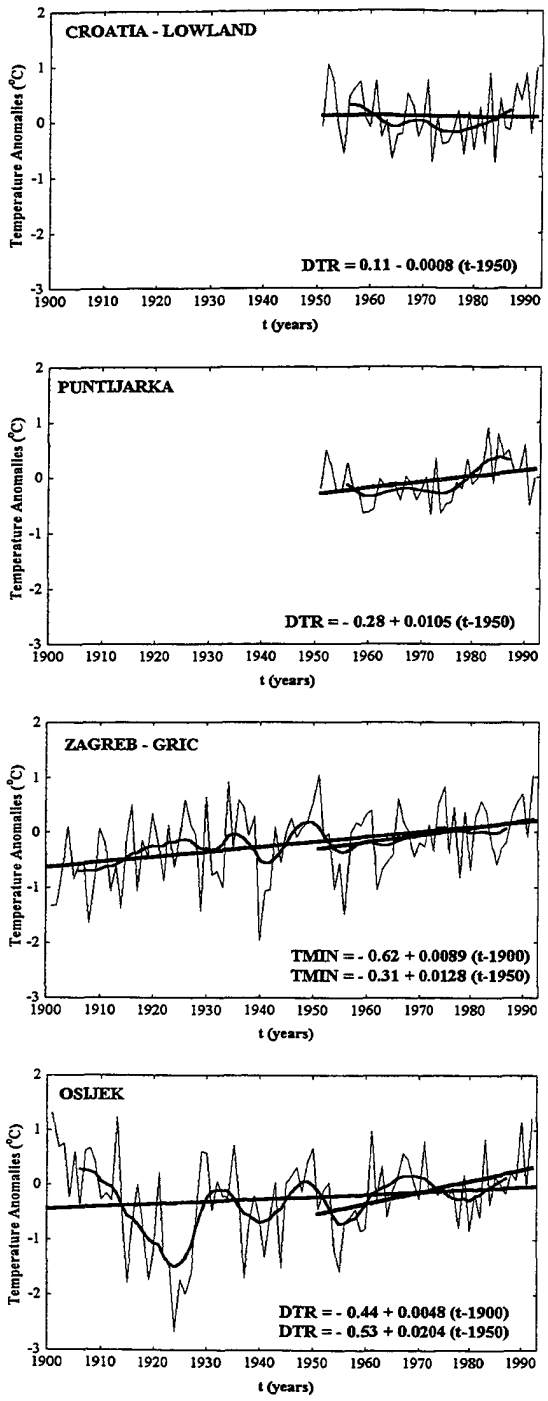


Figure 3. Variations of the mean daily temperature range (DTR), 11-year weighted moving average series and linear trends during the period 1951-1992 and 1901-1992.

REFERENCES

Brazdil, R., Machu, R., Budikova, M., 1994, "Temporal and spatial changes in maxima and minima of air temperature in the Czech Republic in the period of 1951-1993", Contemporary Climatology (eds. R. Brazdil and M. Kolar), Brno, 93-102.

Karl, T.R., Jones, P.D., Knight, R.W., Kukla, G., Plummer, N., Razuvayev, V., Gallo, K.P., Lindseay, J., Charlson, R.J., Peterson, T.C., 1993, "A new perspective on recent global warming: asymmetric trends of daily maximum and minimum temperature", Bull. Amer. Meteor. Soc., 74, 1007-1023.

Lapin, M., Fasko, S., 1994, "Daily air temperature range and relative air humidity correlation at Hurbanovo", Contemporary Climatology (eds. R. Brazdil and M. Kolar), Brno, 359-363.

Niedzwiedz, T., Ustrnul, Z., 1994, "Maximum and minimum temperatures in Poland and the variability of atmospheric circulation", Contemporary Climatology (eds. R. Brazdil and M. Kolar), Brno, 420-425.

Stefanicki, G., Talkner, P., Weber, R.O., 1994, "Temperature trends of the Alpine region in this century", Proceedings of the Internationale Tagung fuer Alpine Meteorologie, Ann. Meteorol., Offenbach, 30, 221-224.

ACKNOWLEDGEMENT

This work was supported by the Ministry of Science and Technology of Republic of Croatia.

CORRESPONDING AUTHOR

M.Sc. Marjana Gajic-Capka
Meteorological and Hydrological Service
Centre for Meteorological Research
HR- 41000 Zagreb, Gric 3
CROATIA
tel: +385 1 421 222 / 270
fax: + 385 1 278 703
e-mail: capka@cirus.dhz.hr

THE Temperature Change at Taipei Basin

H. Y. Tseng

AIR NAVIGATION & WEATHER SERVICES
CAA ROC

ABSTRACT

The Taipei Basin in northen Taiwan is situated in the Subtropic zone. In winter, the weather thereof is controlled by the northern monsoon from the cold air-mass of Mainland China; in summer by the southwestern monsoon from Southern China Sea, or by the southeastern monsoon from the west Pacific.

The annual mean temperature 22.3℃, the absolute maximum in July: 37.3℃, and the absolute minimum in January at Taipei Sungshan Air port: 0.8℃. Due to the population increase, city expansion, Hillside developing, and heavy traffic, the mean temperature increased 0.4℃ in the past 20 years. As a result, haze and airpolution take place frequently.

1. Introduction

The variation of temperature not only has a relation to the dailylife of mankind, but also influences the growth of animals and plants. Taipei Basin (25.0 N, 121.5 E) which situates in subtropic is mainly controlled by the China continental cold air mass in winter and influenced by the warm and moist air mass on the Pacific Ocean in summer. During the spring and summer time, when the stationary fronts appear in the Southern China or southcast coast -- i.e. Mei Yu period (Chen, 1991), usually heavy rainfalls occur. Besides, during summer and autumn, typhoons often invade or influence the Basin, accordingly heavy rainfall and strong wind occur. Because of these reasons, the variation of temperature of the Taipei Basin in a year is deeply influenced by this weather system.

The temperature variation of Taipei: According to the past 86 years (1879-1982) synoptic records of the Taipei weather station which belonged to the Central Weather Bureau, the temperature of Taipei increased nearly 0.97℃ and the annual variation was 0.0114℃ (Wong, 1985). According past 83 years (1902-1984) data of the same station and Cheng (1985) found that the temperature in Taipei had an increasing tendency. The temperature of Taipei city being increasing was caused by the concentrated population, the hot - island effect resulting from city development and the air pollution (Cheng,1968).

Sung Shan Airport is about 5km from the Taipei Weather Station which is in the central part of Taipei. The terrain of the Airport is more expansive, and maybe more representative. Generally , the temperatures of these two places may be different a little bit daily, but the variation is not apparent (Wong, 1985). In view of the mean of a long period, if we pay no attention to the trivial difference of the samples, the result will be similiar. So, if we use the variation of temperature of the Airport to represent that of Taipei could be more suitable. According to the record of past 20 years (1974-1992), when the statistic data of hourly temperature of Sung Shan Airport is compared with the mean temperature of 1953-1972 (Hsiao etc. 1974) -- it is found that the temperature had increased 0.4℃. This increase of temperature is not only closely related to the development of Taipei City (Taipei Basin) but also consistent with the following-facts: the mean temperature of the earth surface has a tendency to turn warmer (Barnett,1984) during the past 100 years due to the greenhouse effect, consequently the temperature of the earth surface has increased nearly 0.3-0.6℃ (Liu,1994).

2. Annual Temperature Variation of Taipei

The Taipei Basin in the northern part of Taiwan is influnced deeply by the marine air mass on the Pacific Ocean extending from the east as much as by the continental air mass from China. The climate of this basin shows the marine features (Sheng 1986, Hsiao 1976), and so when the day time is longer the temperature is higher in summer, but there is no frost and snow in winter when the day time is short.

The annual mean temperature of Taipei is 22.3℃ (Table 1, Fig 1). The warmest month is July, in this month the mean temperature is 28.9℃. From April to November, the mean temperature is all over 20℃; While from June to September is highr than 26.8℃, The coldest month is Jannary in winter, in this month the mean temperature is 15.5℃, and the mean temperature respectively of February, March and December are within 15.8℃--17.8℃.

The Annual mean maximum temperature of Taipei is 25.5℃, which is only 2.3℃ higher than the annual mean temperature.

From June to September, the mean maximum temperature of Taipei ranges from 30℃ to 33℃, as the summer time is long and the weather is extremely hot. The annual mean minimum temperature thereof is 19.3℃. That is only 3℃ lower than the annual mean temperature. From December to March, the mean of minimum temperature thereof is around 13℃ to 15℃ when the winter time is short and the weather is coldest. From May to October, the mean minimum temperature ranges from 21℃ to 25℃.

Table 1. Taipei/Sungshan Airport 1974～1993 Temperature Summary

Month	Mean(℃)	Mean max.(℃)	Mean min.(℃)	Extreme max.(℃) (year)	Extreme min.(℃) (year)	Mean(℃) (1953 ～ 1972)
January	15.5	18.4	12.8	28.3 (1988)	2.3 (1974)	14.8
February	15.8	18.7	13.1	30.8 (1979)	4.8 (1974)	15.4
March	17.8	21.0	14.9	31.8 (1993)	0.8 (1986)	17.6
April	21.3	24.7	18.0	33.8 (1993)	9.6 (1974)	21.1
May	24.4	27.7	21.3	36.8 (1991)	14.6 (1991)	24.4
June	27.0	30.6	23.8	36.4 (1989)	16.2 (1982)	26.5
July	28.9	32.9	25.4	37.3 (1988)	21.8 (1976)	28.3
August	28.6	32.2	25.4	37.0 (1988)	19.4 (1974)	28.1
September	26.8	30.1	23.9	36.2 (1993)	18.5 (1987)	26.4
October	23.8	26.7	21.1	34.5 (1983)	13.4 (1981)	22.9
November	20.4	23.0	17.9	32.6 (1990)	6.7 (1988)	20.3
December	17.2	20.2	14.4	30.1 (1975)	3.2 (1985)	17.2
Annual Mean/Total	22.3	25.5	19.3	Extreme 37.3	Extreme 0.8	21.9

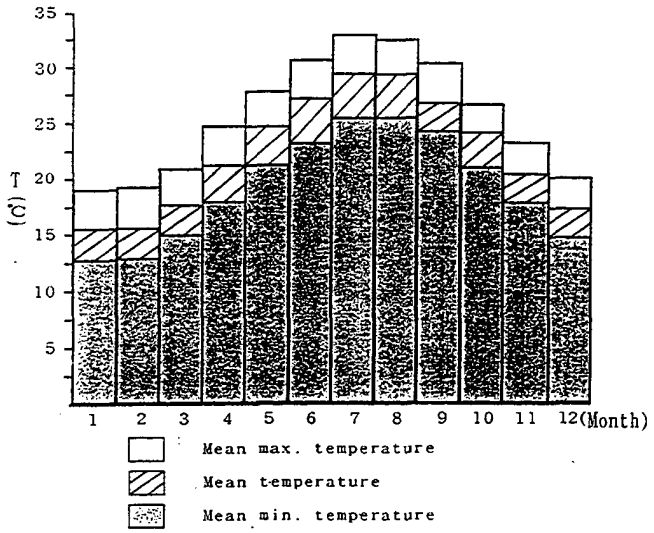


Figure 1. Taipei/Sungshan Airport 1974～1993 Year Mean Temperature

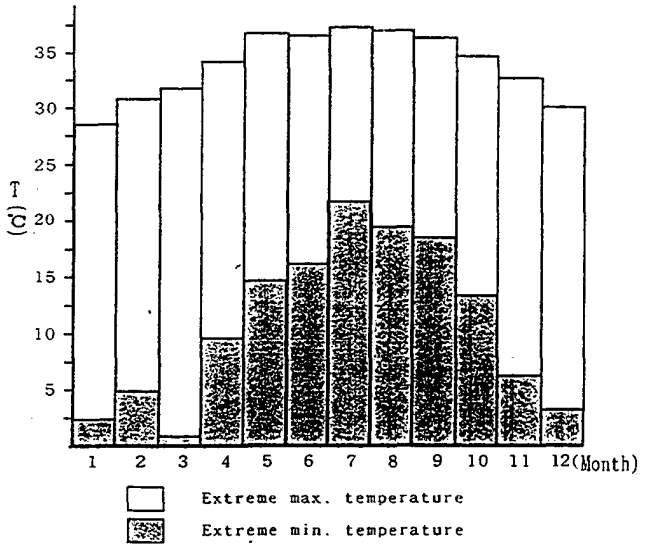


Figure 2. Taipei/Sungshan Airport 1974～1993 Year Extreme Temperature

Taking a look on the past twenty years (1974-1993) record,the extreme maximum temperature (Fig.2) of this basin is 37.3℃ (July 26, 1988). On the day the said temperature appearred, the weather was sunny, and no much rainfall was obtained for a long time, also there was a typhoon moving from the east on the Pacific Ocean and gradually turned to the north and so this basin was influenced by the circulation of the said typhoon, consequently air subsidence was caused and the weather became hotter and hotter. In addition, from May to September, the extreme maximum temperature is higher than 35℃. The extreme minimum temperature of this basin was 0.8℃ (March 3, 1986), on that day there was a cold front just passed through Taiwan, so this basin was influenced by the cold wave and the minimum temperature appeared accordingly. From December to March, the extreme temperature below 5℃ is likely to appear.

3. Diurnal Temperature Variation of Taipei

Except the abnormal variation appearing before and after front passage in winter and spring and the thunderstorm shower days in summer and autumn, as well as that caused by typhoons, the cloud cover condition and the strongness and weakness of wind speed also have a great effect on the diurnal temperature variation of Taipei. Generally, the daily minimum temperature appears at about 0600L

(LST) the morning that is about the time at which the sun just arises from the horizon; the diurnal maximum temperature appears at about 1200L that is the time the sun shines the surface directly (Hsiao, 1976).

From the diurnal hourly temperature statistics of July, 1991 (Fig.3), we can find that the mean minimum temperature of that month appears at about 0500-0600L in the morning, and the monthly mean temperature thereof is about 27 ℃; thereafter the temperature rises rapidly till 1100L, at that time the temperature has been up to the diurnal mean maximum temperature that is about 33℃, thereafter the temperature then is slowly and gradually falling to the lowest point. The monthly mean difference of diurnal temperature variation is about 6℃.

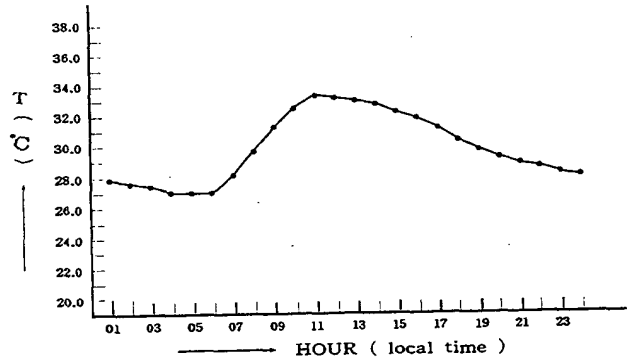


Figure 3. Taipei/Sungshan Airport Hourly Mean Temperature of July, 1991

4. Annual Temperature Variation and Urbanization of Taipei

Among the climate elements of a place, the temperature change is not only directly controlled by the atmospheric circulation, but also has a relation with the variation of weather system in a local area. In the recent ten years, scientists successively consider that the "Green House Effect" is the main cause that makes the surface temperature of the earth rise year by year (Liu, 1994). Besides, the research in this respect also proves that the climate change of various places of the Pacific Ocean Basin is affected by "El Nino " too, as in any place precipitation is also related to temperature variation greatly.

In the recent 20 years, due to the growth of population, the continuous expansion of buildings, the development of the hillside on the rim of this basin,and the air pollution caused by transportation vehicles that makes the phenomenon of "City Forest" become more and more remarkable, consequently the temperature of summer getting warmer gradually. According to the statistics of the latest 20-year temperature data quoted in this article, in Taipei the annual mean temperature is 0.4℃ higher than that shown in the last 20--years (1953 - 1972) statistics made in the past (Table 1). In view of the mean temperature of each month, execpt in May and December the mean temperature has not increased.

Similarly, from the diurnal hourly temperature statistics of January, 1991 (Fig.4), we may learn that the diurnal mean minimum temperature also appears at about 0600L in the morning, it is about 15℃ at that time; from 0800L the temperature begins to rise remarkably, and the mean maximum temperature appears at about 1300L, it is about 18℃ at that time, thereafter the temperature then is slowly and gradually falling again.The mean diurnal temperature variation of the said month is only about 3℃, this is just an half of the mean diurnal temperature variation of July of the same year. From this we may also find again that the diurnal temperature variation in the warm months of summer is larger than that in the cold months of winter.

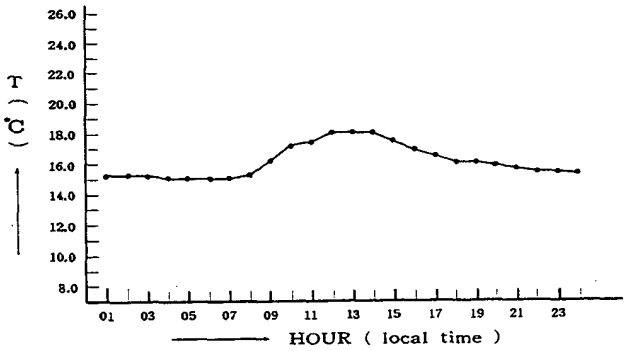


Figure 4. Taipei/Sungshan Airport Hourly Mean Temperature of January, 1991

mean temperature increase is seen in all other months, and this increase ranges from 0.1℃ to 0.9℃

In addition, the Sung Shan Airport is situated in the suburb to the northwest of the urban district of Taipei, since Chungshan highway had been constructed on the north of this airport ten years ago, the heavy traffic on the said highway has formed a "Heat Shield", this not only has blocked the vapor of Keelung River to flow to the said airport, but is also helpful to the rise of the said airport's temperature, accordingly decreasing the occurence of radiation fog at night and in the morning in autumn and winter that was often seen in the past, instead haze days increase,and the air quality becomes worse , consequently causing harm to the health of the public.

5. Conclusion

The annual mean temperature of Taipei is 22.3℃. The mean temperature difference of every month is 6.6℃ to 6.8℃. The monthly mean maximum temperature of this city is 28.9℃ in July, while its mean minimum temperature is 15.5℃ that appears in January. From May to September, the months of summer are the most warmest months of the year. In these months the extreme maximum temperature is higher than 36℃. In the period from 1974 to 1993, the extreme maximum temperature is 37.3℃ which appeared on July 26,1988. From December to March of the next year,in these months the extreme minimum temperature is lower than 5℃, and 0.8℃ minimum temperature had

ever appeared on March 3, 1986. In Taipei, there is no any freeze damage caused by frost or snow.

Because the effect of urbanization in Taipei is getting more and more remarkable, therefore the annual mean temperature in the past 20 years is 0.4℃ higher than that of the 20-year period from 1953 to 1972. The mean temperature increment of each month sums up to 0.1℃ to 0.9℃, but in May and December no variation is seen. This increase in annual mean temperature matches with the "Green House Effect", and scientists hold that such effect may change the global climate of the world.

Due to the rapid economic development and significant advancement in international business activities in the latest 20 years, today Taipei has become one of the most important cities of Eastern Asia. As a result, "City Forest" and urbanization also make the temperature of this city to rise, and the temperature rise has formed a direct influence on the life of the citizens of Taipei, it also becomes an issue which is very much concerned by the government authorities in charge of environment protection and the public, and the said authorities are eagerly intended to find some methods to stop or retard this influence effectively.

References

.Barnett, T.P., 1984 : Long-term Trends in Surface Temperature over the ocean, Mon. Wea. Rev., 112, 303-312.

.Chen G.T.J., 1991: Mesoscale features observed in the Taiwan Mei-Yu season, J. Met. Soc. Japan, 70, 497-516.

.Cheng, S.C.,1985 : An Analysis of Teipei Climate. Bull. of Geog. Soc; No 13, 31-37. (in Chinese With English Abstract)

.Cheng, T.C., 1968 : Taipei Basin Climate, Met. Bull. Vol.14 No.3.1-13, (in Chinese)

.Liu C.M. et al., 1994 : An Assessment of Climate Change of Taiwan in Future, Preprints.C onf. on The Factor of Climate Change and Influnce over Taiwan Area, 2-34, (in Chinese)

.Sheng C.Y., 1986: The Climate of China, Since Publication Co., P.322, (in Chinese)

.Shiao H., et al., 1976: The Aviation Weather. of Taipei International Airport Survey 1963 -1 972, Res.Report, 39-41

.Wong K. Y. et al., 1985: Urbanization and Characteristics of Air Temperature in Summer in Taipei, Bull. of Geog. Soc., No.13, 13-29, (in Chinese With English Abstract)

ESTIMATION OF AGREEMENT AND DISAGREEMENT IN THE INTERANNUAL VARIABILITY OF AIR TEMPERATURE IN HIGH, TEMPERATE AND LOW LATITUDES OF NORTHERN HEMISPHERE.

G.V. Alekseev, P.N. Svyashchennikov, N.E. Harlanenkova

The Arctic and Antarctic Research Institute, St.-Peterburg,Russia.

ABSTRACT

There is a significant negative correlation of interaanual air temperature fluctuation in high and in other latitude zones of the Northern Hemisphere for 1891-1993. A phase-frequency analysis has shown the presence of a both positively and negatively connected components. A contribution of negatively ones is maximum in winter at high frequencies . A positive correlation is noted, as a rule, at low frequencies in summer . It is suggested that negative correlations are related with fluctuations of the winter air exchange between high and lower latitudes. A positive correlation at low frequencies indicate the influence of global factors.

INTRODUCTION

In spite of numerous data on the on-going warming of global climate, the problem of a reliable estimate of its nature has not been fully resolved. One of the reasons for such situation is in the complexity of the variability of the Earth's climate. The strong internal or free variability in the climatic system of the Earth (Lorenz, 1979) screens signals of external or forced climate change. In order to find out and estimate these changes, it is necessary to gain knowledge of the nature, scales and expressions of the free variability of climate. To this end, there are many studies fulfilled that are based both on the analysis of empirical data (for example, Alekseyev, Svyashennikov, 1991) and numerical experiments with atmospheric General Circulation Models (GCM) (for example, Leung and North, 1991). The work presents an analysis of the free and forced variability of midlatitudinal air temperatures manifested over the Northern hemisphere.

DATA AND METHOD

Mean monthly values of surface air temperature in the points of the regular grid 5 degrees of latitude X 10 degrees of longitude for 1891-1993 are used. They were prepared at the Data Center (Obninsk, Russia). Temperature values were interpolated to the grid points from the charts of mean monthly air temperature. Mean latitudinal temperature values and mean temperature in different latitudinal zones were calculated. The obtained temporal series of mean values were subjected to a mutual correlation and spectral analysis using estimates of the correlation functions and spectral characteristics by means of the Blackman-Tukey method. Spectral characteristics (spectral density, coherency, phases) were calculated using a temporal window of Tukey.

RESULTS

Atmospheric circulation fluctuations present the main mechanism forming free oscillations of the climate characteristics. Under conditions of a non-uniform distribution of heat influxes and sinks to the climatic system, the circulation are responsible for most of the observed air temperature fluctuations at some points of the system. Spatial and temporal temperature averaging does not help avoiding completely this weather noise due its large-scale and low-frequency components rather

Table 1.

Correlation coefficient $(\times 10^{-2})$ between mean latitude temperature in January for 1891-1993.

Degr N.Lat	85	80	75	70	65	60	55	50	45	40	35	30	25	20
85	100	96	83	56	26	-4	-22	-31	-27	-20	-16	-8	3	12
80		100	92	66	35	0	-22	-34	-30	-22	-16	-7	6	12
75			100	86	56	20	-7	-27	-30	-31	-23	-6	9	14
70				100	84	52	17	-9	-17	-28	-25	-5	8	10
65					100	81	42	16	4	-8	-19	-13	0	0
60						100	82	59	39	4	-9	-7	-7	-11
55							100	90	72	27	15	11	3	-6
50								100	91	54	37	20	11	-2
45									100	76	58	35	25	6
40										100	77	42	37	19
35											100	81	68	40
30												100	78	48
25													100	75
20														100

than due to the sampling variability of the means. Large-scale atmospheric circulation components are responsible for the teleconnections in temperature fluctuations. These teleconnections are manifested in negative correlations of the anomalies in mean latitudinal air temperature values in the winter season (Table 1).

In December-January significant negative correlations are observed between latitudes of 90 to 70 N and of 55 to 40 N, In February-March negative correlations also become significant between 70-60 N and 35-25 N. During the other months long-range correlations are positive except for July.

Averaged temperature values by latitudinal zones 85-70 N, 85-65 N, 55-40 N, 40-25 N and 35-25 N preserve a significant negative correlation between the polar and other latitudinal zones (Table 2). Negative correlations in this Table do not agree with the conclusions on climate warming at all latitudes which follow from empirical estimates of the changes in mean global temperature and mean temperature over the Hemisphere (Vinnikov et al., 1994). In this connection, the obtained correlation relations were subjected to a mutual spectral analysis with calculations of the estimates of spectral densities, coherencies and phase shifts for mean temperature series of the selected latitudinal zones for all months of the year.

First of all, the estimates of a phase shift and frequencies at which the phase shift was in the intervals $0\pm\frac{\pi}{4}$ or $\pi\pm\frac{\pi}{4}$ were considered. These frequencies correspond to the components of interannual temperature fluctuations that correlate with each other positively or negatively. Further, corresponding estimates of frequency correlations (cocherencies) and spectral densities were selected and a relative contribution of positively or negatively correlated components to the variability of mean monthly temperature of the identified regions was assessed (Table 3).

The contribution of positive correlations increases during the warm half of the year except for July in some zones), and the contribution of negative correlations is maximum in winter reaching 63% in February for low latitudes. Positive correlations prevail over negative ones in all zones under consideration in June and October, and negative - in January and February. In most cases positive correlations make the prevailing contribution in the variability in May and September, and negative in March, November and December. Positive correlations are present at low frequencies (periods more than 20 years) almost in all months of the year, being also observed in the periods of 6-9 years between low and high latitudes.

Table 2.

Correlation coefficient between monthly mean air temperature at different latitudial zones of the Northern Hemisphere for 1891-1993 . (95% significant interval of Zeroth Hypothesis ± 0.20).

Region	MONTH											
	1	2	3	4	5	6	7	8	9	10	11	12
55-40/85-70°N	-0.24	-0.15	-0.05	0.09	0.02	0.39	0.12	0.12	0.33	0.27	-0.08	-0.22
35-25/85-70°N	-0.09	-0.26	-0.14	0.03	0.20	0.08	-0.17	-0.08	0.01	0.15	0.07	0.09
40-25/85-70°N	-0.17	-0.25	-0.17	0.02	0.15	0.10	-0.18	-0.07	0.08	0.21	0.02	0.02

DISCUSSION

Negative correlations of temperature fluctuations in high and low latitudes are, evidently, related to fluctuations of the winter air exchange between them. At the same time positive correlations at low frequencies indicate the effect of global factors providing concurrent temperature changes in high and low latitudes. One of them can be a change in longwave and (or) shortwave transparency of the atmosphere that affects both mean temperature and temperature of high and low latitudes and to a different extent. Let us show this by means of simple ratios of the theory of similarity of the planetary atmospheres (Golitsyn, 1973). The rate of kinetic energy generation (ε) in the atmosphere according to Golytsin is governed by the ratio: $\varepsilon = k\frac{\Delta T}{T_1}\frac{Q}{M} \equiv \gamma\frac{\Delta T}{T_1}$ (1), where K - a constant coefficient; $\Delta T = T_1 - T_2$, where

Table 3.

Relatively contribution (%) of positive and negative correlate components into variability of monthly mean temperature in different latitudial zones .

Region	MONTH											
	1	2	3	4	5	6	7	8	9	10	11	12
	Positive correlation											
55-40/85-70°N	3/17	10/25	22/18	18/21	22/23	65/53	44/41	46/35	60/51	40/31	15/24	12/22
35-25/85-70°N	21/31	19/19	28/27	28/41	32/39	21/33	12/11	24/19	20/18	32/38	20/26	23/33
40-25/85-70°N	18/34	19/33	28/27	25/38	36/40	39/38	9/8	21/12	28/22	35/41	10/24	18/31
	Negative correlation											
55-40/85-70°N	40/32	27/23	19/19	29/32	25/21	5/18	10/16	8/16	10/12	13/8	30/28	46/37
35-25/85-70°N	32/33	60/58	33/48	27/27	16/17	15/7	41/38	43/38	26/29	21/14	27/25	38/30
40-25/85-70°N	46/37	63/52	30/46	32/30	18/17	1/1	39/45	38/46	20/24	26/20	34/28	21/22

T_1 - temperature at equator; T_2 - temperature at the pole; Q - heat influx; M - mass of the atmosphere. The change in longwave atmospheric transparency (δ) results in the air temperature change near the equator (ΔT_1) and the pole (ΔT_2), respectively: $\Delta T_1 = -\frac{1}{4} T_1^3 \frac{\Delta\delta}{\delta}$, $\Delta T_2 = \frac{1}{4} T_2^3 \frac{\Delta\delta}{\delta}$

The difference of temperatures "equator-pole" changes by the value $\Delta T_1 - \Delta T_2 = \frac{\Delta\delta}{4\delta}(T_1^3 - T_2^3)$ i.e. increases at $\Delta\delta < 0$ and vice versa. In accordance with (1), the rate of the kinetic energy generation in the atmosphere changes by the value $\Delta_\delta \varepsilon = \frac{\gamma T_2}{4\delta T}\left[T_2^2 - T_1^2\right]\Delta\delta$, i.e. increases at $\Delta\delta < 0$, since $T_1 > T_2$ .From these ratios it is obvious that at smaller longwave atmospheric transparency the air temperature over the equator and the pole elevates, their difference increases, the rate of kinetic energy generation in the atmosphere grows, i.e. the atmospheric circulation enhances. The latter results in the increased poleward heat transfer and in a significant temperature growth in the polar region and its slight decrease at lower latitudes. In turn, this leads to a decreased temperature difference between them. As a result, the above mentioned correlation signs between the fluctuations of the values under consideration and their dependence on the fluctuation period are obtained.

Another factor that provides a positive temperature correlation of high, mid- and low latitudes on 6-9 year scales can be a phenomenon El-Ninjo-Southern Oscillation. In the estimates of spectra and cocherencies almost for all months there are observed maximum in these periods and they are close to those where a maximum of spectral density of fluctuations of the index of the Southern oscillation is observed.

CONCLUSIONS.

1. Interannual fluctuations of mean monthly air temperature of high, mid- and low latitudes of the Northern Hemisphere are, on the whole, negatively correlated with each other in the winter months. The contribution of negatively correlated components to the variability is maximum at high frequencies (periods less than 6 years) being evident in the range of periods 16-19 years. It decreases many times from a maximum in January-February to minimum values in June.

2. Positively correlated components of the temperature variability in the areas under consideration are observed in all seasons of the year at low frequencies (periods more than 20 years) being noticeable in the range of 6-9 year periods. Their contribution to the total variability is maximum in summer, especially in June and October, when it exceeds the contribution of negatively correlated variability components in all areas.

3. The nature of negatively correlated short-period components in the interannual variability of mean monthly temperature of different latitudinal zones is connected with the atmospheric circulation fluctuations. Positively correlated long-period components indicate the external global effect. One of them can be an increase in carbon dioxide in the atmosphere. Positive correlations of temperature fluctuations with periods 6-9 years can be a result of a global response to the phenomena of El-Ninjo-Southern Oscillation.

4. The change in the contributions of positively and negatively correlated components to the variability of mean temperature of different latitudinal zones points to the fact that the series of mean monthly air temperature in May-June and September-October is more favourable for estimating the climate signals.

ACKNOWLEDGMENT

The research described in this publication was made possible in part by Grant No NSF000 the International Science foundation.

REFERENCE

1. Alekseev G.V., Svyashchennikov P.N., 1991, Natural variability of climate characteristics in the Northern potloar region and in the Northern hemisphere (in Russian), Gidrometeoizdat, Leningrad, Russia, 159 p

2. Golitsyn G.S., 1973, Introduction to dynamics of the planet atmosphere (in Russian). Gidrometeoizdat , Leningrad , Russia,109 p.

3. Leung L.-Y. and North G.R. ,1991, Atmospheric Variability on a Zonally Symmetric Land Planet. Journ. of Climate. vol.4,p.p.753-765.

4. Lorenz E.N., 1979, Forced and free variations of weather and climate. J. Atmos. Sci., v. 763,p.p. 1367-1376.

5. Vinnikov K.Ya., Groisman P.Ya. and Lugina K.M.,1994, Global and hemispheric temperature anomalies from instrumental surface air temperature trends. In: T.A. Boden, D.P. Kaiser, R.J. Sepansky and F.W. Stoss (eds.)> Trends'93. A Compendium of Data on Global Change. ORWL/CDI-AC-65, (Carbon Dioxide Information Analisis Center, Oak Ridge National Laboratory, Oak Ridge, Tenn., USA),p.p. 615-627.

CORRESPONDING AUTHOR

Dr. G.V. Alekseev.
The Arctic and Antarctic Research Institute ,
St.-Petersburg , RUSSIA .

Cycles and Trends in Time Series of Canadian Extreme Rainfall

W.D. Hogg
Climate Research - AES, Toronto, Canada

1. INTRODUCTION

Increasingly, studies of climate trends and variability are concerning themselves with extremes as well as means of climate parameters. This is certainly the case for rainfall, where recent extreme rainfall induced flooding in central North America (1993), Europe (1994-95) and California (1995) have helped focus public and media attention. In addition, Hogg (1992) suggested that measurement program induced inhomogeneities should be less significant for annual extreme series than for annual accumulation series. Thus, the objective of this study is to analyse long time series of annual extremes of daily rainfall.

Regularly recorded climatological measurements have been made in Canada for more than 150 years and are archived for about 2800 locations at present. However, there are only about 50 stations across the country with more than 100 years of data. The majority of these stations use the AES Type B standard rain gauge. The Type B is essentially a can with a funnel and interior clear plastic liner in which the height of accumulated rainfall is manually read once or twice a day. Historically, the details of the gauge used have changed, but not significantly for measurement of annual extremes. The dataset analyzed here was collected using these instruments.

Previous work on long time series of annual extremes of daily rain (Hogg, 1991 & 1992) evaluated inhomogeneities and sampling errors in long recurrence interval statistics. Samples from the extended daily extreme data were used to estimate 100 year return period rainfall amounts. Variability in these estimates were used as a measure of the degree of homogeneity of the annual maximum rainfall series. Samples were selected by choosing contiguous years of data of varying sample size, to better simulate the start-up and closing of recording gauge stations. The visual appearance of these time series suggested the presence of cycles in extreme rainfall, presumably imposed by the climate system. This led to Fourier analysis of the time series of extremes and regression against global atmospheric circulation indices. The results of these analyses are presented here.

2. Data Analysis

Time series of annual extremes of daily rainfall were compiled for 29 stations across Canada. These stations were not subjected to rigorous homogeneity testing but were the survivors of a larger selection of long period stations whose annual accumulation time series were scrutinized for step changes, and whose station history files were searched for major moves, to eliminate unsuitable candidates. For each year at each station, the highest rainfall recorded in a single day was used. To reduce inhomogeneities due to sampling, the stations were grouped by region. Regional annual extremes were determined after normalizing station extremes by dividing by the station mean annual extreme. The regional extreme was simply the largest normalized station extreme. For display purposes, regional extremes were returned to daily precipitation units by multiplying the normalized regional extreme by the mean of regional extreme rainfall of all stations in the region. Regional extremes were considered missing if data for more than one station were missing.

To identify significant cycles, both the station and regional time series were transformed into their harmonic spectra using Fast Fourier Transforms (FFT). Power spectra were computed and expressed as percentage of total variance explained by harmonics of specific frequency (wavelength). Since the presence of trends can obscure the power spectra information (Burroughs 1992), trends were removed prior to application of FFT.

Links between regional time series of annual extremes of rainfall and features in global atmospheric circulation were also sought. Indices were used as indicators of the mode of atmospheric circulation existing during specific months. These oscillation indices were based on Barnston and Livezey (1987) and extracted by J.L. Knox as described in detail by Bonsal (1991). They attempt to quantify the degree of meridional/zonal flow in mid-latitudes, at 50 kPa, for key longitudes on the globe by measuring the mean monthly geopotential height gradient. Indices used in this study included the Western Pacific (WP) estimating gradient along approximately 155E Longitude, the Central Pacific (CP) along 160W, the Pacific North America Index (PNA) from the Gulf of Alaska to the U.S. southeast, the Western Atlantic Index (WA) along 45W Longitude, and the North Atlantic Oscillation Index (NAO) along 30W Longitude. Monthly index values were available for the period 1946-1989. Regression coefficients were determined for each time series of regional annual rainfall extremes with the time series of circulation index value for the month or season of extreme rain. Correlation coefficients of these indices with mean regional extremes were also examined but differences were not significant.

3. RESULTS

Regional time series of normalized annual extreme rainfall were constructed for each region listed in Table 1 and for Canada as a single region, using the 29 stations. Figure 1 depicts this time series for Canada and Table 2 shows the computed linear trend in daily rainfall extremes for each region. Neither station values nor these regional values indicate a significant trend in daily extreme rainfall anywhere in Canada. All trends are positive, but small (<2%/decade). One interesting fact involves a possible correlation between extreme rainfall trends and mean annual temperature trends. Environment Canada (1995) shows that the region of greatest warming in Canada, this century, is the Canadian Prairies and Western Arctic, while the Eastern Arctic is an area of cooling. Regional trend analyses described here indicate that the Eastern Arctic has the highest increase in extreme rainfall while the Canadian Prairies and Western Arctic show little or no trend. If significant, this is the reverse of the expectations of many who speculate that warming will be accompanied by greater atmospheric moisture and a more vigorous hydrologic cycle. Evidence of this contradiction is weak, however, and the most significant finding is that extreme daily rainfall amounts in Canada are not systematically increasing.

Table 1. Linear trend of annual extreme daily rainfall for regions of Canada.

Region (# stns)	Trend/Decade	Period
Canada (20)	1.5 mm (1.8%)	1900-93
Western Arctic (7)	0.3 mm (0.75%)	1925-93
Eastern Arctic (4)	0.6 mm (2.0%)	1930-93
West Coast (4)	0.4 mm (0.5%)	1910-93
Prairies (5)	0.0 mm (0.0%)	1920-93
Great Lakes (5)	0.29 mm (0.4%)	1900-93
Atlantic (4)	0.1 mm (0.1%)	1900-93

Even though absolute amounts are not increasing, it would still be important if the frequency of the larger extreme rainfall events was changing. Professor Yamamoto of Yokohama University, through Mr. Jim Bruce and a presentation by Takeda (1993), suggested a useful depiction of the frequency of extreme events. The year of occurrence of the highest ten daily rainfall events was recorded for every station in a region. The frequency of occurrence, by decade, of these record events was then plotted. Figure 2 shows the frequency histogram for the ten largest daily rainfall events, at twenty stations across Canada. Analysis was restricted to stations with data from 1910 to 1989, but only one event per year was included for each station. Once again, evidence of trend is inconclusive. The 1980's contain the highest frequency of top ten events but the 1950's are just as high and the 1970's contain the lowest frequency of record events. Regional frequency analyses show a similar picture. With the exception of the West Coast region, the 1980's are an exceptional decade for frequency of extreme rainfall, but there is no evidence that this is any sort of continuing trend. The 1950's contain the highest frequency of top ten rainfall events for the West Coast.

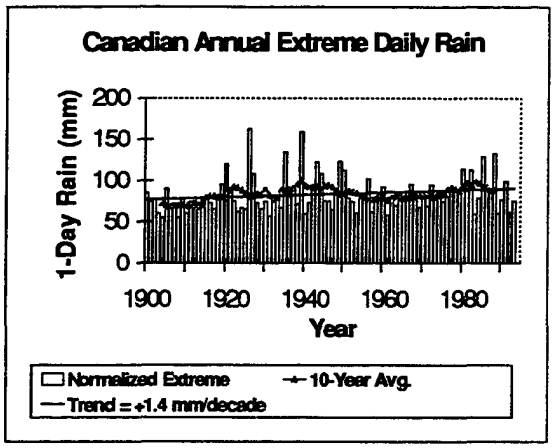


Figure 1. Normalized extreme daily rain for 20 selected stations across Canada.

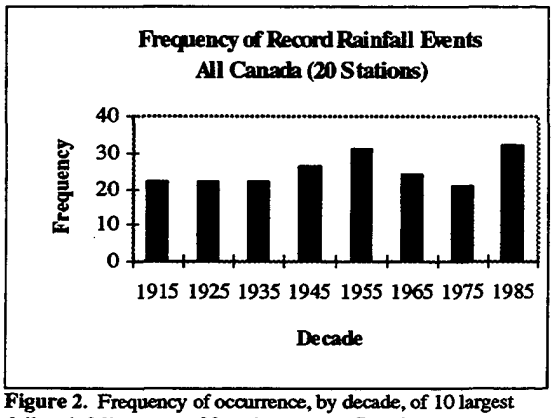
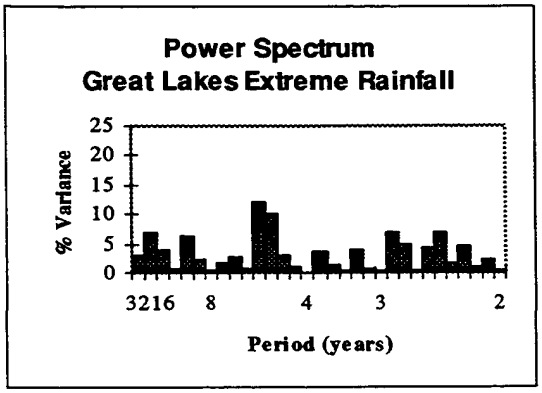


Figure 2. Frequency of occurrence, by decade, of 10 largest daily rainfall events at 20 stations across Canada.

FFT's were applied to the most recent 64 years of the regional extreme rainfall series. The results for two regions, Great Lakes and Atlantic Canada, are shown in Figure 3. The spectra for the two regions are quite dissimilar. The most significant cycles in Atlantic Canada have relatively long periods of 32 and about 9 years with little variance explained by shorter cycles. For the Great Lakes region, however, the most significant cycles have periods of 5-6 years and the longer cycles are not significant. The Arctic regions, Western Arctic in particular, have similar spectra to the Great Lakes, but the spectra for the remaining two regions are quite different. The West Coast spectrum has peaks at both 4 years and 16-20 years while the Prairies have a single significant cycle with period of 2.5 years. This contrasts with cycles identified in United Kingdom one-hour annual extreme rainfall, where Burroughs (1992) reports periodic variations of approximate lengths 7, 11,

20 and 50 years based on data from 1881 to 1986. Obviously, the strength and period of cycles in extreme rainfall vary markedly by region and duration of event. The FFT computational package used for the Canadian data restricted the number of data points to integer powers of two. This confined the analysis for all regions to 64 years, which limits the ability of the FFT to identify and resolve any long cycles. Analysis of different 64-year periods produced spectra similar to those for the most recent 64 years in all regions.



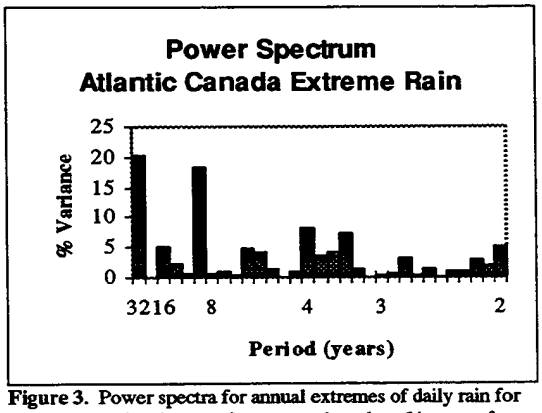


Figure 3. Power spectra for annual extremes of daily rain for two regions. Fourier transforms were based on 64 years of data.

Results of regression of regional extreme rainfall against atmospheric circulation indices were also inconsistent. Monthly values of the six circulation indices were available, so regression against seasonal minimum, maximum and mean value of the index were attempted for each region and index. A scatter plot of extreme rainfall for Prairie Region versus the Central Pacific Index is shown in Figure 4. Values of variance explained (r^2) and index used in regression for all regions are included in Table 2. The variance explained is not large for any region but is significantly greater than zero at the 1% level (based on Fisher z statistic) for Western Arctic, Prairies and Great Lakes. In fact, given the stochastic nature of rainfall, the large number of conditions which must be optimal to generate the annual extreme event, and the very poor sampling density in this study, it can be argued that it is surprising that correlation coefficients are as high as the ones shown in Table 2. There is evidence that a more rigorous selection of stations and regional boundaries would generate improved correlation coefficients for regions with poor correlation coefficients under the current definition. Two stations in Atlantic Canada had values of r over 0.6, in regression with different indices, in years when the station extreme was also the region extreme. This suggests that the stations sample different climate regions and that a better definition of regions would improve correlation coefficients. In all cases of significant regional correlation, the circulation index was thousands of kilometres removed, for either the Central or Western Pacific. Physical explanations for the relationship between these indices and extreme precipitation over continental Canada have not yet been fully developed. Presumably, the indices are one or more planetary wavelengths upstream of the region in question and are indicators of blocking situations, changes in storm tracks and changes in atmospheric moisture supply. This is a topic for additional study.

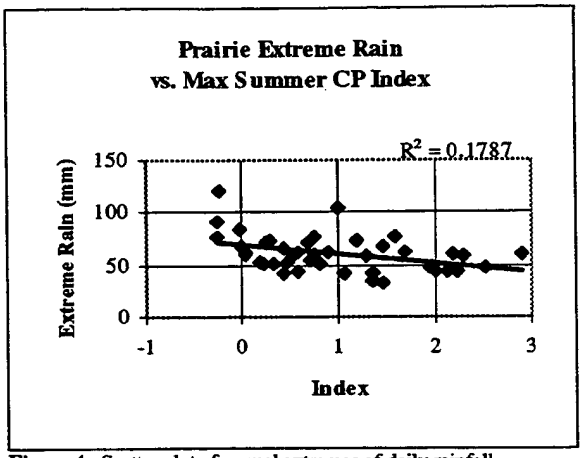


Figure 4. Scatter plot of annual extremes of daily rainfall against the maximum value of the Central Pacific (CP) atmospheric circulation index for the Prairie Region.

Table 2. Correlation coefficient r and variance explained (r^2) in regression against atmospheric circulation indices for the period 1946-1989. CP refers to Central Pacific (160W long.), PNA to the Pacific North America (Gulf of Alaska to U.S. southeast), WP to Western Pacific (155E long.) and WA to Western Atlantic (45W long.).

Region	Circ. Index	r (r^2)
Western Arctic (7)	CP	.46 (.21)
Eastern Arctic (4)	CP	.22 (.05)
West Coast (4)	PNA	.28 (.08)
Prairies (5)	CP	.42 (.18)
Great Lakes (5)	WP	.46 (.21)
Atlantic (4)	WA	.17 (.03)

4. CONCLUSIONS

The trend in extreme rainfall over the last 60-90 years for all regions of Canada is positive, but, in all cases the magnitude is so small as to be considered insignificant when compared with noise levels induced by measurement and sampling difficulties. Similarly, the frequency of the most intense one-day rainfall events has not systematically increased. Statistically significant cycles were found in all regions but cycles of the same length (5-6 years) were only identified in the Arctic and Great Lakes Regions. Evidence of longer periods seemed to be restricted to coastal regions. The most continental type climate (Prairies) had the shortest period (2.5 years) for the most significant cycle found. Correlation with time series of global atmospheric circulation indices was weak but significant for three regions. Correlation was probably weakened by the limited sampling available and by inappropriate region boundaries. The significant correlation was between Regions with continental type climates and indices for the central and western Pacific.

5. REFERENCES

Barnston, A.G. and R.E. Livezey, 1987. Classification, seasonality and persistence of low-frequency atmospheric circulation patterns. Mon. Weather Rev., June, 1987, pp 1083-1126.

Burroughs, W.J., 1992. Weather Cycles: Real or Imaginary. 207 pp. Cambridge U. Press.

Environment Canada, 1995. The state of Canada's climate: monitoring variability and change. Env. Canada, Ottawa.

Hogg, W.D., 1991. Time Series of Daily Rainfall Extremes. Preprints, Fifth Conf. on Climate Variations, 86-89 AMS Boston Ma.

Hogg, W.D., 1992. Inhomogeneities in time series of extreme rainfall. Preprints 5th International Meeting on Statistical Climatology, Toronto, June 1992, pp. 481-484. Env. Canada, AES Downsview.

Takeda, T., 1993. Remote sensing and heavy rainfall disasters. Pres. to Aichi/Nagoya Int. Decade for Natural Disaster Reduction Int. Conf. on Disaster Management in Metropolitan Areas for the 21st Century.

CORRESPONDING AUTHOR

W.D. Hogg
Climate Research, Atmospheric Environment Service
4905 Dufferin Street
Downsview, Ontario, Canada, L3Y 5N7

bhogg@dow.on.doe.ca

PROBABILISTIC DURATIONS OF AGRICULTURAL DROUGHT IN BANGLADESH DURING THE PRE-MONSOON SEASON

Rafique Ahmed

University of Wisconsin - La Crosse
La Crosse, Wisconsin, USA

ABSTRACT

Drought in Bangladesh during the pre-monsoon climatic season affects two crop seasons -- the harvesting period of the spring crop season and the planting period of the summer crop season. Crop stress duration, defined as the consecutive number of days with AE/PE < 0.5, has been used as the index of drought in Bangladesh. Probabilistic durations of drought in Bangladesh during the pre-monsoon season were evaluated for three different time-scales -- in 1 year out of 4, 10 and 25 years. The north-eastern part of the country is less vulnerable to drought than northwestern, and south and southeastern parts of the country

1 INTRODUCTION

Drought is a temporary but complex feature of the climatic system of a given region with wide spread significance. Such natural disasters leave a long lasting effect on the social and economic fabric of a region where it strikes, sometimes requiring relief efforts on a global scale.

Bangladesh, with an area of 145,600 km^2 and a population of nearly 115 million, is dependent on rainfall for agricultural practices. Although this country is known to the outer world as the land of monsoon floods, it is also prone to droughts which cause extensive damage to crops. The pre-monsoon climatic season (March through May) in Bangladesh, which accounts for 15-20% of the annual rainfall in the form of convective storms, encompasses two crop seasons -- the harvesting period of the spring crop season and the planting period of the summer crop season. Rainfall of this season is variable, both temporally and spatially, sometimes leading to drought. So, when drought occurs during this climatic season, it affects both crop seasons -- increasing the food shortage. The nature and extent of drought occurrence in Bangladesh during the pre-monsoon season are presented in this paper.

Crop yield is influenced by AE/PE, which represents the ratio between actual evapotranspiration (AE) and potential evapotranspiration (PE). One study showed that crop yield is maximized when AE/PE ratio is maintained above certain level, other conditions being equal (Lomas and Levin 1979). Experimental results showed that relative yield (the ratio between actual yield and maximum yield) decreases linearly with AE/PE, and the crops suffer from severe moisture stress when AE/PE values are less than 0.5 (Doorenbos and Kassam 1979). It has been shown that an AE/PE of 0.5 over the entire growing season causes 50% reduction in crop yield in the tropics (Doorenbos and Kassam 1979).

2 METHODOLOGY

Drought in Bangladesh has been assessed on the basis of crop stress duration, defined as the consecutive number of days during which AE/PE remains below 0.5, when crops suffer from severe moisture stress. This method was also used by Giambelluca et al (1988) in evaluating the drought in the Pacific Islands.

Using daily rainfall amount (P) and estimated PE as the input data, AE was estimated from the water balance model. The water balance equation is written as

$$P = AE + S + M \qquad (1)$$

In the above equation, S is the soil moisture surplus (drainage and runoff) and M is change in soil moisture.

PE has been evaluated by the Priestley-Taylor (1972) combination model, which is given as

$$PE = 1.26(\Delta/(\Delta+\gamma))(Q^*/\lambda) \qquad (2)$$

where Δ is the slope of the saturation vapor pressure curve at air temperature, γ is the psychrometric constant, Q^* is the net radiation, and λ is the latent heat of vaporization. Q^* was obtained by Nullet's (1987) method as follows:

$$Q^* = (1-\alpha)K_{\downarrow} - L^* \qquad (3)$$

where α is the shortwave albedo (= 0.25), $K\downarrow$ is the incoming solar radiation (MJ m^{-2} day^{-1}) under clear sky, and L^* is the net longwave radiation (MJ m^{-2} day^{-1}). $K\downarrow$ was estimated by the Nullet's (1987) method; and L^* (a function of average daily air temperature, dew point and the fraction of sky covered by clouds) was estimated by the Doorenbos-uitt (1977) method.

AE, which represents the crop water use, was evaluated by a book keeping procedure. This is a function of PE, daily rainfall amount and available soil moisture.

3 DATA

Daily rainfall (mm); and the average daily temperature (°C), dew point (°C) and cloud cover (tenths) data for the months March through May, for the 30-year period (1961 through 1990), for 19 stations were obtained from Bangladesh Meteorological Department. Stations were selected from diverse geographical and climatological areas of the country (Figure 1).

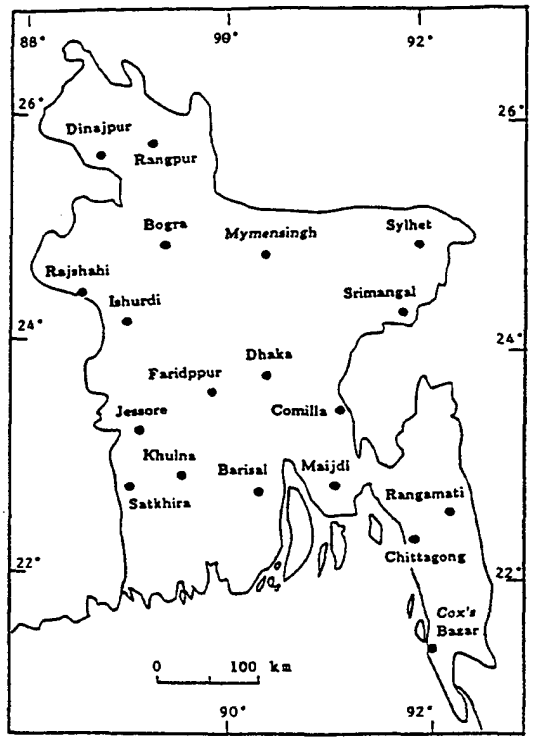


Figure 1. Location of stations.

4 ANALYSIS

For the computation of AE, the values of the moisture holding capacity of the soil used in this study varied from 150 mm in the west-central region to 300 mm in the forested hilly areas of northeast and southeast (Ahmed 1978).

Daily AE/PE values were computed for all 19 stations, for each day of the months March through May for each year, for the 30-year period from 1961 through 1990. These, in turn, were used to identify the periods of crop stress duration during which AE/PE values remained below 0.5. Then the following statistical analyses were performed:

(1) Computation of the mean ($\overline{x}$) and standard deviation (σ) of the crop stress duration.

(2) Probabilistic duration of the crop stress (x') in three different time-scales:

(a) Probabilistic duration of the crop stress in 1 year out of 4 years, which represents a relatively more frequent event. This is obtained as $x' = \overline{x} + 0.67\sigma$.

(b) Probabilistic duration of the crop stress in 1 year out of 10 years, which represents a less frequent event. This is obtained as $x' = \overline{x} + 1.28\sigma$.

(c) Probabilistic duration of the crop stress in 1 year out of 25 years, which represents a least frequent or relatively extreme event. This is obtained as $x' = \overline{x} + 1.75\sigma$.

5 RESULTS AND DISCUSSION

Mean rainfall in Bangladesh during the pre-monsoon season ranges from 200 mm in the west-central region to more than 800 mm in the northeast (Figure 2).

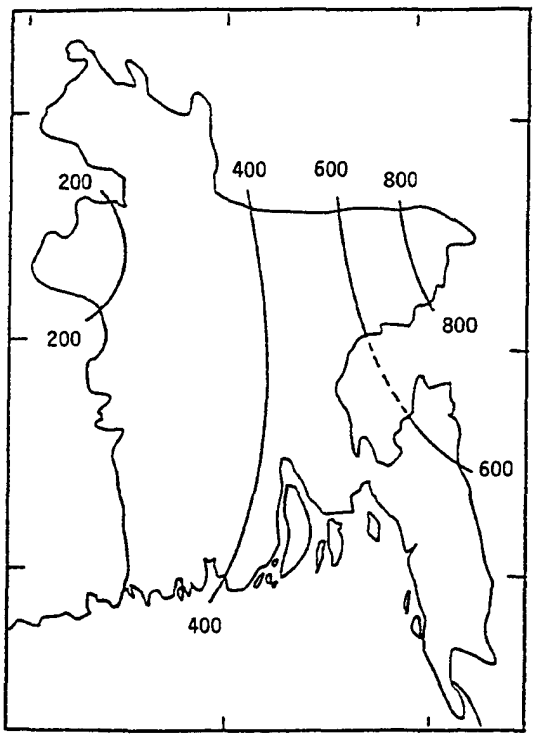


Figure 2. Mean rainfall (mm) during the pre-monsoon season (March through May).

Spatial patterns of the distribution of mean and standard deviation of the crop stress duration (CSD) in Bangladesh during the pre-monsoon season are similar. The mean CSD values vary from less than 8 days in the northeast to over 12 days in the northwest and over 14 days in the southeastern region (Figure 3); while the standard deviations of CSD vary from less than 8 days in the northeast to over 14 days in the northwest and 16 days in the southeastern region (Figure 4).

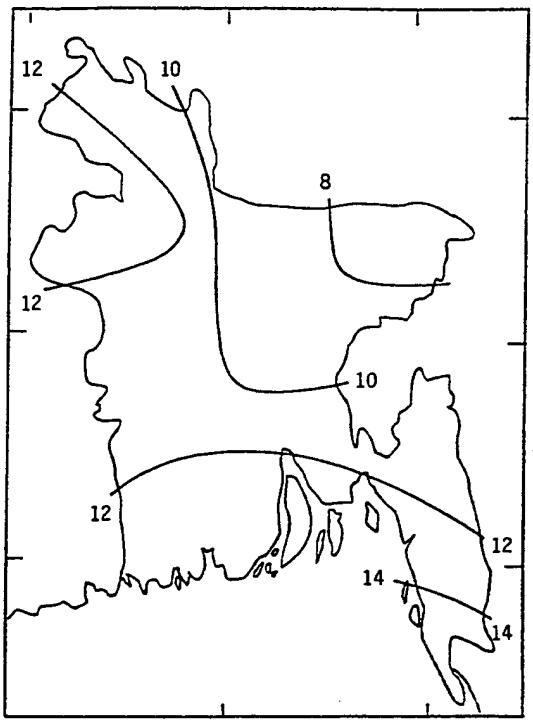


Figure 3. Mean crop stress duration (days).

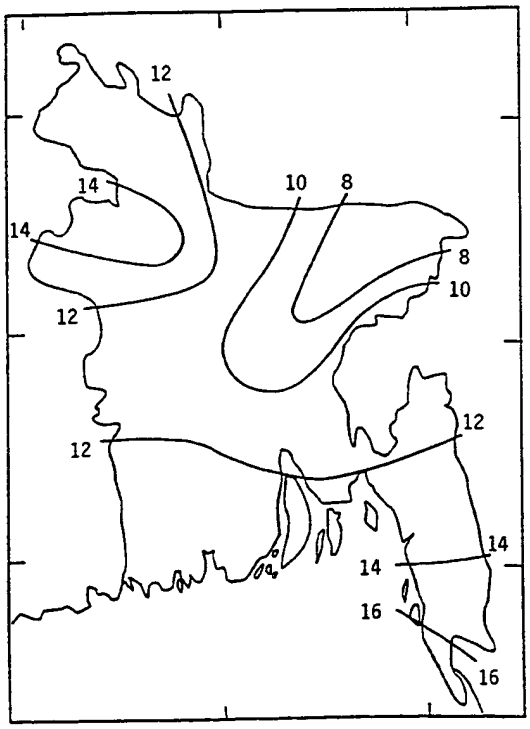


Figure 4. Standard deviation of the crop stress duration (days).

The probabilistic duration of crop stress in 1 year out of 4 years, which represents a relatively more frequent event, varies from 12 days in the northeast to over 22 days in the northwest and over 26 days in the southeast (Figure 5). The probabilistic duration of crop stress in 1 year out of 10 years, representing a less frequent event, ranges from less than 20 days in the northeast to 32 days in the northwest to 36 days in the southeast (Figure 6) .

The probabilistic duration of crop stress in 1 year out of 25 years, which represents an extreme event, varies from less than 24 days in the northeast to 40 days in the northwest and 44 days in the southeast (Figure 7).

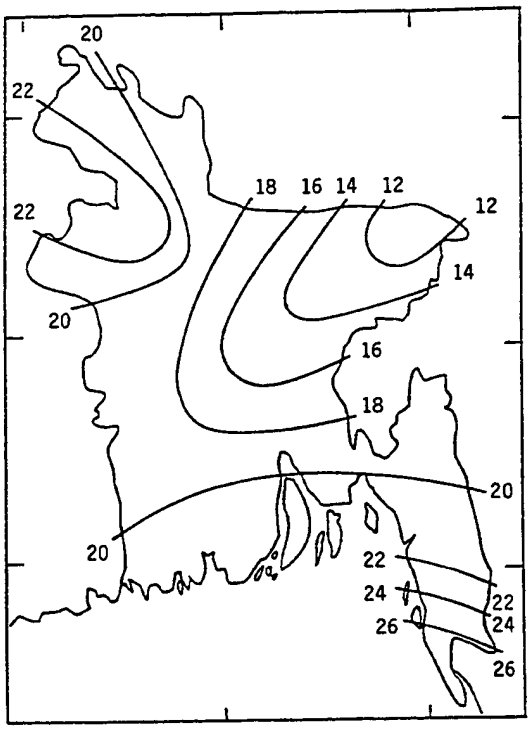


Figure 5. Crop stress duration (days) in 1 year out of 4 years.

6 CONCLUSIONS

The crop stress duration (CSD), defined as the consecutive number of days when AE/PE remains below 0.5, has been used as the index of drought in Bangladesh during the pre-monsoon season (March through May). Using (a) daily estimated PE obtained by the Priestley-Taylor (1972) combination method and (b) daily rainfall as input data in the water balance model, daily AE and AE/PE were evaluated for each day of the months March through May for the thirty year period (1961-1990), at 19 stations of the country. These were then used to obtain various statistical parameters of the CSD in Bangladesh during the season.

The results reveal the mean and standard deviation of CSD, and the probabilistic durations of CSD in Bangladesh during the pre-monsoon season at three time-scales -- in 1 year out of 4, 10, and 25 years, representing relatively more frequent, less frequent and least frequent event, respectively.

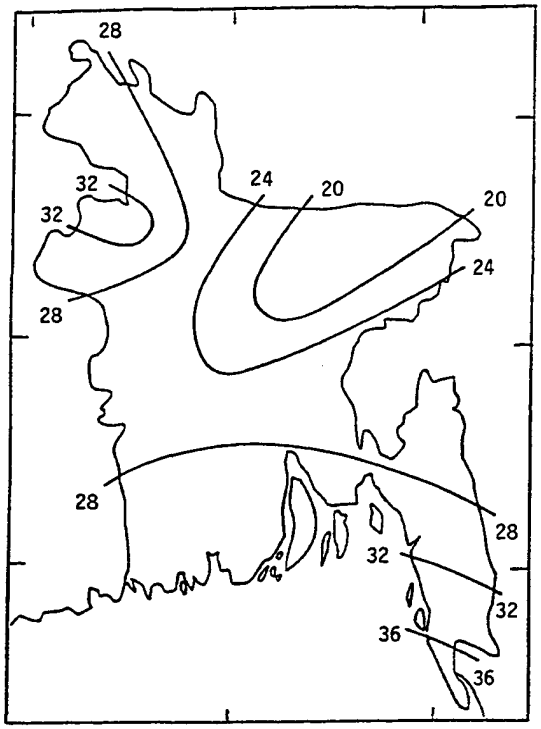


Figure 6. Crop stress duration (days) in 1 year out of 10 years.

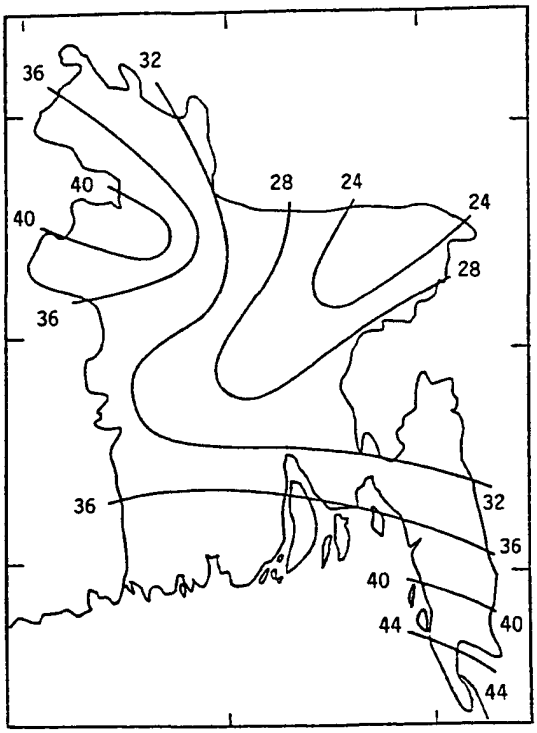


Figure 7. Crop stress duration (days) in 1 year out of 25 years.

Findings of this study will serve two purposes. First, these will be useful to agricultural planners and irrigation engineers of Bangladesh for identifying the areas where agricultural development should be focused as a long-term drought mitigation strategy. Such strategies may include the development and adoption of crops which are resistant to moisture stress, and the determination of irrigation water requirements in different areas of the country. Secondly, this study will contribute toward a better understanding of the climatology of drought in a major monsoon region of the world.

7 REFERENCES

Ahmed, R. 1978, "The Variability of Some Water Balance Parameters of the Pre-monsoon Season in Bangladesh", MA Thesis, Department of Geography, University of Windsor, Windsor, Ontario, Canada.

Doorenbos, J. and Kassam, A. H., 1979, "Yield Response to Water", FAO Irrigation and Drainage Paper No. 33, Rome.

Doorenbos, J. and Pruitt, W. O., 1977, "Crop Water Requirements", FAO Report No. 24, Rome.

Giambelluca, T. W., Nullet, D. and Nullet, M. A., 1988, "Agricultural Drought of South-Central Pacific Islands", Professional Geographer, Vol. 40, pp.404-415.

Lomas, J. and Levin, J., 1979, "Irrigation", in Seaman, J., Chirkov, Y. I, Lomas, J. and Primault, B. (eds.), Agrometeorology, Springer-Verlag, Berlin, pp. 217-264.

Nullet, D., 1987, "Water Balance of Pacific Atolls", Water Resources Bulletin, Vol. 23, pp. 1125-1132.

Priestley, C. B. H. and Taylor, R. J., 1972, "On the Assessment of Surface Heat Flux and Evaporation Using Large Scale Parameters", Monthly Weather Review, Vol. 100, pp. 81-92,

Taylor, J., 1983, "Quantitative Methods in Geography", Houghton Miffin, Boston.

ACKNOWLEDGEMENT

This research project was supported by a Faculty Research Grant from the University of Wisconsin-La Crosse, La Crosse, Wisconsin, USA (1993-1994).

CORRESPONDING AUTHOR

Rafique Ahmed, Ph. D.
Associate Professor
Geography & Earth Science
University of Wisconsin-La Crosse
La Crosse, Wisconsin 54601, USA

Probability Models and Design Values of Extreme Rainfall over China on Various Time Scales

Xiaolan Wang, João Corte-Real and Xuebin Zhang
Department of Physics, Faculty of Sciences, University of Lisbon, Portugal

ABSTRACT

Probability models of Fisher-Tippett types and Gamma types were respectively fitted to annual maximum series of 1, 2, 3, 5, 7, and 10 day rainfall accumulations for 130 stations in China, and the goodness of fit of the candidate models were tested and compared. It is concluded that the Frechét distribution is the most common distribution of annual extreme rainfalls in China, followed by the Pearson Type 3 and 2-parameter Gamma distributions. Precipitation amounts associated with average return periods of 2, 5, 10, 20, 50 and 100 years were estimated from the models of best-fit.

1. INTRODUCTION

Extreme value analysis is concerned with the largest (or smallest) values in a record or in a set of several records. In practical applications, knowledge of the probability distribution of extreme values is particularly important; for example, the probability of flooding is often derived from an extreme value distribution of precipitation amounts. The statistics of precipitation extremes are of interest for a variety of planning and engineering purposes. Conventionally, these statistics are expressed in terms of "average return periods", most often derived from quantiles of a parametric probability model fitted to the largest precipitation values in the climatological record. Fitted models are used both to smooth the data and to extrapolate beyond the available data, i.e., to estimate the precipitation amount (design value) associated with an average return period which is longer than the period of available data.

There have been some studies on the probability models of extreme precipitation in China (Wang, 1991; etc.). However, previous studies generally focused on extreme precipitation at one site or a few stations in a subregion, and on a specific time scale. A more comprehensive study on this topic is still needed.

Studies of extremes in climatological records mostly refer to annual or seasonal maxima. The objective of this study is to fit various probability models to the annual maximum series of rainfall accumulations for durations of 1~10 days at 130 stations in China, to ascertain what probability models are more suitable for describing the extremes, whether the probability distributions of annual extreme rainfall in China vary with the location or duration and to provide a preliminary climatological atlas for precipitation extremes in China.

2. DATA AND PROCEDURES

In general, physical knowledge of the underlying processes does not provide satisfactory information about the probabilities of rare events. It is also not correct to base the choice of a particular distribution merely on mathematical arguments concerning asymptotic properties of extremes. A careful analysis of historic data is needed to find the most appropriate distribution. Usually the fits of two or several candidate distributions have to be compared. By comparing the goodness of fit of Lognormal, Gumbel, 2-parameter Gamma, Pearson Type 3 and Weibull distributions, Wang (1991) concluded that Pearson Type 3 and Weibull distributions are most suitable for describing the annual maxima of daily rainfall in East China, Gumbel and 2-parameter Gamma/Weibull distributions being not suitable for describing annual rainfall extremes in such a region of humid climate. To investigate the extreme precipitation in China (both East and West China) which possesses humid, semi-arid and arid climates, the parametric probability models of Fisher-Tippett types (including Gumbel, Frechét and Weibull distributions) and Gamma types (Pearson Type 3 and 2-parameter Gamma distributions) are chosen as the candidate models. For details about the candidate models, see NERC (1975) and Buishand (1989).

For each of the 130 stations well covering Eastern China (east of 97°E) and Northwest China, annual maxima series $X_0(j)$ of (consecutive) 1, 2, 3, 5, 7 and 10 day rainfall accumulations were sampled from daily rainfall series for the period 1953-1982 (n = 30; j = 1, 2, ..., n), and denoted by AE1d, AE2d, AE3d, AE5d, AE7d and AE10d respectively. Then, each of the five candidate probability models listed above were fitted respectively to each of the six annual maximum series for each of the 130 stations. Various estimators such as conventional Moment, Probability Weighted Moment and Maximum Likelihood (NERC, 1975; Greenwood, et al., 1979; Buishand, 1989; Otten, et al., 1980), as well as the method of Sextiles (Faragó and Katz, 1990; NERC, 1975) were used in the estimation of parameters of the probability models.

The fit of each probability model, combined with some estimator, was first examined by performing the following χ^2 test for goodness of fit (ECTUWR, 1980; Crow et al., 1960):

Suppose the sample values from an experiment fall into r categories. To decide, at the significance level α *, whether the data constitute a sample from a population with distribution function F(x) (including l parameters), we compute*

$$Z=\sum_{i=1}^{r}\frac{(o_i-e_i)^2}{e_i}$$

where o_i *and* e_i *are respectively the observed and expected (theoretical) frequencies for the i-th category (i = 1, 2, ..., r; the grouping should be arranged so that* $e_i \geq 5$ *and* $r \geq 5$*). If Z exceeds the critical value of* χ^2 *distribution for* $\nu = r-1-l$ *degrees of freedom, i.e.,* $Z > \chi^2(\alpha, \nu)$*, reject at the significance level* α *the null hypothesis that the distribution function is F(x).*

Then, the following relative standard error *RSEr* was used as an index of fit:

$$RSEr=\sqrt{\frac{1}{n}\sum_{i=1}^{n}\left[X_o(p_i)-X_e(p_i)\right]^2}\Big/\left[\frac{1}{n}\sum_{i=1}^{n}X_o(p_i)\right]$$

where $X_o(p_i)$ is the i-th smallest observed annual maximum, whose empirical cumulative probability p_i is estimated as

$p_i=(i-0.44)/(n+0.12)$ for Gumbel distribution (Guo, 1990)

$p_i=(i-0.40)/(n+0.20)$ for other distributions (Guo, 1990),

and $X_e(p_i)$ is the estimated value associated with the cumulative probability p_i.

Finally, for each of the 130 stations and for each of the six extreme value series, the model with smallest *RSEr* value is chosen as the model of best fit at the significance level α = 0.05, among the models accepted (not rejected in the χ^2 test). The closeness of fit was also examined by using quantile-quantile (Q-Q) plots, that is, the empirical quantiles $X_o(p_i)$ (on the vertical axes) versus the estimated quantiles (model quantiles) $X_e(p_i)$ (on the horizontal axes). A perfect fit is indicated by all points being on the 1:1 line, while underestimates are indicated by points falling above the line, and overestimates by points located below the line (Wilks, 1992).

3. RESULTS

Probability models of best-fit to the six extreme value series are listed in Table 1, from which one can see that the probability distribution types of annual extreme rainfalls in China vary with both the location and duration of extreme precipitation, except for Urumchi (No. 15), Dunhuang (No. 19), Fuyang (No. 97), Hangzhou (No. 104), Nanchang (No. 105) and Nanning (No. 118), where the Frechét distribution fits best to all the six extreme value series (for six durations), for Hami (No. 18), where all the six extreme value series possess a probability distribution of Weibull type, and for Jiuquan (No. 20) and Yinchuan (No. 27) where the 2-parameter Gamma distribution fits best to all the six series. The numbers of stations in relation to the models and estimators of best-fit to the six extreme value series are given in Table 2, which clearly shows that the most common

Table 1 Models of best fit to the annual maximum series of 1, 2, 3, 5, 7 and 10 day rainfall accumulations (AE1d, AE2d, AE3d, AE5d, AE7d and AE10d) for 130 stations in China (F: Frechét; W: Weibull; G: Gumbel; Γ2: 2-parameter Gamma; P3: Pearson Type 3).

Station No	WMO-No	Annual Extreme series (AE1d	AE2d	AE3d	AE5d	AE7d	AE10d)
1	50527	W	P3	P3	Γ2	P3	W
2	50557	F	P3	G	G	G	G
3	50632	P3	P3	Γ2	G	P3	Γ2
4	50727	W	F	F	F	F	G
5	50745	P3	F	F	W	Γ2	Γ2
6	50756	W	P3	P3	Γ2	Γ2	P3
7	50788	F	F	P3	G	F	F
8	50949	F	W	P3	W	W	W
9	50953	G	Γ2	Γ2	P3	Γ2	P3
10	50963	F	G	P3	W	Γ2	P3
11	50978	P3	Γ2	Γ2	F	Γ2	Γ2
12	51334	P3	P3	P3	W	G	Γ2
13	51379	W	G	F	P3	F	F
14	51431	F	G	Γ2	W	G	G
15	51463	F	F	F	F	F	F
16	51573	F	F	F	Γ2	Γ2	F
17	51644	F	F	P3	F	P3	F
18	52203	W	W	W	W	W	W
19	52418	F	F	F	F	F	F
20	52533	Γ2	Γ2	Γ2	Γ2	Γ2	Γ2
21	52681	P3	P3	Γ2	F	F	W
22	52787	P3	P3	W	F	W	P3
23	52866	G	Γ2	P3	W	W	W
24	52889	F	F	F	Γ2	P3	Γ2
25	53276	F	F	F	F	Γ2	Γ2
26	53463	F	F	P3	F	P3	F
27	53614	Γ2	Γ2	Γ2	Γ2	Γ2	Γ2
28	53646	F	G	G	Γ2	G	G
29	53698	P3	P3	P3	F	F	F
30	53772	F	P3	F	G	G	G
31	53845	F	F	G	F	G	G
32	54026	Γ2	Γ2	Γ2	P3	Γ2	Γ2
33	54094	P3	P3	F	F	W	W
34	54102	F	P3	F	F	F	F
35	54115	P3	F	F	F	F	G
36	54135	Γ2	W	Γ2	F	F	F
37	54161	Γ2	P3	W	P3	Γ2	W
38	54172	W	W	W	Γ2	P3	P3
39	54208	G	F	F	G	P3	P3
40	54218	F	F	P3	F	F	F
41	54237	P3	Γ2	Γ2	Γ2	Γ2	Γ2
42	54292	Γ2	F	G	F	F	F
43	54337	F	F	F	F	Γ2	F
44	54374	F	F	Γ2	Γ2	P3	Γ2
45	54423	F	F	P3	P3	P3	P3
46	54471	F	F	F	F	W	W
47	54483	F	P3	W	Γ2	Γ2	Γ2
48	54497	P3	F	F	F	F	F
49	54511	F	P3	F	F	F	F
50	54527	W	W	P3	P3	P3	W
51	54602	F	F	F	G	F	F
52	54662	Γ2	G	F	W	W	Γ2
53	54776	F	P3	F	F	F	F
54	54823	F	F	F	F	G	G
55	54843	F	Γ2	F	F	G	W
56	54916	P3	F	F	F	G	F
57	56033	F	F	F	F	Γ2	P3
58	56080	F	Γ2	W	P3	P3	P3
59	56093	Γ2	F	Γ2	P3	Γ2	G
60	56146	Γ2	P3	G	G	G	P3
61	56182	P3	Γ2	P3	G	P3	P3
62	56294	P3	P3	F	F	F	F
63	56462	P3	Γ2	Γ2	Γ2	Γ2	F
64	56492	Γ2	Γ2	P3	P3	W	P3
65	56571	G	W	W	F	P3	Γ2
66	56671	P3	G	F	F	P3	F
67	56739	F	Γ2	Γ2	Γ2	P3	P3
68	56964	P3	W	P3	P3	P3	Γ2
69	57006	G	P3	Γ2	Γ2	P3	W
70	57016	F	F	P3	F	F	F
71	57036	P3	F	F	Γ2	G	F
72	57067	P3	F	P3	P3	F	F
73	57083	G	W	Γ2	P3	F	P3
74	57089	P3	Γ2	Γ2	Γ2	Γ2	W
75	57245	P3	P3	P3	P3	F	F
76	57265	F	Γ2	Γ2	Γ2	W	Γ2
77	57290	F	G	F	F	F	F
78	57297	W	P3	G	G	F	F
79	57411	Γ2	P3	P3	W	Γ2	Γ2
80	57447	Γ2	P3	Γ2	Γ2	Γ2	Γ2
81	57461	P3	Γ2	Γ2	P3	W	P3
82	57494	P3	P3	P3	P3	Γ2	Γ2
83	57515	F	F	P3	P3	F	F
84	57662	W	F	F	Γ2	P3	Γ2
85	57679	P3	F	G	F	F	F
86	57707	P3	W	Γ2	Γ2	P3	P3
87	57713	W	Γ2	Γ2	P3	P3	P3
88	57745	P3	F	P3	F	F	F
89	57799	F	G	W	P3	G	G
90	57816	P3	F	P3	F	Γ2	G
91	57872	F	P3	P3	F	F	F
92	57957	P3	P3	F	P3	P3	G
93	57972	P3	Γ2	F	W	P3	Γ2
94	57993	F	F	G	G	P3	F
95	58027	P3	F	P3	P3	P3	Γ2
96	58144	Γ2	G	G	Γ2	Γ2	W
97	58203	F	F	F	F	F	F
98	58221	Γ2	W	P3	W	F	Γ2
99	58238	Γ2	Γ2	Γ2	P3	F	Γ2
100	58251	F	F	P3	G	P3	W
101	58321	W	F	G	P3	F	F
102	58361	F	F	G	W	P3	W
103	58424	F	F	F	F	F	Γ2
104	58457	F	F	F	F	F	F
105	58606	F	F	F	F	F	F
106	58633	P3	G	F	F	F	F
107	58659	F	F	G	G	F	F
108	58834	Γ2	P3	F	F	F	F
109	58847	Γ2	Γ2	P3	Γ2	P3	W
110	59082	F	W	W	Γ2	G	Γ2
111	59134	Γ2	F	F	P3	F	F
112	59211	P3	F	P3	P3	W	P3
113	59265	F	F	F	F	F	G
114	59287	P3	F	Γ2	Γ2	Γ2	Γ2
115	59293	F	F	F	F	F	P3
116	59316	Γ2	F	P3	P3	Γ2	P3
117	59417	F	P3	P3	F	F	P3
118	59431	F	F	F	F	F	F
119	59501	F	W	G	P3	W	Γ2
120	59663	Γ2	Γ2	W	Γ2	Γ2	Γ2
121	59758	Γ2	F	F	F	Γ2	F
122	59838	Γ2	Γ2	Γ2	Γ2	Γ2	W
123	59855	F	P3	Γ2	Γ2	G	G
124	46692	P3	P3	G	Γ2	Γ2	P3
125	46749	F	F	G	F	Γ2	Γ2
126	46708	P3	F	P3	F	F	F
127	46699	P3	Γ2	P3	W	G	G
128	46741	G	F	F	F	F	F
129	46766	F	F	F	P3	F	F
130	46759	P3	P3	W	W	W	W

distribution type of annual extreme rainfalls in China is the Frechét distribution, which fits best for more than one third (44-55) of the 130 stations; the Pearson Type 3 (P3) and 2-parameter Gamma (Γ2) distributions are the second most common distributions, each of them being the model of best-fit for about 20% of the stations. The spatial characteristics of the probability distribution types of the six annual extreme rainfalls will be discussed in more detail later in the subsections. For more details in this regard, readers are referred to Wang (1995).

From Table 2, it can also be concluded that, for a 30-year length series of annual extremes, the method of Probability Weighted Moment (PWM) is the best estimator (among the four estimators used) for estimation of parameters of Frechét and Weibull distributions, while the method of conventional Moment (Mo) is the best estimator for distributions of Gamma (P3 and Γ2) and Gumbel types.

For most stations and durations, the relative standard errors (*RSEr*) of the best-fit models are less than 10%, with Q-Q points generally falling quite near the 1:1 line. Q-Q plots (not shown) reveal that larger standard errors are mostly associated with underestimates on the right tail, that is, underestimates for the largest value(s) in the extreme series, some of which are likely outliers.

Based on the models of best-fit for each of the six durations, the precipitation amounts associated with average return periods of 2, 5, 10, 20, 50 and 100 years (design values) were estimated (cf. Wang, 1995); contour charts of design values for the 50 year return period will be shown and discussed herein below.

3.1 Annual Maximum 1 Day Rainfall

For 1 day duration, the probability distributions of annual extreme rainfalls (AE1d) can mainly be described by the models of Gamma types (P3 and Γ2) in the following regions: Northern and Southern Taiwan, Fujian Province, the coastal areas of Guangdong Province, the upper-middle Yangtze River basin (including Yunnan, Guizhou, Hubei and Sichuan Provinces), Henan and Jiangsu Provinces, the Changbai Mountains, the upper-middle Liaohe River basin, and central Gansu and Lingxia Provinces. The Generalized Extreme Value distributions (G, F and W) fit well the annual extremes in the other regions, especially in North China, the Boyang Lake and upper Huaihe River basins, with shape parameters k ranging from -0.3366 to +0.3206.

The contour chart of annual maximum 1 day rainfalls associated with the 50 year return period is shown in Fig. 1(a), from which it can be seen that the largest design values of AE1d appear in Taiwan (400~475 mm), Hainan, Guangdong and Southern Fujian Provinces (300~400 mm); some large design values of 200~325 mm can be observed in the Changbai Mountains, Eastern Hubei Province, Northern Guangxi Province and Sichuan Basin, constituting secondary centers of design values.

3.2 Annual Maximum Consecutive 2 Day Rainfall

The probability distributions of annual maximum consecutive 2 day rainfalls (AE2d) in East China and the eastern part of North and Northeast China, in the Loess Plateau and Northwest China, as well as in the Yunnan-Guizhou Plateau and the Pearl River basin, can mainly be described by the GEV distributions (G, F and W), with shape parameters k ranging from -0.3501 to +0.2376. The probability models of Gamma types (P3 and Γ2) fit well the annual rainfall extremes in the Hanshui River basin - Sichuan Basin, in Gansu and Lingxia Provinces, as well as in the western part of Northeast China.

The contour chart of annual maximum consecutive 2 day rainfalls (AE2d) associated with the 50 year return period (see Fig. 1(b)) show

that the largest design values of AE2d appear in Taiwan (500~625 mm), Hainan, Guangdong and Southern Fujian Provinces (400~500 mm), while design values of 300~400 mm are estimated for the eastern slopes of Changbai and Taihang Mountains, for Eastern Hubei and Northern Guangxi Provinces, as well as for the regions from Southern Fujian-Jiangxi Provinces southwestward to Eastern Guangxi Province.

3.3 Annual Maximum Consecutive 3 Day Rainfall

For 3 day duration, annual extreme rainfalls in central Northeast China and central South China (around the Qingling-Nanling Mountains) can mainly be described by the probability models of Gamma types (P3 and Γ2), whereas the GEV distributions (G, F and W) generally appear to be the models of best-fit to the annual extremes in North China, and in the region southward and eastward of Dongting Lake (including Taiwan), with shape parameters k ranging from -0.3634 to +0.2732.

As shown in Fig. 1(c), for the 50 year return period, the design values of annual maximum consecutive 3 day rainfalls (AE3d) are about 575~675 mm over Taiwan, and about 500~575 mm over Hainan Island and the coastal areas of Guangdong Province; it ranges from 300 mm to 500 mm over Southern Fujian, Northern Guangdong and Guangxi Provinces; in Eastern Hubei Province and the eastern slopes of Changbai and Taihang Mountains, design values range from 300 to 425 mm, while in the other regions design values are generally less than 300 mm.

3.4 Annual Maximum Consecutive 5 Day Rainfall

The probability models of Gamma types (P3 and Γ2) generally fit well the annual maximum series of consecutive 5 day rainfalls (AE5d) in the coastal areas of Guangdong and Fujian Provinces, in the middle Yangtze River basin and the Qingling Mountains, as well as in Central Liaoling and Eastern Jilin Provinces. The annual extreme rainfalls in the other regions can mainly be described by the GEV distributions (G, F and W), with shape parameters k ranging from -0.4433 to +0.3854.

It is shown in the contour chart of AE5d associated with a return period of 50 years that the largest design values of annual maximum rainfall for 5 day duration appear in Taiwan (600~800 mm), Guangdong and Southern Fujian Provinces (400~600 mm), with secondary centers of large design values (400~500 mm) located in the eastern slopes of Taihang and Changbai Mountains, as well as in the Boyang Lake basin and Northern Guangxi Province, as can be seen from Fig. 2(a).

3.5 Annual Maximum Consecutive 7 Day Rainfall

For 7 day duration, annual extreme rainfalls in the middle Pearl River basin and the middle-lower reaches of Yellow and Yangtze River basins (except Jiangsu Province) generally possess probability models of Gamma types (P3 and Γ2), whereas the GEV distributions (G, F and W) appear to be the models of best-fit to the annual extremes for most stations in Northeast China and the upper reaches of Yellow and Yangtze River basins, with shape parameters k ranging from -0.4065 to +0.5862.

As shown in Fig. 2(b), the largest design values of annual maximum consecutive 7 day rainfall (AE7d), for the 50 year return period, occur in Taiwan, Guangdong and Southern Fujian Provinces, with the amount of 500~950 mm; some large design values (300~500 mm) appear in Northern Guangxi Province and the Boyang Lake basin, as well as in the eastern slopes of Changbai and Taihang Mountains.

3.6 Annual Maximum Consecutive 10 Day Rainfall

In general, the GEV distributions (G, F and W) fit well the annual maximum series of consecutive 10 day rainfalls (AE10d) in the middle-lower Yellow River and the Dongting-Boyang Lake basins, and in the Eastern Coasts and the Liaohe River basin, with shape parameters k ranging from -0.3905 to +0.5048. The annual extreme rainfalls in central Northeast China and Guangdong Province and along the Yangtze River valley, can mainly be described by the probability models of Gamma types (P3 and Γ2).

Contour charts of AE10d associated with a return period of 50 years (see Fig. 2(c)) show that design values of AE10d range from 700 to 950 mm over Taiwan, and from 500 to 800 mm over Hainan and Guangdong Provinces, with design values of 400~600 mm located in the eastern slopes of Taihang and Changbai Mountains, as well as in the Boyang Lake basin and Northern Guangxi Province.

4. CONCLUDING REMARKS

Probability models of Fisher-Tippett and Gamma types have been respectively fitted to annual maximum series of 1, 2, 3, 5, 7 and 10 day rainfall accumulations, and the goodness of fit of the five candidate models have been tested and compared. The results show that probability distribution types of annual extreme rainfalls in China vary with both the location and duration of extreme precipitation; the Frechét distribution is the most common distribution, followed by the Pearson Type 3 and 2-parameter Gamma distributions. For a moderate sample size ($N < 50$), estimations of Probability Weighted Moment (PWM) and conventional Moment (Mo) are preferable to the Maximum Likelihood estimation; among the three estimators, the PWM method is the best estimator for Frechét and Weibull distributions, while the method of conventional Moment leads to the best-fit estimations for distributions of Gamma (P3 and Γ2) and Gumbel types.

Based on the models of best-fit to the six extreme value series, extreme precipitation amounts associated with average return periods of 2, 5, 10, 20, 50 and 100 years have been estimated. The largest design values of extreme rainfalls in China appear in Taiwan and the coastal areas of Southeast China, with some secondary centers of large design values located in Northern Guangxi and Eastern Hubei Provinces, in the eastern slopes of the Taihang and Changbai Mountains, as well as in the Sichuan Basin. These regions of large design values of extreme rainfalls are actually the regions known to be most vulnerable to extreme precipitation in China (cf. Wang, 1995).

Finally, it should be pointed out that the conclusions drawn from this study are restricted within the data limit. An updated data set is needed to corroborate the results and to update the atlas for precipitation extremes in China.

ACKNOWLEDGEMENTS

This research was supported by a doctoral scholarship provided by JNICT (National Board for Scientific and Technological Research, Portugal).

REFERENCES

Buishand, T. A., 1989: "Statistics of extremes in climatology". Statistica Neerlandica, 43 (1989), nr. 1, 1-31.

Crow, E. L., F. A. Davis and M. W. Maxfield, 1960: "Statistics Manual". Dover Publications, INC., New York, 288pp.

ECTUWR (East China Technical University of Water Resources), 1980: "Probability and Statistics in Hydrology". China Water Resources Press, Beijing, 461pp.

Faragó, T. and R. W. Katz, 1990: "Extremes and Design Values in Climatology". WCAP-14, WMO/TD-NO.386. 43pp..

Greenwood, J. A. and J. R. Wallis, 1979: "Probability Weighted Moments: Definition and Relation to Parameters of Several Distribution Expressable in Inverse Form". Water Res. Res., 15, No. 5, 1049-1054.

Guo, S. L., 1990: "A discussion on unbiased plotting positions for the general extreme value distribution". J. Hydrol., 121: 33-44.

NERC (Natural Environment Research Council), 1975: "Flood studies report", Volume I, Whitefriars Press, London.

Otten, A. and M. A. J. Van Montfort, 1980: "Maximum-Likelihood Estimation of the General Extreme-Value Distribution Function Parameters". J. Hydrol., 47, 187-192.

Wang, X., 1995: "Planetary Scale Circulation, Climate and Extreme Events in East Asia". A doctoral dissertation presented to the Faculty of Sciences, University of Lisbon.

Wang, X., 1991: "Distribution model and characteristics of daily extreme precipitation in the East of China". In: Climatological Research — Statistical Climatology (Ed. by Yao, Z.), 69-77 (in Chinese).

Wilks, D. S., 1992: "Comparisons of Parametric Distributions to Describe Precipitation Extremes". In: 12th Conf. on Prob. and Statist. in the Atmosph. Sci., 1992, Toronto, Ontario, Canada. 28-33.

CORRESPONDING AUTHOR

Xiaolan Wang, Department of Physics, Faculty of Sciences, University of Lisbon, Campo Grande, Ed. C1, Piso 4, 1700 Lisbon, Portugal (on leave from the Department of Hydrology and Water Resources, Hohai University, Xikang Road 1, Nanjing 210024, P. R. China).

Table 2 Numbers of stations in relation to the models and estimators of best-fit to the six annual extreme series of rainfalls in China (F: Frechét; W: Weibull; G: Gumbel; Γ2: 2-parameter Gamma; P3: Pearson Type 3).

Extreme	Generalized Extreme Value (GEV) distributions					2-parameter Gamma (Γ2)		Pearson Type 3 (P3)	
Series	G-Mo	G-PWM	F-PWM	W-PWM	GEV-Stl	Γ2-Mo	Γ2-ML	P3-Mo	P3-ML
AE1d	6	1	53	11	0	20	2	35	2
AE2d	9	1	55	12	0	22	1	27	3
AE3d	15	0	44	11	0	25	1	27	7
AE5d	11	1	49	14	0	25	3	26	1
AE7d	15	0	45	13	0	28	2	26	1
AE10d	15	0	45	18	0	25	5	22	0

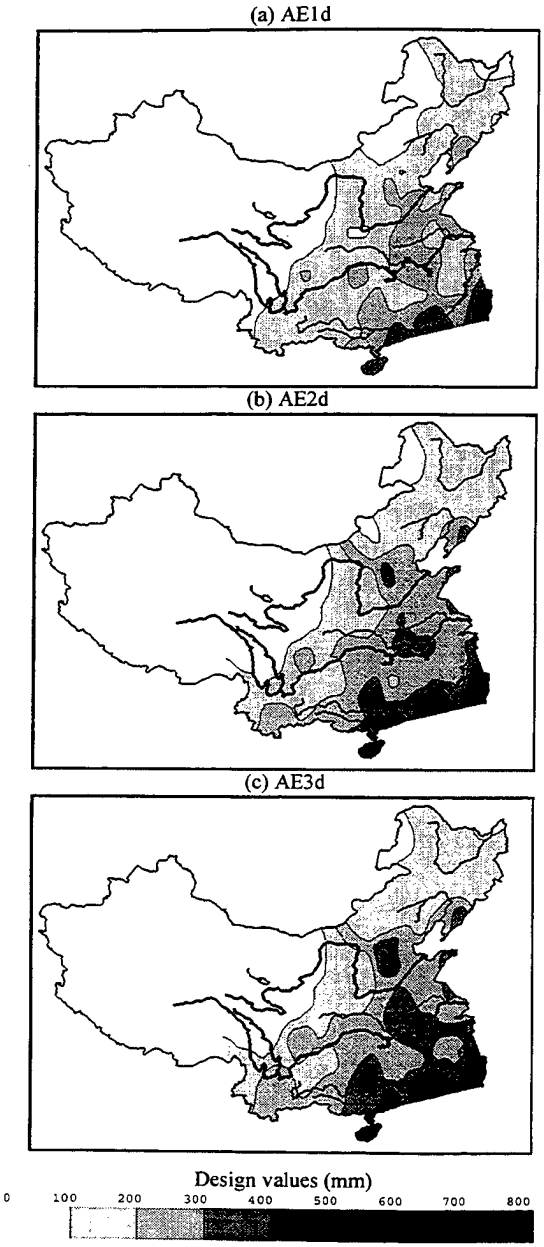


Fig.1 Contour maps of annual maximum 1, 2, and 3 day rainfall accumulations (AE1d, AE2d, and AE3d) associated with an average return period of 50 years. The contour interval is 100 mm.

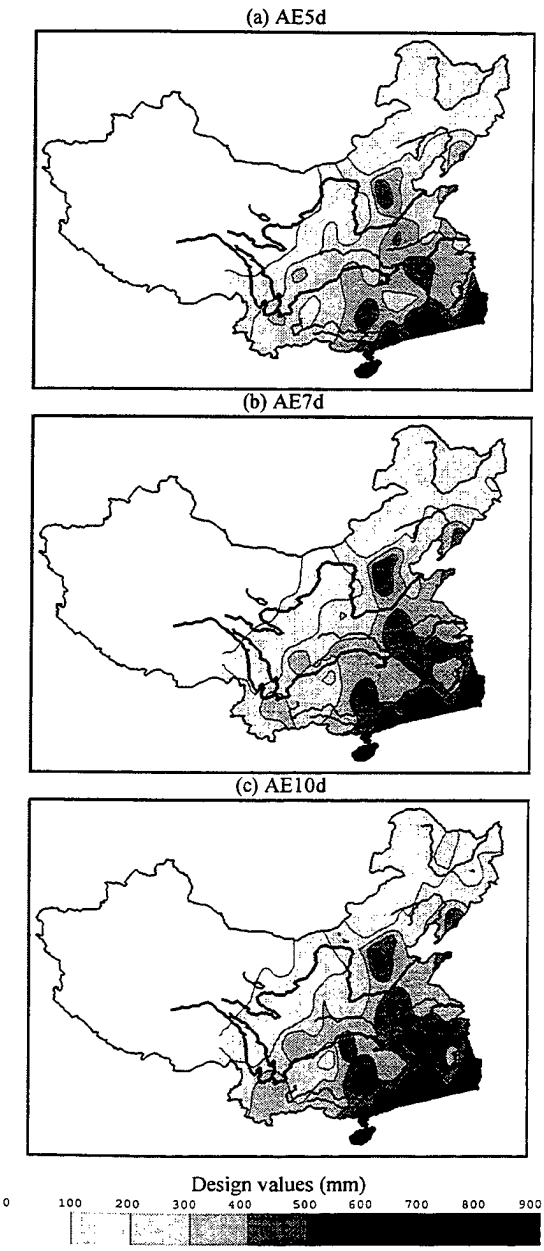


Fig.2 Contour maps of annual maximum 5, 7, and 10 day rainfall accumulations (AE5d, AE7d, and AE10d) associated with an average return period of 50 years. The contour interval is 100 mm.

Probability Models and Design Values of Extreme Rainfall over China on Various Time Scales

Xiaolan Wang, João Corte-Real and Xuebin Zhang
Department of Physics, Faculty of Sciences, University of Lisbon, Portugal

ABSTRACT

Probability models of Fisher-Tippett types and Gamma types were respectively fitted to annual maximum series of 1, 2, 3, 5, 7, and 10 day rainfall accumulations for 130 stations in China, and the goodness of fit of the candidate models were tested and compared. It is concluded that the Frechét distribution is the most common distribution of annual extreme rainfalls in China, followed by the Pearson Type 3 and 2-parameter Gamma distributions. Precipitation amounts associated with average return periods of 2, 5, 10, 20, 50 and 100 years were estimated from the models of best-fit.

1. INTRODUCTION

Extreme value analysis is concerned with the largest (or smallest) values in a record or in a set of several records. In practical applications, knowledge of the probability distribution of extreme values is particularly important; for example, the probability of flooding is often derived from an extreme value distribution of precipitation amounts. The statistics of precipitation extremes are of interest for a variety of planning and engineering purposes. Conventionally, these statistics are expressed in terms of "average return periods", most often derived from quantiles of a parametric probability model fitted to the largest precipitation values in the climatological record. Fitted models are used both to smooth the data and to extrapolate beyond the available data, i.e., to estimate the precipitation amount (design value) associated with an average return period which is longer than the period of available data.

There have been some studies on the probability models of extreme precipitation in China (Wang, 1991; etc.). However, previous studies generally focused on extreme precipitation at one site or a few stations in a subregion, and on a specific time scale. A more comprehensive study on this topic is still needed.

Studies of extremes in climatological records mostly refer to annual or seasonal maxima. The objective of this study is to fit various probability models to the annual maximum series of rainfall accumulations for durations of 1~10 days at 130 stations in China, to ascertain what probability models are more suitable for describing the extremes, whether the probability distributions of annual extreme rainfall in China vary with the location or duration and to provide a preliminary climatological atlas for precipitation extremes in China.

2. DATA AND PROCEDURES

In general, physical knowledge of the underlying processes does not provide satisfactory information about the probabilities of rare events. It is also not correct to base the choice of a particular distribution merely on mathematical arguments concerning asymptotic properties of extremes. A careful analysis of historic data is needed to find the most appropriate distribution. Usually the fits of two or several candidate distributions have to be compared. By comparing the goodness of fit of Lognormal, Gumbel, 2-parameter Gamma, Pearson Type 3 and Weibull distributions, Wang (1991) concluded that Pearson Type 3 and Weibull distributions are most suitable for describing the annual maxima of daily rainfall in East China, Gumbel and 2-parameter Gamma/Weibull distributions being not suitable for describing annual rainfall extremes in such a region of humid climate. To investigate the extreme precipitation in China (both East and West China) which possesses humid, semi-arid and arid climates, the parametric probability models of Fisher-Tippett types (including Gumbel, Frechét and Weibull distributions) and Gamma types (Pearson Type 3 and 2-parameter Gamma distributions) are chosen as the candidate models. For details about the candidate models, see NERC (1975) and Buishand (1989).

For each of the 130 stations well covering Eastern China (east of 97°E) and Northwest China, annual maxima series $X_o(j)$ of (consecutive) 1, 2, 3, 5, 7 and 10 day rainfall accumulations were sampled from daily rainfall series for the period 1953-1982 (n = 30; j = 1, 2, ..., n), and denoted by AE1d, AE2d, AE3d, AE5d, AE7d and AE10d respectively. Then, each of the five candidate probability models listed above were fitted respectively to each of the six annual maximum series for each of the 130 stations. Various estimators such as conventional Moment, Probability Weighted Moment and Maximum Likelihood (NERC, 1975; Greenwood, et al., 1979; Buishand, 1989; Otten, et al., 1980), as well as the method of Sextiles (Faragó and Katz, 1990; NERC, 1975) were used in the estimation of parameters of the probability models.

The fit of each probability model, combined with some estimator, was first examined by performing the following χ^2 test for goodness of fit (ECTUWR, 1980; Crow et al., 1960):

Suppose the sample values from an experiment fall into r categories. To decide, at the significance level α *, whether the data constitute a sample from a population with distribution function F(x) (including l parameters), we compute*

$$Z=\sum_{i=1}^{r}\frac{(o_i-e_i)^2}{e_i}$$

where o_i *and* e_i *are respectively the observed and expected (theoretical) frequencies for the i-th category (i = 1, 2, ..., r; the grouping should be arranged so that* $e_i \geq 5$ *and* $r \geq 5$*). If Z exceeds the critical value of* χ^2 *distribution for* $\nu = r-1-l$ *degrees of freedom, i.e.,* $Z > \chi^2(\alpha, \nu)$*, reject at the significance level* α *the null hypothesis that the distribution function is F(x).*

Then, the following relative standard error *RSEr* was used as an index of fit:

$$RSEr=\sqrt{\frac{1}{n}\sum_{i=1}^{n}\left[X_o(p_i)-X_e(p_i)\right]^2}\Big/\left[\frac{1}{n}\sum_{i=1}^{n}X_o(p_i)\right]$$

where $X_o(p_i)$ is the i-th smallest observed annual maximum, whose empirical cumulative probability p_i is estimated as

$p_i=(i-0.44)/(n+0.12)$ for Gumbel distribution (Guo, 1990)

$p_i=(i-0.40)/(n+0.20)$ for other distributions (Guo, 1990),

and $X_e(p_i)$ is the estimated value associated with the cumulative probability p_i.

Finally, for each of the 130 stations and for each of the six extreme value series, the model with smallest *RSEr* value is chosen as the model of best fit at the significance level α = 0.05, among the models accepted (not rejected in the χ^2 test). The closeness of fit was also examined by using quantile-quantile (Q-Q) plots, that is, the empirical quantiles $X_o(p_i)$ (on the vertical axes) versus the estimated quantiles (model quantiles) $X_e(p_i)$ (on the horizontal axes). A perfect fit is indicated by all points being on the 1:1 line, while underestimates are indicated by points falling above the line, and overestimates by points located below the line (Wilks, 1992).

3. RESULTS

Probability models of best-fit to the six extreme value series are listed in Table 1, from which one can see that the probability distribution types of annual extreme rainfalls in China vary with both the location and duration of extreme precipitation, except for Urumchi (No. 15), Dunhuang (No. 19), Fuyang (No. 97), Hangzhou (No. 104), Nanchang (No. 105) and Nanning (No. 118), where the Frechét distribution fits best to all the six extreme value series (for six durations), for Hami (No. 18), where all the six extreme value series possess a probability distribution of Weibull type, and for Jiuquan (No. 20) and Yinchuan (No. 27) where the 2-parameter Gamma distribution fits best to all the six series. The numbers of stations in relation to the models and estimators of best-fit to the six extreme value series are given in Table 2, which clearly shows that the most common

Table 1 Models of best fit to the annual maximum series of 1, 2, 3, 5, 7 and 10 day rainfall accumulations (AE1d, AE2d, AE3d, AE5d, AE7d and AE10d) for 130 stations in China (F: Frechét; W: Weibull; G: Gumbel; Γ2: 2-parameter Gamma; P3: Pearson Type 3).

Station No	WMO-No	Annual Extreme series (AE1d	AE2d	AE3d	AE5d	AE7d	AE10d)
1	50527	W	P3	P3	Γ2	P3	W
2	50557	F	P3	G	G	G	G
3	50632	P3	P3	Γ2	G	P3	Γ2
4	50727	W	F	F	F	F	G
5	50745	P3	F	F	W	Γ2	Γ2
6	50756	W	P3	P3	Γ2	Γ2	P3
7	50788	F	F	P3	G	F	F
8	50949	F	W	P3	W	W	W
9	50953	G	Γ2	Γ2	P3	Γ2	P3
10	50963	F	G	P3	W	Γ2	P3
11	50978	P3	Γ2	Γ2	F	Γ2	Γ2
12	51334	P3	P3	P3	W	G	Γ2
13	51379	W	G	F	P3	F	F
14	51431	F	G	Γ2	W	G	G
15	51463	F	F	F	F	F	F
16	51573	F	F	F	Γ2	Γ2	F
17	51644	F	F	P3	F	P3	F
18	52203	W	W	W	W	W	W
19	52418	F	F	F	F	F	F
20	52533	Γ2	Γ2	Γ2	Γ2	Γ2	Γ2
21	52681	P3	P3	Γ2	F	F	W
22	52787	P3	P3	W	F	W	P3
23	52866	G	Γ2	P3	W	W	W
24	52889	F	F	F	Γ2	P3	Γ2
25	53276	F	F	F	F	Γ2	Γ2
26	53463	F	F	P3	F	P3	F
27	53614	Γ2	Γ2	Γ2	Γ2	Γ2	Γ2
28	53646	F	G	G	Γ2	G	G
29	53698	P3	P3	P3	F	F	F
30	53772	F	P3	F	G	G	G
31	53845	F	F	G	F	G	G
32	54026	Γ2	Γ2	Γ2	P3	Γ2	Γ2
33	54094	P3	P3	F	F	W	W
34	54102	F	P3	F	F	F	F
35	54115	P3	F	F	F	F	G
36	54135	Γ2	W	Γ2	F	F	F
37	54161	Γ2	P3	W	P3	Γ2	W
38	54172	W	W	W	Γ2	P3	P3
39	54208	G	F	F	G	P3	P3
40	54218	F	F	P3	F	F	F
41	54237	P3	Γ2	Γ2	Γ2	Γ2	Γ2
42	54292	Γ2	F	G	F	F	F
43	54337	F	F	F	F	Γ2	F
44	54374	F	F	Γ2	Γ2	P3	Γ2
45	54423	F	F	P3	P3	P3	P3
46	54471	F	F	F	F	W	W
47	54483	F	P3	W	Γ2	Γ2	Γ2
48	54497	P3	F	F	F	F	F
49	54511	F	P3	F	F	F	F
50	54527	W	W	P3	P3	P3	W
51	54602	F	F	F	G	F	F
52	54662	Γ2	G	F	W	W	Γ2
53	54776	F	P3	F	F	F	F
54	54823	F	F	F	F	G	G
55	54843	F	Γ2	F	F	G	W
56	54916	P3	F	F	F	G	F
57	56033	F	F	F	F	Γ2	P3
58	56080	F	Γ2	W	P3	P3	P3
59	56093	Γ2	F	Γ2	P3	Γ2	G
60	56146	Γ2	P3	G	G	G	P3
61	56182	P3	Γ2	P3	G	P3	P3
62	56294	P3	P3	F	F	F	F
63	56462	P3	Γ2	Γ2	Γ2	Γ2	F
64	56492	Γ2	Γ2	P3	P3	W	P3
65	56571	G	W	W	F	P3	Γ2
66	56671	P3	G	F	F	P3	F
67	56739	F	Γ2	Γ2	Γ2	P3	P3
68	56964	P3	W	P3	P3	P3	Γ2
69	57006	G	P3	Γ2	Γ2	P3	W
70	57016	F	F	P3	F	F	F
71	57036	P3	F	F	Γ2	G	F
72	57067	P3	F	P3	P3	F	F
73	57083	G	W	Γ2	P3	F	P3
74	57089	P3	Γ2	Γ2	Γ2	Γ2	W
75	57245	P3	P3	P3	P3	F	F
76	57265	F	Γ2	Γ2	Γ2	W	Γ2
77	57290	F	G	F	F	F	F
78	57297	W	P3	G	G	F	F
79	57411	Γ2	P3	P3	W	Γ2	Γ2
80	57447	Γ2	P3	Γ2	Γ2	Γ2	Γ2
81	57461	P3	Γ2	Γ2	P3	W	P3
82	57494	P3	P3	P3	P3	Γ2	Γ2
83	57515	F	F	P3	P3	F	F
84	57662	W	F	F	Γ2	P3	Γ2
85	57679	P3	F	G	F	F	F
86	57707	P3	W	Γ2	Γ2	P3	P3
87	57713	W	Γ2	Γ2	P3	P3	P3
88	57745	P3	F	P3	F	F	F
89	57799	F	G	W	P3	G	G
90	57816	P3	F	P3	F	Γ2	G
91	57872	F	P3	P3	F	F	F
92	57957	P3	P3	F	P3	P3	G
93	57972	P3	Γ2	F	W	P3	Γ2
94	57993	F	F	G	G	P3	F
95	58027	P3	F	P3	P3	P3	Γ2
96	58144	Γ2	G	G	Γ2	Γ2	W
97	58203	F	F	F	F	F	F
98	58221	Γ2	W	P3	W	F	Γ2
99	58238	Γ2	Γ2	Γ2	P3	F	Γ2
100	58251	F	F	P3	G	P3	W
101	58321	W	F	G	P3	F	F
102	58361	F	F	G	W	P3	W
103	58424	F	F	F	F	F	Γ2
104	58457	F	F	F	F	F	F
105	58606	F	F	F	F	F	F
106	58633	P3	G	F	F	F	F
107	58659	F	F	G	G	F	F
108	58834	Γ2	P3	F	F	F	F
109	58847	Γ2	Γ2	P3	Γ2	P3	W
110	59082	F	W	W	Γ2	G	Γ2
111	59134	Γ2	F	F	P3	F	F
112	59211	P3	F	P3	P3	W	P3
113	59265	F	F	F	F	F	G
114	59287	P3	F	Γ2	Γ2	Γ2	Γ2
115	59293	F	F	F	F	F	P3
116	59316	Γ2	F	P3	P3	Γ2	P3
117	59417	F	P3	P3	F	F	P3
118	59431	F	F	F	F	F	F
119	59501	F	W	G	P3	W	Γ2
120	59663	Γ2	Γ2	W	Γ2	Γ2	Γ2
121	59758	Γ2	F	F	F	Γ2	F
122	59838	Γ2	Γ2	Γ2	Γ2	Γ2	W
123	59855	F	P3	Γ2	Γ2	G	G
124	46692	P3	P3	G	Γ2	Γ2	P3
125	46749	F	F	G	F	Γ2	Γ2
126	46708	P3	F	P3	F	F	F
127	46699	P3	Γ2	P3	W	G	G
128	46741	G	F	F	F	F	F
129	46766	F	F	F	P3	F	F
130	46759	P3	P3	W	W	W	W

distribution type of annual extreme rainfalls in China is the Frechét distribution, which fits best for more than one third (44-55) of the 130 stations; the Pearson Type 3 (P3) and 2-parameter Gamma (Γ2) distributions are the second most common distributions, each of them being the model of best-fit for about 20% of the stations. The spatial characteristics of the probability distribution types of the six annual extreme rainfalls will be discussed in more detail later in the subsections. For more details in this regard, readers are referred to Wang (1995).

From Table 2, it can also be concluded that, for a 30-year length series of annual extremes, the method of Probability Weighted Moment (PWM) is the best estimator (among the four estimators used) for estimation of parameters of Frechét and Weibull distributions, while the method of conventional Moment (Mo) is the best estimator for distributions of Gamma (P3 and Γ2) and Gumbel types.

For most stations and durations, the relative standard errors (*RSEr*) of the best-fit models are less than 10%, with Q-Q points generally falling quite near the 1:1 line. Q-Q plots (not shown) reveal that larger standard errors are mostly associated with underestimates on the right tail, that is, underestimates for the largest value(s) in the extreme series, some of which are likely outliers.

Based on the models of best-fit for each of the six durations, the precipitation amounts associated with average return periods of 2, 5, 10, 20, 50 and 100 years (design values) were estimated (cf. Wang, 1995); contour charts of design values for the 50 year return period will be shown and discussed herein below.

3.1 Annual Maximum 1 Day Rainfall

For 1 day duration, the probability distributions of annual extreme rainfalls (AE1d) can mainly be described by the models of Gamma types (P3 and Γ2) in the following regions: Northern and Southern Taiwan, Fujian Province, the coastal areas of Guangdong Province, the upper-middle Yangtze River basin (including Yunnan, Guizhou, Hubei and Sichuan Provinces), Henan and Jiangsu Provinces, the Changbai Mountains, the upper-middle Liaohe River basin, and central Gansu and Lingxia Provinces. The Generalized Extreme Value distributions (G, F and W) fit well the annual extremes in the other regions, especially in North China, the Boyang Lake and upper Huaihe River basins, with shape parameters k ranging from -0.3366 to +0.3206.

The contour chart of annual maximum 1 day rainfalls associated with the 50 year return period is shown in Fig. 1(a), from which it can be seen that the largest design values of AE1d appear in Taiwan (400~475 mm), Hainan, Guangdong and Southern Fujian Provinces (300~400 mm); some large design values of 200~325 mm can be observed in the Changbai Mountains, Eastern Hubei Province, Northern Guangxi Province and Sichuan Basin, constituting secondary centers of design values.

3.2 Annual Maximum Consecutive 2 Day Rainfall

The probability distributions of annual maximum consecutive 2 day rainfalls (AE2d) in East China and the eastern part of North and Northeast China, in the Loess Plateau and Northwest China, as well as in the Yunnan-Guizhou Plateau and the Pearl River basin, can mainly be described by the GEV distributions (G, F and W), with shape parameters k ranging from -0.3501 to +0.2376. The probability models of Gamma types (P3 and Γ2) fit well the annual rainfall extremes in the Hanshui River basin - Sichuan Basin, in Gansu and Lingxia Provinces, as well as in the western part of Northeast China.

The contour chart of annual maximum consecutive 2 day rainfalls (AE2d) associated with the 50 year return period (see Fig. 1(b)) show

that the largest design values of AE2d appear in Taiwan (500~625 mm), Hainan, Guangdong and Southern Fujian Provinces (400~500 mm), while design values of 300~400 mm are estimated for the eastern slopes of Changbai and Taihang Mountains, for Eastern Hubei and Northern Guangxi Provinces, as well as for the regions from Southern Fujian-Jiangxi Provinces southwestward to Eastern Guangxi Province.

3.3 Annual Maximum Consecutive 3 Day Rainfall

For 3 day duration, annual extreme rainfalls in central Northeast China and central South China (around the Qingling-Nanling Mountains) can mainly be described by the probability models of Gamma types (P3 and Γ2), whereas the GEV distributions (G, F and W) generally appear to be the models of best-fit to the annual extremes in North China, and in the region southward and eastward of Dongting Lake (including Taiwan), with shape parameters k ranging from -0.3634 to +0.2732.

As shown in Fig. 1(c), for the 50 year return period, the design values of annual maximum consecutive 3 day rainfalls (AE3d) are about 575~675 mm over Taiwan, and about 500~575 mm over Hainan Island and the coastal areas of Guangdong Province; it ranges from 300 mm to 500 mm over Southern Fujian, Northern Guangdong and Guangxi Provinces; in Eastern Hubei Province and the eastern slopes of Changbai and Taihang Mountains, design values range from 300 to 425 mm, while in the other regions design values are generally less than 300 mm.

3.4 Annual Maximum Consecutive 5 Day Rainfall

The probability models of Gamma types (P3 and Γ2) generally fit well the annual maximum series of consecutive 5 day rainfalls (AE5d) in the coastal areas of Guangdong and Fujian Provinces, in the middle Yangtze River basin and the Qingling Mountains, as well as in Central Liaoling and Eastern Jilin Provinces. The annual extreme rainfalls in the other regions can mainly be described by the GEV distributions (G, F and W), with shape parameters k ranging from -0.4433 to +0.3854.

It is shown in the contour chart of AE5d associated with a return period of 50 years that the largest design values of annual maximum rainfall for 5 day duration appear in Taiwan (600~800 mm), Guangdong and Southern Fujian Provinces (400~600 mm), with secondary centers of large design values (400~500 mm) located in the eastern slopes of Taihang and Changbai Mountains, as well as in the Boyang Lake basin and Northern Guangxi Province, as can be seen from Fig. 2(a).

3.5 Annual Maximum Consecutive 7 Day Rainfall

For 7 day duration, annual extreme rainfalls in the middle Pearl River basin and the middle-lower reaches of Yellow and Yangtze River basins (except Jiangsu Province) generally possess probability models of Gamma types (P3 and Γ2), whereas the GEV distributions (G, F and W) appear to be the models of best-fit to the annual extremes for most stations in Northeast China and the upper reaches of Yellow and Yangtze River basins, with shape parameters k ranging from -0.4065 to +0.5862.

As shown in Fig. 2(b), the largest design values of annual maximum consecutive 7 day rainfall (AE7d), for the 50 year return period, occur in Taiwan, Guangdong and Southern Fujian Provinces, with the amount of 500~950 mm; some large design values (300~500 mm) appear in Northern Guangxi Province and the Boyang Lake basin, as well as in the eastern slopes of Changbai and Taihang Mountains.

3.6 Annual Maximum Consecutive 10 Day Rainfall

In general, the GEV distributions (G, F and W) fit well the annual maximum series of consecutive 10 day rainfalls (AE10d) in the middle-lower Yellow River and the Dongting-Boyang Lake basins, and in the Eastern Coasts and the Liaohe River basin, with shape parameters k ranging from -0.3905 to +0.5048. The annual extreme rainfalls in central Northeast China and Guangdong Province and along the Yangtze River valley, can mainly be described by the probability models of Gamma types (P3 and Γ2).

Contour charts of AE10d associated with a return period of 50 years (see Fig. 2(c)) show that design values of AE10d range from 700 to 950 mm over Taiwan, and from 500 to 800 mm over Hainan and Guangdong Provinces, with design values of 400~600 mm located in the eastern slopes of Taihang and Changbai Mountains, as well as in the Boyang Lake basin and Northern Guangxi Province.

4. CONCLUDING REMARKS

Probability models of Fisher-Tippett and Gamma types have been respectively fitted to annual maximum series of 1, 2, 3, 5, 7 and 10 day rainfall accumulations, and the goodness of fit of the five candidate models have been tested and compared. The results show that probability distribution types of annual extreme rainfalls in China vary with both the location and duration of extreme precipitation; the Frechét distribution is the most common distribution, followed by the Pearson Type 3 and 2-parameter Gamma distributions. For a moderate sample size ($N < 50$), estimations of Probability Weighted Moment (PWM) and conventional Moment (Mo) are preferable to the Maximum Likelihood estimation; among the three estimators, the PWM method is the best estimator for Frechét and Weibull distributions, while the method of conventional Moment leads to the best-fit estimations for distributions of Gamma (P3 and Γ2) and Gumbel types.

Based on the models of best-fit to the six extreme value series, extreme precipitation amounts associated with average return periods of 2, 5, 10, 20, 50 and 100 years have been estimated. The largest design values of extreme rainfalls in China appear in Taiwan and the coastal areas of Southeast China, with some secondary centers of large design values located in Northern Guangxi and Eastern Hubei Provinces, in the eastern slopes of the Taihang and Changbai Mountains, as well as in the Sichuan Basin. These regions of large design values of extreme rainfalls are actually the regions known to be most vulnerable to extreme precipitation in China (cf. Wang, 1995).

Finally, it should be pointed out that the conclusions drawn from this study are restricted within the data limit. An updated data set is needed to corroborate the results and to update the atlas for precipitation extremes in China.

ACKNOWLEDGEMENTS

This research was supported by a doctoral scholarship provided by JNICT (National Board for Scientific and Technological Research, Portugal).

REFERENCES

Buishand, T. A., 1989: "Statistics of extremes in climatology". Statistica Neerlandica, 43 (1989), nr. 1, 1-31.

Crow, E. L., F. A. Davis and M. W. Maxfield, 1960: "Statistics Manual". Dover Publications, INC., New York, 288pp.

ECTUWR (East China Technical University of Water Resources), 1980: "Probability and Statistics in Hydrology". China Water Resources Press, Beijing, 461pp.

Faragó, T. and R. W. Katz, 1990: "Extremes and Design Values in Climatology". WCAP-14, WMO/TD-NO.386. 43pp..

Greenwood, J. A. and J. R. Wallis, 1979: "Probability Weighted Moments: Definition and Relation to Parameters of Several Distribution Expressable in Inverse Form". Water Res. Res., 15, No. 5, 1049-1054.

Guo, S. L., 1990: "A discussion on unbiased plotting positions for the general extreme value distribution". J. Hydrol., 121: 33-44.

NERC (Natural Environment Research Council), 1975: "Flood studies report", Volume I, Whitefriars Press, London.

Otten, A. and M. A. J. Van Montfort, 1980: "Maximum-Likelihood Estimation of the General Extreme-Value Distribution Function Parameters". J. Hydrol., 47, 187-192.

Wang, X., 1995: "Planetary Scale Circulation, Climate and Extreme Events in East Asia". A doctoral dissertation presented to the Faculty of Sciences, University of Lisbon.

Wang, X., 1991: "Distribution model and characteristics of daily extreme precipitation in the East of China". In: Climatological Research — Statistical Climatology (Ed. by Yao, Z.), 69-77 (in Chinese).

Wilks, D. S., 1992: "Comparisons of Parametric Distributions to Describe Precipitation Extremes". In: 12th Conf. on Prob. and Statist. in the Atmosph. Sci., 1992, Toronto, Ontario, Canada. 28-33.

CORRESPONDING AUTHOR

Xiaolan Wang, Department of Physics, Faculty of Sciences, University of Lisbon, Campo Grande, Ed. C1, Piso 4, 1700 Lisbon, Portugal (on leave from the Department of Hydrology and Water Resources, Hohai University, Xikang Road 1, Nanjing 210024, P. R. China).

Table 2 Numbers of stations in relation to the models and estimators of best-fit to the six annual extreme series of rainfalls in China (F: Frechét; W: Weibull; G: Gumbel; Γ2: 2-parameter Gamma; P3: Pearson Type 3).

Extreme	Generalized Extreme Value (GEV) distributions					2-parameter Gamma (Γ2)		Pearson Type 3 (P3)	
Series	G-Mo	G-PWM	F-PWM	W-PWM	GEV-Stl	Γ2-Mo	Γ2-ML	P3-Mo	P3-ML
AE1d	6	1	53	11	0	20	2	35	2
AE2d	9	1	55	12	0	22	1	27	3
AE3d	15	0	44	11	0	25	1	27	7
AE5d	11	1	49	14	0	25	3	26	1
AE7d	15	0	45	13	0	28	2	26	1
AE10d	15	0	45	18	0	25	5	22	0

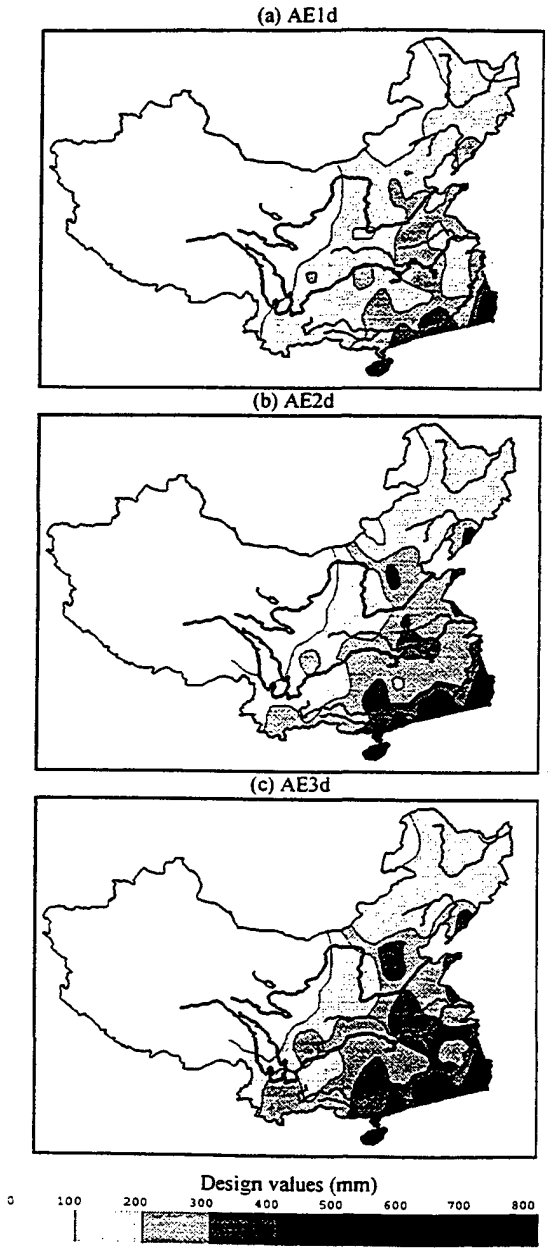


Fig.1 Contour maps of annual maximum 1, 2, and 3 day rainfall accumulations (AE1d, AE2d, and AE3d) associated with an average return period of 50 years. The contour interval is 100 mm.

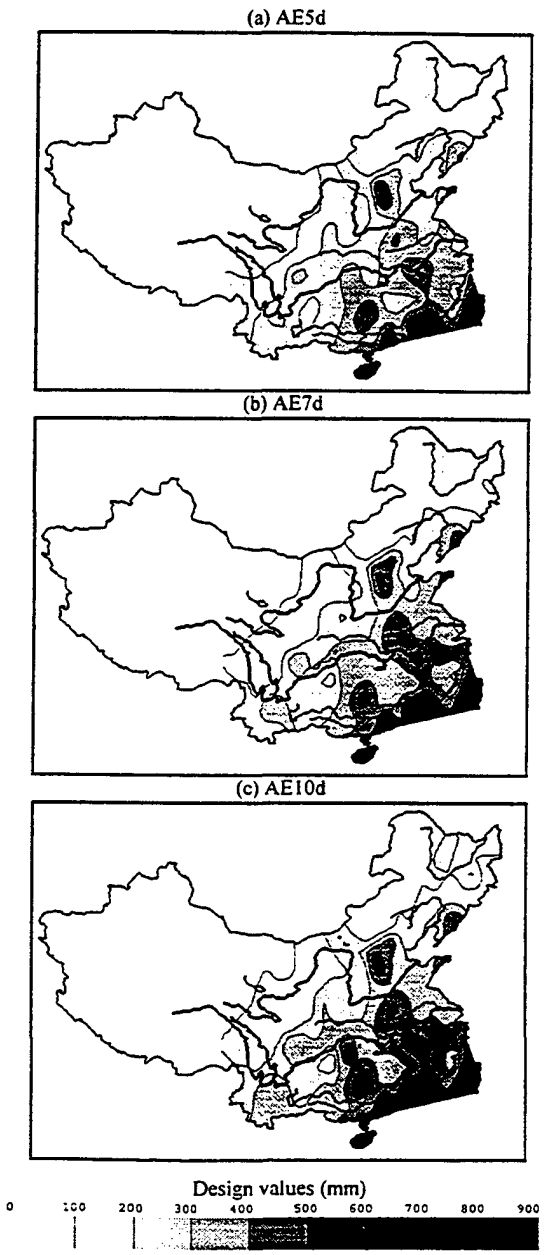


Fig.2 Contour maps of annual maximum 5, 7, and 10 day rainfall accumulations (AE5d, AE7d, and AE10d) associated with an average return period of 50 years. The contour interval is 100 mm.

STATISTICAL-DYNAMICAL ANALYSIS OF EXTREME EVENTS IN TUSCANY (ITALY): DROUGHT AND ANNUAL MAXIMUM DAILY RAINFALL. SPATIAL DISTRIBUTION AND FORECASTING

F. Meneguzzo[1], M. Niccolai[2], N. Musetti[2], F. Tampucci[2]

[1]Ce.S.I.A. - Accademia dei Georgofili, Firenze, Italy; [2]A.R.S.I.A. - Regione Toscana, Pisa, Italy

ABSTRACT

Climatic and meteorological risk analysis and forecasting concerns, among other topics, analysis (and forecasting) of recurrence of long duration droughts and extreme rainfall. Both subjects involve theoretical and immediately practic perspectives.

A statistical-dynamical analysis is carried on to derive a climatological characterization of different areas of Tuscany (Italy) as regards to the recurrence frequency of drought periods (meant as sequences of consecutive dry days) of any given duration. Extraordinary inhomogeneity is derived.

A technique of *regional* statistics based on L-moments of distributions is instead applied to the problem of identification of the underlying distribution, and definition of recurrence periods, of annual maximum daily rainfall for regional data. Target area is a very complex topography one, where a relatively elevated costal range (up to about 1900 m a.s.l.) faces relatively warm Ligurian Gulf (in Mediterranean basin). Objective spatial distribution is derived by means of a multi-regressive methodology.

1. INTRODUCTION

Annual rainfall and drought distributions are relevant limiting factors for organisms: vegetation (and animals) may have to survive long dry spells (Odum, 1983).

Besides, area burned by wildfire seemed to correlate significantly with the duration of dry spells, but not with precipitation (Flannigan and Harrington, 1988).

Effect of climate trend on local drought features has the greatest relevance. Punctual operating forecasts of drought duration (in the course of a dry spell) are also needed for water management and alert for agricultural resources.

On the other hand, soil erosion and flood risks are known to be strictly correlated to rainfall intensity (see, for example, Conese et al., 1993; Klysik and Fortuniak, 1993; Anselmo et al., 1993). Since most historical data refer to daily rainfall, our aim is the identification of the statistical distribution and recurrence features of annual maximum *daily* rainfall, directly useful for limited size basins.

Since flood risk analysis in complex terrain involves mainly spatial distributed rainfall, a multi-regressive technique for spatial objective analysis of recurrence periods of extreme daily rainfalls was employed.

The study concerns all or part of tuscan territory. Figure 1 shows location of Tuscany in Europe, Figure 2 shows (rough) tuscan orography and extremely inhomogeneous distribution of mean annual rainfall.

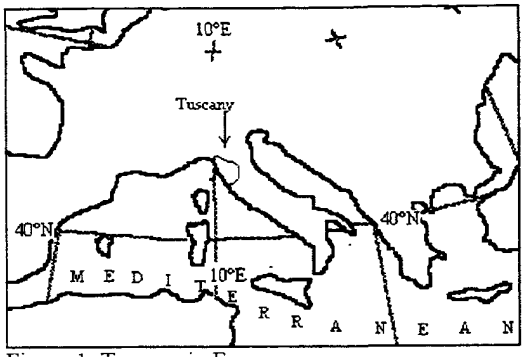


Figure 1. Tuscany in Europe

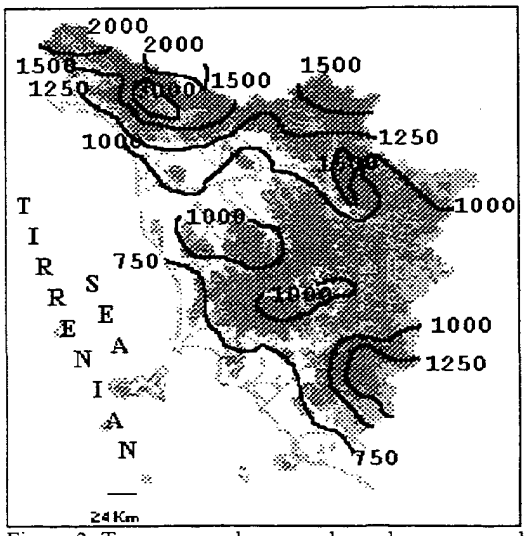


Figure 2. Tuscany: rough orography and mean annual rainfall.

2. STATISTICAL-DYNAMICAL ANALYSIS OF DROUGHT

With the aim to derive recurrence periods of dry spells of any duration at several hystorical meteorological stations in Tuscany (Italy), transitional probability of a *dry day* following a *wet day* or a sequence of several *dry days* (a day is *dry* when total daily rainfall doesn't exceed 1 mm, due to interception by vegetation) was first investigated.

Voluminous literature addressed to this topic is reported in Harrington and Flannigan (1993). We'll

follow the somehow original methodology explained and applied in this last work.

Simple Markov chain models (Gabriel and Neumann, 1962; Berger and Goossens, 1983) generally fail in estimating transitional probabilities of long periods of drought due to the evidence of a rising trend in transitional probability with dry-days sequence lenght.

A plot of the experimental transitional probability of a dry day following a sequence of k dry days is shown in Figure 3 and refers to 43 years of data (1951 - 1993) from *Grosseto* station, located at 42°45' N , 11°07' E at an altitude of 5 meters a.m.s.l. in Tuscany (Italy). Note that the tail of the distribution for long sequences of consecutive dry days is highly irregular due to relative scarcity of data, which makes it apparent the need for a model. Long historical series can in fact hardly provide reliable and operational transitional probabilities for dry spells longer than about 10 to 25 days, even if this lenght may be increased by *smoothing* the data from several similar curves based on observations collected at nearby stations (Figure 4).

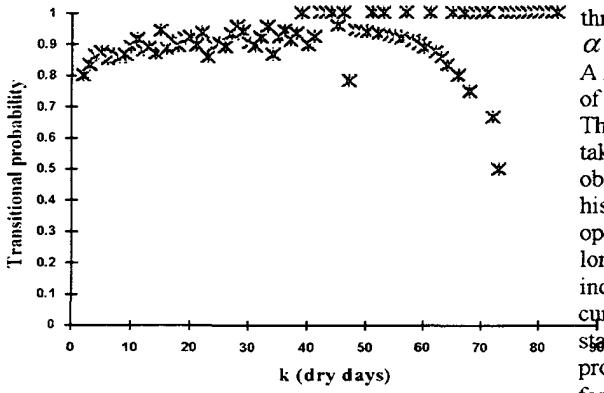


Figure 3. Transitional probability of a dry day following k dry days at Grosseto, Tuscany (Italy).

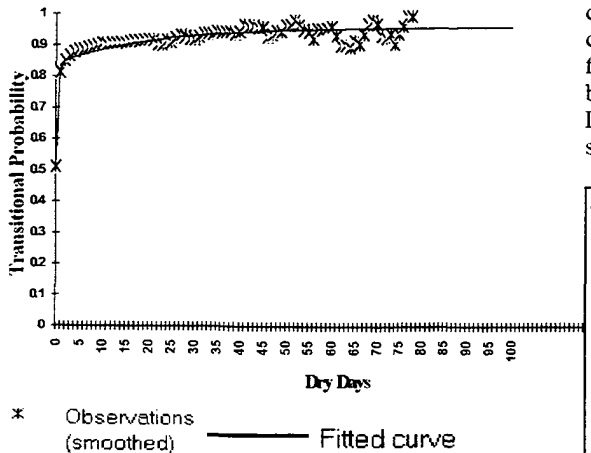


Figure 4. Transitional probabilities: smoothed observations and theoretical fitted curves for *Maremma and Islands*.

According to Harrington and Flannigan (1993), the rising trend may be explained by the hypothesis that curves are composed of two Markov chains corresponding to opposing large-scale atmospheric circulatory regimes: the first one to low-amplitude westerly flows (*non-blocking*, typical of short periods of consecutive dry days), the other one to high-amplitude ridges in the westerlies (*blocking*, typical of the longer persistence of dry days).

By means of an empirical hypothesis on the frequency of occurrence of non-blocking and blocking conditions and an arbitrary correction to account for the imperfect *bimodality* of meteorological circulations, the *predicted* transitional probability that a day will be dry given a preceding sequence of k dry days will be:

$$p(k) = \gamma\left[1 - \beta / (\alpha - t)^{k-\varepsilon}\right]$$
$$\beta = 1 - (\delta / \gamma) \qquad (1)$$
$$\delta = p^*(\varepsilon)$$

where for $k=\varepsilon$ the probability distribution has a characteristic *shoulder* ($\varepsilon = 2$ in Figure 4).

ε , the transitional probability at the *shoulder*, is assigned based on observations (ε is generally rather small, anyway lying in a range where observations are numerous);

γ is estimated as the *asymptotic (large k) value* of the transitional probability from a sequency at least three dry days long to one or more further dry days;

$\alpha - t$ is arbitrarely adjusted to fit the observations.

A notable fact is that no reference is made to the *order* of the Markov chains.

The need for such a model is apparent just as one takes into account scarcity of cases and extreme observational variability, which prevent even long historical series from directly providing reliable and operational transitional probabilities for dry spells longer than about 10 days. This lenght may be increased by *smoothing* the data from several similar curves based on observations collected at nearby stations. The needed *asymptotic* transitional probability (γ) may thus be estimated and the final form of the theoretical transitional probability derived.

Areas which might be considered homogeneous as to drough climate were outlined based on *shape* and characteristic parameters of transitional probability curves derived for single stations. Figure 4 results from a smoothing performed on data from stations belonging to one of such *homogeneous* areas.

Distribution of return periods of 90-days long dry spells all over Tuscany are represented in Figure 5.

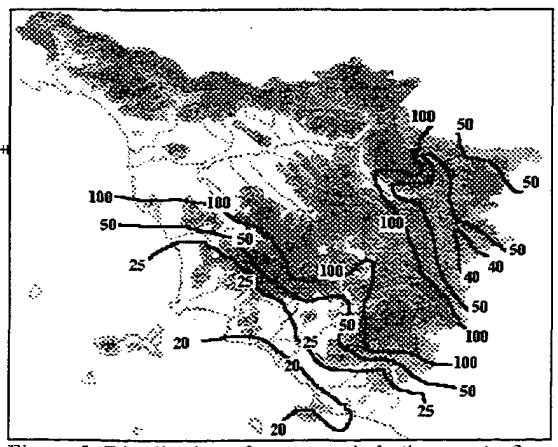


Figure 5. Distribution of return periods (in years) of 90-days long dry spells.

3. STATISTICAL ANALYSIS OF EXTREME RAINFALL

North-westernTuscany, the upper left corner in Figure 2., is an extremely complex topography area: two approximately parallel mountain ranges of similar elevations run south-east to north-west, one of which, Apuan Alps, grows few Km onshore, and the other one, Northern Appennines, is fifteen to thirty Km futher onshore. Apuan Alps face Ligurian Gulf, in northern Mediterranean, where sea surface temperatures range from about 13 °C in late winter to 25 °C in late summer.

Local basins show *lead* times spanning the range from few hours (2 to 3 hours) to 24 hours.

Detailed orography (horizontal step 600 m) of target area (spanning 50.4 Km latitude and 40.2 Km longitude) is shown in Figure 7., where isoline labelled "*0* " represents coastline.

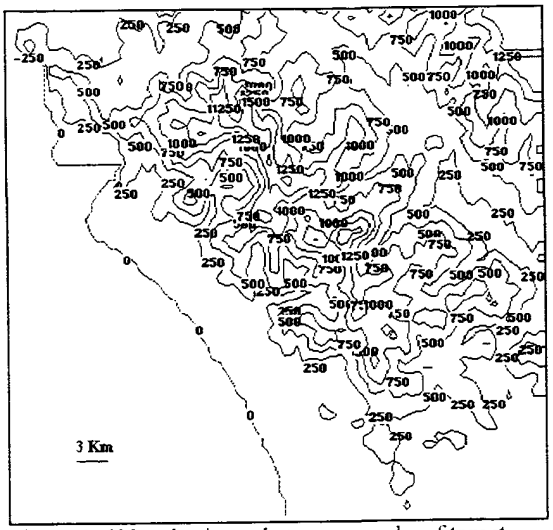


Figure 6. 600 m horizontal step orography of target area.

A methodology which seemed to match our needs was found in literature (Hosking, 1990; Cong et al., 1993), and employs linear combinations of moments (*L-moments*) of observed data and of distribution generated data. For any detail see above references.

We tested three distribution forms, suggested by Cong et al. (1993), which are listed below ($F(x)$ is the *cumulative distribution function*, CDF).

Generalized extreme value (GEV)

$$x = \varepsilon + \alpha \frac{\left[1-(-\log F(x))^{\kappa}\right]}{\kappa} \qquad \kappa \neq 0$$

$$x = \varepsilon + \alpha\left[1-(-\log F(x))\right] \qquad \kappa = 0 \tag{2}$$

Generalized Pareto (PAR)

$$x = \varepsilon + \alpha\left\{1-\left[1-F(x)\right]^{\kappa}\right\} \tag{3}$$

Generalized logistic (LGI)

$$x = \varepsilon + \alpha \frac{1-\left[(1-F(x))/F(x)\right]^{\kappa}}{\kappa} \tag{4}$$

In above equations, α, ε and κ represent parameters.

The identification criterion (for details, see Cong et al., 1993) employs the set of observational data and analogous sets of data drawn (through the Monte Carlo method) from each of above three distributions (Eqns. [2] - [4]).

Since 13 stations data sets were employed, with an average record lenght of about 40 years, 13 data samples each one containing 40 records were drawn from each distribution.

The *random scattering* of observational (t_3, t_4) points (each one computed from a single station data) is then used to identify the underlying distribution (hence the need for *regional* data).

Hypothesis that precipitation data at different stations are mutually independent lets one model multistation precipitation through *independent variables*. The need for *mutual independence* among precipitation amounts at different stations was succesfully checked at several couples of stations in Tuscany and particularly in Arno basin by Bacci et al. (1993).

Each of 13 employed station was provided with at least 35 years long data record. Last year included in computations was 1987.

Our computations clearly led to the choice of ***Generalized extreme value*** (GEV: eqn.[2]) as the underlying distribution form.

We derived an average $\bar{t}_3$, or *L-skewness*, of **0.244** .

According to methodology suggested by Cong et al. (1993), using 10 random samples generated through Monte-Carlo technique, the *conditional probability* that GEV is the *true* underlying distribution given that GEV itself has been identified as the underlying distribution when $\bar{t}_3 = 0.244$ is **0.625**, rather high (even if a larger number of samples should be employed to avoid randomness). Besides, probability that the true underlying distribution form is PAR or LGI is respectively: 0.3125 , 0.0625 .

Parameter estimation was accomplished by equating *sample L-moments* to the corresponding *population* quantities (for details, see Hosking, 1990).

Annual maximum daily rainfall at each station was derived for several return periods. By definition, the relationship between *return period* and *Cumulated Distribution Function* is the following:

$$T(x) = \frac{1}{N\left[1-F(x)\right]} \tag{5}$$

where N is the number of events in a year.

5-years maximum annual daily rainfall ranges from 87 mm at a coastal site to 221 mm at a site located in the upper part (about 800 m a.s.l.) of a south-westerly exposed basin. 100-years values range from 157 mm to 380 mm, at same sites as 5-years extremes. Besides, these two sites are not more than 13 Km apart.

The task to obtain basin distributed values of extreme rainfall related to a given return time was accomplished through a multi-regressive model and a detailed digital terrain model (600 m step). Some topographical variables were identified and assigned to each employed station in the study area. Minimisation of linear relations of extreme rainfall (at

a given return period) with various integer powers of those variables provided best coefficients of the relation. Once each *pixel* of the basin is assigned above variables, linear expression may be evaluated and spatial distribution of extreme rainfall may be drawn. In the following, only 100-years annual maximum daily rainfall will be concerned.
Comparison of computed and observed data provided a relatively small standard deviation of about 7 mm.
Spatial distribution of extreme rainfall is shown in Figure 8 (same domain of Fig. 7). In Figure 9 only 450 mm rainfall is drawn, superimposed to orography.
All this brings the chance to know extreme rainfall in any pixel of a basin; besides, in the *conservative* hypothesis of *simultaneity* among extreme events (plausible only in small size basins), basin extreme average rainfall is immediately known and operational rainfall forecasts gain higher value.

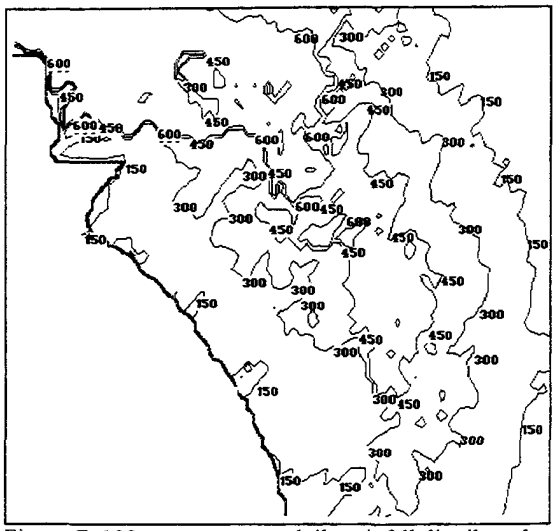


Figure 7. 100-years extreme daily rainfall distributed in study area.

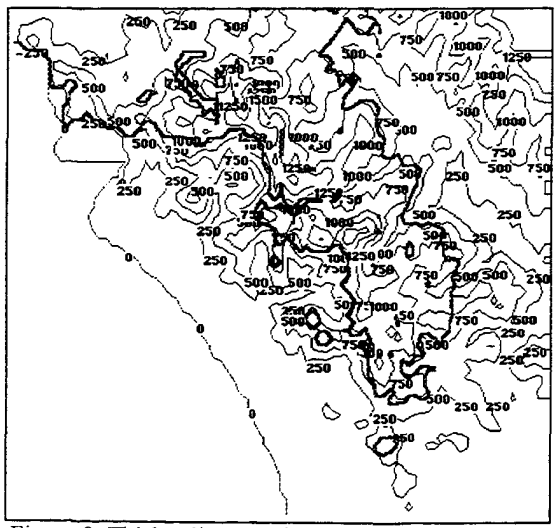


Figure 8. Thicker lines outline areas where 100-years extreme daily rainfall equals or exceeds 450 mm. Orography is the background.

Just a view on last 7 years (1988 to 1994). No peculiarity is apparent, since just one event close to the 100-years event happened, one event close to the 60-years one and most of gauges experienced 10 to 20-years event simultaneously in November 1994, when a basin in the study area experienced a flood.

ACKNOWLEDGEMENTS

Dr. B. Gozzini and Dr. P. Ciapetti, Ce.S.I.A. (Firenze), who provided Digital Terrain Model, Dr. L. Perini, U.C.E.A. (Roma), for a lot of daily rainfall data, Ing. Rivano, Mr. Rapetti and Mr. Pampana, National Idrographical Service, for provided extreme rainfall data for several gauges, are gratefully acknowledged.

REFERENCES

Anselmo, V., Ferrari, S., Mercalli, L., 1993. North-Western Italy Precipitation Long Series: Data and Analysis. In: Precipitation Variability & Climate Change. Proceedings of the International Symposium on Precipitation and Evaporation, Bratislava, 1993, p.52.

Bacci, G., Meneguzzo, F., Musetti, N., Niccolai, M. 1993. Comparison of Precipitation patterns forecast by the General Circulation Model operating at Offenbach German Center with Data collected by a Raingauge Network. Proceedings of the International Symposium on Precipitation and Evaporation, Bratislava, 1993.

Berger, A.L., and C. Goossens, 1983. Persistence of wet and dry spells in Uccle (Belgium). J. Climatol., 3, 21-34

Bras, R.L., 1990. Hydrology. Addison Wesley, Reading, Massachussets.

Cong, S., Y. Li, J.L. Vogel and J.C. Schaake, 1993. Identification of the Underlying Distribution Form of Precipitation by using Regional Data. Water Resour. Res., 29 (4), 1103-1111

Flannigan, M.D., and J.B. Harrington, 1988. A Study of the Relation of Meteorological Variables to Monthly Provincial Area burned by Wildfire in Canada (1953-80). J. Appl. Meteor., 27, 441-452

Gabriel, K.R., and J. Neumann, 1962. A Markov Chain Model for Daily Rainfall Occurrence at Tel Aviv. Quart. J. Roy. Meteor. Soc., 88, 90-95

Giarola, S., G. Grippa and F. Meneguzzo, 1995. DI.M.C.OR., a Software Package for Diagnostic Wind Reconstruction". Environmental Software, In Press.

Harrington, J.B., and M.D. Flannigan, 1993. A Model for the Frequency of Long Periods of Drought at Forested Stations in Canada. J. Appl. Meteor., 32, 1708-1716

Hosking, J.R.M., 1990. L-moments: Analysis and Estimation of Distributions using Linear Combinations of Order Statistics. J. R. Statist. Soc. B, 52 (1), 105-124

Meneguzzo, F., M. Niccolai and G. Bacci, 1994. Climatology of Rainfall in Tuscany: Statistical-Dynamical Analysis of Drought and Statistical Analysis of Annual Maximum Daily Rainfall. Conference Proceedings. Atmospheric Physiscs and Dynamics in the Analysis and Prognosis of Precipitation Fields. Roma, 15-18 Novembre 1994.

Odum, E.P., 1983. Basic Ecology. CBS College Publishing.

Ripley, B.D., 1981. Spatial Statistics. John Wiley & Sons. New York.

CHANGES IN FLOOD FREQUENCIES IN SOUTH AFRICA

Mason, S.J.[1] and Mimmack, G.M.[2]

1. Climatology Research Group,
University of the Witwatersrand, Johannesburg, South Africa
2. Department of Statistics and Actuarial Science,
University of the Witwatersrand, Johannesburg, South Africa

ABSTRACT

Rainfall data at 26 stations in South Africa, where there are at least 90 years of complete daily rainfall records over the 120-year period 1873-1992, are tested for changes in the frequency of extreme flood events. The frequency distributions of the annual one-day rainfall maxima at each of the stations are best described using the three-parameter generalised extreme-value (GEV) distribution. There has been little change in the frequency of extreme flood events in the 120-year period. There is some evidence of an increase in flood events over part of the country during the last 30 years.

INTRODUCTION

Although much of southern Africa lies within arid to semi-arid climatic regions, extreme rainfall events are relatively frequent (eg. Lindesay and Jury, 1991). A number of theoretical, modelling and empirical analyses have suggested that noticeable changes in the frequency of extreme events, including floods, may occur when there are only small changes in climate (Mearns *et al.*, 1984; Wigley, 1985; Rind *et al.*, 1989; Katz and Brown, 1992; Katz and Acero, 1994). Based on output from the CSIRO 9-level general circulation model, increases in extreme rainfall events may be expected over Australia (Whetton *et al.*, 1993) and southern Africa (Mason and Joubert, 1995; Mason *et al.*, 1995) as a result of an enhanced greenhouse effect, even in areas where mean annual rainfall may decrease (cf. Yu and Neil, 1993). It has therefore been suggested that tests for climatic change should focus on changes in the frequency of extreme events rather than on changes in climatic means (von Storch and Zwiers, 1988).

In this paper, evidence of changes in the frequency of extreme daily rainfall events during the last 120 years over South Africa is assessed.

DATA

Daily rainfall data for stations throughout South Africa were obtained up to the end of 1992. Stations were selected on the basis of length and completeness of records. The largest data sets spanned the 120 years from 1873 to 1992. Stations with at least 90 (75%) complete years of daily records were selected. Most of the 26 selected sites are located in the southern half of the country (Fig. 1) for historical reasons.

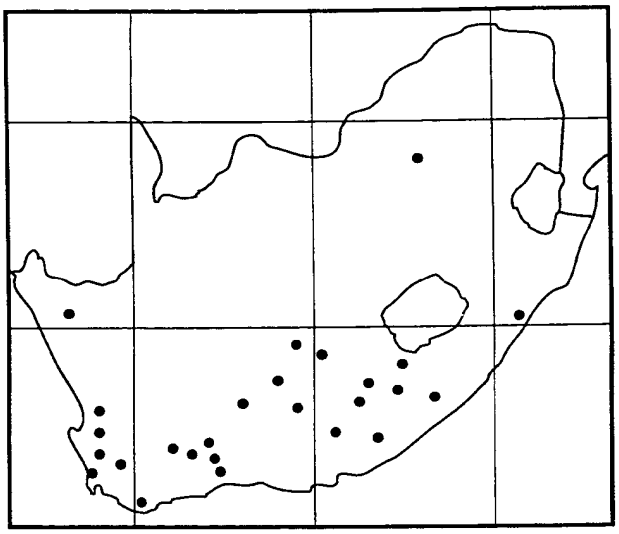


Figure 1: Location of 26 rainfall stations in South Africa with at least 90 complete years of daily rainfall records.

FITTING OF DISTRIBUTIONS

Annual maxima were extracted from the complete years of rainfall records for each of the stations and a number of two- and three-parameter distributions were fitted to the data. The three-parameter distributions fitted were beta-k and beta-p (Mielke and Johnson, 1974), generalised extreme-value (GEV) (Prescott and Walden, 1980) and generalised gamma (Johnson and Kotz, 1970). The two-parameter distributions were the gamma, Gumbel and Weibull distributions (Johnson and Kotz, 1970). Each distribution was fitted to the series of annual maxima from each station using maximum likelihood techniques. Maximum likelihood was used in favour of probability weighted moments since it generally

gives a better fit in the extreme tails with smaller data sets (Hosking *et al.*, 1985; Phien and Emma, 1989). The best two-parameter and the best three-parameter distributions were selected on the basis of the sum of the likelihood functions from the 26 stations.

The Gumbel distribution and the GEV proved to give the best fits to the series of annual maxima from the 26 stations. The fits of these two distributions were then compared using a likelihood ratio test to assess the justifiability of using the third parameter in the GEV distribution. The test statistic for this test is

$$\Lambda = 2\left[\sum_{i=1}^{n} \ln L_i(3) - \sum_{i=1}^{n} \ln L_i(2)\right] \qquad (1),$$

where L(3) is the likelihood function for station *i* for the GEV distribution, L(2) is the likelihood function for the Gumbel distribution and *n* is the number of stations (Wilks, 1992). The significance of the likelihood ratio Λ is obtained from a χ^2 distribution with degrees of freedom equal to the difference in the number of fitted parameters. A total of 78 parameters were fitted using the GEV distribution and 52 parameters using the Gumbel distribution and so the difference is 26, one for each station.

Using all 26 stations, the improvement in likelihood obtained using the third parameter is highly significant. The accuracy of fit of the GEV distribution can be observed visually from the histogram illustrated in Figure 2 and the quantile-quantile plot in Figure 3 (Wilks, 1992). The plot and histogram are illustrated for one station only, chosen because it has the largest number of years of complete data (i.e. number of non-missing years). Other stations do have better fits. Of particular interest is the accuracy of fit in the extreme right tail, represented in the top right section of the quantile-quantile plot.

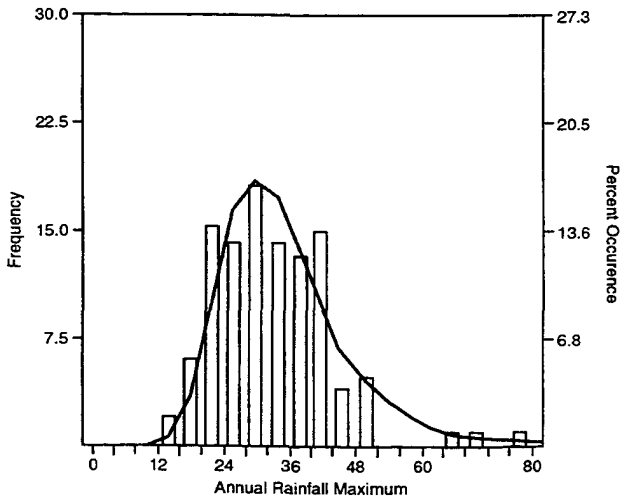


Figure 2: Histogram of annual rainfall maxima for Worcester. The fitted generalised extreme-value distribution is superimposed. Units are in millimetres.

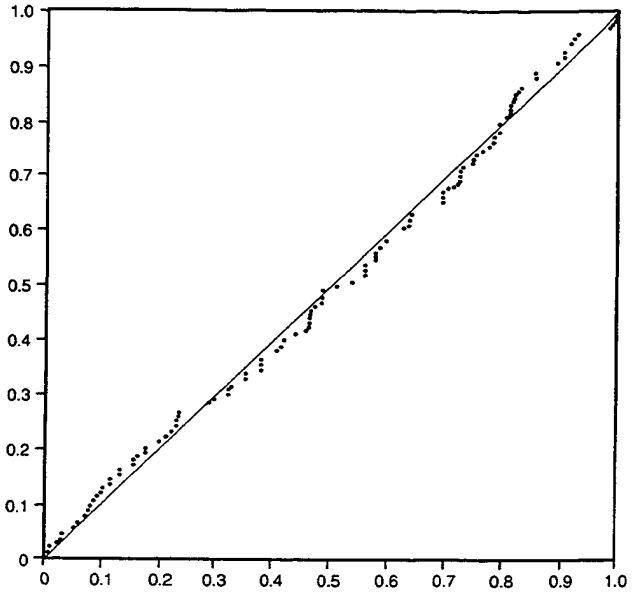


Figure 3: Quantile-quantile plot for the three-parameter generalised extreme-value distribution fitted to annual maxima series for Worcester. Units are in millimetres.

TEST FOR CHANGES IN THE FREQUENCY OF EXTREMES

Tests for changes in the frequency of extreme rainfall events generally assume a linear increase or decrease in frequency (eg. Smith, 1989; Davison and Smith, 1990). The tests involve a time-weighting in the calculation of return periods. The power of such tests can be severely restricted if linearity cannot be assumed.

A resampling method that does not assume linearity was used for testing the significance of changes in the frequency of extreme events. The 120-year period was divided into four non-overlapping periods of 30 years each. GEV distributions were then fitted to the annual rainfall maxima for each of the four periods if at least 25 (85%) complete years were available. Calculations were performed at a stricter level of data availability (i.e. 85% rather than 75%) because of the greater sensitivity of the parameter estimates with smaller sample sizes. The tail areas (or return periods) for pre-defined rainfall thresholds were calculated for each of the 30-year periods at each station. The significance of changes in extreme events can then be assessed by comparing the observed tail areas for each period with the tail area of the empirical distribution that results from assuming that there has been no significant change in the frequency of extreme events during the period of analysis. The empirical distribution was obtained by repeated resampling of 30 years taken at random from the 120-year period. For each station, 1000 random samples were selected and tail areas for the predefined rainfall

thresholds were calculated by counting the number of exceedences.

SIGNIFICANCE OF CHANGES IN THE FREQUENCY OF EXTREME RAINFALL EVENTS OVER SOUTH AFRICA

One-day rainfall totals corresponding to 5-, 10- and 20-year floods over the last 120 years have been calculated for each station. The probabilities of exceeding these thresholds in each of the 30-year periods were then calculated from the fitted GEV distributions and compared with the corresponding probabilities from the empirical distributions. A total of 68 tests for significant changes in flood frequencies were performed for the various return periods. If a 10% level of significance is used, seven of these 68 tests can be expected to erroneously indicate significant changes, and at least 11 significant changes would have to be detected in order to claim that changes in frequency have indeed occurred (Livezey and Chen, 1983). If a specific 30-year period is considered at least 6 stations would have to show a significant change.

At the 10% level of significance there is little evidence of change in the frequency of extreme rainfall events during the 120-year period 1873-1992. The absence of change is significant in the light of increases expected as a result of an enhanced-greenhouse effect (Mason and Joubert, 1995). Over south-western Australia, no change in one-day flood frequencies has been observed, despite a decrease in the mean annual rainfall (Yu and Neil, 1993). Over South Africa there are no long-term rainfall trends, except possibly over the Lowveld in the far eastern part of the country (Mason, 1995), an area not covered in the present analysis.

If one-tailed tests are used to test for increases in frequencies of floods during only the last 30-year period (1963-1992), significant increases are observed in a cluster of five stations to the south-west of Lesotho (fewer than the critical level of 6 stations). The increases are strongest for the 5-year floods and are less marked for the more extreme floods. In contrast, one-tailed tests for decreases in flood frequencies for the same period, show significant decreases at three stations in the winter rainfall region that covers the west and south coasts. Changes in both areas are in agreement with possible future mean annual rainfall trends over southern Africa as simulated by the CSIRO 9-level general circulation model (Joubert, 1994; cf. Brundrit and Shannon, 1989). However, increases in flood frequency are expected even in areas where mean annual rainfall may decrease (Mason and Joubert, 1995).

During the period 1933-1968, two-tailed tests indicate that there were significantly few flood events. However, the stations with few flood events are not spatially coherent. Similarly, during the previous 30 years, 1903-1932, there were four stations with a significantly large number of flood events according to one-tailed tests, but the stations are again not spatially coherent and there are fewer than the critical number required for overall significance. There is no evidence of a large or a small number of floods during the 30-year period at the end of the last century, but tests are based on only the three stations that had sufficient data.

CONCLUSIONS

Two-tailed tests for changes in flood frequencies over South Africa indicate little change in frequencies over the last 120 years. There is weak evidence, however, to suggest that flood frequencies increased during the last 30 years in an area within the summer rainfall region to the south-west of Lesotho. It is not possible to state how extensive the area of increased flood frequencies is since a large proportion of the summer rainfall region has not been covered by this paper: only two stations north of 30S with summer rainfall maxima were considered. The observed changes in flood frequencies over the last 30 years are in agreement with expected changes in the mean annual rainfall over the country as a result of an enhanced greenhouse effect.

REFERENCES

Brundrit, G.B. and Shannon, L.V., 1989, "Cape storms and the Agulhas Current: a glimpse of the future?", *South African Journal of Science*, **85**, 619-620.

Davison, A.C. and Smith, R.L., 1990, "Models for exceedences over high thresholds", *Journal of the Royal Statistical Society, Series B*, **52**, 393-442.

Hosking, J.R.M., Wallis, J.R. and Wood, E.F., 1985, "Estimation of the generalised extreme-value distribution by the method of probability-weighted moments", *Technometrics*, **27**, 251-261.

Johnson, N.L. and Kotz, S., 1970, "Distributions in Statistics: Continuous Univariate Distributions - 1", Wiley, New York, 300pp.

Joubert, A.M., 1994, "Simulations of southern African climatic change by early-generation general circulation models", *WaterSA*, **20**, 315-322.

Joubert, A.M., Mason, S.J. and Galpin, J.S., 1995, "Droughts over southern Africa in a doubled-CO_2 climate", *International Journal of Climatology*, submitted.

Katz, R.W. and Acero, J.G., 1994, "Sensitivity analysis of extreme precipitation events", *International Journal of Climatology*, **14**, 985-999.

Katz, R.W. and Brown, B.G., 1992, "Extreme events in a changing climate: variability is more important than averages", *Climatic Change*, **21**, 289-302.

Lindesay, J.A. and Jury, M.R., 1991, "Atmospheric circulation controls and characteristics of a flood event in central South Africa", *International Journal of Climatology*, **11**, 609-627.

Livezey, R.E. and Chen, W.Y., 1983, "Statistical field significance and its determination by Monte Carlo techniques", *Monthly Weather Review*, **111**, 46-59.

Mason, S.J., 1995, "Climatic change over the Lowveld of South Africa", *Climatic Change*, accepted for publication.

Mason, S.J. and Joubert, A.M., 1995, "Simulated changes in extreme rainfall over southern Africa", *International Journal of Climatology*, submitted.

Mearns, L.O., Katz, R.W. and Schneider, S.H., 1984, "Extreme high-temperature events: changes in their probabilities with changes in mean temperature", *Journal of Climate and Applied Meteorology*, **23**, 1601-1613.

Mielke, P.W. Jr and Johnson, E.S., 1974, "Some generalised beta distributions of the second kind having desirable application features in hydrology and meteorology", *Water Resources Research*, **10**, 223-226.

Phien, H.N. and Emma, F.T-S., 1989, "Parameter estimation for the general extreme value distribution", *WaterSA*, **15**, 57-64.

Prescott, P. and Walden A.T., 1980, "Maximum likelihood estimation of the parameters of the generalised extreme-value disctribution", *Biometrika*, **67**, 723-724.

Rind, D., Goldberg, R. and Ruedy, R., 1989, "Change in climate variability in the 21st century", *Climatic Change*, **14**, 5-37.

Smith, R.L., 1989, "Extreme value analysis of environmental time series: an application to trend detection in ground-level ozone", *Statistical Science*, **4**, 367-393.

von Storch, H. and Zwiers, F.W., 1988, "Recurrence analysis of climate sensitivity experiments", *Journal of Climate*, **1**, 157-171.

Whetton, P.H., Fowler, A.M., Haylock, M.R. and Pittock, A.B., 1993, "Implications of climate change due to the enhanced greenhouse effect on floods and droughts in Australia", *Climatic Change*, **25**, 289-317.

Wigley, T.M.L., 1985, "Impact of extreme events", *Nature*, **316**, 106-107.

Wilks, D.S., 1992, "Comparisons of parametric distributions to describe precipitation extremes", Preprints of the 12th Conference on Probability and Statistics in the Atmospheric Sciences, American Meteorological Society, 28-33.

Yu, B. and Neil, D.T., 1993, "Long-term variations in regional rainfall in the south-west of Western Australia and the difference between average and high intensity rainfalls", *International Journal of Climatology*, **13**, 77-88.

ACKNOWLEDGEMENTS

This research was funded by Technology Research and Investigations, a division of the Technology Group of ESKOM. The rainfall data were supplied by the Computer Centre for Water Research.. Mr P. Stickler drew the diagrams. Useful discussions with A. Boyd and P. Waylen are gratefully acknowledged.

CORRESPONDING AUTHOR
Dr S.J. Mason,
Climatology Research Group,
University of the Witwatersrand,
Private Bag 3,
Johannesburg 2050,
South Africa.

THE INFLUENCE OF THE EXTREMAL INDEX ON THE ESTIMATION OF RETURN PERIODS OF HIGH LEVELS

M. Ivette Gomes

DEIO and CEA, University of Lisbon

ABSTRACT

For particular weakly dependent sequences of observations, and in a context of *Statistical Extremes*, there appears a relevant parameter — equal to one for independent, identically distributed observations —, the so-called *extremal index*. Important parameters of rare events, which are functions of this parameter, are the *high quantiles*, and the *return period for a level*. We shall consider here the influence of the extremal index in the estimation of $T(u)$, the return period of the high level u, and we propose estimators of $T(u)$ whenever working with the *Method of the Annual Maxima*, and with the *Peaks Over Threshold* (POT) *Method*. The derived results have been applied to real data in the most diversified fields of application, from Hydrology to Climatology.

1. INTRODUCTION AND PRELIMINARIES

Whenever dealing with statistical extremes there appear usually two parameters of rare events of primary interest: a *tail index* ξ, which is the shape parameter in the *Generalized Extreme Value* (GEV) distribution function (d.f.)

$$G_\xi(x) = \begin{cases} \exp[-(1+\xi x)^{-1/\xi}] & \text{for } 1+\xi x > 0, \text{ and } \xi \neq 0 \\ \exp[-\exp(-x)] & \text{for } x \in \Re, \text{ and } \xi = 0 \end{cases},$$

the limiting d.f. of the maximum, suitably normalized, of n "weakly" dependent random variables, and an *extremal index* θ, which may roughly be defined as the reciprocal of the expectation of the duration of extreme events. For an adequate dependent stationary sequence $\{X_n\}_{n\geq 1}$, with underlying d.f. $F(.)$, we have a shrinkage of maximum values (Leadbetter Lindgren and Rootzén (1983)) — $P[M_n^X \leq x] \approx F^{n\theta}(x)$, where, as usual, $M_n^X = \max(X_1, X_2, \ldots X_n)$, whereas for an independent, identically distributed (i.i.d.) sequence $\{Y_n\}_{n\geq 1}$ with the same underlying d.f. $F(.)$, $P[M_n^Y \leq x] = F^n(x)$, where we have $M_n^Y = \max(Y_1, Y_2, \ldots Y_n)$. However, the type of limiting law is not modified, since $G_\xi(x)$ is stable for maxima, and consequently,

$$G_\xi^\theta(x) = G_\xi\left(\frac{x-\lambda}{\delta}\right), \quad \lambda = \frac{\theta^\xi - 1}{\xi}, \quad \delta = \theta^\xi.$$

$G_0(x)$ is the well-known *Gumbel* d.f. For $\xi < 0$, we often refer to the GEV as the *Weibull* d.f., and for $\xi > 0$ as the *Fréchet* d.f.

Important parameters of rare events, which are functions of these two parameters, are the *high quantiles* χ_p, i.e., high levels χ_p such that $F(\chi_p) = 1 - p$, with p small, and the *return period for a level*, i.e., the expected waiting time between either "independent" exceedances or consecutive exceedances after a down-crossing of that high level.

The influence of the extremal index in the estimation of high quantiles has been studied in Gomes (1993) and we here consider the influence of the extremal index in the estimation of $T(u)$, the return period of the high level u, defined here as the mean time between a down-crossing and the consecutive up-crossing of that level. We consider, in section 2 of this paper, the Method of the *Annual Maxima* — the best-known method of analyzing extreme values based on the extreme value limiting distributions, and generally applied to annual maxima of the series (Gumbel, 1958). In section 3, we consider the *Peaks Over Threshold* methodology — an alternative approach to Gumbel's model, where we look at exceedances over high thresholds rather than maxima over fixed time periods. Finally, in section 4, we have an example of application.

2. THE METHOD OF ANNUAL MAXIMA

We consider first the *Method of the Annual Maxima* (Gumbel, 1958), i.e. we assume that we have access to a sample of k maximum values of sub-samples of size N/k, from an overall lot of N observations.

Under the general local and asymptotic dependence restrictions pointed out before, any point process limit for the time normalized exceedances of high normalized levels — i.e. levels $u = u_n$ such that $n(1 - F(u_n)) \to \tau$, as $n \to \infty$, for some $\tau > 0$, — associated to a stationary dependent sequence, is a *compound Poisson process*, i.e., there is a clustering of high exceedances, where the underlying Poisson points represent cluster positions, and the multiplicities correspond to cluster sizes. The point process limit for the time normalized upcrossings still

remains a Poisson process, with mean $\theta\tau$ — instead of the mean τ that appears for i.i.d. sequences. More than this: The extremal index θ is, in most practical situations, equal to *the reciprocal of the limiting mean size of cluster exceedances* of a normalized high level.

Then, for the estimation of $T(u)$, the mean time spent between a downcrossing and the consecutive upcrossing of u, for large u, we consider the relation:

$$T(u) = \frac{1}{\theta}\frac{1}{1-F(u)} - \frac{1}{\theta} + 1.$$

This relation, together with the validity of the identification $F^{n\theta}(x) \approx G_\xi(\frac{x-\lambda}{\delta})$, leads us to suggest the estimator

$$T^*(u) = \begin{cases} \frac{N}{k}\left(1+\xi^*\frac{u-\lambda^*}{\delta^*}\right)^{1/\xi^*} - \frac{1}{\theta^*} + 1 & \text{for } \xi \neq 0 \\ \frac{N}{k}\exp\left(\frac{u-\lambda^*}{\delta^*}\right) - \frac{1}{\theta^*} + 1 & \text{for } \xi = 0 \end{cases}$$

Exact and asymptotic properties of T^* will be studied elsewhere.

The estimator θ^* is any convenient estimator of θ (Hsing (1989), Gomes (1990), Nandagopalan(1990), Canto e Castro (1994), Smith and Weissman (1994)). Given the whole sample $(X_1, X_2, \ldots, X_N)$, and once chosen a suitable threshold u, an obvious non-parametric estimator of θ is

$$\theta^* = \frac{\sum_{j=1}^{N-1} I_{[X_j \le u < X_{j+1}]}}{\sum_{j=1}^{N} I_{[X_j > u]}}.$$

The estimators λ^*, δ^* and ξ^* suggested are, due to the numerical simplicity of calculus, when compared to maximum likelihood estimators, the *weighted moments estimators* of location λ, scale δ and shape ξ in the Generalized Extreme Value distribution $G_\xi(\frac{x-\lambda}{\delta})$ (Hosking et al, 1985), given by

$$\xi^* = -(7.8590c + 2.9554c^2), \quad c = \frac{2b_1 - b_0}{3b_2 - b_0} - \frac{\log 2}{\log 3},$$

$$\delta^* = -\frac{(2b_1 - b_0)\xi^*}{\Gamma(1-\xi^*)(1-2^{\xi^*})},$$

and

$$\lambda^* = b_0 - \delta^*\frac{\Gamma(1-\xi^*)-1}{\xi^*},$$

over the range $-1/2 < \xi < 1/2$.

The weighted sample moments b_r are given by

$$b_0 = \bar{X};$$

$$b_r = \frac{1}{k}\sum_{j=1}^{k}\frac{(j-1)(j-2)\ldots(j-r)}{(k-1)(k-2)\ldots(k-r)}X_{j:k}, r > 0$$

where $X_{j:k}$, $1 \le j \le k$, are the ascending order statistics associated to a sample of size k.

The covariance matrix of these weighted moments estimators was obtained numerically by Hosking et al (1985).

3. THE PEAKS OVER THRESHOLD MODEL

Whenever dealing with the Peaks Over Threshold (POT) method, we consider a level u_0, and "independent" excesses of that level are then going to be modelled (Pickands, 1975) by a *Generalized Pareto* (GP) distribution

$$P_\xi(x) = \begin{cases} 1-\left(1+\xi\frac{x}{\beta}\right)^{-1/\xi} & \text{for } 1+\xi x/\beta > 0, \\ & x > 0, \text{ and } \xi \neq 0 \\ 1-\exp(-x/\beta) & \text{for } x > 0, \text{ and } \xi = 0 \end{cases}$$

with the same shape ξ as before, and with a scale parameter $\beta > 0$. The case $\xi = 0$ is the well-known *exponential* distribution.

For this method we have the identification $(1-F(x+u_0))/(1-F(u_0)) = 1-P_\xi(x)$, and thus, assuming that we have k_0 values, out of N, larger than u_0, and k "independent" excesses, we consider the estimator

$$T^{**}(u) = \begin{cases} \frac{1}{\theta^*}\frac{N}{k_0}\left(1+\xi^{**}\frac{u-u_0}{\beta^{**}}\right)^{1/\xi^{**}} & \text{for } \xi \neq 0 \\ \frac{1}{\theta^*}\frac{N}{k_0}\exp\left(\frac{u-u_0}{\beta^{**}}\right) & \text{for } \xi = 0 \end{cases}$$

where θ^* is the estimator of the extremal index considered before or, equivalently, the simpler estimator k/k_0, and β^{**} and ξ^{**} are the weighted moments estimators of scale β and shape ξ in the Generalized Pareto distribution (Hosking and Wallis, 1987),

$$\beta^{**} = \frac{2a_0a_1}{a_0-2a_1}, \quad \xi^{**} = 2 - \frac{a_0}{a_0-2a_1}$$

over the range $\xi < 1$, where $a_0 = \overline{X}$, and for $r > 0$,

$$a_r = \frac{1}{k}\sum_{j=1}^{k} \frac{(k-j)(k-j-1)\ldots(k-j-r+1)}{(k-1)(k-2)\ldots(k-r)} X_{j:k}.$$

The standard errors of these estimators are

$$se(\beta^{**}) = \sqrt{\frac{\beta^2(7-18\xi+11\xi^2-2\xi^3)}{n(1-2\xi)(3-2\xi)}},$$

$$se(\xi^{**}) = \sqrt{\frac{(1-\xi)(2-\xi)^2(1-\xi+2\xi^2)}{n(1-2\xi)(3-2\xi)}}.$$

Exact and asymptotic properties of T** will be derived elsewhere.

4. AN APPLICATION

Available data are daily levels, since 1952 till 1991 for the Portuguese river Douro, at the hidrometric station of Fraga, and in order to have stationarity we have considered the period October/November/December/January. We thus have a sample of $123 \times 40 = 4920$ observations.

A fuzzygram of the annual maxima is shown in Figure 1, and a graph in Gumbel probability paper is shown in Figure 2.

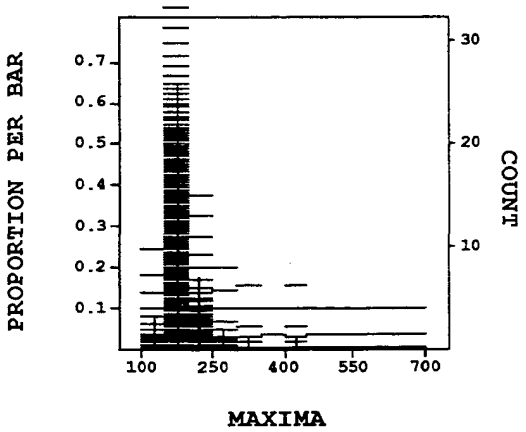


Figure 1. Fuzzygram of the annual maxima

It is clear the positive assymetry of the data, which suggests, together with the shape in the probability paper, a heavy right-hand tail. Consequently a Fréchet model, $\Phi_\alpha((x-\lambda)/\delta) = G_{1/\alpha}(\alpha((x-\lambda)/\delta - 1))$, $\alpha > 0$, for the annual maxima, seems to be appropriate.

The fuzzygram of the independent excesses over the high level 171.5 m^3s^{-1}, and the graph in exponential probability paper are shown in Figures 3 and 4 respectively.

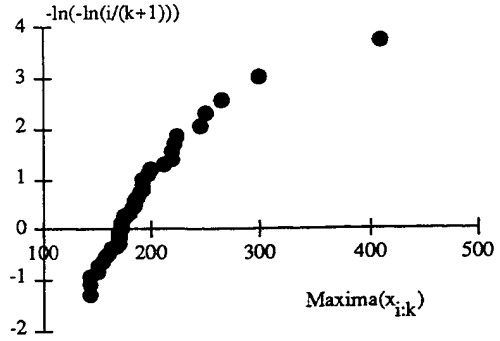


Figure 2. Plotting of the annual maxima in a Gumbel probability paper

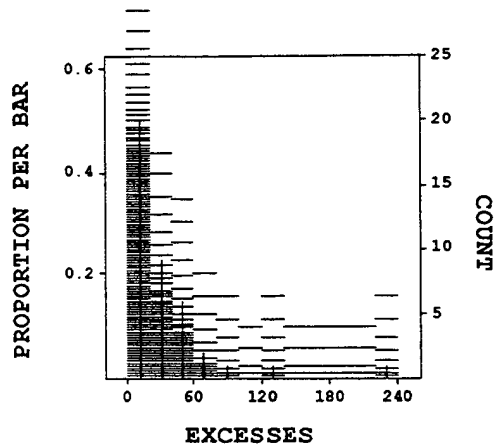


Figure 3. Fuzzygram of the "independent" excesses over the level 171.5 m^3s^{-1}

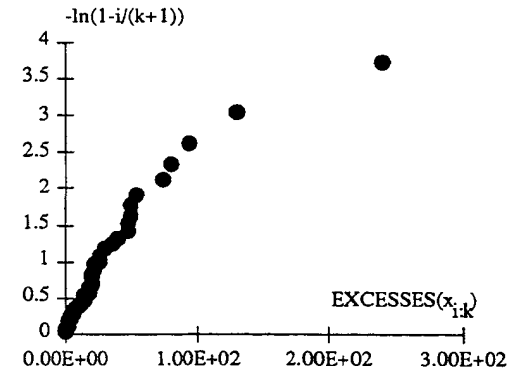


Figure 4. Plotting of the excesses in an exponential probability paper

These figures enhance the data characteristics pointed out before — the excesses should be modelled by a Generalized Pareto P_ξ, with $\xi > 0$.

The choice of the levels for the computation of an estimate of the extremal index was done in a way similar to the one suggested by Tawn (1992). Once too low a value for the level introduces bias, whereas too high a value leads to an estimate with a large variance, we have considered a grid of

levels between the 5% and the 10% top order statistics associated to the raw data, and weighted properly the obtained estimates. We have got here an estimate of the extremal index θ equal to 0.435, i.e. an estimate of 2.299 days for the mean time the river spends above high levels, and consequently the classical methodology that takes $\theta = 1$ may provide under-estimation of parameters of rare events.

For the Gumbel approach, and the weighted moments method of estimation, we have got $\xi^* = 0.2800$ (0.1144). For the POT approach — and a level $u_0 = 171.5$ we have got $\xi^{**} = 0.3203$ (0.1614). These two values agree up to their standard errors. The weighted moments estimates of λ and δ in the GEV model are $\lambda^* = 171.5725$ (4.2222), and $\delta^* = 23.9367$ (2.9965). The weighted moments estimate of the parameter β, in the GP model, is $\beta^{**} = 21.9720$ (5.717).

Notice that since we have, under Gumbel's approach, an estimate for δ not too far away from $\lambda\xi$ (up to standard errors) we can consider that our model should be close to a Fréchet model, with location at zero. The modelling of our data of annual maxima by such a Fréchet model , together with the relation between the GEV and the Fréchet, yield a GEV model with maximum likelihood estimated parameters given by $\tilde{\lambda} = 173.6638$, $\tilde{\delta} = 25.6995$, and $\tilde{\xi} = 0.1480$. This means that we may eventually fit a Fréchet model, $\Phi_{\tilde{\alpha}}(x/\tilde{\delta}')$, with scale $\tilde{\delta}' = \tilde{\delta}\ (n\theta^*)^{-\tilde{\xi}}/\tilde{\xi} = 96.366$, $n = N/k = 123$, and shape $\tilde{\alpha} = 6.7575 = 1/\tilde{\xi}$, to the original data.

Indeed the raw data could be properly modelled by a stationary max-autoregressive process, $X_n = k \max(X_{n-1}, Z_n)$, $n \geq 1$, with d.f. $F(x)$ such that $F(kx)/F(x) = H(x)$, where H is the d.f. of the i.i.d. generating sequence $\{Z_n\}_{n\geq 1}$, with Fréchet margins, with zero location, and for $k = 0.919$ [$= (1-\theta)^{\xi}$]. These markovian models were studied by Alpuim (1989), and have rich properties in what regards clustering of exceedances of high normalized levels.

For the high levels $u = 180,(10)260$, we present in table 1, the estimates of $T(u)$ obtained by the two methods described in sections 2 and 3.

u	T*(u)	T **(u)	$\tilde{T}$(u)	T^S(u)
180	170.52	195.55	155.14	154-3
190	245.42	286.95	224.25	229.0
200	341.35	403.57	317.80	313.1
210	461.55	548.69	442.52	440.3
220	609.47	725.62	606.56	619.5
230	788.69	937.71	819.63	821.6
240	1002.97	1188.35	1093.26	1061.2
250	1256.19	1480.96	1441.04	1513.2
260	1552.42	1818.99	1878.84	1787.3

We also present, in the fourth column of this table the estimation derived from the Fréchet fitting, and in the fifth column the simulated values of $T(u)$ for the max-autoregressive fitted model mentioned before, based on the mean of 1000 values of $T(u)$ for each u. In Figure 5 we represent graphically the above mentioned estimates of the return period.

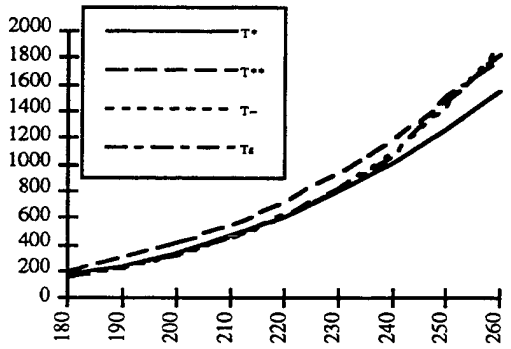


Figure 5. Estimates of return periods

The results obtained through the two approaches are comparable and they do not differ much from the simulated return period.

References:

Alpuim, M.T. (1989). An extremal markovian sequence. *J. Appl. Probab.* **26**, 219-232.

Canto e Castro, M.L. (1994). Estimating the extremal index, under a local dependence condition, by the reciprocal of the average length of successive runs. In J. Galambos et al (eds.). *Extreme Value Theory and Applications*, NIST Special Publ. 866.

Gomes, M.I. (1990). Inference in an extremal markovian model. In Momirovic, K. and V. Mildner (eds.). *Proceedings on Computational Statistics*, 257-262, Physica-Verlag.

Gomes, M.I. (1993). On the estimation of parameters of rare events in environmental time series. In V. Barnett and K.F. Turkman (eds.), *Statistics for the Environment*, 225-241, Wiley.

Gumbel, E.J. (1958). *Statistics of Extremes*. Columbia University Press.

Hosking, J.R.M., Wallis, J.R. and E.F. Wood (1985). Estimation of the GEV distribution by the method of the probability weighted moments. *Technometrics* **27**, 251-261.

Hosking, J.R.M. and Wallis, J.R. (1987). Parameter and Quantile estimation for the GPD. *Technometrics* **29**, 339-349.

Hsing, T. (1989). *Estimating parameters of rare events*. Preprint. Texas A&M University.

Leadbetter, M.R., Lindgren, G. e H. Rootzen (1983). *Extremes and Related Properties of Random Sequences and Processes*. Springer-Verlag.

Nandagopalan, S. (1990). *Multivariate Extremes and Estimation of the Extremal Index*. Ph. D. Thesis, Tech. Report 315, Center for Stochastic Processes, Univ. North-Carolina.

Pickands, J. III (1975). Statistical inference using extreme order statistics. *Ann. Statist.* **3**, 119-131.

Smith, R. and I. Weissman (1994). Estimating the extremal index. *J. Royal Statistical Soc.* **B 56**, 515-528.

Tawn, J. (1992). Estimating probabilities of extreme sea-levels. *Appl. Statistics* **41**, 77-93.

CORRESPONDING AUTHOR
Professor M. Ivette Gomes
Departmente of Statistics
Faculdade de Ciências de Lisboa
Edifício C2, Campo Grande
1700 Lisboa, PORTUGAL

STORM CONDITIONS OVER THE NORTH SEA: A HISTORICAL PERSPECTIVE AND IMPLICATIONS FOR THE 21ST CENTURY

Tom Holt

Climatic Research Unit

University of East Anglia, Norwich, NR4 7TJ UK

ABSTRACT

A gale index is derived for the North Sea using daily atmospheric pressure. A statistical summary of gales in the region is presented for the period 1881-1993. The likely impact of global warming on North Sea storms is examined by computing gale indices from pressure data derived from a General Circulation Model (GCM) and comparing the results with the historical data.

1. INTRODUCTION

The influence of the enhanced greenhouse effect on storminess over the North Sea has important implications for the design of coastal defences against surge damage. To adequately protect vulnerable areas of coast, it would be useful to know if the frequency and intensity of storms is likely to increase under global warming. The issue assumes greater importance when one considers that most climatologists accept that global warming will lead to a rise in sea level, and that there are indications that this may already be happening.

There are a number of methods of assessing the likely future behaviour of climate, usually based on some form of regression technique. A major drawback with this approach, when considering periods more than a few years beyond the available instrumental data, is that assumptions about stationarity of atmospheric processes have to be made. In the context of this study, such assumptions are invalid since we are assuming that non-stationarity will eventually be detected, possibly in storms over the North Sea.

A more appropriate approach was suggested by the availability of climate data from GCMs produced under conditions simulating global warming. Lack of full understanding of atmospheric energetics, and inadequate spatial resolution, prevent the current crop of GCMs from explicitly simulating storm conditions. Surface pressure fields are, however, available and can be used to derive an estimate of windiness.

Using daily mean sea level atmospheric pressure, Jenkinson and Collison (1977) estimated a gale index based on the geostrophic wind and vorticity. This was calibrated to windspeed in knots using station data. Here we update this analysis to 1993, and compare the results with similar indices derived from GCM pressure estimates.

2. THE DATA

Northern Hemisphere daily surface pressure data are available from 1881-1993 on a 5° latitude x 10° longitude grid. We derived daily indices of pressure, wind flow, and vorticity over the full period for the area 45°N to 65°N and 20°W to 20°E. using the Jenkinson technique. The pressure grid points used to represent the North Sea are illustrated in Figure 1.

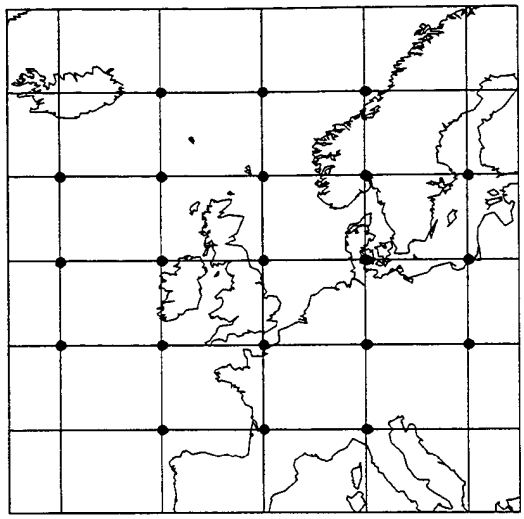


Figure 1 Grid Points used to derive the Gale Indices from Pressure Data

A full description of the derivation of the Gale Index can be found in Jenkinson and Collison (1977).

The GCM pressure data were obtained from Max Planck Institute, Hamburg (Cubasch et al., 1992), for 10 years of 12-hourly point pressure values for the control run, the IPCC 90 Scenario A run (business-as-usual), and the 2 x CO_2 run. These data are on a 5.625° grid and were averaged to a daily value, and then interpolated onto the 5° x 10° grid of the observed data. A gale index was calculated for each of the three runs.

2.1 Validation of the Historical Gale Index

Jenkinson used data from coastal stations to validate and calibrate the original gale index up to 1977. We use observations from Mariner's Weather Log to cross-check Jenkinson's findings and to verify the extension of the index to 1993. Verification was restricted to storms with windspeeds greater than 40 knots.

For storms with windspeeds in excess of 50 knots, the gale index gave values generally within 5% of reported speeds, omitted no recorded storms and inserted no spurious ones. For windspeeds between 40 and 50 knots, the gale index was accurate for about 72% of cases and tended to underestimate by about 12% in 24% of cases. Because lesser storms are often linked to remote systems, 4% of the reported storms were not defined by the gale index.

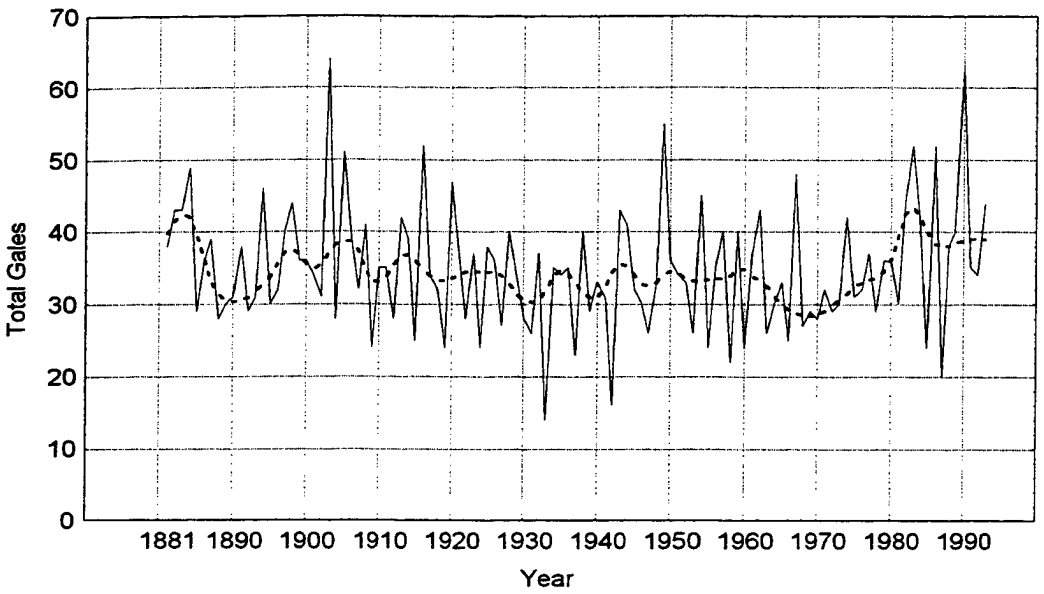


Figure 2 Total Gales per Year (1881-1993)

It should be noted that the observed wind speeds are point observations from ships which might not be in the most severe part of a storm. It is possible that the gale index gives more reliable estimates of storminess. Since we are creating an index of windiness over the North Sea as a whole, an element of spatial averaging is involved which smooths out the effects of relatively local gusts, for example.

For a more complete discussion of the validity of the gale index approach see Holt (1991).

3. HISTORICAL ANALYSIS

For convenience we shall refer to the daily values of the gale index as gales. It is important to understand that these are not gales in the generally accepted sense. The gale index is an assessment of the mean daily windiness and does not necessarily describe discrete storm events. Such events might last only a few hours, or may persist for several days.

In this section we will consider storm frequency and storm intensity, with particular emphasis on changes over time.

3.1 Frequency of Gales

Figure 2 shows the total number of gales over the North Sea for each year from 1881 to 1993. The smoothed curve superimposed on the observations is computed by a 4253H filter which uses a combination of weighted running means and running medians to reveal the important variations in the data and is not unduly influenced by outliers.

The main feature of the plot is that most of the record oscillates about a mean of about 34 gales per year. At the beginning and end of the record, however, there are peaks in the smoothed curve at about 42 storms per year, far higher than in any other period.

Numerous explanations could be offered for this. H. H. Lamb (Lamb, 1991) presents evidence for a cycle of 100 years in North Atlantic cyclone activity. Figure 2 seems to support this hypothesis but at least another 100 years data would be needed before we could conclude that such a cycle exists over the North Sea.

A more likely explanation for the peak at the beginning of the record is that the early pressure data are less reliable than the more recent observations. Several periods of the data require adjustment (see Jenkinson and Collison, 1977) for inhomogeneity before the gale index is calculated. It is possible that the sparse data network in the 19th century gave some spurious results when the pressure data were gridded.

The peak at the end of the record cannot be disregarded so easily. Even allowing for the very low starting point in 1970 (the lowest period of storm activity in the record), the two decades of rising trend warrant further study. After the rise to about 43 gales per year in 1984, the record falls slightly and then starts to climb again. Early data for 1994 show this trend to be continuing with 29 gales by the end of April.

Figure 2 also demonstrates a complete lack of long-term trend in storm frequency.

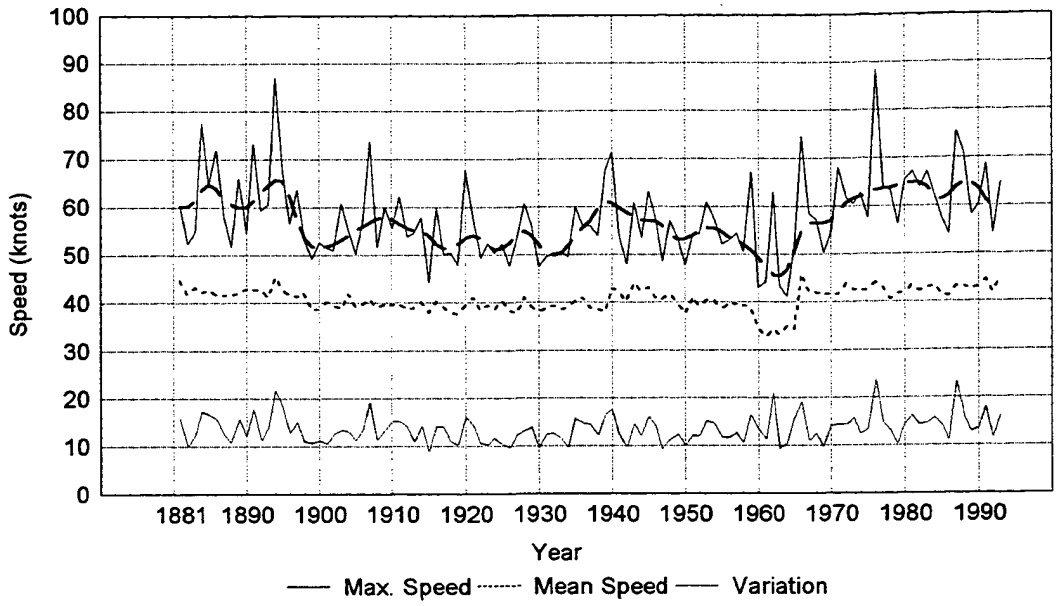


Figure 3 Windspeed and Statistics (1881-1993)

3.2 Wind Intensity

Figure 3 shows three measures of windspeed derived from the gale index. These are the maximum windspeed attained in a given year, the mean windspeed over a year, and the coefficient of variation over a year. The coefficient of variation is the preferred measure of dispersion, since it enables valid comparison between years.

Looking first at the top curve on Figure 3, the maximum windspeed, we can see peaks at the beginning and end of the record just as with the frequency data. Again, the more convincing evidence of short-term trend is in the last couple of decades, and there is no indication of long-term trend.

The second curve in Figure 3, the mean annual windspeed, fluctuates between about 49 knots and 44 knots, with the exception of the 1960-1965 period. This was noted as an inhomogeneity by Jenkinson and was accommodated by adjusting the windspeeds upwards by 25% when computing the gale index. Since this period still manifests very low windspeeds, either the adjustment is inadequate or this was a time of very slack circulation.

The coefficient of variation (the bottom curve in Figure 3) fluctuates between about 9% and 24%, with no indication of any pattern or trend in the variability of windspeeds in time.

3.3 Periodicity

Periodicity in the frequency of gales to 1989 is examined in detail by Holt (1991). Spectral analysis indicates that there is no significant periodicity on any time scale other than a negative autocorrelation at a one year lag. A year with many gales is often followed by a year with few gales. Approximately 40% of the variance in the number of gales in one year is explained by the variance in the previous year.

4. STORMS IN THE 21st CENTURY

Holt (1991) calculated frequency tables from the gale indices computed from the model pressure data, and compared these with frequency distributions from the historical gale index. This is not included in the current analysis since the model records are too short to enable meaningful comparison with frequency distributions derived from 100 years observed data. An exploratory examination, however, reveals that at the highest wind speeds, the observed frequency distributions are mirrored quite well by the model data for the IPCC A and 2 x CO_2 scenarios. This applies equally to storm frequencies and windspeeds, suggesting that the most extreme events are unlikely to be affected by global warming.

Table 1 summarises the statistical properties of the gale indices derived from the model runs. The number of gales in a 2 x CO_2 world is fewer than in the control and IPCC A runs.

Table 1 Summary of the Model Gale Indices

year	con total	con max	sca total	sca max	tco total	tco max
1	20	59	7	57	15	48
2	27	50	9	45	18	51
3	13	52	18	57	15	57
4	11	64	10	49	14	53
5	8	40	11	47	9	65
6	15	50	14	59	14	53
7	12	43	23	46	14	49
8	27	56	10	51	12	49
9	14	46	18	50	15	64
10	10	50	16	67	13	56

key: con, sca, tco, are the control run, IPCC A, and the 2 x CO_2 run respectively. Year is the year of model run, and total and max refer to total number of gales in a year and maximum windspeed in a year.

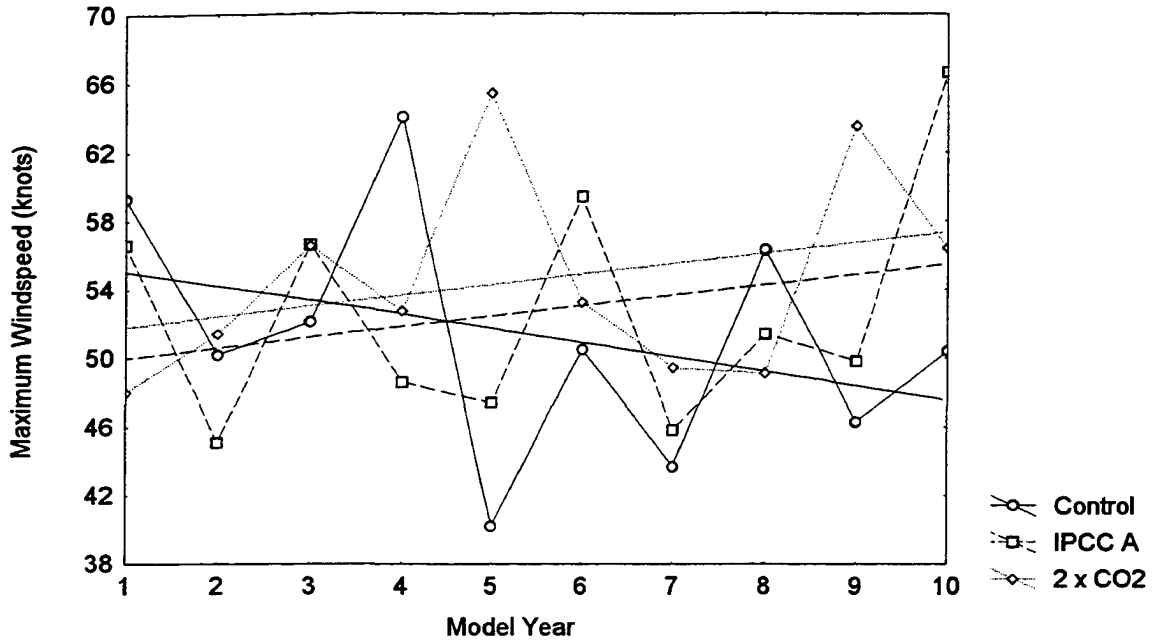


Figure 4 Maximum Windspeed in a Model Year for each Model Run

Figure 4 shows the maximum windspeed information from Table 1. Linear trend lines are included for each model run. Both the IPCC A and 2 x CO_2 scenarios exhibit rising trend, with the latter indicating higher windspeeds. The decline in windspeeds associated with the control run can not be explained without access to a longer time series.

5. CONCLUSIONS

We have presented a preliminary investigation into storminess over the North Sea and the likely implications for the next century under global warming. The historical data indicate a rising trend in the incidence of gales, bigger than any similar trend in the last 100 years, which may be part of the global warming 'signal' or simply an extended 'natural' fluctuation. A similar rising trend in observed wind intensity appears to be declining over the past five years or so.

Evidence from GCM data is inconclusive, with an apparent reduction in storm frequency associated with doubling of atmospheric CO_2. On the other hand, wind intensity under global warming is not only shown to be higher than in the control run, but is also increasing steadily for both the 2 x CO_2 and IPCC A scenarios.

Several inadequacies in the previous study (Holt, 1991) were brought to light when carrying out this research. The problem of using frequency distributions of short model-derived time series has already been mentioned. Also, here we did not attempt to validate the GCM pressure data by comparison with the observed fields. The principle objection to using this method is that no GCM can simulate atmospheric pressure fields with equal accuracy everywhere, leaving the analyst with little alternative but to exercise a subjective assessment of the likely problems arising in the area of interest. The use of a derived climate variable, such as the gale index, should smooth errors in the spatial fields for primary variables and, at the same time, offer a relatively simple, and physically realistic, means of testing the validity of the model data.

In this context, the ability to test model-derived frequency distributions would be invaluable. This requires the modellers to produce time series for the appropriate climate scenarios of at least the same length as the available instrumental data.

6. REFERENCES

Cubasch, U., et al., (1992), "Time dependent greenhouse warming computations with a coupled ocean-atmosphere model". Climate Dynamics, 8, 55-69.

Holt, T., (1991), "Storm Conditions over the North Sea: A Historical Perspective and Implications for the 21st Century". (unpublished) Report to Sir William Halcrow & Partners Ltd. in connection with the Anglian Sea Defence Management Study -Stage III.

Jenkinson, A.F. and P.P. Collison, (1977), "An Initial Climatology of Gales over the North Sea", UK Meteorological Office, Branch Memorandum No. 62.

Lamb, H.H., (1991), "Historic Storms in the North Sea, British Isles and Western Europe", CUP, 204 pp.

Variability and Trends in Minimum, Maximum and Extreme Temperatures For The Niagara Region

Anthony B. Shaw

Department Of Geography
Brock University
St. Catharines, Ontario, Canada L2S 3A1

ABSTRACT

This paper examines temperature changes and occurrences of extreme temperatures over the last fifty years for a number of representative stations in the Niagara Region. The study also compares temperature changes for the two most recent normal periods. The data were analysed using a combination of linear regression models and descriptive statistical methods. Among the findings, the results show a statistically significant increase in annual minimum temperature over the last thirty years and a non-significant increase in maximum temperature. An increase in summer mean temperature will likely produce more days with extreme temperatures.

INTRODUCTION

Although temperature values that display considerable seasonal and inter-annual variability pose major risks to agricultural, economic and recreational activities, occurrences of extreme values can bring disastrous consequences. Extreme maximum and minimum temperatures can also adversely effect crop growth and final yield. Humans and animals can also be at considerable risk from heat stress and photochemical pollutants brought on by abnormally high temperatures. In the Niagara Peninsula, the minimum and maximum temperature extremes present significant threat to climate-sensitive crops. A mild climate favouring extensive cultivation of tender fruits and vinifera grape varieties is the distinctive feature of the Niagara Region. Due to its location just north of the 43rd parallel, the Region is classified as having a continental climate with warm summers and cold winters. However, its peninsular shape with Lake Ontario to the north and Lake Erie to the south helps to moderate seasonal temperatures, giving this region an overall cool climate ideally suited for vineyard crops. Notwithstanding, frequent occurrences of extreme minimum temperature during winter and spring still pose the gravest danger to vineyard and tender fruit crops, while summer high temperature extremes can cause soil moisture stress and fruit and leaf desiccation. High concentrations of low level ozone have also been associated with high summer temperature extremes.

In a global warming scenario, rising temperature will likely have direct impacts on all resource sectors in Ontario. For the Niagara Region, temperature changes will likely lengthen the summer growing season and shorten the winter season. Although considerably moderated by the lakes, winters in this region are likely to be even milder. This situation may diminish risks of damaging freezing temperature, but could induce early budburst and thus increase the risk of frost damage in spring. Accordingly, it is essential to understand the long term temperature variability and occurrences of extreme temperatures in terms of their implications for agricultural activities and air quality of the Region.

This paper examines trends in mean monthly minimum and maximum temperature as well as the frequency of occurrence of extreme maximum temperatures for a number of geographically representative stations of the Niagara Region and contiguous areas. The paper also explores the relationships between summer season mean and maximum temperatures and occurrences of extreme maximum temperatures to determine which one is a better predictor of extreme events. Evidence of the Region's winter becoming more moderate over time should be reflected in trends of higher minimum temperatures and less frequent occurrences of extreme minimum temperatures. Warmer summers should be evidenced by higher maximum temperatures and frequently occurring extreme maximum temperatures.

Previous studies have examined maximum and minimum temperatures and extreme temperatures to determine evidence of climate change and climate variability on different temporal and spatial scales. Coughlan (1979) examined annual mean-maximum temperatures for Australia to determine any evidence of a warming. Relationships between high temperatures and high rainfall intensities in the context of global warming for southeastern Australia have been explored by Yu and Neil, 1990. Others have examined the relationships between changes in mean temperature and corresponding changes in the probabilities of extreme temperature events (Mearns et al., 1984; Takle and Bian, 1993). Their results indicated that as average July temperatures increase so will the frequency of extreme high temperatures in the Midwest. Changnon (1993) also found the behaviour of extreme temperatures sensitive to fluctuations in mean temperature conditions in the southeastern United States. He concluded that potential shifts in average temperature will likely cause significant changes in the frequency and duration of extreme high temperatures in this Region.

Diurnal temperature changes for the past century were also analysed to determine any observed evidence of warming in the Northern Hemisphere landmass (Karl et al., 1991). The results for the contiguous United States, the former Soviet Union and the People's Republic of China mainly indicated an increase in nighttime mean minimum temperatures and a decline in mean daily temperature range. In a similar context, mean monthly maximum, minimum and mean surface temperatures were analysed for climate regions in Canada (Skinner and Gullett, 1993). The authors found a statistically significant rise in national mean annual temperatures as well as significant increase in daytime maximum temperature and nighttime minimum temperature.

DATA AND REGION

The Niagara Region has several climatic stations that offer good spatial representation of the mesoclimates of this area. Of the approximately eleven stations that are currently operating and provide regular daily temperature observations to the Ministry of the Environment, most are located in a rural setting. There is only one first order station, located at the Regional Niagara District Airport. After careful examination of the length and quality of records, five stations were chosen for analysis based on their representation of the Niagara Region from the standpoint of its broad spatial and physical features. Moreover, these stations contain continuous records of daily observations of maximum, minimum and mean temperatures with relatively few missing values. From the beginning of the observation period until the time of this study, each station has remained in the same location. It is assumed that observing practices, instrument types and site conditions have not changed significantly and that the data can be considered homogeneous.

Two threshold values of extreme temperatures have been chosen for analysis in the summer and winter season. Summer extreme temperature is defined as daily observations with maximum temperatures >30° C occurring in the months of June, July and August. This threshold value represents a temperature level that is likely to cause soil moisture stress in plants, heat stress in humans and episodes involving damaging photochemical pollutants. Winter extreme minimum temperature is defined as daily observations with temperatures <-20° C occurring during the months of December, January and February . This extreme value is normally associated with widespread "winter kill" or severe freeze damage to perennial tree and vine crops beyond their threshold limit.

As in most of southern Ontario, the daily weather in the Niagara Region is highly variable. Beginning in the fall, Polar and Arctic air masses sweep into southern Ontario and may bring a diversity of weather conditions as they cross the Great Lakes Region. With the onset of winter, the frequency of moving cyclones increases as they push northeast out of the American Mid-West and east from Alberta. The Niagara Region lies directly under a major storm track running northeast from the Mid-West, up through the Ohio Valley, over the Great Lakes Region and thence through the St. Lawrence Valley. Spring

weather is highly variable and very turbulent, with high winds and frequent cyclones as the transition from winter to spring progresses. Cold spells interspersed with warm spells are common in the months of March and April as migratory cyclones move through the Region in response to large-scale temperature differences. Summer weather is dominated by strong radiative heating and widely scattered precipitation of convective origin. Cyclonic storms are infrequent as the Polar Front Jet is normally north of the Great Lakes Region at this time of the year. Frequent high pressure systems accompanied by lower wind speeds at the surface result in warm summer days.

Annual daily mean temperatures range from 8.0° to 9.0°C. As is typical of most mid-latitude continental locations, the coldest temperatures are in January and the warmest in the month of July, averaging about -4.7°C and 21.4°C, respectively. In spite of the moderating effects of the lakes, the Niagara Region has experienced frequent occurrences of extreme temperatures ranging from a high of 40.6° C to a low of -32.8°C.

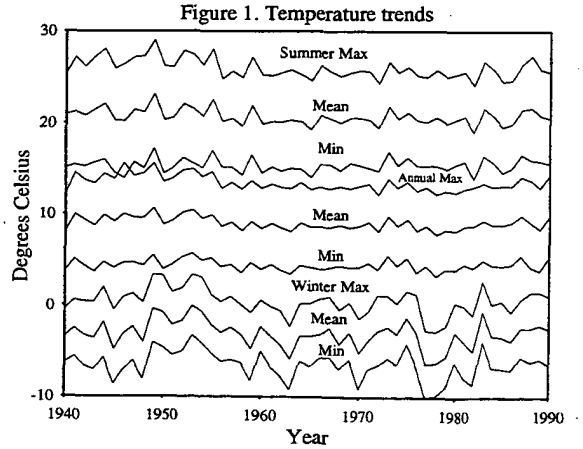
ANALYTICAL METHODS

Deviations in maximum, minimum, and mean temperature were analysed for the period 1940 to 1990 and for two normal periods, 1951-1980 and 1961-1990. Trends for the same periods were analysed using linear bivariate regression models. Tests of linearity were first executed by plotting the standardised residuals against the standardised predicted values. Standard statistical tests of significance of the regression coefficients were performed. The means and standard deviations for the maximum and minimum, and mean temperatures were computed for the forty year period. Trends in extreme temperatures >30°C were also analysed using linear regression methods. Relationships between summer mean maximum and mean temperatures, and the frequency of occurrences of extreme temperatures were also tested using linear regression methods. Frequency analysis of the occurrences of extreme temperatures along with the means and standard deviations were calculated.

TEMPERATURE TRENDS

In Figure 1, shows the distribution of annual maximum and mean temperatures for all stations combined. The period of the 1940s is the warmest decade; temperature subsequently declined markedly from the mid-1950s into the early 1970s and peaked again in the second half of the 1970s. This was followed by a pronounced warming into the 1980s. Annual minimum temperature shows high but declining values from the 1940s into the early 1970s and a weak increasing trend into the 1980s. In every respect, the 1940s and the first half of the 1950s experienced annual maximum temperatures generally unsurpassed in the subsequent decades. There are three periods of comparable high minimum temperatures, which clearly stand out in the record for this period.

Figure 1. Temperature trends



Seasonal distributions of summer (June, July and August) and winter (December, January and February) maximum and mean temperatures reflect trends similar to the annual values. However, a pronounced decline in maximum temperatures is noticeable from the 1940s to the early 1970s for both seasons. In the case of summer minimum temperature, a weak increasing trend is observed for the period as a whole, while winter minimum temperature shows a high degree of variability but a declining trend up to the early 1980s. Except for winter, between 1940 and 1990, mean maximum temperature distribution is generally found to be more highly variable than the mean minimum temperature.

TEMPERATURE CHANGES

Changes in maximum and minimum temperatures for each of the three periods were estimated by linear regression method. Table 1 shows that between 1940 and 1990, annual maximum temperature for all stations combined declined by 1.09°C and mean annual temperature by 0.61°C.

Table 1. Regression Coefficients of Annual Temperature Changes From 1940 - 1990

Stations	Maximum	Minimum	Mean
Harrow	-1.56*	0.01	-0.70*
	$\bar{x}$ 13.78	$\bar{x}$ 4.91	$\bar{x}$ 9.37
	S.D. 0.99	S.D. 0.66	S.D. 0.74
Niagara Falls	-1.56*	0.52	-0.52*
	$\bar{x}$ 13.52	$\bar{x}$ 4.48	$\bar{x}$ 8.96
	S.D. 0.94	S.D. 0.66	S.D. 0.69
St. Catharines	-0.52*	-0.52	-0.52
	$\bar{x}$ 13.50	$\bar{x}$ 4.28	$\bar{x}$ 8.96
	S.D. 0.81	S.D. 0.72	S.D. 0.71
Vineland	-0.52*	0.00	-0.52
	$\bar{x}$ 13.04	$\bar{x}$ 4.59	$\bar{x}$ 8.82
	S.D. 0.71	S.D. 0.56	S.D. 0.60
Welland	-1.56*	0.0	-0.52*
	$\bar{x}$ 13.48	$\bar{x}$ 3.77	$\bar{x}$ 8.64
	S.D. 0.87	S.D. 0.64	S.D. 0.61
All	-1.09*	0.03	-0.61*
	$\bar{x}$ 13.47	$\bar{x}$ 4.46	$\bar{x}$ 9.06
	S.D. 0.82	S.D. 0.58	S.D. 0.66

Significant at the 0.05 probability level, using the students t-test

There was no significant change in minimum temperature. Summer maximum and mean temperatures declined by 1.49°C and 0.66°C, respectively, while a non-significant increase in minimum temperature is noted (Tables 2 and 3). Winter mean temperature for all stations combined declined by 0.79°C. and some individual stations showed a statistically significant decrease in maximum temperature.

Table 2. Regression Coefficients of Summer Temperature Changes From 1940 - 1990

Stations	Maximum	Minimum	Mean
Harrow	-2.03*	0.52	-0.83*
	$\bar{x}$ 26.39	$\bar{x}$ 15.98	$\bar{x}$ 21.23
	S.D. 1.26	S.D. 0.76	S.D. 0.88
Niagara Falls	-2.08*	0.16	-1.04*
	$\bar{x}$ 26.12	$\bar{x}$ 15.70	$\bar{x}$ 20.99
	S.D. 1.45	S.D. 0.83	S.D. 0.95
St. Catharines	-1.04*	0.52	-0.52
	$\bar{x}$ 26.50	$\bar{x}$ 16.09	$\bar{x}$ 20.79
	S.D. 1.23	S.D. 1.84	S.D. 0.96
Vineland	-1.04*	0.52	-0.52
	$\bar{x}$ 25.24	$\bar{x}$ 15.28	$\bar{x}$ 20.28
	S.D. 1.02	S.D. 0.79	S.D. 0.85
Welland	-2.03	0.01	-0.52
	$\bar{x}$ 25.95	$\bar{x}$ 14.76	$\bar{x}$ 20.37
	S.D. 1.17	S.D. 0.87	S.D. 0.86
ALL	-1.49*	0.39	-0.66*
	$\bar{x}$ 25.9	$\bar{x}$ 15.41	$\bar{x}$ 20.73
	S.D. 1.06	S.D. 0.74	S.D. 0.83

* Significant at the 0.05 probability level, using the student's t-test

Table 3. Regression Coefficients of Winter Temperature Changes Between (1940 - 1990)

Stations	Maximum	Minimum	Mean
Harrow	- 1.64*	-0.52	-1.04
1940 - 1990	$\bar{x}$ 0.48 S.D. 1.66	$\bar{x}$ -6.51 S.D. 1.84	$\bar{x}$ -3.14 S.D. 1.69
Niagara Falls	-2.08*	-0.52	-1.04*
1940 - 1990	$\bar{x}$ -0.61 S.D. 1.74	$\bar{x}$ -6.65 S.D. 1.45	$\bar{x}$ -3.04 S.D. 1.55
St. Catharines	0.52	-0.52	0.52
1940 - 1990	$\bar{x}$ 0.55 S.D. 1.42	$\bar{x}$ -6.19 S.D. 1.69	$\bar{x}$ -2.93 S.D. 1.54
Vineland	0.52	-1.04	-1.04*
1940 - 1990	$\bar{x}$ 0.61 S.D. 1.42	$\bar{x}$ -5.61 S.D. 1.60	$\bar{x}$ -2.73 S.D. 1.39
Welland	-1.04*	-0.52	-1.04*
1940 - 1990	$\bar{x}$ 0.42 S.D. 1.52	$\bar{x}$ -7.38 S.D. 1.51	$\bar{x}$ -3.49 S.D. 1.51
All	-0.97	-0.83	-0.79*
	$\bar{x}$ 0.53 S.D. 1.41	$\bar{x}$ -6.47 S.D. 1.49	$\bar{x}$ -3.07 S.D. 1.43

*Significant at the 0.05 probability level, using the student's t-test

Table 4. A Comparison of Regression Coefficients of Annual Temperature Changes for Two Normal Periods

Stations	Maximum	Minimum	Mean
Harrow	- 1.61*	- 0.66*	- 1.15*
1951 - 1980	$\bar{x}$ 13.41 S.D. 0.81	$\bar{x}$ 4.76 S.D. 0.61	$\bar{x}$ 9.12 S.D. 0.66
1961 - 1990	0.29	0.69	0.50
	$\bar{x}$ 13.34 S.D. 0.58	$\bar{x}$ 4.81 S.D. 0.67	$\bar{x}$ 9.09 S.D. 0.60
Niagara Falls	- 1.50	- 0.60	0.90*
1951 - 1980	$\bar{x}$ 13.19 S.D. 0.79	$\bar{x}$ 4.29 S.D. 0.63	$\bar{x}$ 8.74 S.D. 0.65
1961 - 1990	0.60*	0.60*	0.60*
	$\bar{x}$ 13.08 S.D. 0.55	$\bar{x}$ 4.42 S.D. 0.64	$\bar{x}$ 8.72 S.D. 0.56
St. Catharines	- 1.50*	- 0.60*	- 1.20*
1951 - 1980	$\bar{x}$ 13.38 S.D. 0.77	$\bar{x}$ 4.13 S.D. 0.72	$\bar{x}$ 8.81 S.D. 0.71
1961 - 1990	0.30	0.60*	0.30
	$\bar{x}$ 13.25 S.D. 0.53	$\bar{x}$ 4.04 S.D. 0.66	$\bar{x}$ 8.73 S.D. 0.54
Vineland	- 1.50*	- 0.30	- 1.20*
1951 - 1980	$\bar{x}$ 12.97 S.D. 0.67	$\bar{x}$ 4.54 S.D. 0.55	$\bar{x}$ 8.76 S.D. 0.59
1961 - 1990	0.30	0.60*	0.30
	$\bar{x}$ 12.77 S.D. 0.51	$\bar{x}$ 4.51 S.D. 0.53	$\bar{x}$ 8.65 S.D. 0.49
Welland	- 1.50*	- 0.30	- 0.90*
1951 - 1980	$\bar{x}$ 13.22 S.D. 0.71	$\bar{x}$ 3.96 S.D. 0.58	$\bar{x}$ 8.62 S.D. 0.61
1961 - 1990	0.60	0.30	0.18
	$\bar{x}$ 13.04 S.D. 0.48	$\bar{x}$ 3.77 S.D. 0.60	$\bar{x}$ 8.43 S.D. 0.46
ALL	-1.54*	-0.67*	-1.106*
1951 - 1980	$\bar{x}$ 13.23 S.D. 0.72	$\bar{x}$ 4.38 S.D. 0.59	$\bar{x}$ 8.89 S.D. 0.64
1961 - 1990	0.59*	0.54*	0.56*
	$\bar{x}$ 13.09 S.D. 0.51	$\bar{x}$ 4.35 S.D. 0.28	$\bar{x}$ 8.82 S.D. 0.52

*Significant at the 0.05 probability level, using the student's t-test.

Over the last fifty years, maximum temperature seems to have declined significantly but is apparently largely influenced by the period of relatively cool temperatures that prevailed from the mid-1950s to the early 1970s.

COMPARISON OF TWO NORMAL PERIODS

Table 4 compares annual temperatures for the two most recent normal periods. In the first normal period annual maximum temperature declined by 1.54° C and rose by 0.59° C in the second period. Minimum temperature also declined by 0.67° C and increased by 0.54° C in the subsequent period. However, mean and standard deviation values were found to be higher in the first as compared to the second normal period. Analysis of seasonal changes for the summer shows the summer maximum declined by 1.36° C in the first period and a non-significant increase of 0.41° C in the second (Table 5).

Table 5. A Comparison of Regression Coefficients of Summer Temperature Changes For Two Normal Periods

Stations	Maximum	Minimum	Mean
Harrow	-1.74*	0.04	-0.85*
1951 - 1980	$\bar{x}$ 25.98 S.D. 1.06	$\bar{x}$ 15.86 S.D. 0.66	$\bar{x}$ 20.94 S.D. 0.77
1961 - 1990	0.28	0.86*	0.58
	$\bar{x}$ 25.82 S.D. 0.79	$\bar{x}$ 15.98 S.D. 0.69	$\bar{x}$ 20.93 S.D. 0.67
Niagara Falls	-1.50*	-0.30	-0.90
1951 - 1980	$\bar{x}$ 25.96 S.D. 1.07	$\bar{x}$ 15.59 S.D. 0.73	$\bar{x}$ 20.82 S.D. 0.88
1961 - 1990	0.30	0.90*	0.60
	$\bar{x}$ 25.73 S.D. 0.78	$\bar{x}$ 15.70 S.D. 0.75	$\bar{x}$ 20.72 S.D. 0.76
St. Catharines	-1.50*	-0.30	-0.60
1951 - 1980	$\bar{x}$ 26.04 S.D. 1.08	$\bar{x}$ 15.14 S.D. 0.89	$\bar{x}$ 21.05 S.D. 1.19
1961 - 1990	0.60	1.12*	0.90*
	$\bar{x}$ 25.74 S.D. 0.79	$\bar{x}$ 15.29 S.D. 0.97	$\bar{x}$ 20.51 S.D. 0.82
Vineland	-1.20*	-0.30	-0.60
1951 - 1980	$\bar{x}$ 25.50 S.D. 1.25	$\bar{x}$ 16.03 S.D. 1.27	$\bar{x}$ 20.81 S.D. 1.20
1961 - 1990	0.30	1.20*	0.60
	$\bar{x}$ 25.15 S.D. 1.12	$\bar{x}$ 16.09 S.D. 1.13	$\bar{x}$ 20.67 S.D. 1.09
Welland	-0.90*	0.01	-0.30
1951 - 1980	$\bar{x}$ 25.59 S.D. 0.86	$\bar{x}$ 14.96 S.D. 0.77	$\bar{x}$ 20.31 S.D. 0.76
1961 - 1990	0.30	-0.30	-0.09
	$\bar{x}$ 25.38 S.D. 0.74	$\bar{x}$ 14.74 S.D. 0.76	$\bar{x}$ 20.05 S.D. 0.67
All	-1.36*	0.05	-0.69
1951 - 1980	$\bar{x}$ 25.75 S.D. 0.91	$\bar{x}$ 15.36 S.D. 0.67	$\bar{x}$ 20.58 S.D. 0.76
1961 - 1990	0.41	0.77*	0.61
	$\bar{x}$ 25.52 S.D. 0.73	$\bar{x}$ 15.40 S.D. 0.67	$\bar{x}$ 20.47 S.D. 0.67

*Significant at the 0.05 probability level, using the student's t-test

The only statistically significant change in temperature for the 1951 to 1990 normal period is noted with respect to summer minimum temperature, which increased by 0.77° C. Table 6 shows that winter temperatures in the first period have declined significantly in all cases and there have been non-significant increases in the subsequent period.

Table 6. A Comparison of Regression Coefficients of Winter Temperature Changes For Two Normal Periods

Stations	Maximum	Minimum	Mean
Harrow	-2.28*	-2.54*	-2.40*
1951 - 1980	$\bar{x}$ -0.05	$\bar{x}$ -6.74	$\bar{x}$ -3.43
	S.D. 1.60	S.D. 1.96	S.D. 1.77
1961 - 1990	1.06	0.78	1.03
	$\bar{x}$ -0.13	$\bar{x}$ -6.98	$\bar{x}$ -3.65
	S.D. 1.64	S.D. 1.85	S.D. 1.68
Niagara Falls	-3.30*	-2.10*	-2.7*
1951 - 1980	$\bar{x}$ 0.21	$\bar{x}$ -6.93	$\bar{x}$ -3.34
	S.D. 1.70	S.D. 1.49	S.D. 1.52
1961 - 1990	0.90	1.20	0.90
	$\bar{x}$ -0.10	$\bar{x}$ -7.00	$\bar{x}$ -3.56
	S.D. 1.36	S.D. 1.44	S.D. 1.34
St. Catharines	-2.1*	-2.7*	-1.5*
1951 - 1980	$\bar{x}$ 0.47	$\bar{x}$ -6.27	$\bar{x}$ -3.10
	S.D. 1.45	S.D. 1.93	S.D. 1.70
1961 - 1990	0.90	0.60	1.20
	$\bar{x}$ 0.35	$\bar{x}$ -6.61	$\bar{x}$ -3.32
	S.D. 1.43	S.D. 1.67	S.D. 1.52
Vineland	2.40*	-3.9*	-2.40*
1951 - 1980	$\bar{x}$ 0.50	$\bar{x}$ -5.52	$\bar{x}$ 2.89
	S.D. 1.52	S.D. 1.74	S.D. 1.47
1961 - 1990	0.90	0.60	1.05
	$\bar{x}$ 0.30	$\bar{x}$ -6.01	$\bar{x}$ -3.00
	S.D. 1.47	S.D. 1.59	S.D. 1.51
Welland	-2.40*	-2.10*	-2.40*
1951 - 1980	$\bar{x}$ 0.11	$\bar{x}$ -7.26	$\bar{x}$ -3.61
	S.D. 1.58	S.D. 1.79	S.D. 1.67
1961 - 1990	1.50	-0.30	0.60
	$\bar{x}$ -0.11	$\bar{x}$ -7.75	$\bar{x}$ -3.97
	S.D. 1.36	S.D. 1.60	S.D. 1.41
ALL	-2.53*	-2.72*	-2.52*
1952 - 1980	$\bar{x}$ 0.25	$\bar{x}$ -6.53	$\bar{x}$ -3.27
	S.D. 1.50	S.D. 1.66	S.D. 1.54
1961 - 1990	1.05	0.54	1.06
	$\bar{x}$ 0.06	$\bar{x}$ -6.88	$\bar{x}$ -3.5
	S.D. 1.34	S.D. 1.48	S.D. 1.38

*Significant at the 0.05 probability level, using the student's t-test

The comparison of temperature for two most recent normal periods found maximum temperatures have declined in the first period but showed a non-significant increase in the second. Minimum temperature values have shown a statistically significant increase primarily in the last normal period.

EXTREME TEMPERATURES

This study also tested the relationship between summer mean and maximum temperatures and the occurrences of extreme temperatures >30° C to determine which one is the better predictor of extreme events. It is expected that as summer mean and maximum temperatures increase, the frequency of occurrences of extreme temperature events will likely increase. The number of days with extreme temperature average about 15 days for the Niagara Region. Table 7 shows the mean maximum temperature to be the better predictor with R^2 values ranging from 0.71 to 0.86.

Table 7. R^2 Values and Regression Coefficients For Summer Mean and Maximum Temperatures and Frequency of Days With Temperatures >30°C

Stations	T - Mean		T - Max	
	R^2	Coefficient	R^2	Coefficient
Harrow	0.65	10.5	0.86	8.04
Niagara Falls	0.72	9.05	0.78	7.80
St. Catharines	0.54	7.02	0.71	7.07
Vineland	0.59	6.43	0.73	5.86
Welland	0.53	9.64	0.79	8.63

However, as compared to maximum temperature, one degree increase in mean temperature is likely to add 8 days to the current average.

CONCLUSIONS

This study analysed mean maximum, minimum and mean temperatures for the Niagara Region for the period 1940 to 1990 and the two most recent normal periods to determine whether there are any significant trends. Based on linear regression models, significant changes in annual and seasonal temperatures were found for the three periods examined. Maximum temperatures showed the highest degree of variability and significant changes in all three periods. Minimum temperatures displayed comparatively weak variability but a weak increasing trend in the most recent normal period. The relationship between summer mean and maximum temperature and occurrences of extreme temperature show maximum temperature to be the better predictor. However, in the context of a future warming scenario, one degree warming in mean summer temperature for the Niagara Region will likely increase the average number of days with extreme temperature from 15 to 23 days.

REFERENCES

Changon, D., 1993, Variability in high temperature extremes in the southeastern United States, Physical Geography, 14, pp. 599-611.

Coughlan, M. J., 1979, Recent variations in annual-mean maximum temperatures over Australia, Journal of Royal Meteorological Society, 107, pp. 707-719.

Karl, T. R., Kukla, G., Rasuvayev, V. N., Quayle, R. G., Heim, R.R., Easterling, D.R., and Fu, C.B., 1991, Global warmin: Evidence for Asymmetric Diurnal Temperature Change, Geophysical Research Letters, 18, No. 12, pp. 2253-2256.

Mearns, L. O., Katz, R.W., and Schneider, S.H., 1984, Extreme high- temperature events : Changes in their probabilities with changes in mean temperature, Journal of Climate and Applied Climatology, 23, 1601-1613.

Skinner, W. R., and Gullett, D.W., 1993, Trends of Daily Maximum and Minimum Temperature in Canada during the past Century, Climatological Bulletin, 27, pp. 63-77.

Tackle, E. S., and Bian, X., 1993, Preliminary evaluation of temperature means, extremes, and variability, and their relation to agricultural yields. Preprints from the Eight Conference on Applied Climatology, AMS, pp. 32-37.

Yu, B. and Neil, T., 1991, Global warming and regional rainfall: The difference between average and high intensity rainfalls, International Journal of Climatology, 11, pp. 653-661.

OPERATIONAL MULTI-SEASON OUTLOOKS OF SEASONAL MEAN TEMPERATURE AND PRECIPITATION

Edward O'Lenic

Climate Prediction Center
5200 Auth Road
Camp Springs, MD 20746

ABSTRACT

This paper will discuss NWS's new operational, long lead, seasonal outlooks, including the scientific basis of the new outlooks. The three models used to prepare the outlooks will be described. They are canonical correlation analysis (CCA), optimal climate normals (OCN) and the coupled model predictions (CMP). The paper also discusses the skill of the forecast methods, the new paradigm which has been developed for producing the outlooks, the new map format for the probabilistic outlooks, and finally, the modes by which the outlooks are dissenimated, including Internet (the Internet address is **http://nic.fb4.noaa.gov**).

1. INTRODUCTION

The first operational seasonal long-lead Climate Outlook for the continental United States, Alaska and Hawaii, consisting of a 0.5 month lead-time outlook of seasonal mean temperature and total precipitation for January-March 1995, was issued on December 15, 1994. On January 16, 1995, Outlooks for February through April 1995 through February through April 1996 (lead-times of from 0.5 to 12.5 months) were issued. These events mark the culmination of several years of development work and have benefited from several decades of research on low-frequency variability. Implementation of these outlooks also required a major effort to render them understandable to users. In particular, new methods were developed for graphically displaying both the tools used to prepare the outlooks and the final products. This paper gives an overview of the new outlooks and the new production/display methods employed.

2. THE SCIENTIFIC BASIS OF CLIMATE OUTLOOKS

During the last 25 years our understanding of processes operating within the global climate system on timescales of 10 days to interdecadal has grown greatly. With respect to seasonal prediction, the most important low frequency atmospheric phenomena is the El Nino/Southern Oscillation (ENSO), which produces statistically significant climate anomalies over large areas of the United States during much of the year, particularly winter.

Three "tools" are used to prepare the Outlooks. They are:

a) Canonical correlation analysis (CCA)(Barnston, 1993) capitalizes upon ENSO. This multivariate statistical technique relates future spatial and temporal patterns of U.S. surface temperature to spatial and temporal patterns of observed seasonal mean tropical Pacific SST, hemispheric 700-mb height, and U.S. surface temperature.

b) Optimal Climate Normals (OCN)(Huang et al., 1994) is also used. It is an objective statistical technique based upon the simple notion that one can obtain a useful estimate of the climate (temperature or precipitation) for a future season by formulating the predicted climate for that season from the average of the most recent k years for that season, where k is less than the standard 30 years. For operational use, k is now fixed at 10 years. OCN isolates the effects of trends or recent multi-year regimes in the seasonal temperature and precipitation time series. OCN forecasts are expressed as the difference between the optimal normals and the official 30-year climatology.

c) Finally, a coupled ocean-atmosphere model forecast (CMF) (Leetmaa and Ji, 1992) has been developed and made operational. This model is operationally integrated out to 6 months of simulated time in two modes, one using an underlying SST field which is persisted from the intial time and the other which uses an evolving SST field.

3. ACCURACY OF LONG-LEAD CLIMATE OUTLOOKS

The accuracy of long-range empirical outlooks has always been modest because the predictions are drawn from distributions which necessarily acknowledge a large number of possible outcomes, while the observed single event against which the outlook is verified includes the noise created by the unpredictable (on monthly and seasonal timescales) synoptic disturbances which occur (Epstein, 1988). According to some estimates of potential predictability (Madden and Shea, 1978), the noise is generally larger than the signal in middle latitudes. Therefore, **our climate outlook products must be accompanied by information about the accuracy of the products.**

The likely accuracy of the OCN and CCA is gauged by a seasonal and spatial accuracy record based upon 30 or more years of outlooks. For the CCA this is done by cross-validation (CV). For the NWP-based CMF, the model must be rerun and verified for at least 10 years (cases) for a given season. The accuracy of the OCN technique is measured by correlating predicted and observed anomalies during 1961-93. These OCN correlation scores are lowered to account for the shinkage expected on independent data (Huang et al., 1994, Barnston and van den Dool, 1993).

The correlation scores of CCA and OCN projections of seasonal mean temperature, averaged over the continental United States, (Figs. 1a, b) have accuracy maxima in the cool and warm seasons with minima in between. The score of a random prediction on these graphs would be zero. The annual cycles of accuracy of CCA and OCN seasonal precipitation predictions (not shown) both have wintertime maxima, however, the CCA has a summertime accuracy minimum, while the OCN has a maximum during that season. For both methods, skillful areas on the precipitation maps (not shown) are much smaller and more spotty than those for temperature. One remarkable property of the CCA forecasts (Fig. 1a) is that there is little drop in accuracy between 1 month and 7 month lead times. Something similar to this occurs for the OCN short and long lead forecasts (Fig 1b).

The accuracy of CCA and OCN also vary regionally (Figs. 2a and 2b). Both have correlation scores in excess of 50 percent over large portions of the eastern U.S. for outlooks of seasonal mean temperature, at a lead-time of 6.5 months for the CCA and lead-times of 0.5-12.5 months for the OCN, during January - March (JFM) and over the Great Basin during July - September (JAS) (JAS chart are not shown, however, electronic copies are available via Internet).

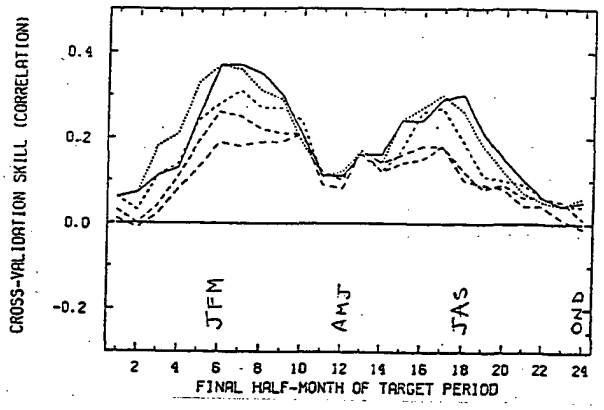


Figure 1a. Cross-validation correlation skill of CCA projections of seasonal mean temperature averaged over 59 stations across the continental U.S. Season 1 is the 3-month period ending in mid-January, etc. Shown are the annual cycles of skill of CCA outlooks at lead-times of one month (solid curve), 4 months (shortest dashed curve), 7 months (second shortest dashed curve), 10 months (next longest dashed curve), and 13 months (longest dashed curve).

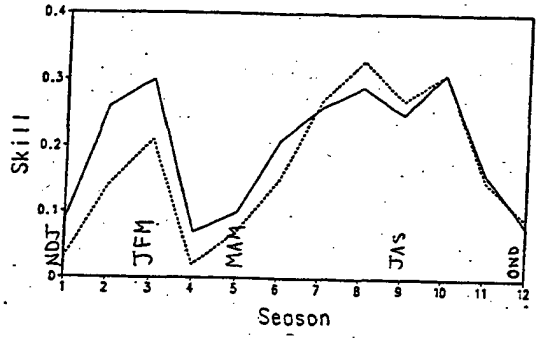


Figure 1b. Correlation skill of OCN projections of seasonal mean temperature, averaged over 325 climate divisions across the contintental U.S. Solid curve is for the (short lead-time) 0.5-8.5 month leads, dashed curve is for the (long lead-time) 9.5-20.5 month leads.

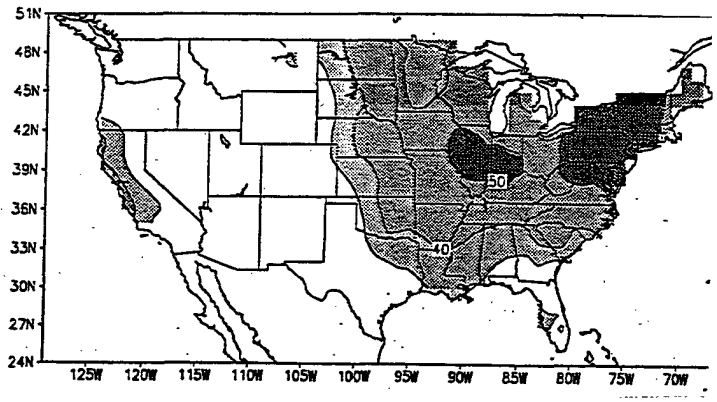


Figure 2a. Cross-validation-determined correlation skill of CCA projections of seasonal mean temperature at a lead-time of 6.5 months for the January-March target season. Based upon independent data from 1956-93. Correlations are scaled by a factor of 100. Contour interval is 10. Scores < 30 are not contoured.

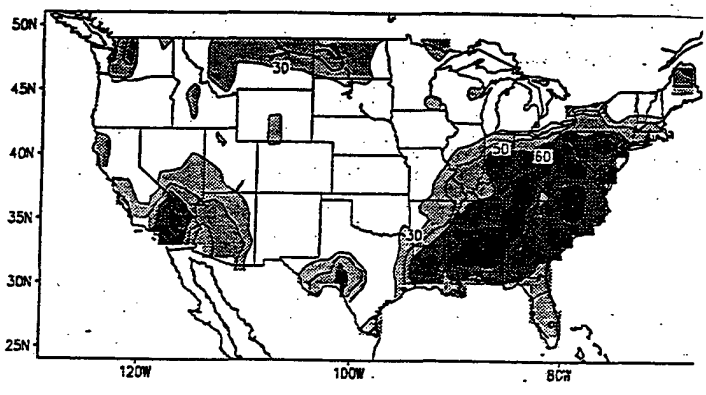


Figure 2b. Correlation skill of OCN projections of seasonal mean temperature at lead-times of 0.5-8.5 months for the January-March target season. Based upon predictions from 1961-1993. The correlations are lowered to reflect the expected shrinkage of skill on independent future forecasts. Correlations are scaled by a factor of 100. Contour interval is 10. Scores < 30 are not contoured.

Simulations based upon perfect SSTs indicate that CMF-based projections of temperature have a cold season U.S. average maximum correlation with observations of about 0.50 and a warm season minumum (not shown). The average maximum accuracy is reduced by about half when strong ENSO years are excluded. ENSO-related U.S. average CMF precipitation skill has early winter and early spring maxima (0.30-0.40) (not shown). Non-ENSO forecasts have about 0.10 to 0.15 correlation with observations.

4. NEW OPERATIONAL PROCEDURES

A new suite of procedures has been developed to formulate long lead outlooks. One of the most important requirements for these procedures is that they be formulated so as to take the known accuracy of the predictive tools into account, as objectively as possible. Other requirements include use of work-station computing and communication technologies for display, evaluation and forecast creation. The new procedures are as follows:

1. Projections of seasonal mean surface temperature (T) and total precipitation (P), for the conterminous U.S., Alaska, and Hawaii, are derived from a mostly objective combination of CCA, OCN, and CMF. Maps from each method, in the same format, for all leads and variables, are produced by computer and placed on a workstation.

2. Map values, plotted at stations, are standardized so that the results of all of the methods may be intercompared. The physical size of the numbers on the maps corresponds to three tool correlation skill levels - - largest numbers correspond to 0.60 or greater, mid-size numbers indicate 0.45-0.59 , smallest numbers correspond to 0.30-0.44 , and no numbers indicate skill below 0.30. In the near future, a single map which optimally combines all of the methods, will be produced via multiple linear regression. Time sequences of the maps for the various methods may be easily viewed in order to examine their temporal consistency.

3. Two persons examine the maps for each lead-time and variable and resolve any conflicts among the methods. Confidence is low in regions where two or more tools are in opposition and high when they are in agreement and when the skill of tools is high. There is also a consolidated tool which linearly combines all three tools into a single graphical tool.

4. Probability anomalies are used to depict the confidence of theforecasters in the tools. We arbitrarily divide the observed distribution of T and P during 1961-90 into three equally likely categories, BELOW, NORMAL, and ABOVE, for T, and BELOW, MODERATE, and ABOVE, for P. The average likelihood, or *climatological probability*, of these categories is 1/3 - 1/3 - 1/3. We designate this category on the maps as "CL", which signifies "CLimatological probabilities." Deviations from CL are indicated by the probability anomalies. A legend is included on the maps.

5. A total of 26 probability anomaly maps are drawn, i.e., one T and P map for each of 13 lead-times of from 0.5 to 12.5 months. In regions of high skill and good agreement among tools, probability anomaly values may reach values as high as 15% to 20%. Generally, however, map contour values range from zero (or CL) to 10%. Figure 3a, b shows a sample of the new climate outlook maps.

6. The outlook for seasonal mean SST in the equatorial Pacific Ocean is formulated from CCA and is displayed as an x-y plot of SST versus lead-time (not shown). A prognostic map discussion covering all outlook leads is written, as is a bulletin describing the details of both the 0.5 month lead-time monthly and the long-lead-time seasonal outlooks for Hawaii.

7. An electronic document, intended for use on Internet and for backup copies (hardcopy or fax, available through mid-late 1994 from the Regional Climate Centers), is composed via desk-top publication techniques. After 3 PM Eastern Time, all of the outlook maps are disseminated via AFOS, Family of Services (FOS), AFOS Graphics Service, and Internet (address: **nic.fb4.noaa.gov**) (Note: Internet is not an official mode of dissemination). Tools and skill maps are placed on anonymous FTP and Internet.

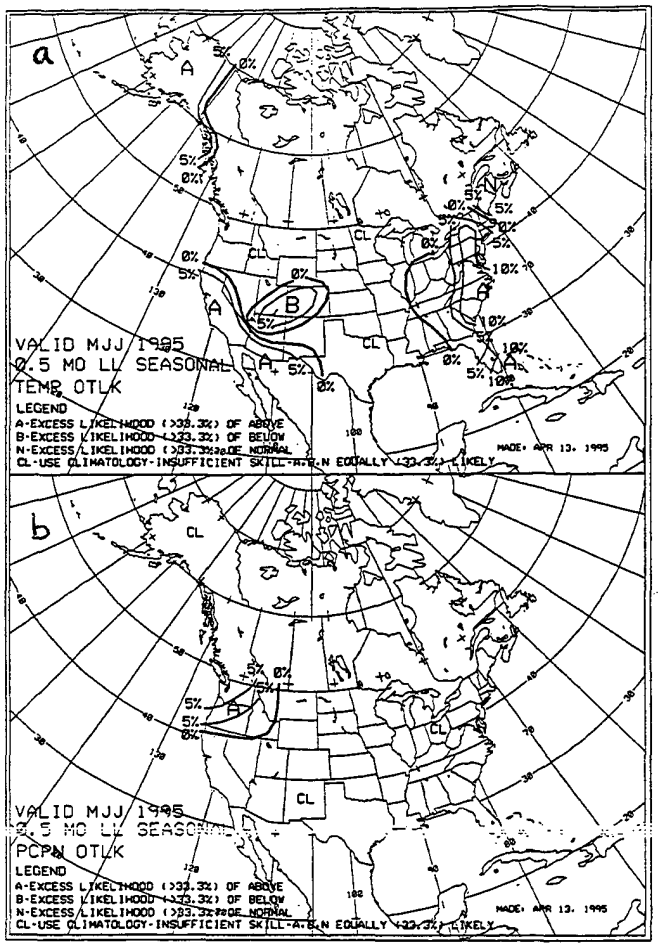


Figure 3. Samples of long-lead outlook maps (2 out of a total of 26). Map contours are probability anomalies with respect to three (BELOW, NORMAL or MODERATE and ABOVE) climatologically equally likely (33-1/3% each) categories. Probabilities are scaled by a factor of 100. Contour interval is 5. In regions labeled "CL" the probability anomaly is zero (see legend).

7. REFERENCES

Barnston, A.G., and H.M. van den Dool, 1993: A degeneracy in cross-validated skill in regression-based forecasts. *J. Climate*, **5**, 963-977.

_____, 1993: Linear statistical short-term climate predictive skill in the Northern Hemisphere. NOAA Technical Report NWS 49, September 1993, U.S. Dept. of Commerce, NOAA, National Weather Service. 137 pp. Available from the Climate Prediction Center, Room 604 WWB, Camp Springs, MD, 20746.

Epstein, E.S., 1988: Long-range weather prediction: Limits of predictability and beyond. *Wea. and Forecasting*, **3**, 69-75.

Huang, J., and H.M. van den Dool, 1993: Monthly precipitation-temperature relation and temperature prediction over the U.S. *J. Climate*, **6**, 1111-1132.

_____, _____, and A.G. Barnston, 1994: Long-lead seasonal temperature prediction using optimal climate normals. Submitted to *J. Climate*, (in press).

Madden, R.L. and D.J. Shea, 1978: Estimates of the natural variability of time-averaged temperatures over the United States. *Mon. Wea. Rev.*, **106**, 1695-1703.

CURRENT DEVELOPMENTS IN STATISTICAL SEASONAL RAINFALL PREDICTION IN AUSTRALIA

Wasyl Drosdowsky
Bureau of Meteorology Research Centre,
Melbourne, Australia

ABSTRACT

Past research has highlighted the significant impact of climate variations on the Australian economy, and the value of timely forecasts of these climate variations. Current predictions, based on the state of the El Nino / Southern Oscillation show some skill (above chance, persistence or climatology) of forecasts of seasonal climate variations. Current empirical work in the Bureau of Meteorology Research Centre has two directions; firstly to utilise global scale sea surface temperature anomaly (SSTa) patterns as predictors of inter-annual Australian climate variability, and secondly to document and understand the intraseasonal variability of Australian rainfall and the impact of this variability on seasonal prediction. The results of extensive testing of the SSTa predictors is described.

1. INTRODUCTION

A significant relationship exists in some seasons between eastern Australian rainfall and the Southern Oscillation (SO, McBride and Nicholls, 1983). This relationship provides the basis for a Seasonal Climate Outlook, (SCO) issued by the National Climate Centre (NCC) of the Australian Bureau of Meteorology. The major emphases of this service, which uses the Troup Southern Oscillation Index (SOI), are seasonal (3 monthly) rainfall forecasts for eastern Australia. Forecasts are also made of the timing of the onset of north Australian wet season (monsoon), and the expected number of tropical cyclones.

Since the commencement of the SCO, various forecast techniques have been employed in order to extract the maximum information from the SOI. Initially actual seasonal rainfall was predicted using simple linear regression with the past season (three months) value of the SOI as the predictor. This predicted rainfall was then expressed as a decile value. These categorical forecasts were replaced by probabilistic forecasts in 1992, partly in response to user's requests for some error or probability estimates to be included with the forecast. The forecasts are produced using linear discriminant analysis, with the past season, or the trend in the SOI as the predictor.

In addition, a number of more subjective techniques are employed. These include two forms of phase categories of the SOI (Stone 1992, Zhang and Casey 1992) and an analogue selection technique (Drosdowsky 1994). These methods give further qualitative guidance of the probability forecast.

The relations with the SO are weak, however, during the late southern summer and autumn period, when extreme events decay, and over the western third of the continent throughout the year. This has lead, in recent years to attempts to find other independent predictors. Nicholls (1989) and Drosdowsky (1993a,b) have documented a major mode of winter rainfall variability, consisting of a broad band running northwest to southeast from the northwest of Western Australia through central Australia to the south coast. Nicholls (1989) showed that this pattern was related to the gradient in sea surface temperature (SST) between the central Indian Ocean and Indonesia. This anomaly pattern has been called the Indian Ocean Dipole. Drosdowsky (1993c) showed that the strongest precursor to this dipole pattern was found in the SSTa in the eastern Indian Ocean near the west coast of Australia during the preceding summer and autumn.

Large scale SSTa patterns have been shown to be related to seasonal rainfall anomalies in other

regions of the globe. Ward and Folland (1991) have linked rainfall anomalies in the Sahel and Northeast Brazil with large scale patterns of Pacific and Atlantic Ocean SST anomalies.

A major project is therefore underway within BMRC to systematically examine the potential of near global sea surface temperature anomaly (SSTa) patterns as predictors of Australian seasonal rainfall. This project involves three components; improved empirical seasonal predictions, GCM simulations of climate variations, and the impact of intraseasonal variability on seasonal prediction.

2. DATA

Three Australia-wide rainfall data sets, with different spatial and temporal resolution are being utilised.

1. Monthly district averages, as used by NCC. These are available from 1913 to the present for 107 districts of highly variable size covering the Australian continent. This data set was used by Nicholls (1989) and Drosdowsky (1993a).
2. A high quality station data set of approximately 400 stations, with daily and monthly data from 1910. This data set is intended primarily for climate change detection but is also suitable for climate variability studies.
3. A one degree grid of daily (from 1950) and monthly (from 1910) data. This is the major data set used currently. The rotated S-mode principal component analysis of Drosdowsky (1993a) has been repeated using this data set (but for a slightly longer period, 1950 to 1993). While the eight regions found earlier are broadly reproduced, the relative importance is altered, due to the uniform coverage of the grided data compared to the rainfall districts. In particular the centre of the first principal component shifts markedly northwards.

Two sea surface temperature data sets are used:
1. The UK Meteorological Office Global Ice and Sea Surface Temperature data set (GISST), from January 1949 to December 1991, and
2. The NMC/CAC optimum interpolation analysis from 1982 to the present.
Both these data sets have 1° x 1° spatial resolution.

3. SST VARIABILITY

Previous studies of the relationships between Australian rainfall and near-global SSTa (Nicholls 1989, Drosdowsky 1993a,b) had reduced the dimensionality of the rainfall data using principal component analysis, and searched for teleconnections using simultaneous and lagged linear correlations between the principal component time series and the SST. From these teleconnections a number of simple "box indices" similar to Nino1 to Nino4 have been identified as potential predictors, eg Nicholls (1984) North Australia/Indonesia Index and the Indian Ocean Index (Drosdowsky 1993c).
A more systematic approach to finding potential predictors in the SST data is to compute the principal components of the SSTa and the relate these to the rainfall.

The GISST data for the 43 years from 1950 to 1991 were averaged to a 6° by 6° degree grid, with 627 boxes covering the region from 60°N to 54°S and 30°E to 60°W used in the analysis. The analyses were performed using both monthly and seasonally (2 and 3 monthly) averaged data, and on each ocean basin separately as well as the entire domain.

For all three ocean areas, the spatial patterns (principal component loadings) produced by the monthly and seasonal data sets are virtually identical, as are the resulting principal component time series when the monthly series are averaged into the appropriate seasons.

Only the monthly sea surface temperatures are therefore used in the following analyses, since the seasonal values can be easily reproduced by averaging the appropriate monthly principal components.

Apart from the first component, the combined basins analysis, however is not simply the sum of the two separate analyses. The time series of the first component in all three ocean areas is significantly correlated with the SO, and the spatial patterns represent the mature phase of an El Nino / Southern Oscillation event.

In the combined analysis, the much greater number of grid points (and greater variability) of the Pacific

Ocean tends to dominate over the contribution from the Indian Ocean. The percentage of explained variance is very similar for the Pacific Ocean and combined basins, which is to be expected since the Pacific Ocean basin covers the majority of the combined oceans area. In each case the first principal component accounts for about 15% and the first 10 components about 42% of the variance. For the Indian Ocean the first component explains only 11% of the variance, however the first 10 account for 55% of the basin variance.

The dipole pattern, which is primarily a winter-time Indian Ocean phenomenon, is not a prominent feature of the all-months, combined oceans analysis. The principal component analysis was undertaken primarily for data reduction purposes and no rotation of the principal components was performed. A relatively large number of components (eleven for the combined ocean basins) were retained to ensure that the variance associated with the regional and seasonal patterns, such as the Indian Ocean dipole was retained.

4. RAINFALL PREDICTION

Initial hindcast experiments were performed using stepwise multiple linear regression, with the rainfall principal components as predictands The predictors were the principal component time series of the seasonal or monthly values of the Pacific Ocean, the Indian Ocean or the combined ocean analysis or the Southern Oscillation Index.

These regression forecasts were performed in order to determine which components contribute to the forecast skill. The significant components were found to vary from month to month, although all contributed at some time of the year.

Although reasonable predictions were obtained using this regression method its applicability to operational forecasting is limited since it is in terms of categorical values for the rainfall principal components and does not easily give error or probability estimates. For this reason linear discriminant analysis has used. Monthly or seasonal rainfall totals have been classified into either three (terciles) or five (quintile) categories. A discriminant analysis, with the classes calculated separately was performed for each grid point.

The forecasts have been carried out for one, two or three month rainfalls, using one or two months SSTa, with a lead time of zero or one month. The predictors have been the principal components of the three oceans areas and the SOI. Most of the hindcasts are performed using a training period of 31 years from 1950 to 1980 and an 11 year test period from 1982 to 1991.

Overall the results show significant increase in skill of the SSTa over the SOI used alone, although this may be offset slightly if we make use of the longer time series of the SOI. In particular the SSTa show much higher skill through the so-called "predictability barrier" in late summer - early autumn. Not unexpectedly, there is more skill in predicting on a coarser grid (smaller number of larger grid boxes), and in forecasting only three rainfall categories rather than five.

All three oceans basins perform equally well, suggesting that most of the variance is common to both the Indian and Pacific basins, although there may be regional variations in skill.

5. INTRA-SEASONAL VARIABILITY

Much of Australia lies in the tropics and is potentially influenced by the tropical intra-seasonal oscillation. The extent to which this signal can be detected, both in the extreme north and its southern limits have not been extensively documented. More generally, the relationship between intraseasonal variability and seasonal rainfall anomalies has not been explored, either in Australia or elsewhere around the globe.

Principal component analyses of 43 years of one degree grided pentad (five day) rainfall totals over the Australian continent have been performed. A Varimax rotated S-mode analysis of standardised anomalies produced a very similar regionalisation of the Australian continent to that reported (using a different, seasonal district average data set) in Drosdowsky (1993a). For those pentad components which most closely resembled the seasonal patterns, the resulting pentad time series, when averaged into seasonal values, where also highly correlated with the seasonal values. A much closer fit between the pentad and seasonal principal components is found when the grided seasonal rainfall is used.

Examination of the pentad time series through a number of individual seasons suggest that the seasonal anomaly is generally the result of a small number of significant pentads, rather than a uniform departure over the entire season. Further research is needed to determine whether large positive (negative) seasonal rainfall anomalies are the result of a greater (fewer) number or more (less) intense intraseasonal rainfall events.

A second aspect of intraseasonal variability that is being examined is the onset or commencement of a seasonal rainy period. In the north of Australia this is related to the onset of the Australian summer monsoon. In contrast the southern and western parts of the continent have a "Mediterranean" climate with dry summers and cool wet winters. While the onset of the monsoon is related to the SO in the prior season, predictors of the timing of the first significant autumn and winter rainfall over southern Australia have not yet been found.

6. DISCUSSION

The work carried out to date has raised a number of questions concerning the basic assumptions and the application of SSTa patterns as predictors in a practical, operational seasonal forecasting system.

1. Are principal components (or any other eigenfunctions) the best way of representing the SSTa patterns? Some recent research suggests that it is necessary to perform combined analysis of the predictor and predictand fields together using, for example canonical correlation or singular value decomposition to accurately capture the inter-relationships. Alternatively can we simply use the simple "box indices" such as Nino3 or the Indian Ocean Index (Drosdowsky 1993c), which can be shown to produce skilful forecasts.

2. The expectation of most users of seasonal predictions is for forecasts expressed in probabilistic terms. Is Linear Discriminant Analysis the most appropriate forecasting methodology? Discriminant analysis assumes the data can be divided into classes based on the classification variable. This requires prior knowledge of the number of classes and estimates of the class properties.

3. How should probability forecasts for a large number of spatial points be verified, and the optimal spatial resolution determined. This verification has been carried out on a point-by-point basis, using the LEPS (linear error in probability space, Ward and Folland 1991) technique, and then averaged over the spatial domain. Should we instead employ some form of pattern correlation, ie can we expect to be able to forecast with some skill at every spatial point, or are we restricted to the overall spatial pattern.

References

Drosdowsky, W., 1993a: An analysis of Australian seasonal rainfall anomalies: 1950-1987. I: Spatial patterns. ***Intl. J. Climatol.,*** **13,** 1-30.

Drosdowsky, W., 1993b: An analysis of Australian seasonal rainfall anomalies: 1950-1987. II: Temporal variability and teleconnection patterns. ***Intl. J. Climatol.,*** **13,** 111-149.

Drosdowsky, W., 1993c: Potential predictability of winter rainfall over southern and eastern Australia using Indian Ocean sea surface temperature anomalies. ***Aust. Meteor. Mag.,*** **43,** 1-6.

Drosdowsky, W., 1994: Analogue (non-linear) forecasts of the Southern Oscillation Index time series. ***Wea and Forec, 9,*** 78-84.

McBride, J.L. and Nicholls, N., 1983: Seasonal relationships between Australian rainfall and the Southern Oscillation. *Mon. Weath. Rev.,* 111, 1998-2004.

Nicholls, N., 1984: The Southern Oscillation and Indonesian Sea surface temperature. *Mon. Wea.Rev.,* 112, 424-432.

Nicholls, N., 1989: Sea surface temperatures and Australian winter rainfall. *Jnl Climate.,* 2, 965-973.

Stone, R.C., (1992): SOI phase relationships with rainfall in Australia. *Ph.D. Thesis, The University of Queensland, St, Lucia, Queensland.*

Ward, N.M., and C.K. Folland, 1991: Prediction of seasonal rainfall in the north Nordeste of Brazil using eigenvectors of sea surface temperature. ***Intl. J. Climatol.,*** **11,** 711-743.

Zhang, X.-G., and T.M. Casey, 1992: Long-term variations in the Southern Oscillation and relationships with Australian rainfall. *Aust. Meteor. Mag.,***40,** 211-225.

CORRESPONDING AUTHOR
Wasyl Drosdowsky,
Bureau of Meteorology Research Centre
PO Box 1289K,
Melbourne, 3001
AUSTRALIA

SEASONAL FORECASTING OF TROPICAL RAINFALL

M Neil Ward, Charles Mutai[1], Ishiaku Mohammed[2], Andrew W Colman

Hadley Centre for Climate Prediction and Research, UK Meteorological Office. [1] Drought Monitoring Centre, Nairobi, Kenya. [2] African Centre of Meteorological Applications for Development, Niamey, Niger.

INTRODUCTION: Seasonal forecasting for some tropical regions is now a reality. It is based mainly on statistical and numerical modelling of the impact of sea-surface temperature (SST) anomalies on the tropical atmosphere. Seasonal forecasting is advancing through the efforts of a number of research groups and climate centres. In 1986, the UK Meteorological Office made its first experimental forecast of seasonal rainfall for the Sahel. Since then, forecasts have been made each year for the Sahel, and the effort has been expanded to include NE Brazil (since 1987), other regions of West Africa (since 1992) and East Africa (1994). This paper reports on recent developments of this work, which have involved collaboration with ACMAD and the Nairobi DMC (see author affiliations).

DATA: Rainfall data in this study were provided by Hulme (1992, personal communication) who has interpolated monthly station values to a regular 2.5°lat x 3.75°long grid. Then, area-average rainfall indices were created by averaging standardised grid-box values. Some of the areas and series used are in Figs. 1 and 2. SST data were taken from the Meteorological Office Historical SST dataset (MOHSST) version 4 (Bottomley et al., 1990). SST anomalies were averaged to create a 10°lat x 10°long SST anomaly dataset (described in Ward and Folland, 1991).

FORECAST METHODOLOGY: Statistical analysis and general circulation model (GCM) simulations support the contention that seasonal rainfall totals in some tropical regions are strongly determined by SST anomaly patterns (e.g. see Rowell et al., 1995). Persistence of SST anomalies over a few months is often sufficient to bring a degree of predictability to seasonal rainfall totals. Forecasts can be made using atmospheric GCMs forced with the SST anomalies observed prior to the rainy season (Ward et al., 1993), but in this paper, simple statistical methods are discussed. It can be useful to represent some of the principal SST anomaly patterns in the form of Empirical Orthogonal Functions (EOFs). The global covariance SST EOF analysis of Folland et al. (1991) yielded three patterns that are related to tropical rainfall in many regions: EOF2, which represents ENSO; EOF3, which represents interhemispheric contrast in SST anomalies; Rotated EOF2 (REOF2), which mainly represents variability in the tropical South Atlantic, but also has some weight in the tropical North Atlantic and Indian Oceans (See Fig. 3).

To create a statistical forecast system, one must first identify which SST anomaly patterns are statistically related to the rainfall in the forecast region. Then, a forecast model is made by relating the seasonal rainfall index (Fig. 2) to SST EOF time-coefficients measured before the rainfall season. Discriminant Analysis is used to forecast the probability of rainfall ranges (Ward and Folland, 1991). A simpler approach (Hastenrath et al., 1984) is to construct a multiple regression that predicts the value of the rainfall index from the pre-rainfall season values of the EOF time-coefficients.

FORECAST REGIONS IN JULY-SEPTEMBER (JAS): The Sahel rainy season is concentrated in JAS, when the ITCZ reaches its most northerly location. During these months, the Guinea Coast region to the south usually experiences its "Little Dry Season". However, in some years, the rains continue through JAS on the Guinea Coast, while the rains are deficient further north in the Sahel. This pattern is strongly correlated with Equatorial and South Atlantic SST, represented by REOF2 in Fig. 4. The Equatorial and South Atlantic SST anomalies in May-June provide very skilful forecasts of the JAS Guinea Coast rainfall, explaining some 50% of interannual variance (i.e. multiple regression predictions correlate at about 0.7 with the observed rainfall index). For the Sahel, EOF2 and EOF3 are also used in the forecast model (Ward et al., 1993). The Soudan region has a forecast model similar to the Sahel, but with little weight given to REOF2, since the Soudan region is a transition between positive correlations with REOF2 on the Guinea Coast and negative correlations further north (Fig. 4).

FORECAST REGIONS IN OCTOBER-DECEMBER (OND): The Guinea Coast and East African regions receive most rain in the transition seasons. The OND rains show some predictability in both regions. Note that in the transition seasons, Guinea Coast rainfall shows a decline in rainfall similar in shape to the Sahel region in JAS (Fig. 2). Potentially useful predictability is found for the Guinea Coast from regression models which combine REOF2 in September (now a negative correlation with OND Guinea Coast rainfall) with specific SST measures in the tropical North Atlantic SST in September.

For East Africa, REOF2 is combined with REOF4 and REOF5, both of which represent different

aspects of Pacific SST variability. The regression model performs well on historical data 1945-1988 (Fig. 5). Note that the model is trained on one half of the data and tested on the remaining half, to reduce the danger of inflating skill through over-fitting.

ISSUED FORECASTS: The history of the UK Met. Office experimental seasonal forecasts for the Sahel and NE Brazil is summarised in Fig. 6. The forecasts shown were made and issued about one month before the rainy season, though the policy now is also to make an updated forecast using the latest available SST information as the season starts. The forecasts are expressed in terms of five rainfall categories, which are climatologically equally likely to occur (i.e. they are quints). The issued forecast shown in Fig. 6 is a subjective combination of all information available to the forecasters. In some years, numerical model information was available, but the forecasts mostly reflect the input of statistical models.

The Northeast Brazil rainy season is March-May. Forecasts are made using a combination of Atlantic and Pacific SST (Ward and Folland, 1991). The issued forecasts show extremely good skill (Fig. 6a). The NE Brazil series contains no multi-decadal variability, which makes identification of stable forecast relationships easier. The JAS Guinea Coast series also has little multi-decadal variability, and has a stable statistical relationship with SST, so the real-time forecasts can be expected to have clear skill over a long period. The Sahel region (and Soudan region, not discussed in this short paper) are more problematical because of the strong multi-decadal component in their rainfall series. It may be necessary to continually refer the forecast to recent climatologies, and monitor rather than forecast the multi-decadal component of the series. Nonetheless, for the Sahel, the correct quint has been forecast 50% of the time (Fig. 6b), but there have also been some seriously misleading forecasts. The forecast failure in 1988 also highlights the need for SST prediction, since a strong La Nina developed in the Pacific after the forecast was issued, and this probably led to the enhanced rainfall in 1988 (Palmer et al., 1992; Rowel et al., 1995; Ward et al., 1993). Indeed, lead-times beyond a few months require the use of numerical (or statistical) models to predict the evolution of the coupled ocean-atmosphere system (Cane et al., 1986).

The UK Met. Office forecasts are made available to National Met. Services and regional climate centres (like the DMCs and ACMAD) who combine the information with other forecasts made around the world, to provide advice to users such as aid agencies and the agricultural sector. The development of rational strategies to make best use of the new information is an important challenge.

References

Bottomley, M., Folland, C.K., Hsiung, J., Newell, R.E., and Parker D.E., 1990: Global ocean surface temperature atlas (GOSTA). Joint Meteorological Office/Massachusetts Institute of Technology Project. Project supported by US Dept. of Energy, US National Science Foundation and US Office of Naval Research. Publication funded by UK Depts. of Energy and Environment. pp20 and 313 Plates. HMSO, London.

Cane, M.A., Dolan, S.C., and Zebiak, S.E., 1986: Experimental forecasts of El Nino. Nature, 321, 827-832.

Folland, C.K., Owen, J.A., Ward, M.N., and Colman, A.W., 1991: Prediction of seasonal rainfall in the Sahel region of Africa using empirical and dynamical methods. J. Forecasting, 10, 21-56.

Hastenrath, S., Wu, M.-C and Chu, P.-S., 1984: Towards the monitoring and prediction of north-east Brazil droughts. Quart. J. Roy. Met. Soc., 110, 411-425.

Hulme, M., 1992: A 1951-80 global land precipitation climatology for the evaluation of general circulation models. Climate Dyn., 7, 57-72.

Nicholson, S.E., 1985: Sub-Saharan rainfall 1981-84. J. Climate Appl. Meteor., 24, 1388-1391.

Palmer, T.N., Brankovic, C., Viterbo, P., and Miller, M.J., 1992: Modeling interannual variations of summer monsoons. J. Climate, 5, 399-417.

Rowell, D.P., Folland, C.K., Maskell, K., and Ward, M.N., 1994: Variability of summer rainfall over tropical North Africa, 1906-92: Observations and modelling. Quart. J. Roy. Met. Soc., 121, 669-704.

Ward, M.N., and Folland, C.K., 1991: Prediction of seasonal rainfall in the North Nordeste of Brazil using eigenvectors of sea-surface temperature. Int. J. Climatol., 11, 711-743.

Ward, M.N., Folland, C.K., Maskell, K., Colman, A.W., Rowell, D.P, and Lane, K.B., 1993: Experimental seasonal forecasting of tropical rainfall at the U.K. Meteorological Office. In Prediction of interannual climate variations (Ed J. Shukla), 197-216. Springer-Verlag, Berlin.

ACKNOWLEDGEMENTS

The authors thank Mr Chris Folland and Dr Mike Davey for their contribution to the forecasts and forecast methods.

CORRESPONDING AUTHOR (Current Address): Dr M Neil Ward, IMGA-CNR, Via Emilia Est 770, 41100 Modena, Italy. Permanent e-mail: mnward@meto.govt.uk.

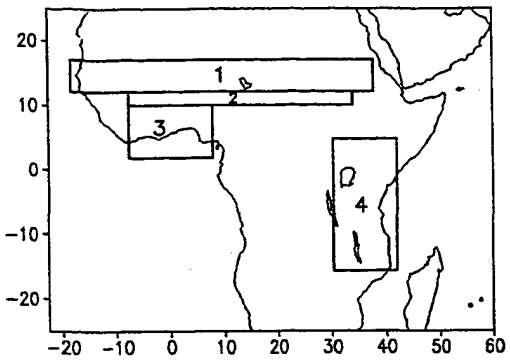


FIG. 1. Relatively homogeneous rainfall regions used for analysis and prediction: 1=Sahel, 2=Soudan, 3=Guinea Coast, 4=East Africa. The Sahel region approximately covers the same region used by Nicholson (1985) as the Sahel.

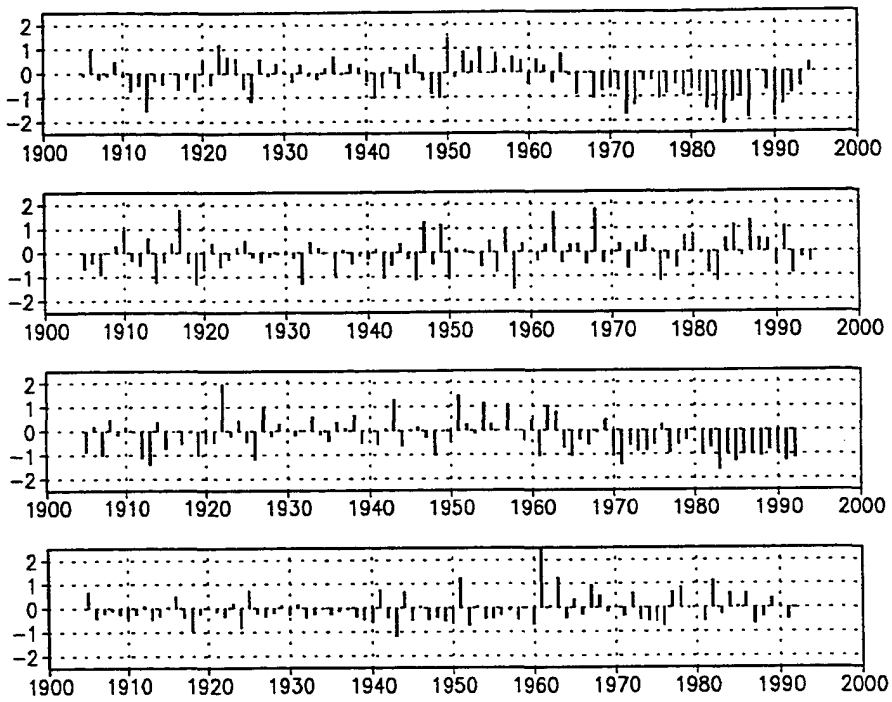


FIG. 2. Standardised rainfall anomaly indices for (a) Sahel in JAS, (b) Guinea Coast in JAS, (c) Guinea Coast in OND, (d) East Africa in OND.

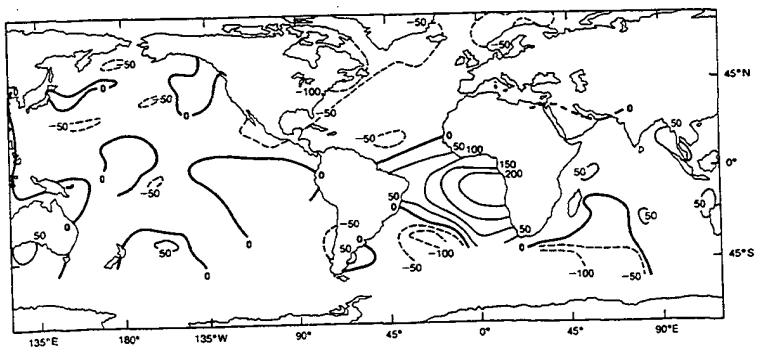


FIG. 3. Global Covariance SST anomaly EOF mainly representing variability in the Equatorial and tropical South Atlantic. The pattern was derived by rotating global EOFs 4-13. This is the second of these rotated EOFs.

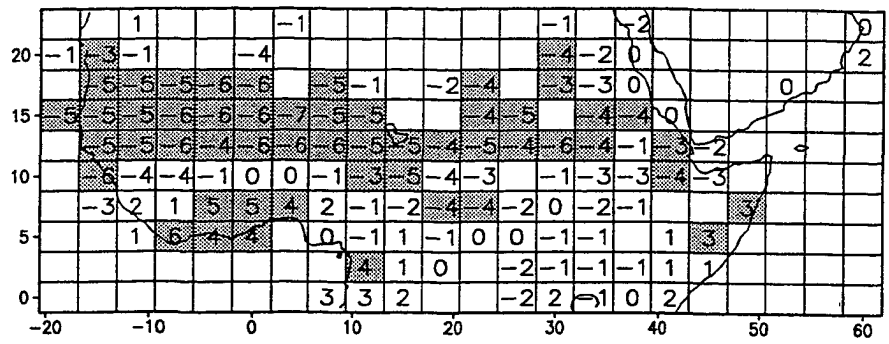


FIG. 4. Correlation (in tenths) between the JAS time-coefficients of SST REOF2 and JAS rainfall in each grid-box (1946-88). Shaded values are statistically significant at the 5% level (allowing for the reduction of degrees of freedom due to serial correlation in the series).

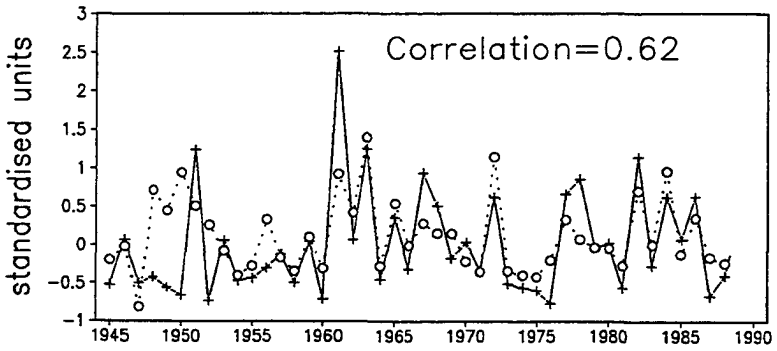


FIG. 5. Forecasting East African OND rainfall. The forecasts (dashed line with circles) for 1945-1966 are from a regression model trained on the 1967-88 period; forecasts for 1967-88 are from a model trained on 1945-66. The predictors are September values of REOF2 and REOF4, and JAS values of REOF5.

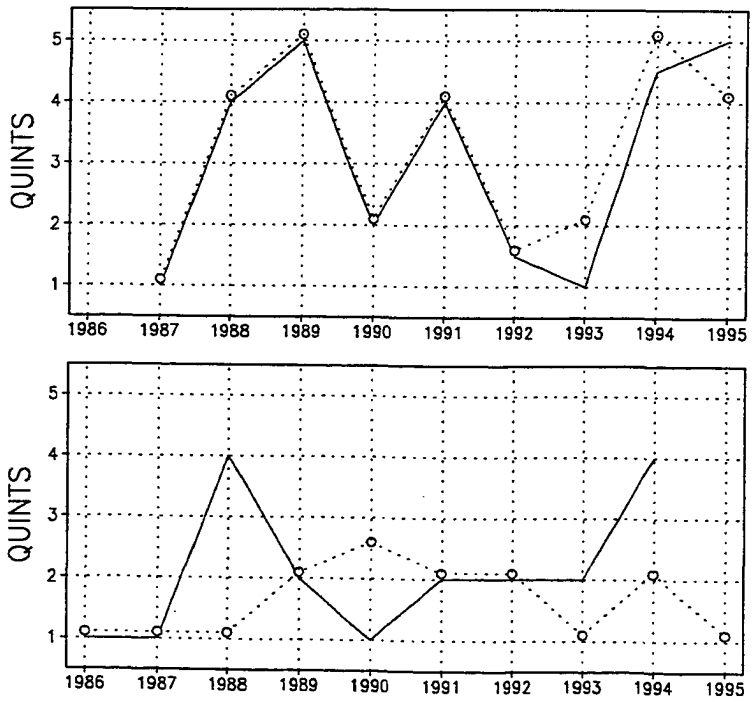


FIG. 6. Issued experimental forecasts for (a) NE Brazil, (b) Sahel region as defined by Nicholson (1985). Observed (solid) and Forecast (dashed with circles). The forecast line is raised slightly to distinguish it from the observed line. These forecasts were made and issued about one month before the main rainy season. Quint 1 = Very Dry, Quint 5 = Very Wet.

DOWNSCALING OF LARGE-SCALE GCM OUTPUT TO REGIONAL RAINFALL IN AUSTRALIA USING WEATHER STATE CLASSIFICATION BY RECURSIVE PARTITIONING

Reiner Schnur and Dennis P. Lettenmaier

Dept. of Civil Engineering, University of Washington, Seattle, USA

ABSTRACT

Due to their coarse resolution General Circulation Models (GCMs) lack the ability to reliably predict effects of increased greenhouse gas concentrations on surface parameters on a regional scale. In this paper, a semi-empirical downscaling method is applied to project large-scale GCM output to daily precipitation in different regions of Australia.

It is shown that the effects of a 2xCO2 signal in an equilibrium GCM run on local rainfall is not dramatic. There is an indication of more rainy days and a decrease of the length of dry periods in Southwest Australia in the winter season for a transient climate change experiment where the CO2 concentrations are increased gradually. The simulated rainfall sequences are more sensitive for dry regions and seasons.

1 INTRODUCTION

Output from current large-scale general circulation models (GCMs) cannot be used directly as boundary conditions for climate impact models on the regional/local scale due to the lack of spatial detail in GCMs and the need for parameterizations of small scale physics. During the last decade significant interest from scientists, politicians and the public has evolved in such regional impact studies because of the effects possible climatic changes, e.g. of the hydrological cycle, can have on society (Rind et al., 1992).

In particular, precipitation is important as a forcing variable for many impact models in hydrology and agriculture/ecology but is not well represented in GCMs on a regional scale. To evaluate the performance of newer, higher-resolution GCMs in this respect the simulated precipitation of a T106 (~ 1° resolution) GCM is compared to observations and a T21 GCM (~ 5° resolution, which is the resolution for which long-term climate experiment runs are available nowadays). The higher resolution maps necessarily include more detail than those for the T21 model but still show significant differences on the regional scale to the observations.

One possible way out of this dilemma is to use the fact that GCMs do reliably simulate large-scale features of the atmosphere (e.g. Hadley cell, storm tracks, jet streams) for variables like pressure, temperature or winds. In this paper we use this information to "downscale" GCM output to regional daily rainfall sequences in Australia after empirically establishing a relationship between the large and the small scale parameters using historical data (see e.g. Giorgi and Mearns, 1991 for a review of dynamical and statistical downscaling methods). Australia has been chosen as study region since it is characterized by several distinct climate regions which allows the evaluation of the method in different climate regimes. Because of the large arid regions in Australia the performance of any downscaling method for dry regimes is especially crucial for regional hydrologic impact studies.

2 METHOD

Classifying large-scale free-atmosphere variables into typical circulation patterns (CPs) and building a statistical model of precipitation conditional on these CPs has been used in several previous studies (e.g. Bardossy and Plate, 1992). The main difference between these studies have been the way how the classification is carried out (e.g. objectively or subjectively) and how the conditional statistical model for the local surface variable is built.

The method of recursive partitioning (or Classification and Regression Analysis, see Breiman et al., 1984, Hughes et al., 1993) discussed in this paper consists of classifying in an objective way the observed large-scale atmospheric circulation (measured here in terms of sea level pressure, after retaining the first few Empirical Orthogonal Function coefficients) into different weather types. This is done in such a way that each

weather state is most strongly connected to a certain state of the concurrent daily precipitation occurrences at multiple stations so that the joint rainfall distribution functions for each weather state are optimally separated in a certain sense. Having established this relationship from observed data the joint distributions of rainfall amounts for each weather state define a stochastic model of precipitation amounts at several stations conditional on each weather state (weather generator). This model can then be applied in any (GCM) climate to simulate local precipitation.

3 RESULTS

Results are discussed for both the verification of the weather generator and its application to different scenario runs of the Hamburg MPI GCM. The variables which are especially of interest both for verification and for application in hydrological impact models are rainfall occurrences (wet/dry), the distribution of storm interarrival times and rainfall amounts including their spatial correlations.

The method outlined above has been applied to different regions in Australia, and for the winter and summer seasons separately. The statistical model has been trained by using observed SLP analyses and station precipitation records from 1972-89. However, in several cases, the procedure was not able to classify the SLP fields into circulation patterns which are connected to different rainfall patterns. This problem occurred e.g. for the Southwest of Australia in summer and for the North in winter when very dry conditions are prevalent.

For the verification of the model station rainfall has been simulated using SLP analyses from a different source and for the years 1957-77. Mean daily rainfall, mean intensities and probabilities of precipitation are fairly well simulated whereas the distribution of the length of dry periods is sometimes underestimated. Also, the spatial correlation structure for rainfall between the stations is reproduced very well which is important if the generated data are to be used in a regional hydrologic model.

The comparison of the downscaled rainfall sequences using SLP from the control and 2xCO2 equilibrium runs of the Hamburg GCM show, in general, no significant change due to doubling CO2.

The downscaling procedure was also applied to decades 1, 5 and 8 of the Hamburg GCM transient 100-year run (decade 5 corresponds to 2xCO2). In general, there were no significant changes in the means of the resulting rainfall simulations between decade 1 and decade 5 and 8. For the Southwest of Australia in winter the probability of precipitation increased (95% significant), whereas the length of dry periods decreased.

When impact modelers use downscaled data they also need to know the connected uncertainties since these have to be compared to their model sensitivities. Therefore, 25 Monte Carlo simulations of daily rainfall have been performed. Twice the standard deviations of mean daily rainfall, mean intensities and probabilities of precipitation are generally less than 10% of the values, except for very dry stations where the uncertainty is greater.

4 Discussion

It has been shown that even the most recent higher resolution GCMs are unable to correctly simulate regional precipitation in Australia. An objective classification technique has been used to downscale the more reliable large-scale output of a GCM to daily rainfall sequences at multiple stations in Australia. The method is only successful when there is a strong relationship between different circulation patterns and rainfall occurrence patterns (e.g. summer monsoons in North Australia). In particular, this is a problem in very dry climate regimes (e.g. North Australia in winter). Also, for region/seasons where the method can be applied successfully the results are more sensitive for dry stations. Because the effect of climate change on precipitation in dry regions is important for water resource planning this problem of dealing with dry climate regimes has to be further investigated.

Another problem is the bias of the control runs of current GCMs compared to observations. Consequently, the differences for downscaled rainfall between 1xCO2 and observations are often larger than the differences between 1xCO2 and 2xCO2. This makes it difficult to derive with some confidence realistic projections of regional parameters in a changed climate to be used in desicion making and risk assessment.

References

Bardossy, A., and E. J. Plate, 1992, "Space-time model for daily rainfall using atmospheric circulation patterns", Water Resour. Res., 28(5), pp. 1247-1259.

Breiman, L., J. H. Friedman, A. Olshen, and J. C. Stone, 1984, "Classification and Regression Trees", Wadsworth and Brooks, Monterey, Calif.

Giorgi, F., and L. O. Mearns, 1991, "Approaches to the simulation of regional climate change: a review", Rev. Geophys., 29(2), pp. 191-216.

Hughes, J. P., D. P. Lettenmaier, and P. Guttorp, 1993, "A Stochastic Approach for Assessing the Effect of Changes in Synoptic Circulation Patterns

on Gauge Precipitation", Water Resours. Res., 29(10), pp. 3303-3315.
Rind, D., C. Rosenzweig, and R. Goldberg, 1992, "Modeling the hydrological cycle in assessment of climate change", Nature 358, pp. 119-122.

Corresponding author
Reiner Schnur
Dept. of Civil Engineering, Univ. of Washington
170 Wilcox Hall, FX-10
Seattle, WA, 98195, USA
phone: +1 206 543 5454 fax: +1 206 685 3836
e-mail: reiner@ce.washington.edu

NOTE

Statistical downscaling of monthly mean North Atlantic air-pressure to sea level anomalies in the Baltic Sea

Hauke Heyen
Max-Planck-Institut
für Meteorologie
Hamburg

Eduardo Zorita
LODYC, Université
Pierre et Marie Curie
Paris

Hans von Storch
Max-Planck-Institut
für Meteorologie
Hamburg

Abstract

A relationship between the North Atlantic air-pressure at sea-level and the anomalies of sea level at several Baltic gauges is identified. Monthly means from twenty observed winters are used to fit a statistical model and further observations from this century are used to validate it. The model is able to estimate sea level anomalies from the air-pressure field to a good level of approximation. As main forcing for the sea level anomalies, zonal wind-stress is identified. For the past 89 years, we found that a slight decrease of sea level anomalies was induced by air-pressure. A slight increase is found when air-pressure from a GCM-"greenhouse"-experiment is downscaled.

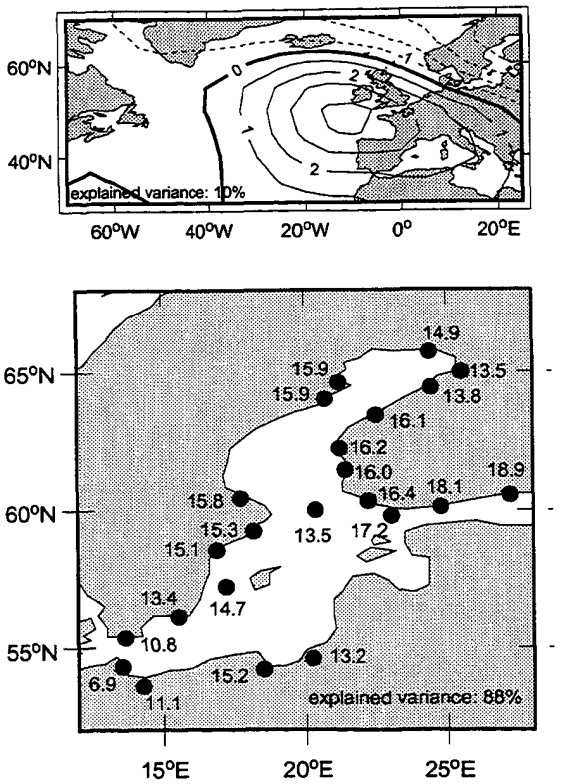


Figure 1: The 1st pair of CCA-patterns. Numbers depict typical anomalies in hPa and cm.

1 Introduction

General Circulation Models (GCMs) are a powerful tool in studies of the global climate. While they are able to reproduce "large-scale" climate features to a good level of approximation ("large-scale" refers to processes with a characteristic length scale of several grid lenghts) values at single grid points are questionable and should not be interpolated to derive information about processes on smaller scales. Thus LAM-"nesting", analogue models or statistical techniques are needed to relate large-scale information to small-scale one.

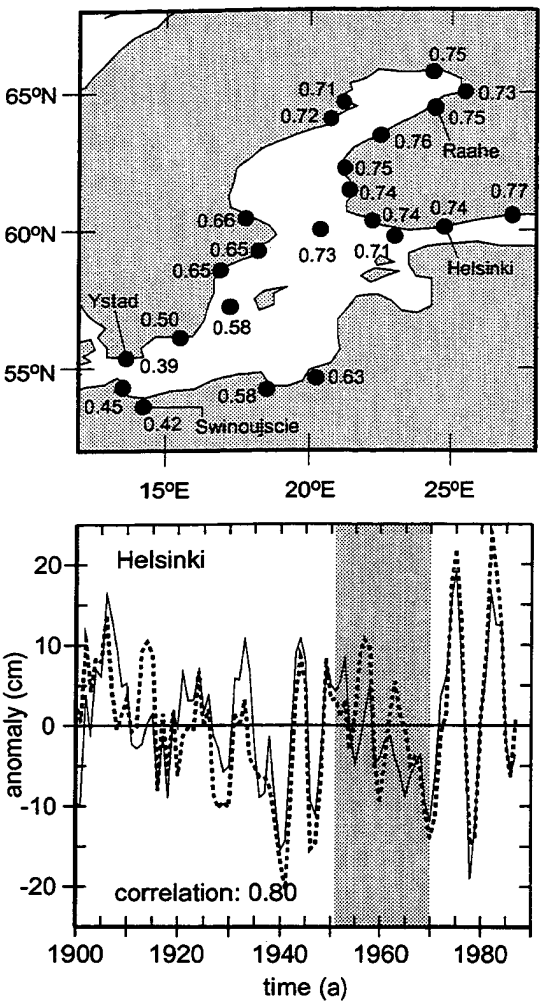


Figure 2: Local correlation between observations and estimates (top). Below, estimates (solid) and observations (dashed) at Helsinki (3-yr running mean). The fitting period is hatched.

2 The statistical model

We use the same approach as von Storch et al.(1993) or Cui et al.(1995). The steps are:

1. Identify a large-scale parameter G which controls the local parameter L by $L = \mathrm{f}(G, \vec{\alpha})$, where $\vec{\alpha}$ is an unknown stochastical vector. If the intent is to calculate L for climate experiments, G should be simulated well by climate models.
2. Use observations to fit $\vec{\alpha}$ such that $||L - \mathrm{f}(G, \vec{\alpha})|| = \min$
3. Validate the relationship with independent data.
4. If the relationship is confirmed, G can be derived from GCM-experiments to estimate L.

3 The datasets

In the present paper we used winter data from the months December to February. The analysis could, of course, also be done for other seasons.

Baltic Sea sea level data: We used the BODC dataset and selected 23 stations which reported between 1899 and 1987.

Sea-level air-pressure data: We utilized data from NMC/NCAR. We interpolated it on a 5° by 5° grid and selected a box within 70°W to 25°E and 30°N to 70°N.
As climate experiment we choose the "early industrial" 150-year integration carried out by Cubasch et al.(1995) with a global coupled ocean-atmosphere model (ECHAM1/LSG). The first 50 years of this experiment were forced with observed atmospheric CO_2-concentrations from 1935 to 1985, afterwards a continous yearly CO_2-increase of about 1.3% was assumed.

4 Fit and validation of the statistical model

4.1 Correlation between sea level and air-pressure

In a first step we search the *main modes of variability* of sea level and pressure, since we do not expect to find a relationship between all details of both parameters. Thereafter we conduct a Canonical Correlation Analysis (CCA) for these main modes. We find a leading pair of patterns (Figure 1) with time series that are correlated with 0.8. The sea level pattern

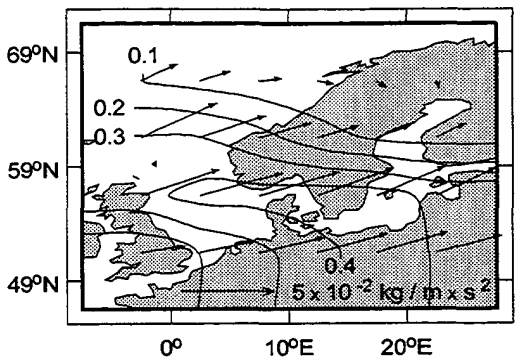


Figure 3: Vectors indicate wind-stress that is associated with the leading sea level CCA-pattern. Isolines depict the explained variance of the wind-stress

describes a simultaneously rise of all Baltic gauges and explains 90% of the total sea level variance.

4.2 Validating the relationship with observational data

To validate the obtained relationship we estimate sea level anomalies for the periode 1899 to 1987 and compare it with the observations (Figure 2).

We find that the estimated anomalies generally have the correct sign. In addition, they contain variations on the decadal time scale that are in good correspondance with the observations. This is not self-evident, since our model was fitted with 20 years of detrended data and thus is familiar with monthly and yearly variations only. That it produces decadal variations though, makes it probable that it may guess trends in sea level in a realistic manner, too - e.g. when we downscale climate experiment data.
The decreasing local correlations between estimated and observed values for stations situated in the southwest may be due to a more complex behaviour of sea level there: In this region in- and outflow situations lead to high velocities and strong haline gradients. This results in a more complex behaviour of the gauges situated there, that is not represented within the selected signal-subspace.

When not-detrended air-pressure is downscaled, a slight mean decrease for the estimated sea level is found (Figure 4). Its magnitude is about -.05 cm/yr between 1899 and 1987, thus it is certainly much smaller than sea level trends induced by iso- and eustacy.

5 Links between air-pressure and sea level

We found that large-scale air-pressure and local sea level are related *statistically*, but what is the *physical* reason for this relationship? Since the air-pressure field contains indirect information about precipitation, wind-stress etc., too, it is not clear which parameter really forces the sea level variations. To separate the more important forcing-parameters from those that are less important we take possible parameters and calculate that portion of their variance that is correlated with 1. to the variance of the sea level. If that portion is high, that parameter is presumably an important forcing for sea level.
We find that (for winter monthly means) zonal wind-stress forces the first Baltic Sea CCA-pattern (Figure 3: 40% of wind-stress variance in the transition area is correlated with 1. to 90% of sea level variance). This forcing might be directly, by pushing water into the Skagerrak, or indirectly, by piling up water in the German Bight. Both effects promote inflow into the Baltic Sea or suppress outflow and thus change the entire water volume of the Baltic Sea.

6 Downscaling GCM-data

When air-pressure data from a climate experiment is downscaled, we find that

- the air-pressure induced sea level anomalies show no further decrease, but seem to increase, especially for the later years of the GCM-experiment. Over the 150 years of the experiment we have a total increase of about 0.01 cm/yr.

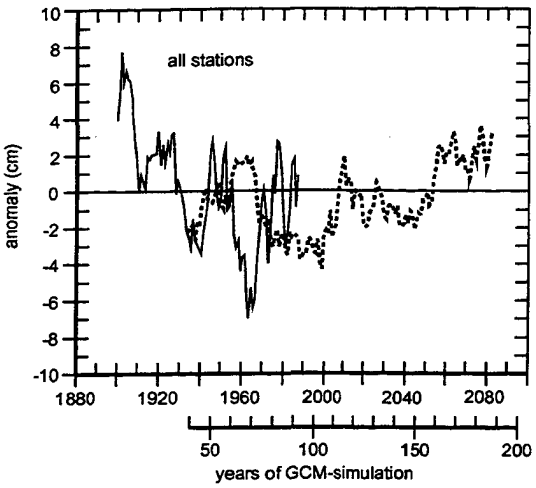


Figure 4: Mean sea level, downscaled from air-pressure observations (solid) and GCM-air-pressure (dashed).

- the variance of the guessed anomalies is smaller than that of the observed anomalies or that of the anomalies downscaled from air-pressure observations.

The loss of variance can be explained partly by a lower variance of GCM-pressure itself, and partly due to flawy modelation of location and intensity of main air-pressure signals. Nevertheless the GCM is able to reproduce the main modes of variability to a good degree of approximation and we believe it to be trustworthy. The most important result is therefore the slight increase of sea level in the long-term mean (Figure 4). Though this increase has a small magnitude, it has an opposite sign then in the observations from this century and might become important in that region, where iso- and eustacy cancel each other.

7 Acknowledgements

The idea for this work originates from a fruitful communication between Hans von Storch and Jan Backhaus (Institut für Meereskunde, Universität Hamburg). Financial support was provided by the European Community through project EV5V-CT91-0051. For the informative figures we like to thank Marion Grunert (Max-Planck-Institut für Meteorologie).
A more complete desription of this work was submitted to Tellus.

References

Cubasch, U., Hegerl, G., Hellbach, A., Höck, H., Mikolajewicz, U., Santer, B.D. and Voss, R., 1995. A climate change simulation starting at an early time of industrialization. Clim.Dyn., in press

Cui, M., von Storch, H. and Zorita, E., 1995. Coastal sea level and the large-scale climate state: a downscaling exercise for the Japanese Islands. Tellus, **47A**, 132-144

von Storch, H., Zorita, E. and Cubasch, U., 1993. Downscaling of global climate change estimates to regional scales: an application to Iberian rainfall in Wintertime. J.Climate,**6**, 1161-1171.

Corresponding Author Hauke Heyen, Max-Planck-Institut für Meteorologie, Bundesstraße 55, D-20146 Hamburg, internet: heyen@dkrz.d400.de

A SPACE-TIME DOWNSCALING APPROACH IN TERMS OF PATTERNS RECOGNITION AND STOCHASTIC GENERATION

XIA Jun

Faculty of Hydrology, Department of River Engineering, Wuhan University of Hydraulic & Electric Engineering, Wuhan, 430072, China

ABSTRACT

This paper addresses the problem of weather generation. A space-time downscaling approach in terms of patterns recognition, grey clustering and stochastic generation was developed for the weather variables such as air temperature and precipitation. The method described in this paper were preliminary verified for rainfall data set in Shun Tian ctchment. It was found that the proposed method can yield a good simulation and provide an uncertainty information for both temporal and spatial scale in the downscaling from GCMs to hydrological models

1. INTRODUCTION

The weather generator involves the collection of algorithms and methods for the generation, downscaling, and interpolation of appropriate climatic variables from GCMs to ecological and hydrological models. The weather generator method developed in this paper is one of stochastic analysis in terms of pattern recognition and clustering . Main ideas involves three-folds: (a) Feature information extraction of climate variables, where weather patterns were expanded by the Karhunen- Loeve (K-L) orthogonal functions; (b) Grey associative clustering of the feature vectors. The measurement of patterns similarity is represented by the grey associative degree rjo; (c) Stochastic weather generation in terms of the Monte Carlo simulation, which provide temporal and spatial downscaling information in terms of weather patterns recognition and clustering.

2. FEATURE INFORMATION EXTRACTION OF WEATHER PATTERNS

The pattern recognition is a new technique which was used to extract the feature information of studied processes and make classification (Tou and Gonzaleg, 1974). As far as weather process is concerned, their distribution in temporal and spatial scale, such as precipitation and air temperature in each year, can be defined as a pattern. Let the monthly or daily weather variable amount at time t and point s as x(s,t). The discrete time series with m patterns are expressed as

$$X_{m\times n}=\begin{pmatrix} x(s_1,t_1) & \cdots & x(s_1,t_n) \\ \vdots & \ddots & \vdots \\ x(s_m,t_1) & \cdots & x(s_m,t_n) \end{pmatrix} \qquad (1)$$

Generally, { x(s,t) } can be taken as a stochastic weather process due to climate uncertainty. To extract main information from weather patterns and variables, a pattern recognition method in terms of the Karhunen-Loeve(K-L) orthogonal expansion was developed, which is not required any priori hypothesis about pattern's stochastic distribution. The arbitrary weather processes might be expanded by the K-L orthogonal function series:

$$x(s,t)=\sum_{l=1}^{L} a_l(t)q_l(s) \qquad (2)$$

where a_l (t) is feature coefficients of orthogonal expansion.

For the discrete variables with m patterns , the equation (2) can be represented by the product of feature vector matrix, A , and orthogonal matrix , Q,

$$X = Q(S)A(t) \qquad (3)$$

where:

$$Q(S)=\begin{pmatrix} q_1(s_1) & \cdots & q_L(s_1) \\ \vdots & \ddots & \vdots \\ q_1(s_m) & \cdots & q_L(s_m) \end{pmatrix}, \quad A(t)=\begin{pmatrix} a_1(t_1) & \cdots & a_1(t_n) \\ \vdots & \ddots & \vdots \\ a_L(t_1) & \cdots & a_L(t_n) \end{pmatrix}$$

It is proved that the covariance matrix of weather patterns, { X } , can be derived as

$$\begin{aligned} C_x &= E\{ [X-EX][X-EX]^T \} \\ &= E\{ [Q(S)A(t)-E(Q(S)A(t))][Q(S)A(t)-E(Q(S)A(t))]^T \} \\ &= E\{ [Q(S)A(t)-Q(S)E(A(t))][Q(S)A(t)-Q(S)E(A(t))]^T \} \\ &= Q(S)C_A Q^T(S) \end{aligned} \quad (4)$$

Let

$$C_A = D_\lambda = diag\{\lambda_1 , \lambda_2, \dots , \lambda_n\} \quad (5)$$

The following relationship is also obtained

$$C_x Q(S) = Q(S)D_\lambda Q^T(S)Q(S) = Q(S)D_\lambda \quad (6)$$

It is shown that $\{\lambda_j\}$ is a set of eignevalue of the covariance matrix Cx, q_j is corresponding eignevector. Because the Cx is a real symmetrical matrix, the eignevector corresponding eignevalue must be orthogonal each other. The feature vector, A(t) ,can be identified by

$$A(t) = Q^T(S)X(S,t) \quad (7)$$

Accordingly, weather patterns feature, { Xj } , can be approximately represented by the orthogonal vector { aj }, j=1, 2,..., L; where L ∈ n. By comparisons of original weather patterns with transformed feature vectors in terms of K-L orthogonal expansion, it was found that there are some distinguishing features for the pattern recognition approach. The first, the original weather patterns, { X(k) }, is a set of correlative series, but the feature vector, { aj(k) }, is a set of independent variables due to the orthogonality of vector { qj }. The secondly, the order of eignevalues can be arranged from the maximal value to minima value in order. The precision of pattern modelling is then defined as

$$S(L) = \frac{\sum_{j=1}^{L} \lambda_j}{\sum_{j=1}^{n} \lambda_j} \quad (8)$$

If available allowed precision S* is selected, the dimension of weather patterns in feature vector space will be less than the dimension defined in original patterns space. This process is called as an information compression. On the other hand, the relationship between the original patterns and feature vector can be transformed in terms of the equation (3) and (7).

3.GREY ASSOCIATIVE CLUSTERING OF FEATURE VECTOR

In consideration of the uncertainty and imprecision in the pattern division, a Grey Associative Clustering Approach (GACA) was developed (Xia, 1993). This approach is of a dynamic clustering with soft division EPS ∈[0,1]. The measurement of patterns similarity, { $a_j(t)$}, is represented by the grey associative degree, r_{jo}, given by

$$r_{jo} = w(k)\xi_{jo}(k) \quad (9)$$

where: $r_{jo} \in [0,1]$, j=1,2,..., s; w(k) is a weight that is defined by the ratio of individual eignevalue to the total eignevalue obtained from weather patterns, i.e.

$$w(k) = \frac{\lambda(k)}{\sum_{j=1}^{n} \lambda(j)} \quad (10)$$

$\xi_{jo}(k)$ is the kth discrete point associative function that can be selected in terms of the theory of grey associative space (i.e.the normality, even-symmetry, systematisation and closeability; see Deng, 1985). An available structure is here suggested as

$$\xi_{j0}(k) = \frac{1}{1+\Delta_{j0}(k)} \quad (11)$$

where $\Delta_{jo}(k) = | z_j(k) - z_o(k) |$; $z_j(k)$ is feature vector with linear normality given by $zj(k) = (Z_j(k) - Z_{min}) / (Z_{max} - Z_{min})$ and Z_{min} = min.min { $Z_j(k), Z_o(k)$}, Z_{max} = max.max { $Z_j(k)$, $Z_o(k)$ }; $z_o(k)$ is reference series.

Main ideas in grey clustering procedure are explained as follows:

(a) Let initial clustering step number i = 1, and determine the reference series $Z_o(k)$ = { aj(k) } according to the principle of maxim modules, i.e. max { ||aj|| }. Other feature vectors {a_j } are defined as { $Z_j(k)$} where j=1,2,...,m-1;

(b) Calculate the associative degree rjo for all feature vectors in terms of the equation (9) - (11). Then, find the total similar index:

$$\varepsilon^{(i)} = \frac{r_N - r_0}{r_N} \quad (12)$$

where: r_N = max.{ r_{jo} }, or = min{ r_{jo} }.

(c) Input a soft division index EPS ∈ [0,1]. If $\varepsilon^{(i)}$ ≤EPS, then all samples will be looked as a class $C^{(i)}$, i.e. $C^{(i)} = (Z_1, Z_2, \dots, Z_m)$. If $\varepsilon^{(i)}$ >EPS, then the samples $C^{(i)}$ will be divided into two sub-samples, in which the set satisfying the condition $(r_N - r^*)/r^*$ ≤EPS will be taken as a class, i.e. $Ci^{(1)} = (Z_1^*, Z_2^*,\dots,Z_n^*)$. Others will be looked as a new samples,

i.e. $Ci^{(2)} = (Z_1', Z_2', ..., Z_n,)$, where m=n*+m';(d) Let m' as m, go on the above steps until K different clusters were obtained. Then, calculate statistical parameters of each K class such as the mean and derivation etc. Evidently, when EPS is taken as unit (i.e. 100%), the clustering will be full relaxation in which only one class is obtained. If EPS is taken as zero, then this clustering will be very rigorous. In reality, EPS is usually taken as a number in the grey interval $[\varepsilon_{min}, \varepsilon_{max}] \in [0,1]$. We call this clustering as a soft division. By preliminary comparison with the present fuzzy clustering method , it was found that the grey associative clustering approach (GSCA) might be more workable and practical (Xia, 1989,1990, 1993).

4. STOCHASTIC WEATHER GENERATION

In consideration of the weather generation and their uncertainty, the independent structure in stochastic feature vector { ai } is here modelled by a multiple-normal distribution model. Of cause, if available testing show that the stochastic distribution of studied weather variables did not obey this hypothesis, an initialization called as the Box-Cox transformation will be suggested (Box & Cox, 1964). Accordingly, the probability density function (PDF) of class ci can be assumed as

$$P(a/C_i) = (2\pi)^{-\frac{1}{2}}|C_A|^{-\frac{1}{2}} \exp[(a-u_i)^T C_A^{-1}(a-u_i)] \quad (13)$$

where C_A is given by the equation (5), u_i is determined by the clustering. The validity of the formulation (13) was verified by comparison to Monto-Carlo simulations.

On the other hand, the empirical probability happening in the class C_i event is approximately estimated by

$$P(a/C_i) = \frac{n_i}{N} \times 100\% \quad (14)$$

where ni is the sample number of sub-class Ci.

The formulation of feature vector generation in terms of the Monte-Carlor simulation is given by

$$a_i = BR + u_i \quad (15)$$

where R is a standard random vector, i.e.R = $\{R_1,...,R_L\} \sim N(0,I)$; u_i is the mean of sub-class C_i.

Using the relation $C_A = E\{aa^T\} - u_i u_i^T = BB^T = D_\lambda$, the matrix B can be derived as $B = dig.\{\sqrt{\lambda_1}, \sqrt{\lambda_2}, ..., \sqrt{\lambda_m}\}$.

On the basis of above stochastic simulation and the equation (3), the weather generations relative to different pattern classes can be obtained by

$$X^{(i)}(S,t) = Q(s)a^{(i)}(t), \quad (i=1,2,...,K) \quad (16)$$

As a result, we can have statistics for the characteristic parameters. Finely, the stochastic weather inferences and predictions about the climate change impact can be made.

4

5. PRELIMINARY APPLICATIONS

Two examinations applied to weather generation were given in this paper. One is monthly air temperature or precipitation generation and perdition in both current and projected future climates. Another is the generation of precipitation in spatial scale.

The monthly air temperature data series from 1905 to 1990 at Wuhan station, located the middle stream in the Yangtze River, were collected to set up a stochastic weather generator in temporal scale. The first step in the examinations consisted in temperature pattern recognition. The results of grey associative clustering in the feature vector sample indicate that the similarity of temperature distribution is of significance. The total samples from 1905 to 1990 can be divided into four classes when whitening value of the index EPS is taken as 3%. Furthermore, the stochastic simulations of air temperature in monthly changes can be obtained according to the equation (13)-(17). The comparisons of statistic characteristics of simulated patterns with observed patterns of the monthly temperature for the Whuan station is listed in the Table 1. It was shown that quite good results was obtained, indeed. The Table 2 give the other results about comparisons of temperature prediction in existing condition with climate change condition, where the scenario prediction for the objective year 2030 was provided by GCMs. Air temperature prediction is shown in the Fig.1

Another example for spatial downscaling of precipitation was applied to the Shun Tian catchment, Donjiang basin, China. The precipitation records from six distributed gauging stations (1972 - 1988) were collected, in which each spatial distribution for the same time scale such as monthly or yearly will form a precipitation patterns. The patterns will be represented in the same way given by the equation (1), where the variable $x_i(j)$is a monthly or yearly precipitation corresponding to the jth station or grid with the ith sample. All { $x_i(j)$ } in area distribution will form a spatial pattern in the studied catchment.

The results of precipitation patterns recognition and grey clustering indicate that there are four

different spatial distributions for the yearly precipitation patterns at the Shun Tian catchment. The feature vectors of precipitation patterns for each classes is also quite different. These feature vectors and correspondent frequency happening in total precipitation events can be evaluated. The precipitation generations of spatial downscaling with 500 samples, and comparisons of statistic characteristics were listed in the Table 3. Preliminary examination show that the downscaling approach in terms of the patterns recognition, the grey clustering and stochastic simulation method could provide a technique to generate weather variables applied to spatial downscaling at each gauging stations.

6. CONCLUSION REMARK

(a) A pattern recognition techniques including clustering and stochastic simulation was developed. The weather feature vector with arbitrary stochastic distribution can be extracted without prior hypothesis. The clustering and generation could be carried out in lower dimension space.

(b) The method of weather generation was preliminary verified by two basin weather data in China, and comparisons of stochastic characteristic parameters. The results indicated that there are evidently uncertainty in weather patterns. The stochastic generator can give a probability prediction with maxim and minima in high resolution data. The climate scenario provided by GCMs can be easily linked with monthly or daily mean changes.

(c) The applications on spatial downscaling with daily scale remains to be examined and improved.

References

Bass.B, Summary Report on Activity 4.1: Data requirements for ecological and hydrological studies nd related management purposes; Biosphere Aspects of the Hydrological Cycle (BAHC), *Focus 4: the Weather Generator Project, Bratislava, Slovakia, 16-18 Sept., 1993.*

Box,G.E.P.and Cox, D.R.:An analysis of transformation, Journal of the Royal Statistical Society, Vol.B26,211-252, 1964.

Chien,Y.T., and Fu,K.S., On the generalised Karhunen-Loeve expansion, IEEE Trans. Inf. Theory, IT-13, 518-520, 1967.

Deng,J.L., Special Issue of grey system approach (in Chinese), Fuzzy Mathematics 5(2), 1985.

Tou,J.T.and Gonzalez, R.C.,Pattern Recognition Principles, Addison-Wesley, Reading, Massachusetts, 11974.

Xia, J. , A grey correlative analysis and pattern recognition applied to mid-long term runoff forecasting(in Chinese), Advances in Water Science, Vol.4, No.3, 190-197, 1993.

Xia, J. , Grey system theory approach and preliminary application to downscaling component of weather generation, Research report on activity 4.2: Development of the weather generator, BAHC,Karlsruhe Workshop, Karlsruhe, Germany, June 26-28, 1994.

Table 1 Comparison of statistic characteristics for the temperature generation in the Wuhan station (Data samples: 1905-1990; Simulation 500 years)

Item \ Month		J	M	M	J	S	N
Mean	X_{act}	3.474	10.200	21.710	28.791	23.630	11.582
	X_g	3.377	10.374	22.023	29.144	23.905	12.223
S.D	σ_{act}	1.484	1.318	1.058	1.187	1.052	1.161
	σ_g	1.578	1.343	1.206	1.369	0.940	1.082
C.V	$Cv._{act}$	0.427	0.129	0.049	0.041	0.045	0.100
	$Cv._g$	0.467	0.129	0.055	0.047	0.039	0.088
C.S	$Cs._{act}$	0.273	0.078	0.019	0.238	0.035	0.403
	$Cs._g$	0.267	0.012	0.248	0.089	0.136	0.159

Table 2 Comparison of temperature prediction in present condition with climate change , Whuan (GCMs provide the scenario prediction for the objective year 2030)

Item \ Month		J	M	M	J	S	N
X_{mean}	Present	3.377	10.374	22.023	29.144	23.905	12.223
	Change	4.467	11.464	23.113	30.234	24.995	13.313
X_{min}	Present	-1.615	6.725	19.173	25.275	20.647	9.397
	Change	-0.525	8.905	20.263	26.365	21.737	10.487
X_{max}	Present	7.009	13.867	25.645	32.987	26.857	14.998
	Change	8.099	14.857	26.735	34.077	27.947	16.088

Table 3 Comparison of statistic characteristics for the yearly precipitation spatial generation at Shun Tian catchment (Simulation 500 years)

Item \ Station No.		1	2	3	4	5	6
Mean	Xact	1531.9	1227.7	1813.2	1764.3	1768.1	1742.4
	Xg	1611.2	1280.6	1860.2	1782.4	1757.0	1749.4
Max.	Xact	2345.4	1828.7	2698.0	2694.8	2401.0	2489.7
	Xg	2797.0	2201.8	3596.2	3308.9	2929.9	2903.6
Min.	Xact	1141.5	801.3	823.6	1255.6	1360.9	1393.0
	Xg	633.3	159.9	132.5	669.2	623.8	918.1
C.V	Cv.act	0.193	0.232	0.241	0.193	0.183	0.160
	Cv.g	0.250	0.296	0.310	0.233	0.232	0.192

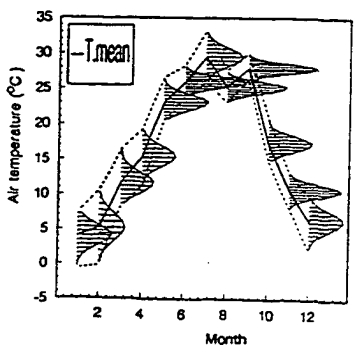


Fig.1 Stochastic Generation and Prediction of Monthly Air Temperature Series in Wuhan, China.

Downscaling Techniques for Snowfall Prediction in Global Change Studies

by

David L. McGinnis, Ph. D.

Cooperative Institute for Environmental Sciences
Campus Box 449, University of Colorado, Boulder, CO 80309-0216, USA.

Abstract

This study develops observed climate-based downscaling transfer functions which are used with General Circulation Model (GCM) output to assess potential global-change impacts on Upper Colorado Plateau, USA, water resources. Daily automated snow-water equivalent stations are used with 700 mb synoptic circulation to determine the downscaling functions. Multiple regression and neural network downscaling techniques are investigated explaining approximately 34% and 70% of the daily snowfall variance respectively. The neural-network-based transfer functions are used with the GENESIS General Circulation Model (GCM) to simulate snowfall characteristics in both a 1xCO_2 and a 2xCO_2 climate.

Introduction

Global climate change studies often make use of General Circulation Models (GCMs) of the atmosphere and oceans. These models have coarse resolution ranging from 2.5° by 2.5° up to 8° by 10° latitude and longitude. Such resolution poses distinct problems when trying to investigate regional impacts of climate change. The use of downscaling transfer functions allows better sub-GCM grid scale information to be derived while using the best features of GCM output (large-scale atmospheric circulation).

GCMs are notoriously poor regarding individual grid point comparisons with observed regional climate (Grotch and MacCracken, 1991), especially temperature and precipitation fields. Wilson and Mitchell (1987) find that local geographic and topographic sub-grid scale features, that are not accounted for in the model, cause modeled surface variables to disagree with observed climate. Wigley et al. (1990) suggest large-scale variability may be used to determine useful local information; Karl et al. (1990) and Portman et al. (1992) discuss methods to determine local variables from large-scale atmospheric variability.

Linear-based transfer functions applied to GCM output to simulate circulation-based temperature changes in a 2xCO_2 atmosphere are developed by Hewitson and Crane (1992a). Their downscaling methodology demonstrates the value of relating synoptic-scale circulation to local surface variables. Subsequent downscaling studies show the increased predictive ability obtained by using non-linear methods such as neural networks (Hewitson and Crane, 1992b).

The primary purpose of this paper is to compare linear and non-linear downscaling techniques using the same data and once the best technique is determined, use the transfer functions with validated GCM output to simulate potential climate changes under 2xCO_2 conditions. The surface variable of interest is high-elevation snowpack over the Colorado Plateau, USA, which is the primary water source for much of the dry southwest United States. Over 70% of the water in the Colorado River begins as snowpack, thus better simulation of snowfall is paramount to assessing future water resources in a 2xCO_2 climate.

Data Preparation

The atmospheric data used here come from the National Meteorological Center (NMC) and are part of an observational data set supplied by the National Center for Atmospheric Research (NCAR) (Jenne, 1975). 700 mb geopotential heights are chosen to best mimic surface pressure conditions on the 3000-4000 meter elevation Colorado Plateau. Using a synoptic-scale atmospheric window (125° W to 100° W longitude and 30° N to 50° N latitude), 44 gridpoints are used from the NMC octagonal grid (figure 1); the time series of daily 1200 Z observations from 1981 to 1989 is selected to best match the time domain of the available snowfall data.

The GCM used in this study is the GENESIS (Global ENvironmental and Ecological Simulation) model being developed at NCAR by S. Thompson and D. Pollard (personal communication). Daily 12 Z 700 mb data are extracted for both control climate and 2xCO_2 simulations. Because the observed climate and the GCM grids differ, they must first be interpolated to the same gridpoints to facilitate comparative analyses; in this case, the GCM data are interpolated to the NMC octagonal grid (figure 1).

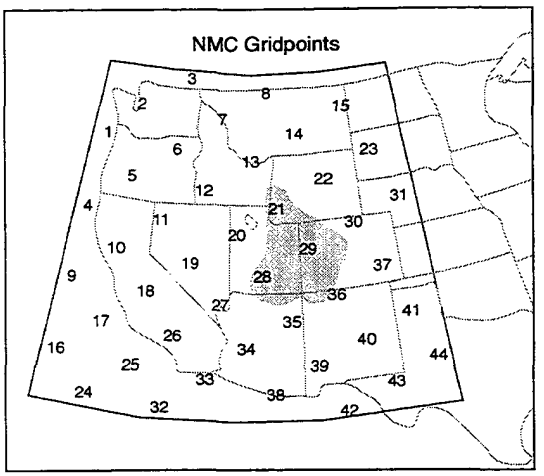


Figure 1. NMC 700 mb gridpoints; The Upper Colorado Plateau is shaded light gray.

Each 700 mb height time series undergoes a rotated S-mode principal component analysis (PCA) as a data-reduction effort. The input matrix has 44 gridpoint variables forming the columns and 2644 days forming the rows. The resulting component loadings represent the spatial variance patterns associated with the 700 mb data series (figure 2) and the component scores are the manifestation of those spatial patterns on a given day. These scores become the input (independent) variables in the downscaling analyses. The three retained orthogonal components for observed climate explain 93% of the 700 mb circulation variance; the 1xCO_2 and 2xCO_2 simulation PCAs explain 97.6% and 97.8% respectively. The component scores for each analysis represent the temporal manifestation of the associated spatial variance patterns--a synoptic index. The synoptic circulation on a given day is a product of the component scores and their attendant loading patterns; it is impossible to separate the components into climatological features. Rather, they must be considered together.

Daily snowfall data are available from the Soil Conservation Service Snow Telemetry (SNOTEL) historic data base. Automated sensors provide daily measurement of snow-water equivalence (SWE). There are more than 100 Upper Colorado Plateau SNOTEL sites currently operational; however, only 54 stations are used in this study due to data record length and quality. The SNOTEL sites are distributed over various elevations, aspects and drainage basins thus representing the spatial distribution of Upper Colorado Plateau snowfall. The individual SNOTEL site time series were correlated and subsequently divided into five groups (figure 3); the daily snowfall within each group were then averaged to create a regional snowfall variable. This reduced some of the high-frequency noise in the data set and smoothed the daily snowfall record.

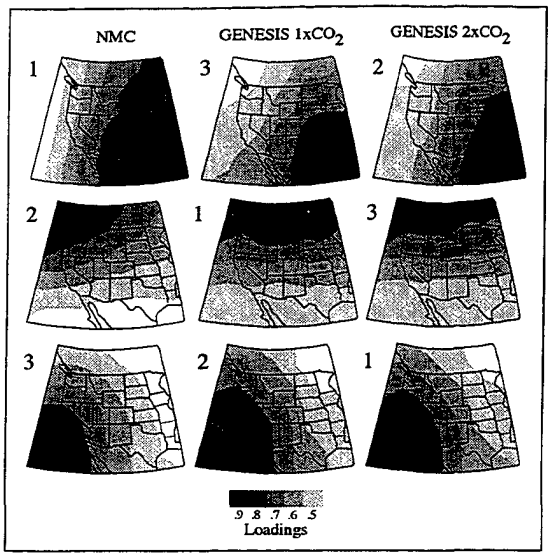


Figure 2. Loadings maps showing matched components.

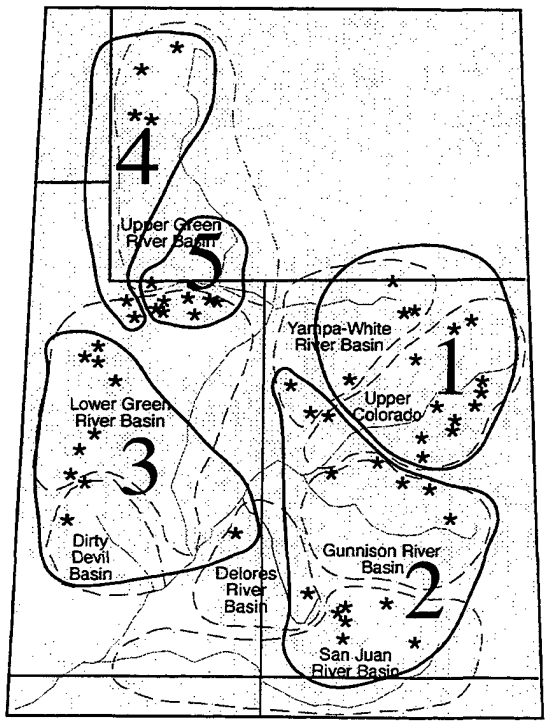


Figure 3. SNOTEL site groups. Asterisks indicate location of SNOTEL sites, solid dark lines indicate corelation-based groups, light solid lines are the rivers and light dashed lines indicate drainage basins.

Various configurations for both the multiple regression and neural network downscaling approaches were tested. Only the best results from each methodology are reported.

Multiple Regression Downscaling

Stepwise multiple regression is a standard climatology tool applied when a set of independent variables might affect the prediction of a dependent variable. In the present analysis, polynomial regression (in an attempt to incorporate certain non-linear relationships) is used where the 700 mb PCA score time series (three components), along with their squares and cross products, predict daily SWE. Thus, a total of nine independent variables are used to characterize synoptic circulation conditions.

Initially, all 54 stations are analyzed individually using raw (not smoothed) data with r^2 values ranging from 0.08 to 0.48, with a 54-site mean of 0.25. These results, however, are not as good as many climatological studies. Therefore, the SWE and the 700 mb data are smoothed before subsequent multiple regression analyses.

The 700 mb data are conditioned using a 5-day smoothing filter (because most synoptic event pass through the study region in this time frame). The regression results (r^2) for the 5-day smoothed synoptic index and the averaged regional SWE groups range between 0.29 and 0.45 with an mean of 0.34 (table 1). The best regional results, unfortunately, occur in the Colorado Plateau regions that contribute the least snowpack water resource to the Colorado River flow. Regardless, while the variance explained is relatively small for climatological research, this analysis demonstrates a definite synoptic control on Colorado Plateau snowfall.

Table 1. Comparison of r^2 values for the regional groups.

Group:	1	2	3	4	5
Regression	0.29	0.33	0.45	0.42	0.29
Neural Net	0.64	0.77	0.77	0.68	0.62

Neural Network Downscaling

Climate does not always act in linear relationships, particularly in complex mountainous terrain. Neural networks provide new approaches to problem solving that utilize non-linear mathematics and are applicable to a wide variety of applications.

The data are preconditioned for the neural network analysis differently than the multiple regression study described above. Here, the 700 mb component scores remain unsmoothed (raw) but are lagged from day 0 to include the previous four days. Thus, a total of five days of synoptic circulation information (day 0 to day -4) are included. With three lagged components, the total number of inputs to the neural network procedure is 15; these represent the synoptic circulation and its recent antecedent conditions that affect snowfall. The SNOTEL data are the group averages as described above.

A feed-forward backpropagation neural network, much like a linear regression, takes independent variables and predicts a dependent variable. The net configuration (figure 4) takes the 15 input data as the input layer and multiplies each value by a random weight value (Wij) along each linkage between the input layer and the hidden layer (comprised of 22 nodes). At each hidden layer node, the input value-weight products are summed and passed through a non-linear sigmoid function. These values are then passed along another set of weighted linkages to the single output node. Here, the net-predicted value is compared to the observed value and the error calculated. This error is then passed through all the linkages and nodes (output layer--hidden layer--input layer) and the error term updates and corrects the weights on each link. The entire procedure iterates until the root mean squared error of the net predictions reaches a global minimum. A more complete description of neural network functions may be found in Hewitson and Crane, 1994). Once the net has developed the best set of weights on each linkage, these weights become the non-linear transfer function that relates synoptic circulation characteristics to the regional SWE output variable.

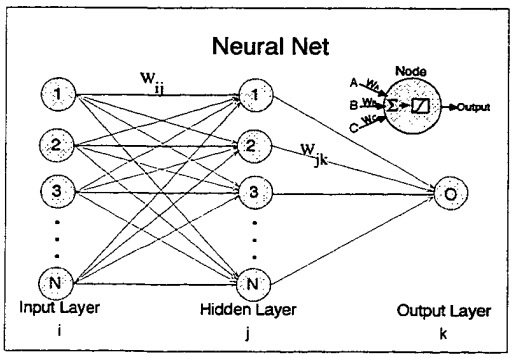


Figure 4. Neural net configuration. An individual processing node is in upper right portion of diagram.

The results of the neural network analysis nearly double the variance explained by the linear regression methodology (see table 1). Snowfall associated with SNOTEL regions 1 and 2 is the primary high-elevation source of Colorado River water. The neural net results for region 2 are shown in figure 5. Note that the net matches the phase and magnitude of snowfall variance quite well; however, the net tends to underestimate some extreme events. The total annual accumulation (which most water managers use) is well predicted, remembering that these daily snowfall simulations result from synoptic circulation variables only. Adding temperature and other hydrologic variables (i.e., humidity) would likely improve these results. On the other hand, such additions would not be appropriate in the climate change analyses described below.

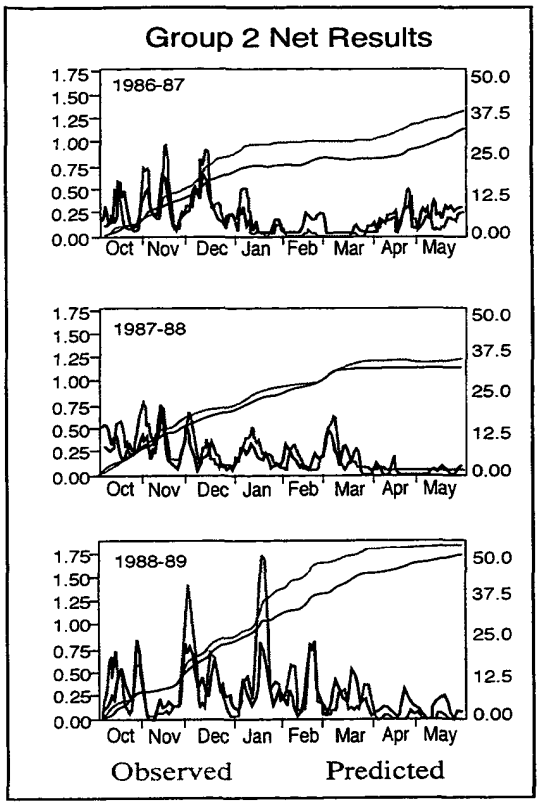


Figure 5. Observed and neural-net based daily SWE prediction (cm). Seasonal accumulation is also shown.

The neural net results are significantly better than the multiple regression in each SNOTEL group. Although the two analyses were performed with different data conditioning, they represent the best results for their methodology. The neural net results match both phase and magnitude of daily snowfall variance remarkably well (figure 5). Here, daily snowfall amounts for three years exhibit excellent agreement on snowfall events. While the magnitude of extreme events is sometimes underestimated, the annual accumulations, especially in years without extreme events like 1987-88, are closely simulated by the net. Thus, the neural net-based transfer functions become the method of choice to downscale from synoptic-scale atmospheric circulation to regional daily snowfall.

GENESIS GCM Validation

Before the neural net transfer functions can be applied to GCM simulations, the GCM synoptic circulation must be validated against observed climate. While the patterns in figure 2 may be visually compared, it is valuable to calculate pointwise and gradient correlations. The primary comparison is between NMC observed climate and the GENESIS $1xCO_2$ simulation. The pointwise correlations range from 0.90 to 0.97 but the gradient patterns show less agreement. Regardless, the spatial variance patterns are similar enough to warrant use of the observed-climate transfer functions with the GCM circulation. The $2xCO_2$ circulation spatial variance must be similar too in order to apply the transfer functions to the climate-change scenario. The pointwise correlations as well as the gradient correlations between the $1xCO_2$ and $2xCO_2$ circulation are all excellent--in fact, better than between observed climate and the $1xCO_2$ simulation. This suggests that the patterns of synoptic activity will likely remain spatially similar under climate change scenarios.

However, the temporal realm must also be validated. The $1xCO_2$ climate must be similar in event frequency and persistence (events are defined as days with component scores with an absolute value greater than 1.0) to observed climate. For brevity, the temporal comparisons between observed and $1xCO_2$ climate are very good. There is no *a priori* reason to suspect the $2xCO_2$ circulation should temporally match either modeled or observed data sets.
The GCM circulation is considered valididated by both spatial and temporal comparisons; therefore, the observed-climate transfer functions may be applied to the modeled circulation.

GCM Snowfall Simulations

The main purpose of using the downscaling methodologies described here is to allow use of large-scale GCM features that are much better modeled than individual grid point or regional climate variables. However, any discussion using $2xCO_2$ GCM output must be preceded with a few caveats. The transfer functions merely demonstrate possible climate changes based on atmospheric circulation alone; any general temperature trends (whether warming or cooling) are not included in this analysis. In addition, the neural net only captures approximately 70% of the daily snowfall variance, tends to underpredict extreme events and may overpredict snowfall by treating some rainfall events as snowfall. Regardless, the total seasonal SWE should be relatively accurate. If the climate warms, the season length may shorten and may affect the transfer function relationship.

Finally, the five SNOTEL regions have slightly different snowfall characteristics and several of the net-derived seasonal accumulations are too low due to missing data. Twenty nine days are missing from 1981-82 while 33, 18 and 20 days are absent from the next three winter seasons. The remaining years all have fewer than seven missing days. These missing days cause the net-derived data to not calculate snowfall on those days because the score values (or the appropriate lagged information) are not available; therefore, with approximately 6% of the potential snowfall days not accounted for, the net-derived seasonal accumulations should be slightly less than observed climate.

Transfer function derived average seasonal SWE in all five SNOTEL regions are within 5% of actual SWE in observed climate. Thus, the transfer functions perform quite well. The GENESIS $1xCO_2$ simulation produces slightly too much snowfall (less than 8% for any group). Table 2 summarizes the comparison between observed climate (predicted with the transfer functions) and the GCM simulations. To no surprise, the total annual precipitation rises slightly under climate change conditions. Although this analysis is related to synoptic circulation based changes only, it is apparent that total precipitation is likely to at least remain nearly the same, if not increase.

Table 2. Full-season net-based transfer function SWE averages.

Region	Model	Average SWE (cm)
1	Observed	58.52
	$1xCO_2$	59.66
	$2xCO_2$	60.33
2	Observed	59.28
	$1xCO_2$	63.25
	$2xCO_2$	60.25
3	Observed	53.82
	$1xCO_2$	57.05
	$2xCO_2$	54.25
4	Observed	60.68
	$1xCO_2$	60.76
	$2xCO_2$	69.70
5	Observed	52.71
	$1xCO_2$	56.74
	$2xCO_2$	58.34

However, temperature is not taken into account by the analysis in table 2. These results relate to accumulation over the entire snow season from 1 October through 31 May. If temperature is added to the analysis, some of these snowfall events will occur as rain rather than snow. Work is currently underway to assess temperature with the similar transfer functions in order to better model rainfall events and melt periods. In the meantime, it is possible to use output directly from the GCM that indicates whether there is snow cover within the grid cells that cover the Upper Colorado Plateau region. The GCM reports a fractional snow coverage which indicates when snow is present (this surface variable is highly questionable, however, due to the poor topography of the Rocky Mountains). When this factor is added to the analysis, a different picture of seasonal snowfall emerges (table 3). The amount of water resource stored in snowpack is dramatically reduced. It must be noted, however, that the $1xCO_2$ seasonal totals are also reduced; this suggests that the temperature conditions and the evaluation of fractional snow cover are highly suspect (and drive research using downscaling methods). Regardless, the $2xCO_2$ seasonal totals are up to 50% less than observed. While the results shown in table 2 suggest similar seasonal totals, adding temperature information suggests much less snow accumulation. Therefore, it is logical to expect that the snow season will shorten and more precipitation will occur as rain instead of snow.

Table 3. Seasonal SWE accounting for "no-snow cover" days.

Region	Model	Average SWE (cm)
1	Observed	58.52
	$1xCO_2$	41.38
	$2xCO_2$	29.41
2	Observed	59.28
	$1xCO_2$	41.68
	$2xCO_2$	32.74
3	Observed	53.82
	$1xCO_2$	41.68
	$2xCO_2$	30.91
4	Observed	60.68
	$1xCO_2$	39.14
	$2xCO_2$	40.79
5	Observed	52.71
	$1xCO_2$	38.25
	$2xCO_2$	31.78

The suggestion that more precipitation will fall as rain is supported by the changes in winter season length. Table 4 summarizes these modifications. The start date (end date) are the averages for the dates when snow continuously covers (is absent from) the ground for one week. Both the GENESIS present-day and $2xCO_2$ simulations demonstrate reduced snow seasons. The $2xCO_2$ season has over 50% fewer potential snow days according to this analysis. However, further transfer function development currently being undertaken may prove a better measure of potential temperature changes, and hence season length modifications, than is reported here using direct GCM output.

Table 4. Average snow season dates.

	Start date	End date	No-snow days
Observed	10 October	23 May	0
$1xCO_2$	6 November	17 April	13
$2xCO_2$	26 November	21 March	24

Conclusions

The primary purpose of this paper was to investigate multiple regression and non-linear neural networks as potential downscaling methodologies. Downscaling from synoptic-scale atmospheric circulation to regional snowfall using observed climate developed transfer functions modeled daily snowfall quite well. The neural network approximately doubled the variance explained by the multiple regression methods and became the methodology of choice for examining climate change related snowfall modifications.

The GENESIS GCM was used to simulate both present day and $2xCO_2$ atmospheric circulation. This circulation was validated before being used with the neural net based transfer functions to predict snowfall. The synoptic atmospheric variability over the study region changes little between observed, $1xCO_2$ and $2xCO_2$ circulation. The GENESIS model tends to produce too little snow in both the $1xCO_2$ and $2xCO_2$ analyses with the $2xCO_2$ simulation showing seasonal reductions in the range of 17% to 29% in all regions except one. The $2xCO_2$ season is approximately half as long as the currently observed snow season.

Therefore, water resources are likely to change in a $2xCO_2$ climate. If more precipitation falls as rain instead of snow, the storage capacity of the snowpack will change the timing of the seasonal peak flows on the Colorado River. Water managers will have to adjust dam and reservoir operations to account for this modified flow pattern.

Before these conclusions are appropriate for policy makers, more research must be done to better model the precipitation characteristics. The $2xCO_2$ atmosphere is likely to produce more precipitation, but more evaporation is likely to occur as well. Furthermore, temperature modifications complicate the picture and may cause more rain and less snow while keeping the general precipitation amount nearly the same as today. Further research is underway to address temperature concerns, snowpack melt period characteristics and how these might change in a $2xCO_2$ climate.

References

Grotch, S.L. and M.C. MacCracken, 1991, "The use of general circulation models to predict regional climate change", *J. Climate*, 4, 286-303.

Hewitson, B.C. and R.G. Crane, 1992a, "Regional-scale prediction from the GISS GCM", *Paleogeography, Paleoclimatology (Global and Planetary Change Section)*, **97**, 249-267.

Hewitson, B.C. and R.G. Crane, 1992b, "Large-scale xontrols on local precipitation in tropical Mexico", *Geophys. Res. Ltrs.*, 19, 18, 1835-1838.

Hewitson, B.C. and R.G. Crane, eds., 1994, "*Neural Nets: Applications in Geography*", Kluwer Academic Publishers, Boston, MA, USA.

Jenne, R.L., 1975, "Data sets for meteorological research", *NCAR-TN/1A-111*, National Center for Atmospheric Research, Boulder, CO, 194 pp.

Karl, T.R., W.C. Wang, M.E. Schlessinger, R.S.W. Knight and D.A. Portman, 1990, "A method of relating general circulation model simulated climate to the observed local climate, part I: seasonal statistics", *J. Climate*, **3**, 1053-1079.

Portman, D.A., W.C. Wang and T.R. Karl, 1992, "Comparison of general circulation model and observed regional climates: daily and seasonal variability", *J. Climate*, **5**, 343-353.

Thompson, S.L. and D. Pollard, personal communication, "A global climate model (GENESIS) with a land-surface-transfer scheme (LSX), part 1: present-day climate", submitted to *J. Climate*.

Wigley, T.M.L., P.D. Jones, K.R. Briffe and G. Smith, 1990, "Obtaining sub-grid scale information from coarse-resolution general circulation model output", *J. Geophys. Res.*, **95**, 1943-1953.

Wilson, C.A. and J.F.B. Mitchell, 1987, "A doubled CO2 climate sensitivity experiment with a global climate model including a simple ocean", *J. Geophys. Res.*, **92**, D11, 13,315-13,343.

Acknowledgements

This research was performed under NASA Grant NAGW-2686 to E. J. Barron, and DOE Grant DE-FG02-93ER61717.A000 to R. G. Crane, The Earth System Science Center, Pennsylvania State University, USA. I would also like to recognize Dr. B. C. Hewitson, University of Cape Town, South Africa, for his tireless support. The NevProp program was kindly made available by Phil Goodman, University of Nevada, Reno, USA.

Author's email address: mcginnis@nsidc2.colorado.edu

A TWO-STEP METHOD TO TRANSFORM CLIMATE MODEL OUTPUTS INTO REGIONAL AND LOCAL WEATHER ELEMENTS

W. Enke and A. Spekat

Free University of Berlin, Germany

ABSTRACT

The increasing demand of climate impact research, driven by a public interest in the local and global consequences of possible climate change has given rise to a need in data of high spatial and temporal resolution. A statistical regionalization method is presented which uses expertise gained in 25 years of operational weather forecast. It consists of two steps: Cluster analysis using the minimum distance method in combination with a conditional, linear, multiple regression analysis. Clustering is performed in three steps: (i) generation of a starting partition predefining the number of classes and using the method of radius restriction; (ii) allocation of all objects to their most similar class; (iii) iterative performance of the minimum distance method in order to optimize the classification for all objects.

The characteristical time scale of weather phenomena is taken into account by using daily fields of 1000, 700, and 500 hPa absolute topography and the relative topography 1000/500 hPa for each day and its successor. The data used in this study cover the Atlantic-European sector from 60W to 50E and from 80N to 30N on a 5x5 degree grid. The local weather is taken from 52 climate stations in Germany. The study starts in 1966 and extends into 1994. It turned out that a combination of 6 to 10 classes for clustering, the subsequent regression step, and the division into seasonal subsets lead to a maximum information gain. This promising approach for valid downscaling will be applied to evaluate climate model scenarios.

1 INTRODUCTION

For a global scenario in a large scale, climate models forecast a global temperature rise of at least 2 degrees K. However, the coarse results do not shed enough light on possible local effects which might be even larger. Regions that have been identified as extremely sensible to climate changes, like semi-arid or permafrost areas might be affected by even smaller magnitudes of temperature or precipitation change. We all have to aware that climate change as such is only one part of global change. There is a multitude of interactions between natural and human-influenced ecosystems on one hand and our earth's climate system on the other hand. **Climate Impact Modellers** from different communities (e.g. Hydrology, Forestry, Sociology) have data demands ranging from local (a few m^2) to large (several 10^3 km^2) scale in space and daily extremes to annual averages in the temporal scale.

The required long-time simulations of > 100 a, so far can only be produced by coarse-mesh global climate model versions. Therefore statistical downscaling methods are an option to approach the data demands mentioned above. The method presented here was developed for statistical short and medium range weather forecasting. Its operational experience proves that it is suitable for downscaling purposes. Essentially, this approach combines clustering and subsequent multiple regression analysis.

2 DATA

For the classification of weather patterns (see 3.1) our archive consists of 5x5 gridpoint values of 1000, 700, and 500 hPa geopotential height, and 700 hPa relative humidity in the North Atlantic/European sector. Regression analysis (see 3.2) was performed for T_{max}, T_{min}, T_{mean}, relative humidity, cloudiness, sunshine duration, and precipitation using a set of 52 German climate observation stations. Both archives consist of German Weather Service (DWD) data and cover the period 1966-1994.

3 SHORT DESCRIPTION OF THE METHOD

The method features a two-step approach:

- Cluster analysis using the S1 score as a distance measure
- Multiple linear regression analysis using cross validation

3.1 Classification Step

The Cluster Analysis is performed in three steps

3.1.1 Selection of a starting partition of weather situations with maximum unsimilarity with empirically determined number of classes and starting situations (see Fig. 1).

For clustering the distance measure S1 score is used:

$$S1_j = \frac{\sum_{i=1}^{m} (|d_{p,j} - d_{j,i}| * \alpha_i)}{\sum_{i=1}^{m} (\max(|d_{p,i}|, |d_{j,i}|))}$$

$d_{p,i}$ Horizontal differences of the mean weather pattern of the given classes.

$d_{j,i}$ Horizontal differences of the daily weather patterns.

α Weights of the differences, depending on the distance from the central reference point

m number of horizontal differences

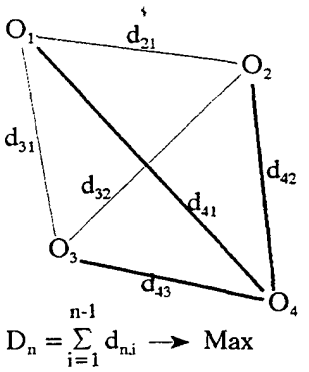


Fig. 1: Stepwise selection of the most unsimilar weather patterns ($O_1 \ldots O_n$) n: number of classes

3.1.2 Allocation of all objects to their most similar class. Centroids successively change in mean value and variance during this procedure (see Fig. 2).

3.1.3 All objects are exchanged iteratively between the classes until a stable state is reached (see Fig. 2). The similarity within classes is to be maximized.

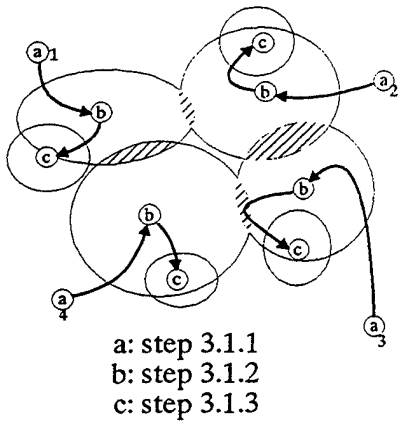


Fig. 2: Schematic representation of the three classification steps. Note the shift in centroid position and the variance-reducing effect of iteratively exchanging objects

3.2 Regression step

For each class a separate regression analysis is performed. Cross validation technique is used to estimate the optimal complexity of the regression equations. The following types of predictors have been used (or will be used in future project stages):

- Geopotential height at the central point and as an areal average
- Relative topography 500/1000, 500/700 and 700/1000hPa
- Approximated persistence
- Subjectively classified air masses
- Vorticity at the reference point and as an areal average
- Humidity of the 700hPa level at the reference point and as an areal average.

The 52 stations from the area investigated are grouped into 6 regions including two mountain regions to further account for subset climate. Temperature, humidity, cloudiness, sunshine duration and precipitation (mean values and different thresholds) are downscaled.

Because of a lack of relation between climate forecasts and observed weather elements, it is in principle not possible to obtain "real" persistence as a predictor. For this reason, approximated, or pseudo-persistence (today's persistence is the forecast of yesterday's predictand instead of its observation) is used.

4 RESULTS

Composite charts of the averaged weather patterns of 1000 hPa for summer and winter, obtained after the classification step are given in Figs. 3 and 4 for warm, cold, dry, wet and two other frequent weather situations. It is evident that clustering already yields well interpretable synoptical patterns. Please note that the distance measure for used clustering takes into account other levels as well.

The tables attached to each chart of Figs. 3 and 4 display the relative frequency of each class and mean values of seven weather elements. Their variance, expressed as RMSE is derived from the regression step using absolute topographies of 1000 hPa, relative topographies 500/1000 hPa and pseudo-persistence (see 3.2).

Clustering—even though it is performed on atmospheric geopotential patterns—very well separates temperature regimes at the surface as shown in the splitting between coldest and warmest class which amounts to 8.3K in summer and 7.8K in winter for T_{max}. Similar values are obtained from minimum and daily mean temperature. Introducing 700 hPa humidity fields into clustering **and** regression — a work in progress — will probably improve the accuracy of humidity, cloudiness, sunshine and precipitation results.

Furthermore, pronounced differences in variance among the classes is in accordance with synoptical experience.

As a measure of skill for downscaling the integral reduction of variance over all classes is shown in Table 1. It represents the improvement relative to sample variance is used (cf. Tab. 1).

Element	Winter	Summer
Maximum Temperature	50,9	56,6
Minimum Temperature	43,9	35,1
Daily Mean Temperature	49,1	53,8
Relative Humidity	8,1	31,4
Cloudiness	9,6	40,1
Sunshine Duration	6,7	32,5
Precipitation	15,7	16,0

Table 1: Reduction of variance (in %) for 7 weather *elements in winter and summer.*

Obviously, the quality of regionalization has a high seasonal dependency, expressed by humidity, cloudiness and sunshine duration. Moreover, the temperature regime bears a higher potential for improvement. These results are in accordance with synoptical and statistical weather forecasting verifications.

5 THE FUTURE

It is feasible, that there is still a potential for ameliorating the method. Current activities include: optimizing the clustering step, and using other predictors, such as advection, vorticity, and atmospheric stability.

Necessarily, this development and testing phase of the downscaling method is performed using a diagnostic data set. The next step will be the application to global climate model simulations of the present state (control runs) and future scenarios.

6 SUGGESTED READING

Balzer, K., 1980: Mittelfristige Interpretationsvorhersage mittels fester Klassifizierung oder/und Regressionsanalyse. F/E-Bericht des Met. Dienstes Potsdam.

Frey-Bunness, F., D. Heimann and R. Sausen, 1995: Statistical-dynamical downscaling procedure for global climate simulations. Theor. Appl. Climat., **50**, 117-131.

International Geosphere-Biosphere Programme (IGBP), 1994: Biospheric Aspects of the Hydrological Cycle (BAHC) Focus 4: The Weather Generator Project, Report No. 4, Brad Bass (ed.), BAHC Core Project Office, Potsdam, 131 pp.

Storch, H.v., E. Zorita and U. Cubasch, 1993: Downscaling of global climate change estimates to regional scales: An application to Iberian rainfall in wintertime. J. Climate, **6**, 1161-1171.

ACKNOWLEDGEMENT

This work is being sponsored by grant 07VKV01/1-30 of the German Ministry for Education, Research, Science, and Technology (BMBF) as a part of its research programme "Climate Variability and Signal Detection".

CORRESPONDING AUTHOR

Arne Spekat
Institute of Meteorology
Free University of Berlin
Carl-Heinrich-Becker-Weg 6-10
D-12165 Berlin, GERMANY
Tel.: +49 30 838 71139/71118
Fax.: +49 30 838 71217
e-mail: as@zedat.fu-berlin.de

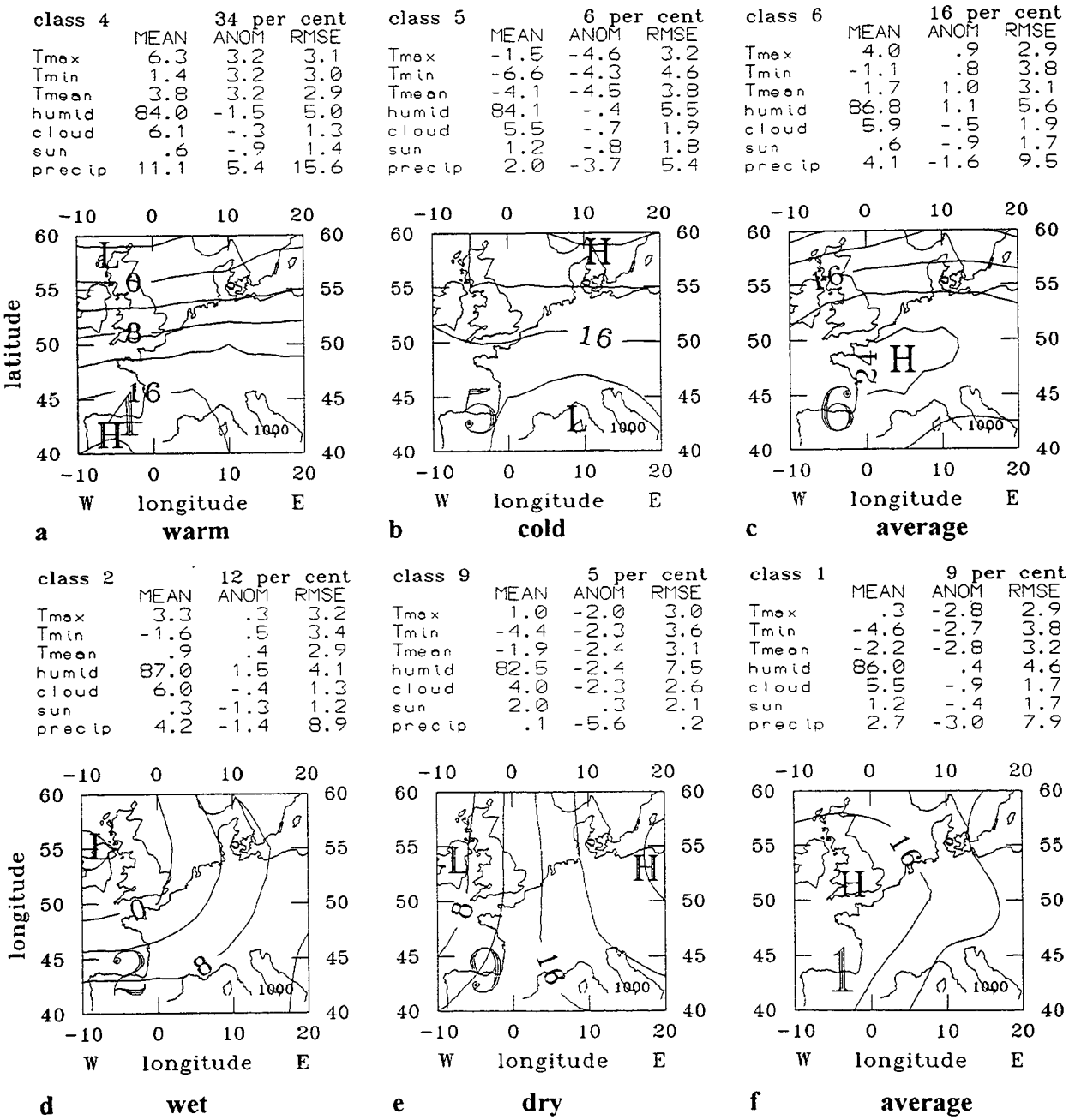
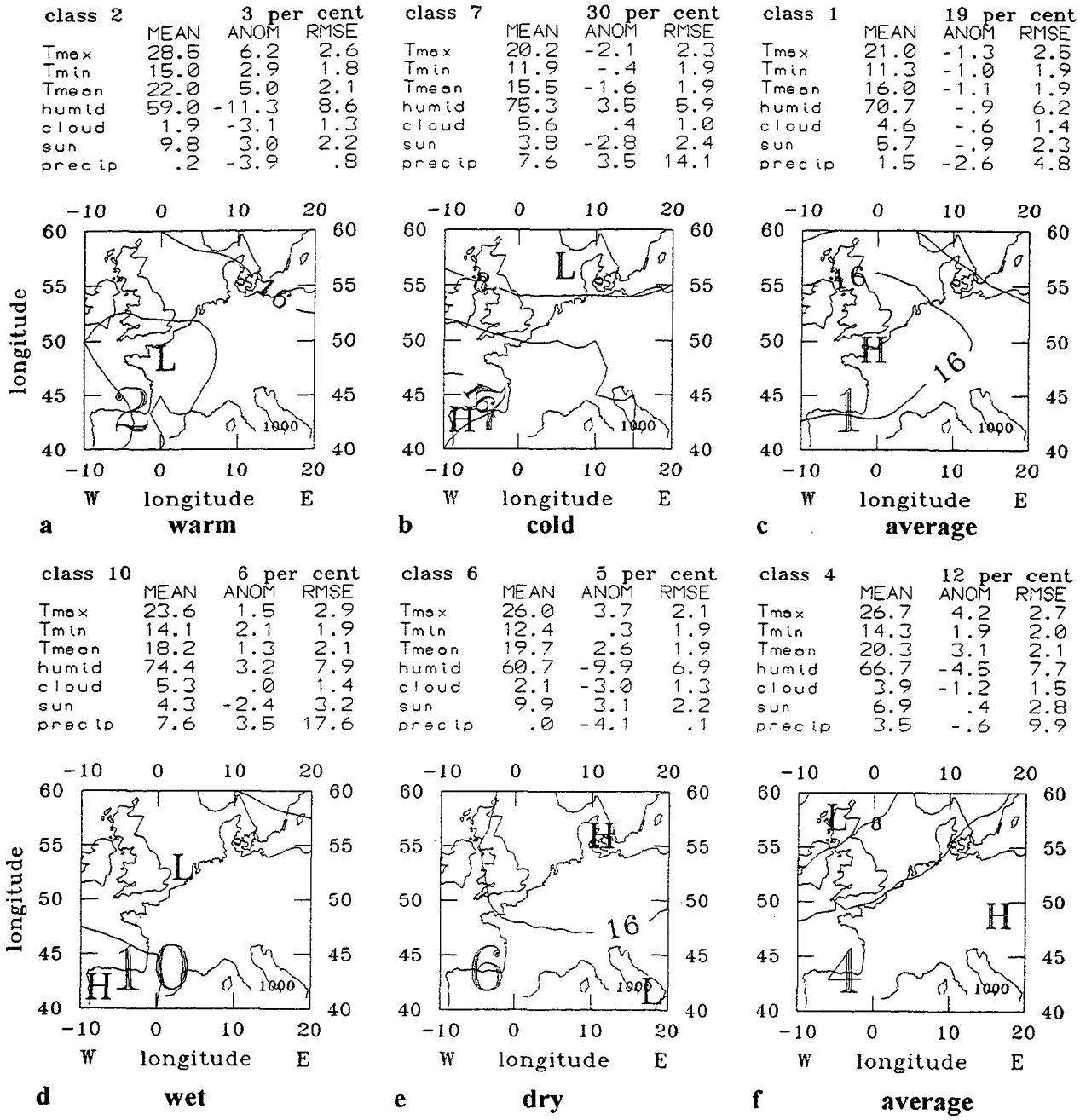


Fig 3: Composite 1000 hPa geopotential charts for Central and Western Europe **WINTER (December-January-February)**. Classes selected represent cold (3a), warm (3b), average temperature (3c), wet (3d), dry (3e) and average humidity (3f) weather situations for Northern Germany (below 500m elevation, excluding the coastal zones of the Baltic and the North Sea). Isoline spacing is 4 gpm. The table above each chart lists the averaged weather elements maximum, minimum and mean daily temperature (in °C), relative humidity (in %), cloudiness (in octas), absolute sunshine duration (in hours), and precipitation (in mm) for each class, followed by its anomaly (deviation from the weighted mean of that element for that particular class) and its root mean square error. Furthermore, the frequency of occurence of each class is given. Data cover the period 1966-1993. See Table 1 for comparing the reduction of variance for each weather element.



SUMMER

Fig 4: Composite 1000 hPa geopotential charts for Central and Western Europe **SUMMER (June-July-August)**. Classes selected represent cold (4a), warm (4b), average temperature (4c), wet (4d), dry (4e) and average humidity (4f) weather situations for Northern Germany (below 500m elevation, excluding the coastal zones of the Baltic and the North Sea). Isoline spacing is 4 gpm. The table above each chart lists the averaged weather elements maximum, minimum and mean daily temperature (in °C), relative humidity (in %), cloudiness (in octas), absolute sunshine duration (in hours), and precipitation (in mm) for each class, followed by its anomaly (deviation from the weighted mean of that element for that particular class) and its root mean square error. Furthermore, the frequency of occurence of each class is given. Data cover the period 1966-1993. See Table 1 for comparing the reduction of variance for each weather element.

A COMPARATIVE ANALYSIS OF PRINCIPAL COMPONENT ANALYSIS AND BISERIAL CORRELATION TECHNIQUE TO SPECIFY PRECIPITATION

Nora E. Ruiz and Walter M. Vargas

Department of Atmospheric Sciences
University of Buenos Aires. Argentina

ABSTRACT

In this work, PCA is applied to identify 500 mb patterns associated with local precipitation and compared to those obtained by using biserial correlation fields. The purpose is to examine the skill of both techniques to discriminate precipitating weather conditions.

First, to address the need for a better pattern classification, PCA was carried out in s-mode to visualize possible similarities by regions by means of this technique in relation to precipitation occurrence. Then, biserial correlation fields between 500 mb relative vorticity and precipitation as a binary variable are evaluated and compared with eigenvectors and principal components results. The two different schemes are tested to determine if the individual loading fields would yield comparatively similar information in terms of precipitation. This is accomplished by quantitatively comparing the differences in the resulting probabilities of precipitation and their associated distributions.

Based on the examination of the information in terms of precipitation given by PC and biserial correlation solutions, the spatial patterns of the latter are meaningful and enhance physical interpretability, whereas the PC solutions lack synoptic meaning and effectiveness.

1 INTRODUCTION

Objective synoptic climatological methods to identify homogeneous weather types and precipitation situations may be used in forecast problems (Lorenz, 1956; Lund, 1963; Yarnal and White, 1987). The choice of the predictor selection method is often dependent upon objectives of the synoptic study. In this work, the predictand variable is the occurrence or non-occurrence of precipitation in a given locality. So, the methodologies applied for this goal should maximize differences between groups of local occurrence of this phenomenon and groups related to non-occurrence. Our purpose is to evaluate the results of two different selection procedures as applied to daily probability of precipitation since different methods yield highly diverse results (Kalkstein et al, 1987).

Firstly, the methodology that requires the application of Principal Component Analysis to reduce the original data by representing them in fewer than the initial number of variables while retaining most of the information will be utilized (Lorenz, 1956; Ehrendorfer, 1987). Secondly, the biserial correlation technique used to identify the grid-points or regions that better separate the precipitation and non-precipitation groups (as a binary variable) will be applied to the same dataset (Barry and Perry, 1973; Ruiz and Vargas, 1993).

In order to compare both methodologies, the discriminant functions (Miller, 1962) obtained taking into account the best predictors coming from both methods will be examined to determine which set of predictors is most synoptically meaningful in terms of probability of precipitation, and, additionally, a determination will be made regarding the selection procedure which produces the best results.

2 DATA

Data used are 500 mb geopotential heights from ECMWF analyses covering the period January 1983 to December 1985, for the South American region between 15°S and 70°S, and 120°W and 20°W. The derived variable relative geostrophic vorticity was evaluated and utilized in this study. In order to take into account the seasonal cycle, the total sample was stratified in six cool months and six warm months. Daily precipitation data of three stations in Buenos Aires are also used. The precipitation event is defined as the occurrence of ≥ 0.1 mm of average precipitation at the three stations in a 24-h period (from 12Z day i to 12Z day i+1).

3 RESULTS

Principal Component Analysis

PCA is a frequently used technique to extract useful information from fields that may be then utilized as predictors in a regression scheme (Baptistan, 1989).

Eigenvalues λ and their corresponding explained variances produced by the 500 mb relative vorticity winter fields (943 grid-points and 552 days) are shown in the following table:

	λ	Variance (%)	Accumulated Variance(%)
1)	41.6	4.4	4.4
2)	39.5	4.2	8.6
3)	35.2	3.7	12.3
4)	32.9	3.5	15.8
5)	30.8	3.3	19.1
6)	26.1	2.8	21.9
7)	23.5	2.5	24.4
.	.	.	.
.	.	.	.
.	.	.	.
100)	1.9	0.2	86.4

Based on these results, there is obviously no λ which explains a significant part of the total variance and more than a hundred eigenvectors would be necessary to represent the fields rather satisfactorily.

The main associated factor loadings are illustrated in Figs. 1a, 1b and 1c.

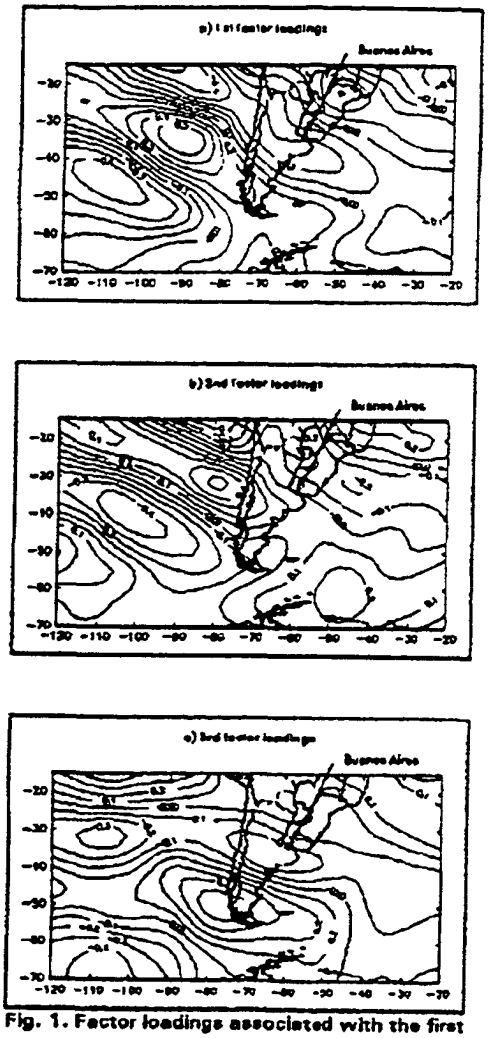


Fig. 1. Factor loadings associated with the first component (4.4%), a), with the second component (4.2%), b), and with the third component (3.7%), c).

The patterns shown in these figures indicate the regions correlated with the respective factor scores or principal components. But it should be noted that the percentage of the total variance accounted for by each pattern is very low.

As the PC representation allows us to describe the temporal evolution of this meteorological field, the first three PC will be chosen as predictors.

Biserial Correlation Technique

Biserial correlation fields (Panofsky and Brier, 1965) between 500 mb vorticity fields and rainfall in Buenos Aires are evaluated to determine regions or grid-points where the contributions of this dynamic variable to precipitation are significant (Ruiz y Vargas, 1993). The pattern obtained is displayed in Fig. 2.

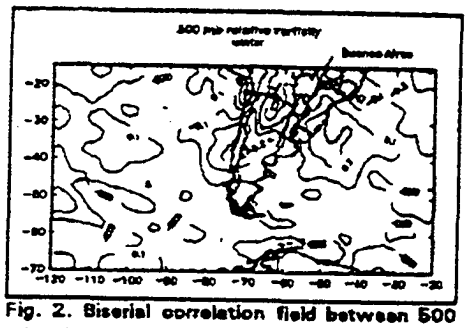


Fig. 2. Biserial correlation field between 500 mb relative vorticity and precipitation in Buenos Aires, during winter.

Biserial correlation coefficients higher than 0.17 are statistically significant to the confidence level of 99%. In this case, the "best" grid-points, that is to say: vorticity at 37.5°S,72.5°W (on the cordillera de los Andes), at 35°S,50°W (in the Atlantic ocean), and at 20°S,70°W (in the north of Chile), are selected as predictors.

Comparative Analysis

As it is known, Multiple Discriminant Analysis (Miller, 1962) is a linear statistical technique that calculates the probability that a forecast predictand will fall into a particular class. It is thus ideally suited to the two category problem of precipitation and non-precipitation. By means of MDA applied to each set of selected predictors and the precipitation as predictand perfomances of both solutions are tested. In both cases the developing sample is used.

To visualize to what extent the discriminant function (Y) separates occurrence from non-occurrence groups in each case, frequency distributions of Y are calculated.

Relative frequency distributions of Y based on PC solutions and on selected grid-points (biserial correlation-based method) are shown in Figs. 3 and 4, respectively. Each interval is 0.00018 wide. Every distribution is gaussian. As the separation of the means (yes/no precipitation) is the fundamental signal detection index of discrimination, their difference is tested by means of t-Student statistic (critical value: 2.58, to 1%), whose values are 4.8 (Fig. 3) and 9.2 (Fig. 4). Accordingly, it is observed that the second solution reveals a better skill to discriminate precipitation. Additionally, the biserial correlation coefficient between Y and the precipitation event is 0.27 in the first experiment, and 0.48 in the second one.

It is also convenient to describe the quality of the forecast estimations (in a categorical way) throgh contingency tables.

For the first approach:

	Forecast	
Observed	yes	no
yes	59%	41%
no	42%	58%

For the second approach:

	Forecast	
Observed	yes	no
yes	65%	35%
no	30%	70%

The association coefficient $\underline{a}$ (Panofsky and Brier, 1965)
for each table are 0.17 and 0.35, respectively ($\underline{a}$ equals 0 for no association, and 1 for perfect association). The values of percentage correct are 58% and 68%, respectively.

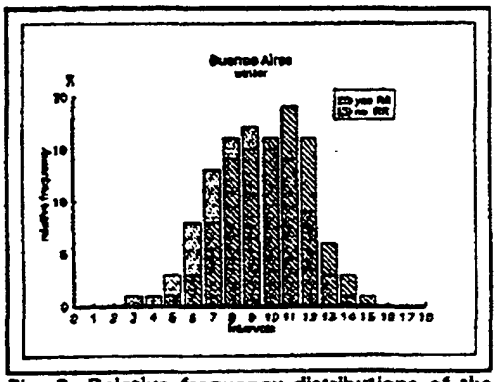


Fig. 3. Relative frequency distributions of the discriminant function Y for occurrence and non-occurrence of precipitation in Buenos Aires during winter, using PC predictors.

4 CONCLUSIONS

The comparison between two different selection schemes, one based on the principal component method and the another one on the biserial correlation technique, as applied to daily probability of precipitation and their associated distributions is performed. The results show that equations developed on specific grid-points were significantly better. In spite of the information comes from only one meteorological field, 500 mb relative vorticity fields), it is, however, interesting to note that PCA method doesn't necessarily resume the best results. It may be concluded that the biserial correlation-based technique may be considered most efficient when

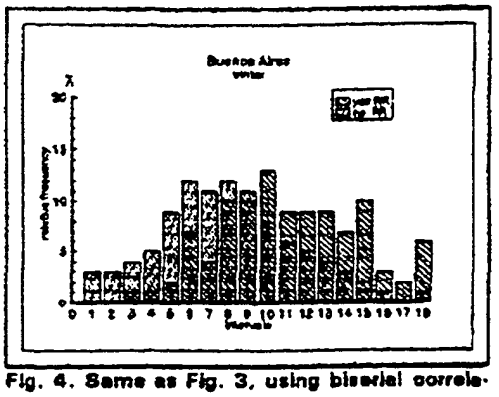


Fig. 4. Same as Fig. 3, using biserial correlation-based predictors.

dealing with identifying predictors of occurrence of precipitation. By introducing predictors selected using the latter scheme, we tried to take into account physical relationships between predictand and predictors such as position and intensity of cyclonic and anticyclonic disturbances in 500 mb, vorticity advection and vorticity gradients indicating strong winds in the middle troposphere. They proved to be informative in spite of they were not selected by usual procedures. PC solutions lack synoptic meaning and effectiveness as applied to this experiment.

References

Baptistan, P., 1989, "Application de l'Analyse en Compo-santes Principales pour la prévision du cycle diurne de la température par adaptation statistique des sorties du modèle dynamique PERIDOT", Note de travail du CRMD, N°6, pp 85.

Barry, R.G. and Perry, A.H., 1973, "Sinoptic Climatology: Methods and Applications", Methuen and Co. Ltd., London.

Craddock, J.N. and Flood, C.R., 1969, "Eigenvectors for representing 500 mb geopotential surface over the Northern Hemisphere", Quart. J. R. Met. Soc., 95, 576.

Ehrendorfer, M., 1987, "A regionalization of Austrias's precipitation climate using Principal Component Analysis", J. Climatol., 7, 71-89.

Lorenz, E. N., 1956, "Empirical orthogonal functions and statistical weather prediction", Cambridge, M.I.T., Department of Meteorology, Scientific Report N° 1.

Lund, I.A., 1963, "Map-pattern classification by statistical methods", Journal of Applied Meteorology, 2, 56.

Miller, R.G., 1962, "Statistical Prediction by Discriminant Analysis", Meteorological Monographs, AMS, 4, N°25.

Panofsky, H.A. and Brier, G.W., 1965, "Some Applications of Statistics to Meteorology", The Pennsylvania State University, Pennsylvania.

Ruiz, N.E. and Vargas, W.M., 1993, "Estudio de diagnóstico sinóptico de la precipitación de Buenos Aires en base a análisis de 500 mb del ECMWF", METEOROLOGICA, 18, 3-12.

Ruiz, N.E. and Vargas, W.M., 1994, "Ensayo de pronóstico objetivo de probabilidad de precipitación en Buenos Aires en base a análisis de 500 mb del ECMWF", METEOROLOGICA, 19, 3-12.

Yarnal, B. and White, D.A., 1987, "Subjectivity in a computer-assisted synoptic climatology I: Classification results", J. Climat., 7, 119-128.

CORRESPONDING AUTHOR

Nora E. Ruiz

Dpto. Ciencias de la Atmósfera, Univ. de Buenos Aires

Ciudad Universitaria, Pab. II, 1428, Buenos Aires ARGENTINA. e-mail: ruiz@meteor.uba.ar

Downscaling GCM information to regional scales: A non-parametric multivariate regression approach

João Corte-Real, Xuebin Zhang and Xiaolan Wang
Department of Physics, University of Lisbon, Lisbon, Portugal

ABSTRACT

Multivariate Adaptive Regression Splines (MARS) was used to relate observational SLP anomalies over Euro-Atlantic and wintertime monthly rainfall in Portugal; possible anthropogenic changes of rainfall were estimated by using a GCM simulated SLP. The MARS model was fitted and tested with two different 45-year data sets. Though GCM control simulation successfully reproduced main features of large-scale circulation, the observational relationship between SLP and rainfall was not well preserved. In a 54-year experiment, rainfall of statistical estimation and the relevant direct GCM output possess similar multi-annual variation and a reduction tendency; however, there are substantial differences regarding details.

1. INTRODUCTION

The impact of climate change manifests itself in natural and social environments, which vary widely from place to place. For this reason, it is crucially important to understand climate change on a local basis. Although no one can predict future climate, nevertheless, it is possible to estimate possible outcomes of how the climate system will respond to changes in atmospheric composition, especially the increasing of greenhouse gases. The state-of-art General Circulation Models (GCMs) simulate large-scale circulations in a realistic manner and it is believed that they are adequate tools to predict future large-scale circulation. However, in GCMs, local parameters, such as rainfall, are dependent on subgrid-scale processes, which are treated by the so-called parameterization schemes; thus it is very difficult to estimate the impact of climate change on the local scale without an adequate tool to relate GCM output to local climate. Various methods have been developed to scale down GCM simulated large-scale information to regional parameters (e.g. Karl *et al.* 1990; Wigley *et al.* 1990; Giorgi 1990; von Storch *et al.* 1993); some of them have even been incorporated in ecosystem models (Gyalistras *et al.* 1994).

We propose in this study a strategy which utilises a non-parametric mutilvariate regression technique, the Multivariate Adaptive Regression Splines (MARS) (Friedman 1991), to examine the relationship between wintertime rainfall in Portugal and mean sea level pressure over North Atlantic-Europe. This relationship is then used to downscale GCM simulated large-scale information to deduce possible anthropogenic changes of rainfall in the region.

2. DATA AND STRATEGY

2.1 Observational data

In this study two kinds of observational data were used: (1) monthly rainfall series of 8 stations well covering Portugal (see Fig. 1) for the period 1901-1991 (91 years); (2) monthly mean sea level pressure field series (SLP) with 264 5°×5° longitude-latitude grid-points covering the sector 85°W-30°E and 20°N-70°N. The SLP data were calculated from two daily data sets provided by NCAR: one covers the period from January 1946 to August 1992 with few gaps being filled by linear interpolation; another covers the period from January 1900 to August 1944; for this data set, monthly mean values were computed as the mean of all observed daily values at a grid in the month if there are more than 20 observations; otherwise SLP is treated as missing; missing values were then interpolated with nearest grid values.

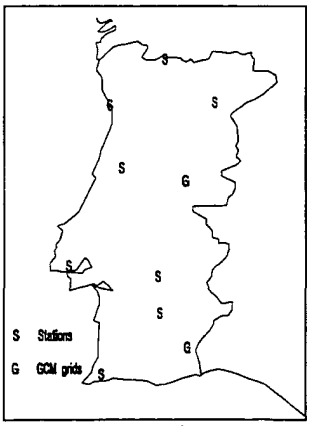


Fig. 1 Locations of stations and GCM grids for rainfall data.

2.2 GCM output

This study makes use of results from the Hadley Centre's High Resolution GCM Transient Experiment (UKTR) which was performed with a coupled Atmosphere-Ocean General Circulation Model (AOGCM). The reference climate was obtained by a 75-year control integration with a constant CO_2 concentration of 323 ppmv. In the perturbed simulation, the atmospheric concentrations of CO_2 were allowed to rise by 1% per annum (compound), resulting in a double after 70 years (Hadley Centre 1992). Monthly mean sea level pressure, temperature and monthly rainfall data for a 75-year period of both control and perturbed simulations were kindly provided by Climate Impacts LINK Project.

The perturbed run data goes from January, year 1 to August, year 75 of the experiment. Since there are 49 missing months in the first 20 years, only the data for the period from January of year 21 to December of year 74 (54 years) were employed in this study. The control run data starts in September, year 50 and ends in August Year 125 of the experiment. In order to infer the atmospheric response to the increasing of CO_2, only the last 54 years (January of year 70 to December of year 124) of control data were used. One missing month was linearly interpolated in time. The area means of monthly rainfall over Portugal were taken from the means of respective values at two grid points located in the country (see Fig. 1). The SLP data were linearly regrided to 5°×5° latitude-longitude from the original grids and extracted for the same sector as the observed SLP. According to Viner *et al.* (1994), it is assumed that the last 54 years of transient run, which were used in this study, correspond to the period from year 2010 to 2065.

2.3 Strategy

MARS is a newly developed non-parametric mutivariate regression method. To our knowledge, it has not been widely used in the field of climatology. Various mutivariate regression methods, such as linear regression or threshold regression are subsets of MARS model. Detailed descriptions about MARS can be found in Friedman (1991). Friedman's MARS 3.5, available from statlib, was used in the work reported here.

Principal component analysis (PCA), a powerful and effective tool for extracting large-scale circulation patterns and for reducing the dimensionality of large climatic data set, has been widely used (e.g. Kutzbach 1970; Corte-Real et al. 1994). In order to ascertain large-scale circulation features over the North Atlantic-Europe and to reduce the number of variables to be used as predictors in MARS model, PCA was first applied to observed wintertime monthly SLP deviation field-series for the period 1946-1991. Thus the predictors in the MARS model are the first few principal components (PCs) which account for most part of the variance of SLP and are the most important factors controlling the winter rainfall; the predictand is the area mean wintertime monthly rainfall in Portugal. The stability of observed large-scale circulation patterns and the ability of the GCM in simulating these features was evaluated by performing PCA on wintertime SLP for the period 1900-1943 and on GCM simulated SLP.

The observational data of both rainfall and SLP for the period 1946-1991, which we shall call reference data, were used to calibrate the MARS model; the stability of the MARS model was confirmed by fitting 1000 randomly resampled subsets of the reference data with sampling length of 125. The prediction skill of the model can be demonstrated by its ability to reproduce the wintertime rainfall for 1900-1943. Possible changes in wintertime rainfall in Portugal were assessed by comparing the rainfall series obtained from GCM control and perturbed runs, as well as from applying the statistical model to SLP anomalies of GCM perturbed simulation.

3. LARGE-SCALE CIRCULATION ANOMALIES OVER ATLANTIC-EUROPE AND PRECIPITATION ANOMALIES IN PORTUGAL

3.1 Wintertime EOFs of SLP over Atlantic-Europe

The total variance explained by the first six PCs of wintertime (Dec., Jan. and Feb., hereafter denoted as DJF) SLP for the periods 1946-1991 and 1900-1943 are 89.2% and 88.2%, respectively. The spatial structures of the first two Empirical Orthogonal Functions (EOFs) for one period are very close to those in the other period, and are also in good agreement with previously published results (Glowienka-Hense 1990). Besides, the EOFs of orders 3, 4, 5, 6 and their variance fractions in one period are also close to those in the other period. In order to show how close the EOFs in one period are to those in the other period, the correlations between the first six PCs for the period 1900-1943 and the projections of SLP field-series for 1900-1943 onto the corresponding EOFs relative to the period 1946-1991 were calculated. It was found that they are highly correlated with correlation coefficients between 0.995 and 0.861 (sample length 129). Thus it can be concluded that differences of large-scale circulation patterns in the two periods are not significant, though their corresponding time amplitudes may vary in a wide range. Clearly, the first six observed patterns of SLP are most suggestive of the main characteristics of large-scale circulation over the Atlantic-Europe, as they were also reproduced in the period 1900-1943, and thus their associated principal components were retained as predictors for the subsequent statistical modelling.

3.2 Statistical reconstruction of area mean rainfall for Portugal in this century

The wintertime (DJF) observations for the period 1946-1991 (135 samples) of both rainfall and SLP data were used to calibrate the MARS model. As can be seen in Fig. 2, MARS fits the data quite well.

The prediction skill of the above constructed MARS model can be tested by comparing its predictions of the area mean rainfall for the period 1901-1943 with in situ observations. To accomplish this, the monthly SLP anomalies in wintertime for the period 1901-1943 were obtained by subtracting the relevant climatological mean, calculated from the period 1946-1991, from the SLP series; then this field-series of SLP anomalies was projected onto the first six EOFs of DJF SLP for 1946-1991; the resulting time series (PCs) were finally used as predictors in the MARS model to estimate the area mean rainfall for the period 1901-1943. As shown in Fig. 2, the time evolution in both curves are highly coherent, with an correlation coefficient of 0.77 (sample size=129), although a slight overestimation of rainfall can be found in the period 1910-1930.

The stability of the MARS model was also tested as follows: 1000 subsets with sample length of 125 were randomly drawn from the reference data sets (both SLP and rainfall); MARS model was fitted to each of the subsets; the correlations between estimated and observed rainfalls were calculated; the 100 best-fit models (100 highest correlations) were used to estimate rainfall for 1901-1943. The average

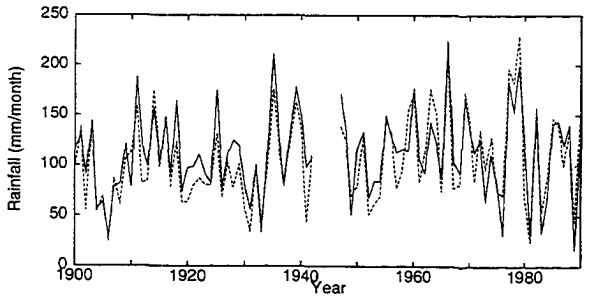


Fig. 2 Area-averaged winter mean rainfall (mm/month) calculated from observations at 8 station (dashed lines) and derived from SLP data (solid lines) by using MARS model. The statistical model was constructed by using the data for the period 1946-1991.

of estimations of rainfall from these 100 MARS models were then calculated as another estimation for the period. It was found that there is no significant difference between this estimation and the reconstruction from the MARS model based on the full reference data sets (not shown). Thus it can be concluded that the MARS model constructed by using the full reference data set is indeed stable.

The successful reconstruction of 90-year wintertime monthly rainfall from the first six PCs of SLP indicates that these PCs and their associated spatial structures effectively capture the characteristics of large-scale circulation of the atmosphere which are directly responsible for the variations of wintertime rainfall in Portugal.

4. DOWNSCALING GCM OUTPUT TO REGIONAL SCALE

4.1 Control simulation

The annual cycle of rainfall in control run roughly agrees with the observational one. There are, however, major differences with respect to details. The simulated rainfall in almost all months are overestimated, except for October and November when it is too small.

A fundamental assumption in down-scaling GCM large-scale information into regional scale is that the GCM simulated large-scale circulation is credible. Thus, it is of interest to ascertain whether GCM simulation reasonably reproduces the main features of large-scale circulation. For this purpose, PCA was performed on the wintertime SLP of the last 46-year control simulation. It was found that the first two observed patterns are similar to the first two simulated ones respectively; the 3rd, 4th, 5th, 7th simulated patterns respectively resemble the 3rd, 5th, 4th, 6th EOFs of the relevant observations. The total variance explained by the associated six EOFs account for 90.1%. The first few PCs in the control simulation are also highly correlated with the projections of SLP field-series in the control run, onto the observed first few EOFs of observed SLP. The correlation coefficients are between 0.975 and 0.725 (sample length 138). Thus, it can be concluded that the GCM control simulation has successfully reproduced the main features of large-scale circulation patterns over the Atlantic-Europe; if taking into account the fact that EOFs are subject to significant sampling variabilities, the difference between GCM simulated patterns and observed ones are possibly within the sampling uncertainty.

Another important point in trying to assess the possible changes in regional rainfall with the help of GCM simulated large-scale information is the relationship between large-scale circulation and regional rainfall. An estimation of wintertime precipitation was made by using the projections of simulated SLP onto the first six EOFs of the reference SLP (observations) as the input to the MARS model. The output of the model shows a quite different time evolution from that of the rainfall directly obtained from the GCM, though their interannual variabilities are similar (Fig. 3). This indicates that the relationship between SLP and rainfall in observed climate is not well reproduced by the GCM control simulation on intra-annual scales. Hulme et al. (1993) also reported that the relationships between model circulation regimes and model surface climate variables do not always reproduce those observed in reality. But does the GCM produces an internally stable relationship between SLP

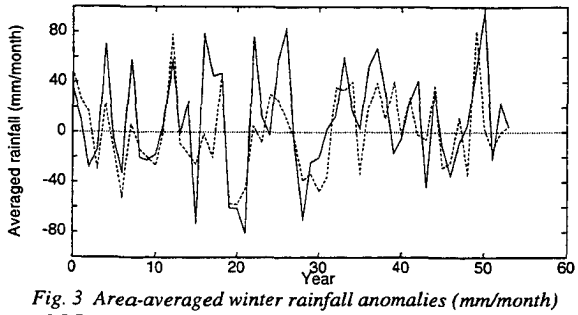


Fig. 3 Area-averaged winter rainfall anomalies (mm/month) of GCM control simulation as derived from GCM simulated rainfall (dashed line) and as derived from GCM simulated SLP field (sold line) using the relationship between rainfall and SLP in observed climate.

and rainfall which is different from the observed climate? In order to answer this question, the 54-year control data were split into two equal parts. The first five PCs and the 7th PC of GCM simulated SLP (their associated spatial structures are similar to the first six EOFs of the reference SLP, as discussed before) were used as predictors, and the mean of rainfalls at the two grids as the predictand. MARS model was set up by using one half of the data in control run, and then employed to estimate the rainfall in the other half of the period. The model fits the data quite satisfactorily, and interannual variability is also predicted, but smaller time scale variations may be out of phase (not shown) relative to those in the testing data set. In this experiment, both the PCs directly

obtained from the GCMs SLP and those obtained from projecting GCM's SLP onto the reference EOFs were used. It seems that the relationships between large-scale circulation and regional rainfall in the GCM control simulation is not as strong and stable as those in the observations.

4.2 Possible changes in wintertime rainfall over Portugal

a). Information directly provided by GCM

The climate model does not simulate the present climate perfectly. However, the simulated changes from the present to future climate, which we are more interested in, may be more reliable than the simulations themselves for either the present or future since the state-of-art GCMs do provide a good representation of the large-scale circulation of the atmosphere. A reduction of rainfall in all months of year except August and September was found. In wintertime, the mean reduction of monthly rainfall is 16.9 mm in 54 years, accounting for 11.5% of the relevant long-term mean in control simulation. A comprehensive comparison of the statistical characteristics of the GCM simulated rainfall in the control run with those in the perturbed run may provide a better perspective in this regard. One method of making this comparison is the quantile-quantile (q-q) plot which is an extremely effective method of comparing the distributions of two variables. Here, the q-q plot is actually a plot of a data value in the control run versus a specific data value in the perturbed run which corresponds to the same percentage in their relevant cumulative frequency distributions. The 54-year GCM monthly rainfall both present (control run), and future (perturbed run) climates are ranked for all calendar months; the largest value in the perturbed run is then plotted against the largest one in the control run and the second largest value in the perturbed data against the second largest one in the control data, and so on. If the distributions of rainfall in control and perturbed runs were identical, the q-q plot would be a straight line, with slope equal to one, crossing the origin. Fig. 4 shows q-q plots of control against perturbed data for three winter months. It seems that the way rainfall changes may be quite different in different calendar months. The q-q plots for February, December are parallel to and below the line of identical distributions (except very few points near or higher the line), indicating that there is a systematic reduction of rainfall in perturbed simulation for those months, but no evident changes in central tendency. The reduction in long-term mean of January rainfall is mainly caused by the systematic decrease of normal precipitation events; the increase of rainfall for larger precipitation events is also apparent, which amplifies the range of rainfall variation for the month.

b). Information indirectly obtained from GCM simulated large-scale circulation

The variability of SLP over the Atlantic-Europe, which is directly responsible for variations of wintertime rainfall in Portugal, has been reasonably well simulated by the GCM. A natural way to infer the possible anthropogenic changes in rainfall is to apply the strong and stable relationship between rainfall and SLP in observed climate, represented by MARS model, to the GCM simulated SLP. To do this, the differences between perturbed run GCM's SLP and long-term means of control run SLP were projected onto the first six EOFs of the reference SLP; these projections were then used as MARS input to estimate possible changes in wintertime rainfall. Fig. 5 shows the resulting rainfall anomaly curve, together with the mean anomalies of GCM rainfall at the two grid-points for Portugal; a 5-year moving average filter has been applied to both curves.

The two curves vary coherently on multiannual scale, as shown in Fig. 6, but their amplitudes differ. Differences exist in the estimations of future changes in wintertime rainfall: the statistical model estimates monthly rainfall reductions of 19.0 mm, 23.8mm and 5.1mm in 54 years for December, January and February, respectively; while relevant GCM direct estimations are 20.9mm, 9.6mm and 20mm; however the mean rates of change in wintertime monthly rainfall are in relatively good agreement (16.0 mm and 16.9 mm per 54-year for statistical model and GCM estimation respectively).

For climatic change impact studies, not only changes in means, but in the distribution itself as well are important. The observed distributions of rainfall for three wintertime months (DJF) in last 54-year were therefore compared with the MARS model estimations. The model estimation of rainfall is the sum of the MARS model estimated anomalies and long-term mean of rainfall in the last 54-year for the corresponding calendar months. Q-q plots for observations against model estimations for three wintertime months are shown in Fig. 6. In different winter months, the possible changes of rainfall distribution are quite different: there is a systematic change in January; reductions in December and February are mainly caused by the decrease of larger rainfall events.

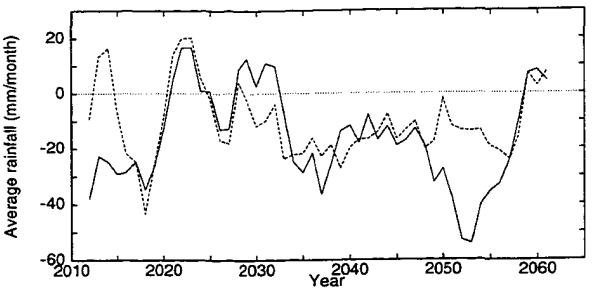


Fig. 5 Possible anthropogentic changes of winter rainfall for Portugal as derived directly from rainfall values at two grids in UKTR (dashed line) and as indirectly derived from the GCM simulated SLP field with the statistical model (solid line). 5-year moving average filter was applied to both curves.

5. DISCUSSION AND CONCLUSIONS

The relationship between large-scale circulation features (SLP) over North Atlantic-Europe and the wintertime rainfall in Portugal has been examined and applied to assess possible changes in wintertime rainfall caused by increasing the concentration of greenhouse gases in the atmosphere, based on a GCM simulated circulation. The stability of this relationship was tested by fitting a statistical model to each of 1000 randomly resampled subsets. It was demonstrated the MARS model is able to reproduce satisfactorily, from the observed SLP distributions, the wintertime rainfall in Portugal in this century. This study draws some important conclusions, respecting the methodology of downscaling GCM information to regional scale and to the possible anthropogenic changes of rainfall in Portugal.

The statistical approach proposed in this paper is formally similar to Karl et al. (1990) and Wigley et al. (1990), and close to Storch et al. (1993). Karl et al. (1990) used local free-atmosphere parameters, Wigley et al. (1990) used area averages; both established the relationship between local and regional-scale (some grid point values) climates. Different from these two approaches, Storch et al. (1993) chose a parameter representing the large-scale flow variability or principal components to relate regional parameters for different sites, by searching optimal linear correlations between the two fields, with canonical correlation technique. We related large-scale flow variability to area mean rainfall with nonparametric multivariate regression method, allowing not only the linear relationship, but non-linear interactions as well, to be established between the predictors and predictand. Comparing with the step-wise regression technique, it can not only select the most relevant predictors into the model, but also provides the information regarding the importance of each predictor; besides, the model also delivers the possibility for considering non-linear relationships. The advantages of this strategy are apparent; first of all, it is technically very simple; second, it offers certain confidence in the context of consistence with observations, and third, it may be used for a wide range of parameters, such as temperature, precipitation, or discharge in rivers and even economic parameters. However, this method is not without limitation: it can only be used if the local parameters bear a strong relationship with the large-scale circulation, and one can not be sure if the relationship between predictand and predictors will still be valid beyond the range of model fitting.

The change of wintertime monthly rainfall in Portugal directly simulated by UKTR at two grid points is about -16.9 mm in a 54-year period (approximately equivalent to years 2010-2065), whereas the change estimated by the MARS method is about -16 mm in the same period. Both the UKTR direct output and the empirical estimation possess similar interdecadal variation. This result is consistent with what is reported by Storch et al. (1993), who showed a decrease of 7 mm per 100 years (statistical model) and 9 mm per 100 years (GCM) in Iberian wintertime monthly rainfall by using a 100-year transient simulation undertaken at MPI (Cubasch et al. 1992) with greenhouse emission rate of IPCC. It should be noted that, when running in transient mode with similar greenhouse emission rates, both the UKTR and MPI models

show marked reduction of rainfall in Portugal in both their direct output and the relevant empirical estimations, although the two models not only have different spatial resolutions but some other different details. This shows the possible direction of anthropogenic changes of wintertime rainfall in Portugal in the perturbed future climate. It also indicates that both transient simulations (UKTR and MPI) yielded similar SLP structures and variations. It should also be noted that the reliability of the results presented in this paper regarding the future changes of rainfall in Portugal is highly dependent on the reliability of GCM simulated large-scale circulation changes; with the improvement of current climate models, our uncertainty in this respect will greatly be reduced.

ACKNOWLEDGEMENTS

This work was supported mainly by CEC under the contracts EV5V-CT94-0510 and EV5V-CT92-0164, partly by JNICT, Portugal, under the contract PEMA/C/CVC/12/91. The GCM data were supplied by the Climate Impacts LINK Project (UK Department of Environment Contract PECD7/12/96) on behalf of the UK Meteorological Office and Dr. David Viner of Climate Research Unit kindly extracted the GCM data. The authors are grateful for the Instituto Nacional da Águe, Portugal, who kindly provided rainfall data.

REFERENCES

Corte-Real, J., Wang, X., Zhang, X, 1994, "Modes of variability in northern hemisphere's mid-tropospheric large-scale circulation", Theor. Appl. Climatol., in press.

Cubasch, U., Hasselmann, K., Höck, H., Maier-Reimer. E., Mikolajewicz, U., Santer, B.D., Sausen, R., 1992, "Transient greenhouse warming computations with a coupled ocean-atmosphere model", Clim. Dyn. **8**, 55-69.

Friedman, J.H., 1991, "Multivariate adaptive regression splines", Annals of Stat. **19**, 1-141.

Giorgi, F., Marinucci, M.R., Visconti, G., 1990, "Use of a limited-area model nested in a general circulation model for regional climate simulation over Europe", J. Geophys. Res. **95**, 18413-18431.

Glowienka-Hense, R., 1990, "Performance of the ECMWF T21 model in simulating the North Atlantic Oscillation in the Atlantic-European SLP field", Tellus **42A**, 497-507.

Gyalistras, D., von Storch, H., Fischlin, A., Beniston, M., 1994, "Linking GCM-simulated climatic changes to ecosystem models: case studies of statistical downscaling in the Alps", Climate Research, **4**, 167-189.

Hadley Centre, 1992, "The Hadley Centre Transient Climate Change Experiment. Hadley Centre", Bracknell, UK, 20pp.

Hulme, M., Briffa, K.R., Jones, P.D., Senior, C.A., 1993, "Validation of GCM control simulations using indices of daily airflow types over the British Isles", Clim. Dyn. **9**, 95-105.

Karl, T.R., Wang, W.C., Schlesinger, M.E., Knight, R.W., Portman, D., 1990, "A method of relating general circulation model simulated climate to observed local climate. Part I: Seasonal statistics", J. Clim. **3**, 1053-1079.

Kutzbach, J., 1970, "Large-scale features of monthly mean northern hemisphere anomaly map of sea level pressure", Mon. Wea. Rev., **98**, 708-716.

Viner, D., Hulme, M., 1994, "Construction of climate change scenarios for the British Isles from GCM transient climate change experiments. Technical note, No.5, prepared for the UK Dept. of Environment", CRU, Norwich, UK.

von Storch, H., Zorita, E., Cubasch, U. 1993, "Downscaling of global climate change estimates to regional scales: An application to Iberian rainfall in wintertime", J. Clim. **6**, 1161-1171.

Wigley, T.M.L., Jones, P.D., Briffa, K.R., Smith, G., 1990, "Obtaining subgrid scale information from coarse-resolution general circulation model output", J. Geophys. Res., **95**, 1943-1953.

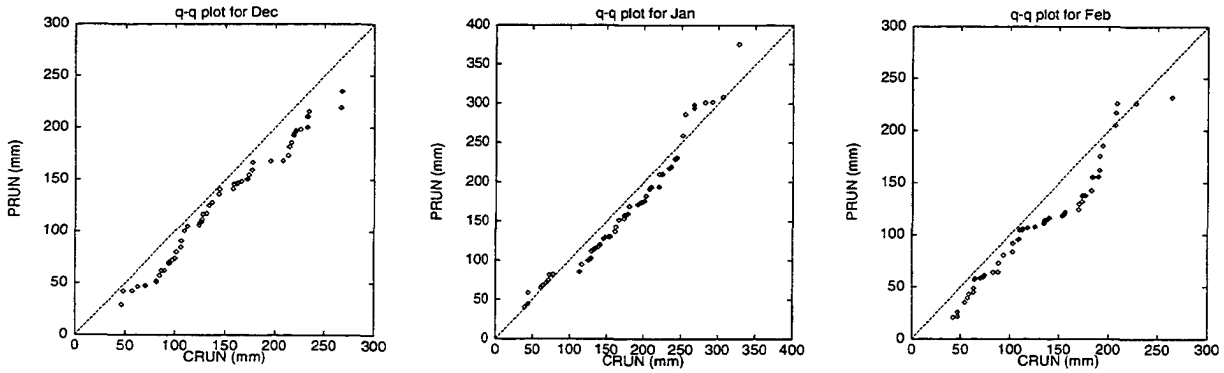


Fig. 4 Quantile-quantile plots of area-averaged winter rainfall for Portugal from GCM control (CRUN) and perturbed (PRUN) simulations.

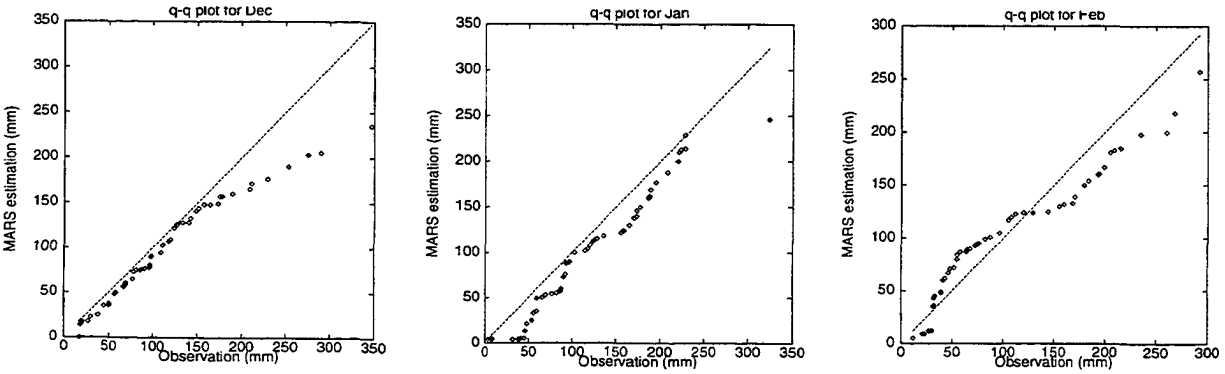


Fig. 6 Quantile-quantile plots of area-averaged winter rainfall: Observations in last 54-year against statistical model derived future rainfall from SLP of GCM perturbed simulation.

Intra-seasonal Oscillations and Associated Spatial-Temporal Structures of Precipitation over China

Xiaolan Wang, João Corte-Real and Xuebin Zhang

Department of Physics, Faculty of Sciences, University of Lisbon, Portugal

ABSTRACT

Based on field series of daily rainfalls in eastern China, intra-seasonal oscillations of the monsoonal precipitation and the associated *spatial-temporal structures* were explored by performing multi-channel Singular Spectrum Analysis. Three oscillations with periods of 43, 21 and 13 days were found to be robust and independent. The spatial-temporal structures, i.e. the propagations of rainfall anomalies, associated with these quasi-periodicities are presented. Also, some information about the amplitudes and seasonalities of these oscillations is provided by using composite analysis. Interestingly, the quasi-20 day oscillation is associated with the transition process between the first two dominant regimes of the monsoonal rainfall.

1. INTRODUCTION

The East Asian Monsoon circulation possesses a wide range of spatial and temporal scales of variability; and so does the monsoonal rainfall. There have been many studies on rainfall variability over China, based on various data sources and using different methods, including Principal Component Analysis (PCA); in the intra-seasonal scale, strong signals of the 30-60 days, 20 days and biweekly oscillations have been found in southern to central China, but reportedly they need to be confirmed (Lau, 1988; Lau, 1992; Yihui, 1994). Also, there is still little knowledge about the *spatial-temporal structures* of the intra-seasonal oscillations of precipitation over China. The main purpose of this study is to provide a more complete description of the spatial-temporal structures of oscillatory variability of precipitation over China.

2. DATA AND PROCEDURES

Based on a data set of daily rainfall series for 122 stations well covering eastern China (east of 97°E), for a period of 30 years (1953-1982), field series of 5-day rainfall totals and 2-day mean rainfalls (183 samples per year) were sampled. To detect the potential intra-seasonal oscillations and, furthermore, to explore the *spatial-temporal structures* of these oscillations, multi-channel Singular Spectrum Analysis (mcSSA) was adopted here. For detailed descriptions of mcSSA, readers are referred to the papers of Plaut and Vautard (hereafter PV; 1994) or Corte-Real and Wang (hereafter CW; 1994).

First of all, to extract the permanent annual cycle and its harmonics, mcSSA with a window length of 74 pentads (M = 74) was carried out on the field-series of 5-day rainfall total. Besides the annual cycle (365 days) and its second and third harmonics (182 and 120 days), which were isolated respectively as oscillatory pairs 1-2, 3-4 and 5-6, strong signals with periodicities in the range 13-70 days were also found (see Table 1). The spatial-temporal structures of the annual cycle and its harmonics will be discussed later in section 3.

Since mcSSA is typically successful in isolating oscillations with periods in the range [M/5, M] (Vautard et al., 1992a), a shorter window length is needed for a better localisation of intra-seasonal oscillations. Therefore, to focus on the oscillations with periods of 13~70 days, the annual cycle and its second and third harmonics, represented by the relevant reconstructed components (cf. PV, 1994; CW, 1994; Wang, 1995), were removed from the 5-day rainfall field-series, and a second experiment of mcSSA with a window length of 15 pentads (75 days) was carried out on the filtered data set. Three intra-seasonal oscillations, with quasi-periods of 57, 21 and 13 days, were isolated in this experiment.

For a more precise description of these intra-seasonal oscillations, a smaller sampling interval is needed. Thus, mcSSA with a window length of 72 days (M = 36) was applied to the deviation series of 2-day-mean rainfall (i.e., deviations from the annual cycle defined by the long-term mean values for each of the 183 sampling intervals of year). The reason for using the deviation series here is just to remove the annual cycle (another possible approach for removing the annual cycle). In this experiment, intra-seasonal oscillations with quasi-periods of 43, 21 and 12 days were clearly isolated as pairs 1-2, 6-7 and 10-11 respectively. No phase-locking between these oscillations are apparent, indicating that they seem independent of each other.

Table 1 Oscillatory pairs and their peak variance fractions, identified from mcSSA performed on the field-series of 5-day rainfall, with a window length of 74 pentads.

Pair	1-2	3-4	5-6	7-8	9-10	11-12	15-16	17-18
Periods (day)	**365**	**182**	**120**	63	58	70	35	38
Peak variance fraction (%)	99.97	99.09	87.28	14.42	77.40	74.88	44.85	11.58

Table 2 Oscillatory pairs and their peak variance fractions (in parenthesis), identified from experiments of mcSSA with different window lengths (M = 72 or 64 days).

M = 72 days		M = 64 days		M = 72 days		M = 64 days	
Pair	Periods (day)	Pair	Periods (day)	Pair	Periods (day)	Pair	Periods (day)
Basic dataset (1953-1982)				**Randomly resampled dataset (1953-1982)**			
1-2	43 (87.99%)	1-2	41 (79.23%)	1-2	27 (16.58%)		
6-7	21 (40.40%)	5-6	21 (42.00%)				
10-11	12 (18.96%)	10-11	12 (25.50%)				
Dataset for the period 1953-1967				**Dataset for the period 1968-1982**			
1-2	40 (77.14%)			3-4	41 (31.45%)		
6-7	24 (19.87%)			5-6	19 (65.13%)		
8-9	11 (44.42%)			34-35	14 (9.39%)		

Furthermore, these three intra-seasonal oscillations are reproducible, when different window lengths (72 and 64 days) are used and when mcSSA is applied to two equal-length subsets of the relevant data set (see Table 2). They are also qualitatively different from those obtained from a *randomly resampled* data set. Therefore, it can be concluded that there do exist three independent intra-seasonal oscillations in the precipitation over China, with quasi-periods of about 43, 21 and 12 days, respectively. The spatial-temporal structures, i.e. the movements of the rainfall centers, associated with these quasi-periodicities will be presented later in section 4. Also, to obtain some reliable information about the amplitudes of the intra-seasonal oscillations, composites of the deviations of 2-day mean rainfall keyed to eight equally populated phase-categories of these oscillations were carried out, with the phase-categories being defined by using the reconstructed components RCs

(PV, 1994; CW, 1994; Wang, 1995), which are directly comparable with the (multi-channel) deviation series of 2-day mean rainfall.

3. SPATIAL-TEMPORAL STRUCTURES OF THE ANNUAL CYCLE AND ITS HARMONICS

As represented by the first eigenvector-sequence ST-EOF01 (not shown), the spatial-temporal structures of the permanent annual cycle can be described as follows: the rainy season of China first starts in Southern China, with a rainfall center appearing in the Dongting-Boyang Lake basins; this rainfall center extends northward, forming a rain-band over southeast of the Yellow River valley; then, dry weather follows to prevail over Southern China, while the rain-band splits into two parts, one of them moving further northward to North China where the rainy season consequently starts, the other dominating over the Sichuan Basin; as the rainy season ends in North China and the rainfall center retreats from the Yunnan-Guizhou Plateau (Southwestern China), dry weather follows to dominate in the entire eastern China.

The second harmonic of the annual cycle was well isolated as the oscillatory pair 3-4. As shown in Fig. 1 (an interval of 9 pentads is placed between maps), it is associated with a striking contrast of weather conditions between Southern and Northern China, with Taiwan and Southwestern China being in phase with Northern China (cf. ST-EOF03_05 and ST-EOF03_23 in Fig. 1): when the rainy season in Southern China is replaced by a dry spell, rainy weather starts to dominate in Northern and Southwestern China, as well as in Taiwan; and *vice versa*.

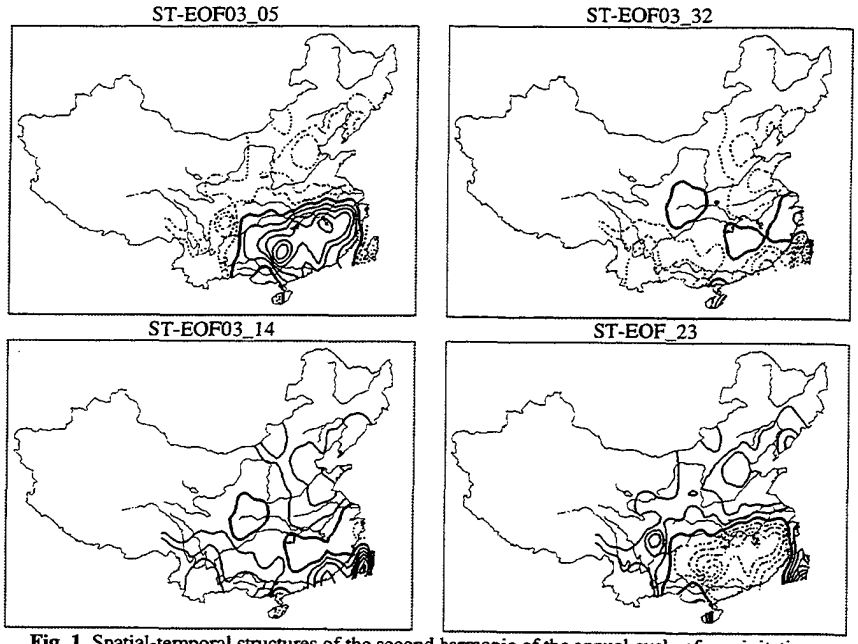


Fig. 1 Spatial-temporal structures of the second harmonic of the annual cycle of precipitation over China, represented by the eigenvector-sequence ST-EOF03 derived from mcSSA performed on the 5-day rainfall field-series, with a window length of 74 pentads.

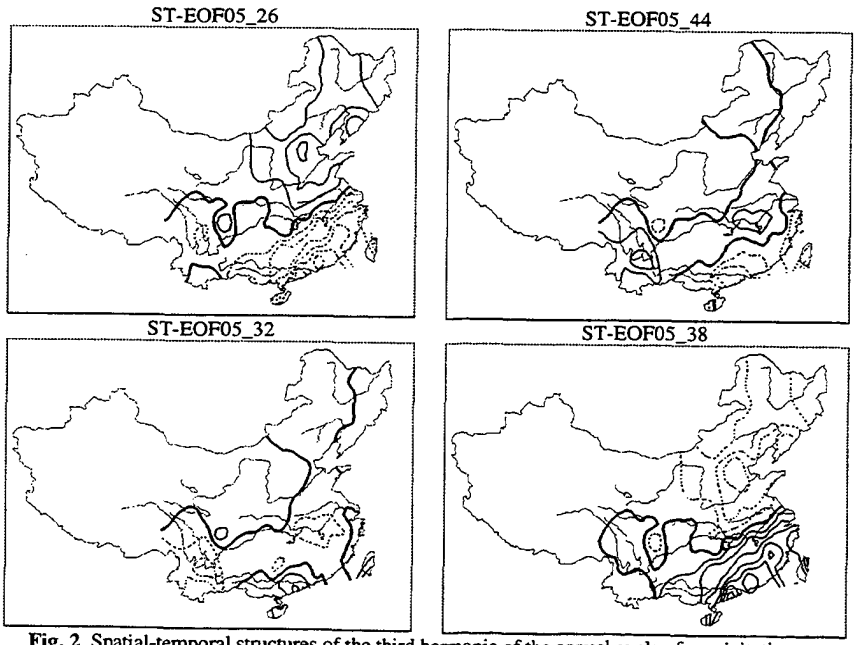


Fig. 2 Spatial-temporal structures of the third harmonic of the annual cycle of precipitation over China, represented by the eigenvector-sequence ST-EOF05 derived from mcSSA performed on the 5-day rainfall field-series, with a window length of 74 pentads.

As represented by the eigenvector-sequence ST-EOF05, the third harmonic is related to a northwestward propagation of rainfall anomalies. As shown in Fig. 2 (with an interval of 6 pentads between maps), a rainfall center appearing in the coastal areas of Southeastern China may first extend northwestward (cf. ST-EOF05_32 in Fig. 2); then, it moves to the Yangtze River basin (cf. ST-EOF05_44) and decays there, while a rainfall center appears in North China and dry weather systems dominate in Southeastern China (cf. ST-EOF05_26). When the rainfall center over North China decays, dry weather systems prevail over the Yangtze River basin, and a rainfall center revives in Southern China. Consequently, another cycle of this oscillation follows.

4. SPATIAL-TEMPORAL STRUCTURES OF INTRA-SEASONAL OSCILLATIONS

From the experiments of mcSSA described in section 2, it was concluded that in the precipitation over China, three intra-seasonal oscillations with quasi-periods of about 43, 21 and 12 days exist, respectively accounting for about 88%, 40% and 19% of the total variance in the relevant frequency bands (cf. Fig. 3).

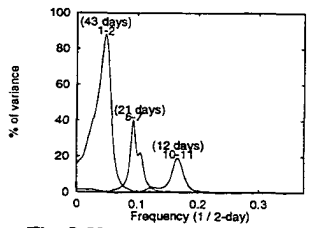


Fig. 3 Variance fraction of the indicated pairs of ST-PCs of the deviation series of 2-day mean rainfall, derived by mcSSA with a window length of 72 days.

The spatial-temporal structures of these oscillations can be represented by the eigenvector-sequences ST-EOF1, ST-EOF6 and ST-EOF10 derived from an experiment of mcSSA performed on the deviation series of 2-day mean rainfall, with a window length of 72 days (cf. section 2). It should be pointed out that some

principal patterns of precipitation variability (defined by 5-day rainfall deviations; cf. Wang, 1995) turn out to be associated with certain phases of these intra-seasonal oscillations.

The quasi-40 day oscillation is confined to the region south of 40°N, as can be seen from Fig. 4, which shows about half a complete cycle of this oscillation represented by the eigenvector-sequence ST-EOF1, with an interval of 6~8 days (3~4 × 2-day) between maps. Symmetric phases of this oscillation display structures of opposite phases. It is associated with the following spatial-temporal structures: a rainfall center first appears in Taiwan (cf. ST-EOF1_05 in Fig. 4), extending *northwestward* to Southeastern China (southeast of the middle-lower Yangtze River; cf. ST-EOF1_09); then, it moves *westward* and decays in the Pearl River basin, while dry weather systems follow to prevail in Southeastern China, advancing northwestward; the region from the Wushan Mountains northeastward to the Huaihe River basin experiences weather conditions opposite to those of Southeastern China. This is in good agreement with Lau's (1988) finding, based on 10-day mean rainfall, that the quasi-40 day modes of precipitation over China are consistent with a northwestward inland migration of the major rain-band from the coastal region. The high-amplitude phases of this oscillation (cf. ST-EOF1_09) reveal the most dominant regime r-EOF1 (Fig. 5) of the monsoonal rainfall. The composites (not shown) keyed to the eight phase-categories of this quasi-40 day oscillation display spatial-temporal structures similar to ST-EOF1, with the maximal positive and negative deviations of 2-day mean rainfall, +6.0 mm and -3.7 mm, occurring over Taiwan in the two symmetric high-amplitude phases (Phases 3 and 7) respectively.

Fig. 6 shows the spatial-temporal structures associated with half a complete cycle of the quasi-20 day oscillation, represented by the eigenvector-sequence ST-EOF6. Symmetric phases of this oscillation exhibit patterns of opposite phases. This oscillation is also confined to the region south of 40°N. It is characterized by a striking contrast of weather conditions between Southeastern China and the middle-lower reaches of Yangtze River valley, displaying a dipole structure which fully develops over South China and then retreats *southward* and collapses, followed by the development of a dipole structure of opposite phase. The fully developed dipole structure (cf. ST-EOF6_20 in Fig. 6) resembles the first dominant rainfall regime (r-EOF1 in Fig. 5), whereas the ST-EOF6_22 (see Fig. 6) is similar to the second dominant

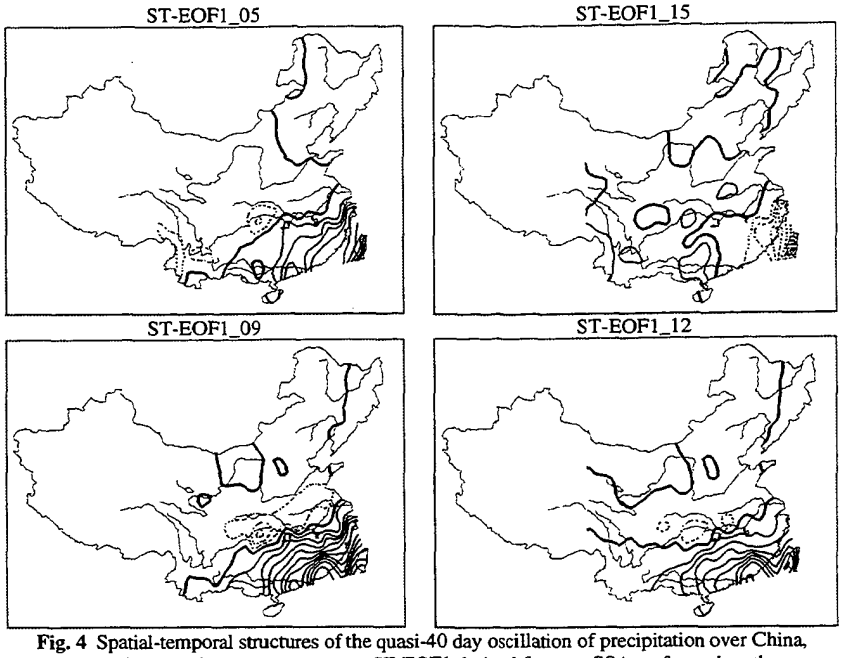


Fig. 4 Spatial-temporal structures of the quasi-40 day oscillation of precipitation over China, represented by the eigenvector-sequence ST-EOF1 derived from mcSSA performed on the deviation series of 2-day mean rainfall, with a window length of 72 days.

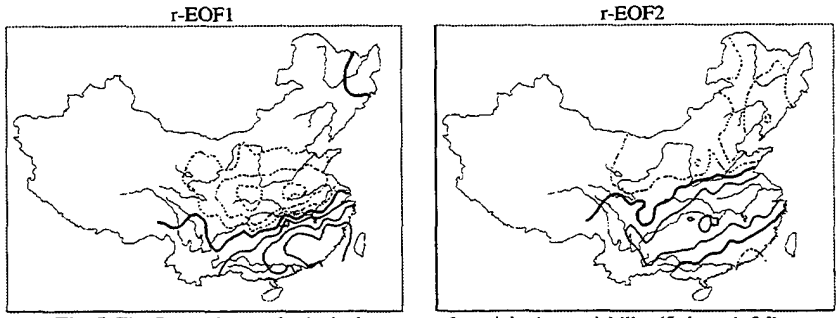


Fig. 5 The first and second principal patterns of precipitation variability (5-day rainfall deviations) in China (quoted from Wang, 1995).

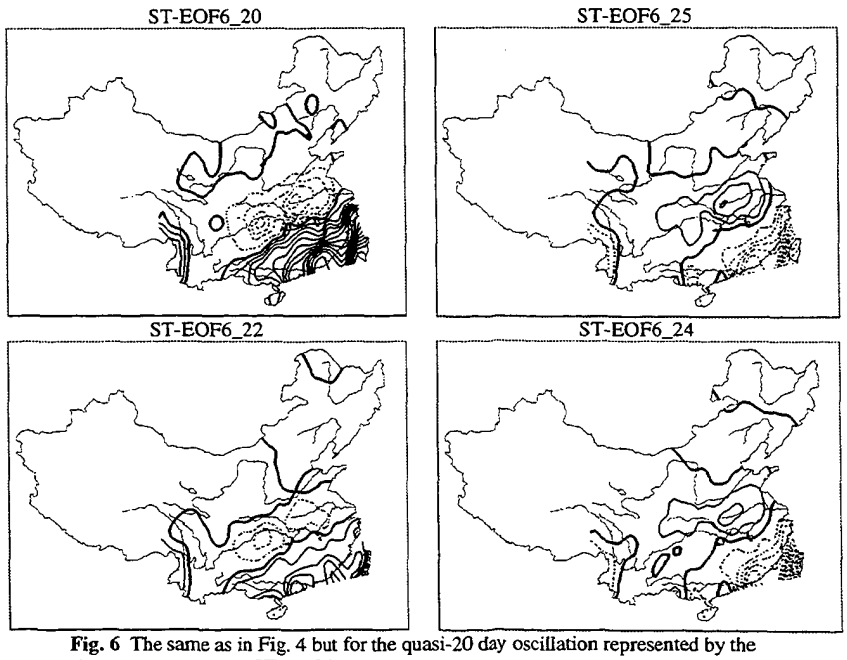


Fig. 6 The same as in Fig. 4 but for the quasi-20 day oscillation represented by the eigenvector-sequence ST-EOF6.

rainfall regime (r-EOF2 in Fig. 5). Thus, this quasi-20 day oscillation is associated with the transition process between the first and second dominant regimes of the monsoonal rainfall, namely between r-EOF1 and r-EOF2. The corresponding composites (not shown) of deviations of 2-day mean rainfall display spatial-temporal structures similar to ST-EOF6, with amplitudes of +5.96 mm and -3.54 mm occurring over Taiwan in the two symmetric high-amplitude phases (Phases 3 and 7) respectively.

Since symmetric phases of the quasi-biweekly oscillation also display structures of opposite phases, only half a round cycle of this oscillation represented by the eigenvector-sequence ST-EOF10 is shown in Fig. 7, with an interval of 2-day between maps. This oscillation is mainly confined to Southeastern China. It is associated with a center of rainfall anomalies which appears first in Taiwan, extending and propagating *westward* to Southeastern China in about one week, and then, rapidly retreating *southward* or decaying in Southwestern China, while a center of opposite phase anomalies develops in Taiwan. Consequently, another half cycle of the quasi-biweekly oscillation succeeds. The relevant composites (not shown) reveal the similar spatial-temporal structures, with the maximal deviations of 2-day mean rainfall of +4.9 mm (over Taiwan) and -3.0 mm (over Kantong Province) respectively occurring in the two symmetric high-amplitude phases (Phases 4 and 8).

5. SUMMARY

Based on the daily rainfall series for 122 stations well covering eastern China, for the period 1953-1982, and with focus on periods of two weeks to a year, low-frequency oscillatory variabilities of precipitation over China were explored by performing multi-channel Singular Spectrum Analysis (mcSSA). Besides the annual cycle and its second and third harmonics (182 and 120 days), three intra-seasonal oscillations with quasi-periods of about 43, 21 and 12 days were clearly isolated, accounting for about 88%, 40% and 19% of the total variance in the relevant frequency bands. No phase-locking between these oscillations are apparent, indicating that they seem to be independent of each other. These quasi-periodicities are robust, since they are reproducible, when different window lengths (72 and 64 days) are used and when mcSSA is applied to two equal-length subsets of the relevant data set, and since they are qualitatively different from those obtained from a *randomly resampled* data set. The spatial-temporal structures, i.e. the propagation of rainfall anomalies, associated with these quasi-periodicities are presented, as well as those related to the annual cycle and its harmonics. Also, some reliable information about the amplitudes and seasonalities of these oscillations is provided by using composite analysis.

Actually, all these intra-seasonal oscillations are confined to the region south of 40°N. The quasi-40 day oscillation is associated with *northwestward* propagation of rainfall anomalies, exhibiting the most dominant regime of monsoonal rainfall in its high-amplitude phases. The quasi-20 day oscillation is related to a dipole structure which fully develops over the region south of 40°N and then retreats *southward* and collapses; it displays the transition process between the first and second dominant regimes of rainfall over China. The quasi-biweekly oscillation is characterized by precipitation episodes which start in Taiwan, propagate *westward* to Southeastern China in one week, and then rapidly retreat *southward* or decay in Southwestern China, replaced by a dry spell.

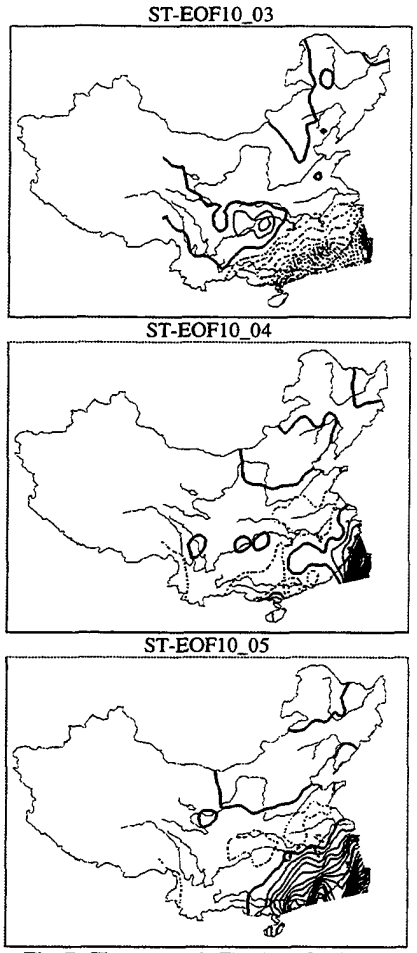


Fig. 7 The same as in Fig. 4 but for the quasi-biweekly oscillation represented by the eigenvector-sequence ST-EOF10.

ACKNOWLEDGEMENTS

This research was supported by a doctoral scholarship provided by JNICT (National Board for Scientific and Technological Research, Portugal). We greatly appreciate Prof. Gongbing Peng's kind help on obtaining the data. Professors G. Peng, Enji Zhou and Zhongxiu Fan offered their warm-hearted help and strong encouragement to Wang and Zhang on many aspects.

REFERENCES

Corte-Real, J. and X. Wang, 1994: "Low-frequency Oscillations and Associated Wave Motions over Eurasia". In: Proc. Intern. Conf. on Monsoon Variability and Prediction, Trieste, Italy, WCRP-84 (WMO/TD-No. 619), **Vol. I**, 166-173.

Lau, K.-M., 1992: "East Asian Summer Monsoon Rainfall Variability and Climate Teleconnection". J. Meteor. Soc. Japan, **Vol. 70**, No. 1, 211-241.

Lau, K.-M., G. J. Yang and S. H. Shen, 1988: "Seasonal and Intraseasonal Climatology of Summer Monsoon Rainfall over East Asia". Mon. Wea. Rev., **116**, 18-37.

Plaut, G. and Vautard, R., 1994: "Spells of Low-Frequency Oscillations and Weather Regimes in the Northern Hemisphere". J. Atmos. Sci. **51**, 210-236.

Tian, S.-F. and T. Yasunari, 1992: "Time and Space Structures of Interannual Variations in Summer Rainfall over China". J. Meteor. Soc. Japan, **Vol. 70**, No. 1, 585-595.

Vautard, R., et al., 1992: Singular-spectrum analysis: A toolkit for short, noisy chaotic signals. Physica D **58**, 95-126.

Wang, X., 1995: "Planetary Scale Circulation, Climate and Extreme Events in East Asia". A doctoral dissertation to be presented to the Faculty of Sciences, University of Lisbon in July 1995.

Yihui, D., 1994: "Monsoons over China". Kluwer Academic Publishers, The Netherlands, 419pp.

CORRESPONDING AUTHOR

Xiaolan Wang, Department of Physics, Faculty of Sciences, University of Lisbon, Campo Grande, Ed. C1, Piso 4, 1700 Lisbon, Portugal (on leave from the Department of Hydrology and Water Resources, Hohai University, Xikang Road 1, Nanjing 210024, P. R. China).

THE BREAKPOINT REPRESENTATION OF RAINFALL

John Sansom

National Institute of Water & Atmospehric Research, Wellington, New Zealand

ABSTRACT

Rainfall is generated by at least 2 processes each of which can be characterised by its distribution of rain rates and durations. The breakpoint representation captures the information required to parameterise the processes and so describe the rainfall climatology. However, the currently available breakpoint data is poor for low rates and short durations. A version of the EM algorithm suitable for a truncated dataset was checked with simulations and then used so that the poor data was ignored. The results at low truncation agreed with previous estimates but a new picture emerged at higher truncation. Verification is required from a gauge sensitive in the low-rate/short-duration region which gives breakpoints directly.

INTRODUCTION

Pluviographs show that rainfall strongly tends to occur in variable length periods during which the rate of fall is steady on the scale of one or two minutes. Distinct breaks occur where the rate changes; these are the breakpoints and a detailed record of the rainfall at a point is just the times when changes occur and the rate of fall after a change, which can be zero.

This representation is distinctly different to that in which the amount of rain accumulated during a fixed period — fixed in length and with respect to the clock — is recorded e.g. hourly rainfalls. The normal means of studying in greater detail the rainfall process is to examine accumulations at shorter time scales i.e. monthly then daily then hourly then 10 minute and so on but not much further. A comparison by Sansom (1992) between such accumulations at short periods and the breakpoint data indicates that the latter give a more realistic or natural view of the behaviour of rainfall on short time scales. This is important because rainfall processes operate at similar time scales.

An overview of the data (Sansom and Thomson, 1992) shows that it can be statically modelled as a mixture of log-normal components; univariate for the lengths of dry periods, and bivariate for the lengths of wet periods and the steady rate during the period. The technique used to decompose the data into modes was the Expectation Maximisation (EM) algorithm which yields estimates of the fractional representation of each component and the parameters defining them.

The EM algorithm generally will provide details on as many modes as are requested of it and it is necessary through other means to determine how many modes are needed or are correct. The chosen means was to extend the static model temporally since the modes, which represent processes, should have significant persistence. The underlying idea is that rainfall occurs either due to large scale uplift (rain) or due to convective activity (showers) and that these rain or shower event last longer than any particular period of steady precipitation. Thus using the parameters estimated by the EM algorithm, Sansom (1995) made discriminant analyses and by looking for persistence and agreement with manual weather observations a "best" model was chosen.

A long standing problem with the data and its subsequent decomposition into modes concerns the distinction between when it is raining and when it is not. The "raw" data from the gauge is not labelled as representing a wet or dry period. But, generally, this is not a problem because far away in time from any precipitation there will be a strong implication in the data that it is not raining and, in contrast, during a time of significant rain there will be a strong implication that it is raining. However, there can be periods of doubt when from the data alone a decision on whether it was raining or not can be hard to make.

For periods of a given length the doubtful ones are associated with the lower rain rates observed for periods of that length i.e. a low rain rate will be well defined over a long enough period but the same rate very doubtful over much shorter periods. If this problem is ignored the parameters estimated by the EM algorithm are badly contaminated. The way around this problem is to use a modified version of the EM algorithm (Sansom and Thomson, 1995) suitable for a truncated data set. This modified EM algorithm is set out in the next section then some results from simulations. The application to 15 years of data from Invercargill, New Zealand (46°25'S, 168°20'E) and the results obtained is presented in the last section.

THE EM ALGORITHM

Many attempts at resolving the components from a mixture of distributions have been made since first tried by Pearson (1894); Everitt and Hand (1981) and Titterington (1985) present comprehensive reviews. The EM algorithm described by Redner and Walker (1984) provides for the decomposition of mixtures of distributions from the exponential family which includes the multivariate normal and hence log-normals when the technique is applied to the data after logarithmic transformation.

The model is that of a mixture of m distributions from the same parametric family so that the overall density is $p(x|\Theta) = \sum_{i=1}^{m} \alpha_i p_i(x|\theta_i)$ where $x = (x_1, \ldots, x_n)$,

n is the number of variates, $\alpha_i \geq 0 \forall i$, $\sum_{i=1}^{m} \alpha_i = 1$ and the p_i are density functions from the same family parameterised by θ_i. Here Θ denotes the collection of all the parameters α_i, θ_i. For the multivariate normal p_i is given by:

$$p_i(x|\theta_i) = \frac{1}{(2\pi)^{n/2}|\Sigma_i|^{1/2}} \exp(-\tfrac{1}{2}(x-\mu_i)'\Sigma_i^{-1}(x-\mu_i))$$

where $\theta_i = (\mu_i, \Sigma_i)$ in which the μ_i are real and the Σ_i are positive definite $n \times n$ matrices.

The EM algorithm originated as a means of dealing with incomplete data. In this case, not knowing which mode any particular datum comes from represents the "incompleteness" of the data. Noting that parameters without "hats" refer to the values for the current iteration then where:

$$a_{ik} = \frac{\alpha_i p_i(x_k|\theta_i)}{p(x_k|\Theta)}$$

the algorithm gives:

$$\begin{aligned}
\hat{\alpha}_i &= f_1 \sum_{k=1}^{N} a_{ik} + f_2 \\
\hat{\alpha}_i\hat{\mu}_i &= f_1 \sum_{k=1}^{N} a_{ik}x_k + f_2\mu_{ic} \\
\hat{\alpha}_i\hat{\Sigma}_i &= f_1 \sum_{k=1}^{N} a_{ik}(x_k - \hat{\mu}_i)(x_k - \hat{\mu}_i)' \\
&\quad + f_2(\Sigma_{ic} + (\mu_{ic} - \hat{\mu}_i)(\mu_{ic} - \hat{\mu}_i)')
\end{aligned}$$

where the $\hat{\alpha}_i$ derived in the first equation is used to estimate the $\hat{\mu}_i$ in the second which in turn is used in the third equation and for non-truncated data $f_1 = \frac{1}{N}$ and $f_2 = 0$.

If the sample has been truncated such that only those x satisfying $t'x > c$ are retained then:

$$f_1 = \frac{1}{\frac{N+1}{F_0} - 1}, \qquad f_2 = \frac{\alpha_i F_{ic}}{1 - \frac{F_0}{N+1}}$$

where

$$F_0 = P(t'X > c|\Theta), \qquad F_{ic} = P(t'X \leq c|I = i, \theta_i)$$

or

$$F_0 = 1 - \sum_{i=1}^{L} \alpha_i F_{ic} \text{ and } F_{ic} = \Phi\left(\frac{c - t'\mu_i}{\sqrt{t'\Gamma_i t}}\right)$$

since for a given $I = i$, $t'X$ is distributed as $N(t'\mu_i, t'\Gamma_i t)$ and thus Φ is the standard normal cumulative function. Also

$$\begin{aligned}
\mu_{ic} &= E(X|I = i, t'X \leq c, \theta_i) \\
\Sigma_{ic} &= \text{Var}(X|I = i, t'X \leq c, \theta_i)
\end{aligned}$$

and standard results are available for these although where the truncation line is neither horizontal or vertical the data must be rotated before the standard results can be used.

SIMULATIONS

To check the algorithm it was applied to data sets simulated using parameter values which had been found previously for a 3 mode fit using the version of the EM algorithm for non-truncated data. It was found sufficient to use samples of size 10000 and iterate only until convergence to 4 significant figures was reached. However, to find a satisfactory estimate of the parameters' estimation standard deviation (i.e. column σ in Tables 1,2) through the Fisher information, it was found necessary to take the mean of 10 estimates each using

Table 1: Results from 50 simulations plus 10 estimates of σ with non-truncated data.

	μ	σ	$\bar{x}$	s	t	χ^2
α_1	0.500	0.009	0.501	0.009	1.0	49.2
α_2	0.300	0.008	0.298	0.009	-1.4	60.0
α_3	0.200	0.006	0.200	0.007	0.4	56.1
μ_{1_1}	3.401	0.016	3.400	0.017	-0.6	57.2
μ_{2_1}	0.693	0.020	0.689	0.018	-1.7	41.7
σ_{1_1}	0.693	0.010	0.692	0.011	-0.8	57.5
σ_{2_1}	0.916	0.014	0.920	0.013	1.8	44.2
ρ_1	0.000	0.020	0.002	0.021	0.6	50.7
μ_{1_2}	2.565	0.018	2.559	0.017	**-2.3**	40.3
μ_{2_2}	-0.223	0.018	-0.219	0.016	1.9	36.2
σ_{1_2}	0.693	0.013	0.692	0.012	-0.6	35.9
σ_{2_2}	0.693	0.013	0.693	0.014	0.0	60.0
ρ_2	-0.900	0.006	-0.901	0.006	-1.0	44.4
μ_{1_3}	1.609	0.031	1.609	0.028	-0.1	38.7
μ_{2_3}	1.609	0.033	1.606	0.029	-0.8	39.3
σ_{1_3}	1.099	0.019	1.100	0.018	0.5	42.7
σ_{2_3}	1.386	0.024	1.384	0.027	-0.6	59.7
ρ_3	0.800	0.011	0.799	0.011	-0.4	52.3

Table 2: Results from 50 simulations plus 10 estimates of σ with 15% truncated data.

	μ	σ	$\bar{x}$	s	t	χ^2
α_1	0.500	0.012	0.503	0.011	**2.1**	42.4
α_2	0.300	0.013	0.297	0.015	-1.3	62.9
α_3	0.200	0.012	0.199	0.012	-0.4	45.8
μ_{1_1}	3.401	0.020	3.395	0.016	**-2.9**	**31.5**
μ_{2_1}	0.693	0.028	0.693	0.027	-0.1	47.6
σ_{1_1}	0.693	0.012	0.694	0.009	1.0	**28.5**
σ_{2_1}	0.916	0.020	0.921	0.021	1.7	54.2
ρ_1	0.000	0.027	-0.001	0.027	-0.1	49.9
μ_{1_2}	2.565	0.023	2.559	0.038	-1.1	**138.7**
μ_{2_2}	-0.223	0.025	-0.217	0.044	1.0	**150.4**
σ_{1_2}	0.693	0.018	0.696	0.025	0.9	**96.3**
σ_{2_2}	0.693	0.020	0.692	0.032	-0.3	**121.6**
ρ_2	-0.900	0.006	-0.902	0.009	-1.3	**116.8**
μ_{1_3}	1.609	0.088	1.588	0.085	-1.8	46.6
μ_{2_3}	1.609	0.107	1.592	0.111	-1.1	52.7
σ_{1_3}	1.099	0.044	1.106	0.036	1.5	32.7
σ_{2_3}	1.386	0.066	1.394	0.064	0.8	46.5
ρ_3	0.800	0.027	0.806	0.020	**2.0**	**26.7**

a sample of size 10000. Estimates were necessary since the required expectations could not be made analytically.

Results like those tabulated in Tables 1 and 2 were examined. In these tables the first column shows the values of the simulating parameters and is headed μ since for large enough samples the algorithm should recover the parameter values without bias. The second column is the expected standard deviation of the estimates of the μ's found through the Fisher information. The third column is the mean over 50 runs of the recovered parameter values while the fourth is the standard deviations over the 50 runs. The last 2 columns show the validity of the algorithm by giving test statistics for the $\bar{x}, s$ against the μ, σ columns i.e. t and χ^2 values. Where a 95% confidence interval based on the $\bar{x}, s$ would not include the μ, σ, the test statistic is show in boldface type.

The initial set of simulating parameters was found to give more occasions where the 95%CI excluded the μ, σ than acceptable — 17% for μ and 64% for σ. Even in the no truncation case, one of the 50 runs was found to have 7 out the 18 parameters lying more than 2 standard deviations from the mean values over the 50 runs. It could be that for such a case numerical effects led the algorithm to a local rather than the global maximum of the likelihood. However, the convergence found was stable with respect to the initial values used for the iterative process; thus, the solution is a property of the data values and is not a numerical effect. Thus, in such cases it appears that the sample emphasises what is usually a local maximum in the likelihood to such an extent that it dominates the normal global maximum. However, values within acceptable limits were found for the parameters when the sample was re-sampled at 50 and 60% and usually at 70% but not when 80% of the data was retained.

The values shown in Tables 1 and 2 resulted from making the "problem" easier for the EM algorithm by changing the ρ's from $-.4, -.9, -.8$ to $0, -.9, .8$ and changing μ_{1_1} from 2.3026 to 3.4012. With these values the number of parameters whose 95%CI excluded the simulating value decreased to acceptable levels especially since for repeated sets of 50 runs different parameters were involved. The exception to this was for the χ^2 values of mode 2 in the truncated case (i.e. μ_{1_2}, σ_{1_2} etc) where in several sets of 50 runs at several levels of truncation $\geq$15% the χ^2 values showed that s significantly exceeds σ. The mode in question is the one where most of the truncation is taking place and the enhanced variation in its parameter estimates starts to be significant when it itself is being truncated by about 40%.

Overall the simulations showed that for both versions of the EM algorithm the values of the simulating parameters are recovered well with the mean values over several runs showing no bias and, since the standard deviations are usually under 10% of the mean values, values close to the "real" ones can be expected on any particular run. Also, the EM algorithm is not sensitive to the initial values it is given and will, generally, find the global maximum in the likelihood. However, there can be difficulties where parameter estimates are highly correlated but re-sampling may help in such cases.

DATA ANALYSIS

Initially, at steps of 6% from 6% to 36% truncation, 3 component fits were found using randomly selected (but reasonable) starting values. Ten runs to convergence, each from different initial values, were made for each level of truncation. A half of all the fits were similar to the pattern shown in Figure 1C which is distinctly different to previous fits using non-truncated data where the pattern was similar to that of Figure 1B. A quarter of the fits, including fits from all but the lowest level of truncation, were dominated by a single mode and the remaining fits were not well grouped.

The likelihood for any particular truncation level was greatest for those runs included in the large group which had representatives from all levels of truncation and was most popular for a truncation of 24%. Using this level of 24%, 4 mode fits were also made to the data giving a similar pattern to that for the 3 mode, however, 5 and 6 mode fits did not follow the same pattern.

In order to follow the change from the pattern of modes for non-truncated data to the pattern for data with a 24% truncation, finer truncation steps were used ($\approx$ 1%) and the result from one step was used to initiate the fit for the next step. The series of fits resulting from increasing truncation was compared to that when truncation was slowly decreased from 24%. For 3 modes the "increasing" series had the greatest likelihood for truncation below 5% and the "decreasing" series thereafter; for 4 modes the change over was at 12%. Furthermore, the changeovers were well-defined at these truncation levels with one pattern being maintained through low truncations and the other through high truncations.

Figure 1 shows the 3 and 4 mode patterns in panels B and D for low truncation with the lower line indicating the least (i.e. zero) level of truncation and the higher line the highest level for that pattern. In panels C and E, the patterns for higher truncation are shown again with lines indicating the least and highest levels of truncation that gave the pattern. (Higher truncation may still give the pattern but eventually a single mode would probably dominate). In panel A a smoothed scatter plot of the data is given; it can be seen that the B and D fits are like the data but the C and E fits imply that much data is missing. Indeed, estimates of the "true" sample size are 53000 for C and 48000 for E but only about 41000 for B and D; the size of the non-truncated data set was 40570.

CONCLUSION

Sansom (1995) interprets the modes of Figure 1B and D as rising from large scale or convective precipitation i.e. rain (R) and showers (S) respectively. In addition the inability to digitise the pluviographs exactly leads to an error mode (E) and when 4 modes are considered then a general mode (G) captures some of the R and S. The identification of these modes was established through discriminant analysis for the R,S and G (Sansom, 1995) and by simulation for E (Sansom and Thomson, 1992). The E mode does not appear in panel

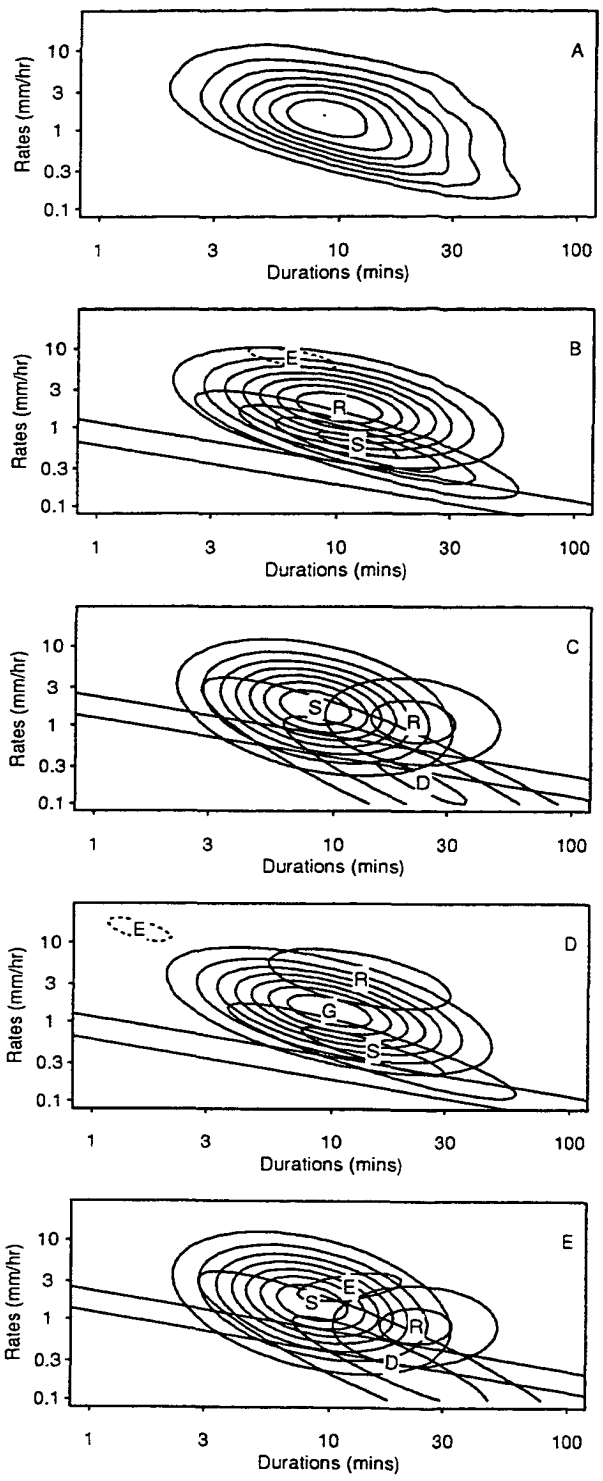


Figure 1: A: Contour plot of the data. B,C: 3 mode fits for slight (B) and heavier truncation (C). D,E: as B,C for 4 modes. In B,C,D and E the range of truncations involved are shown and the contours in each panel are the same with any mode not reaching the lowest contour value shown dashed at a level of 95% of that mode's maximum value.

C but a mode labelled D appears in the low-rate/long-duration region. This remains in panel E where the possible re-appearance of the E mode is shown.

The E mode arises from the inability to digitise short wet periods without biasing the resulting rain rate to a higher than actual value. The D mode might also be explained by poor digitising but in this case the problem is the near absence on the pluviographs of exactly horizontal lines during dry (D) periods and the certainty that even if they existed they could not be digitised as such. Thus most dry periods will be digitised as if some rain fell during the period and in transforming the data digitised off the pluviographs into amounts of rain during periods of time, empirically established rules are used to decide whether or not it was raining during any period. Furthermore, the truncation has been used to remove any remaining doubtful data. The patterns shown in panels B and D show that the transformation rules may well be operating as intended. On the other hand the S modes may well be vestiges of the D mode which is only seen properly when the effect of the rules is removed by higher truncation.

The dilemma is whether the "true" picture is more like D or E and resolution of this may be possible through appropriate simulations but would properly be done through the gathering of data from a gauge giving breakpoints directly. This gauge, which is not currently available, should also be sensitive in the low-rate/short-duration region.

REFERENCES

Everitt,B.S.;Hand,D.J. 1981, "Finite mixture distributions." Chapman and Hall, London.

Pearson,K. 1894, "Contributions to the mathematical theory of evolution." Philosophical transactions of the Royal Society pp71–96.

Redner,R.A.;Walker,H.F. 1984, "Mixture densities, maximum likelihood and the EM algorithm." Society for Industrial and Applied Mathematics review, Vol 26 pp192–239.

Sansom,J.;Thomson,P.J. 1992, "Rainfall classification using breakpoint pluviograph data." Journal of Climate, Vol 5 pp755–764.

Sansom,J. 1992, "Breakpoint representation of rainfall." Journal of Applied Meteorology, Vol 31 pp1514–1519.

Sansom,J. 1995, "Rainfall discrimination and spatial variation using breakpoint data." Journal of Climate, Vol 8 pp624–636.

Sansom,J.;Thomson,P.J. 1995, "Application of the EM Algorithm to detecting components in censored and truncated meteorological data" In preperation.

Titterington,D.M. 1985, "Statistical analysis of finite mixture distributions." John Wiley.

CORRESPONDING AUTHOR

John Sansom,
NIWA,
PO Box 3047,
Wellington, New Zealand.

CHANGES OF PRECIPITATION CHARACTERISTICS IN FINLAND

Raino Heino

Finnish Meteorological Institute, Helsinki, Finland

ABSTRACT

Long-term records of precipitation parameters are studied. The records need necessarily corrections, because of the improvements of the measuring instruments and of various other disturbances in the records. Statistical characteristics of the frequency distributions and their changes are studied. In spite of some secular changes (e.g. the wet 1920s and the dry 1940s), the annual precipitation amounts have remained roughly at the same level during the whole century. The interannual variability of precipitation has, in general, decreased in Finland. Changes of the other distribution parameters can mostly be regarded as part of the "normal" year-to-year variability.

1. INTRODUCTION

Precipitation climatology of a region and its changes are quite difficult to monitor, because the variations of precipitation in space and time are rather large. Although the network of precipitation stations is generally far denser than the networks established for the observation of other climatic elements, the difficulties of the measuring technique and their changes as well as relocations of stations may cause strong inhomogeneities in the long-term records and make the results of studies spurious. A short review based on earlier studies is given on the major inhomogeneity problems of the Finnish long-term precipitation records.

The total number of stations, which have made precipitation measurements in Finland, is around 1000, 120 of which have been in operation since 1931 or earlier. In addition to the precipitation amounts the other standard long-term precipitation records in Finland include the number of days with precipitation exceeding specific amounts (>0.1, >1.0, >10 mm and snowfall > 0.1 mm) and the daily maximum amounts. However, they are not included in this study.

Studies of the long-term changes of the Finnish precipitation climate are very few. This may be due to the fact that precipitation variations or changes have not been accorded as much importance as temperature, because precipitation amounts in Finland are generally sufficient for most activities in all seasons, and flooding is not a great problem, either. A recent study by Heino (1994), however, reviews the precipitation data, data homogeneity as well as changes of precipitation amounts in Finland.

This study is a part of the SILMU-national climate programme (cf. Heino and Tuomenvirta, 1994) and the North Atlantic Climatological Dataset - project (cf. Frich, 1994).

2. HOMOGENEITY OF THE RECORDS

Measurements of precipitation are highly dependent on the structure of the precipitation gauge and its exposure, and consequently introduce many complications. The records of precipitation amounts are always underestimates of the real amounts and they are usually expected to contain great inhomogeneities in both space and time. In addition, most of the random-type inhomogeneities are also negative resulting from reduction in the catch (e.g. due to a leaking gauge, spilling of water). Of particular concern is the measurement of snowfall from conventional gauges, where large errors are known to occur.

The main source of inhomogeneity in precipitation records for the whole country originates from 2-3 changes of precipitation gauges, which have produced apparent increases in precipitation amount of up to 30% in winter. These errors were corrected in all the data used in this study (examples of corrections in Fig. 1).

Precipitation measurements are extremely dependent on the local exposure of the gauge, so any changes in measuring sites or their surroundings may introduce severe inhomogeneities into the data records. The relocation of many stations to nearby airports is a dominant feature in the Finnish network of long-term precipitation records. The winter precipitation at open airport stations is 10-40% smaller than at the neighbouring (sheltered) town stations. These corrections are also taken into account in the examples of Fig. 1.

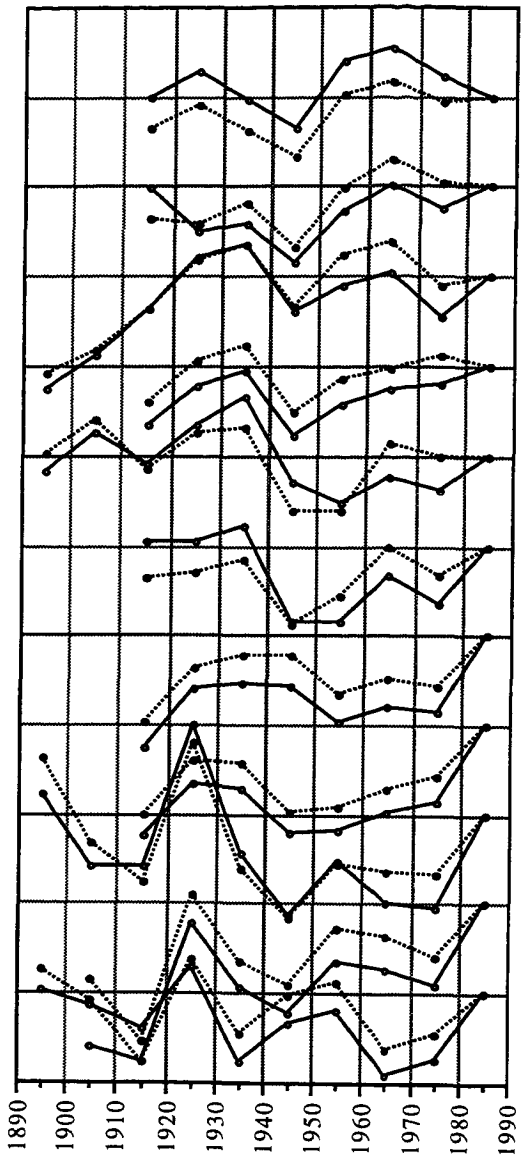


Fig. 1. Decadal averages of annual precipitation in Finland during 1891-1990 as deviations from the 1981-1990 mean value for each station. Stations are from south to north (60-70°N 25-30°E). For each station there are two curves, the original (solid) and corrected (dotted).

The "stability" of the difference between two adjacent stations for annual precipitation is shown in Fig. 2. In 1914 the surroundings of Ilmala observatory changed considerably, as trees were felled in order to fortify the observatory hill. The gauge was also moved, but to an open site. This effect can well be seen in the precipitation records. In 1924 the measurement site was moved to a sheltered location and thereafter the difference remained at about the same level until the 1960s, after which both stations were relocated.

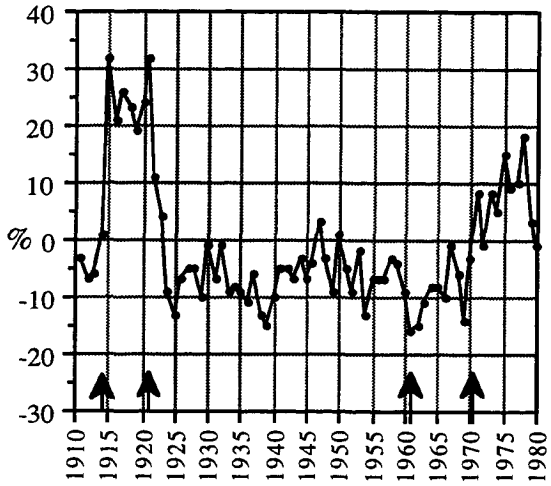


Fig. 2. Differences (%) of annual amounts of precipitation in Helsinki between the centre station and Ilmala observatory (4 km apart) during 1911-1980. The positive numbers mean greater amounts at the centre station. Site changes of the gauges and the local environment are marked by arrows.

Any station relocations across a strong isohyetal gradient, as is normally observed in coastal regions, may also create a significant inhomogeneity in the precipitation records.

The corrections needed in the course of time would require most detailed information on the history of each gauge (position, near-environment, etc.). These details are catalogued quite well for the present network of stations measuring precipitation in Finland, using photographs from a fish-eye camera (full sky images down to the horizon) for most stations, but this information is not available for the previous observing sites. Photographs and drawings of the observation sites included in the inspection reports, however, offer some possibilities to estimate the near-environment of previous sites.

3. PRECIPITATION TOTALS

Non-overlapping averages of annual precipitation during the last 100 years are already given in Fig. 1 for some Finnish stations which have records of 80 years or more in duration and which were found or corrected to be homogeneous. Quite large differences are seen between the stations, although in many cases certain decades (e.g. the 1920s and the 1980s) received more precipitation than the others. A notable rising trend is seen at most stations in southern and central Finland. However, visual examination does not reveal any long-term changes.

Corresponding seasonal curves of decadal averages show variable features. Due to the large variability of precipitation, the changes from decade to decade as well as between stations are largest in summer. A recent increase in precipitation is also evident in summer, especially in the south. A recent decrease, on the other hand, dominates the autumn curves in the north.

Due to the great interannual (and interdecadal) variability of precipitation a longer averaging period reveals more readily possible trends in the data. The spatial distribution of the annual mean precipitation for the latest normal period 1961-1990 were compared with the previous normal period 1931-1960.

Annual mean precipitation has increased at almost all the Finnish stations. Thus it is plainly clear that precipitation has really increased in Finland between the two latest normal periods. The improvement of the measuring equipment is no longer an explanation for the increase, because it was excluded from the records. The standard error of 30-year annual mean precipitation in Finland ranges from 15 to 20 mm and since the increase at several stations has been around 30-40 mm, the change has therefore been significant at the 95% level.

The changes of seasonal mean precipitation between the two latest normal periods have mostly been positive, as for the annual precipitation.

According to Førland et al. (1995) precipitation has increased in most parts of Northwest Europe.

4. VARIABILITY OF PRECIPITATION

Studies of the variability of precipitation and their changes over time are totally absent in Finland, and are quite rare elsewhere, as well. The results, however, are quite inconclusive. To illustrate, in a separate study Auer (1993) did not find any changes in the variability of annual precipitation in Austria during the course of the last 100 years.

The standard deviation is not a proper measure for studying the variability of precipitation, because it is closely related to the mean. When examining the change of the coefficient of variation between the two standard normal periods 1931-1960 and 1961-1990, a decrease was found at almost all stations, amounting to as much as a 5-7% decline at several stations. Random variations would result in values within about 2 standard errors of the mean, so by this criterion the changes have not occurred by chance.

The dependency of the coefficient of variation on mean annual precipitation was also studied. However, the variability was found to be independent of the precipitation amounts themselves. The same result was reported by Tabony (1977) for precipitation in Great Britain.

Examples of the annual course of the coefficient of variation are shown in Fig. 3 for the period 1891-1990. They show maxima in late spring and early summer, while the variability of precipitation is usually at a minimum in November-January. The annual course is, however, quite irregular.

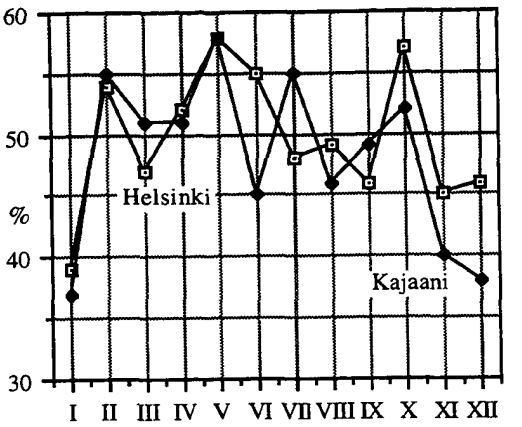


Fig. 3. Annual course of the coefficient of variation (%) of precipitation at Helsinki and Kajaani in 1891-1990.

5. OTHER CHARACTERISTICS

Skewness and kurtosis of precipitation

Precipitation distributions are known to be generally skewed and irregular, especially on a monthly basis. On a seasonal and annual basis the distribution is expected to be closer to a normal distribution. Since the shape of the frequency distribution affects the interpretation of other features of precipitation, it is important to examine the main shape characteristics and their changes.

The coefficient of skewness of annual precipitation is presently (1961-1990) positive. However, only at a few stations in inland region are the values significantly skewed (values >0.9), which is probably due to local shower activity.

When comparing the change between the two latest normal periods, it was found that the negative skewness of annual precipitation (mostly non-significant) of the period 1931-1960 has changed to positive (also mostly non-significant) values in the present normal period.

On a monthly basis a high positive (right side) skewness is expected, because the distribution is limited to zero on the left side, but is capable of reaching very high values on the right side. This

is well illustrated in Fig. 4, which shows that monthly precipitation distributions are positively skewed, most of them significantly (>0.5). The values, however, are very unstable without any clear consistency. The same is true for the curves of the coefficient of kurtosis.

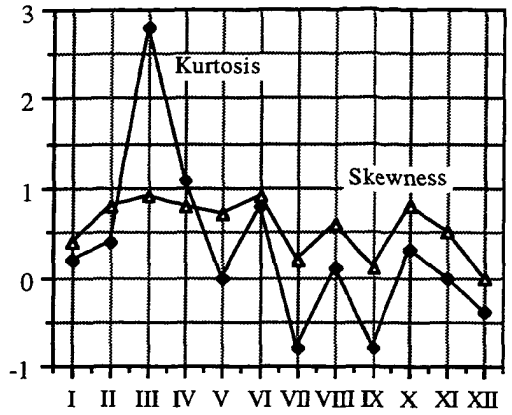


Fig. 4. Annual course of the coefficient of skewness and kurtosis of precipitation at Helsinki in 1891-1990.

Autocorrelation

Correlations between consecutive months were calculated for all the stations with long-term records. As expected the correlations were small and variable. Negative values were also common. Insignificant correlations have also been found by several researchers around Europe (e.g. Auer, 1993) and they can be attributed to the relative independence of the synoptic conditions characterising the precipitation in each season.

Spatial correlation

The spatial correlation of mean precipitation is generally low between the stations. The pattern is basically the same: a sharp reduction of correlation to between 0.7 and 0.8 even in the case of the closest stations. A value of 0.5 is reached at a distance of 300-400 km.

One interesting regional feature is noteworthy. Since the routes of depressions bringing precipitation to Finland are most often from south-west to the north-east, the correlations are higher in that direction.

Correlation coefficients between the Finnish stations and a few available longer-distance stations in Europe with 100-year records showed very irregular features. The correlation was, however, related to distance, except in summer, when the precipitation is mostly influenced by local shower activities. In the Baltic Sea region the correlations in autumn and winter were around 0.5, but in the summer months considerably less. The same was true towards the east. For example, the correlation coefficient between Helsinki and Moscow was 0.1-0.3. On the other hand, almost significant negative correlations were found between Finland and Iceland.

6. CONCLUDING REMARKS

The precipitation climate of Finland has remained basically unchanged during the present century and most of the changes can be regarded as the part of the natural climatic variability. The expected human-induced climate changes are not (yet) detectable in Finland. The monitoring of future climatic variations, complemented with reliable background information, will be continued as an important task of climatology in Finland.

REFERENCES

Auer, I., 1993. Niederschlagsschwankungen in Österreich seit Beginn der Instrumentallen Beobachtungen durch die Zentralanstalt für Meteorologie und Geodynamik. *Österreichische Beiträge zu Meteorologie und Geophysik 7*, 73 p.

Frich, P., 1994. North Atlantic Climatological Dataset (NACD) - towards an European Climatic Data Centre (ECDC). In: Heino, R. (ed.), Climate Variations in Europe. Proceedings of the European Workshop held in Kirkkonummi (Majvik), Finland 15-18 May 1994. *Publications of the Academy of Finland 3/94*, 81-96.

Førland et al., 1995. Changes in "normal" precipitation in the North Atlantic region (in preparation).

Heino, R., 1994. Climate of Finland during the period of meteorological observations, *Finnish Meteorological Institute Contributions 12*, 209 p.

Heino, R. and H. Tuomenvirta, 1994. Climatic changes in Northern Europe. In: Kanninen M.. and P. Heikinheimo, The Finnish Research Programme on Climate Change, Second Progress Report. *Publications of the Academy of Finland 1/94*, 31-36.

Tabony, R.C., 1977. The variability of long-duration rainfall over Great Britain.*Meteorological Office Scientific Paper 37*, Bracknell, UK, 40 p.

CORRESPONDING AUTHOR

Dr. Raino Heino
Finnish Meteorological Institute
Climatology Division
P.O. Box 503
FIN-00101 Helsinki
Finland

FRACTAL PROPERTIES OF PRECIPITATION IN SPAIN

J.J. Oñate Rubalcaba

Departamento Universitario de Ecología. Universidad Autónoma de Madrid. 28049-Madrid, Spain

ABSTRACT

Application of rescaled range analisys to the 10 annual precipitation series in Spain for the period 1901-1989, reveals that the series of precipitations fits a fractal distribution, with a mean fractal dimension of 1.32±0.01. This lies in the same order of magnitude as the fractal dimensions obtained from other macrometeorological and paleoclimatic registers. This favourable comparison between fractal dimensions of the variables on both small time scales and long-term time spans suggests that such values are characteristic of climatic change over the spectral range of 10 to 10^6 years. The results contribute to the establishment of this assumption as a valid hypothesis for the interpolation of climatic change from one scale to the next, and also in aplicationes such as hydrological design.

1 INTRODUCTION

Self-similarity and scale invariance are characteristic properties of the real world exploted by fractal geometry to find simple rules for the assembly of complex natural objects or processes. Many natural phenomena manifest scale invariance and may be studied in the framework of fractal geometry (Lovejoy and Mandelbrot, 1985, Turcotte 1992).

Mandelbrot (1982) defined fractal distribution as one in which the number of objects N with a characteristic size greater than r, scales with the relation

$$N=Cr^{-D} \qquad (1)$$

where C is a constant of proportionality and D is a similarity or fractal exponent wich can be related to the fractal dimension (Mandelbrot, 1975).

Very long time scales, usually associated with climate, were studied by Hurst (1951, 1956) who found that fluctuations in the Nile River outflows reveal long-term correlations. Hurst's rescaled range analysis (R/S) has been applied to a number of macrometeorological, climatic and paleoclimatic variables (Mandelbrot and Wallis, 1968, 1969, Lovejoy and Schertzer, 1983, Lovejoy and Mandelbrot, 1985, Fluegeman and Snow, 1988, Bodri, 1994). The results of these analyses indicate fractal geometry of the variables and yield Hurst's exponent values in the interval $0.5<H<1$.

This paper analyzes 10 annual precipitation secular series in order to determine the fractal dimension of their curves. If the fractal dimensions calculated on this centenary time scale are found to be similar in order of magnitude to those obtained for the longer-term climatic data, we have new proof that climatic changes are characterized by a general fractal dimension over the spectral range 10 to 10^6 years, with a heavy statistical interdependence of data.

2 DATA

Ten series of annual precipitations in Spain between 1901 and 1989 were computed from daily figures kindly provided by Spanish Institute of Meteorology (Table 1).

Table 1. Meteorological Station Locations

Station	Lat. (°N)	Long. (°W)	Alt. (m)
Albacete	38.56	01.51	699
Alicante	38.22	00.30	82
Badajoz	38.52	06.58	186
Huesca	42.07	00.26	503
Jaén	37.48	03.48	503
La Coruña	43.22	08.25	57
Salamanca	40.58	05.41	797
San Fernando	36.27	06.12	30
San Sebastián	43.19	02.03	258
Soria	41.46	02.28	1063

Homogeneity of the original records was tested by means of the application of run test (Thom, 1966), and was considered acceptable in all cases ($p<0.1$). Since there was a considerable variability of the original records (Table 2), 5-year moving average filters were computed to smooth the series.

Trends in the series for the last century were examined using the Mann-Kendall trend

analysis (Mitchell *et al.*, 1966). Statistically significant and negative tendencies were found in three series, while another three had significant and positive tendencies. No statistically significant trends were found in the remaining four series (Table 3).

Table 2. Average Annual Precipitation (mm) and Variation Coefficient of Records

Station	Mean	CV
Albacete	343.6	347.5
Alicante	333.3	497.5
Badajoz	499.5	331.7
Huesca	529.2	336.3
Jaén	586.1	341.6
La Coruña	892.7	214.9
Salamanca	419.1	312.1
San Fernando	604.9	350.0
San Sebastián	1423.9	209.3
Soria	546.2	271.5

Table 3. Trend Analysis. Mann-Kendall Statistic U(t) and Probability Level: *p<0.05; **p<0.01

Station	U(t)	p
Albacete	1.06	-
Alicante	-0.22	-
Badajoz	0.12	-
Huesca	1.24	-
Jaén	-3.36	**
La Coruña	4.10	**
Salamanca	1.99	*
San Fernando	-2.31	*
San Sebastián	4.93	**
Soria	-1.94	*

3 METHODS

Detailed descriptions of the *R/S* analysis can be found in the bibliography (e.g. Hurst, 1965, Mandelbrot and Wallis, 1969, Feder, 1988) but a brief outline is provided here. The present study obtained 10 discrete records in time of annual precipitation. By choosing a time period s (referred to as a lag) shorter than the total record T, we first calculate the increments I, the change in precipitation between two adjacent years, for this lag and then the average A and the standard deviation S of the increments. By constructing a set of new increments $(I-A)$ and sequentially adding them, we reconstruct an image of the original curve in this lag along a horizontal axis. Range R is defined as the maximum value minus the minimum value of this curve, and by dividing R by S we obtain a dimensionless number R/S (rescaled range value) for the lag in question. For each lag s we obtained $(T-s)$ number of R/S values. The average of all of them is the final representative value of each specific time span.

The record is said to satisfy Hurst's law if the plot of R/S values versus time spans in log-log space is closely aligned along a straight trendline, the slope of which shall be designated as H. For many natural phenomena, Hurst and later Mandelbrot found that $R/S \sim (\text{lag})^H$, where H is now referred to as the Hurst exponent. Mandelbrot and Wallis (1969) discussed the effect of R/S ratios for high and low values of s when drawing conclusions from the plot. They concluded that when fitting a straight trendline, high and low values of s should be given less weight than values far from both $s=1$ and $s=T$. The present analysis therefore adopts time spans of 5, 7, 10, 20, 40, and 70 years.

The Hurst exponent is easily shown (Feder, 1988) to be 0.5 for a random record in time where observations are statistically independent. Mandelbrot and Wallis (1969) found that for many geophysical records $H \uparrow 0.5$, being a common characteristic for persistent data values of $H>0.5$ and for antipersistent data values of $H<0.5$.

According to Mandelbrot (1982), the Hurst exponent in the interval $0.5<H<1$ is related to fractal dimension D by

$$D=2-H \qquad (2)$$

which leads to the values of D in the interval $1<D<1.5$. Mandelbrot and Wallis (1969) qualified this feature as a usual characteristic of many geophysical records, meaning some degree of long-term persistence in the data.

4 RESULTS AND DISCUSSION

Given that plot of R/S values versus time are virtually repetitive, figure 1 only shows the the plots for two of the meteorological stations.,

Plotted lines represent linear regressions for time spans of 5, 10, 20, 40 and 70 years (Mandelbrot and Wallis 1969).

The presence of clearly visible breaks is a characteristic feature of each diagram (Fig. 2). Near a lag of $s \sim 18$ the trendline shows a reduction in the scatter of the log (R/S) values being the slope interrupted by an almost horizontal segment and quickly reestablished after the break. Similar breaks also appear near a lag of $s \sim 22$ and $s \sim 33$. These characteristics may be linked to periodic

phenomena with the wavelength equal to s (Mandelbrot and Wallis, 1969).

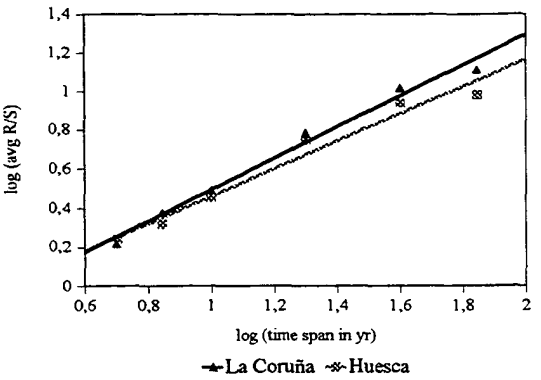


Figure. 1. Plot of Averaged Rescaled (R/S) Values versus Time Spans for La Coruña and Huesca Meteorological Stations.

The second and third breaks might correspond respectively to twice and threefold the wavelength of the well-known periodic element in solar activity. Many other climatic records from instrumental as well as proxy data (see review by Burroughs, 1992), also indicate the sunspot cycle and the multiples of the 11-year period.

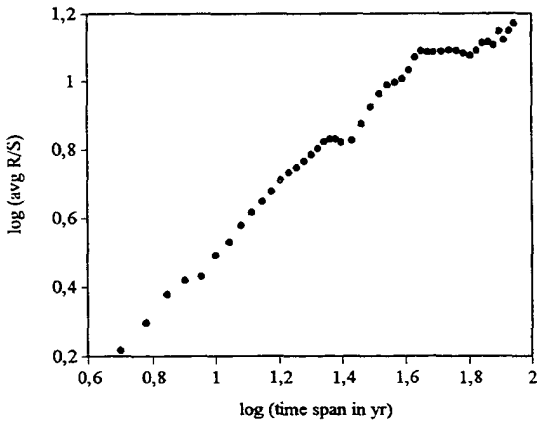


Figure. 2. Detailed Version of fig. 1 for La Coruña Meteorological Station. Values of s range from 5 to 25 uniformly in increments of 1, then from 25 to 50 uniformly in increments of two, and from 50 onwards in increments of 3.

Most surprisingly is the first break, which may be linked to the 20-year cycle detected in other rainfall records (Currie & O'Brien, 1988; Hamseed, 1983; Tyson, 1986). No conclusions should be advanced at this point about whether it is due to lunar tidal effects or to some other cause. As Burroughs (1992) remarks, until we have looked at all the evidence, all we can say is that on the basis of instrumental records, the case for many aspects of precipitation being modulated by a 20-year cycle is apparently formidable.

The presence of several periodic elements complicates the panorama, but it does not alter the validity of the *R/S* diagrams. Table 4 shows estimates for slope H and the calculated fractal dimensions D.

Table 4. H Values and Fractal Dimensions for the Series

Station	H	D
Albacete	0.70±0.0	1.30
Alicante	0.71±0.0	1.29
Badajoz	0.79±0.0	1.21
Huesca	0.70±0.0	1.30
Jaén	0.56±0.0	1.44
La Coruña	0.80±0.0	1.20
Salamanca	0.68±0.0	1.32
San Fernando	0.59±0.0	1.41
San Sebastián	0.64±0.0	1.36
Soria	0.68±0.0	1.32
Mean	0.68±0.0	1.32±0.01

There is no apparent link between the trends in the data sets and the fractal dimension values obtained. Values of D lie in the range 1.20-1.44 with a mean of 1.32 in accordance with those obtained in previous studies. Furthermore, all estimated values of H lie in the range 0.5-1, indicating long-term persistence of the data.

5 CONCLUSIONS

Values of H exceeding 0.5 infer that the span of statistical interdependence of climatic data is large. The good agreement of fractal dimensions in the range $1<D<1.5$ on both short and long-term time scales, indicate a persistence in the climatic records over the spectral range of 10 to 10^6 years. The similarity in the irregularity characteristics of the records suggest that the system has a "memory" of past conditions over at least this range.

Further quantitative studies of the climatic elements in the whole hierarchy of time scales may have a comparative basis in the fractal dimension, which is independent of specific units of measurement. This potential opens up new opportunities in climatic research, particularly in the interpolation of climatic change from one scale to the next.

ACKNOWLEDGMENTS

The author is indebted to the Spanish National Meteorology Institute (I.N.M.) for kindly providing the daily data and to F. Suárez for programming assistance. The study was sponsored by I.N.M. contract n° 9416.640.08.51.

References

Bodri, L., 1994, "Fractal analysis of climatic data: Mean annual temperature records in Hungary", Theor. Appl. Climatol., 49, 53-57.

Burroughs, W.J., 1992, "Weather cycles: Real or imaginary", Cambridge, Cambridge University Press, 207 pp.

Currie, R.G., O'Brien, F., 1988, "Periodic 18.6 year and cyclic 10- to 11-year signals in Northeast United States precipitation data", Int. J. of Climatology, 8, 255-281.

Feder, J., 1988, "Fractals", New York, Plenum Press, 235 pp.

Fluegeman, R.H., Snow, R.S., 1989, "Fractal analysis of long-range paleoclimatic data: oxygen isotope record of Pacific core V28-239", PAGEOPH, 131, 307-313.

Hamseed, S., 1983, "An analysis of periodicities in the 1470 to 1974 Beijing precipitation record", Geophys. Res. Letters, 10, 436-439.

Hurst, H.E., 1951,"Long-term storage capacity of reservoirs", Trans. Am. Soc. Civil Engrs., 116, 770.

Hurst, H.E., 1956, "Methods of using long-term storage in reservoirs", Proc. Inst. Civil Engrs., Part 1, 519.

Hurst, H.E., Black, R.P., Simaika, Y.M., 1965, "Long-term storage, an experimental Study", London, Constable.

Lovejoy, S., Schertzer, D., 1983, "Evidence of a 40,000 year scaling regime in climatological temperatures", IInd Inter. Meeting on Statistical Climatology, Lisbon, Portugal, 26-30 Sept. 1983, 16.1.1-16.1.5, Lisbon, Instituto Nac. de Met. e Geof.

Lovejoy, S., Mandelbrot, B.B., 1985, "Fractal properties of rain, a fractal model", Tellus, 37 A, 209-232.

Mandelbrot, B.B., 1975, "Les objects fractals: forme, hasard et dimension", Paris, Flammarion, 187 pp.

Mandelbrot, B.B., 1982, "The Fractal Geometry of Nature", New York, Freeman, 461 pp.

Mandelbrot, B.B., Wallis, J.R., 1969, "Some long-run properties of geophysical records", Water Resources Res., 5, 321-340.

Mitchell, J.M., Dzerdzeevskii, B., Flohn, H., Hofmeyr, W.L., Lamb, H.H., Rao, K.N., Wallen, C.C., 1966, "Climatic Change", WMO Tech. Note No. 79, Geneva, World Meteorological Organization, 79 pp.

Thom, H.C.S., 1966, "Some methods of climatological analysis", WMO Tech. Note No. 81, Geneva, World Meteorological Organization, 53 pp.

Turcotte, D.L., 1992, "Fractals and Chaos in Geology and Geophysics", Cambridge, Cambridge University Press, 221 pp.

Tyson, P.D., 1986, "Climatic Change and Variability in Southern Africa", Oxford, Oxford University Press, 197 pp.

CORRESPONDIG AUTHOR

J.J. Oñate
Departamento Interuniversitario de Ecología
Universidad Autónoma de Madrid
28049-SPAIN

RAINFALL DISTRIBUTION IN THE GISBORNE REGION, NEW ZEALAND, IN DIFFERENT SYNOPTIC SITUATIONS.

G.M. Daw

Meteorological Service of New Zealand Limited.

INTRODUCTION

The Gisborne region is located in the northeast of the North Island of New Zealand. The province boasts a complex topography, and can be a difficult one to forecast for. It lies to the east of a substantial mountain range, and due to the prevalence of westerlies over New Zealand, can often be affected by drought. There is a desire to improve the forecast skill of moderate or heavy rainfall events in the area, due to its "rain sensitivity."

The purpose of this study was to identify distinct spatial precipitation patterns in moderate or heavy rainfall events in the region, and to link these with synoptic class. This research used the technique of principal component analysis to identify spatial rainfall pattern, with the aim of integrating the results into the forecast process.

METHOD

An economical description of the variation in rainfall over the Gisborne region was achieved using the method of principal component analysis (PCA). Characteristic spatial patterns were identified. Corresponding synoptic mechanisms were then linked to these favoured modes, helping the forecaster to build a better conceptual model of the mesoscale rainfall patterns in the area.

PCA was applied to data from a network of twenty eight rain gauges in the Gisborne Province. The data spanned two and a half years, from March 1989 to August 1991, and consisted of consecutive 24 hour rainfall totals.

Excessively light precipitation days were not the focus of this study, and were removed from the analysis to avoid spurious precipitation patterns emerging.

Analysis was performed using the Systat package. A correlation matrix was used and three significant components emerged by the usual criteria Jolliffe (1986, 1990); Salinger et al. (1986). Components were rotated for ease of interpretation, employing the varimax criterion Jolliffe (1987); Richman (1986). The three rotated components explained 84% of the total variance.

RESULTS

Figures 1, 2 and 3 display the plotted components, contoured using a Cressman (1959) analysis scheme. The three abstract precipitation patterns are distinct-

Pattern 1 shows a rainfall maximum in the south and southeast of the area, with a corresponding minimum on the northern side of the main divide. The main range is aligned in a southwest/northeast direction, yet the rainfall gradient is slightly westsouthwest/eastnortheast. The influence of the coastal hills in the northeast of the district can be seen.

The second pattern is strongly defined, with a large precipitation maximum to the north and northwest, mirrored by a minima to the south and southeast. The effect of the main divide is clear .

Pattern 3 has a small but distinct rainfall maximum in the northeast of the region. This maximum occurs close to the coast over the coastal hills mentioned previously.

These patterns are statistical notions. Daily rainfall will consist of more than one component pattern, usually with one particular component dominant. In order to link synoptic situation with component rainfall pattern, operational charts were investigated for the most dominant days for each component (highest score days). Mean Sea Level, 1000-500hpa Thickness and upper level charts were utilised.

Component one was defined synoptically by a moist flow from the southeast between a trough to the north or northeast of the North Island and a ridge to the east of the South Island. (A conveyor belt of moisture). The upper winds over Gisborne were usually a light or moderate southerly, with an upper level ridge pushed well south over the South Island and an upper level trough over the Gisborne area. A meridional flow is evident over New Zealand, with a omega-shaped jet structure common. A cold trough was evident over or just to the east of Gisborne.

The distinguishing feature of the synoptic situation linked to component two was the strong, long fetch northwest flow over the North Island. An active cold front, normally oriented in a north/south direction, is moving east onto the country. An associated wave is common. A large amplitude upper trough west of New Zealand ensures a *deep* northwesterly to the Gisborne area, most often with a subtropical jet on its downstream side. A warm tongue lies over the country, with strong warm advection ahead of the surface front.

The synoptic situation associated with component three was similar but subtly different to that of component one. A surface *northeast* flow between around a ridge east of the country and a trough west of Gisborne brings a moist airmass onto the Gisborne coast. The upper level features are cut-off and there is marked meridional flow, similar to the pattern for component one. In this case the upper level *high* is positioned east of or over Gisborne. Upper winds over the entire country are light, with an indeterminate thermal pattern. Wind maxima exist both to the north *and* south of New Zealand.

Three conceptual models were developed from this research, detailing spatial precipitation patterns in the Gisborne region and the associated synoptic features.

CONCLUSION

The mathematical rainfall patterns correlated well with actual spatial precipitation variations for selected case studies. It was evident that the 24 hour time period was too coarse for certain events. A moderate proportion (20%) of actual rainfalls in a certain situation type were best explained by a *combination* of the component one and three mathematical patterns.

Further investigation revealed a temporal relation in component dominance. Component one and three were strongly linked, with an almost invariable transition from one to the other on time scales of one day or less. This was consistent with the synoptic situations that had been identified for each component.

Seasonal trends in component dominance were also noticed, possibly linked to the medium and long waves in the westerlies. Further research would need to be done to prove this.

It is intended that this type of research be applied to other forecast districts in New Zealand, with more statistical models of this type being integrated into the forecast process.

Figure 1

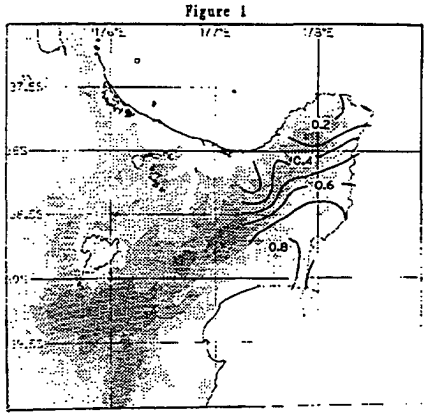


Figure 2

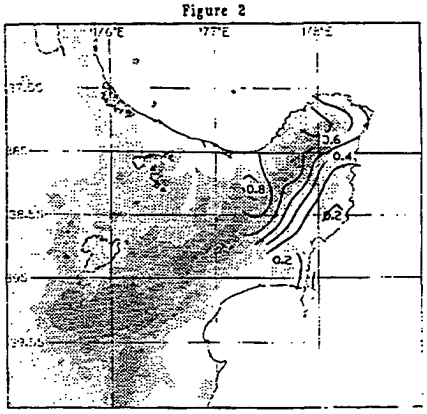
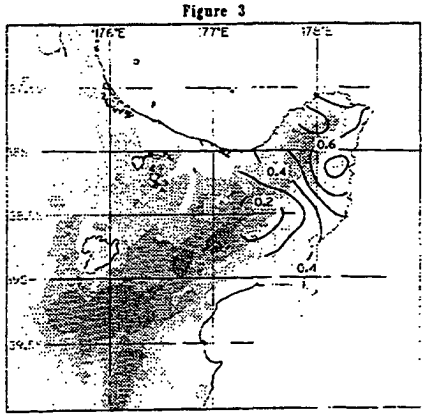


Figure 3



Light shading 300-600m AMSL
Medium shading 600-900m AMSL
Dark shading >900m AMSL

ACKNOWLEDGEMENTS

The author acknowledges

- The efforts of the Gisborne District Council and the National Institute of Water and Atmosphere Research (NIWA) in supplying data for this research.
- Dr Mark Sinclair of NIWA for making his orographic rainfall model available.

REFERENCES

Craddock, J.M., and Flood, C.R., 1969, "Eigenvectors for representing the 500mb geopotential surface over the Northern Hemisphere", Quarterly Journal of the Royal Meteorological Society, Vol 95, pp. 576-593.

Flury, B., 1988, "Common Principal Components and related multivariate models", Wiley, New York.

Hessell, J.W.D., 1980, "The climate and weather of the Gisborne Region", New Zealand Meteorological Service Misc. Publication, Vol 115 (8).

Jackson, J.E., 1991, "A user's guide to Principal Components", Wiley, New York.

Jolliffe, I.T., 1986, "Principal Component Analysis", Springer-Verlag, New York.

Jolliffe, I.T., 1987, "Rotation of Principal Components: some comments", J. Climatology, Vol 103, pp. 507-510.

Jolliffe, I.T., 1990, "Principal Component Analysis: A beginner's guide- Introduction and application", Weather, October 1990, pp. 375-382.

Jolliffe, I.T., 1993, "Principal Component Analysis: A beginner's guide- Pitfalls, myths, and extensions", Weather, August 1993, pp. 246-253.

Kidson, J.W., 1975, "Eigenvector analysis of monthly mean surface data", Monthly Weather Review, Vol 103, pp. 177-186.

Mulaik, S.A., 1971, "The foundations of factor analysis", McGraw Hill, New York.

Neale, A.A., and Thompson, G.H., 1978, "Rainfall distribution near Manawatu Gorge in a simple west and northwest airstream", New Zealand Meteorological Service Technical Note 233.

Preisendorfer, R.W., 1988, "Principal Component Analysis in meteorology and oceanography", Elsevier, Amsterdam.

Richman, M.B., 1986, " Rotation of principal components", J. Climatology, Vol 6, pp. 293-335.

Salinger, M.J., Smith, R.M., and Tweeddale, M., 1986, "Mesoscale precipitation patterns around Wellington, New Zealand", New Zealand Journal of Geology and Geophysics, Vol 29, pp. 99-114.

Seber, G.A.F., 1984, "Multivariate observations", Wiley, New York.

Sinclair, M.R., 1993, "A diagnostic model for estimating orographic precipitation", Internal NIWA paper.

CORRESPONDING AUTHOR
Miss Georgina Daw
Meteorological Service of New Zealand Limited.
PO BOX 722 Wellington
New Zealand
email DAW@MET.CO.NZ

ON THE CONNECTION OF PRECIPITATION SYSTEMS WITH SPATIAL CORRELATION FIELDS IN THE PROVINCE OF ENTRE RIOS

D.F. Barrera

Universidad de Buenos Aires, Buenos Aires, Argentina.

ABSTRACT

Meso-scale correlation fields of precipitation in a flatland centered at 31^0 S, 58^0 W, were estimated from computed point values of spatial autocorrelation. Typical, differentiated fields were found for each season and time integration lapse, and possible causes of the observed particular paths were discussed and related to basic descriptions of present theories about mid-latitude mesoscale precipitation systems and about convective storms evolution. Patterns are elliptic; their inter-seasonal variations, such as orientation, decrease with distance and excentricity, were studied.

1 INTRODUCTION

Correlation fields of precipitation in a flatland (centered at 31^0 S, 58^0 W) belonging to the Province of Entre Rios (east of Argentina) were estimated from computed point values of spatial autocorrelation. Spatial dimensions of the area studied and observing sites interdistances correspond to those of atmospheric meso-ß scale. Daily precipitation series from 40 pluviometric posts and 3 meteorological stations irregularly distributed over an area of 30000 km^2 belonging to the National Meteorological Service Network were processed in this work. Simultaneous records processed cover the period 1962-1975.

The region has a mid-latitude climate in winter and a subtropical climate in summer. It is a temperate sub-humid flatland with a mean anual precipitation of about 100 cm.

A methodology developed by Barrera (1995) was used to obtain correlation fields from the above mentioned series. The selected time integration lapses were 5, 30 and 90 days. The lapse of 5 days was chosen in order to capture the effect on precipitation of frontal passages due to synoptic pressure waves (Madden and Julian, 1972). The lapses of 30 and 90 days were chosen in order to know how the effects of synoptic and sub-synoptic origin decrease as time integration increases.

We referred to latitude and longitude as Φ and θ repectively. Consequently with the above mentioned methodology, a value of 280 km on the side for the "homogeneity area" was selected and divided into 49 square sub-areas of 40 km on the side. This enabled us to have 730 points on the correlation domain (plane $\Delta\Phi$, $\Delta\theta$) to fit the correlation field.

2 MAIN CHARACTERISTICS OF THE FIELDS FOUND

In spite of the smoothing carried out by means of non-parametric and robust fittings, the field isolines found show distorsions concerning the fields that would be analitically derived from superpositions of one or more anisotropic effects. These distorsions can be explained as caused by climatic fluctuations characteristic of the time-space variability of precipitation during the 14-year-period selected. They should diminish as the computation period extends.

2.1 BASIC SHAPE OF CORRELATION PATTERNS

Typical, differentiated fields were found for each season and time integration lapse.

The obtained fields are characterized by their anisotrophy, with elliptic patterns varying in shape and orientation depending on season, separation between localities and time integration lapse.

In order to explain the anisotropy detected for every season, we highligth the fact that convective precipitation (which has strong presence even in winter) is almost always limited to narrow areas such as rainbands and squall lines (Houze and Hobbs, 1982), which have seasonal predominant orientations in the region. The anisotropy of the fields found for 5 and 30-day periods in the four seasons is evident, its basic shape being elliptic for each isoline. For example, in the case of rain accumulated for 5 days in winter (it does not snow in the area), for correlations between 0.70 and 0.50, there is a basic elliptic pattern, with its mayor axis pointed in the direction WNW-ESE, shaping an approximated angle of 130^0 from the north. This means that with equal separation between locations, separation vectors pointing in that direction are the most correlated, whereas in its

normal direction the correlation between precipitation totals is minimum (minor axis of the ellipse). Major axes of ellipses indicate spatial orientations for which the decrease in correlation with separation is minimum.
It arises as a more or less immediate hipothesis that this basic shape es mainly due to the dominant orientation of cold fronts and squall lines passing across the region, which are associated with cyclonic centers originated at the subpolar low-pressure belt.

2.1.1 INTER-SEASONAL VARIATIONS OF PATTERNS

2.1.1.1 ORIENTATION

In summer and fall, the basic elliptic patterns are directed with their major axes at approximately 100^0 and 110^0 respectively (Figures 1c and 1d). This mayor axes layout, nearer to the direction E-O than in winter and spring (Figures 1a and 1b) might be due to the fact that in summer and fall cold fronts arrive with less strength to the area studied, and this migth cause its advance to head more to the north, not to the northwest as would be the case in winter and spring, according to what was observed. Another explanation for what was observed could originate in the variation of the mean thermal field along the year, which might result in a more E-W orientation in summer of the convective systems such as squall lines and mesoscale convective complexes. The frequency of squall lines is higher in summer in the studied region (see Lichtenstein and Schwarkopf, 1970).
As a result of this study, we presumed that the mean seasonal orientation of fronts and squall lines in the region vary from one season to another, and are coincident whith the orientations of the major axes of the corresponding obtained elliptic correlation patterns.

2.1.1.2 DECREASE WITH DISTANCE

In summer, in the same integration period, the correlation values are much smaller than in winter for any direction and separation. The corresponding values in spring and fall are intermediate. This fact depends on the kind of prevailing pr. The stratiform rain is more incident in winter. On the other hand, convective activity, with major presence in summer, generates rain fields less uniform and much less extended than the ones caused by stratiform cludiness.

2.1.1.3 EXCENTRICITY

In fall, the fields found are of similar shape to the ones in summer but with slower decrease; whereas spring correlation fields are more similar to the ones in winter, but with a faster decrease with distance than these ones. These characteristics apply to accumulated precipitation in 5 days as well as in 30.
The degree of anisotropy (excentricity) was found to be maximum in winter and minimum in summer. This fact was related to the greater activity of synoptic weather systems over the region in winter, with predominance of narrow frontal rainbands associated to cold fronts as rain provider. Houze and Hobbs (1982) pointed out that frontal rainbands are more or less paralell to the front.
The obtained fields show basic elliptic patterns for the four seasons and the three time integration lapses, except in the case of 90 days cumulative precipitation for summer and winter.

2.1.2 ROTATION OF ELLIPTIC PATTERNS WITH DISTANCE

Rotation of elliptic patterns with distance were found for the four seasons. For separations between localities greater than 100 km, the relative orientation of maximum correlation was found to be approximately 120^0 (west northwest - east southeast) in winter and spring, and 100o in summer and fall.
For separations lesser than 80 km, relative orientations of maximum correlation were rotated about 30^0 counter-clockwise with respect to greater separations. It was presumed that this rotation as a function of separation is due to the displacement of convective clusters along the rainbands towards the synoptic lower pressure center.
In winter, spring and fall there is a gradual clockwise rototion af the major axis od the dominant elliptic shape, as the separation between localities increases" In the case of rain accumulated for five days in winter (Figure 1a), the correlation for 40 km of distance is approximately 0.8 in the direction of minimum variation, which es about 100^0 from the north. This contrasts with the 130^0 of the major axis for a separation of 200 km. This fact is consistent with observations on storms carried out with radar and with outlines of storm displacements and convective cells (Marwitz, 1972 ; Newton and Frankhauser, 1975). These authors showed that the convective cells grouped in the SMSAs move in the approximate direction of the average wind of the cloudy layer; and that consequentrly the relative movement of the cells is not parallel to the advance direction of the storm and front, but rotated to the left in the northrn hemisphere. This must go together with a rotation to the right in the southern hemisphere, en the direction of the synoptic

center of low pressure associated with the front. Therefore, the movemente of the cells is not along the rainband axis (or the squall line), but rotated to the elft of the axis, forming a sharp angle. We can expect that this angle is approximately equal to the one formed by the isobars on the hot side of the front and the frontal line. In the area being studied, and following this pattern of typical movement, the logical consequenceis that this same angle appears in the correlation field also: the axis of the cell movement is represented by the axis of the internal elliptic shape, and that of the band by that of the external elliptic shape.

2.1.3 VARIATION WITH INTEGRATION LAPSES

For 30-day periods of accumulated rain, in spite of the fact that the effects of 4 or 5 synoptic waves are added to the integration lapse, the preferential orientation is present, thogh the elliptic shape is more rounded (Figures 2a and 2d).
As it was to be expected, the correlationes greater for this lapse than for 5 days, for whatever distance values given and direction. This is due to the fact that the greater the number of storms included in the same lapse, the more uniform the accumulated rain field will be. For totals accumulated of 90 days, values turned out even greater, as it was to be expected. Moreover, the correlation isolines are approximately circular in winter and summer for distances of 120 km or more, evidencing the effect produced by the superposition of about 5 synoptic perturbations causing pr. For example, in summer, for localities 120 km distant form each other, the correlation are 0.80 and 0.76 for the directions E-W and N-S respectively.

3 CONCLUSIONS

It can be concluded that the results confirm that precipitation in the area is a mesoscale phenomenon, because the correlation decreases rapidly. For example, for an integration lapse of 5 days in winter (which typically contains one frontal passage), two localities which are separated by 160 km and oriented WNW-ESE (maximum correlation direction) have a correlation value of 0.70; this means that only 49% of the variance of the time series in a locality is explained by what occured in the other locality. In the other seasons and especially in summer, for equal conditions only a small percentage of the variance is explained by the process in the other locality, and this percentage decreases as the separation between localities increases.

Likewise, possible causes of the observed particular paths were discussed and related to basic descriptions of present theories about mid-latitude mesoscale precipitation systems and about convective storms evolution (Marwitz, 1972; Newton and Frankhauser, 1975). In this sense, the results of this work support these basic descriptions, because they are consistent with the correlation fields found.

References

Barrera, D.F., 1995, "Una metodología para estimar el campo de correlación de la precipitación en mesoescala a partir de redes pluviométricas convencionales", Avances en Geofísica y Geodesia, Madrid, Volume 1, in press.

Houze, R.A., and Hobbs, P.V., 1982, "Organization and structure of precipitating cloud systems", Adv. in Geophys., 24, 225-315.

Lichtenstein, E.R. and Schwarzkopf, M.L., 1970, "Aspectos estadísticos de las líneas de inestabilidad en la Argentina", Meteorológica, 1(1), 3-12.

Madden, R. and Julian, P., 1972, "Further evidence of global-scale, 5 day pressure waves", J. Atmos. Sci., 29, 1464-1469.

Marwitz, J.D., 1972, "The structure and motion of severe hailstorms. Part II: Multicell storms", J. Appl. Meteor., 11, 180-188.

Newton, C.W. and Frankhauser, J., 1975, "Movement and propagation of multicellular convective storms", Pure Appl. Geophys., 113, 747-764.

ACKNOWLEDGEMENTS

The author wishes to acknowledge Prof. Erich Lichtenstein for his useful comments.
This work has been done with economic support of National Council of Scientific and Technological Research of Argentina (CONICET) and University of Buenos Aires.
The data used belong to the pluviometric network of the National Meteorological Service of Argentina.

CORRESPONDING AUTHOR
Professor D.F. Barrera
Department of Atmospheric Sciences
Universidad de Buenos Aires
Ciudad Universitaria
1428 Buenos Aires, ARGENTINA.

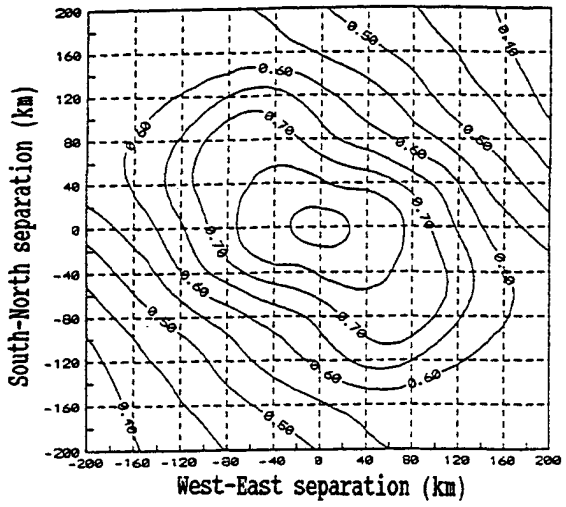


Figure 1a. Correlation field.
5-day periods. Winter

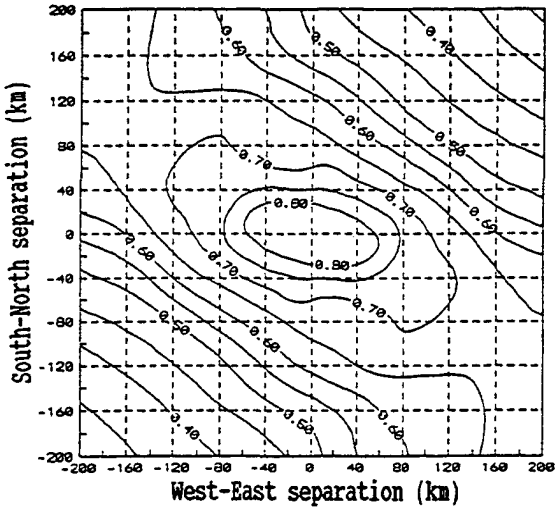


Figure 1b. Correlation field.
5-day periods. Spring

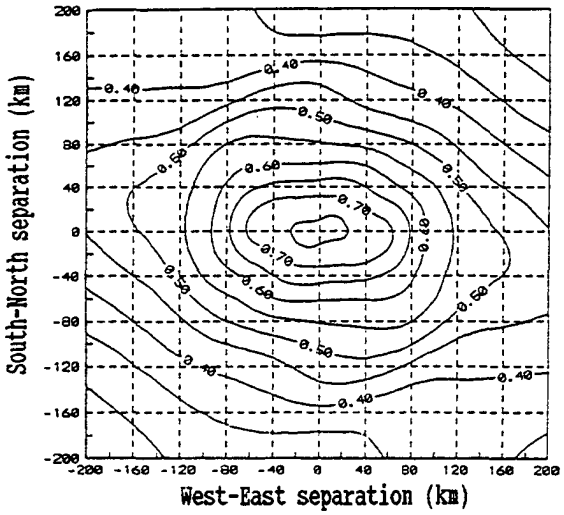


Figure 1c. Correlation field.
5-day periods. Summer

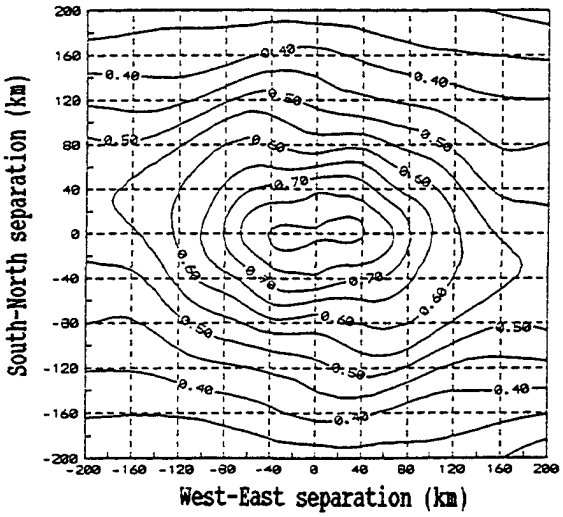


Figure 1d. Correlation field.
5-day periods. Fall

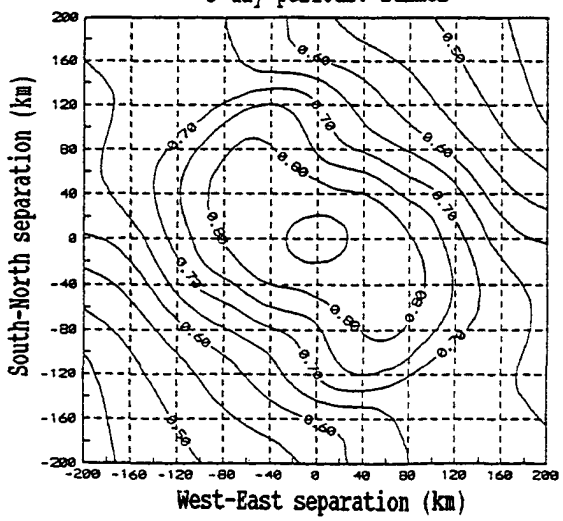


Figure 2a. Correlation field.
30-day periods. Winter

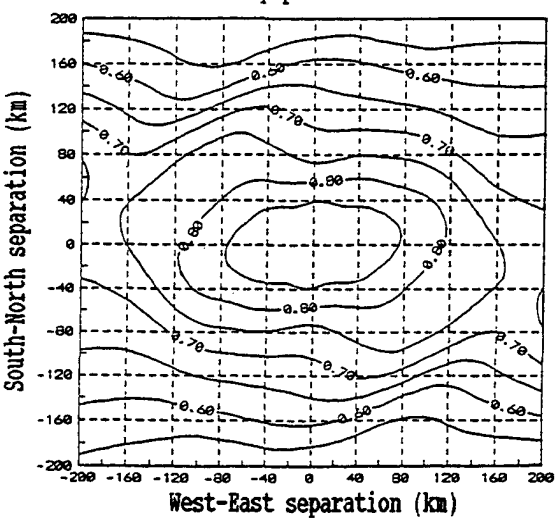


Figure 2d. Correlation field.
30-day periods. Fall

METHODOLOGIC ASPECTS OF EVALUATING THE CORRELATION FIELD OF PRECIPITATION IN MESOSCALE FROM PLUVIOMETRIC DATA

D.F. Barrera

Universidad de Buenos Aires, Buenos Aires, Argentina.

ABSTRACT

Certain procedures dealing with the estimation of spatial correlation fields of precipitation from daily series of pluviometric posts belonging to a conventional meso-network were proposed. They are related to the following issues: a) the days to be considered for computations; b) the sizes of terrain areas associated with cloud clusters and rainbands, which have to be considered; c) sparse and irregular distribution of observing sites, and density maximization of information in the correlation domain; d) detection of anisotrophy and secondary maximums in the correlation field; e) smoothing of isolines at the graph stage.

1 INTRODUCTION

Most operational meso-networks for measuring precipitation all over the world are formed mainly by pluviometric posts. Due to the fact that storms are governed by mesoscale processes, daily data series from these stations are crucially needed for describing both temporal and spatial structure of precipitation. But these series are, generally, significantly affected by observational errors. The most frequent errors are due to the known fact- already reported in Argentina by Hoffmann (1970)- that small totals are frequently omitted. Series affected by this type of errors are easily spotted by their low frequency of small values. In the consisted series, other types of errors that may affect the statistical structure of series (Sevruk, 1982) were eliminated almost completely.

Despite of this fact, affected series are needed to estimate the correlation field of precipitation in mesoscale due to sparse and irregular distribution of observing sites. The gauging network used in this study is shown in Figure 1.

Barrera (1988) showed that omission errors lead to an underestimation of spatial correlation values obtained from affected series, and developed a method to estimate the true value.

Another issues related to the obtention of correlation fields in mesoscale are discussed in this paper, and ways to deal with them are proposed.

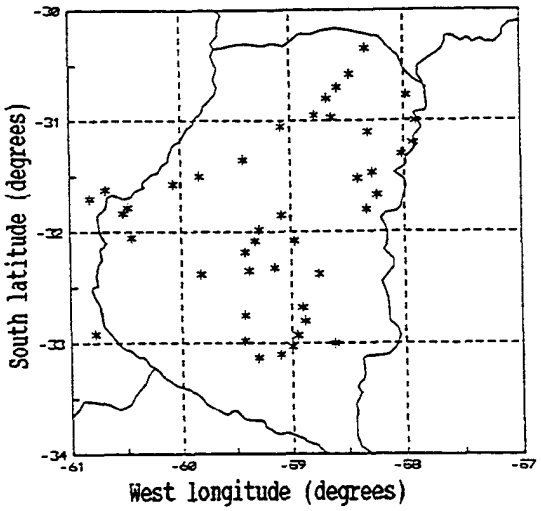


Figure 1. Pluviometric network in the Province of Entre Ríos (Argentina).

2 METHODOLOGIC ASPECTS

2.1 ABOUT THE DAYS TO BE INCLUDED FOR COMPUTATION

A criterion was proposed to determine the series terms (days) to be computed based on observed precipitation at gauging stations. It takes into account scale aspects of rainbands and cloud clusters.

Stol (1972) studied the problem of selecting the days that should be taken into account when computing the spatial correlation of daily precipitation over a region of mesoscale dimensions. He proposed to consider only the "potentially rainy" days. In this way, the days with no precipitation processes in the studied region are excluded for computations. He suggested to take as such days the ones where at least 0.5 mm. were registered at all the observing sites of the region. This criterion could be satisfactory for regions where stratiform and broad precipitation systems are dominant, such as The Netherlands where it was

applied. But it is inadequate for regions where convective cloud systems are sometimes the only source of precipitation. In mid to low latitudes, such as the central region of Argentina, precipitation systems associated with extratropical cyclons, such as rainbands accompanying cold and warm fronts and squall lines, many times present no stratiform rain outside the rainbands. Sharon (1974) proposed to consider the days in which at least one station belonging to the studied area registered an amount of rain greater than certain limit.
We adopted this last criterion, but applied it to sub-zones belonging to the studied region instead of considering the whole region. We choose a daily total of 5 mm as limit.

2.2 ABOUT THE "POTENTIALLY RAINY AREA"

We sought for an area of territory which can be "dragged" by a typical rainband during a storm. Taking into account that rainbands have typical lengths of 200 km to 300 km (Houze et al, 1976) we can expect that a circular area of about 250 km in diameter can be "dragged" by a rainband coming from any direction and get rain from it. Austin and Houze (1972) called "small meso-scale area" (SMSA) to the horizontal atmospheric region containing a cloud cluster (10^2 to 10^3 km^2). Later Houze et al (1976) applied the same concept to a rainband (10^3 to 10^4 km^2) and defined the "large meso-scale area" (LMSA). We followed this terminlogy and applied it to territorial areas that are affected ("dragged") by a SMSA or a LMSA. An area of about 5000 km^2 was defined as "large meso-scale potentially rainy area" (LMSPRA) for a given day being analysed, provided that at least one interior gauging site registered at least 5 mm of rain.
In the same way, an area of about 500 km^2 was defined as "small meso-scale potentially rainy area" (SMSPRA) by considering horizontal dimensions and discharge time of cloud clusters (Houze and Hobbs, 1982). Potentially rainy areas are not geographically fixed.

2.3 ABOUT THE PAIRS OF OBSERVING SITES TO BE CORRELATED

In order to apply the definition of "potentially rainy area" to fixed territorial areas, we proposed to take as the study area a zone of the dimension of a LMSPRA.
Depending on the goal of the study, the zone can be divided into sub-zones of the dimensions of a SMSPRA.
Some of the available observing sites can be located outside the chosen zone (or sub-zone). We call "reference sites" to the observing sites interior to the zone (or sub-zone). If a particular day the zone (or sub-zone) is a LMSPRA (or a SMSPRA), then each of the reference sites must be correlated to the rest of the observing sites, no matter they are reference sites or not. Three different ways of selecting the reference sites were proposed, depending on the particular purpose of the study. Each of these ways leads to a different correlation field, as it is explained below.
a) We seek for a correlation field associated to rain from cloud clusters dragging the center of the zone, and therefore associated to rainbands or squall lines affecting a great part of the zone. In this case, we define a central sub-zone. The days to be kept for computations are those for which the centered sub-zone is a SMSPRA. The reference sites are those interior to the sub-zone. This is appropriate to study the correlation structure associated to severe individual storms.
b) We want to estimate the correlation field associated to rain affecting any part of the zone, no matter if the central area had rain or not. The days to be kept for computations are those for which the zone is a LMSPRA. The reference sites are those interior to the whole zone. In this case computation will include a greater number of pairs of observing sites with no rain at both sites, than in case a); this, in turn, leads to a higher value of correlation.
c) We seek for the correlation field of accumulated precipitation over an integration lapse including more than one rainstorm (i.e., monthly precipitation). In this case, cloud clusters of different storms generally dragged different parts of the zone. Therefore, it is convenient to divide the zone into sub-zones. For each of the sub-zones, the days to be kept for computations are those for which the sub-zone is a SMSPRA, and the reference sites are those interior to the sub-zone. The integration lapses computed will differ from one sub-zone to another, because in a particular lapse not all the sub-zones could registered rain.
For ease of computations, and in order to avoid overlapping of sub-zones, we propose to define square sub-zones in this case.
Fitted correlation functions following procedures b) and c) are shown in Figure 2.

2.4 ABOUT THE POINTS IN THE CORRELATION DOMAIN TO BE INCLUDED

We assumed that precipitation field is homogeneous with respect to their covariance function within an area of mesoscale dimension, provided that it is free of surface discontinuities and orographic features. This property of homogeneity of a two-dimensional

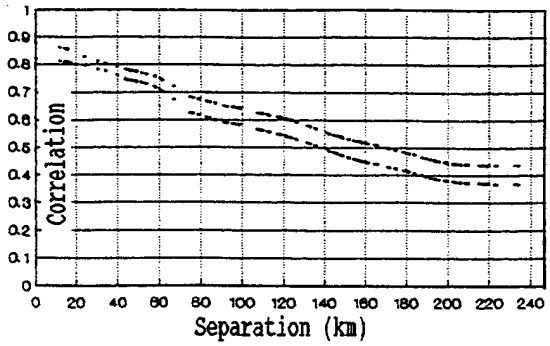


Figure 2. Fitting by procedures b and c
Points are at interdistances between gauges

field was used in order to increase the density of information in the correlation domain: This assumption permits to shift vectors joining pairs of observing sites (relative position) to a common origin in the correlation plane. In this way, it is possible to get enough points in the correlation plane even from an irregular and sparse observing network as the used in this work (see Figure 3). By testing homogeneity over a control region (a plain in the east of Argentina), we verified that a sized area up to 300 km in diameter can be considered as "homogeneous area". The derived correlation field can be centered at any place inside the study area.

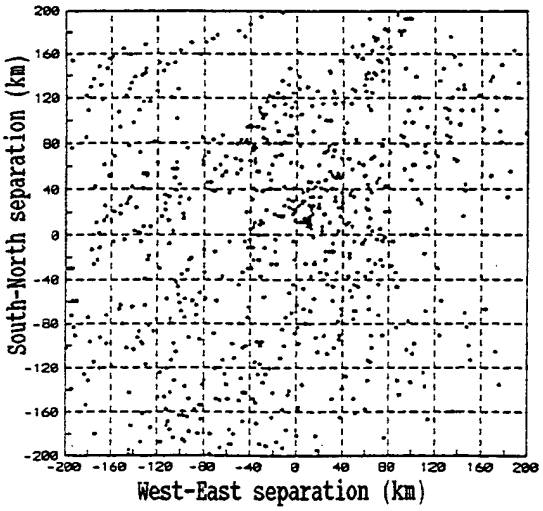


Figure 3. Points in the correlation domain

2.5 ABOUT THE FITTING OF THE CORRELATION FUNCTION

Scatter diagrams in the plane "correlation vs. separation" for 18 equally spaced orientations coincident with the radial grid-lines (see next section) were proposed in order to detect anisotropy in the correlation field (Huff and Shipp, 1969). Separation vectors falling inside an angle of 20 degrees around a radial grid-line were grouped to fit the respective correlation function.

A non-parametric, robust statistical fitting method developed by Boente and Fraiman (1991) was used to estimate, from a scatter diagram of computed values, the spatial correlation function for a given orientation. A typical fitting is shown in Figure 4. This way was preferred over parametric fitting because the last one does not allow us to detect possible secondary maximums (due to mesoscale processes) in the function.

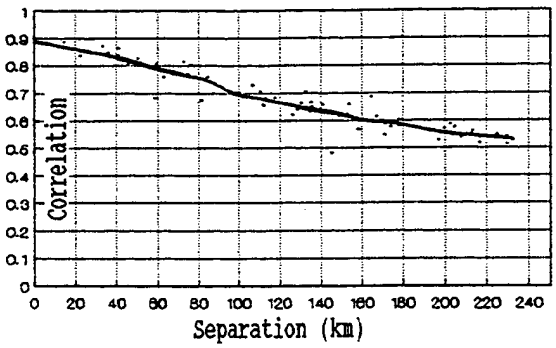


Figure 4. Non-parametric and robust fitting
Scatter diagram and correlation function

Thiébaux (1976) proposed several parametric functions of correlation versus separation, all of them with monotonous decrease; some of these functions were derived analytically by considering as been generated by a stochastic autoregressive anisotropic bidimensional process. An example of correlation functions fitted by the proposed method for six different orientations is shown in Figure 5.

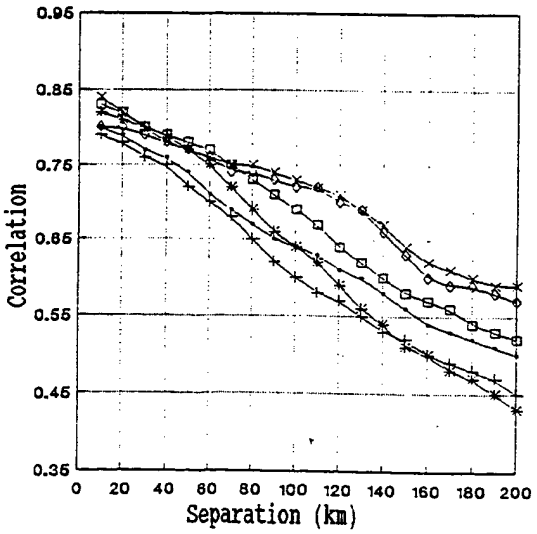


Figure 5. Correlation functions fitted for 6 different directions every 30^0

2.6 ABOUT THE INTERPOLATION GRID

A radial-circular grid (i.e., radial grid-lines intersected by concentric circles) (see Figure 6) was proposed instead of the commonly used square grid, for depiction of correlation isolines.

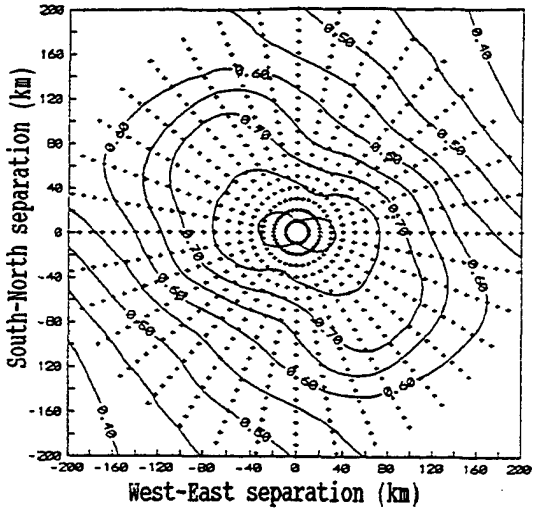


Figure 6. Grid-points and correlation field

In the grid, the number of grid-points on each circle is the same, so curved features of correlation isolines, which resemble concentric circles or ellipses, follow the same degree of smoothing, no matter how far from the center they are. In the case of a square grid, smoothing becames greater when reducing the distance to the center. Then, the proposed grid is more adequate than the conventional square grid for capturing patterns formed by concentric curved lines (see Figure 6).

3 CONCLUSIONS

The methodology presented in this paper allowed us to estimate spatial correlation fields of precipitation from daily series of pluviometric posts belonging to a conventional meso-network. Obtained geometric patterns of correlation structure are in agreement with what can be expected from basic descriptions of present theories of mid-latitude mesoscale precipitation systems and from synoptic characteristics of the selected testing region.

References

Austin, P.M. and Houze, R.A., 1972, "Analysis of the structure of precipitation patterns in New England", J. Appl. Meteor., 11, 926-935.

Barrera, D.F., 1988, "Análisis climático-estadístico de las estructuras temporales y espaciales de la precipitación en mesoescala. Aplicación al filtrado de errores de observación", PhD Tesis, Universidad de Buenos Aires, 147 pp.

Boente, G., and Q. Fraiman, 1991, "A functional approach to robust nonparametric regression", in WEMER STAHEL & SANFORD WEISBERG (ed.), Directions in robust statistics and diagnostics, 35-46, Proceedings of the IMA Institute, USA, Vol.33, Part I.

Hoffmann, J.A.J., 1970, "Características de las series de precipitación en la República Argentina", Meteorológica, 1(3).

Houze, R.A.; Hobbs, P.V.; Biswas, K.R., y Davis, W.M., 1976, "Mesoscale rainbands in extratropical cyclones", Mo. Wea. Rev., 104, 868-878.

Houze, R.A., y Hobbs, P.V., 1982, "Organization and structure of precipitating cloud systems", Adv. in Geophys., 24, 225-315.

Huff, F.A. y Shipp, W.L., 1969, "Spatial correlations of storm, monthly and seasonal precipitation", J. Appl. Meteor., 8, 542-550.

Sevruk, B., 1982, "Methods of correction for systematic error in point precipitation measurement for operational use". Operational Hydrology Report, 21, WMO Nº589.

Sharon, D., 1974, "On the modelling of correlation functions for rainfall studies", J. Hydrol., 22, 219-224.

Stol, Ph., 1972, "The relative efficiency of the density of raingage networks", J. Hydrol., 15, 193-208.

Thiébaux, H.J., 1976, "Anisotropic correlation functions for objective analysis", Mon. Wea. Rev., 104, 994-1002.

ACKNOWLEDGEMENTS

This work has been done with economic support of National Council of Scientific and Technological Research (CONICET) and University of Buenos Aires (Argentina).

CORRESPONDING AUTHOR

Professor D.F. Barrera
Department of Atmospheric Sciences
Universidad de Buenos Aires
Ciudad Universitaria
1428 Buenos Aires, ARGENTINA.

30-day periods. Winter

Daily Alpine Precipitation and its Relation to the Synoptic Scale Flow
A Principal Component and Singular Value Decomposition Approach

Martin Widmann, David Bresch, Christoph Frei and Christoph Schär

Atmosperic Physics ETH, Zürich, Switzerland

April 28, 1995

1 INTRODUCTION

Precipitation in the Alpine region is to a high degree governed by the interaction of synoptic scale weather systems with the Alpine topography. Typically these "primary precipitation events" have a time-scale around one day. The main objectives of the present work are the description of the spatial variability of daily precipitation totals by means of Principal Component Analysis (PCA) and the investigation of the relationship between Alpine precipitation and synoptic scale flow on a daily basis.

With respect to the latter, two approaches will be discussed. The first one uses a disjunct weather classification scheme designed for Switzerland (Schüepp [5]) in conjunction with an approximative representation of precipitation provided by the leading Principal Components (PC). The second method is applied to the whole Alpine region and objectivly identifies coupled anomaly patterns in this mesoscale precipitation field and in the synoptic scale pressure field by means of Singular Value Decomposition (SVD).

The precipitation analysis is based on 3 different data sets: A data set including 100 Swiss Stations for the period 1901-1992, a data set including 300 Swiss stations for the period 1961-1992 [1] and a high resolution gridpoint data set for the whole Alpine region [2] covering the period 1977-1992. In addition a gridpoint data set of geopotential heights [3] was used to provide information on the synoptic situation.

2 EOFS FOR SWITZERLAND

The first 4 leading Empirical Orthogonal Functions (EOFs) calculated from 304 Swiss stations for the years 1961-1992 are indicated in Fig.1. They account for 76% of the total variance. EOF1 describes an uniform mode of variability showing a great similarity to the mean distribution. North-south gradients are explained by the bipolar EOF2 highlighting the Ticino region with the boundary line between the two signs close to the main crest of the Alps, whereas the second bipolar pattern EOF3 roughly spoken describes west-east gradients with some presumably topographic induced deviations from a standard bipolar pattern which would show straighter isolines. The fraction of spatial variability directly correlated to the underlying topography is explained by EOF4, wherein the main crest of the Alps and the Swiss Jura mountains can clearly be seen.

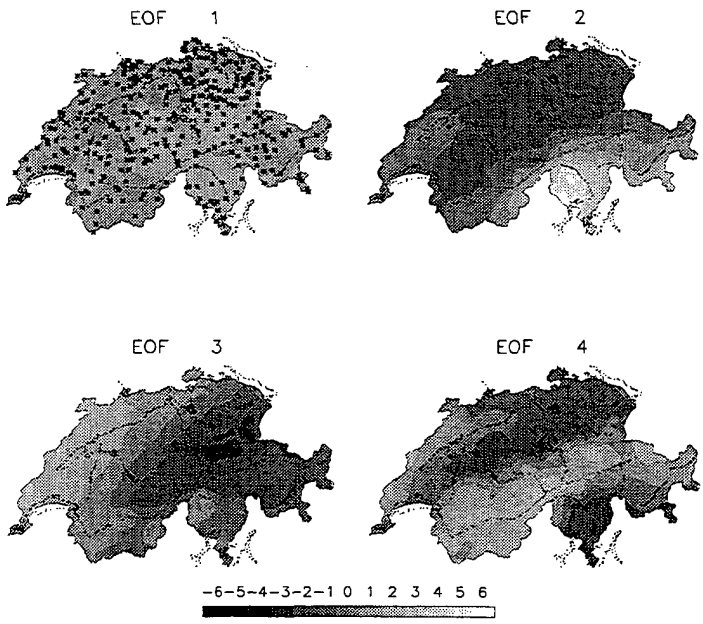


Fig.1: The leading 4 EOFs (in arbitrary units) of daily precipitation in Switzerland as calculated from the years 1961-1992. The observation sites are overlaid to EOF1.

3 ROTATED EOFS

In order to investigate the question of regionalisation, i.e. the identification of areas with highly correlated precipitation, we performed Varimax rotations in different dimensions. The most satisfactory results were obtained in 3 dimensions, where the 3 regions western Switzerland, north-eastern Switzerland and the Ticino area are clearly dominated by one of the rotated PC (RPC).

It should be noted, that besides requiring the loadings of the rotated EOFs (REOFs) to satisfy certain algebraic criteria, as done dealing with the region-

[1] Both provided by the Swiss Meteorological Institute.

[2] Compiled at the Institute of Atmospheric Physics, ETH Zuerich, for details see acknowledgments.

[3] Produced by the Department of Atmospheric Sciences, University of Washington and Data Support Section, NCAR.

alisation problem (cf. e.g. Richman [3]), algebraic criteria can be applied as well to the RPC scores to chose linear transformations of the PCs (cf. e.g. R.Preissendorfer [2], chap.7).

This kind of linear transformations were investgated as well using again the Varimax criterion. In this case the transformation tries to produce RPCs which tend to be small in some situations and large in others but seldom take intermediate values. If this objective were achieved, the RPCs and corresponding REOFs would become interpretable in the sense of a classification. However, applied to the Alpine precipitation data set, this method was not able to produce the desired dense data distribution aligned to the RPC-axes. In 2-dimensional sections the individual data points revealed a quite homogeneous distribution in both the unrotated and the rotated PC-space. Thus, there are strong indications, that the daily precipitation totals do not show a pronounced cluster-like structure.

4 EXCITATION CONDITIONS

The synoptic excitation conditions for the PCs were analysed using the Schuepp weather classification scheme designed for Switzerland. It takes into account the pressure distribution at the ground and the geopotential height of the 500 hPa-level. With respect to the surface pressure, there is a distinction in 8 classes, namely high and low pressure situations, situations without pronounced pressure distribution, advective situations divided in 4 classes according to the wind direction and low pressure situations with an active cyclone or trough centered above Switzerland. This main classes are further subdivided with regard to the upper level pressure distribution, leading finally to the 40 "Schüepp Wetterlagen"(SWLs), which will not be discussed in detail here.

Fig.2 indicates the mean values and standard deviations of the first 4 (standardised) PCs as a function of the SWL. The salient feature of the diagrams is a large variability for all PCs and SWLs. For several weather classes and PCs this leads to standard deviation intervals containing both positiv and negativ values and overlapping considerably with a large number of other intervals. On the other hand there are SWLs which show intervals laying clearly on the positive or negative side for certain PCs. For example southerly flow situations (weather classes 31-35) lead to a pronounced excitation of PC2 which describes north-south gradients.

In order to combine these unrelated 1-dimensional views of the excitation conditions to a multidimensional view, we investigated the separation of the 4-dimensional data clouds associated with each SWL. For this purpose boxes in the data space were constructed for each SWL by centering them at the respective PC-means in the various SWLs and giving to them side lengths equal to a multiple of the standard deviations of the PCs (which depend on the PC and the SWL).

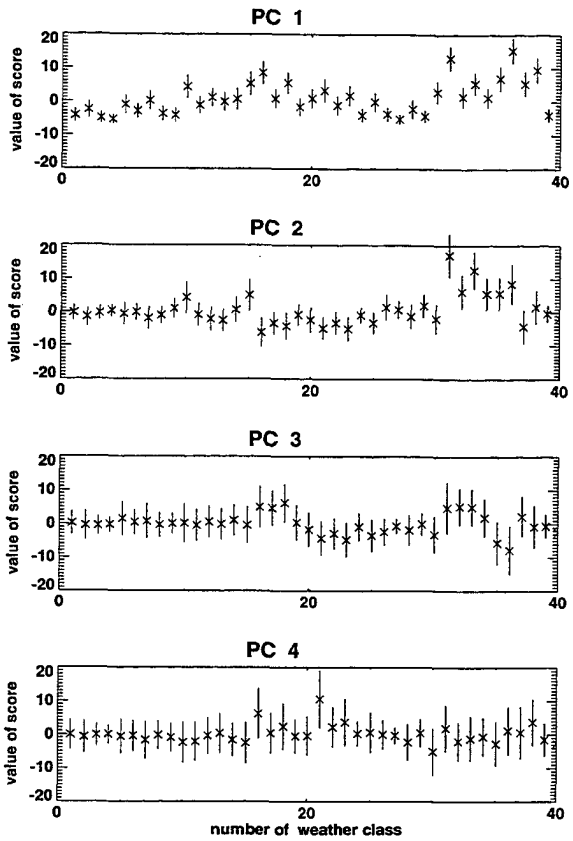


Fig.2: Average and standard deviation of PC-scores as a function of Schüepp weather classes.

It was found, that at box side lenghts of 0.6 times the standard deviations the first box becomes isolated, i.e. does not overlap with any other box. Since we can not assume a gaussian or any other simple distribution of the PCs, we now have to ask what fraction of the data is actually contained in these boxes. Depending on the SWL these are between 0% and 87%, reflecting the different shapes of the PC-distributions. This shows, that *on the level of individual situations* the SWLs do not produce unique, characteristic precipitation situations.

To analyse to what extent the mean precipitation associated with the SWLs are distinguishable, the side lenghts of the boxes were further decreased to 0.2 times the standard deviations. Despite the uncertainty about the actual distributions, we regard this as an approximation to the error of the mean value, since the number of data points for each SWL is between 100 and 500. About 50% of this boxes are not overlapping with other ones and hence characteristic *mean* precipitation distributions can be attributed to the respective SWLs.

In addition the "box-problem" was investigated in 4-dimensional spherical polar coordinates leading to a "segment problem", but the separation of the data clouds associated with the SWLs was not improved by this construction. Similarly the inclusion of more than 4 PCs did in both cases not lead to a further separation of the data.

5 TRENDS OF PCS

The compact description of the precipitation data set provided by the leading PCs can be used as the starting point for a trend analysis, which was carried out for Swiss daily precipitation totals with respect to the period 1901-1992 and the period 1961-1992. The resulting PC-trends can be regarded as trends of weighted means with weights defined by the EOFs.

Considering the first 3 PCs the most significant trend (at a significance level of 95%) is revealed for autumn and PC2 describing a decrease of precipitation in the Ticino region (southern Switzerland) in the years 1961-1992. On the 90% level we obtained a trend for PC1 in winter for the whole period 1901-1992 associated with overall increasing precipitation. On the same level of significance a trend in spring occured for PC3 in the 1961-1992 period showing an increasing precipitation in the (south-) western and a decrease in the (north-) eastern regions of Switzerland.

As expected, these trends are in very good agreement with conventional trend studies (Schoenwiese [4]) which analyse the trends at individual stations, but the EOF-technique serves to increase the significance.

6 ALPINE EOFS

In order to investigate the spatial variability of daily precipitation in the whole Alpine region, a PCA was also performed for the gridpoint data set mentioned above. In this case the first 16 PCs are needed to explain 75% of total the variance. It was found, that some of the features of the Swiss EOFs can be seen in the Alpine EOFs as well. This shows, that domain shape dependence is not a dominant influence for the leading EOFs, but that characteristic structures of this EOFs are determined by the data distribution.

As an example Fig.3 depicts EOF3 which now describes north-south gradients. The comparison of the zero-isoline of this EOF with the respective one of EOF2 from the Swiss data set (Fig.1) confirmes the previous statement.

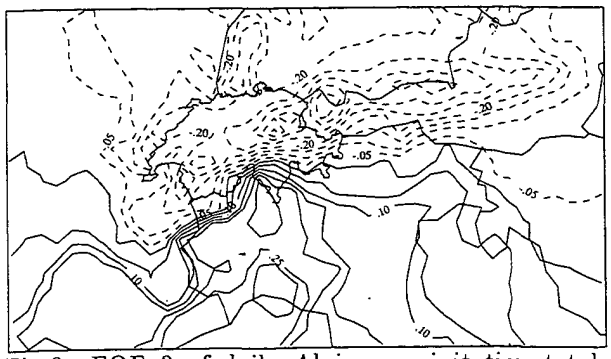


Fig.3: EOF 3 of daily Alpine precipitation totals as calculated from the years 1978-1991 (arbitrary units). Positive (negative) anomalies are indicated by solid (dashed) isolines.

7 SINGULAR VALUE DECOMPOSITION

The second approach we utilized to analyse the relation between Alpine precipitation and the synoptic situation is a Singular Value Decomposition (SVD) of the cross-covariance matrix between daily precipitation and sea level pressure fields (see Bretherton et al. 1992 [1]) including the period 1978-1988. This method successively maximizes the covariance of the timedependent amplitudes of spatially orthogonal anomaly patterns in the two fields. Thus, unlike in Canonical Correlation Analysis, the leading SVD anomaly patterns are not only highly correlated but are guaranteed to have large amplitudes.

The first 3 coupled anomaly patterns of SLP in the domain indicated and the Alpine precipitation distribution are depicted in Fig.4. Negative SLP anomalies centered over north-western Europe are associated with positive precipitation anomalies in the whole Alpine region. The respective positive SLP anomalies lead to negative precipitation anomalies. SLP anomalies producing northerly or southerly (geostrophic) flow anomalies towards the Alps are linked to a north-south gradient precipitation anomaly pattern which is nearly identical to EOF3 (Fig.3). Negative SLP anomalies over Ireland and positive anomalies in south-eastern Europe are connected to decreasing west-east precipitation gradients and vice versa.

8 CONCLUSIONS

Despite the high spatial variability, daily precipitation fields in the Alpine region can be described with good accuracy by the leading EOFs. The structure of the leading EOFs is to a high degree dominated by the data distribution, corroborating their meteorologigal relevance.

Data analysis in the low dimensional spaces defined by the leading EOFs provides a convenient starting point for further studies, e.g. linear trend analysis, which identified some significant trends of the Swiss precipitation PCs. Based upon the leading PCs we also showed that about 50% of the Schuepp weather classes are associated with a distinctive mean precipitation distribution, but that on the level of individual daily cases we can not find a pronounced relation between this disjunct weather classes and the precipitation distribution. These results are further discussed in Widmann and Schär (1995) [6].

By means of a Singular Value Decomposition we constructed coupled anomaly patterns of synoptic scale SLP and mesoscale precipitation which are physically/synoptically interpretable. The approximation of individual situations as a linear combination of anomaly patterns enables a more precise description than disjunct classifications. Therefore the analysis of coupled anomaly patterns seems a promising way to describe the relation between different fields. Such methods have some potential in the realm of semi-empirical downscaling.

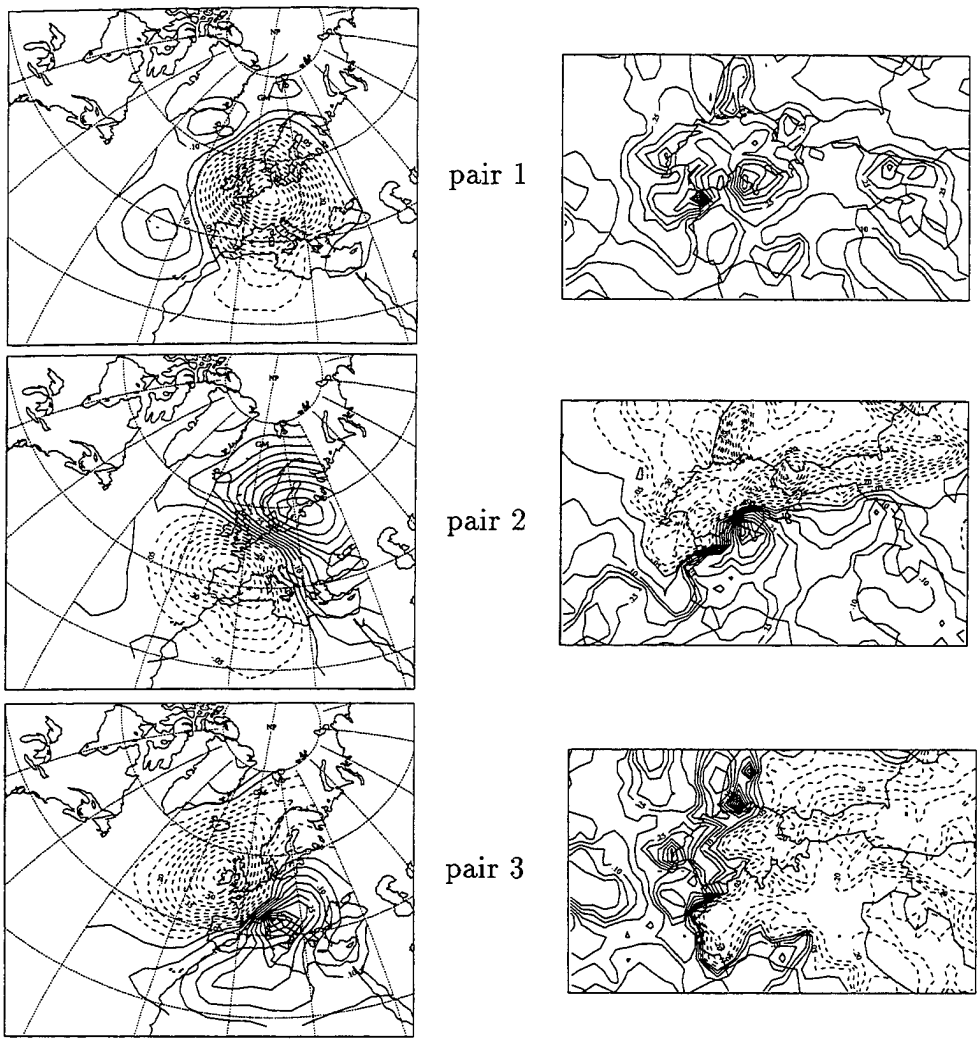


Fig.4: The first 3 coupled anomaly patterns (arbitrary units) of daily SLP and daily precipitation calculated by Singular Value Decomposition. Positive (negative) anomalies are indicated by solid (dashed) isolines.

REFERENCES

[1] Bretherton, C.S., C. Smith, and J.M. Wallace, 1992: An Intercomparison of Methods for Finding Coupled Patterns in Climate Data, *J. Climate*, **5**, pp. 541-560

[2] Preisendorfer, R.W. and C.D. Mobley, 1988: Principal component analysis in meteorology and oceanography, Elsevier (Seattle)

[3] Richman, M.B., 1986: Rotation of principal components. *J. Climatol.*, **7**, pp. 511-520

[4] Schönwiese, C.D., J. Rapp, T. Fuchs and M. Denhard, 1993: Klimatrend-Atlas Europa 1891-1990. Verlag Zentrum für Umweltforschung, Frankfurt.

[5] Schüepp M., 1979: Witterungsklimatologie, Beiheft zu den Annalen der Schweizerischen Meteorologischen Anstalt (Jahrgang 1978)

[6] Widmann, M. and C. Schär, 1995: Principal Components of daily Swiss precipitation, submitted to *Theor. Appl. Climatol.*

ACKNOWLEDGEMENTS

We are indepted to the following Institutes for providing access to daily precipitation data: German Weather Service, Hydrographisches Zentralbüro des Bundesministeriums für Land- und Forstwirtschaft/Republik Österreich, Meteo France and the Swiss Meteorological Institute. The SLP data set was provided by the Department of Atmospheric Sciences, University of Washington and the Data Support Section at NCAR. The research was supported by the Swiss Priority Program (contract SPP-U 5001-035166).

CORRESPONDING AUTHOR

Martin Widmann

Atmospheric Physics ETH

CH-8093 Zürich, Switzerland

tel.: +41/1/633 36 24

fax: +41/1/633 10 58

e-mail: widmann@atmos.umnw.ethz.ch

Using EOF Analysis to create a new GISST Data Set.

N.A.Rayner, M.N.Ward, C.K.Folland and D.E.Parker.
Hadley Centre for Climate Prediction and Research,
Meteorological Office, Bracknell, UK.

The Meteorological Office Global sea-Ice and Sea Surface Temperature (GISST) data set is used both within the Met. Office and in a large number of other groups around the World to force atmospheric General Circulation Model (GCM) simulations of the climate of the twentieth century.

In order to produce a complete GISST data set for forcing GCMs, sea surface temperature (SST) data must first be interpolated into data-sparse regions of the in situ Meteorological Office Historical SST data set (MOHSST). Empirical Orthogonal Function (EOF) analysis has been used to capture the essential characteristics of the spatial and temporal variation of the record, in order that these characteristics may be used to reconstruct the field in data-sparse areas in a manner most in keeping with the available observed data.

Individual covariance matrices for the Atlantic, Indian and Pacific ocean basins were formed and EOFs calculated on an equal area grid. The existing version of GISST[1] for 1901-1990 was used to calculate the EOFs as a complete set of data is needed. Only the first few EOFs are necessary to explain the majority of the spatial variance of the data. The remainder are viewed as noise (e.g. non-coherent SST anomalies or erroneous observations) and are discarded for the data reconstruction process. Once the significant EOFs have been identified, they are used to interpolate missing data by reconstruction of the whole field. This is achieved using the data which **are** available in the MOHSST data set to identify how strong the contribution from each EOF pattern is in each individual month. Reconstructed values are only used where data were missing previously; observed anomalies are retained.

The strength of the kth EOF pattern for any month is given by a scalar quantity known as the time coefficient, z_k. We are able to make a first estimate of this, z_k^*, the coefficient calculated from the incomplete observed data. After manipulation of the EOF equations, it is shown that z_k^* can then be used to calculate an estimate of z_k via:

$$z_k = (1 - c_{kk})^{-1} z_k^*$$

c_{kk} here is the sum of squares of the weights of the kth EOF over all missing data positions[2].

The method is verified using data-sparse periods simulated by removing data from the decade 1981-1990. Reconstructed portions of data (reconstructed using EOFs calculated over 1901-1980) are compared with observed data; measures of skill are attached to the reconstruction using various statistics, including the new Linear Error in Probability Space (LEPS)[3], which is sensitive to both the phase and absolute magnitude of reconstruction errors.

Initial results have been encouraging. The method is being developed to incorporate the additional teleconnection information included in global EOFs and the seasonality of teleconnections as revealed in seasonal EOFs. It is planned to directly assess the skill of the reconstruction by the level of success of GCM simulations forced with fixed-grid reconstructed fields for 1981-1990 compared to those forced with the complete observed field.

---

[1] D.E.Parker, C.K.Folland, A.Bevan, M.N.Ward, M.Jackson and K.Maskell 'Marine Surface Data for Analysis of Climatic Fluctuations on Interannual to Century Timescales.'(1994) in press in 'Natural Climate Variability on Decade-to-Century Time Scales.' National Academy Press, Washington.

[2] N.A.Rayner and M.N.Ward. Hadley Centre Internal Note (1994).

[3] J.M.Potts, C.K.Folland, I.T.Jolliffe and D.Sexton,'Revised 'LEPS' Scores for Assessing Climate Model Simulations and Long-Range Forecasts'(1994) submitted to Journal of Climate.

Reconstruction of Global SST using EOF Analysis and COADS Data

T. M. Smith, R. W. Reynolds, and R. E. Livezey

NOAA/NWS/National Meteorological Center
(Corresponding address: T. Smith, Climate Analysis Center/NMC,
W/NMC52, Washington, D.C. 20233
e-mail: wd52ts@sgi25.wwb.noaa.gov)

Abstract

We use EOFs based on twelve years (1982-93) of high resolution analysis with COADS observations to reconstruct global SST anomalies from 1950 to 1992. The high resolution analysis uses satellite and *in situ* data. Our goal is to give an improved analysis before 1982 for which satellite observations are not available. This method interpolates COADS SST anomalies into data-sparse regions by using the statistical structure defined by the EOFs, thus avoiding physically unrealistic patterns that may result from horizontal or temporal interpolation. Reconstruction is done by finding weights for each EOF mode such that the mean-squared error of the reconstruction is minimized.

1. Introduction

A number of climate studies require an accurate historical sea surface temperature (SST) anomalies. These include extended integrations of climate models, attempts to relate observed climate variations to SST variations, and atmospheric reanalyses. Here we produce a more accurate global SST analysis using an empirical orthogonal function (EOF) based reconstruction method. We compute global anomalies of monthly SST for 1950-92. The method uses the observed SST anomaly spatial covariance structure from a densely sampled period to reconstruct the field of SST anomalies in a more sparsely sampled period.

2. Data and Method

The EOF reconstruction uses the 1° gridded optimal interpolation (OI) of SST anomalies for the period 1982-93 (Reynolds and Smith 1994). The OI uses satellite and *in situ* observations to produce a high resolution analysis. The EOF spatial patterns are fit to *in situ* data from the monthly 2° COADS SST (Slutz *et al.* 1985) from January 1950 to December 1992. Within each 2° COADS square we use median SST. For comparisons we use the Global Sea-Ice SST (GISST) analysis. The GISST is produced and provided to us by the U.K. Meteorological Office (Parker *et al.* 1994). For all SST analyses and data we use the adjusted OI climatology of Reynolds and Smith (1995) to form anomalies. All data are interpolated to the COADS 2° grid.

We do no analysis south of 45°S, where there is little *in situ* data in the region between the Antarctic Circumpolar front and Antarctica. That front, located between 40°S and 50°S, separates northern and southern regions that may not be reliably correlated with each other. In the Northern Hemisphere, we limit our analysis to regions south of 69°N to avoid areas that commonly contain sea ice. Data are multiplied by the cosine of the latitude before computation of EOFs and reconstruction. After reconstruction the SST anomalies are divided by the cosine of the latitude to remove the weighting.

The global EOF spatial patterns for the first few modes show that large loadings tend to be located in the tropics and the extratropics poleward of 30° latitude, which show a strong correspondence to the OI standard deviation. Because these centers of action occur in separate regions, we did EOF reconstructions in six regions separately: the Tropical Atlantic, Tropical Pacific, Tropical Indian, North Atlantic, North Pacific, and a southern ocean strip. Tropical regions are between 30°N and 30°S, and extratropical regions from 20° latitude to their poleward limit. In the 10° overlap regions reconstructed anomalies are joined using linear interpolation.

We use the twelve years of OI SST anomalies with the time-mean anomaly (μ) removed to compute the EOFs. The time-mean anomaly is removed so that the modes are not forced to try to represent long-term trends in the anomalies. Thus at each of the x locations and t times the OI SST can be represented by

$$OI(x,t) = \mu(x) + \sum_{n=1}^{N} X_n(x)\, T_n(t) \qquad (1)$$

where N is the maximum number of modes, X_n is the loading and T_n the time series for mode n. We wish to find a best fit function

$$F(x,\tau) = \sum_{n=1}^{M} X_n(x)\, W_n(\tau)\,, \qquad (2)$$

which is a weighted sum over M modes (M < N), using a different weight, W_n, for each mode. The functions $W_n(\tau)$ are determined by a least squares fit to the COADS *in situ* data with v(x), the eleven year running mean, subtracted. We then compute the reconstruction

$$R(x,\tau) = v(x) + F(x,\tau) \qquad (3)$$

Experiments computing the reconstruction with and without removal of the long-term mean show that removing the mean from the data before reconstruction, and then adding it back in afterwards as in equation (5), gives a slightly more accurate reconstruction over the 1982-92 period. To decide the best number of modes to use, M, we compute cross-validated reconstructions for the 1982-92 period and compare to the OI for the same period. Cross validation is done by computing a set of modes for each month that exclude data from eight months before the target month to eight months after the target month. We also use the data distribution of the 1950s for the cross validation experiments. We compare cross validated reconstructions to the OI to show how many modes we can retain without overfitting (i.e., keeping higher modes that lower the accuracy of the reconstruction compared to the OI).

3. EOF Reconstruction for 1950 to 1992

We compute the reconstructions using the EOFs for all OI months (1982-1993) and all available *in situ* COADS super observations for the month being reconstructed Fig.1 shows the global RMS difference with respect to the OI for the reconstruction and GISST. Globally, the reconstruction has lower RMS difference than GISST. Because GISST heavily relies on interpolated *in situ* observations, its RMS difference is largest in those regions where *in situ* sampling is most sparse, which include the Southern Hemisphere and the Tropical Pacific. In regions where sampling is dense, such as the North Pacific, the GISST analysis is comparable to the reconstructions. Fields of SST anomalies from the reconstruction and the OI are similar, but the reconstruction is spatially smoother and shows slightly weaker anomalies.

An example during a Tropical Pacific cool episode in January 1971 (Fig. 2) shows apparent distortions in the GISST analysis, which stretches anomalies north-south. This stretching, which is absent in the reconstruction, is apparently caused by horizontal interpolation. Both analyses show the same phase and approximately the same magnitude of large-scale interannual variation throughout the oceans. The major differences are that the reconstruction does not distort the anomaly pattern in under sampled regions.

4. Summary

We have shown that monthly SST anomalies can be reconstructed from *in situ* data from 1950 to present using the EOF basis functions and a least-squared fit. This method gives results that are generally more accurate than traditional horizontal and temporal interpolation. This is demonstrated in our comparisons with the OI SST anomalies from 1982 to 1992. In general, the EOF reconstruction gives a more spatially coherent field of SST anomalies than traditional methods. This method is particularly effective in the Tropical Pacific, where anomalies can be large and persistent and where *in situ* sampling is often sparse. In regions where *in situ* sampling is dense, the EOF based reconstruction does not have as clear an advantage over more traditional methods.

The EOF reconstructed SST may be useful to modelers simulating atmospheric variations. For example, details of the position and magnitude of Tropical Pacific Ocean SST anomalies may affect extra-tropical responses in atmospheric models. The GISST analysis also has much more spatial variability than the reconstruction, which in part may be caused by unrealistic stretching of anomalies into data-void regions or from questionable data in the analysis. Such unrealistic variations may cause an unrealistic atmospheric response when used as the lower boundary for an atmospheric model. Area-average results show much less difference between the reconstruction and GISST anomalies.

Acknowledgements: We thank J. O'Brien for suggesting this project, D. Stokes for much help in setting up the SST data and for help with programming, and N. Rayner and D. Parker who gave us valuable suggestions and advice

throughout the course of this work. The U.K. Meteorological Office provided the GISST data, and NCAR made the COADS data available.

Parker, D.E., P.D. Jones, C.K. Folland, and A. Bevan, 1994: Interdecadal changes of surface temperature since the late nineteenth century. *J. Geophys. Res.*, **99**, 14373-14399.

Reynolds, R.W., and T.M. Smith, 1994: Improved global sea surface temperature analyses using optimum interpolation. *J. Climate*, **7**, 929-948.

Reynolds, R.W., and T.M. Smith, 1995: A high resolution global sea surface temperature climatology. Accepted for publication by *J. Climate*.

Slutz, R.S., J. Lubler, J.D. Hiscox, S.D. Woodruff, R.J. Jenne, D.H. Joseph, P.M. Steurer, and J.D. Elius, 1985: *Comprehensive Ocean Atmosphere Data Set.* National Oceanic and Atmospheric Administration. [Available from Climate Research Program, ERL, R/E/AR6, 325 Broadway, Boulder, CO 80303.]

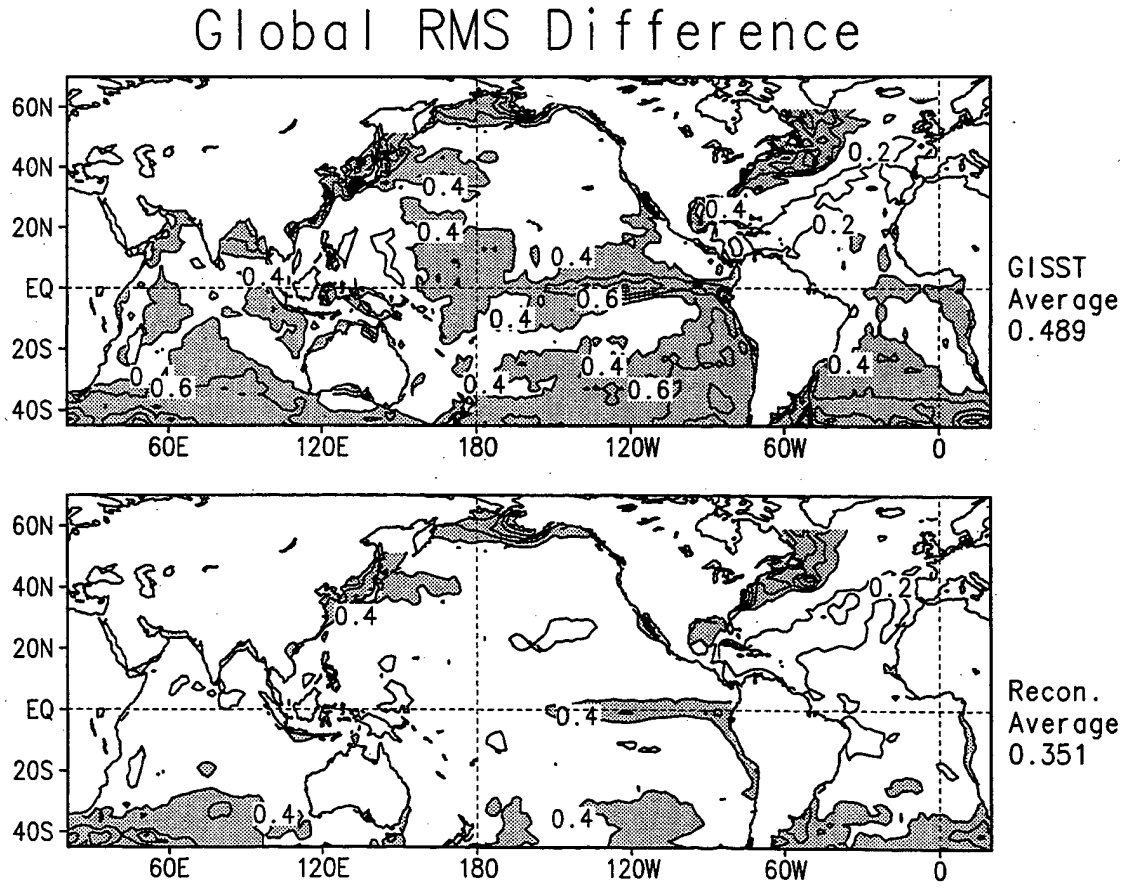


Fig. 1 Global RMS difference from the OI (°C) over the 1982-92 period for GISST (top panel) and the reconstruction (bottom panel) . The global average for each is shown to the right of the panels. The contour interval is 0.2, values > 0.4 are shaded.

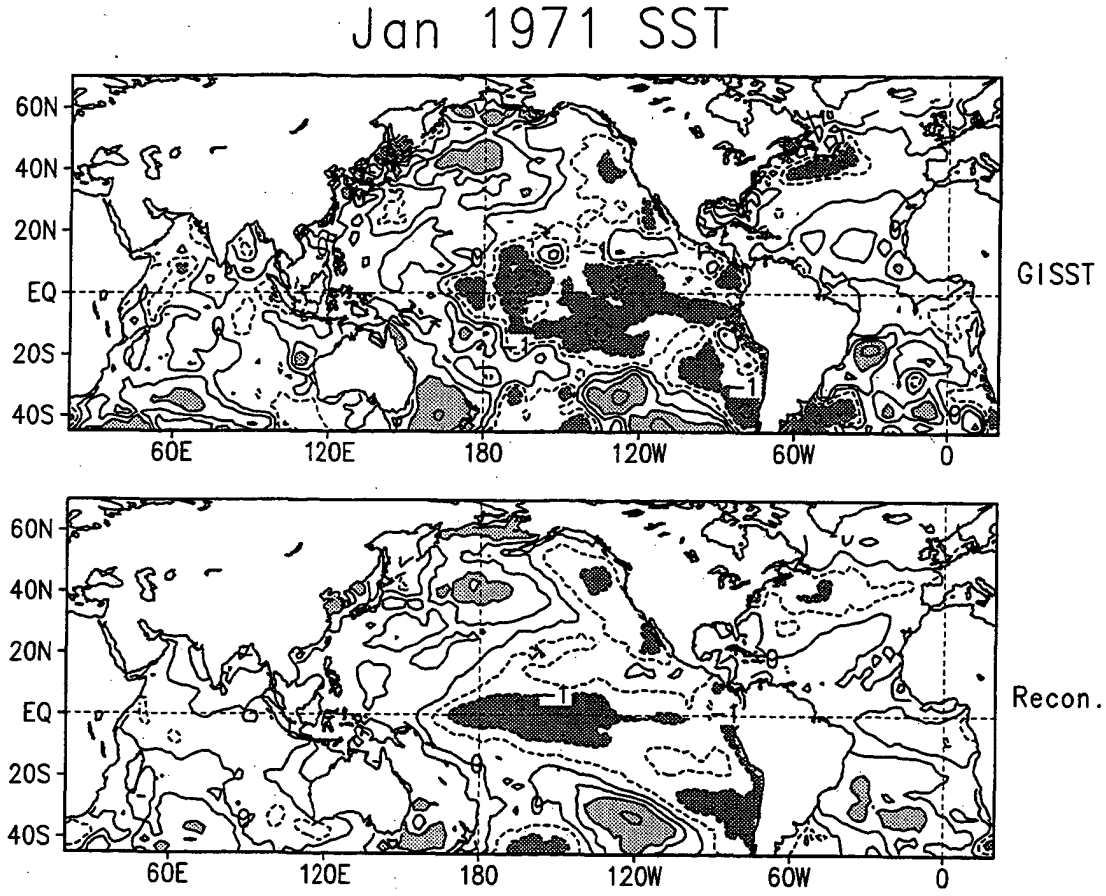


Fig. 2 GISST (top panel), and reconstructed (bottom panel) SST anomalies for January 1971 (°C). The contour interval is 1°C, except that the ±0.5°C contour is also shown. Dark shading shows values > 1, light shading shows values < -1.

Smoothing Spline ANOVA and the spatio-temporal analysis of climate data

Grace Wahba
University of Wisconsin,
Madison, WI, USA

We show how Smoothing Spline ANOVA methods may be used to analyzes spatio-temporal climate data. In particular, the method may be used to model monthly, yearly and spatial main effects and interactions. Some computational problems and open questions will be discussed.

APPLICATION OF STATISTICAL OBJECTIVE ANALYSIS TO RAINFALL FIELDS FROM A CONVENTIONAL MESO-NETWORK: COMPARISON WITH THE EMPIRICAL WEIGHING SCHEME

D.F. Barrera and A.B. Basualdo

Universidad de Buenos Aires, Buenos Aires, Argentina.

ABSTRACT

Two methods of spatial interpolation were applied to 10-day periods of accumulated precipitation: 1) The empirical weighing scheme of data, in which weighing factors are a function of distance between the analysed point and observing sites; and 2) The "optimal interpolation" method. Grid-point estimations were performed following both methods for a 20 km interval square-grid built over the study area. Estimations by method 1) were used as "first guess" (preliminary field) in method 2). In order to control and compare both methods, estimations at 20 observing sites were performed and then compared with the observations (assumed as true values). Sums of cuadratic errors were always significantly lesser when using the optimal interpolation method.

1 INTRODUCTION

A strong limitation of data from a pluviometric meso-network to estimate rainfall amounts at ungauged sites in the area is due to the fact that spatial variability of precipitation is very high even at scales much smaller than typical interdistances between gauges.

Due to this fact, estimation of accumulated precipitation at ungauged sites have associated errors. A measure of these interpolation errors can be estimated in a statistical way as a "typical error"; the lesser the typical error, the better the estimation. The choice of the interpolation method is of fundamental importance on this issue.

In the present paper, two methods of interpolation were applied and compared using 10-day accumulated precipitation data from a conventional meso-network (see Figure 1) over a study area of about 60000 km^2 in the east of Argentina: 1) The traditionally used empirical weighing scheme of data, in which weighing factors are a function of distance between the analysed point and observing sites (method 1); and 2) The "optimal interpolation" method, in which information derived from structural properties of the variable, as well as quality of information is utilized (method 2).

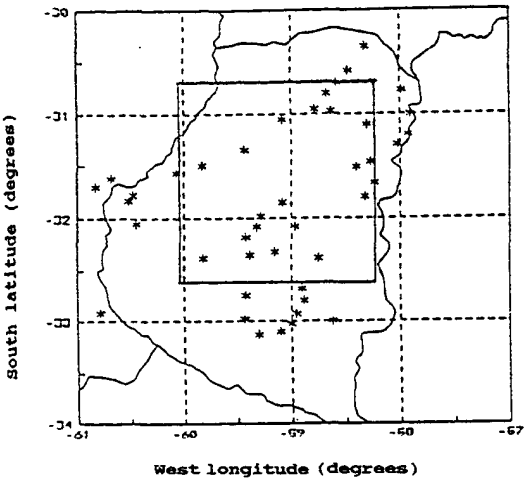


Figure 1
Study area and location of gauging stations

2 IMPLEMENTATION OF METHODS

2.1 EMPIRICAL WEIGHING SCHEME

This method is based on the following scheme:

$$A_0 = \Sigma\, h_{0,i}\, O_i \qquad \text{where}$$

A_0: Analysis value at location o.
O_i: Observed value at location (gauging site) i , i=1,...,n.
$h_{0,i}$: Weighing coefficient associated to points o,i.

The weighing coefficient is generally an inverse polinomial function of the separation d between the observing site and the analysis point. As it is widely accepted by hydrologists, we used the following weighing function (Bedient and Huber, 1988):

$$h_{0,i} = d_{0,i}^{-2} \,/\, (\Sigma d_{0,i}^{-2})$$

if $d > r_0$, and $h_{0,i} = 1$ for the nearest point if $d < r_0$. A value of 5 km for r_0 is typical for the case of 10-day precipitation a conventional

observing network, and was chosen in this work.

2.2 OPTIMAL INTERPOLATION METHOD

Also known as "statistical objective analysis", this method has some theoretical advantages over empirical weighting schemes. One of them is that weighs are directly related to correlations instead of distances, thus including structural properties of the field; another one is that relative correlations (separations) between influencing points are taken into account, which allows to diminish the influence of observing sites with redundant information (Thiébaux and Pedder, 1987).

This method due to L. Gandin (1963) assumes the existence of a true field (noted T) and the availability of a preliminary field, or first guess of the analysis field (noted P). It is based on the following scheme:

$$A_0 = P_0 + \Sigma\, h_{0,i}\,(O_i - P_i)$$

where

P_0: Preliminary value (first guess) at location o.

P_i: Preliminary value at observing site i.

Analysed values have an associated error E which is defined as:

$$E^a = \langle (A - T)^2 \rangle$$

where the symbol <> denotes time average over a large number of events. The optimum interpolation weigths are those that minimize the cuadratic error E_a^2. In order to calculate them, observed values are assumed as belonging to the true field. For two observing points influencing an analysis point, the expression of the weigh 1 is (Thiébaux and Pedder, 1987):

$$h_1 = \frac{(1+\sigma_2)\mu_{01} - \mu_{02}\mu_{12}}{(1+\sigma_1)(1+\sigma_2) - \mu^2_{12}}$$

where:

μ_{ij} = correlation between locations i and j (subscript o indicates the analysis point.

σ_i = normalized mean cuadratic error of observations at station i.

Gandin (1963) stated that the preliminary field must be the climatic mean field. Following Gustavsson (1980) and Thiébaux and Pedder (1987) the preliminary field can be another first guess of the true field, provided the correlation field of deviations with respect to that field can be estimated. We decided to use estimations by method 1) as "first guess" (preliminary field) in method 2), and to take as an estimate of the respective correlation field, the one obtained by Barrera (1995) which was built from computed correlation values of deviations from the average of observed data. The series of daily totals used were collected at 43 stations (see Figure 1) during the period 1961-1975. Correlation values μ_{ij} were taken from the respective field of 10-day accumulated wintertime precipitation for the study region. This field was used instead of those of deviations from the average preliminary values, whose were not available (see Figure 2).

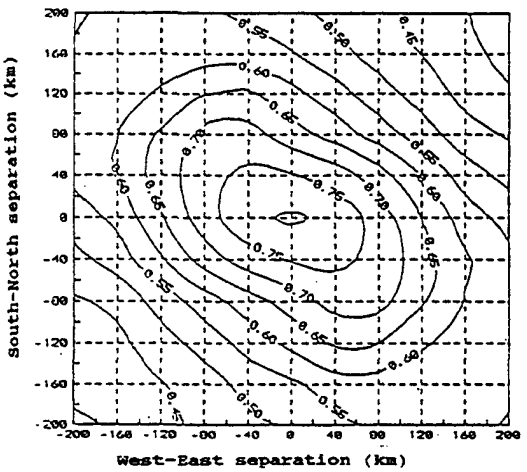


Figure 2
Correlation field of 10-day periods
Province of Entre Ríos

3 EVALUATION OF METHODS

Grid-point estimations were performed following both methods for a 20 km interval square-grid built over the study area (of about 60000 square km). For selecting the observing sites that influence a particular grid-point, two different criterions were adopted: for method 1, the nearest sites to the analysed point; while for method 2, the sites having greater correlation with the analysed point were chosen.

As regards the number of influencing points to be taken, tests were performed varying this number from 1 to 20; the best results, for this highly variable field and the network used, were obtained for 3 influencing sites in both methods. This quantity was adopted. We think that it would be greater for a denser network.

Rainfall contours obtained by methods 1 and 2 are shown in Figures 3 and 4 respectively.

In order to control and compare both methods, estimations at the 20 observing sites interior to

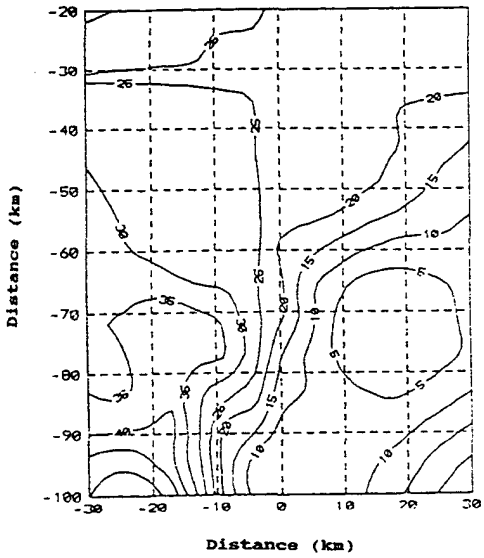


Figure 3
Case study. Rainfall contours obtained by method 1.

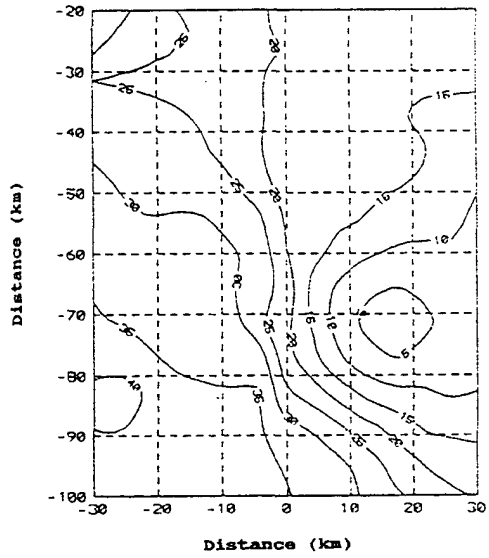


Figure 4
Case study. Rainfall contours obtained by method 2.

a testing 200 km-sided square area in the studied region (see Figure 1) were performed by interpolation from grid-point values, and then compared with the observations, assuming that these were the true values. Sums of cuadratic errors (i.e., squared differences between estimated and observed values) over the 20 sites were used in both cases as measure of error variance. These values were computed for 20 independent periods of 10-day cumulative precipitation (see Figure 5). In the average of the 20 10-day periods considered, the error was about 20% lower in the case of method 2.

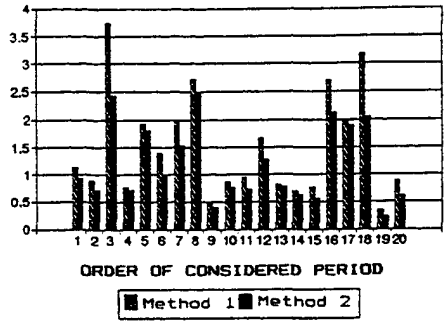


Figure 5
Normalized cuadratic error

Fitting of a function of normalized error (divided by areal average precipitation) versus that average showed that normalized error decreases when areal precipitation increases. The obtained functions were $y=0.55\ x^{-0.43}$ for method 1, and $y=0.42\ x^{-0.43}$ for method 2, with 78.4% and 79.8% of variance explained, respectively (see Figure 6); this implies that fitted normalized error in method 2 is 24% lower than in method 1.

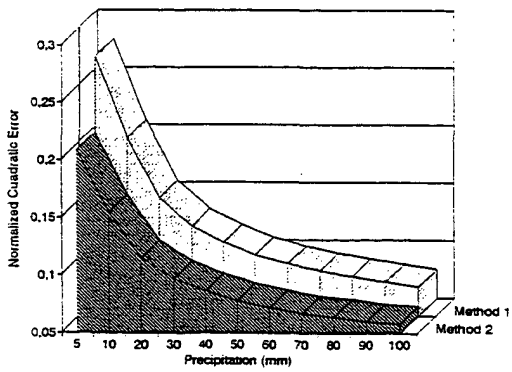


Figure 6
Regression multiplicative model
$y = a\ x^{b}$

4 CONCLUSION

Computed error variance values were always significantly lesser when using the optimal interpolation method, showing that this one is

better than the traditional weighing scheme method when applied to mesoscale 10-day precipitation fields.

References

Barrera, D.F., 1995, "La estructura de correlación espacial de la precipitación en la Provincia de Entre Ríos: su relación con los sistemas precipitantes", Avances en Geofísica y Geodesia, Madrid, Volume 1, in press.

Bedient, P.B. and W.C. Huber, 1988, "Hydrology and floodplain analysis", Addison-Wesley, 650 pp.

Gandin, L.S., 1963, "Objective analysis of meteorological fields", Gidrometeorol Izdat (original in russian), Israel Program for Scientific Translations, Jerusalem, 1966, 242 pp.

Gustavsson, N., 1980, "A Review of Methods for Objective Analysis". In Bengtsson, L., Ghil, M. and Kallén, E. (eds), Dynamic Meteorology- Data Assimilation Methods, Springer-Verlag, New York, 330 pp.

Thiébaux, H.J. and M.A. Pedder, 1987, "Spatial Objective Analysis". London, Academic Press, 299 pp.

ACKNOWLEDGEMENTS

This work has been done with economic support of National Council of Scientific and Technological Research (CONICET) and University of Buenos Aires (Argentina).

CORRESPONDING AUTHOR

Professor D.F. Barrera
Department of Atmospheric Sciences
Universidad de Buenos Aires
Ciudad Universitaria
1428 Buenos Aires, ARGENTINA.

INFLUENCE OF NETWORK DESIGN ON ESTIMATION OF PRECIPITATION

H. Kutiel[1]; P. A. Kay[2] and L. Dickey[2]

[1]University of Haifa, Haifa , Israel
[2]University of Waterloo, Waterloo, Ontario, Canada

ABSTRACT
Rainfall fields are simulated as random elliptical events. Each simulation is sampled by six different fixed network designs of 9 points. Isohyet maps for each network design provide volumetric estimates, which are compared to the known volume of the events comprising the simulations. Additionally, 100 random network designs for each simulation provide sampling distributions of the number of dry points sampled, from which the efficiency of each network design is inferred. The choice of the "best" design depends on the criterion of greatest importance to satisfy, and the spatial characteristic of the rainfall events across the study area.

1 INTRODUCTION

Kay and Kutiel (1994) examined the effect of rain gauge network density on the representation of rainfall by isohyet maps. Using a simulation study, we showed that a very dense network, on the order of 0.1 the median event size, is required for adequate depiction. Given that national networks are far short of this ideal density, we may ask if the way the network is arranged has any influence on the resulting interpolation. That is, is there a "best" arrangement for a limited number of gauges? The purpose of the present study is to evaluate the importance of network design to the interpolation of the rain field (both its pattern and the volume of rainfall it represents).

2 METHODOLOGY

We tested six different regular arrangements of nine rain gauges each (corresponding to network densities of 0.60-0.75 median storm size). Four different simulations, each comprising 10 random elliptical events, were prepared; two distinctly different ones are discussed here (Figure 1). In one, the events were clustered close to the centre of the area, without any rain on the perimeter. Maximum rainfall occupied much of the centre of the area. In the other, the events were located around the perimeter of the area; no event was captured entirely within the area. Maxima of rainfall occurred in the northwest corner and on the western edge of the area.

The volume of rain in each event was approximated by a cone with an elliptical base; therefore the known volume represented by the ten rainfall events was

$$V = \frac{\pi}{3}\sum_{i=1}^{10} a_i b_i h_i \qquad (1)$$

where a and b are the major and the minor axes and h is the maximum precipitation total of each event.

Isohyet maps were interpreted from the values sampled by each regular 9-gauge network (the dots in Figure 2 depict the gauges). The MacGridzo software package used for the mapping also provided estimates of volume represented by each isohyet map (calculated by a set of interpolated pyramidal facets). The comparison of estimated volumes, to the known volume, was one criteria by which the adequacy of network design was judged. A second criterion was the shape of the rainfall field depicted by the isohyet map.

A third criterion was the efficiency of the network in sampling the spatial distribution of rainfall, here indicated by the frequency of wet and dry points. A Monte Carlo simulation of 100 randomly designed 9-gauge networks, for each of the rainfall fields, provided sampling distributions. These distributions were very nearly binomial, and the probability of the number of dry points (out of 9) could be assigned for each network design.

3 RESULTS

Despite the quite different distribution of events in the two simulations, the isohyets for the regular 9-gauge networks reveal some

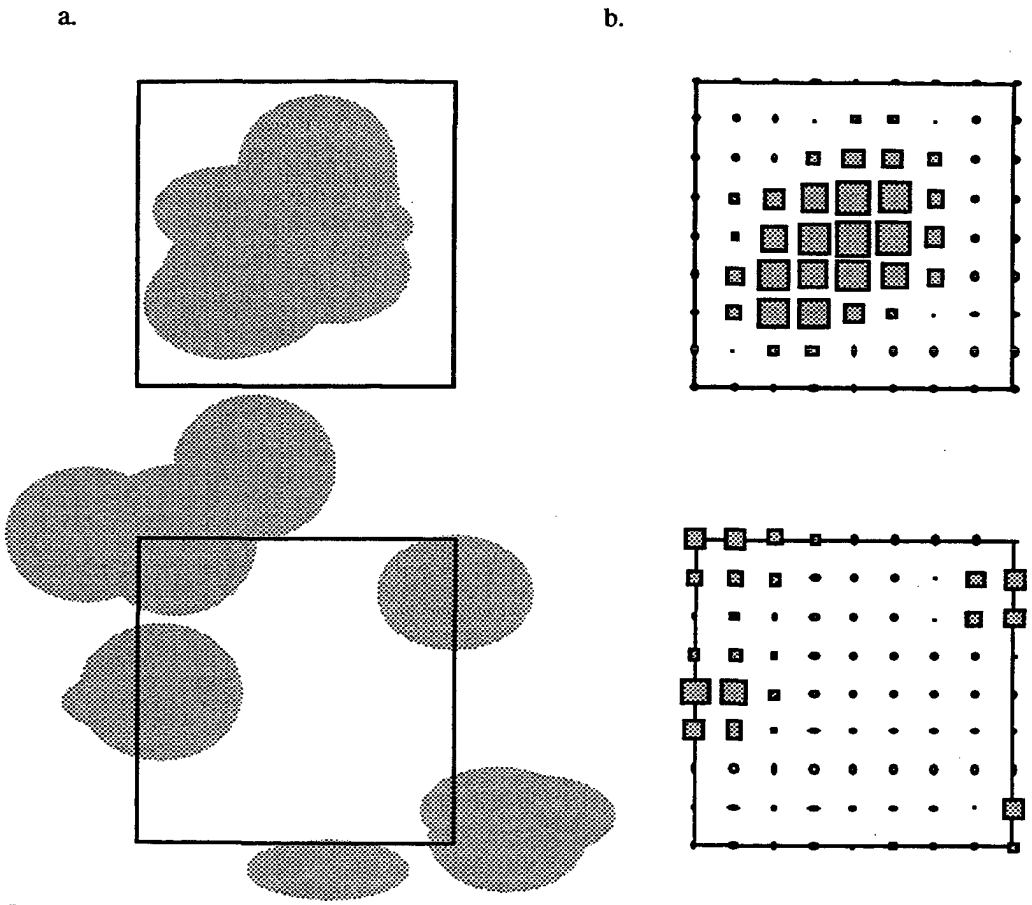


Figure 1. (a) Rainfall events and (b) rainfall amounts for first (top) and second (bottom) simulations. Area of squares in (b) proportional to rainfall amount.

considerable similarity (Figure 2). In particular, the coincidence of a sample point with any amount of rainfall tends to have pronounced effect on the interpolated isohyets. In the second simulation, for example, the absence of a gauge in the middle of the western perimeter leads to isohyet maps that completely misses the maximum known to occur there (e.g., the combined and X networks). Similarly, a gauge in the northwest corner, sampling the maximum there, leads to maps that more correctly depict the pattern (e.g., square, combined, X networks). In simulation one, the slight SW-NE orientation of the rainfall maximum is best detected when there are sample points with a similar arrangement (e.g., circle, X, diamond networks). Thus the mapped rainfall field, interpolated from a limited number of gauges, can appear distinctly different due to the arrangement of the gauges.

When we turn to the efficiency of sampling wet and dry points, the binomial distributions suggested the mean number of dry points in the first simulation as 5.1, and in the second as 5.7. In the first simulation, the cross and diamond grids both had 5 dry points (out of 9), and were thus best by this criterion. The square, with 8 dry points, was clearly inadequate; there was less than a 5% probability of a random design producing 8 or 9 dry points. In the second simulation, all designs except the square had 5 or 6 dry points. The square had 4 dry points; the probability of this few dry points in a random design was approximately 14%.

With regard to volume estimation, there is large variation for the same event among the various network designs (Table 1). In simulation 1, all designs except the square and circle over-estimate true volume; the square is closest. In simulation 2, the direction of over- and under-estimation reverses, with the square and circle greatly over-estimating true volume; the cross design is closest.

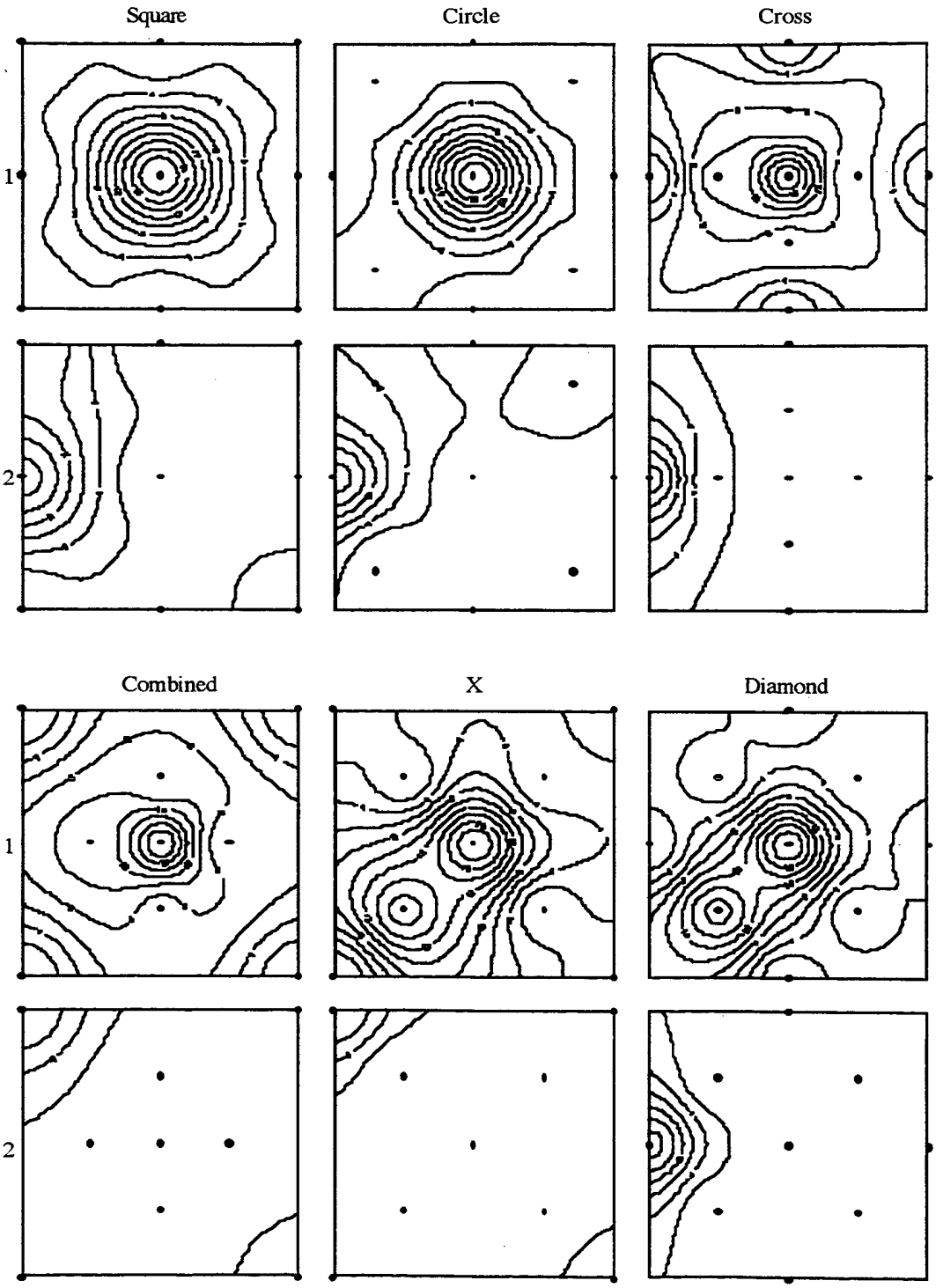


Figure 2. Isohyet maps for the six network designs for each of the two simulations. Dots indicate gauge locations.

Table 1. Estimated volumes of water for network design, as percentage of true volume for each simulation.

Simulation	Square	Circle	Cross	Combined	X	Diamond
1	92	72	142	161	131	113
2	181	153	102	79	50	78

4 DISCUSSION

Our main conclusion is that the arrangement of the network, and not only its density, has a major influence on the maps that one might generate for a series of events. This is true for all arrangements, symmetrical (as discussed here) or random (not shown). If rainfall is concentrated on the margin of an area, with a relative minimum in the centre, network designs that place most gauges on the perimeter will sample the rainfall distribution best (e.g., square or circle). If rainfall is concentrated within an area, with relative minima on the perimeter, then network designs that place most gauges within the area will sample the rainfall distribution best (e.g., X or diamond; perhaps circle).

Based on efficiency of sampling the distribution of precipitation, the X and diamond network designs sampled a number of dry points consistent with theoretical expectation. With points both in the area and on the perimeter, these two designs seem most utilitarian. The exact match, however, would be conditioned on the orientation of the rainfall maximum and of the network.

With regard to volume estimation, again we see the influence of the spatial distribution of rainfall on the indication of which network design is best. When rainfall is concentrated in the centre, designs with most points in the centre work best. With rainfall on the periphery of the area, designs with points on the perimeter work best.

The choice of the "best" design depends on the criterion of greatest importance to satisfy, and the spatial characteristic of the rainfall events across the study area. Of course, prior to the measurement of rainfall, we may not know the spatial characteristics of the field, and therefore have no guidance to the choice of the "best" network design. Therefore, decisions may be based on whether the primary purpose is to depict the spatial distribution or to estimate total volume most accurately.

References

Kay, P. A. and Kutiel, H., 1994, "Some remarks on climatic maps of precipitation", Climate Research, Volume 4, pp. 233-241.

CORRESPONDING AUTHOR

Dr. Haim Kutiel,
Department of Geography,
University of Haifa,
Haifa 31905, ISRAEL

INTERMITTENT CLOUD STRUCTURE AND RADIATION

Robert F. Cahalan
Goddard Laboratory for Atmospheres
NASA-Goddard Space Flight Center, Greenbelt, MD 20771

ABSTRACT

Liquid water clouds are primary controllers of both incoming solar radiation and outgoing infrared radiation in Earth's atmosphere. Current climate models treat clouds as plane-parallel, and thus neglect the observed variability in cloudiness on scales smaller than about 100 km, aside from assigning a ``cloud fraction" to each gridcell. However, computations show that mean radiative fluxes are sensitive to small-scale variability in cloud optical properties (Cahalan et al., 1994a). A family of 2-parameter bounded cascade models has been shown to reproduce the observed one-point and two-point distributions of liquid water observed in California marine stratocumulus. The radiative fluxes in the model are computable by a simple "independent pixel approximation," which neglects 3D photon transfer (Cahalan et al., 1994b). This approach breaks down when the cloud field becomes highly intermittent, as was observed for example in ASTEX, where the cloud fields were often riddled with small gaps (Cahalan et al., 1994c). Such intermittency may be generated by singular cascades, but these produce wavenumber spectra that are flatter than observed. Bounded cascades may also be intermittent, if they generate gaps in the liquid water field with a probability which vvanishes as the spatial scale vanish. We consider a simple intermittent bounded model with a "gap probability", $0 < g_n < 1$, which takes the form $g_n = gc^n$ as a function of cascade number, n, where $0 < g, c < 1$. The distribution of gaps is compared with FIRE and ASTEX data. The influence of the parameters on thestatistical moments and on the radiative fluxes is determined. Lessons of the model for the cloud parameterization problem, and for the estimation of sampling errors in remote sensing and in situ field studies, are considered.

REFERENCES

Cahalan, R. F., W. Ridgway, W. J. Wiscombe, T. L. Bell and J. B. Snider, 1994a: The albedo of fractal stratocumulus clouds, J. Atmos. Sci. 51, 2434-2455.

Cahalan, R. F., W. Ridgway, W. J. Wiscombe, S. Gollmer and Harshvardhan, 1994b: Independent pixel and Monte Carlo estimates of stratocumulus albedo, J. Atmos. Sci. 51, 3776-3790.

Cahalan, R. F., D. Silberstein and J. B. Snider, 1994c: Liquid water path and plane-parallel albedo bias during ASTEX, J. Atmos. Sci. , to appear.

Detection of Strong-ENSO Forced Signals in the Northern Extratropics

Robert E. Livezey, Michiko Mautani, Ming Ji, Hualan Rui, Ants Leetma and Arun Kuman
W/NMC51, Climate Prediction Center
NOAA Science Center, USA

Observational composites and prescribed-SST GCM experiments are employed to describe the seasonality of tropical-extratropical teleconnections when SSTs in the central tropical Pacific ocean are unusually warm or cold as they often are in strong ENSO episodes.

Cold and warm episode composites are constructed for each month of the year for Northern Hemisphere 700 hpa heights and North American temperature and precipitation according to whether or not the magnitude of the departure from normal of SSTs in the region surrounding the equator and just east of the Dateline exceed a critical amount. This is in sharp contrast to techniques that have relied on designation of specific years as warm or cold ENSO episodes. The resultant samples are also constrained to contain between four and ten cases an all composites are test for field significance using randomization techniques.

The composite fields are compared to the month by month model climatology from a 20-year GCM run in which the standardized SST anomalies are fixed to those for January 1992 (the height of a strong warm episode). The comparison are made through use of anomaly correlations and decomposition of composites and ensemble averages as well as their constituent members in Rotated PCA.

Early results suggest significant signals outside of the a priori expected wintertime North America that can potentially be detected in real-time situations with reasonably sized GCM ensembles.

Statistical-dynamical analysis of multiple decadal long atmospheric simulations using the ECHAM3 model under GISST forcing

Ulrich Römer[†], Andreas Hense[†], C. K. Folland[‡]

[†] Meteorologisches Institut der Universität Bonn, Auf dem Hügel 20, 53121 Bonn, Germany

[‡] Hadley Center for Climate Prediction and Research, Bracknell

ABSTRACT

The changes of climate means between the decades 1904/13 and 1951/60 have been examined. This is done by data from the ECHAM3 model under GISST forcing. The analysis is done in the subspace of amplitudes of suitably defined three dimensional modes derived from simplified models. The covariance matrix of the joint signal resulting from the boundary conditions of these amplitudes is estimated by three methods. It is shown that the variable sea surface pressure, velocity potential and stream-function changed significantly in the tropics in 300 hPa between the two decades.

1 INTRODUCTION

The focus of interest in this study lies in the examination of the interaction between ocean and atmosphere. Numerous studies have been carried out on this subject and these should form the basis for an examination of the large-scale structure and for finding a physical reason for a change in climate based on SST changes. The decades 1904/13 and 1951/60 are generally recognised as *cold* and *warm* sea surface temperature (SST) episodes, respectively. The SST data of these periods are used to provide the boundary conditions for atmospheric climate simulations and are taken from the Global Ice and Sea Surface Temperature data set (Parker, Jones, Folland and Bevan 1994). This data are used to study wether there are significant atmospheric flow differences between the two decades associated with the externally varying boundary conditions. The analysis (Hotelling T^2 and a variant of linear discrimant analysis for monthly means) is done in the subspace of amplitudes of suitably defined three dimensional modes derived from simplified models. The covariance matrix of the joint signal resulting from the boundary conditions of these amplitudes is estimated by three methods representing different levels of the internal noise.

2 THEORY

2.1 Statistics

This study aims at establishing whether the climate means of two decades with different Sea Surface Temperature (SST) - 1904-1913 (*cold*), 1951-60(*warm*) - differ significantly from one another. This is examined by means of describing selected climate parameters. These parameters are integrated into a phase state vektor $\vec{x}$. Let us suppose that the phase state vector $\vec{x}$ is a random variable of dimension m. This random variable $\vec{x}$ is drawn from a multivariate normally distributed ensemble with mean $\vec{\mu}$ and covariance matrix Σ. By means of simulation two samples of size T_c and T_w taken from the *cold* and *warm* phases are available. It is assumed that due to the different boundary conditions the average vektors $\vec{\mu}_c$ und $\vec{\mu}_w$ of both decades have changed. In simple cases second order moments like the covariance matrix Σ are not expected to change simultaneously. Based on the given samples we will examine if the null hypothesis of equal expectation values

$$H_0 : \vec{\mu}_c = E(\vec{x}_c) = \vec{\mu}_w = E(\vec{x}_w) \qquad (1)$$

or the alternative hypothesis of different expectations is valid

$$H_A : E(\vec{x}_c) \neq E(\vec{x}_w)\,. \qquad (2)$$

The appropriate test variable for the above pair of hypotheses is the Hotelling T^2 statistics (Morrison 1990):

$$T^2 = \frac{T_c T_w}{T_c + T_w} D^2 = \frac{T_c T_w}{T_c + T_w} (\overline{\vec{x}_c} - \overline{\vec{x}_w})^t \mathbf{S}^{-1} (\overline{\vec{x}_c} - \overline{\vec{x}_w}) \qquad (3)$$

where $\overline{\vec{x}}_{w,c}$ are the estimated climatic means and $\mathbf{S}$ is an estimate of the covariance matrix Σ. The variable D^2 is an estimate of the so-called Mahalanobis distance which is a distance measurement in phase space and invariant to scaling transformations (Zwiers 1987). In order to determine the T^2 test variable the invertability of $\mathbf{S}$ is essential. The matrix $\mathbf{S}$ holds the field dimension m and maximum $\mathrm{rang}(\mathbf{S}) = T_w + T_k - 2 = p$ and as a result of the short time series in relation to the field quantity $p \ll m$ $\mathbf{S}$ is not invertible. This problem is solved by a projection of the fields on appropriately chosen guess vectors. The T^2 variable is, by assumption of the zero hypothesis Fisher-F distributed by $(p\,, T_w + T_k - p - 1)$ degrees of freedom (Morrison 1990).

The Hotelling test does not specify how strongly the signal is realised within each 30-d sample compared to the internal variability as measured by the covariance matrix. To derive an index of relative strength we additionally apply the recurrence analysis (Zwiers and von Storch 1989) after finding a significant signal. The method is based on linear discriminant analysis and estimates the probability of correctly placing a single 30-d realisation into the appropriate ensemble *cold* or *warm*. If this probability is high (e.g. recurrence larger than 75%) the two ensembles are separated by a large Mahalanobis distance such that on average three out of four realisations are assigned to the correct ensemble. The combination of the Hotelling test *and* recurrence analysis assures the significance and stability of the results.

2.2 Estimator of the covariance matrix

Simulations of climate with a AGCM are influenced by boundary conditions and the initial conditions. So it is possible that changes in the boundary conditions (e.g. changes in the sea surface temperature) lead to an external variation of the model climate expressed by a shift of the mean climate state vector. Different initial conditions result in an internal variation around the mean model climate possibly leading to a random shift between the two climates.

To allow for a separation of the externally generated variability (by SST and ice) from the internal noise we performed five integrations for each decade separately differing only in their initial conditions and thereby generating different realisations of the atmospheric climate state vector. It will be assumed that every random variable $\vec{x}_j(t)$ $(j = 1, \ldots, n_{c(w)})$ can be described as a sum of a climate variable $\vec{\nu}(t)$ according to the external SST forcing and an internal variable $\vec{\varepsilon}_j(t)$ caused by the initial conditions.

$$\vec{x}_{j_{c(w)}}(t) = \vec{\nu}_{c(w)}(t) + \vec{\varepsilon}_{j_{c(w)}}(t) \qquad (4)$$

In the following we will omit the indices c and k for the "*cold*" and "*warm*" simulations because the following arithmetics is realized separately for the *cold* and *warm* simulations.

The covariance matrix of the joint signal resulting from the boundary conditions of these amplitudes is estimated at present by three methods

1. **Pool-method** pooling all integrations of one decade into a single simulation and estimation of covariance matrix $\mathbf{S}_{p_w}$ and $\mathbf{S}_{p_c}$.
2. **Average-method** averaging all realisations for one decade at a fixed time and calculating a biased estimate of the joint signal covariance matrix $\mathbf{S}_m$.
3. **Anova-method** removing that bias according to a one-sided ANOVA analysis by performing permutations of the single realisations at a fixed time within each decade, thus enhancing the number of realisations.

1. Pool-Method The initial conditions for all simulations are independent from each other so that all simulations of the atmospheric climate state are an independent realisation of the ensemble. Therefore it is possible to pool all simulations of one decade to a single, long simulation. The sample size increases by the factor of the number of simulations n. The expectation value $E(\vec{x})$ is estimated by

$$\overline{\vec{x}} = \frac{1}{nT} \sum_{t=1}^{T} \sum_{j=1}^{n} \vec{x}_j(t)$$

and the covariance matrix $\mathbf{S}_p$ is defined as

$$\mathbf{S}_p = \frac{1}{n} \sum_{j=1}^{n} \frac{1}{T-1} \sum_{t=1}^{T} \left(\vec{x}_j(t) - \overline{\vec{x}}\right) \left(\vec{x}_j(t) - \overline{\vec{x}}\right)^t$$

With the pool method it is not possible to separate the external from the internal signal. The resulting T^2 variable is biased by the noise of the signal and so it is difficult to get a correct sample mean value.

2. Average-method We are interested in the examination of the mean state of the climate caused by an SST forcing. Therefore we have to separate the external signal. With this goal in mind we take the mean of all simulations. So we decrease the variance and reduce the internal signal caused by the initial conditions and the internal variability. We look for an estimator of the covariance matrix $\mathbf{S}_m$ with an external signal caused by SST forcing and an estimator for the climate variable $\vec{\nu}(t)$. We get $\vec{\nu}(t)$ as a mean value over all simulations for every sample vector $\vec{x}(t)$ at all grid points. We make the assumption that the internal variation $\vec{\varepsilon}(t)$ are identical, independly distributed random variables. With this the estimator $\vec{\nu}(t)$ is calculated as

$$\vec{\nu}(t)) = \frac{1}{n} \sum_{j=1}^{n} \vec{x}_j(t) \qquad j = 1, \ldots, \text{simulation}$$

with the assumption $\frac{1}{n} \sum_{j=1}^{n} \vec{\varepsilon}_j(t) = 0$.

The estimator for the expectation value of the externally forced parameter $E(\vec{\nu})$ and the covariance matrix $\mathbf{S}_m$ determine as

$$\overline{\vec{\nu}} = \frac{1}{T} \sum_{t=1}^{T} \vec{\nu}(t)$$

$$\mathbf{S}_m = \frac{1}{T-1} \sum_{t=1}^{T} \left(\vec{\nu}(t) - \overline{\vec{\nu}}\right) \left(\vec{\nu}(t) - \overline{\vec{\nu}}\right)^t$$

This estimator makes it possible to separate the signal caused by external SST forcing but this estimator has a bias because of the internal variability.

3. ANOVA Method We get by combination of the pool and average methods a better estimate for the external signal and particularly a removal of the bias due to the internal variation. The value of the covariance matrix of the external forcing can be determined by averaging all *cold* and *warm* simulations or from all single simulations. The covariance matrix $\mathbf{S}_m$ and the covariance matrix $\mathbf{S}_p$ are both biased estimators for the covariance matrix $\mathbf{S}_{sst}$ because of the internal variance. From both resulting value $\mathbf{S}_m$ and $\mathbf{S}_p$ we get the studied estimator $\mathbf{S}_{sst}$.

Since every simulation is independent of the initial conditions, it follows that they do not correlate. Therefore the terms $\vec{\varepsilon}_j(t) \cdot (\vec{\nu}(t) - \overline{\vec{\nu}})^t$ and $(\vec{\varepsilon}_j - \overline{\vec{\varepsilon}_j}) \cdot (\vec{\varepsilon}_{j'} - \overline{\vec{\varepsilon}_{j'}})^t$ for $j \neq j'$ disappear and for the covariance matrices $\mathbf{S}_m$ and $\mathbf{S}_p$ follow:

$$\mathbf{S}_m = \mathbf{S}_{sst} + \frac{1}{n}\mathbf{S}_\varepsilon$$

$$\mathbf{S}_p = \mathbf{S}_{sst} + \mathbf{S}_\varepsilon$$

$$\Rightarrow \quad \mathbf{S}_{sst} = \frac{n}{n-1}\left(\mathbf{S}_m - \frac{1}{n}\mathbf{S}_p\right) \qquad (5)$$

The equation 5 shows the dependence of the estimator $\mathbf{S}_{sst}$ on the internal variability. The larger the number of simulations and the better the estimator of the mean climate signal according to the SST boundary conditions, the smaller the bias will be. On the other hand the matrix $\mathbf{S}_{sst}$ is no more absolutely positive definit. Because of this we have to increase the number of simulations. Preisendorfer and Barnett (1983) show that we can use all simulations as a pool of possible simulations of a ensemble. For this the year to year autocorrelation has to be small. The autocorrelation has a value of $r \sim -0.1 \pm 0.3$ by a significance level of 95%, so that we can increase the number of simulations according to the following scheme.

The n simulation of size T for each decade is sorted so that every simulation is classified to the corresponding month. With a random generator one of the n realisations of each month will be chosen. In this way we get a new simulation. We define this random simulation as a new sample with a sample size of T. According to this scheme we need 200 additional realisations to make the estimate $\mathbf{S}_{sst}$ positiv definit. The distribution function for the T^2 variable and this ANOVA-method is not Fisher-F distributed. A bootstrap method is used to estimate nonparametric quantiles of the null hypothesis.

2.3 Information compression

To determine the T^2 test variable we need the inverse of the sample covariance matrix $\mathbf{S}^{-1}$. The variables of investigation Ψ, χ, Φ and $\ln p_s$ are integrated into the state vector $\vec{x}(t)$. With it $\vec{x}(t)$ will have a very high dimension.

The sample covariance matrix is invertible, if the dimension of the state vector $\dim(\vec{x}(t))$ is lower than $(T_w + T_m - 2)$. We therefore split the state vector $\vec{x}$ into a part which is accessible by statistics and into an unresolvable part. The accessible part is characterized by being spanned by a (low dimensional) set of so called guess vectors $\vec{g}_k, k \in [1, \tilde{q}], \tilde{q} \ll q$ (von Storch 1987). These guess vectors are q dimensional vectors being designed as to represent typical patterns in grid point space. The guess vectors are defined a-priori using a physical model. If we arrange the guess vectors as column vectors of a $q \times \tilde{q}$ matrix G and the amplitudes of the guess vectors in a $\tilde{q}$ dimensional column vector $\vec{y}$ we can write

$$\vec{x} = G\vec{y} + \vec{r} \tag{6}$$

where $\vec{r}$ denotes the unresolved part of the state vector $\vec{x}$. Eq. (6) can be solved for the unknown amplitudes $\vec{y}$ by requiring the residual variance $\vec{r}^t W \vec{r}$ to be a minimum, where W is a yet unspecified, but freely chosen metric of the scalar product. The solution reads

$$\vec{y} = (G^t W G)^{-1} G^t W \vec{x} \tag{7}$$

which is well defined provided that the guess patterns form a linearly independent set. The dimension of the projected state vector $\vec{y}$ is $\tilde{q}$ which depends only on the numbers of guess vectors specified a-priori. Thus, if we specify only $\tilde{q} < T_c + T_w - 2$ guess vectors, the estimated covariance matrix of the projected state vector $\vec{y}$ is most probably of full rank and can be inverted and the T^2 statistics in the subspace of the phase space which is well defined and can be used to test H_0, H_A.

2.4 Guess modes

This studie concentrates on changes in the tropics based on the study of Hense and Römer (1995) We use a linearized reduced gravity model with only the first internal baroclinic mode included and driven by a deep internal heat source against frictional effects, which provides a sufficient description of the long term mean tropical flow (Robertson and Frankignoul 1990). The eigenmodes of the linearized model were sorted according to the modulus of the eigenvalue thus defining the guess vectors. We will use the eigenmodes $\vec{e}_{k,m}$ of the linear system as the a-priori defined, physical based guess vectors $\vec{g}_k$ of Eq. 7. Firstly the eigenmodes were separated into those propagating eastward and westward relative to a zero basic flow $u_0 = 0$. This differentiates between the Kelvin / gravity modes and the Rossby / gravity modes. Secondly, within each of these two subsets, the eigenmodes were sorted according to the modulus of their respective eigenvalue with nonzero basic flow. Both subsets were merged again by choosing as guess vectors an alternating one eastward and one westward moving mode.

These guess vectors depend on the strength of the superrotational flow u_0, the Rossby radius of deformation R_0 and the damping constantγ. Details of the model used can be found in Hense and Römer (1995).

2.5 The data

Globally and monthly varying mean fields of SST and ice boundaries for the period January 1904- December 1913 and January 1951-December 1960 have been taken from the Global Ice and Sea Surface Temperature (GISST) data set prepared by the Hadley Center for Climate Prediction and Research (Parker, Jones, Folland and Bevan 1994) and used as boundary conditions for the ECHAM3 model (Roeckner et. al. 1990) at resolution T21 and 19 vertical layers. Five integrations for each decade separately differing only in their initial conditions are performed thereby generating different realisations of the atmospheric climate state vector. Spin-up time was two years for every simulation so that even the long time surface processe should have adjusted on the boundary conditions. Input into the analysis are stream-function, velocity potential, sea level pressure and the geopotential at different levels.

3 RESULTS

Based on the study of Hense and Römer (1995) we test the parameter streamfunktion, velocity potential in 300 hPa and 750 hPa and the sea level pressure. The results of the T^2 test are strongly dependent on the Rossby radius. For the parameter χ, Ψ in 300 hPa and the sea level pressure p_s we get the best results for a Rossby radius of 900 km. This agrees well with the Rossby radius used by Gill (1980) for dry atmosphere. We use for the damping rate γ a value of $5.0 \cdot 10^{-5}$ 1/s (this corresponds to 2.5 day) and for the mean velocity a value of 10 m/s.

By utilizing the eigenmodes and the pool-method, the H_o hypothesis can be rejected with an error level of 1%. The recurrence is 80% (table 1). Figure 1 shows the significant field by transforming the modal amplitudes representation back into grid-point space for sea level pressure p_s. The GCM shows a significant drop of about 2 hPa in SLP over the Pacific and an increase over the tropical Atlantic and Africa of the same magnitude in the case of the *cold* simulation compared to the *warm* one. In terms of spatial pattern correlations (squared) between the statistically filtered and the raw fields, the significant differences account for 9% of the stream-function, 88% of the velocity potential and 8% for the sea level pressure of the total difference pattern. One has to keep in mind that the choice of the guessmodes is solely restricted to the tropical region. In contrast to this, the large parts of the variance and energy of the stream-function and the sea level pressure come from the extratropics. If we compare this result with the results of the average and ANOVA-methods we see that the H_0 hypothesis can be rejected (table 1). As expected the variance decreases and the recurrence increases. This shows that the external variance caused by SST has a significant effect on the mean climate. A comparison of the significant sea level pressure fields p_s shows (figure 1-3) that the variance is lower in the pool-method than in the average-method. If we take off the bias caused by the internal variance in the ANOVA-method the variance and the recurrence increase (table 1). So we can see that the ANOVA-method shows a better and more significant result for the T^2 hypothesis test. The variables χ, Ψ in 300 hPa and p_s show significant differences between the two decades caused by SST forcing.

A test of the Ψ, χ – fields in 750 hPa and p_s shows that for the pool-method the H_A hypothesis has to be accepted with an error level of 5% (table 1). But if we take only the covariance matrix of the external signal (ANOVA) the H_0 hypothesis is true. So there is no significant difference between the two decade for the external variance alone. Furthermore it shows that because of the different SST forcing the internal variance is increased and therefore the mean climate is different.

4 CONCLUSION

The statistical dynamical analysis of the difference between two GCM experiments under GISST using the ECHAM3 GCM is described. An analysis scheme which deals with the multivariate test problem, the problem of separation of the externally generated variability and

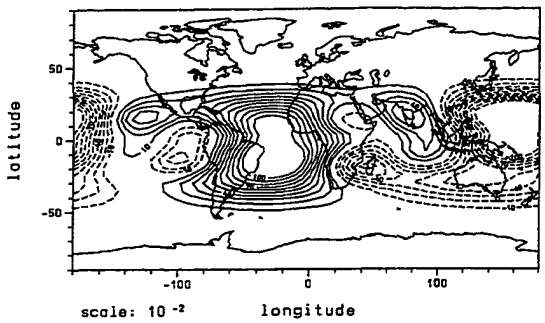


Figure 1 Significant difference field *cold - warm* of the p_s field using the Pool method. Values have to be multiplied by the indicated scale factor, units are hPa, zero contour is omitted, negative contours are dashed, contour interval is 0.10.

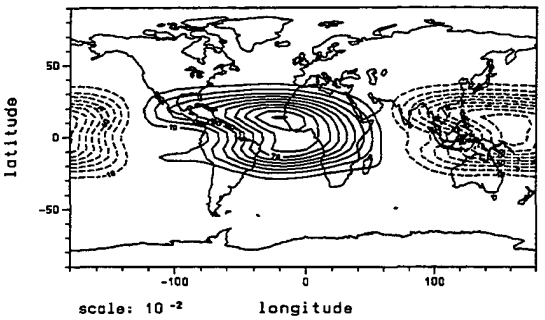


Figure 2 Significant difference field *cold - warm* of the p_s field using the average method. Plotting convention, units and contour interval as in Fig. 1.

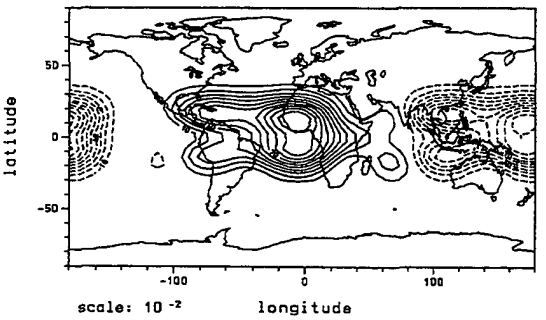


Figure 3 Significant difference field *cold - warm* of the p_s field using the ANOVA method. Plotting convention, units and contour interval as in Fig. 1.

the information compression problem is presented. Input into the analysis has been streamfunction and velocity potential describing the flow field and sea level pressure.

Three different methods to obtain the covariance matrix have been set up to find out if this hypothesis is true. The first method – the pool method – shows that there is a difference in all analysed variables. The second and third methods – average and ANOVA methods – show that the treated variables are not significantly different in all levels. This shows that it is possible and necessary to distinguish between the internally and externally introduced variability.

	T^2	Rec.	Correlation			M
300 hPa			χ	Ψ	p_s	
1.	1%	80%	88%	9%	8%	40
2.	5%	92%	81%	6%	6%	7
3.	10%	93%	82%	7%	6%	8
750 hPa			χ	Ψ	p_s	
1.	1%	84%	92%	29%	11%	40
2.	>10%	<75%	–	–	–	–
3.	>10%	<75%	–	–	–	–

Table 1 Error level by rejecting the H_0 hypothesis (T^2), Recurrence (Rec.), squared global spatial pattern correlation coefficient and number of used eigenmodes (M) for the significant χ, Ψ at 300 hPa and 750 hPa and p_s field as a function of used three covariance methods.

References

Gill, A. E. (1980). Some simple solution for heat-induced tropical circulation, *Q.J.R. Meteorol. Soc.* **106**: 447 – 462.

Hense, A. and Römer, U. (1995). Statistical analysis of tropical climate anomaly simulations, *Clim. Dyn.* **11**: 178 – 192.

Morrison, D. F. (1990). *Multivariate Statistical Methods*, McGraw-Hill, New York.

Parker, D. E., Jones, P. D., Folland, C. K. and Bevan, A. (1994). *Interdecadal changes of surface temperature since the late nineteenth century, J. Geophys. Res.* **99**(D7): 14373 – 14399.

Preisendorfer, R. and Barnett, T. P. (1983). Numerical model-reality intercomparison tests using small-sample statistics, *J. Atmos. Sci.* **40**(8): 1884 – 1896.

Robertson, A. W. and Frankignoul, C. (1990). The tropical circulation: Simple model versus general circulation model, *Q.J.R. Meteorol. Soc.* **116**: 69 – 87.

Roeckner, E. et. al. (1992). *Simulation of the Present-Day Climate with the ECHAM Model: Impact of Model Physics and Resolution*, Vol. 93, Max-Plank-Institut für Meteorologie, Hamburg Report.

von Storch, H. (1987). A statistical comparison with observations of control and el niño simulations using the ncar ccm, *Beitr. Phys. Atmosph.* **60**(4): 464 – 477.

Zwiers, F. W. (1987). Statistical considerations for climate experiments. part ii: Multivariate tests, *J. Climate Appl. Meteor.* **26**: 477 – 487.

Zwiers, F. W. and von Storch, H. (1989). Multivariate recurrence analysis, *Journal of Climate* **2**: 1538 – 1553.

CORRESPONDING AUTHOR

Andreas Hense
Meteorologisches Institut der Universität Bonn
Auf dem Hügel 20, 53121 Bonn, Germany

EXTERNAL AND INTERNAL SEASONAL VARIABILITY SIMULATED WITH THE LMD AGCM DURING THE NORTHERN HEMISPHERE WINTER.

C. Dichampt*, S. Parey, J.Y. Caneill

EDF/DER, Environment department, 6 quai Watier, 78401 Chatou Cedex, France.
* PhD thesis student

ABSTRACT

Fifteen simulations of the 1970-1988 period are firstly studied to identify characteristic patterns of the 500 hPa geopotential height field and of the 850 hPa temperature field simulated on the monthly scale during the Northern Hemisphere winter with the LMD AGCM (cycle 5.1). Two selected winter (1970-71 and 1983-84) are then more precisely studied from seasonal ensemble integrations with a higher resolution version of the same model (cycle 5.3).

1 INTRODUCTION

The potential predictability of the atmosphere on the seasonal scale can be investigated using Atmospheric General Circulation Models, forced with observed oceanic variables (Sea Surface Temperature and ice cover anomalies) observed on past periods. This is the present approach used to characterise some properties of the atmospheric seasonal variability at middle latitudes during the Northern Hemisphere winter, as simulated with the LMD (Laboratoire de Météorologie Dynamique) AGCM.

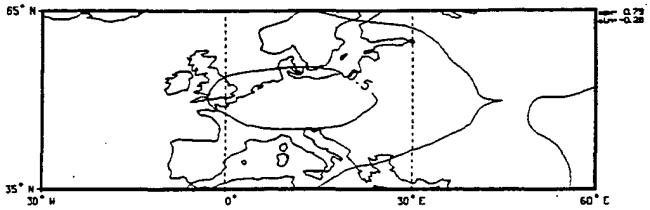
2 IDENTIFICATION OF LOW-FREQUENCY STRUCTURES SIMULATED ON EUROPE

Fifteen simulations of the same 19-year period (1970-1988) are firstly studied. They have been computed using the LMD AGCM (cycle 5.1 : resolution 64x50x11) forced with observed SSTs. The study focuses on the low-frequency features of the 500 hPa geopotential height field and of the 850 hPa temperature field simulated during the Northern Hemisphere winter on the Atlantic/European area, from the study of monthly means and variance fields of individual realisations and of the ensemble mean simulation.

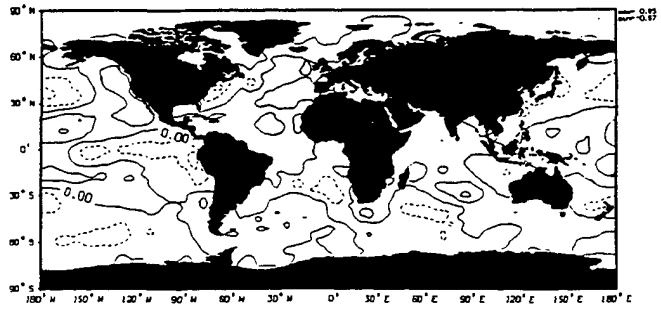
The size of the sample allows for an investigation of the external variability (induced by oceanic forcing variability) as well as of the internal (inter-realisations) variability. Different methods have been used to characterise the main climatic situations simulated by the model and to identify its principal modes of external and internal variability on the monthly scale (estimations of EOFs, distributions of the variables associated with specific events in the physical space and in the phase space).

One of the main results of the study is the connection that has been found between El Nino/La Nina oceanic events and the situation simulated on Europe, from a classification method applied to the monthly means on the European window (figures 1 to 4).

The impact of the oceanic forcing variables on the internal variability is also discussed, and a special attention is paid to the depiction of well reproduced winter events on the European sector, from a comparison of the diagnostic results with similar ones obtained on NMC data of the same period.



(a)



(b)

Figure 1. (a) Centroid of the cluster 1 (ensemble mean calculated on all the elements of the cluster 1), from a classification on European 850 hPa temperature anomalies maps ; (b) SST anomalies centroid for the cluster 1 previously defined.
This cluster agregates 431 elements on the 855 initial ones (19 years x 3 winter months x 15 realisations).
The significativity (at a 95% level) of the presence of a given winter in a cluster is assessed by comparing the number of its realisations (within the 15 ones) which belong to the cluster with the distribution of occurence that would be obtained from random drawing . The winters that are found significatively represented in this cluster are : 1981, 1984.

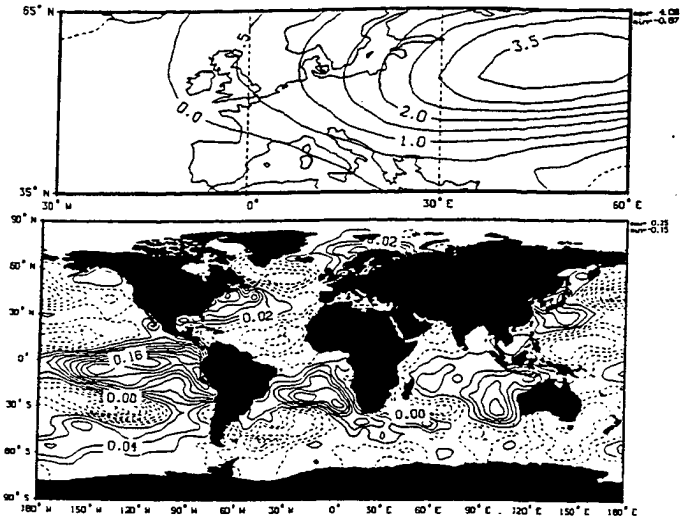


Figure 2. Same as fig. 1, but for the cluster 2. This cluster agregates 199 elements, and the winters significatively represented are : 1983, 1987 (two El Nino years).

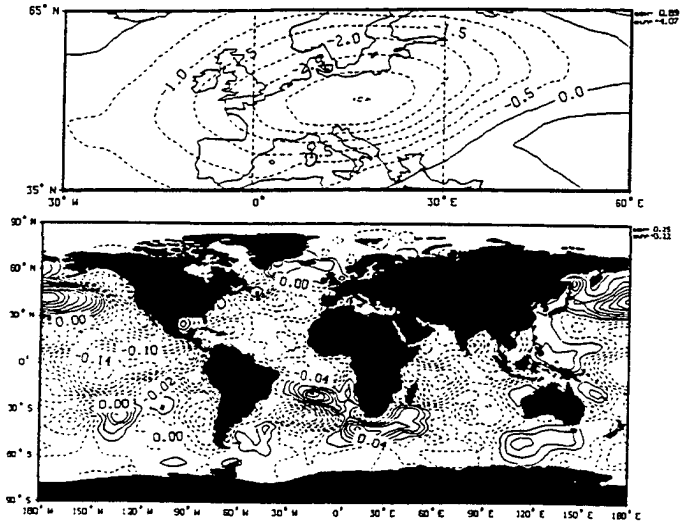


Figure 3. Same as fig. 1, but for the cluster 3. This cluster agregates 82 elements, and the winter significatively represented is : 1971 (La Nina year).

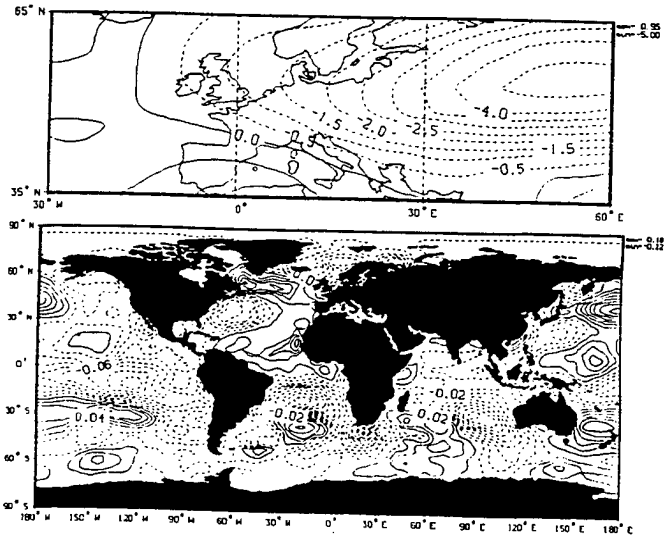


Figure 4. Same as fig. 1, but for the cluster 4. This cluster agregates 143 elements, and the winters significatively represented are : 1974 (La Nina year), 1979,1982.

3 STUDY OF TWO PARTICULAR CASES : 1970-71 AND 1983-84 EUROPEAN WINTERS

Two particular winters have been selected from this analysis, to be more precisely studied from seasonal integrations with a higher resolution version of the LMD model (cycle 5.3, resolution 96x72x15) : the cold 1970-1971 winter, a case of strong La Nina oceanic anomaly, and the warm 1983-1984 winter on Europe. One 23-year long simulation of the 1970-1992 period has been computed with the latter version of the model to constitute a climatic reference, and fifteen realisations of the both selected winters have been integrated respectively until the end of March 1971 and of March 1984, starting with "simulated time-lagged" initial states : they have been obtained from previous short integrations with the model around the 1st of September 1970 and the 1st of September 1983 extracted from the long reference simulation.

The two ensemble mean simulations of the 1970/71 winter and of the 1983/84 winter scores are evaluated on different geographical areas (anomaly correlation coefficients, climatological skill scores), and the spreads of the simulated individual atmospheric trajectories are examined. The statistical significance of the results is assessed from Student/Fisher tests on the means/variances anomalies.

The simulated variability on time scales from one week to one month is compared between these two cases : simulation of anticyclonic blocking events (estimated from a blocking index), and reproduction of the main atmospheric large-scale oscillations (from the calculation of teleconnection index).

4. CONCLUSION

Thie study shows characteristic situations simulated on Europe during winter, and it links these features to oceanic forcings. It allows to compare on two particular seasonal cases the results from two versions of the LMD model.

References

Déqué, M. and J.F. Royer, 1992 : The skill of extended-range extratropical winter dynamical forecasts, *Journal of Climate*, 5, 1346-1356.

Murphy, A.H. and E.S. Epstein, 1989 : Skill scores and correlation coefficients in model verification, *Monthly Weather Review*, 117, 572-581.

Palmer, T.N., 1988 : Medium and extended range predictability and stability of the PNA mode, *Quarterly Journal of Royal Meteorological Society*,114, 691-713.

Palmer, T.N., and D.L.T. Anderson, 1994 : The prospects for seasonal forecasting - a review paper, *Q.J.R. Meteorol. Soc.*, 120, 755-793.

STATISTICAL ANALYSIS OF THE RELATIONSHIP BETWEEN TRANSIENT EDDY SENSIBLE AND LATENT HEAT FLUXES IN THE SOUTHERN HEMISPHERE

Marilyn Raphael
Department of Geography
University of California, Los Angeles
405 Hilgard Avenue, Los Angeles, CA 90024-1524

ABSTRACT

The relationship between the 850mb, transient eddy, latent (LHF) and sensible (SHF) heat fluxes in the Southern Hemisphere, are studied using bandpass-filtered European Centre for Medium Range Weather Forecasts (ECMWF) analyses for January. Eleven-year averages of the fluxes show that they are of comparable magnitudes in the middle latitudes and that the LHF exceeds the SHF equatorward of 45°S. Correlations of the zonal averages of the flux anomalies show that they are most strongly linked in the middle latitudes. Principal components analysis (PCA) and singular value decomposition (SVD) show that the two fluxes act together and that the first two PCs explain the majority of the variance in the datasets. The strong covariation between the fluxes suggest that there is a reinforcing relationship between them. This reinforcement occurs in the region of flux divergence.

INTRODUCTION

Research on atmospheric processes shows that the latitudinal imbalances of energy that result from differential radiative heating are redressed by the poleward transport of energy in latent and sensible forms. Much of the research has focused upon the individual fluxes in particular the SHF (eg. Haines and Winston, 1963; Lau, 1979; Oort and Rasmusson, 1971; Raphael and Rogers, 1992). These forms of energy are transported chiefly by the mean meridional circulation in the Tropics and by the quasi-stationary and transient eddies in the extratropics. The transient eddies are baroclinic and therefore depend upon the meridional temperature gradient. The SHF is shown to be closely related to the latitudinal temperature gradient through the mechanism of flux divergence (van Loon, 1979; van Loon and Kidson, 1993). Other studies indicate that the SHF is reinforced by LHF convergence.

General circulation model (GCM) studies suggest that one of the results of global warming would be a reduced meridional temperature gradient which would be most apparent in winter. A change of this nature can have several effects. One of these is that the LHF may increase because of warmer temperatures and the SHF may decrease simultaneously. Another is that the LHF transport to and release at higher latitudes may result in a reduced temperature gradient and associated smaller eddies (Held, 1993).

To understand the effect of global warming on the fluxes of energy it is necessary to understand how the flux components as well as the fluxes themselves vary among themselves in present day climate. The relationships between the flux components in the Southern Hemisphere have been described by Trenberth (1991). The LHF and SHF are positively related to each other through their common variable the meridional wind. The strength of the wind derives directly from the intensity of the baroclinic eddy and is therefore dependent upon the meridional temperature gradient. The LHF is also dependent upon the availability of moisture. While the reality of a relationship between the fluxes is accepted, it is still useful to assess the strength of the relationship and the importance of the factors contributing to it. It would be useful to know the strength of relationship between the fluxes and the contribution of these factors to the strength of the fluxes.

The importance of this study lies in its attempts to describe and determine the strength of the relationship between the fluxes. In addition this study attempts to separate the fluxes into their important modes of variation and from these, determine the source of their common variation. Then it may be possible to comment on the probable effects of changes in these sources on the heat fluxes themselves.

DATA

The data used in this analysis are January, monthly averages of the bandpass filtered (to retain 2-8 day fluctuations) covariances $v'T'$ (SHF) and $v'q'$ (LHF) at 850mb in the Southern Hemisphere. They are derived from the ECMWF global analyses and span the period 1979-1989. The details of these data are discussed extensively elsewhere (Trenberth, 1991, 1992). The 850mb level was chosen since it is the level at which both the LHF and SHF peak in magnitude. The Southern Hemisphere is chosen because the complicating influences of the land/sea distribution are reduced. The month of January was chosen because it represents the time during

which the Southern Hemisphere temperature gradients are strong and the associated fluxes are quite large.

METHOD

Simple correlations between the flux anomalies (departures from the mean) are calculated and mapped for the entire globe. Spatial averages of the fluxes and their divergence are also presented. Zonal averages of the flux anomalies are calculated for each year for the latitudes ranging from 24°S - 64°S. These zonal averages are correlated and also subjected to PCA and the matrix form of SVD. PCA produces pairs of eigenvectors and expansion coefficients which allow the spatial and temporal description of the factors that contribute most to the variation of the fluxes. From the SVD analysis, reduced rank Hovmoller plots that correspond to the modes of the PCA are produced. These plots are essentially spatial time series of the data therefore they contain a combination of the information contained in the eigenvectors and the expansion coefficient and are used to substantiate the information produced by PCA. These plots are an improvement on the ones produced using the raw data since the raw data may possess noise, thus obscuring meaningful patterns.

RESULTS and DISCUSSION

The mapped averages of the fluxes (Figure 1) show that the flux maxima occur over the midlatitude oceans and eastern North America. The flux maxima occur in the region of greatest variation in the geopotential height field also identified as storm tracks. In the Southern Hemisphere they are similar in magnitude while in the Northern Hemisphere the SHF is markedly larger than the LHF.

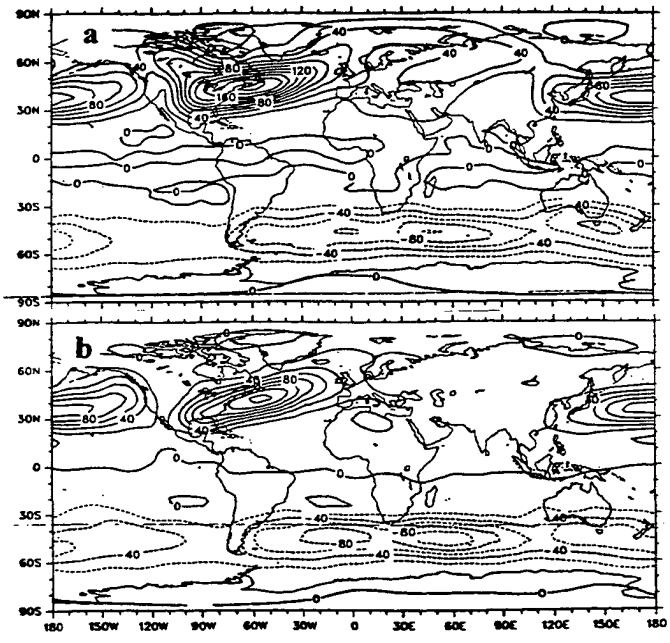


Figure 1. Spatial distribution of latent (a) and sensible (b) heat flux averages in January. Units are Joules.

Statistically significant correlations of the zonal averages indicate that the heat fluxes are strongly positively correlated with each other in the mid and high latitudes and weakly correlated in the subtropics. The geographical distribution of these correlations (Figure 2) shows that they are zonally coherent and unlike the zonal averages, they peak in the storm track region. Similar correlations exist in the Northern Hemisphere.

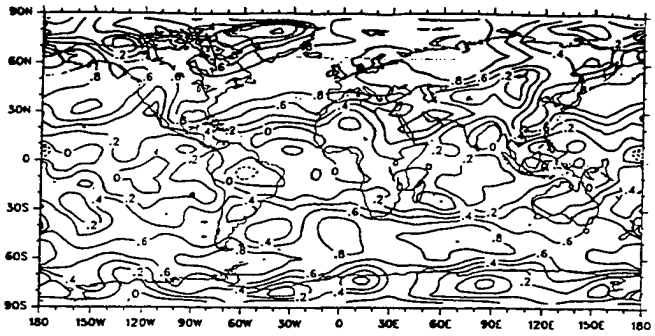
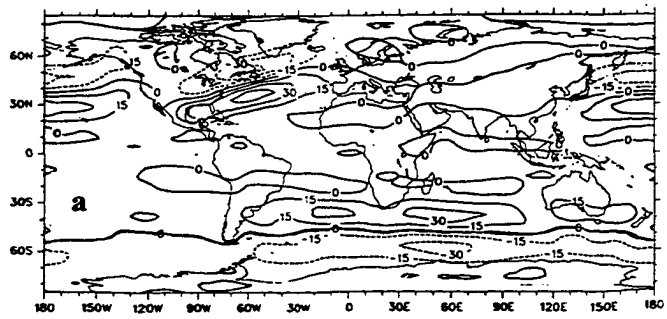


Figure 2. Latent and Sensible heat flux anomaly correlations in January. Values greater than 6 are statistically significant.

These strong correlations arise partly because both fluxes have a common component, the meridional wind (v') and also because of the positive relationship between temperature and available moisture. The strong coupling of the fluxes may also be due to the reinforcing relationship that is thought to exist between them.

Figure 3 shows the flux divergence calculated from the spatial averages of Figure 1. It indicates that divergence is greatest in the regions of strongest flux. Also the LHF appears to be a greater source of energy than the SHF in the Southern Hemisphere. In the Northern Hemisphere this is true only over the North Pacific Ocean since the SHF appears to be a greater source of energy than the LHF over the western Atlantic Ocean and eastern United States.



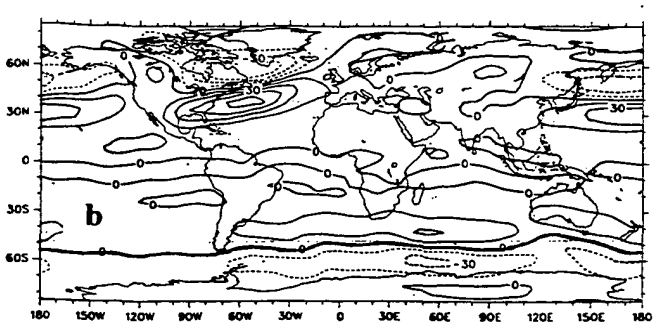


Figure 3. Latent (a) and sensible (b) heat flux divergence for July. Units are Joules.

The PCA procedure reveals that most of the variance in the datasets is explained by the first two eigenvectors (EOF). This suggests that the fluxes have not experienced much spatial, interannual variation over the period of study and that they are affected by few controlling factors in January. Figure 4 displays the first three EOFs and their accompanying expansion coefficients for both fluxes, and it is apparent that the LHF and SHF

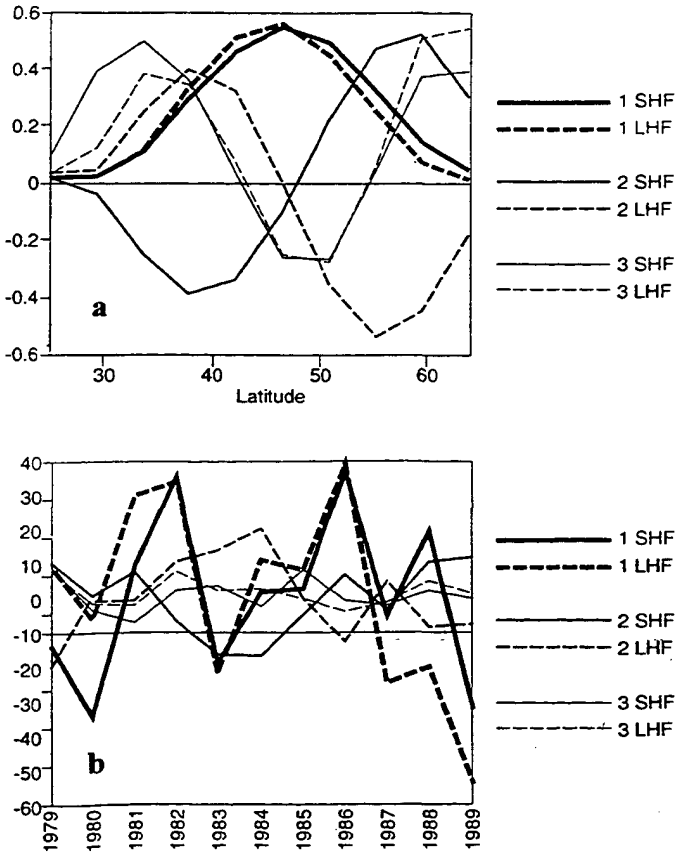


Figure 4. Eigenvectors (a) and expansion coefficients (b) of the zonal averages of the latent and sensible heat flux.

act in an almost identical manner. The first EOF explains 87.3% and 83.4% of the variation in the dataset for the LHF and SHF respectively. It appears to be a weighted average of the heat fluxes with the center of action lying between 40°S - 50°S. The second EOF appears to be a contrast between the fluxes in the northern and southern extremes of latitude and the centers of action lie poleward of 50°S and equatorward of 40°S. In PCA such a pattern of contrasting modes is not uncommon because of the way in which these modes are forced to be orthogonal to each other. However, the results of the SVD analysis (Figure 5) are similar to that of PCA.

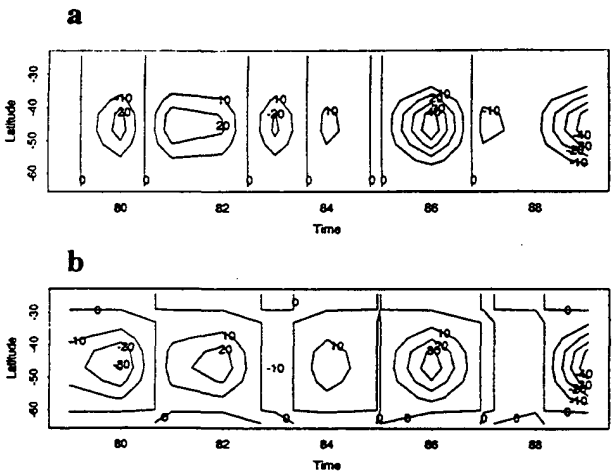


Figure 5. Rank 1 approximations to the latent (a) and sensible (b) heat flux. Units are Joules.

The rank 1 approximation to the data is a combination of the first EOF and its expansion coefficient. It explains approximately 87% and 83% of the variation in the latent and sensible heat flux datasets respectively. It shows a peak in activity at the same latitudes as the first EOF. The second mode indicates a clear north/south contrast which is more distinct in the sensible heat flux field and the polarity of which changes over time. The rank 2 approximation which is the sum of the first two modes of activity, explains 98% of the variation in the dataset.

The patterns extracted from the data can be related to some actual physical processes. The similarity of the first EOFs (and the rank 1 approximations) might be expected since the flux anomalies are almost perfectly correlated in the middle latitudes. The LHF and SHF are at their maximum in the middle latitudes and are sharply reduced at the higher and lower latitudes. The centre of action of the first EOF lies in the latitudes of the strongest temperature gradients and increased atmospheric water vapor content (Figure 6).

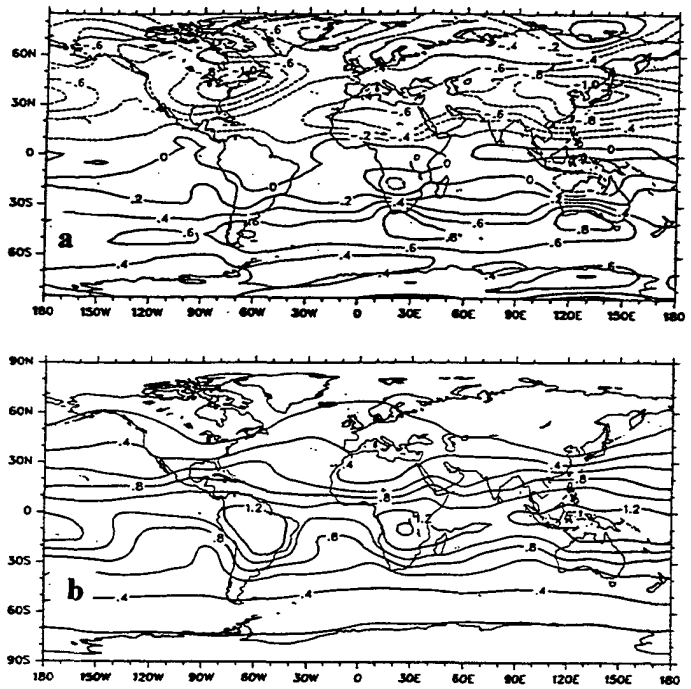


Figure 6. Average meridional temperature gradients (a) (Units are $X10^{-2}$K/m) and mixing ratio (b) (Units are $X10^{-2}$g/kg) for January.

The SHF is largely a function of the meridional temperature gradient while the LHF also depends upon the availability of moisture. The similarity of the first EOFs may then be due to the spatial coincidence of strong temperature gradients and increased water vapor in the atmosphere. The strong January temperature gradients are the result of the influence of Antarctica while the increased water vapor content of the atmosphere is due to summer conditions in the Southern Hemisphere.

The expansion coefficients of the first two EOFs (Figure 4b) indicate that the LHF and SHF vary closely together in time. The first coefficient suggests a strong interannual variation in the fluxes as well as an underlying quasi-biennial fluctuation. The dataset however, is too short to allow a good analysis of this variation. The first mode of variation in the SVD analysis shows that there is a definite wave pattern with an approximate period of two years. This structure is present in both fields but is more distinct in the LHF field. The expansion coefficients for the second EOF do not lend themselves as easily to interpretation.

SUMMARY and CONCLUSIONS

The LHF and SHF are similar in magnitude and the regions of strongest flux occur over the midlatitude oceans and eastern North America. The LHF and SHF are shown to be positively related to each other, very strongly in the midlatitudes and weakly in the subtropics. PCA and SVD analysis show that the two fluxes have common modes of variation, the first mode explaining the majority of the variation in the dataset. It is suggested that the fluxes vary similarly because of the spatial coincidence of the strong temperature gradients and increased water vapor content of the atmosphere. The former influences the SHF while the latter influences the LHF. Before more general conclusions may be drawn it necessary to look at the flux relationships during other periods (eg. July) and in more detail for the Northern Hemisphere where the land/sea arrangements may introduce more complexity into the relationship between the fluxes.

References

Held, I.M., 1993, Large-scale Dynamics and Global Warming. Bulletin of the Americam Meteorological Society, 74, 228-241.

Lau, N.-C., 1978, On the three-dimensional structure of the observed transient eddy statistics of the Northern Hemisphere wintertime circulation. Journal of Atmospheric Science, 35, 1900-1923.

Oort, A.H. and E.M. Rasmusson, 1971, Global Atmospheric Circulation Statistics, NOAA Prof. Paper 5, USDC/NOAA Rockville, MD 323 pp.

Raphael, M.N. and J.C. Rogers, 1992, The Meridional Flux of Eddy Sensible Heat at 700mb in the Nothern Hemisphere Winter. Physical Geography, 13, 1-13.

Trenberth, K.E., 1991, Storm Tracks in the Southern Hemisphere. Journal of the Atmospheric Sciences, 48, 2159-2177.

Trenberth, K.E., 1992, Global Analyses from ECMWF: an Atlas of 1000 to 10 mb Circulation Statistics. National Center for Atmospheric Research, Boulder, Colorado.

van Loon, H.V.L., 1979, The association between latitudinal temperature gradient and eddy transport. Part I: Transport of Sensible Heat in Winter. Monthly Weather Review, 107, 525-34.

van Loon, H.V.L. and J.W. Kidson, 1994, The association between latitudinal temperature gradient and eddy transport Part III: the Southern Hemisphere, Australian Meteorological Magazine, 42, 31-37.

ACKNOWLEDGEMENTS

I thank Steve Cherry, Montana State University for his advice on the statistics used in this study. I also thank Kevin Trenberth and Harry van Loon for their comment during this study. This research was completed while the author was on sabbatical at the National Center for Atmospheric Research.

STUDY OF OCEAN - ATMOSPHERE INTERACTION USING A MARKOV CHAIN MODEL

Ileana Mares, C. Mares, Mihaela Mihailescu

National Institute of Meteorology and Hydrology, Bucharest, Romania

ABSTRACT

Blocking type circulation is analysed over the Atlantic - European region (50W - 40E, 35N - 65N) at 500 hPa height, for the period 1965 - 1987 associated with the state of the Atlantic Ocean in the tropical zone (39N - 3N, 74W - 10E). First the teleconnections between the two fields using canonical correlation were studied. The months with a good dependence, have been considered in order to define the state of the ocean which determines the occurrence or non-occurrence of the blocking type circulation. In this way, 4 states of the atmospheric circulation were defined and they were studied using a first order Markov chain.

1 INTRODUCTION

The ocean - atmosphere interaction has been often studied with coupled ocean - atmosphere models. But investigations exist, in which the study of this interaction using a statistical modelling is tried. So, Deque (1989) studied teleconnections between sea surface temperature (SST) from the tropical Atlantic and the field from 500 hPa height, using the canonical correlation analysis with different lags. At the same time DaCamara et al. (1992), have investigated the blocking type circulation in winter for which they associated some characteristics of the SST anomalous fields for Pacific and Atlantic. The main purpose of our study is to analyse the way in which the transition of a blocking circulation type into other type without blocking is conditioned by the ocean state over the tropical Atlantic zone.

For this, the SST monthly values obtained from Comprehensive Ocean - Atmosphere Data Set (COADS), (Woodruff et al., 1987) were considered, in the period 1965 - 1987 for the area from (39N - 3N, 74W - 10E). For the same period the blocking index for the geopotential at 500 hPa defined in the sector (50W - 40E, 35N - 65N) has been also calculated. First, teleconnections with different lags between the blocking index and the sea surface temperatures anomaly (SSTA) were achieved using canonical correlation analysis.

Using the state of the ocean in the predictor months 4 states of the atmosphere circulation were defined , for which a first order Markov chain model was applied.

Using the rows of the transition matrix a simulation of the states of the chain has been achieved, the limiting matrix, the mean matrix of the first transition time, as well as the variance matrix have been calculated. The test of the transition probabilities has been made using a Monte Carlo simulation (Vautard, 1990).

For the months in which SSTA is a good predictor, the blocking type circulation can be predicted approximately knowing the SST prediction a year before, as Latif and Graham (1991) mentioned .

2 TELECONNECTIONS BETWEEN BLOCKING INDEX AND SSTA

In order to test the teleconnections between the blocking index and SSTA from the tropical Atlantic Ocean the canonical correlation with different lags was used. For this reason SSTA field was first analysed using the decomposition in EOFs.

In this paper we considered as significant components those for which the eigenvalue was greater than 1. The number of significant components for each month, their variance, as well as the variance of the first component are presented in Table 1.

Table 1. Significant EOFs components, their cumulative variance (%) and variance of EOF-1 for the SSTA over the region (39 N - 3 N, 74 W - 10 E)

Month	No.of signif. EOFs	Variance of signif. EOFs	Variance of EOF-1
1	15	97	32
2	14	97	36
3	12	97	50
4	12	96	43
5	15	98	42
6	14	97	38
7	15	97	34
8	14	97	33
9	16	98	31
10	15	97	28
11	15	97	29
12	13	96	36

For each month from the period 1965 - 1987, the blocking index I_B, for the longitude λ, was evaluated as follows:

$$I_B(\lambda) = \phi\ (\lambda, 57.5N) - \phi\ (\lambda, 37.5N) \quad (1)$$

where ϕ is geopotential at 500 hPa height.

The positive values of I_B indicate the existence of an anticyclone or of an well defined ridge. For each month of the period 1965 - 1987, canonical correlation with lags from 1 to 12 months, between the monthly values of the blocking index over the Atlantic - European sector and the monthly values of SSTA over the tropical Atlantic sector (only in the Northern Hemisphere) has been realised for which only the significant components were considered.

The best results are presented in Tab. 2.

First column of this table contains the month for which the blocking index is forecast. The second column contains climate change point (CCP), occurred in this index series; in the third column, the signal - to - noise ratio, calculated using first and second order statistical moments (Mares, 1994), is presented, the forth column contains first canonical correlation coefficient; V represents significant level. In the sixth column there are presented the months with the highest significance level of

correlation between SSTA (predictor) and blocking index. The climate change points were sought using Pettitt and Mann - Kendall nonparametrical tests, in the manner described according to Sneyers (1992); m represents a minimum point, M a maximum point. In the case of SSTA these change points were detected using only EOF - 1.

Table 2. Canonical correlation analysis between blocking index and SSTA.
CCP - climate change point; R - signal - to - noise ratio ; ρ_1 - first canonical correlation; V - significance level (%).

Blocking index					*SSTA (EOF - 1)*		
Mon.	CCP	R	ρ_1	V	Mon.	CCP	R
1	1974 (M)	.42	.98	1	9	1975 (m)	.58
2	1978 (m)	.76	.95	1	10	1976 (m)	.67
3	1976 (M)	.56	.93	1	11	1976 (M)	.59
4	1973 (m)	.45	.96	0.1	7	1976 (m)	.79
5	1976 (m)	.58	.95	1	9	1975 (m)	.58
6	1973 (m)	.42	.94	2	9	1975 (m)	.58
7	1971 (m)	.45	.92	5	9	1975 (m)	.58
8	1977 (M)	.22	.94	1	10	1976 (m)	.67
9	1977 (M)	.42	.94	1	11	1976 (M)	.59
10	1975 (M)	.46	.94	1	10	1976 (m)	.67
11	1972 (M)	.45	.92	1	12	1976 (m)	.63
12	1977 (M)	.75	.92	5	12	1976 (m)	.63

In Fig. 1, Mann - Kendall test is presented, forward and backward, for EOF - 1 - SSTA for October (fig. 1 a) and for blocking index for February (fig. 1 b).
The intersection points of the curves from Fig. 1 indicate climate change points near those obtained by Pettitt test.
In Figure 2 it is presented only forward side of the Mann - Kendall test for blocking index for February (1966 - 1987) and for EOF - 1 - SSTA for October (1965 - 1986), seeking in this way the good concordance between the trends of the two correlated series.
Climate change points obtained for each month for SSTA are closed to the point obtained by Bojariu (1994), who has examined EOF - 1 unless the months, but considering a more extended zone (39N - 37S; 74W - 10E) and who has found a change point in 1978.
After verifying the canonical correlation, the best results were obtained for circulation index for February determined by the sea state in October (in 86% of the cases); for the index values for August determined by the sea state from October (91% cases), as well as for the atmospheric state in October determined by the sea state in the same month but a year before (86% cases). These good results can be explained by the fact that climate change points of the atmospheric state occurred after the years with changes in the ocean. This thing is also proofed by the weakest results of the verify (64% of the cases), for the month pairs (1, 9) and (7, 9) when the change points from SSTA occurred after the ones from the atmospheric circulation.

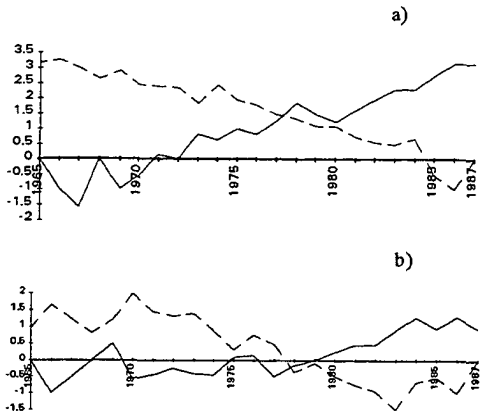


Figure 1. Mann - Kendall test for EOF - 1- SSTA (a) and for the blocking index (b) ;
forward (____) and backward (_ _ _)

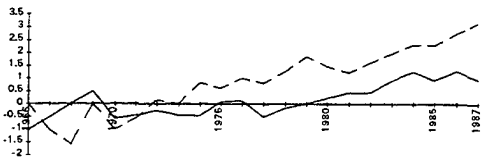


Figure 2. Forward side of the Mann - Kendall test for blocking index for February (1966 - 1987) (____) and for EOF - 1 - SSTA for October (1965 - 1986) (_ _ _).

In Fig. 3, the simple correlation coefficients r_i between the blocking index (February) and SSTA (October) for each point from the considered sector are presented. In Fig. 3 , the key zones ($|r| > 0.4$) over the tropical Atlantic in the Northern Hemisphere are noticed , which determine the occurrence the blocking type circulation. So, the cold water from the equatorial key zone from October influences the blocking in February while in the tropical key zone the warm water from October influences the occurrence of the blocking type circulation of February.

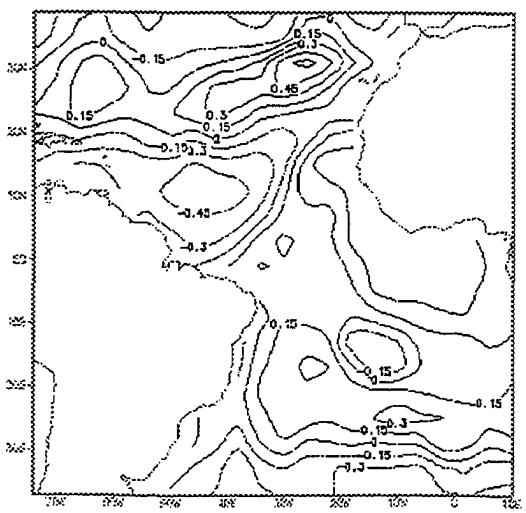


Figure 3. Correlation coefficients between blocking index and SSTA

3 MODELLING BY A FIRST ORDER MARKOV PROCESS

According to Kemeny and Snell (1960), we make the following considerations.

A finite Markov chain is a finite Markov process such that the transition probabilities p_{ij} (t) do not depend on t (t - being discrete time).

If we have the transition matrix for a Markov chain P, with entries p_{ij}, this matrix is regular if and only if for some N, P^N has no zero entities.

We suppose that there is a regular Markov chain, in this case, we have following properties :

(i) the powers P^N approach a probability matrix A;

(ii) each row of A is the same probability vector:

$$a = \{a_1, a_2, \ldots, a_n\} \tag{2}$$

The fundamental matrix for the Markov chain determined by P is:

$$Z = (I - (P - A))^{-1} \tag{3}$$

The first passage time f_k is a function whose value is the number of steps before entering S_k for the first time after the initial position.

The mean first passage matrix , denoted by M, is matrix with entries $m_{ij} = M_i [f_j]$

$$M = (I - Z + E.Z_{dg})D \tag{4}$$

where: E - unity matrix

D - diagonal matrix

(the diagonal elements are $d_{ii} = 1 / a_i$)

The variance of the first passage time is:

$$W = M(2Z_{dg}D - I) + 2(ZM - E(ZM)_{dg}) \tag{5}$$

One of the well-known methods of generating Markov chains uses the rows of the transition matrix P, in a manner described by Naylor (1966).

If the last state of the system was i, then the next state is j if:

$$\sum_{k=1}^{j-1} p_{ik} < r \leq \sum_{k=1}^{j} p_{ik} \tag{6}$$

where r is a uniform random number in the (0,1) interval. Each random number generated will cause a transition from state i to j and the frequency of being in any of the finite states can be counted.

According to the analysis made in paragraph 2 in which we determined the SSTA predictor months for circulation index, we realised the following classification for the entire analysed series (264 values):

1 - zonal circulation associated with cold water;

2 - zonal circulation with warm water;

3 - blocking type circulation with cold water;

4 - blocking type circulation with warm water.

As blocking type circulation it was considered the case in which $I_B \geq 0$ and as zonal circulation the case in which $I_B < 0$. As cold water it was considered the case in which the anomalies averaged over the 150 points over the tropical Atlantic in Northern Hemisphere is negative; the warm water is otherwise.

The transition probabilities matrix for a first order Markov chain, with the four states defined above , is:

$$P = \begin{pmatrix} 0.371 & 0.043 & 0.529 & 0.057 \\ 0.138 & 0.328 & 0.069 & 0.466 \\ 0.432 & 0.081 & 0.405 & 0.081 \\ 0.066 & 0.492 & 0.049 & 0.393 \end{pmatrix} \tag{7}$$

The limiting matrix is found after 23 steps . Each row of the matrix has the form :

$$A = (0.266 \quad 0.220 \quad 0.282 \quad 0.232) \tag{8}$$

By means of limiting matrix , the maximum duration of the anticipation can be determined.

The mean first passage matrix is :

$$M = \begin{pmatrix} 3.76 & 9.53 & 2.88 & 9.83 \\ 7.35 & 4.53 & 7.82 & 4.47 \\ 3.76 & 9.08 & 3.55 & 9.44 \\ 7.91 & 3.42 & 8.30 & 4.31 \end{pmatrix} \tag{9}$$

The variance of the first passage time is:

$$W = \begin{pmatrix} 23.55 & 65.83 & 16.95 & 74.69 \\ 45.09 & 37.33 & 45.05 & 43.73 \\ 25.05 & 65.63 & 22.31 & 74.23 \\ 45.35 & 26.92 & 45.66 & 39.68 \end{pmatrix} \tag{10}$$

Because after the simulation of the Markov chain using 1000 transition the following probabilities

$$A_S = (0.263 \quad 0.218 \quad 0.274 \quad 0.245) \tag{11}$$

of appearing the states are closed to the limiting vector A it means that a good modelling was realised .

In order to assess the statistical significance of the transition matrix elements according to Vautard et al. (1990), we used the nonparametrical and robust method of the Monte Carlo simulation. This way is suitable not only because it makes no apriori supposition concerning the transition probabilities from a state to another, but also for the fact that the deficiency of the short data series is partially eliminated.

Generating random numbers in order to simulate the transition matrix according to empirical transition matrix for a sufficient great number of steps, we obtain results with a desired confidence level . In this way, for a process of 10000 time steps, that we used, the significant elements of the transition matrix must not exceed 100 in order to obtain a 99 % confidence level.

In the analysed case, transition 1 $\longrightarrow$ 3 has a 96 % confidence level and transition 3 $\longrightarrow$ 1 is realised with a 86 % confidence level. Transitions 3 $\longrightarrow$ 3 and 4 $\longrightarrow$ 2 can be also considered to have statistical significance, but the calculated confidence levels are only 80 %.

4 CONCLUSIONS

The main purpose of our study to find whether a systematic influence of anomalies types of SST from the tropical Atlantic in the Northern Hemisphere upon the atmospheric blocking over the Atlantic - European sector at mid and higher latitudes, has been only partially fulfilled. This situation is, first of all, due to the fact that although the interaction between ocean and atmosphere exists almost the whole year - result obtained from the canonical correlation - the active role of the ocean in the atmospheric blocking is evident only in some of the months. The major role of SSTA in the respective months in atmospheric blocking over the Atlantic - European zone of the mid and higher latitudes, is also explained by the occurrence of some climate change points, first in the ocean state and then in atmosphere.

The results concerning the climate jump (1975 / 1976) in EOF 1 - SSTA which we obtained for the northern tropical Atlantic, are in a good agreement with the ones found by Xu (1993), for mode 5 of the Principal Oscillation Pattern (POP), considering the tropical zone of the Planetary Ocean.

For the months in which the results didn't show an active state of the ocean which would influence the atmospheric blocking one can suppose that the atmosphere has the active role, as Deque (1989) has shown.

Analysis by canonical correlation remains to be done for the two components of the ocean - atmosphere system with different lags in which the atmosphere leads the ocean, in order to seek for the active role of the atmosphere.

The modelling of the ocean - atmosphere interaction, using a Markov chain model , has shown preferable states of interaction considered in this study. In this way the great confidence level was obtained in the case of transition $1 \longrightarrow 3$, that is the change of the zonal circulation associated with cold water in the blocking circulation associated also with cold water.

Limiting matrix is found after 23 steps, which means that until 23 months, the initial state influences the behaviour of the process. The great transition probability of the limiting matrix elements is the one referring to the third state, namely transition to the blocking type circulation associated with cold water.

References

Bojariu, R., 1994: "Change Points in Variability of SST and Surface Wind for Central Atlantic". CAS/JCS WGNE Res. Act. Atmos. Oc. Modelling Rep. 19pp.248-249.

DaCamara, C.C., E.C. Kung, W.E. Baker, B.C., Lee and J.A.M. Corte - Real, 1992, "Long - Term Analysis of Planetary Wave Activities and Blocking Circulation in the Northern Hemisphere Winter "Beitr.Phys. Atmosph. Volume 64,No.4,pp.295 - 298.

Deque, M.,J.Servain , 1989, "Teleconnections between Tropical Atlantic Sea Surface Temperatures and Midlatitude 50 kPa Heights during 1964 - 1986",Journal of Climate, Volume 2,No.9,pp.929-944.

Kemeny, J. and L.Snell, 1960, "Finite Markov Chains", (Princeton New Jersey),Wan Nostrand Co.Inc., pp 1-50.

Latif, M. and N. Graham, 1991, "How much Predictive Skill is contained in the Thermal Structure of an OGCM", (Max - Planck - Institut fur Meteorologie , Hamburg, Germany),Report No. 63.

Mares , Ileana and C. Mares, 1994, "Statistical Methods for estimating the Signal - to - Noise Ratio", Contemporary Climatology, edited by R. Brazdil and M. Kolar, (Brno, Czech Republic), pp. 373 - 379.

Naylor, Th., H., J. L. Balintfy, D. S. Burdick, Chu Kong, 1966, "Computer Simulation Techniques", John Wiley and Sons, Inc. New York, London, Sydney, pp 1-200.

Sneyers, R., 1992, "Use and misuse of Statistical Methods for the Detection of Climate Change", Proc. Amer. Meteor. Soc., 12th Conference on Probability and Statistics in the Atmos. Sci. and 5th Inter. Meet. on Statis.Clim. (Toronto, Canada), pp-j 76-81.

Vautard , R., Kingtse C. Mo, M. Ghil, 1990, "Statistical Significance Test for Transition Matrices of Atmospheric Markov-Chains", J. Atmos. Sci., Volume 47, No. 15,pp 1926-1931.

Woodruff, S. D., R. J. Slutz, R. L. Jenne and P. M. Steurer, 1987, "A Comprehensive Ocean-Atmosphere Data Set",Bull. Amer. Meteor. Soc., Volume 68,pp. 1239-1250.

Xu, J., 1993, " The Joint Modes of the Coupled Atmosphere - Ocean Observed from 1967 to 1986", Journal of Climate, Volume 6, No. 5, pp. 816 - 838.

ACKNOWLEDGEMENTS

This research was supported by the European Community (Contract No. 1, CIPDCT 925046). The authors are grateful to dr. H. Cattle from Hadley Centre, coordinator of this project.

CORRESPONDING AUTHOR

Ileana Mares
National Institute of Meteorology and Hydrology
Sos. Bucuresti - Ploiesti, no. 97, sector 1
Bucharest, ROMANIA

CLOUD COVER AND TYPE OVER THE FORMER USSR, 1936–83; TRENDS DERIVED FROM THE RIHMI-WDC 223-STATION 6- AND 3-HOURLY METEOROLOGICAL DATABASE

Dale P. Kaiser
Carbon Dioxide Information Analysis Center, Environmental Sciences Division,
Oak Ridge National Laboratory, Oak Ridge, Tennessee, USA

Vyacheslav N. Razuvaev
Research Institute of Hydrometeorological Information – World Data Centre, Obninsk, Russia

ABSTRACT
This paper presents trends analyses of sky cover data from the former U.S.S.R. for the period 1936–83. Observations of total cloud amount, low cloud amount, and low-, middle, and high-cloud type from 223 stations were obtained from a database of 6- and 3-hourly meteorological observations compiled at the Research Institute of Hydrometeorological Information – World Data Centre in Obninsk, Russia. Station data were averaged over various-sized grid boxes and linear trends in seasonal mean total cloud amount, low cloud amount, frequency of occurrence of cirrus clouds, cirrus amount, and frequency of clear sky were computed for the period 1936–83.

1 INTRODUCTION

In recent years a great deal of meteorological and climatological data have been exchanged between the two principal climate data centers of the United States and the former Soviet Union: the National Climatic Data Center (NCDC), in Asheville, North Carolina, and the Research Institute of Hydrometeorological Information – World Data Centre (RIHMI-WDC; hereafter referred to as RIHMI) in Obninsk, Russia. This was accomplished via Working Group VIII (*Influence of Environmental Changes on Climate*) of the bilateral initiative known as the *Agreement on Protection of the Environment*, established on May 23, 1972 by the United States and the USSR.

One of the key datasets compiled by RIHMI includes 6- and 3-hourly meteorological observations from 223 USSR stations for the period 1936–83. Six-hourly observations were made from 1936–65; 3-hourly observations were made from 1966 onward. RIHMI has chosen to use daily and hourly data from these stations as the basis for considerable climate research efforts. These data (hereafter referred to as the RIHMI database) have been made available by the Department of Energy's Carbon Dioxide Information Analysis Center (CDIAC) in Oak Ridge, Tennessee (Razuvaev et al. 1995). The data have undergone quality assurance checks at RIHMI, NCDC, and CDIAC. The data contain observations of some 22 meteorological variables, including near-surface air temperature, sea level pressure, precipitation amount, weather type, total cloud cover, and cloud type.

In a previous study, Kaiser et al. (1995) compared seasonal and annual mean total cloud cover from the RIHMI database to data presented in the atlas: *Global Distribution of Total Cloud Cover and Cloud Type Amounts Over Land* (Warren et al. 1986; hereafter referred to as W86) for the common data period 1971–81. RIHMI means were found to be an average of 2-4% higher over much of the country, with the largest differences found over central Siberia in winter. The reasons for these generally systematic differences are still unclear; the analysis methods of Kaiser et al. (1995) intentionally paralleled those described in W86. It is anticipated that these differences will be explored further, but in this paper we will use the RIHMI database to examine trends in sky cover variables over the USSR for the database's entire period of record (1936–83).

2 DATA

The RIHMI database includes 6- and 3-hourly observations from 223 stations across the USSR. Records are of good quality and for the most part serially complete. Cloud information used here include: total cloud amount (N); low-cloud amount (NL); low, middle, and high cloud type; and present weather (ww). N and NL are given in tenths of sky cover, i.e., as an integer ranging from 0 (no clouds or <1/10 sky cover) to 10 (overcast or >9/10 sky cover with or without openings), whereas in raw World Meteorological Organization (WMO) synoptic code reports cloud amount is expressed in octas (eighths of sky cover), where N=0 indicates clear sky and N=8 indicates complete overcast. A sky nine-tenths covered with clouds or an overcast sky with openings are both reported as N=7 (equivalent to 0.875 sky cover) in the WMO code. (This influences our treatment of the RIHMI cloud amounts, as detailed in the next section.) Descriptions of cloud type and ww in the RIHMI observations essentially conform to those prescribed by the WMO.

3 METHOD OF ANALYSIS

Analysis of RIHMI cloud data paralleled the methods used in W86. Only a brief description will be given here; a complete description may be gained by referring to W86. The USSR was divided into latitude/longitude boxes ranging in size from 5 × 5° from 35°N to 50°N; 5 × 10° from 50°N to 70°N; to 5 × 20° poleward of 70°N. (The dimensions of each box are increased poleward of 50°N to maintain approximately equal area in each box.) The northernmost RIHMI station is at ~73°N, so the analysis area was extended only to 75°N. The locations of the RIHMI stations and the grid boxes chosen for analysis are shown in Fig. 1. Several grid boxes within the USSR contain no RIHMI stations, whereas several boxes along its borders extend into other countries. Land grid boxes on the border were only analyzed if at least half the box's area lay in the USSR. This resulted in 219 RIHMI stations over 84 grid boxes being used in the analysis. Using records which passed certain cloud- and ww-related internal consistency checks, grid box means of cloud parameters were computed for the four standard meteorological seasons over the period 1936–83. This included mean N and NL, and means of several derived parameters: frequency of occurrence of cirrus clouds (fci), amount of cirrus clouds when present (awp), total cirrus amount (aci), and frequency of occurrence of completely clear sky (fclr). These and many other cloud parameters were examined in W86. Space constraints here necessitate our selecting only a handful of basic variables. Their descriptions are given in the following.

Means of N and NL (percent sky cover) were computed using all valid observations from a given season. Daytime and nighttime observations were given equal weight in the averaging (as in W86), although observers' estimates of nighttime cloud cover are known to often be too low (cf. Schneider et al. 1989). As mentioned previously, in the RIHMI database an overcast sky with or without gaps is denoted by N=10. (The presence of gaps is indicated by a flag code.) Numerically, this is the equivalent of 100% sky cover in either case. In the synoptic observations used in W86, nine-tenths sky cover or an overcast sky with gaps is coded as N=7 (equivalent to 87.5% sky cover). Kaiser et al. (1995), so as to ensure valid comparisons between the RIHMI and W86 data, assigned RIHMI entries of N=9 or N=10 with gaps a value of 87.5% sky cover. This practice was continued in the present analysis.

Cirrus clouds are known to exhibit significant radiative effects on the surface and lower troposphere (Liou 1992). W86 found that over the period 1971–81, cirrus clouds were the most frequently observed cloud type over most of the USSR. For these reasons we chose to examine cirrus cloudiness here. The determination of seasonal fci is made by simply dividing the number of times cirrus was reported as present by the number of *non-missing* observations of high cloud type. Non-missing in this instance means that an observer could report *something* about the presence of cirrus; be it that cirrus was/wasn't present or was unable to be assessed due to a lower overcast. The awp was determined in two ways: (1) When cirrus was present with no lower-level clouds awp was obtained directly from N, and (2) When cirrus was present with lower-level clouds, awp was estimated using the random-overlap equation (W86):

$$1 - N = (1 - awp)(1 - NL), \qquad (1)$$

where all variables are expressed as fractional amounts ranging from 0.0 to 1.0. Equation (1) states that the clear fraction of the sky is the product of the clear fractions of the layers; it is valid only for instantaneous cloud amounts. However, as noted in W86, there are three situations in which awp cannot be computed using (1): (a) when clouds are reported at all three levels (as the equation has two unknowns and cannot be solved); (b) when NL=0.9 (since awp is constrained to being equal only to 0.0 or 1.0); and (c) when NL=1.0 the presence or absence of cirrus clouds cannot be determined. Seasonal means of aci were estimated as the product of seasonal mean fci and awp. Seasonal fclr was obtained by simply dividing the number of N=0 observations by the number of non-missing observations of N.

4 RESULTS

Due to space constraints, we have chosen to focus our discussion of results on the cloud variables and seasons which show the greatest changes over 1936–83, however, all variables and seasons exhibit important findings which will be dealt with more thoroughly in the presentation of this work at 6IMSC. Simple linear regression was performed on the seasonal grid box means of the six variables described in the preceding section. Testing for significance of linear trends in the data using the 5% confidence level revealed significant regional trends in the data over all seasons. The magnitudes of regional changes were generally found to be greatest in winter for all variables. Winter linear trend values for N, NL, fci, aci and fclr are mapped in Figs. 2a–e. (The map of awp trends is not shown, as trends were generally not significant.) Grid boxes with trends significant at the 5% level include the magnitude of the trend; those which are not significant simply give the sign of the linear trend. The region showing the most dramatic changes stretches from central to eastern Siberia, where large wintertime *increases* in N (percent sky cover), fci (percent of observations), and aci (percent sky cover) are observed. Large *decreases* are observed in NL (percent sky cover) and fclr (percent of observations) over this same general region. Analyses of these same variables for spring, summer, and fall (not shown) revealed similar patterns of significant change over this part of the country, with magnitudes being generally smaller. Another contiguous, but smaller region of the country showing significant wintertime changes lies in the vicinity of the Black and Caspian Seas. Here the sign of changes in N and fclr are opposite those in the Siberian region and evidence of increasing cirrus cloudiness is much weaker.

To depict actual seasonal values of variables and their changes over time in the Siberian region, grid box means of all variables over the region encompassed by 90° and 160° E, and 50° to 70° N were averaged over the period 1937–83 and plotted as time series in Fig. 3. (Winter means for 1936 were not calculated due to the lack of December, 1935 data.) The units of N, NL, awp, and aci are percent sky cover; those of fci and fclr are percent of observations. The time series show evidence of marked change in all variables but awp. Large increases in fci and aci are evident, and these series exhibit a positive correlation with each other (r=0.95) as would be expected, but correlate much more weakly with N (r=0.31 and r=0.43, respectively), which shows a weaker, but significant increase. The smaller increase in aci relative to fci is explained by awp being relatively unchanged over the period (recall aci is estimated from the product of fci and awp). N shows a strong negative correlation with fclr (r=-0.95).

It seems reasonable that the large decrease in NL over the period would contribute to increases in fci and therefore aci due to the opportunity to detect cirrus more often. There may be other causes however. Evidence for increasing cirrus cloudiness has been presented elsewhere in the literature, e.g., Machta and Carpenter (1971) reported increases in cirrus amount in the absence of lower level clouds at a number of U.S. stations between 1948 and 1970. Other studies have correlated observed increases in cirrus cloud amount and observed decreases in the number of clear days with the advent and increasing frequency of high-altitude jet traffic (Changnon 1981). The work of Changnon (1981), however, looked at sky conditions over the heart of the United States, where condensation trails from jets would presumably be much more common than over Siberia.

5 SUMMARY AND CONCLUSIONS

Seasonal, grid box means of several basic sky cover variables were computed from USSR 6- and 3-hourly meteorological observations over the period 1936–83. The most significant findings show evidence of substantial changes in cloud amount over a large part of the USSR stretching from central to eastern Siberia. There is strong evidence for (1) wintertime increases in total cloud amount and cirrus cloud amount, and (2) wintertime decreases in low cloud amount and frequency of clear sky. While no conclusions may be drawn at this point regarding the causes of these cloudiness changes over the Siberian region, these data seem to show evidence of real changes and much more research is warranted. If indeed cloudiness has changed over the Siberian region as shown by this analysis, we would expect to find strong feedbacks in surface and atmospheric temperatures.

References

Changnon, S. A., Jr., 1981, "Midwestern Cloud, Sunshine and Temperature Trends since 1901: Possible Evidence of Jet Contrail Effects", *Journal of Applied Meteorology* 20, pp. 496–508.

Kaiser, D. P., R. S. Vose, T. R. Karl, and V. N. Razuvaev, 1995, "The Distribution of Cloud Cover Over the Former USSR

as Derived from the RIHMI 223-Station 3-Hourly Meteorological Database", Proceedings of the Ninth Conference on Applied Climatology, (Dallas, Texas, USA), pp. 81–86.

Liou, K. N., 1992, "Radiation and Cloud Processes in the Atmosphere", Oxford University Press, 487 pp.

Machta, L., and T. Carpenter, 1971, "Trends in High Cloudiness at Denver and Salt Lake City" In *Man's Impact on the Climate*, MIT Press, pp. 410–415.

Razuvaev, V. N., E. G. Apasova, and R. A. Martuganov, 1995, Six- and Three-hourly Meteorological Observations from 223 U.S.S.R Stations, ORNL/CDIAC-66, NDP-048, Carbon Dioxide Information Analysis Center, Oak Ridge National Laboratory, Oak Ridge, Tennessee.

Schneider, G., P. Paluzzi, and J. P. Oliver, 1989, "Systematic error in the synoptic sky cover record of the South Pole", J. Climate, 2, 295–302.

Warren, S. G., C. J. Hahn, J. London, R. M. Chervin, and R. Jenne, 1986, "Global Distribution of Total Cloud Cover and Cloud Type Amounts Over Land", DOE/ER/60085-H1, NCAR Tech. Note TN-273 + STR, 231 pp.

ACKNOWLEDGMENTS

CDIAC is sponsored by the Global Change Research Program of the Environmental Sciences Division, Office of Health and Environmental Research, U.S. Department of Energy. Oak Ridge National Laboratory is managed by Martin Marietta Energy Systems, Inc. for the U.S. Department of Energy under contract DE-AC05-84OR21400.

CORRESPONDING AUTHOR

Dale P. Kaiser,
Carbon Dioxide Information Analysis Center,
Oak Ridge National Laboratory,
P.O. Box 2008, MS-6335,
Oak Ridge, TN 37831-6335, USA.

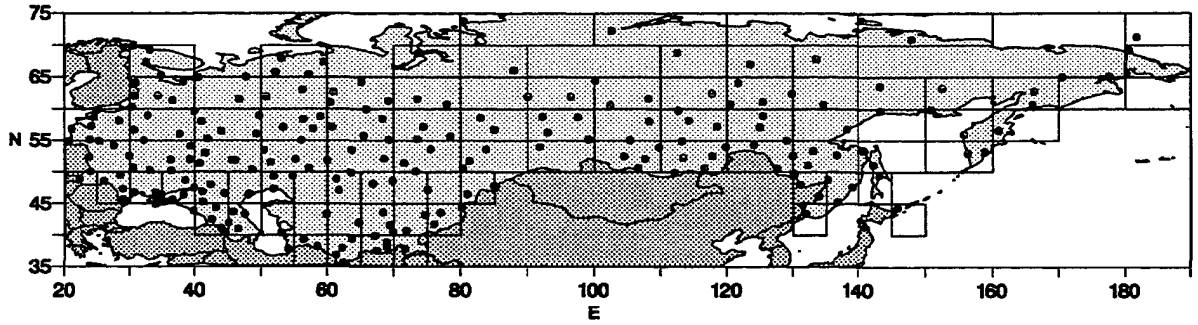
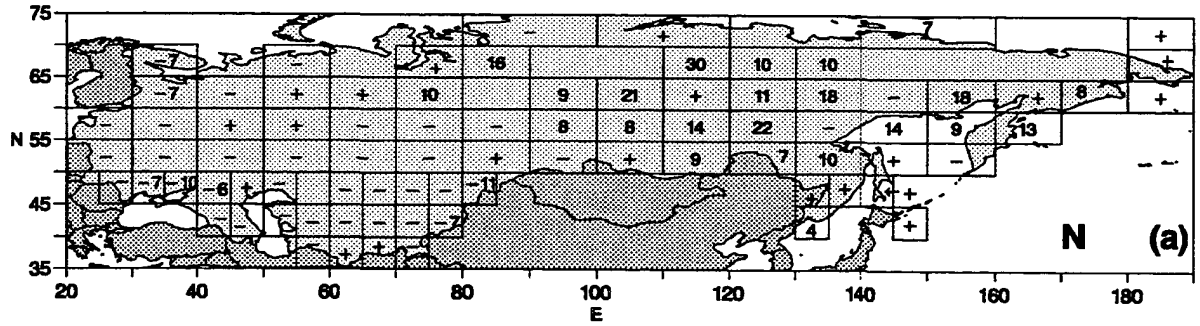
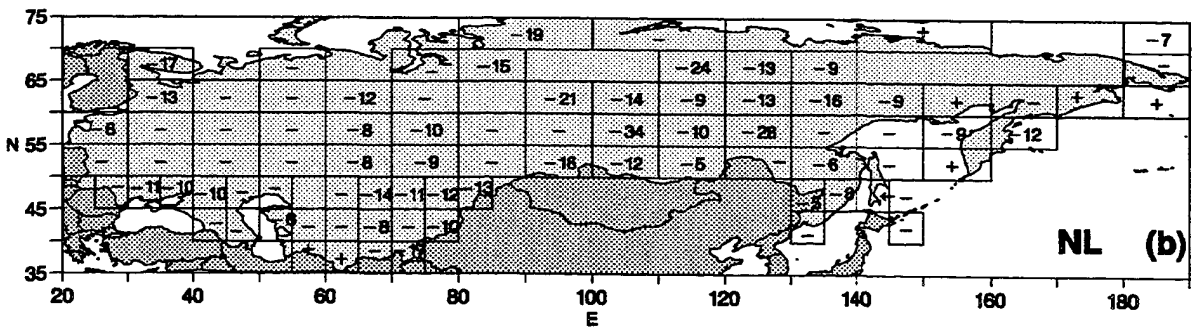


Figure 1. Locations of the 219 RIHMI stations and 84 grid boxes chosen for analysis.





Figures 2a–e. (Above and next page) USSR winter means of (a) total cloud amount (N); (b) low cloud amount (NL); (c) frequency of occurrence of cirrus (fci); (d) total cirrus amount (aci); and (e) frequency of occurrence of clear sky (fclr) for the period 1937–83.

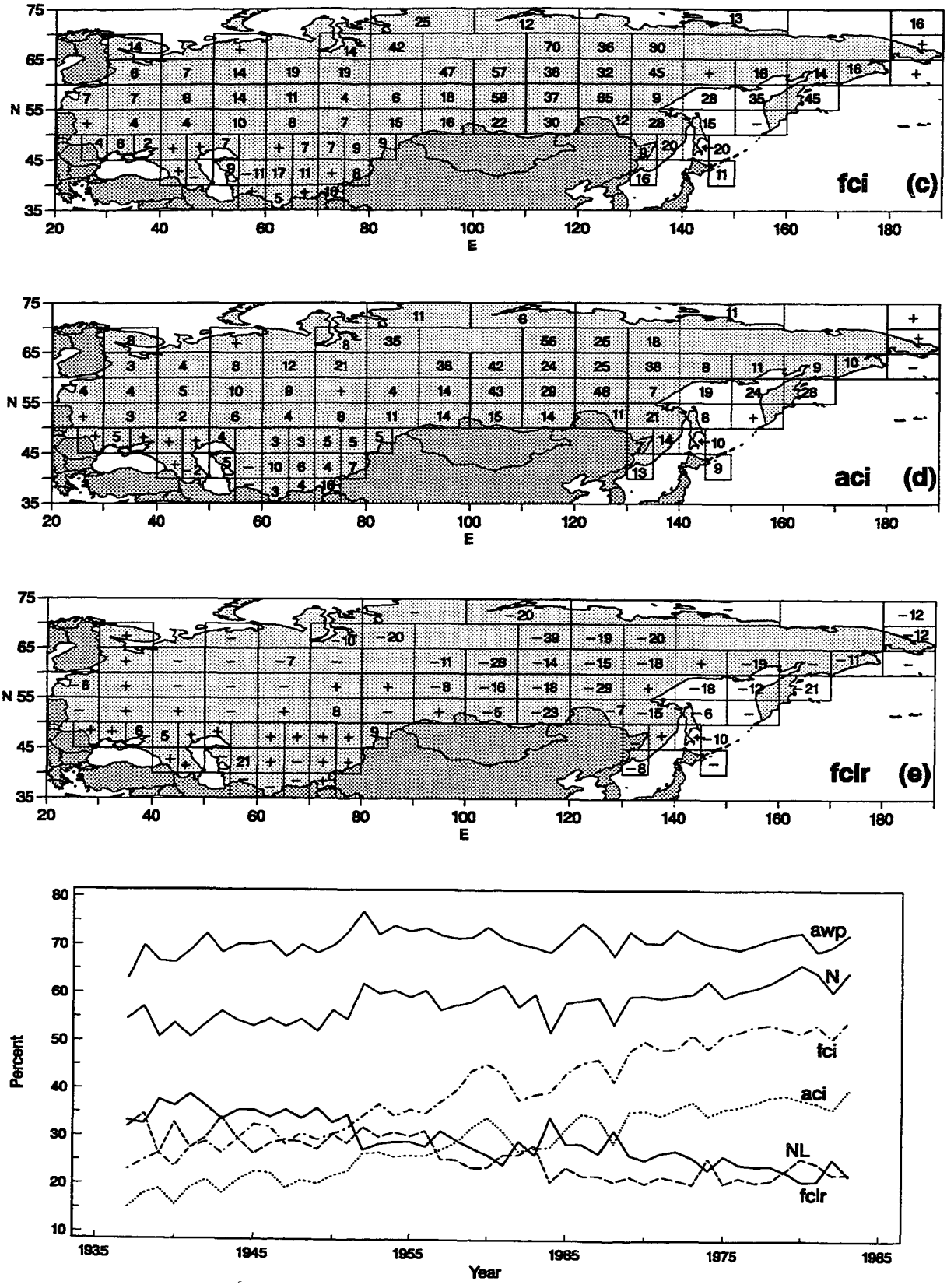


Figure 3. Winter means of total cloud amount (N); low cloud amount (NL); frequency of occurrence of cirrus (fci); amount of cirrus when present (awp); total cirrus amount (aci); and frequency of occurrence of clear sky (fclr) for the region encompassed by 90° and 160° E, and 50° to 70° N, over the period 1937–83.

SPACE-TIME COVARIANCE MODELLING

Wendy Meiring, Peter Guttorp and Paul D. Sampson

University of Washington, Seattle, USA

Abstract

We present an approach for modelling spatial covariance structure that varies periodically in time. This is an extension of Sampson and Guttorp's spatial covariance modelling approach, which does not assume spatial stationarity or isotropy. Possible temporal periodicities include seasonal or diurnal changes. There are many potential applications in climatological research.

We discuss an application to hourly surface ozone monitoring data, and model a diurnal periodicity in spatial covariance structure. We use data from a region of California during July and August 1990.

1 INTRODUCTION

Geophysical scientists, including meteorologists and atmospheric chemists, develop complex geophysical models. These models must be evaluated by comparing model output with data. The data and the model output may be on different spatial and temporal scales. The motivation for the spatial covariance estimation work discussed in this paper is the continued development of techniques for comparing air quality model gridded ozone output, with ozone records from a number of point monitoring sites. Our aim is not to model ozone per se.

It may be valuable to use information from all point monitoring sites in a region to estimate the average for a specific grid cell. This is particularly important when there is reasonably strong spatial correlation on the spatial scales being considered, or when there are several sites located close together in a grid cell. Section 6 describes an approach for estimating the average for a grid cell. This approach requires a model for the spatial association between records at different sites. Modelling this spatial association is the subject of this paper.

Hourly surface ozone data exhibit strong diurnal structure in mean, and in temporal and spatial correlation. This is due to the diurnal photochemical reaction cycle, which is influenced by emissions and meteorology. A National Research Council report (1991) describes ozone chemistry, measurements, modelling and model evaluation in more detail than can be presented here. We illustrate an approach for modelling spatial covariance structure which varies in time.

Outline of Paper

The paper proceeds as follows. In section 2 we briefly introduce the ozone data and some data analysis issues. Section 3 gives some spatial covariance estimation definitions. The Sampson-Guttorp spatial covariance estimation approach is described in section 4. It is used to estimate the spatial covariance structure for different hours of the day in section 5. Section 6 is a discussion section which describes an approach for estimating block (grid cell) averages.

2 DATA

We use hourly surface ozone data collected as part of the SARMAP project, an air quality modelling project for the San Joaquin Valley of California.

Aircraft and surface records of many pollutant and meteorological variables were collected during the SARMAP field study. Surface measurements were made at 326 monitoring stations in the San Joaquin Valley and environs for 62 days during the summer of 1990 (July 1 - August 31). Of these, 131 sites measured ozone. In this paper we consider surface ozone records from 32 of these sites. The locations of these sites are indicated in Figure 1.

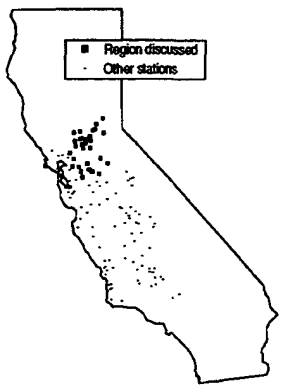


Figure 1: Map indicating location of SARMAP ozone monitoring sites in California.

More details about the SARMAP project goals, field study (monitoring) and modelling are given in Solomon (1993).

Data Analysis Issues

Figure 2 shows time series plots of ozone data after a square root transformation for four sites in the region of interest. These plots show that there are missing data and different degrees of discretization at different sites. They also show a diurnal structure in the ozone records. We consider ozone

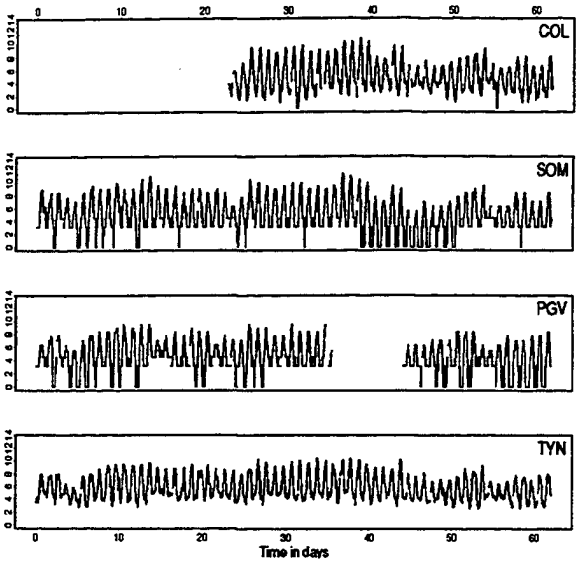


Figure 2: Time series of $\sqrt{\text{ozone}}$ in ppb$^{\frac{1}{2}}$ for four sites.

on the square root scale to deal with problems of skewness and inhomogeneity of variance. The estimated diurnal mean structure (the mean for each hour of the day) is subtracted. We estimate the covariance structure of the residuals after subtracting the hourly means.

The cross-correlogram between two time series may be mis-interpreted if one doesn't adjust for the temporal correlation in some way (see eg. Diggle, 1990). One might use a space-time model incorporating both spatial and temporal correlation, or one might prewhiten the series from each site before estimating the spatial correlation. Prewhitening is an attempt to explain some of the temporal correlation and obtain residuals that are almost uncorrelated in time. Sampson et al. (1994) take the former approach, while Guttorp et al. (1994) use the prewhitening approach. In this paper we use AR(2) models to prewhiten the residuals after subtracting the diurnal hourly mean structure.

Model

For time t, corresponding to hour j of the day, $j \in \{0, \ldots, 23\}$, the model we fit here is

$$Z_{it} = \sqrt{Y_{it}} - H_{ij(t)} \quad (1)$$

$$Z_{it} = \alpha_{i1} Z_{i,(t-1)} + \alpha_{i2} Z_{i,(t-2)} + e_{it} \quad (2)$$

where

$$\begin{aligned} Y_{it} &= \text{the ozone at site } i \text{ at time } t \\ H_{ij(t)} &= \text{mean for hour } j \text{ of } \sqrt{Y_{it}} \\ \alpha_{i1}, \alpha_{i2} &\text{ are AR(2) parameters} \\ e_t &= \left[\, e_{1t} \quad \ldots \quad e_{Nt} \,\right]^{\mathrm{T}} \sim \mathrm{N}(0, \Sigma_j) \end{aligned}$$

for the spatial covariance structure Σ_j for hour j.

3 SPATIAL COVARIANCE ESTIMATION

We address the spatial covariance structure Σ_j in terms of the spatial dispersion between sites x and y, defined as the variance of the spatial increments of the process,

$$D(x,y) = \mathrm{var}[\, Z(x,t) - Z(y,t) \,].$$

This function of site location is known as the variogram in the geostatistical literature, and as the structure function in the atmospheric science literature.

$$D(x,y) \to 2\sigma_\epsilon^2, \qquad \text{as } x \to y \quad (3)$$

where σ_ϵ^2 is known as the nugget effect, and is a measure of the small scale variability and measurement error.

Sample estimates can be obtained for each pair of monitoring sites. A model for the spatial dispersions as a function of geographic locations in space provides an estimator of the spatial dispersion between any two points in space. Simplifying assumptions may be made in developing such a model. These include spatial stationarity where $D(x,y)$ is assumed only to depend on the difference between coordinates $x - y$. A special case of spatial stationarity is isotropy, where $D(x,y)$ is assumed to be a function only of the Euclidean distance between sites x and y. See Cressie (1991) for more details about valid variogram models and assumptions.

In air quality applications, topographic and meteorological influences, as well as chemical emissions vary in space, so spatial stationarity may not be a reasonable assumption.

4 SAMPSON-GUTTORP APPROACH

The Sampson Guttorp approach transforms the geographic plane (G-plane) into a dispersion plane (D-plane) so that spatial dispersions depend only on Euclidean distances between sites in the D-plane. We model isotropic structure in the D-plane representation, corresponding to nonstationarity in the G-plane. The spatial covariance is assumed to be a smooth function of the geographic coordinates. The location x for each geographic site is mapped onto a location x^* in the D-plane. This mapping is computed as two thin-plate spline mappings.

The transformation is obtained by moving the positions of the monitoring sites relative to each other to minimize a penalized weighted least squares criterion between the sample dispersions and the fitted dispersions. The fitted dispersion between sites x_i and x_j, f_{ij}, is calculated by fitting a valid isotropic variogram model γ as a function of distances in the D-plane.

$$f_{ij} = \gamma\left(\left|x_i^* - x_j^*\right|\right). \quad (4)$$

The fitted dispersions change as the sites are moved in the D-plane. The criterion is

$$\sum_{j=2}^{N} \sum_{i=1}^{j-1} \left[\frac{(d_{ij} - f_{ij})}{f_{ij}}\right]^2 + \lambda \,\mathrm{BEP}, \quad (5)$$

where d_{ij} is the sample estimate of the dispersion and BEP is a *bending energy penalty* for the deformation (transformation) of the G-plane to the D-plane. λ is a smoothness parameter.

In general terms, sites with relatively strong correlation are moved closer together, while sites with weaker correlation are moved further apart. Two sites are fixed at their geographic coordinates in order to fix the scale, rotation and location of the D-plane configuration.

See Guttorp and Sampson (1994) for more details about the estimation approach.

5 ESTIMATES FOR DIFFERENT HOURS

After removing hourly means and pre-whitening, we use the Sampson-Guttorp approach to estimate the spatial covariance structure for each hour j, based on sample dispersion estimates from the prewhitened residuals in a three hour window, hours $(j-1)$, j and $(j+1)$. We use the exponential variogram model for γ in equation 4. Results presented here are for the spatial correlation structure (ie. the time series have been scaled to variance one).

Figure 3 shows a pair of plots for each of hours 8, 10, 12, 14, 16 and 18. The first plot indicates how a rectangular grid in the geographic plane is deformed to give the D-plane coordinates. (Lines are closer together where sites have been moved closer together.) In the second plot, sample dispersion estimates between pairs of monitoring sites are plotted against the D-plane distance between the sites. There is one dot for each pair of sites. The fitted variogram γ is shown as a line passing through the sample dispersions.

These figures indicate differences in the correlation structure for different hours of the day. There is stronger correlation structure in the afternoon hours than there is at hour 8. (Lower dispersion corresponds to higher correlation.) The changes in spatial dispersion structure may be explained by the diurnal structure in emissions and photochemical activity, since ozone is produced in photochemical reactions. In the map for hour 10 one can see stronger correlation in the NW-SE direction. This hour has a transformation map which is closest to that of a linear mapping from the G-plane to the D-plane.

A simplified overview of a possible diurnal ozone cycle is as follows. At night there is depletion of the surface ozone due to surface deposition. In the morning there is mixing of atmospheric layers, and an increase in ozone due to transport from other layers and photochemical action. During the afternoon there is photochemical action on the ozone precursors to produce ozone. Local patterns in emissions and ozone transport may lead to stronger spatial correlation in the afternoon than at other hours. Factors such as altitude, transport and meteorology may cause different cycles at some sites.

6 DISCUSSION

We use a procedure analogous to that described by Cressie (1991, sect. 3.2.2) to estimate block averages. Point kriging calculations are performed for each of M regularly spaced points in a grid cell, using the estimated covariance structure of the prewhitened residuals. This gives an estimated prewhitened residual at each of the M points.

The prewhitening coefficients and the diurnal mean structure are also interpolated to these unmonitored sites. The estimated prewhitened residuals, prewhitening coefficients and diurnal means are used to calculate point estimates of ozone levels on the transformed scale at each of the regularly spaced sites in the block. Block average ozone estimates at a particular time point are based on these point estimates with a correction for the bias of the simple back-transform to the original scale of ozone measurements (ppb). This methodology is described in Sampson et al. (1994). These point kriging calculations assume a known covariance function, and therefore variance estimates may underestimate the true variability of the estimation procedure. A bootstrap procedure on the covariances may be used to assess better the variability of the estimates.

The block average estimates may be compared with gridded photochemical air quality model output as part of operational model evaluation.

There are many climatological applications and extensions of the work discussed here. For example, spatial covariance of a meteorological field might be modelled for different climatic regimes. One extension of this work involves modelling spatial covariances from satellite records which have irregularly recorded observations in space and time due to the satellite path.

References

[1] Cressie, N.A.C. (1991). *Statistics for spatial data.* Wiley-Interscience.

[2] Diggle, P.J. (1990). *Time Series. A Biostatistical Introduction.* Oxford Science Publications.

[3] Guttorp, P., W. Meiring, and P.D. Sampson (1994). A Space-time Analysis of Ground-Level Ozone Data. *Environmetrics* **5:** 241-254.

[4] Guttorp, P., and P.D. Sampson (1994). Methods for Estimating Heterogeneous Spatial Covariance Functions with Environmental Applications. *in* Patil, G.P. and Rao, C.R. (eds), *Handbook of Statistics XII: Environmental Statistics,* Elsevier/North Holland, New York, pp. 663-690.

[5] National Research Council (1991). *Rethinking the Ozone Problem in Urban and Regional Air Pollution.* National Academy Press, Washington, D.C.

[6] Sampson, P.D., P. Guttorp, and W. Meiring (1994). Spatio-Temporal Analysis of Regional Ozone Data for Operational Evaluation of an Air Quality Model. *ASA Proceedings.*

[7] Solomon, P.A. (1993). *Planning and Managing Regional Air Quality. Modeling and Measurement Studies.* Lewis Publishers/Pacific Gas and Electric Company, Chelsea, MI.

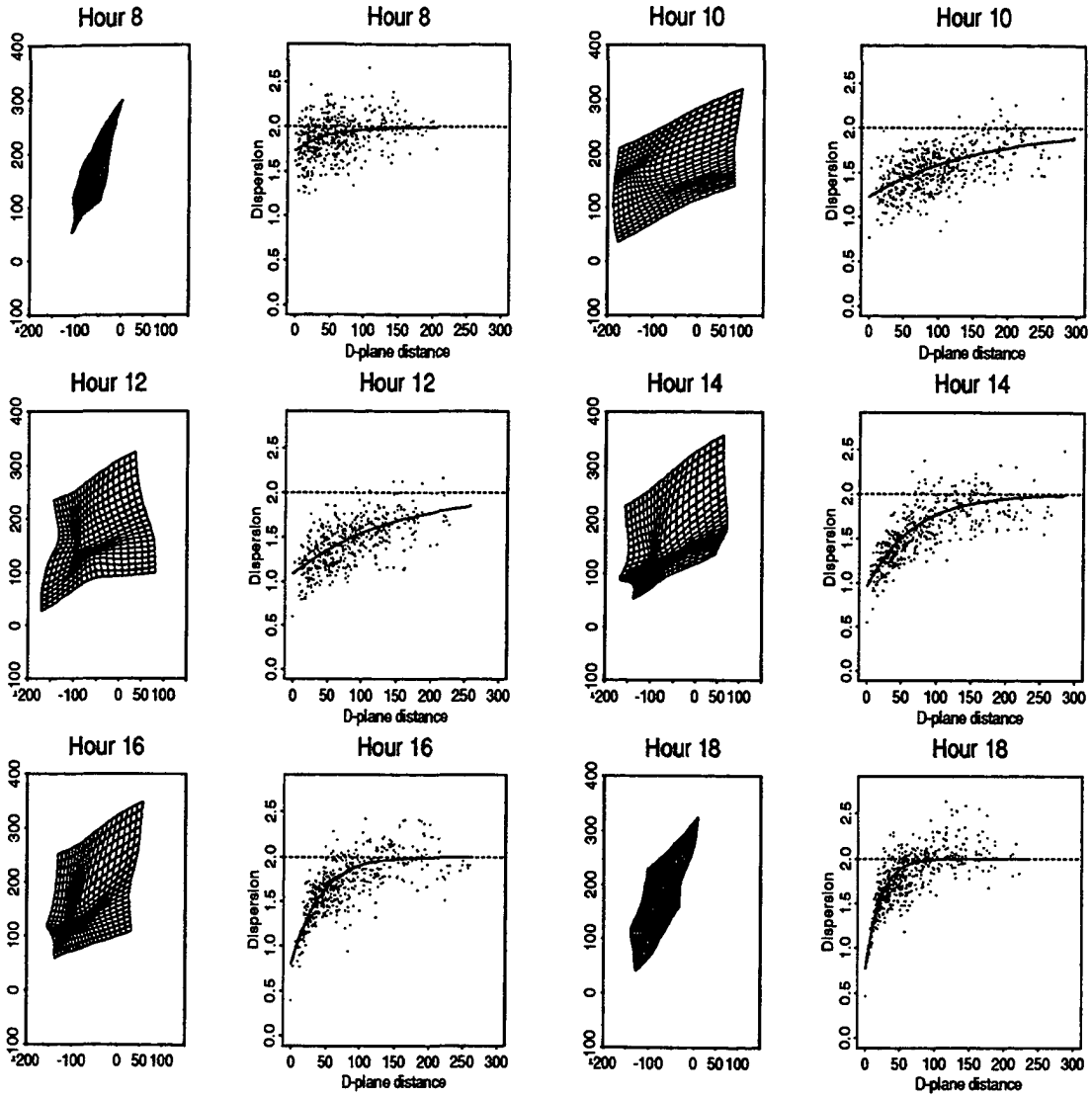


Figure 3: Transformation maps and fitted variograms for several hours.

7 ACKNOWLEDGEMENTS

This research was sponsored by a contract with the Electric Power Research Institute, Palo Alto, CA. The authors thank Alan Hansen of EPRI for his continued support. They also thank Paul Solomon of PG&E and Rich Hackney of the California Air Resources Board for their assistance in providing the SARMAP database.

8 CORRESPONDING AUTHOR

Wendy Meiring
University of Washington
STATISTICS
Box 354322
Seattle, WA 98195-4322

LINEAR MODELS FOR SPATIAL OR TEMPORAL MULTIVARIATE DATA

H. Wackernagel and M. Grzebyk

Ecole des Mines de Paris, Fontainebleau, France

ABSTRACT

In geostatistics, methods for characterizing the spatial or temporal variation at different scales of a multivariate system have attracted much attention during the last decade. Applications have been particularly numerous in soil science. Most work was based on the linear model of coregionalization (LMC) which is suitable for the description of a system using direct and cross variograms, because cross variograms are even. Recently, work done on complex kriging (for estimating vector variables in 2D geographical space) has inspired the bilinear model of coregionalization (BMC) which is more general in the sense that it allows the description of a system for which the cross-covariance functions are not even.

1 INTRODUCTION

Cross-covariance functions are useful in describing the cross-correlations in a set of variables which can be:

- different types of measurements located in space or time,
- measurements of one quantity in a spatial region at different times,
- measurements of one quantity along time at different sites of a spatial region.

The cross-covariance functions are not necessarily even as there can be various kinds of delay or shift effects at different charateristic space or time scales between the variables. At each charateristic scale of index u we shall however assume that the space or time correlation is governed by one correlation function $\rho_u(\mathbf{h})$.

The real linear model of coregionalization has the limitation that it can only serve to model a set of covariance functions in which the cross-covariance functions are even. It is necessary to introduce a complex linear model of coregionalization and to take its real part, the bilinear model of coregionalization, when the cross-covariance functions in a real covariance function matrix are not even.

In geostatistics, the estimation of two dimensional vector variables as complex variables was studied by Lajaunie and Béjaoui (1991), who examined ways of modeling the complex covariance function. This work inspired Grzebyk (1993) in formulating the bilinear model of coregionalization.

2 COVARIANCE FUNCTION MATRIX

We denote $C_{ij}(\mathbf{h})$ the cross-covariance function between two jointly second-order stationary random functions $Z_i(\mathbf{x})$ and $Z_j(\mathbf{x})$, where $\mathbf{x}$ is the vector of the coordinates of a point in space or time, $\mathbf{h}$ is a vector linking a pair of points in space or time, Z is a real or complex random variable, i and j are indices of a set of N random functions.

The matrix $\mathbf{C}_{ij}(\mathbf{h})$ of direct and cross covariance functions for a given set of random functions is charaterized by Cramér's generalization of the Bochner-Khintchine theorem (Cramér, 1940).

3 INTRINSIC CORRELATION MODEL

The simplest model for real random functions is the following

$$\mathbf{C}(\mathbf{h}) = \mathbf{V}\,\rho(\mathbf{h}) \tag{1}$$

where $\mathbf{V}$ is the matrix of variances and covariances σ_{ij} and $\rho(\mathbf{h})$ is a direct correlation function.

It is called the *intrinsic correlation* model (Matheron, 1965) because the correlation between two random functions

$$\frac{\sigma_{ij}\,\rho(\mathbf{h})}{\sqrt{\sigma_{ii}\,\rho(\mathbf{h})\,\sigma_{jj}\,\rho(\mathbf{h})}} = \frac{\sigma_{ij}}{\sqrt{\sigma_{ii}\,\sigma_{jj}}} = r_{ij} \tag{2}$$

does not depend upon spatial scale.

The linear model associated to the intrinsic correlation model is written

$$Z_i(\mathbf{x}) = \sum_{p=1}^{N} a_{pi}\,Y_p(\mathbf{x}) \tag{3}$$

where $Y_p(\mathbf{x})$ are N uncorrelated random functions whose direct covariance functions $\rho(\mathbf{h})$ do not depend on the index p and a_{pi} are transformation coefficients.

From a known intrinsic correlation model, one possible method to specify the transformation coefficients is based on the eigenvalue decomposition of the variance-covariance matrix $\mathbf{V}$ and the factors Y_p can then be interpreted as principal components.

The intrinsic correlation model is an important reference case when the variables are all measured at the same locations, because their estimation is simplified (Wackernagel, 1994).

4 NESTED MODEL

A more sophisticated model for a set of real random functions is the multivariate nested covariance function model

$$\mathbf{C}(\mathbf{h}) = \sum_{u=0}^{S} \mathbf{B}_u \, \rho_u(\mathbf{h}) \tag{4}$$

where u is an index for a set of $S+1$ characteristic spatial or temporal scales and the *coregionalization matrices* $\mathbf{B}_u$ are variance-covariance matrices describing multivariate correlation at these charateristic scales of the phenonenon.

The associated random function model is the *linear model of coregionalization* (LMC)

$$Z_i(\mathbf{x}) = \sum_{u=0}^{S} \sum_{p=1}^{N} a_{piu} \, Y_{pu}(\mathbf{x}) \tag{5}$$

where a set of N uncorrelated factors is defined at each of the $S+1$ charateristic scales. A possibility to specify the LMC from a known multivariate nested covariance function model is by performing a principal component analysis based on the eigenvalue decomposition of the coregionalization matrices which yields the transformation coefficients $Y_{pu}(\mathbf{x})$.

5 COMPLEX COVARIANCE FUNCTION

A model for univariate complex covariance function $C(\mathbf{h}) = C^{\mathrm{Re}}(\mathbf{h}) + \mathrm{i}\, C^{\mathrm{Im}}(\mathbf{h})$ with a known real part $C^{\mathrm{Re}}(\mathbf{h})$ can be defined on the basis of an application of the Radon-Nikodym theorem by the relation

$$\mathrm{i}\, C^{\mathrm{Im}}(\mathbf{h}) = \left(\Phi * C^{\mathrm{Re}}\right)(\mathbf{h}) \tag{6}$$

where Φ is a complex distribution whose Fourier transform is a real odd function φ with values in the interval $[-1, 1]$. The class of $C^{\mathrm{Im}}(\mathbf{h})$ corresponding to a given real continuous covariance function $C^{\mathrm{Re}}(\mathbf{h})$, such that $C(\mathbf{h}) = C^{\mathrm{Re}}(\mathbf{h}) + \left(\Phi * C^{\mathrm{Re}}\right)(\mathbf{h})$ is a complex covariance function, are called *compatible* imaginary parts.

A simple class of compatible imaginary parts can be obtained using $\Phi = \mathrm{i}/2\,(\nu - \check{\nu})$ and the compatible imaginary parts are given by $C^{\mathrm{Im}}(\mathbf{h}) = \frac{1}{2} \int \left[C^{\mathrm{Re}}(\mathbf{h} - \boldsymbol{\tau}) - C^{\mathrm{Re}}(\mathbf{h} + \boldsymbol{\tau})\right] \nu(d\boldsymbol{\tau})$ with $\left| \int \sin(\mathbf{u}^{\mathrm{T}} \boldsymbol{\tau}) \, \nu(d\boldsymbol{\tau}) \right| < 1$.

The class can be extended (Grzebyk, 1993) by considering real covariance functions $C^{\mathrm{c}}(\mathbf{h})$ compatible with a given $C^{\mathrm{Re}}(\mathbf{h})$ in the sense that the positive measures $\mu^{\mathrm{c}} \leq \mu^{\mathrm{Re}}$ and then

$$C^{\mathrm{Im}}(\mathbf{h}) = \frac{1}{2} \int \left[C^{\mathrm{c}}(\mathbf{h} - \boldsymbol{\tau}) - C^{\mathrm{c}}(\mathbf{h} + \boldsymbol{\tau})\right] \nu(d\boldsymbol{\tau}) \tag{7}$$

is a compatible imaginary part, provided that $\left| \int \sin(\mathbf{u}^{\mathrm{T}} \boldsymbol{\tau}) \, \nu(d\boldsymbol{\tau}) \right| < 1$.

In practice a finite sum based on translations $\boldsymbol{\tau}_k$ is used

$$C^{\mathrm{Im}}(\mathbf{h}) = \frac{1}{2} \sum_{k=1}^{K} p_k \left(C^{\mathrm{c}}(\mathbf{h} - \boldsymbol{\tau}_k) - C^{\mathrm{c}}(\mathbf{h} + \boldsymbol{\tau}_k)\right) \tag{8}$$

with weights $p_k \geq 0$ and $\sum p_k \leq 1$. Instead of only one function $C^{\mathrm{c}}(\mathbf{h})$, K functions $C^{\mathrm{c}}_k(\mathbf{h})$ can be introduced which represent a family of covariance functions compatible with a given $C^{\mathrm{Re}}(\mathbf{h})$.

6 BILINEAR MODEL

The complex analogue to the intrinsic correlation model is

$$\mathbf{C}(\mathbf{h}) = \mathbf{B}\,\rho(\mathbf{h}) = \mathbf{E}\,\chi(\mathbf{h}) - \mathbf{F}\,\kappa(\mathbf{h}) + \mathrm{i}\left(\mathbf{E}\,\kappa(\mathbf{h}) + \mathbf{F}\,\chi(\mathbf{h})\right) \tag{9}$$

where $\rho(\mathbf{h}) = \chi(\mathbf{h}) + \mathrm{i}\,\kappa(\mathbf{h})$ is a scalar complex covariance function and $\mathbf{B}$ is a hermitian positive semi-definite matrix with $\mathbf{B} = \mathbf{E} + \mathrm{i}\,\mathbf{F}$. The matrix $\mathbf{E}$ is a symmetric positive semi-definite matrix while $\mathbf{F}$ is antisymmetric.

Naturally we can consider a nested complex multivariate covariance function model of the type $\mathbf{C}(\mathbf{h}) = \sum_u \mathbf{B}_u \, \rho_u(\mathbf{h})$ with a corresponding complex LMC.

The real LMC is in particular not adequate for multivariate time series analysis where delay effects or phase shifts are common and cannot be included in a model with even cross covariances. A model for real random functions with

non even real cross covariance functions can be derived from the complex LMC by taking its real part. We obtain the *bilinear model of coregionalization* (BMC) which is composed of the linear combination of two sets of factors $U_{pu}(\mathbf{x})$ and $V_{pu}(\mathbf{x})$ with two sets of transformation coefficients c_{piu} and d_{piu}.

In the case of only one spatial scale (the nested case is analog) we can drop the index u and we have the BMC

$$Z_i(\mathbf{x}) = \sum_{p=1}^{N} c_{pi}\, U_p(\mathbf{x}) - \sum_{p=1}^{N} d_{pi}\, V_p(\mathbf{x}) \quad (10)$$

with

$$\sum_{p=1}^{N} (c_{pi}\, c_{pi} + d_{pi}\, d_{pi}) = e_{ij} \quad (11)$$

$$\sum_{p=1}^{N} (c_{pi}\, d_{pi} - c_{pi}\, d_{pi}) = f_{ij} \quad (12)$$

where e_{ij} and f_{ij} are respectively the elements of matrices $\mathbf{E}$ and $\mathbf{F}$ such that $\mathbf{B} = \mathbf{E} + \mathrm{i}\,\mathbf{F}$.

Restraining the covariance functions for $U(\mathbf{x})$ and $V(\mathbf{x})$ to be of the form

$$C_{UU}(\mathbf{h}) = C_{VV}(\mathbf{h}) = \frac{1}{2}\chi(\mathbf{h}) \quad (13)$$

$$C_{UV}(-\mathbf{h}) = -C_{UV}(\mathbf{h}) = \frac{1}{2}\kappa(\mathbf{h}) \quad (14)$$

where $\chi(\mathbf{h}) + \mathrm{i}\,\kappa(\mathbf{h})$ is a complex covariance function with an odd imaginary part, the cross-covariance function between two real variables is

$$C_{ij}(\mathbf{h}) = \sum_{p=1}^{N} (c_p^i\, c_p^j + d_p^i\, d_p^j)\, \frac{\chi(\mathbf{h})}{2} - \sum_{p=1}^{N} (c_p^j\, d_p^i - c_p^i\, d_p^j)\, \frac{\kappa(\mathbf{h})}{2} \quad (15)$$

The multivariate covariance function model associated to the BMC is thus

$$\mathbf{C}(\mathbf{h}) = \frac{1}{2}\left(\mathbf{E}\,\chi(\mathbf{h}) - \mathbf{F}\,\kappa(\mathbf{h})\right) \quad (16)$$

and is real. See Grzebyk (1993) for details on fitting algorithms.

7 APPLICATIONS

Grzebyk (1993) provides an example of the fit of a covariance model with non even cross covariance functions using a BMC to the coregionalization of data from three remote sensing channels of a Landsat satellite.

The BMC certainly has many applications in meteorology. It can for example serve in modeling wind and geopotential (like in Chauvet et al. (1976) or Thiébaux et al. (1990)) because the extension of the BMC to the case of a set of variables including their first order derivatives is straightforward (Grzebyk and Wackernagel, 1994).

REFERENCES

Chauvet, P., Pailleux, J. and Chilès, J.P., 1976, "Analyse objective des champs météorologiques par cokrigeage", La Météorologie, 6. Série, No 4, pp. 37–54.

Cramér, H., 1940, "On the theory of stationary random processes", Annals of Mathematics, 41, pp. 215–230.

Grzebyk, M., 1993, "Ajustement d'une Corégionalisation Stationnaire", Doctoral thesis, Centre de Géostatistique, Ecole des Mines de Paris, Fontainebleau, 154p.

Grzebyk, M. and Wackernagel, H., 1994, "Multivariate analysis and spatial/temporal scales: real and complex models", Proceedings of XVIIth International Biometrics Conference, Hamilton, Ontario, Canada, Volume 1, pp. 19–33.

Lajaunie, C. and Béjaoui, R., 1991, "Sur le krigeage des fonctions complexes", Report N-23/91/G, Centre de Géostatistique, Ecole des Mines de Paris, Fontainebleau, 24p.

Matheron, G., 1965, "Les Variables Régionalisées et leur Estimation". Masson, Paris, 305p.

Thiébaux, H.J., Morone, L.L. and Wobus, R.L., 1990, "Global forecast error correlation. Part 1: isobaric wind and geopotential", Monthly Weather Review, 118, pp. 2117–2137.

Wackernagel, H., 1994, "Cokriging versus kriging in regionalized multivariate data analysis", Geoderma, 62, pp. 83–92.

CORRESPONDING AUTHOR

Dr. Hans Wackernagel,
Centre de Géostatistique,
Ecole des Mines de Paris,
35 rue Saint Honoré,
77305 Fontainebleau, FRANCE.

SPATIAL-TEMPORAL RAINFALL PROCESSES: STOCHASTIC MODELS AND DATA ANALYSIS

Richard Chandler Valerie Isham
Anastasia Kakou Paul Northrop

University College London

ABSTRACT

A brief overview is given of some current work of the authors, in building stochastic spatial-temporal models of precipitation, and of the statistical data analyses that are being used to guide informed choices of model structure.

1 INTRODUCTION

Stochastic spatial-temporal models of precipitation have a vital role to play in addressing problems in hydrology. In particular, we want to provide models that can be simulated to generate synthetic rainfall data. These data are used, for example, in the design of water storage or flood drainage systems, where the data form the input to hydrological models such as those for soil run-off. In cases of this sort, the spatial scale of interest will be the catchment (either urban, of size perhaps 10^2 km^2, or a river basin of maybe 10^4 km^2) while the temporal scale could be daily/monthly (in the case of water resources) or less than an hour (for storm water sewerage design).

Our aim is to represent only the main physical features of the rainfall process, and to allow for the detailed complexities of the actual process using stochastic elements. The models that will be described are constructed in continuous time, and have a limited number of parameters that are interpretable in terms of rain cells clustered within moving storm events. These models are not developed for predictive purposes, except perhaps locally in space and time, for the storms are assumed to occur at random.

We note that synthetic data are needed because real data are only available to a limited extent (for example, in short runs; as daily data only; at isolated gauges). We shall be interested in models for the temporal precipitation process at a single site and the multivariate temporal process at a (small) set of sites, as well as for the full spatial-temporal process.

Our models may also provide a means to tackle the problem of disaggregating precipitation totals, for a large spatial region over successive time-periods (such as those that are predicted by a General Circulation Model for a grid square of order 10^4 km^2), into a spatial-temporal pattern of rainfall over that region with realistic local properties. Existing methods of disaggregation (Eagleson 1978, Warrilow, Sangster & Slingo 1986, Onof & Wheater 1994) model only the marginal properties of rainfall at a particular site and do not incorporate any temporal or spatial memory. The disaggregated precipitation is then used to estimate expected soil run-off by integrating the run-off contribution from each site over the grid square (and appropriate time interval). However, in order to determine the variability of the soil run-off, more detailed joint distributional properties of the spatial-temporal rainfall process are needed.

2 DATA

The work described in this paper is being carried out under the umbrella of the HYREX (= Hydrological Radar Experiment) special initiative currently being funded by the Natural Environment Research Council (NERC). In addition to providing support for individual researchers, HYREX is responsible for collecting high quality data. A dense network of 52 (0.2 mm tipping bucket) raingauges has been installed in a catchment, roughly 120 km^2 in area, in SW England, resulting in the availability of data recording the rainfall intensity aggregated in disjoint time intervals; *e.g.*, 15 minutes, 1 hour, ..., 24 hours. A radar installation sited close to this network is monitoring the region continuously; data are collected for 5×5 km^2 pixels up to a distance of 210 km from the installation, and for 2×2 km^2 pixels up to a distance of 75 km, every 5 minutes. Data from other radar beams covering this region are also available. The calibration of radar data against raingauge data is an important issue, but not one that will be discussed here.

Precipitation is normally classified as either *convective*, which is generally short-lived and very intense rain (as in a summer thunderstorm), or *non-convective*, which is associated with the large-scale uplift of warm air above colder air, and is more-prolonged but less intense rainfall. In either case, the rain *cells* (the smallest precipitation elements visible on radar, of order 10–50 km^2) occur in clusters that we shall call *storms*, and these may themselves be clustered within *precipitation fields*.

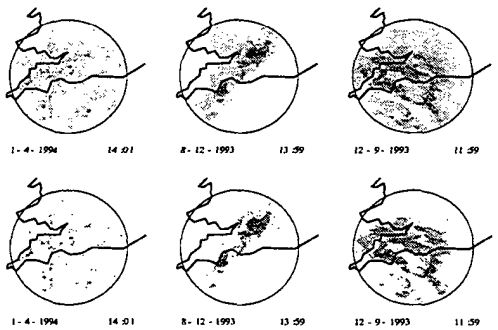


Figure 1: Different patterns of UK rainfall. Left to right: (i) showers (ii) rainband (iii) large rain mass. The bottom sequence shows the same events with all rainfall intensities under 1mm/hr removed. The HYREX raingauge network appears as a small black blob near the centre of each image.

3 MODEL DEVELOPMENT

Precipitation models fall into several categories. There are the dynamic meteorological models (Mason 1986) that use complex nonlinear deterministic models and seek accurately to represent the details of the physical process. At the other extreme are the empirical statistical models (see *e.g.*, Stern & Coe (1984) for a model based on a marked second-order Markov chain; Lovejoy & Schertzer (1987), Gupta & Waymire (1990) and Foufoula-Georgiou & Kumar (1994) for multiscaling processes and fractal cascades; Goodall & Mardia (1994) for a smoothing method based on kriging and Kalman filtering).

As mentioned in the Introduction, we shall concentrate on intermediate stochastic models, in which modest number of parameters are used to represent the rainfall process. These parameters relate to underlying physical phenomena like rain cells

and storms. The models are constructed in continuous time and are then aggregated over disjoint time periods as necessary, for fitting to empirical data. For simplicity, in this paper, we shall include only one level of clustering, of cells within storms, and assume stationarity. Thus, in fitting the models, typically we treat each month separately. Assuming explicit periodic functional forms for the seasonal variation of the model parameters has not been found to be especially helpful in reducing the number of parameters to be fitted (Onof 1992) and will not be considered here. Our models are most appropriate for fine-resolution data and are useful for data reduction (*e.g.*, for comparing the rainfall processes at distinct sites or in different seasons) and for gaining scientific understanding, as well as for the purposes already mentioned.

SINGLE SITE MODELS

The spatial-temporal models that we consider are generalisations of point process-based models with rectangular cells that have been used to represent rainfall at a single site. In these models, cells arrive at the site at times determined by a clustered point process. Each cell has a rectangular profile, with a random intensity (or *depth*) that is fixed for the random duration of the cell. Some simple models of this sort were investigated in Rodriguez-Iturbe, Cox & Isham (1987) and Rodriguez-Iturbe, Cox & Isham (1988). There, cell origins occur in a Poisson cluster process (either Neyman-Scott or Bartlett-Lewis, see *e.g.*, Cox & Isham (1980)) in time, and the durations of the cells are assumed to be exponentially distributed. The form of the distribution of the cell depth is not critical for most properties and can usually be left arbitrary. Note that both individual cells and storms (*i.e.* clusters of cells) can overlap (this is plausible as these phenomena may occur at different levels in the atmosphere, while only their projections affect the raingauge). The rainfall intensity $Y(t)$ at time t is the sum of the depths of all cells active at time t. The data recorded at a single raingauge are successive observations of $Y_i^{(h)} = \int_{T_i} Y(t)\,dt$ over disjoint time intervals T_i of width h.

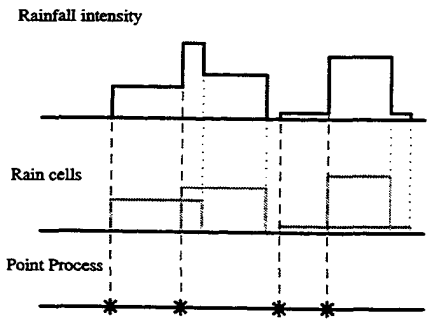


Figure 2: Schematic diagram of point process model for rainfall at a single site.

The simplest case of this model has five parameters: three for the point process (specifying the cluster rate, mean number of cells per cluster, and spacing of cells within each cluster) and two for the cells (one each for the distributions of depth and duration). Many properties of such models can be derived explicitly; for example, the probability that it is dry at time t and the distribution of the length of a dry period, the distribution and moments of $Y(t)$, the autocovariance of the process $\mathrm{cov}(Y(t), Y(t+\tau))$ at lag τ, and the corresponding properties for the aggregated data $Y_i^{(h)}$. Other properties of interest have to be determined by simulation (given particular parameter values); for example, the distributions of extremes, the joint and conditional distributions of $Y_{i+1}^{(h)}$ given $Y_i^{(h)} = 0$. Note that because the precipitation process is *not* Gaussian, it is not adequately summarised by the second-order properties that are available explicitly.

Various generalisations of this basic model have been made: Rodriguez-Iturbe et al. (1988) allow the parameter η of the exponential distribution of cell duration, L, to be random between storms but fixed for all cells within a cluster. This allows additional variation in cell durations and dependence between cells within storms. Cowpertwait (1994) investigates a multi-type cell model that distinguishes convective and non-convective cells within a storm. We have recently considered models incorporating (negatively correlated) dependence between the cell depth and duration, as an alternative way to allow for different cell types. In particular, we have retained the exponential distribution for L and assumed that the conditional distribution of depth, X, given L, has either a χ^2 or exponential distribution with a mean of the form $\mathrm{E}(X|L) = fL^\nu \exp(-cL)$ where ν takes the value 0 or 1 and f may be fixed at $f = 1$. Note that the properties typically used in fitting these models require only expressions for $\mathrm{E}(XL)$ and $\mathrm{E}(X^2L)$, so that the explicit distributional forms are unimportant once these moments are fixed. Our analysis has shown that, of these alternatives, the model using the exponential conditional distribution with mean $\mathrm{E}(X|L) = L\exp(-cL)$ does best in reproducing the observed properties of the rainfall process.

SPATIAL-TEMPORAL MODELS

An immediate extension of the single-site models is to consider multivariate analogues in which the precipitation processes are modelled simultaneously at a small set of sites. The challenge is to find suitable ways of incorporating inter-site dependence, where this must depend on the spatial separations of the sites, whilst retaining the structure of the single-site models for the marginal processes. Some possible models, and their theoretical properties, are discussed in Cox & Isham (1994) and this work is now being extended to include a larger set of models, to compare their qualitative properties with those of the HYREX data, and to fit some of the models to these data.

For many purposes, however, models in continuous space, as well as time, are essential. As in the multi-site case, in developing fully spatial-temporal models, we seek to preserve the structure of the single-site models in their marginal properties. Spatial-temporal modelling of rainfall based on point-process models originated in the fundamental work of Le Cam (1961) and was developed in the 1980s in a number of papers (see *e.g.*, Waymire, Gupta & Rodriguez-Iturbe (1984)). The basic elements comprising such models are *rainfall fields* occurring in a temporal Poisson process; *rain bands* (storms) occurring within each field in a spatial Poisson process, the rate of which may depend on location (reflecting orography) and time (seasonality); *cells* occurring in each storm, clustering in space and time, usually with either a Neyman-Scott or Bartlett-Lewis structure. Typically the cells, storms and fields move with velocities that may be in common.

The cell depths are often assumed to be random constants at the cell centres, and decaying in a quadratic exponential form in space and a linear exponential form in time. This type of assumption is fine when only a single storm is modelled, but poses problems for the full model of the process because each storm has infinite extent in both space and time, and there can be no dry periods or regions without imposing an arbitrary cut-off value to define this. An alternative cell structure that we have assumed (Cox & Isham 1988) is that the single-site rectangular cell is replaced by a cylinder, each cell consisting of a random depth that is constant over a circular region with random radius, for the duration of a random lifetime.

The models that we describe here have a single level of clustering (of cells within storms). Whether there is any need for a further layer (fields) of clustering depends on the resolution of the data and the application being considered. With 5 km radar data, a cell of perhaps 100 km^2 occupies only 4 pixels,

and even with 2 km resolution is only a small block of 25 pixels. Thus, whereas with raingauge data we have fitted cells within storms, with radar data it may be more appropriate to think of these as storms within fields. The apparent self-similar structure of rainfall processes (Waymire 1985) makes this approach plausible and consistent.

The model explored by Cox & Isham (1988) consists of storms that occur as a Poisson process in *space and time*, and cells that form a Bartlett-Lewis cluster in time, but are located at the same spatial point as the storm origin. All cells move with the same velocity relative to the storm origin. Thus the cells within a storm tend to string out in a band in the direction of motion. This now seems implausible, for although bands of cells are clearly visible on many radar pictures, analysis of the HYREX and other data shows that the cells will often move in a direction that is orthogonal to the band.

In current work, extensions of this model are being investigated. One important feature is that the storm origin is given the same velocity as the individual cells. This is plausible and increases the mathematical tractability of the models. In addition, the cell origins are spatially displaced from the storm origin to form a Neyman-Scott cluster in space. Various possibilities have been considered including Gaussian displacements, where the covariance matrix of the bivariate normal distribution reflects the storm shape (and as an extra layer of generality may be taken itself as a random matrix with, for example, an inverse Wishart distribution). Another possibility is that the cell origins are uniformly displaced over an elliptical *storm region* which has random scale, eccentricity, and orientation. Varying the distributions of these variables determining the shape of the ellipse, has the effect of generating very different storm shapes.

Both of these types of displacement give rise to plausible-looking simulations of storm evolution. The elliptical structure leads more easily to useful theoretical properties. A variant of the model is to assume that the cells within a storm are elliptical rather than circular, and are all scaled versions of the storm ellipse. The geometrical properties of intersections of similar ellipses makes this variant especially tractable.

With all such models, we obtain explicit expressions for the marginal properties of the process at a single site and the joint properties between pairs of sites; for example, the cross-covariance between sites i and j, $\mathrm{cov}(Y_i(t), Y_j(t+\tau))$, and joint probabilities, of the form $\mathrm{P}(Y_i(t) = Y_j(t+\tau) = 0)$, that it is dry at both sites. We can also look at the empirical properties of simulated data; for example, we can compare the simulated and real rainfall data in terms of their agreement with the Taylor hypothesis (Zawadski 1973).

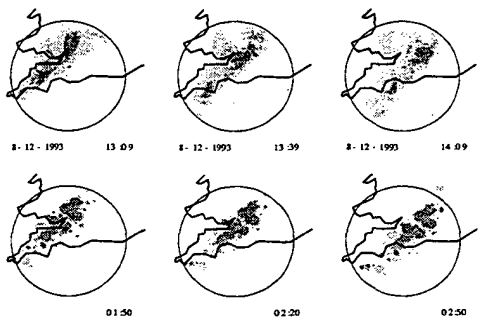


Figure 3: Simulation of a spatial-temporal rainfall model. Temporal separation of images is 30 mins. Top sequence: actual data. Bottom sequence: simulation.

4 MODEL FITTING

Fitting spatial-temporal models poses many challenges. In the case of our models, there are problems because of the very complicated dependence structure of the observed variables. At a single site, the data are temporally aggregated, which adds an additional level of dependence to the data and complication to the theoretical properties. Similarly, radar data are spatially (but not temporally) aggregated. However, because of the scaling properties of rainfall processes mentioned above, it may be appropriate to treat raw radar data as *non*-spatially aggregated and fit our models, interpreting the basic elements as storms clustered within rainbands. In this case there is no need to determine theoretical properties of spatially-aggregated data for model-fitting purposes.

In the case of raingauge data, the temporal aggregation (over periods of at least an hour, for most data sets) means that individual storms cannot be separately identified. In contrast, the sequence of much more frequent radar 'snapshots' (every 5 minutes) enables the storms to be identified and fitted one at a time.

FITTING METHODS

We have investigated two approaches to model fitting: the *method of moments* approach in which unknown parameters are estimated by the minimisation of a weighted sum of squared differences between (suitably chosen) explicit properties and their corresponding sample values, and a *spectral approach* (Chandler 1995) that uses maximum likelihood fitting based on the Fourier coefficients of the data, under the approximation that these coefficients have a multivariate normal distribution. A third approach to fitting, that we have not yet explored, is based on Markov chain Monte Carlo simulations, (Smith & Robinson (1994) fit a model with a rather similar structure to daily data).

The adequacy of fit of a model can be assessed by comparison of the fitted properties (both explicit and simulated) of particular interest, with their corresponding sample properties. Inevitably, the choice of properties used for this will be application-led. In some cases these properties may be indirect, resulting from the input into other hydrological processes of data simulated from the fitted model. For example, in a particular case (Rodriguez-Iturbe et al. 1988), this method of assessing the fit of a single-site model, accentuated the importance of the observation that the proportion of wet periods was being slightly underestimated. Such underestimation has a crucial effect on the soil run-off properties.

A general problem of fitting models of this sort, is the lack of identifiability of their parameters. For example, there is typically a trade-off between a small number of clusters containing many cells and a large number of small clusters. The result is that distinct, and well-separated, local optima in the parameter space may correspond to comparable values of the objective function and give similar sets of fitted values.

Of the two methods that we have considered, the spectral method has a number of advantages *a priori*. The method of moments involves an arbitrariness of the choice of properties to be used in the fitting whereas the spectral method makes more objective use of the data. The moments method requires the model to have a strong Markov behaviour (in particular, the assumption of exponentially distributed cell lifetimes is important) in order that algebraic derivations of properties are feasible; also, the temporal aggregation of the empirical data complicates these derivations. By contrast, the spectral method requires weaker assumptions (for example, non-exponential cell lifetimes are not a problem) and it copes well with data filtering (aggregation). In addition, because this method uses the entire data set rather than some summary statistics, it generally needs shorter runs of data.

COMPARISONS

We have compared the use of the two methods of fitting our models in the single-site and multi-site cases, and are currently working on results for the fully spatial-temporal model. We

note that there seems to be little to choose between the Bartlett-Lewis and Neyman-Scott based models as far as their fits to data are concerned. If we use only first and second-order properties in the method of moments fitting, our experience so far is that the two methods give broadly similar results, though the spectral method gives parameter estimates that vary more smoothly from one month to the next. Presumably the explanation for this is that the latter method is using second order properties at long lags as well as short ones, whereas the former properties were not used with the moments method. It is also encouraging to note that the parameter estimates and their seasonal variation are meteorologically sensible: for example, in summer there are fewer storms with fewer, deeper, shorter-lived cells that are more widely dispersed about the storm origin . However we already know that, in the single-site case, we can obtain a much better fit with the moments method by incorporating the proportion of hourly intervals that are dry, into the model fitting. It seems likely that some analogue of this would be advantageous in the spectral fitting case also, and an obvious possibility that we shall investigate is to combine appropriately the spectrum for the rainfall intensity with that for the dry intervals in the observed rainfall process.

5 CONCLUDING REMARKS

Unfortunately, space constraints have ruled out the inclusion of the technical details and results of our work, and of more than the barest minimum of references necessary to set this work properly in the context of the literature. Both model-building and data analyses are ongoing, and much remains to be done. The class of models is both broad and flexible and provides a viable means of simulating 'artificial' data. It is encouraging that the models are being used to address real hydrological problems. Recent examples of its use are illustrated by Glasbey, Cooper & McGechan (1995) with regard to rainfall disaggregation and Faulkner, Onof & Wheater (1995) in the context of extreme rainfall in flood design.

ACKNOWLEDGEMENTS

We acknowledge with thanks the support of the NERC (RC, VI) through a research grant under the auspices of the HYREX project, of the Greek State Scholarships Foundation (AK) and of the EPSRC (PN) for research studentships. We are most grateful to our colleagues on this project, Sir David Cox, Christian Onof and Howard Wheater for their continuing collaboration.

CORRESPONDING AUTHOR

Professor Valerie Isham
Department of Statistical Science
University College London
London WC1E 6BT, UK.

REFERENCES

Chandler, R. E. (1995), A spectral method for estimating parameters in rainfall models, Technical report, no. 142, University College London, London WC1E 6BT.

Cowpertwait, P. (1994), 'A generalised point process model for rainfall', *Proc. R. Soc. Lond.* **447**, 23–37.

Cox, D. & Isham, V. (1980), *Point Processes*, Chapman and Hall, London.

Cox, D. & Isham, V. (1988), 'A simple spatial-temporal model of rainfall', *Proc. R. Soc. Lond.* **A415**, 317–328.

Cox, D. & Isham, V. (1994), Stochastic models of precipitation., *in* V. Barnett & K. Turkman, eds, 'Statistics for the Environment 2: Water related issues', Wiley, Chichester, pp. 3–18.

Eagleson, P. (1978), 'Climate, soil and vegetation, 2. the distribution of annual precipitation derived from storm sequences', *Water Resources Research* **14**, 713–721.

Faulkner, D., Onof, C. & Wheater, H. (1995), 'Simulating storms for flood design with a Poisson cluster rainfall model', *Ann. Geophys.* **13, Suppl.II**, C532.

Foufoula-Georgiou, E. & Kumar, P. (1994), 'Multi-scale analysis of rainfall fields', *Ann. Geophys.*

Glasbey, C., Cooper, G. & McGechan, M. (1995), 'Disaggregation of daily rainfall by conditional simulation from a point process model', *J. Hydrol.* **165**, 1–9.

Goodall, C. & Mardia, K. (1994), Challenges in multivariate spatio-temporal modeling, *in* 'Proceedings of the 17th International Biometric Conference, volume 1'.

Gupta, V. & Waymire, E. (1990), 'Multiscaling properties of spatial rainfall and river flow distributions', *J. Geophys. Res.* **95 (D3)**, 1999–2010.

Le Cam, L. (1961), A stochastic description of precipitation, *in* J. Neyman, ed., 'Proceedings of the Fourth Berkeley Symposium on Mathematical Statistics and Probability, 3', Berkeley, California, pp. 165–186.

Lovejoy, S. & Schertzer, D. (1987), 'Physical modelling and analysis of rain and clouds by anisotropic scaling multiplicative processes', *J. Geophys. Res.* **92 (D8)**, 9693–9714.

Mason, J. (1986), 'Numerical weather prediction.', *Proc. R. Soc. Lond.* **A407**, 51–60.

Onof, C. (1992), 'Stochastic modelling of British rainfall data using Poisson processes', PhD thesis, University of London.

Onof, C. & Wheater, H. (1994), Analysis of the spatial coverage of British rainfall fields, Technical report, Department of Civil Engineering, Imperial College, London SW7 2BU.

Rodriguez-Iturbe, I., Cox, D. & Isham, V. (1987), 'Some models for rainfall based on stochastic point processes.', *Proc. R. Soc. Lond.* **A410**, 269–288.

Rodriguez-Iturbe, I., Cox, D. & Isham, V. (1988), 'A point process model for rainfall: further developments.', *Proc. R. Soc. Lond.* **A417**, 283–298.

Smith, R. & Robinson, P. (1994), A Bayesian approach to the modeling of spatial-temporal precipitation data, Technical report, University of North Carolina, Chapel Hill.

Stern, R. & Coe, R. (1984), 'A model fitting analysis of rainfall data (with discussion).', *J. R. Statist. Soc.* **A147**, 1–34.

Warrilow, D., Sangster, A. & Slingo, A. (1986), Modelling of land surface processes and their influence on the European climate, Technical report, no. DCTN38, UK Meteorological Office, Bracknell, Berks.

Waymire, E. (1985), 'Scaling limits and self-similarity in precipitation fields', *Water Resources Research* **21**, 1271–1281.

Waymire, E., Gupta, V. & Rodriguez-Iturbe, I. (1984), 'A spectral theory of rainfall intensity at the meso-β scale.', *Water Resources Research* **20**, 1453–1465.

Zawadski, I. (1973), 'Statistical properties of precipitation patterns', *J. Appl. Meteor.* **12**, 459–472.

On the Development and Use of Homogenized Climate Data Sets

David R. Easterling
Thomas C. Peterson
Thomas R. Karl

NOAA/NESDIS
National Climatic Data Center
151 Patton Avenue
Asheville, NC 28801 USA

ABSTRACT.
At the NCDC we have developed a number of climate data sets that have been adjusted for inhomogeneities. In this paper we review adjustment methodologies we have developed and compare the results between the two main adjustment methods.

1. INTRODUCTION.
At the National Climatic Data Center (NCDC), we have developed a number of climate data sets, in collaboration with the Carbon Dioxide Information and Analysis Center of the Oak Ridge National Laboratory, that are high quality (subjected to rigorous quality assurance procedures), and have had a series of data adjustments designed to improve the homogeneity of the data. These data sets include the United States Historical Climatology Network (USHCN: Karl, *et al.* 1990), and the Global Historical Climatology Network (GHCN: Vose, *et al.* 1992). As the developers of these data sets, we are often contacted by researchers who have questions regarding various aspects of the data. These questions range from the proper use of the data, to the data adjustments and their validity. It is the purpose of this note to review the adjustment methodologies, why adjustments are necessary, and to attempt to provide guidelines regarding the use of these data.

2. CREATION OF HOMOGENEOUS DATA SETS. Adjustment techniques for inhomogeneities have been developed to address both gradual trends and discontinuities. Furthermore, these techniques may be based on metadata (station history) or they may be purely statistically (non-metadata) based, but in each case the data are adjusted to the most recent homogeneous period of the record. In developing data sets at the NCDC, we use each approach depending on the data set. For the USHCN we use a series of techniques based on metadata (station histories) as described in Karl, *et al.* (1986), Karl and Williams (1987) and Karl, *et al.* (1988). However, for the GHCN which we do not have extensive metadata files for, we have developed a non-metadata adjustment scheme which starts by creating homogeneous reference series for each candidate station as described in Peterson and Easterling (1994). The reference series is then used in a statistically-based scheme for detecting undocumented discontinuities which is described in Easterling and Peterson (1994a).

3. DISCUSSION.
Figure 1 shows a number of time series of mean annual temperature anomalies for Spokane, WA and for its region (the east slope of the northern Cascades) as defined in Karl, *et al.* (1988). Homogeneity adjustments were performed on the data using two methodologies, the standard USHCN (metadata based) adjustments, and the non-metadata adjustment scheme outlined above. The time series for the region, computed using the unadjusted data for all USHCN stations (35) in the region is nearly identical to Spokane from the 1960s to the present (Figure 1a). However, a series of discontinuities due to instrument changes and station moves causes the Spokane time series to be much warmer prior to the 1960s, resulting in a overall linear trend that is strongly negative. On the other hand, the regional trend for the unadjusted data is slightly positive, but not statistically significant.

The time series calculated from the data adjusted using the USHCN metadata based methodology (Figure 1b) shows a distinct change in the trend characteristics both for Spokane and the region. There is now only a slight negative trend in the Spokane time series, but a statistically significant positive trend in the regional time series. The time series for Spokane adjusted using the non-metadata methodology (Figure 1c) shows a slight positive trend which is virtually identical to the

regional trend.

It is clear from Figure 1 that data adjustments do cause large changes both in the individual station and area-averaged time series. However, these differences decrease as the area size increases, particularly as the area size approaches the hemispheric scale (Easterling and Peterson 1994b). This raises a number of questions regarding the differences in the unadjusted and adjusted data. First, why is the trend in the regional time series for the USHCN adjusted data considerably more positive than the unadjusted data, or for that matter the non-metadata adjusted data and even the Spokane time series? The answer to this is mainly in the time-of-observation bias adjustments. Karl, *et al.* (1986) have shown that changing the observing time from midnight to earlier in the day causes a distinct cool bias in monthly averaged temperatures. However, in the USA this bias occurs mainly at Cooperative stations that take observations only once per day. Since the trend has been to earlier observing times due to hydrological forecasting needs, and the USHCN is composed mainly of Cooperative stations, adjustments for this bias will cause area-averaged time series to have a more positive trend.

The changes to the time series at Spokane, however, are mainly due to adjustments for station moves and instrument changes. Spokane is a USA First-order station, and has had a number of documented changes (see Table 2 in Easterling and Peterson 1994a) that caused the earlier years of the unadjusted time series to be much warmer.

If we consider the unadjusted time series in parts, the data observed during a period when no changes occurred at the observing station, or in the way the data were processed can be considered homogeneous since they are representative of the observing site, conditions and methods in place during that period. However, as soon as a change occurs the data become inhomogeneous, and are now representative of new conditions. Any adjustments to the data can only attempt to ensure that the data are "relatively homogeneous", since the property of "true homogeneity" is irretrievably lost (Conrad and Pollak 1962). It then follows that, if a station has undergone changes, as all stations have, and the data have been "homogenized" using a methodology like those described above, the time series for that station does not truly represent any one site, but is more like the composite of a number of sites.

This is particularly evident if we compare data adjusted using different methodologies. Since a discontinuity causes an unknown change in the statistical characteristics of the time series, and adjustments for random effects are generally made through comparison with reference time series, different methodologies can make different adjustments for the same discontinuity. This is shown by comparison of the two time series for Spokane adjusted using the two methodologies described above (Figure 1d). The two time series are identical from 1960 to the present. However, they begin to diverge prior to 1960 due to the differences in the adjustments made with the two methodologies. It is clear that since both of the adjusted time series are closer to the regional time series than the unadjusted time series, both are more homogeneous than the unadjusted Spokane time series. However, it is also evident that the adjustments, although very similar are not identical, resulting in slightly different trends.

The question of which adjusted time series is correct is impossible to answer satisfactorily since the only way to determine this would be by comparison with the "true homogeneous" time series for Spokane. However, if we consider the basis for adjustments it follows that a set of recommendations can be made regarding a hierarchy of preferred adjustment methodologies. The metadata approach used to adjust the USHCN data uses two basic assumptions: that the bias associated with known effects (e.g. the time-of-observation bias) can be estimated and applied with a reasonable degree of confidence, and that knowing the date of changes that can cause a discontinuity allows us to test that change for statistically significant biases. Thus, an approach based on prior knowledge is preferable. However, in many cases station history files (metadata) are incomplete or missing altogether which requires a non-metadata approach for homogeneity adjustments. In reality, even the most extensive station history files probably do not contain information on all changes at a station that can cause a discontinuity (e.g. simply replacing a broken thermometer). Therefore, it is likely that the optimal approach to homogeneity adjustments when metadata are available is a combined approach where both metadata and non-metadata methods are applied. However, the

question remains as to the proper application strategy if both are to be used.

As for the use of individual station data that have been subjected to homogeneity adjustments, we recommend that the researcher keep in mind the points of the preceding discussion. In particular, the adjusted time series represents an attempt to make the data appear as if they have been observed at one site under consistent methods and conditions when in reality those conditions may have existed only briefly during the most recent period. Due to the need for reference series comparisons to make most data adjustments, the adjusted time series often has statistical characteristics more consistent with the regional time series than with the unadjusted data for that same station. Therefore, care must be taken when using either the adjusted or unadjusted time series for an individual station, and it is our opinion that the optimal use of adjusted climatological time series is in the development of more robust regional analyses.

4. REFERENCES.

Conrad, V., and C. Pollak, 1962: **Methods in Climatology,** Harvard University Press, Cambridge, Mass., 459 pp.

Easterling, D.R., and T.C. Peterson, 1994a: A new method for detecting undocumented discontinuities in climatological time series, **Int. J. Climatol.**, in press.

Easterling, D.R., and T.C. Peterson, 1994b: The effect of artificial discontinuities on recent trends in minimum and maximum temperatures, **Atmos. Res.**, in press.

Karl, T.R. and C.N. Williams, Jr., 1987: An approach to adjusting climatological time series for discontinuous inhomogeneities, **J. Climate Appl. Meteor., 26,** 1744-1763.

Karl, T.R., C.N. Williams, Jr., P.J. Young, and W.W. Wendland, 1986: A model to estimate the time of observation bias associated with monthly mean maximum, minimum, and mean temperatures for the United States, **J. Climate Appl. Meteor., 25,** 145-160.

Karl, T.R., C.N. Williams, Jr., F.T. Quinlan, and T.A. Boden, 1990: **United States Historical Climatology Network (HCN) Serial Temperature and Precipitation Data.,** Environmental Sciences Division, Pub. No. 3404, Carbon Dioxide Information and Analysis Center, Oak Ridge National Laboratory, 389 pp.

Karl, T.R., H.F. Diaz, and G. Kukla, 1988: Urbanization: its detection and effect in the United States climate record, **J. Climate, 1,** 1099-1123.

Peterson, T.C., and D.R. Easterling, 1994: Creation of homogeneous composite climatological reference series, **Int. J. Climatol,** 671-679.

Vose, R.S., R.L. Schmoyer, P.M. Steurer, T.C. Peterson, R.R. Heim, T.R. Karl, and J.K. Eischeid, 1992: **The Global Historical Climatology Network: Long-term MonthlyTemperature, Precipitation, Sea-level, and Station Pressure Data,** Environmental Sciences Division, Pub. No. 3912, Carbon Dioxide Information and Analysis Center, Oak Ridge National Laboratory, 189 pp.

ACKNOWLEDGMENTS: Partial support for this work was provided to the National Climatic Data Center by the USA Department of Energy through Interagency Agreements: DE-AI05-90ER60952 and DE-AI05-900R21956.

CORRESPONDING AUTHOR
Dr. David R. Easterling,
NOAA/NESDIS, National Climatic Data Center,
Federal Building,
Asheville, NC 28801,
USA
deasterl@ncdc.noaa.gov

Figure 1: (a) Annual average temperature for Spokane (solid) and USHCN Region 5 (dotted) both unadjusted; (b) same except that both were adjusted using the USHCN metadata methodology; (c) same except that both were adjusted using the non-metadata methodology; (d) annual average temperature for Spokane adjusted using metadata methodology (solid) and non-metadata methodology (dotted).

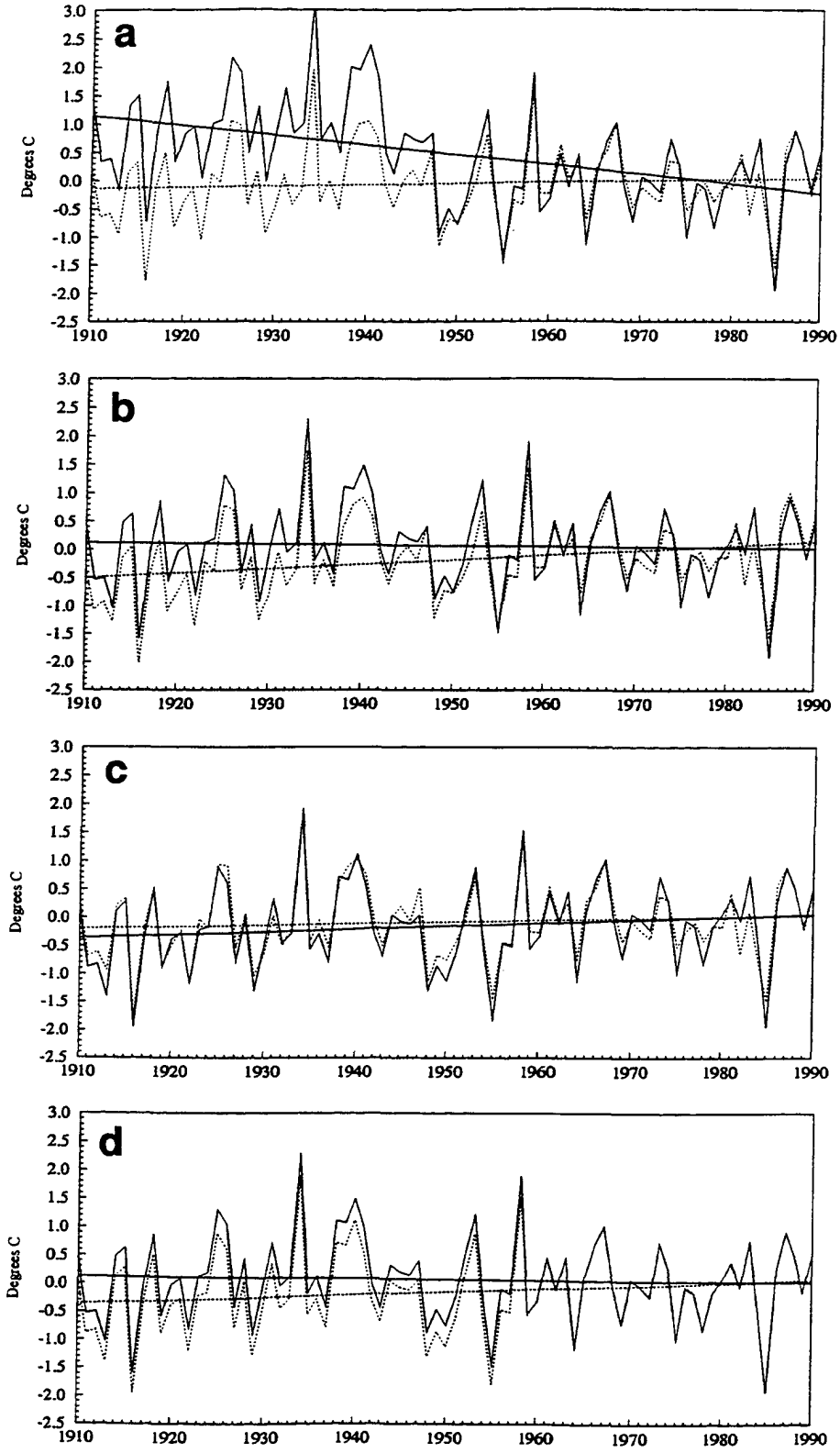


Figure 1. See preceding page for caption.

Homogeneity testing, multiple breaks and trends

Hans Alexandersson
Swedish Meteorological and Hydrological Institute

ABSTRACT

Climate change research is often much disturbed by more or less unknown non-homogeneities in the data series used. Also analyses of anomalies, when monthly values are compared with averages from a normal period, become difficult or sometimes almost meaningless because of non-homogeneities in the climate records.

Two attempts to identify single shifts in the mean level comparing data from nearby stations and using stringent mathematics and parametric tests were first tested on precipitation data (Potter, 1981 and Alexandersson, 1984 and 1986). The latter, mathematically simplest, method is easy to generalize to more complex types of breaks e.g.

1/ multiple breaks
2/ a linear trend of arbitrary length

Multiple breaks can, in principle, be fairly well detected and quantified by successive use of a single shift test analyzing the series in separate time sections. Artificial linear trends are perhaps most likely to occur in temperature data from growing cities.

1 INTRODUCTION

The Standard Normal Homogeneity Test (SNHT) - for single shifts - was developed and applied on precipitation data by Alexandersson (1984, 1986) and then further adapted to climate data problems by e.g. Hanssen-Bauer and Førland (1994). In an extensive intercomparison (Easterling and Peterson, 1992) of different tests this test was found most effective in revealing and dating single and sudden shifts in artificial data. The SNHT has also, in a slightly different version, been discussed in the statistical literature (Hawkins, 1977).

The null hypothesis will, for all the tests, be

$H_0 : Z_i \in N(0,1)$

where Z is a standardized variable which, in turn, is a ratio or difference between a value at the test site and a weighted reference value created from surrounding sites with data of good quality.

Just as for the single shift test the distributions of the test statistics are complicated and we must use simulations to obtain critical levels. It is not straightforward to compare different tests (e.g. is one or two breaks most probable when both test quantities are above the critical levels). But it is reasonable to use ratios of test quantities to critical levels. All tests here have positive variables as test statistics.

The trend test will be a close analogue to the SNHT for a single shift. The basic difference will be the alternative hypothesis. The generalization to multiple breaks is mathematically easy but requires substantially more computer time for each new break introduced in the model.

2 THE REFERENCE VALUE

We will use Y to denote our test site and then Y_i to denote a specific value (e.g. annual accumulated precipitation or annual mean temperature) at year (or other time unit) i. Further X_j will denote one of the surrounding reference sites (the j:th one out of a total of k) and X_{ji} a specific value from that site. Then, to detect relative non-homogeneities, we form ratios (by tradition used in precipitation studies) or differences (often used in temperature studies) according to

$$Q_i = Y_i / \left[\sum_{j=1}^{k} \rho_j^2 X_{ji} \bar{Y} / \bar{X}_j\right] / \sum \rho_j^2 \qquad (1)$$

$$Q_i = Y_i - \sum_{j=1}^{k} \rho_j^2 \left[X_{ji} - \bar{X}_j + \bar{Y}\right] / \sum_{j=1}^{k} \rho_j^2 \qquad (2)$$

We call the denominator in Eq.1 and the second term at the right side of Eq.2 reference values as they intend to be reasonable and stable estimates for the test site using a set of neighbouring stations. In these equations the weight ρ_j denotes the correlation coefficient between the test site and a surrounding station (but also other weights may be used or other techniques to derive reference values). This coefficient must be positive. Bars denote mean values for some certain specific period, like 1961-90. This normalizing has the important effect that we can use different sets of neighbouring stations at different years, including also somewhat shorter and non-complete records, when we calculate reference values. The normalizations also cause the ratios to fluctuate around one for Eq.1 and around zero for Eq.2. Reformulations of the reference values can be done without influencing the theory of the tests.

Then we standardize these series.

$$Z_i = (Q_i - \bar{Q}) / \sigma_Q \qquad (3)$$

We use n-1-weighted standard deviations. This is of some importance to mention as it influences the test statistic and the critical levels.

3 THE SNHT FOR TRENDS AND MULTIPLE BREAKS

For the single shift test we refer to the references above. Now we will introduce a model where the q-series, the series of relative values, change gradually, or more precisely linearly, from time a to b. To be more precise we can then say that this is a test for a relative trend of arbitrary length.

The alternative hypothesis can then be written

$$H_1:\quad \begin{array}{ll} Z_i \in N(\mu_1,1) & i\in\{1,..,a\} \\ Z_i \in N(\mu_1+(i-a)(\mu_2-\mu_1)/(b-a),1) & i\in\{a+1,..,b\} \\ Z_i \in N(\mu_2,1) & i\in\{b+1,..,n\} \end{array}$$

The whole curve described by the mean values is then assumed to be continuous. The trend may extend throughout the whole length of the series.

Forming the likelihood ratio and then differentiating with respect to μ_1 and μ_2 will finally lead to a scheme from which the test statistic T can be obtained as

$$T=\max_{a,b}[-a\mu_1^2+2a\mu_1\bar{z}_1-\mu_1^2 SB-\mu_2^2 SA+2\mu_1 SZB \quad (4)$$
$$+2\mu_2 SZA-2\mu_1\mu_2 SAB-(n-b)\mu_2^2+2(n-b)\mu_2\bar{z}_2]$$

where

$$SA=\sum_{i=a+1}^{b}(i-a)^2/(b-a)^2 \quad (5)$$

$$SB=\sum_{i=a+1}^{b}(b-i)^2/(b-a)^2 \quad (6)$$

$$SZA=\sum_{i=a+1}^{b} z_i(i-a)/(b-a) \quad (7)$$

$$SZB=\sum_{i=a+1}^{b} z_i(b-i)/(b-a) \quad (8)$$

$$SAB=\sum_{i=a+1}^{b}(b-i)(i-a)/(b-a)^2 \quad (9)$$

$$\mu_1=\frac{a\bar{z}_1+SZB-SL\cdot SAB}{a+SB+SK\cdot SAB} \quad (10)$$

$$\mu 2=\frac{\mu_1(-SAB)}{SA+n-b}+\frac{(n-b)\bar{z}_2+SZA}{SA+n-b}=\mu_1 SK+SL \quad (11)$$

Note that for b=a all sums (SA to SAB) are zero and μ_1 and μ_2 are equal to the corresponding arithmetic averages z_1 and z_2 so that T reduces to the single shift test.

This SNHT for trends of arbitrary length might seem a bit awkward at first but, just as for the single shift test, it can in fact be considered as a minimization of squared distances to the mean level curve given by the alternative hypothesis H_1. We will, tentatively, use five years as a minimum number (b-a) for trends to be accepted!

It turns out that the critical levels for the single shift and the trend test are almost equal. This is so because in the simulations under H_0, i.e. using homogeneous random numbers, the largest breaks practically always are of the sudden shift type.

For a double shift the alternative hypothesis will be

$$H_1:\quad \begin{array}{ll} Z_i \in N(\mu_1,1) & i\in\{1,..,a\} \\ Z_i \in N(\mu_2,1) & i\in\{a+1,..,b\} \\ Z_i \in N(\mu_3,1) & i\in\{b+1,..,n\} \end{array}$$

and then the test statistic becomes

$$T=\max_{a,b}(a\bar{z}_1^2+(b-a)\bar{z}_2^2+(n-b)\bar{z}_3^2) \quad (12)$$

in complete analogy to the single shift test. It is now also obvious how higher order breaks can be handled although we will not use them here. They are a bit cumbersome to use because of the explosive increase in computer time for each break. In Table 1 critical levels at the 95% level are given for the single shift (and then also the trend) and the double shift tests for some values on the number n.

Table 1. 95% critical levels as a function of n.

n	single+trend	double
20	6.95	10.5
40	8.10	13.2
60	8.60	14.7
80	8.95	15.6
100	9.15	16.3
150	9.35	17.4
250	9.70	18.3

4 AN EXAMPLE

Figure 1 shows an example of these tests when applied on annual temperature data from Kvikkjokk (66°57'N, 17°45'E) and using Abisko (68°21'N, 18°49'E), Kiruna (67°49'N, 20°14'E), Jokkmokk (66°37'N, 19°50'E), Stensele (65°04'N, 17°09'E) and Vuoggatjålme (66°34'N, 16°34'E) as reference stations. Some minor corrections were applied for the series from Jokkmokk and Stensele. These stations are situated in northwestern Sweden with hilly terrain and complex temperature patterns.

The Q-series for Kvikkjokk might first be thought of as a slow trend downward but in this case the objective trend test picks out the downward shift 1964-65 just as the single shift test. The double shift test gives 1924 and 1964 as break points. Comparing the T-values versus the critical levels give

31.1/9.2=3.4 for the single shift
38.2/16.4=2.3 for the double shift

This would indicate that one break might be enough. Performing single shift tests on two equal parts (1889-1941 and 1942-1994) gives, however, that also the early break is significant (T=12.1).

Testing the four seasons individually shows that the early break is most pronounced in spring and summer while the latter break only can be seen in autumn and winter data. Comparing with known station changes the first break probably can be coupled to a change from wall screen (on a north-facing wall but note that we are north of the arctic circle!) to a free standing Stevenson screen. The latter break is associated with an exchange of screen as the old one was rotten. Although within the same yard the new screen was mounted some metres lower (hilly terrain) and then more exposed to the very frequent inversions during the winter half year.

This one and only example demonstrates the tough work a climatologist has to go through with every series. And the work is not easier with several tests but it seems that sometimes the trend test is a better model than an abrupt shift, while two or more breaks as a rule can be handled by performing successive tests with the single shift model.

References

Alexandersson, H., 1984: "A homogeneity test based on ratios and applied to precipitation series", Reports No. 79, Dept. of Meteorology, Uppsala Un., Sweden, 55 p.

Alexandersson, H., 1986: "A homogeneity test applied to precipitation data", J. of Climatology, vol 6, 661-675.

Easterling, D. and T. Peterson, 1992: "Techniques for detecting and adjusting for artificial discontinuities in climatological time series: a review", In Proc. 5th Int. Meeting on Stat. Climatology, Toronto, Canada. 5 pp.

Hanssen-Bauer, I. and E. Førland, 1994: "Homogenizing long Norwegian precipitation series", J. of Climate, vol 7, nr 6, 1001-1013.

Hawkins, P.M., 1977: "Testing a sequence of observations for a shift in location", J. of Amer. Stat. Assoc., vol 72, 180-186.

Potter, K.W., 1981: "Illustration of a new test for detecting a shift in mean in precipitaion series", Mon. Wea. Rev., vol 109, 2040-2045.

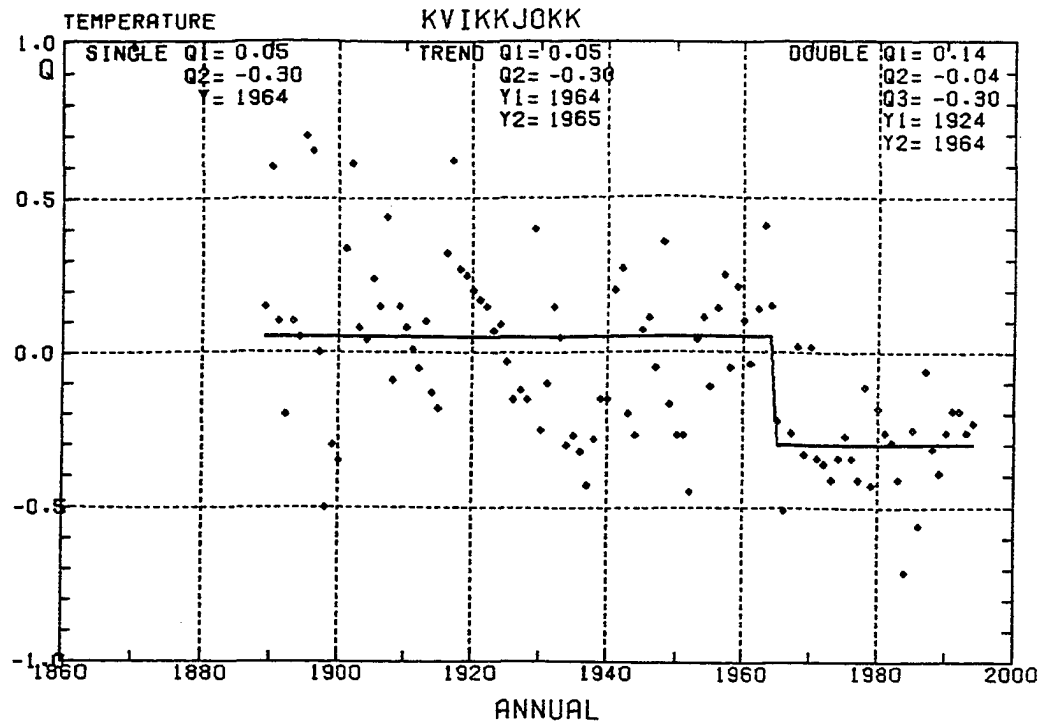


Figure 1. Q-series 1889-1994 for annual temperatures, Kvikkjokk, Lappland, Sweden.

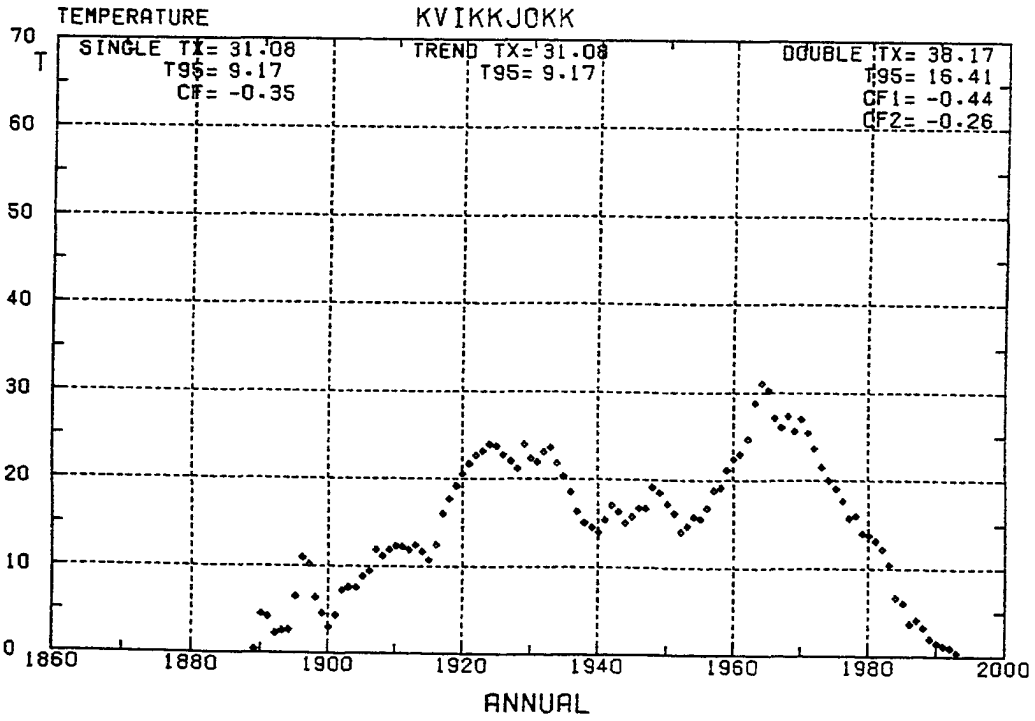


Figure 2. T_t-series (single shift) 1889-1993 for annual temperatures, Kvikkjokk, Lappland, Sweden.

ADJUSTMENT OF APPARENT CHANGES IN VARIABILITY OF TEMPERATURE TIME SERIES

Heikki Tuomenvirta
Finnish Meteorological Institute
and
Hans Alexandersson
Swedish Meteorological and Hydrological Institute

ABSTRACT

Long climatological time series are seldom homogeneous. Besides real climatic changes, they show apparent changes. A 'linear' method, based on linear regressions between stations being adjusted and reference series, can adjust also changes of variability whereas constant correcting adjusts only changes of mean level of time series. According to Finnish data, especially, winter time monthly mean temperature series have homogeneity breaks in variability, which could be adjusted with 'linear' method.

1 INTRODUCTION

Climate research and monitoring of climatic changes requires long, homogeneous time series of meteorological observations. However, the adjectives long and homogeneous can seldom at the same time be used to characterise time series. The long meteorological observation records suffer from changes of instruments, sites, observing hours, etc., which can easily cause breaks in the homogeneity of the same order of magnitude as the long-term climate variability.

There are several statistical tests in use for detecting inhomogeneties, e.g. Alexandersson (1986), Craddock (1979). Recently, some new methods have been developed by Young (1993) and Szentimrey (1994). Statistical testing can detect inhomogeneties that should be verified from station history information. If a physical reason for homogeneity break can be found from station history (or 'metadata'), it minimises the risk of removing real climatic changes from data.

The procedure of homogenising of climatological time series includes, besides testing, also the adjusting of detected inhomogeneities. This article will discuss on simple methods for adjusting artificial, sudden breaks in homogeneity of mean temperature time series. Methods requiring several meteorological elements, like correction methods for 'true' precipitation presented in Sevruk (1982), will not be discussed. The related problem of detecting discontinuities in homogeneity is relevant to the question of adjusting, but it will not be consulted anymore.

2 ADJUSTMENT METHODS

Relative techniques to adjust time series for inhomogeneties require homogeneous reference series. Petterson and Easterling (1994) describe the creation of climatological reference series for data that has not previously been tested. Data, used in this study, had been tested earlier (Heino, 1994) and stations used for creating reference series have passed homogeneity testing.

Reference anomaly series (r_i) were constructed in the following way:

$$r_i = \sum_j w_j \left[\left(x_{ij} - \overline{x_j} \right) \sigma_y / \sigma_{xj} \right] / \sum_j w_j \qquad (1)$$

Here x_j is the jth reference station's series, overbar denotes time mean, σ is standard deviation and w_j is weighting factor, in this study, square of correlation coefficient between test and reference station. Station being adjusted, test station, is marked with symbol y. If reference series are constructed according to equation (1), the standard deviations of reference series are same as at test stations.

Next we present three simple ways to adjust time series with the help of reference series. The common way to do the adjusting is to use the difference (ratio for precipitation), q_i, between reference and test station (y_i) anomaly series. Here defined as:

$$q_i = y_i - r_i \qquad (2)$$

The q-series are divided into two parts: part before the homogeneity break, and part after the break (denoted with subsymbols 1 and 2, respectively). The adjustment is difference between time means of q-series after and before the discontinuity $\left(\overline{q2} - \overline{q1} \right)$. In this presentation we will call this method, constant monthly (CM) adjustments, if it is defined on monthly level. If same method is used to define adjustment on annual level, it will be called constant annual (CA) method.

Above method adjusts the mean levels of series to be the same before and after break. CM does that for all months, separately, and CA for annual means. However, they don't consider possible changes in variability. Therefore, adjustments of individual months or years may not be very good and trends can be over- or underestimated.

To take into account possible changes in variability a following method to define adjustments was developed: (i) linear regression between test and reference series, before and after the break, is performed, (ii) the change of slope of regression line is used as amplification/dumping factor in the adjustment procedure. Linear regression lines are $y1 = a1r1 + b1$ and $y2 = a2r2 + b2$. The adjusted values at the test site (y_i^a) can be calculated with formula:

$$y_i^a = \overline{y_1} + \Delta y + (a_2 / a_1)(y_i - \overline{y_1}) \qquad (3)$$

Here Δy is change the of mean level. The last term of (3) is the amplification/damping term, which is ratio of slopes times anomaly. In this article, method is called 'linear' adjustment (LINEAR).

Example data are from Oulu, Finland. December mean temperature series for period 1972-1982 are adjusted to the level of period 1983-1994. The physical reason for the break was station relocation from town centre to University campus. The old site had the warming effects of sea, river and town centre. Figure 1a shows the linear regression of temperature anomalies when station was in town centre and Figure 1b at the University. The regression line at the University is steeper than in town indicating larger temperature amplitude.

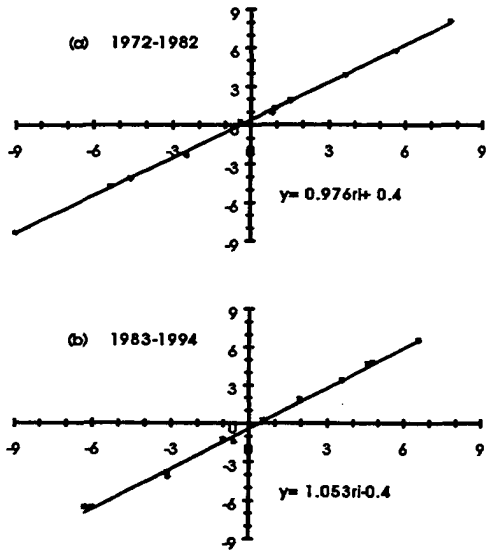


Figure 1. Linear regressions of December mean temperature anomalies at Oulu (a) before and (b) after station relocation in 1983 (units: degrees Celsius).

The December temperature adjustments at Oulu are shown in Figure 2 as a function of temperature anomaly. The old site at town centre was more 'maritime' and temperature variations were smaller than at present site. Therefore, cold Decembers require large negative adjustments.

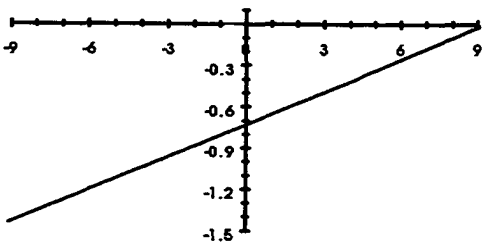


Figure 2. December adjustments at Oulu as a function of temperature anomaly (units: degrees Celsius).

3 COMPARISON OF METHODS

To evaluate, if 'linear' adjustment is giving better corrections than constant methods, we organised following comparison. Two homogeneous, closely situated stations were selected. The stations are located in different microclimatic environments. The data from one station are adjusted to simulate the data from the other station. Simulated data are then compared with real observed data.

Three pairs of stations were selected and simulations were done. The correlation coefficient of monthly mean temperatures between station pairs is at most months 0.99 or better. The worse monthly correlation was 0.97. Table 1 describes the differences of pairs of stations (Helsinki, Kuopio and Rovaniemi) used in this study. The most important difference between Helsinki stations is maritimity, in Kuopio local orography and openness play important role, and in Rovaniemi the altitude difference is relevant. First station of pair is adjusted to represent the second station. For example, Helsinki Kaisaniemi monthly mean temperatures were adjusted to represent Helsinki airport temperatures. Time periods are rather short because criteria for homogeneity used in this comparison was very strict.

Table 1. Characteristics of station pairs used in comparison.

station/period	altitude	location	remarks
Helsinki Kaisaniemi 1970-1994	4 m	botanical garden in city centre	1 km from sea
Helsinki airport 1970-1994	53 m	airport	16 km from sea open
Kuopio airport 1972-1994	94 m	airport	open
Kuopio Inkilänmäki 1972-1994	119 m	family house suburb	on a slope
Rovaniemi airport 1960-1994	198 m	airport	open
Rovaniemi Apukka 1960-1994	103 m	agricultural research station	

The time periods are divided in half. To make comparison similar to real use of an adjustment method, time series were constructed where old part of series needs adjustment (predictor, e.g. Helsinki Kaisaniemi 1972-1982) and new part is from station which will be simulated (e.g. Helsinki airport 1983-1994). The changes of mean levels and slopes are defined against reference series and they are used to adjust old parts of the series to represent the other station (e.g. Helsinki Kaisaniemi is adjusted, predictant, to represent Helsinki airport 1972-1982).

We tried to evaluate the significance of change between slopes of linear regression lines. This was done with Student's t-test. Null hypothesis is that a_2 is equal to a_1. Alternative hypothesis $a_2 \neq a_1$, means that slopes of regression lines, before and after break, are different. The test parameter (t) is computed in the following way:

$$t = \frac{|a_2 - a_1|}{\sqrt{se(a_2)^2 + se(a_1)^2}} \qquad (4)$$

Here *se* is standard error. Table 2 shows the monthly changes (or differences) of mean levels (Δy), ratios of slopes (a_2 / a_1) and probability of getting larger t-value (*prob*) than in (4).

Table 2. Monthly changes of mean levels, ratios of slopes and probability of slope changes (Student's t-test). Unit of mean level temperature change is degrees Celsius.

Helsinki	Δy	a_2 / a_1	*prob*
Jan	-1.19	1.102	0.00
Feb	-0.91	1.073	0.00
Mar	-0.70	1.006	0.86

Apr	0.05	1.035	0.62
May	0.25	1.099	0.21
Jun	-0.23	0.990	0.81
Jul	-0.33	1.033	0.39
Aug	-0.70	1.020	0.77
Sep	-1.03	1.063	0.02
Oct	-0.98	1.073	0.19
Nov	-1.24	1.108	0.00
Dec	-1.16	1.054	0.01
Kuopio			
Jan	0.75	0.934	0.01
Feb	0.87	0.926	0.01
Mar	0.62	0.877	0.01
Apr	0.33	1.062	0.35
May	0.08	0.993	0.88
Jun	-0.18	1.040	0.30
Jul	-0.33	1.003	0.95
Aug	-0.46	0.945	0.40
Sep	-0.17	1.056	0.17
Oct	-0.06	0.951	0.06
Nov	-0.01	1.008	0.75
Dec	0.28	0.912	0.00
Rovaniemi			
Jan	-1.63	1.173	0.00
Feb	-1.35	1.117	0.00
Mar	-1.04	1.358	0.00
Apr	-0.08	1.049	0.33
May	0.06	0.917	0.07
Jun	0.18	0.968	0.27
Jul	0.16	0.978	0.68
Aug	-0.08	0.958	0.51
Sep	0.04	1.042	0.18
Oct	0.03	1.134	0.00
Nov	-0.26	1.121	0.01
Dec	-1.22	1.168	0.00

It can be seen that Helsinki airport is colder than Kaisaniemi most of the year (Δy is negative). It is also more variable, i.e. temperature variations within month are larger (a_2 / a_1 is greater than one). The significant slope changes occur during winter and autumn (*prob* small). Kuopio was chosen a case where the temperature variations are generally damped with 'linear' method (airport has larger temperature amplitude than Inkilänmäki). In Rovaniemi winter time mean level and slope changes are largest of three examples. Frequent inversion situations cause large changes because altitude difference of sites is almost 100 meters. From April to September mean temperatures are quite similar.

Values presented in Table 2 were used with three adjustment methods ('linear', CM and CA) to create series which simulate the other station. Simulated series were compared with real observed temperatures. The mean errors between observed and adjusted temperatures are presented in Table 3.

Generally, 'linear' method gives smallest errors. In Helsinki, CM wins 'linear' in number of months with smallest errors, but differences are small. During months when slope change is statistically significant, 'linear' method is clearly better than others. From above results it is clear, that monthly or seasonal adjusted means with CA shouldn't be used. Actually, CA method should be applied to annual values, not to monthly.

The errors of adjusted temperatures are largest in Rovaniemi where the temperature variability is also largest. Similarly errors have maximum during winter months in Kuopio and Rovaniemi. In Helsinki, the maritime effect at Kaisaniemi station causes largest errors to occur during spring.

4 POTENTIAL USE OF 'LINEAR' METHOD

The earlier homogeneity testing results were used to evaluate, if 'linear' method could be used in practical work. There are preconditions that must be fulfilled before method can be applied. First, homogeneity breaks must be found. Secondly, there must exist reference stations with good correlations and sufficiently long series.

In an earlier work, Standard Normal Homogeneity Test (SNHT) was applied together with station history information to long mean temperature series from Finland (Tuomenvirta and Drebs, 1994). The reasons for breaks, detected by SNHT, were sought from station history material. For almost 90% of breaks, a physical reason could be found from 'metadata'. For these cases and some recently identified breaks, the Student's test for change of regression line slope was performed, see equation (4). The results of testing 36 breaks are summarised in Table 4.

Clearly December and January are the months when homogeneity breaks cause also discontinuities in variability. Almost half of significant slope changes occur during winter months. The temperature variability has maximum in winter. Probably, the local environmental factors like water bodies, elevation and openness have larger effect on mean temperature in winter than during other seasons.

5 CONCLUSIONS

The constant adjustment methods discussed in this paper are commonly applied, e.g. Hanssen-Bauer and Förland (1994), Heino (1994), Böhm (1992). The 'linear' adjustment doesn't use any other elements or information than what can be derived from element being adjusted. Therefore, it can be considered as simple as constant corrections, but it still tries to capture the possible changes in variability.

In the comparison, the 'linear' method gave better corrections than constant adjustments. The corrections were best when adjusting homogeneity breaks of winter months. To avoid artificially changing the variability, 'linear' adjustments can be restricted only to cases when the change of regression line's slope is statistically significant. It should be kept in mind that relative testing and adjustment methods rely on the presence of good quality, well correlating reference stations. Here, only monthly mean temperatures were corrected, but at least in principle, other climatic elements can be adjusted in this way, too.

These results suggested that 'linear' method gives better adjustments, when change of slope is statistically significant. If this is true, roughly about one third of winter time temperature adjustments of Finnish long term temperature series could be improved with 'linear' adjustment.

The detection of inhomogeneities was not studied, but the winter time results suggest that there are discontinuities in the variability of temperature time series. Presently SNHT uses sums of ratios or differences between test and reference series. To detect the variability changes, value to be tested in SNHT could be composed of sums of linear regression line terms.

Table 3. Monthly mean errors of three adjustment methods at three test sites (in degrees Celsius). Bold numbers indicate smallest error of the month at site. Asterisk shows statistically significant (95% level) slope changes.

	HELSINKI			KUOPIO			ROVANIEMI		
month	LINEAR	CM	CA	LINEAR	CM	CA	LINEAR	CM	CA

Jan	**0.110***	0.255	0.578	**0.242***	0.383	0.433	**0.575***	0.827	1.153
Feb	0.230*	**0.229**	0.444	**0.192***	0.343	0.837	**0.463***	0.522	0.621
Mar	0.177	**0.177**	0.193	**0.285***	0.340	0.770	**0.475***	0.878	0.941
Apr	**0.352**	0.358	0.364	**0.186**	0.190	0.313	**0.287**	0.291	0.440
May	0.306	**0.304**	0.830	**0.133**	0.133	0.148	**0.207**	0.247	0.543
Jun	0.232	**0.222**	0.553	0.131	**0.075**	0.272	0.174	**0.172**	0.671
Jul	0.204	**0.198**	0.259	0.112	**0.112**	0.372	**0.197**	0.213	0.566
Aug	0.188	**0.185**	0.190	**0.268**	0.268	0.322	**0.258**	0.268	0.470
Sep	**0.153***	0.161	0.385	0.214	0.200	**0.105**	**0.158**	0.174	0.504
Oct	0.200	**0.192**	0.462	**0.094**	0.105	0.122	**0.229***	0.346	0.607
Nov	**0.130***	0.185	0.555	0.101	**0.100**	0.150	**0.283***	0.401	0.430
Dec	**0.133***	0.177	0.608	**0.153***	0.272	0.270	**0.593***	0.846	0.900

Table 4. Monthly and seasonal frequencies of statistically significant (95% level, t-test) slope changes in homogeneity breaks of temperature series. Seasons defined as three month periods, e.g. winter is from December to February.

month	Jan	Feb	Mar	Apr	May	Jun	Jul	Aug	Sep	Nov	Oct	Dec
breaks	11	7	5	3	2	3	2	5	4	4	6	13
season	winter (DJF)			spring (MAM)			summer (JJA)			autumn (SON)		
breaks	30			10			11			14		

References

Alexandersson, H., 1986, "A homogeneity test applied to precipitation data", J. of Climatology 6, 661-675.

Böhm, R., 1992, "Description of procedure of homogenizing temperature time series in Austria", CERI, Proj. Gr. Met. WP 2, 1-14.

Craddock, J.M., 1979, "Methods for comparing annual rainfall records for climatic purposes", Weather 34, 332-346.

Hanssen-Bauer, I. and E.J. Förland, 1994, "Homogenizing long Norwegian precipitation series", J. Climate 7:6, 1001-1013.

Heino, R., 1994, "Climate in Finland during the period of meteorological observations", Finnish Meteorological Institute Contributions 12, 209 pp.

Petterson, T.C. and D.R. Easterling, 1994 "Creation of homogeneous composite climatological reference time series", Int. J. Climatol. 14, 671-679.

Sevruk, B., 1982, "Methods of correction for systematic error in point precipitation measurement for operational", WMO-No.589, 91 pp.

Szentimrey, T., 1994, "Statistical problems connected with the homogenization of climatic time series", Climate variations in Europe, Publications of the Academy of Finland 3/94, 330-339.

Tuomenvirta, H. and A. Drebs, 1994, "Homogeneity testing and management of metadata in Finland", Climate variations in Europe, Publications of the Academy of Finland 3/94, 321-329.

Young, K.C., 1993, "Detecting and Removing Inhomogeneities From Long-Term Monthly Sea Level Pressure Time Series", J. Climate 6, 1205-1220.

CORRESPONDING AUTHOR
Heikki Tuomenvirta
Finnish Meteorological Institute
P.O. Box 503
00101 Helsinki
FINLAND

Correcting mean annual maxima for data discretization

I.J. Dwyer and D.W. Reed

Institute of Hydrology, Wallingford, UK.

ABSTRACT

Rainfall accumulations are generally measured between fixed hours of the day. The maximum over some time period will underestimate the true maximum that would be derived from continuous data. A correction model is derived empirically by reference to hourly rainfall data from the UK and Australia. Some of the variation in the results between sites is shown to be linked to climate.

INTRODUCTION

Important to natural hazard risk assessment is the accurate statistical modelling of environmental extremes. This is often achieved by analysing 'extreme events' extracted from long data records. The data recording process inevitably contains some form of discretization, however, such as averaging over discrete time steps, which can adversely affect the estimation of extremes and hence the risk assessment. For example, *fixed* daily rainfall accumulations are conventionally measured between the hours of 0900 each day and the annual maxima, taken as representative of the extremes, are subject to frequency analysis; the *sliding* 24-hour maxima, obtained from hourly data, will generally be higher and, in the context of river flooding, would more faithfully represent the extremes, since the clock timing of rainfall is irrelevant. Both fixed and sliding maxima are only approximations to the *true* maxima that would be obtained by sliding a time window smoothly across continuous data (were it available).

A number of *correction factors* have been proposed for converting one type of maxima to another. Hershfield and Wilson (1958) suggest a multiplier of 1.13 for converting fixed one-day into sliding 1440-minute rainfalls. The Flood Studies Report (Natural Environment Research Council, 1975), studying data from around the UK, reports a correction factor of 1.11 for converting one-day to 24-hour rainfalls (of five year return period). More recently, van Montfort (1991) suggested a procedure for estimating a GEV distribution for sliding 24-hour rainfalls from observed one and two-day rainfalls: his analysis of 58 years of rainfall data for Kelburn, New Zealand, suggests correction factors of 1.15 for 2.33-year rainfalls. The commonly cited result of Weiss (1964) is based upon theoretical arguments which are, unfortunately, flawed (see Dwyer and Reed, 1995).

These and other investigations use data of varying extent and quality and employ disparate methods for estimating correction factors. The study reported here uses good quality rainfall data from the UK and Australia to estimate correction factors by a direct method. It is unique in that correction factors are also suggested for converting fixed to *true* maxima, a range of rainfall durations is examined, and systematic variation in the results with climate regime is investigated.

ANALYSIS

Rainfall data were divided into *records* of length $n=2^{14}$ (16384) data values which corresponds to nearly 2 years of hourly data. Each record was analysed separately as described below.

Analogous to the subdivision of data records into years, a record is divided into m=32 *periods* of equal length. Denoting the data values in period i by $x_i(1)$, $x_i(2)$, ... , fixed accumulations of duration D are formed by

$$\begin{aligned} f_{i1} &= x_i(1)+x_i(2)+\ldots+x_i(D) \\ f_{i2} &= x_i(D+1)+x_i(D+2)+\ldots+x_i(2D) \\ &\vdots \quad \vdots \end{aligned} \tag{1}$$

and sliding accumulations of duration D by

$$\begin{aligned} v_{i1} &= x_i(1)+x_i(2)+\ldots+x_i(D) \\ v_{i2} &= x_i(2)+x_i(3)+\ldots+x_i(D+1) \\ &\vdots \quad \vdots \end{aligned} \tag{2}$$

So that each period contains a whole number of fixed accumulations, the length of the periods are set to the greatest integer multiple of D not greater than 512 ($=2^{14}/32$), thus maximizing the amount of data used in the record. Also, so as not to miss a storm which is split across two periods, a sliding accumulation which straddles a border is assigned to the period in which it is mostly contained (and the former if it is equally split).

The fixed maximum of duration D, for period i, is $F_i(D)=\max[f_{i1}, f_{i2},\ldots]$. Similarly, the sliding maximum is $V_i(D)=\max[v_{i1}, v_{i2},\ldots]$. Thus, the fixed and sliding *mean period maxima* (of duration D) are given by

$$\bar{F}(D) = \frac{1}{m}\sum_{i=1}^{m} F_i(D) \tag{3}$$

$$\bar{V}(D) = \frac{1}{m}\sum_{i=1}^{m} V_i(D) \tag{4}$$

respectively (m=32). For a particular record then, the sample correction factor for converting the fixed into the sliding mean period maximum, for duration D, is defined as

$$R(D) = \bar{V}(D)/\bar{F}(D) \tag{5}$$

Thus, graphs of R(D) against D are constructed for each data record. Dropping the notation D, an estimate of the standard error of R(D) is given by

$$s^2(R) = \frac{1}{m(m-1)\bar{F}^2}\sum_{i=1}^{m}(V_i - R.F_i)^2 \tag{6}$$

giving rise to confidence intervals calculated from Normal percentage points (Barnett, 1974).

DATA

A number of hourly rainfall records were available at each of six sites. In the UK, eight such records (labelled A-H) were available at Eskdalemuir, central southern Scotland, five (A-E) at Leeming in North Yorkshire and eight (A-H) at Ringway, Manchester. In Australia, five were available at Brisbane, five at Melbourne and six at Sydney.

GRAPHS OF R(D)

Graphs of R(D) against D were obtained for each data record. Some examples are shown in Figure 1 with a model function fitted by nonlinear regression (details below). All graphs demonstrate the following common features:

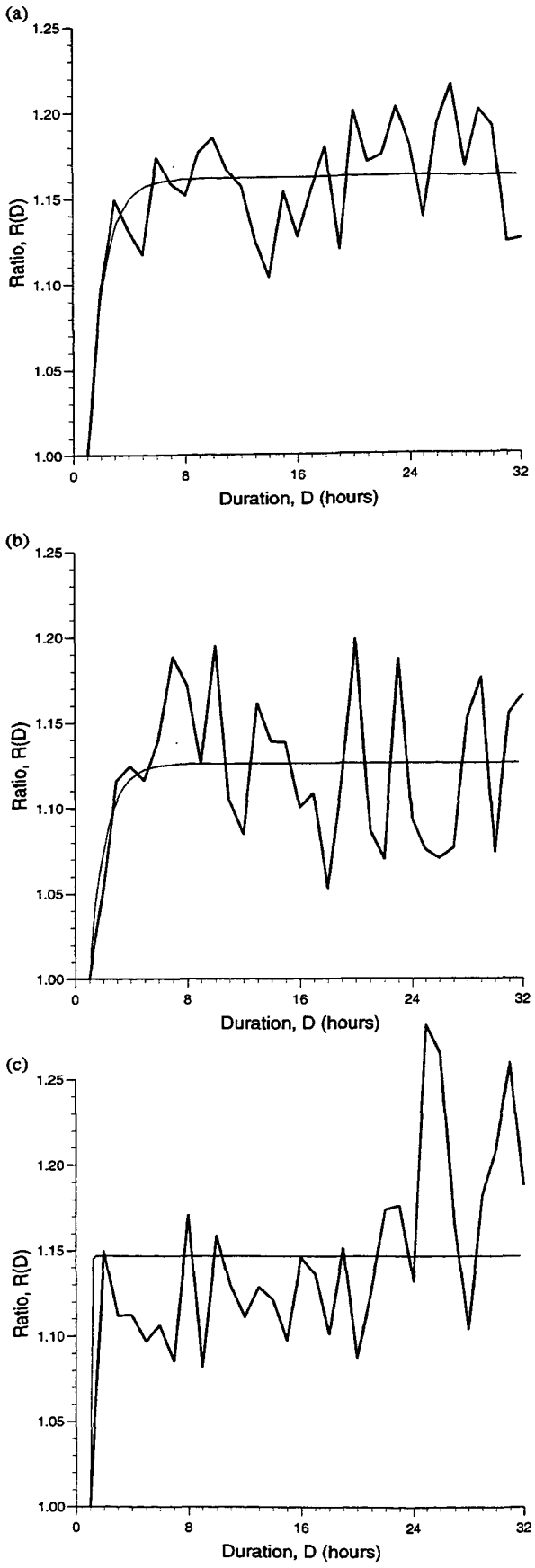


Figure 1 Graphs of R(D) against D, with fitted model, for (a) Eskdalemuir record C, (b) Leeming C and (c) Brisbane D.

Table 1 Values of a and b for each record

Site	Record	a	b
Eskdalemuir	A	0.169	0.388
	B	0.160	0.563
	C	0.162	0.841
	D	0.180	0.402
	E	0.161	0.700
	F	0.177	0.330
	G	0.170	0.343
	H	0.158	1.564
	means:	0.167	0.556
Leeming	A	0.171	0.717
	B	0.168	0.796
	C	0.126	0.865
	D	0.155	1.038
	E	0.151	0.387
	means	0.154	0.734
Ringway	A	0.159	0.432
	B	0.153	0.643
	C	0.154	0.620
	D	0.148	1.198
	E	0.166	0.631
	F	0.169	0.512
	G	0.162	0.285
	H	0.144	0.269
	means:	0.157	0.517
Brisbane	A	0.139	0.723
	B	0.151	0.657
	C	0.124	-
	D	0.147	-
	E	0.162	0.208
	means:	0.144	0.462
Melbourne	A	0.175	-
	B	0.157	0.510
	C	0.164	0.198
	D	0.135	-
	E	0.150	0.973
	means:	0.156	0.486
Sydney	A	0.144	0.771
	B	0.160	0.501
	C	0.158	0.612
	D	0.176	0.261
	E	0.164	0.529
	F	0.169	0.479
	means:	0.162	0.500
Overall means:		0.158	0.571

- R(1)≡1 by definition, since no difference can be distinguished between fixed and sliding accumulations when the duration is equal to the data resolution.
- R(D) generally increases over small D.
- R(D) appears to level off at higher D to fluctuate about some constant value, R^* say.

The levelling off of R(D) is to be expected. Recall that the fixed and sliding maxima are both approximations to the true maximum as would be obtained from continuous data. As D increases, the ratio of the sliding to true maximum approaches unity since the discrepancy between them gets increasingly small compared to their overall size. Thus, as D increases, the ratio R(D) approaches the ratio of the *true* to fixed maximum. Under the hypothesis that extreme rainfall across a range of durations exhibit some self-similarity, this ratio is assumed to be independent of D, whence R^* is interpreted as the correction factor for converting the mean fixed maximum to the mean true maximum for that data record.

A MODEL FOR R(D)

The behaviour of R(D) described above is modelled as exponentially diminishing growth to the limiting constant R^*. With the constraint R(1)≡1, the model function ρ(D) takes the form

$$\rho(D) = 1 + a[1 - \exp\{-b(D-1)\}] \qquad (7)$$

where a and b are parameters estimated by nonlinear least-squares regression. The limiting value, R^* is modelled by

$$\rho^* = \lim_{D \to \infty} \rho(D) = 1 + a \qquad (8)$$

Parameter b relates to the growth rate of ρ(D). The maximum duration, D_{max}, used to model R(D) by ρ(D) should be large enough to adequately define the limiting value but not so large that it becomes a significant proportion of the period length: D_{max} of 32 or 64 was found to be sufficient.

RESULTS

The values of a and b are given in Table 1 for each record analysed. In some cases (eg Figure 1c) there appears to be no growth period and so the value for b (effectively infinite) is not given. Site averages are indicated as well as overall averages; the arithmetic mean is computed for parameter a whereas the geometric mean is computed for the more variable parameter b. Close inspection of the results suggests inter-site differences for parameter a. No systematic differences are evident for parameter b.

An examination of a number of the data records revealed that for most D the regression curve ρ(D) lies within the sample 95% confidence interval for R(D) (as from equation 6). This substantiates the assumptions that variation about the regression curve is due to sample error (rather than a poor model) and that R(D) converges for large D.

The above results were investigated for their sensitivity to various peculiarities of the methodology. The start time of each record was changed from 0900 to midnight on the first day; this affects the timing of the fixed intervals (particularly for D=24 when the fixed intervals all occur between the same hours each day). Whilst this did change the value of parameter a for individual records, the site and overall means changed very little (the overall means being 0.158 for 0900 start and 0.160 for midnight start). So, for climates considered here, mean correction factors are independent of the timing of the fixed intervals. This may not hold for climates where heavy rainfall is subject to strong diurnal cycles. Next, the period length over which maxima are extracted was varied. This was achieved for each UK site by concatenating the consecutive records to form one long record and dividing it up into various numbers of periods each resulting in a given period length. Thus, correction factors (1+a) for period lengths of about 21, 43, 85 and 171 days were examined. For any given site, correction factors did change with period length but not systematically or in a way that was consistent across sites.

CLIMATE

It is reasonable to conjecture that any inter-site differences in parameter a are due to differences in climate, and in particular rainfall regime. The rainfall regime is investigated for each site and used to construct hypotheses regarding differences between the site means for parameter a.

Eskdalemuir in central southern Scotland and Ringway near Manchester are subject to mainly frontal rainfall arriving from the Atlantic Ocean, with October to January being the rainiest season. Leeming, in North Yorkshire, sheltered from these westerly fronts by the Pennine mountains, experiences a greater number of convective summer storms. Sydney, on the south-east coast of Australia, experiences mainly frontal rainfall which peaks in autumn (May to June), while Melbourne on the south-east tip experiences more moderate rainfall evenly distributed throughout the year. Brisbane, on the east coast, is perhaps the most extreme of the climates, being subject to short, heavy monsoonal rains in the summer and lighter frontal rain in the winter.

It is the 'storm concentration' in particular which is expected to have a direct bearing on correction factors. For, if a typical storm at a site arises from relatively few hours of intense rainfall then, by simple probability, there is less chance of it being split at 0900 across two observational days (and hence under-recorded) than for a site where the typical storm is of longer duration.

The concentration of the typical storm for a given site is indexed by the mean number of wet hours comprising the period maxima for D=24. That is, for each *fixed* 1-day period maximum, the number of wet hours (greater than 0.2mm) is recorded and the mean calculated and denoted N_{wet}. The results are shown for each site in Table 2.

Table 2 Value of N_{wet} for each site

Site	N_{wet} (hours)
Eskdalemuir	11.7
Sydney	8.8
Ringway	8.4
Melbourne	8.2
Leeming	8.1
Brisbane	7.2

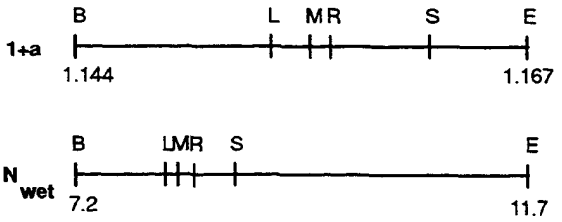


Figure 2 Comparing 1+a with N_{wet} (with each site denoted by its first letter)

The values of N_{wet} are compared to the mean correction factors in Figure 2. The similarity in the site order is striking, and drives the

hypotheses that Eskdalemuir requires higher correction factors than other sites, Brisbane requires lower correction factors than other sites, with the rest do not significantly differ one to another. These hypotheses are tested by using paired Student's t tests to discern significant differences in the site mean correction factors (at the 90% confidence level). A test statistic is used which assumes equal but unknown variances. One sided tests indicate that Eskdalemuir has a significantly greater mean correction factor than all sites except Sydney, and Brisbane has a lower mean correction factor than all sites except Leeming and Melbourne. Two sided tests result in no significant differences between mean correction factors at the other sites. These results lend support to the conjecture that sites experiencing long-duration frontal rainfall require higher correction factors than sites subject to shorter duration events.

APPLICATIONS

The following advice relates to rainfall time-series for a single gauge, measured by accumulations over a fixed time interval. The correction factors suggested pertain to mean period maxima for rainfall durations one to 32 hours obtained from sub-daily data.

Using parameter values a=0.16 and b=0.57, four types of correction can be performed:

Converting Fixed to Sliding Maxima

The multiplier $\rho(D)$ may be used to convert the mean fixed maximum of duration D to the mean sliding maximum of duration D.

Converting Fixed to True Maxima

The multiplier ρ^* may be used to convert the mean fixed maximum of duration D, to the mean true maximum of duration D.

Converting Sliding to True Maxima

It may occur that the mean sliding maximum of duration D is available but the mean true maximum is required. The former can be converted to the latter using the correction factor

$$\alpha(D) = \frac{\rho^*}{\rho(D)} \qquad (9)$$

This can be seen by considering the conversion in two stages: first, convert the mean sliding maximum into the mean fixed maximum by dividing by $\rho(D)$; second, convert this mean fixed maximum into the mean true maximum using the multiplier ρ^*.

Converting Sliding to Sliding Maxima

The mean sliding maximum of duration D, as measured from data of resolution τ, may be converted into the mean sliding maximum of the same duration but as if measured from data of finer resolution $\tau'=\tau/\lambda$ ($\lambda>1$) using the multiplier

$$\beta(D) = \frac{\rho(\lambda D)}{\rho(D)} \qquad (10)$$

This can be seen by considering the conversion in three stages: first convert the mean sliding maximum of duration D, measured at resolution τ, into the mean true maximum by multiplying by $\alpha(D)$; second, use the reasonable assumption that ρ^* is independent of data resolution to obtain the mean fixed maximum for the same duration but expressed in terms of the resolution τ' (namely, duration λD) by dividing by ρ^*; lastly, convert this mean fixed maximum of duration λD into the mean sliding maximum (as measured at resolution τ') using the multiplier $\rho(\lambda D)$.

Examples

Let the mean *fixed* 3-hour maximum be denoted by F. The mean *sliding* 3-hour maximum, V, is obtained using equation 7:

$$V = \rho(3)F \approx 1.11F \qquad (11)$$

The mean *true* maximum of duration 3 hours, T, can be obtained using equation 8, namely

$$T = \rho^*F = (1+a)F = 1.16F \qquad (12)$$

If the sliding 3-hour maximum, V, is available, then T can be obtained from V using equation 8 as follows:

$$T = \alpha(3)V = \frac{\rho^*}{\rho(3)}V \approx 1.045V \qquad (13)$$

Suppose that the mean sliding 3-hour maximum, V1, has been calculated from hourly data (τ=1 hour). Although it is sliding, there is still a considerable discretization effect at such a short duration (D=3). To calculate the mean sliding 3-hour maximum as if it were extracted from, say, 15-minute data (τ=¼ hour), denoted by V2, use equation 10 to obtain

$$V2 = \beta(3)V1 = \frac{\rho(3\lambda)}{\rho(3)}V1 = \frac{\rho(12)}{\rho(3)}V1 \approx 1.045V1 \qquad (14)$$

The Special Case of Daily Rainfall

Special guidelines apply when converting fixed to true maxima for daily rainfall. As well as the correction factor ρ^*=1.16, as suggested above, correction factors of 1.15 and 1.17 may also be employed: the former for sites with rainfall regimes which tend to generate concentrated events of short duration (such as tropical storms); the latter for sites with rainfall regimes tending to generate longer events (such as those produced by large frontal systems).

OTHER WORK

Correction factors are investigated for rainfall, wind speed and air temperature data in Dwyer and Reed (1994). Dwyer and Reed (1995) examine correction factors for longer duration rainfalls as well as investigating the effect of discretization upon the L-skewness and L-kurtosis of period maxima.

REFERENCES

Barnett, V. 1974. Elements of sampling theory. English University Press, London. Chapter 3.

Dwyer, I.J. & Reed, D.W. 1994. Effective fractal dimension and corrections to the mean of annual maxima. J. Hydrol., 157, 13-34.

Dwyer, I.J. & Reed, D.W. 1995. Allowance for discretization in hydrological and environmental risk estimation. Report number 123, Institute of Hydrology, Wallingford.

Hershfield, D.M. & Wilson, W.T. 1958. Generalizing of rainfall-intensity-frequency data. IUGG/IAHS publication no. 43, 499-506.

Natural Environment Research Council. 1975. Flood Studies Report (in five volumes). NERC, London. Vol. II, Chapter 3.

van Montfort, M.A.J. 1990. Sliding maxima. J. Hydrol., 118, 77-85.

Weiss, L.L. 1964. Ratio of true to fixed-interval maximum rainfall. J. Hydraul. Div. Proc. ASCE, 90, 77-82.

ACKNOWLEDGEMENTS

The research was funded by the UK Natural Environment Research Council.

CORRESPONDING AUTHOR

Mr. Ian J. Dwyer, Institute of Hydrology, Maclean Buildings, Crowmarsh Gifford, Wallingford, Oxon OX10 8BB, UK.

LONG TIME SERIES OF TEMPERATURE IN NORWAY

P. Ø. Nordli

Norwegian Meteorological Institute

ABSTRACT

As a part of the international NACD-project[1] 18 Norwegian time series of air temperature have been checked for inhomogeneities by statistical methods and studies of metadata. Inhomogeneities occur as a consequence of relocations, changes of instruments and observational procedures. During winter when inversion situations are predominant, even small relocations may lead to inhomogeneities in the series.

Eleven rural series scattered over an area from 58° N to 78°N and from 9°W to 31°E are found acceptable for use in the analyses. The data is smoothed by a low pass filter involving Gaussian weighting. Warm and cold spells seem to be present almost in the same years throughout the entire area. The series are also checked for trends by the Mann-Kendall test.

Principal component analysis is performed on annual temperatures. The first four PCs have been interpreted. Together they accounts for 94 % of the variance (the two first ones for 85 %).

1 THE HOMOGENEITY OF THE NORWEGIAN TEMPERATURE TIME SERIES

Some of the oldest Norwegian temperature time series have earlier been tested for inhomogeneities using subjective methods. They are, however, now under testing with the "Standard Normal Homogeneity Test" (SNHT), (Alexandersson, 1986) which is chosen as the main testing procedure in the NACD-project. The principal idea of the test is to compare a test station with a group of homogenous reference stations.

Our main concerns about inhomogeneity are:

Changes of formula. Fortunately the formula used to calculate monthly mean temperature has been unchanged since January 1876 when the minimum thermometer was introduced in the Norwegian network. Changes of observation hours are adjusted for by a constant in the formula.

Shrinking of the glass in thermometers This was a problem for early thermometers used as late as in the first part of the present century. As the thermometers grew older they tended to show higher temperature which required adjustment of instrument corrections. In Norwegian inspection reports it is seen that thermometer comparisons have been done, but they are far from frequent.

Changes from wall screen to Stevenson screen. This is one of the greatest problems for the Norwegian series because, as far as we know, no parallel measurements have been made. The use of the SNHT is also questionable since the change took place at all stations at almost the same time.

A temperature series from Dombås (1881-1965, 62.05°N, 9.08°E) was therefore analysed as a stand alone series (Demarée, Derasse, 1993). They found a highly significant change in the second part of 1929. This was relatively close to the real change which took place in September 1933. The statistical results remain, however obscured by the occurrence of a general warming in the 1930's.

The effects of the change are also studied in a test field at Dombås, only 100 m from the old site. A wall screen was located at the northern wall of a old dwelling house and the Stevenson screen some 10 m outside the east wall. The differences between the wall screen and the Stevenson screen are shown on Fig 1.

The differences change systematically during the year. In winter and autumn the Stevenson screen is warmer than the wall screen and vice versa in spring and summer.

One can question whether this result is caused by different screening only or are there other factors involved? The test field is situated at a slope and consequently a down slope drainage flow is present under inversion conditions. The house causes the cold air to stagnate. Therefore the temperature on

[1]North Atlantic Climatic Data set

the upslope northern side of the house may be colder than the air nearby the house. Preliminary results indicate that this effect explains most of the difference in winter.

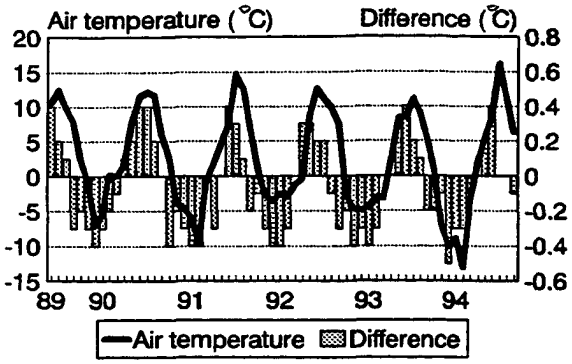


Fig. 1 Difference between the mean monthly temperature inside wall screen and Stevenson screen at Dombås test field.

Sunshine on wall screens. In the network of stations direct sunshine on the wall screens was normally avoided at the observation hours. Nevertheless, a few occasions are known. One method to avoid direct sunshine was to build extra screens on the walls. An extra screen was also mounted at Dombås for test purposes.

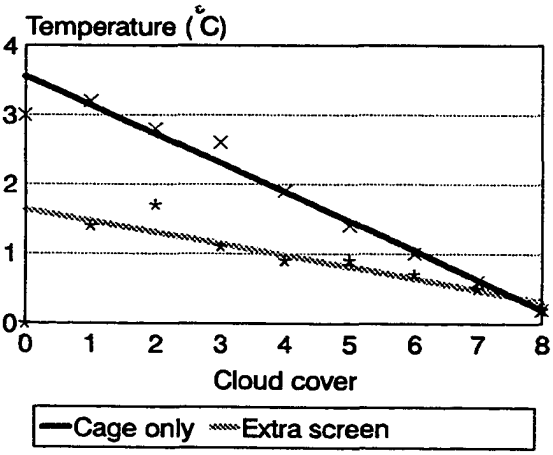


Fig. 2 Mean difference wall screen - Stevenson screen at Dombås test field as a function of cloud cover. Observation hours 18 and 19 in the season May - July. Regression lines without and with an extra screen on the wall.

At observation hours 18^h and 19^h at Dombås in the months May - July direct sunshine is possible at the wall. Results show that when it is overcast it does not matter whether an extra screen is mounted or not. If not overcast the wall screen is overheated as compared to the Stevenson screen, but the extra screen reduces the effect to about one half. Direct sunshine on a wall screen at Oksøy from 1883-1892 is documented by station history. Test results with SNHT applied on the 14^h observation leads to an adjustment of about 1°C in Jun.-Aug. which is in good agreement with results from the test field.

Relocations of the screens. One of the most frequent causes of inhomogeneities is relocations. On high latitude inversions are frequent during winter and consequently relocations which changes the height of the station above the valley floor are likely to cause inhomogeneities. Even elevation changes as small as 10 m may influence on the measurements of about 0.5 °C, (Nordli, 1995).

Changes of the environment near the screen. (buildings, trees or ground vegetation). These changes certainly influence the observations strongly for the observations at fixed hours and also the extremes. Often the changes have opposite signs for maximum and minimum temperature so that the change in the mean temperature is less pronounced, and may be difficult to discover when only mean temperature is tested.

The homogeneity testing is not completed. Some of the series may therefore be further adjusted. We expect those adjustments to be small and of minor importance for the results of the analyses.

2 CLIMATOLOGICAL ANALYSES OF THE SERIES

Three stations in the Arctic (Bjørnøya, Svalbard Airport and Jan Mayen) together with the stations plotted on the map comprising the Norwegian mainland are used in the analyses. Series with serious inhomogeneities and urban stations are avoided. The southern station Oksøy is situated at latitude 58°N and the northern station Svalbard Airport at 78°N.

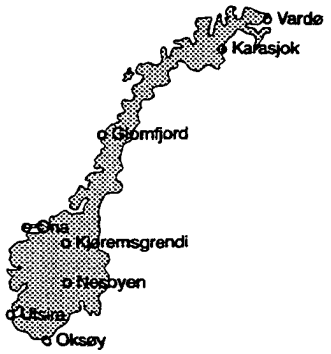


Fig. 3 The stations at the Norwegian mainland.

The correlations between some of the time series are shown in table 1 for individual years in the period 1922 - 1994. The chosen start year 1922

was the first year the three Arctic stations were in operation simultaneously.

Table 1 Correlation table, annual values.

	Oks.	Ona	Glom.	Var.	J.M.	Bjø.	Sva.
Oksøy	1.00	0.84	0.67	0.64	0.26	0.40	0.34
Ona	0.84	1.00	0.87	0.72	0.36	0.49	0.42
Glomfjord	0.67	0.87	1.00	0.78	0.50	0.57	0.50
Vardø	0.64	0.72	0.78	1.00	0.49	0.72	0.65
Jan Mayen	0.26	0.36	0.50	0.49	1.00	0.65	0.72
Bjørnøya	0.40	0.49	0.57	0.72	0.65	1.00	0.92
Svalbard	0.34	0.42	0.50	0.65	0.72	0.92	1.00

From table 1 it is seen that all series are positively correlated. Jan Mayen is poorly correlated with the rest of the series, not higher than 0.72 with any of them. From Glomfjord the distance is approx. the same to Oksøy, Vardø and Jan Mayen. Glomfjord is, however, better correlated with the two stations along the Norwegian coast than with Jan Mayen. This may be caused by the common path of winter cyclones moving along the Norwegian coast into the Barents sea so that Svalbard and the coastal stations of Norway often get the same air masses.

The series may be smoothed by a low pass filter including Gaussian weighting which is used on Fig. 4 for all stations. They are normalised to zero mean and unit standard deviation. All of them have cold spells in the 1960's and around 1980 and warm spells in the 1930's, 1970's and around 1990.

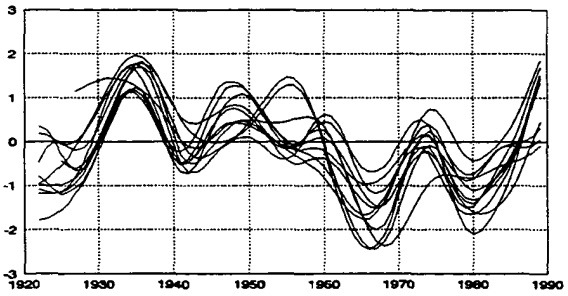


Fig. 4 Normalised annual Norwegian temperature series smoothed by a low pass filter.

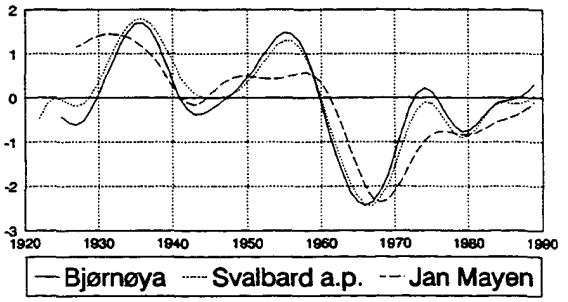


Fig. 5 Normalised annual temperature series from the Arctic smoothed by a low pass filter.

Three series in the Arctic are shown on Fig. 5. Bjørnøya and Svalbard are closely correlated. The main pattern of the series from the mainland are easily recognised in the two Arctic series. They have, however, maximum values in the 1950's which is not seen at the series from the mainland.

Many of the stations on the mainland started in the 1860's but the method used to calculate monthly mean temperature before the minimum thermometer was introduced in 1876 seems not to be satisfactory. In the present analyses data from before this year is therefore rejected.

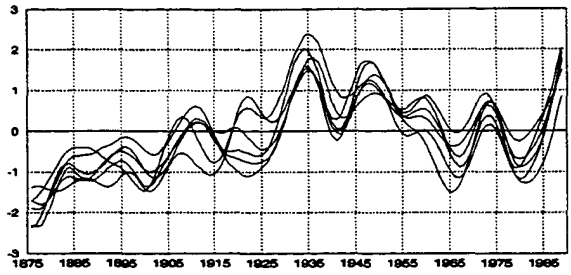


Fig. 6 Normalised annual Norwegian temperature series smoothed by a low pass filter.

All series reveal the well known increasing temperature trend from the start of the series to the 1930's. In the first part of the diagram the maxima and minima are less pronounced than in the last part. Around 1920 the northern series Vardø and Karasjok have maxima and the southern stations Oksøy and Utsira have minima. The two last ones have maxima 10 years earlier.

The Mann-Kendall trend test is applied to the series in two partly overlapping periods, 1876-1994 and 1922-1994 for annual and seasonal values, winter (Dec.-Feb.), spring (Mars-May), summer (June-Aug.), autumn (Sep.-Nov.). The results are shown in table 2.

Table 2 Mann-Kendall test for trend. The + sign denotes positive trend and the - sign negative. Not significant values (5 % level) are marked within brackets. The test comprise the periods 1876-1994 (first columns) and 1922-94 (second columns).

Series	Year		Winter		Spring		Summer		Autumn	
Oksøy	(+)	(+)	(+)	(+)	(+)	(+)	(-)	(-)	+	(+)
Utsira	+	(+)	(+)	(+)	+	(+)	(+)	(-)	+	(+)
Nesbyen		+		(+)	+	+		(-)		+
Kjøremsgrendi	+	+	(+)	(-)	+	+	(+)	(-)	+	+
Ona	+	(+)	(+)	(-)	+	(+)	+	(-)	+	(+)
Glomfjord		(-)		(-)		+		(-)		+
Karasjok	(+)	(-)	(-)	-	+	(+)	+	(-)	(+)	(+)
Vardø	+	(-)	(+)	(-)	+	+	+	(-)	+	+
Jan Mayen		-		-		(-)		-		(-)
Bjørnøya		(-)		-		+		(+)		+
Svalbard		(-)		-		+		(-)		+

For the entire period (1876-1994) the trends of the annual values are positive although not significant for all of them. This is true also in spring and autumn. In winter no series have significant trend. In summer there are significant positive trends in northern Norway and at the lighthouse station Ona.

For the period 1922-94 negative trends occur more frequently than during the entire period. In the Arctic and at Karasjok the trends are significantly negative during winter. Negative trends are found at Jan Mayen at all seasons although not significant in spring and autumn. Significant positive trends in the annual values are only found for the two stations around 62°N, Kjøremsgrendi and Ona.

The two stations Karasjok and Vardø are situated around 70°N. Vardø is an island outside the eastern tip of the Varanger peninsula and the maritime influence is consequently great. Karasjok on the other hand has continental climate, situated in the bottom of a valley, close to the Finnish border.

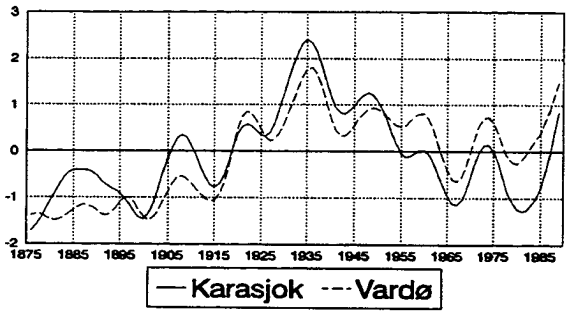


Fig. 7 Normalised annual temperature series of two stations near 70° N smoothed by a low pass filter.

Although high mutual correlation Karasjok seems to have been colder relative to Vardø in the second half of the series (Fig. 7). This makes the trend of the continental series (Karasjok) weaker than the maritime one (Vardø). At 62° N, however, the maritime station Ona and the continental station Kjøremsgrendi have almost the same trend (not shown at a diagram).

Principal component (PC) analysis is performed on the data set of annual values (1922-1994). The loadings are normalised to represent the correlations between the PCs and the original variables. Some results are shown in table 3.

The first PC explains 2/3 of the entire variance. From table 3 it is seen that all of the loadings have the same sign. The PC accounts for the general correlation between the stations over the entire area.

Table 3 Correlations between normalised annual temperature and the first four PCs. The stations are listed from south to north.

Station	1. PC	2. PC	3. PC	4. PC
Oksøy	0.87	-0.40	0.22	-0.02
Utsira	0.87	-0.40	0.13	0.08
Nesbyen	0.86	-0.34	0.29	-0.05
Kjøremsgrendi	0.90	-0.36	0.04	0.04
Ona	0.91	-0.23	-0.08	0.08
Glomfjord	0.89	0.00	-0.35	0.12
Karasjok	0.86	0.15	-0.39	-0.05
Vardø	0.87	0.20	-0.22	-0.25
Jan Myen	0.56	0.62	-0.12	0.52
Bjørnøya	0.71	0.60	0.19	-0.23
Svalbard A.p.	0.65	0.67	0.20	-0.13

The loadings of the second PC increases nearly monotonically in the table i.e. from south to north. Therefore the second PC is interpreted to account for the north-south variability in the data set. Adding this PC to the first one 85% of the entire variance is explained.

The third and four PCs explain 5 % and 4 % of the variance respectively which means that 94 % is explained by the first four PCs. After having removed the two first components the third one accounts for temperature anomalies in mid latitudes versus the areas to the north and south. Finally the fourth PC accounts for the contrast in the area between east and west. Thus Jan Mayen's load is heavy in this component.

REFERENCES

Alexandersson, H., 1986, "A homogeneity test applied to precipitation data" Journal of climatology, VOL 6, 661-675 (1986).

Demarée, G.R. and Derasse, Sl., 1993 (KMI), with co-operation of P.Ø.Nordli (DNMI), "Trend analysis of a stand-alone Norwegian temperature series". Proceedings from the Forth Nordic Climate Workshop, Reykjavik, Iceland. Edited by DMI, Copenhagen.

Nordli, P.Ø., 1994, "Adjustments of temperature time series in winter topoclimate. Results from the Dombås test field". DNMI-klima, report no 05/95. Oslo.

ACKNOWLEDGEMENTS

My colleague at DNMI Inger Hanssen-Bauer having performed the factor analysis is gratefully acknowledged.

CORRESPONDING AUTHOR

Per Øyvind Nordli
The Norwegian meteorological Institute
Box 43, Blindern, N-0313 OSLO, Norway.

ANALYSIS OF ANNUAL RAINFALL SERIES IN IVORY COAST IN ORDER TO DETECT CLIMATIC VARIATIONS

H. Lubès (1), J. E. Paturel (2), E. Servat (2), J. M. Masson (3), B. Kouamé (2)

(1) Orstom, Département des Eaux Continentales, Laboratoire d'hydrologie, B. P. 5045, 34032 Montpellier Cedex 1, France.
(2) Orstom, Département des Eaux Continentales, Antenne hydrologique, 06 B. P. 1203 Cidex 1, Abidjan 06, Côte d'Ivoire.
(3) Laboratoire Géofluides-Bassins-Eau, URA-CNRS 1765, Université Montpellier II, place Eugène Bataillon, 34095 Montpellier Cedex, France.

ABSTRACT

Countries around the Guinea Gulf seem to have undergone climatic variations since the beginning of the 1970's.
The objective of the research programme Iccare (Identification et Conséquences d'une variabilité du Climat en AfRique de l'ouest non sahElienne) is to identify these climatic changes by analyzing rainfall and hydrometric time series homogeneity.
This paper presents the results of graphical methods and statistical tests performed to study annual rainfall series in Ivory Coast. They conclude that a rainfall deficit has been occurring for the last twenty-five years in the country.

1. INTRODUCTION

Drought that has been rampant in West Africa for about twenty years often has tragic effects in sahelian countries. This situation explains and justifies why many researchers have been focusing their interest on these regions. However the more southern countries around the Guinea Gulf, too, seem to have undergone climatic variations over the same period of time. Changes in rainfall and flow regimes may negatively interfere with agriculture development projects and with the management of water resources even in these generally wet regions. Consequently studies must be undertaken to characterize these changes.

This paper presents the first steps and results of the research programme named Iccare (Identification et Conséquences d'une variabilité du Climat en AfRique de l'ouest non sahElienne) (Servat, 1994). This programme is part of the FRIEND-AOC Project, and attempts to identify an *a priori* change in rainfall and hydrometric time series in wet West Africa.

The different symptoms of a climatic change are studied. Has rainfall been decreasing since the beginning of the 1960's ? Have the isohyets been moving ? Is this change spatially uniform ? Has the rainy season been starting earlier or later ? Has the depth of precipitation over the year, undergone changes ?

The results presented here concern annual rainfall in Ivory Coast.

Climatic variations are generally pointed out using graphical approaches and statistical tests adapted to the study of time series homogeneity.

We present hereafter some applications of these various approaches.

2. DATA

Rainfall data are provided by the rainfall network of Ivory Coast. The oldest time series begin in 1920. Some rainfall stations are not taken into account because they were installed too recently, or they were removed too early, or they are not reliable enough (significant percentage of missing values).

Twenty-six annual rainfall series beginning before 1950 are statistically analyzed.

Data are considered to be reliable until at least 1980, having been checked by C. I. E. H (Comité Interafricain d'Etudes Hydrauliques), and Orstom up to then.

3. RAINFALL REGIMES IN IVORY COAST

The studied stations cover the whole country with non-uniform density. However they are able to represent the spatial variability of annual rainfall (see Figure 1). The mean annual precipitation varies between 2400 mm (extreme south-west) and 950 mm (extreme north-east). The shape of the interannual isohyets is a U which is bowed towards the north-east. Their axis is a line which crosses Ivory Coast through Tabou (station 2-1), Gagnoa (station 6-5) and the east of Béoumi (station 5-3) . Rainfall regularly decreases from the south-west to the north-east along this axis. It increases when going away from this axis towards the north-west as well as towards the south-east (Mott MacDonald, BCEOM, SOGREAH, Orstom, 1993).

Table 1. Classification of the stations

Station / Group	Period of observation	Identification in Figure 1
Group 1		
Abidjan	1938-1992	1-1
Adiaké	1945-1993	1-2
Lamé	1930-1984	1-3
Sassandra	1923-1993	1-4
Group 2		
Tabou	1935-1992	2-1
Group 3		
Man	1923-1992	3-1
Group 4		
Boundiali	1934-1992	4-1
Odienné	1933-1993	4-2
Group 5		
Abengourou	1920-1992	5-1
Agnibilékro	1945-1992	5-2
Béoumi	1940-1992	5-3
Bondoukou	1937-1980	5-4
Bongouanou	1948-1992	5-5
Bouna	1920-1980	5-6
Dimbokro	1922-1992	5-7
Katiola	1949-1991	5-8
M'Bahiakro	1945-1992	5-9
Group 6		
Adzopé	1945-1992	6-1
Bouaflé	1924-1992	6-2
Daloa	1920-1992	6-3
Divo	1946-1992	6-4
Gagnoa	1930-1993	6-5
Lakota	1945-1992	6-6
Oumé	1945-1992	6-7
Soubré	1940-1992	6-8
Tiassalé	1930-1982	6-9

A hierarchic classification procedure has been used to distribute the twenty-six series into six homogeneous groups. These groups correspond to the six commonly identified rainfall regimes in Ivory Coast, with respect to the amount of precipitation and to its seasonal distribution. This classification is presented in Table 1.

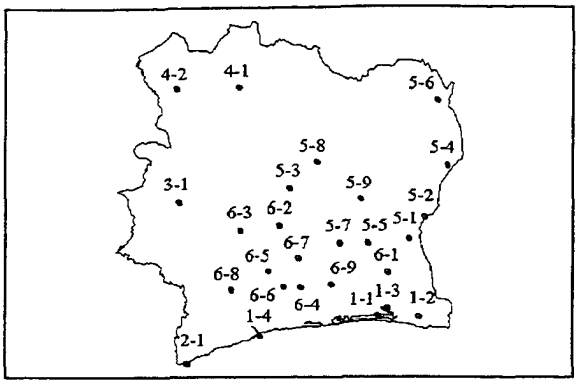


Figure 1. Location of rainfall stations in Ivory Coast

4. STATISTICAL PROCEDURES

Graphical methods are often used to give some insight into the homogeneity of time series. Some examples will be presented.

However it is always advisable to test the significance of departures from homogeneity by statistical methods. The different procedures used are briefly described in this section. They are drawn from the considerable amount of literature published on the general subject of the homogeneity of hydrological series (Lubès et *al.*, 1994). They have been previously applied in other geographic contexts.

In the following, (x_i), i=1, N is the studied time series, $\bar{x}$ is its mean.

Pettitt's test (1979), derived from Mann-Whitney's is based on the properties of a rank statistic. The null hypothesis is homogeneity of the series.
It is supposed that for any time t between 1 and N, the time series (x_i), i = 1, t and (x_i), i = t+1, N belong both to the same population.
The tested variable is the maximum absolute value of the variable $U_{t,N}$ for t between 1 and N-1 :

$$U_{t,N} = \sum_{i=1}^{t} \sum_{j=t+1}^{N} D_{ij}$$

with $D_{ij} = \mathrm{sgn}(x_i - x_j)$ and sgn(x) = 1 if x>0, 0 if x = 0, -1 if x<0.

If the null hypothesis is rejected, an estimate of the date of the change is given by the time t which provides the maximum absolute value of $U_{t,N}$.

Other tests, Statistic U (Buishand, 1982, 1984), Bayesian approach (Lee and Heghinian, 1977), amount to comparing means before and after an *a priori* supposed change. These tests are built on the following model :

$$x_i = \begin{cases} \mu + \varepsilon_i & i = 1,\ldots\ldots, \tau \\ \mu + \delta + \varepsilon_i & i = \tau+1,\ldots\ldots, N \end{cases}$$

The ε_i's are independent random normal variables with zero means and common unknown variance σ^2. Parameters τ, μ, δ et σ are unknown and independent.
$1 \le \tau \le N-1, -\infty < \mu < \infty, -\infty < \delta < \infty, \sigma > 0$.

τ and δ are the time point and the amount of shift respectively.
If an *a priori* uniform distribution is supposed for the shift time τ, Buishand 's U statistic is defined by :

$$U = \left[N(N+1)\right]^{-1} \sum_{k=1}^{N-1} \left(S_k^* / Dx\right)^2 \quad \text{with}$$

$$S_k^* = \sum_{i=1}^{k} (x_i - \bar{x}) \quad \text{for k = 1,....., N and}$$

$$Dx^2 = N^{-1} \sum_{i=1}^{N} \left(x_i - \bar{x}\right)^2$$

The null hypothesis is homogeneity of the series. If it is rejected, this test does not propose an estimate for the time point of shift.

Lee and Heghinian' Bayesian method yields an estimate of the *a posteriori* probability distribution of the time point of shift.
When the distribution is unimodal, the mode is an estimate of the time point of shift. All the more reliable is this estimate as the distribution dispersion is low.

Hubert's procedure (Hubert et *al*, 1989) of series segmentation deals with the detection of several change points of the mean value. A specific algorithm provides one or more time points of shift which divide the series into different segments. Scheffé's test (Dagnélie, 1975) checks that the means of adjacent segments are significantly different.

Finally a confidence ellipse is used to analyze homogeneity of the series (x_i).

According to the model already presented, if the null hypothesis is true, the variable S_k^* has a normal distribution with zero mean and a variance estimated by :

$$k(N-k)\left(N-1\right)^{-1} Dx^2, k = 0,\ldots\ldots, N$$

Consequently for a given confidence threshold, it is possible to define a confidence ellipse which includes the series S_k^* if the null hypothesis is true. If the series is partly outside the ellipse, a shift can be considered as significant for the chosen confidence threshold.

5. INTERANNUAL ISOHYETS AND RAINFALL INDEX ANALYSIS

The stations have been used to define the interannual isohyets by decade since 1950 (Kouamé et *al.*, 1994).
These graphs show that precipitation have been decreasing since 1970 over Ivory Coast. Figure 3 compares the decades 1950-59 and 1980-89.

Evolution of the 1200 mm isohyet shows that the zone receiving less than 1200 mm rainfall has been growing since the beginning of the 1970's. At the same time above 1700 mm zones have been narrowing. Nowadays the only region with such precipitation represents a narrow fringe close to Liberia.

To assess annual precipitation variations, Nicholson et *al.* (1988) defined a rainfall index. It is calculated every year over the 1950-1989 period by $\frac{x_i - \bar{x}}{s}$.

x_i is the precipitation for the ith year, $\bar{x}$ and s are the mean rainfall and the standard deviation over the 1950-1989 period, respectively.

Graphs of interannual rainfall indices conclude that rainfall has been decreasing since 1970 and more considerably since 1980. The Atlantic coast and the north, north-west part of the country are especially hit by the rainfall deficit. Figure 4 shows the maps for the decades 1950-59 and 1980-89.

6. RESULTS OF STATISTICAL PROCEDURES

Tests for detecting a shift in annual rainfall series have been used. The results are analyzed considering a regional point of view.

Table 2 presents the results. A shift is considered as a significant change in the mean of the series detected by all the procedures. When a change is not detected by all the procedures, it is called a "deviation".

The conclusions are the same as those of the graphical analyses with some more details.

A shift in the series mean has been detected in all regions excepted in the eastern part north of Bongouanou-Abengourou where rainfall is the lowest in Ivory Coast, and around Tabou in the south-west where rainfall is the highest in the country. In group 5 three stations only show a shift : Béoumi, Dimbokro and Katiola (see Table 1). In fact, these stations are close to the sixth zone where a general shift has been detected.

The shifts occurred at different time points, in the beginning of the 1960's at Béoumi for example, around the year 1980 at Abidjan, Adiaké and Odienné. Generally speaking they have been located from 1968 to 1975. This is in accordance with studies on sahelian regions.

A more definite conclusion is that a shift of the annual rainfall regime can clearly be identified. The dates of shift and the percentages of deficit with regard to the mean must be cautiously considered because they are not independent of the series duration.

Table 2. Results of statistical procedures

Station / Group	Time point of shift	Deficit expressed in % with regard to the mean before shift
Group 1		
Abidjan	1982	22
Adiaké	1982	25
Lamé	1968	24
Sassandra	1971	18
Group 2		
Tabou	no shift	
Group 3		
Man	1966 (deviation)	13
Group 4		
Boundiali	1975	20
Odienné	1979-1982	23
Group 5		
Abengourou	no shift	
Agnibilékro	no shift	
Béoumi	1963-1964	15
Bondoukou	no shift	
Bongouanou	no shift	
Bouna	no shift	
Dimbokro	1968	13
Katiola	1968	22
M'Bahiakro	no shift	
Group 6		
Adzopé	1968	15
Bouaflé	1972	18
Daloa	1971	16
Divo	1972	18
Gagnoa	1966	12
Lakota	1970	25
Oumé	1976-1979	17
Soubré	1970	21
Tiassalé	1969 (deviation)	17

7. STUDY OF VERY LONG TIME SERIES

The longest series (more than six decades) provide information on the intrinsic variability of the time series variable.
The shift that has previously been identified in these series can then be compared to other changes that occurred in the past.
Consequently the time series of rainfall indices can be used to define wet and dry periods according to the positive or negative values of the index, respectively. These values are considered to be significant with regard to the confidence interval of the mean at 95%. Each period is characterized by its duration and by a value taken as a linear combination of the annual indices, thereby representing the relative impact of the wet or dry period. All periods of the same type, i.e. wet or dry, can be compared by making a plot of impact indices against durations for this particular type.

Figure 2 shows the dry periods of the annual precipitation series of Bouaflé. Data begin in 1924. It can be observed that the last dry periods (since around 1970) are both the longest and the most severe at this station.
Since 1973, only years 1980 and 1985 have a positive index.
Before 1970 wet and dry periods generally lasted less than 3 years and followed one another.

Consequently the current deficit can be considered to be peculiar.

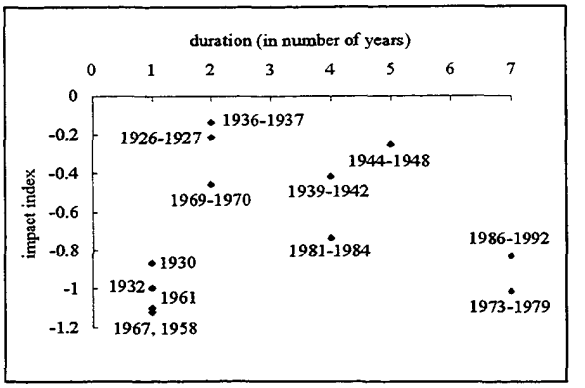


Figure 2. Dry periods of the annual precipitation series of Bouaflé

8. CONCLUSION

This study deals with annual rainfall series at different stations in Ivory Coast.

Graphics and statistical tests conclude that a rainfall deficit has been occurring for the last twenty-five years in 80% of the country. Most of the series reveal a change of mean between 1968 and 1975. These results are consistent with studies concerning sahelian regions.
The other countries of the Guinea Gulf, Ghana, Togo, Benin, are being studied in the same way. A first analysis of the interannual isohyets and indices graphs by decade already reveal that the rainfall deficit has been extending in these countries since the beginning of the 1970's. The same kind of studies will be conducted in the other countries of non-sahelian West Africa. They will confirm or not the climatic variability hypothesis with a large geographic extent in this part of Africa.

REFERENCES

Buishand, T.A. , 1982, "Some methods for testing the homogeneity of rainfall records", *Jour. of Hydrol.*, Volume 58, pp. 11-27.

Buishand, T. A. , 1984, "Tests for detecting a shift in the mean of hydrological time series", *Jour. of Hydrol.*, Volume 73, pp. 51-69.

Dagnélie, P. , 1975, *"Analyse statistique à plusieurs variables"*, Presses agronomiques de Gembloux, 362 pages.

Hubert, P. , Carbonnel, J. P. , 1987, "Approche statistique de l'aridification de l'Afrique de l'Ouest", *Jour. of Hydrol.*, Volume 95, pp. 165-183.

Hubert, P. , Carbonnel, J. P. , Chaouche, A. , 1989, "Segmentation des séries hydrométéorologiques. Application à des séries de précipitations et de débits de l'Afrique de l'ouest", *Jour. of Hydrol.*, Volume 110, pp. 349-367.

Hubert, P. , Carbonnel, J. P. , 1993, "Segmentation des séries annuelles de débits de grands fleuves africains", Bulletin de liaison du CIEH, No. 92, pp. 3-10.

Kouamé, B. , Paturel, J. E. , Servat, E. , Boyer, J. F. , Lubès, H. Masson, J. M. , 1994, "Inventaire des données. Pré-traitement pour la Côte d'Ivoire, le Togo et le Bénin", Programme Iccare, Report. No. 2. Orstom, 62 pages.

Lee, A. F. S. , Heghinian, S. M. , 1977, "A shift of the mean level in a sequence of independent normal random variables - A bayesian approach.", *Technometrics*, Volume. 19, No. 4, pp. 503-506.

Lubès, H. , Masson, J. M. , Servat, E. , Paturel, J. E. , Kouamé, B. , Boyer, J. F. , 1994, "Caractérisation de fluctuations dans une série chronologique par application de tests statistiques. Etude bibliographique", Programme Iccare, Report. No. 3. Orstom, 21 pages.

Mott MacDonald, BCEOM, SOGREAH, Orstom, 1993, "Evaluation hydrologique de l'Afrique Sub-Saharienne. Pays de l'Afrique de l'Ouest. Rapport de pays : Côte d'Ivoire", 232 pages.

Nicholson, S. E. , Kim, J. , Hoopingarner, J. , 1988, "Atlas of African Rainfall and its Interannual Variability", Department of Meteorology, Florida State University Tallahassee, Florida.

Pettitt, A. N. , 1979, "A non-parametric approach to the change-point problem", *Applied Statistics*, Volume.28, No. 2, pp. 126-135.

Servat, E. , 1994, "Iccare, Identification et Conséquences d'une variabilité du Climat en AfRique de l'ouest non sahElienne, Présentation du programme", Programme Iccare, Report No. 1 Orstom, 23 pages.

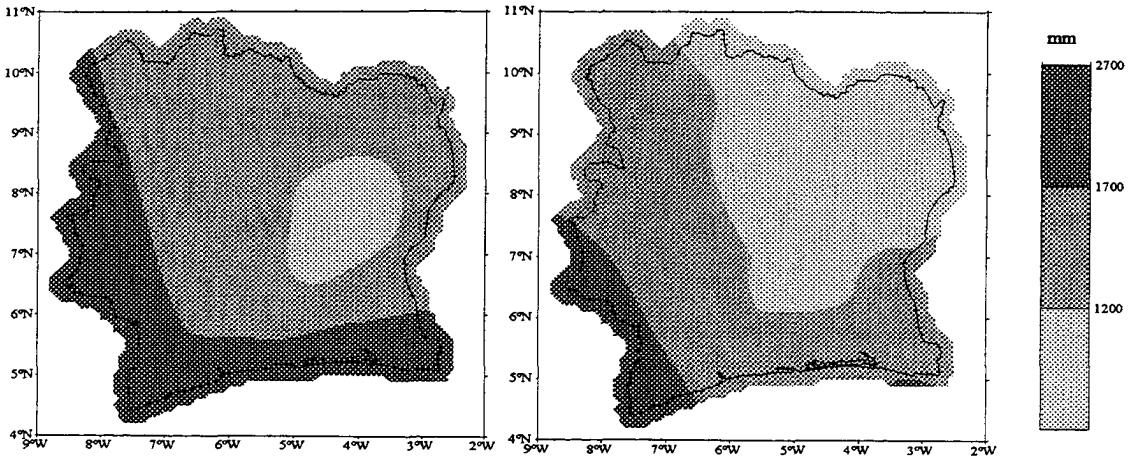


Figure 3. Interannual isohyets over the decades 1950-59 (left) and 1980-89 (right)

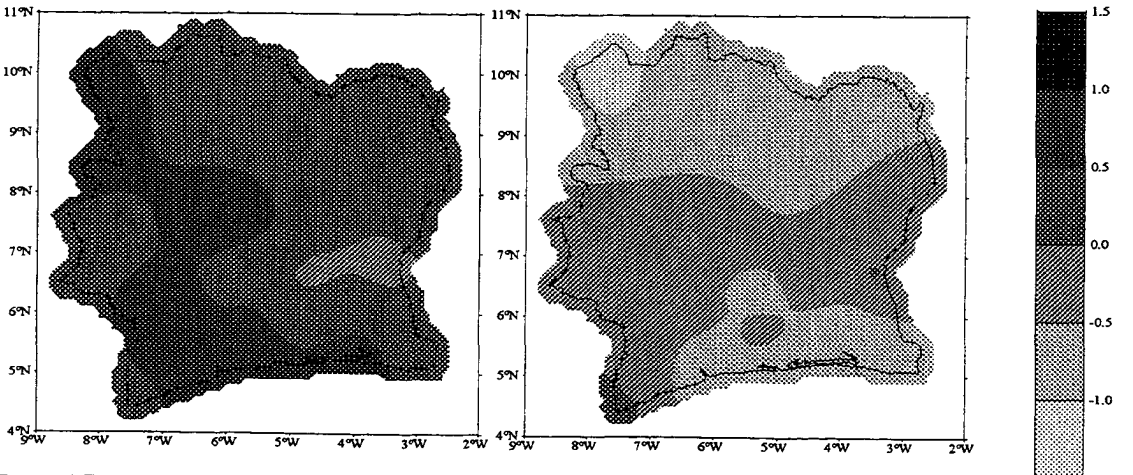


Figure 4. Interannual rainfall indices over the decades 1950-59 (left) and 1980-89 (right)

CORRESPONDING AUTHOR
Mme Hélène Lubès
Orstom
B. P. 5045, 34032 Montpellier Cedex 1, France.

TRENDS OF MAXIMUM AND MINIMUM TEMPERATURES IN NORTHERN SOUTH AMERICA (VENEZUELA AND COLOMBIA) DURING THE PERIOD 1918-1990. HOMOGENEITY TEST.

RAMON A. QUINTANA-GOMEZ

UNIVERSIDAD NACIONAL EXPERIMENTAL DE LOS LLANOS "EZEQUIEL ZAMORA", BARINAS, EDO. BARINAS, VENEZUELA.

ABSTRACT

This research first tested the homogeneity of the temperature data of the climatological stations' longest records of Venezuela and Colombia. Second, evaluated the trends and deviations of maximum and minimum temperatures and diurnal thermal ranges (DTR) during the period 1918-1990. Eleven stations, the ones with less inhomogeneities, after applying the Alexandersson homogeneity test (1986), were selected for minor and partial data adjustments (according to Easterling and Peterson, 1994). The temperature and DTR deviations were examined. The most remarkable feature is a sustained increase of the minimum and DTR partial series during the last 25 years of the period.

1 INTRODUCTION

Before attempting to start any climate research on temperature and its fluctuations in time and space, especially when it is dealing with deviations and 'anomalies', it is very important to have access to reliable data which are free form artificial trends or changes.

In order to obtain the best results, the time series being analyzed must be homogeneous (trends and variations caused only by effects of weather and climate). One of the most effective way of checking the reliability of a climate series is to compare it with surrounding stations' data (Alexandersson, 1986, Easterling and Peterson, 1994).

The study tested the homogeneity of the basic information provided, the mean monthly maximum and minimum temperature and DTR series of the climatological stations with the longest and continuous data in venezuela and Colombia. After this, the fluctuations and 'anomalies' of these parameters were evaluated during the period 1918-1990 in northernmost South America.

2 DATA AND METHODS OF ANALYSIS

For the period 1918-1990, a group of 14 long-term stations in Venezuela (9) and Colombia (5), all with less than 10% missing monthly temperature data and available metadata were first preselected to be tested for homogeneity. It was used the test developed by Alexandersson (1986) which locates basically where (and when) an inhomogeneity occurs and whether the change is significant. However, not all discontinuities were detected through this test, others were located with the stations' metadata (also used to verify the Alexandersson's) and through examinations of decadal data series arrays and application of the t-test for statistical significance.

3 RESULTS

Eleven stations, the ones with less inhomogeneities, 6 in Venezuela and 5 in Colombia, were finally selected for partial data adjustments. These stations are shown in Fig 1.

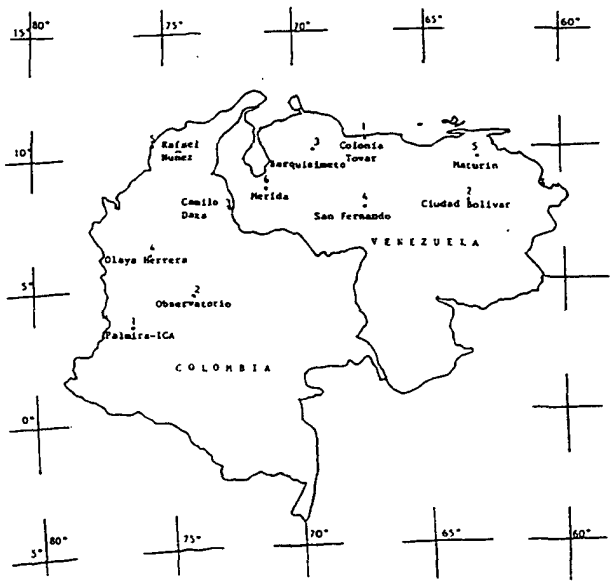


Figure 1. The eleven climatological stations with relatively homogeneous temperature data.

The adjustments of the discontinuities were made following the technique developed by Easterling and Peterson (1994), which is basically adding (or substracting) the difference between two means to (or from) each value of the original candidate partial series being tested before (or after) the 'break' point. After this, the variations and fluctuations of maximum and minimum temperatures and diurnal thermal ranges (DTR) were examined for the period under study. Before defining a procedure for extracting temperature change from measurements for large areas, it is important to have a quantitative measure of the size of the surrounding area for which a given station's data may provide significant information on temperature change. Therefore, it was computed the correlation coefficient between the temperature variations for all pairs of the selected stations having at least fifty common years in the whole area. A procedure similar to the one used by Hansen and Lebedeff (1987) on a global scale and Gaffin (1994) who focused his research on Texas, USA. The results are presented in Table 1 for Venezuela and Colombia, separately and Table 2, for both countries togheter, and Fig. 2.

Table 1. Correlation coefficients between annual DTR variations for station pairs with at least fifty common years of records. The station pair common (years) is shown in parentheses.

VENEZUELA	Correlation Coefficients					
	Col. Tovar	C. Bolivar	Barquisimeto	S. Fernando	Maturin	Merida
Col. Tovar	/	0.68	0.84	0.88	0.91	0.88
C. Bolivar	500,(32)	/	0.48	0.57	0.71	0.71
Barquisimeto	220,(52)	670,(48)	/	0.81	0.80	0.80
S. Fernando	290,(49)	450,(49)	310,(49)	/	0.89	0.92
Maturin	470,(46)	190,(46)	670,(46)	320,(46)	/	0.85
Merida	470,(51)	850,(51)	260,(47)	410,(48)	890,(45)	/

COLOMBIA	Correlation Coefficients					
	Palmira-ICA	Observatorio	Camilo Daza	Olaya Herrera	Rafael Nunez	
Palmira-ICA	/	0.48	0.42	0.33	0.59	
Observatorio	270,(48)	/	0.51	0.59	0.49	
Camilo Daza	650,(37)	410,(38)	/	0.75	0.77	
Olaya Herrera	310,(42)	240,(41)	390,(39)	/	0.56	
Rafael Nunez	790,(36)	660,(39)	440,(37)	470,(37)	/	

Separation Distance in Km. (Common Part in Years)

Table 2. Same as Table 1 but for Venezuela and Colombia togheter. The straight separation between stations (in km.) is shown in boxes.

VENEZUELA —— COLOMBIA					
	Col. Tovar	C. Bolivar	Barquisimeto	S. Fernando	Maturin	Merida
Palmira-ICA	0.73(51) [1250]	0.40(50) [1510]	0.75(47) [1060]	0.71(45) [1090]	0.69(42) [1610]	0.75(50) [800]
Observatorio	0.33(46) [990]	0.17(51) [1230]	0.36(45) [800]	0.22(41) [820]	0.15(41) [1330]	0.40(51) [560]
Camilo Daza	0.03(42) [630]	-0.25(40) [990]	0.20(42) [430]	-0.25(39) [560]	-0.01(38) [1050]	-0.06(39) [170]
Olaya Herrera	-0.03(44) [1020]	-0.27(41) [1340]	0.07(43) [820]	-0.05(41) [920]	-0.06(40) [1420]	0.09(40) [560]
Rafael Nunez	0.34(41) [900]	0.11(38) [1350]	0.30(40) [700]	0.07(38) [930]	0.24(37) [1360]	0.17(38) [530]

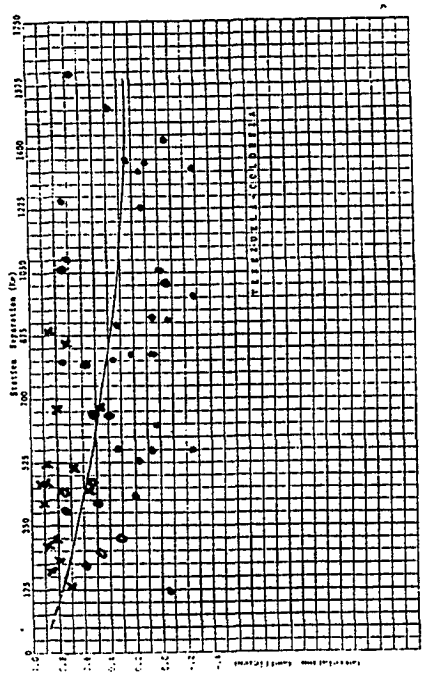


Figure 2. Correlation between annual DTR deviations for each station pair. A **x** is for Venezuela, a **o** for Colombia, and a **•** for both countries.

There exists a noticeably high correlations of the temperature variations among each country's stations data, especially observed in Venezuela. This is considered significant for purposes of evaluating thermal deviations and anomalies in the region. Analyzing the complete trends of maximum and minimum temperature and DTR series of the eleven stations during the period 1918-1990, it is observed that the minimum temperature series of all stations show a sustained increase during the last 25 years of the period (1966-1990). See Fig. 3 and 4. This increase proved to be statistically significant in almost all stations, and so was the DTR decrease, especially at the Colombian stations (Table 3). On the other hand, 8 stations exhibit a decrease of the maximum temperatures during the lapse 1966-1990. See also Fig. 3 and 4. But these results are not as significant as the minimum and DTR trends.

4 RESULTS DISCUSSION AND CONCLUSIONS

Using the Alexandersson test in conjuction with the station's metadata proved to be the most effective way to detect data discontinuities and inhomogeneities. Some particular inhomogeneities (Venezuela) not detected through the Alexandersson test and revealed from the metadata were 'handled' with the t-test. When adjusting discontinuous values detected from both the Alexandersson's and t-test, the procedure was simply adding or substracting the differences between two means to or from each value of the original candidate partial series before or after the break point. But it is possible that while adjusting the discontinuous values, which might be mathematically correct, there was a possibility of introducing physical inconsistences in the records. Thus, it is not realistic to expect that the adjusted (or unadjusted) series would represent the real conditions at each individual station.

Examining the temperature variations in both countries represented by the 11 stations, it is interesting to notice the high correlation among all the stations, especially in Venezuela (averaged 0.80). This is statistically significant for purposes of evaluating thermal fluctuations and anomalies in this region.The minimum temperature series of all the stations show an increase statistically significant starting by the middle of decade of 1960, throughout the end of the series in 1990. This relative warming is not easily explained. There are several possible factors that influence the minimum temperature to increase and the DTR reduce, i.e., the cloud cover, aerosols, and greenhouse gases which have been observed to increaese in many areas on earth also might have been affecting the northernmost South America.

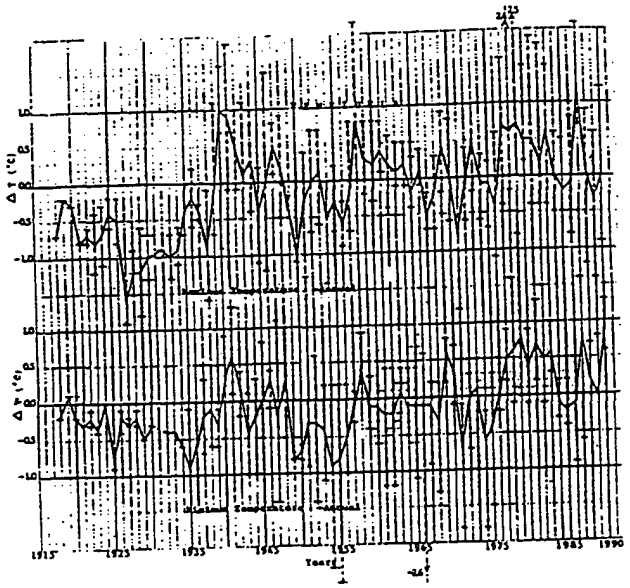


Figure 3. Time series of the variations of the maximum and minimum temperatures for Venezuela.

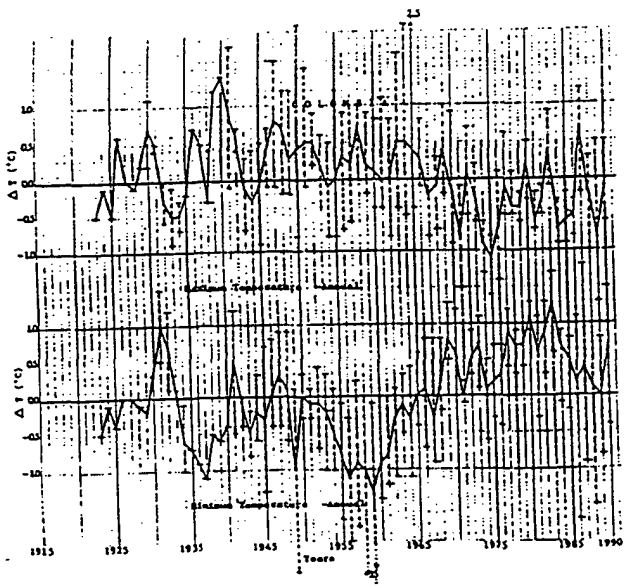


Figure 4. Same as Fig.3. but for Colombia.

References

Alexandersson, H., 1986 : A homogeneity test applied to precipitation data. J. Climatol., Vol. 6, pp. 661-675.

Easterling, D. R. and T. C. Peterson, 1994 : A new method for detecting and adjusting for undocumented discontinuities in climatological time series. Sith Conference on Climate Variations, January 23-28, 1994, Nashville, TN, USA.

Gaffin, D. M., 1994 : Comparison of point and areal estimates of temporal fluctuations of climatic elements: A case study for Texas. MS Thesis, Dept. of Meteorology of Texas A&M University, 115 pp.

Hansen, J. and S. Lebedeff, 1987 : Global trends of measured surface air temperatures. J. of Geoph. Res., Vol. 92, NO. D11, pp. 13,345 - 13,372.

ACKNOWLEDGEMENTS

The author thanks the Dept. of Meteorology of Texas A&M University for giving him the opportunity and facilities to carry out this research. This gratitude goes in special way to Prof. John F. Griffiths, a great and valuable friend for his worthy advisory, suggestion, and comments regarding this and other previous works.

CHANGES IN THE WINTER PRECIPITATION IN ROMANIA INDUCED BY CHANGES IN THE LARGE SCALE CIRCULATION

Aristiţa Busuioc

National Institute of Meteorology and Hydrology, Bucharest, Romania

ABSTRACT

The link between Romanian precipitation and large-scale circulation (represented by sea level pressure field) is studied with the Canonical Correlation Analysis (CCA). Then the "change-points" in the time series associated to the first two CCA pairs are detected by using the Pettitt's statistic.

The simultaneous and physically plausible "change-points" have been found in both parameters: an upward shift around 1933 and a downward shift around 1969 are related to a change of the southwesterly flow which brings moist Mediterranean air to Romania; the downward shift in the mid 1920s is related to a change of the northwesterly flow.

1 INTRODUCTION

The study of the climate variability is important for many reasons. The users from agriculture and hydrology require in formation about the range of the natural climate variability. To understand why some changes in the climate variability occur, it is essential to consider the atmospheric dynamics, as well as the local physical processes. The atmospheric circulation is the main forcing for the regional variability of wind, temperature, precipitation and other climatic variables.

In this paper the variability in the winter Romanian precipitation in connection with the variability in the atmospheric circulation on the European scale is studied. The Pettitt's statistic is used to detect the changes of the mean and variance of the analysed series. Pettitt (1979) has presented in detail this statistic which detects only the changes in the mean. Following the suggestion given by Sneyers (1975) for the Mann-Kendall's test, the Pettitt's statistic has been used to detect the change in the variance too (see Section 2). Busuioc and von Storch (1995) have shown that the performance of the test is highly sensitive to the presence of the serial correlation and linear trend in the time series. If the problem of the serial correlation can be solved by "prewhitening" the time series, the trend-problem is not so simple; the substraction of the estimated trend seems to reduce the power of the test in such a manner that the test becames useless. Therefore , the Pettitt's statistic is used not as a confirmatory tool but only as an exploratory tool to identify possible change points without attempting to make any probability statements.

The relationship between the Romanian precipitation and large-scale circulation is studied with the Canonical Correletion Analysis (CCA). As a parameter to represent the large-scale circulation we use the seasonal mean sea level pressure (SLP) field at the European scale. Then the time series associated to the most significant CCA pairs of precipitation and SLP to detect "change-points" in the both time series have been analysed.

2 DATA AND METHODS

The data used in this paper are the time series of the winter seasonal precipitation amount at the 14 Romanian stations and seasonaly mean sea level pressure (SLP) over 1901-1988 interval during the winter season (December to February). For the SLP the area between 30°N - 55°N and 5°E - 50° E was selected. The monthly SLP data have been taken from the National Center for Atmospheric Research (USA) with a resolution of $5^0 \times 5^0$. For both parameters the anomalies have been computed by subtracting the long term seasonal mean from the original values. Only a brief description about the mathematical methods used in the paper is presented in this section.

The CCA is a tool to find out linear relationships between two space-time dependent variables (e.g.,Barnett and Preisend orfer, 1987; von Storch, 1985). The CCA selects a pair of spatial patterns of two space-time dependent variables so that their time coefficients are optimally correlated. Since the coefficients are normalized to unity, the canonical correlation patterns represent the typical strength of the signal. Thus, the coefficients may be seen as time series of weights which describe the strenght and the sign of the patterns for each realization in time.

Prior to the CCA, the original data are projected onto their empirical orthogonal functions (EOFs) and only a limited number of them are retained, explaining most of the total variance. This also serves as a data-filtering procedure to eliminate noise (although it can exclude potentially useful information). Note that the canonical correlation are overestimated when derived from a finite sample (e.g., von Storch, 1995).

The Pettitt's statistic is a non-parametric technique to approach the change-point at the level of the time series. More details are given by Pettitt (1979), Sneyers (1975), Busuioc and von Storch (1995). Mainly, this test is sensitive only to change in the time series mean.

To detect the change of the variance, in this paper the original time series are transformed into absolute anomalies relative to the long term mean and then the Pettitt's test is applied. This result has been proved by means Monte-Carlo experiments.

The performance of the test is highly affected by the linear trend and serial correlation of the analysed series. The serial correlation can be filtered by a "prewhitening". All Pettitt's statistics used bellow are calculated from such prewhitened time series. For the trend-problem a cure is not possible to be offered; the subtraction of the estimated trend seems to reduce the power of the test in such a manner that the test becames useless. More details about this problem are presented by Busuioc and von Storch (1995). Therefore, the Pettitt's statistic has been used only as an exploratory tool to identify possible change-points without attempting to make any probability statement (such as the risk of rejecting the null hypothesis of no change-point).

3 RESULTS

The changes in the winter Romanian precipitation and SLP fields are discussed in several steps. First, the individual time series of winter mean precipitation at 14 locations are examined. Next, EOFs for precipitation and the European pressure distribution are derived and their coefficient time series are analysed with respect to change points. Finally, the CCA of precipitation and pressure is done and the coefficient time series associated to the first two significant CCA pairs are analysed to detect the simultaneous change points.

3.1 Trends and change-points in the Romanian precipitationrecords

The trend of the winter precipitation in Romania during the 1901-1988 interval is presented in Table 1 (first column). As on average over the country the precipitation is increasing by

Table 1: Trends (mm/season/100 years), change points (year; an ↑ represents an upward shift and a ↓ a downward shift) over the compet interval 1901-1988 and the sub-interval 1935-1988 for the winter precipitation in Romania.

Stations	trend	1901-1988 change-point	1935-1988 change-point
Ocna Sugatag	22	1939 ↑	1969 ↓
Baia Mare	-33	1923 ↓	1967 ↓
Bistrita	25	1955 ↑	1954 ↑
Brasov	-31	1969 ↓	1969 ↓
Sibiu	11	1918 ↑	1970 ↓
Timisoara	16	1949 ↑	1948 ↑
Tr. Severin	58	1933 ↑	1970 ↓
Tg. Jiu	67	1933 ↑	1969 ↓
Bucuresti	56	1919 ↑	1969 ↓
Calarasi	-5	1969 ↓	1969 ↓
Sulina	-4	1970 ↓	1970 ↓
Constanta	20	1951 ↑	1969 ↓
Roman	-30	1970 ↓	1969 ↓
Iasi	17	1930 ↑	1969 ↓

17 mm/100 years. At nine stations the amount of precipitation has increased and at five the amounts have decreased.

Pettitt's statistics derived from all original anomalies, indicates upward change-points in the early 1930s and downward change-points around 1969/1970 for several stations (Table 1, second column). The Pettitt's statistic calculated only for the time after the first change-point exhibits a downward shift around 1969/1970 for almost all stations (Table 1, 3rd column).

The Pettitt's statistics derived from the absolute anomalies do not indicate significance change in the variance.

3.2 EOFs of the Romanian precipitation and Central European SLP

The first EOFs for the winter Romanian precipitation and SLP have been computed from the full data set 1901-1988. These patterns show the main spatial features of the two analysed variables and their coefficient time series describe the dominant variability in the data sets.

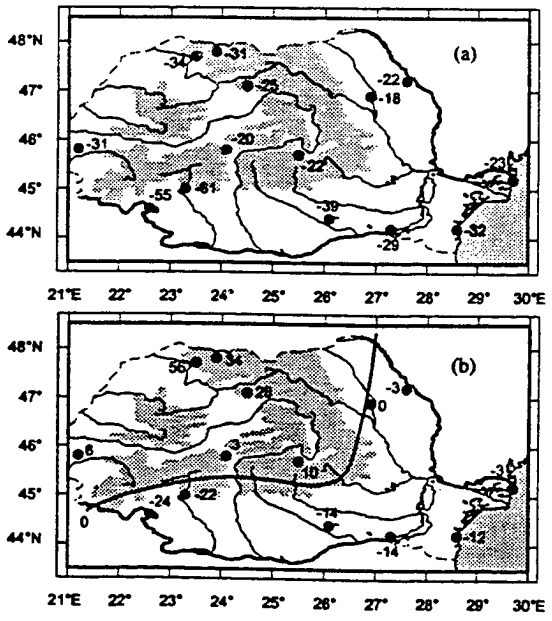


Figure 1. The patterns of the first (a) and second (b) EOFs for the winter Romanian precipitation (1901-1988). The coefficients are normalized to one so that the patterns represent typical dimensional distributions (in mm). From Busuioc and von Storch (1995).

The first two EOFs for the Romanian precipitation are shown in Figure 1. The first EOF explains 48% of the total variance and has the same sign over the entire area with the highest values in the southwestern part and decreasing to the northeast. This pattern suggests that in spite of the highly irregular topography of the region, there is a common physical process dominating the winter precipitation variability and this process could be linked to large-scale processes. We will return to this aspect bellow. The second EOF (20% explained variance) has a dipol structure, the positive and negative values being separated by a line which follows almost exactly the Carpathian topography. This pattern suggest the influence of the Carpathian (especially in the higher southern part) on the precipitation variability.

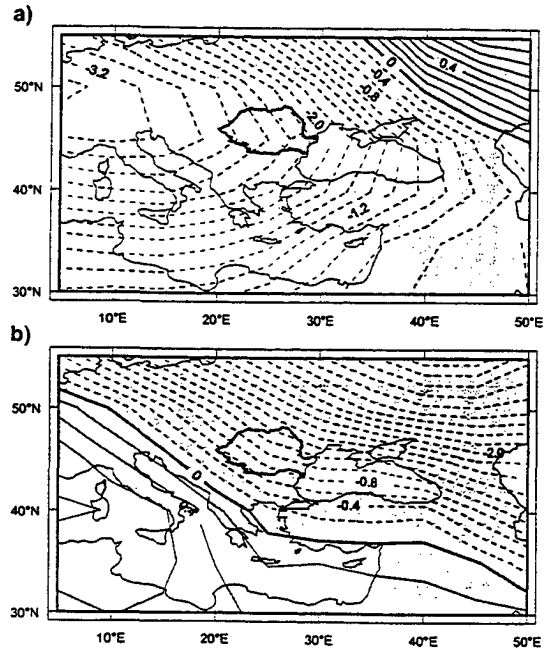


Figure 2. The patterns of the first (a) and second (b) EOFs for the winter SLP (1901-1988). Continous lines mark positive values, and dashed lines negative values (contour interval of 0.2 hPa). From Busuioc and von Storch (1995).

The first two SLP EOFs explaining 45% and 33% of the total variance are presented in Figure 2. The first EOF shows a large anomaly area with the same sign and the second EOF shows a dipole structure with the gradient oriented from northeast to southwest.

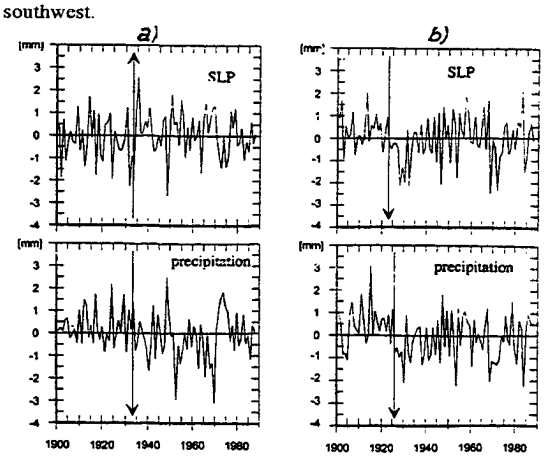


Figure 3. Coefficient time series of the first (a) and second (b) EOFs of the winter mean SLP and total winter Romanian precipitation. The change-point is marked. From Busuioc and von Storch (1995).

The coefficient time series of the first two EOFs of SLP and Romanian precipitation are presented in figure 3. The Pettitt's statistic signals the presence of a downward shift in the precipitation-related first EOF coefficient and an upward shift in the first SLP EOF coefficient around 1933. The Pettitt's statistic also offers some evidence that there might be a secondary change point around 1969/1970. The 2nd EOF coefficient time series of precipitation and SLP have also joint downward change-points (1923 for SLP and 1926 for precipitation).
Considering the EOFs patterns of the two parameters (Figures 1 and 2) these quasisynchronous change-points seem to be dynamically consistent and indicate a possible link between them. The coefficient time series of the first SLP EOF was before 1933 on average negative so that the rain-bringing southwesterly circulation over Romania was less frequent. Consistently the first EOF coefficient of precipitation was on average positive so that less precipitation, with maximum deficits at the southwesterly flank of the Carpathians, was observed (Figure 1a). Between 1934 and 1969 the situation was reversed, and after 1969 the southweterly circulation became again less frequent. A similar interpretation is suggested by the patterns of the second pair of EOFs with less rainfall in the extra-Carpathian region (Figure 1b). The intensity and/or frequency of the northwesterly circulation which mainly affects the intra-Carpathian region changed in the mid 1920s.

3.3 Link between Romanian precipitation and large-scale circulation

The link between simultaneous variability of the two parameters is giving by CCA analysis. The first 6 EOFs for the SLP and 5 EOFs for the Romanian precipitation have been retained for the CCA.

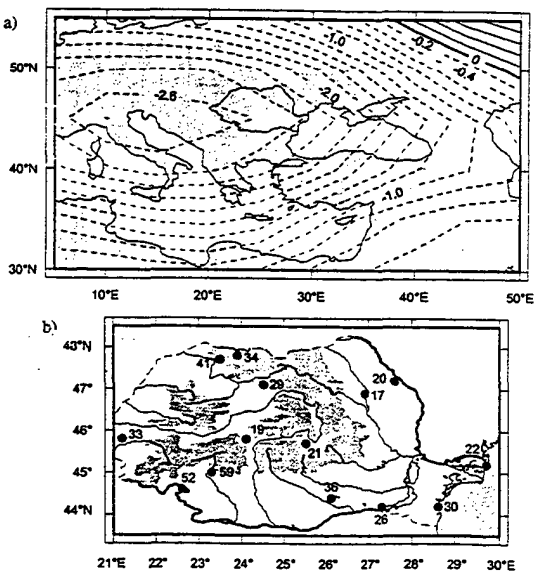


Figure 4. The patterns of the first canonical pair of the winter mean SLP (contour interval of 0.2 hPa) and total winter Romanian precipitation (contour interval of 5 mm). Continous lines mark positive values, and dashed linews negative values. From Busuioc and von Storch (1995).

The first CCA pair exhibits a correlation between the precipitation and SLP coefficient time series of 0.84. They explain 35% of the total seasonal mean SLP variance and 47% of the total precipitation variance. The patterns (Figure 4) are similar to the first EOFs for both variables (Figures 1a and 2a) and represent a link that is very reasonable from the physical point of view. Low pressure over Europe and the Mediterranean basin guides maritime air and precipitating weather systems into Romania, so that above normal precipitation is recorded. The maximum values of nearly 59 mm are in the southwest and the minimum values of 17 mm in the northeast that shows the orographic perturbation effect of the Carpathian mountains.

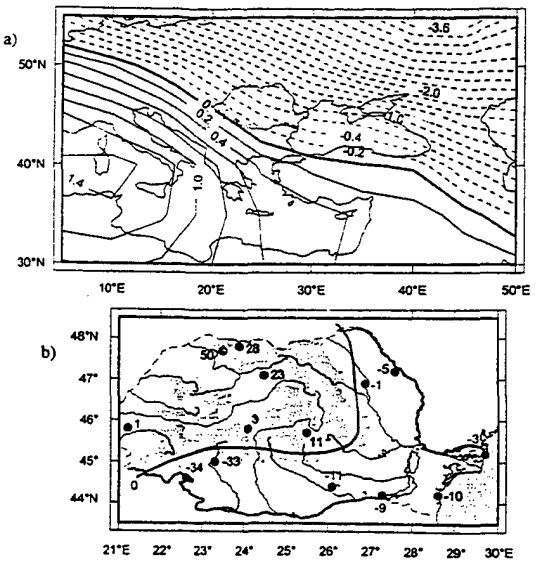


Figure 5. The patterns of the second canonical pair of the winter mean SLP (contour interval of 0.2 hPa) and total winter Romanian precipitation (contour of 5 mm). Continous lines mark positive values, and dashed lines negative values. From Busuioc and von Storch (1995).

The second CCA (0.65 correlation) explains 31% of the total SLP variance and 20% of the total precipitation variance. The patterns (Figure 5) are similar to the second EOFs for both variables (Figure 1b and 2b). Again a physically plausible link is suggested by the patterns. The SLP pattern describes a northwesterly flow that affects mostly the intra-Carpathian region where the positive precipitation anomalies are emphasized, the highest being in the northwest.

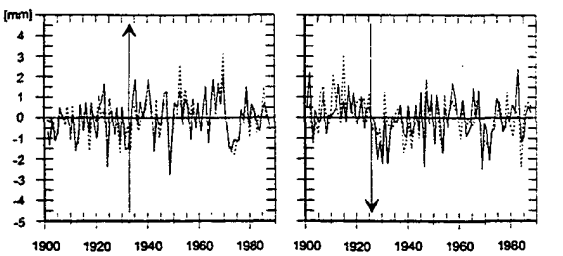


Figure 6. Normalized time components of the first (a) and second (b) CCA patterns of SLP anomalies (continous line) and Romanian precipitation (dashed line).

In Figure 6a the time coefficients of the first CCA pair are shown. The year-to year variation are highly coherent. Both curves have an upward change-point around 1933. The change is strong and now we can assert that changes in the Romanian winter precipitation are due to changes in the large scale circulation. This phenomenon is very clear for the southwestern stations which are controlled by the first CCA. An upward change-point around 1919 for Bucuresti (Bucharest) station is possibly caused by the local process of urbanization.
A secondary downward change-point around 1969 is signalled by the Pettitt's statistic when the time interval is limited to 1935-1988. This secondary change-point is again consistent with the analysis of the individual precipitation time series (Table 1).

Figure 6b shows the time coefficients of the second CCA pair. The year-to year variations are fairly coherent. Both curves share a simultaneous downward change-point in the mid 1920s. The CCA patterns of the SLP and Romanian precipitation (Figure 5) suggest the following physical link: an intensification of the northwesterly circulation over Romania leads to more precipitation in the intra-Carpathian region, with the strongest effect in the northwest. The downward shift for the Baia Mare stations seems to be related to this mechanism.

4 CONCLUSION

The link between Romanian winter precipitation variability and the European SLP variability is strong. This link appears to be primarily related to the first SLP EOF or, equivalently to the strength of the southwesterly circulation from the Mediterranean. A significant intensification of this circulation type since 1933 has been found. Because of the topographic structures, related to the Carpathians, this change has an impact mainly on the southwestern stations which have an upward change-point around the same period. Since 1969 the southwesterly flow has slightly weakened leading to the decreasing of the precipitation at some central and eastern stations.

Another mechanism, which seems to be responsible for a change-point in the mid 1920s is the strength of the northwesterly circulation which has weakened affecting the precipitation at some stations in the intra-Carpathian region.

We can not assert whether the dynamics of these changes in the large-scale circulation found in this study are natural fluctuations of the climate system or are determined by the external forcings.

References

Barnett, T., and R.Preisendorfer, 1987, "Origin and levels of monthly and seasonal forecast skill for United States surface air temperatures determined by canonical correlation analysis, Mon. Wea. Rev., pp.1825-1850.

Busuioc, A., and H. von Storch, 1995, "Changes in the winter precipitation in Romania and its relation to the large scale circulation", Max-Planck-Institut für Meteorologie, Report No. 151 (Hamburg, Germany).

Pettitt, A. N., 1979, "A non-parametric approach to the change-point problem, Appl. Statist., pp.126-135.

Sneyers, R., 1975, "Sur l'analyse statistique des series d'observations, WMO Note technigue No 143, 189 pp.

Von Storch, H., 1995, "Spatial Patterns: EOFs and CCA. In: H. Von Storch and A. Navara (eds). "Analysis of Climate Variability: Applications of Statistical Techniques", Springer Verlag (in press).

ACKNOWLEDGEMENTS

This study was made possible through fundings by the Commision of the European Community (ERB-CIPA-CT-92-2045) and the Max-Planck Society to finance two extended visits of the author to the Max-Planck-Institut für Meteorologie. The author thanks Prof. Dr. K. Hasselmann for making this visit possible and Dr. H. von Storch for his useful help in preparing this study. Dr. E. Zorita and H. Heyen helped with the computational/graphic routines and providing the large-scale SLP data sets, Dr. F. Zwiers with useful comments about climate variability. A. Argeşiu helped me to improve the English.

CORRESPONDING AUTHOR

Aristiţa Busuioc
National Institute of Meteorology and Hydrology
Bucharest, ROMANIA

AN EMPIRICAL ATMOSPHERIC MODEL FOR USE IN FORECASTS OF THE COUPLED ATMOSPHERE/OCEAN SYSTEM

Grant Branstator[1] and Sue Ellen Haupt[2]

[1]National Center for Atmospheric Research, Boulder, CO, USA
[2]University of Colorado, Boulder, CO, USA

ABSTRACT

A linear model of the atmosphere is proposed that may be suitable for use in place of conventional linear models commonly applied to simulations of the coupled atmosphere/ocean system. The model's prognostic equation is based on empirical relationships found between atmospheric state and tendency rather than on physical principles. As a test, such an empirical model is developed for prediction of the barotropic streamfunction and its behavior is found to be physically reasonable and superior to the linear, nondivergent barotropic vorticity equation. Data requirements for the construction of the empirical model and the optimum choice of a basis for the model are considered.

1 INTRODUCTION

Successful predictions of ENSO are currently being produced by coupled models in which the atmosphere is represented by a simple model based on the linearized equations of motion. As an alternative, in this study we develop a linear model that is based, not on a physical principle, but rather on the statistics of the past history of the atmosphere. The model operator $\mathbf{L}$ is defined so that it minimizes $< (s_t - \mathbf{L}s)^2 >$, where s is the state of the atmosphere, s_t is the tendency of s and $< >$ denotes averaging over the domain and history. This is the same operator used by Hasselmann (1988) to find Principal Oscillation Patterns (POPs). In our application, however, rather than confine our attention to a few prominent modes, we use either the full or nearly full dimensionality of the operator and treat it as a replacement for a physically-based model of the form $s_t = \mathcal{L}s + r$, where r is an anomalous forcing distribution. Since by construction $\mathbf{L}$ is an optimal model, it necessarily is a more complete representative of the true atmospheric dynamics than any physically-based model can be. For example, it should automatically include processes, like the effect of the climatological planetary waves and feedbacks from high-frequency transients and moisture, not represented in traditional linear atmospheric models.

2 COMPARISON WITH PHYSICAL MODELS

Given the large number of possible degrees of freedom in atmospheric flow, we anticipate that a large dataset will be needed to construct such a model. Because the data record for nature is short and possibly nonstationary, we choose to construct a test model using data produced by a perpetual January general circulation model (GCM) running with fixed boundary conditions. 108,000 samples of half-daily data are available.

The GCM has 13,888 spatial degrees of freedom and an empirical model could be constructed to represent all of these, but to reduce the complexity of the computation, we consider models that do not include all of the fields present in the GCM state vector. Following the reasoning commonly used with simple, physically-based models, we assume that midtropospheric streamfunction is rather independent of other fields and construct models whose state vector consists of this field at just one level, requiring 495 degrees of freedom. For example, calculating the optimal $\mathbf{L}$ operator for half-daily 300mb streamfunction, we find that it is able to predict .517 of the (spatial and temporal) variance of the 300mb streamfunction tendency field. We find that the empirical technique is even more skillful at predicting tendencies of the streamfunction averaged for 850 and 300mb. In this case .671 of the tendency variance is explainable as a linear function of the state. For the remainder of our study, we use this barotropic streamfunction as the model's dependent variable. By way of comparison, we note that the nondivergent barotropic vorticity equation when linearized about the GCM's time mean 300mb streamfunction explains only about one quarter as much tendency variance.

As a second test of the empirical model, we reproduce some of the idealized calculations often done with simple physical models. For example, if we introduce a disc of perturbation vorticity into it at (30S, 0E) and integrate forward in time, we see (Fig. 1) that the disturbance disperses with large scales experiencing westward group velocities and small scales eastward velocities, just as would be expected in a physical model (cf., Hoskins *et al.*, 1977). Similarly, if we switch on steady, localized sources in the model, its reaction is to generate wave trains emanating from the source, again, as expected on physical grounds. The shapes of these wavetrains depend on the location of the source, suggesting that local conditions (presumably features like the planetary waves and stormtracks) are influencing the evolution of the modeled state.

As a third test of the model, we use a set of 24 time-average GCM solutions to assess its capabilities. These 24 solutions are for cases with imposed steady heating anomalies at various equatorial locations. We calculate the forcing required to produce each of the 24 GCM

anomalies in forced, steady solutions of the empirical model. These forcing fields, which are simply found by calculating $\mathbf{L}s$, where s is an anomalous flow from the GCM, are influenced by all processes that are in the GCM but not in the empirical model. In addition to containing the effect of processes that are outside the realm of streamfunction dynamics (like the vorticity source generated by outflow over the heated region), dynamics inaccurately represented by the empirical operator must be compensated for by this residual forcing. Thus, this field is partially an indication of empirical model shortcomings. The 24 forcing fields calculated in this way have a great deal in common; they all have the expected strong features in the vicinity of the equatorial heated region. Longitudinally translating each of these fields in order to put the associated heat source in the same position, one finds the composite forcing associated with the average case (Fig. 2a). A similar calculation with the nondivergent barotropic vorticity equation linearized about time-average control conditions produces the distribution in Fig. 2b. The larger amplitude and more widespread distribution in this second panel is an indication that the physically-based model does not include as many of the dynamical mechanisms that are important in these equatorial heating cases.

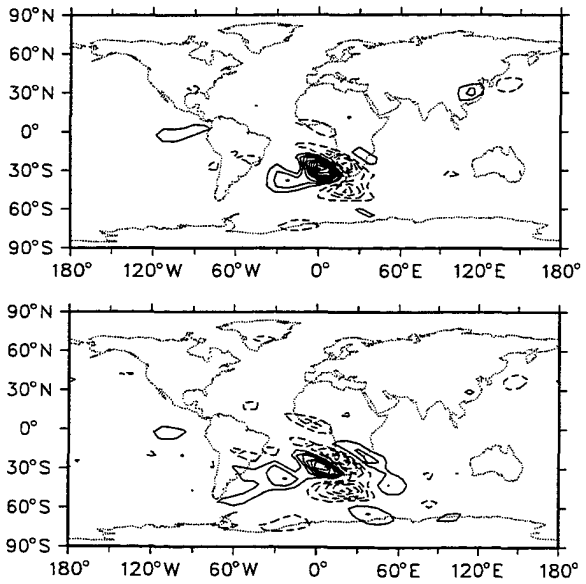


Figure 1. Perturbation vorticity after a) one and b) two days in an empirical dynamical model when an initial circular perturbation is introduced at (30S, 0E).

Another test of the simple models' ability to reproduce the GCM's behavior in these 24 cases is to force them by stationary sources of the form $-fD$, where f is the Coriolis parameter and D is a disc of divergence, assumed to be caused by the heating anomaly. If D is given a radius of 3000 km and centered in the same location as the imposed heating anomaly, we find that the pattern correlation between the empirical model's response and the GCM's actual upper tropospheric anomaly is on average .62. This is in contrast to the average pattern correlation of .48 achieved when the same source is introduced into the physically-based model.

3 DATA REQUIREMENTS

Being encouraged by the behavior of the empirical model, we now consider whether such a model is practical. One important question is how much data is needed to construct such a model. This issue we address by calculating the tendency variance that the empirical model explains as a function of the length of the dataset used to construct the model. Setting aside 10,000 half-days of barotropic streamfunction to use as an independent dataset, we use more and more data from the remainder of our dataset to construct the empirical model. As expected (Fig. 3), as more data is used to calculate the model, less of the tendency variance in that dependent data is explained by the model but more of the variance in the independent data is explained. After about 50,000 half-days the variance explained in the dependent and independent data asymptote to the same value (.67), indicating that this is enough data to find the true relationships between state and tendency. Rather than insisting on complete convergence, one might be satisfied with an operator that contains somewhat less than the maximum potential skill. For example, in the remaining experiments described in this paper, we have used 20,000 half-days to construct it; this model explains .65 of the barotropic streamfunction tendency variance. Of course even this is far more data than is available from nature. The GCM-generated data suggest that by using the 5,000 to 10,000 half-daily observations available for any one season, one could produce an empirical model that explains about .60 of the barotropic streamfunction tendency variance.

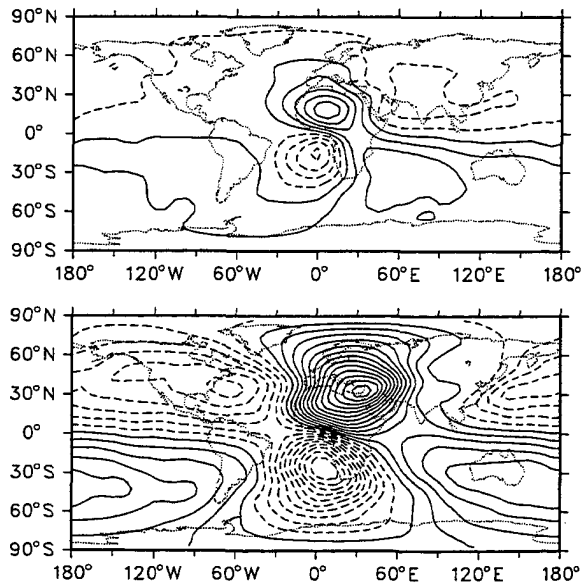


Figure 2. a) Ensemble average forcing required by an empirical dynamical model to maintain the time-mean streamfunction anomalies produced by equatorial heating in 24 GCM experiments. b) Same as (a) except the residual forcing is for the linearized barotropic vorticity equation. Same contour interval in both panels.

4 OPTIMUM BASIS

One may not need to include all spatial degrees of freedom to construct an adequate empirical model. This could prove useful for more advanced models than the one we have been testing, in particular, ones in which

many fields are used to define the state of the atmosphere. Furthermore, with fewer degrees of freedom, it is possible that the length of the timeseries required to construct the model might be shortened.

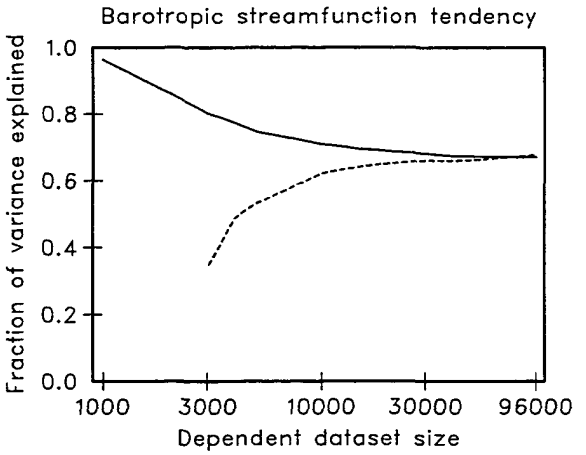


Figure 3. Barotropic streamfunction tendency variance explained by an empirical model in dependent (solid) and independent (dashed) datasets as a function of the size of the dependent dataset.

One natural means of reducing the degrees of freedom in the empirical model is to use empirical orthogonal functions (EOFs) as a basis and ignore those EOFs that explain little variance. We have tried this by making use of the EOFs of half-daily barotropic streamfunction from our GCM dataset and find there is some cause for concern with this approach. We produce a series of empirical models, each of which is constructed from data that is more and more highly EOF truncated. As seen in the solid line of Fig. 4, with higher truncation the accuracy of the linear model (as measured by the explained variance of the *truncated* tendencies) decreases. This could mean a) that the least significant modes are the most accurately forecast, or b) that these modes provide predictive information about the tendencies associated with the more significant modes. The solid line in Fig. 5 shows the variance in the tendency of each individual EOF coefficient that can be explained by the untruncated empirical operator. There is some indication that the trailing EOFs are better forecast than the leading EOFs, so the first possibility has some validity. But it also seems that the least significant EOFs make important contributions to the prediction of tendencies of the leading EOFs. This fact is seen in the dashed line of Fig. 4, which shows the tendency variance of that part of the barotropic streamfunction represented by the leading 10 EOFs as a function of model truncation. Whereas .41 of the variance of the tendencies in these structures can be explained when all EOFs are used as predictors, only .11 is explained when the coefficients of just those same 10 patterns serve as predictors.

The source of the loss of accuracy in predicting the evolution of the most vigorous structures when the least vigorous structures are truncated from the problem is simply that the tendencies in one EOF are not independent of the amplitude of other EOFs; the dynamics of the system allow one pattern to evolve into another. To overcome this we try a second basis, one which does not have this attribute, namely the eigenvectors of the empirical operator. For the test of this possibility, we start with the empirical model for barotropic streamfunction at full resolution and calculate its eigenvalues and eigenvectors. Ordering these modes by the magnitude of the eigenvalues, we can calculate the variance in the tendency of each of these modes explained by the empirical model (dashed line in Fig. 5) and find that the accuracy is highly modally dependent. Evolution of the modes with small magnitude eigenvalues is least well forecast; perhaps these are the structures most influenced by external processes like heating. The way in which this situation differs from that for the EOFs is that if some of these modes are removed from the system, our ability to predict the remaining modes does not suffer.

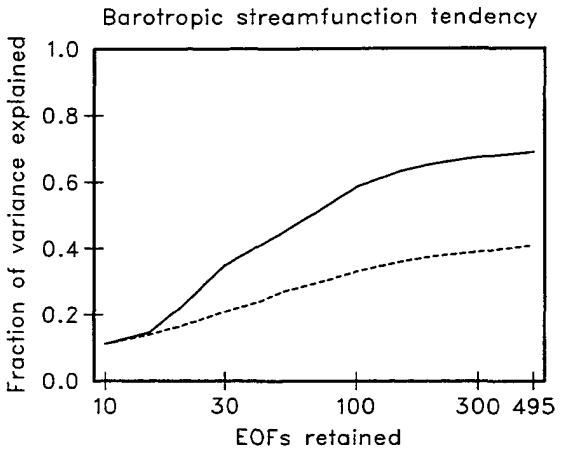


Figure 4. Barotropic streamfunction tendency variance explained as a function of the EOF truncation of the model. Solid: Resolved variance explained. Dashed: Variance explained in the tendencies of the leading 10 EOFs.

If we want to use a reduced basis in the empirical model, we could choose an EOF basis (to maximize representation of the state) or an eigenmode basis (to take advantage of modal independence). To examine the consequences of this tradeoff, we apply the empirical model to cases of equatorial forcing and compare its behavior when truncated in both ways. An example is shown in Fig. 6. The top panel of that figure shows the steady response of the model to a dipole source straddling the equator at 60W. The second panel shows the solution when only the leading 20% of the EOFs are retained in the model formulation. The general character and placement of the wavetrains into each hemisphere is retained, but the phasing of the main midlatitude lobes is degraded. If instead one retains the 20% of the model eigenmodes with the smallest magnitude eigenvalues (the modes that on average should make the largest contribution to steadily forced cases), the solution of the bottom panel results. The midlatitude arches are present and the phasing of many of the lobes is more accurate here than in the EOF-truncated solution, but the solution is noisier. This would be consistent with more accurate tendencies but less variance explainable by the resolved modes. Clearly each method of truncation has its strengths and weaknesses.

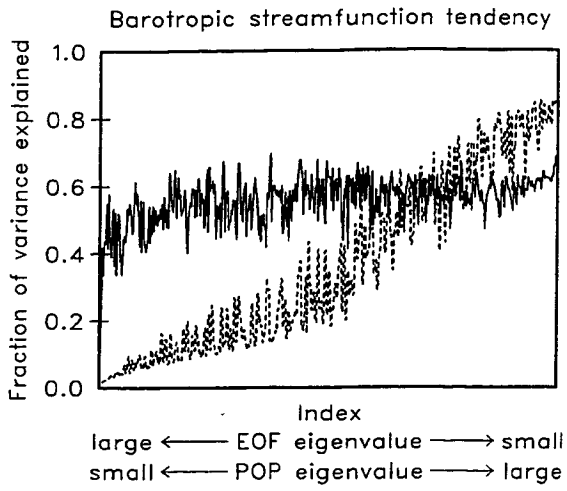


Figure 5. Variance explained in streamfunction tendencies for the coefficients of individual EOFs (solid) and model eigenmodes (dashed).

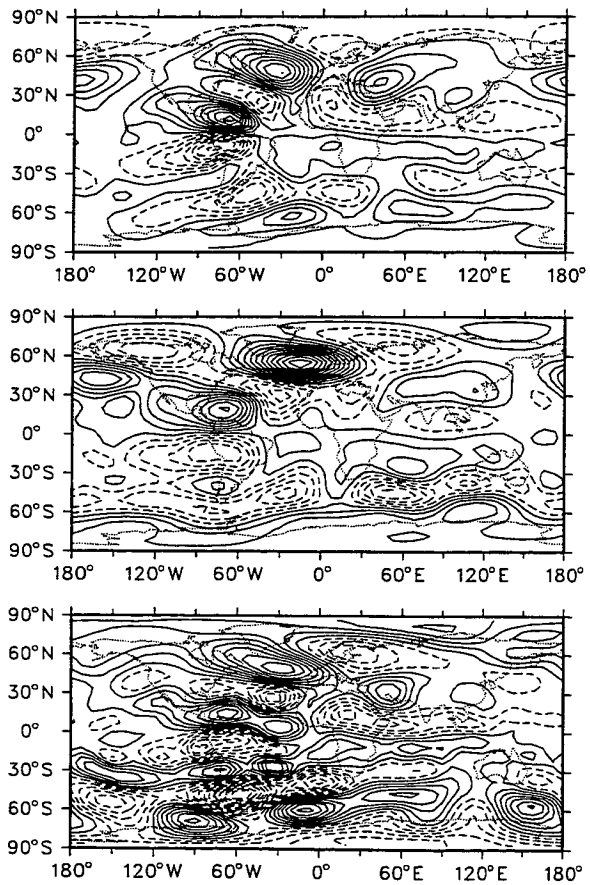


Figure 6. Steady streamfunction response of the empirical model to a dipole equatorial source at 60W. Top: Model at full resolution. Middle: Model using 101 EOFs for a basis. Bottom: Model using 101 eigenmodes as a basis.

5 SUMMARY

Our tests suggest that an empirically-defined dynamical model of the atmosphere may be a viable candidate for situations where a simple atmosphere is needed. Such a model gives physically reasonable solutions and has been found to be superior to conventional linear models in reproducing the low-frequency behavior of a GCM. To attain its full potential, much more data than is available from the historical record of nature is needed to construct such an empirical model, but the reduction in accuracy resulting from the short observed record may be acceptable for some purposes. Alternatively one may use long records from GCMs to construct the model. Our calculations indicate that one may be able to reduce the degrees of freedom in an empirical model, but care must be taken that it be done in such a way that model accuracy is not overly affected. This could help pave the way for multi-level, multi-variable models of this kind that would include the fields (surface winds and temperature) needed in coupled applications.

REFERENCES

Hasselmann, K., 1988, PIPs and POPs: The reduction of complex dynamical systems using principal interaction and oscillation patterns. *J. Geophys. Res., 93*, 11,015–11,021.

Hoskins, B.J., A.J. Simmons, and D.C. Andrews, 1977, Energy dispersion in a barotropic atmosphere, *Quart. J. Roy. Meteor. Soc., 103*, 553–567.

CORRESPONDING AUTHOR
Grant Branstator
National Center for Atmospheric Research
P.O. Box 3000
Boulder, CO 80307-3000, USA

PREDICTABILITY LIMITS OF ENSO; THE ROLE OF STOCHASTIC FORCING

Ch. Eckert & M. Latif

Max-Planck-Institute for Meteorology,
Hamburg, Germany

ASTRACT

The El Niño/Southern Oscillation (ENSO) phenomenon is modeled as a stochastically driven system. This is accomplished by adding to a Hybrid Coupled Model of the tropical Pacific ocean–atmosphere system a stochastic wind stress anomaly field which was derived from observations. The results obtained indicate that stochastic forcing is an essential ingredient in modelling ENSO, limiting its predictability to less than the average oscillation period.

1. INTRODUCTION

Observational records of ENSO, e.g. the UKMO Global Ice and Sea Surface Temperature (GISST) data set, Parker et al. (1994), exhibit a high degree of variability, manifested by the irregular occurence of the ENSO extremes and their varying amplitudes. There are different approaches available to explain these characteristics. Jin et al. (1994) and Tziperman et al. (1994), for instance, explain the irregularity of ENSO by non-linear interactions between the annual cycle and the fundamental ENSO frequency. Here, we investigate the influence of random perturbations added to a coupled model system designed to simulate ENSO. This contrasts those studies concerned with uncertain initial conditions. The amplification of errors may be caused by different mechanisms such as unstable modes, Goswami & Shukla (1991), or the non-selfadjoint nature of the linearised system dynamics, Blumenthal (1991). Apart from these uncertainties, the perpetual action of weather events and longer lasting random anomalies in the tropical Pacific ocean–atmosphere system may influence ENSO. To investigate the influence of these processes on ENSO, we designed a stochastically forced ocean–atmosphere system which mimics the observed statistics to some extent.

We will proceed as follows. A description of the stochastically forced ocean–atmosphere model and ensemble integrations performed are decribed in sections 2 and 3, respectively. The optimal fit of a linear stochastic process in a reduced state space to the ensemble data is carried out in section 4. We address the predictability of the optimal linear model in section 5, and summarise and discuss results in section 6.

2. THE MODEL

The coupled ocean–atmosphere model we use to simulate ENSO consists of an ocean general circulation model (OGCM) of the equatorial Pacific limited to the domain 130°W–80°E, 30°S–30°N and a statistical atmosphere model which was derived from observations. The OGCM is described in detail in Latif (1987). However, vertical mixing is Richardson number dependent. The ocean model is driven by annual cycles of wind stress and heat flux. The latter enters as a Newtonian relaxation term only. The statistical atmosphere model relates sea surface temperature anomalies (SSTA) linearly to wind stress anomalies. The regression matrix is derived from observations for the period 1970 to 1985. The SST data were taken from the data set of Reynolds (1988), and the wind stress from the Florida State University (FSU) dataset, Goldenberg & O'Brien (1981). The linear regression is done in EOF space, retaining the first 5 EOFs of the respective anomalies. Coupling is done on a monthly basis with linear interpolation inbetween. This coupling methodology is analogous to the one described by Barnett et al. (1993). To account for deficiencies of the OGCM its simulated SSTA is corrected according to the procedure of Barnett et al. (1993) before passed to the atmosphere model. The coupling strength was tuned in such a way that the HCM oscillates regularly with a period of about 60 months in a 120 year integration shown in Figure 1. Apart from the dissimilarity of the spectra of observed and simulated SSTA, the HCM underestimates the amplitudes of the ENSO extremes slightly.

The wind stress data set shows a high degree of variability at time scales short compared to a typical oscillation period, e.g. Kleeman & Power (1994). In order to investigate the effects of stochastic forcing on the model variability, we added wind stress noise to the HCM in a second integration. The noise was constructed as follows. First, the observed wind stress anomalies were high-pass filtered (retaining variability with time scales less than 16 months) and subjected to EOF analysis. We then combine the leading 10 EOFs with random amplitudes according to the variance of their corresponding principal components. The residual part of the noise is assumed to be uncorrelated in

space and time. The variance of the latter matches the variance of the residual wind stress field obtained after subtracting the linear combination from the original field.

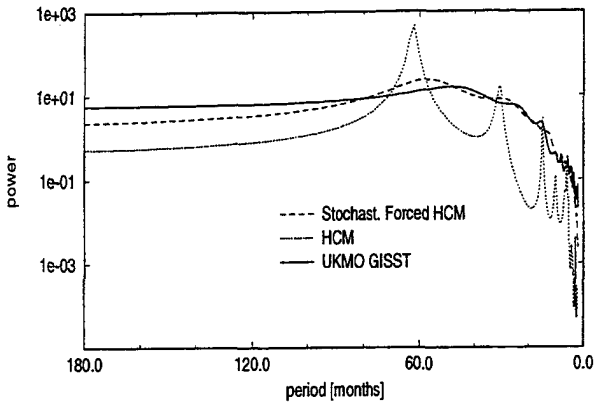


Figure 1 Maximum entropy spectrum of monthly values of SSTA averaged over the Niño3 region for the 120 year integrations of the Hybrid Coupled Model, its stochastically driven version, and the UKMO GISST data set lasting from 1900–1992. Each time series was scaled to unit variance before computing its spectrum.

We performed a second 120 year integration with the HCM, but now with stochastic forcing included. The HCM oscillates now irregularly as witnessed by the power spectrum of this integration (Fig.1). Although the variability at long time scales is clearly underestimated, the aggreement at interannual and shorter time scales is much better than without stochastic forcing.

3. RESTART EXPERIMENTS

To study the model variability further, we initialise the model at selected months of the 120 year integration, corresponding to different phases of the model ENSO cycle. We generate ensembles of 216 trajectories for each restart month by integrating the model forward in time for 72 months with different realisations of the stochastic part. Fig.2 displays the time evolution of one particular ensemble. Shown is the mean and standard deviation of SSTA averaged over the Niño3 index region. The standard deviation quickly saturates after about 20 months. To further investigate the influence of the random perturbations on the interannual variability, the ensemble data were then used to derive an approximating linear stochastic model.

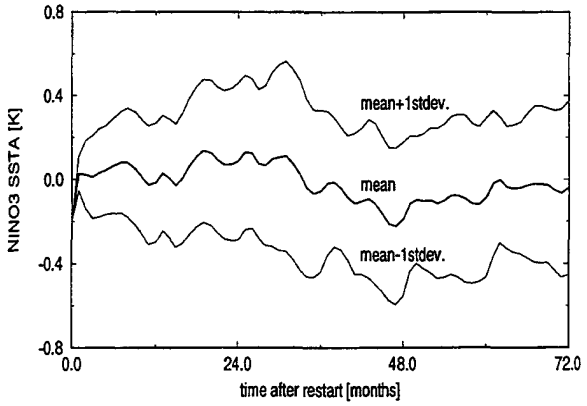


Figure 2 Time evolution of the mean and standard deviation of SSTA averaged over the Niño3 region. The restart ensemble was initialised at month 468 of the 120 year integration.

4. LINEAR STOCHASTIC PROCESS

The time evolution of a linear stochastic system is given by the differential equation

$$\dot{x}(t) = Ax(t) + B\eta(t) \quad . \tag{1}$$

The vector $x(t)$ represents the state of the n dimensional system at time t, A and B denote $n \times n$ matrices, and $\eta(t)$ is meant to be an n dimensional gaussian random vector with mean 0 and the identity matrix as covariance matrix. In our application A and B are assumed to be constant in time. This implies that the diffusion matrix of the random process is given by BB^T. The time evolution of the mean $\langle x \rangle$ and the covariance matrix $\Sigma_{ij} = \langle (x_i - \langle x_i \rangle)(x_j - \langle x_j \rangle) \rangle$ then obey the differential equations

$$\dot{\langle x \rangle} = A\langle x \rangle \quad , \quad \langle x \rangle(0) = x_0 \tag{2}$$

and

$$\dot{\Sigma} = A\Sigma + \Sigma A^T + BB^T \quad , \quad \Sigma(0) = \Sigma_0 \tag{3}$$

not explicitly denoting the time dependence of $\langle x \rangle$ and Σ for notational convenience. For a derivation of equations (2) and (3) see for instance van Kampen (1992). $\Sigma(0)$ vanishes since the ensemble members start from the same initial state. To obtain an optimal linear model in a least squares sense, we define a cost function which measures the misfit between the linear model characterised by the entries of A and B and the ensemble data:

$$F(A,B) = \sum_{t=1}^{T} [(\langle x \rangle - \langle x \rangle_{ens})^T \mathbf{M}_{1,t} (\langle x \rangle - \langle x \rangle_{ens}) + (\vec{\Sigma} - \vec{\Sigma}_{ens})^T \mathbf{M}_{2,t} (\vec{\Sigma} - \vec{\Sigma}_{ens})] \quad . \tag{4}$$

$\vec{\Sigma}$ denotes a column vector with its entries given by the main diagonal and upper triangle of the covariance matrix. The weighing matrices $\mathbf{M_{1,t}}$ and $\mathbf{M_{2,t}}$ were derived from the ensemble assuming normal variates:

$$\mathbf{M_{1,t}} = N \cdot \Sigma_{ens}^{-1} \quad (5)$$

$$\mathbf{M_{2,t}} = cov(\Sigma_{ij,ens}, \Sigma_{kl,ens})^{-1} = \left[\frac{1}{N}(\Sigma_{il,ens}\Sigma_{jk,ens} + \Sigma_{ik,ens}\Sigma_{jl,ens})\right]^{-1} \quad (6)$$

To mimise F in parameter space one could choose various methods. We chose a software tool, developed by Giering; Giering & Kaminski (1995). This tool generates the adjoint of the above model and uses this for the subsequent minimisation of $F(A, B)$.

It remains to specifiy the dimension of the state space for the linear model. To get a reduced state space representation of the stochastically forced HCM, we performed a combined EOF analysis of SSTA, sea level anomalies, and zonal wind stress anomalies of the 120 year model run and retain the leading EOFs, typically 4 to 6, which are then used to derive the linear model.

5. PREDICTABILITY

We first compute the eigenvalues and eigenvectors of the system matrix to get more insight into the interannual variability of the linear model. Afterwards, we transform the system matrix into the basis of normal modes, yielding a system matrix which has block diagonal form and the covariance matrix of the transformed stochastic process:

$$\Sigma^* = L\Sigma L^T \quad . \quad (7)$$

L denotes the applied linear transformation. Since our concern is the investigation of the interannual variability of the linear model, we project the system onto the subspace of the normal modes associated with these time scales. The covariance matrix is transformed analogously to (7), the matrix L being replaced by the appropriate projection operator.

As a measure of predictability we define

$$s(t) = \alpha[det(\Sigma(t))]^{1/4} \int dx p(x;t) p_{stat}(x) \quad , \quad (8)$$

which quantifies the degree of similarity among the time dependent and stationary probability distributions of the stochastic process. At the starting point t=0, s vanishes, whereas the constant $\alpha = (2\sqrt{\pi})^n [det(\Sigma_{stat})]^{1/4}$ is chosen such that s approaches 1 for large t. The behaviour in the intermediate range depends on the underlying stochastic process. Calculated for the linear model fit, the predictability measure reaches large values well before the dominant cycle period.

6. SUMMARY AND CONCLUSION

Extending a Hybrid Coupled Model by a stochastic part yielded better agreement with observations. The model ENSO extremes occur irregularly and with varying amplitudes. Restart experiments showed considerable spread among trajectories, which implies that stochastic forcing is a significant limiting factor to the model's predictability. To investigate this further, we approximated the HCM by a linear stochastic process yielding a predictability measure which reaches critical values before a dominant cycle period has elapsed.

There are, however, some caveats. The estimate of the stochastic forcing may suffer from mesurement errors in the underlying dataset, the way of constructing the random perturbation cannot be justified rigorously, and the dominant period of the model ENSO mode is longer than observed. Further, the approximating linear system does not fit the stochastically forced HCM perfectly, since it is formulated in a reduced state space, and a misfit remains after optimisation.

In summary, our study reveals the importance of stochastic forcing to model ENSO and in limiting ENSO predictability.

REFERENCES

Barnett, T.P., Latif, M., Graham, N., Flügel, M., Pazan, S., White, W., 1993, ENSO and ENSO-related Predictability. Part I: Prediction of Equatorial Pacific Sea Surface Temperature with a Hybrid Coupled Ocean–Atmosphere Model, J. Climate, **8**, 1545-1566.

Blumenthal, B., 1991, Predictability of a Coupled Ocean–Atmosphere Model, J. Climate, **4**, 766-784.

Giering, R., Kaminski. Th., 1995, Recipes for Adjoint Code Construction, Internal Report (Max-Planck-Institut für Meteorologie).

Goldenberg, S., O'Brien, J., 1981, Time and Space Variability of the Tropical Pacific Wind Stress, Mon. Wea. Rev., **109**, 1190-1207.

Goswami, B.N., Shukla, J., 1991, Predictability of a Coupled Ocean–Atmosphere Model, J. Climate, **4**, 3-22.

Jin, F.-F., Neelin, D., Ghil, M., 1994, El Niño on the Devil's Staircase: Annual Subharmonic Steps to Choas, Science, **246**, 70-72.

Kleeman, R., Power, S.B., 1994, Limits to Predictability in a Coupled Ocean–Atmosphere Model due to Atmospheric Noise, Tellus, **46A**, 529-540.

Latif, M., 1987, Tropical Ocean Circulation Experiments, J. Phys. Oceanogr., **17**, 246-263.

Parker. D.E., Folland, C.K., Bevan, A., Ward, M.N., Jackson, M., Maskell, K., 1994, Marine Surface Data for Analysis of Climatic Fluctuations on Interannual to Century Time Scales, National Research Council: Natural Climate Variability on Decade to Century Time Scales, Eds. D.G. Martinson, K. Bryan, M. Ghil, M.M. Hall, T.R. Karl, E.S. Sarachik, S. Soroostian, and L.F. Talley, National Academy Press, Washington.

Reynolds, R.W., 1988, A Real–Time Global Sea Surface Temperature Analysis, J.Climate, **1**, 75-86.

van Kampen, N.G., 1992, Stochastic Processes in Physics and Chemistry, North - Holland, 210ff.

CORRESPONDING AUTHOR
Christian Eckert
Max-Planck-Institut für Meteorologie
Bundesstraße 55
D-20146 Hamburg
GERMANY.

The Potential for Long–Range Prediction of Precipitation over India for the Southwest Monsoon Season An Analysis of Variance Approach

Dennis J. Shea, N. A. Sontakke[1], Roland A. Madden, Richard W. Katz

National Center for Atmospheric Research, Boulder, CO, USA 80307
[1]Indian Institute for Tropical Meteorology, Pune, India

ABSTRACT

The details of daily weather variations cannot be predicted more than, say, two weeks in advance. These variations, which are due to the atmosphere's internal dynamics, introduce variance into time-averaged meteorological quantities. This variance is referred to as "climate noise" and is not predictable at long lead times. Here, estimates of the climate noise of monthly precipitation over India during the monsoon season (June–September) are made and compared with the actual interannual variability of monthly precipitation. The observed interannual variability of monthly precipitation is assumed to consist of a "climate signal" and the climate noise. The climate signal, which may be composed of many components, is presumed to arise from changing external conditions such as slowly varying sea surface temperatures, soil moisture, the greenhouse effect, etc. Generally, any physical process whose time scales are long relative to daily weather variations are considered to be external. Where the interannual variability of monthly precipitation exceeds that suggested by climate noise it is concluded that the signal is large enough to *potentially* be predicted at long–range.

The potential for long-range prediction is approached as an analysis of variance problem. The variance *between* seasons (*i.e.*, the interannual variability) which contains the climate noise and, possibly, a climate signal is compared to the variance *within* seasons as estimated by a two-state first-order Markov model (*i.e.*, the climate noise). Regions where the ratios exceed one are considered to be potentially predicatable at long lead times.

1 INTRODUCTION

The potential for long-range prediction of monthly time averages as defined by Madden (1976), Madden and Shea (1978; hereafter MS) and Shea and Madden (1990; hereafter SM) is estimated by the ratio of the observed interannual variability of monthly means (σ_A^2) to the variability due to "climate noise" (σ_T^2). The square root of the climate noise is synonymous with the standard error of estimating monthly means. from statistical sampling fluctuations. It is a result of daily variability introduced by the internal dynamics occurring within the atmosphere and as such can not be predicted at long lead times. Thus it represents an unpredictable component in the climate system. σ_A^2 is assumed to consist the climate noise and variance introduced by slowly changing external conditions (*i.e.*, climate signals). Assuming σ_T^2 is independent of σ_A^2 then the amount by which the observed interannual variability exceeds the climate noise is a measure of the potential long–range prediction. For example, F-ratios (σ_A^2/σ_T^2) of 1.5 and 2.0 would indicate that it would potentially be possible to explain 33% and 50% of the variance of monthly means, respectively. It is important to note that large estimates of σ_T^2 do not necessarily imply low potential for prediction.

The estimates of climate noise were evaluated within the conceptual framework outlined by Leith (1975, 1978). Briefly, this may be described as follows. Under the influence of constant external conditions individual realizations from an ensemble of realizations occurring within a climate allowing a unique set of statistics are sampled. The resulting time means from each realization will exhibit fluctuations about the ensemble mean. This variability is the climate noise. In fact, under these ideal conditions the climate noise and the interannual variability would be nearly identical since all variability would be due to internal dynamics alone. In this ideal case, there would be no potential for long-range prediction since the F-ratios would be approximately one everywhere.

Unfortunately, climate noise in the 'real world' can not be estimated under these ideal conditions. Neglecting possible atmospheric intransitivity (Lorenz, 1968, 1976), the continuously changing external conditions (e.g., sea-surface temperature, snow-ice cover, etc.) within the ensemble of realizations (approximated by daily data within, say, a season) and even within an individual realization affect daily weather and, thus, the estimates of the climate noise. Nevertheless, it is important to assess the magnitude of the climate noise and to estimate the potential for long range prediction. In the following, we briefly describe the method used to estimate σ_T^2 for precipitation.

2 DATA

The daily rainfall data used in this study were from the India Meteorological Department (IMD-Pune) and from the Climate Analysis Center (CAC), Washington, D.C. The dataset contained data from 1596 Indian stations and 61 stations from countries bordering India. These stations were selected based upon length of record and the desire for representative spatial coverage. Generally, stations within India spanned more than 60–65 years of data. Thirty-seven stations spanned

1901–4/93 and 100+ stations spanned 1901-84 with the period 1971-74 missing. The data for surrounding countries spanned, at most, 14 years. Results from these areas should be viewed as tentative. For this reason, the emphasis in this study will be on India. Shea and Sontakke (1995; hereafter SS) provide more details on this dataset. SS also presents various statistics computed from these data.

3. ESTIMATING CLIMATE NOISE

The climate noise associated with monthly and seasonal precipitation totals was estimated by assuming that daily precipitation could be modeled by a two-state first-order Markov process as described by Katz and Parlange (1995):

$$\sigma_T^2 = T\left[qp\sigma^2 + p(1-p)\frac{1+d}{1-d}u^2\right] \qquad (1)$$

where T is the length of the noise process (*e.g.*, 30 or 31 for monthly totals and, say, 92 for a 3-month seasonal total); q is a term which includes the effects of autocorrelation within sequences of wet days ($\geq$2.5mm); p is the unconditional probability of precipitation; σ^2 and u^2 are the variance and squared mean of precipitation amounts utilizing wet days only; and, d is a 'persistence parameter'. This model is a more general version of the model first proposed by Katz (1977, 1983). Equation (1) includes the occurrence and intensity of the precipitation process and the autocorrelation of sequences of wet days. Madden and Shea (1982) and Singh and Kriplani (1986; hereafter SK) have applied the original version of the model to precipitation data from the USA and India. Although a first order Markov model may not be appropriate for any individual monsoon season, Singh *et. al.* (1981) have shown that overall it provides an adequate description.

Because it is more difficult to lessen the effects of slowly varying external conditions on precipitation during a season (as opposed to temperature; see MS and SM), it is possible that the estimates of climate noise are inflated. This would cause the F-ratios presented in Section 4 to be conservative.

4 RESULTS

Estimates of the noise and the F-ratios for different time periods within the monsoon season (June through September; JJAS) were calculated. These provided some insight into the robustness of the the model parameters used and the noise estimates obtained using (1). Qualitatively, all periods exhibited the same pattern. The largest noise estimates coincided with the areas of largest total precipitation (see SS). For example, the values of σ_T for combined July–August (JA; $T = 62$) are presented in figure 1. These values of σ_T may be interpreted to mean that 62-day JA precipitation totals would have a standard deviation of about 142 mm near Bhopal in central India strictly as a result of fluctuations due to daily weather variability.

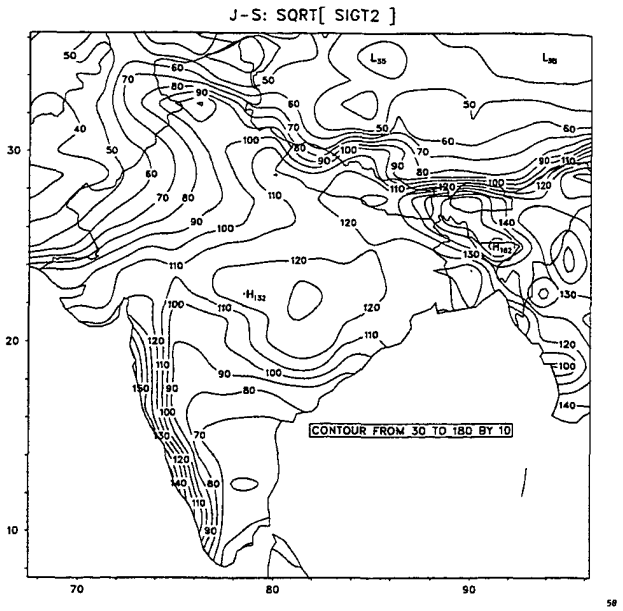


Fig. 1 Estimates (mm) of σ_T for the combined July–August precipitation totals.

Figures 2 and 3 present F-ratios for for the entire monsoon season (JJAS) and for the peak monsoon months (JA). Both figures show that throughout India there exists variance above that attributable to climate noise. The largest F-ratios ($\geq$2.5) are along the west coast where the southwesterly winds associated with the monsoon impinge on the Western Ghat mountain range which runs parallel to the coast. Stronger (weaker) than normal southwesterly monsoon winds will produce above (less than) normal rainfall in these areas. The central and northwestern portions of India show ratios of 1.4 to 2.0. These regions are affected by low pressure systems which originate in the northern region of the Bay of Bengal. These systems travel west-northwestwards along the monsoon trough which generally in located over the Ganges Valley. Periods when the monsoon trough move northwards to the foot of the Himalaya mountains are characterized by short period drought over central India and copious rainfall near the Himalaya. The smallest F-ratios (~1.25 or less) are located over southeastern India. During JJAS this region is less affected by the southwest monsoon. This region generally gets the majority of its rainfall during the northeast monsoon which occurs from October through December.

The results presented here are consistent with those presented by SK over the west coast of India. However, they are less optimistic over central and eastern India where SK indicate ratios of 2 to more than 3. There are several possible reasons for the differences between the the SK study and the present work: (i) SK used the original version of the model which did not take into account the autocorrelation within sequences of rainy days; (ii) SK used only 19 years of daily data for 220 stations; and, (iii) SK spatially averaged the data into 33 meteorological regions. The reasons for the different estimates are being investigated.

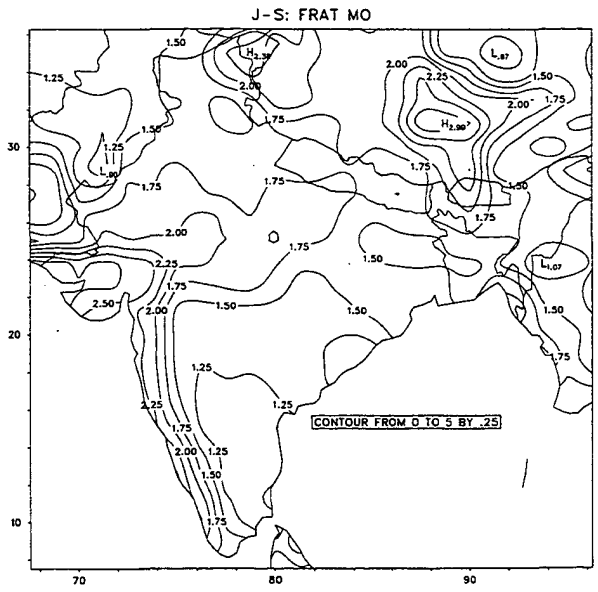


Fig. 2 Estimates of F-ratios for the entire southwest monsoon season (June through September).

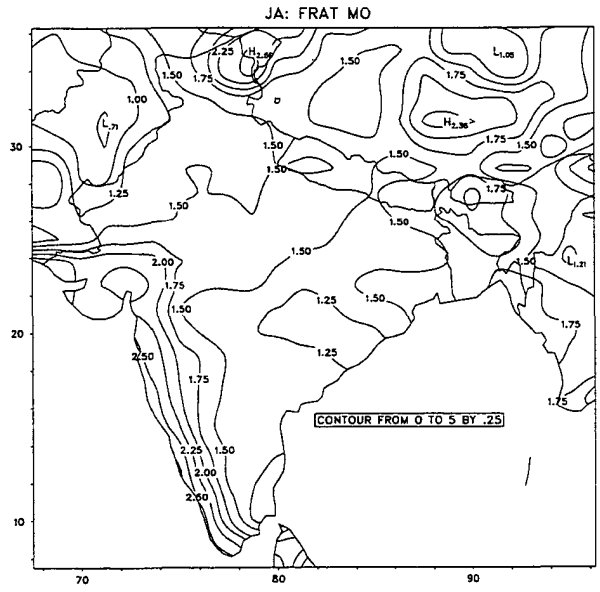


Fig. 3 Estimates of F-ratios for the peak southwest monsoon months (July and August).

5 SUMMARY

A Markov model which includes the occurrence and intensity of a precipitation process and the autocorrelation of sequences of wet days has been used to estimate the variance in monthly and seasonal precipitation totals over India during the southwest monsoon season (June through September). F-ratios calculated using the observed interannual variability of monthly and seasonal precipitation totals in the numerator (σ_A) and the variance associated with weather fluctuations (σ_T) in the denominator indicate that it may be possible to predict fluctuations of rainfall totals over India with long lead times.

The numerator, σ_A^2, contains variance information from daily weather variations which are unpredictable at long lead times and, possibly, variance from potentially predictable low-frequency signals. In the current application σ_A^2 is estimated from monsoon seasons sampled at one year intervals. Thus, the estimates of potential for prediction strictly apply to lead times of one or more years. Nonetheless, we believe that the general patterns for potential prediction apply to shorter lead times.

REFERENCES

Katz, R.W., 1977: Precipitation as a chain-dependent process. *J. Appl. Meteor.*, **16**, 671-676.

——, 1983: Statistical procedures for making inferences about precipitation changes simulated by an atmospheric general circulation model. *J. Atmos. Sci.*, **40**, 2193–2201.

——, and M.B. Parlange, 1995: Generalizations of chain-dependent processes: Application to hourly precipitation. *Water Resources Research* (in press).

Leith, C. E., 1975: The design of a statistical-dynamical climate model and statistical constraints on the predictability of climate. Appendix 2.2, *The Physical Basis of Climate and Climate Modeling.* WMO No. 16, 265 pages.

——, 1978: Predictability of climate. *Nature* **276**, 352–355.

Lorenz, E. N., 1968: Climate determinism. Meteor. Monogr., **30**, 1–3.

——, 1976: Nondeterministic theories of climate change. *Quat. Res.*, **6**, 495–506.

Madden, R. A., 1976: Estimates of the natural variability of time-averaged sea-level pressure. *Mon. Wea. Rev.*, **104**, 942–952.

——, and D. J. Shea, 1978: Estimates of the natural variability of time-averaged temperatures over the United States. *Mon. Wea. Rev.*, **111**, 1696–1703.

——, and D. J. Shea, 1982: Potential long range predictability of precipitation over North America. *Proceedings of the Seventh Annual Climate Diagnostics Workshop*, 18–22 October, NCAR, Boulder, CO, 423–426.

Shea, D. J. and R. A. Madden, 1990: Potential for Long-Range Prediction of Monthly Mean Surface Temperatures over North America. *J. Climate*, **3**, 1444–1451.

——, and N. A. Sontakke, 1995: The annual cycle of precipitation over the Indian subcontinent: Daily, Monthly and Seasonal Statistics. NCAR/TN-401+STR, 168pp.

Singh, S.V., R.H. Kriplani, P. Shaha, P.M. Ismail, and S.D. Dahale, 1981: Persistence in daily and 5-day summer rainfall over India. *Arch. Meteor. Geophs. Biklim., Ser. A* **30**, 261–277.

——, and R.H. Kriplani, 1986: Potential Predictability of Lower Tropospheric Monsoon Circulation and Rainfall over India. *Mon. Wea. Rev.*, **114**, 758–763.

PREDICTING SOUTH AFRICAN SEASONAL RAINFALL BY MEANS OF CANONICAL CORRELATION ANALYSIS

W. A. Landman

South African Weather Bureau

ABSTRACT

Equations relating to prediction by canonical variates, are used to make categorical rainfall forecasts for South Africa. Forecast skill measures are presented, as well as a prediction scheme used operationally at the South African Weather Bureau. Sea surface temperatures of the oceans adjacent to southern Africa, as well as the equatorial Pacific Ocean, are used as predictors. Forecasts are made for homogeneous rainfall regions, covering six consecutive months.

1 INTRODUCTION

Canonical Correlation Analysis (CCA) is used as an advanced statistical technique to forecast rainfall for South Africa, using sea surface temperatures (SST) as the only predictor. South Africa is divided into eight homogeneous rainfall regions. These regions were obtained by correlating the standardised time series of each district with their significant rotated (Varimax) principal component time series. The districts that correlated best with a particular significant rotated pc, were subsequently grouped.

2 DATA

Global Ocean Global Atmosphere (GOGA) SST data (Pan and Oort 1990, Lau and Nath 1994) of the ocean next to southern Africa, and the equatorial Pacific Ocean, are used as predictors. The climate period is 39 years (1946/1947 to 1984/85). Blended SST (Reynolds 1988) is used as predictor for the period that follows the climate, up to the end of 1994. Optimum Interpolation (OI) SST data (Reynolds and Smith 1994) is used from 1995. The ocean regions are:

1. Indian Ocean: 20.25°N to 38.25°S,
2. Atlantic Ocean: 6.75°N to 38.25°S, and
3. equatorial Pacific Ocean: 120°E to 85°W, 11.25°N to 11.25°S).

The district rainfall data set of the South African Weather Bureau (Van Rooy 1972) is used as predictand.

3 METHOD

Both the predictor and predictand data sets are standardised, separately orthogonalised and truncated using Empirical Orthogonal Function (EOF) analysis. The truncation rule used here is the "Average Root" or "Guttman-Kaiser" criterion (Jackson 1991). The resulting predictor and predictand principal component time series are then analysed in the CCA procedure.

The mathematical method to obtain the canonical vectors and canonical correlations, follows that of Tatsuoka (1988). Equations relating to prediction by canonical variates are constructed in a least-squares sense (Glahn 1968). The prediction equations are subsequently used to make categorical (above-normal, normal, below-normal) rainfall forecasts for six consecutive months.

Model skill measures (local and global skill) as determined by cross-validation (one year withdrawn for each model), are discussed by Barnett and Preisendorfer (1987). A "Skill Score" is obtained for a test period that follows the training period. The Skill Score is the percentage of years during the test period, where both the predicted and observed mean indices are in the same category (below-normal, normal or above-normal). For a model to be considered useful, it has to meet the following criteria:

1. Global skill significant at 95% level,
2. Average local skill larger than 33.3%,
3. Skill Score larger than 33.3%.

4 CASE STUDIES

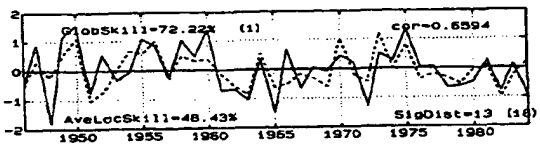


Figure 1. Cross-validated forecast for homogeneous rainfall region 6 for December, using September to November mean SST of the equatorial Pacific as predictor. The solid line is the observed mean index and the dashed line the predicted mean index. "Globskill" is the global skill, "AveLocSkill" the average local skill, "SigDist" the number of significant districts, "cor" the correlation between the observed and predicted mean indices.

Two case studies will be presented. Firstly, September to November mean SST of the equatorial Pacific as predictor, and the December rainfall of a homogeneous rainfall region that forms part of the central interior of South Africa, as predictand. It is clear from inspection of the global and local skill values, and also the correlation in Figure 1, that this is a model with high skill. Take note that the La Niña years of 1973/74 and 1975/76, and the El Niño year of 1982/83 are particularly well predicted.

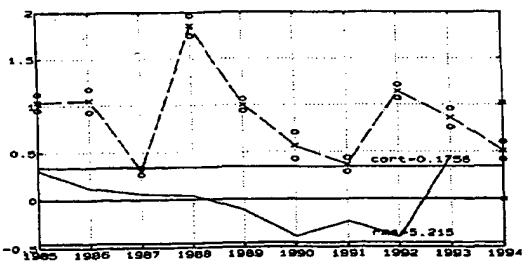


Figure 2. Forecast for homogeneous rainfall region 6 for December, using September to November mean SST of the equatorial Pacific as predictor. The solid line is the observed mean index, and the dashed line the predicted mean index. The horizontal lines on either side of the zero-line define the middle tercile. "cor" is the correlation between the observed and predicted mean indices, "rms" is the root-mean-square error.

The forecast for the test period that follows the climate is shown in Figure 2. For this case, the Skill Score is only 22.2%

(two of the nine years of the test period were predicted correctly, i.e. in the same category - 1987, and 1993). Also, the correlation between the mean predicted indices and the mean observed indices is low. This example shows that high skill obtained from cross-validation, does not guarantee a good forecast. The forecast for December 1994 will be rejected.

The second example depicted in Figures 3 and 4, has the Atlantic mean SST of June to August as predictor, and the rainfall of October of a homogeneous rainfall region in the far northeastern parts of South Africa as predictand.

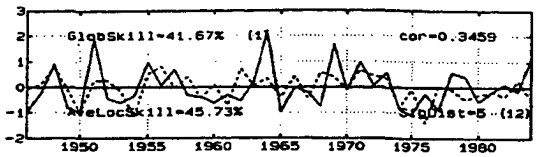


Figure 3. As in Figure 1, but for homogeneous rainfall region 8 for October, using June to August mean SST of the Atlantic Ocean as predictor.

According to the cross-validation criteria listed above, this can also be considered a useful model, even though the local and global skill scores (Figure 3) are lower than those of the previous example.

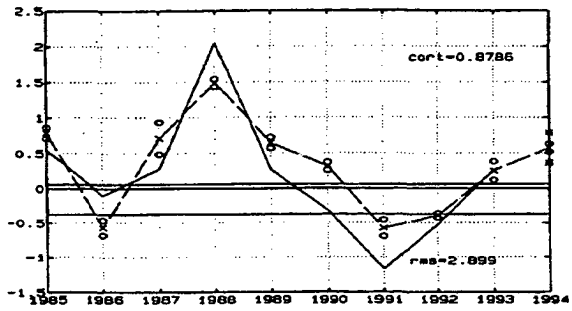


Figure 4. As in Figure 2, but for homogeneous rainfall region 8 for October, using June to August mean SST of the Atlantic Ocean as predictor.

Figure 4 shows the prediction for the test period. A very high Skill Score of 78% (seven of the nine years were predicted correctly) is found here, with a correlation between the predicted and observed mean indices close to 0.9. The forecast for October 1994 is "above-normal". From the above examples it can thus be concluded that it is better to evaluate each model during a test period that is independent of the climate period.

5 CONFLICTING FORECASTS

Three different ocean regions predict for a particular rainfall month. It could happen that more than one ocean can produce a significant model, but with conflicting forecasts. If this happens, the forecast of the model with the highest Skill Score is considered correct. With equal Skill Scores, the correlation between the observed and predicted mean indices is compared. If this correlation is not significant, the global and local skill measures are compared, and finally, the correlation between the predicted and observed mean indices of the cross-validated climate period is considered.

6 CONSTRUCTING THE FINAL FORECAST

Forecasts are made for six consecutive months, with three different SST lags. The first predictand month leads the first SST period (three months) by one month, the second SST period by two months, and the third by three months. A forecast map is constructed for each SST period, with three separate forecast maps the result. The final forecast map is constructed by blending the three maps into one map. This final map shows the predictions that have the highest skill.

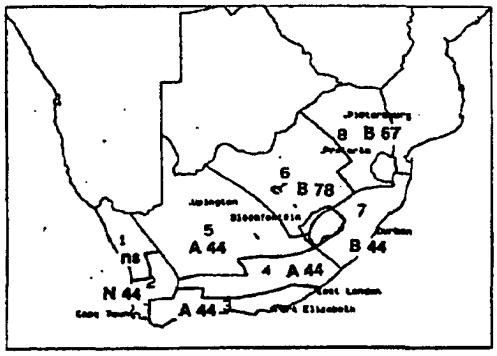


Figure 5. Blended forecast map of the homogeneous rainfall regions. A: above-normal, N: normal, B: below-normal, ns: not statistically significant. Skill scores are shown next to the predicted rainfall category.

Figure 5 is an example of a blended forecast map. By comparing the forecast map with what was actually observed during December 1994, it can be seen that this technique has only modest prediction skill. Table 1 shows the normal rainfall intervals for each homogeneous rainfall region with their associated measured rainfall numbers, as well as the predicted and observed rainfall categories.

Table 1.

Hom Region	Prediction (Skill Score)	"Normal" Interval (mm)	Observed	mm
1	ns	2-7	N	3
2	N (44)	8-20	N	12
3	A (44)	20-32	A	93
4	A (44)	32-53	A	56
5	A (44)	23-40	B	8
6	B (78)	70-100	B	67
7	B (44)	104-128	N	107
8	B (67)	96 - 131	N	97

The forecast was particularly bad for homogeneous rainfall region 5.

7 CONCLUSIONS

1. High global and local skill measures do not guarantee a good forecast - a test period independent of the training period has to be evaluated.
2. CCA as forecast tool, using SST to predict South African rainfall, has modest skill.

8 REFERENCES

Barnett, T.P., R. Preisendorfer, 1987, "Origins and levels of monthly and seasonal forecast skill for United States air temperature determined by Canonical Correlation Ana-

lysis", Mon. Wea. Rev., Volume 115, pp. 1825-1850.

Glahn, H.R., 1968, "Canonical Correlation and its relationship to discriminant analysis and multiple regression", J. Atmos. Sci., Volume 25, pp. 23-31.

Jackson, J.E., 1991, "A User's Guide to Principal Components", John Wiley & Sons, inc. New York, pp. 47-48.

Lau, N.-C. and M. J. Nath, 1994, "A modelling study of the relative roles of tropical and extratropical SST anomalies in the variability of the global atmosphere-ocean system", J. Climate, Volume 7, pp. 1184-1207.

Pan, Y. H. and A. H. Oort, 1990, "Correlation analyses between sea surface temperature anomalies in the eastern equatorial Pacific and the world ocean", Climate Dyn., Volume 4, pp. 191-205.

Reynolds, R.W., 1988, "A real-time global sea surface temperature analysis", J. Climate, Volume 1, pp. 75-86.

Reynolds, R.W., 1994, "Improved global sea surface temperature analyses using Optimum Interpolation", J Climate, Volume 7, pp. 929-948.

Tatsuoka, M., 1988, "Multivariate Analysis", Macmillan, pp. 241-249.

Van Rooy, M.P., 1972, "Climate of South Africa, Part 10: District rainfall for South Africa and the annual march of rainfall over southern Africa", Weather Bureau, Pretoria. WB35, pp. 1-116.

9 ACKNOWLEDGEMENTS

The assistance of A.F. Diaz, Universidad de la República, Uruguay, with the CCA model code, is greatly appreciated, as well as discussions with S.J. Mason, University of the Witwatersrand, South Africa.

CORRESPONDING AUTHOR

Mr W.A. Landman
South African Weather Bureau
Private Bag X097
Pretoria
0001
SOUTH AFRICA

GLOBAL SEA SURFACE TEMPERATURE VARIABILITY ASSOCIATED WITH WEST AFRICAN RAINFALL ANOMALY TYPES. APPLICATION TO SEASONAL FORECAST OF SAHEL RAINFALL

Serge Janicot*, Bernard Fontaine**, Vincent Moron***

* Météo-France, Laboratoire de Météorologie Dynamique du CNRS, Palaiseau, France
** CNRS, Centre de Recherches de Climatologie de l'Université de Bourgogne, Dijon, France
*** Centre de Recherches de Climatologie, Université de Bourgogne, Dijon, France

ABSTRACT

Linear discriminant analyses have been performed between ten classes of West African rainfall anomaly patterns and a priori selected rotated SST low frequency and high frequency components on the period 1945-1993. Results for observed/predicted Sahel rainfall quints occurrences on the dependent period are presented, and statistical significance is assessed through Monte Carlo simulations.

1. INTRODUCTION

Folland et al. (1986) showed that interannual Sahel rainfall variability could be explained by sea surface temperature (SST) anomalies on a global scale. Folland et al. (1991) pursued this investigation and performed a seasonal forecast of the amount of monsoon rainfall. Three SST predictors were selected : unrotated EOF2 of seasonal SST anomalies associated with El Nino / La Nina events in the tropical Pacific, unrotated EOF3 of seasonal SST anomalies exhibiting weights of opposite signs north and south of the equator except for the Northern Indian ocean where they have the same sign as those in much of the Southern Hemisphere, and rotated EOF2 (extracted from Varimax rotation of unrotated EOFs 4-13) of seasonal SST anomalies depicting localized weights in the tropical South Atlantic. Linear discriminant analysis (LDA) was performed between occurrences of five quints of Sahel standardized rainfall total and the three April-May SST predictors over the training highly persistent period 1946-1986 (resp. 1901-1945), and the discriminant function was used to forecast quints over the independent weakly persistent period 1901-1945 (resp. 1946-1986). 21 quints out of 45 (resp. 15 out of 41) were correctly predicted on the independent period 1901-1945 (resp. 1946-1986). However it must be noticed that the EOF analysis was performed on the whole period 1901-1986.

Tanaka et al. (1975), then Nicholson (1981, 1986), showed that most of the West African rainfall anomaly patterns can be summed up by four basic rainfall types delineated '++', '--', '+-','-+', in reference to the rainfall departure signs north/south of 10°N. Janicot (1992), Fontaine and Bigot (1993), and more recently Fontaine and Janicot (1995), demonstrated that these four rainfall anomaly types are associated with statistically different mean SST anomaly fields. These considerations have been also developed by Ward (1994).

Ward (1994) and Rowell et al. (1995), discriminating linkages between Sahel rainfall and SST at decadal and interannual time scales, also pointed out different statistical relationships.

In this paper, we have performed linear discriminant analyses between Sahel rainfall and SST predictors by using information derived from analysis of West African rainfall anomaly types and from separation between low frequency and high frequency time scales. Preliminary results are presented hereafter.

2. DATA ANALYSIS

Seasonal July-September standardized rainfall indexes have been defined for "continental Sahel", "western Sahel" and "Guinea Coast" region over the period 1945-1993 by using rainfall dataset and results presented in Moron (1994). A "Sahel" index has been computed by combining continental and western Sahel indexes with respect to their representative areas. This Sahel index has been categorized according to its rank in the cumulative distribution calculated over the period 1945-1993, by using thresholds of -1 σ, -0.35 σ, +0.35 σ, and +1 σ, where σ is the standard deviation. This provides five near equiprobable categories : 8 cases for the very dry quint, 12 cases for the dry quint, 11 cases for the mean quint, 10 cases for the wet quint, and 8 cases for the very wet quint. The Guinea Coast standardized index has been also categorized into two classes separated by the threshold -0.1 σ, what provides 25 cases for the dry class and 24 for the wet class. Then ten rainfall types are available by combining Sahel quints and Guinea Coast classes.

The SST dataset is an updated version of the UKMO dataset described in Bottomley et al. (1990). It provides global monthly SST anomalies on as many 5° latitude/longitude grid mesh as available, derived from ship measurements, and corrected from presumed observational biases. The period 1945-1993 has been retained, as for rainfall indexes, in order to increase the space/time density of the data. For the same reason, the SST field has been limited between the latitudes 60°N and 40°S. Oceanic grid points with more than 20% of

missing data have been no more included. The remaining missing values have been replaced by their monthly mean computed over the period 1945-1993 in order to avoid any spatial extent of large anomalies over poor documented areas.

A lot of papers pointed out that after the second world war, Sahel rainfall variability has had a strong low frequency component. As we want to discriminate Sahel quint occurrences over the period 1945-1993, we chose to analyse SST variability through its low and high frequency components. We first performed a principal component analysis of the covariance matrix of monthly SST departures after having weighted each oceanic grid-point by the cosine of the latitude. A Varimax orthogonal rotation was applied to define more localized areas of SST signals. The O'Lenic and Livezey (1988) test defined the number of rotated components (here 10). Spectral analyses (not shown) were performed on the rotated modes and a threshold of 96 months (8 years) was pointed out between low frequency and high frequency variability. Then a low-pass Butterworth filter (Murakami, 1979) with a response of 0.5 at 90 months was applied to each grid-point SST time series. The low-filtered SST component is called low-frequency component, and the residual SST component is called high-frequency component. The same Varimax rotated principal component analysis was then applied separately on the low-frequency and on the high-frequency SST components. Rotated SST components have been selected at each of the two frequency scales, in order to be used in the LDA. This has been an a priori choice since we did not select the rotated components best correlated with the ten rainfall types occurrences, but components whose spatial pattern has been shown in previous studies to have a physical impact on West African monsoon dynamics.

The four selected rotated components are shown in Figures 1 to 4. At the low frequency scale, the first rotated component (called hereafter BF1; Fig.1) explains 25% of variance and displays the interhemispheric dipole with positive weights (expressed here in term of correlations) in all the Southern Hemisphere oceans and the Northern Indian ocean, and negative weights in the Northern Hemisphere oceans. The associated time series shows a slow reversal of sign between 1966 and 1979, with negative values before and positive ones after. The second selected low frequency component is the fourth rotated one (called hereafter BF4; Fig.2). It explains 8.7% of variance and displays an in-phase boreal Atlantic mode with strong positive weights in the latitude belts 0°N-20°N and 30°N-50°N. At the high frequency scale, the first rotated component (called hereafter HF1; Fig.3) explains 6.3% of the variance and refers to El Nino / La Nina pattern with positive weights in the Eastern equatorial Pacific and negative one to the West. The associated time series reproduces quite well the El Nino and La Nina occurrences. The second selected high frequency component is the fourth rotated one (called hereafter HF4; Fig.4). It explains 2.27% of variance and displays positive weights in equatorial and tropical parts of the Southern Atlantic. The second rotated component (HF2) was also considered since it has a spatial pattern similar to those of BF4 but it was rejected by a stepwise process (see Tab.1). Each couple of components is not (or very weakly) time-correlated.

3. LDA RESULTS

Linear Discriminant Analysis (LDA) has been performed with the a priori selected BF1-BF4-HF1-HF4 times series for mean three-month values averaged on July-August-September in order to quantify their separating power in relation to the ten rainfall anomaly types occurrences. Then the discriminating power related to the five Sahel quints is infered and compared to the one computed from a LDA working directly on the five Sahel quints without taking into account the Guinea Coast rainfall anomaly occurrences. Computations have been also performed with June-July-August, May-June-July, ..., January-February-March mean values of the four SST rotated components to evaluate the predictive skill of the process. Tab.1 shows that the four SST predictors are selected at a significance level lower than 5%.

Table 1 : Stepwise selection of five July-August-September SST predictors (partial correlation square, F-test and significance level).

	r**2	F	Prob
BF1	0.60	5.94	0.01%
BF4	0.52	4.29	0.08%
HF4	0.51	4.14	0.1%
HF1	0.39	2.60	2%
HF2	0.10	0.45	87%

LDA (Hand 1981, SAS 1989) uses the Bayes probability theorem to forecast the posterior probability of each rainfall anomaly type occurrence, given the predictor values. The prior probability of each type is proportional to the observed one, and not equal (samples vary from 4 to 7 but one class has only one case). For each case, posterior probabilities of occurrence are provided for the ten rainfall anomaly types and the type forecasted with the highest probability is retained. The skill significance has been tested throught two different Monte Carlo simulations. First 1000 discriminant analyses were performed by using each time four pseudo-random normal series to simulate the SST predictors series in the discriminant model. Second, each SST predictor series has been decomposed through a FFT. For each harmonic component, a new phase is computed throught a pseudo-random uniform distribution, and the series is recomposed with these new harmonic components. This new series has the same energy spectral density than the original one but with random dephasings included in each harmonic component. Then the spectral properties of the series are conserved (for example the low frequency signal of BF1 and BF4 is included in each associated simulated series). The Monte Carlo process has been achieved 1000 times for each SST predictor and 1000 LDA have been performed, each time with four different simulated series associated respectively with BF1, BF4, HF1, HF4. Significance levels obtained with the two Monte Carlo processes have been computed and are nearly similar. Then the following results are defined relatively to their statistical significance computed with the second process. One, two, three stars indicate results significant to a 5%, 1%, 0.1% level, respectively.

Table 2 shows the contingency table of the observed/predicted Sahel quints infered from the LDA

performed on the ten classes by using July-August-September SST predictors.

Table 2 : Contingency table of the observed/predicted five Sahel quints infered from the LDA performed on the ten classes with July-August-September SST predictors over the period 1945-1993.

P./O.	--	-	0	+	++
--	6**	2	2	0	0
-	1	8	2	1	0
0	1	1	5	0	0
+	0	0	1	7*	0
++	0	1	1	2	8***

31** out of 49 cases are well classified in the ten classes distribution and 34*** in the five Sahel quints distribution (hit score of 69%), with good scores for the extreme quints. LDA performed with only the five Sahel quints discriminates 30*** out of 49 cases (hit score of 61%; not shown). Then the Guinea Coast rainfall data have provided 8% more well predicted Sahel quints. Table 3 shows the number of well predicted Sahel quints infered from LDA on ten classes with observed values of SST components series for the previous mean three-month periods. Predictability appears larger with inclusion of May values.

Table 3 : Number of well predicted Sahel quints over the period 1945-1993 with observed values of SST components series for the previous mean three-month periods (ex : JFM for January-February-March).

period	skill
JFM	24*
FMA	23*
MAM	27**
AMJ	28**
MJJ	28**
JJA	30***
JAS	34***

4. CONCLUSION

Linear discriminant analyses have been performed to predict Sahel rainfall quints occurrences on the period 1945-1993 with low and high frequency SST components. Results show that Guinea Coast rainfall variability improves the discrimination skill on the dependent and very specific period 1945-1993. Monte Carlo simulations have provided information on the predictive skill. A test on an independent period is necessary whereas the available period 1901-1944 does not provide good quality datasets.

REFERENCES

Bottomley, M., C.K. Folland, J. Hsiung, R.E. Newell and D.E. Parker, 1990, "Global ocean surface temperature Atlas 'GOSTA'", Joint Met. Office / Massachusetts Institute of Technology Atlas. Printed by HMSO, London, 20pp, 313 plates.

Folland C.K., T.N. Palmer and D.E. Parker, 1986, "Sahel rainfall and worldwide sea temperature 1901-1985", Nature, 320, 602-607.

Folland, C.K., J.A. Owen, M.N. Ward and A.W. Colman, 1991, "Prediction of seasonal rainfall in the Sahel region of Africa using empirical and dynamical methods", J. Forecasting, 10, 21-56.

Fontaine, B. and S. Bigot, 1993, "West African rainfall deficits and sea surface temperatures", Int. J. Climatology, 13, 271-285.

Hand, D.J., 1981, "Discrimination and classification", John Wiley and Sons, New-York.

Janicot, S., 1992, "Spatiotemporal variability of West African rainfall; Part II: Associated surface and airmass characteristics", J. Climate, 5, 499-511.

Janicot, S. and B. Fontaine, 1995, "Near-global sea surface temperature variability associated with West African rainfall anomaly types", submitted to J. Climate.

Moron, V., 1994, "Guinean and Salelian rainfall anomaly indices at annual and monthly time scales (1933-1990)", Int. J. Climatology, 14, 325-341.

Murakami, M., 1979, "Large scale aspects of deep convection activity over the GATE area", Mon. Wea. Rev., 107, 994-1013.

Nichoson, S.E., 1981, "Rainfall and atmospheric circulation during drought periods and wetter years in West Africa", Mon. Wea. Rev., 109, 2191-2208.

Nicholson, S.E., 1986, "The spatial coherence of African rainfall anomalies : interhemispheric teleconnections", J. Clim. Appl. Met., 25, 1365-1381.

O'Lenic, E.A. and R.E. Livezey, 1988, "Practical considerations in the use of rotated principal component analysis (RPCA) in diagnostic studies of upper-air height fields", Mon. Wea. Rev., 116, 1682-1689.

Rowell D.P., C.K. Folland, K. Maskell and M.N. Ward, 1995, "Variability of summer rainfall over tropical North Africa (1906-1992): observations and modelling", Quart. J. Roy. Met. Soc., in press.

SAS, 1989, "SAS/STAT, User's Guide", Version 6, 4th edition, Vol.1, Cary, NC: SAS Institute Inc., 943 pp.

Tanaka, M., B.C. Weare, A.R. Navato and R.E. Newell, 1975, "Recent African rainfall patterns", Nature, 255, 201-203.

Ward M.N., 1994, "Tropical North African rainfall and worldwide monthly to multi-decadal climate variation", Thesis Univ. Reading, 312pp.

ACKNOWLEDGEMENTS

The authors are largely thankful to the UKMO for providing the SST dataset.

CORRESPONDING AUTHOR
Dr Serge Janicot
Laboratoire de Météorologie Dynamique
Ecole Polytechnique
91128 Palaiseau Cédex, FRANCE.

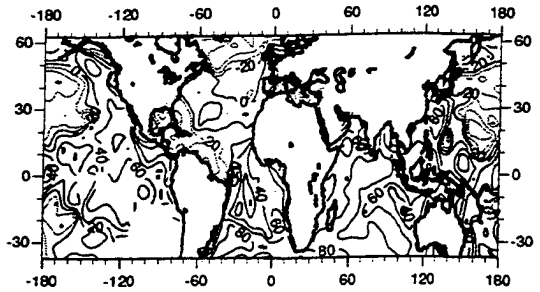


Figure 1a : Rotated component BF1 of low-frequency filtered monthly SST anomalies for 1945-1993; spatial loadings represent correlations between the eigenvector component series and the SST series.

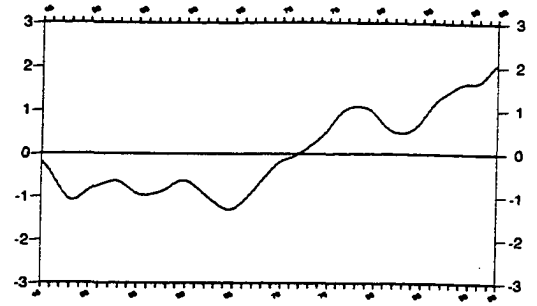


Figure 1b : Rotated component BF1 of low-frequency filtered monthly SST anomalies for 1945-1993; standardized time series of component scores.

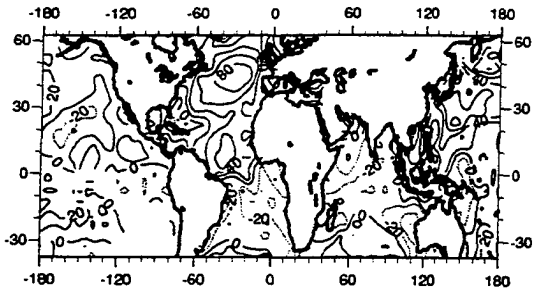


Figure 2a : Rotated component BF4 of low-frequency filtered monthly SST anomalies for 1945-1993; spatial loadings represent correlations between the eigenvector component series and the SST series.

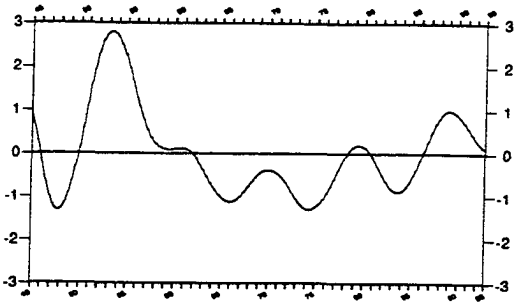


Figure 2b : Rotated component BF4 of low-frequency filtered monthly SST anomalies for 1945-1993; standardized time series of component scores.

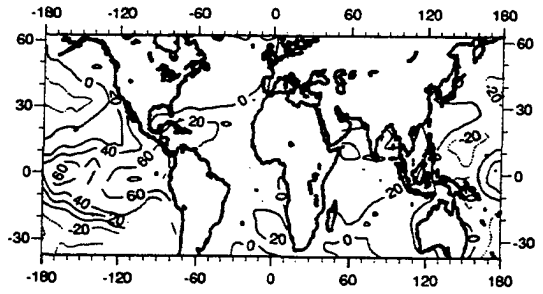


Figure 3a : Rotated component HF1 of high-frequency filtered monthly SST anomalies for 1945-1993; spatial loadings represent correlations between the eigenvector component series and the SST series.

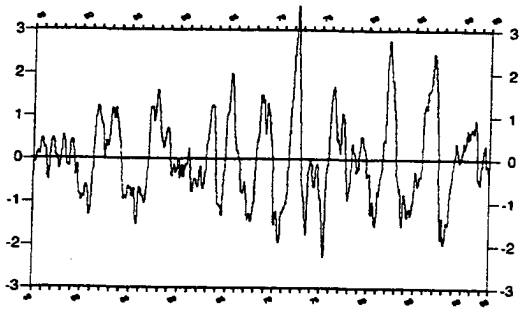


Figure 3b : Rotated component HF1 of high-frequency filtered monthly SST anomalies for 1945-1993; standardized time series of component scores.

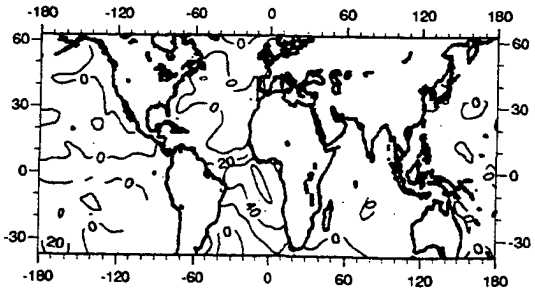


Figure 4a : Rotated component HF4 of high-frequency filtered monthly SST anomalies for 1945-1993; spatial loadings represent correlations between the eigenvector component series and the SST series.

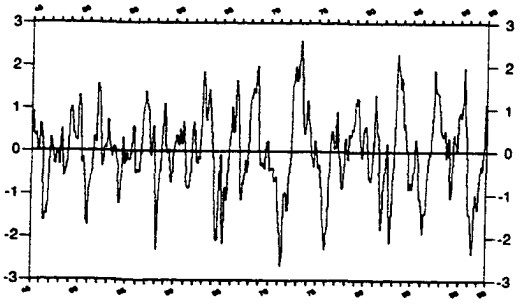


Figure 4b : Rotated component HF4 of high-frequency filtered monthly SST anomalies for 1945-1993; standardized time series of component scores.

The Use of Equatorial Indices for Winter Climate Prediction in the Yukon

Eric Taylor
Climate Section, Science Division
Environmental Conservation Branch
Environment Canada, Pacific and Yukon Region

ABSTRACT

Winter temperatures and precipitation at three sites in the Yukon are compared to the monthly sea surface temperature of the eastern equatorial Pacific and the monthly Southern Oscillation Index (SOI) occurring in the previous summer and autumn. The highest correlations between winter Yukon temperatures and these equatorial indices occur with the August SOI and the September equatorial sea surface temperatures. The highest correlation between winter Yukon precipitation and the equatorial indices occur with the August SOI and the October equatorial sea surface temperatures. Linear relationships between winter Yukon temperature and both the SOI and equatorial sea surface temperatures are developed as a winter temperature forecasting tool.

1. INTRODUCTION

This paper explores the use the Southern Oscillation Index (SOI) and equatorial sea surface temperatures as a tool in forecasting the winter climate in the Yukon (figure 1). The SOI is the standardized difference in sea level pressure between Tahiti and Darwin. This index is linked to the cyclical warming of the ocean surface near the equator in the eastern Pacific, known as El Niño. Negative values of the SOI generally occur during this oceanic warming.



Figure 1. The Yukon with the locations of the three climate stations used in this study.

Previous work has shown that the winter climate in most of the Yukon is related to El Niño (Ropelewski and Halpert 1986; Clark 1990, Shabbar 1993). Ropelewski found that the December through March season is generally milder during El Niño events in the Yukon and that the January temperature of Whitehorse is most highly effected. A possible cause for this link between equatorial climate and Yukon climate are is that the warmer water along the equator increases the north-south atmospheric temperature gradient across the north Pacific. This in turn strengthens the westerly jet stream in the middle atmosphere and results in a stronger push of mild Pacific air over northwestern North America during the winter, including the Yukon (Kousky, 1991, personal communication).

This paper builds on this previous work by developing a forecast tool to help predict winter temperature and precipitation anomalies in the Yukon based on equatorial sea surface temperatures and the SOI from the previous summer and autumn.

2. DATA

Monthly values of the SOI from 1951 to 1993 and sea surface temperature anomalies (SST) from the Niño 3 region from 1970 to 1993 were obtained from the Climate Analysis Center, Washington, D.C. The Niño 3 region is a 10 degree latitude wide band along the eastern equatorial Pacific from 150° West to 90° West longitude.

Monthly average temperatures and precipitation from three Yukon climate stations having climate records since 1951 were obtained from the Canadian Climate Centre, Downsview, Ontario. Locations and elevations of these stations are given in Table 1.

Table 1. Yukon climate stations from which temperature and precipitation were analysed.

Climate Station	Location	Elev. (m)
Whitehorse	60° 43' N, 135° 04'W	703
Watson Lake	60° 07' N, 128° 49'W	690
Mayo	63° 36'N, 135° 53'W	504

Winter temperatures in this study are the average of the monthly temperatures of December through March. Winter precipitation is the sum of the monthly precipitation for these months.

3. ANALYSIS

The initial objective was to find the summer or autumn month(s) during which there was a significant correlation between the equatorial indices and following winter climate. Correlation coefficients were generated between the winter climate variables and the monthly SOI and Niño 3 region SSTs of the five to seven months preceding the winter period. Correlation coefficients were also generated between the two to four-month averages of these monthly SOI and SSTs and the winter temperature and precipitation.

The second objective was to use linear regression to develop relationships between Yukon climate and the summer and fall equatorial indices where significant correlations existed.

a) Temperature

Winter temperature at the three climate sites is negatively correlated to the monthly SOI for all summer and fall months (Figure 2, top).

The best correlation is between winter temperatures and the previous August SOI. The August correlation coefficients range from -0.33 at Watson Lake to -0.43 at Mayo. These are statistically significant at the 5% level. The correlations between winter temperature and SOI values from the months of October and November are markedly lower than those in August. This is a non-intuitive result, since climate conditions occurring in the December through March period would be expected to be most highly correlated with the SOI of the most recent month, November.

Winter temperatures at the three sites are positively correlated to SSTs in all summer and fall months preceding the winter (Figure 2, bottom). The highest correlation is between September SSTs and Yukon winter temperatures. The September correlation coefficients range from 0.48 at Watson Lake to 0.51 at Mayo. All September correlations are statistically significant at the 5% level.

These results reveal a one-month lag between the months of highest correlations of Yukon winter temperatures and equatorial SSTs and SOI. This may be due to the dependence of the SSTs on the wind field, and therefore the SOI, at the equator. Anomalous westerly winds tend to move more warm water into the eastern equatorial Pacific. This is likely due an eastward-propagating equatorial Kelvin wave initiated by these anomalous westerly winds. This Kelvin wave takes about two months to travel from New Guinea to South America (Gill, 1982). This relatively slow speed could be the explanation for the time lag between SOI and SST correlations. Similarly, it is reasonable to expect that there will be a time lag between the onset of anomalous easterly winds at the equator and cooler equatorial SSTs caused by increased upwelling along the northwest coast of South America.

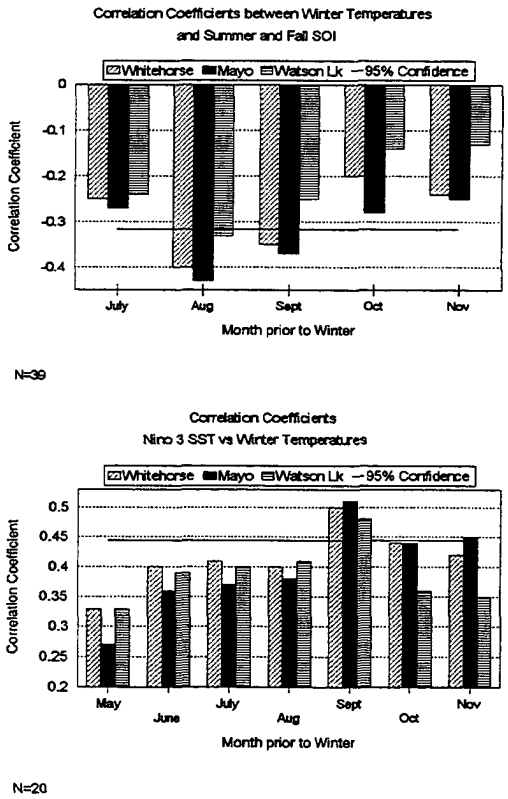


Figure 2 Correlations between winter Yukon temperatures and the Southern Oscillation Index (top) and SST from the Nino 3 region (bottom) from the previous summer and fall. The horizontal lines indicates the value for which the correlation coefficient becomes significant at the 5% level.

Table 2 shows the results of using linear regression to estimate a relationship between Yukon winter temperature and the SOI or SST. The August SOI or the September SST is chosen as the independent variables due to their better correlations with winter temperatures. The winter temperature anomaly at each climate site is the dependent variable. Plots of the regression lines and data for Whitehorse are shown in Figures 3 and 4. As the correlation coefficients are not

large, less than 25% of the variance in winter temperatures is explained by these equatorial indices at all three climate sites.

Table 2. Equations linking equatorial indices and winter temperature at three Yukon climate sites, based upon linear regression. *T* is the winter (December through March) temperature anomaly (°C) at each site, *SOI* is the standardized Southern Oscillation Index of the previous August, and *SST* is the anomaly (°C) in the sea surface temperature in the Niño 3 region of the equatorial Pacific of the previous September. Correlation coefficents (r) vary slightly from those displayed in figure 2 where the sample size (N) is sometimes smaller. p is the significance level.

Site	Regression Equation	r	N	p
Whitehorse	T = - 0.079 - 1.4 * SOI	-0.42	41	.007
	T = 0.092+ 2.0 * SST	0.49	22	.019
Mayo	T = 0.025 - 1.5 * SOI	-0.43	39	.007
	T = 0.37 + 2.1 * SST	0.51	20	.020
Watson L.	T = 0.38 - 0.95 * SOI	-0.34	40	.034
	T = 0.32 + 1.5 * SST	0.48	21	.028

Correlations of the average of several months of summer and fall SOI or SST with winter Yukon temperatures were not as high as the highest single month correlations and are therefore not shown here.

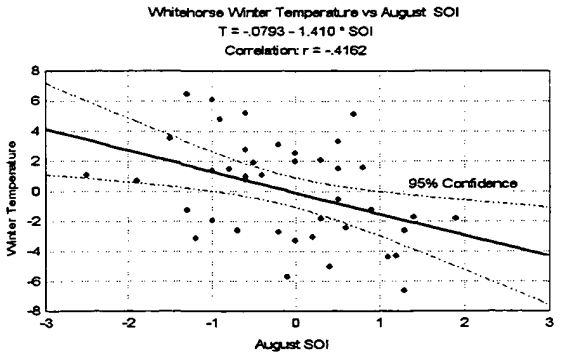


Figure 3 Scatter plot of the Whitehorse winter temperatures as a function of the August SOI. Regression lines with 95% confidence limits are also plotted.

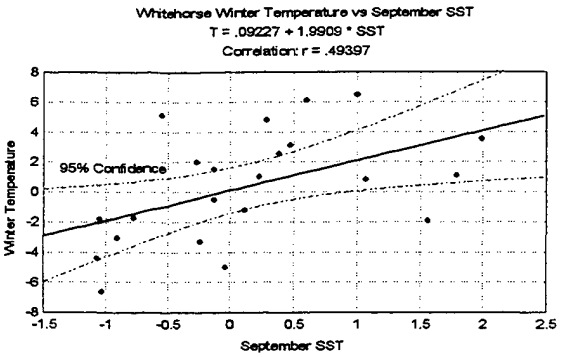


Figure 4. Scatter plot of the Whitehorse winter temperatures as a function of the September SST from the Nino 3 region. Regression lines with 95% confidence limits are also plotted.

b) Precipitation

The correlation between winter precipitation at the three Yukon climate sites and the equatorial indices is lower than that for Yukon temperature. Correlation coefficients between winter precipitation and summer and fall SOI are all positive (Figure 5, top) except for one near-zero correlation in July for Mayo. The highest correlation coefficient between winter precipitation and SOI is 0.39 at Whitehorse for the August SOI. Watson Lake also showed a peak in August (0.25), although the November SOI is almost as high. Only the August SOI correlation with Whithorse winter precipitation is significant at the 5% level.

Correlations between winter precipitation and summer and fall SSTs is higher than with SOIs (figure 5, bottom). All correlations are negative The only correlation coefficient that is significant at the 5% level is between winter precipitation at Whitehorse and the October SST (-0.43). . Watson Lake also shows a peak in October with an correlation coefficient of -0.38. There is only a weak correlation between SST and Mayo winter precipitation.

Due to the generally poor correlation coefficients between winter precipitation and the summer and fall equatorial indices, and the resulting relatively small amount of precipitation variance explained by the equatorial indices, linear regression was not used to determine relationships between the variables.

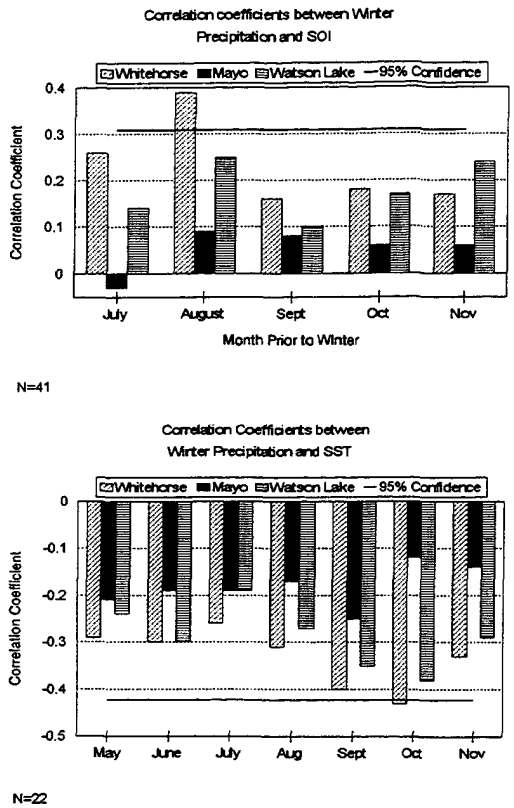


Figure 5 Correlation coefficients between winter Yukon precipitation and the SOI (top) and the SST from Nino 3 region (bottom) for the summer and fall months prior to the winter. The horizontal line in the graph indicates the value of the correlation coefficient at which correlation is significant at the 5% level.

4. SUMMARY AND CONCLUSIONS.

The SOI of the previous summer and fall is negatively correlated to winter temperatures (December through March) in three climate sites in the Yukon. August SOIs have the best correlation to subsequent winter temperatures. Correlation coefficients between temperature and August SOIs varies between -0.34 and -0.43.

The SST in the Niño 3 region of the equatorial Pacific of the previous months is positively correlated to winter temperatures in the Yukon. September SSTs have the best correlation to subsequent winter temperatures. Correlation coefficients between winter temperature and September SSTs varies between 0.48 and 0.51.

Linear relationships were developed between winter temperature and both SOIs and SSTs. All relationships show that negative SOIs or positive SSTs in the previous summer tend to result in warmer Yukon winters, with the opposite also being true. The variance explained by these equatorial indices is not large, but these relationships can be used as one tool in forecasting the winter temperature at the three Yukon sites.

The correlation between the equatorial indices and Yukon winter precipitation is not as high as the winter temperature correlations. Correlation coefficients between winter precipitation and SOI varies between near zero to 0.39, with the highest correlations occurring with the August SOI. Correlation coefficients between winter precipitation and SSTs varies between -0.12 and -0.43, with the highest correlations occurring in with the October SST. Due to the generally small amount of precipitation variance explained by the equatorial indices, regression methods to estimate a linear relationship between the variables were not attempted.

The cause of the time lag of up to 4 months between the most highly correlated summer and fall equatorial indices and the Yukon winter temperatures is not well understood. Warming of the sea surface at the equator appears to be linked with warming in the Gulf of Alaska. This warming would likely result in a milder winter climate in the Yukon. However, a cursory analysis of sea surface temperature anomalies along the west coast of North America does not reveal a significant time lag between warming at the equator and at 50°N.

Further work to expand this analysis into other areas of northwestern North America would be beneficial.

REFERENCES

Clarke, K.J. 1990, "Some Effects on Yukon's Weather", Unpublished internal Environment Canada report.

Gill, Adrian 1982, "Atmosphere-Ocean Dynamics", Academic Press. p 437.

Ropelewski, C.F., and M.S. Halpert, 1986, "North American Precipitation and Temperature Patterns Associated with the El Niño/Southern Oscillation (ENSO)". Monthly Weather Review, **114**, pp 2352-2362.

Shabbar, Amir 1993, "Explosive Volcanoes, ENSOs and the Canadian Climate". Internal Canadian Climate Centre Report no. 93-6.

30-DAY MEAN PREDICTION OF A DYNAMIC-STOCHASTIC MODEL

Weidong Jiang, William Gutowski, Jr.

Iowa State University, Ames, Iowa, U.S.A.

Hongxing Cao

Chinese Academy of Meteorological Sciences
Beijing, P. R. China

ABSTRACT

Applying the multi-time prediction method, a multi-layer dynamic-stochastic prediction model is established based on a primitive equation, global spectral model. In this paper, the principle of the multi-time prediction method and the structure of the prediction model are presented. Also, experimental predictions of 30-day mean temperature at 250 hPa and 750 hPa by the model are described and evaluated.

1. INTRODUCTION

One basic principle of numerical weather prediction is that given an initial state of the atmosphere, the future state is predictable through integrating the differential equations governing the atmospheric motions. Different from this idea, a "conventional" procedure used by experienced weather forecasters is analyzing historical multi-time states of the atmosphere and then making subjective prediction. Koo (1958) pointed out the above difference and suggested a modification of the definition of numerical weather prediction in order to use long-term accumulated observational data which has a lot of meteorological information to be deciphered. Since then, several multi-time numerical prediction models were proposed and tested (Cheng and Tu, 1973; Chou, 1974; Cao, 1981; Zhu and Cao, 1991; Cao et al, 1992). These multi-time models try to take advantage of physics included in the differential equations of the atmosphere as well as the meteorological data series. The experimental short to medium-range weather forecasts have quite good skills.

Following the basic idea of Cao (1981), we established a multi-time prediction model in which the dynamic core is modified form the US National Meteorological Center's (NMC) global, primitive equation, spectral model (GSM) (Brenner et al, 1982). Our main interest is to make global /hemispheric ensemble average prediction using the multi-time prediction method. More specifically, we made 30-day average prediction experiments.

2. PRINCIPLE OF THE MULTI-TIME PREDICTION METHOD

Dynamic or thermodynamic equations governing atmospheric motions at a given location can be generalized in this form,

$$\frac{\partial x(t)}{\partial t} = F(x, \lambda, t), \qquad (1)$$

where x denotes an atmospheric variable, such as temperature, pressure, vorticity, or divergence. λ represents a physical parameter, t time. Eqn. (1) describes the relationship between a local time change rate of x and a space term F(x, λ, t) at the time t. F(x, λ, t) can also be called a source function.

The forward time difference form of Eqn. (1) can be written as

$$x(t_0 + \Delta t) = x(t_0) + F(x, \lambda, t)\Delta t, \qquad (2)$$

which can be used to predict $x(t_0 + \Delta t)$ in terms of information at time t_0. Δt is the time interval and is set to 1 unit hereafter. When Eqn. (2) is actually solved on a computer, there exists computational errors. Considering the errors as stochastic processes, we can modify the difference equation and write a stochastic-difference form of Eqn. (1),

$$x(t_0 + 1) = x(t_0) + \theta_0 F(x, \lambda, t_0) + \delta_0, \qquad (3)$$

where stochastic parameters θ_0 and δ_0, which change with time, are used to implicitly consider errors. t_0 stands for a specific time. According to the above recursive relation, we may similarly write the x values at p+1 time points before t_0+1 as the following expressions,

$$x(t_0) = x(t_0 - 1) + \theta_1 F(x, \lambda, t_0 - 1) + \delta_1, \qquad (4)$$

$$x(t_0-1)=x(t_0-2)+\theta_2F(x,\lambda,t_0-2)+\delta_2, \quad (5)$$

$$\vdots$$

$$x(t_0-p+1)=x(t_0-p)+\theta_pF(x,\lambda,t_0-p)+\delta_p, \quad (6)$$

where θ_i, δ_i (i=0,1,2,...,p) are stochastic parameters at different time. Assuming that x values before time t_0-p has little effect on $x(t_0+1)$ and backward substituting Eqns. (6), (5), and (4) successively into Eqn. (3), we finally obtain the expression as

$$x(t_0+1)=x(t_0-p)+\sum_{i=0}^{p}\theta_iF(x,\lambda,t_0-i)+\delta, \quad (7)$$

where δ is used to represent the summation of all noise terms. Eqn. (7) shows that we can predict $x(t_0+1)$ according to the information of previous p+1 time levels. The physical meaning of Eqn. (7) is that $x(t_0+1)$ is a modified value of x at time t_0-p after considering all the changes from t_0-p to t_0. We note that Eqn. (7) can be viewed as a mathematical expression of the "conventional" forecasting method mentioned in the introduction part. It is also noted that when p=0, $\theta_0=1$, and $\delta=0$, Eqn. (7) reduces to the difference equation (2) used for deterministic prediction.

Assuming that δ behaves as white noise and ignoring it in Eqn. (7), the stochastic parameters θ_i (i=0,1,2,...,p) can be estimated from historical data series according to the least-square principle, and then the prediction for $x(t_0+1)$ can be made.

Following the above principle, we established a multi-time prediction model for the large-scale system in the atmosphere.

3. MULTI-TIME SPECTRAL PREDICTION MODEL

The modified NMC GSM (Brenner et al. 1982) is adapted to be the dynamic kernel of our multi-time prediction model. The GSM part is flexible in vertical resolution and wavenumber truncation. Excluding parameterized physics, the prognostic equations of spectral coefficients of vorticity, divergence, temperature, and surface pressure can be expressed as the follows:

$$\frac{\partial\eta_n^m}{\partial t}=-L_n^m(A_m,B_m)\equiv F1, \quad (8)$$

$$\frac{\partial D_n^m}{\partial t}=L_n^m(B_m,-A_m)+\frac{n(n+1)}{a^2}(E_n^m+\Phi_n^m+RT_0q_n^m)\equiv F2, \quad (9)$$

$$\frac{\partial T_n^m}{\partial t}=-L_n^m((UT')_m,(VT')_m)+I_n^m\equiv F3, \quad (10)$$

$$\frac{\partial q_n^m}{\partial t}=-\bar{C}_n^m-\bar{D}_n^m\equiv F4, \quad (11)$$

where η_n^m, D_n^m, T_n^m, and q_n^m respectively are spectral coefficients of vorticity, divergence, temperature, and logarithmic surface pressure. Others notations are explained in Brenner et al. (1982) except that F1, F2, F3, and F4 are respectively used here to represent the total right-hand side terms of Eqns. (8), (9), (10), and (11).

Applying the method introduced in Section 2 to the above four equations, we get the multi-time prognostic equations of spectral coefficients,

$$\eta_n^m(t_0+1)=\eta_n^m(t_0-p)+\sum_{i=0}^{p}\theta_{1i}F1(t_0-i), \quad (12)$$

$$D_n^m(t_0+1)=D_n^m(t_0-p)+\sum_{i=0}^{p}\theta_{2i}F2(t_0-i), \quad (13)$$

$$T_n^m(t_0+1)=T_n^m(t_0-p)+\sum_{i=0}^{p}\theta_{3i}F3(t_0-i), \quad (14)$$

$$q_n^m(t_0+1)=q_n^m(t_0-p)+\sum_{i=0}^{p}\theta_{4i}F4(t_0-i), \quad (15)$$

where θ_{1i}, θ_{2i}, θ_{3i}, and θ_{4i} are complex stochastic parameters. Therefore, when using multi-time observational data, prediction can be made using the multi-time prognostic equations (12)-(15) instead of the time integration from one initial state.

According the above consideration, four basic parts are needed to construct the multi-time spectral prediction model. The first part, preprocessor, computes the time series of spectral coefficients of vorticity, divergence, temperature, and logarithmic surface pressure from observational data, which could utilize the products of a global prediction model. Results of the preprocessor are fed into the second part, dynamic kernel, to compute the time series of space terms F1, F2, F3, and F4. Predictions of spectral coefficients according to Eqns (12), (13), (14), and (15) is realized in the third part, the complex least-square predictor, which requires the results from the part 1 and part 2. The last part, postprocessor, converts the forecasting spectral coefficients into final results.

4. PREDICTION EXPERIMENTS

To test the long-range forecasting ability of the model, we made four 30-day mean forecasting experiments (February 23-March 24, February 28-March 29, April 14-May 13, and May 29-June 27, 1991) with leading time 5 days. The results were compared with the real fields and the anomaly correlations between them were computed (Tables 1 and 2).

In our experiments, the atmosphere was divided into two even sigma layers and spectral truncation in the meridional direction is equivalent to rhomboidal 30. To simplify computation, the earth's surface was assumed to be flat and parameterized physics was not considered in the experiments. Since the two sigma layers are close to 250 hPa and 750 hPa,

vertical interpolation to the σ-coordinates was skipped in the preprocessor. We used the NMC global analytical data set from September 30, 1990 to July 31, 1991 to compute 30-day average-field time series. When running 5 days was applied, the time series has 61 samples. The p value mentioned in the Section 2 was estimated as the minimum lag length when the correlation is small . We used p=29 in the experiments. The sample size (N in the Section 3) used to estimate the stochastic parameters was set to 34 .

For the 250 hPa temperature field averaged from February 23 to March 24 (Fig. 1), comparing with the real field, we can see that major systems are reasonably shown in the forecasted field, such as the warm ridge over the Northern Atlantic Ocean and the cold trough over the Southern Atlantic Ocean. The cold centers over North America and over North Europe are also reflected in the forecast. However, some details in the real field are not well predicted. The forecast for the high-latitude region of Southern Hemisphere is quite different from the real. Downstream regions of main mountain ranges in the Northern Hemisphere also have the forecasting problem. The forecast field is relatively smoother than the real field.

Similarly, in the 750 hPa fields (Fig. 2), the warm ridge over Europe is consistently located in the forecast although it is smoothed. The position of cold center over North America is shifted northward in the forecast field. The forecast in the Asia has little skill. We note that the Southern Hemisphere forecast is quite good. The baroclinic zone around the Antarctic is captured well by the model forecast. The overall forecast is better than that for 250 hPa temperature .

Similar features can be found in other experiments (not shown). Overviewing our experiments, we note that there is an obvious seasonal trend of forecast skill in Northern Hemisphere. In Table 1, from February to June, the forecast skill of 250 hPa temperature in Northern Hemisphere decreases from 0.911 to 0.718, which leads to a decrease of 55% of the global forecast skill. In Southern Hemisphere, the forecast skill appears relatively stable. The seasonal trend of the temperature field at 750 hPa is qualitatively the same.

Since the parameterized physics for 30-day average variables is not clear, radiative heating and land-atmosphere interaction were not considered in the dynamic computations. When they are relatively small terms, our model may implicitly include these parameterized physics into the stochastic parameters. However, radiative heating and land-atmosphere interaction can not be treated as stochastic processes when they are strong. This may explain the seasonal trend of the model's forecast skill.

ACKNOWLEDGMENTS

We thank the US Air Force Phillips Laboratory and Atmospheric and Environmental Research, Inc., for providing us with the PL/GD-AER global spectral model that was adapted into the dynamic kernel of our model.

The support by NSF grant ATM-913522 to Iowa State University is gratefully acknowledged.

REFERENCES

Brenner, S., C. J. Chang, and S. Y. K. Yee, 1982: The AFGL spectral model of the moist global atmosphere: Documentation of the base line version. AFGL-TR-82-0393, 65pp.

Cao, H., S. Zhu, and W. Jiang, 1992: Dynamic-stochastic model of weather forecasting. Chinese Journal of Computational Physics, 9, 765-766 (in Chinese).

Cheng, C.-L. and H.-Y. Tu, 1973: Anew numerical weather prediction model, utilizing multiple-instant observation data. Scientia Sinica, 16, 396-406.

Chou, G.-F., 1974: A problem of using past data in numerical weather forecasting. Scientia Sinica, 17, 814-825.

Koo, C.-C., 1959: On the equivalency of formulations of weather forecasting as an initial value problem and as an evolution problem. The atmosphere and sea in the motion. The Rossby Memorial Volume.

Zhu, S. and H. Cao, 1991: Preliminary study of barotropic stochastic difference model applied to weather prediction. Acta Meteorologica Sinica, 5, 90-100.

CORRESPONDING AUTHOR

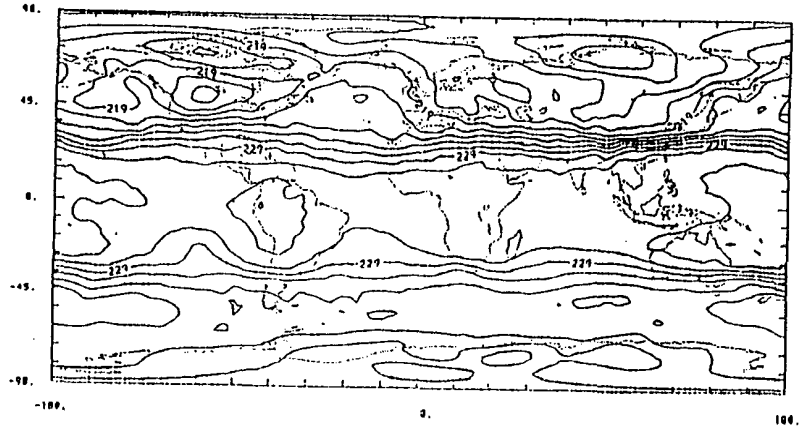
Weidong Jiang, 3010 Agronomy Hall, Iowa State University, Ames, IA 50011 USA.

Table 1. Anomaly correlations between the real temperature fields and the forecasted temperature fields leading 5 days at 250 hPa

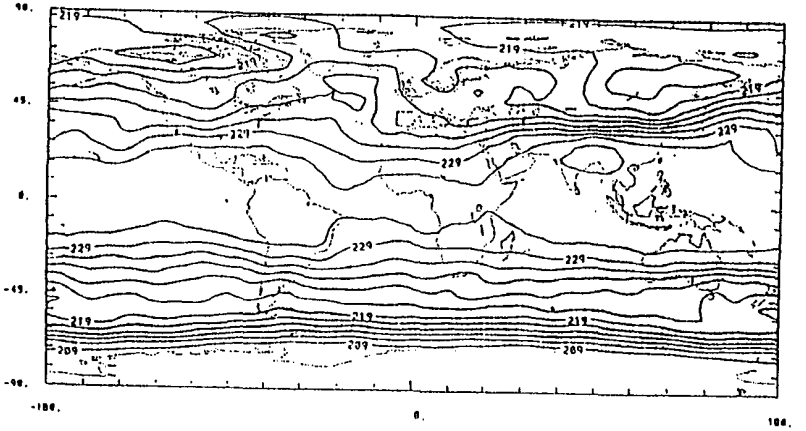
Average	250 hPa		
period	Globe	N. H.	S. H.
2/23-3/24	0.610	0.911	0.904
2/28-3/29	0.659	0.898	0.905
4/14-5/13	0.796	0.741	0.916
5/29-6/27	0.277	0.718	0.932

Table 2. Same as Table 1 but at 750 hPa

Average	750 hPa		
period	Globe	N. H.	S. H.
2/23-3/24	0.923	0.958	0.989
2/28-3/29	0.942	0.962	0.988
4/14-5/13	0.892	0.967	0.953
5/29-6/27	0.671	0.892	0.947

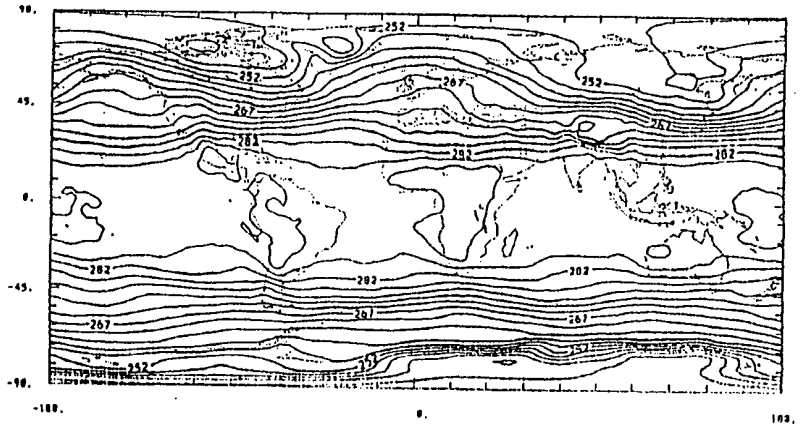


(a)

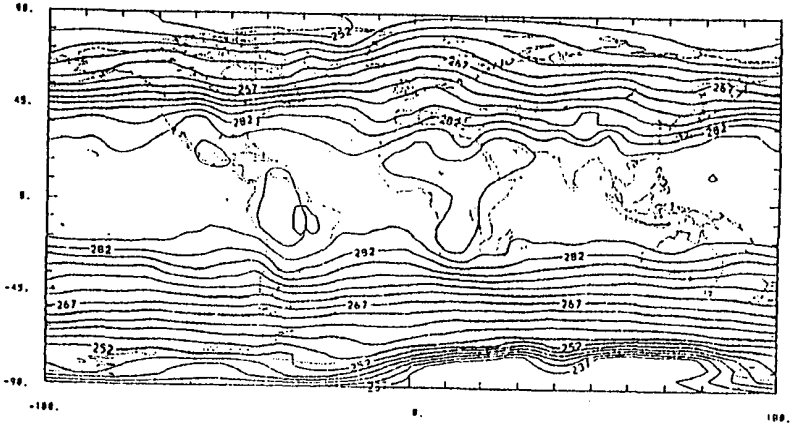


(b)

Fig. 1 (a) The real and (b) the forecasted temperature fields at 250 hPa averaged from Feb. 23 to March 24, 1991. Contour interval is 2K.



(a)



(b)

Fig. 2 (a) The real and (b) the forecasted temperature fields at 750 hPa averaged from Feb. 23 to March 24, 1991. Contour interval is 3K.

WEAKLY QUADRATIC STRUCTURE OF THE SPECTRUM OF ATMOSPHERIC PRESSURE VARIATIONS ON TIMES SCALES OF MONTHS TO YEARS

Sultan Hameed and Robert G. Currie

State University of New York, Stony Brook, New York, USA

ABSTRACT

Computed Fourier spectra of solar flux to the atmosphere at all latitudes yields a discrete spectrum with lines at 12, 6, 4, 3, 2.4, 2 months, etc., and occurs necessarily so from the earth's orbital characteristics. This structure is found in spectra of observed sea level air pressure (SLP), which also show subharmonic peaks with periods $T_1 \approx 40$ and $T_2 \approx 26$ months, the quasi-triennial QTO and quasi-biennial QBO oscillations, and with period $T_3 \approx 14$ months, the atmospheric pole tide (APT). The spectra also yield evidence for a further 33 peaks. These are explained as summation and difference tones caused by interaction of the annual and its five harmonics (first set of parents) with the subharmonics T_i, i = 1-3 (second parents), and the theoretical expression for the tones is

$$f_{i\pm j} = 1/T_i \pm (j + 1)/12 \qquad (1)$$

cycles per month (cpm), where j = 0.5. The only requirement physically for these interactions is that the atmosphere be weakly nonlinear.

1 INTRODUCTION

We show that on a time scale of 2 to ≈70 months (mon) the spectrum of observed sea level pressure SLP is discrete, and characteristic of a weakly nonlinear system; it is not chaotic. This result emerges from applying the Fourier transform to monthly SLP data of the Northern Hemisphere for 1899-1982 prepared by Trenberth and Paolino (1980). At a latitude of 30°, based on 216 spectra, we find discrete line spectra at 12, 6, 4, 3, 2.4, and 2 mon corresponding to j = 0-5 in Equation (1). They account for 63 percent of total variance in the monthly sampled data.

Peaks at subharmonic periods of 42.3, 29.1, and 14.2 mon are also found corresponding to T_i, i = 1-3 in Equation (1). In addition, we find evidence for 31 out of 33 possible summation and difference tones described by Equation (1); physically, the generation of these tones only assumes a weakly quadratic response of atmospheric pressure variations to a seasonal forcing.

Hameed and Currie (1995) present a more lengthy investigation for latitudes 20° to 85°N of the Trenberth and Paolino (1980) data set, which leads to the same conclusions drawn herein for 30°N. The results encompassed in Equation (1) for observed SLP data confirm the comprehensive worldwide study of Hameed et al. (1995), who found the same structure in SLP series simulated by two different versions of the Oregon State University OSU coupled ocean-atmosphere GCM. Earlier papers on more limited aspects of the phenomena described by Equation (1) are Currie and Hameed (1988, 1990) and Hameed and Currie (1989).

2 SPECTRUM OF THE SOLAR FLUX

Prior to analysis of SLP data, it is important to establish the modes of variability exhibited by incident solar flux at the top of the atmosphere. The fact that incident solar radiation has discrete periods in the daily and monthly period ranges is due to the effects of the earth's diurnal rotation, and inclination of its rotation axis with the ecliptic as it orbits about the sun. It thus follows that the spectrum of incident solar flux is discrete. Hameed et al. (1995) computed daily averaged solar flux at the top of the atmosphere at different latitudes using the analytic expression given by Sellers (1965, equation 3.7). The Fourier transform was applied to these time series and they verified (their figure 1) that the input energy of solar flux to the atmosphere is discrete with periods 12, 6, 4, 3, 2.4, 2, 1.7 mon, etc. It was shown that: (1) at the equator more energy is input to the atmosphere at 6 mon than at 12, a factor responsible for the dominant semi-annual variability of equatorial climates. (2) As latitude increases there is a substantial and monotonic decrease of power with increasing harmonic number, a feature responsible for the dominant role of the 12 mom period in mid-latitude climate. (3) Because solar flux is zero for nearly half the year at the poles the available energy is distributed into a large number of harmonics, and power in the 6 mon harmonic is only moderately less than in the 12 mon term; this indicates that climate in the polar regions is expected to be much more variable on monthly time scales than at mid-latitudes, as was observed in SLP data by Maksimov (1960).

The relative amplitudes and phases of the 12 mon period and its harmonics have been used to characterize different climate regimes (e.g., Kirkyla and Hameed, 1989). But the more interesting problem is the following: What other modes of variability will be excited by the interaction of the discrete frequency (12, 6, 4, 3, 2.4, 2 mon) solar flux with the non-linear climate system?

3 SAMPLE SPECTRUM AT 30°N

Figure 1 shows the mean spectrum based on 3 x 72 individual spectra at 30°N from the Trenberth and Paolino (1980) data set from 1899-1982. The grid spacing for each time series is 5° yielding 72 records. Each record was broken into three series spanning 1914/36, 1937/59, and 1960/82. Thus each of the 216 series consists of 276 monthly values. This length was chosen because it corresponds with the length of simulated SLP series in the OSU2 GCM studied earlier by the writers (see citations).

Figure 1 is obtained as follows: (i) a linear trend is fitted to each time series and subtracted from the corresponding 276 monthly values to obtain residuals, (ii) the fast Fourier transform is calculated for each series of residual values, (iii) the resulting 216 spectra are averaged, and (iv) the average spectrum is multiplied by 1000 and the log taken. Taking the log enables one to cover a wide dynamic range and multiplication by 1000 avoids negative values in Figure 1.

In Figure 1 one observes line spectra with enormous power at 12, and 6 mon periods, and smaller lines at periods 4, 3, 2.4, and 2 mon. This is the same structure as that due to the solar flux at the top of the atmosphere discussed in Section 2, and the Fourier spectrum of this flux for 30°N is given in Fig. 1 of Hameed et al. (1995). The contribution of the 12 mon term to total variance in the data is 53 percent, that of the 6 mon signal is 6 percent, and that of the 4-2 mon terms is 4 percent. Thus, 63 percent of the total variance is explained by the seasonal cycle.

Note in Figure 1 peaks with periods $T_1 = 42.3$, $T_2 = 29.1$, and $T_3 = 14.2$ mon. These are respectively identified as the quasi-triennial oscillation or QTO, the quasi-biennial oscillation or QBO, and the atmospheric pole tide or APT found by Currie and

Hameed (1990) and Hameed et al. (1995) in simulated SLP for two OSU-GCMs. The analog of the APT in astronomy is known as the "Chandler wobble" of the solid earth's rotation axis, and the "pole tide" in oceanography (Currie, 1975). Since the phenomenon is little known in atmospheric science a brief discussion is given in Hameed et al. (1995).

It has long been known (e.g., Stoker, 1950) that nonlinear systems can display discrete oscillatory modes in addition to those associated with external forcing. For a large variety of systems, modes are excited at frequencies that are lower than the forcing frequency. In this, the "subharmonic range", periods that are integral multiples of the external periods are commonly detected. The generation of such modes is sometimes referred to as the "subharmonic cascade" in the modern literature on nonlinear systems (see Berge et al., 1984, Chap. 8). We identify the QTO and QBO as such a phenomena with the period lengthened for reasons still unclear.

4 THEORETICAL MODEL FOR TONES

The existence of combination tones in weakly non-linear systems subject to periodic external forcing has been discussed by Stoker (1950) and Feynman et al. (1963). Since T_1, T_2, T_3 are not exact integral multiples of the periods of the annual cycle and its harmonics one expects that the sums and differences of their frequencies may be generated due to nonlinearlity. If one considers a weakly quadratic response, i.e., if an input signal $\chi_{in}(t)$ generates a response

$$\chi_{out}(t) = K[\chi_{in}(t) + \varepsilon\chi_{in}^2(t)]$$

where $\varepsilon << 1$ and $\chi_{in}(t)$ has two frequencies ω_1, ω_2 written as

$$\chi_{in} = A\cos(\omega_1 t) + B\cos(\omega_2 t),$$

then $\chi_{out}(t)$ contains the term

$$AB/2[\cos(\omega_1+\omega_2)t + \cos(\omega_1-\omega_2)t].$$

In such weakly nonlinear systems one expects combination tones, summation and difference, with frequencies $(\omega_1 \pm \omega_2)$ [Feynman et al. (1963), equation 50.25]. The condition $\varepsilon << 1$, that is, that the system has a weakly quadratic response to forcing, is the only assumption made.

Consider two sets of parent frequencies ω_1 and ω_2. One set consists of the annual term and its harmonics present in the external forcing with periods 12, 6, 4, 3, 2.4 and 2 mon. The other set contains the three subharmonic responses of the system—the QTO (T_1), the QBO (T_2), and APT (T_3) seen in Figure 1. These periods are not external, but because they are not in a rational proportion to the external periods the two sets of parents interact to generate combination tones.

The combination of the three subharmonic frequencies $f_i = 1/T_i$ and the annual cycle and its 5 harmonics give rise theoretically to 33 combination tones described by Equation (1). It should be noted that tones f_{1+5} in Equation (1) cannot be detected in data sampled monthly because they lead to frequencies higher than the Nyquist $f_N = 0.5$ cpm, that is to say, periods shorter than 2 mon.

In order to gain familiarity with Equation (1), consider the difference tones predicted by the parents observed in Figure 1 with periods 42.3 (i = 1), 29.1 (i = 2), and 14.2 mon (i = 3), interacting with the first harmonic of period 6 mon (j = 1). Equation (1) predicts that these interactions will produce tones with frequencies f_{1-1}, f_{2-1}, and f_{3-1} whose periods are 6.99, 7.56, and 10.39 mon. These predicted periods are quite close to three peaks seen in Figure 1 whose periods are 7.07, 7.66, and 10.4 mon. As a second example consider the summation tones with frequency f_{1+1}, f_{2+1}, and f_{3-1} whose periods are 5.25, 4.97, and 4.22 mon. These predicted periods are quite close to another two peaks seen in Figure 1 whose periods are 4.97, and 4.28 mon. The observed peak which should be near 5.25 mon is missing as denoted by as asterisk in Figure 1. In a similar manner one could construct the combination tones of the 12 mon annual and its 4, 3, 2.4, and 2 mon harmonics interacting with the three subharmonics.

5 SAMPLE TABLE FOR TONES AT 30°N

Columns 1-2 of Table 1 list the tone numbers 1-33 and symbols in terms of Equation (1) for increasing frequency. Column 3 contains the predicted frequencies according to Equation (1) with the T_1 = 42.31, T_2 = 29.05, and T_3 = 14.16 mon parents interacting with the seasonal term and its five harmonics. Column 4 lists the corresponding frequencies observed in Figure 1. These 31 tones and their three subharmonic parents contribute 22 percent of total variance in the data. And, since the second set of parents contributes 63 percent to total variance in the data as noted earlier, it follows that the remaining 15 percent of variance is accounted for by noise.

Column 5 shows the percentage of spectra out of 216 total where evidence for each frequency was found. The mean is 56 percent. Column 6 lists the discrepancies between predicted and observed frequencies. The root-mean-square rms error between prediction and observation for the 31 tones identified is 0.00254 as shown. Thus, the errors are on the order of a few parts in 1,000. Columns 7-8 give the corresponding predicted and observed periods. Out of 33 predicted tones only tones 1 and 11 are not found in the spectrum of Figure 1, and they are identified by the two asterisks.

The Trenberth and Paolino (1980) data set is sampled at 5° intervals in northern latitudes, beginning at latitude 20°N. Hameed and Currie (1995) have prepared 14 tables analogous to Table 1 for each latitude from 20°N to 85° inclusive, as well as a table giving the weighted average predicted and observed frequencies for all latitudes. For all latitudes the mean periods of the three sub-harmonic periods were T_1 = 38.75 mon for the QTO, T_2 = 28.35 mon for the QBO, and T_3 = 14.31 mon for the APT. The APT was detected in 79 percent of all spectra, whereas detection for the much better known QBO was low at 49 percent (the QTO was intermediate at 58 percent).

6 COMBINATION TONES OF THE SOLAR CYCLE

We note the two sets of dark arrows drawn about the 4 and 3 mon harmonic lines in Figure 1 with periods (3.89, 4.12 mon) and (2.94, 3.07 mon). Also note the arrow with period 138 mon or 11.5 years. When one takes the sum and difference frequencies of the 4 mon and 3 mon terms, respectively, with the long period 138 mon period one gets two sets of frequencies, (0.25725, 0.24275 cpm) and (0.34050, 0.32608); their periods are (3.89, 4.12 mom) and (2.94, 3.07 mon), the same as observed in Figure 1.

Currie (1993) has reported two long period signals in climate data with periods ≈ 11 and ≈19 years, identifying them as the solar cycle and 18.6-year luni-solar effects on climate. Figure 1 shows two sets of tones generated by summation and difference frequencies of the solar cycle signal interacting with the 4 and 3 mon harmonics. If one expands the length of the SLP records to 408 months, rather than 276 to increase resolution one finds good evidence for two combinations lines about the 12, 6, and 2.4 mon lines in addition to the two sets of lines seen in Figure 1 about the 4 and 3 mon harmonics. Such structure has been found in other climate parameters such as air temperature (Currie and Hameed, unpublished data 1993), but further discussion is outside the scope of this paper.

7 DISCUSSION

Certain features of Figure 1 are well understood, for we know that solar flux to the top of the atmosphere has a discrete spectrum. This structure consists of lines with periods 12, 6, 4, 3, 2.4, and 2 mon, and it contributes 63 percent to total variance in SLP at 30° N.

Similarly, certain other spectral features of Figure 1 have also been reported such as the QTO, QBO, and APT with periods ≈40, ≈26, and ≈14 mon. The novel aspect is that we see in Figure 1 many other peaks which correspond to summation and difference tones as first identified in simulated GCM data, and now seen in observed SLP at 30°N. These 33 tones are generated, as described by Equation (1), by weakly quadratic interactions between two sets of parents, the seasonal term and its harmonics, and the QTO-QBO-APT subharmonics.

This result shows that on time scales of months to several years the atmosphere is a weakly quadratic system and not a chaotic system. The suggestion of atmosphere being chaotic arises from models, such as that of Lorenz (1963), in which temporal variation of the external forcing is suppressed, and therefore the discrete nature of the spectrum of the atmospheric response, seen in Fig. 2, is not simulated.

The results presented here suggest that the seasonal variation of the external forcing imposes order on the atmosphere by concentrating power in certain predictable frequencies. This is consistent with the work by Prigogine (1947) who showed that energy input into physical systems results in steady non-equilibrium states, characterized by a minimum of entropy production; that is to say, by order. Wyant et al. (1987) demonstrate that Prigogine's theorem is applicable to the atmosphere only if time dependence of solar radiation is included in model calculations.

REFERENCES

Berge, P., Pomeau, Y., and Vidal, C., 1984, "Order within Chaos, Wiley, New York.

Currie, R. G., 1975, "Period, Q, and amplitude of the pole tide", Geophys. J. Roy. Astr. Soc., Volume 43, pp. 73-86.

Currie, R. G., 1993, "Luni-solar 18.6- and 10-11 year solar cycle signals in USA air temperature records, Int. J. Climatol., Volume 13, pp. 31-50.

Currie, R. G. and Hameed, S., 1988, "Evidence of quasi-biennial oscillations in a general circulation model", Geophys. Res. Lett., Volume 15, pp. 649-652.

Currie, R. G. and Hameed, S., 1990, "Atmospheric signals at high latitudes in a coupled ocean-atmosphere general circulation model:, Geophys. Res. Lett., Volume 17, pp. 945-948.

Feynman, R. P., Leighton, R. B. and Sands, M., 1963, "The Feynman Lectures on Physics", Volume 1, Addison-Wesley, Reading.

Hameed, S. and Currie, R. G., 1989, "Simulation of the 14-month Chandler wobble in a global climate model", Geophys. Res. Lett., Volume 16, pp. 247-250.

Hameed, S. and Currie, R. G., 1995, "Signals in atmospheric pressure variations from 2 to ≈70 months: Part II, observed sea-level pressure variations over the northern hemisphere", Int. J. Climatol., in review.

Hameed, S., Currie, R. G. and LaGrone, H., 1995, "Signals in atmospheric pressure variations from 2 to ≈70 months: Part I, simulations by two coupled ocean-atmosphere GCMs, Int. J. Climatol., in press.

Kirkyla, K. I. and Hameed, S., 1989, "Harmonic analysis of the seasonal cycle in precipitation over the United States: a comparison between observations and a general circulation model", J. Climate, Volume 2, pp. 1463-1475.

Lorenz, E. N., 1963, "Deterministic nonperiodic flow", J. Atmos. Sci., Volume 20, pp. 130-141.

Lean, J., 1991, "Variations in the Sun's radiative output", Revs. Geophys., Volume 29, pp. 505-535.

Maksimov, I. V., 1960, "Nutational phenomena in the high latitude atmosphere and their role in the formation of climate", in Problems of the North, Volume No. 1, National Research Council Canada, pp. 103-123.

Prigogine, I., 1947, "Etude Thermodynaminque Des Phenomenes Irreversibles", Desver, Liege.

Sellers, W. D., 1965, "Physical Climatology", University Chicago Press, Chicago.

Stoker, J. J., 1950, "Nonlinear Vibrations in Mechanical and Electrical Systems", Interscience, New York.

Trenberth, K. E. and Paolino, Jr. D. A., 1980, "The Northern Hemisphere sea-level pressure data set: trends, errors and discontinuities", Mon. Wea. Rev., Volume 108, pp. 855-872.

Wyant, P. H., Mongroo, A. and Hameed, S., 1988, "Determination of heat transport coefficient in energy-balance climate models of extremization of entropy production", J. Atmos. Sci., Volume 45, pp. 189-193.

ACKNOWLEDGEMENTS

This work was performed under the auspices of the CO_2 Research Division, Office of Basic Energy Sciences, U. S. Department of Energy through Grant DEFG0285ER60314A007 to the State University of New York at Stony Brook.

CORRESPONDING AUTHOR

Dr. Sultan Hameed
Institute for Terrestrial and Planetary Atmospheres
State University of New York
Stony Brook, New York 11794-5000, USA

Figure 1. Mean Fourier spectrum of sea level pressure at 30°N. It is the average of 216 spectra as described in section 3. The periods associated with the peaks are shown in months. Spectral peaks that appear as doublets are indicated by vertical lines and triplet peak structure is identified by light arrows (see Hameed et al. (1995) for details). The dark arrows point to the combination tones of the 138 month peak assumed to be related to the solar cycle (see Sect. 6).

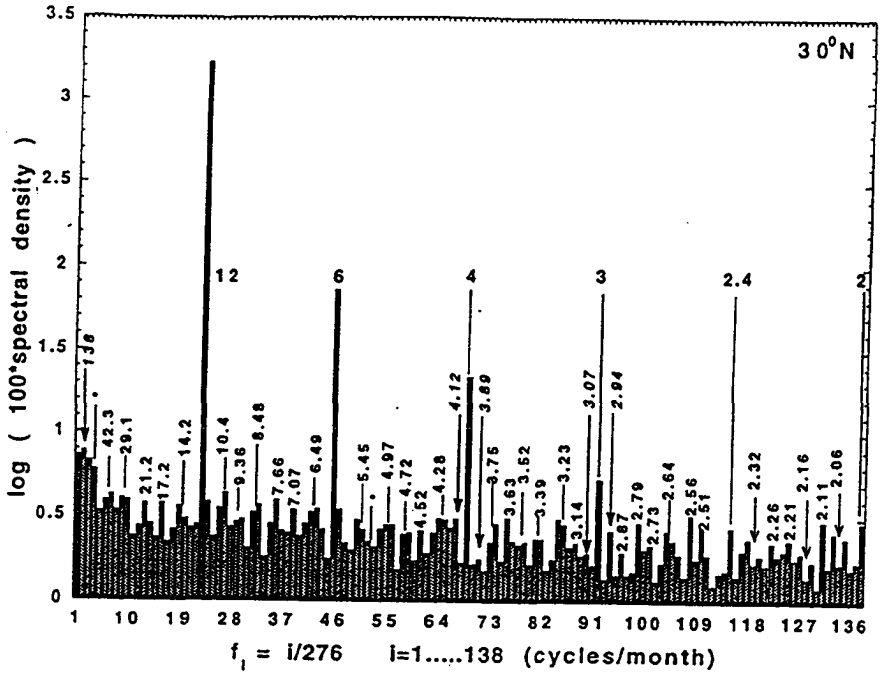


Table 1. Summary of theoretical (according to Eq. 1) and observed summation and difference tones in terms of frequencies and periods for Trenberth air pressure data at 30°N. The subharmonic periods shown in Fig. 1 have periods T_1=42.3, T_2=29.1, and T_3=14.2 mon.

Tones	$f_{i\pm j}$ Eqn. 1	Predicted frequency (cpm)	Observed frequency (cpm)	% out of 216 spectra	Discrepancies	Predicted period (months)	Observed period (months)
1	f_{3-0}	0.01270				78.72	
2	f_{2-0}	0.04891	0.04718	40	0.00173	20.44	21.20
3	f_{1-0}	0.05969	0.05800	46	0.00169	16.75	17.24
4	f_{3-1}	0.09604	0.09638	77	-0.00134	10.41	10.38
5	f_{1+0}	0.10697	0.10687	69	0.00010	9.35	9.36
6	f_{2+0}	0.11775	0.11793	81	-0.00018	8.49	8.48
7	f_{2-1}	0.13225	0.13052	40	0.00173	7.56	7.66
8	f_{1-1}	0.14303	0.14135	49	0.00168	6.99	7.07
9	f_{3+0}	0.15396	0.15419	75	-0.00023	6.50	6.49
10	f_{3-2}	0.17937	0.18341	71	-0.00404	5.58	5.45
11	f_{1+1}	0.19031				5.25	
12	f_{2+1}	0.20109	0.20102	71	0.00007	4.97	4.97
13	f_{2-2}	0.21558	0.21200	79	0.00358	4.64	4.72
14	f_{1-2}	0.22636	0.22108	39	0.00528	4.42	4.52
15	f_{3+1}	0.23730	0.23387	77	0.00343	4.21	4.28
16	f_{3-3}	0.26270	0.26644	75	-0.00374	3.81	3.75
17	f_{1+2}	0.27364	0.27544	39	-0.00180	3.65	3.63
18	f_{2+2}	0.28442	0.28616	38	-0.00174	3.52	3.49
19	f_{2-3}	0.29891	0.29548	75	0.00343	3.35	3.38
20	f_{1-3}	0.30969	0.30976	73	-0.00007	3.23	3.23
21	f_{3+2}	0.32063	0.31701	66	0.00362	3.12	3.15
22	f_{3-4}	0.34604	0.34779	38	-0.00175	2.89	2.88
23	f_{1+3}	0.35697	0.35875	42	-0.00178	2.80	2.79
24	f_{2+3}	0.36775	0.36588	44	0.00187	2.72	2.73
25	f_{2-4}	0.38225	0.37844	78	0.00381	2.62	2.64
26	f_{1-4}	0.39303	0.39132	50	0.00171	2.54	2.56
27	f_{3+3}	0.40396	0.39852	37	0.00544	2.48	2.51
28	f_{3-5}	0.42937	0.43103	85	-0.00166	2.33	2.32
29	f_{1+4}	0.44031	0.44207	39	-0.00176	2.27	2.26
30	f_{2+4}	0.45109	0.45285	35	-0.00176	2.22	2.21
31	f_{2-5}	0.46558	0.46370	90	0.00188	2.15	2.16
32	f_{1-5}	0.47636	0.47466	54	0.00170	2.10	2.11
33	f_{3+4}	0.48730	0.48566	85	0.00164	2.05	2.06
				56	0.00254		

CLIMATOLOGY OF THE CYCLONE IN GLOBAL ATMOSPHERE

V.E. LAGUN (THE ARCTIC & ANTARCTIC RES. INS.),

38, Bering st., St. Petersburg, 199397, RUSSIA

Global distribution and short term variability cyclone climatology parameters have been investigated using a developed method of numerical diagnosis. Twice-daily US NMC surface pressure field (1981-1992) are used to estimate temporal and spacial frequencies, number, square, speed drift and other cyclone parameters. Spacial frequency is defined as ratio of the total sumcyclones square on hemisphere to hemisphere square. It was found that the mean global and hemispheric values of local temporal and spacial frequency is quasi-constant. The clear increase of the mature cyclone number in the last decade have been presented. Hypothetical causes of the tendencies of the climatic change of cyclonic activity parameters are discussed.

Variations in Anticyclonicity across the eastern Australasian Region for the 29-year period (1965 - 1993)

R.M. LEIGHTON and H. NOWAK
National Meteorological Centre
Bureau of Meteorology
Melbourne
Australia

ABSTRACT

Anticyclonicity variations for the 29-year period (1965-1993) for each season and annual are presented for the area centred on eastern Australia. Maps of those regions which display long term variations are shown and discussed. A presentation of time-series of the anticyclonicity at selected points highlights where significant variations have been observed.

INTRODUCTION

The term 'anticyclonicity' ('cyclonicity') is defined as the time in hours during which anticyclone (cyclone) centres occupy a given 5 degree latitude-longitude "square" in a given period. Anticyclonicity (cyclonicity) is computed from the locations of anticyclone (cyclone) centres in the Australian Bureau of Meteorology Centre's 0000 and 1200 UTC sea level pressure analyses, assuming a uniform speed of movement for systems that can be tracked. Single centres which are not part of a track are assigned a lifetime of 6 hours.

The representation of the surface circulation in the Australian region (including New Zealand), for long periods (months or seasons), by means of charts of anticyclonicity and cyclonicity was developed during 1951-53, in connection with the problem of extended range forecasting in Australia. Charts of 7-year averages (1946-1952) of monthly and seasonal anticyclonicity and cyclonicity were presented and discussed by Karelsky (1954). Updated charts for the 15 years 1946-60 were later published (Karelsky 1961).

Since 1960, satellite imagery has substantially enhanced the date base available to analysts in the National Meteorological Centre. Leighton and Deslandes (1991a) published monthly charts of anticyclonicity and cyclonicity for the 23 years 1965-87, for the Australasian region including the eastern Indian Ocean. Synoptic discussions of the averages for this later period were also presented (Leighton and Deslandes 1991b)

A paper illustrating how (anti)cyclonicity anomalies can relate to significant prolonged weather events in the Australian region was published by Leighton (1994).

The anticyclonicity data base for the Australasian region has been extended to 1993. This time period was considered long enough to provide some significant variations (trends) in anticyclonicity totals over a region. This paper highlights the areas across eastern Australia, the Tasman Sea, New Zealand and the Southern Ocean where such variations (trends) in seasonal and annual anticyclonicity have occurred.

Data and Methodology

The monthly cyclone-anticyclone data base (MCAHD) for the Australasian region covers the 29 year period 1965-1993. The anticyclonicity data base for the eastern Australasian region (130°E-180°E, 25°S-55°S) was extracted from MCAHD and monthly totals were summed to give seasonal and annual totals.

All seasonal and annual anticyclonicity values were correlated with the year to examine linear trends. From the correlation co-efficients obtained isopleths of +0.37 and -0.37 were drawn for each season and year (a correlation co-efficient of ±0.37 is significant at the 5% level for the sample size of 29). Areas within the +0.37 isopleth are described as showing an increase in anticyclonicity and areas within the -0.37 isopleth are described as displaying a decrease in anticyclonicity.

DISCUSSION

Winter

During the winter months a notable decrease in anticyclonicity has occurred across western Victoria, central New South Wales and southeastern Queensland (Fig 1a). An increase in anticyclonicity is evident across southwestern Queensland, central New South Wales and eastern South Australia. Fig 1b shows a winter anticyclonicity time series for central New South Wales.

Spring

During the spring months a decrease in anticyclonicity has occurred across most of New Zealand and over waters to the west of Tasmania. Increases in anticyclonicity are evident over western New South Wales and waters to the east of Norfolk Island (Fig 2a). A spring anticyclonicity time series is shown for the region near Norfolk Island (Fig 2b).

Summer

During the summer months a notable decrease in anticyclonicity has occurred near Tasmania and to the southeast of New Zealand (Fig 3a). Fig 3b shows the summer time series for the region to the west of Tasmania.

Autumn

The autumn months show a notable increase in anticyclonicity over the western Tasman Sea and Tasmania and decreases in anticyclonicity across the northern Nullarbor Plain, over central New South Wales and to the east of New Zealand (Fig 4a). Fig 4b shows the autumn time series for the western Tasman Sea.

Annual

Annual anticyclonicity totals show some interesting variations across the eastern Australasian region (see fig 5). Annual totals have shown an increase across eastern South Australia, western New South Wales and southwestern Queensland. These increases have occurred mainly in the winter and spring totals. The increase over waters to the east of Norfolk Island has been more uniform throughout the year. Decreases in annual totals across central New South Wales and western Victoria have occurred mainly in winter and annual decreases over waters to the west of Tasmania have occurred mostly in spring and summer. The annual anticyclonicity decreases over the New Zealand region have been predominantly in winter and spring and the decreases over South Australia have been in autumn and winter. There has been a noted decrease in totals in a small area near Macquarie Island which ia already a low anticyclonicity average area.

From 1965 cloud satellite photographs were available for the Australasian region which greatly increased the data base for synoptic analyses. Changes in satellite imagery especially the introduction of GMS satellites from 1982 improved the data base and additional data has been supplied by drifting buoys deployed at various times since 1978 at differing locations in the oceans around the Southern Hemisphere. The authors believe that the ability of experienced analysts to identify centres of anticyclones from cloud photos could affect the accuracy of synoptic analyses. On many occasions there is no obvious cloud structure related to anticyclone centres and positioning of centres often relies on surface pressure and wind observations. Across ocean areas when no surface or satellite wind observations are available differing interpretations could lead to some inaccuracies on location of centres on occasions. Across Australia positioning of anticyclone centres is more reliable because of the network of surface observation stations.

Reasons for these variations are not clear. Continual improvements of the data base for synoptic analysis during the 29-year period could have led to variations in locations of anticyclone centres particularly over the oceans but these are not expected to be large enough to show a definite shift of centres of anticyclonicity.

References

Karelsky, S. 1954. Surface Circulation in the Australasian Region, Bureau of Meteorology Study No. 3, Australian Government Printing Service, Canberra, 45pp.

Karelsky, S. 1961. Monthly and Seasonal Anticyclonicity and Cyclonicity in the Australian region - 15 Year Average (1946-1960), Bureau of Meteorology Study No. 13, Australian Government Printing Service, Canberra, 11pp.

Leighton, R. M. and Deslandes, R. 1991a. Monthly anticyclonicity and cyclonicity in the Australian region: 23 year (1965-1987) Averages, Bureau of Meteorology Technical Report No 64, Melbourne, 29pp.

Leighton, R. M. and Deslandes, R. 1991b. Monthly anticyclonicity and cyclonicity in the Australasian region: averages for January, April, July and October, Aust. Meteorol. Mag., 39, 149-154.

Leighton, R. M. 1994. Relationship of anomalies of (anti)cyclonicity to some significant weather events over the Australian Region, Aust. Meteorol. Mag., 43,

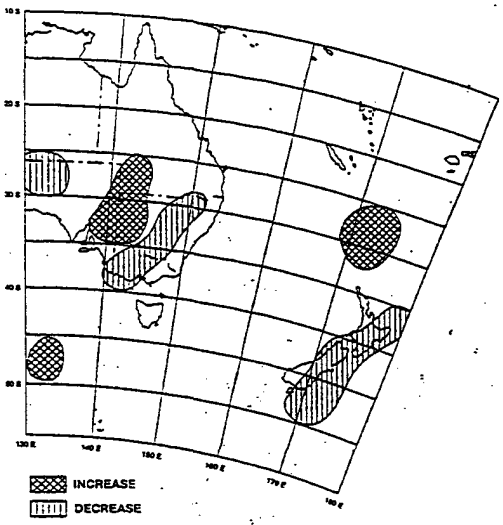


Fig 1a. Winter anticyclonicity trends sig. at 5% level, from 1965-1993

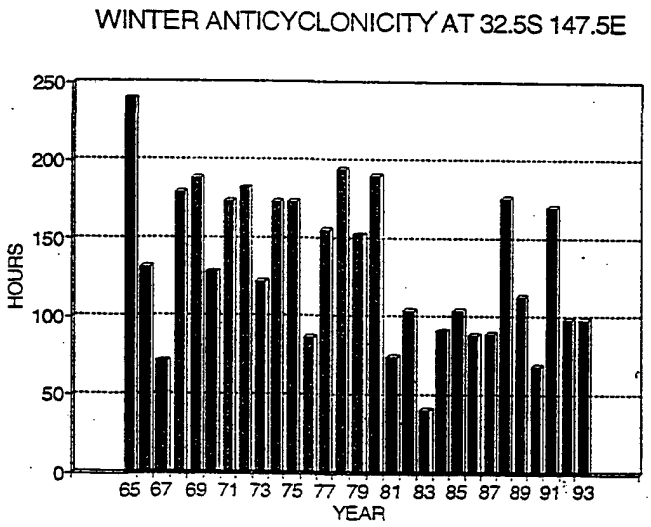


Fig 1b. Winter anticyclonicity time series for central New South Wales

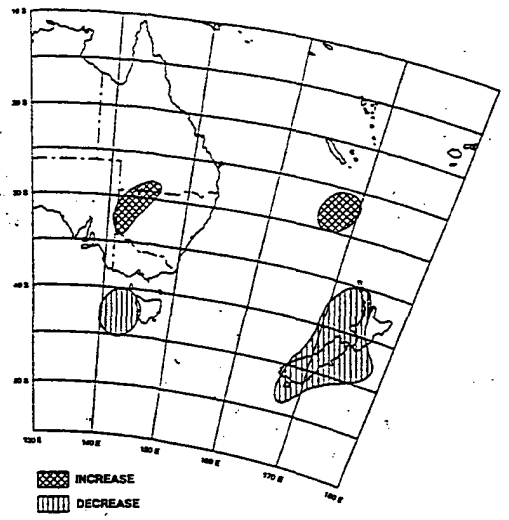


Fig 2a. Spring anticyclonicity trends sig. at 5% level from 1965-1993

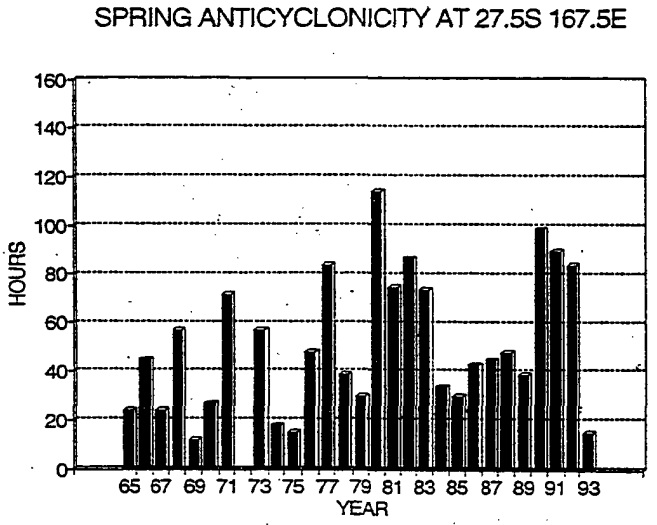


Fig 2b. Spring anticyclonicity time series for near Norfolk Island

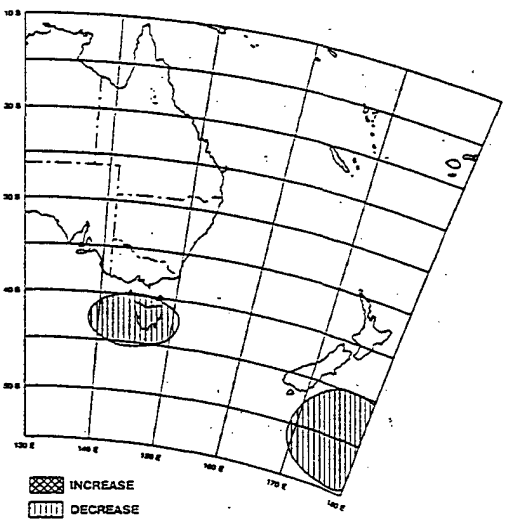


Fig 3a. Summer anticyclonicity trends sig. at 5% level, from 1965-1993

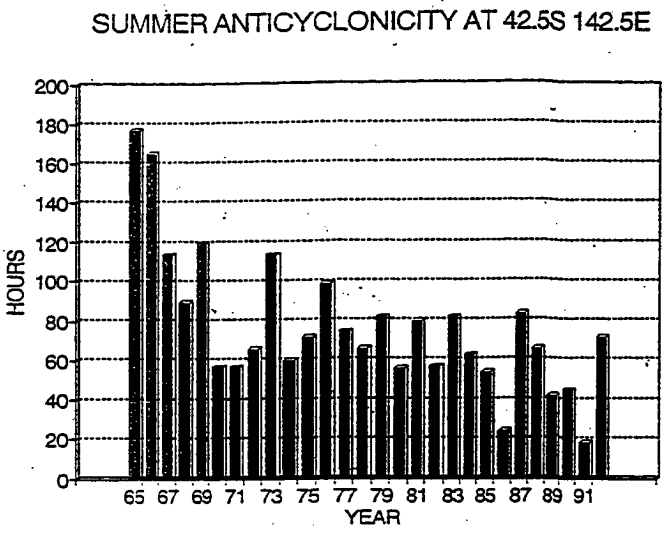


Fig 3b. Summer anticyclonicity time series for west of Tasmania

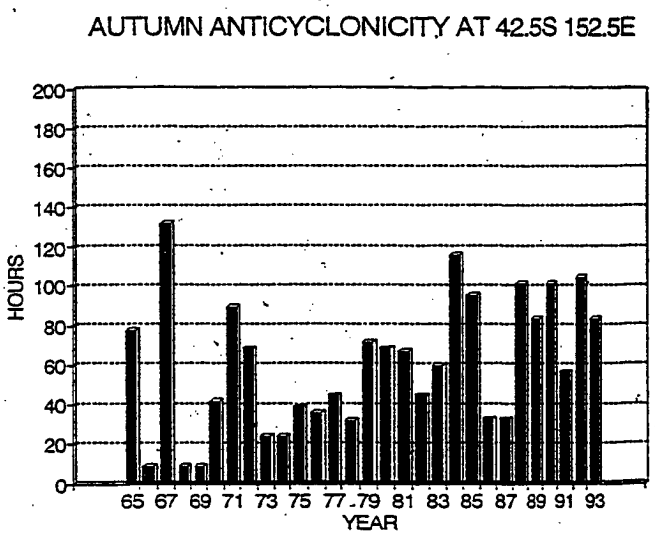


Fig 4b. Autumn anticyclonicity time series for western Tasman Sea

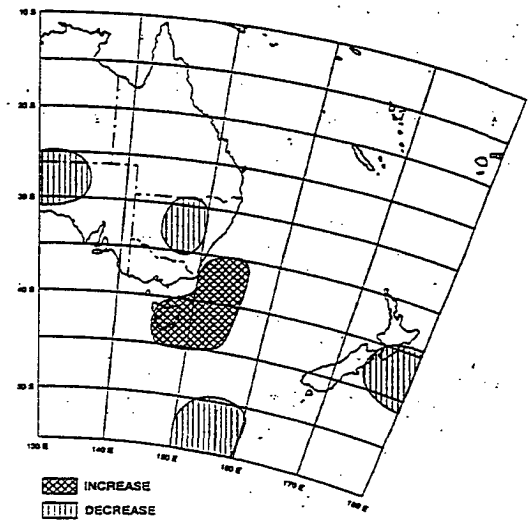


Fig 4a. Autumn anticyclonicity trends sig. at 5% level, from 1965-1993

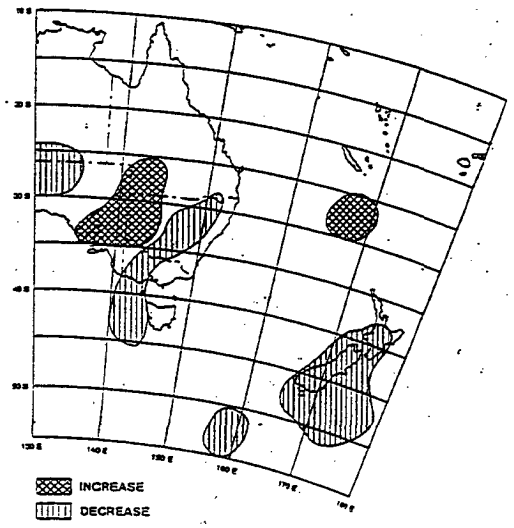


Fig 5. Annual anticyclonicity trends sig. at 5% level, from 1965-1993

ON THE EFFECTS OF NONLINEARITY ON THE VARIABILITY OF LONG CLIMATIC RECORDS

J. A. García-Miguel, F. Valero, J. F. González, F. J. Doblas

Departamento de Astrofisica y Ciencias de la Atmósfera. Facultad de Físicas. Universidad Complutense. Ciudad Universitaria. 28040. Madrid. Spain.

ABSTRACT

The largest monthly windrun series in Spain has been studied from a spectral point of view. After applying high and band-pass filters some of the resulting significant frequencies may be identified as related to a known dynamic or radiative phenomenon, as the annual cycle, the luni-solar and solar cycles (Mn and Sc), the QBO and the 14-month atmospheric Chandler tide. Most of the remaining peaks can be interpreted recalling the fact that combination tones are generated in nonlinear systems. The time evolution of the signals can be understood from this same point of view.

1 INTRODUCTION

A common spectral aproach to the study of climatic variability is carried out to assess the influence of nonlinearities on the variability of climatological series. In studies of climatic variability it is always desirable that samples are as large in time as possible. Firstly, this allows obtaining more information about the long term behaviour of the record, which is particularly important in trend studies. Secondly, it improves the reliability in signal detection. This is a consecuence of the fact that the signal-to-noise ratio increases proportionally to the number of samples in the series (Scargle, 1982). In this paper, the largest series of monthly windrun in Spain has been used; windrun is a very noisy variable which shows great variability in all timescales.

One problem with signal detection is associating the significant peaks obtained in the analysis with physical phenomena. Though significant fluctuations can be found in a great variety of frequencies, in many cases they are considered as more of a random than a physically fundamented nature. Herein, we provide a simple way in which some of the detected signals may be identified based on the fact that combination tones are expected to be generated in nonlinear physical systems. This interpretation has been used before in atmosphere applied studies by Hameed and Currie (1989) and Currie and Hameed (1990) to identify peaks detected in GCM simulated data spectra. We find that nonlinear interactions also seem to explain adequately the long term amplitude behaviour of the detected signals and consequently of the variance of the series.

In section 2 a brief description of data is provided. An overall view of the effects of nonlinearities on a physicall system is supplied in section 3. In section 4 results of filtering and spectrum analysis are provided together with a discussion following the guidelines proposed in section 3.

2 DATA

Data consist of monthly mean values of daily windrun records. There are seven sites in Spain which have available windrun data for a period of at least one hundred years (a reasonable length to attempt signal detection with simple methods). The series which has been used in this work is the largest of them all (1867-1992) and was built using data provided by two observatories sited in Madrid (Valero et al., 1995).

3 NONLINEAR INTERACTIONS

Herein, some possible nonlinear effects are shown: i) generation of harmonics; ii) generation of tones (sum and difference of frequencies); iii) amplitude modulation of waves; and iv) variance modulation of the series.

Following Currie and Hameed (1990) let us take the response $x_{out}(t)$ to be related to the input $x_{in}(t)$ in a nonlinear system as it could be the case of the climatic system (ε small compared to unity) by

$$x_{out}(t) = K\left[x_{in}(t) + \varepsilon\, x_{in}^2(t)\right] \qquad (1)$$

where K is constant.

i) Harmonics generation

Let us consider an input function $x_{in}(t) = \cos \omega t$; there will be a component in the output, $x_{out}(t)$, given by

$$K\frac{\varepsilon}{2}\cos 2\omega t \qquad (2)$$

Therefore, if we consider a second order nonlinearity a harmonic term is generated in a frequency double of the original frequency. If the order of the nonlinear term is greater (say **n**) the generated harmonic would be a frequency n times that of the original frequency.

ii) Combination signals

Further, if we assume an input function

$$x_{in}(t) = A\cos\omega_1 t + B\cos\omega_2 t \quad (3)$$

where ω_1 and ω_2 are not in harmonic relation, apart from the harmonics generated according to (2), there will be a component in the output given by

$$2K\varepsilon AB\cos\omega_1 t\cos\omega_2 t \quad (4)$$

This term can be re-written into two components with frequencies corresponding to the sum and difference of the "parents" frequencies, namely

$$K\varepsilon AB\left[\cos(\omega_1+\omega_2)t + \cos(\omega_1-\omega_2)t\right] \quad (5)$$

Thus, considering the smallest order perturbation (second order) from linearity as in (1), two new signals of frequencies $\omega_1 \pm \omega_2$ should be expected to appear (sum and difference tones).

iii) Modulation of amplitude

When spectrum analysis is applied to a series of N data, values of espectral density will be evaluated for a set of N/2 frequencies separated by a frequency distance of 1/N. Therefore, for any frequency ω_2 lower than 1/N the possible sum and difference tones that would be produced by its interaction with ω_1 would be separated from ω_1 by less than one frequency interval. In those cases it is not possible to distinguish ω_1 from the sum and difference tones and expression (4) would then be interpreted as a single term: the modulation of the amplitude of a signal of frequency ω_1 by a sinusoidal function of frequency ω_2 ($f(B,\omega_2,t) = 2B\cos\omega_2 t$). Expression (4) can be re-written as

$$K\varepsilon A f(B,\omega_2,t)\cos\omega_1 t \quad (6)$$

Further, by substituting (3) in (1) and using (6), the whole contribution of ω_1 to the output would be given by

$$K\left\{A\left[1+\varepsilon f(B,\omega_2,t)\right]\right\}\cos\omega_1 t \quad (7)$$

iv) Variance modulation

The modulation stated in **iii)** for nonlinear systems can also affect the variance of the series. Let us consider a series x_t which can be expressed using Fourier analysis as

$$x_t = \bar{x} + \sum_{p=1}^{N/2}\left[R_p\cos(\omega_p t + \phi_p)\right] \quad (8)$$

where R_p and ϕ_p are the mean amplitude and phase of the p-th Fourier harmonic of frequency ω_p in the considered time period (t=1...N). According to Parseval's theorem (Chatfield, 1984) the variance of the series can be written as a function of the amplitudes R_p

$$\hat{\sigma}^2 = \sum_{p=1}^{N/2-1}\left[R_p^2/2\right] + R_{N/2}^2 \quad (9)$$

According to (7), in case a low frequency ω (<1/N) exists the amplitude of the p-th Fourier harmonic, R_p, of frequency ω_p would be given by the temporal average of a function $R_p'\left[1+\varepsilon f(R,\omega,t)\right]$ where R_p' (similarly to A in section **iii)**) is the amplitude of the ω_p-wave modulated by the ω-wave. Allowing that each one of the amplitudes may be modulated by ω, the variance of the series can also vary in time modulated by a function of frequency ω(*i.e.*, the amplitudes and the variance can have different values for different subperiods in the series).

4 RESULTS

Periodograms have been used as spectral estimators (Bloomfield, 1976). Though it is more noisy than other smoothed spectral estimators, it provides more resolution and allows the user to identify single peaks. Care must be taken in identifing this peaks and therefore it is essential making use of an appropiate powerful test. In this work, Fisher's test of significance (Fisher, 1929; Shimshoni, 1971) has been applied.

After applying the Fisher's test (99% significance) to the monthly windrun series eleven cycles and trend were found to be significant (Table 1; marked with *). Most of the variance is explained by the annual cycle and its six and four month harmonics (17.5%). There is also an important amount of variability produced by very low frequency oscillations (VLFO) of a period around 60 years. This cycle has been pointed out by Folland *et al.* (1984) and Schlesinger and Ramankutty (1994) and it is characterized by a deep minimum around the 1920's, a maximum around the 1950's followed by a downward trend which reaches a new minimun in the 1960's. Figure 1 shows a 4-years centered moving average of the original series. The above mentioned long term features are apparent. Luni-Solar cycle (Mn) and solar cycle (Sc) have also been detected, together with other signals of periods around 25 years, 9 years, 5 years and 10 months.

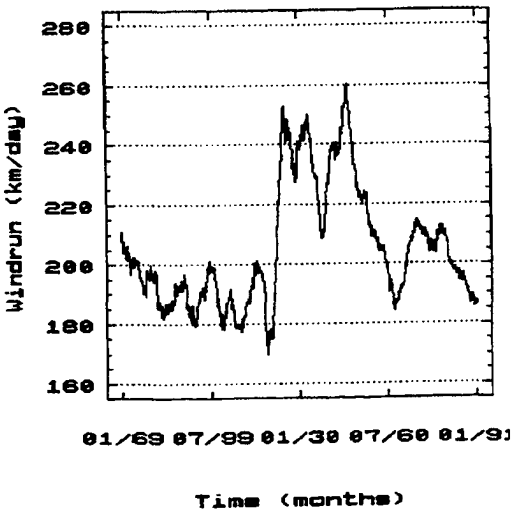


Figure 1. 48-month centered runing average of original series (x axis units are months/year)

High and band-pass filters have been applied to the data to eliminate the VLFO and the annual cycle and harmonics. The high-pass filter has been applied through subtraction of the low pass filter output to the data (Bloomfield 1976, p. 129; filter length n=180 and cutoff frequency, ω_c= 0.0035 cycles/month). The band-pass filter has been designed using complex demodulation (Bloomfield, 1976; n= 175 and ω_c= 0.0034 cycles/month). Finally, the 12, 6 and 4 month signals have been remodulated and subtracted to the series. Thirty five cycles which could be grouped and identified as contributions of several signals have been found to be significant after applying the same analysis as before (see Table 1). In particular, the QTO (Quasi-

Table 1. Frequencies, periods and possible associated fenomena of detected significant signals. * indicates signals detected before filtering. Values in brackets below associated phenomenon indicate estimated tone frequencies.

	FREQUENCY (cycles/month)	*PERIOD (months or years)*	*ASSOCIAT. PHENOM.*
*1**	*0.00066*	*126 yr*	***Trend***
*2**	*0.00132* *0.00198*	*63yr* *42yr*	***VLFO***
*3**	*0.00331*	*25.2 yr*	***I(Mn-VLFO)***
*4**	*0.00397* *0.00434* *0.00520*	*21 yr* *19.2 yr* *16 yr*	***Mn***
*5**	*0.00694* *0.00727* *0.00779*	*12 yr* *11.45 yr* *10.7 yr*	***Sc***
*6**	*0.00868* *0.00926* *0.00958* *0.01045*	*9.6 yr* *9 yr* *8.7 yr* *8 yr*	***I(VLFO+Sc)***
7	*0.01388*	*6 yr*	***I(A12-Ch) (71.1 m)***
*8**	*0.01595* *0.01585* *0.01650*	*5.6yr* *5.25yr* *5.1yr*	
9	*0.02170*	*46.1 m*	***QTO***
10	*0.03831*	*26.1 m*	***QB0***
11	*0.04348*	*23.0 m*	***I(A12-QBO) (21.82 m)***
12	*0.06849* *0.07042*	*14.6 m* *14.2 m*	***Ch***
*13**	*0.08333*	*12 m*	***A12***
*14**	*0.09900*	*10.1 m*	***I(A12-QTO) (10.27 m)***
15	*0.07463*	*13.4 m*	***I(A12-Sc) (13.2 m)***
16	*0.13812*	*7.24 m*	***I(A6-QBO) (7.74 m)***
17	*0.14493*	*6.9 m*	***I(A6-QTO) (7.06 m)***
18	*0.15456*	*6.47 m*	***I(A6-QBO) (6.55 m)***
*19**	*0.16777*	*6 m*	***A6***
20	*0.19608*	*5.1 m*	***I(A6+QTO) (5.22 m)***
21	*0.20408*	*4.9 m*	***I(A6+QBO) (4.9 m)***
22	*0.20492*	*4.88 m*	***I(A4-QBO) (4.71 m)***
*23**	*0.25*	*4 m*	***A4***
24	*0.5*	*2 m*	***A2***

Triennial Oscillation, influence of El Niño in the Atlantic Ocean) has been found with a period of 46.1 months. Significant evidence of the QBO (26.1 months), the 14-month Chandler wobble (Ch) and the 2-month harmonic of the annual cycle have also been found. The rest of the cycles cannot be directly associated to a dynamic or radiative physical phenomenon.

Nonlinear effects

Possible sum and difference tones were generated according to (5) using the annual cycle and its harmonics with the QBO, QTO and Ch-tyde as "parents" frequencies. The resulting estimated tones agreed well with some of the found frequencies. These generated signals are indicated in Table 1 by *I(A,B)* where *A* and *B* are the generating frequencies. Most of them were also detected by Currie and Hameed (1990) using model data. In Table 1 estimated tones are indicated in brackets below *I(A,B)*. Only in cases where *VLFO* is involved it is not possible to make an adecuate estimation due to the wide range of uncertainty in estimating its frequency.

The time evolution of the signals has been studied using moving periodograms (periodograms applied to 30 year data subsets 5-years shifted in time). All amplitudes show similar oscillations to the VLFO (see Figure 2) pointing out a modulation of by this signal according to (7).

The time evolution of the variance is described through calculating 48-month centered moving variances in a similar way to the usual centered moving averages. Figure 3 shows a plot of the resulting curve. Once again the resulting trends agree with the long term trends found for the original series (see Fig. 1). There are other low frequency signals also apparent in Figure 1 that also seem to drive the evolution of the variance. Anual oscillations (*i.e.*, annual maximum minus minimun) were also calculated providing the same results (not shown here).

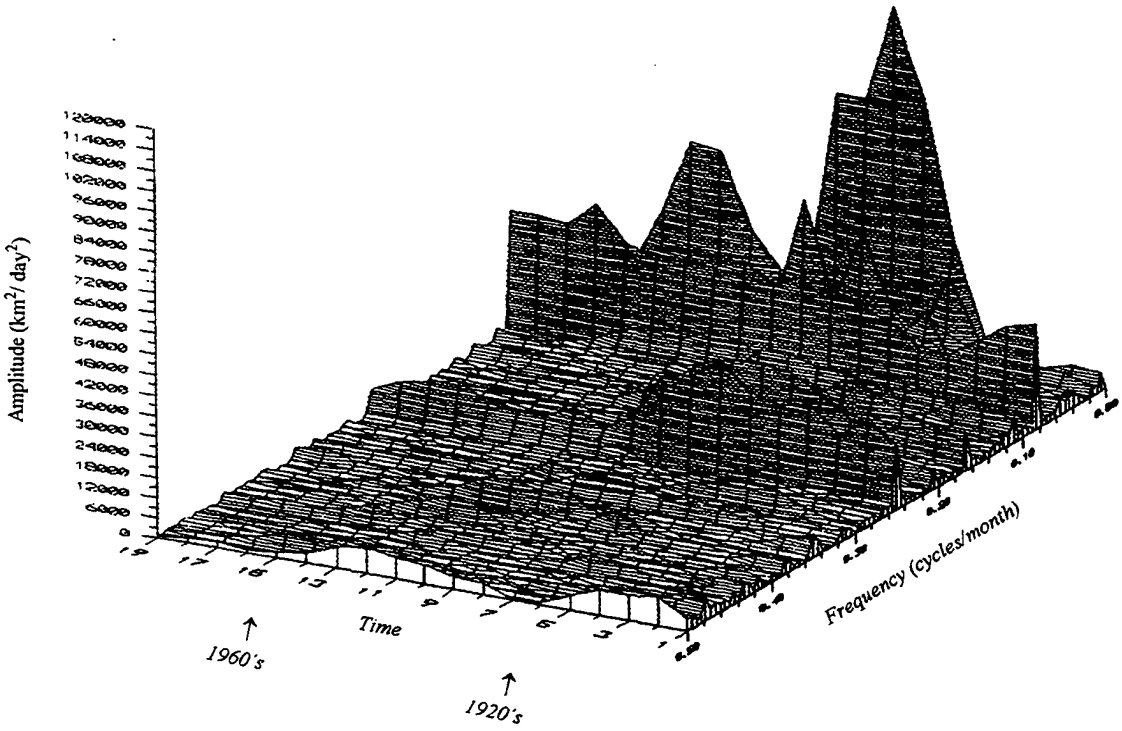


Figure 2. Moving periodograms of original series. Periodograms have been calculated for 30 year periods shifted 5 years in time.

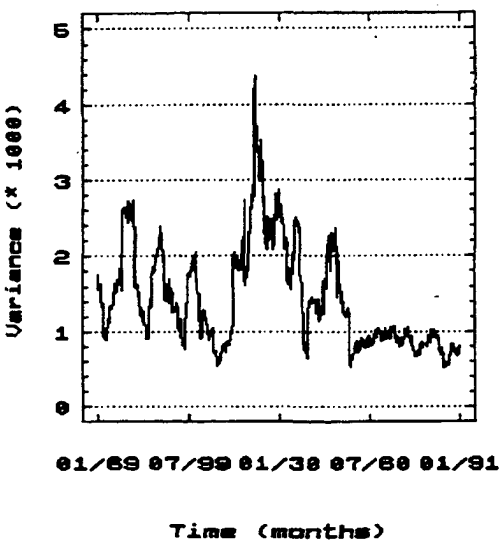


Figure 3. 48-month centered runing variance of original series (x axis units are months/year)

5 CONCLUSIONS

In this work an example is given of the effects of nonlinearities in the variability of a series, both in the generation of combination tones and in the modulation of the constituent signals and the variance of the series. The values expected according to a nonlinearity of second order agree quite well with the results obtained from direct meassurement. Also, the amplitudes of the constituent signals of the series seem to be modulated by a very low frequently oscillation that causes relative minima in the 1920's and 1960's and relative maxima in the 1940's and at the end of the record. The time evolution of the variance of the series shows a similar pattern.

Recent calculations for windrun data from other sites are being carried out by the authors. Results seem to confirm on the whole the results presented here.

ACKNOWLEDGEMENTS

This work was supported by the Comunidad Autonoma de Madrid (Spain), under Contract CAM 286/92 and grants 316/92.

6 REFERENCES

Bloomfield, P., 1976, "Fourier Analysis fo Time Series: An Introduction", John Wiley & Sons, New York.

Chatfield, C., 1984,"The Analysis of Time Series. An Introduction", Chapman and Hall Ltd. (London), 3rd ed..

Currie, R. G. and S. Hameed, 1990, "Atmospheric Signals at High Latitudes in a Coupled Ocean-Atmosphere General Circulation Model" , Geophys. Res. Lett., 17, 7, pp. 691-694.

Fisher, P. A., 1929, "Test of Significance in Harmonic Analysis", Proc. R. Soc., A, 125, pp. 54-59.

Folland, C. K., D. E. Parker and F. E. Kates, 1984, "Worldwide Marine Temperature Fluctuations", Nature, 310, pp. 670-673.

Hameed, S. and R. G. Currie, 1989, "Simulation of the 14-Month Chandler Wobble in a Global Climate Model", Geophys. Res. Lett., 16, 7, pp. 691-694.

Scargle, J. D., 1982, "Studies in Astronomical Time Series Analysis. II.", Ap. J., 263, pp. 835-853.

Schlesinger, E. and N. Ramankutty, 1994, "An Oscillation in the Global Climate System of Period 65-70 Years", Nature, 367, 24, pp. 723-726.

Shimshoni, M., 1971, "On Fisher's Test of Significance in Harmonic Analysis", Geophis. J. R. Astr. Soc., 23, pp. 373-377.

Valero, F., J. F. González, F. J. Doblas and J. A. García-Miguel, 1995, "A Method for the Reconstruction and Temporal Extension of Climatological Time Series", Int. J. Climatol. Accepted.

Climatological Variability in Regional Air Pollution

Jack D. Shannon
Environmental Research Division
Argonne National Laboratory
Argonne, IL 60439

and

Edward C. Trexler, Jr.
Office of Fossil Energy
U.S. Department of Energy
Washington, DC 20545

ABSTRACT: Effects of climatological and meteorological variability on means and distributions of air pollution parameters, particularly those related to regional visibility, are illustrated. Over periods of up to a decade climatological variability may mask or overstate improvements resulting from emission controls. The importance of including climatological uncertainties in assessing potential policies, particularly when based partly on calculated source-receptor relationships, is highlighted.

Although some air pollution modeling studies examine events that have already occurred (*e.g.*, the Chernobyl plume) with relevant meteorological conditions largely known, most pollution modeling studies address expected or potential scenarios for the future. Future meteorological conditions, the major pollutant forcing function other than emissions, are inherently uncertain although much relevant information is contained in past observational data. For convenience in our discussions of regional pollutant variability unrelated to emission changes, we define meteorological variability as short-term (within-season) pollutant variability and climatological variability as year-to-year changes in seasonal averages and accumulations of pollutant variables. In observations and in some of our simulations the effects are confounded because for seasons of two different years both the mean and the within-season character of a pollutant variable may change. Note that climatological and meteorological variability do not refer here to the variability of climate or meteorology but rather to their induced effects on pollutant behavior.

Expressed in relative terms, climatological variability usually increases as the spatial and temporal scales over which the pollutant parameters are averaged decrease. Seasonal variability from one year to the next tends to be greater than annual variability (Shannon *et al.*, 1985). Similarly, the climatological variability at a single location tends to be greater than the variability averaged over a region. Climatological variability can enhance or mask the effects of emission trends. For evaluation of past data there is frequently less interest in examining climatological variability for its own sake than in being able to quantify and remove climatological variability before performing trend analysis. Such quantification of climatological variability requires the aid of a model or models, ranging from relatively simple conceptual models (*e.g.*, assuming that wet deposition of pollutants varies with aggregated precipitation) to regional models that examine different aspects of variability. One might quantify climatological variability by multiple exercise of a model with the climatology from a series of individual years while holding emissions temporally constant. Results can then be used to adjust an observed trend. After removing temperature-related effects on ozone concentrations, Rao *et al.* (1995) concluded that ozone concentrations have decreased in recent years in the northeastern United States. Shannon (1992) isolated the 1979-1988 trends in regional wet deposition of sulfate associated with SO_2 emission trends, and deduced that emission reductions were dominant during the first four years and that climatological variability controlled regional variability thereafter.

Climatological variability should be considered in evaluating the probable effectiveness of potential future emission control policies. The primary reason is to create a realistic distribution of possible pollutant outcomes rather than a single deterministic estimate without associated uncertainty. In addition, quantification of climatological variability is desirable so that the likelihood of detecting the pollutant trend associated with the control action, perhaps as a function of the number of years of monitoring, can be assessed. Trexler and Shannon (1995) examined the expected improvement in visibility from SO_2 emission reductions mandated by recent legislation. We use source-receptor relationships from the Advanced Statistical Trajectory Regional Air Pollution (ASTRAP) model (Shannon, 1985), together with emissions vectors aggregated at the state level,

observed means and variations on various temporal scales of relative humidity (RH) and concentrations of particulate species, and light attentuation equations for those species as functions of RH and concentration, in the Visibility Assessment Scoping Model (VASM) (Trexler and Laulainen, 1992). To generate realistic short-term distributions of visual impairment, VASM varies RH and particulate concentrations of sulfate, nitrate, elemental carbon, organic carbon, fine-particle dust, and coarse-particle dust through Monte Carlo techniques by assuming lognormal distributions for the particulate species and a diurnal curve superimposed on a normal distribution for RH.

A recent series of applications of VASM/ASTRAP has examined potential future distributions of visual impairment in scenic parks in the United States. Although the research is still in progress, some preliminary results can be shown here. In Figure 1, distributions of summer visibility impairment in deciviews (dv), an increasingly accepted visibility metric that is analogous to the logarithmic decibel scale for sound, are estimated for Shenandoah National Park in the eastern United States for conditions before and after the approximately 50% reduction in SO_2 emissions currently underway. The distributions, which are quite smooth because each curve represents the average of 9,000 (90 days * 100 years) simulations of 15 daylight hours per day, reflect a mean overall improvement of about 3 dv. Although this improvement may seem small, the typical observer can detect a difference of between 1 and 2 dv in a scenic view. In addition, limits exist as to how much improvement can be obtained solely by SO_2 controls because sulfate causes only about one-half of visibility impairment in the nonurban East and about one-fifth in the nonurban West, with the remainder due to other particulate species, NO_2 gas, and natural Raleigh scattering (Trijonis *et al.*, 1990).

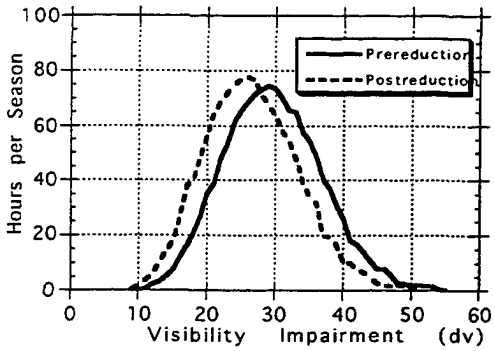


Figure 1: Mean expected summer distributions of visual impairment at Shenandoah National Park before and after the emission reductions mandated by the 1990 Clean Air Act Amendments, as calculated with VASM.

VASM results indicate a typical mean shift of 2-3 dv between sunrise (maximum RH) and midafternoon (minimum RH) due to the RH difference. Light attentuation by hygroscopic particles such as sulfate increases exponentially for RH values above 70%; visibility thus tends to be worst at sunrise. Sometimes researchers have a greater interest in the change in the frequency of relatively dirty or relatively clean days; by selecting a critical deciview value, one can easily estimate such changes from the expected distributions. Our calculations indicate that the occurrences at Shenandoah of visual impairment above 40 dv can be expected to be reduced over 50% after the emission reductions are completed.

A particular season will typically exhibit a much more irregular distribution of visual impairment, because only about 20 to 40 changes of air mass will occur during the season. A set of VASM simulations of visual impairment for a single summer are shown in Figure 2 for mean prereduction and postreduction sulfate concentrations; also shown are two cases representing mean sulfate conditions 14% higher and 18% lower than the expected postreduction mean. This corresponds to the range of ASTRAP results calculated with each of 11 summers of meteorological data.

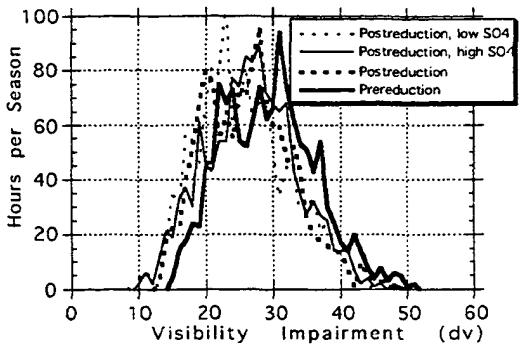


Figure 2: Single-year simulations from VASM of summer distributions of visual impairment at Shenandoah before and after emission reductions, plus postreduction cases of higher and lower mean concentrations of sulfate from ASTRAP estimates of climatological variability. Within-season meteorological variability differs for each case.

A range of about ±15% in the post-reduction seasonal average of sulfate results in relatively modest changes in the distribution of visual impairment (roughly ±1 dv). This is not unexpected because (1) the deciview parameter is logarithmic and (2) we have not yet included climatological variability of the other particulate species. For clarity in assessment and policy analysis, expected mean distributions as in Figure 1 are the most useful modeling output. Changes expected after a sufficiently long period of averaging can be clearly depicted. Observations of visual impairment for a single season, on the other hand, can be expected to exhibit the irregularities illustrated in Figure 2 (Trexler and Shannon, 1995). Both presentations are useful in demonstrating expected outcomes and potential variations about those outcomes.

An evaluation of visibility should examine variations in both mean conditions and distributions about those mean conditions. In evaluation of acidic deposition, for which the most important ecological effects are largely controlled by long-term loading, long-term variability is more emphasized than short-term variability (Streets *et al.*, 1985). Climatological variability can be the major factor controlling year-to-year variability of pollutant parameters, particularly when emission changes are relatively small. In some cases, an apparent trend over a period of 5 to 10 years can simply be the result of the particular sequence of climatological conditions. This point is illustrated in Figure 3, in which ASTRAP simulations for average summer atmospheric concentrations of sulfate at Shenandoah National Park indicate a significant upward trend from 1982 through 1990, even though the model simulations hold emissions temporally constant at 1985 levels. The slope of the modeled trend is similar to that of the observations, in large part because aggregated emissions of SO_2 changed little during the period. Little direct correlation is seen between modeled and observed concentrations because of the sharply lower observed concentrations in 1986 and 1987. In addition to the usual suspects (model inadequacies), the discrepancies may be due to substate emission changes that are not reflected in aggregated totals or to calculations of observed seasonal means from limited sampling (two days per week at best).

ASTRAP calculations indicate that Ohio and Pennsylvania SO_2 sources contribute the greatest shares (aggregated by state) of the summer sulfate concentrations at Shenandoah. Their source-receptor contributions, normalized by emission rate, can change significantly from year to year (Figure 4). A targeted emission control strategy based upon the 1983 source-receptor relationships might be very different than a strategy based upon 1982 calculations. Such variations indicate that emission control policies should reflect the best estimate of source-receptor relationships averaged over multiple years, rather than for any single, perhaps atypical year.

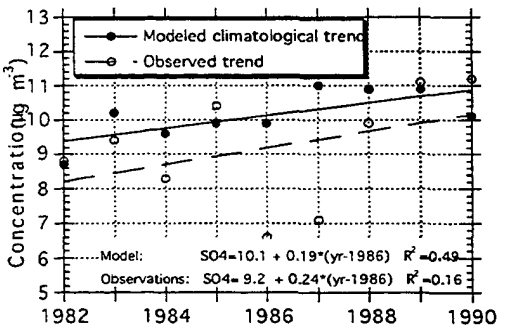


Figure 3: Comparison of the observed trend in average summer atmospheric concentration of sulfate at Shenandoah with a modeled trend from ASTRAP simulations in which climatology varies but emissions

are held constant. Equations describing the linear trends are shown.

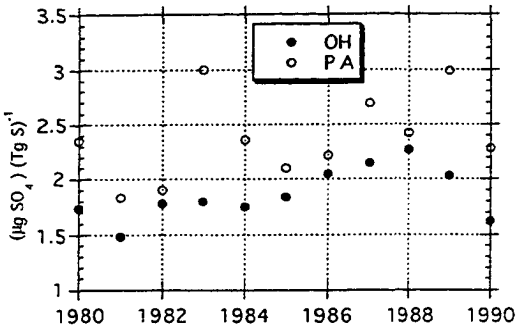


Figure 4: ASTRAP estimates of the normalized contribution of aggregated SO_2 sources of Ohio and Pennsylvania to average summer sulfate concentrations at Shenandoah.

Models invariably simplify nature. Although other meteorological parameters such as mixed-layer depth, temperature, or incident radiation may influence pollutant variability, often by affecting chemical transformation rates, here we examine only climatological variability related to patterns of a single-layer transport wind (resolved over grids of either 150- to 175-km or 300- to 350-km spacing and updated four times daily) and total precipitation (resolved over a grid of 100- to 115-km spacing and updated 2 to 4 times daily). The mean diurnal and seasonal effects of other variables, such as RH and temperature, are parameterized without year-to-year variability in our approach. Because we cannot address all relevant meteorological variables in our study, we likely underestimate overall climatological variability.

ACKNOWLEDGMENTS: This work was supported by the Office of Planning and Environment, Office of Fossil Energy of the U. S. Department of Energy, under contract W-31-109-Eng-38. Jeff Camp assisted in model revisions for different computer systems.

REFERENCES

Rao, S.T., Zalewsky, E. and Zurbenko, I.G., 1995: Determining temporal and spatial variations in ozone air quality. *J. Air and Waste Management Assoc.*, **45**, 57-61.

Shannon, J.D., 1985: *User's Guide for the Advanced Statistical Trajectory Regional Air Pollution (ASTRAP) Model.* U. S. Environmental Protection Agency Report EPA/600/8-85/016 (NTIS PB85-236784/XAB).

Shannon, J.D., 1992: Regional analysis of S emission-deposition trends in North America from 1979 through 1978. In: *Air Pollution Modeling and its Application IX* (H. van Dop and G. Kallos, eds.), Plenum Press, New York, 57-64.

Shannon, J.D., Lesht, B.M., and Samson, P.J., 1985: Variability in patterns of acid deposition resulting from climatological variability. In: *Proceedings of the 9th Conference on Probability and Statistics in Atmospheric Science*, American Meteorological Society, Virginia Beach, VA, 72-79.

Streets, D.G., Lesht, B.M., Shannon, J.D. and Veselka, T.D., 1985: Climatological variability: Effect on strategies to reduce acid deposition. *Environ. Sci. and Technol.*, **19**, 887-893.

Trexler, E.C. Jr. and Laulainen, N., 1992: Techniques for computing and presenting annual visibility characterizations for locations of interest. In: *Proceedings of the 86th Annual Meeting*, 93-RP-135.02, Air and Waste Management Association, Pittsburgh.

Trexler, E.C. Jr., and Shannon, J.D., 1995: The impact of climatological variability on visibility impairment distributions. In: *Proceedings of the International Specialty Conference on Aerosols and Atmospheric Optics: Radiative Balance and Visual Air Quality*, Snowbird, Utah, Sept. 26-30, 1994, Air and Waste Management Association, Pittsburgh, 681-692.

Trijonis, J.D., Malm, W.C., Pitchford, M., White, W.H., Charlson, R., and Husar, R., 1990: *Visibility: Existing and Historical Conditions - Causes and Effects.* NAPAP Report 24, National Acid Precipitation Assessment Program, Washington, DC.

Global and local climatic changes in the West African upwelling ecosystems.

Marie-Helene DURAND
Centre ORSTOM de Bondy - 70 route d'Aulnay - 93143 Bondy Cedex - France.

Claude ROY
Centre ORSTOM de Brest- BP 70 - 29280 Plouzane - France.

The marine resources of the coastal upwelling regions of the world oceans represent up to 30% of the total world marine fish production. Mostly constituted by short lived pelagic fish species, the abundance of these resources is known for being highly variable and strongly influenced by the fluctuations of the oceanographic environment. The variability of the environment in these upwelling systems has never been fully documented, however this is crucial for understanding the dynamic of the exploited marine resources in the context of climate change. Meteorological observations collected by ships of opportunity along trade routes (COADS dataset) are used to build time series of several surface meteorological parameters (sea-surface temperature, wind speed, etc.) along the coast of the West African coastal upwelling, from Morocco to Senegal, during the last 45 years. A spatial grid is designed by taking into account the data density and topographical and ecological features. Detecting and analyzing changes in these data series using time series analyses is a difficult problem that requires careful thinking about the meaning of change and about the ways change can occur in the data. Change, in the context of climate change, is often used in context such as "global warming", meaning that the long term behavior of worldwide temperature is characterized by a positive trend. In the coastal upwelling areas of the oceans, due to the complex circulation processes and to the interaction with the atmosphere, even if the trend of the underlying process is uniform and global in scale, the observed changes could have different behavior and could vary between areas. New techniques developed in economy (seasonal cointegration) are applied here to the fields of oceanography and climate change in order to analyze the dominant patterns of the variability of the physical environment in the West African upwelling ecosystem. This allow to distinguish between changes in the common trend (which affect an entire region in the same manner) and stationary cyclical swings or even non-stationary components (which remain isolated in space).

MODELLING CURRENT AND FUTURE DISTRIBUTIONS OF NATIVE SPECIES

T.H. Sparks[†], T.W. Parr[§] & S.M. Wright[†]

NERC Institute of Terrestrial Ecology, [†]Monks Wood & [§]Merlewood, UK.

ABSTRACT

This paper compares alternative methods for linking the geographic distribution of species in Britain to climatic data. Many researchers convert the geographic distribution of species into a distribution in 'climate-space' and then model the distribution in this orientation. We consider five different approaches to this modelling and examine the relative fits of the models. The potential for extending some of these models to make predictions post climate change is discussed. Logistic regression appears to be the most suitable method for this purpose.

1 INTRODUCTION

The geographic distribution of species is the result of many inter-relating factors. These include historical, geological and economic reasons. It is not uncommon for different factors to appear to be of primary importance at different scales of interest. In Britain, it is customary to publish national atlases of flora and fauna on a 10km grid, and national databases generally hold data at this resolution. At this scale it is expected that climate will play an important role in determining the distributional limits of species. The response of species in relation to climate can be of particular importance when contemplating the consequences of climate change on the general distribution of our native flora and fauna.

2 DATA

The Biological Records Centre at Monks Wood holds distributional data for a wide range of flora and fauna. Because the data are not collected in a systematic way it is appropriate to consider species distributions only as presence or absence, rather than as a measure of density. Three dissimilar example species (Globe Flower *Trollius europaeus*, Rusty-back Fern *Ceterach officinarum* subsp. *officinarum*, Turnip Moth *Agrotis segetum*; Figures 1-3) with different geographical distributions were selected to illustrate the methods used.

The Climatic Research Unit (CRU) at the University of East Anglia has produced climate data gridded on the same 10km scale as the distributional records (Viner & Hulme, 1994). Of the available variables, eight for which data from climate change scenarios will be available have been selected (Table 1).

Table 1. The Pool of Eight Climatic Variables (all at mean altitude)

Minimum January temperature
Mean January temperature
Maximum July temperature
Mean July temperature
Annual precipitation
Annual sunshine hours
Average wind speed
Relative humidity

3 METHODS

The methods used in examining the distributions in climate space (Figure 4) were as follows

1 A rectangular climate envelope (as used in the BIOCLIM package; Nix, 1986) was placed around the presence records. All geographic locations within this envelope are considered to have suitable climate. A more restricted envelope (5-95%) is created by ignoring the lower and upper 5% of presence records on each axis (Figure 5). All locations within either of these envelope specifications can then be mapped.

2 A climate envelope based on a convex hull (cf the HABITAT package; Walker & Cocks, 1991). Locations within the hull are considered to have suitable climate (Figure 6). This definition of suitable climate can be improved by 'peeling' layers from the convex hull until it contains approximately x% of presence records (we have used x=90).

3 Linear discriminant analysis (LDA) was used to allocate each 10km square to a presence or absence category. An alternative is to use the distance measure produced by LDA as an indication of the suitability of climate. Either the binary allocation, or the continuous distance measure can then be mapped.

4 Logistic regression was used to relate presence and absence records to climate variables. The basic linear model was extended to include quadratic and crossproduct terms. The output from the model, continuous on the 0-1 scale, is a measure of climate

suitability.

5 A grid-based approach. The climate space is divided into a regular grid and the proportion of presence records to all records is calculated for each grid cell. These proportions can then be re-mapped. We concentrated on a 10x10 grid, but also investigated 5x5, 20x20 and an irregular decile grid.

These methods are examined in two dimensions for clarity of presentation using two climatic variables. As indicated, output from the method variants was either of a binary nature, indicating suitable or non-suitable climates, or continuous within the range zero to one, indicating a probability of suitable climate. The methods were compared in their ability to model the current distribution using the residual sums-of-squares(RSS) as a yardstick.

4 RESULTS

Method variants producing a binary outcome generally, and as expected, produced a poorer fit (larger RSS) to the distributions (Table 2); LDA produced the lowest RSS of this group. Of the examined methods, logistic regression and the grid method most satisfactorily modelled the current distribution.

Table 2. Model fits (RSS) from the examined methods. (GF=globe flower, RF=rusty-back fern, TM=turnip moth)

Binary output methods	GF	RF	TM
BIOCLIM style 100%	1852	1909	2128
BIOCLIM style 5-95%	804	1202	1001
Convex hull 100%	1466	1656	1673
Convex hull c.90%	959	1208	1231
LDA	487	1062	783
Continuous output methods			
LDA distance measure	355	583	511
Logistic linear terms	311	398	434
+quadratic	302	352	434
+crossproduct	302	352	433
Grid 10x10	286	361	431
5x5	313	405	442
20x20	262	326	412
decile	283	336	417

5 DISCUSSION

It is most likely that the methods that will be most useful for predicting the future distribution of species will be those that most accurately model the current distribution. This would suggest that the logistic regression (Figure 7) and grid approaches will be the most satisfactory of the compared methods. Where extrapolation beyond observed climate is not necessary, all of the methods described here can be used to predict the consequences of climate change. However, extrapolation creates problems for the rectangular climate envelope, convex hull and grid approaches. LDA and logistic regression cope easily with unexperienced climate values in the formula used to determine climate suitability (Figure 8 shows logistic regression predictions following a 3°C warming). However, the further that predictions extend beyond observed climate space, the greater the risk of ecological nonsense!

The example species occur at the extremes of Britain in geographical and climate space. Hence we would anticipate that LDA would perform well in separating the absence/presence categories. In other situations where a species' optimum is central within observed climate then the climate envelope, hull or logistic regression approaches would be more appropriate and LDA would perform poorly.

The distribution modelling reported here is based on the relatively small geographic area of Britain. Since reports from Australia and elsewhere indicate satisfactory modelling of distributions at the continent scale, an ideal approach might be to establish species-climate relationships Europe-wide and then apply the results to Britain.

References

Nix, H.A.(1986). A biogeographic analysis of Australian elapid snakes. *Atlas of Australian Elapid Snakes* (ed R. Longmore) pp 4-15, Bureau of Flora and Fauna, Canberra.

Viner, D. & Hulme, M. (1994). *The climate impact LINK project: providing climate change scenarios for impacts assessment in the UK.* Climatic Research Unit, Norwich.

Walker, P.A. & Cocks, K.D. (1991). HABITAT: A procedure for modelling a disjoint environmental envelope for a plant or animal species. *Global Ecology and Biogeography Letters*, **1**, 108-118.

ACKNOWLEDGEMENTS

This work was supported by the Department of the Environment's "Core model project: the impacts of climate change on natural and semi-natural ecosystems" and NERC's TIGER (Terrestrial Initiative in Global Environment Research) programme.

CORRESPONDING AUTHOR

T H Sparks
ITE Monks Wood
Abbots Ripton
Huntingdon
Cambs PE17 2LS
UK

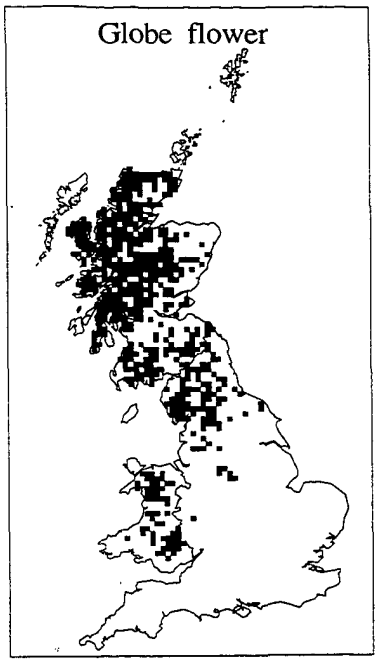


Figure 1

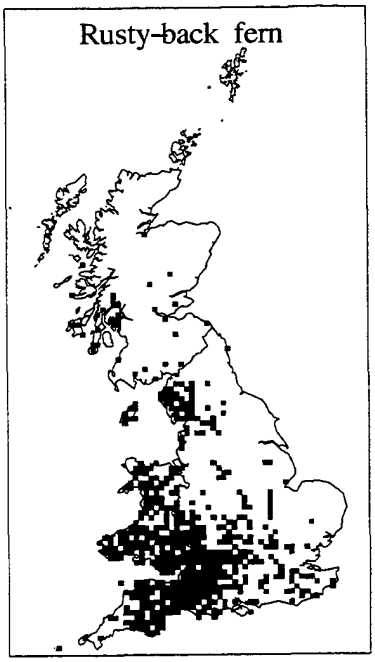


Figure 2



Figure 3

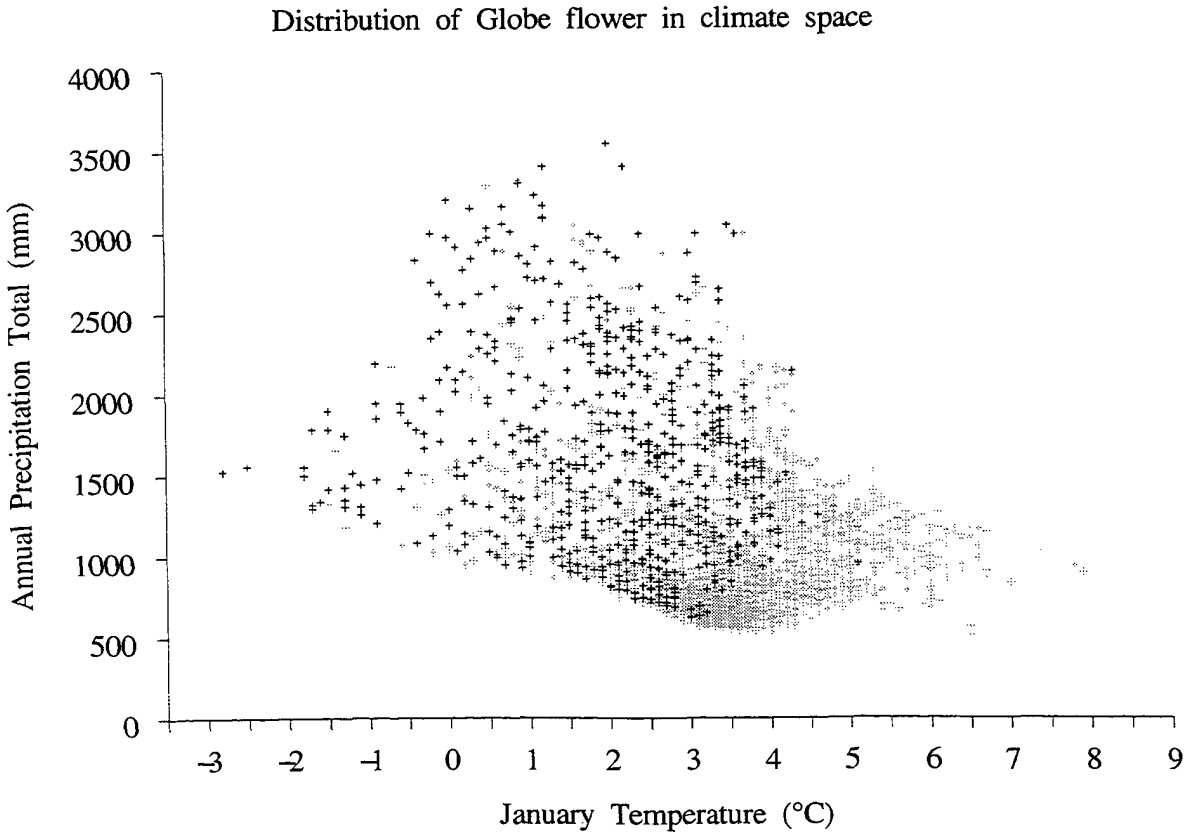


Figure 4

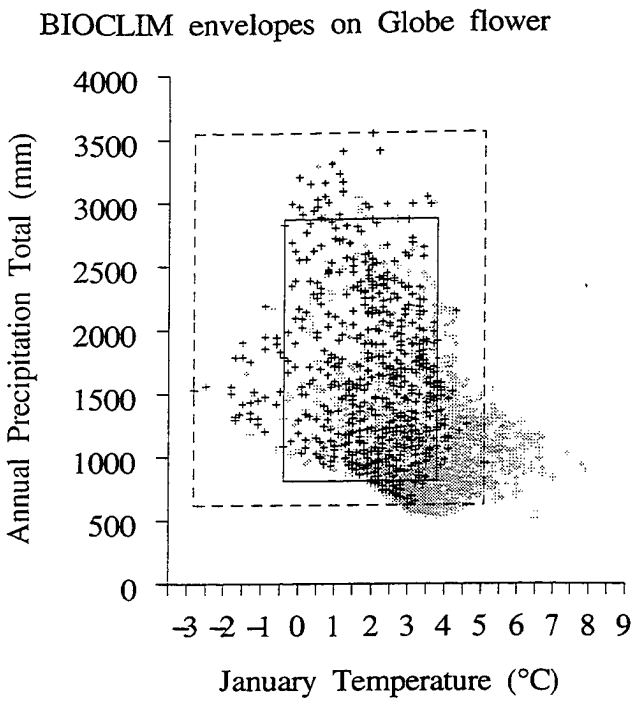


Figure 5

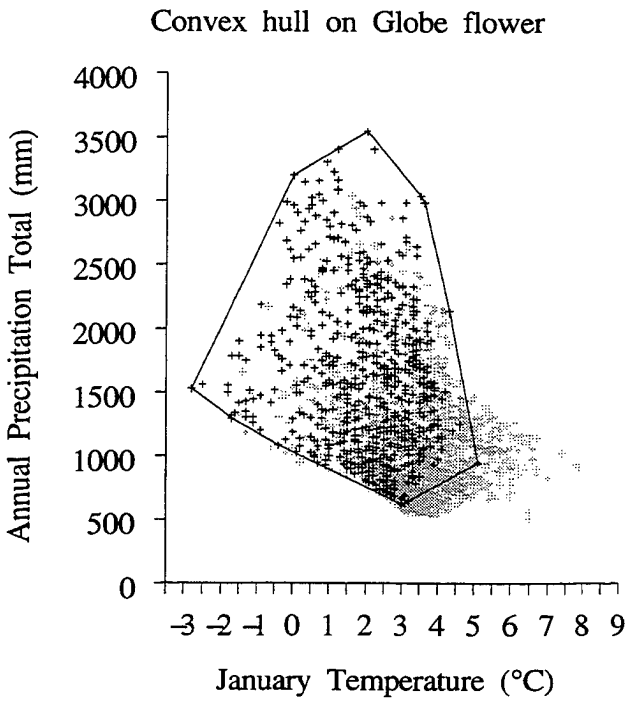


Figure 6

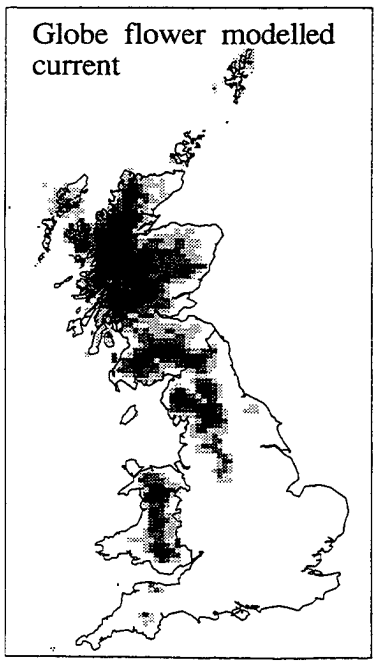


Figure 7

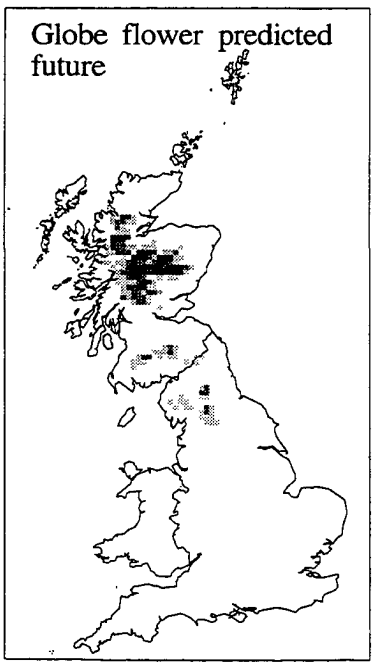


Figure 8

INTERANNUAL AND INTERDECADAL VARIABILITY IN A FIXED-SST, PERPETUAL JANUARY GCM RUN

G. Nitsche and J. M. Wallace

University of Washington, Seattle, Washington, USA

ABSTRACT

The low-frequency variability in a 100,000 day perpetual January, fixed-SST GCM run is analyzed by means of a number of different techniques. It is found that there is no intrinsic variability on timescales beyond about 200 days in the model. Between about 50 and 150 days, the variability is concentrated in one equivalent barotropic, largely zonally symmetric mode per hemisphere. Other modes of variability exhibit white-noise like behavior on time scales longer than about 50 days. It is speculated that fluctuations in the dominant mode corresponds to index cycles like the ones found in Southern Hemisphere observations.

1 INTRODUCTION

The question of whether there are detectable signs of anthropogenic global warming has been an issue of extensive debate recently. The point of contention in this debate has been not so much the quality of atmospheric and oceanic observations, but rather the interpretation of these observations, particularly in making the distinction between signals that are part of the natural variability of the climate and signals induced by anthropogenic influences on the atmosphere. To make this distinction, a thorough understanding of the nature of the natural low-frequency climate variability is essential.

Studies using coupled atmosphere-ocean general circulation models (e.g., Delworth et al. 1993) have established that, as was first hypothesized by Bjerknes (1964), the dominant climatic signals on interdecadal timescales are due to fluctuations in the oceanic thermohaline circulation. However, it is less clear how large a role pure (not ocean-driven) atmospheric variability plays on interannual time scales.

Even before the onset of the global warming debate, Madden (1976) investigated the structure of low-frequency atmospheric variability in connection with the issue of predictability. He posed the question of whether the observations of sea-level pressure in the Northern Hemisphere showed any sign of an intrinsic, low-frequency signal (which would imply that climate tendencies might be predictable on the time scale of this signal) or whether the observed long-term variability could be interpreted as a white noise process without any low-frequency structure (which would imply that long-term climate prediction is essentially impossible). Madden found that intrinsic variability on interseasonal to interannual time scales exists poleward of about 60°N and equatorward of about 40°N, whereas it could not be clearly determined whether it exists between 40° and 60°N. However, Madden had only 73 years of observational data available, part of which are of questionable quality.

The purpose of the present study is to determine whether intrinsic variability on interseasonal to interdecadal timescales exists in a fixed-SST, perpetual January GCM run or if the variability present on these time scales in such a model can simply be explained as sampling fluctuations due to the presence of variability at higher frequencies. Unlike Madden (1976), we base our analysis on Empirical Orthogonal Functions (EOFs) instead of individual gridpoints since we are mainly interested in large-scale features of the circulation. Furthermore, EOF analysis provides us with a tool for analyzing and describing the principal modes of variability on different low-frequency timescales. The results are compared to observational studies.

2 MODEL

The model used is the Geophysical Fluid Dynamics Laboratory (GFDL) Climate group's Atmospheric GCM. The version of the model used for this run (M. J. Nath, personal communication) has R15 resolution and nine vertical levels. It uses standard model orography. For insolation, January values are used, and sea-ice cover and SST are fixed to January climatology. Soil moisture and snow depth are set to fixed values that were previously determined as the means of a 100-year seasonal control run. Cloud cover is predicted. The run which is investigated here is a 100,200 day run with orbital parameters fixed in perpetual January and sea surface temperatures fixed to January climatological values. The model run was facilitated by support from the GFDL Consortium project.

A comparison of the mean and variance of the model output 500 hPa geopotentential height fields with the observed climatology shows that the model reproduces the basic features of Northern Hemisphere winter atmospheric flow reasonably well. One apparent weakness is that the zonally symmetric circulation in the model is stronger than the observed.

In this study, the following fields are analyzed:

- 500 hPa geopotential height;
- sea level pressure;
- 200 hPa streamfunction.

Since the emphasis of this study is on extratropical wintertime variability, most analyses are performed on the part of the fields north of 16°N only. However, in Section 7 we use analyses of the extratropical (summer) Southern Hemisphere (south of 16°S) for control purposes.

3 METHODOLOGY

In the analysis of the model output, we proceed as follows. First, we form running means for a wide range of lengths (two days to 1,500 days; it turns out that for a model run of the length available here, 1,500 days represents the largest length for which stable results can be obtained in the following analyses). For most analyses, running means of length N days were evaluated every $N/2$ days, so that successive means overlap. First, we investigate the behavior of the total variance in the fields as a function of the length of the

running mean. We then perform Empirical Orthogonal Function (EOF) analyses of the fields and analyze the change in the structure of the leading EOFs as a function of averaging length as well as the percentage of variance explained by the individual modes and the spectra of the corresponding principal components (PCs).

4 RESULTS FOR THE 500 HPA GEOPOTENTIAL HEIGHT FIELD

Fig. 1 shows the (area-averaged) variances of the Northern Hemisphere 500 hPa geopotential height (GPH) field as a function of the averaging length. The dashed lines indicate inverse proportionality, which corresponds to white noise. The Northern Hemisphere variance is larger than the globally averaged variance, reflecting the fact that the winter hemisphere is dynamically more active. Other than that, the similarity between the two curves is striking. Intrinsic low-frequency variability seems to be present in the model for averaging times up to about 100 days, corresponding to intraseasonal and intermediate time scales; beyond that, the variance behaves as if the fluctuations were white noise, i.e. there is no intrinsic variability on longer time scales.

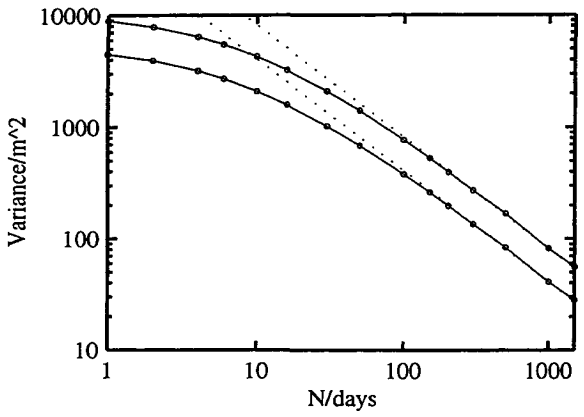


Figure 1: Area-averaged variance of extratropical Northern Hemisphere (upper curve) and global (lower curve) variance of running means of 500 hPa geopotential height in the GFDL model run.

Fig. 2 shows the percentages of variance explained by the first five EOFs, again as a function of the length of the running mean. It is evident that the variability inherent in time averages longer than about a month is dominated by the first EOF. On the other hand, the percentage of variance explained by this mode does not grow monotonically, but reaches a saturation value of about 30% at around 100 to 150 days, corresponding well to the upper time scale limit found earlier. The structure of EOF 1 changes very little with the averaging interval; Fig. 3 shows its structure for N=100 days. The pattern is mainly zonal in structure, representing a difference between high values of GPH at high latitudes and low values at low latitudes (or vice versa), corresponding to changes in intensity in the westerlies at around 60°N. It exhibits a superimposed zonal wavenumber 2 structure, with maximum intensities near the dateline and at the longitude of Greenland. This mode is not found in observational studies of the 500 hPa height field (e.g., Wallace and Gutzler 1981), which could indicate that the zonal mean flow in the model is too strong; however, it is found to be the leading EOF of observed Northern Hemisphere sea surface pressure. The Western Hemisphere part of the pattern bears a strong resemblance to the North Atlantic oscillation or NAO (Walker and Bliss 1932); the most notable difference between EOF 1 for short (N~10) and long (N~1000) running means (not shown) is that the NAO pattern becomes progressively more important as the averaging time is increased and that the maximum over Greenland becomes dominant compared to that over the Chukchi Sea. EOFs 2, 3 and 4 (not shown) are less clearly defined and change in shape as the length of the running means is changed. To further investigate the variability associated with the first few EOF modes, we calculated Principal Component (PC) time series for the first three EOF corresponding to different sampling intervals.[1] The variances of various running means of these PCs are shown in Fig. 4. The variance associated with EOF 2 and 3 exhibits white-

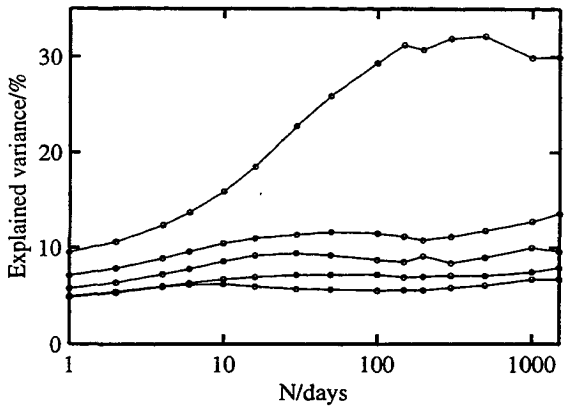


Figure 2: Percentages of variance explained by EOF 1 to 5 (top to bottom) as a function of sampling length.

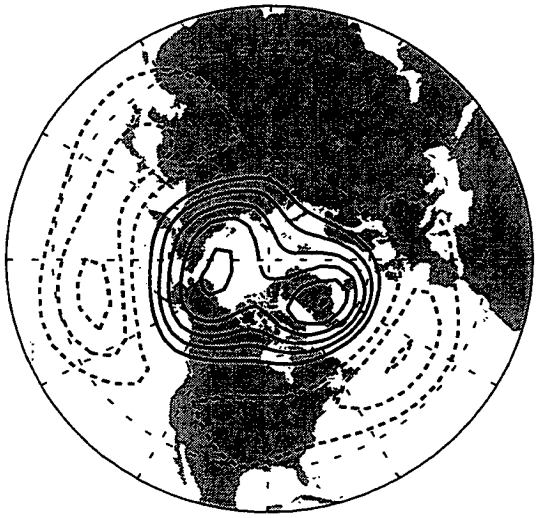


Figure 3: EOF 1 of Northern Hemisphere 30-day running mean 500 hPa geopotential height (arbitrary units; negative contours dashed).

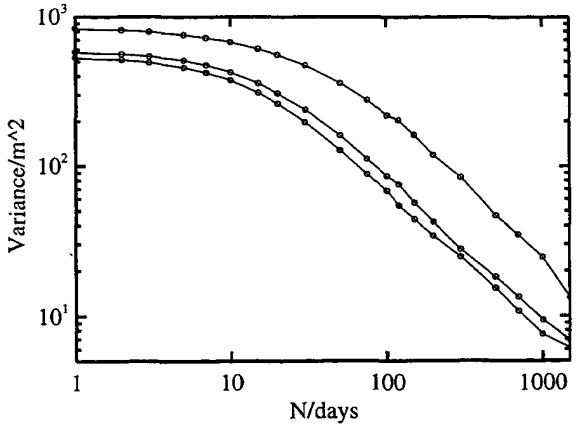


Figure 4: Variance explained by projections of daily NH 500 hPa geopotential height data onto EOFs of 30-day running means.

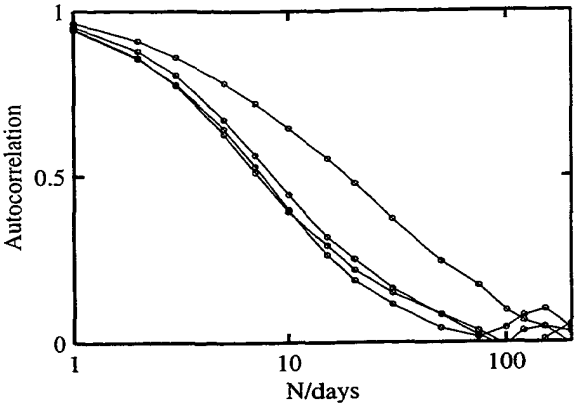


Figure 5: Lag-1 autocorrelation function for the leading four PCs (top to bottom) as a function of N.

noise like behavior on timescales beyond about 30 to 50 days, whereas the variance associated with EOF 1 shows this behavior only on time scales beyond about 100 days. This point is further illustrated by the lag-1 autocorrelation function of the first four PCs for different values of N, which is shown in Fig. 5. The figure shows that the autocorrelations for all PCs are close to 1 for daily data and that they approach zero for N=200. However, it appears that for intermediate values of N, autocorrelations for the first PC are substantially higher than for the following ones, and the curve corresponding to PC 1 seems to intersect the abscissa at a value between 150 and 200, rather than about 80 to 90 as found for the following PCs. This once again seems to indicate the presence of intrinsic variance in only one mode on timescales roughly corresponding to 100-day means.

5 VERTICAL STRUCTURE OF THE DOMINANT MODE

To test whether similar low-frequency behavior is present at different levels in the model atmosphere and to what extent the dominant patterns at various levels are correlated, we investigated the structure of the variability in the sea-level pressure and 200 hPa streamfunction fields in a similar manner. To avoid spurious variance associated with the extrapolation of sea level pressure over mountainous terrain, we disregarded all grid points corresponding to elevations higher than 1,000m in the SLP analysis, which means that the region of the maximum in the 500 hPa height EOF 1 over Greenland is largely ignored in this analysis. Nevertheless, we find a similar behavior in the fraction of variance explained by individual EOF modes as for the 500 hPa height field, with the first EOF explaining about one third of the total variance for long running means and all further modes explaining distinctly less. A visual inspection of the corresponding EOF pattern (not shown) shows that it is similar to the pattern found in the 500 hPa height field (they are spatially correlated at 88.2%), and that it corresponds to the first EOF mode in the observations (Wallace and Gutzler 1981).

1. To avoid random variability that might be associated with fluctuations in the shape of the EOF for different sample sizes, and for the ease of computation, we are using projections on the 30-day EOFs throughout.

In analyzing the 200 hPa streamfunction field, we again find similar behavior of the distribution of variance onto the EOF modes. The dominant pattern is very similar to that of the 500 hPa GPH field; both patterns are spatially correlated at 95.4%. The corresponding principal components are correlated at 89.7% for unfiltered data; the correlation reaches a value of 94.3% for 30-day running means. For all values of N, the variance explained by EOF 1 in the streamfunction field is slightly smaller than the corresponding figure for the 500 hPa GPH field. This is not surprising, considering that in the streamfunction field, a larger percentage of the total variance comes from subtropical latitudes. The signals in these latitudes are typically less coherent than those in mid- and high latitudes.

6 ANALYSIS OF THE SOUTHERN HEMISPHERE 500 HPA GPH FIELD

In order to establish whether similar results hold in a very different basic state, we analyzed the low-frequency variability of the 500 hPa geopotential height in the extratropical Southern Hemisphere in the same model run. Due to the more zonally symmetric land-sea distribution and orography, the Southern hemisphere circulation is much more zonally symmetric than that of the Northern Hemisphere, in both model and observations; since the conditions of the model run correspond to perpetual summer in the Southern Hemisphere, the latitudinal temperature gradients and there-

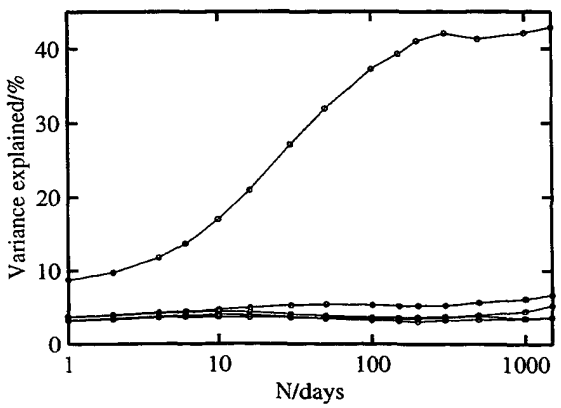


Figure 6: As Fig. 2, but for the Southern Hemisphere.

fore the intensity of the midlatitude zonal flow are lower than in the Northern Hemisphere case. The distribution of variance among the EOFs for various lengths of running means, shown in Fig. 6, exhibits a similar, but more extreme picture than in the Northern Hemisphere case. The first EOF corresponds to a nearly completely zonally symmetric flow pattern (not shown), in agreement with results from observational studies (Kidson 1987). It explains a percentage of variance that increases from 9% for unfiltered data to more than 40% for 200-day running means and stabilizes there, whereas the fractions of variance explained by all other EOFs do not exhibit much of an increase and do not exceed 7% even for 1,500 day running means. The Southern hemisphere low-frequency variance in the model seems to be concentrated almost entirely in the zonally symmetric mode.

7 DISCUSSION AND CONCLUSION

Our analyses show that intrinsic low-frequency variability exists on intraseasonal timescales. The variability is largely confined to one mode, which corresponds to an increase (decrease) of the zonally symmetric flow in high midlatitudes, with maximum intensity at the longitudes of Greenland and the Bering Strait, and is largely barotropic. This mode dominates the variability in all Northern Hemisphere fields investigated on timescales longer than about 10 days. Similar behavior is found in the Southern Hemisphere. There does not appear to be any intrinsic atmospheric variability on interannual and longer time scales.

The structure of the EOFs corresponds well to the index cycles which have been documented in the Southern Hemisphere and which represent vacillations in the width of the zonal jet (e.g., Kidson 1987). This suggests that the dominant mode in the Northern Hemisphere represents a similar phenomenon in the model, which does not exist in the real atmosphere due to the weaker zonally symmetric flow. However, the frequency distribution of the corresponding PCs does not give any indication for the presence of multiple modes in either hemisphere.

Since the absence of an annual cycle in the model removes all timescales, except the diurnal one, from the forcing, the question arises how the 200-day timescale for the cutoff of intrinsic variability in the model is determined. One possible explanation is that this timescale is determined by the time needed for the atmosphere to reach radiative equilibrium with space.

For the future, we are planning to perform a similar analysis the output of a long-term run of the same atmospheric model, but coupled to a mixed layer ocean. By adding the mixed layer, the heat capacity of the coupled atmosphere-ocean system is increased by a factor of almost ten; on the other hand, the mixed-layer ocean should not make any dynamical contribution. It remains to be seen how this influences the low-frequency cutoff of intrinsic variability in the model.

REFERENCES

Bjerknes, J., 1964, "Atlantic Air-Sea Interaction", Adv. Geophys., Vol. 10, pp.1-82.

Delworth, T., S. Manabe, and R. J. Stouffer, 1993, "Interdecadal Variations of the Thermohaline Circulation in a Coupled Ocean-Atmosphere Model", J. Climate, Vol. 6, pp. 1993-2011.

Kidson, J. W., 1988a, "Indices of the Southern Hemisphere Zonal Wind", J. Climate, Vol. 1, pp. 183-194.

Kidson, J. W., 1988b, "Interannual Variations in the Southern Hemisphere Circulation", J. Climate, Vol. 1, pp. 1177-1198.

Madden, R. A., 1976, "Estimates of the Natural Variability of Time-Averaged Sea-Level Pressure", Mon. Wea. Rev., Vol. 104, pp. 942-952.

Walker, G. T., and E. W. Bliss, 1932, "World Weather V", Mem. Roy. Meteor. Soc., Vol. 4, pp. 53-84.

Wallace, J. M., and D. S. Gutzler, "Teleconnections in the Geopotential Height Field during the Northern Hemisphere Winter", Mon. Wea. Rev., Vol. 109, pp. 784-812.

ACKNOWLEDGMENTS

We are thankful to Mary Jo Nath at GFDL for her help in accessing the data, and to Valentin Dymnikov and Ileana Bladé for helpful discussions.

CORRESPONDING AUTHOR

Gregor Nitsche
JISAO, University of Washington
4909 25 Ave NE
Seattle WA 98105-4107
USA
email: nitsche@atmos.washington.edu

Caveats in the application of statistical analysis in climate research

Hans von Storch
Max-Planck-Institut fuer Meteorologie, Hamburg

Statistical Analysis is one of the three methodical pillars of climate research (simplified dynamical reasoning and experimentation with numerical climate models are the other two). As such it is worthwhile to examine whether the problems encountered in climate research are "normal" in the sense of mainstream statistical wisdom.

All empirical evidence must be gathered from the one observational record the (hopefully stationary and ergodic) climate system realizes since real experiments can not be done. The past observational record has been screened intensely and has shaped our understanding and perceptions of how the dynamics of climate are. Therefore, new hypotheses of the character of the climate system, independently whether they originate from exploratory data analyses, GCM experiments or from dynamical reasoning, is implicitly based on the past record - and no independent data is at hand to verify the hypothesis. Most climatic processes have a large (temporal) memory so that a significant amount of new independent observational evidence cannot be collected in a practically reasonable period of time. The consequence of this adverse situation is that the confirmatory tools of statistical analysis, in particular null hypothesis tests, can hardly be used. However, within the artificial and restricted world of a GCM, new independent evidence can be created through additional experiments and exploratory analysis becomes possible. The problem with GCM data is that any result applies to the GCM world which might, or might not, match the real climate system.

The dilemma of exploratory analysis is demonstrated by the absurd case of the Mexican Hat and with the sometimes furiously discussed sun-weather connection.

Another specific aspect refers to the always present interdependence between any two observations in space and time. Therefore many standard routines cannot be used as specified in mainstream statistical textbooks. This problem is illustrated with the tests by Mann-Kenndall and Pettitt to detect trends and change points.

A particularity of the climate system is its enormous (infinite) phasespace which does not allow to determine a-priori suitable low-dimensional subspaces to which a statistical analysis, or a theoretical argument, might be limited. Statistical approaches help to identify such sub-spaces, conditional upon the problem under consideration. The general idea of Principal Interaction Patterns is discussed.

MIXTURES OF STOCHASTIC PROCESSES: APPLICATION TO GENERATION OF CLIMATE CHANGE SCENARIOS

Richard W. Katz

National Center for Atmospheric Research, Boulder, Colorado, USA

ABSTRACT

Mixtures of stochastic processes have increasingly arisen in climate research in recent years. Some general properties of mixtures that are well known within statistics, but not ordinarily utilized in complete generality in climate applications, are reviewed. These properties are illustrated for Richardson's model (or WGEN), a popular form of stochastic weather generator. The question of how best to adjust the parameters of this model to generate scenarios of climate change is examined. Finally, how these same issues apply to statistical "downscaling" is briefly outlined.

1. BACKGROUND

Most often the concept of a "mixture" of stochastic processes is not explicitly recognized as such in climate research, but instead only appears indirectly through consideration of conditional stochastic models for climate time series. For instance, certain forms of stochastic weather generators are expressed in a conditional form convenient for simulation algorithms (e.g., Richardson, 1981). Such models have been advocated for use in producing climate change scenarios for impact assessments (Wilks, 1992). Another instance arises with what is sometimes termed statistical "downscaling" (von Storch *et al.*, 1993). For example, stochastic models for local daily precipitation have been fitted conditional on an index of large-scale atmospheric circulation (Katz and Parlange, 1993).

In these circumstances, the overall "unconditional" (or "induced") stochastic process for the climate variable (that has been specified conditionally) can be viewed as a mixture of "conditional" stochastic processes. For various reasons, it may be helpful to consider the statistical properties of the unconditional process. When employing Richardson's model to produce climate change scenarios, it is difficult to determine how to achieve the desired changes without explicit treatment of the unconditional process.

2. MIXTURES OF STOCHASTIC PROCESSES

2.1. Distributions

Typically in climate applications, the conditional distribution of a continuous random variable X given a discrete random variable I (e.g., an index), say with density function $f_{X|I}(x|i)$, is specified. The unconditional distribution of X, say with density function $f_X(x)$, can be obtained from this conditional distribution by

$$f_X(x) = \Sigma_i \; f_{X|I}(x|i) \Pr\{I = i\}. \qquad (1)$$

That is, the unconditional density function is a weighted average of the conditional densities.

Much research in statistics has dealt with the problem of estimating the components on the right-hand side of (1) when I is not actually observed, the case of a "hidden" mixture (e.g., Titterington *et al.*, 1985). Nevertheless, climate applications have not tended to make use of these methods, but to focus instead on related, but not equivalent problems like detecting multimodality (e.g., Nitsche *et al.*, 1994).

2.2. Moments

For an accessible treatment of the geometric approach to conditional expectation based on Hilbert space theory, see Chapter 2 of Brockwell and Davis (1991). The key idea requires recognizing that the mean of the conditional distribution of the random variable X, $E(X|I = i)$, is itself a random variable. Then X has an orthogonal decomposition

$$X = E(X|I) + [X - E(X|I)] \qquad (2)$$

(Bhattacharya and Waymire, 1990, p. 642).

A well known property of conditional expectation is

$$E(X) = E[E(X|I)], \tag{3}$$

or that the unconditional mean is just a weighted average of the conditional means. This relationship (3) can be regarded as "conservation of center of mass."

Making use of (2), the unconditional variance is related to the conditional mean and conditional variance by

$$\text{var}(X) = E[\text{var}(X|I)] + \text{var}[E(X|I)]. \tag{4}$$

That is, the unconditional variance is not simply a weighted average of the conditional variances, but reflects the variation in the conditional means as well. This property (4) can be viewed as a statistical version of the Pythagorean Theorem.

Let Y denote another arbitrary random variable (e.g., X and Y might represent observations of the same climate variable at consecutive time periods). Making repeated use of (2), the unconditional covariance can be expressed in terms of the conditional covariance and conditional mean as

$$\text{cov}(X, Y) = E[\text{cov}(X, Y)|I)] + \text{cov}[E(X|I), E(Y|I)]. \tag{5}$$

This relationship (5) is a natural generalization of (4). Note that in all of these expressions, (2)—(5), the conditioning variable I could actually be a set of variables (e.g., the past history of an index).

3. RICHARDSON'S MODEL

These theoretical properties of unconditional processes are applied to a particular stochastic model due to Richardson (1981), sometimes known as WGEN (Richardson and Wright, 1984). This model is employed to simulate joint daily time series of precipitation amount and other climate variables, such as minimum and maximum temperature and solar radiation.

3.1. Definition of model

A simplified version of Richardson's model is briefly described. Rather than simultaneously considering all of these variables, only one variable at a time (e.g., daily mean temperature) is modeled conditional on the occurrence of precipitation. Further, any seasonal cycles in the model parameters are ignored.

Let $\{J_t: t = 1, 2, \ldots\}$ denote the sequence of daily precipitation occurrences (i.e., $J_t = 1$ indicates a wet day, $J_t = 0$ a dry day). Assume that this process is a first-order Markov chain, with parameters the probability of a wet day π and the first-order autocorrelation coefficient (or persistence parameter) d; that is,

$$\pi = \Pr\{J_t = 1\}, \quad d = \text{corr}(J_{t-1}, J_t). \tag{6}$$

Note that $d > 0$ for daily precipitation occurrences.

Let $\{X_t: t = 1, 2, \ldots\}$ denote the time series of daily mean temperature. The X_t-process is defined conditional on the J_t-process, with a "residual" time series $\{Z_t: t = 1, 2, \ldots\}$ being employed to link these two processes. The Z_t-process is a first-order autoregressive [AR(1)] process with autocorrelation ϕ, and Z_t being normally distributed with zero mean and unit variance. Given $J_t = i$, set

$$X_t = \mu_i + \sigma_i Z_t, \quad i = 0, 1. \tag{7}$$

That is, the conditional distribution of X_t is normal with mean μ_i and variance σ_i^2.

As an example, the parameter estimates when this model is fitted to the daily precipitation occurrence and daily mean temperature observations for the month of January for 30 years (1965—1994) at Denver, Colorado, are:

$$\hat{\pi} = 0.178, \quad \hat{d} = 0.219, \quad \hat{\mu}_0 = 32.2\ ^\circ\text{F},$$

$$\hat{\sigma}_0 = 10.8\ ^\circ\text{F}, \quad \hat{\mu}_1 = 21.8\ ^\circ\text{F}, \quad \hat{\sigma}_1 = 11.0\ ^\circ\text{F},$$

$$\hat{\phi} = 0.663. \tag{8}$$

It is evident that the daily mean temperature is substantially lower on the average, and perhaps more variable, on wet days than on dry days, with the effect on the mean being physically plausible.

3.2. Unconditional model

To produce scenarios of climate change, it is tempting simply to change the parameters of Richardson's model about which some knowledge might be available. The other parameters, whose

possible changes are unknown, would be held fixed at their present values. In this way, it might be anticipated that the statistical (if not physical) relationship between daily precipitation occurrence and mean temperature would be preserved. To see that this is not necessarily the case, the two conditional models for daily mean temperature need to be converted into a single, consistent unconditional model.

The statistical properties of the unconditional temperature process can be derived using the general properties stated in section 2.2. Applying (3) and (4), the unconditional mean, μ_X say, and variance, σ_X^2 say, of the daily mean temperature X_t are given by

$$\mu_X = (1 - \pi)\,\mu_0 + \pi\,\mu_1,$$

$$\sigma_X^2 = (1 - \pi)\,\sigma_0^2 + \pi\,\sigma_1^2 + \pi\,(1 - \pi)\,(\mu_1 - \mu_0)^2. \tag{9}$$

Applying (5), the cross correlation function between the daily precipitation occurrence J_t and the daily mean temperature X_{t+l}, $\rho_{JX}(l)$ say, can be expressed as

$$\rho_{JX}(l) = \left([\pi\,(1 - \pi)]^{1/2}\,d^l\,(\mu_1 - \mu_0)\right) / \sigma_X, \tag{10}$$

$l = \ldots, -1, 0, 1, \ldots$ Here an expression for σ_X is included in (9). Note that $\rho_{JX}(l) < 0$, because $\mu_1 < \mu_0$.

The autocorrelation function of daily maximum temperature, $\rho_X(l)$ say, is quite complex, but follows directly from (5):

$$\sigma_X^2\,\rho_X(l) = \phi^l\,[(1 - \pi)\,\sigma_0^2 + \pi\,\sigma_1^2]$$

$$+ \pi\,(1 - \pi)\,[d^l\,(\mu_1 - \mu_0)^2 - \phi^l\,(1 - d^l)\,(\sigma_1 - \sigma_0)^2], \tag{11}$$

$l = 1, 2, \ldots$ It depends on the autocorrelation functions of both the residual temperature time series, $\rho_Z(l) = \phi^l$, and the precipitation occurrence process, $\rho_J(l) = d^l$. If $0 < d < \phi$, as is the case for daily mean temperature, then $\rho_X(l) < \rho_Z(l)$.

When the parameter estimates for the Denver data (8) are substituted into (9)–(11), the following unconditional temperature statistics are obtained:

$$\mu_X = 30.4\ ^\circ\text{F},\quad \sigma_X = 11.6\ ^\circ\text{F},$$

$$\rho_{JX}(0) = -\,0.343,\quad \rho_X(1) = 0.611. \tag{12}$$

These values necessarily reproduce the corresponding sample statistics, with the exception of the first-order autocorrelation. Its observed value is 0.729, indicating that Richardson's model only preserves the residual first-order autocorrelation ϕ, *not* the unconditional autocorrelation. Note that the unconditional distribution of daily mean temperature is quite close to the normal, despite being a mixture of two normals (1).

3.3. Climate change

To see what effect varying certain parameters of Richardson's model has on the unconditional process for daily mean temperature, consider the following hypothetical example. Suppose that the probability of a wet day for Denver in January doubled to $\pi^* = 0.355$, holding all the other parameters of Richardson's model fixed. From (9)–(11), the unconditional temperature statistics for this case of a "wetter" climate are:

$$\mu_X = 28.5\ ^\circ\text{F},\quad \sigma_X = 12.0\ ^\circ\text{F},$$

$$\rho_{JX}(0) = -\,0.415,\quad \rho_X(1) = 0.586. \tag{13}$$

Comparing these values with those for the current climate (12), the wetter climate is cooler on the average, as is physically reasonable. Less obvious are the results that the temperature is more variable, that its day-to-day persistence has decreased, and that the contemporaneous cross correlation between precipitation occurrence and mean temperature has increased (in absolute value). It would be interesting to investigate whether such effects have any physical justification.

The effect of the increase probability of precipitation on the unconditional daily temperature mean μ_X could be counteracted by simultaneously increasing the two conditional means to $\mu_0^* = 34.1\ ^\circ\text{F}$ and $\mu_1^* = 23.7\ ^\circ\text{F}$. Likewise, its effect on the unconditional standard deviation σ_X could be counteracted by decreasing the two conditional standard deviations to $\sigma_0^* = 10.4\ ^\circ\text{F}$ and $\sigma_1^* = 10.6\ ^\circ\text{F}$. Nevertheless, for this climate change scenario, the contemporaneous cross correlation and first-order autocorrelation differ even further from their present values. In this case, (9)–(11) yield

$$\mu_X = 30.4\ ^\circ\text{F},\quad \sigma_X = 11.6\ ^\circ\text{F},$$

$$\rho_{JX}(0) = -\,0.430,\quad \rho_X(1) = 0.581. \tag{14}$$

It would be difficult, if not impossible, to devise a way in which to preserve as well the current values of

$\rho_{JX}(0)$ and $\rho_X(1)$. See Katz (1995) for a more detailed discussion of the generation of climate change scenarios.

4. STATISTICAL DOWNSCALING

Impact assessments require climate change scenarios on small spatial and short temporal scales and for variables, especially precipitation, that are not predicted well by physical/numerical models of climate. On the other hand, these models do have substantial skill in predicting large-scale patterns in atmospheric circulation that are long-lived. Statistical downscaling attempts to relate empirically these two disparate forms of climate information.

For instance, Katz and Parlange (1993) studied the relationship between daily precipitation at individual gauges in California and gridded monthly mean sea level pressure off the coast in the Pacific Ocean. The methodology involved fitting separate conditional stochastic models to daily time series of precipitation amounts depending on whether or not the pressure was above or below normal. When the same form of stochastic model is fitted to daily precipitation amounts without conditioning on pressure, a pronounced tendency to underestimate the observed variance of monthly total precipitation results. On the other hand, the unconditional model obtained by combining the two conditional ones has much less of a tendency to underestimate the same monthly variance. This behavior is referred to as "over dispersion" in the statistics literature, with the use of mixtures being a popular remedy.

Zucchini and Guttorp (1991) have applied a technique called "hidden Markov modeling" to treat the same problem when the conditioning variable is not observed (e.g., as if pressure data were not available). This methodology can be viewed as generalizing hidden mixtures to allow for temporal dependence.

REFERENCES

Bhattacharya, R.N., and E.C. Waymire, 1990: *Stochastic Processes with Applications*. Wiley, New York.

Brockwell, P.J., and R.A. Davis, 1991: *Time Series: Theory and Methods* (second edition). Springer-Verlag, New York.

Katz, R.W., 1995: Use of stochastic models to generate climate change scenarios. Submitted for publication.

Katz, R.W., and M.B. Parlange, 1993: Effects of an index of atmospheric circulation on stochastic properties of precipitation. *Water Resources Research*, **29**, 2335–2344.

Nitsche, G., J.M. Wallace, and C. Kooperberg, 1994: Is there evidence of multiple equilibria in planetary wave amplitude statistics? *Journal of the Atmospheric Sciences*, **51**, 314–322.

Richardson, C.W., 1981: Stochastic simulation of daily precipitation, temperature, and solar radiation. *Water Resources Research*, **17**, 182–190.

Richardson, C.W., and D.A. Wright, 1984: WGEN: A model for generating daily weather variables. USDA, ARS-8, NTIS, Springfield, VA.

Storch, H. von, E. Zorita, and U. Cubasch, 1993: Downscaling of global climate estimates to regional scales: An application to the Iberian rainfall in wintertime. *Journal of Climate*, **6**, 1161–1171.

Titterington, D.M., A.F.M. Smith, and U.E. Makov, 1985: *Statistical Analysis of Finite Mixture Distributions*. Wiley, Chichester, U.K.

Wilks, D.S., 1992: Adapting stochastic weather generation algorithms for climate change studies. *Climatic Change*, **22**, 67–84.

Zucchini, W., and P. Guttorp, 1991: A hidden Markov model for space-time precipitation. *Water Resources Research*, **27**, 1917–1923.

ACKNOWLEDGMENTS

The National Center for Atmospheric Research is sponsored by the National Science Foundation. Research was partially supported by NSF Grant DMS-9312686.

CORRESPONDING AUTHOR

Richard W. Katz
Environmental and Societal Impacts Group
National Center for Atmospheric Research
P.O. Box 3000
Boulder, CO 80307 USA

A NEW METHODOLOGY FOR INVESTIGATING LONG RANGE PREDICTABILITY

Richard H. Jones, Roland Madden, Dennis J. Shea

National Center for Atmospheric Research, Boulder, CO, USA

ABSTRACT

Time domain methods are used to investigate the potential for long range prediction. Daily observations of a continuous variable (e.g., temperature) over a season, repeated for a number of years, are used. Observations may be missing. The basic methodology is regression with correlated errors. The regression part of the model can include sines and cosines to remove the annual cycle. Alternatively, the daily means can be estimated using a regression model which includes a regression coefficient for each day of the year. This gives improved estimates when there are missing observations and the data are serially correlated, compared to subtracting the long term daily means. The errors in the regression model are assumed to have an autoregressive moving average (ARMA) structure of arbitrary order, ARMA(p,q), or the sum of first order autoregressive (AR(1)) models. Maximum likelihood estimation, using nonlinear optimization, is used to estimate the regression coefficients and ARMA parameters, assuming that the errors in the model have Gaussian distributions. An estimate of the spectral density can be calculated from the coefficients. Within this framework, it is possible to test whether various predictor variables can significantly improve long range forecasts by using likelihood ratio tests. It is also possible to model a random between year effect which models unpredictable year to year variability. Examples are presented using winter temperature data, and it is shown that the temperature anomalies are well modelled as an ARMA(2,1) with observational error, or, equivalently, as the sum of two AR(1) processes plus observational error.

1 INTRODUCTION

Using daily observations of a meteorological variable over a season, and repeated for a number of years, it is possible to look for long term trends or year to year variability in the mean of the variable. Properly accounting for the annual cycle is necessary since, otherwise, the spectral density near zero frequency will be distorted. The subtraction of the sample mean, annual cycle and several harmonics leaves a hole in the spectral density near zero frequency. If these harmonics are based on climatological data rather than the data being analyzed, the spectral density is still distorted near zero frequency. If there are no missing observations, the day by day means can be subtracted without distorting the spectral density (Jones, 1964). By subtracting the day by day means, we mean subtracting the mean of all December firsts in the data set from each December first, etc.

An unbalanced situation exists when some of the observations are missing. In this case, the day by day means can be estimated by regression and subtracted from the data. Now we are faced with a regression problem with serially correlated errors. In meteorology, these errors are often referred to as anomalies. Once we are set up to handle regression with serially correlated errors, other independent variables can be added to the regression such as a variable that increases linearly with year to look for a linear trend over time.

Another concept that has become popular in the area of biostatistics, is to consider data from different years to be statistically independent and include a random between year effect to the model (Jones, 1993). A random between year effect is a random year to year shift in the mean. Some years are higher than usual and some years are lower than usual. This random year to year shift can be caused by some outside factor that is not included in the model such as sea surface temperature. The variance of this random effect can be estimated along with the regression coefficients using maximum likelihood, and the variance estimate can be tested to see if it is significantly different from zero.

2 A REGRESSION MIXED MODEL

A mixed model is a regression model with more than one random error term. These random errors are referred to as components of variance (Jones, 1993). In our situation there is the error or anomaly associated with each observation, ϵ_{ij}, where i denotes the year, and j denotes the observations within a year. The second random error term is γ_i which denotes the random year to year shift in the mean level. The regression model for year i is

$$y_{ij} = \beta_j + \gamma_i + \epsilon_{ij}, \qquad (1)$$

where β_j is the mean for day j. For example, if there are observations for 92 days within a season each year, there will be 92 β's to estimate. γ_i is the random year effect for year i, assumed to have a Gaussian distribution with zero mean and variance σ^2_γ. The errors, ϵ_{ij}, are assumed to have zero means, variance σ^2_ϵ, to be independent from year to year, and have a Gaussian ARMA(p,q) structure

within years. The ARMA(p,q) model is

$$\epsilon_j = \sum_{k=1}^{p} \phi_k \epsilon_{j-k} + \eta_j + \sum_{k=1}^{q} \theta_k \eta_{j-k}, \qquad (2)$$

where η_j is the unpredictable random input at time j, sometimes called an innovation or shock (Box and Jenkins, 1976), with mean zero and variance σ_η^2. The ϵ_{ij} are independent of the γ_i's. If a model contains observational error, the actual temperature anomaly is

$$\epsilon_j + \xi_j,$$

where the ξ_j are assumed to be independent Gaussian random variables with zero mean and variance σ_ξ^2, i.e. white noise.

Let m be the number of years of data, and n be the number of observations per year. If the data set is balanced, i.e. there are no missing observations, the maximum likelihood estimates of the β's are simply the day by day averages,

$$\hat{\beta}_j = \frac{1}{m} \sum_{i=1}^{m} y_{ij}.$$

If there are missing observations, the β's should be estimated by regression. For days when all m years of data are available, the estimate of the beta for that day is still just the average. For days that contain missing observations, the maximum likelihood estimates of the corresponding β's are not the simple averages since data from adjoining days improves the estimates by using the serial correlation in the error structure.

Equation (1) can be written in matrix form as

$$\mathbf{y}_i = \mathbf{X}_i \beta + \mathbf{1}\gamma_i + \epsilon_i, \qquad (3)$$

where $\mathbf{y}_i$ is a column vector of the observations from year i, and $\mathbf{X}_i$ is the identity matrix. If there are missing observations in the $\mathbf{y}_i$ vector, the corresponding rows of $\mathbf{X}_i$ are removed, so $\mathbf{X}_i$ is the identity matrix with missing rows. This is a special case corresponding to model (1). In general, $\mathbf{X}_i$ can be any design matrix for year i as would be used in any regression analysis. In the random part of the model, $\mathbf{1}$ is a column vector of ones, γ_i is the random year effect for year i, and ϵ_i is the vector of errors assumed to have an ARMA(p,q) structure within years.

A method for the maximum likelihood estimation of the parameters of an ARMA(p,q) model when there are missing observations is given in Jones (1980). This method uses state space representations and the Kalman filter to calculate the likelihood function. Using the methods in Jones (1993), maximum likelihood estimates of the regression coefficients and variance parameters in (3) can be obtained along with the estimates of the ARMA parameters. Two nested models can be compared statistically by calculating the change in −2 ln likelihood between the two models, and comparing the change to the percentage points of the chi-square distribution with degrees of freedom equal to the change in the number of estimated parameters. The model with more parameters should have a lower value of −2 ln likelihood since −2 ln likelihood is being minimized by the optimization program. Nested models are models that can be obtained from each other by setting some of the parameters equal to zero, or by applying constraints to some of the parameters. The number of parameters includes both regression coefficients and the parameters in the error structure such as the ARMA coefficients. When many models are being compared, AIC (Akaike, 1974) is useful for comparing models. AIC is defined as −2 ln likelihood plus twice the number of estimated parameters. This provides a penalty for estimating parameters and attempts to avoid over fitting.

3 A TWO COMPONENT AR(1) MODEL

Mitchell (1966) suggested that a possible model for air temperature anomalies is the sum of two autoregressions, one with a time constant on the order of a few days, and one with a much longer time constant. He referred to this process as a *compound first-order linear Markov process.* At the time he postulated this model, tools for the maximum likelihood estimation of the parameters were not available. Now, this model can be formulated in state space form and the parameters estimated. If the two autoregressions are

$$x_1(t) = \phi_1 x_1(t-1) + \eta_1(t)$$

$$x_2(t) = \phi_2 x_2(t-1) + \eta_2(t)$$

they can be written as a matrix state equation,

$$\begin{bmatrix} x_1(t) \\ x_2(t) \end{bmatrix} = \begin{bmatrix} \phi_1 & 0 \\ 0 & \phi_2 \end{bmatrix} \begin{bmatrix} x_1(t-1) \\ x_2(t-1) \end{bmatrix} + \begin{bmatrix} \eta_1(t) \\ \eta_2(t) \end{bmatrix}$$

The observation equation defines what linear combination of the elements of the state vector are observed,

$$y(t) = \begin{bmatrix} 1 & 1 \end{bmatrix} \begin{bmatrix} x_1(t) \\ x_2(t) \end{bmatrix} + v(t),$$

where $v(t)$ is observational error. Note that this model contains five unknown parameters, the two ϕ's, the two variances of the random input's, σ_1^2 and σ_2^2, and the observational error variance.

Once a model is in state space form consisting of a state equation and an observation equation, and assuming that the errors are Gaussian, the Kalman filter can be used to calculate the likelihood for given values of the unknown parameters. Nonlinear optimization (Dennis and Schnabel, 1983) can then be used to obtain maximum likelihood estimates.

4 EXAMPLES

The first data set analyzed was 28 years of daily temperature (°C) data for 96 winter days at Saint Bernard, Alabama. Instead of using (3) to estimate day by day means, a grand mean across all years and the annual cycle and several of its harmonics were estimated and removed by regression within the data set. Only the first harmonic (one

cycle per year) and the grand mean were significant. There was no significant random between year effect. The best model, based on AIC, contained a grand mean, the first harmonic, no random year effect, and an ARMA(4,3) error structure. Switching to model (3) where the day by day means are removed by regression, the best error structure is an ARMA(2,2), a much simpler model. The ARMA(2,2) model fit to the data is equivalent to an ARMA(2,1) with observational error (Jones, 1993). The reason for this change in the error model is that by removing the mean by fitting the annual cycle leaves a hole in the spectral density near zero frequency, and the ARMA process is trying to model the hole as well as the remaining structure at higher frequencies. Removing the day by day means does not change the shape of the spectrum near zero frequency.

The second data set analyzed was 41 years of daily temperature (°C) data for 96 winter days at Redlands, California. Of the potential 3,936 observations, 93 were missing. Model (3) was used to remove the daily means by regression since the data set contained missing observations. Again, an ARMA(2,1) plus observational error provided the best fit to the error structure. The estimated ARMA(2,1) model is

$$\epsilon_j = 1.7552\epsilon_{j-1} - 0.7561\epsilon_{j-2} + \eta_j - 0.9809\eta_{j-1},$$

where η_j is the random one day forecast error if the past temperatures were measured exactly. The standard deviation of this forecast error is estimated as 2.081°C. The observational error in the model has an estimated standard deviation of 1.503°C. The estimated standard deviation of the difference between a one day forecast and the observed temperature on that day is $\sqrt{(2.081)^2 + (1.503)^2} = 2.567$°C.

The roots of the characteristic equation,

$$1 - 1.7552z + 0.7561z^2 = 0,$$

determine the time constants of the ARMA model. The roots of the characteristic equation are

$$z_1 = 0.759$$

$$z_2 = 0.996$$

Fitting a model consisting of the sum of two AR(1) processes plus observational error to the Redlands data gave the identical likelihood as fitting the ARMA(2,1) model with observational error. The estimated parameters are

$$\hat{\phi}_1 = 0.758$$

$$\hat{\phi}_2 = 0.996$$

$$\hat{\sigma}_1 = 2.035°\text{C}$$

$$\hat{\sigma}_2 = 0.168°\text{C}$$

and the estimated observation error standard deviation is 1.481.

Observational errors appear in the observation equation of the state space models for the ARMA error structure and the two component AR(1) model. The observational error standard deviation may not be the standard deviation of the actual observational errors. They may also be looked at as an extra parameter to help give a better fit to the actual error spectrum and serial correlation. For example, an ARMA(2,1) with observational error is an ARMA(2,2) process without observational error (Box and Jenkins, 1976). Any actual observational error that exists has been absorbed into the ARMA parameters. Two models are equivalent if they have the same spectral density and covariance function. The spectral density of an ARMA(p,q) model with observational error is

$$s(f) = \sigma_\eta^2 \frac{|1 + \sum_{k=1}^{q} \theta_k \exp(2\pi i k f)|^2}{|1 - \sum_{k=1}^{p} \phi_k \exp(2\pi i k f)|^2} + \sigma_\xi^2$$

The spectral density of the sum of AR(1) processes with observational error is

$$s(f) = \sum_k \frac{\sigma_k^2}{|1 - \phi_k \exp(2\pi i f)|^2} + \sigma_\xi^2$$

The spectral density of the Redlands temperature data calculated from both these equations are very similar. The plot using the sum of AR(1) processes is shown in Figure 1.

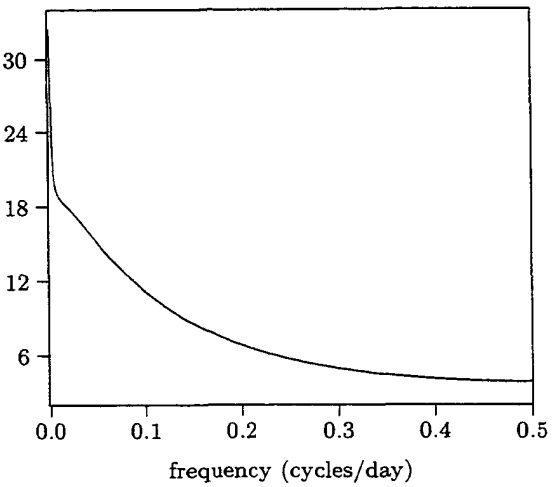


Figure 1: Estimated spectral density from the double AR(1) model with observational error on a log scale in $db = 10 \log_{10} s(f)$.

Prediction variances can be calculated for a prediction of any number of steps into the future using the state space representations. It is easy to see how predictions are made in the case of a simple AR(1) process without observational error. The current anomaly is multiplied by ϕ for a one step prediction, ϕ^2 for a two step prediction, etc. This is not as easy when the process is observed with observational error, or when the two component AR(1) processes is observed with observational error. The power of the state space formulation is that the state of the process is estimated based on all the past data. In the case of the two component AR(1) processes, the state is the current value of both of the processes. Predictions are then made

by predicting both of the AR(1) processes based on the best current estimates of their values. This is demonstrated in Figure 2. The two points at

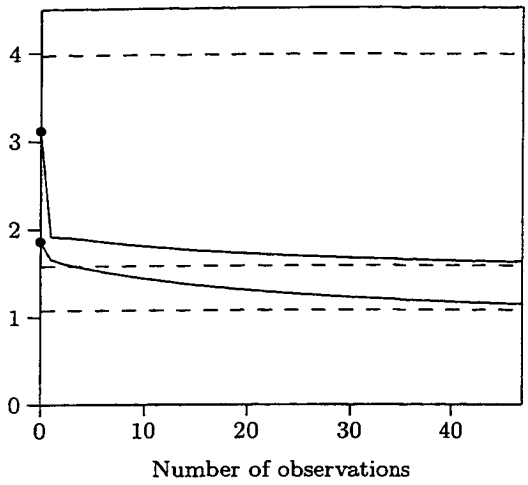


Figure 2: Standard deviations of the estimates of the two component AR(1) processe as a function of the number of days of available data. The top dashed line is the standard deviation of the temperature anomalies. The points at 0 denote the standard deviations of the two AR(1) processes. The lower dashed lines are the limits of the curves.

zero are the standard deviations of the two AR(1) processes, the upper point being the process with short term predictability, and the lower point being the long term process. These points are calculated as

$$\frac{\sigma_k}{\sqrt{1-\phi_k^2}}.$$

The upper dashed line is the standard deviation of the sum of the two AR(1) processes plus observational error, which is the square root of the variance,

$$\frac{\sigma_1^2}{1-\phi_1^2} + \frac{\sigma_2^2}{1-\phi_2^2} + \sigma_\xi^2.$$

When one observation is available, estimates of the level of the sum of the two AR(1) processes is obtained, and the standard deviations of the estimates of the two processes drops to the first point on each curve. As more observations are collected, the estimates of the states have lower standard deviations, and, in the limit, approach the dashed lines.

Predictions are made starting with any number of past observations to obtain the best estimate of the current elements of the state vector, and these are projected into the future. The prediction error standard deviation calculated from the two component AR(1) model is shown in Figure 3.

5 DISCUSSION

It is clear that there is some long range predictability in the temperature data analyzed. Since there is no significant year to year variability, it looks as if there is some long range persistence within years.

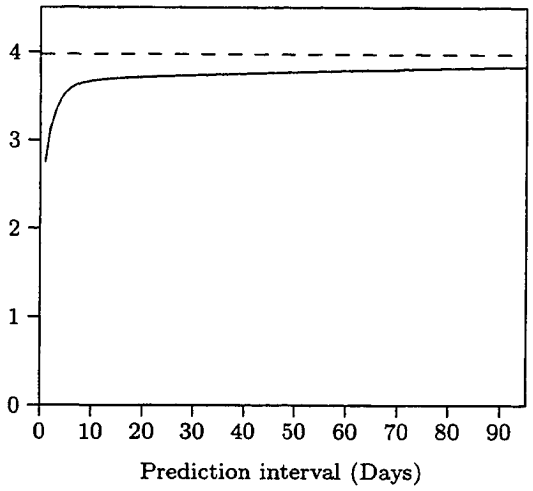


Figure 3: Estimated prediction error standard deviation from the two component AR(1) model with observational error. The dashed line is the standard deviation of the temperature anomalies.

The high peak in the spectrum near zero frequency indicates this, as do the prediction standard deviation curves. This could be caused by differences in the conditions around where the temperature is recorded from year to year. Such things as sea surface temperature, snow cover, soil moisture could possibly be responsible. If these variables could be identified and included in the regression equation, it is possible that the high peak near zero frequency in the residual spectrum would go away, and these variables could be part of the prediction equation.

REFERENCES

Akaike, H. (1974) A new look at the statistical model identification. *IEEE Trans. on Automatic Control*, **AC-19**, 716–23.

Box, G.E.P. and Jenkins, G.M. (1976) *Time Series Analysis, forecasting and control*, Revised Edition, Holden-Day, San Francisco.

Dennis, J. E. and Schnabel, R. B. (1983) *Numerical Methods for Unconstrained Optimization and Nonlinear Equations*, Englewood Cliffs, New Jersey: Prentice-Hall.

Jones, R. H. (1964) Spectral analysis and linear prediction of meteorological time series. *Journal of Applied Meteorology*, **3**, 45–52.

Jones, R. H. (1980) Maximum likelihood fitting of ARMA models to time series with missing observations. *Technometrics*, **22**, 389–395.

Jones, R. H. (1993) *Longitudinal Data Analysis with Serial Correlation: A State-space Approach*, Chapman and Hall, New York and London.

Mitchell, J. M. (1966) Stochastic models of air-sea interaction and climatic fluctuations. *Proceedings of the Symposium on Arctic Heat Budget and Atmospheric Circulation*, Rand Corporation.

Multivariate Tests for Comparison of Temporal Variability in Observed and Simulated Climates

Jules J. Beersma and T. Adri Buishand

Royal Netherlands Meteorological Institute (KNMI)
P.O. Box 201, 3730 AE De Bilt, The Netherlands

1 Introduction

Climate variability occurs on a range of different time scales varying from hours, days, years to millennia and beyond. For impact assessment of anthropogenic climate change we are primarily interested in changes in the present mean state and in fluctuations about this mean. The frequency of extreme events is e.g. very sensitive to changes in the variability. Validation of the variability within general circulation models (GCMs), which are the 'state of the art' tools for predicting anthropogenic climate change, is despite its importance somewhat neglected.

This paper discusses (jackknife) tests for variances. The method bears strong resemblance with the use of the jackknife in Buishand and Beersma (1993) for a test on the autocorrelation coefficients. Tests are presented for both daily variability (within month variance) and interannual variability (between month variance).

2 A test for daily variability

Daily values of an atmospheric variable are generally correlated and their distribution differes from the normal distribution. The traditional F-test cannot be used in that situation. In this section Welch's (1938) t-solution to the Behrens-Fisher problem is presented for testing for differences in the within month variances. For other variance components similar tests can be derived using the jackknife. A multivariate extension provides a very powerful test in situations that the differences in daily variability have the same sign for the different seasons or across a region.

Let $x_{i,j}$ denote the value of an atmospheric variable on day i ($i = 1, \ldots, n$) of a certain calendar month in year j ($j = 1, \ldots, J$). The within month variances $s^2_{\mathrm{w},j}$ are defined by:

$$s^2_{\mathrm{w},j} = \frac{1}{n}\sum_{i=1}^{n}(x_{i,j} - \overline{x}_{\cdot j})^2 \qquad (1)$$

with $\overline{x}_{\cdot j} = \sum_{i=1}^{n} x_{i,j}/n$ the monthly average in year j. The $s^2_{\mathrm{w},j}$'s represent the variance of the daily values within the calendar month under consideration in year j.

Since the distribution of $\hat{\theta}_{\mathrm{w},j} = \ln(s^2_{\mathrm{w},j})$ is closer to normality than that of $s^2_{\mathrm{w},j}$, Welch's t-solution works better when the test is based on $\overline{\theta}_{\mathrm{w}} = \sum_{j=1}^{J}\hat{\theta}_{\mathrm{w},j}/J$ instead of the average of the $s^2_{\mathrm{w},j}$'s. An estimate of the variance of $\overline{\theta}_{\mathrm{w}}$ is given by:

$$\hat{\mathrm{V}}_{\mathrm{w}} = \frac{1}{J(J-1)}\sum_{j=1}^{J}\left(\hat{\theta}_{\mathrm{w},j} - \overline{\theta}_{\mathrm{w}}\right)^2 . \qquad (2)$$

A suitable statistic to test for equality of the daily variances of two mutually independent climate time series is:

$$T_{\mathrm{w}} = \frac{\overline{\theta}_{\mathrm{w}}(\mathrm{II}) - \overline{\theta}_{\mathrm{w}}(\mathrm{I})}{\left[\hat{\mathrm{V}}_{\mathrm{w}}(\mathrm{I}) + \hat{\mathrm{V}}_{\mathrm{w}}(\mathrm{II})\right]^{1/2}} , \qquad (3)$$

with $\overline{\theta}_{\mathrm{w}}(\mathrm{I})$ and $\overline{\theta}_{\mathrm{w}}(\mathrm{II})$ the averages of the $\hat{\theta}_{\mathrm{w},j}$'s for climates I and II, respectively, and $\hat{\mathrm{V}}_{\mathrm{w}}(\mathrm{I})$ and $\hat{\mathrm{V}}_{\mathrm{w}}(\mathrm{II})$ the estimates of the variances of $\overline{\theta}_{\mathrm{w}}(\mathrm{I})$ and $\overline{\theta}_{\mathrm{w}}(\mathrm{II})$. The critical values can be derived from the t-distribution with an effective number of degrees of freedom given by:

$$d^* = \frac{\left[\hat{\mathrm{V}}_{\mathrm{w}}(\mathrm{I}) + \hat{\mathrm{V}}_{\mathrm{w}}(\mathrm{II})\right]^2}{\hat{\mathrm{V}}^2_{\mathrm{w}}(\mathrm{I})/(J-1) + \hat{\mathrm{V}}^2_{\mathrm{w}}(\mathrm{II})/(K-1)} \qquad (4)$$

with J and K the number of years in climates I and II respectively. The value of d^* cannot be larger than $J+K-2$. The test is similar to that of Welch (1938) for comparing means of two normal populations with possible unequal variances. This famous Behrens-Fisher problem comes up in the tests discussed in this paper when the two climates have different kurtosis[1] and when the two climates have different spatial correlations in the multivariate extension of Section 4.

[1] The kurtosis γ_2 refers to a standardized fourth-order moment. For the normal distribution $\gamma_2 = 0$.

3 Jackknife tests

The variance estimate in (2) requires a value of the within month variance for each individual month. For other variance components such an estimate can not be given. The jackknife provides a distribution-free estimate of the variance of a statistic $\hat{\theta}$ by recomputing the statistic a large number of times after successive deletion of one observation or a group of observations from the entire dataset. The method requires that the data in different groups are independent. To accomplish this requirement a complete month is deleted each time.

For the description of jackknife tests it is convenient to introduce the pseudo-values θ_j^*:

$$\theta_j^* = \hat{\theta} + (J-1)(\hat{\theta} - \hat{\theta}_{-j}) \,, \tag{5}$$

with $\hat{\theta}_{-j}$ the value of the statistic after omitting the data for year j in the pooled sample of the calendar month under consideration. The key idea behind a jackknife test is that these pseudo-values may often be treated as independent normal variables. This holds in particular when a group of observations is deleted each time. The test can then be based on the mean of the pseudo-values:

$$\hat{\theta}_{\text{jack}} = \frac{1}{J}\sum_{j=1}^{J} \theta_j^* \tag{6}$$

and its variance. The latter and the variance of $\hat{\theta}$ can both be estimated by the jackknife variance:

$$\hat{\text{V}}_{\text{jack}} = \frac{1}{J(J-1)}\sum_{j=1}^{J}\left(\theta_j^* - \hat{\theta}_{\text{jack}}\right)^2 \,. \tag{7}$$

The expression for the test statistic then reads:

$$T = \frac{\hat{\theta}_{\text{jack}}(\text{II}) - \hat{\theta}_{\text{jack}}(\text{I})}{\left[\hat{\text{V}}_{\text{jack}}(\text{I}) + \hat{\text{V}}_{\text{jack}}(\text{II})\right]^{1/2}} \,, \tag{8}$$

with $\hat{\theta}_{\text{jack}}(\text{I})$ and $\hat{\theta}_{\text{jack}}(\text{II})$ the averages of the pseudo-values for climates I and II, and $\hat{\text{V}}_{\text{jack}}(\text{I})$ and $\hat{\text{V}}_{\text{jack}}(\text{II})$ the jackknife variances for these climates. In many cases the null distribution of T can be approximated by the t-distribution with d^* degrees of freedom, where d^* is obtained by replacing $\hat{\text{V}}_{\text{w}}(\text{I})$ and $\hat{\text{V}}_{\text{w}}(\text{II})$ in (4) by $\hat{\text{V}}_{\text{jack}}(\text{I})$ and $\hat{\text{V}}_{\text{jack}}(\text{II})$.

The test in the previous section is obtained when $\hat{\theta} = \sum_{j=1}^{J} \ln(s_{\text{w},j}^2)/J$. The pseudo-values θ_j^* are then equal to $\hat{\theta}_{\text{w},j}$. An alternative test on the within month variances is possible by taking: $\hat{\theta} = \ln(\sum_{j=1}^{J} s_{\text{w},j}^2/J)$. A slight modification of the jackknife statistic for testing for equality of between month variances is considered in Section 5.

4 Multivariate extensions

The jackknife tests in Section 3 refer to data in a specific calendar month at a given location. Such tests can be applied simultaneously to a number of successive calendar months and to various points on a grid. An important problem is then the determination of the global significance of these tests. When the tests are not independent, as for different climate time series on a GCM grid, computationally intensive permutation techniques are required to determine the global significance.

The use of a single multivariate test statistic avoids the above multiplicity problem. The data for the individual (calendar) months can be combined into a single seasonal or annual test statistic as follows. First, the pseudo-values θ_1^*, θ_2^*, ... ,θ_J^* are calculated for each month separately. These pseudo-values are then averaged over the various months, giving $\overline{\theta_1^*}$, $\overline{\theta_2^*}$, ... ,$\overline{\theta_J^*}$. The jackknife statistic T is finally obtained by applying (6) and (7) to these average pseudo-values. Because a larger sample is considered than just an individual calendar month these combined tests are more powerful than those in Section 3.

The data at several grid points in a region can be combined by a similar averaging procedure. The result is a simple multivariate test which does not require permutation techniques. The test will be most powerful when the differences in climate I and climate II have the same sign across the whole region.

5 A corrected jackknife test for between month variances

Let $\overline{x}_{\cdot j}$ again denote the monthly mean of a certain calendar month in year j ($j = 1, \ldots, J$). The between month variance or interannual variance s_{b}^2 is defined as:

$$s_{\text{b}}^2 = \frac{1}{J}\sum_{j=1}^{J}(\overline{x}_{\cdot j} - \overline{x})^2 \tag{9}$$

where $\overline{x} = \sum_{j=1}^{J} \overline{x}_{\cdot j}/J$. The jackknife procedure in Section 3 can provide a statistic T_{b} for comparing the between month variances. Because only one value is now deleted each time the correlation between the pseudo-values θ_1^*, θ_2^*, ... , θ_J^* may not be neglected in samples of about 10 years, which are often encountered in GCM simulations. Furthermore, the distribution of these pseudo-values can then deviate from the normal distribution. The t-approximation of the null distribution of the jackknife statistic T_{b} is therefore more uncertain than for the daily variances.

Averaging over successive months or grid points as explained in Section 4 provides pseudo-values that are almost normally distributed. Departures from the

assumed t-distribution are then mainly due to correlation between the pseudo-values. If the correlation coefficient ρ is known the test statistic can easily be corrected (Walsh, 1947) using an adjusted estimate of the variance of $\hat{\theta}_{\text{jack}}$:

$$\tilde{\text{V}}_{\text{jack}} = \frac{1+(J-1)\rho}{1-\rho}\hat{\text{V}}_{\text{jack}} \ , \qquad (10)$$

leading to the modified test statistic

$$\tilde{T}_{\text{b}} = \frac{\hat{\theta}_{\text{jack}}(\text{II}) - \hat{\theta}_{\text{jack}}(\text{I})}{\left[\tilde{\text{V}}_{\text{jack}}(\text{I}) + \tilde{\text{V}}_{\text{jack}}(\text{II})\right]^{1/2}} \ . \qquad (11)$$

From the Satterthwaite procedure in Welch (1938) it follows that the variance estimate $\tilde{\text{V}}_{\text{jack}}$ should also be used in (4) for the degrees of freedom.

The value of ρ depends on J and on the distribution of the monthly means. In particular, the kurtosis γ_2 is important. For monthly means γ_2 is generally close to zero. The correlation coefficient in (10) can therefore often be based on the value of ρ for the normal distribution. A Monte Carlo experiment shows that this value can be approximated as:

$$\tilde{\rho} = -J^{-1.7} \ . \qquad (12)$$

Wigley and Santer (1990) used a rather similar statistic than our jackknife statistic:

$$\text{SPRET1} = \overline{s^2_{\text{b}}}(\text{I})/\overline{s^2_{\text{b}}}(\text{II}) \qquad (13)$$

where $\overline{s^2_{\text{b}}}(\text{I})$ and $\overline{s^2_{\text{b}}}(\text{II})$ are the spatial averages of the between month variances for climate I and climate II, respectively, for a particular calendar month. There is, however, not a simple approximation to the distribution of SPRET1 under the null hypothesis. Wigley and Santer (1990) used a pooled permutation procedure to determine the statistical significance of the observed value of SPRET1.

6 Examples

The tests in the previous sections have been applied to time series of daily near surface temperature over Europe. Temperature variances of ECMWF analyses and two simulations of the coupled ECHAM/LSG model (Cubasch et al., 1992) are considered and compared for the area extending from 34° to 67°N and 14°W to 26°E. The ECMWF analyses refer to the period 1984–1993. For the ECHAM GCM daily temperatures were considered for the last 10 years (2075–2084) in the 100-year control run with constant 1985 CO_2 equivalents and in the scenario-A run with an average CO_2 concentration of 2.8 times that of 1985.

Table 1 summarizes some relevant sample statistics. The values in this table are averages of monthly estimates over a season or year and over the grid. The table shows that in the control run the average temperature is underestimated in winter (DJF) and overestimated in summer (JJA). The control run of the ECHAM model overestimates the within month variance in all seasons and underestimates the between month variance in most seasons. For the within month variance the differences are significant at the 5% level in all seasons, but for the between month variance this is only the case in the summer season.

Table 1: Mean (°C), variances (°C^2) and kurtosis estimates of near surface temperature over Europe. E refers to the ECMWF analyses, C to the ECHAM control run and A to the ECHAM scenario-A run.

Season	Data	$\bar{x}$	Variance s^2_{w}	Variance s^2_{b}	$\hat{\gamma}_2$ $\{x_{i,j}\}$	$\hat{\gamma}_2$ $\{\bar{x}_{\cdot,j}\}$
DJF	E	4.2	6.65	4.10	0.15	-0.42
	C	2.1	14.06*	4.24	0.48	-0.67
	A	5.7	8.09*	3.20*	0.36	-0.53
MAM	E	8.1	5.14	2.29	0.51	-0.60
	C	7.8	7.79*	1.67	0.14	-0.55
	A	10.5	5.35*	1.22	0.05	-0.36
JJA	E	16.3	3.82	1.68	0.66	-0.57
	C	17.8	4.30*	1.18*	0.14	-0.61
	A	20.5	3.87	1.52	0.08	-0.55
SON	E	11.3	5.56	2.33	0.34	-0.59
	C	11.3	6.63*	1.63	0.17	-0.67
	A	14.0	5.72	1.30	0.29	-0.51
Year	E	10.0	5.29	2.60	0.41	-0.54
	C	9.7	8.19*	2.18*	0.23	-0.62
	A	12.7	5.75*	1.81	0.20	-0.49

* differences significant at the 5% level (two-sided test, C versus E for the control run, A versus C for the scenario-A run).

In the scenario-A run the average temperature is about 3°C higher for all seasons and both the daily and interannual variances are generally lower than in the control run. The reduction in the variances as a result of enhanced greenhouse gas concentrations is statistically significant for both components in winter and for the within month variance in spring, but there is no statistical evidence of a change in the variances in the summer and autumn seasons. For the daily variance the reductions in the first two seasons are strong enough to yield a significant reduction over the year.

As expected the monthly mean temperatures $\bar{x}_{\cdot,j}$ have the smallest kurtosis. For independent normally distributed data $E(\hat{\gamma}_2) = -0.55$ for $J = 10$ (Cramér, 1946). The kurtosis estimates of the monthly means in Table 1 are all close to this theoretical value. This justifies the use of (12) to correct for correlation between the pseudo-values in the jackknife test for equal-

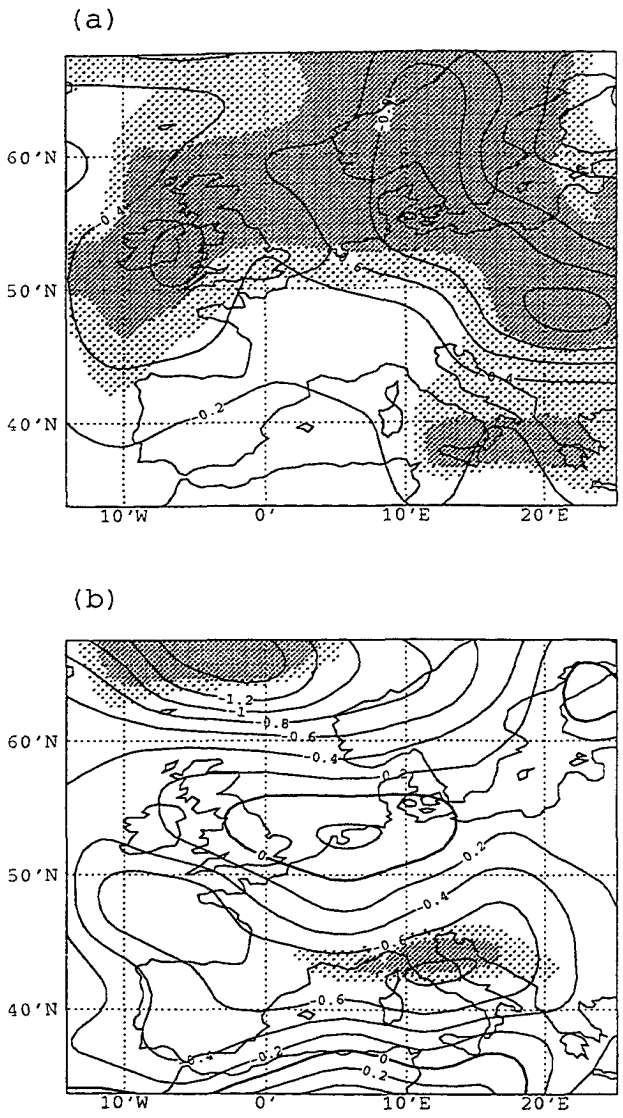


Figure 1: Logarithm of variance ratios (ECHAM scenario-A divided by control run) for winter (DJF) near surface temperature; (a) within month variance and (b) between month variance. Areas with significant differences at the 5% (1%) level are (heavily) shaded.

ity of between month variances.

The magnitude of the differences varies over the study area. Figure 1 presents maps of the logarithm of the local variance ratios for the winter season. Significant differences in the local variances based on jackknifing of single grid point data are shaded.

7 Conclusions

Tests for equality of variances based on the jackknife have a much wider applicability than the traditional F-test. In most cases the null distribution of the jackknife statistic can be approximated by Student's t-distribution. For the between month variances it is necessary, however, to correct for the correlation between the pseudo-values in the jackknife procedure. A multivariate test statistic can be obtained by averaging the pseudo-values over successive months and/or grid points in a region.

The examples indicate that the multivariate jackknife tests are able to detect differences of about 15% between the seasonal averages of the within month variances when 10-year samples over Europe are combined (two-sided test, significance level 5%). For the between month variances the differences should generally be larger than 30% to obtain a statistically significant result under similar conditions. Especially for the latter averaging over months or grid points is desirable to gain power.

Acknowledgments. The GCM data were kindly provided by the Max-Planck-Institut für Meteorologie in Hamburg, Germany.

References

[1] Buishand, T.A. and J.J. Beersma, 1993: Jackknife tests for differences in autocorrelation between climate time series. *J. Climate*, **6**, 2490–2495.

[2] Cramér, H., 1946: *Mathematical Methods of Statistics.* Princeton University Press, Princeton, New Jersey, 575 pp.

[3] Cubasch, U., K. Hasselmann, H. Höck, E. Maier-Reimer, U. Mikolajewicz, B.D. Santer and R. Sausen, 1992: Time-dependent greenhouse warming computations with a coupled ocean-atmosphere model. *Clim. Dyn.* **8**, 55–69.

[4] Walsh, J.E., 1947: Concerning the effect of intraclass correlation on certain significance tests. *Ann. Math. Statist.*, **18**, 88–96.

[5] Welch, B.L., 1938: The significance of the difference between two means when the population variances are unequal. *Biometrika*, **29**, 350–361.

[6] Wigley, T.M.L. and B.D. Santer, 1990: Statistical comparison of spatial fields in model validation, perturbation, and predictability experiments. *J. Geophys. Res.*, **95**, 851–865.

ENTROPY ESTIMATION OF JOINT DISTRIBUTIONS

Niels C. Lind

University of Victoria, BC and University of Waterloo, ON, Canada

ABSTRACT

Design for high-uncertainty high-consequence climatic hazards makes special demands on statistical methods. Information-theoretical methods to estimate univariate random variables, useful when data are scarce, are surveyed. These methods are extended to estimate jointly distributed random variables. No single method can be best for all applications, but information-theoretical methods offer both theoretical and practical advantages in the context of high-uncertainty high-consequence hazards. An example illustrates the methods.

1 INTRODUCTION

Large scale engineering projects such as dams or dikes present challenging demands on statistics. The catastrophic potential calls for high reliability under extremes of flood, wind and earthquake. Unavoidably, high reliability is connected with high uncertainty because information on extremes is deficient, requiring extrapolation beyond the range of experience. In Switzerland, for example, dams must be designed for a flood peak 50% higher than one having a 1000-year return period (Salmon and Hartford 1995) while data, at best, cover only a few centuries.

The statistical methods available were developed mostly for purposes other than the estimation of extreme events from scarce data. Hypotheses about distribution type, if at all tested, are often accepted in engineering merely because there are no grounds for rejection. No two projects are alike, requiring situation-specific analysis that goes beyond mathematical manipulation (Klemes 1993).

Engineering science is empirical; engineers must learn from the profession's collective experience. This is difficult unless the methods of analysis are standardized, applied to a sufficient number of instances, and kept constant for a sufficient length of time to give meaningful feedback. Practical requirements for engineering administration in big organizations over large areas, similarly, also fosters standardization of methods of analysis. This need can go to almost ridiculous extremes, such as standardizing all floods to follow a Pearson Type III distribution. Engineers must never lose sight of the potential for failure. After a failure, the legal system will assign probable cause(s), which are ascertained by peer consensus over whether "accepted" analysis methods were followed. Beside nurturing the tendency towards standardization of methods, this circumstance has created a need for methods that have firm rationales and are logically defensible.

Some information-theoretical methods to assign distributions to random variables of unknown mathematical type have emerged recently (Lind and Solana 1988, Kapur and Kesavan 1992, Lind 1994). These methods offer distinct advantages when there is high uncertainty but high reliability and high defendability are required. Section 2 gives an overview of the information-theoretical methods of univariate estimation and their rationales. Section 3 suggests extensions to joint distributions. Application is illustrated in Section 4.

2 INFORMATION-BASED ESTIMATION

Jaynes (1957) showed that the important probability distributions in statistical mechanics can be derived by maximizing Shannon's information-theoretical entropy - $\Sigma p \log p$ subject to appropriate moment constraints. The distribution type is completely defined by the choice of which moments to constrain. This is why application of Jaynes' principle with moment constraints is so elegant in statistical mechanics, but also why it is unsuited to estimating climatic variables since their distribution type is never known.

The Sample Rule

The *sample rule* is the proposition that if a number is chosen at random from any set of m numbers then the probability that it is the i-th element when the set is ordered equals 1/m. The sample rule is a consequence of randomness in sampling. When applied to rare extremes of natural quantities with m = n+1, the sample rule implies that the probability of a future observation being greater than any of n values observed so far equals 1/(n+1). The sample rule is generally violated by conventionally fitted distributions, although independent random sampling is assumed in the estimation. This lack of self-consistency may well be unimportant, generally speaking, but it is important when, as in engineering climatiology, it is the extremes that matter.

Quantile-Based Estimation

If the moment constraints for a continuous univariate random quantity are replaced by quantile constraints based on the sample rule, then the maximum entropy estimate turns out entirely different. In this quantile-based formulation the random sample of size n subdivides the range of the random variable X into m=n+1 intervals I_i each representing a compound event of probability 1/m. A distribution with parameter vector θ, $F(x,\theta)$, assigns probability $p_i(\theta)$ to interval i that is generally different from 1/m. Various methods to estimate θ have been proposed, based on the idea that all p_i should be made as nearly equal as possible to 1/m.

The Principle of Minimum Information

Thus, Cheng and Amin (1983) proposed the Maximum Products of Spacings method (MPS), equivalent to the information-theoretical method of minimizing the Shannon *information* $-\Sigma \log p$ (Lind 1994). The *principle of minimum information* states that the distribution should be selected from a set of candidates $\{F(x,\theta)\}$ such that the Shannon information conveyed about the events I_i is minimized.

This minimum information estimate has several useful properties. The principle of minimum information yields a unique solution F(x) when other methods fail. The algorithm is the same for all types of distributions. The estimation process introduces a minimum of information, thus approaching objectivity. The solution is invariant under a monotonic transformation of the variable. The method involves optimization of θ, but is computationally simple (Lind 1994).

Maximum Entropy Estimation
An alternative is the principle of maximum entropy: Select the distribution from the set of candidates $\{F(x,\theta)\}$ such that the Shannon *entropy* $H(\theta) = -\Sigma p \log p$ is maximized. Formally, the Shannon entropy is the expected value of the information. When the distribution is well fitted, all the p_i are nearly equal, so that there is little difference in practice between the distributions of maximum entropy and minimum information.

Relative Entropy Methods
A difficulty with moment-based methods of estimation is the lack of invariance under a monotonic transformation of the variable. For example, it makes a difference whether the engineer estimates the maximum wind pressure from a distribution of pressures or from a distribution of velocities derived from the same observations.

Let I(.) denote the integral operator, and let p and q denote probability density functions, all on the same domain.The Kullback-Leibler *cross-entropy* $K(p,q) = I[q \log (q/p)]$ is a semi-metric and is invariant under monotonic transformations of the variable. K(p,q) may be considered as a directed distance from p to q in the space of distributions defined on the domain of X.

K(p,q) is also called a *relative entropy*, the entropy of q relative to p. Distribution p serves as *reference distribution;* q is called the *posterior*. If p and q are piecewise proportional in all intervals I_i, then K(p,q) is minimum and equals $\Sigma q_i \log (q_i/p_i)$ (Lind and Solana 1988).

Various applications of relative entropy to estimate continuous distributions are possible, depending on the choice of reference distribution. One may (A) select the type of the reference distribution or a set of candidate distribution types, or (B) choose the distribution that is necessary to minimize the relative entropy of a distribution of given type. Alternatively, one may (C) select the reference distribution *a priori.*

(A) Reference Distribution Type(s) Given
The reference distribution p may be any distribution on the domain of X. Generally, such a distribution does not satisfy the sample rule. However, there always exists uniquely a distribution q that does satisfy the sample rule and is closest to p in the sense of minimizing K(p,q). This *posterior distribution* q may be considered a correction of p. This distribution is of the form c(x)p(x), where $c(x) = (mp_i)^{-1}$ is piecewise constant over the domain of x, generally discontinuous at the data points (Lind and Solana 1987). When q thus minimizes K(p,q), then the minimum value equals $-\Sigma (1/m)\log (mp_i)$ and is a measure of the goodness of the fit. This minimum value is an increasing linear function of the information of p. So, if p is the minimum information distribution of its type and if q(x) equals $p(x)/(mp_i)$, then K(p,q) is minimum.

It is possible to consider a *candidate set* C composed of one or more classes of distributions of different type (normal, lognormal, etc.) and compare globally the best fitting distribution in each class. The *principle of least information* says that p and q should be selected jointly to minimize the relative entropy K(p,q) (Lind 1994).

(B) Posterior Distribution Type Given
Reversing the role of p and q gives an alternative method of estimation. Then q is to belong to a suitable candidate set C and is chosen by maximizing the entropy $-\Sigma q_i \log q_i$, while p(x), only piecewise continuous, is chosen to satisfy the sample rule in the form q(x)/c(x), where $c(x) = \text{const.} = q_i m$.

(C) Approximations
Some simple approximate solutions are readily suggested. The reference distribution p may be any distribution on the domain of X and the posterior q can be considered as a correction of p to satisfy the sample rule. Thus, p may be selected by the method of moments or any other convenient method.

A different class of estimation procedures is obtained by relaxing some of the n sample rule constraints furnished by the data. If the object of interest is extreme high values of the variable, then low values observed are of little interest - indeed, to the extent they contribute to the estimate of high extremes they are detrimental to the estimate (Klemes 1994). The estimated distribution need only fit well in the high end. A reasonable selection for a one-parameter distribution is to fit only the highest observed value, x_n. For a two-parameter distribution it would be reasonable to fit also to the median if n is small or the upper quartile if n is large.

The two-parameter case is common. Denote the two selected points by (x'_i,z_i) and (x'_j,z_j), where $z=N^{-1}(p)$ is the inverse of the standardized distribution chosen as model for X. The resulting distribution for X' is

$$F_{X'}(x')=N[z_j+(z_j-z_i)(x-x_i)/(x_j-x_i)]. \quad (1)$$

If a k-parameter distribution type is chosen as the candidate set and k quantile constraints are selected to be fitted, then K(p,q) vanishes and the posterior distribution q coincides with the reference distribution p. This yields by simple calculations an approximation for F that at once is of the desired type, satisfies the most important quantile constraints, minimizes the information and cross-entropy, and maximizes the entropy.

A probability plot of the data sometimes shows that extreme observations do not fit the trend. Then it is tempting to try to reject them as "outliers." But since the distribution type is unknown for natural phenomena variables, this cannot be done on statistical grounds. The "outlier" cannot be rejected rationally if a plausible source for the supposed gross error cannot be identified. Instead, one may consider resampling: deleting each observation with probability 1/n and recombining the resulting n samples of size n-1.

3 JOINT DISTRIBUTIONS
Information-theoretical methods cannot easily be extended to the estimation of jointly distributed random variables (X,Y) because the information I, entropy H and relative entropy K are not generally invariant under a rotation of the coordinate system (X',Y')=T(X,Y). If and only if two variables are independent, then I, H, and K for the pair are the sum of those of the individual variables. Only then is it sensible to assign that sum to the joint distribution as well.

The joint distribution of two random variables is incompletely determined by its marginals. This is a major difficulty in the estimation of jointly distributed random variables, because the distribution type generally depends on the correlation, but must be determined before the parameters can be estimated. The distribution of any linear combination of the two variables is generally complex, must be determined by integration, and is therefore mathematically intractable in applications.

Gaussian distributions are the only exception. If the two components are Gaussian, there is no assurance that the joint distribution is also Gaussian; still, if the joint distribution is Gaussian, all marginals and any linear transform thereof are also Gaussian. For distributions of the common hat-shaped type, it therefore seems a good idea to begin estimation by making a

transformation of the variables that renders them Gaussian. In practice it is easy to transform the observed components X and Y of such variables into standardized Gaussian variables X" = $T_X X$ and Y" = $T_Y Y$ by means of normal probability plots. If after such transformations T the sum and the difference of the data pairs also plot nearly on straight lines on a normal probability graph, then it may be reasonable to model the transformed variables as jointly Gaussian. This greatly facilitates estimation. The transform may be called the *underlying* Gaussian distribution.

The sums and differences of the normalized observed variables are expected to be uncorrelated, independent Gaussian random variables. They may each be estimated by any method described in Section 2. Inverse transformation then gives the distribution estimates for X and Y.

In summary, the joint distribution of a pair of variables X and Y can be modelled by: (1) transforming them into standardized normal variates, (2) modelling their sum and difference and (3) applying the inverse transformation. Steps (1) and (2) can both be done by conventional methods, minimum information, maximum entropy, or quantile approximation. Minimizing the relative entropy yields two distributions, one of which is non-gaussian (discontinuous). This distribution cannot be processed in step (3) in any simple way. The procedures are illustrated in the following example.

4 EXAMPLE

Table 1 shows 49 joint observations of two random variables X and Y. Lognormal probability plots, Figure 1, suggest that X and Y both are approximately lognormally distributed. Figure 2 is a log-log plot indicating that X and Y are correlated. By the logarithmic transformations x'=ln x and y'=ln y the two variables are mapped into variables X' and Y' that are taken as normally distributed. Table 2 gives the various estimates of these distributions and the normalizing mappings $x"=(x'-m_{x'})/s_{x'}$ and $y"=(y'-m_{y'})/s_{y'}$.

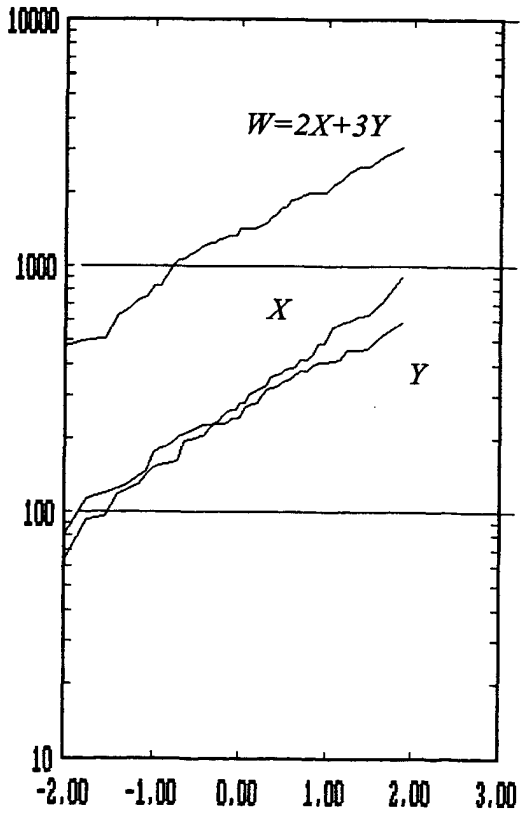


Figure 1. Lognormal probability plots of the data X and Y in Table 1 and the linear combination W=2X+3Y.

The transforms u=rx"+ry" and v=rx"-ry", where $r=2^{1/2}$, give the uncorrelated Gaussian variables U and V. They are estimated by the same procedures. The results are listed in Table 2. By the inverse transformations (u,v) > (x",y") > (x',y') > (x,y) the joint distribution follows.

Table 1. 49 Joint Observations of X and Y

x	119	75	716	390	258	140	235
y	279	118	455	589	272	158	239
x	261	228	597	315	224	260	583
y	129	395	230	197	204	241	408
x	304	248	380	130	213	354	226
y	459	417	276	157	336	196	265
x	210	192	365	173	437	125	483
y	233	346	376	95	375	142	524
x	303	369	331	146	384	226	113
y	229	465	162	59	409	125	93
x	181	626	562	278	906	415	320
y	155	244	205	299	414	218	230
x	279	185	630	416	202	486	218
y	152	319	324	199	343	318	361

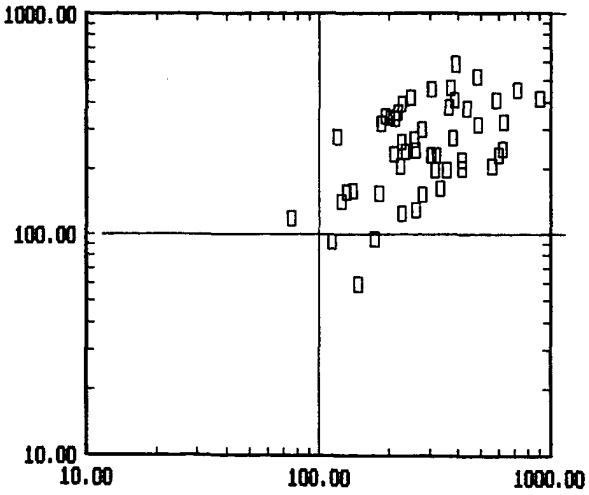


Figure 2. Log-log plot of the data Y versus X in Table 1.

Table 2. Estimates of X', Y,' U and V

Method	$m_{X'}$	$s_{X'}$	$m_{Y'}$	$s_{Y'}$
Moments	5.64129	0.53213	5.50486	0.49555
MinInfo	5.64515	0.57221	5.50334	0.53297
MaxEnt	5.63408	0.59407	5.53002	0.53070
Quantile	5.62762	0.57513	5.49717	0.42901

Method	m_U	s_U	m_V	s_V
Moments	0	1.24109	0	0.67800
Quantile	0	1.13133	0	0.75363*
				0.61540**

* used when v is positive
** used when v is negative

In applications, although sometimes the complete joint distribution is required for convolution with a capacity-type variable, the quantity of interest is typically a linear

combination W=aX+bY with fixed coefficients a and b. Then it makes sense to transform the observations first into observations of W and then use any method of estimation.

Consider the variable W=2X+3Y, and suppose that the 99th and 99.9th percentiles are required. Although the estimates may be made from U and V by convolution (which does not conserve the distribution type), a more convenient approach is to model W directly. As it turns out, the upper end of the distribution of W appears sensibly linear on a lognormal plot, so it may be processed in the samer fashion as X and Y. Resulting estimates are shown in Table 3.

Table 3. Estimated parameters and percentiles of W= 2X+3Y.

Method	Median	StdDev	99 %	99.9%
Moments	7.1999	0.4501	3818	5385
Quantiles	7.2598	0.3721	3380	4492

5 DISCUSSION

The example illustrates the kind of data that is typically available for climatic variables used in engineering. The information-theoretical methods yield results that are comparable with the method of moments. Median and standard deviations appear in close agreement within a few per cent but, not unexpectedly, there are significant differences in the quantiles that may govern design. Although the information-theoretical methods have some advantages in terms of rationale and simplicity of calculation, it remains to be seen if their performance as estimators is as good as the established methods. This question can be examined by simulated data drawn from known distributions.

Unlike the method of moments, the information-based methods presented in this paper can easily accommodate a mixture of joint and isolated observations.

6 CONCLUSION

Estimation of univariate distributions by information-theoretical methods can be extended to a pair of jointly distributed random variables. In statistical climatology this can be used in the estimation of spatial covariance and, for stationary processes, covariance in time. Their use for this purpose may be of practical interest, because the information-theoretical estimation mehods have many advantages, though these have not been demonstrated in this paper. They yield solutions when other methods fail. The solutions are unique for each method. The objective functions (Shannon's information, entropy, or the Kullback-Leibler relative entropy) have information-theoretical rationales; for each, in a certain sense, it can be said that arbitrary bias is minimized. The algorithms are universally applicable to all sets of candidate distributions. The solutions are invariant under monotonic transformations of the variables.

References

Jaynes, E. T., "Information Theory and Statistical Mechanics," *Physical Reviews*, 106, pp. 620-630, 1957.

Kapur, J. N. and Kesavan, H. K., 1992, *Entropy Optimization Principles with Applications*, Academic Press, Inc., San Diego, CA.

Klemes, V., 1994, "Statistics and Probability: Wrong Remedies for a Confused Hydrologic Modeller," Chapter 19 in *Statistics for the Environment*, V. Barnett and K. Turkman (eds.), pp. 345-366, John Wiley and Sons, Inc.

Lind, N. C., 1994, "Information theory and maximum product of spacings estimation," *Journal of the Royal Statistical Society, Series B*, Vol. 56, No.1.

N. C. Lind and V. Solana, 1988, "Estimation of Random Variables With Fractile Constraints," *IRR paper No. 11*, Institute for Risk Research, University of Waterloo, Waterloo, ON, Canada.

Salmon, G. and Hartford, D. N. D., 1995, "Risk Analysis for Dam Safety," *Seminar and Workshop on Risk-Based Dam Safety Evaluation*, B. C. Hydro, Burnaby, BC, March.

ACKNOWLEDGMENTS

Financial support of the Natural Sciences and Engineering Research Council is gratefully acknowledged. Thanks are due to Mr. John Leung for assistance with computer programming and calculations.

CORRESPONDING AUTHOR

Professor Niels C. Lind
504 - 640 Montreal Street
Victoria, BC, Canada V8V 1Z8
Tel (604) 382 2699 * Fax (604) 721 6051
e-mail: nlind@hamilton.uvic.ca

The asymptotic behaviour of the maximum of a random sample subject to trends in location and scale.

C S Withers
Applied Mathematics Group
The New Zealand Institute for Industrial Research and Development
P O Box 31-310, Lower Hutt, New Zealand

April 19, 1995

Abstract

We study the behaviour of the maximum of a series of independent observations subject to trends in both location and scale. The trend functions are arbitrary smooth functions and may be non-linear.

It turns out that **trend in scale dominates trend in location**, at least for an upper tail of power type or gamma type.

Implications for climate change will be discussed.

1 Introduction and summary

We give the asymptotic behaviour of the maximum from a random sample subject to trends in location and scale.

Suppose we observe real r.v.s,

$$Y_{jn} = \mu(j/n) + \sigma(j/n)e_j,\ 1 \le j \le n \quad (1.1)$$

where the scaled residuals $\{e_j\}$ are i.i.d. $F(x)$ and $\mu(t)$, $\sigma(t)$ are non-random functions on [0, 1] with finite derivatives at 0+ and 1−. Set

$$M_n = max_{j=1}^n Y_{jn},\ n_1 = \log n,\ n_2 = \log n_1. \quad (1.2)$$

In §2 we prove the following results.

THEOREM 1.1 *(Power type tail). Suppose that*

$$1 - F(x) = K\ x^{-\theta}\{1 + O(x^{-\beta})\}\ as\ x \to \infty$$

$$where\ K > 0,\ \theta > 0,\ \beta > 0. \quad (1.3)$$

Then as $n \to \infty$,

$$n^{-1/\theta}\ M_n = \{K \int_0^1 \sigma(t)^\theta\ dt\}^{1/\theta}\ Y_\theta + O_p(n^{-\delta}) \quad (1.4)$$

$$where\ Y_\theta \sim EV2(\theta) = \exp(-x^{-\theta})\ on\ (0,\infty), \quad (1.5)$$

and $\delta = \min(1, \theta^{-1},\ \beta\theta^{-1})$.

So dependency of Y_n on σ is $O_p(n^{1/\theta})$ while that of Y_n on μ is at most $O_p(n^{1/\theta-\delta})$.

THEOREM 1.2 *(Gamma type tail). Suppose that for some* $K > 0$, $\delta > 0$, $\beta > 0$ *and* θ *in R,*

$$1 - F(x) = Kx^{-\theta}\exp(-\delta x)\{1 + O(x^{-\beta})\} \quad (1.6)$$

as $x \to \infty$.

$$Set \qquad K_\delta = \log K + \theta \log \delta, \quad (1.7)$$

and $Y_0 \sim Gumbel\ (x) = \exp(-e^{-x})\ on\ (0,\infty)$

(a) If $\sigma(t) \equiv 1$, *then as* $n \to \infty$

$$M_n = \delta^{-1}(n_1 - \theta n_2 + K_\delta + \lambda + Y_0) + O_p(\theta n_2\ n_1^{-1}\ + n_1^{-\beta}) \quad (1.8)$$

$$where\ \lambda = \log \int_0^1 \exp\{\delta\mu(t)\}dt.$$

(b) Suppose $\sigma(t)$ *has a unique maximum at* t_0 *in [0, 1] with finite derivatives at* t_0.

If $0 < t_0 < 1$, $\sigma^{(1)}\ (t_0) = 0$ *and* $\sigma^{(2)}(t_0) < 0$, *then as* $n \to \infty$

$$M_n = \delta^{-1}\{n_1 - (\theta + 1/2)n_2 + K_\delta + \lambda_1(t_0) + Y_0\}\sigma(t_0) + O_p(n_2 n_1^{-1} + n_1^{-\beta}), \quad (1.9)$$

where

$$\lambda_1(t) = \delta\mu(t)\sigma(t)^{-1} + 2^{-1}\log\{2\pi\sigma(t)^{-3}|\sigma^{(2)}(t)|^{-1}\}.$$

If $t_0 = 0$ *or* 1 *and* $\sigma^{(1)}(t_0) \neq 0$, *then as* $n \to \infty$

$$M_n = \delta^{-1}\{n_1 - (\theta+1)n_2 + K_\delta + \lambda_2(t_0) + Y_0\}\sigma(t_0) + O_p(n_2 n_1^{-1} + n_1^{-\beta}), \quad (1.10)$$

where $\lambda_2(t) = \delta\mu(t)\sigma(t)^{-1} + \{\sigma(t)^2|\sigma^{(1)}(t)|^{-1}\}$.

So dependency of M_n on σ is $O_p(n_1)$, but that of Y_n on μ is only $O_p(1)$.

If $O(x^{-\beta})$ in (1.3), (1.6) is replaced by say a series in $x^{-\beta}$, then an expansion for the distribution of M_n may be obtained: see Withers (1993, 1994) for the case $\sigma(t) \equiv 1$.

§3 makes a comparison with related results.

2 Proofs

Proof of Theorem 1.1. Suppose $c_n \to \infty$ and $P_n = P(c_n^{-1} M_n \leq x) = \Pi_{j=1}^n P(Y_{jn} \leq c_n x)$. Then

$$-\log P_n = -\sum_{j=1}^n \log F(x_{jn}) \quad (2.1)$$

where $x_{jn} = \{c_n x - \mu(j/n)\}/\sigma(j/n)$.

$$\text{As } x \to \infty, \ -\log F(x) = \sum_{k=1}^\infty (1 - F(x))^k/k \quad (2.2)$$

$= Kx^{-\theta}\{1 + O(x^{-\beta})\} + O(x^{-2\theta})$.
So $-\log P_n = K\sum_{j=1}^n x_{jn}^{-\theta} + O(\epsilon_{n1})$.
where $\epsilon_{n1} = nc_n^{-\theta-\beta} + nc_n^{-2\theta}$.
Also $x_{jn}^{-\theta} = (c_n x)^{-\theta}\sigma(j/n)^\theta\{1 + O(c_n^{-1})\}$
so $-\log P_n = Kn(c_n x)^{-\theta}\{A_n + O(c_n^{-1})\} + O(\epsilon_{n1})$
where $A_n = n^{-1}\sum_{j=1}^n \sigma(j/n)^\theta = A + O(n^{-1})$
for $A = \int_0^1 \sigma(t)^\theta\, dt$ for smooth $\sigma(\cdot)$
by the Euler-McLaurin expansion.
Taking $nc_n^{-\theta} = 1$ this gives
$-\log P_n = K_\theta^\theta\, x^{-\theta} + O(\epsilon_{n2})$ for $K_\theta^\theta = KA^\theta$
and $\epsilon_{n2} = n^{-1} + c_n^{-1} + \epsilon_{n1} = O(n^{-\delta})$.
So $P(n^{-1/\theta} M_n \leq x) = \exp(-K_\theta^\theta\, x^{-\theta}) + O(n^{-\delta})$
$= P(K_\theta\, Y_\theta \leq x) + O(n^{-\delta})$
for Y_θ of (1.5). So M_n can be represented as

$$n^{-1/\theta}\, M_n = K_\theta\, Y_\theta + O_p(n^{-\delta}).\square$$

Proof of Theorem 1.2. Suppose $c_n \to \infty$ and $P_n = P(\delta M_n - c_n \leq x)$

$$= \Pi_{j=1}^n P(Y_{jn} \leq x_n) \text{ for } x_n = (c_n + x)/\delta.$$

Then (2.1) holds with

$$x_{jn} = \{x_n - \mu(j/n)\}g(j/n) \text{ for } g(t) = \sigma(t)^{-1}.$$

By (2.2) as $x \to \infty$,

$$-\log F(x) = Kx^{-\theta}\exp(-\delta x)\{1 + O(x^{-\beta})\},$$

so $-\log P_n = KB_n + O(\epsilon_n)$
where $\epsilon_n = nx_n^{-\theta-\beta}\, exp(g_0\delta x_n)$,

$$B_n = \sum_{j=1}^n x_{jn}^{-\theta}\exp(-\delta x_{jn})$$

$$= x_n^{-\theta}\sum_{j=1}^n \{1 + O(x_n^{-1})\}\sigma(j/n)^\theta$$

$$\exp\{-\delta x_n g(j/n) + b(j/n)\}$$

$$= x_n^{-\theta}\{1 + O(x_n^{-1})\}B_n(\delta x_n)$$

$b(t) = \delta\mu(t)\sigma(t)^{-1}, a(t) = \sigma(t)^\theta \exp b(t)$,

$$B_n(\lambda) = \sum_{j=1}^n d_\lambda\ (j/n),$$

and $d_\lambda(t) = a(t)\exp\{-\lambda g(t)\}$.
By the Euler-McLaurin expansion

$$B_n(\lambda) = \sum_{i=0}^\infty n^{1-i}\alpha_i(d_\lambda) \quad (2.3)$$

$$\text{where } \alpha_0(f) = \int_0^1 f(t)dt,\ \alpha_1(f) = \{f(1) - f(0)\}/2,$$

$$\alpha_2(f) = \{\dot{f}(1) - \dot{f}(0)\}/12,\ \alpha_3(f) = 0, \ldots$$

(a) Suppose $\sigma(t) \equiv 1$. Then $d_\lambda(t) = e^{-\lambda}\, a(t)$. So

$$-\log P_n = K\delta^\theta c_n^{-\theta}\{1 + O(c_n^{-1})\}e^{-\delta x_n} n\{\alpha_0(a) + O(n^{-1})\}.$$

Also $c_n^{-\theta}e^{-c_n}n \approx 1 \Longrightarrow \theta\log c_n + c_n \approx n_1$
so take $c_n = n_1 - \theta n_2$. Then $c_n^{-\theta}\, e^{-c_n} n = 1 + O(\nu_n)$
where $\nu_n = n_2\, n_1^{-1}$. So

$$-\log\, P_n = e^{-x+\lambda_0}\, + O(\nu_n + \epsilon_n)$$

for $\lambda_0 = \log\{K\delta^\theta\, \alpha_0(a)\}$.

$$\text{So } P_n = P(Y_0\ < x - \lambda_0) + O(\nu_n + \epsilon_n)$$

and M_n can be represented as
$\delta M_n = c_n + Y_0 + \lambda_0 + O_p(\nu_n + \epsilon_n)$.
Also $\epsilon_n = O(n_1^{-\beta})$.

(b) Suppose $g(t) = \sigma(t)^{-1}$ has a unique minimum at t_0 in $[0,1]$.

If $0 < t_0 < 1$, a saddlepoint expansion about t_0 (for example apply Withers (1994) with $M = 2$, $\lambda = 0$) gives

$$\alpha_0(d_\lambda) = e^{\gamma - \lambda g_0}\ \lambda^{-1/2}\{1 + O(\lambda^{-1})\}$$

where $g_i = g^{(i)}(t_0)$ and
$e^\gamma = a(t_0)(2\pi g_2^{-1})^{1/2}$. So

$$-\log P_n = O(n x_n^{\theta - 1/2}\ e^{-\delta x_n g_0}) = O(e^{-\psi_n})$$

where $\psi_n = (\theta + 1/2)\log c_n + c_n g_0 - n_1$.

Taking $c_n = g_0^{-1} n_1 - g_0^{-1}(\theta + 1/2)\log(g_0^{-1} n_1)$

gives $\psi_n = O(\nu_n)$ where $\nu_n = n_2 n_1^{-1}$.

Setting $\lambda = \delta x_n = c_n + x$,

$$-\log P_n = K\delta^\theta \lambda^{-\theta}\{1 + O(n_1^{-1})\} n I_n + O(\epsilon_n)$$

$$\begin{aligned} \text{where } I_n &= \alpha_0(d_\lambda) + n^{-1}\alpha_1(d_\lambda) + \ldots \\ &= e^{\gamma' - x g_0} + O(\nu_n + \epsilon_n) \end{aligned}$$

$$\text{and } \gamma' = \gamma + \log(K\delta^\theta). \tag{2.4}$$

$$\text{So } P_n = P(Y_0 < x g_0 - \gamma') + O(\nu_n + \epsilon_n), \tag{2.5}$$

and M_n can be represented as

$$\delta M_n = c_n + g_0^{-1}(\gamma' + Y_0) + O_p(\nu_n + \epsilon_n). \tag{2.6}$$

Also $g_2 = -\sigma(t_0)^{-2}\sigma^{(2)}(t_0)$ and
$\epsilon_n = O(n c_n^{-\theta-\beta} e^{-g_0 c_n}) = O(n_1^{-\beta})$
so (1.10) holds.

If $t_0 = 0$ or 1 then an expansion about t_0 (apply Withers (1994) with $M = 1$, $\lambda = 0$) gives

$$\alpha_0(d_\lambda) = g_1^{-1} a_0 e^{-\lambda g_0}\{1 + O(\lambda^{-1})\}$$

where $a_0 = a(t_0)$ and $\alpha_1(d_\lambda) = O(e^{-\lambda g_0 - \lambda\epsilon})$
where $\epsilon > 0$, so at $\lambda = \delta x_n = c_n + x$,

$$\begin{aligned} -\log P_n &= K x_n^{-\theta}\{1 + O(x_n^{-1})\} B_n(\lambda) + O(\epsilon_n) \\ &= K\delta^\theta\ c_n^{-\theta}\{1 + O(c_n^{-1})\} n e^{-\lambda g_0}\{\lambda^{-1}\ g_1^{-1}\ a_0 \\ &\qquad [1 + O(\lambda^{-1})] + O(n^{-1}\ e^{-\lambda\epsilon})\} + O(\epsilon_n) \\ &= K\delta^\theta\ \{1 + O(c_n^{-1})\} e^{-\psi_n}\{g_1^{-1}\ a_0 + \\ &\qquad O(\lambda^{-1} + \lambda n^{-1} e^{-\lambda\epsilon})\} + O(\epsilon_n) \text{ where} \end{aligned}$$

$$\psi_n = (\theta + 1)\log c_n + \lambda g_0 - n_1 = x g_0 + O(\nu_n)$$

for $\nu_n = n_2 n_1^{-1}$ taking

$$c_n = g_0^{-1}\ n_1 - g_0^{-1}(\theta + 1)\log(g_0^{-1} n_1).$$

So (2.4) – (2.6) hold with
$e^\gamma = g_1^{-1} a_0 = -\sigma_0^{\theta+2}\ \sigma_1^{-1}\ e^{b_0}$
where $\sigma_i = \sigma^{(i)}(t_0), b_0 = b(t_0)$. □

3 A comparison with other results

The only results at all comparable in the literature, are those of Ballerini and McCormick (1989).

They replace $\mu(j/n)$ by $\mu(j)$ and $\sigma(j/n)$ by $\sigma(j)$, and assume that $\sigma(j)$ has period p.

Their results imply

(i) if (1.3) holds, so $F(x/c_n)^n \to P(Y_\theta \le x)$ with $c_n = (Kn)^{-1/\theta}$, then $c_n M_n \xrightarrow{\mathcal{L}} b^{1/\theta}\ Y_\theta$ where $b = p^{-1}\sum_{j=1}^p \sigma(j)^\theta$, provided that

$$\max_{i=1}^n\ |\mu(i)| = o(n^{1/\theta}); \tag{3.1}$$

(ii) if (1.6) holds, so $F(x/\delta + m_n/\delta)^n \to$

$$P(Y_0 \le x) \text{ for } m_n = n_1 - \theta n_2 + K_\delta,$$

for K_δ of (1.7), then

$$M_n = \mu(1) + \sigma(1)\delta^{-1}(m_n - \log p + Y_0) + o_p(1)$$

provided that μ also has period p, σ has a unique maximum on $\{1, \ldots, p\}$, and either $\mu(i) \equiv 0$ or

$$\delta \max_{i=1}^n |\mu(i)| - m_n \to 0. \tag{3.2}$$

Condition (3.1) holds for example for $\mu(i) = a + ib$ with $b \ne 0 \iff \alpha\theta < 1$

Condition (3.2) will nearly always be false, but presumably can be weakened to .

$$\max_{i=1}^n |\mu(i)| = o(n_1).$$

References

Ballerini, R. and McCormick, William.P. (1989) Extreme value theory for processes with periodic variances. *Commun.Statist.-Stochastic Models*, 5, 45-61.

Withers, C.S. (1993) Expansions for the distribution of the maximum from Distributions with a Power Tail when a Trend is present. *Technical Report No. 414*, Department of Statistics, University of North Carolina, Chapel Hill, New York.

Withers, C.S. (1994) Expansions for the distribution of the maximum from distributions with an asymptotically gamma tail when a trend is present. Submitted.

CLIMATE INSTABILITY DETERMINATION DISCUSSION OF METHOD AND EXAMPLES

R. Sneyers

Royal Meteorological Institute, Brussels, Belgium

ABSTRACT

For characterizing their internal structure, randomness of time-series is verified by testing both mean and dispersion for independence of their elements against serial correlation and, sequentially, for identity of distribution against trend. The discussion concerns testing ranks instead of elements, bias of the asymptotic distribution of test statistics, power of the considered tests and optimal estimation of change-points separating random (i.i.d.) subseries. The relative importance to be given to significance levels is also examined.

Examples of global, regional and local temperature time-series are given.

1 INTRODUCTION

Climate instability determination is of paramount importance as well for practical as for theoretical purposes.

In fact, if its knowledge is the unavoidable base for the elaboration of reliable designs involving elements depending on climate variability, an objective approach of the problem of possible man-made climate changes is unthinkable without this knowledge. Long series of observation being the single available witness of the long term climate evolution, characterizing their internal statistical structure appears, thus, as the first problem to be considered.

In Sneyers (1992_1 and 1992_2), review and comments were made on solutions used for solving this problem and an objective method developed and illustrated with some examples. This paper answers the need for a complete theoretical justification of the procedure. Moreover this opportunity has been taken for illustrating more completely the methodology by examples, the results of which suggesting, at the same time, the diversity of the climate instability at least in the northern hemisphere.

2 TESTING RANDOMNESS

Randomness being defined by independence and identity of distribution of the elements of the series, its verification may be made with testing the randomness of the series against serial correlation and against trend.

For the choice between parametric tests, assuming the knowledge of a given distribution (generally the normal one), and distribution-free (non-parametric) tests, it should be noted that in case of rejection , with the first tests, ambiguity may rise due to the possibility that the underlying normality hypothesis may be responsible for this rejection. Thus, use of the second ones avoids this drawback.

Moreover, it is obvious that the power of a distribution-free test varies with the type of the actual underlying distribution and, when this distribution is the normal one, that this power is generally lower than the one of the most powerful corresponding parametric test. Therefore, choice is made of the distribution-free test having the highest power-efficiency relative to this most powerful corresponding parametric one.

Finally, taking account of the fact that the set of order statistics $t = (x_{(1)}, x_{(2)}, \dots, x_{(n)},)$ form a sufficient statistic (Kendall and Stuart, 1967, Vol. 2, p. 472), advantage may be taken of replacing in the series the order statistic $x_{(i)}$ by its rank r_i, noting that if F(x) is the underlying distribution function, under the hypothesis of randomness, we have (Sneyers, 1990, p. 19)

$$(1) \qquad E[F(x_{i})] = r_i/(n+1).$$

In particular, in case of an outlier, this procedure reduces the resulting bias in the computed test statistic.

3 TEST OF INDEPENDENCE

By definition, the joint distribution function F(x, y) of two random variables x and y gives the probability for having for any couple of values x_0, y_0 simultaneously $x<x_0$ and $y<y_0$, that is

$$(2) \qquad F(x_0, y_0) = Pr(x<x_0, y<y_0).$$

Moreover, if $F(y|x)$ is the conditional distribution function of y given x, (2) becomes

$$(3) \qquad F(x, y) = F(x)F(y|x)$$

Finally, if y is independent of x, $F(y|x) = F(y)$ and we have

$$(4) \qquad F(x, y) = F(x)F(y).$$

It follows that, given an independent sample (x_i, y_i) of n simultaneous observations of x and y, and if r(x) and r(y) are respectively the ranks of x and y in such a sample, with (1) and (4), we have:

$$(5) \qquad E[F(x_i, y_i)] = E[F(x_i)F(y_i)] = r(x_i)r(y_i)/(n+1)^2.$$

Moreover, $r(x_i)$ and $r(y_i)$ being also independent variables, their correlation coefficient has for large n asymptotically a normal distribution with 0 mean and $(n-1)^{-1}$ variance (Kendall and Stuart, 1967, Vol. 2, p. 476).

Thus, the rank correlation coefficient gives an equivalent test statistic for testing independence.

4 SERIAL CORRELATION TESTS

In the case of a time-series, it is obvious that the rank correlation test may be used for testing the independence of its consecutive elements. In this case the sample of couples being tested for independence is (x_i, x_{i+1}) for i = 1, 2, ... , n-1 or n, with, in the last case, $x_{n+1} = x_1$.

Under the hypothesis of randomness, the distribution of the test statistic, actually the sample serial correlation coefficient of first order r, is asymptotically normal with mean and variance

$$(6) \qquad E(r) = -(n-1)^{-1} \text{ or } 0,$$

whether the form of the test statistic is circular or not, and

(7) $\quad \text{var } r = (n-1)^{-1}.$

The circular version of the serial correlation coefficient is the test statistic of the Wald-Wolfowitz test of randomness.
An equivalent test statistic against serial correlation is given by the so called von Neumann's ratio defined by the statistic

(8) $\quad RVN = n\Sigma_k(x_i - x_{i+1})^2 / k\Sigma_n(x_i - m)^2$

where m is the series average and Σ_k indicates the summation from 1 to k or to n with k = n or (n-1) whether the version is circular or not.
Note that the circular version of this ratio is twice the inverse of Abbe's criteria RA of homogeneity quoted by Conrad (1925), which is related to the serial correlation coefficient r by the relation (Sneyers, 1955)

(9) $\quad RA(1 - r) = 1.$

Thus, the tests based on each of those three statistics are equivalent.
The rank version was suggested already by Wald and Wolfowitz, but its asymptotic relative efficiency is reduced to .91 (Bartels, 1982, p. 40).
In this case, mean and variance defined in (6) and (7) become respectively

(10) $\quad E(r) = -(n-1)^{-1}$ or 0 and $\text{var } r = n^{-1}.$

Moreover, due to the asymptotic character of the normality of the considered statistics distribution, care has to be taken of its validity for small samples.
Considering the problem for the von Neumann test statistic in the non circular version and using the better fit obtained by a Beta function adjusted to the exact moments, Bartels (1982) has listed critical values for 10 to 100.
In particular, for the standardized values of the test statistic, from Bartels critical values appears that, at the .05 level, the normal approximation gives too low critical values with an error of about .15 for n=10, but approaching the correct value of 1.645 with less than .04 for $n \geq 30$.

5 TEST OF IDENTITY OF DISTRIBUTION

Assuming that the distribution of the elements of the series is defined by its central moments, their stability is the necessary and sufficient condition for the stability of the distribution.
On the other hand, stability of the moments inferring stability of the powers of the deviations from the mean and inequalities remaining unchanged for odd powers in all cases and for even powers when the compared elements are positive, stability of moments is ensured by the single stability of the mean and of the dispersion (absolute deviation from the mean).

The Mann trend test

For testing this desired stability, the Mann test seems to be the most appropriate one, due to the fact that its statistic is the result of a progressive comparison of each element of the series with its preceding ones.
This comparison consists in determining for each element x_i the number n_i of smaller preceding ones and the test statistic t is defined by the relation

(11) $\quad t = \Sigma_n n_i.$

Under the hypothesis of randomness, its distribution has mean and variance

(12) $\quad E(t) = n(n-1)/4$ and $\text{var } t = n(n-1)(2n+5)/72$

For $n \geq 10$, the normal approximation is sufficiently accurate and its asymptotic power-efficiency relative to normal linear trend is .98 (Kendall and Stuart 1967, Vol. 2, p. 483-486).
A peculiar computational advantage of the Mann trend test is the recurrence

(13) $\quad t_i = t_{i-1} + r_{i,i} - 1,$

which relates the test statistic t_i of the subseries ending with x_i to the test statistic t_{i-1} of the subseries ending with x_{i-1} and to the rank $r_{i,i}$ of x_i in the first one. The successive standardized values computed in this way for t_i, i=1, 2, ... , n, whether oscillating near or diverging from zero, show then the absence or the existence of internal or ending trends in the series.

6 CHANGE-POINT DETERMINATION

When, in a time series, the element x_k with $1<k<n$ divides the total series into two random subseries (x_1, x_k) and (x_{k+1}, x_n) having different distributions, k is called a change-point.
When one such point exists, when computing successively the standardized values $u(t_k)$ and $u(t'_{k+1})$ for the subseries (x_1, x_k) and (x_{k+1}, x_n), there will be a value of k for which the two test statistics will be simultaneously nearest to zero (Sneyers, 1958).
From the above considerations, it follows that the search for a possible change-point should be covered by testing the stability as well of the mean as of the dispersion.
Moreover, in the case that k is the existing change-point, generally characterized by a significant value for t_n, its mathematical estimate will be given by the minimum value of the statistic X(t) defined by the relation

(14) $\quad X(t) = u^2(t_k) + u^2(t'_{k+1})$

Pettitt's change-point determination

Pettitt's approach of the change-point search problem (Sneyers, 1992_1 and 1992_2), is to test the homogeneity of the two subseries (x_1, x_k) and (x_{k+1}, x_n), for k = 1, 2, ... , n.
Using the Mann-Whitney test, Pettitt's test statistic X_k becomes

(15) $\quad X_k = 2R_k - k(n+1),$

where $R_k = \Sigma_k r_i$ and r_i are the ranks of x_i for i=1, 2, ... , k in the complete series. Under the null hypothesis of randomness and thus of absence of change-point, $E(X_k) = 0$ and extreme values X_E are significant for an abrupt decreasing or increasing shift at the significance level

(16) $\quad \alpha = \exp\{-6(X_E)^2/(n^3+n^2)\}$

in a one-sided test and 2α in a two-sided test.

Several change-points determination

In the case of several change-points in a time series, when shifts are compensating, the standardized Mann test $u(t_n)$ may have a near zero value while intermediate $u(t_k)$ have significant values. Moreover, Pettitt's statistic being a cumulated sum corrected for the mean, in this case, the change-points will produce absolute or relative extremes of X_k in the neighbourhood of the change-points. For their estimation, the joint consideration of $u(t_k)$, $u(t'_k)$ and X_k will thus be useful.
In particular, for the determination of the first one, say k_1, it should be noted that the subseries x_i, for i=1 to k_1, being then stable, the series $u(t_k)$ will be characterized by values oscillating near zero up to k_1, followed by values systematically increasing or decreasing. Thus, a first estimate of k_1 may be obtained by taking account of this property. Proceeding then in the same way to the analysis of the series x_i, reduced to $i = k_1+1$, k_1+2, ... , n, first estimates will successively be obtained for the different change-points. If these estimates are k_1, k_2,... , k_m,

improved estimates will then be realized by applying the Mann test analysis to subseries defined by two estimated change-points separated by only one change-point, beginning backwards with the series defined by the points $(k_{m-1}+1, n)$ to produce a new estimate k'_m of k_m. Re-estimating successively k_{m-1}, k_m-2,..., k_1, using each time the preceding new estimate, and repeating the procedure successively onwards and backwards, estimates of the change-points will be considered as optimal when the successive onward and backward scannings made in this way, lead to stabilized estimates.

Significance levels and power

For what concerns the probability level to which the different estimated change-points are significant, it should be remembered that for a subseries of length n' with significance level α, this significance level reduced to the total length of the series becomes (Sneyers, 1990, p. 5)

$$(17) \qquad \alpha_0 = 1 - (1 - \alpha)^{n/n'}.$$

On the other hand, care has also to be taken of the fact that, when independent events have respectively the probabilities α_1, α_2,... , α_m, their global probability:

$$(18) \qquad \alpha_0 = \alpha_1\alpha_2 \ldots \alpha_m$$

is found considering the fact that $-2 \ln\alpha_0$ is chi-square distributed with 2m d.f., small values of α_k leading to large values of the chi-square (Sneyers, 1990, p. 3, The Fisher test).

It follows that when dealing with significance levels of independent subseries, relation (17) enables levels to be made comparable, while with (18), the distribution of α_0 allows to compute the global level associated to the found reduced significance levels.

For instance, when a test statistic has a standardized normal distribution and if the complete series is divided into three independent series of equal length for which the reduced test statistic takes a critical value at least equal to 1.2, the global α_0 is found to be less than .05. It follows that working systematically with the intermediate .05 levels raises the risk of missing significant features inside the complete series.

Similarly, detection of increasing or decreasing trend being of equal interest, one-sided tests should be applied here as well as for serial correlation.

Finally, let be mentioned that, if the serial correlation test has power-efficiency zero against a linear trend alternative (Kendall and Stuart, 1966, Vol. 3, p. 360), under the hypothesis of alternating change-point shifts, this power-efficiency is, on the contrary, very high. If this property justifies the ancient use of Abbe's criteria for testing the observational homogeneity of data series, it emphasises also its full consideration for the search of change-points.

7 EXAMPLES

The considered examples give, for the northern hemisphere, a sample of the results found at the global, regional and local scale, by applying the above described method of analysis to surface air temperature series.

These results are extensively reproduced for the global series and more briefly for the other examples.

Northern hemisphere surface air temperature, 1851-1987 (°C)

The monthly data published by Jones et al, 1986 and 1988, are monthly averages of deviations in .01°C referring to the period 1951-1970. The analysed series are the annual and seasonal averages derived from these deviations. Though extended, at present, up to 1993, this series has been chosen for comparison of our results with previous ones.

The results have been characterized for each series or subseries by the set of data: P_k, n, m, s, u(r), u(t), $u_x(t)$ and $u(t_k)$, where P_k is the year of the considered change-point or of the end of the series and where, for the subseries ending at this point, we have: n = size, m = average, s = standard deviation, u(r) = standardized serial correlation statistic, u(t) = standardized trend statistic, $[u_x(t), u_x(t')]$ are the intermediate extremes given respectively by the onward and backward trend analysis and $u(t_k)$ is the value of the trend statistic for the subseries $(P_{k-1} + 1, P_{k+1})$.

For the complete series of annual averages, the results (0.01°C):

1987	137	-11.29	25.19	5.63	6.99	-

show strongly significant serial correlation and trend test statistics.

Moreover, Pettitt's statistic (15) and change-point trend statistic (14) are in perfect agreement with preceding results giving respectively maximum and minimum values for k = 1920 (Sneyers, 1992_2). For this change-point the derived subseries give:

1920	70	-27.67	20.20	.65	.12	(1.81, 2.41)
1987	67	5.82	17.28	1.14	.06	(2.95, 2.83)

This decomposition giving still relatively high values for the intermediate trend statistic, continuing the analysis gives the final results:

1880	30	-24.36	24.98	-1.46	.34	-1.51
1892	12	-40.29	11.01	1.38	.14	2.13
1920	28	-25.81	15.39	1.30	-.10 (2.92,-)	2.51
1929	9	-13.44	12.07	-.50	-.10	1.97
1953	24	12.32	13.31	1.01	-.27 (-,-1.85)	-3.03
1978	25	-3.10	16.08	-.45	-.28 (2.56,-)	1.90
1987	9	20.43	18.99	-.51	-.42	

results which reveal the successive shifts: -15.93, +14.48, +11.87, +25.76, -15.42, +23.53.

The intermediate values for the trend statistic mentioned here do not have any significance, given the shortness of the corresponding subseries.

For the residual dispersion (absolute value), which explains 54% of the total variance, the analysis of the complete series gives the result:

1987	137	12.99	11.20	.91	-.85 (-2.84,2.25)

which shows again the existence of internal trends. The full analysis leads to the different standard deviations: 1885 (23.45), 1955 (13.16) and 1987 (16.93).

Noting that the Shapiro-Wilk test for normality (Sneyers, 1990, p. 77) applied to the six subseries concludes to acceptance of the hypothesis at the .05 level and that the adjustment of a gamma-distribution function with α = 4.49 and β = 4.36 fits to the distribution of the lengths of these series, the complete statistical characterization of the full series has been achieved.

For the four seasons, from the complete analysis, we will quote only the change-points P_k of the mean, with the corresponding shifts.

In particular, the change-points of the mean are:

for the winter series (1852-1987): 1901 (+18.82), 1922 (+19.58), 1931 (+14.42), 1961 (-18.73), 1978 (+38.63), explaining 27% of the total variance (s = 46.68);

for the spring averages (1851-1987): 1863 (-7.35), 1864 (-6.08), 1923 (-10.75), 1937 (+5.09), 1955 (+10.67), 1961 (-9.23), explaining 39% of the total variance (s = 31.17);

for the summer series (1851-1987): 1868 (+18.03), 1878 (-47.16), 1895 (+18.88), 1902 (-26.34), 1913 (+15.99), 1920 (+43.59), 1930 (-9.91), 1941 (-11.99), 1961 (-12.84), 1978 (+18.85), explaining 60% of the total variance (s = 21.01);

for the autumn series (1851-1987): 1894 (+15.34), 1924

(+45.94), 1950 (-17.41), explaining 41% of the total variance (s = 32.30).

USA regional air temperature, 1895-1991 (°F)
Monthly data sets were kindly communicated by the US national data center in Asheville, NC.
For the derived annual averages, change-points of the mean and corresponding shifts: 1924 (+.78), 1942 (-.29), 1961 (-.43), 1984 (+.94) explain 22% of the total variance (s = .77).
For the seasonal averages, change-points appear only for winter, spring and summer respectively in numbers: 3, 1 and 3; they explain 12%, 12% and 31% of the total variances, (s = 1.77, 1.24, .88, 1.02 for each season).

Central England air temperature, 1659-1991 (°C)
Annual and seasonal averages were derived from the monthly data sets taken from Manley (1974) and from Parker et al. (1992).
For the annual averages, change-points of the mean and following shifts: 1668 (-.43), 1690 (-.67), 1699 (+1.11), 1725 (+.63), 1739 (-.74), 1824 (+.51), 1836 (-.87), 1845 (+.63), 1878 (-.48), (1894 (+.48), 1929 (+.25) explain 30% of the total variance (s = .62).
For the seasonal averages, change-points appear for winter, spring, summer and autumn respectively in numbers: 5, 21, 14 and 10; they explain 9%, 33%, 16% and 28% of the total variances (s = 1.35, .85, .80 and .84).

Austria regional air temperature, 1775 - 1989 (°C)
Annual and seasonal averages were derived from Böhm (1992).
For the annual averages, change-points of the mean and following shifts: 1777 (+1.14), 1828 (-.78), 1861 (+.69), 1868 (-.62), 1884 (-.30), 1891 (+.43), 1919 (+.34), 1946 (+.78), 1951 (-.71), 1973 (+.36) explain 28% of the total variance (s = .74).
For the seasonal averages, change-points appear for winter, spring, summer and autumn respectively in numbers: 3, 4, 4 and 4; they explain 8%, 10%, 19% and 15% of total variances (s = 1.67, 1.15, .92 and 1.02).

Uccle - Brussels (Belgium) air temperature, 1833 - 1994 (°C).
For the annual averages, change-points of the mean and following shifts: 1884 (-.71), 1892 (+.91), 1910 (+.46), 1943 (+.23), 1989 (+.78) explain 41% of the total variance (s = .78).
For the seasonal averages, change-points appear in each season, respectively in numbers: 3, 5, 3, and 2; they explain 11%, 37%, 17% and 34% of total variances (s = 1.72, 1.12, .97 and .97).

Genova (Italy) air temperature, 1833 - 1990 (°C)
For the annual averages derived from monthly averages kindly communicated by Prof. R. Rossetti (Pavia), change-points of the mean and following shifts: 1841 (+.51), 1862 (+.68), 1869 (-.72), 1878 (-.75), 1894 (+.32), 1918 (+.57), 1940 (+.37), 1949 (-.73)), 1987 (+1.01) explain 40% of the variance (s = .61).
For the seasonal averages, change-points appear respectively in number: 7, 8, 5, and 5 explaining 19%, 30%, 26% and 21% of the total variances (s = 1.14, .92, .90, .90).

Oulou (Finland) air temperature, 1847-1990 (°C)
For the annual averages kindly communicated by our colleague Dr. R. Heino (Finnish Meteorological Office), the change-points and following shifts: 1872 (+.43), 1933 (+1.50), 1939 (-2.90), 1942 (+2.06), 1954 (-1.00), 1970 (+1.11), 1976 (-1.22), 1987 (+1.55) explain 23% of the total variance (s = 1.13).

Remarks and conclusions
The serial corrrelation test statistic being sensitive to groupings of consecutive high or low values and the trend test statistic, to groupings of such values at the beginning or at the end of the tested series, the method reduces to testing simultaneously randomness against short and long range persistence. In case of rejection of the null hypothesis, the search for change-points allows determination of the simplest model, when valid.
For what concerns our results, the comparison of global, regional and local series confirms and shows:
(1) the abrupt character at all scales of climate changes already evidenced for Brussels and Paris in Sneyers, 1958;
(2) the smallness of the shifts at global scale compared to the higher ones occurring at middle and higher latitudes with, for the global scale , the highest part of explained variance.
An explanation may be found in the instability of the frequency of weather types at middle and higher latitudes determined by the perturbation flow generated by the General Circulation and in compensating effects of given circulations, due to location and geographical situation (neighbouring mountains, seas and oceans). The connection of the rainfall amounts instability in Milan (Italy) to the eastern neighbourhood of the Adriatic sea (Sneyers et al., 1994) enlightens sufficiently this opinion.

References

Bartels, R., 1982, " The rank version of the von Neumann's ratio test for randomness", J. Amer. Statist. Assoc., Volume 77, pp. 40-46.

Böhm, R., 1992," Lufttemperaturschwankungen in Österrreich seit 1775", Öster. Beitr. Meteor. Geoph., Heft 5, Wien , 96p.

Conrad, V, 1925, "Homogenitätsbestimmung meteotologischer Beobachtungen. Met. Zeitschr., Volume 42, pp. 482-85.

Jones, P.D., Raper, S.C.B., Bradley, R.S., Diaz, H.F., Kelly, P.M. & Wigley, T.M.L., 1986, "Northern hemisphere surface air temperature variations: 1851-1984", J. Climate Appl. Meteor., Volume 25, pp. 161-79.

Jones, P.D., 1988, "Hemispheric surface air temperature variations: recent trends and an update to 1987", J. Climate, volume 1, pp. 654-60.

Kendall, M.G. & Stuart, A., 1967, 1966, The Advanced Theory of Statistics, Vol. 2, Vol. 3, London, Griffin, 690 p., 552 p.

Manley, G., 1974, "Central England temperature data 1941-1979, Quat. J. R. Meteor. Soc., volume 100, pp. 389-405.

Parker, D.E., Legg, T.P. & Folland, C.K., 1992, " A new daily Central England temperature series, 1772-1991", Inter. J. Climatol., volume 12, pp. 317-42.

Sneyers, R., 1955, "Sur la détermination de l'homogénéité des séries climatologiques", J. Scient. Météor., Paris, Volume 28, pp. 359-72.

-, 1958, Connexions Thermiques entre Saisons Consécutives à Bruxelles-Uccle, Institut Roy. Météor. de Belgique, Pub. N° 23, 23 p.

-, 1990, On the Statistical Analysis of Series of Observations, W.M.O., Technical Note N° 143, Geneva, 192 p.

-, 1992_1, "Use and misuse of statistical methods for the detection of climate change", Preprints, 12th Conference on Probability and Statistics in the Atmospheric Sciences, Amer. Meteor. Soc, pp. J76-J81.

-, 1992_2, "On the use of statistical analysis for the objective determination of climate change", Meteor. Zeitschr., N. F. 1, pp. 247-56.

Sneyers, R., Siani, A.M. & Palmieri, S., 1994, "Climate change detection in Alpine Valleys, The example of the Brera Observatory (Milan) rainfall series (1790-1990)". Annalen der Meteorologie, 30, pp. 247-50.

CORRESPONDING AUTHOR

Dr. R. Sneyers
Institut royal météorologique de Belgique
3, avenue Circulaire, B-1180 Bruxelles, Belgium

A BAYESIAN APPROACH TO MODELLING SPATIAL-TEMPORAL PRECIPITATION DATA [1]

Richard L. Smith [2] and Peter J. Robinson [3]

Most precipitation data comes in the form of daily rainfall totals collected across a network of rain gauges. Research over the past several years on the statistical modeling of rainfall data has led to the development of models in which rain events are formed according to some stochastic process, and deposit rain over an area before they die. Fitting such models to daily data is difficult, however, because of the absence of direct observation of the rain events. In this paper, we argue that such a fitting procedure is possible within a Bayesian framework. The methodology relies heavily on Markov chain simulation algorithms to produce a reconstruction of the unseen process of rain events. As applications, we discuss the potential of such methodology in demonstrating changes in precipitation patterns as a result of actual or hypothesized changes in the global climate.

1. Introduction

This paper represents the first part of research directed towards the question "What influence will future climate change have on the spatial and temporal patterns of precipitation?" General circulation models typically produce spatial averages of temperature and rainfall over large grid cells. However, the questions concerning rainfall that are of interest in hydrology, agriculture, etc., typically concern patterns of rainfall over a much smaller spatial scale. Thus there is a very general problem, sometimes referred to as "downscaling" or "disaggregation", concerned with turning predictions over large spatial scales into predictions over small spatial scales. As a first step to doing this, we need some understanding of current patterns of rainfall over the temporal and spatial scales of interest. This task motivates the present paper, which is concerned with contructing statistical models for the spatial- temporal distribution of rainfall.

It seems reasonable to try to construct models which reflect, even if only in a very crude and incomplete way, our physical understanding about precipitation, and in this connection there is a long history of stochastic models based on superpositions of point processes. An early attempt was that of Le Cam (1961), who proposed a three-level hierarchy of "storms", "fronts" and "rain cells". Subsequent modifications include the model of Waymire, Gupta and Rodriguez-Iturbe (1984). However, these papers did not directly attempt to fit the models to real data. Statistical methods were proposed by Rodriguez-Iturbe *et al.* (1987, 1988) and Cox and Isham (1988), using "method of moments" fits based on equating the theoretical and sample values of various quantities that can be calculated directly, such as moments and correlations. They pointed out the difficulties of a likelihood-based approach for these models. For recent discussion see Barnett and Turkman (1993).

In this paper we argue that a Monte Carlo simulation approach, making use of the Gibbs sampler and Hastings-Metropolis algorithms (see, e.g., Smith and Roberts 1993, for a review) provides a viable methodology for fitting these models and constructing Bayesian estimates (which, with a diffuse prior, should also approximate maximum likelihood estimates). Space permits only a brief outline of the method here; a fuller description is in preparation for publication elsewhere. The method is applied to daily rainfall data from North Carolina, and deliberately uses a somewhat simplified form of the model; however, once the general methodology becomes established, it should be relatively easily extended to other models.

2. The model and its Bayesian analysis

Our model is as follows. All random variables are mutually independent except where specified otherwise.

[1] Research supported by NSF grants DMS-9115750 and DMS-9205112, and by the EPSRC

[2] Address for correspondence: Statistical Laboratory, 16 Mill Lane, Cambridge CB2 1SB, U.K.

[3] Department of Geography, University of North Carolina, Chapel Hill, N.C. 27599-3220, U.S.A.

(1) Each day is either "wet" or "dry" over the region of study. The process of wet and dry days has a first-order Markov structure where

$$\Pr\{\text{Day } n \text{ is wet} \mid \text{Day } n-1 \text{ is wet}\} = p_1,$$
$$\Pr\{\text{Day } n \text{ is wet} \mid \text{Day } n-1 \text{ is dry}\} = p_2,$$

with $0 < p_1 < 1$, $0 < p_2 < 1$.

(2) Given that a day is wet, the number of rain events N has a geometric distribution with parameter q, $0 < q < 1$, i.e.

$$\Pr\{N = k \mid N > 0\} = (1-q)q^{k-1},\ k = 1, 2, 3, \ldots$$

Dry days, of course, correspond to $N = 0$.

(3) Given $N > 0$ on a particular day, the kth rain event for $1 \leq k \leq N$ is specified by an origin (X_k, Y_k) (in cartesian coordinates), a direction Φ_k (in radians, measured clockwise from north), a duration D_k and a radius R_k. It is assumed that (X_k, Y_k) are uniformly distributed over a rectangle $(x_l, x_u) \times (y_l, y_u)$ containing all the measurement stations, D_k has a gamma distribution with parameters (a_D, b_D) and R_k has a gamma distribution with parameters (a_R, b_R). These random variables can reasonably be assumed independent from one rain event to the next, but there is a difficulty with the directions Φ_k because we would expect them to be highly correlated within a particular day. We therefore adopt the following hierarchical model for the event directions $\{\Phi_k,\ k = 1, \ldots, N\}$:

(a) For each day there is a dominant direction Φ_0 which has a von Mises distribution centred at some "prevailing wind direction" Φ^* and with concentration parameter κ_0,

(b) Conditionally on Φ_0, the individual directions $\Phi_1, \ldots, \Phi_N$ are independently drawn from the von Mises distribution centred at Φ_0 with concentration parameter κ_1.

The centre of the kth rain event begins at (X_k, Y_k), moves a distance D_k in the direction Φ_k, and then dies. Throughout this time the rain event is assumed to be a circle of radius R_k, whose centre is the centre of the rain event. From this it is possible to calculate the extent to which each rain event covers each measurement station. This is defined to be the distance that the rain event moves while the measurement station is inside the event. A rain event which does not cover a particular station at all is said to have coverage extent 0 for that station.

(4) Suppose the total extent of rain events covering station j in a particular day is denoted T_j. Then conditionally on T_j, we assume the actual amount of rainfall at station j has a gamma distribution with parameters $(T_j\alpha_j, \beta_j)$. The gamma parameters (α_j, β_j) are assumed fixed but different for each station.

Evidently this model has many arbitrary features, but our main purpose here is to demonstrate the feasibility of fitting such a model rather than trying too hard to justify the model itself.

We now turn to the details of a Bayesian analysis of this system. We can think of the model conceptually as consisting of five boxes.

Box A: the top-level parameters p_1, p_2, q, Φ^*, κ_0, κ_1, a_D, b_D, a_R, b_R.

Box B: N, Φ_0 and the rain events $\{X_k, Y_k, \Phi_k, D_k, R_k,\ 1 \leq k \leq N\}$ for each day.

Box C: The coverage extents T_j for individual stations.

Box D: The gamma parameters for individual stations, i.e. the constants α_j, β_j, $1 \leq j \leq m$.

Box E: The observed rain gauge data.

The logical dependence between these boxes is given by the following diagram:

$$\begin{array}{ccccccc} & & & & & & \mathrm{D} \\ & & & & & & \downarrow \\ \mathrm{A} & \rightarrow & \mathrm{B} & \rightarrow & \mathrm{C} & \rightarrow & \mathrm{E} \end{array}$$

Here arrows represent direction of dependence. Given A we can generate the contents of B, given B we can calculate C, and given C and D together we can generate E. Note that the dependence from B to C is deterministic but the other dependencies define probability distributions rather than specifying exactly the contents of the box at the head of the arrow.

We assume proper but diffuse prior distributions for each of the parameters in boxes A and D. The Bayesian inference problem is then to compute the joint distribution of the boxes A, B, C and D, given E. We approach

this via Gibbs sampling: set up a Monte Carlo simulation of the whole system, and then update the contents of each of the boxes A, B, C and D in turn, conditionally on the contents of all the other boxes. For A and D, this is an application of what are by now routine Bayesian calculations, while C is a direct calculation given B. For box B itself, we adopt a method based on randomly deciding whether to add a rain event, to delete a rain event, or to do both, with probabilities $\frac{1}{4}$, $\frac{1}{4}$, $\frac{1}{2}$ respectively, and then applying the Hastings (1970) rule to decide whether to accept or reject the new configuration. The whole procedure is repeated a very large number of times until it appears to converge. In the studies which follow this is based on 20,000 iterations.

3. Results

The procedure of Section 2 has been applied to five years' daily rainfall data from 13 stations in the flat coastal plain region of North Carolina. Separate analyses were performed for "summer" (June, July, August) and "winter" (December, January, February) data. One of the main features of interest is the contrast between these, since winter rainfall in North Carolina tends to consist of cyclonic events of long temporal and spatial extent, whereas summer rainfall is much more dominated by small but intense convective storms.

Fig. 1 shows a time series plot for the summer data of the principal parameters across the 20,000 iterations. In the case of the distance and radius parameters, the mean distance a_D/b_D and mean radius a_R/b_R were plotted in place of the parameters b_D and b_R. Similar plots were obtained for the winter data. Although these plots do not provide any conclusive evidence that the Markov chain has reached stationarity, the visual impressions suggests that they have.

Fig. 2 shows estimated (smoothed) posterior densities for each of the ten principal parameters, computed separately for the summer data (solid curve) and the winter data (broken curve). Despite the uncertainties over such issues as whether the model is appropriate or whether enough iterations have been taken, some interesting comparisons can be made. The p_1 and p_2 values show that the overall probability of rain somewhere in the region is substantially higher in summer than in winter. On the other hand, the summer rain events have smaller mean radius, and also cover a smaller distance before they die. This is highly consistent with our expectations, given the contrast between winter cyclonic events and summer convective events mentioned above.

One the other hand, Fig. 3 shows that not everything is satisfactory about this model. In this plot, spatial correlations based on occurrences (i.e. code the data =1 if rainfall occurs on a given day, 0 otherwise) are computed using both the real data, and simulated data from the fitted model. The simulated correlations decay much faster with distance than the true correlations. Work is currently in progress to find more realistic models that will reflect the true correlations more accurately.

References

Barnett, V. and Turkman, F. (eds.) (1993), *Statistics for the Environment, Volume 2: Water Related Issues*. Chichester: John Wiley.

Cox, D.R. and Isham, V. (1988), A simple spatial-temporal model of rainfall. *Proc. Roy. Soc. Lond. A* **415**, 317-328.

Hastings, W.K. (1970), Monte Carlo sampling methods using Markov chains and their applications. *Biometrika* **57**, 97-109.

Le Cam, L. (1961), A stochastic description of precipitation. *Proceedings of the Fourth Berkeley Symposium on Mathematical Statistics and Probability*, **3**, ed. J. Neyman, Berkeley, CA, pp. 165-186

Rodriguez-Iturbe, I., Cox, D.R. and Isham, V. (1987), Some models for rainfall based on stochastic point processes. *Proc. Roy. Soc. Lond. A* **410**, 269-288.

Rodriguez-Iturbe, I., Cox, D.R. and Isham, V. (1988), A point process model for rainfall: further developments. *Proc. Roy. Soc. Lond. A* **417**, 283-298.

Smith, A.F.M. and Roberts, G.O. (1993), Bayesian computation via the Gibbs sampler and related Markov chain Monte Carlo methods. *J.R. Statist. Soc. B* **55**, 3-23.

Waymire, E., Gupta, V.K. and Rodriguez-Iturbe, I. (1984), Spectral theory of rainfall intensity at the meso-β scale. *Water Resources Research* **20**, 1453-1465.

Fig. 1: Time series plots of parameters

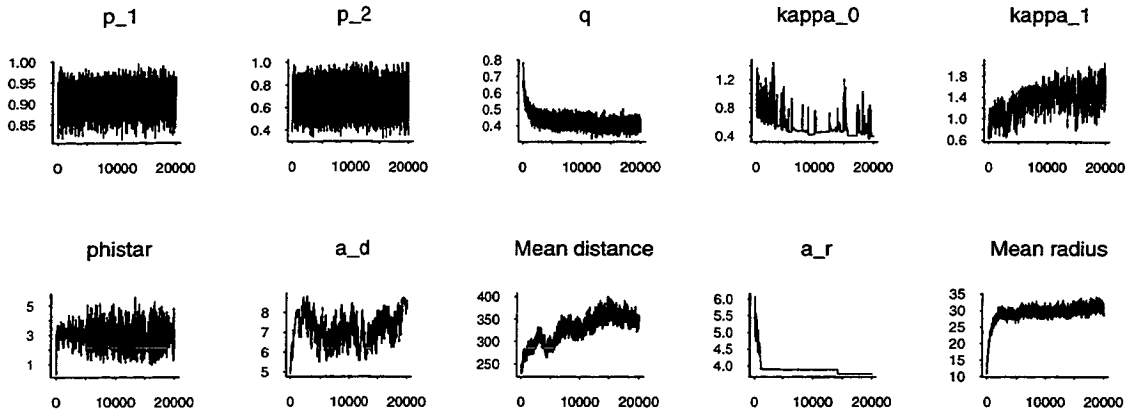


Fig. 2: Posterior densities (Solid curve summer, broken curve winter)

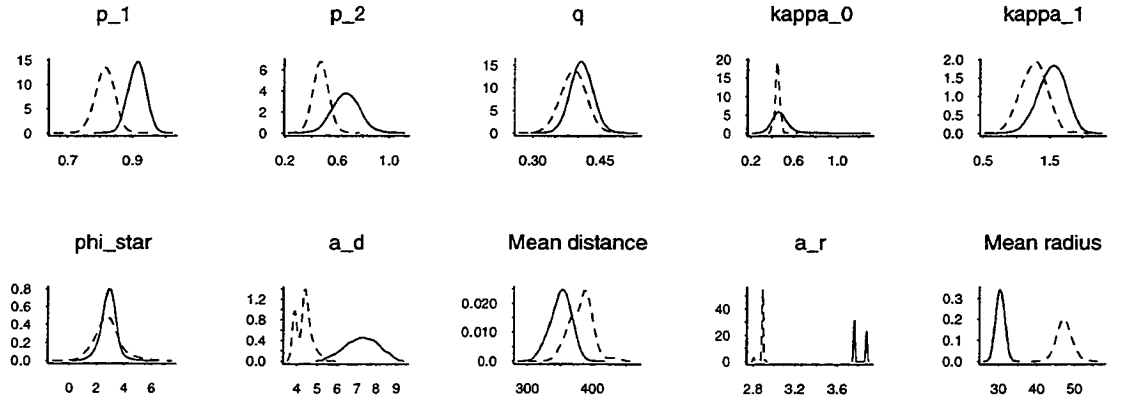
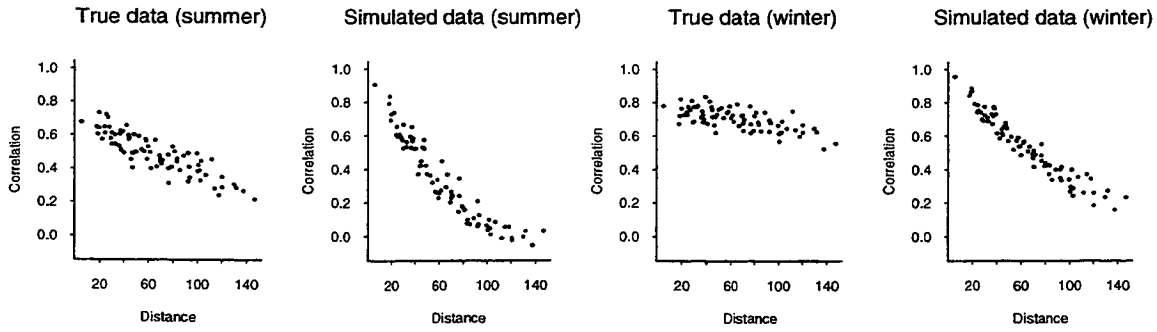


Fig. 3: Spatial correlations based on occurrences



Optimum averaging of incomplete climatological data

Bettina Kusserow, Andreas Hense

Meteorologisches Institut der Universität Bonn, Auf dem Hügel 20, 53121 Bonn, Germany

ABSTRACT

The aim of the study is to obtain homogeneous data from incomplete climatological data sets, while retaining the largest possible amount of information, based on Gandin's method (1965) of optimum averaging. The entire information from the climatic data is optimally utilized as the spatial-temporal correlation between the fields is incorporated into the estimations by means of a transformation of the data into EOF's. The analysis procedure not only serves to homogenize the data but also to inspect if the values are integrated into the spatial-temporal structure of the data set. Moreover it is possible to assign an error estimate to each value of the homogeneous data set.

1 INTRODUCTION

During the last few years large climatological data sets such as the Comprehensive Ocean Atmosphere Data Set (COADS) or the Monthly Climatic Data (MCD) have become available. Two features are typical of these data sets:

- Similar measurements of a certain variable – although of different quality – are available at a rather limited number of observation points
- Although data has been recorded over a rather long time period (> 100 years), the spatial coverage at the above mentioned observation locations can vary considerably.

For the analysis of climatic fluctuations or for the validation of model simulations, climatological data on a regular space-time grid are necessary. Since the total amount of information is limited, a homogenziation always implies an averaging in time and/or space. The represented analysis method is a way to define spatial means based on a least squares approach. The weighting coefficients are calculated from the (second moment) statistics of the data field itself by minimizing the variance of analysis error. Specifically it is the spatial-temporal correlation between the observations which make use of all the available information contained in the data. Therefore we will term this approach the optimal averaging technique. Furthermore the statistical approach will also allow conclusions to be drawn about the quality or representativeness of single observations.

Due to large gaps in the data rows or to non-representative values it appears that it is not always possible to calculate an (optimal) mean, so that the analysed parameter field may also be incomplete. This problem has been overcome by a moving window analysis of the above described optimal average method.

The optimum averaging method is further developed and tested by interpolating selected parameters from the COADS $2° \times 2°$ grid onto a coarser $5,625° \times 5,625°$ grid according to the T21-ECHAM model. For the analysis tests restrictions are initially made to the Atlantic $(100°W - 30°E)$ and to the months of January and June for the period 1951 to 1989. Due to its day-to-day variability, sea level pressure (SLP) has proved to be appropriate as test parameter, which provides an opportunity to test the error detection of the method.

2 THEORY

2.1 Formulation of the problem

Suppose we have a continuous random field $X(\vec{r})$, the probability density of which is completely determined by the first moment

$$E(X(\vec{r})) = m(\vec{r})$$

and the second moment covariance function

$$\Phi(\vec{r}, \vec{r}') = E((X(\vec{r}) - m(\vec{r}))(X(\vec{r}') - m(\vec{r}')))$$

We will assume that we know from the continuous field $X(\vec{r})$ only the values at K_t locations $(X_k = X(\vec{r}_k); k = 1, K_t)$. The index t for K_t indicates that the number of spatial sampling points may vary randomly. We want to derive an estimator $\mathcal{L}^*(X)$ for the spatial average $\mathcal{L}(X)$ of the random field $X(\vec{r})$, which will be computed by a linear combination of

the spatially sampled values

$$\mathcal{L}^* = \sum_{k=1}^{K_t} \lambda_k X(\vec{r}_k)$$

This estimator is subjected to two constraints

- the unbiasedness

$$E(\mathcal{L}^*) = E(\mathcal{L}(X))$$

- the minimum error variance

$$\mathrm{Var}(\mathcal{L}^* - \mathcal{L}(X)) = \text{Minimum}$$

  where the variance is defined as the diagonal elements of the covariance function.

Without loss of generality we will assume that the expectation field $m(\vec{r})$ can be expanded a-priori in a series of linearily independent known functions f_l

$$m(\vec{r}) = \sum_l a_l f_l(\vec{r})$$

If we now insert the definition of the estimator $\mathcal{L}^*$ into the unbiasedness constraint we can derive a constraint for the weights λ_k in $\mathcal{L}$.

$$\sum_l a_l (\sum_{k=1}^{K_t} \lambda_k f_l(\vec{r}_k) - \mathcal{L}(f_l)) = 0$$

Since the last equation is valid for any a_l and with the assumption that $m(\vec{r}) = 0$ (analysis of anomaly values) we may chose $f_1 = 1; f_l = 0 \text{ for } l > 1; a_1 = 1$, so that the constraint for the weights from the unbiasedness simplifies to

$$\sum_{k=1}^{K_t} \lambda_k = 1 \quad .$$

The computation of the weights themselves follows from the minimization requirement where the minimization is subjected to the above constraint which will be taken into account by a Lagrangian multiplier γ. It results at the minimum

$$\sum_{k=1}^{K_t} \lambda_k < X(\vec{r}_k), X(\vec{r}_{k'}) > = < X(r_{k'}), \mathcal{L}(X) > \gamma$$

where

$$< X(\vec{r}_k), X(\vec{r}_{k'}) > = \Phi(\vec{r}_k, \vec{r}_{k'})$$

is the covariance function sampled at the spatial sample points of the covariance matrix and

$$< X(\vec{r}_k), \mathcal{L}(X) >$$

is the covariance between the sample points and the spatial mean. This linear system of equations will be formulated in a matrix equation. As the expected error we obtain

$$\mathrm{Var}(\mathcal{L}^* - \mathcal{L}) =$$
$$\mathrm{Var}(\mathcal{L}) - \sum_{k=1}^{K_t} \lambda_k < X(\vec{r}_k), \mathcal{L}(X) > + \gamma$$

2.2 EOF expansion

For the continuous case the eigenvalue-problem of the covariance function $\Phi(\vec{r}_k, \vec{r}_{k'})$ of any random process $X(\vec{r})$ on a set S is solved by the Karhunen-Loeve (K-L) functions $\widehat{e}_i(\vec{r})$ with their eigenvalues $\widehat{\mu}_i$.

$$\int_S \Phi(\vec{r}_k, \vec{r}_{k'}) \widehat{e}_i(\vec{r}_{k'}) d\vec{r}_{k'} = \widehat{\mu}_i \widehat{e}_i(\vec{r})$$

whereby it is valid that: $\widehat{\mu}_i \geq 0$ and $\widehat{\mu}_i \in \mathbb{R}$. Thus any random process $X(\vec{r})$ can be represented in the following way

$$X(\vec{r}) = \sum_i a_i \widehat{e}_i(\vec{r}_k)$$

In the discrete case i.e. the covariance between J discrete points ($k = 1, .., J$) the analogs of the K-L functions are the empirical orthogonal functions (EOF's) $e_i(\vec{r})$ with their eigenvalues μ_i. Then the covariance matrix can be written as

$$\Phi_J(\vec{r}_k, \vec{r}_{k'}) = \sum_{i=1}^{J} \mu_i e_i(\vec{r}_k) e_i(\vec{r}_{k'})$$

The discrete covariance $\Phi_J(\vec{r}_{k'}, \mathcal{L}(\vec{r}_k))$ is given by

$$\Phi_J(\vec{r}_{k'}, \mathcal{L}(\vec{r}_k)) = \sum_{i=1}^{J} \mu_i e_i(\vec{r}_{k'}) \mathcal{L}\left(e_i(\vec{r}_k)\right)$$

In the same way it is possible to pass over the analysis error $Var(\mathcal{L}^* - \mathcal{L})$ from the continuous to the discrete case. Here K_t means the number of spatially locations with observations at the moment t and $\lambda_k, k = 1, K_t$ the unknown coefficients at this points.

$$Var(\mathcal{L}^* - \mathcal{L}) = \sum_{k=i}^{J} \mu_i \mathcal{L}(e_i(\vec{r}_k)) \mathcal{L}(e_i(\vec{r}_k))$$
$$- \sum_{k=1}^{K_t} \lambda_k \left(\sum_i^J \mu_i e_i(\vec{r}_{k'}) \mathcal{L}(e_i(\vec{r}_k)) \right) + \gamma$$

2.3 Estimation

In order to work with the above equations we have to estimate the covariance matrix from

discrete values derived from a sample. We will assume that we have N realizations $t, t = 1, \ldots, N$ of the field X sampled at the K_t locations $(\vec{r}_k, k = 1, \ldots, K_t)$. The maximal number of spatial sample points shall be K

$$K = \max(K_t, t = 1, \ldots, N) .$$

We will denote the statistical sample of the random field X as

$$x(\vec{r}_k, t), \quad k = 1, \ldots, K_t, \quad t = 1, \ldots, N$$

The estimate of expectation is given as the arithmetic mean over all valid data

$$\overline{x}_k = \frac{1}{N_k} \sum_{t=1}^{N_k} x(\vec{r}_k, t)$$

In order to fulfil the assumption of a zero expectation we define a new statistical sample x'

$$x'(\vec{r}_k, t) = (x(\vec{r}_k, t) - \overline{x}_k)$$

If the maximal number of observation points K is smaller than the number of sample elements N we can estimate from the given sample the covariance matrix $\Phi_J(\vec{r}_k, \vec{r}_{k'})$.

Since Wilk (1932) there have been many examinations about the problem of estimating the covariance matrix from an incomplete data matrix. In one special case of missing data (data matrix with "monotonic" or "nested" pattern) Morrison (1976) has developed a scheme which permits the direct calculation of the covariance. Another way to estimate the covariance matrix is to compute the sum only over data points where both observations k and k' at time t are available.

From this covariance matrix we estimate the eigenvalues μ_i and the EOF's e_i. This are plugged in into the above equations for the covariances $\Phi_J(\vec{r}_k, \vec{r}_{k'})$ and $\Phi_J(\vec{r}_{k'}, \mathcal{L}(\vec{r}_k))$ to define estimators for this variables. Furthermore it is useful to have some influence on the smoothness of the covariance structure since the estimator Φ_J also contains statistical fluctuations which disturb the true spatial correlation structure. (Obled and Creutin, 1986).

This problem can be solved by using a truncated EOF expansion ($I < K$). Then the linear system of analysis equations (matrix equation) can be solved.

However a problem occurs if the data matrix has too many missing values. In this case it is not imperative that the respective covariance matrix is positive-definite and its eigenvalues may no longer be greater than zero. This means that the covariance matrix is not of full rank. In this case the analysis-scheme includes two different ways to reduce the dimension of the matrix:

- calculating I as the number of EOF's whose eigenvalues are not negative
- reducing the data set by excluding that spatial grid point with the smallest number of observations. Then a new covariance matrix is estimated and its eigenvalue problem is solved. This procedure is repeated until there are only positive eigenvalues.

Now the matrix equation has to be solved particularly for each realization. Since K_t is smaller than K the matrix which we need to calculate the optimal weights

- varies with the sample t
- is obtained from the K dimensional covariance matrix by omitting those rows and columns which correspond to spatial sample points without an observation at sample t.

The variance of the population linear operator $\mathrm{Var}(\mathcal{L}(X))$ and thus the estimated analysis error can also be estimated from the EOF expansion.

2.4 Filling of partially data-void areas

We have to expect that for certain boxes of the analysis-grid the optimal area average cannot be estimated for every month due to initially missing data. To fill in these partially data-void areas, the data grid is interpolated onto another analysis-grid of the same resolution as the data-grid, using the analysis method based on the above theory within a moving window of e.g. 16 grid points.

3 PRESENTATION OF METHODS

As a working example for the above theory we used the monthly values for January atmospheric sea level pressure (SLP) from the COADS data set over the Atlantic for the area :

90°N – 70°S
100°W – 30°E

and for the period 1951-1989. We have chosen the SLP field as it is a scalar atmospheric field with a high day-to-day variability. In regions of small data coverage and strong gradients this will probably lead to observations which do not

represent the monthly means (e.g. observations in storms, which are not counterbalanced by observations of high pressure systems). This will give us the opportunity to test the error detection part of our method.

3.1 The data base

The quality of the data of the COADS data set is not homogeneous. The COADS data set is a simple collection of observations from ships navigating at any time during the month concerned and at any point in the respective $2° \times 2°$ grid box. Thus the individual pieces of data are composed of a very variable number of observations and represent the "real" monthly average with a different quality. Due to large gaps in the data rows or to non-representative monthly values (as a result of sparse observations in these areas), it was found that particularly in the regions north of 60° N and south of 40° S an efficient homogenization of the data is not possible. In those areas the analysis error is large than 1 hPa, of the exceeding even 10 hPa. In regions of large data coverage the analysis error is always very much smaller than 1 hPa.

4 CONCLUSION

This paper presents a method of homogenizing incomplete data sets in which the space-time structures of the investigated fields are incorporated into the analysis by means of a data transformation into empirical orthogonal functions (EOF's). The method presented has the additional advantage that values which are not integrated into the spatial-temporal structure of the data set become apparent during the analysis procedure and, if required, can be excluded from the analysis immediately. As the analysis error is determined for each evaluation, it is possible to assign an error bar to each value of the new data set. The monthly values of the parameters sea level pressure (SLP) of the COADS data set are estimated on two different analysis-grids. If the aim of the analysis is to check the individual data with regard to its integration in the time-space field structure, the following analysis procedure has proved suitable:

- The covariance matrix is only estimated on the basis of monthly values in pairs.
- If negative eigenvalues occur, this is seen as a kind of natural smoothing, and respective EOF's are not used any further in the analysis.

The main objective of this study i.e. the homogenization of incomplete data sets while retaining the maximum amount of information, is reached by an analysis procedure as follows:

- The covariance matrix is estimated according to Morrison's modified procedure.
- If negative eigenvalues occur, COADS boxes with the worst distribution of values are successively excluded from the analysis until exclusively EOF's with positive values solve the eigenvalue problem.

Significal differences between these two analysis occur if the time scale of the variability of the parameter concerned is shorter than the period which the examined data is supposed to represent. Thus it is possible in the case of the SLP parameter - due to its day-to-day variability - to determine any COADS monthly values which deviate from the "actual" monthly mean. On the other hand the analysis fo SST observation as a "slow" variable produces very similar results.

References

Gandin, L. S. (1965). *Objective analysis of meteorological fields*, (Translated from Russian, Israel Program for Scientific Translations, Jerusalem 1965).

Morrison, D. F. (1976). *Multivariate Statistical Methods*, McGraw-Hill, New York.

Wilks, S. S. (1932). *Moments and distributions of estimates of population parameters from fragmentary samples*, Annals of Mathematical Statistics, **3**, 163 – 195.

CORRESPONDING AUTHOR

Andreas Hense
Meteorologisches Institut
der Universität Bonn
Auf dem Hügel 20, 53121 Bonn, Germany

FINE-MESH ANALYSIS OF THE MONTHLY MEAN TEMPERATURE AND PRECIPITATION FIELDS OVER FINLAND

Jaakko Helminen

Finnish Meteorological Institute, Helsinki, Finland

ABSTRACT

Normal value fields of the monthly mean temperature and precipitation over Finland for the period 1961-1990 are analyzed on a fine-mesh 10 km * 10 km grid. This study focuses on the differences between the kriging and the Gandin (optimum interpolation) methods. In this context the local anisotrophy due to the topography and the closeness of lakes as well as the sea is considered. Moreover the spatial weighting function of the Gandin analysis scheme is based on a sample, which is statistically independent of the period considered in the intercomparison experiment.

1. INTRODUCTION

In many climate applications and impact studies a fine, unified resolution of the climate variable values is essential. At the same time one is mainly interested in smoothed fields, e.g. monthly mean value fields. This combination offers realistic possibilities to develop different analysis methods suitable for fine-mesh analysis purposes and furthermore to test their feasibility.

This study applies the kriging and Gandin methods to the normal-value (1961-1990) monthly mean temperature and precipitation fields of Finland. The station values are interpolated to a GIS, 10 km * 10 km, fine-mesh grid. Moreover the methods have been modified so that anisotrophic effects of topography and the closeness of lakes as well as the sea are taken into consideration.

We describe first the data we have used in this study. Then we proceed to methodological questions with special emphasis on the anisotrophic effects we have taken into account.

2. DATA

The data consists of July mean values of temperature and precipitation of the Finnish synoptic and climate stations. The station network is given in Fig. 1.

The digitalized, quality checked data starts from 1959 and we have used the time interval 1959-1994. The data of 1959-1960 and 1991-1994 have been used for various numerical analysis scheme parameter estimations.

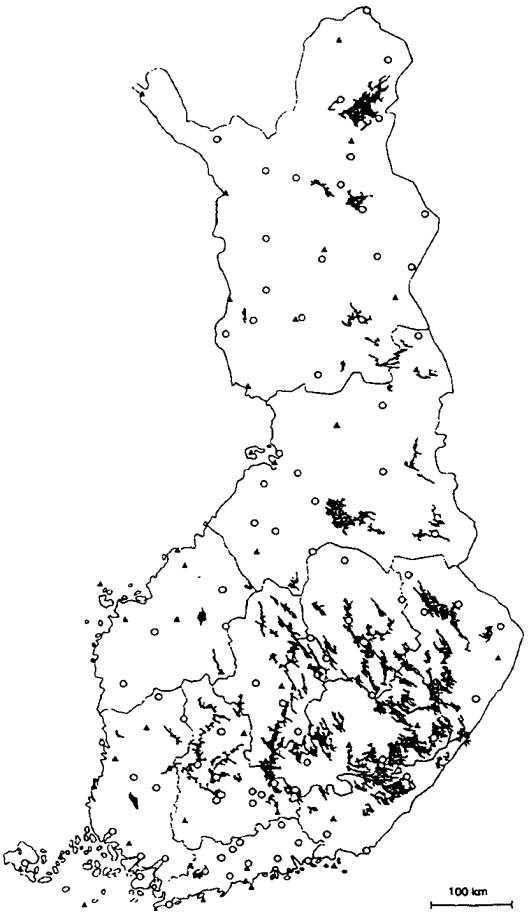


Figure 1. The Finnish synoptic and climate station network. synoptic station; o climate station

3. METHODS

Both the kriging and the Gandin method consist of two parts. First we determine the long-term field. Second, the numerical analysis schemes

employed on deviations from the long-term field are based on linear interpolation.

Using the universal kriging approach as in Ripley (1981) and Henttonen (1991) we assume that the long-term field m/x) is not known. Moreover m(x) is assumed to follow the form $m(\mathbf{x})=\mathbf{f}'(\mathbf{x})\beta$, where $\mathbf{f}(\mathbf{x})$ is a known vector-valued function and β is the regression coefficient vector. When we know the error covariance function, β can be estimated through the generalized least squares estimates **b**.

By denoting

$$\mathbf{Z}_N = \begin{bmatrix} Z(x_1) \\ . \\ . \\ . \\ Z(x_N) \end{bmatrix},$$

where $Z(x_1),...,Z(x_N)$ are the sample point values of the variable Z. When the covariance function $\mathbf{K}= C(x_i,x_j)$ is known and **b** has been estimated the best linear, unbiased estimate Z(x) at an intermediant point is obtained by minimizing the mean squared error

$$MSE(\hat{Z}(\mathbf{x})) = E(\lambda\, \mathbf{Z}_N - Z(\mathbf{x}))^2$$

subject to the unbiasedness constraint

$$E(\lambda'\, \mathbf{Z}_N) = E(Z(\mathbf{x})).$$

With this constraint we get

$$\hat{Z}(\mathbf{x}) = \mathbf{f}'(\mathbf{x})\mathbf{b} + \mathbf{k}'\mathbf{K}^{-1}(\mathbf{Z}_N - \mathbf{F}\mathbf{b}), \qquad (1)$$

where

$$\mathbf{F} = \begin{bmatrix} f_1(x_1) .... f_r(x_1) \\ . \quad . \\ . \quad . \\ . \quad . \\ f_1(x_N) .... f_r(x_N) \end{bmatrix} \quad \text{and}$$

$$\mathbf{b} = (\mathbf{F}'\mathbf{K}^{-1}\mathbf{F})^{-1}\mathbf{F}'\mathbf{K}^{-1}\mathbf{Z}_N.$$

Moreover, according to Ripley (1981), the kriging provides the following estimate for the error

variance $\sigma_E^2(\mathbf{x})$ at the point **x**

$$\sigma_E^2(\mathbf{x}) = \sigma^2 - \mathbf{k}'(\mathbf{x})\mathbf{K}^{-1}\mathbf{k}(\mathbf{x}) + \qquad (2)$$

$$(\mathbf{f}(\mathbf{x}) - \mathbf{F}'\mathbf{K}^{-1}\mathbf{k}(\mathbf{x}))'(\mathbf{F}'\mathbf{K}^{-1}\mathbf{F})^{-1}$$

$$(\mathbf{f}(\mathbf{x}) - \mathbf{F}'\mathbf{K}^{-1}\mathbf{k}(\mathbf{x})),$$

where

$$\sigma^2 = \text{var}\,(Z(\mathbf{x})).$$

According to the expression (3) for kriging the covariance matrix has to be inverted at each of the N data points. The inverse is used at several stages: in computing the generalized least squares estimates **b**, in smoothing the residuals, and in computing the estimates of the analysis error. The Cholesky decomposition of **K** is utilized in the inversion step.

To summarize the following computational procedure is used for the kriging.

1) Form the covariance matrix of the data points $\mathbf{K} = C(x_i,x_j)$. Construct a non-singular lower triangular matrix **L** such that $\mathbf{K}=\mathbf{L}\mathbf{L}'$. (Cholesky decomposition of **K**).

2) Solve the regression coefficients **b** from

$$\mathbf{L}^{-1}\mathbf{Z}_N = \mathbf{L}^{-1}\mathbf{F}\mathbf{b},$$

where

$$\mathbf{F} = \begin{bmatrix} f_1(x_1) .... f_r(x_1) \\ . \quad . \\ . \quad . \\ . \quad . \\ f_1(x_N) .... f_r(x_N) \end{bmatrix} \quad \text{and}$$

$$\mathbf{Z}_N = \begin{bmatrix} Z(x_1) \\ . \\ . \\ . \\ Z(x_N) \end{bmatrix}.$$

3) Form the residual vector at data points:

$$\mathbf{w}_N = \mathbf{Z}_N - \mathbf{F}\mathbf{b},$$

where **b** is a generalized least squares estimate of the regression coefficients (step 2).

4) Form **y** such that $\mathbf{L}(\mathbf{L}'\mathbf{y}) = \mathbf{w}_N$.

5) Predict Z(x) by $\mathbf{y}'\mathbf{k}(\mathbf{x}) + \mathbf{f}'(\mathbf{x})\mathbf{b}$,

where $\mathbf{k}(\mathbf{x})$ is the vector of covariances between data points and the point **x**.

The error variance (2) is given by

$$\sigma_E^2(\mathbf{x}) = \sigma^2 \,\|\mathbf{e}\|^2 + \|\mathbf{g}\|^2$$

$$\mathbf{L}\mathbf{e} = \mathbf{k}(\mathbf{x}),$$

$$(\mathbf{L}^{-1}\mathbf{F})'\mathbf{g} = \mathbf{f}(\mathbf{x}) - (\mathbf{L}^{-1}\mathbf{F})'\mathbf{e}.$$

In our kriging application we restrict the long-term fields to quadratic surfaces so that r = 2.

When we apply the Gandin method we first estimate the long-term field as the mean $E(\mathbf{Z}_N)$ of observations, which are statistically independent of the period we want to analyze. After having determined the stationwise mean values the mean values at the grid points are estimated graphically.

The analysis is based on deviations from the mean field, i.e.

$$\mathbf{dZ(x)} = \mathbf{Z(x)} - E(\mathbf{Z(x)}),$$

so that it is estimated as the linear combination of deviations at neighbouring observation sites. In other words

$$dZ(\mathbf{x}) = \sum_i s_i dZ_i \qquad (i = 1,...,n).$$

The values of the weights s_i are determined by the least squares method. If we denote the autocorrelation matrix of the deviations dZ_i by

$$\mathbf{R} = \begin{bmatrix} 1 & \mu_{12} & .... & \mu_{1n} \\ \mu_{21} & 1 & .... & \mu_{2n} \\ . & . & & . \\ . & . & & . \\ & & & \\ & & & \\ . & . & & . \\ \mu_{n1} & \mu_{n2} & .... & 1 \end{bmatrix},$$

$$\mathbf{s} = \begin{bmatrix} s_1 \\ s_2 \\ . \\ . \\ s_n \end{bmatrix},$$

$\eta = \eta\mathbf{I}$ (relative observation error matrix) and

$$\mathbf{r_0} = \begin{bmatrix} \mu_{01} \\ \mu_{02} \\ \\ \\ \mu_{0n} \end{bmatrix},$$

we can write

$$\mathbf{s} = (\mathbf{R} + \eta\mathbf{I})^{-1}\mathbf{r_0}. \qquad (3)$$

The relative interpolation error ε can be written as

$$\varepsilon = 1 - \sum_i \sum_j s_i s_j \mu_{ij} - \eta \sum_i s_i^2. \qquad (4)$$

According to Gandin (1965) the number n of observation sites neighbouring the grid point 0 is typically less than N (the total number of the observation sites). Moreover to ensure a representative sample the sites are selected one by one from the adjacent grid point squares according to the following scheme.

.	.	.	.	.	.
	22	19	11	17	21
.	.	.	.	.	.
	14	6	3	5	13
.	.	.	.	.	.
	10	2	0	1	9
.	.	.	.	.	.
	16	8	4	7	15
.	.	.	.	.	.
	24	20	12	18	23
.	.	.	.	.	.

Figure 2. The scheme according to which the neighbouring observation site values for the basic grid point 0 are chosen. The indices i = 0,1,... refer to squares with the grid point i as its centerpoint. The neighbouring sites will be chosen one by one from the squares i as far as the total number n has been reached. In case there are several sites within a square the site closest to the basic grid point will be chosen.

The determination of the autocorrelation function is usually done by using appropriate theoretical functions and by estimating their parameters.

In kriging we have used Whittle's autocorrelation function, which has the form

$$C(r,\nu) = \frac{\sigma^2}{2^{\nu-1}\Gamma(\nu)} \left(\frac{r}{r_0}\right)^{\nu} K_\nu \left(\frac{r}{r_0}\right) \qquad (5)$$

Some examples of its form can be seen in Fig. 3.

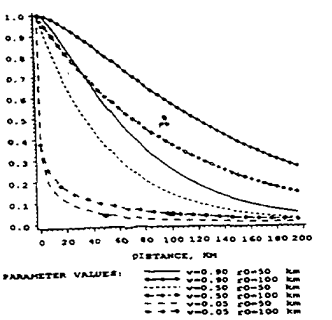


Figure 3. Examples on Whittle's autocorrelation function (5).

In Gandin's method we use as autocorrelation function

$$\mu(r) = e^{-ar^b} \cos(cr). \quad (6)$$

It should be emphasized that this function allows negative values at some distances.

In kriging the anisotropic effects have been taken into account by using the following regression model

$$E(\mathbf{Z}(x,y,z,l,s) = \beta_0 + \beta_1 x + \beta_2 y + \beta_3 x^2 + \beta_4 y^2 + \beta_5 xy + \beta_6 z + \beta_7 z^2 + \beta_8 xz + \beta_9 yz + \beta_{10} l + \beta_{11} s,$$

where z is the altitude of the point (x,y) in meters, l is the proportion of lakes inside the radius of 15 km from the point, and s is the proportion of sea inside the radius of 20 km from the point.

In the Gandin method the anisotrophy is taken into account by setting constraints to the choice of neighbouring sites so that the chosen sites represent approximately the same altitude and closeness to lakes and/or the sea.

4. PRELIMINARY RESULTS

Since some of the calculations have not been finished only some kriging results are presented here.

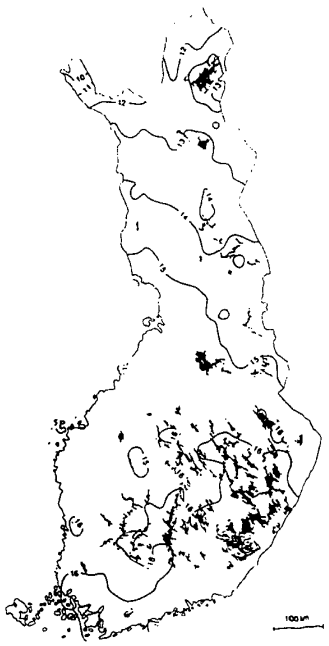


Figure 4. July mean temperature for the normal period 1961-1990 (Heikinheimo & Hellsten, 1995)

According to Fig. 4 the effect of the lakes can be seen especially in the Southeastern Finland. In Northern Finland the isotherms reflect mainly topographical features.

References

Heikinheimo, M. and E. Hellsten, 1995: Personal communication.

Gandin, L.S., 1965: Objective Analysis of Meteorological Fields. Jerusalem: Israel Program for Scientific Translations.

Henttonen, Helena, 1991: Kriging in interpolating July mean temperatures and precipitation sums. Reports from the Department of Statistics, University of Jyväskylä, 12/1991, Jyväskylä, Finland.

Ripley, Brian D., 1981: Spatial Statistics. John Wiley & Sons, New York City, NY, USA.

ACKNOWLEDGEMENTS

The assistance of Eino Hellsten, Finnish Meteorological Institute, Helsinki, Finland, in preparing this paper is gratefully acknowledged.

CORRESPONDING AUTHOR

Jaakko Helminen
Finnish Meteorological Institute
P.O.Box 503
FIN-00101 Helsinki
Finland

OBJECTIVE ANALYSIS USING A HIERARCHY OF CLIMATE FEATURES

Albert R. Boehm
Hughes STX Corporation

ABSTRACT
Current objective analysis methods - optimal interpolation, Barns interpolation, Cressman interpolation, smoothing splines, and Kriging - are founded on a continuous field and a correlation structure that falls off in space and/or time. The atmosphere has, on occasion, very sharp gradients that separate one statistically similar region from another. These separations occur at all scales in time and space. A number of statistical procedures are available to effectively analyze this type of structure.

1 TYPES OF STRUCTURE

Objective analysis is the automated numerical specification of a field given some measurements of the field. In general, a field can be quite complicated indeed, but here attention is focused on atmospheric fields such as the spatial variation of wind or the vertical variation of temperature as a function of time. Automated means that the computation is done with little or no human intervention except, of course, in the development of the method.

Continuous Variables

A great number of schemes have been developed and successfully used for objective analysis of the atmosphere. These include optimal interpolation, Barns interpolation, Cressman interpolation, smoothing splines, and Kriging all of which are well described in Thiebaux and Pedder (1987). Smoothing splines and Kriging have been compared recently by Laslett (1994). These methods are founded on a continuous field and a correlation structure that is high for nearby points but lower for more distant points. Figure 1 provides a conceptual motivation for these objective analysis methods.

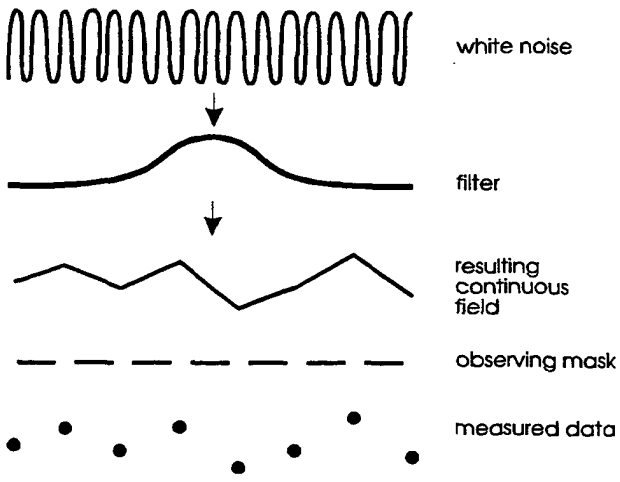


Figure 1. Conceptual generation of measurements of a continuous variable

Discrete Variables

But let us consider another analysis problem. Suppose we are viewing a parking lot with some vehicles on it, and we want to know how many there are, their size, and the model type, e.g. car, truck, van, of each vehicle. The concept is illustrated in figure 2 if we desire to know the height, width and location of each entity.

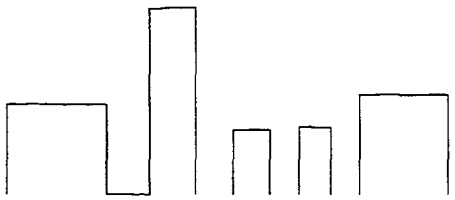


Figure 2. A set of discrete internally uniform objects

The above mentioned objective analyses are not suited for such an analysis. But consider a cloud analysis. Is not this situation closer to the concept portrayed in figure 2 than that in figure 1?

Correlation Structure

The fundamental difference between the two concepts is that in figure 1 the variable is continuous while in figure 2 the variable has jumps or discontinuities. Which is more appropriate for the atmosphere? A clue is found in the observed correlation structure. Correlation as a function of separation distance for a continuous variable must have a zero derivative at zero separation. This shape is often found in empirical correlation (Bertoni and Lund, 1964) of such things as pressure heights or temperatures aloft.

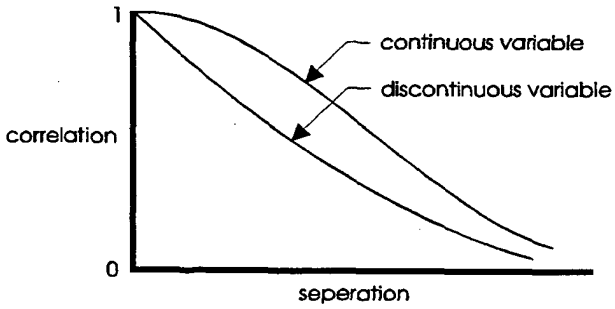


Figure 3. The slope at the origin indicates the fundamental difference between a correlation structure for a continuous versus a discontinuous variable

On the other hand, the correlation curve for a discontinuous function has a non-zero derivative at zero separation. This type of correlation has been found in the spatial analysis of clouds and surface temperature (Bertoni and Lund, 1964) and in the temporal analysis of most surface variables such as visibility, wind speed, and ceilings.

The effect of measuring a smoothed variable is worth considering. Suppose in our parking lot analysis we were viewing from a great distance and could only measure the mean value over a 10 meter disk. If the parking lot was black and all the vehicles were white and none wider than 5 meters and none further apart than 9 meters, than no 10 meter disk would contain all black or all white. All we

would measure is shades of gray. Further, the shade of gray would be a continuous function. A smoothing process has converted a discontinuous function into a continuous function.

Hierarchical Domains with Diverse Boundaries

In figure 4 the structure contains domains which contain statistical structure that is similar within a domain but is measurably different from statistical structure in (most) other domains. The boundary between domains may be very sharp, effectively a discontinuity, or it may consist of a gradual change from one domain to the next. Note that each domain consists of an aggregation of smaller scale domains each with the basic properties of internal statistical similarity and sharp or gradual boundaries.

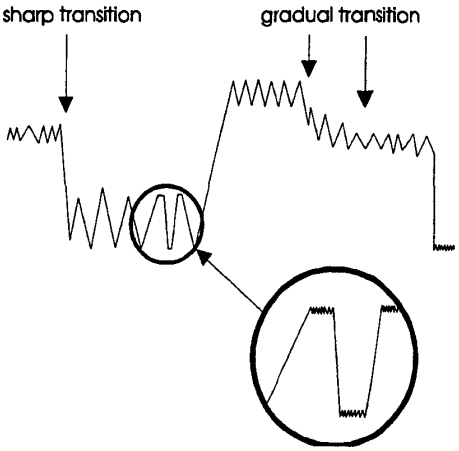


Figure 4. Hierarchical domains each with nearly homogeneous statistical structure but with varying degrees of transition

This structure was postulated after observing many cloud fields. The structure in one area tends to be very similar while the structure in another area is quite different. By similar is meant that if a small section of a domain is compared with another small section of the same domain, the human eye or just about any statistical measurement such as correlation structure, distribution of cloud size or distances between clouds show a similarity but if compared to another domain, the small sections appear to be quite different even in adjacent domains.

There is the case where a section from a domain is similar to a section in another domain that is far away in space or time. But it is perhaps worth recording the impression that like snowflakes, no two clouds nor cloud fields are exactly alike.

Discontinuities in the Atmosphere?

Many sharp boundaries are observed in the atmosphere. These are observed at all scales and include fast moving cold fronts, mirage-producing inversions, cloud or not, and shock waves. Whether these are true mathematical discontinuities has important theoretical fluid mechanics implications. From a practical point of view, the fact that there is at least very high gradients is sufficient to model discrete objects.

2 HEFeS

HEFeS (Hierarchical Environmental Feature Structure) consists of a hierarchy of objects - weather features - that correspond to the different scales of motion found in the atmosphere. Here a distinction is made between an atmospheric physical feature and an object which is the computer representation of the feature. An introduction to HEFeS is found in Boehm (1994). Here only the motivation for using HEFeS is presented along with an illustrative example.

HEFeS was initially set up to provide realistic environmental effects in training and other types of simulation. It was only when devising the selection process that it was realized that there was an objective analysis application.

Scales of Propagation

Meteorologists have for many years divided atmospheric motion into various scales - since the importance of various forces in the equations of motion vary depending on what size (scale of motion) they are applied to. The Coriolus force caused by the spin of the earth is a major factor in causing the high and low pressure systems seen on a synoptic weather map. On the other hand, the Coriolus force is negligible in describing dust devils.

Thus in analyzing various scales of motion, although there are similarities, there are also significant differences particularly with respect to the measuring sensor.

Consider remote sensing. A meteorological satellite Infrared sensor may have a beam width of 3 km or more at the height of the clouds. A high resolution surface based infrared sensor may have a beam width of less than 5 meters when looking at the same cloud. What they see will not have the same emissivity nor structure. If both measurements are to be used in the same analysis or if one is used to validate the other, the scale of structure that they each measure must be known.

HEFeS Objects

HEFeS specifies objects at various scales - a cascade of objects as shown in Table 1.

TABLE 1. HEFeS object classes

OBJECT CLASS	TYPICAL SIZE	TYPICAL TIME	EXAMPLE
Climate regime	global	1 month	hot summer
planetary wave	5000km	1 week	zonal jet
synoptic feature	1000km	3 days	cold front
meso feature	100km	12 hours	squall line
cluster	1km	1 hour	cloud cluster
cell	30m	10 min.	cloud cell
sheet	5m	5 min	rain streamer
voxel	1m	1 min	droplet dist.
Particle	1mm	30 sec	single droplet

For a given simulation, a master HEFeS object is selected. This is usually climate regime. An example of a climate regime is {very cold winter}. A more complicated climate regime is {warm winter followed by an early spring}. All other objects are subordinate to the master object and must be consistent with it. Each sub-object must be consistent with its parent object. Rain virga is prohibited from being attached to a clear sky object. In the selection process these prohibitions are enforced by object conditional probability. A zero probability completely prohibits a sub-object while high probability facilitates the likelihood of a sub-object being attached.

3 OBJECTIVE ANALYSIS USING OBJECTS

Objects have a history of use in objective analysis. Lund's (1963) map typing method selects a type given a pressure field. Analog methods, particularly analog methods that designate a set of proto types are a form of objective analysis. Even the Bergeron air mass analysis (Berry et al. 1945) may be considered a type of objective analysis. However, these methods are more in line with the concepts of figure 2, that is, they are founded on a distinct set of types.

A number of more modern schemes have been developed to extend this concept. The problem has two parts. The first is to define a set of potential objects. The second is given a set of measurements, from what object do they most likely come.

Informative Priors

Frigessi and Stander (1994) present a method of classification using satellite images. They formalize the concepts of figure 2 by defining spatial homogeneity. They define each point in a scene as belonging to one of many homogeneous regions. Posing the problem in a Bayesian framework allows not only a classification, but also the probability of belonging to a given region. The application is agricultural not meteorological. However, the fundamental problem is nearly the same.

Hierarchical Templates

A model more like that of the concepts of hierarchical domains with diverse boundaries has been described by Phillips and Smith (1994). They use stochastically deformable templates for objects in the underlying image scenes. Their application is capturing of facial features for compressed image transmission for teleconference etc. over low bandwidth communications. Being able to recognize a face from different angles seems a little remote from meteorology, but consider recognizing a cloud field given different satellite views.

Climatological Spatial-Temporal Modeling

An application of interest to climate change investigators is the work of Handcock and Wallis (1994). They used kriging within a Bayesian framework to obtain a posterior distribution to calibrate temperature shifts. This method defines a theoretical model of specifying smoothness and variance within a field. While this particular work focuses on long-term change, the statistical concepts are just as applicable to small scale change. That is, where does one domain end and another start.

Wavelets And The Haar Function

Wavelet theory has the potential to provide powerful new techniques for nonparametric inference (Antoniadis et al., 1994). Wavelets are a set of functions that can be fitted to data. In particular, they can represent data that has intrinsically local properties. They can be used to find edges or boundaries. Serrano et al. (1992) used wavelets for climatic estimates. Haar functions, a form of wavelets, have been used to detect climate change (Howell and Mahrt, 1993).

Categorized Regression - CART

Classification And Regression Trees (CART) is a simplified neural net using only binary decisions (Breiman et al, 1984). It produces a tree of binary decisions using binary regression at each stage. CART is quite robust and in addition its decision tree can be displayed graphically to help understanding.

Neural Networks

Neural networks provide a very flexible statistical method of categorizing data. However, their very flexibility is part of the problem when applied to atmospheric data. Neural nets require a large amount of data when applied to multidimensional problems. Perlovsky (1991) has improved the data efficiency of neural nets by adding logical subjectively determined sub models as preprocessors. The sub models do not have to be perfect nor exhaustive since the statistical fitting of the neural nets take defects into account. Results with tracking algorithms have been impressive. The equivalent sub models in the current application are the various scaled climate objects.

4. HIERARCHICAL ANALYSIS

There are four analysis topics that feature analysis attempts to cover: sharp boundaries, pattern identification, multiple dependent variables, and hierarchical structure. The above methods address the first three of these topics; hierarchical structure requires a different kind of analysis.

One of the more famous hierarchies is the biological taxonomy classifying each living thing into species, genus, etc. This kind of hierarchy consists of exclusive categories at all levels and results in a tree structure where each small branch belongs to one and only one larger branch.

Weather, on the other hand, tends to have many sub categories that can be assigned to more than one higher scale category. Rain can result from upslope advection or from convective activity. But the observation - rain - does not make the distinction. Consequently, subcategories are found to belong to more than one category.

However, given a sub category, not all categories have the same probability. Thus, this hierarchical structure is defined by a series of scale sizes each with a set of features at that scale and with the features at one scale size related to the next higher and next lower scale size by conditional probability.

Quantitative Attributes

HEFeS features are not just a selection from a set of classes. They are variable in size and shape and have quantitative attributes such as temperature and pressure. Each feature has a climatic distribution of these variables assigned to it. Thus, while a temperature of 35 degrees may be possible in several features, it is usually more probable in one of the features.

Specifying The Hierarchy

First the sets in the hierarchy must be specified. The levels themselves are more or less subjective but based on considerable meteorological experience and literature.

At each level, specifying a rich enough set of features to cover nearly all possibilities is not a simple chore. Rather then try to find the optimal set of features, an extensible strategy is employed. First a reasonable set of features is specified. Observed patterns are classified. When an observed pattern can not be adequately represented by the current feature sets, a new feature is added. Often a reduced set is adequate for a given task.

The foundation for a set of features is not unique. At the cloud feature level for example, the standard cumulus, stratus, etc. designations can be used. However, a completely different categorization can be based simply on specific humidity, turbulence, and height.

Feature Selection

Given a set of observations, O_i, i=1 to n, what is the most probable feature, F_{max}, out of a set of features, F_j, j=1 to m? There are two degrees of complexity. The simpler case is when all observations are of the same scale and higher and lower feature scales are either known or can be ignored. The more general case considers observations of different scales.

For the single scale case, the probability of each category requires an analysis analogous to objective analysis of a scalar. Probability is the dependent variable, and the conditional probability of an observation given another observation is equivalent to the variance functions use in optimal interpolation.

One way to analyze a multi-scale case is to use multiple versions of the single scale case but varying them according to the possible features of a different scale.

These procedures sound quite complicated, and in the general case they are. However, when applied to a specific problem such as what is the height of the tropopause or where is the cold front, simple solutions are possible; even straightforward.

5 SUMMARY

The atmosphere has numerous sharp gradients if not discontinuities. Current operational objective analysis methods presuppose a continuous atmosphere. A different view of the atmosphere is that it consists of features that may have sharp or gradual boundaries. A number of statistical methods are available to analyze this type of atmosphere.

REFERENCES

Antoniadis, A., Gregoire, G., and Mckreague, I.W., 1994: "Wavelet Methods For Curve Estimation", *Journal ot the American Statistical Association*, 89, 1340-1353.

Bertoni, E.A., and Lund, I.A., 1964: *Winter Space Correlation Of Pressure, Temperature and Density to 16km*, Environ. Res. Pap., No. 75, AFCRL-64-1020, NTIS AD 611-002.

Berry, F.A., and Bollay, E., 1945: "Air Masses", *Handbook Of Meteorology*, McGraw-Hill Book Co., New York, 604-637.

Boehm, A.R., 1994: *Introduction To HEFeS (Hierarchical Environmental Feature Simulator)* , PL-TR-94-2013, Phillips Lab., Directorate of Geophysics, Hanscom AFB, MA, AD A283 244/2/DDM.

Breiman, L., Freidman, J.H., Olshen, R.A., Stone, C.J., 1984: *Classification and Regression Trees*, Wadsworth & Brooks/Cole Advanced Books & Software, Pacific Grove, CA, 358p.

Frigessi, A. and Stander, J., 1994: "Informative Priors For The Bayesian Classification of Satellite Images", *Journal of The American Statistical Association*, 89, 703-709.

Handcock, M.S., and Wallis, J.r., 1994: "An Approach to Statistical Spatial-Temporal Modeling of Meteorological Fields", *Journal of The American Statistical Association*, 89, 368-378.

Howell, J. and Mahrt, L., 1993: "Haar Filters For Signals With Embedded Rapid Changes", *Eighth Conference On Applied Climatology*, Amer. Meteor. Soc., Boston, 112-115.

Laslett, G. M., 1994: "Kriging and Splines: An Empirical Comparison of Their Predictive Performance in Some Applications", *Journal of the American Statistical Association*, 89, 391-400.

Lund, I.A., 1963: "Map-Pattern Classification by Statistical Methods", *J. Appl. Meteor.*, 2, 56-65.

Perlovsky, L.I. and McManus, M.M., 1991: "Maximum Likelihood Neural Networks For Sensor Fusion and Adaptive Classification", *Neural Networks*, 4, 89-102.

Phillips, D.B., and Smith, A.F.M., 1994: " Bayesian Faces Via Hierarchical Template Modeling", *Journal of The American Statistical association*, 89, 1151-1163.

Serrano, E., Compagnucci, R., and Fabio, M., 1992: "The Use of the Wavelet Transform For Climatic Estimates", *5th International Meeting On Statistical Climatology*, Atmospheric Environment Service, Toronto, Canada.

Thiebaux, H. J., and Pedder, M. A., 1987: *Spatial Objective Analysis: with applications in atmospheric science*, Academic Press, London.

ACKNOWLEDGMENTS

This research was sponsored by the Phillips Laboratory, Geophysics Directorate under contract F19628-93-C-0051 with Donald D. Grantham as contract monitor. Additional Support was provided by the US Army Space and Strategic Defense Command with Charles LaMar as project leader.

CORRESPONDING AUTHOR

Albert Boehm

109 Massachusetts Ave., Lexington, MA 02173 USA

Spatial interpolation of rainfall statistics at different time scales

L. Guenni
Universidad Simón Bolívar, Caracas, Venezuela

ABSTRACT

Ten years of common records for 25 stations in Guárico state, Venezuela, were used to spatially interpolate mean and total rainfall for different time scales (annual, quarterly, monthly and 10-day periods). Thin plate smoothing splines were used in the interpolation procedure in different ways: by considering rainfall statistics as dependent on latitude and longitude only, as well as considering dependencies on elevation. For rainfall means, elevation is essential to assure reduced surfaces error estimates. For total rainfall, separation of signal from noise is difficult for data too spatially skewed and short time scales.

1.INTRODUCTION

Spatial estimation of rainfall data in locations without measurement records has always been an important problem in hydrology and climatology. Thin plate smoothing splines (Wahba,1990; Hutchinson,1991,1994) have been succesfully used to interpolate mean rainfall values including the effects of topography. The spatial interpolation of rainfall means is a very different problem from the spatial interpolation of actual rainfall totals for a particular time period. In the first case, the error estimates of the data model consider the year to year variability in adition to defficiencies in the model. In the second case, only deficiencies in the model are considered, and the measurement errors which are usually unknown, are included in this error estimate in both cases. In this paper, spatial interpolation of mean rainfall values and actual rainfall totals at different time scales (annual, quarterly, monthly and 10-day periods) is carried out by thin plate smoothing splines, firstly, independently of elevation; secondly, with two different dependencies on elevation: a spline function of position and a varying dependence on elevation and, a spline function of position with a linear parametric dependence on elevation. Twenty five stations from Guárico state at the central plains of Venezuela were used to analize the different error estimates of the interpolation technique for mean and total rainfall at different time scales and dependencies on elevation.

Mean Rainfall		Total Rainfall	
Period	Mean	Period	$\lvert Skewness \rvert$
Annual			
Annual	1103.45	Year 1972 (h)	1.7736
		Year 1976 (l)	0.3829
Quarterly			
1st Quarter	36.03	1st Quarter (h) 1976	4.0124
3rd Quarter	506.32	3rd Quarter (l) 1972	0.0335
Monthly			
March	8.71	March (h) 1971	4.2087
July	187.50	August (l) 1972	0.0008
10-day periods			
8th period	1.5270	9th period (h) 1978	4.2087
21st period	66.16	22nd period (l) 1972	0.0543

Table 1: Selected periods for the spatial interpolation mean and total rainfall values
h = highest skewness coefficient; l = lowest skewness coefficient

2. DATA ANALYSIS

The elevation stations varied from around 80 to 980 meters above sea level with a clear gradient in precipitation which decreases from the northern part of the state located at the central mountain range, towards the southern part of the state where the lowland areas or "llanos" are dominant.

Ten common but non-contiguous years of data were selected for each station from the period 1967-1982. Data quality restrictions determined the selection of non-contiguous years. There is a very distinctive seasonal pattern for all the stations in the region with a rainy season from May to September and a dry season from October to April. The state has an area

of about 65,000 km^2 with a lower density of stations in the south-east part of the state. For each station, the following statistics were calculated: mean annual rainfall, mean quarterly rainfall, mean monthly rainfall and mean 10-day accumulated rainfall. For each location i, the mean variance estimate, σ_i^2/n_i was calculated, where σ_i^2 is the variance of the corresponding rainfall statistic at location i and n_i is the number of years of records. For each time scale, periods with the highest and lowest mean rainfall were selected for interpolation. For the actual rainfall totals, the spatial skewness coefficient was calculated with data from all stations with total rainfall for a particular period. It is assumed that actual rainfall values for periods with high skewness coefficient will be more difficult to interpolate than stations with low skewness (in absolute value) coefficient . A period with actual rainfall values with the highest and the lowest skewness coefficient was selected for annual, quarterly, monthly and 10-day rainfall totals. In Table 1, the selected periods for each time scale are present for mean rainfall values and actual rainfall values. Seven mean rainfall statistics and 8 actual rainfall totals were selected for interpolation. If the total number of 10-day periods were to be interpolated for 10 years of data, 360 surfaces had to be produced for this data set.

3.DESCRIPTION OF THE SPATIAL INTERPOLATION PROCEDURE

Thin plate smoothing splines have been described extensively by Wahba(1990) and Hutchinson(1995). Let $z(x_i)$ n data values located at position x_i such that:

$$z(x_i) = f(x_i) + \varepsilon_i, \quad i = 1, \ldots, n \qquad (1)$$

where $f(x_i)$ is a continuous and unknown function to be estimated from the data points and ε_i are the error terms which are usually assumed independent with zero mean and variance $\sigma_i^2\sigma^2$, where σ_i^2 is the local variance at each point and σ^2 is a common variance usually unknown. x_i are the coordinates representing the space (for example, longitude, latitude and elevation). The z_i are estimated by a suitable smooth function g which minimizes:

$$(z-g)^T V^{-1}(z-g) + \rho J_m(g) \qquad (2)$$

where $g = (g((x_1), \ldots, g(x_n))^T$, $z = (z(x_1), \ldots, z(x_n))^T$; V is a diagonal matrix with components $\{v_{ii}\} = \sigma_i^2$ and $J_m(g)$ is a measure of the roughness of the function g defined in terms of the mth order partial derivatives of g. The parameter ρ is the smoothing parameter which is usually estimated by minimising the Generalized Cross Validation (GCV). This is a measure of the predictive error of the surface calculated by leaving out each data point in turn and estimating the mean square residuals between the observed data points and the fitted values estimated by using the remaining data points.

In a similar fashion to linear regression the vector estimates of z (g) can be calculated as Az where A is the influence matrix. The value of ρ can be calculated by minimising an implicit GCV estimate given by Craven and Wahba (1979):

$$\frac{(z-Az)^T V^{-1}(z-Az)/n}{[trace(I-A)/n]^2} \qquad (3)$$

The trace of $(I-A)$, where I is the identity matrix, may be interpreted as the degrees of freedom of the residual sum of squares given by the first term of (2). Two extreme cases can occur during the interpolation procedure: if trace of $(I-A)$ is zero, the interpolation procedure is exact and there is no smoothing. ($\rho = 0$ in (2)). On another hand, if trace of $(I-A)$ is equal to $n - n_1$ with $n_1 = (dim(x_i) + 1)$ ($dim(x_i)$ is the space dimension of the vector of independent variables x_i), we get the maximum degree of smoothing and the fitted surface is a plane in R^{n_1} ($\rho = \infty$ in (2)). In both cases there is an unrealistic situation. The trace of $(I-A)$ is a useful diagnostics tool and it is expected to exceed $n/2$, if the data are not too sparse to support spline smoothing (Hutchinson and Gessler, 1994). The error variance estimate ($\hat{\sigma}^2$) is given by:

$$\hat{\sigma}^2 = \frac{(z-Az)^T V^{-1}(z-Az)}{trace(I-A)} \qquad (4)$$

If trace of $(I-A)$ is less than $n/2$ the GCV would be greater than $2\hat{\sigma}^2$

Partial thin plate splines

It is posible to incorporate linear sub-models within the splines framework in order to determine empirical lapse rates. In this case:

$$z_i = f(x_i) + \sum_{j=1}^{p} \beta_j \psi_j(x_i) + \varepsilon_i$$

where $i = 1, \ldots, n$, f is an unknown but smooth function which will be estimated, ψ_j is a set of known functions and β_j are coefficients to be estimated. ε_i are defined as before. If x_i represents for example, latitude and longitude and $\psi_1(x_i) = h_i$ where h_i represents the elevation at location i, the model:

$$z_i = f(x_i) + \beta_1 * h_i + \varepsilon_i \qquad (5)$$

assumes a constant dependence rate of z_i with respect to elevation overimposed on the 2-dimensional spline function $f(x_i)$ and β_1 is the gradient with respect to h_i.

4.RESULTS

The fifteen variables described in Table 1, were interpolated with thin plate smoothing splines by using the algorithm developed by Hutchinson (1989) in three different ways:

- As a function of longitude and latitude only (bivariate thin plate spline (2D))
- As a function of longitude, latitude and elevation (tri-variate thin plate splines (3D)).
- A bi-variate spline as function of longitude and latitude and a constant linear dependence on elevation (partial thin plate splines (3DP))

In all cases longitude and latitude are in degrees and elevation in kms.

Interpolation of rainfall means

For the interpolation of rainfall means, the components of the diagonal matrix $V(\{v_{ii}\})$ to minimize (2) were estimated as s_i^2/n_i, where s_i^2 is the variance estimate of the rainfall variable at location i and n_i is the number of years of records. This value represents the local relative variance at each point. The residual degrees of freedom, the square root of the GCV and the estimated error standard deviation (square root of values given by (4)) are presented in Table 2 for some of the variables described in Table 1, which correspond with the periods with the highest rainfall means. In all cases the tri-variate splines had the best performance with a lower square root of the GCV values and a lower standard deviation of the residuals than in the other cases. For mean July rainfall with tri-variate splines, the residual degrees of freedom (4.4) is much less than $n/2$ (12.5) and the predictive error of the surface as given by RGCV outweighs the standard deviation of the surface errors by a factor greater than 2. While for annualy to monthly mean data, the predictive error of the surface is between 7-9% of the rainfall mean for all stations, for 10-day periods the errors increased up to 16% of the corresponding rainfall mean. For the driest periods, this gets even worst (values not shown), with predictive errors greater than 50% of the rainfall mean even for the best interpolated surfaces. For the driest month, a tri-variate spline produced an exact interpolation which is an unrealistic result. For the driest 10-day period the data did not support the spline interpolation, and a plane was fitted to the data set in each case. It is evident that a varying dependence on elevation should be included in the model for annual, quarterly, and monthly mean values during the wet season. This result agrees with the results reported by Hutchinson (1995) for mean annual rainfall for an australian location.

Period	Type	Res. df	$\hat{\sigma}$	RGCV
Annual	2D	15.2	134.56	173.0
	3D	10.7	62.83	95.7
	3DP	16.9	90.83	110.0
3rd Quarter	2D	19.2	55.68	63.7
	3D	10.1	24.9	39.1
	3DP	18.1	35.02	41.1
July	2D	22.0	27.44	29.2
	3D	4.4	6.566	15.6
	3DP	21.0	16.68	18.2
21st 10-day period	2D	22.0	15.12	16.1
	3D	12.2	7.32	10.5
	3DP	18.5	10.84	12.6

Table 2: Error estimates of the interpolation of rainfall means
Res. df: Residual degrees of freedom; $\hat{\sigma}$: Square root of values given by eq. (4); RGCV: Square root of GCV

Interpolation of rainfall totals

For the interpolation of rainfall totals, the components of the diagonal matrix $V(\{v_{ii}\})$ were set to 1.0 for all data points. The results are presented in Table 3 for selected annual and monthly totals as indicated in Table 1. For both time scales, rainfall totals with high spatial skewness coefficient and low spatial skewness coefficients are presented for comparisons. The annual total mean for all stations with high and low spatial skewness are 929.14 mm and 972.23 mm respectively. The corresponding values for monthly totals are 2.78 mm and 105.83 mm. It is observed that periods with lower spatial skewness coefficients are better interpolated than periods which are highly nonsymmetryc in space. The former case is usually associated with periods with higher rainfall means. However the predictive errors of the fitted surfaces increase when the time scale decreases, going from 16% of the station mean for total annual values to 39% of the station mean for the 10-day total values. For periods with high spatial skewness, predictive errors are considerably high (more than 100% of the mean for all stations for quarterly and monthly totals) while for annual values errors are 16% of

Period	Type	Res. df	$\hat{\sigma}$	RGCV
	2D	19.6	199.0	223.0
Year	3D	5.1	67.2	149
1972(h)	3DP	16.9	161.0	181.0
	2D	8.3	116.0	198.0
Year	3D	14.5	121.0	155.0
1976(l)	3DP	17.5	138.0	162.0
	2D	22.0	7.31	7.79
March,	3D	0	0.0	3.61
1971(h)	3DP	21.0	6.92	7.55
	2D	21.3	38.8	35.6
August,	3D	4.8	14.8	33.8
1972(l)	3DP	20.3	33.5	37.2

Table 3: Error estimates of the interpolation of rainfall means
Res. df: Residual degrees of freedom; $\hat{\sigma}$: Square root of values given by eq. (4); RGCV: Square root of GCV h = highest skewness coefficient.; l = lowest skewness coefficient

the station mean. With highly non-symmetric data in space, the interpolation procedure produces an exact interpolation condition ($\rho = 0$) for quarterly, monthly and 10-day periods data when using a tri-variate spline. For the same time scales, the technique is unable to cope with small local scale variation and produces the second degenerated case ($\rho = \infty$) for bi-variate and partial thin plate splines. In this case signal dectection is limited by data sparsity and the low number of stations.

5. CONCLUSION

The ability of splines to separate signal from noise in order to determine the spatial variation of different rainfall statistics has been demonstrated. This separation is possible in an efficient way for mean rainfall values at different time scales varying from annual to 10-day periods, even for a low to moderate number of stations. Including a spatially variant dependence on elevation is essential for this task. However, as expected, surface predictive errors increased when the time scale decreased. For drier periods, the signal to noise identification becomes more difficult due to small scale variations undetected by the data set or due to the data sparsity. A more difficult problem is the spatial interpolation af actual rainfall totals, specially for time periods in which the data are highly non-symmetric in space. Although spatial interpolation of rainfall totals for lower time scales than accumulated 10-day periods were not attempted, it is expected that the signal to noise separation will be a difficult task, specially if the number and spatial distribution of stations is not adequate. However it is possible to fit point stochastic rainfall models to the existing rainfall stations at a daily time step whose parameters are more spatially coherent than the raw rainfall totals and could be more easily interpolated. An example of this methodology have been presented by Guenni (1991).

References

Craven, P. and Wahba, G., 1979, "Smoothing noisy data with spline functions", Numerische Mathematik, Volume 31, pp. 377-403.

Guenni. L., 1991, "Seasonal and spatial variability of weather patterns for crop model applications", PhD thesis, Griffith University, Brisbane, Australia.

Hutchinson, M.F., 1984, "Some surface fitting and contouring programs for noisy data", Consulting report ACT 84/6. CSIRO Divison of Mathematics and Statistics, Canberra.

Hutchinson, M.F., 1991, "The application of thin plate smoothing splines to continent-wide data assimilation", J.D. Jasper(Ed.), Data Assimilation Systems, BMRC Res. Rep. No. 27, Bureau of Meteorology, Melbourne, pp. 104-107.

Hutchinson, M.F., 1995, "Interpolating mean rainfall using thin plate smoothing splines", International Journal of Geographic Information Systems, (in press).

Hutchinson, M.F. and Gessler, P.E., 1994, "Splines-more than just a smooth interpolator", Geoderma, Volume 62, pp. 45-67.

Wahba, G., 1990, "Spline models for observational data", CBMS-NSF Regional Conference Series in Applied Mathematics. SIAM, Philadelphia.

ACKNOWLEDGEMENTS

I wish to thank Dr. Mike Hutchinson, from CRES, Australian National University, Australia, and Prof. András Bárdossy, from University of Stuttgart, Germany, for useful discussions and suggestions.

CORRESPONDING AUTHOR

Lelys Guenni
Universidad Simón Bolívar Departamento de Matematicas Puras y Aplicadas Centro de Estadística y Software Matemático APDO. 89.000. Caracas 1080-A Venezuela
email: lbravo@cesma.usb.ve.

CORRECTION OF SOLID PRECIPITATION

H. Madsen

The Danish Meteorological Institute, Copenhagen, Denmark

ABSTRACT

The measured amount of precipitation is underestimated compared to the precipitation falling on the ground. The losses in precipitation amount are particularly large for snowfall, and this is mainly due to aerodynamic effects and depends primarily on wind speed. However, the aerodynamic effect also depends on the temperature, since this effect depends on the shape of the snow flakes, which is again dependant on temperature.

A statistical model for describing this systematic error in precipitation measurements has been developed. The model is based on 12 hour measurements of snowfall and wind speed and temperature during precipitation from an experimental field in Finland. Corrections due to snow for the Hellmann raingauge are presented. Further, the statistical errors on the corrections are estimated.

1 INTRODUCTION

Numerous national and regional studies have been conducted to assess and quantify precipitation (particularly solid precipitation) measurement errors. Hamon (1973), Goodison (1978), Sevruk (1983). Tammelin (1984), Aune and Førland (1985) and Allerup, Madsen and Vejen (1995) have described methods for correcting solid precipitation considering wind speed and temperature during snowfall.

In 1985 the Commission for Instruments and Methods of Observation of the World Meteorological Organization (WMO/CIMO) decided, that an international comparison of measuring solid precipitation should be conducted. In the light of this a Nordic field comparison was organized in Finland. The comparisons were carried out from 1987 to 1993 and observations of solid precipitation from this period have been submitted to statistical analysis. These studies concern results from comparing the Danish raingauge Hellmann to a reference gauge.

The intercomparison field is situated at the meteorological observatory at Jokioinen (about 120 km northwest of Helsinki) on fairly flat ground surrounded by cultivated fields. The Danish raingauge is a 200 cm^2 unshielded Hellmann gauge placed with its orifice 1.5 cm above the ground. In winter the gauge is provided with a metal "snowcross" preventing the snow from blowing out of the gauge. The reference gauge DFIR is a shielded Russian Tretyakov gauge with its orifice 3.0 m above the ground and placed in the center of a double Valdai fence (see Figure 1). This double fence reduces the wind speed around the gauge rim, giving rise to a very small wind error.

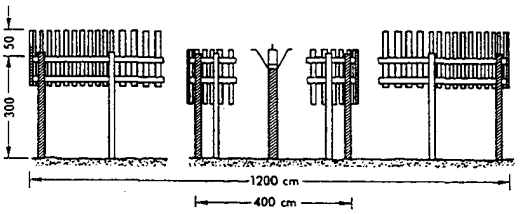


Figure 1. Shielded Tretyakov raingauge placed in the center of a double Valdai fence

For detailed studies of the precipitation an automatic gauge, the Norwegian GEONOR, is used, and this gauge is also installed in a double fence. Wind speed having been measured at seven masts at 2 m level has been reduced to precipitation gauge level (1.5 m) considering the snow depth. Further, temperature is measured.

2 DATA

For the period November 1987 - April 1993 about 300 twelve-hour values of solid precipitation ≥ 0.2 mm, measured at the Hellmann gauge and the DFIR, have been available for statistical analysis.

10 min. values are taken from the GEONOR to calculate the duration of precipitation for all the twelve-hour values, and for the same periods 10 min registrations from the wind and temperature mast are providing average values of wind speed and temperature. Furthermore, synoptic weather observations give detailed informations about

precipitation types (rain, sleet, snow etc.) Wind speed and temperature are calculated as mean values for periods when precipitation have occured.

3 RESULTS

The essential systematic errors in precipitation measurements are due to aerodynamic effect and wetting loss, the first mentioned being by far the most significant factor. Wetting loss is owing to adhesion from the bottom and inner walls of the raingauge, which will influence the measured amount of precipitation. However, these amounts are resulting from weighing, thus wetting errors are excluded.

The general model for correction of systematic errors in precipitation measurements (Nordic Working Group for Precipitation (NWGP) (1995)) is

$$P_c = k(P_m + \Sigma\Delta P_{im}) \qquad (1)$$

where P_m is the measured amount of precipitation, P_c is the corrected or "true" amount, $\Sigma\Delta P_{im}$ are wetting and evaporation losses and k is the correction factor for aerodynamic effect. In practice P_c is estimated as $P_r + \Sigma\Delta P_{ir}$, where P_r is precipitation measured at a reference gauge, and P_{ir} are wetting and evaporation losses. Then (1) can be expressed as

$$P_r + \Sigma\Delta P_{ir} = k(P_m + \Sigma\Delta P_{im}) \qquad (2)$$

As mentioned the precipitation values used in this analysis is a result from weighing which means, that wetting loss practically can be excluded. Further, the evaporation losses for both of the gauges (the reference (DFIR) and the Hellmann) are very small and can be neglected. Now the correction factor k can be rewritten as the ratio between weighing amounts of precipitation from the DFIR P_c and the Hellmann P_H

$$k = P_c / P_H \qquad (3)$$

Since k depends on wind speed at gauge level v_g (m/s) and temperature T (°C), data have been devided in the combinations of v_g and T classes (v_g,T) representing the range of measured wind speed and temperature. At the same time we also have insured, that every combination (v_g,T) are represented by a sufficient number of snowfall events in the interests of the subsequently statistical analysis.

In the following a stochastic correction model is tested by studying the empirical structure between twelve-hour values of solid precipitation P_c and P_H from the DFIR and the Hellmann respectively. This structure is analyzed for fixed combinations of wind speed and temperature and for each (v_g,T) combination a scatter plot of log P_c versus log P_H has been studied; one of these plots for 2.0 m/s $\leq v_g <$ 3.0 m/s and -4.0° $< T \leq$ -2.0° appears from Figure 2. This example is typical for all other (v_g,T) combinations and it is seen, what is fundamental for the following, that a linear structure emerge:

$$\log P_c = \alpha(v_g,T) + \beta(v_g,T)\log P_H \qquad (4)$$

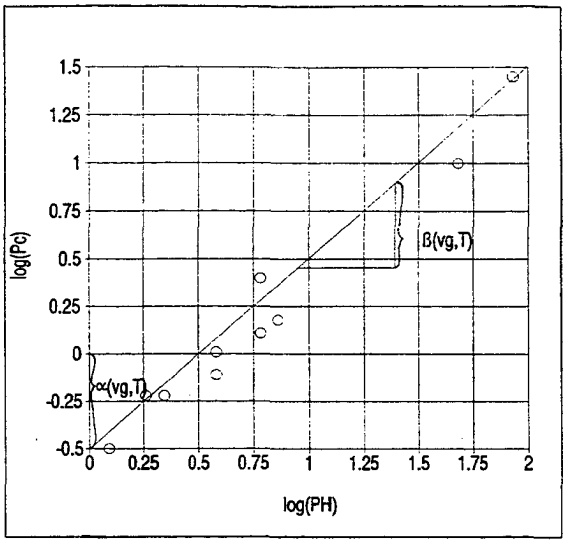


Figure 2. Scatter plot of log P_c versus log P_H

The linear relation is specified for fixed (v_g,T)-classes, and estimates of intercept α (v_g,T) and the slope ß (v_g,T) can be readily obtained through ordinary regression analysis techniques. Notice, that this linear structure is found for all (v_g,T) combinations!

The basic structure (4) was used again and more detailed studies of estimated α (v_g,T), ß (v_g,T)-values for varying wind speed (v_g) and temperature (T) led to the following hypothesis:

$$\begin{aligned} \alpha(v_g,T) &= \eta_0 + \eta_1 v_g + \eta_2 T + \eta_3 v_g T \\ \beta(v_g,T) &= \kappa_0 + \kappa_1 v_g + \kappa_2(T) \end{aligned} \qquad (5)$$

As a consequence, wind speed v_g and temperature T are now introduced explicitly in $\alpha(v_g,T)$ together with an interaction $v_g \cdot T$ between v_g and T while ß(v_g,T) is additive in wind speed v_g and temperature T leaving temperature to enter through an unknown function κ_2 (T) of temperature T.

This model specification was testet succesfully with high value of the multiple correlation R^2, and

no systematic deviations were found using the residuals.

Accepting these structures, a final, simplified model was introduced:

$$\log \frac{P_c}{P_H} = \beta_0 + \beta_1 v_g + \beta_2 T + \beta_3 v_g \cdot T = \psi(v_g, T) \quad (6)$$

$\psi(v_g, T)$ represents a simple bi-linear model using explicit values of wind speed v_g and temperature T. Notice, that model (6) for any fixed value of temperature $T = T_0$ represents the type of model traditionally applied to the differences between the reference gauge (P_c) and the Hellmann gauge (P_H); in fact $T = T_0$ provides a simple linear model depending on the wind speed v_g:

$$\log \frac{P_c}{P_H} = \tau_0(T_0) + \tau_1(T_0) \cdot v_g \quad (7)$$

where $\tau_0(T_0) = (\beta_0 + \beta_2 T_0)$ and
$\tau_1(T_0) = (\beta_1 + \beta_3 T_0)$

Consequently, a test of the bi-linear structure in the model (6) can be done by verifying (7) and estimating $\tau_0(T_0)$ and $\tau_1(T_0)$ for fixed T_0-values. The proposed linearity of $\tau_0(T_0)$ and $\tau_1(T_0)$ can then be investigated by analyzing the estimates of τ_0 and τ_1.
The test of the model structure (6) can, of course, be undertaken by a symmetric argument leading to the consequence (7) by fixing the wind speed $v_g = v_{g0}$ and obtain the following (8):

$$\log \frac{P_c}{P_H} = \delta_0(v_{g0}) + \delta_1(v_{g0}) \cdot T \quad (8)$$

where $\delta_0(v_{g0}) = (\beta_0 + \beta_1 v_{g0})$ and
$\delta_1(v_{g0}) = (\beta_2 + \beta_3 v_{g0})$

wich is a linear expression in the temperature T for given wind speed $v_g = v_{g0}$.

Both types of tests of the model (6) were applied to the data and it was concluded, that this model provides a good fit to the data.

The coefficients in the model (6) β_0, β_1, β_2 and β_3 have been estimated. Now the correction factor can be expressed as:

$$k = P_c / P_H = e^{0.04587 + 0.23677 v_g + 0.01798 T - 0.01541 v_g T} \quad (9)$$

It is seen, that this factor increases with increasing wind speed and decreasing temperature as one would expect.

The statistical error on the corrections can be stated by means of 95% confidence limits on the estimated regression function $\psi(v_g, T)$, leading to the following approximate expression $k e^{\pm 0.06}$

4 CONCLUSIONS

The wind induced errors in precipitation measurements results in systematic deficits, which are particularly large when snowfall occurs. To correct the measured precipitation due to this aerodynamic effect, a statistical model based on twelve-hours temperature has been constructed.

Finally, estimation of variances on the corrections has been done for the aerodynamic effect.

References

Allerup, P., et al., 1995. "A Comprehensive Model for Correcting Point Precipitation". (To be published).

Aune, B. and Førland, E.J., 1985. "Comparison of Nordic methods for point precipitation correction", ETH/IAHS/WMO Workshop on the correction of precipitation measurements. Zurich 1-3 April 1985.

Goodison, B.E., 1978. "Accuracy of Canadian snow measurements", J.Appl.Meteorol., 17(10), 1542-48.

Hamon, W.R., 1973. "Computing actual precipitation", WMO/OMM No. 326, Geneva.

Nordic Working Group for Precipitation, 1995. "Manual for Operational Correction of Precipitation Data". (To be published).

Sevruk, B. 1983. "Correction of measured precipitation in the Alps using the Water Equivalent of New Snow". Nordic Hydrology, 1983, 49-58.

DETERMINATION OF DROUGHT/FLOOD INDEX BY STATISTICS AND ITS APPLICATION TO EASTERN CHINA

Jinmei Shen

Department of Geo. & Atmospheric Sciences, Iowa State University, 3010 Agronomy Hall, Ames, Iowa 50011, USA

Xiaomin Dong

Jiangsu Institute of Climate Application, Nanjing 210009, PRC

ABSTRACT Based on the principle of statistics and the actual characteristics of drought/flood, we proposed a method for quantitative and objective droughts/floods index. Comparisons with the results of the previous investigations and the actual data of disasters show that this method is feasible to the quantitative, precise and objective analysis on the modes of droughts/floods occurred in the eastern China, and the proposed drought/flood index has a higher accuracy than those of previous investigators. Now, this index is being widely used in China.

1. INTRODUCTION

Drought/flood is the most severe one of natural disasters in the eastern China. The economic loss caused by drought/flood is gigantic. For example, in 1991, the economic loss in the eastern China resulted from the special great floods was millions of dollars. How to quantitatively, precisely and objectively determine the extent of drought/flood and its level is a key to reduce the economic loss. Many studies have been done on the division of the drought/flood index. However, no ideal drought /flood index is suitable to the eastern China.

In this paper, we designed a mode of drought/flood index and applied it to the eastern China by improving "Bhalme and Mooley" method (Bhalme and Mooley, 1980). According to the actual characteristics, i.e., drought/flood forms easily and transfers rapidly from drought to flood (or from flood to drought) in the eastern China, a dekad is chosen as the time scale to compute drought/flood index. Considering the similarity and difference of the climatic characteristic between the counties, we divided the eastern China into 5 subdivisions.

2. METHODOLOGY

The present study has been made using daily precipitation measurements of 60 meteorological stations in the eastern China for a period of 30 years (1961-1990). The procedures for development of our drought/flood index mode are divided into the following steps.

a. By using statistical analysis of a long record, compute the long-term (30 years) mean precipitation $\overline{X}_{i,k}$ and standard deviation $S_{i,k}$ for every station and every dekad, where i denotes the station and k is the dekad.

b. Compute the moisture index $M_{i,k,l}$ for every station and every dekad in every year. The moisture index is the precipitation anomaly weight by the reciprocal of coefficient of variation, given as

$$M_{i,k,l}=100\frac{X_{i,k,l}-\overline{X}_{i,k}}{S_{i,k}} \qquad (1)$$

where l represents the year.

c. Compute the regional dekadly moisture index $N_{J,k}$ for every year.

$$N_{J,k,l}=\frac{1}{i_0}\sum_{i=1}^{i_0} M_{i,k,l} \qquad (2)$$

where J represents the subdivision and i_0 the number of the stations in the J subdivision.

d. Rearrange the regional dekadly moisture index $N_{J,k,l}$ for every year according to its positive and negative value, and calculate its regional mean moisture index $\overline{N}_{J,k}^{(+)}$ and $\overline{N}_{J,k}^{(-)}$.

$$\overline{N}_{J,k}^{(+)}=\frac{1}{l_1}\sum_{l=1}^{l_1} N_{J,k,l} \qquad (3)$$

$$\overline{N}_{J,k}^{(-)} = \frac{1}{l_2}\sum_{l=1}^{l_2} N_{J,k,l} \qquad (4)$$

where l_1 and l_2 are the number of the year which $N_{J,k,l}$ is positive and negative, respectively.

e. Give the changes of regional mean moisture indexes $\overline{N}_{J,k}^{(+)}$ and $\overline{N}_{J,k}^{(-)}$ as a function of time (every dekad). For example, Figs.1a and 1b show the changes of $\overline{N}_{5,k}^{(+)}$ and $\overline{N}_{5,k}^{(-)}$ with time (dekad, k=1,2,...,36) in 5th subdivision.

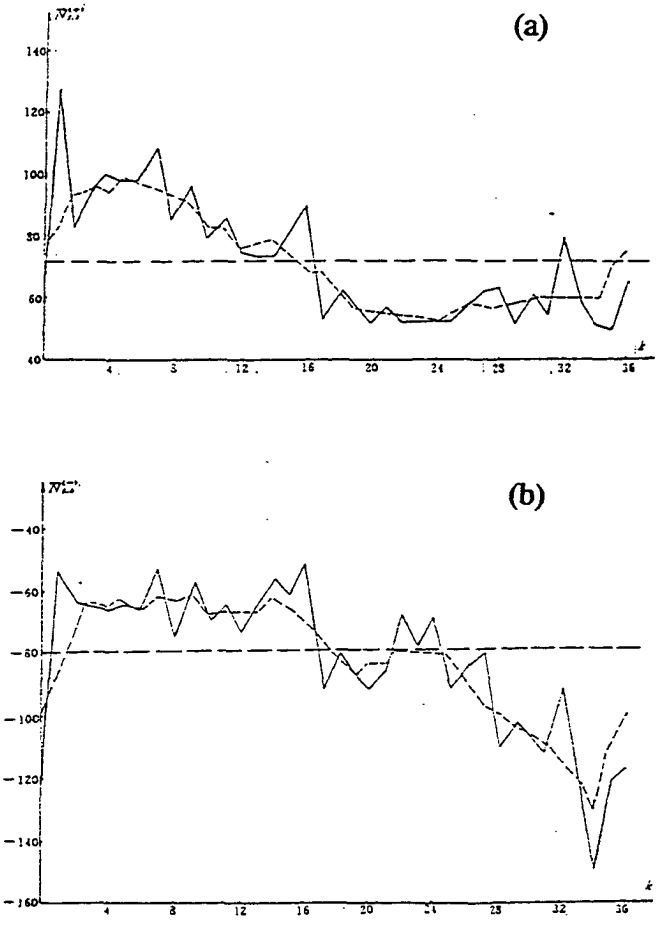


Fig.1 Changes of regional mean moisture indexes (a) $\overline{N}_{5,k}^{(+)}$ and (b) $\overline{N}_{5,k}^{(-)}$ as a function of time. Solid line: no smooth; dash line: 5 dekads smooth; and dot dash line: annual mean value.

f. According to above two curves of $\overline{N}_{J,k}^{(+)}$ and $\overline{N}_{J,k}^{(-)}$, determine the durations of flood index equation (k_1) and of drought index equation (k_2) for every subdivision (Table 1).

g. Among the value of $M_{j,k,l}$ for every subdivision and every dekad, chose the maximum positive $N_{J,k}^{(+)max}$ and the maximum negative $N_{J,k}^{(-)max}$.

h. According to the above durations of flood index equation k_1 and of drought index equation k_2, calculate the highest accumulated values of the maximum positive moisture index $N_{J,S}^{(+)}$, and the highest accumulated values of the maximum negative moisture index $N_{J,S}^{(-)}$, respectively.

$$N_{J,S}^{(+)} = \sum_{k=1}^{k_1} N_{J,k}^{(+)max}$$
$$N_{J,S}^{(-)} = \sum_{k=1}^{k_2} N_{J,k}^{(-)max} \qquad (5)$$

Table 1. The initial and last dekad of the durations of flood index equation (k_1) and of drought index equation (k_2) for 5 subdivisions in the Eastern China

Region	Flood equation		Drought equation	
	initial & last dekad	k_1	initial & last dekad	K_2
1	33-6*	10	19-32	14
	7-18	12		
2	32-15*	20	16-31	16
3	29-7*	15	8-28	21
4	27-9*	19	10-26	17
5	1-15	15	16-36	21

Note: * represents the dekad of the next year

i. By using least-square method, determine the coefficients a_1, b_1 and a_2, b_2 in equation (5), and then obtain the extreme flood line and the extreme drought line, respectively. The extreme flood line (solid line) and its corresponding the extreme drought line (dash line) are shown in Fig.2. The extreme drought line (solid line) and its corresponding the extreme flood line (dash line) are shown in Fig.3.

$$N_{J,S}^{(+)} = a_1 + b_1 ks, \quad ks = 1, 2, \ldots, k_1 \qquad (6)$$
$$N_{J,S}^{(-)} = a_2 + b_2 Ks, \quad ks = 1, 2, \ldots, k_2$$

The distance between the extreme drought line and its corresponding the extreme flood line (Figs.2 and 3) is then divided into eight equal lengths and the body of the graph is corresponding divided by six more lines, labeled severe, moderate and mild

drought, mild, moderate and severe flood, as the same as that of Bhalme and Mooley (1980). Numerical values are assigned to these lines, i.e. ± 4 for extreme flood (drought), ± 3 for severe flood (drought), ± 2 for moderate flood (drought) and ± 1 for mild extent of flood (drought). Table 2 lists the descriptive terms of the character of drought/flood represented by various intervals of the index. $I_{i,k,l}$ represents the drought/flood index.

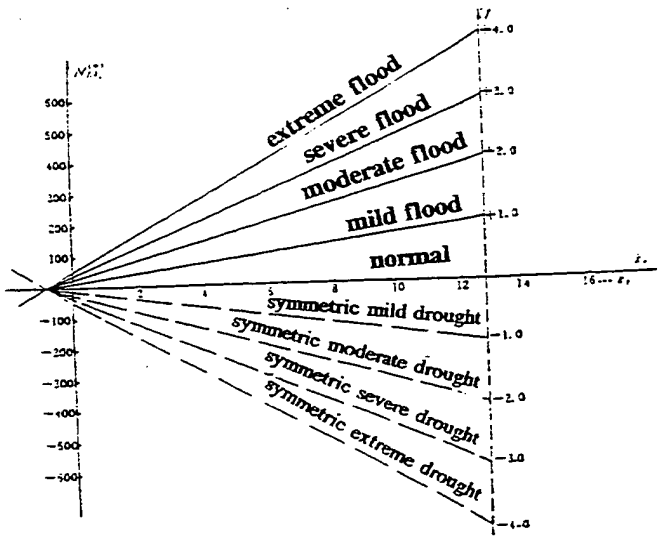


Fig.2 Extreme flood line and its symmetric extreme drought line

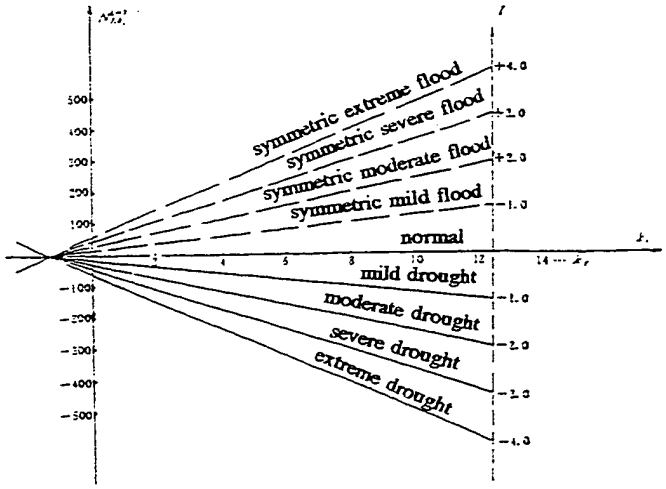


Fig.3 Extreme drought line and its symmetric extreme flood line

Table 2. Range of drought/flood index $I_{i,k,l}$ vs the extent and grade of climatic drought/flood

Index $I_{i,k,l}$	Climatic drought/flood Extent	Grade
≥ 4.00	extreme flood	4
[3.00, 3.99]	severe flood	3
[2.00, 2.99]	moderate flood	2
[1.00, 1.99]	mild flood	1
[-.99, 0.99]	normal	0
[-1.99, -1.00]	mild drought	-1
[-2.99, -2.00]	moderate drought	-2
[-3.99, -3.00]	severe drought	-3
≤ -4.00	extreme drought	-4

j. Adjust the discontinuity of drought/flood index for the transient period between drought-equation and flood-equation as well as for the adjacent subdivisions by means of temporal and spatial adjustment at the same time-step. Finally, we obtain the drought/flood index equations for every subdivision and different durations of drought and flood, as shown in Table 3, where subscript k stands for the current dekad.

Table 3. Drought/flood index $I_{i,k,l}$ model for every dekad and every subdivision in the eastern China

Region	Character	Drought/flood index $I_{i,k,l}$ mode
1	drought	$I_{i,k,l}=(M_{i,k,l}/66.47)+0.56xI_{i,k-1,l}$
	flood	$I_{i,k,l}=2.8[(M_{i,k,l}/105.92)+0.042xI_{i,k-1,l}]$
		$I_{i,k,l}=2.8[(M_{i,k,l}/110.21)+0.052xI_{i,k-1,l}]$
2	drought	$I_{i,k,l}=(M_{i,k,l}/30.8)+0.157xI_{i,k-1,l}$
	flood	$I_{i,k,l}=2.8[(M_{i,k,l}/110.04)+0.208xI_{i,k-1,l}]$
3	drought	$I_{i,k,l}=(M_{i,k,l}/34.75)+0.1xI_{i,k-1,l}$
	flood	$I_{i,k,l}=2.8[(M_{i,k,l}/107.787)+0.097xI_{i,k-1,l}]$
4	drought	$I_{i,k,l}=(M_{i,k,l}/49.97)+0.412xI_{i,k-1,l}$
	flood	$I_{i,k,l}=2.8[(M_{i,k,l}/98.31)+0.112xI_{i,k-1,l}]$
5	drought	$I_{i,k,l}=(M_{i,k,l}/43.74)+0.422xI_{i,k-1,l}$
	flood	$I_{i,k,l}=2.8[(M_{i,k,l}/85.0)+0.028xI_{i,k-1,l}]$

3. CALIBRATION AND APPLICATION IN THE EASTERN CHINA

The calibration of our computed drought/flood index $I_{i,k,l}$ with the actual data is divided into two parts: comparing with the previous investigations from 1949 to 1974 (Jiangsu Meteorological Bureau, 1975) as listed in Table 4 and the actual data of typical droughts/floods disasters occurred in the eastern China during the past 30 years as listed in Table 5. According to our comparison, we found that (1) no matter what the extent and grade of drought or flood, and the temporal and space distributions, our results have higher accuracy than the previous disaster records (Jiangsu Meteorological Bureau, 1975, hereafter JMB), (2) our results are fitted to the actual drought/flood disaster data occurred in last 30 years very well.

TABLE 4 Comparisons of two different methods for describing four typical drought/flood modes

Mode	Period Mon. Dekad	grade of $I_{i,k,l}$ North to South	JMB North to South
	Mar 1st	-1 -1	-3 -1
	2nd	-1 -3	-3 -1
	3rd	-2 -3	-3 -1
1962	Apr 1st	-1 0	-3 -1
whole	2nd	-1 0	-3 -1
region	3rd	-1 0	-3 -1
drought	May 1st	-1,-2* -1,-2	-3 -1
	2nd	-1,-2* -2,-3	-3 -1
	3rd	-1,-2* -2,-3	-3 -1
1963	Apr 2nd	0,1 2 2,3	1 3
whole	3rd	0,1 2 3	1 3
region	May 1st	0,1 2 3	1 3
flood	2nd	1,2 3 1	1 3
1972			
North-	June 3rd	-2,-3* 2 3 2↓	-3 3→2
drought	Aug 1st	-2,-3* 2 3 -2*	-3 3→2
South-			
flood			
1963	July 1st	3 3 -2,-3*	3 -1
North-	2nd	3 1 -2,-3*	3 -1
flood	3rd	3 1 -1,-2*	3 -1
South-	Aug 1st	2,3 1 -1,-2*	3 -1
drought			

* stands for local value.

In 1991, a special severe flood occurred in the eastern China. We first put this drought/flood index in practical use, obtained the temporal and space distribution of this flood in time, and simulated the damaged extent and grade of this rare severe flood. The first application showed that it had a good effect on the actual cases. Now this drought/flood index model has been widely used in the eastern China.

TABLE 5 Comparisons our index of drought/flood modes with actual situation of disastrous level

Year	Period Mon. Dekad	Subdivisions 1	2	3	4	5	Actual situation
1978	Mar 3rd	-2	-2	-3	-3	-3	70-year
	Apr 1-3	-2	-2	-3,-2	-3	-3	record-
	May 1st	-1,-2*	-2	-3,-2*	-3	-3	breaking
	2nd	-1,-2*	-2	-2→3	-1→2	,-3	drought
	3rd	-2*	-2	-2→3	-1→2	,-3	
	June 1st	-2*	-2	-2→3	-1→2	,-3	
	2nd	-2*	-2	-2→3	-1→2	,-3	
1987	July 1st	0	-2	3	3	3	water-level
	2nd	0	-3*	2	3	3	of all rivers
	3rd	0	-3	2	-3	-3	above the
	Aug 1st	0	-3	2	2	2	warning-
	2nd	0	-1	2	2	2	level
1988	May 2nd	-1	-1	1	2*	2*	Drought in
	3rd	-1	-1	0	0	0	most of
	June 1st	0	-2	0	-1*	-1*	region and
	2nd	0	-2	3	-1*	-1*	no water
	3rd	-1	-3*	3	-1*	-1*	for living
	July 1st	-2	-3	-3	-2	-2	in July
	2nd	0	2	-2	-1	-2*	

* stands for local value.

4. CONCLUSION

Based on the principle of statistics and actual characteristics of droughts/floods in the eastern China, a quantitative and objective droughts/floods index has been obtained. The droughts/floods index is divided into 9 levels, from 4,"extreme flood" , to -4, "extreme drought", its corresponding value of the index is from "more than 4.00" to "less than -4.00". The droughts and floods which occurred in the eastern China were analyzed quantitatively and objectively. Compared with the results of the previous investigations and the actual data of disasters, it indicated that the model is feasible to the quantitative, precise and objective analysis on the droughts/floods occurred in the eastern China, and this index has a higher accuracy.

REFERENCE

Bhalme, N. H., and D.A., Mooley, 1980: Large-scale droughts/floods and monsoon circulation. *Mon. Wea. Rew.*, **108**, pp. 1197-1211.

Jiangsu Meteorological Bureau, 1975, droughts and floods occurred in Jiangsu Province (1949-1974), pp 80.

On the Statistical Significance of "Optimal Climate Normals"

Daniel S. Wilks
Cornell University, Ithaca, New York, USA

ABSTRACT

A simple approach to long-range forecasting of monthly or seasonal quantities is as the average of observations over some number of the most recent years. Finding this "optimal climate normal" (OCN) involves multiplicity problems in both time and space. These problems are addressed here using nonparametric resampling tests, applied to U.S. Climate Division Data in order to investigate operational viability of OCN forecasts by the U.S. Climate Prediction Center. The seasonal (3-month average) temperature forecasts are found to be good enough that their performance is unlikely to have arisen by chance for most times of year, while seasonal precipitation forecasts are significantly better than chance only during the fall.

1. INTRODUCTION

Very long-range forecasting — with lead times on the order of a year — is a difficult problem, even when the predictand is an average over a month or season. The accuracy of such forecasts is currently quite limited, and accordingly relatively unsophisticated methods can be competitive. A very simple and operationally straightforward method for constructing such forecasts is as the average over that number of the most recent years' values found to give the best "hindcast" performance on a set of historical data. Forecasts prepared according to this method have a lead time of approximately 11 months when the predictand is a monthly average, or 9 months when the predictand is a 3-month average.

Searching the climatic record at a location for that averaging period yielding the apparently best forecast performance is not a new idea. Some relatively recent discussions of the screening different of different averaging periods as long-range predictors are provided in Dixon and Shulman (1984), Lamb and Changnon (1981), and Sabin and Shulman (1985). A variety of earlier studies addressing this issue, some dating to the first half of the century, are also cited in the above papers.

This simple procedure is currently used as one contributor to new operational long-lead forecasts produced by the U.S. Climate Prediction Center (Huang et al. 1995, hereafter HVB), who call the average over that number of years yielding the best performance the "optimal climate normal" (OCN). Operating on area-averaged (U.S. Climate Division) data for seasonal (i.e., averages over 3 months) temperature, HVB selected averaging periods that yielded best hindcast performance for the years 1961–1993.

While the procedure for computing the OCN forecasts is operationally straightforward, an objective evaluation of the results on the dependent data is conceptually more difficult. At individual locations, the procedure of blindly screening the hindcast performances of all averaging periods between one and thirty years involves a multiplicity of comparisons. Choosing the single best averaging period from many possibilities should accordingly lead to some degree of "artificial skill," or misleadingly positive results for the developmental data. While a cross-validation approach would be a desirable safeguard, the procedure by which it might be constructed is not clear, due to the overlapping of the averaging periods and the shortness of the available record relative to the thirty-year maximum averaging period. Recognizing this problem, HVB used a deflator due to Barnston and van den Dool (1993) to better estimate forecast performance on independent data.

An equally serious problem relates to the multiplicity of simultaneous evaluations of hindcast performance at many locations. Because of the strong spatial correlation typically exhibited by monthly- and seasonal temperature and precipitation data, the apparently (but erroneously) good hindcast performances occasionally arising by chance will tend to occur with spatial coherency, and these areas accordingly have the potential to be confused with regions for which there may be real predictability. This aspect of the problem is especially of concern because the selection of averaging periods at the individual locations are, by the nature of the searching procedure, "tuned" to the sampling variations particular to the available data record.

This study approaches both the local and spatial OCN multiplicity problems through nonparametric hypothesis testing procedures. Seasonal and monthly temperature and precipitation data from U.S. climate divisions for the years 1931-1993, as in HVB and described in Section 2, are used in order to allow valid comparisons with that study. The statistical significance of the OCNs for single-location dependent data predictions is assessed using a resampling procedure, described in Section 3, in which the data series are repeatedly shuffled to produce distributions of various performance measures under the null hypothesis that the OCNs exhibit no predictive skill relative to the conventional 30-year normals. The "field significance" of the collections of local tests described above is similarly assessed in Section 4, by simultaneously and coherently shuffling the time series for all the climate divisions, and summarizing the results of individual-location tests under this sampling scheme.

2. FORECASTS AND VERIFICATION

The U.S. Climate Division data, for 1931-1993 (National Climatic Data Center 1994) is used in the following, in order to maintain maximum comparability with HVB. Analyses of both the raw monthly, and composited seasonal, data series are reported below. Monthly series for temperature and precipitation for each calendar month were used directly. For each "season," comprised of triplets of consecutive months (January-February-March, February-March-April, etc.), the respective monthly temperatures for each division were averaged, and the monthly precipitation values were totaled. The result in each case is a time series, T_i, i = 1, . . . , 63; in which i = 1 corresponds to the year 1931, and i = 63 indicates the year 1993. This notation will be applied to both the temperature and the precipitation data.

The k-year "climate normal" predictor for the data value T_i is simply the average over the previous k values in that time series, i.e.,

$$\bar{T}_{i,k} = \frac{1}{k} \sum_{j=1}^{k} T_{i-j} \quad . \qquad (1)$$

The averaging period is allowed to vary between k = 1 (the "persistence" forecast) and k = 30 (the annually updated "30-year normal"). Accordingly, the first year for which hindcasts can be computed for the present data set is 1961 (i = 31). For each data series, the averaging period for which Eq. 1 produces the best specifications for the years 1961-1993 is chosen as "optimal."

One measure used in HVB to judge the correspondence between the OCNs and data for the years being hindcast was a correlation measure of the form

$$COR(k) = \frac{\sum_{i=31}^{n} \hat{T}_i^f \, \hat{T}_i^{ob}}{\left[\sum_{i=31}^{n} (\hat{T}_i^f)^2 \sum_{i=31}^{n} (\hat{T}_i^{ob})^2 \right]^{1/2}} \quad , \qquad (2)$$

where n = 63 years for the present data set, the superscript "f" denotes forecast, and the superscript "ob" indicates the target observed datum to be specified, and the circumflex accents indicate anomalies constructed as

$$\hat{T}_i^f = \bar{T}_{i,k} - \bar{T}_{i,30} \qquad (3a)$$

and

$$\hat{T}_i^{ob} = T_i - \bar{T}_{i,30} \quad . \qquad (3b)$$

Also considered here is the normalized mean-squared error,

$$MSE^*(k) = \frac{\sum_{i=31}^{n} (\bar{T}_{i,k} - T_i)^2}{\sum_{i=31}^{n} (\bar{T}_{i,30} - T_i)^2} \quad , \qquad (4)$$

where the normalizing factor in the denominator of Eq. 4 is included to allow MSE*(k) values for different locations to be comparable, regardless of their intrinsic degrees of interannual variability.

3. LOCAL STATISTICAL SIGNIFICANCE

Determining the "optimal" value of the averaging period, k, involves examining the accuracy with which the data values for each station can be specified using Eq. 1, as reflected by measures such as Eq. 2 or Eq. 4, for each of the thirty values of k considered. That value of the averaging period yielding the single best hindcast performance among these thirty values on the available data is chosen. Although this procedure is intuitively appealing, the results are difficult to interpret because of the many trial values that are considered. Even if there is little real relationship between the predictor in Eq. 1 and the data values T_i, there may be ample opportunity for chance variations in the relatively short data series to yield a value of k for which a chosen accuracy measure indicates appreciable predictability. The consequence of this multiplicity of comparisons is that some degree of "artificial skill," or misleadingly positive results for the developmental data, is expected.

From a hypothesis testing perspective, any significant predictive skill (with respect to the 30-year "normals") exhibited by the OCN forecasts presumably derives from the data series T_i exhibiting at least somewhat consistent trends or cycles in time. Accordingly, the null hypothesis of no predictive skill implies that each 63-member data series exhibits no real time dependence, and to the extent that the data appear to contradict this condition it is as a result of chance orderings of the data. The reference, or null, distribution for either of the performance measures can be constructed by shuffling the T_i values sufficiently many times to sample adequately the 63! possibilities, computing the value of the test statistic for each of the 30 values of k in each random re-ordering, and recording the largest COR(k) or smallest MSE*(k) of each set of thirty test statistics.

For the temperature data, it is not actually necessary to repeat the resampling process for each of the 344 climate divisions and each of the twelve months or seasons, because the distributions of monthly and seasonal temperatures are very nearly Gaussian. Since the performance measures in Eqs. 2 and 3 are nondimensional, their behavior under the null distribution for Gaussian variates can be simulated once and for all using standard Gaussian random numbers. Table 1a shows the 10%, 5%, and 1% critical values for the null distributions of COR(k) and MSE*(k), computed using 10,000 separate samples of n = 63 independent standard Gaussian variates. These values agree quite closely with those obtained through the resampling of actual seasonal temperature series of the same length. The values in Table 1b were produced in the same way, except for the crucial difference that the thirty possible values of k were not searched for the one yielding the best specifications. Rather, for each of the 10,000 trials, a single value of k was chosen randomly. The differences between the

corresponding entries in Tables 1a and 1b illustrate the potential danger involved in searching a wide range of possibilities when choosing an "optimal" averaging period. The spatial distribution of locally significant tests for seasonal temperatures at the 344 climate divisions (not shown) indicates substantial numbers of locations for which local tests are significant at the 1% and 5% levels for most of the twelve possible 3-month seasons.

The precipitation data is sufficiently strongly skewed over much of the U.S. that the Gaussian critical levels presented in Table 1a are not appropriate. For the local precipitation tests, critical levels for each location and time period were derived through individual resampling tests, using 10,000 samples each. The spatial distribution of locally significant tests for divisional precipitation totals is much sparser than for seasonal temperature, with largest significant areas in the fall months.

4. FIELD SIGNIFICANCE

In order to fully evaluate the promise of the OCN forecasts, it is necessary to evaluate the statistical significance of the overall spatial pattern of forecast performance, i.e., the "field significance" (Livezey and Chen 1983) of observed patterns of locally significant tests. This is a testing multiplicity problem that is complicated by the spatial correlation of the divisional temperature and precipitation data: false rejections of local null hypotheses will tend to occur with spatial coherency, and accordingly have the potential to be confused with regions for which there may be real predictability.

The field significance of the collections of sets of local tests described above is assessed by simultaneously and coherently shuffling the individual time series for all the climate divisions. That is, for this resampling test the data consist of time series of 344-element vectors $\mathbf{T}_i$, i = 1, . . ., 63. Sampling from the 63! permutations of these vectors simulates the condition implied by the null hypothesis, that the particular time ordering of the data is arbitrary, while preserving the spatial relationships of the data in each year. Ten thousand permutations of the vectors $\mathbf{T}_i$ were drawn, and local tests were conducted on these samples for each of the 344 divisions as described in Section 3. The null distribution then consists of the areas (not numbers of tests, because sizes of the climate divisions vary widely) over which nominally significant tests occurred, over the 10,000 trials. The statistical significance of the actual area over which locally significant tests occur is then assessed by comparison to the corresponding distribution of areas of (falsely) significant local tests under the null hypothesis.

Figure 1 summarizes the results of these field significance tests for (a) seasonal temperature, and (b) seasonal precipitation. The local tests upon which these results are based were conducted at the 5% level for temperatures, but at the 10% level for precipitation since relatively few local precipitation tests were significant at the 5% level. The vertical scale for the field significance p-values is inverted and logarithmic, and horizontal dashed lines indicate field significance at the 1%, 5%, and 10% levels. The symbols "C", and "M" indicate tests using the COR(k), and MSE*(k) statistics, respectively.

Table 1. Critical values (10%, 5%, and 1% levels) for the performance statistics in Eqs. 2 and 3, for underlying data following Gaussian distributions, and n = 63; when (a) the best averaging period, k, among thirty is chosen, and (b) when the averaging period is chosen randomly.

	Measure	10%	5%	1%
(a)	COR(k)	0.364	0.404	0.484
	MSE*(k)	0.928	0.901	0.828
(b)	Measure	10%	5%	1%
	COR	0.198	0.254	0.354
	MSE*	0.980	0.960	0.914

Figure 1a indicates that the OCN forecasts for seasonal temperature are significantly better than the 30-year average, except for the seasons September-October-November, October-November-December, and November-December-January. The results for seasonal precipitation in Figure 1b are much weaker, with the most consistent statistical significance occurring only for September-October-November, and October-November-December. The corresponding figures for monthly OCN forecasts (not shown) indicate that their statistical field significance is considerably weaker. For temperature, the strongest results are for January, April, July, August, and October, and few of the tests achieve field significance at the 1% level. The results for monthly precipitation are worst of all, and indicate that the OCNs are essentially indistinguishable from the results on randomly re-ordered data. Evidently the OCN forecasts for monthly precipitation have no significant predictive value.

5. SUMMARY AND CONCLUSIONS

The extent to which the apparent predictive capacity of seasonal and monthly OCN hindcasts of temperature and precipitation is larger than would be expected by chance has been examined here using nonparametric hypothesis tests. At the local level, the sampling distributions of forecast performance statistics under the null hypothesis were constructed by repeatedly re-ordering the data. The field significance of these local tests was approached in the same way, by re-ordering the underlying fields consisting of data at 344 individual climate divisions, and computing the areas exhibiting nominally significant local tests.

Field significance results for seasonal temperature forecasts indicate strongly that, with the exception of the fall and early winter seasons SON through NDJ, significant local forecast skill is sufficiently widespread that it is unlikely to have occurred by chance. Significant results for seasonal precipitation are much less widespread in space, and

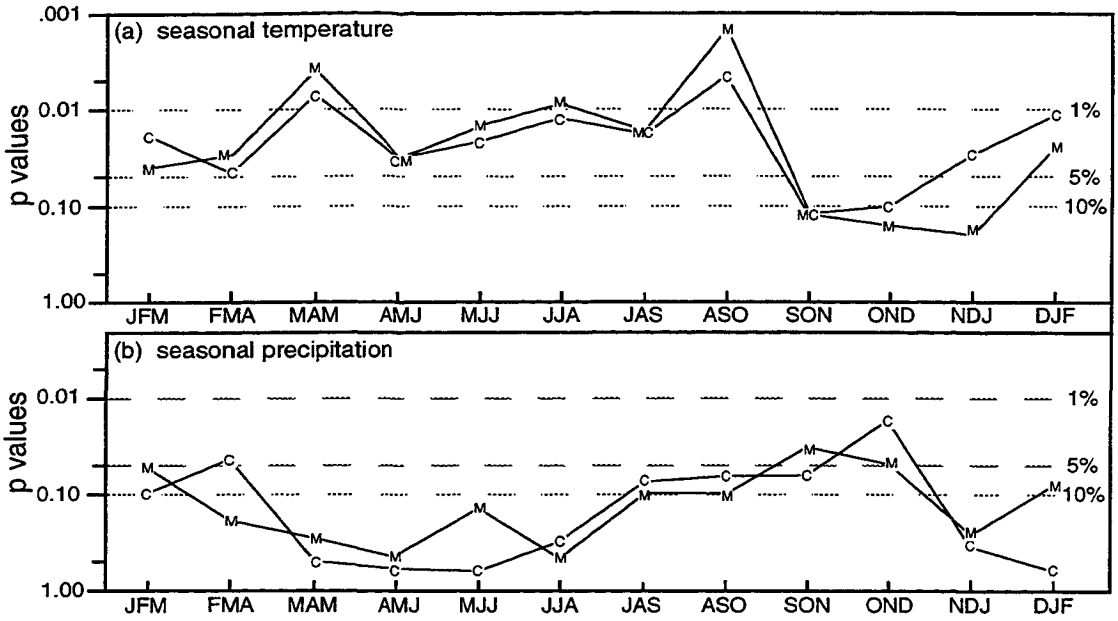


Figure 1. P-values summarizing field significance tests for OCN forecasts of (a) seasonal temperature, and (b) seasonal precipitation. Local tests for temperatures were conducted at the 5% level, and local precipitation tests were at the 10% level. The symbols "C", and "M" indicate tests using the COR(k) and MSE*(k) statistics, respectively.

convincingly achieve field significance only for SON and OND. Results for monthly temperature forecasts are somewhat better than those for seasonal precipitation, but less impressive than those for seasonal temperature. Results for monthly precipitation forecasts appear to be no better than would be expected by chance.

The significance testing approach adopted here is less than ideal, but has been resorted to because cross-validation does not seem practicable given the available data. The testing framework does allow identification of levels of local forecast performance that are too great to have plausibly arisen by chance, and provides reassurance that many of the spatial patterns of significant forecast performance are unlikely to have resulted only from sampling variations. However, this analysis does not yield estimates of those forecast performance measures that could be expected for independent (i.e., future) data. Rather, the critical values used here (e.g., in Table 1a) are better than can be expected for forecasts of future independent data, precisely because they have been constructed to reproduce the factors that lead to artificial skill for hindcasts. On the other hand, the critical values in Table 1b, which are based on randomly chosen averaging periods, are probably overly conservative. Respective pairs of values in Tables 1a and 1b might be expected to bracket future forecast performance.

ACKNOWLEDGEMENT

This work was supported by the Northeast Regional Climate Center under NOAA grant NA16CP-0220-02.

REFERENCES

Barnston, A.G., and H.M. van den Dool, 1993. A degeneracy in cross-validated skill in regression-based forecasts. *Journal of Climate*, 5, 963-977.

Dixon, K.W., and M.D. Shulman, 1984. A statistical evaluation of the predictive abilities of climatic averages. *Journal of Climate and Applied Meteorology*, 23, 1542-1552.

Huang, J., H.M. van den Dool, and A.G. Barnston, 1995. Long-lead seasonal temperature prediction using optimal climate normals. *Journal of Climate*, submitted.

Lamb, P.J., and S.J. Changnon, Jr., 1981. On the "best" temperature and precipitation normals: the Illinois situation. *Journal of Applied Meteorology*, 20, 1383-1390.

Livezey, R.E., and W.Y. Chen, 1983. Statistical field significance and its determination by Monte Carlo techniques. *Monthly Weather Review*, 111, 46-59.

National Climatic Data Center, 1994. Time bias corrected divisional temperature-precipitation drought index. Documentation for dataset TD-9640. NOAA/NCDC, Asheville, NC, 12 pp.

Sabin, T.E., and M.D. Shulman, 1985. A statistical evaluation of the efficiency of the climatic normal as a predictor. *Journal of Climatology*, 5, 63-77.

CORRESPONDING AUTHOR:

Prof. D.S. Wilks
Dept. Soil, Crop and Atmospheric Sciences
Cornell University, Ithaca, NY USA 14853
wilks@metvax.cit.cornell.edu

Divergent Influences in Intraseasonal Teleconnections: An Observational Study Using ISCCP Cloud State and ECMWF Wind State Data

Steven A. Mauget
Atmospheric Science Program
Department of Land, Air, and Water Resources, University of California, Davis, CA 95616
(SAMAUGET@.UCDAVIS.EDU)

ABSTRACT

Rasmusson (1991,1988) proposes that large scale vertical circulations may be key elements in teleconnection dynamics. The 2-D diagnostic study of Sardeshmukh & Hoskins (1988) reveals the importance of divergent vorticity advection in determining the ultimate positioning of a convectively induced vorticity source, which suggests the influence of a Hadley driven mechanism in the 3-D general circulation. Previous observational studies have sought out cause and effect relationships between tropical convection and extratropical circulation over intraseasonal time scales, but have not employed methods capable of distinguishing the divergent nature of tropical-extratropical interactions. By contrast, the methods of the current observational effort are specifically intended to detect a divergent "signature" in intraseasonal teleconnections.

INTRODUCTION

Rasmusson (1991,1988) and Mo & Rasmusson (1993) suggest that Walker and Hadley circulations may play a important role in intraseasonal teleconnections by coupling tropical convection to dominant vorticity sources in nearby subtropical regions. This view contrasts with that of earlier models (i.e., Hoskins & Karoly,1981; Simmons et.al. 1983) which described teleconnection dynamics in the context of Rossby wave propagation driven by vorticity sources co-located with tropical convection. In these earlier scenarios the influence of divergence was limited to a stretching source term, thus the divergence that takes place above regions of tropical convection was considered to drive an anticyclonic source situated directly over the rising motion. With the addition of a divergent advection term Rasmusson(1988) and Sardeshmukh & Hoskins (1988) have proposed a revised effective source term [S],

$$\frac{\partial \xi}{\partial t} + V_\psi \bullet \nabla(\xi + f) = -(\xi + f)\nabla \bullet V_\chi - V_\chi \bullet \nabla(\xi + f)$$
$$= -\nabla \bullet V_\chi(\xi + f) = [S] \qquad \text{(Eq.1)}$$

and a revised teleconnection scenario, with a relatively weak stretching influence in the vicinity of the tropical heating and a stronger source region in the subtropics that Rasmusson (1991) associates with the poleward *descending* branches of Hadley circulations. The magnitude of the rotational flow in such subsidence dominated regions is weak: if the related advection term is neglected, the result is a local subtropical vorticity balance strongly influenced by the convergence of Hadley-borne vorticity fluxes into the subtropical sinking branch of the circulation (Fig. 1). Within this latter context, Rasmusson (1991) suggests a Hadley driven northern winter teleconnection mechanism in which tropical heating anomalies in the ascending portion of the circulation indirectly force vorticity sources in the Northern Hemisphere descending branch of the circulation. The goal of the current research is to conduct an observational study which explicitly seeks out the influence of such a mechanism in intraseasonal teleconnections.

In the past investigators have explored the relationships between tropical convection and extratropical circulation over intraseasonal time scales, but have not sought out evidence of divergent circulations as intermediaries in these relationships (Lau & Phillips, 1986; Liebmann & Hartmann,1984). More recent work has focused on gathering evidence of a divergent connection between the tropics and subtropics. Chen & Yen's [CY] (1991) analysis of subtropical vorticity balances in FGGE IIIb data (May-Aug. 1979) suggests a link between 30-60 day oscillations in 200 mb tropical divergence and subsequent fluctuations in subtropical vorticity convergence and streamfunction. Mo & Rasmusson [M&R] (1993) also suggest a Hadley driven link between tropical convection and dominant vorticity sources in nearby subtropical regions, based on their analysis of northern winter (JFM) mean 200 mb vorticity budgets during the 1986-89 ENSO cycle. Although the results of both studies imply the vorticity convergence mechanism of Fig. 1, the compositing approach of CY and M&R's analysis of mean seasonal data are not suited to providing explicit evidence of the existence and nature of this three dimensional tropical-extratropical link. As a result, the methods used here more closely resemble that which a synoptic meteorologist would adopt; that is, a case study approach that avoids the consideration of mean behavior and composites derived from a number of events, concentrating instead on individual instances of tropical convection and extratropical response. A potential advantage to such an approach is that in addition to directly showing the influence of a divergent mechanism, the resulting individual case studies may provide clear information regarding *how* the mechanism works. The method chosen to conduct these case studies is a multiple variable, multiple channel implementation of Singular Spectral Analysis (Vautard & Ghil, 1989; Vautard et. al. 1992). This analysis involves both cloud and wind state data, the former derived from the ISCCP "C1" data set (Rossow et.al., 1988), the latter from ECMWF wind analyses.

SINGULAR SPECTRUM ANALYSIS

Single Channel-Single Variable SSA is essentially a data adaptive means of spectral analysis, achieved by dividing a time series into a series of overlapping sub-sequences of a specified duration (m) and subjecting the resulting m-element sequences to eigenanalysis. If, for example, the time series in question is 200 elements long and spectral peaks at and above a frequency of (20 time units)$^{-1}$ are being sought out, 181 overlapping subsequences of 20 unit duration could be formed.

$$Z_1 = 1..20,\ Z_2 = 2..21, \ldots\ldots\ldots Z_{181} = 181..200$$

Given these 181 elements, a T-mode eigenanalysis yields a data adaptive eigenbasis spanning R^{20}. These basis vectors result from the solution of;

$$\lambda_l = e_l^T D \quad D^T e_l \qquad \text{(Eq. 2)}$$

where the 181 subsequences occupy COL(D).

$$D = \left[\begin{bmatrix} 1 \\ 20 \end{bmatrix} \begin{bmatrix} 2 \\ 21 \end{bmatrix} \cdots\cdots\cdots \begin{bmatrix} 181 \\ 200 \end{bmatrix} \right]$$

$Z_1 \quad Z_2 \qquad\qquad Z_{181}$

The application to spectral analysis stems from the fact that clusters of subsequences possessing spectral variance at angular frequency ω will yield eigenvectors with forms similar to $\sin(\omega t)$ and $\cos(\omega t)$. In this particular example a 181 element principle component would result from projecting a given 20 element eigenvector onto $Z_1, Z_2 \ldots Z_{181}$, with the variance of the PC proportional to the percentage of the total variance explained by that eigenvector/spectral component. As applied to the current research, this method has been extended to isolating clusters of spectral variance common to different variables at different points in time, over a number of grid locations.

Multiple Channel, Multiple Variable SSA

Again, the goal is to observe individual episodes of tropical convection and subtropical response, and to test for a sequence of events in various data fields that indicate a divergent mechanism. For example, a chain of events with a Hadley/Walker signature might involve a surge in tropical convection followed by a distinguishing sequence of related subtropical effects. The initial convective stage of such a sequence of events can be observed through the mean and variance of satellite observed cloud top temperatures, as large scale rising motion in the tropics occurs in cumulonimbus complexes possessing a wide range of cloud top temperatures/heights with relatively cold/high mean values. Throughout the course of this work, the dimensionless index of Vernekar (1982) has been used to distinguish events of tropical convection.

$$VI = \sigma/(T - 165.0) \qquad \text{(Eq. 3)}$$

The cloud state statistics σ and T are ISCCP reported variables indicating the standard deviation and mean of cloud top temperatures respectively. Under clear sky conditions, the Vernekar Index value is driven to zero. Subtropical effects might include a shift in 500 Mb vertical motion indicating the associated subtropical subsidence, and a shift in 200 Mb subtropical vorticity in response to vorticity convergence in the circulation's descending arm.

How might SSA be used to detect such a sequence of events? The premise made here is that if the tropical event and the extratropical response were bracketed by m-element subsequences, then both event and response sequences might form a co-spectral cluster in R^m, which might in turn be distinguished by eigenanalysis. As such, the observational method pursued here could be considered as a data adaptive co-spectral analysis. As practiced thus far, this SSA-based analysis has taken place in 5 stages:

1) A prospective low frequency tropical convective event is identified. Given the location and duration of the event, a tropical grid of Vernekar Index time series are formed that bracket the event in both space and time. In the example of Fig. 3, an oversized grid of $N_r = 377$ grid locations, spanning 32.5 S- Equator, 95E- 170 E was chosen. As the event in question took place over Northern Australia during approximately Dec. 26 1983 - Jan. 15 1984, an embedding dimension (m) of 22 days was decided upon.

2) Extratropical comparison grids are defined for a number of related variables, in this case ECMWF vertical motion at 500 mb and vorticity at 200 mb. As the emphasis in this study is on northern winter teleconnections in the North Pacific, a grid of $N_c = 855$ locations covering most of this region was chosen, as highlighted in Fig. 3.

3) Next, the $2 * N_c$ comparison time series are subdivided into m-element overlapping subsequences, each potentially capable of bracketing shifts in the extratropical variables occurring *subsequent* to the convective event. As these extratropical effects were expected to take place at a lag of no more than 35 days, 35 subsequences were formed from the time series at each comparison grid location; i.e., Z_1 = days 1..22, Z_2 = 2..23, ... Z_{35} = 35..57, where day 1 is Dec. 26 1983. Comparison subsequences are derived from seasonal time series that have been detrended, normalized to the seasonal (DJFM) standard deviation, and subjected to a $(40\ day)^{-1}$ -$(4\ day)^{-1}$ Lanczos bandpass filter (Duchon,1979). The Vernekar Index subsequences of the tropical grid were extracted from time series treated in an identical manner.

4) As in the single variable-single channel case Eq. 3 is solved, where COL(D) is now occupied by the $(2*N_c*35) + N_r$ m-element subsequences of both comparison grids and the tropical reference grid

$$D = \left[\begin{bmatrix} 1 \\ 22 \end{bmatrix} \cdots \begin{bmatrix} 1 \\ 22 \end{bmatrix} \begin{bmatrix} 1 \\ 22 \end{bmatrix} \cdots \begin{bmatrix} 35 \\ 56 \end{bmatrix} \cdots \begin{bmatrix} 1 \\ 22 \end{bmatrix} \cdots \begin{bmatrix} 35 \\ 56 \end{bmatrix} \begin{bmatrix} 1 \\ 22 \end{bmatrix} \cdots \begin{bmatrix} 35 \\ 56 \end{bmatrix} \cdots \begin{bmatrix} 1 \\ 22 \end{bmatrix} \cdots \begin{bmatrix} 35 \\ 56 \end{bmatrix} \right]$$

-Tropical- ω_{500} ξ_{200}

VI --(1)-- $-(N_c)-$ --(1)-- $-(N_c)-$

$-N_r-$ N_c*35 N_c*35

Given an embedding dimension of 22, the solution to this analysis yields 22 eigenvectors. In the January 1984 case study of Fig. 3 , the first and second eigenvectors were found to be paired; that is, both eigenvectors explained roughly the same amount of fractional variance and are of the form $\sin(\omega t)$ and $\cos(\omega t)$, where ω is the fundamental angular frequency $(2*\pi*(22\ days)^{-1})$. In addition, a break is apparent between the percentage of variance explained by the second eigenvector and that explained by higher order modes. A more rigorous test for a spectral break could be attempted using the eigenvalue uncertainty derived by North, et.al., (1982),

$$\delta\lambda = \lambda\sqrt{2/N} \qquad \text{(Eq.4)}$$

where the number of degrees of freedom (N) is an estimate of the total number of independent measurements in time and space, summed for each variable. The uncertainty bars of Fig. 2 assume that adjacent, non-overlapping 22 day data subsequences are statistically independent in time, thus each 56 day time series contains ~ 3 temporal DOF. At this time an analysis of the number of spatial DOF in the Northern Pacific wind fields has not been conducted. Until these parameters are estimated the results of Livesey & Chen(1982) for 700 mb heights over a comparable area will be adopted, thus the vorticity and vertical motion fields are assumed to possess 10 spatial DOF each. As a result, for the Jan. 1984 case study, $N \cong 3*10 + 3*10 = 60$ for the two wind variables over the Northern Pacific grid.

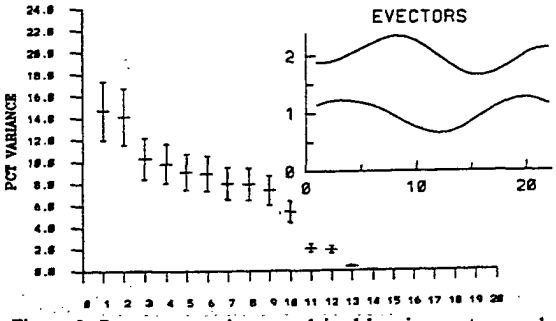


Figure 2: Percentage variance explained by eigenvectors, and first and second eigenvector of the January 1984 case study.

5) The final stage involves the formation of principal component maps. By projecting the first eigenvector onto each of the N_r subsequences of the tropical grid and forming a map of the resulting values, those subsequences with the spectral characteristics of the first eigenvector can be distinguished. By

repeating this process on elements 1-22 of the N_c time series of the ω_{500} data and mapping the results on the subtropical grid, the spectral characteristics of that field is tested for at zero lag. Continuing this process on elements 2-23, 3-24, ...35-57 of the ω_{500} data results in 34 additional PC maps, each indicating where the vertical motion field was co-spectral with the first eigenvector, and the lag at which this occurred with respect to the initial tropical event (i.e., +1 day, +2 day,.....+34 days). This PC generating process takes place for all extratropical variables involved in the eigenanalysis. The approach thus far has been to normalize all data-eigenvector projections to correlations, and to only consider PC/correlation values exceeding a 95% confidence level. Local confidence levels have been calculated by modeling the first eigenvector as a first order Markov process, and correlating m-element segments of the model with a sufficient number of m-element data segments to estimate independent 95% confidence levels for each data field.

Discussion of the January 1984 Case Study

Figure 3 shows a sequence of principal component maps generated via the process outlined above, where the reference eigenvector is the inverse of the first eigenvector found in Fig. 2. As a result;

- positive correlations in the Vernekar Index PC indicate transitions to vertically extended cloud states consistent with convective activity,
- positive(negative) correlations in the ω_{500} PCs indicate transitions to sinking(rising) motion.,
- positive(negative) correlations in the ξ_{200} PCs indicate transitions to cyclonic(anticyclonic) flow.

In Fig. 3, the lag 0 inset indicates positive Vernekar Index correlations in the vicinity of Northern Australia, which marks the initial convective event of Dec. 26 - Jan. 15. At a lag of +15 days, correlations consistent with the onset of large scale subsidence off the U.S.-Mexican coast begin to appear. At subsequent lags this subsidence migrates westward and towards the equator, and increases in extent. Animation of the vertical motion fields over this period hints at the development of an extensive anticyclonic arc of subsidence in the northeast Pacific, and this transition is evident in Fig. 3 at lags +19 - +21 days. The ξ_{200} PCs of Fig. 3 give more direct evidence of the dynamic response implied in the anticyclonic arcing of the subsidence fields, specifically in the arc of negative correlations that appear between lags +19 - +21 days, indicating a concurrent transition to an anticyclonic flow state, and apparently enhanced subtropical ridging, in the northeast Pacific over this period.

CONCLUSION

The principle component sequences of Fig. 3 appear to show a distinct transient event of convection, subsidence, and subtropical dynamic response in the northern hemisphere arm of the Pacific Walker regime, similar to that depicted in the schematic of Fig. 1. However, determining the true statistical significance of these results requires a direct estimate of the spatial degrees of freedom of both wind and cloud state fields. These parameters are necessary to confirm both the existence of a spectral break in explained variance via the error bar estimates of North et.al. (1982), and the global significance of correlation fields (Livesey & Chen , 1983). It will be noted in closing that given the assumed number of spatial DOF and the conservative estimate of temporal DOF, the first eigenvalue barely fails the first test, while the +23 day PC/correlation fields pass the second. An analysis to determine the actual number of spatial DOF is currently taking place.

ACKNOWLEDGEMENTS

This work was supported by the NASA Global Change Fellowship Program (Grant # NGT-30200).

References

Chen, T.C. and M.C. Yen, 1991, "Interaction between intraseasonal oscillations of the midlatitude flow and tropical convection during 1979 northern summer: The Pacific Ocean.", Journal of Climate, 4, 653-671.

Duchon, C.E., 1979, "Lanczos filtering in one and two dimensions", Journal of Applied Meteorology, 18, 1016-1022.

Hoskins, B.J., and D.J. Karoly, 1981, "A steady linear response of a spherical atmosphere to thermal and orographic forcing.", Journal of Atmospheric Science, 38, 1179-1196.

Lau, K.M. and T.J. Phillips, 1986, "Coherent fluctuations of geopotential height and tropical convection in intraseasonal time scales", J. Atmos. Sci., 43 , 1164-1181.

Liebmann, B. amd D.L. Hartmann, 1984, "An observational study of tropical-midlatitude interactions on intraseasonal time scales during winter", J. Atmos. Sci., 41 , 3333-3350.

Livesey,R.E., and W.Y.Chen, 1983, "Statistical field significance and its determination by Monte Carlo techniques", Monthly Weather Review,111, 46-59.

Mo, K., and E.M. Rasmusson, 1993, "The 200-mb climatological vorticity budget during 1986-1989 as revealed by NMC analyses", J. of Climate, 6 , 577-594.

North, G.R., et.al., 1982, "Sampling errors in the estimation of empirical orthogonal functions", Mon. Wea. Rev., 110, 699-706.

Rasmusson, E.M., 1988, "Atmospheric teleconnections during the 1986-1989 ENSO cycle. Proceedings, 3rd International Conference on Southern Hemisphere Meteorology and Oceanography", Boston, Amer. Met. Soc.., pp 361-365.

Rasmusson, E.M., 1991, "Observational aspects of ENSO cycle teleconnections", In: Teleconnections Linking Worldwide Climate Anomalies. M.H. Glaatz, R.W. Katz and R.W. Nichols Eds. Cambridge, Cambridge Univ. Press. pp. 309-343.

Simmons, A.J., J.M. Wallace and G.W. Branstator, 1983, "Barotropic wave propagation and instability, and atmospheric teleconnection patterns", J. Atmos. Sci., 40, 1363-1392.

Sardeshmukh,P.D. and B.J. Hoskins, 1988, "The generation of global rotational flow by steady idealized tropical divergence", J. Atmos. Sci., 45 , 1228-1251.

Vautard, R. and M Ghil: 1989, "Singular spectrum analysis in nonlinear dynamics with applications to paleoclimatic time series", Physica D, 35, 395-424.

Vautard,R., P. Yiou and M Ghil: 1992, "Singular spectrum analysis: A toolkit for short,noisy chaotic signals", Physica D, 58, 95-126.

Vernekar,A.D., "Spatial and temporal variations of large scale subsidence and convection regions derived from satellite data", In: Annual Climate Diagnostic Workshop, 6th, Palisades, N.Y., Oct 14-16, Proceedings. Wash. D.C., NOAA, Mar. 1982.

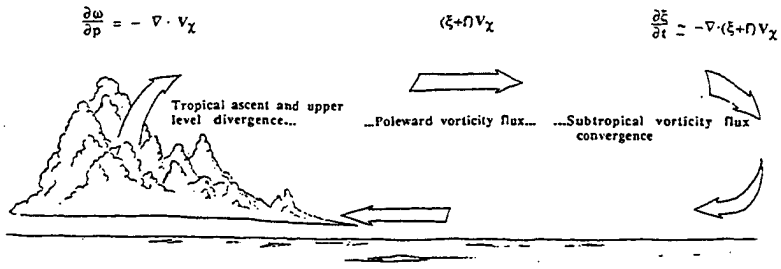


Figure 1. Schematic illustrating tropical convection, divergent vorticity advection,and subtropical vorticity convergence

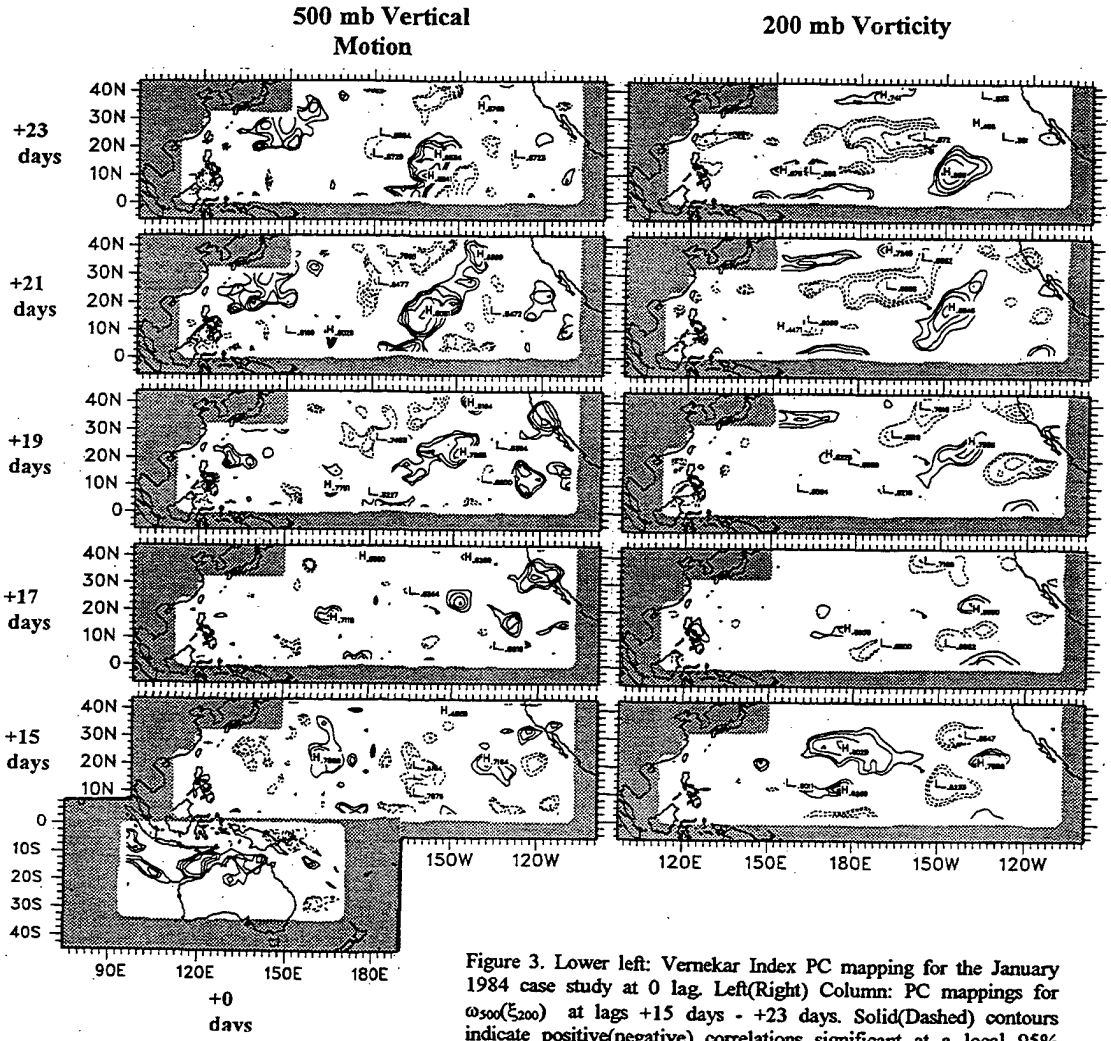


Figure 3. Lower left: Vernekar Index PC mapping for the January 1984 case study at 0 lag. Left(Right) Column: PC mappings for $\omega_{500}(\xi_{200})$ at lags +15 days - +23 days. Solid(Dashed) contours indicate positive(negative) correlations significant at a local 95% confidence level.

PREFERRED CLIMATE PATTERNS IN THE UNITED STATES ASSOCIATED WITH CATEGORIZED EL NINO/SOUTHERN OSCILLATION (ENSO) EVENTS

D.W. Presnell

National Weather Service, Daytona Beach, Florida, USA

ABSTRACT

Preferred modes of temperature and precipitation anomalies in the contiguous United States prior to, during, and after El Nino/Southern Oscillation (ENSO) events have been examined for 27 events during 1895-1990. Attention is given to preferred climate modes associated with an ENSO classification scheme that considers time of initiation and dissipation of events. Factor analysis of temperature and precipitation anomalies during a 15 month period beginning with June of the year in which the event began (0) and ending with August of the subsequent year (1) was performed. Factors were examined based on the classification of each ENSO event as indicated by the Wright Rainfall Index (WRI).

1 INTRODUCTION

This research focuses on monthly climate patterns in the contiguous United States associated with categorized ENSO events. These patterns could be used in conjunction with predictions of ENSO event occurrences. Once an event is predicted to occur, the proposed categories and associated preferred climate patterns could be used to predict climate anomalies in the United States during a particular type of ENSO event. Results of this research are also valuable as a climatology of the monthly patterns of climate in the United States during particular types of ENSO events.

Factor analysis was conducted using monthly temperature and precipitation data for the 27 ENSO events. The factors were then examined based on the strength of each ENSO event as indicated by the WRI. Analyses of factor loadings in space produced three factors for both monthly temperature and precipitation anomalies, with each factor exhibiting principal patterns. From the principal patterns, three idealized surface temperature and precipitation patterns were created as a means of identifying where, in the continental United States, positive or negative monthly climate anomalies might occur during categorized ENSO events.

2 METHODOLOGY

Defining An ENSO Event

ENSO events from 1895-1990 were studied for this research because in the United States, state temperature and precipitation data sets were only available for the period 1895-1990. In defining events during 1895-1978, the ENSO events defined by Quinn et al. (1978) were used as guidelines. It was desired to have the largest sample size possible so events that occurred after the Quinn et al. (1978) article, 1879-1990, were also defined using those guidelines.

If an event defined by Quinn et al. (1978) had two consecutive 6 month mean Southern Oscillation Index (SOI) values $\leq$ -1.0, then it was defined as an event for this research. This process created 18 ENSO events during the period 1895-1978. For the period 1979-1990, an ENSO event was also said to occur when two consecutive 6 month mean values of the SOI were $\leq$ -1.0. This process extended the sample size to 21 events (Table 1).

Table 1. Chronological listing of ENSO events used for the factor analysis. Asterisks indicate the events which lasted for 2 years.

1. 1896-97	12. 1951-52
2. 1899-00	13. 1953-54
3. 1902-03	14. 1957-58
4. 1904-05-06 *	15. 1963-64
5. 1911-12	16. 1965-66
6. 1913-14-15 *	17. 1969-70
7. 1918-19-20 *	18. 1972-73
8. 1923-24	19. 1976-77-78 *
9. 1925-26	20. 1982-83
10. 1929-30-31 *	21. 1986-87
11. 1939-40-41 *	

Although most ENSO events typically last for one year, six of the 21 events persisted for two years. These events were defined to exist for 27 months [June (0)-August (2)]. They were split into two separate events in order to extend the sample size to 27 years for the factor analysis. The largest sample size was desired in order to have the most reliable results possible from the factor analysis.

Classification Methods

The 27 events were classified to identify climate modes associated with particular types of ENSO events. Each event was categorized according to its behavior as described by the WRI. Due to the small sample size of each category (< 30), rigorous statistical testing could not be performed.

The classification scheme is based upon the onset, duration, and demise of each ENSO event as indicated by the WRI. In classifying the 27 ENSO events, four categories were defined (Table 2). These categories are not mutually exclusive as some events matched criteria for more than one category.

Table 2. ENSO events included in the (a) Early Starters, (b) Early Enders, (c) Late Enders, and (d) Early Starters and Late Enders categories. Criteria for each category is listed at the top of each table.

Table 2a.
Criteria for beginning: WRI > 120% by August (0)
Criteria for ending: None

Events included:	*Aug. (0) WRI*	*Peak WRI*
1. 1896-97 *	115	Dec. 160
2. 1899-00	129	Oct. 177
3. 1902-03	134	Nov. 223
4. 1904-05	124	Jan. 153
5. 1905-06	126	Oct. 159
6. 1914-15	121	Oct. 191
7. 1918-19	160	Feb. 181
8. 1919-20	146	Oct. 168
9. 1923-24	146	Nov. 163
10. 1925-26	123	Nov. 182
11. 1929-30	135	Nov. 142
12. 1930-31	152	Sep. 191
13. 1939-40	120	Dec. 163

14. 1940-41	133	Oct. 206
15. 1951-52	140	Aug. 140
16. 1953-54	125	May. 155
17. 1957-58	134	Nov. 201
18. 1963-64	129	Oct. 180
19. 1965-66	149	Oct. 189
20. 1972-73	159	Nov. 223
21. 1976-77	150	Oct. 165
22. 1977-78	120	Dec. 161
23. 1982-83	138	Oct. 199
24. 1986-87	122	Dec. 179

Table 2b.
Criteria for beginning: None
Criteria for ending: WRI < 120% in March (1) and April (1)

Events Included:	*March (1)*	*April (1) WRI*	*Peak WRI*
1. 1896-97	115		Dec. 160
2. 1902-03	82		Nov. 223
3. 1905-06	91		Oct. 159
4. 1923-24	103		Nov. 163
5. 1929-30	136	99	Nov. 177
6. 1930-31	137	83	Nov. 142
7. 1951-52	102		Dec. 131
8. 1953-54	122	88	Oct. 144
9. 1963-64	107		Oct. 180
10. 1972-73	124	92	Nov. 223
11. 1977-78	112		Nov. 160
12. 1982-83	113		Oct. 199

Table 2c.
Criteria for beginning: None
Criteria for ending: WRI >120% in March (1) and April (1)

Events Included:	*March (1)*	*April (1) WRI*	*Peak WRI*
1. 1899-00	124	120	Oct. 177
2. 1904-05	120	147	Jan. 153
3. 1911-12	138	140	Dec. 185
4. 1913-14	173	139	Mar. 173
5. 1914-15	164	147	Oct. 191
6. 1918-19	161	164	Feb. 181
7. 1919-20	156	120	Oct. 168
8. 1925-26	173	172	Oct. 182
9. 1939-40	149	151	Dec. 163
10. 1940-41	150	141	Nov. 206
11. 1957-58	149	130	Nov. 201
12. 1965-66	132	121	Oct. 189
13. 1969-70	121	124	Apr. 124
14. 1976-77	132	128	Oct. 165
15. 1986-87	162	162	Dec. 179

Table 2d.
Criteria for beginning: WRI > 120% by August (0)
Criteria for ending: WRI > 120% in March (1), and April (1)

Events included:	*Aug. (0) WRI*	*March (1)*	*April (1) WRI*	*Peak WRI*
1. 1899-00	129	124	120	Oct. 177
2. 1904-05	124	120	147	Jan. 153
3. 1914-15	121	164	147	Oct. 191
4. 1918-19	160	161	164	Feb. 181
5. 1919-20	146	156	120	Oct. 168
6. 1925-26	123	173	172	Oct. 182
7. 1939-40	120	149	151	Dec. 163
8. 1940-41	133	150	141	Oct. 206
9. 1957-58	134	149	130	Nov. 201
10. 1965-66	149	132	121	Oct. 189
11. 1976-77	150	132	128	Oct. 165
12. 1986-87	122	162	162	Dec. 179

The fact that these categories are not mutually exclusive might raise some doubts on their usefulness. However, this research was not affected by any prior assumptions regarding intercorrelation of event types. There has been no literature that has shown any one of these categories to be associated with a particular type of climate anomaly pattern in the United States. Thus, there is no reason to assume that mutually exclusive categories based on known relationships are needed.

This decision allowed for an increase in the number of cases examined in each category. Since the categories appear to lack any intercorrelation, there is reduced risk of "contaminating" the results if a particular event is used in more than one category.

Factor Analysis of Climate Data

The main advantages of using factor analysis are that the method provides an efficient way of compressing geophysical data in both space and time, and secondly, it yields results that may be regarded as independent modes of the variability of the temperature and precipitation fields [Peixoto and Oort (1992)].

Each eigenvalue pattern is associated with a series of time coefficients that describes the time evolution of the particular spatial mode. Patterns that account for a large percentage of the variance are assumed to be associated with important centers of action in the atmosphere [Peixoto and Oort (1992)]. All patterns are temporally and spatially independent; thus, no one pattern has within itself any relationship to any other pattern [Peixoto and Oort (1992)].

The eigenvalue elements of the data covariance matrix are formed from the difference of the observations from their long-term means [Kim and Mueller (1978)]. Thus, the results depend on the coherence of the departures from normal for both temperature and precipitation.

While state data was employed in this study, most of the New England area has been eliminated from the factor analysis. These states represent small areas and their climate data could possibly bias the results if the data points are clustered and not equally spaced [Kim and Mueller (1978)]. A reduction in the number of states used in the factor analysis was necessary because the factor analysis requires more ENSO events than states to be viewed as statistically sound or stable through time [Kim and Mueller (1978)]. In this case, there were 27 events and 40 states as there were no data available for Alaska or Hawaii.

3 PREFERRED MONTHLY CLIMATE PATTERNS

Temperature

Each factor of the analysis of space coefficients is associated with a pattern of monthly temperature anomalies. Three idealized surface temperature patterns for the United States have been identified (Fig. 1) from these patterns associated with each factor. Idealized surface temperature pattern 1 (Fig. 1a) indicates the temperature anomaly pattern associated with factor 1. Idealized temperature pattern 2 (Fig. 1b) indicates the monthly temperature anomaly pattern associated with factor 2 and temperature pattern 3 (Fig. 1c) indicates the anomaly pattern associated with factor 3.

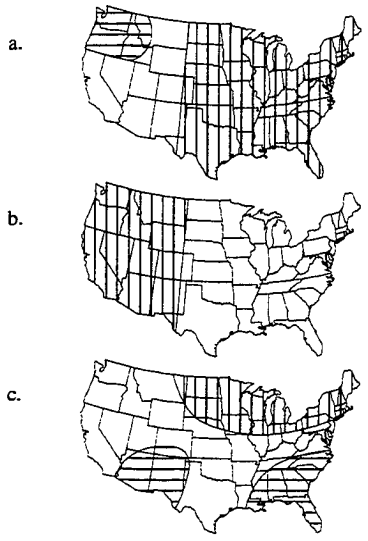


Figure 1. Idealized monthly temperature patterns (a) 1, (b) 2, and (c) 3. Vertical lines indicate areas of expected positive monthly temperature anomalies and horizontal lines indicate areas of expected negative monthly temperature anomalies.

The monthly factor loadings of time (time coefficients) for each factor were examined and if the value was > 1.2 (< -1.2) the month qualified as having a similar (opposite) temperature anomaly pattern of the idealized temperature pattern associated with a particular factor. A factor loading is a term referring to a coefficient (time) in a factor pattern and it is equivalent to correlations between factors (ENSO events) and variables (climate anomalies). Generally, values of time coefficients > 1.0 or < -1.0 are considered to be high correlations between factors and variables [Kim and Mueller (1978)]. The values of 1.2 and -1.2 were chosen to increase the amount of correlation between ENSO events and monthly temperature anomalies.

Frequency distributions of the results of this examination were conducted for each category of ENSO events (Table 3). A +P1 indicates that a month's "preferred" temperature pattern is similar to idealized surface temperature pattern 1. A -P1 indicates that a month's "preferred" temperature pattern is similar to the reverse of pattern 1. Likewise, a +P2 (-P2) and +P3 (-P3) indicate the same except the monthly temperature pattern is similar to idealized temperature patterns 2 and 3 respectively. These have been labeled as "preferred temperature patterns."

Table 3. Frequency distribution of the preferred patterns of monthly temperature for (a) Early Starters, (b) Early Enders, (c) Late Enders, and (d) Early Starters and late Enders. A +Pl (-Pl) indicates that Idealized monthly temperature pattern 1 (or opposite) occurred most often in the month indicated etc. etc. If more than one preferred pattern is given, then each occurred the percentage indicated. No preferred pattern is given when its % of occurrence is less than 10%.

	J(0)	J(0)	A(0)	S(0)	O(0)	N(0)	D(0)	J(1)	F(1)	M(1)	A(1)	M(1)	J(1)	J(1)	A(1)
(a)	P1 P2	P3	-P3	P2	P1	P1 -P2 P3 -P3	P3	-P3	P3	P1	P2	-P3	P3	P3	P3
%	17	25	13	17	13	13	17	17	17	17	25	25	13	13	13
(b)	-P1 -P3	P1 P3 -P1	-P3	P2	P1	P3	P1 -P2 -P3	-P2 P3	P1 P3 -P2	-P2	P2 -P2	-P3	-P3	P1 P3	P3
%	17	17	33	25	17	17	17	25	17	25	17	25	17	17	17
(c)	P1	P3	P1	P1	-P1	P1 P3	P3	-P1	P3 -P2	P1 P2 P3 -P3	P2	P3	P2		P2
%	33	33	20	20	13	20	20	20	13	13	20	27	13		13
(d)	P1 P2	P3	P1	P1	-P1	P1 P3	-P1 P3	-P1 -P3	-P2 P3	P1 P2 P3 -P3	P2 P3	P3	P2 P3	P3	
%	25	33	17	17	17	25	17	17	17	17	25	33	17	17	

The ENSO events categorized as Early Starters (Table 2a) have idealized monthly temperature pattern 3 (Fig. 1c) as the preferred pattern for 10 of the 15 months examined. Pattern 3 is preferred during the initial summer, winter, and ending summer months. The highest percentage of occurrence for pattern 3 is during July (0) at 25%. Pattern 1 (-P1) is the preferred pattern in the months of June (0), October, November, and March (Table 3a). Pattern 1 occurs 17% of the time in June(0) as its highest rate.

The analysis of the Early Enders type of ENSO events (Table 3b) reveals that there is no consistent occurrence of an idealized monthly temperature pattern. In June, July, and August (JJA), patterns 1 and 3 are the preferred patterns. Each of the three idealized monthly temperature patterns occur as the preferred pattern during September, October, and November (SON) and December, January, and February (DJF). During March, April, and May (MAM), pattern 2 is the preferred pattern. The ending summer has pattern 3 as the preferred pattern. The highest percentage of occurrence for pattern 1 is 17% in October. For patterns 2 and 3, it is 25% in September and August respectively.

In the Late Enders category of ENSO events (Table 2c), idealized monthly temperature patterns 1 and 3 are the preferred patterns during the initial JJA, SON, and DJF (Table 3c). Pattern 1 is preferred four times during JJA and SON with 33% as its highest occurrence rate in June (0). The DJF period alternates between a +P3 and -P1 preferred pattern. The highest rate of occurrence for pattern 3 is 33% in July (0). In the seasons of northern spring and summer (1), pattern 2 occurs four times as the preferred pattern with 20% in April as the highest rate of occurrence (Table 3c).

In the category of Early Starters and Late Enders ENSO events (Table 2d), idealized monthly temperature patterns 1 and 3 occur the most as the preferred patterns of this category (Table 3d). Pattern 3 occurs often in the initial and ending summer and during spring. Pattern 1 is preferred during SON (+P1) and DJF (-P1). Monthly temperature pattern 2, along with pattern 3, is the preferred pattern in April (1) and June (1). Pattern one's highest percentage of occurrence is 25% in June (0) while pattern three's highest is 33% during July (0) and May (1).

Precipitation

The same processes used in determining preferred temperature patterns were used in determining preferred precipitation patterns. Each factor of the analysis of space coefficients was associated with a pattern of monthly precipitation anomalies. Three idealized precipitation patterns for the United States were identified (Fig. 2) from these patterns associated with each factor. Idealized precipitation pattern 1 (Fig. 2a) indicates precipitation anomalies associated with factor 1. Idealized precipitation pattern 2 (Fig. 2b) shows the anomalies associated with factor 2 and likewise for pattern 3 (Fig. 2c).

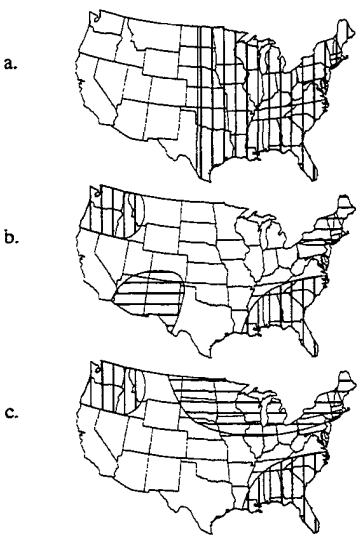


Figure 2. Idealized monthly precipitation patterns (a) 1, (b) 2, and (c) 3. Vertical lines indicate areas of expected positive monthly precipitation anomalies and horizontal lines indicate areas of expected negative monthly precipitation anomalies.

Frequency distributions of the results of this examination were conducted for each category of ENSO events (Table 4). The notation is the same as for the preferred temperature patterns with +P1 (-P1) indicating that a month's precipitation anomaly pattern is similar (opposite) to idealized precipitation pattern 1 etc. etc.

Table 4. Frequency distribution of the preferred patterns of monthly precipitation for (a) Early Starters, (b) Early Enders, (c) Late Enders, and (d) Early Starters and Late Enders. A +PI (-PI) indicates that Idealized monthly precipitation pattern 1 (or opposite) occurred most often in the month indicated etc. etc. If more than one preferred pattern is given, then each occurred the percentage indicated. No preferred pattern is given when its % of occurrence is less than 10%.

	J(0)	J(0)	A(0)	S(0)	O(0)	N(0)	D(0)	J(1)	F(1)	M(1)	A(1)	M(1)	J(1)	J(1)	A(1)
(a)	P1	P1	P1	-P2	P1	-P1	-P1	P1 -P2 -P3	P1	P1		-P1,-P1	P3	P3	-P1
%	17	21	17	21	21	29	21	13	25	17		38	17	21	17
(b)	P3	P1	-P1 -P3	P1	-P1	P2	P1	P2	P1	P1		P1	-P3	-P3	-P3
%	25	50	17	25	33	25	42	17	25	25		42	33	33	25
(c)	-P2	P1 -P1	P1	-P2	P1	-P1	-P2	-P1	P2	-P1		-P1	P3	P3 -P1	P3
%	20	20	20	27	27	40	27	27	27	13		40	13	33	20
(d)	P1 P2 -P2 -P3		P1	-P1	P1	-P1	-P2	-P1	P2	-P1		-P1		P3	P3
%	17		17	42	33	50	17	17	33	17		42		33	25

The Early Starters type of ENSO events has pattern 1 (Fig. 2a) as the preferred precipitation pattern during the initial summer season (Table 4a). During SON, -P2 P1, and -P1 are the preferred respectively. The December through May period has P1 as the preferred pattern while the ending summer has P3 as the preferred precipitation pattern. Pattern one's highest percentage of occurrence is 38% in May (1). Twenty-one percent represents the largest percentage of occurrence for patterns 2 and 3 in July (0) and July (1) respectively.

In the Early Enders category of ENSO events, idealized precipitation pattern 1 is the preferred pattern of precipitation anomalies during JJA (0) and the early fall (Table 4b). November (0) and January (1) prefer pattern 2 (Fig. 2b) while December prefers pattern 1. Pattern 1 (Fig. 2a) is the preferred pattern during the February-May period. In the ending summer, pattern 3 (-P3) represents the preferred pattern of precipitation anomalies. Pattern 1 occurs 50% of the time in July (0) for its largest occurrence rate. The largest for pattern 2 is 25% in November (0) and for pattern 3, it is 33% in June (1).

For the Late Enders category, idealized monthly precipitation patterns 1 and 2 alternate as the preferred patterns from the initial JJA through DJF (Table 4c). During MAM, pattern 1 (-P1) is the preferred pattern. Once again, pattern 3 is the preferred pattern during the ending JJA period. The highest rate of occurrence for pattern 1 is 40% which occurs in November and May. Pattern two's highest rate is 27% and this occurs in September, December, and February. A 33% rate of occurrence represents the largest for pattern 3 (Table 4c).

Pattern 1 and the reverse of it are preferred from June (0) through November (0) for the Early Starters and Late Enders category of ENSO events (Table 4d). Pattern 2 is the preferred precipitation pattern for December and February while pattern 1 is preferred in January, March, and May. Pattern 3 is preferred during the ending summer. Pattern one's largest percentage of occurrence is 50% in November (0). Thirty-three percent represents the highest rate for pattern 2 and 3 during February (1) and July (1) respectively.

The three idealized monthly patterns for both temperature and precipitation were created as a means of identifying where, in the continental United States, positive or negative monthly climate anomalies might occur during particular types of ENSO events. They do not suggest that these are the only climate anomalies which can occur during ENSO events.

The previous tabular analyses indicate the monthly climate anomaly patterns which occur most frequently in the continental United States during these type of ENSO events. Unfortunately, the frequency distributions reveal that these preferred patterns usually occur a small percentage of the time. This limits the use of these results in climate prediction during ENSO; however, they also can be valuable as a climatology of monthly climate patterns in the United States associated with categorized ENSO events.

SUMMARY AND CONCLUSIONS

ENSO events which occurred during the period 1895-1990 were categorized according to the behavior of each as indicated by the WRI. Factor analysis of monthly climate anomalies in the United States associated with these ENSO events was conducted. The analysis produced three factors, with each factor exhibiting patterns of factor loadings. These patterns of factor loadings were used to create three idealized temperature and precipitation anomaly patterns in the continental United States as a means of identifying climate modes which occur during the categorized ENSO events.

A possible reason that the preferred climate patterns occurred a low percentage of the time is that the sample size of ENSO events (27) was too small for rigorous statistical testing and that the number of events was considerably less than the 40 states (points) used in the factor analysis. The factor analysis requires more points (state data) than cases (ENSO events) to be statistically sound or stable through time. If more events are added to the sample, the number of cases will be closer to the points used, making the factor analysis less unstable with time.

Future monthly climate anomaly patterns associated with ENSO can be compared to the ones of this research. This will hopefully allow for a better understanding of these anomalies in the United States. A similar approach could be used in determining ENSO-related climate anomalies for other countries. This would allow for a better understanding of the well documented effects by the ENSO phenomena on the global climate.

REFERENCES

Kim, J.O., and Mueller, C.W., 1978, "Introduction to Factor Analysis: What Is It and How To Do It", Sage Publications.

Peixoto, J.P., and Oort, A.H., 1992, "Physics of Climate", American Institute of Physics.

Quinn, W.H., Zopf, D.O., Short, K.S., and Yang, R., 1978, "Historical Trends and Statistics of the Southern Oscillation, El Nino, and Indonesian Droughts", Fishery Bulletin 76 pp. 663-678.

ACKNOWLEDGEMENTS

I would like to thank Dr. Arthur Douglas of Creighton University, USA, for his guidance in preparing this research.

CORRESPONDING AUTHOR

Mr. Wayne Presnell
National Weather Service Office,
1580 Aviation Center Parkway
Daytona Beach, Florida, USA 32114

LONG-TERM ANOMALIES AND TRENDS IN THE MID TROPOSPHERE OF THE NORTHERN HEMISPHERE.

Igor I. Zveryaev and Olga A. Razoryonova

P.P.Shirshov Institute of Oceanology, RAS, Moscow, Russia

ABSTRACT

Diagnosis of interannual variability of the 500 hPa geopotential height and temperature is carried out. Winter anomalies of geopotential heights and temperatures are in a good agreement with each other over the oceans and the continents. During the winter period geopotential heights anomalies are strongly linked to the sea level pressure anomalies. Analysis of the relationships between January zonal means of 500 hPa geopotential heights at different latitudes for oceanic and continental regions is presented. Some characteristics of the North Atlantic and the North Pacific oscillations patterns are considered. There is a remarkable relation of the long-term (interdecadal) trends over the North Pacific and over the northern part of Eurasia, namely, positive trends over the North Pacific are associated with negative tendencies over the Eurasia and vice versa. The north-south and the ocean-continent structure of the long-term variations of 500 hPa heights and temperatures are investigated.

1.INTRODUCTION

The majority of articles concerning empirical and modeling study of climatic variability and large-scale ocean-atmosphere interaction deals with the long-term variability of the mid tropospherical parameters. There are a number of well known reasons for this. Climatic signal is more pronounced in 500 hPa heights variations than in sea level pressure variability (SLP) because of the natural low-pass filtering. Thus investigations of such phenomena as El-Nino - Southern Oscillation, North Atlantic and North Pacific oscillations (Palmer and Sun (1985), Wallace and Gutzler (1981), Rogers (1984)) include analysis of the long-term variability of parameters in the mid troposphere.

In this paper we consider climatic variability of the 500 hPa heights and temperatures in the areas of their most intensive variations and some relationships between this variability and long-term changes of the SLP. To investigate the north-south and the ocean-continent structure of climatic variability of 500 hPa heights and temperatures we consider anomalies of zonal means calculated separately for oceanic and continental regions.

2. LONG-TERM ANOMALIES AND TRENDS OVER THE NORTH ATLANTIC, THE NORTH EURASIA AND THE NORTH PACIFIC

The data set used in this study consists of monthly mean 500 hPa geopotential height and temperature and SLP, presented on NMC (United States National Meteorological Center) octagonal grid, spanning the period 1946-1989 (geopotential height and SLP) and 1962-1989 (temperature). The data have been converted into 5° by 5° latitude-longitude grid.

To investigate characteristics of the long-term variability of the parameters of the mid troposphere during the Northern Hemisphere winter we have chosen three regions over the North Atlantic, the northern part of Eurasia and the North Pacific. Centers of these regions are sited at 50°N 30°W, 75°N 90°E and 50°N 170°W respectively. Wallace and Blackmon (1983) define these regions as those characterized by the most intensive variability of the winter monthly means of 500 hPa geopotential height.

Time series of the January anomalies of 500 hPa height and temperature as well as of SLP have been computed. Winter anomalies of geopotential heights and temperatures are in a good agreement with each other over the oceans and the continent. In wintertime, geopotential heights anomalies are also strongly linked to the SLP anomalies. Correlation coefficients between geopotential heights anomalies and SLP anomalies over the oceans are higher ($r=0.89$ and $r=0.93$ for the North Atlantic and the North Pacific, respectively) than those over the continent ($r=0.80$ for the Eurasia). The values of the correlation coefficients are statistically significant at the 95% confidence level. It is found out that beginning from the mid 60's positive anomalies over the North Atlantic are usually associated with negative anomalies over the North Pacific and vice versa.

Time series of the annual means of 500 hPa geopotential heights demonstrate remarkable relation between the long-term (interdecadal) trends over the North Pacific and over the northern part of Eurasia (fig.1), namely, beginning from about 1963 positive trend over the Eurasia are accompanied by negative trend over the North Pacific. This relation may result from the large scale interdecadal air masses redistribution between these two regions.

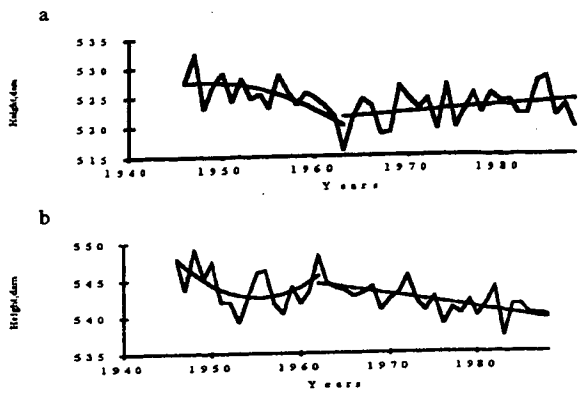


Figure 1. Annual mean 500 hPa geopotential heights (dam) and long-term trends over the North Eurasia (a) and the North Pacific (b).

Analysis of the connections between January zonal means of 500 hPa geopotential heights calculated for oceanic and continental areas shows that the highest negative correlation coefficient (r=-0.78) (fig.2) over the North Atlantic is observed between 35° and 65° northern latitudes zonal means. The highest negative correlation coefficient (r=-0.77) over the North Pacific is obtained between 25° and 60° northern latitudes zonal means. These results indicate the manifestation of the North Atlantic and the North Pacific oscillations. Over the Eurasia the highest negative correlation coefficient (r=-0.61) is obtained between 45° and 70° northern latitudes zonal means. Presented values of the correlation coefficients are statistically significant at the 95% confidence level.

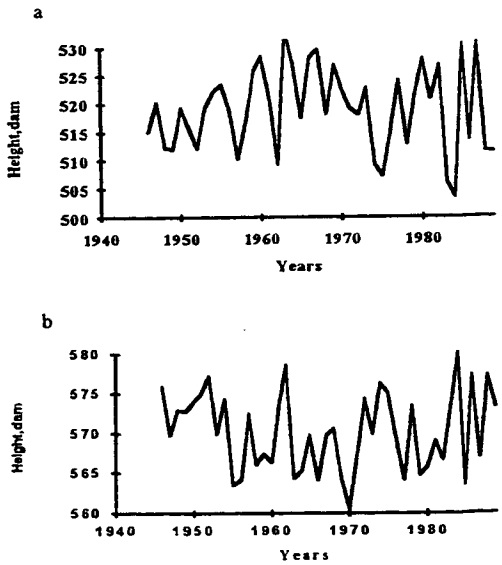


Figure 2. January monthly means of 500 hPa geopotential heights over the North Atlantic at 65°N (a) and 35°N (b).

3. THE NORTH-SOUTH AND THE OCEAN-CONTINENT STRUCTURE OF THE LONG-TERM VARIATIONS

To study the north-south and the ocean-continent structure of the long-term variations of 500 hPa heights and temperatures we have constructed zonal time series of the annual mean anomalies, calculated separately for the North Atlantic, the Eurasia, the North Pacific and the North America. Anomalies are calculated with respect to the 1946 to 1989 averaged for the geopotential heights and to the 1963 to 1989 averaged to the temperature. These time series are presented in figure 3. We have added heavy solid curves to indicate decadally smoothed trends. The smoothed curves were obtained by applying Potter's low-pass filter with 10-year window.

As it is clearly seen in figure 3 the values of anomalies of 500 hPa geopotential heights vary within the range from -2 dam to 2 dam in mid and low latitudes over the continents and in low latitudes over the oceans. There is remarkable increase of the anomalies in mid latitudes over the oceans. For example, at 50°N over the North Pacific the 500 hPa geopotential heights anomalies values vary from -4 dam to 6 dam. At the same time, we observe well defined negative trend during the whole period from 1946 till 1989 in the mid latitudinal North Pacific only. The dominant feature of the long-term variability of 500 hPa geopotential heights both over the continents and the North Atlantic is the transform of the negative trend to positive one in the late 70's. Zonal time series of the temperature in mid latitudes over the North America exhibit negative anomalies during the period from 1963 till about 1977 and positive anomalies in later years. Of considerable interest are the diverging interdecadal trends in mid latitudes over the North Pacific and the North America during the whole period with relative cooling over the North Pacific and relative heating over the North America. There are no such long-term trends over the North Atlantic and the Eurasia, where the quasi-decadal fluctuations are dominant. In low latitudes temperature anomalies vary coherently over the oceans and the continents.

4. CONCLUSIONS

This paper has considered climatic variability of the 500 hPa geopotential height and temperature over Northern Hemisphere. Long-term anomalies and trends in the regions of the most intensive variations of the winter monthly means of 500 hPa geopotential height are studied. Opposite trends of 500 hPa geopotential heights over the North Pacific and the North Eurasia are defined. Some characteristics of

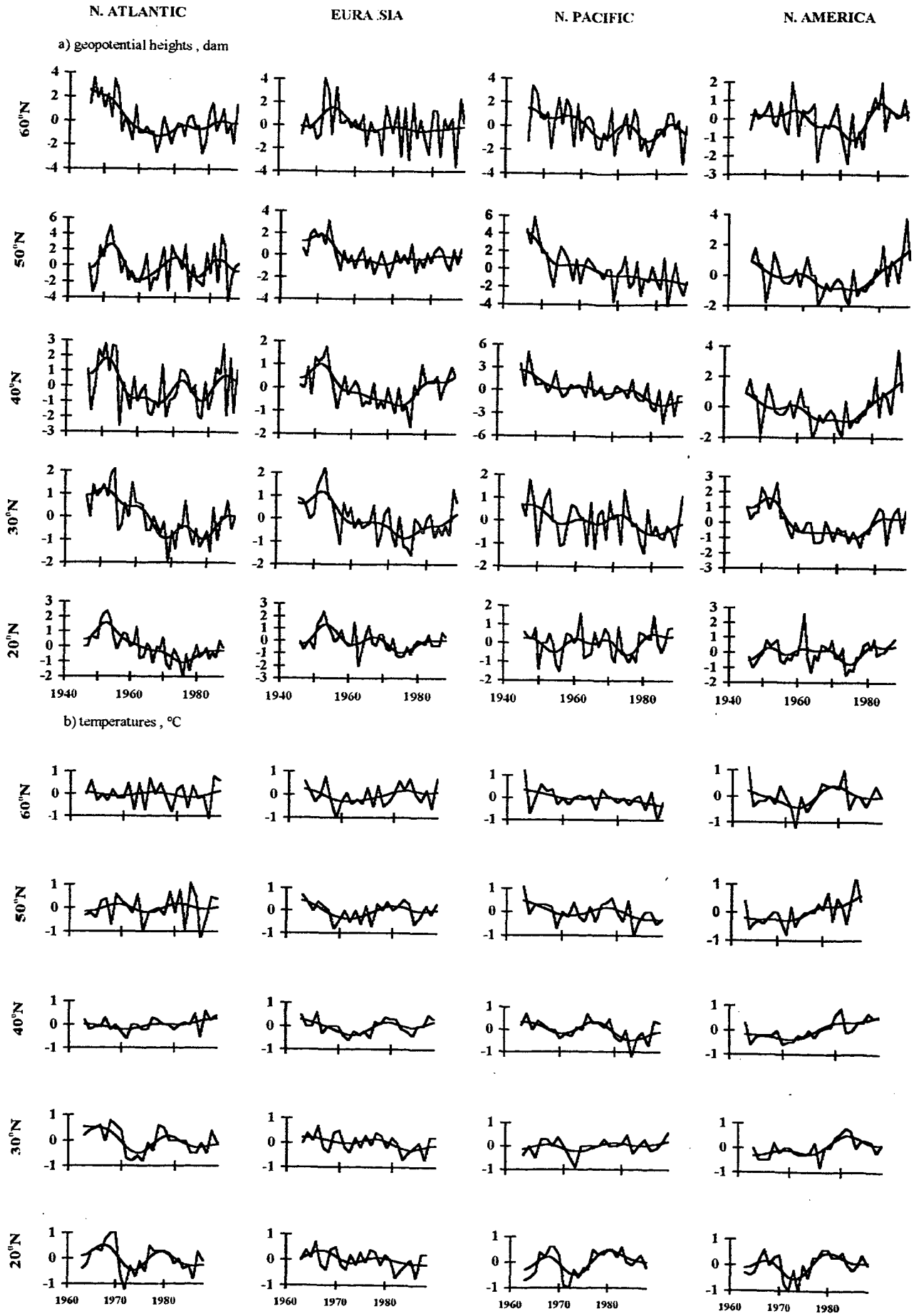


Figure 3. Annual mean 500 hPa geopotential heights and temperatures anomalies averaged along the latitudes from 20°N to 60°N . The dominant trends are shown by solid curves.

connection between long term variations of 500 hPa geopotential heights and SLP are presented.

The north-south and the ocean-continent structure of the long-term variations of 500 hPa heights and temperatures are investigated. It is shown that the long-term variations of 500 hPa heights intensify sufficiently in the mid latitudes over the oceans. The diverging interdecadal trends in mid latitudes over the North Pacific and the North America during the whole period with relative cooling over the North Pacific and relative heating over the North America are defined.

5. REFERENCES

Blackmon, M. L.,Y.-H. Lee, J. M. Wallace, 1984, "Horizontal structure of 500 mb height fluctuations with long, intermediate and short time scales." J. Atmos. Sci., volume 41, pp. 961-979.

Graham, E.N., T. P. Barnett, R. Wilde, M. Ponater, S. Schubert, 1994, "On the roles of tropical and midlatitude SSTs in forcing interannual to interdecadal variability in the winter Northern Hemisphere circulation.", J. Climate, volume 7, pp. 1416-1441.

Palmer, T.N., and Z. Sun, 1985, "A modeling and observational study of the relationship between sea surface temperatures in the north-west Atlantic and the atmospheric general circulation.", Quart. J. Roy. Meteor. Soc., volume 111, pp. 947-975.

Rogers J.C., 1984, "The Association between the North Atlantic Oscillation and the Southern Oscillation in the Northern Hemisphere.", Mon. Wea.Rev., volume 112, pp. 1990-2015.

Wallace, J. M., and D. S. Gutzler, 1981, "Teleconnections in the geopotential height field during the Northern Hemisphere winter.", Mon. Wea. Rev., volume 109, pp. 784-812.

6. ACKNOWLEDGMENTS

This work was supported under International Science Foundation Grant ME5000 and under the Grants "Global Climate Change" and "World Ocean" sponsored by the Russian Ministry of the Science and Technological Policy.

CORRESPONDING AUTHOR
Doctor I.I. Zveryaev,
P.P.Shirshov Institute of Oceanology,
RAS, Krasikova st., 23,
Moscow, 117218, RUSSIA.

□

MONTHLY MEAN PRECIPITATION AND TEMPERATURE OVER THE UNITED STATE -- EOF ANALYSIS

Robert F. Cahalan, Lawrence Wharton, and Man-Li Wu
Goddard Laboratory for Atmospheres
NASA/Goddard Space Flight Center, Greenbelt, MD 20771 U.S.A.

The January and July monthly mean precipitation and temperature at 61 stations over the United States during1900-1990 are analyzed in terms of empirical orthogonal functions (EOFs) and their variances. The eigenvalue spectra are compared with an analytic form for the sample variance spectrum of uncorrelated noise, and also with a generalized form which accounts for time correlations. The number of signal modes increases with the ratio of months-per-gridpoint in either field, and more modes are distinguishable from noise in the temperature field than in precipitation for any given ratio. More signal modes occur in January than July, consistent with the increased importance of local heating and convective rainfall in summer. The effect of temporal correlation on the noise spectrum, and the effect of spatial correlation on the EOFs are clarified. Comparison of the signal modes with homogeneous and isotropic noise illustrates: 1. structure due to the nature of the spatial domain of the data rather than the nature of the climate ("domain error"); and 2. structure due to contamination by other EOFs having similar variance ("mixing error").

Long term Variability of Intensity and Frequency of Indian Monsoon Rainfall

A. Kulkarni and S.V. Singh
Indian Institute of Tropical Meteorology
Pune, INDIA

It is well known that a large part of annual rainfall at a station is contributed by a small number of heavy rain days. The behaviour of daily rainfall distribution at different stations over entire country is very important aspect of Indian monsoon rainfall as well as Indian climatology.

The daily 24 hour rainfall data for monsoon months (June- September) for 29 stations well distributed over entire India for the period of 89 year, 1901-1989, has been used in this study. The daily rainfall series of every station has been categorised in 3 categories -scanty, moderate and heavy rainfall by using appropriate thresholds. The long term variability of total, frequency and intensity of these three categories have been studied using nonparametric tests. Since the daily rainfall series is highly noisy and serially uncorrelated in time the Mann-Kendall test has been used for trend analysis. Also Petitt (1975) test has been applied to detect the shift in time series of these quantities. Characteristic features of the extreme rainfall events defined as upper 10% daily rainfall values are also studied. The difference in distributions of high intensity rainfalls and extremes have been studied using Mann-Whitney test in contrasting situations.

It has been observed that total rainfall and number of rainy days are increasing over Northern and Western parts of India. North-east India shows decreasing trend, but not significant. Also all stations over Northern India, and West Coast shows a shift in extremes and high intensity rainfalls in the period 1920-1940.

Thus the high intensity rainfalls and the number of days giving them are increasing over western parts of India but their distribution in drought and flood situations is much different.

Ensemble Predictions and Chaotic Systems

Leonard A. Smith

Mathematical Institute, University of Oxford, Oxford, GB

ABSTRACT

Forecast evaluation with a single prediction determined from each imperfectly observed initial state is incomplete; observational noise implies that an ensemble of initial states of the system are consistent with the current observed state. In a nonlinear system, this distribution will develop non-Gaussian structure, even if the forecast model is perfect. The case of a perfect model is contrasted with a forecast model for temperature observations from a thermally-driven, rotating fluid annulus. Ensemble prediction of nonlinear systems reveals shortcomings in the traditional evaluation of forecast-verification pairs with least-squares cost functions.

1. INTRODUCTION

Self-consistent prediction requires accounting for observational noise not only when constructing the model, but also in the observation from which predictions are initiated. One approach is to forecast an ensemble of initial conditions, each of which is consistent with the observation, see Palmer (1992). We will consider a single observable, s_i, and investigate the implications which imperfect models of the system and inexact characterisation of the observational noise hold for prediction. Our concern here is to interpret the results of "fast" models, independent of the details of the model itself, whether it be based on radial basis functions, neural nets, or parameterised physics. The data comes from a laboratory system where the application of nonlinear dynamical systems theory can be put to the test using ensembles orders of magnitude larger than those practical in numerical weather forecasting models.

Given a model, F, there are (at least) two barriers to perfect prediction: (i) F, while potentially very good, will not be a perfect model, so the prediction error, if initially small, will grow with time, (ii) the initial condition will not be "perfect" either - any observational error will result in the growth of error even in the case of a perfect model. Even in the lab, significant observational error in unavoidable; at the very least, there will be truncation errors due to an analog-to-digital (A/D) converter. This has, of course, been recognised in numerical weather forecasting for some time (*e.g.* Thompson (1957)), and has repeatedly been posed as limiting the predictability of chaotic dynamical systems.

2. ENSEMBLE PREDICTIONS

Given an ensemble of points, each consistent with a particular observation, we can observe how the initial uncertainty grows with time by evolving the ensemble of initial conditions under our model. We then estimate the reliability of the forecast by interpreting the distribution of the ensemble as the probability density function (PDF) of the observation after time t, which we denote as $\psi_t(s)$. The evolution of $\psi_t(s)$ with time is shown in the figures. If our models of both the dynamics and the ensemble are perfect, we will have the optimal predictions of this deterministic system; the statistical aspect is unavoidable. Our incomplete knowledge of the initial condition forces this interpretation even when we can extract exact deterministic dynamics (Epstein(1969)). For chaotic systems, $\psi_t(s)$ may "quickly" spread over the full range of s and, given a perfect model, it will evolve toward an invariant PDF, $\psi_\infty(s)$, which corresponds to the projection of the invariant measure onto the quantity we are measuring. In the absence of any knowledge of the current state of the system, our best prediction is summarised by $\psi_\infty(s)$ (*i.e.* the climatological distribution).

3. THE LORENZ SYSTEM

To distinguish the complications arising from an imperfect model from those of inexact knowledge of the initial state, we assume a perfect model of the deterministic system, the Lorenz equations themselves, see Lorenz(1963), and consider a perfect ensemble of initial conditions. In this case we have data on a strange attractor subject only to quantisation error; while we may form an ensemble of uniformly distributed values over the range mapped into the observed value by truncation, the true values of the system will *not* be uniformly distributed in this range. Two obvious implications are: (1) that stability may be distorted by perturbations off the attractor which fall back onto it, and, worse yet, (2) that not all initial conditions in this region need be in the same basin of attraction as the system we are studying!

Figure 1 shows the evolution of a set of 2^{12} points on the attractor, all of which are indistinguishable given an 8-bit observation of their location in phase space; the two columns show the evolution of the PDF for the Lorenz variable x, the left column for time zero to six, the right column continues the graph for time six to twelve. Several nonlinear aspects of the decay of predictability are obvious: [1] The

decay is not monotonic, as expected by Tong and Moeanaddin (1988); there is "return of skill" in that predictions for time $t = 0.4$ are sharper than predictions for $t = 0.2$; [2] The distribution is not Gaussian, indeed, it is not uni-modal. This implies that least-squares solutions are not optimal, for instance at $t = 2.75$ the correct least-squares prediction would be the center of the graph, $x = 0$ where there is no probability of observing the system; [3] Although the PDF spreads quickly, $\psi_t(s)$ appears different from $\psi_\infty(s)$ for quite some time.

The time at which $\psi_t(s)$ becomes indistinguishable from $\psi_\infty(s)$ (and therefore, in our context, useless), defines the true "limit of predictability" given this triplet of observation, model and ensemble size.

4. ROTATING CONVECTION

Now contrast the Lorenz case with a rotating, thermally stressed fluid annulus believed to exhibit low dimensional, chaotic dynamics. A time series of temperature measurements from a co-rotating probe was used to construct a radial basis function model of this system. The data series has been divided into a learning set and a test set, the first is used in the construction of the model and the second for out-of-sample evaluation. The details of the experiment and this analysis are given in Read *et al.*(1992) and Smith(1992, 1994b). Figure 2 shows a series of 27 evolutions of $\psi_t(s)$, each for a duration of 16 iterations; the initial ensembles were Gaussian with standard deviation 0.02 degrees. Every 16 iterations, the true observation is noted and a new ensemble is started (there is a vertical gap in the graph to mark each of these points in time), the extent to which the predicted PDF reflects the new observation determines the accuracy of the prediction.

Note that some members of the ensemble fall outside the basin of attraction and diverge immediately from the range of observed values (as in ensembles 1, 2, 4, 10, 12 ...). Ignoring such points, the evolution of ensembles under this forecast model does appear to reflect the evolution of the system fairly well. Rapid, non-Gaussian evolution of ensembles reflects a rapid, and variable, decay of predictability; the final PDFs (each just before a gap) agree fairly well with the observations. An exception is ensemble 12, where we have a sharp well defined PDF which does not reflect the observation at the time ensemble 13 is initialised. Also note that ensemble 11 correctly indicates an impending rapid drop in temperature, without giving the precise timing; while ensemble 26, gives an indication of the timing of the drop and also reflects the initial state observed for ensemble 27 indicating some "return of skill." Each of these behaviours has a parallel in numerical weather forecasting, but in this situation, the simplicity of the models and the availability to obtain large data sets will allow us to resolve questions with a statistical certainty not obtainable for the atmosphere. One example involves determining the best method of forming imperfect ensembles; there are many others.

5. CONCLUSIONS

In both examples considered, the PDF quickly becomes multi-modal, this holds deep implications for the appropriateness of model fitting and verification in the least-squares sense. Specifically, the predictor with the least squared prediction error may consistently predict physically unreasonable results, while forecast models making predictions consistent with the observations, or for that matter even a perfect forecast model, may rank low in a least squares sense. As expected (see Smith(1994b) and references therein), both the predictability and model forecast skill for chaotic systems varies widely between different initial states. Finally, the selection of initial conditions consistent with the model is a nontrivial problem, even when the noise process is known.

The ensemble forecast *can* contain usable information as long as it is distinguishable from $\psi_\infty(s)$. As noted by Murphy (1993), the question of whether or not a given prediction is "useful" is a complicated one, depending on the goals of the user of the forecast. What we can be sure of is that once the image of the ensemble remains indistinguishable from $\psi_\infty(s)$, then the forecast is definitely "useless". The time scales for the onset of uselessness, however, can be significantly longer than those suggested by simple error growth models.

RE.ERENCES

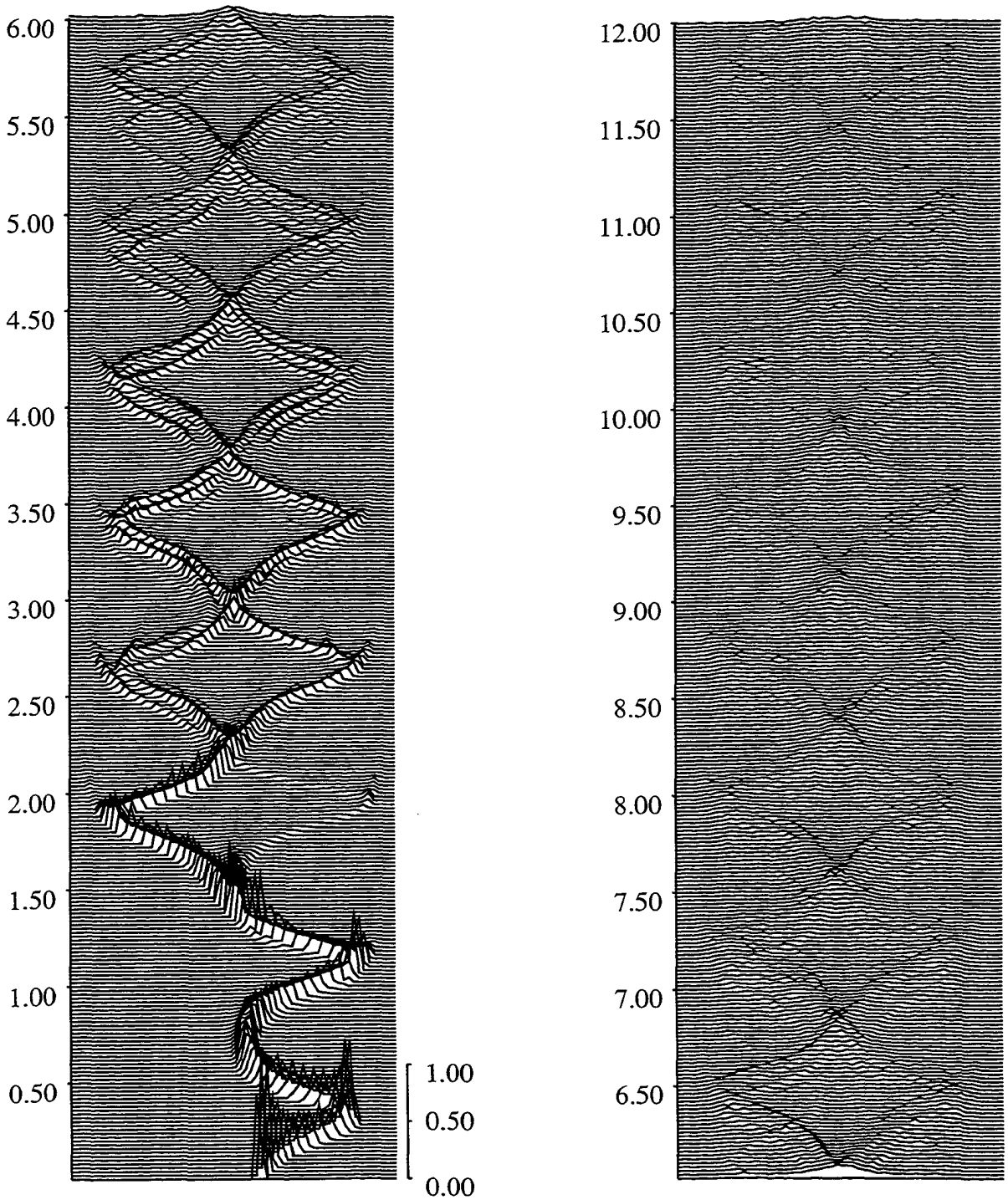
1. E.S. Epstein. *Tellus*, 21(6):739–759, 1969.
2. E. N. Lorenz. *J. Atmos. Sci.*, 20:130–141, 1963.
3. Allan H. Murphy. *Weather and Forecasting*, 8:281–293, 1993.
4. T. N. Palmer. *Meteorological*, (58):5–15, June 1992.
5. P. Read, M. J. Bell, D. W. Johnson, and R. M. Small. *J. Fluid Mech.*, 238:599–632, 1992.
6. L. A. Smith. *Physica D*, 58:50–76, 1992.
7. L. A. Smith. In F.T. Luk, editor, *Advanced Signal Processing: Algorithms, Architectures and Implementations*, volume 2296, pages 293–304, Bellingham, WA, 1994. SPIE.
8. L. A. Smith. *Phil. Trans. R. Soc. Lond.*, A 446, 1994b.
9. P. D. Thompson. *Tellus*, 9:275–295, 1957.
10. H. Tong and R. Moeanaddin. *The Statistician*, 37:101–110, 1988.

ACKNOWLEDGEMENTS

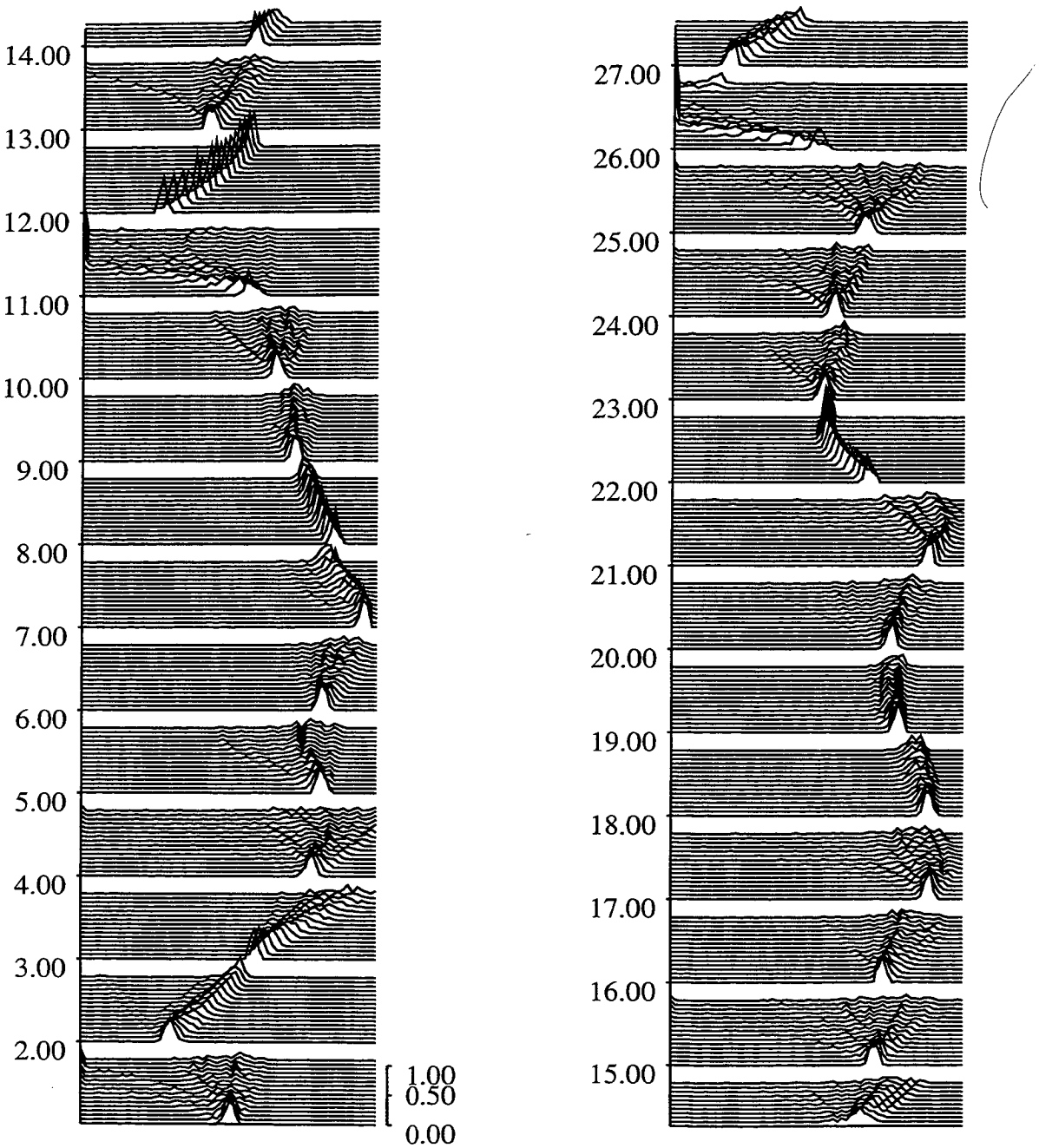
LAS is supported by a Senior Research Fellowship at Pembroke College, Oxford.

CORRESPONDING AUTHOR

Leonard A. Smith
Mathematical Institute
26 St Giles'
University of Oxford
Oxford OX1 3LB, ENGLAND
email: lenny@maths.ox.ac.uk



A perfect forecast of the evolution of a perfect ensemble of initial conditions, each on the Lorenz attractor and indistinguishable under an 8-bit observation. Each horizontal curve reflects $\psi(x)$ at a time t, the left column for times $0 < t < 6$, the right for $6 < t < 12$. The scale for ψ is given just to the right of the left column.



Evolution of $\psi(T)$ for the predicted temperature, T, for the rotating annulus. The evolution of 27 ensembles are shown, each re-initialisation is preceded by a gap for clarity. The PDFs are initially Gaussian, they are evolved under an (imperfect) radial basis function forecast model for 128 sample times (only 16 PDFs are plotted), the last PDF is followed by a gap, after which a new ensemble is initiated about a fresh observation.

"Testing (and I mean testing) for the presence of chaos"

Rodney C.L. Wolff
University of Glasgow, Scotland
(moving to: Queensland University of Technology)
(EMAIL: r.wolff@qut.edu.au)

ABSTRACT

There are many instances of `real data' whose manifestly erratic behaviour appears to be largely attributable to the presence of low-dimensional chaos. A bench-mark of deterministic chaos is the tendency of nearby initial conditions to diverge exponentially fast in the short term. The global rate of such (exponential) divergence is given by the Lyapunov exponent(s) of the system. Where equations governing a strictly deterministic dynamical system can be written down, it may be possible to calculate an expression for the Lyapunov exponent(s), even approximately. In other cases, there exist various methods to construct non-parametric estimators of the Lyapunov exponent(s). A necessary condition for the existence of chaos is that the dominant Lyapunov exponent is positive, and this is often (reasonably) taken to be a sufficient condition. To date, however, all inferential methods based on Lyapunov exponents seem only to use point estimates thereof: little or no careful attention is given to the precision of such estimates. In this talk, we consider the efficacy of bootstrap methods for the interval estimation of Lyapunov exponents. Further, by way of setting the scene for allied inference on noisy dynamical systems, we construct a bootstrap percentile test which can be applied to hypothesis tests on Lyapunov exponents and related sensitivity measures.

CLIMATE VARIABILITY UNDER CLEAR SKIES: APPLICATIONS FOR THE CLOUD AND SNOW COVER FEEDBACK PROBLEMS

Pavel Ya. Groisman,
University of Massachusetts
Amhesrt, MA, USA

Pan-Mao Zhai
National Climate Center
Beijing, PRC

ABSTRACT

Climatology of clear skies for northern extratropical land is presented in the form of deviations from the average climate conditions. Clouds are an internal component of the climate system, and these deviations indicate specific climate conditions associated with clear skies. At the same time, they may be considered as estimates of the *overall "forcing"* of the regional climate by clouds. A similar approach is applied to estimation of the potential effect of the presence of snow on the ground and an attempt is made to divide the effects of snow and clouds.

INTRODUCTION

Many satellite measurements heavily rely on clear skies for quality observations (Gutman et al. 1995). The composite average based on such measurements differs from the averages made under mean climate conditions. To develop the appropriate adjustments, a knowledge of the clear-sky climatology is required. Moreover, observations under clear skies play a key role in contemporary studies of the cloud and snow cover feedbacks (cf., Harrison et al. 1990; Cess et al. 1991; Potter et al. 1992; Gaffen and Elliott 1993; Groisman et al. 1994). Thus, precise characterization of clear-sky climate conditions can help to resolve these important problems of modern climate modeling and climate change studies. This is a main aim of our paper. Additionally, we use hourly observational data stratified (sliced) by constant values of some of meteorological parameters (surface temperature, cloudiness, snow on the ground) to estimate relationships between different meteorological elements. Some of these relationships may be loosely named "feedbacks".

DATA

Figure 1 shows the stations used on the current stage of the study (totally 115 primary and 34 supplementary stations from China, the former USSR, Canada, and the United States). In North American and Chinese stations surface, aerological and snow cover data were jointly analyzed. Only surface data (including station data on snow cover) have been currently processed for Russia. The data

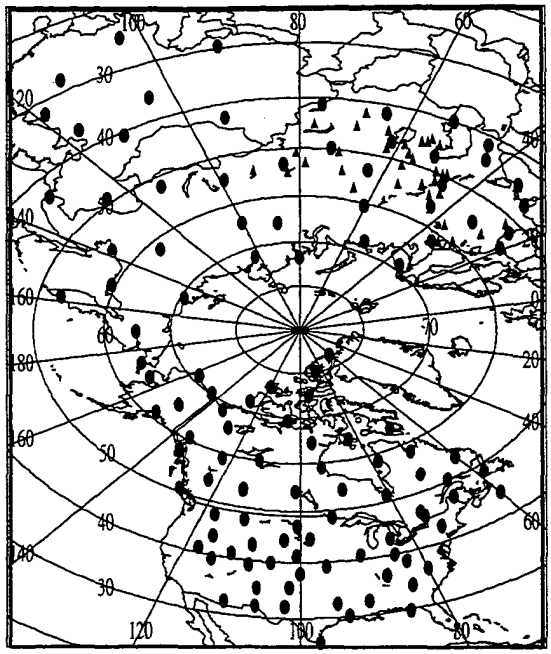


Figure 1. Stations used in this analysis, primary (•) and supplementory (▲) networks.

characteristics are:

A. Russia: near-surface 3-hour-meteorological observations (Razuvaev et al. 1995) period 1966-1990 for primary and 1966-1984 for supplementory stations; *B.* China: near-surface 6-hour meteorological observations, period 1951-1990, 00Z and 12Z aerological observations at standard levels, period 1972-1992; *C.* Canada and United States: hourly surface observations from circa 1950 to 1993; 00Z and 12Z aerological observations at standard levels, period 1972-1992 (NCDC 1993). *D.* Snow cover satellite data in the grid cells collocated to selected stations from 1972 to 1992, weekly data for North America and China (Matson 1986). For Russia instead of satellite data we used daily station reports on presence and type of snow cover on the meteorological ground.

CLOUD "EFFECTS"

For the network depicted in Figure 1, we analyzed hourly surface and aerological data for the

past several decades to obtain the climate distribution under clear sky conditions and compared it with average long-term normals. Some results of this comparison are presented in Figures 2 through 4. The sample size for these estimates varies significantly depending on time and season. While average conditions were estimated using more that 750 observations for each hour and month, the sample size for mean clear sky conditions varied from 250 (night in winter and spring) to 30 (afternoon in summer). ***Clouds are an internal component of the climate system; nevertheless, the results of this comparison may be considered as estimates of the overall "forcing" of the regional climate by clouds.***

Clear-sky weather conditions possess some special features that place them aside from average climate. Besides such obvious features as an absence of precipitation and clouds, clear skies in extratropical regions are characterized by (a) mostly anticyclonic conditions (on average the atmospheric pressure is 5hPa above its long-term mean values), (b) weaker advective processes (wind speed at the anemometer height is usually 20 to 50% less under clear skies than on average), (c) a reduced water vapor content of the troposphere by 20 to 50%, (d) significant changes in near-surface temperature field and heat fluxes, (e) a stronger diurnal cycle in near-surface climate characteristics and heat fluxes. We have quantified all these properties for most of North America and Eurasia (in the boundaries of the above-mentioned four countries).

SNOW COVER "EFFECTS"

The absence of clouds makes more prominent all effects of surface conditions on the heat and vapor fluxes. That's why we used the clear-sky conditions to delimit possible effects of the presence of snow on the ground on the water vapor distribution near the surface and in the lower troposphere (Table 1). To obtain these values the near-surface and aerological data at each station were stratified by surface air temperature, cloudiness, and presence of snow on the ground. Only those temperature ranges (±0.5°C) were selected for which both surface conditions (snow / no snow) were observed under clear skies at least ten times during the analyzed period (1972-1992 for North America and 1966-1990 for the former USSR. The difference: $(e_{snow}-e_{bare})/e_{bare}$ then was calculated for each selected temperature range and for each station. The average values of these differences for Russian, Alaskan, Canadian, and U.S. stations are presented. Accuracy (standards) of these estimates varies from less than 1 (Russia) to 5 (Canada) percent. Examples for single stations are presented in Table 2.

Table 1. Mean average decrease (percent) of the water vapor content of the clear-sky atmosphere under the same surface air temperatures with snow on the ground. For temperatures above the freezing point this decrease is higher than shown below.

Level	Alas-ka	Cana-da	Cont. U.S.	Former USSR
surface	-18	-17	-14	-13
850mb	-23	-18	-15	N/A
700mb	-21	-19	-16	N/A
500mb	-23	-27	-23	N/A

For temperatures much below the freezing point, the presence of snow on the ground under clear skies corresponds to higher water vapor concentration in the lower troposphere above it (cf., Table 2). For temperatures about and above 0°C, the presence of snow on the ground is associated with a water vapor decrease in the lower troposphere under clear sky conditions. For North America (as well as for the most of Eurasia) this latter effect of snow cover prevails on average. Table 1 contains the result for the former USSR territory: a 13% average decrease of the water vapor content when snow is on the ground compared to bare soil conditions. Sorting by equal ground surface temperatures (for Russia we have such data) refines and strengthens this effect to a 22% average decrease (Table 3). It is worth noting that this *decrease* of atmospheric water vapor pressure over snow covered soil under the same surface temperatures corresponds to *an increase* of evaporation rates. For the same data set in Table 4, we estimated the average

Table 3. The same as in Table 2 but for near-surface 3-hourly data from 35 stations well distributed over the former USSR territory. The data were compared in the same temperature ranges (±0.5°C) of surface air and ground temperatures.

Sorting by surface	Average conditions	Clear sky conditions
air temperature	-4%	-13%
ground temperature	-8%	-22%

Table 4. Mean average increase (W m^{-2}) of turbulent heat fluxes under the same ground surface temperatures with snow on the ground (Groisman et al. 1995). These estimates are based on the results of Genikhovich and Osipova (1984) and pertain to the former USSR territory.

Heat flux	Average conditions	Clear sky conditions
Sensible	13	27
Latent	9	19

Table 2: Clear-sky cold season vertical distribution of water vapor pressure (e) at International Falls, Minnesota, USA for various intervals of surface air temperature for bare ground, and its change for snow-covered ground (De = $(e_{snow}-e_{bare})/e_{bare}$).

Temperature interval	Surface		850 mb		700 mb		500 mb	
	e(mb)	De(%)	e(mb)	De(%)	e(mb)	De(%)	e(mb)	De(%)
-12°C to -8°C	1.15	4	0.42	37	0.18	22	0.15	-6
-8°C to -4°C	1.69	5	0.63	29	0.25	24	0.16	-13
-4°C to -1°C	2.36	0	0.98	14	0.38	7	0.20	-22
-1°C to 1°C	2.84	-14	1.22	-3	0.48	-19	0.21	-34

The same, but at Grand Junction, Colorado, USA.

Temperature interval	Surface		850 mb		700 mb		500 mb	
	e(mb)	De(%)	e(mb)	De(%)	e(mb)	De(%)	e(mb)	De(%)
-8°C to -4°C	2.73	3	2.56	-3	1.44	0	0.37	-9
-4°C to -1°C	3.33	2	3.01	-2	1.65	0	0.37	-2
-1°C to 1°C	4.05	-9	3.58	-14	1.91	-10	0.43	-18
1°C to 5°C	4.33	-8	3.77	-15	2.21	-22	0.44	-26
5°C to 8°C	4.77	-10	3.46	-18	2.50	-21	0.52	-23

increase of latent heat flux to be about 20 W m^{-2} when snow is on the ground compared to bare soil.

CONCLUSIONS

Clear skies are characterized by conditions which are significantly different from the average near-surface climatology and heat fluxes. That has to be taken into account in any studies that rely on them as a reference (feedback studies, satellite measurements).

The presence of snow on the ground generally is associated with less water vapor in the lower troposphere under clear sky conditions (while the evaporation rate is higher than on average).

References:

Cess, R.D., and 32 others, 1991: Interpretation of snow-climate feedback as produced by 17 general circulation models. *Science*, 253, 888-892.

Gaffen, D.J. and W.P. Elliott, 1993: Column water vapor content in clear and cloudy skies. *J. Climate*, **6**, 2278-2287.

Genikhovich, E.L. and G.I. Osipova, 1984: Determination of the exchange coefficient using data of routine meteorological observations. *Transactions of the Main Geophysical Observatory*, **479**, 62-69 (in Russian).

Groisman, P.Ya., T.R. Karl, and R.W. Knight, and G.L. Stenchikov, 1994: Changes of snow cover, temperature, and the radiative heat balance over the Northern Hemisphere, *J. of Climate*, **7**, 1633-1656.

_____, P.-M. Zhai, and E.L. Genikhovich, 1995: Cloud and snow cover effects on the surface-atmosphere interactions. Paper presented at the Joint Meeting of the Canadian Geophysical Union -Hydrology Section (CGU-HS) and International GEWEX Workshop on Cold-Season/Region Hydrometeorology, Banff, Alberta, Canada, May 22-26, 1995.

Gutman, G., D. Tarpley, A. Ignatov, and S. Olson, 1995: The enhanced NOAA global land dataset from the Advanced Very High Resolution Radiometer. *Bull. Amer. Meteorol. Soc.*, **76**, No.7 (in press).

Harrison, E.F., P. Minnis, B.R. Barkstrom, V. Ramanathan, R.D. Cess, and G.G. Gibson, 1990: Seasonal variation of cloud radiative forcing derived from the Earth Radiation Budget Experiment. *J. Geophys. Res.*, 95, 18687-18703.

Matson, M., 1986: The NOAA satellite-derived snow cover data base: Past, present, and future. *Glaciological Data Report GD-18: Snow Watch '85*, 115-124 (World Data Center-A for Glaciology-Snow and Ice, Boulder, Co).

National Climatic Data Center (NCDC), 1993: *Radiosonde Data of North America, 1946-1992*, CD-ROM, Version 1.0, August 1993.

Potter, G.L., J.M.Slingo, J-J. Morcrette, and L. Corsetti, 1992: Modeling Perspective on Cloud Radiative Forcing.*J. Geophys. Res.*, **97**, No D18, 20,507-20,518.

Razuvaev, V.N., E.B. Apasova, R.A. Martuganov, D.P. Kaiser, 1995: Six- and Three-hourly Meteorological Observations From 223 USSR Stations. ORNL/CDIAC-66, NDP-048. Carbon Dioxide Information Analysis Center, Oak Ridge National Laboratory, Oak Ridge, Tennessee, April 1995. 68 pp. + Appendices.

ACKNOWLEDGEMENTS

This work was initiated while the authors worked as visiting scientists at the U.S. National Climatic Data Center, Asheville, North Carolina. Currently the study has been supported by the U.S. National Science Foundation grant #ATM-9501320.

CORRESPONDING AUTHOR

Dr. Pavel Ya. Groisman
Department of Geosciences, Morrill Science Center,
University of Massachusetts,
Amherst, 01003, USA
phone: +1 413-545-9573; fax: 413-545-1200;
email:pasha@climate1.geo.umass.edu

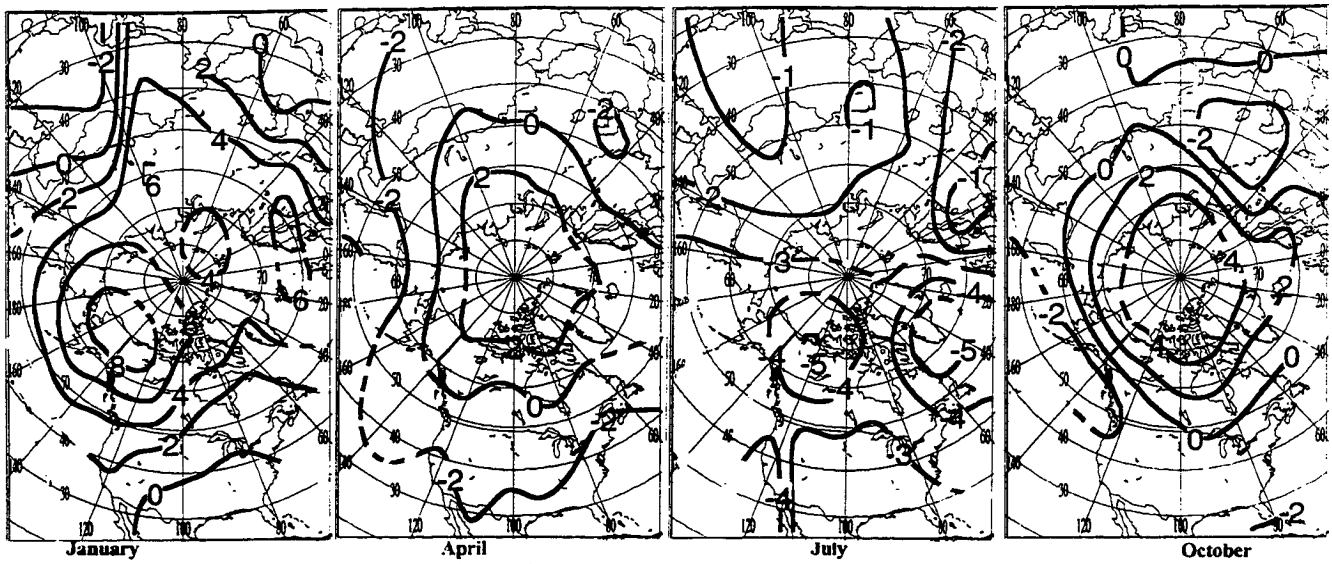


Figure 2a. Mean monthly change (°C) of the surface air temperature under clear skies (T_{clear}) compared to T_{all} under average afternoon climate conditions, $T_{all} - T_{clear}$.

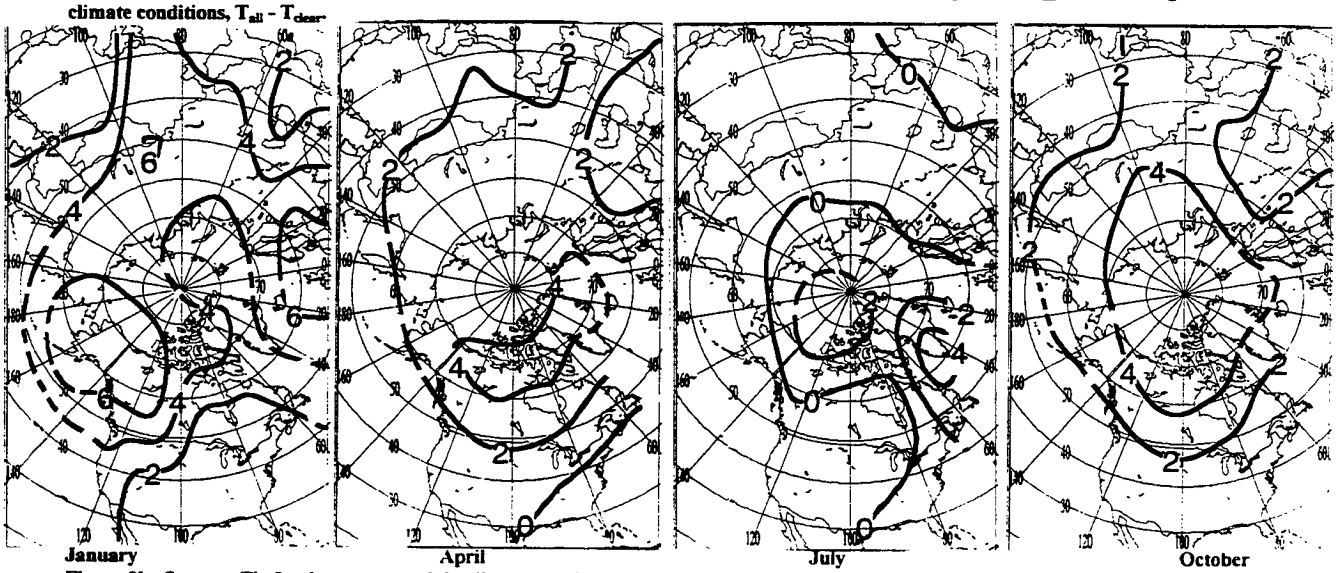


Figure 2b. Same as Fig.2 a, but average night climate conditions.

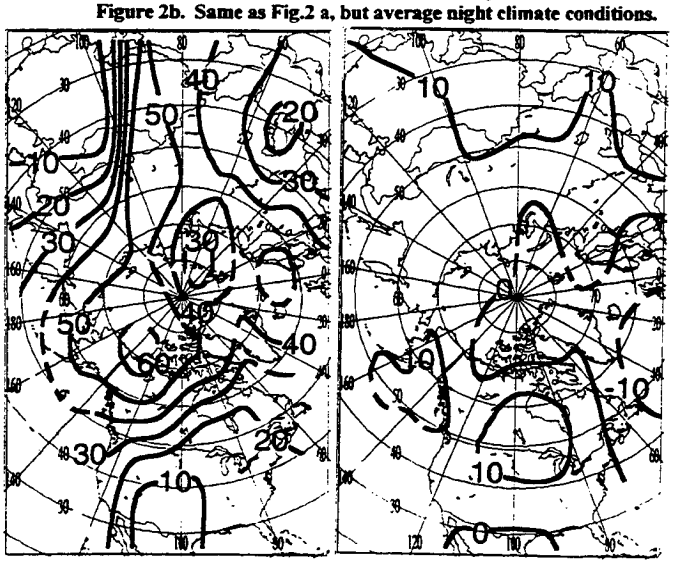


Figure 3. Mean monthly reduction (%) of the near-surface water vapor pressure under clear skies (e_{clear}) compared to e_{all} under average afternoon climate conditions, $100\% * (e_{all}-e_{clear})/e_{all}$.

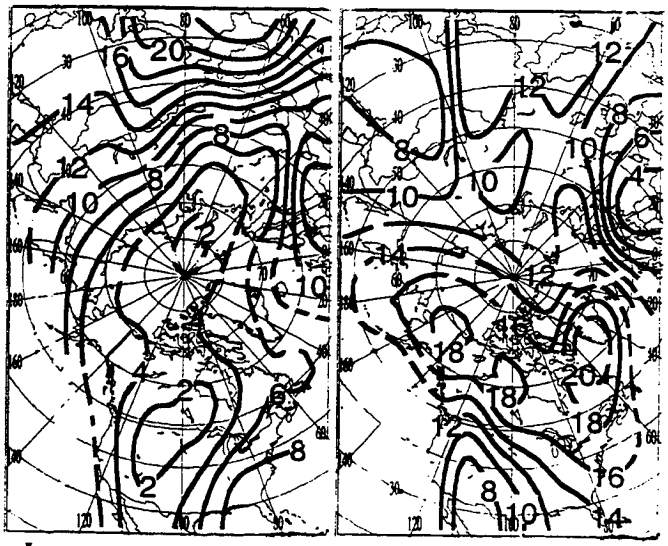


Figure 4. Mean monthly reduction (%) of the near-surface relative humidity under clear skies (f_{clear}) compared to f_{all} under average afternoon climate conditions, $f_{all} - f_{clear}$.

On Temporal Variability of the Zonal and Global Average Radiation and Cloudiness

Olavi Kärner

IAAP, Tõravere, ESTONIA

April 20, 1995

Abstract

Most of the meteorological variables contain a certain annual cycle overshadowed by some interannual variability. This leads to a situation that seasonal autoregressive moving average models (SARIMA) can give a better approximation (in terms of residual variance) than Fourier series. Simple models from the SARIMA family yield good approximation for globally averaged radiation series (residual variance less than 17% of the initial one), but remarkably worse result for cloud amounts (residual variance generally more than 40%). For zonal mean variables the annual cycle is not obvious. Zones with and without annual cycle are situated alternately over the tropics and Northern Hemisphere.

1 Introduction

Clouds play important role in modifying the Earth radiation budget, water cycle etc. Investigations of statistical properties of large scale cloudiness variability can provide new information necessary for the validation of atmospheric circulation models.

It is hard to introduce a quantitative method to measure cloud amount (e.g. Malberg 1973, Stowe et al. 1989, Kärner and Keevallik 1993 among many others). Moreover, the global cloud field is changing very rapidly further complicating the measurements (Mokhov and Schlesinger 1993,1994). Therefore, some new comparatively simply and accurately measurable terms like Cloud Radiative Forcing (Charlock and Ramanathan 1985) and (radiatively) Effective Cloud Amount (Kärner and Keevallik 1993) have been used to investigate cloudiness variability. Recently, the cloud forcing terms were succesfully used in validation of general circulation models (Kiehl and Ramanathan 1990), especially focusing on annual cycle (Randall and Tjemkes 1991, Bony et al. 1992).

Due to rapidly developing satellite measurements during last decades methodically homogeneous global data sets of several important climate variables have been archived (e.g. NASA 1986). This enables one to use time series analysis methods to investigate their variability. In the present report stochastic models are employed to represent the contemporary variability of the earth radiation budget and cloudiness on global and zonal basis. The technique, introduced by Box and Jenkins (1976) will be followed for that purpose.

2 Data

Selected variables from three sources of satellite data are used to illustrate temporal variability of largely averaged cloudiness and radiation fields. All used time series are consisting of monthly averaged values from the time period: 1978-1990.

Measurements of the outgoing longwave radiation (OLR) at the top of the atmosphere (TOA) are archived by NASA (NASA 1986) from the Nimbus 7 earth radiation budget (ERB) wide field of view radiometer (WFOV) registrations during 1978-1986. Details are described by Jacobowitz et al. (1984).

Total cloud amount (NCLE) is used from the estimates by the Nimbus-7 Cloud Data Processing Team (Stowe et al. 1988). Cloud amount is estimated using a bispectral algorithm, which determines areal cloud averages separately for two channels. One part is a pixel-counting threshold algorithm applied to Temperature Humidity Infrared Radiometer (THIR) radiances, and other is a linear-scaling algorithm applied to Total Ozone Mapping Spectrometer (TOMS) ultraviolet reflectivities. These separate estimates

are afterwards combined into a weighted average estimate for the area and for the period 1979-1985.

The International Satellite Cloud Climatology Project (Rossow et al. 1988) has produced 8-year (1983-91) time series of total cloud amount (CA) on global basis. Cloud amount is estimated by means of a bispectral pixelcounting algorithm, where the cloud/no cloud decision for each pixel is based on logic which combines visible and infrared radiances, rather than separates them. Thus, the total cloud amount estimates NCLE and CA are actually two physically different variables. The difference is described in detail by Stowe et al.(1989).

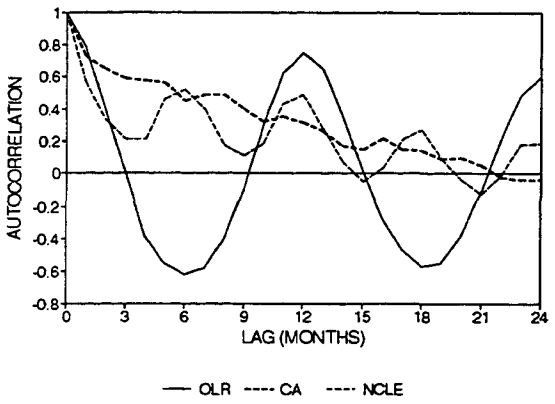


Figure 1: Sample autocorrelations for three globally averaged variables

3 Model fitting

Radiation series are strongly influenced by the Earth-Sun distance, thus an adequate model (if exists) belongs likely to the class of seasonal autoregression integrated moving average (SARIMA) models (e.g Box and Jenkins 1976).

Sample autocorrelations give initial information about possibly applicable model. Figure 1. shows sample autocorrelations (maximum time lag equals to two years) for three selected (globally averaged) variables. Sample autocorrelations for many globally averaged variables show an annual cycle, similar to that expressed by curve for OLR, or a semiannual one (NCLE). Autocorrelations for zonally averaged variables behave similarly. One possible way to model series x_t $(t = 1, \ldots n)$ with remarkable annual cycle is by means of the following autoregressive model (Kärner 1993,1995)

$$x_t = \phi_1 x_{t-1} + \phi_{12} x_{t-12} + \phi_{13} x_{t-13} + a_t. \quad (1)$$

Here, a_t is white noise and the minimum residual variance is usually reached if the sum of the fitted coefficients equals to 1: $\phi_1 + \phi_{12} + \phi_{13} = 1$. An exception to that is CA, the autocorrelations of which reveal no hint on any cycle. Slow decay in its autocorrelation points at the first order moving average model for monthly increments:

$$x_t - x_{t-1} = a_t + \Theta_1 a_{t-1}. \quad (2)$$

where Θ is fitted by least squares.

4 Results

Detailed results connected to the estimation of coefficients and testing an adequacy of the chosen model by means of residual series a_t, are presented by Kärner 1995 and Kärner and Rannik 1995. Next some comments on the most important results are presented.

4.1 Globally Averaged Series

Two types of models, i.e., those expressed by (1) and (2), are applicable to represent the interannual variability of the analyzed series. The first of them is seasonal, i.e. it explicitly takes into account an annual cycle of the modelled variable. Another model is more simple denoting that the monthly increments in initial series can be modelled via a first order moving average model, which allows an interpretation of random walk overshadowed with white noise (see Box and Jenkins 1976 for details). It is remarkable that two methodically independent total cloud amount records, (NCLE and CA) show different structure of temporal variability. Model (1) for NCLE points out that there is a dominant cycle (the annual, thus likely brought about solar input) in the globally averaged total cloud amount. Model (2) allows to conclude that the monthly increments of the globally averaged cloud amount may be random (i.e. without any cycle in cloud amount). This contradiction is a statistical supplement to the methodical differences between the ISCCP and NCLE, discussed by Stowe et al. (1989).

4.2 Zonally Averaged Series

Modelling leads to significantly different results in respect to residual variance. Whole tropical belt and Northern Hemisphere can be separated into two classes depending on that. Low residual variance belts (each of them about 10° wide)

are centered at 15°S, 15°N, 38°N, and 65°N, respectively if to rely on NCLE record. Low residual variance is a result of significant annual cycle in the corresponding zonal cloud amounts. The results point out that there exists no annual cycle with a permanent amplitude and phase even on high latitudes. Such an attempt always gives correlating residuals. Using SARIMA models enables one to take account of the mutual influence of shortterm (1 or 2 months) and longterm (1 or 2 years) correlations. Less than 10% residual variance in three belts ($9°S-18°S$; $4.5°N-18°N$; $36°N-40.5$°N) shows that empirical models may be useful for validation of cloud parameterization schemes in general circulation models.

Between the low residual variance belts zones with high residual variance are located (centered at 0°, 25°, 50°, and 75°N, respectively). They are less than 10° wide, and connected to low (or negligible) annual amplitude of the zonal mean cloud amount. As a result the zonal mean cloud amount is much closer to white noise than in previous case. Consequently these zones are less important as long as new information towards cloud parameterization is considered.

It is remarkable that the corresponding zonal structure holds for several independent cloud amount and cloud forcing estimates. High residual variance belts correspond to zones without annual cycle in total cloud amount as seen from ground based climatologies and first results of nephanalysis (Kärner and Keevallik 1993). Recently Mokhov and Schlesinger (1993, 1994) obtained similar latitudinal distribution of annual amplitude analysing cloud amounts, produced for one and the same time period by means of three different satellite methods. The same disposition of low and high annual amplitude zones was also obtained by Bony et al. (1992) analysing annual cycles of longwave cloud radiative forcing (LWCF) and cloud albedo perturbations from the ERBE observations. Figure 2. illustrates the situation. Curves for OLR and NCLE show the explained variance by means of model (1), relative to initial one (left scale). Curve for LWCF, taken from Bony et al. 1992, shows the zonal distribution of amplitudes for the annual harmonic, relative to the maximum amplitude (right scale).

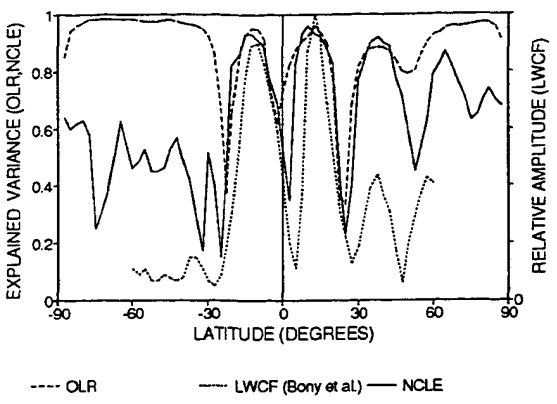


Figure 2: Different zonal mean variability (see text for explanations)

5 Conclusions

The result that two terms pretending to estimate total cloud amount for the same time period have different structure in their temporal variability on global basis, is something to be expected. The existing cloud detection methods still provide very dispersed estimates of cloud amount. Nevertheless, a common structure is apparent in temporal variability of the cloud forcing and cloud amount terms on zonal basis.

References

[1] Bony S., H. Le Treut, J-P. Duvel, R.S. Kandel, 1992: Satellite validation of GCM-simulated annual cycle of the earth radiation budget and cloud forcing. *J. Geophys. Res.* **D97**, 18 061–18 081.

[2] Box G.E.P., G.M. Jenkins 1976: *Time series analysis, forecasting and control,* (revised edn). Holden-Day, San Francisco.

[3] Charlock, T.P. and V. Ramanathan 1985: The albedo field and cloud radiative forcing produced by a general circulation model with internally generated cloud optics. *J. Atmos. Sci.* **42**, 1408–1429.

[4] Jacobowitz H. H., V.Soule, H.L.Kyle, F.B.House and the Nimbus-7 ERB Experiment Team 1984: The earth radiation budget (ERB) experiment: An overview. *J. Geophys. Res.* **D89**, *5021-5038.*

[5] Kärner O. 1993: Global average net radiation sensitivity to cloud amount variations. *J. Atmos. Sci.* **50**, *3994-4000.*

[6] Kärner O. 1995: Stochastic models to represent the temporal variability of global

average radiation budget, cloudiness and temperature. To appear in Proceedings of NATO Advanced Researh Workshop "Climate Sensitivity to Radiative Perturbation", Paris, France. 11–15 July 1994.

[7] Kärner O. and S. Keevallik 1993: *Effective Cloud Cover Variations* A. Deepak Publ., Hampton, Virginia.

[8] Kärner O. and Ü. Rannik 1995: Stochastic Models to represent the temporal variability of zonal average cloudiness and cloud forcing. Submitted to *J. of Climate.*

[9] Kiehl, J.T. and V. Ramanathan 1990: Comparison of cloud forcing derived from the Earth Radiation Budget Experiment with that simulated by the NCAR Community Climate Model. *J. Geophys. Res.* **D95**, 11 679–11 698.

[10] Malberg H. 1973: Comparison of mean cloud cover obtained by satellite photographs and ground based observations over Europe and the Atlantic. *Mon. Wea. Rev.* **101**, 893–897.

[11] Mokhov, I.I. and M.E. Schlesinger 1993: Analysis of global cloudiness. Part 1. Comparison of Meteor, Nimbus 7, and International satellite Cloud Climatology Project (ISCCP) satellite data. *J. Geophys. Res.* **D98**, 12 849–12 868.

[12] Mokhov, I.I and M.E. Schlesinger 1994: Analysis of global cloudiness. Part 2. Comparison of ground-based and satellite-based cloud climatologies. *J. Geophys. Res.* **D99**, 17 045–17 065.

[13] NASA 1986: ERB Matrix Summary Tape, Modification 2, NASA, GSFC, Greenbelt, MD. 44pp.

[14] Randall, D.A. and S. Tjemkes 1991: Clouds, the Earth's radiation budget, and the hydrological cycle. *Paleogeogr., Paleoclimatol., Paleoecol.*, **90**, 3–9.

[15] Rannik Ü. 1994: On the impact of clouds to variability of shortwave radiation. Master Thesis at Tartu University, 56pp.(in Estonian)

[16] Rossow W.B., L.C.Garder, P.J.Lu and A.Walker 1988: International Satellite Cloud Climatology Project (ISCCP). Documentation of cloud data. World Climate Research Programme, WMO/TD - No 266, 75 pp.

[17] Stowe L.L., G.G.Wellemeyer, T.F.Eck, H.Y.M.Yeh and the Nimbus-7 Cloud Data Processing Team 1988: Nimbus-7 global cloud climatology, part I: Algorithm and validation. *J.Climate* **1**, *445–470.*

[18] Stowe L.L., H.Y.M. Yeh, T.F. Eck, C.G. Wellemeyer, H.L. Kyle and The Nimbus-7 Cloud Data Processing Team 1989: Nimbus-7 global cloud climatology, part II: First year results. *J. Climate* **2**, *671–709.*

ACKNOWLEDGEMENTS

This work was supported by the European Union contract ERBCIPDCT 930026 at IAAP.

CORRESPONDING AUTHOR

Dr. O. Kärner
Institute of Astrophysics and Atmospheric Physics, Estonian Academy of Sciences
EE 2444, Tõravere
ESTONIA.

THE RELATIONSHIP BETWEEN THE DRAG COEFFICIENT AND THE EXTENT OF WHITECAPPING, AS INFERRED FROM OBSERVATIONS MADE IN THE NORTHEAST PACIFIC OCEAN

E.C. Monahan[1], I.G. O'Muircheartaigh[2] W. Wang[1] and Q. Wang[1]

1) University of Connecticut at Avery Point, Groton, CT, USA
2) University College, Galway, Ireland

ABSTRACT

It has been determined that the relationship between the sea surface drag coefficient, C_{10}, the magnitude of which is required to assess the extent of air-sea coupling, and the extent of wave breaking, or of Stage A whitecap coverage, WCF, which is quantity amenable to monitoring from satellite, is well described by an expression of the following form:

$$WCF^{0.2} = \beta_0 + \beta_1 C_{10} + \beta_2{}^2 (C10)^2 \quad (1)$$

The appropriate transformation of the dependent variable (exponentiation to the power of 0.2) is that which enables the data to meet the standard assumptions of multiple regressions (normality of errors, and homoscedasticity), and the form of the equation was determined by stepwise regression. Two separate analyses were performed for each of three data sets - one where the model included an intercept term and one where it did not.

1. INTRODUCTION

The wind stress, τ, the rate at which forward momentum is transferred downward through the sea-surface from the atmosphere to the ocean, can be expressed as in Equation (1), where

$$\tau = \rho C_D U_{10}^2, \quad (2)$$

ρ is the density of the air, U_{10} is the wind speed as measured at an elevation of 10 meters and C_D is the drag coefficient. In turn, C_D is itself a function of U_{10} (e.g., Smith, 1980; Large and Pond, 1981), of the thermal stability of the marine atmospheric boundary layer, and of the dynamic surface roughness (e.g., Roll, 1965; Smith, et al, 1992). The drag coefficient, C_D, in part as a consequence of its dependence on sea surface roughness, varies with the sea state, i.e. with the wave field (e.g., Geerhaert, et al, 1986; Toba, et al, 1990). More specifically, it has been suggested (Katsaros and Atakturk, 1991) that C_D is a function of the intensity of wave breaking.

Now the intensity of wave breaking, or equivalently, the prevalence of Stage A whitecapping (Monahan and Lu, 1990), can potentially be monitored routinely from space (e.g., Monahan and O'Muircheartaigh, 1986), and since there are several alternative remote sensing procedures available for the independent determination of low elevation wind fields, it may be possible to obtain, for use in global, coupled, air-sea circulation models, improved surface stresses fields by combining satellite derive fields of Stage A whitecaps and low elevation winds.

2. DATA

The ideal data set for the determination of the dependence of C_D, or sea surface stress, on the extent of Stage A whitecapping, would be one where images showing the extend of whitecapping had been recorded in the field at the same time that the surface stress had been obtained from the same platform by the dissipation or eddy correlation methods, as was the case in the HEXOS experiment (Smith, et al, 1990).

For the current investigation Stage-A whitecap observations (Monahan and Wilson, 1990; Wilson, et al, 1992), and C_D values inferred from wind and atmospheric stability data using the approach of Smith (1981), obtained from the April 1990 CST-4 experiment (Hanson and White, 1991) and the winter 1992 CST-7

experiment (Root and Hanson, 1992) were taken as the data base. Both the CST-4 and CST-7 experiments were conducted in the open Gulf of Alaska.

3. ANALYSES

Based on the following statistical considerations, it was concluded that the following form for the dependence of Stage-A whitecapping on the drag coefficient is to be preferred:

$$WCF^{0.2} = \beta_0 + \beta_1 C_{10} + \beta_2{}^2 (C10)^2 \quad (3)$$

and, in particular, the model with $\beta_0 = 0$ is preferred based on physical considerations of the occurrence of whitecap. The quantity WCF is the fraction of the sea surface covered by spilling wave crests, W_A, multiplied by 10^4, while C_{10} is the 10-meter-elevation drag coefficient multiplied by 10^3.

When fitting a model of this type to data, it is necessary, if one is to perform statistical test of the model, that a number of underlying assumptions must hold. In particular, normal distribution of the errors, and homoscedasticity in relation to the error variances, must apply before statistical tests are applied. The raw data do NOT satisfy these assumptions, but it was determined that a power transformation (using a power of 0.2) applied to the dependent variable (WCF) ensures that the (transformed) data satisfy the assumptions, and that one can therefore proceed with applying a stepwise regression to establish an appropriate polynomial model for the dependence of whitecapping on the drag co-efficient.

The application of the stepwise procedure established that in the case of each of the datasets a quadratic model provided a significant improvement over a simple linear model. Although, as one would expect (because an extra parameter is fitted) a model with an intercept term gave a better fit than one without such a term, it was felt (from physical considerations, and in particular the fact that when there is zero windspeed there will be no whitecap cover) that a model with no intercept term (i.e. passing through the origin) was more appropriate.

This conclusion is qualitatively similar to the findings that one of the authors (W. W.) obtained from a preliminary analysis of the data from the HEXOS experiment.

The results of the individual analyses of the one CST-4 data set and the two CST-7 sets are as follows (for completeness the estimated coefficients for both the intercept and no intercept models are presented):

	Estimated coefficients (t-values in parentheses)		
Data set	β_0	β_1	β_2
cst-4			
intercept	0.64 (0.78)	0.05 (0.04)	0.71 (1.23)
no intercept		1.12 (7.21)	0.27 (2.15)
cst-7 (r1)			
intercept	2.63 (3.39)	-4.18 (-3.27)	2.43 (4.71)
no intercept		0.11 (0.60)	0.74 (5.43)
cst-7 (tc)			
intercept	2.92 (0.82)	-5.04 (-0.94)	2.86 (1.44)
no intercept		-0.67 (-2.40)	1.24 (5.80)

4. CONCLUSIONS

The quadratic expression

$$WCF^{0.2} = \beta_1 C_{10} + \beta_2{}^2 (C10)^2 \quad (4)$$

is deemed the best descriptor of the dependence of WCF on C_{10}. Plots of the three data sets, together with the fitted curves in each case, are presented in Figures 1 and 2.

It is clear from a comparison the two figures that the difference between the intercept and no intercept models is not sustantial except in the case of low C10 values for data set 2. However, as previously pointed out, physical considerations strongly suggest that the no intercept model is the more appropriate.

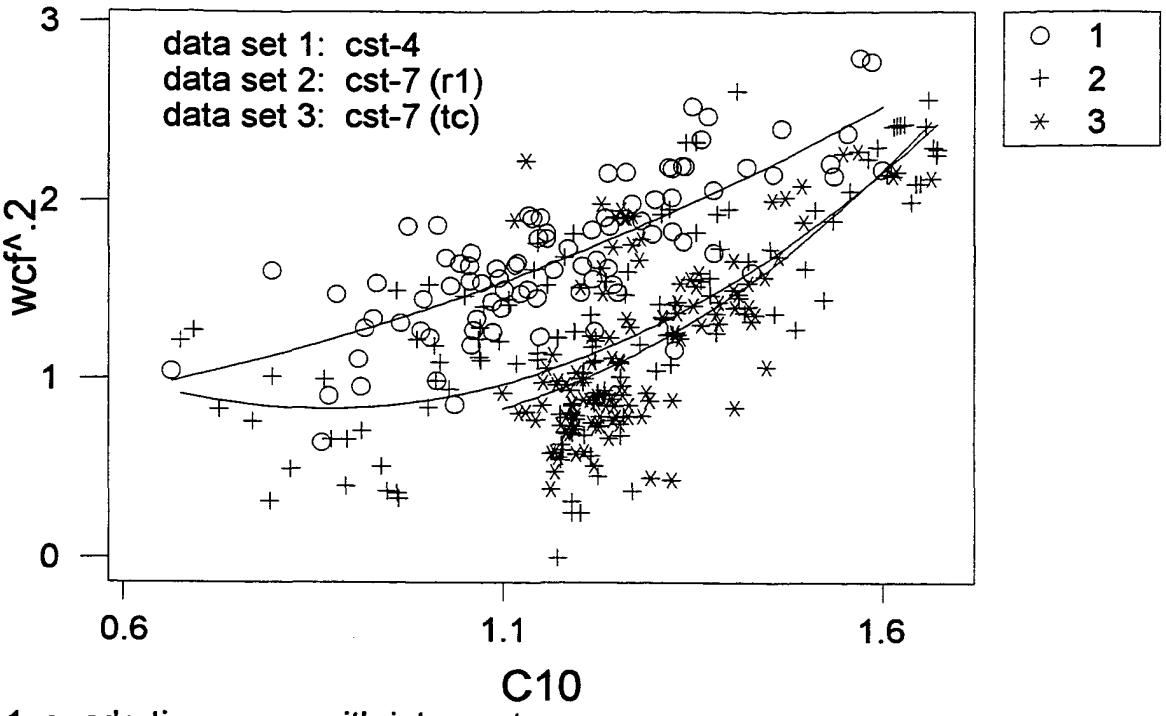


Figure 1: quadratic curves, with intercept

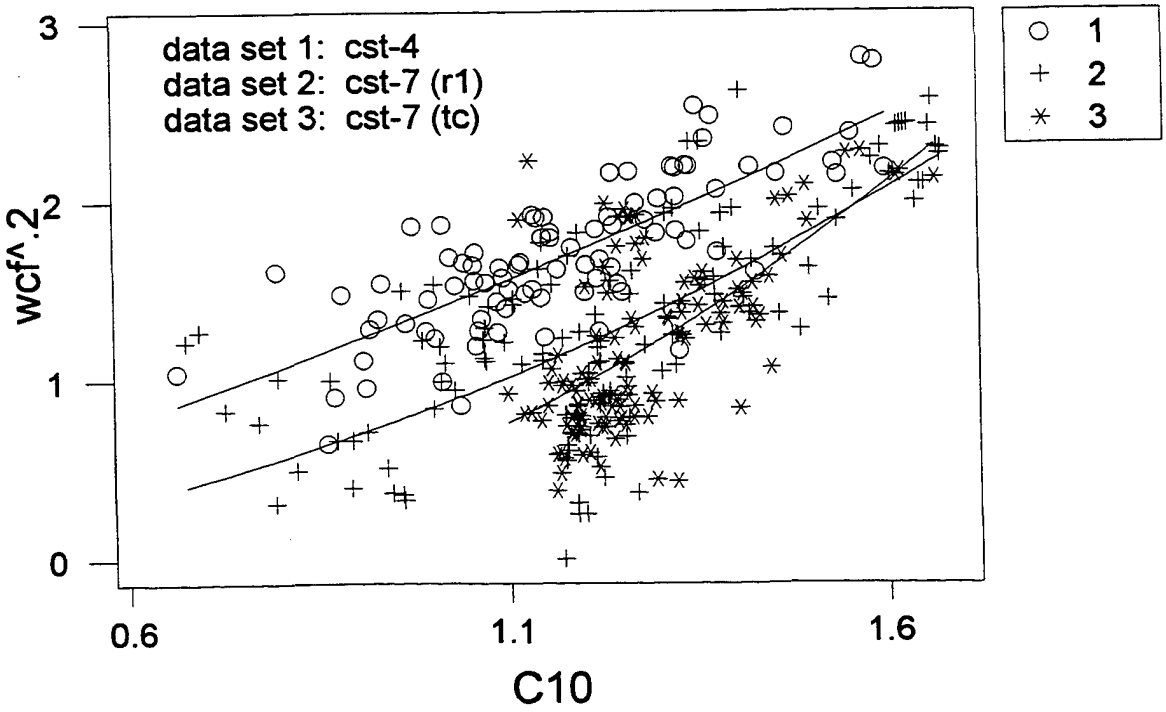


Figure 2: quadratic curves, no intercept

ACKNOWLEDGMENTS
The initial analyses of the several whitecap data set at UConn were supported by contract 605337-0 from the Applied Physics Laboratory of Johns Hopkins University and by Grant N00014-92-J-1167 from the U.S. Office of Naval Research.

REFERENCES

Geerhaert, G.L., K. B. Katsaros, and K. Richter, 1986. "Variation of the Drag Coefficient and Its Dependence on Sea State", Journal of Geophysical Research, 91, 7667-7679.

Hanson, J. L., and L. H. White, 1991. "Assessment of the Air-Sea Boundary Zone During Critical Sea Test 4, Report STD-R-1978", Applied Physics Laboratory, Johns Hopkins University, Laurel, MD, 1-116.

Katsaros, K. B., and S. S. Atakturk, 1991. "Dependence of Wave Breaking Statistics on Wind Stress and Wave Development", in R.

Grimshaw and M.L. Banner, Eds. Proceedings, IUTAM Breaking Waves Symposium, Sydney, Australia, 1-14.

Large, W. G., and S. Pond, 1981. "Open Ocean Momentum Flux Measurements in Moderate to Strong Winds", Journal of Physical Oceanography, 11, 324-336

Monahan, E. C. and M. Lu., 1990. "Acoustically Relevant Bubble Assemblages and Their Dependence on Meteorological Parameters", IEEE, Journal of Oceanic Engineering, 15, 340-349.

Monahan, E. C., and I. G. O'Muircheartaigh, 1986. "Whitecaps and the Passive Remote Sensing of the Ocean Surface", International Journal of Remote Sensing, 7, 627-642.

Monahan, E. C. and M. B. Wilson, 1990. "Characterization of Oceanic Whitecap Coverage Observed During CST IV Cruise", Whitecap Report No. 8, to APL, Johns Hopkins U., MSI, UConn, 1-117.

Roll, H. U., 1965. "Physics of the Marine Atmosphere", Academic Press, N.Y., 1-426.

Root, S.L., and J. L. Hanson, Eds., 1992. "Critical Sea Test 7, Phase II, Quick-Look Report", Report STD-R-2119, Applied Physics Laboratory, Johns Hopkins University, Laurel, MD, 1-610.

Smith, S.D., 1980. "Wind Stress and Heat Flux over the Ocean in Gale Force Winds", Journal of Physical Oceanography, 10, 709-726.

Smith, S.D., 1981. "Factors for Adjustment of Wind Speed over Water to a 10 Meter Height", Report BI-R-81-3, Bedford Institute of Oceanography, Dartmouth, N.S. Canada, 1-29.

Smith, S.D., R. J. Anderson, W.A. Oost, C. Kraan, N. Maat, J. DeCosmo, K. B. Katsaros, K. L. Davidson, K. Bumke, L. Hasse, and H. M. Chadwick, 1992. "Sea Surface Wind Stress and Drag Coefficients: The HEXOS Results", Boundary-Layer Meteorology, 60, 109-142.

Smith, S. D., K. B. Katsaros, W. A. Oost, and P. J. Mestayer, 1990. "Two Major Experiments in the Humidity Exchange over the Sea (HEXOS) Program", Bulletin of the American Meteorological Society, 71, 161-172.

Toba, Y., N. Iida, H. Kawamura, N. Ebuchi, and I. S. F. Jones, 1990. "Wave Dependence of Sea-Surface Wind Stress", Journal of Physical Oceanography, 20, 705-721.

Wilson, M. B., S. L. Wilson, and J. C. Wilson, 1992. "Analysis of Foam Cover (Stage A Whitecaps) during Cruise of R/V CORY CHOUEST (Feb/Mar 1992) and R/V J. P. TULLEY (Feb/Mar 1992)", Tech. Report, Sea Surface Physics Laboratory, UConn to APL Johns Hopkins, 3 Volumes, 1-305

CORRESPONDING AUTHOR

Professor E.C. Monahan,
Institute of Marine Sciences,
University of Connecticut,
Avery Point,
Groton, CT 06340, USA.

USE OF CLIMATIC DATA IN MATHEMATICAL MODELS APPLIED TO AGRICULTURE IN NORTHERN IRELAND

S.D. Lennox[1], E.A. Goodall[1] and R.V. Smith[2]

[1]Biometrics Division,
[2]Agricultural and Environmental Science Division,
Department of Agriculture for Northern Ireland, Newforge Lane, Belfast BT9 5PX Northern Ireland.

ABSTRACT

Climatic data collected at a number of sites in Northern Ireland have many practical applications in the agricultural industry. This paper presents two specific applications of climatic data in the development of mathematical models. The first model presented relates the annual level of cattle condemned due to liver fluke in terms of temperature in the period June-August. The second model is also applied to cattle and describes the relationship between the utilised metabolisable energy from grass and forage in terms of climatic variables and the dry matter content of the available silage.

FASCIOLOSIS PREVALENCE IN CATTLE

INTRODUCTION

Fasciolosis (liver fluke) is a serious economic disease of cattle and sheep. It is a parasitic disease which can result in the death of heavily affected animals although many less severely affected animals can suffer a substantial reduction of growth and production. The most important measure for controlling the disease is the strategic use of modern flukicidal drugs. However, both the drugs and their administration are expensive and the frequency and most cost effective timing of their use should be dependent on the annual risk of the disease forecasted in a particular year (Urquhart *et al* 1987).

Basic systems for forecasting the estimated risk of the disease which use general climatic conditions have been developed and used in Europe (Ollerenshaw and Rowlands, 1959). Such systems lack accuracy as they can only estimate the risk of infection as being either high, medium or low. In Northern Ireland, a more accurate forecasting system has been developed which uses abattoir condemnation data recorded since 1976 (McIlroy *et al*, 1988). Data from this database was integrated with a computerised database of climatic variables in the formulation of the proposed model (Goodall *et al*, 1993).

METHODS and RESULTS

Data was extracted from the abattoir condemnation database specific to the recorded cases of liver condemnations due to fasciolosis in cattle. The monthly level of condemnations due to fasciolosis lesions in the period 1976-91 was expressed as a percentage of the total number of cattle slaughtered and the data subjected to time series analysis techniques. The data exhibited a consistent degree of seasonality which implied that a more practical measure of time period would be the period from August to the end of the following July. Fig. 1 shows the annual prevalence level of liver condemnations due to fasciolosis in cattle calculated for this time period.

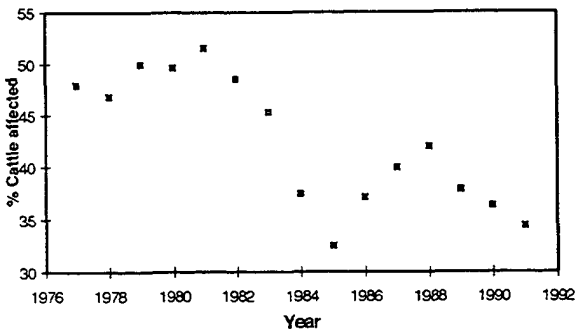


Fig. 1 The mean annual prevalence of liver condemnations due to fasciolosis in cattle

A correlogram of the series of annual fasciolosis data indicated a lag 1 autocorrelation coefficient of 0.79 which was statistically significantly different from 0 ($P<0.001$). The correlogram indicated that the series was non-stationery and that it would be appropriate to fit an autoregressive AR(0,1) process to the data. A wide variety of autoregressive integrated moving

average (ARIMA) processes were fitted to the time series of annual prevalence data using the methodology described by Box and Jenkins (1970).

A process is defined to be autoregressive of order p AR(p) if:

$$X_t = \alpha_1 X_{t-1} + \ldots + \alpha_p X_{t-p} + E_t$$

where E_t is a random error with mean zero and variance $\sigma^2 z$ and $\alpha_1, \ldots \alpha_p$ are constants. ARIMA models are normally fitted to series which are stationary and exhibit no time-trends or periodic behaviour. If a non-stationary series is identified then working with differences between consecutive terms (e.g. $Y_t = X_t - X_{t-1}$) is a simple way of making a new series stationary. Differencing may be repeated and autoregressive models fitted to the new series. An AR(p) model fitted to data that has been differenced d times is denoted by AR(p,d).

All meaningful weighted averages of monthly values were calculated for a range of climatic variables. These were all constructed as individual time series and were developed on a bi-monthly, tri-monthly... basis as it was felt to be practical. These series of data were stored permanently in a computerised database for ease of retrieval as they have many applications. All the formulated time series of the meteorological variables were found to be stationary with an AR($0,0$) process always found to be the most appropriate. The differenced fasciolosis time series (Y) (i.e. $Y_t = X_t - X_{t-1}$) was found to be correlated with the time series of mean air temperature (T) for the period June until August inclusive:

$$Y = 39.3 - 2.9\,T \quad (R^2 = 0.51)$$

The slope coefficient was statistically significantly different from 0 ($P<0.05$). A bivariate autoregressive model for fasciolosis condemnations in cattle was then formulated to be:

$$X_t = X_{t-1} - 2.9\,(T - 13.6) + E_t$$

where X_t = annual level of fasciolosis condemnations in year t; X_{t-1} = annual level of fasciolosis condemnations in year $t-1$; T = mean June-August air temperature (deg C) between year t and year $t-1$; E_t is a random error term.

Fig. 2 shows the fitted values from this new model and the observed values for individual fasciolosis years. The mathematical model formulated to predict annual risk of fasciolosis in cattle accounted for 0.8 of the variation in the original condemnation series. More important, however, the model fitted to August 1990 and 1991 forecast the next year's fasciolosis level to deviate absolutely by only 0.03 and 0.04, respectively, from the levels which were actually observed.

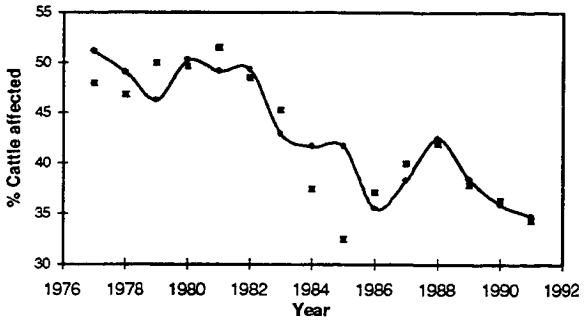


Fig. 2 The observed annual prevalence of liver condemnations due to fasciolosis in cattle and the predicted annual prevalence.

UME FROM GRASSLAND

INTRODUCTION

Stocking rate has been used in the past as an indicator of the general level of grassland utilisation. However, stocking rate does not take into account the feeding of concentrates or the contribution of grassland to total feed requirements. A more accurate measurement of the level of grassland utilisation is utilised metabolisable energy (UME) and is a useful indicator of the physical performance of grassland and of the level of management of the livestock carried. Using prior knowledge of the energy requirements of livestock, it is possible to calculate the total amount of metabolisable energy required to support this animal population (Smith *et al*, 1995). A model is formulated which defines the UME from grass and forage in terms of climatic variables and silage dry matter content.

METHODS AND RESULTS

In this study the aim has been to express the net utilised metabolisable energy from forage in terms of an annual rate per unit area (i.e. GJ ha^{-1}). Data for total grassland area and total area of rough grazing for Northern Ireland were extracted from the annual Northern Ireland Agricultural Census (HMSO, 1991) for the years 1970-1991. The use of fertilisers, and hence the intensity of animal production on the rough grazing area, is about one fifth of that for improved grassland. Total forage area was therefore calculated by adding the total area of grassland and 0.2 x the area of rough grazing and also data for the non-grass area.

A relationship between animal weight and forage consumption is often used to relate different classes and ages of grazing livestock. A measure known as the "dairy cow equivalent" is used in the analysis of Northern Ireland farm management data in which a

dairy cow is standardised to have the value 1.0 and all other stock are related to this base depending on their weight and forage demands. Using the total number of DCE's, the total energy requirements of livestock were estimated using the energy allowance data from ARC (1980). Subtracting the energy contribution for non-forage feeds such as concentrates, from the total energy required by the livestock, gives a value for the net utilised metabolisable energy by the livestock. Dividing this by the total forage area results in the net UME per ha of grass and forage. Fig. 3. shows the estimated values of UME per ha of grass and forage for the years 1970-1991.

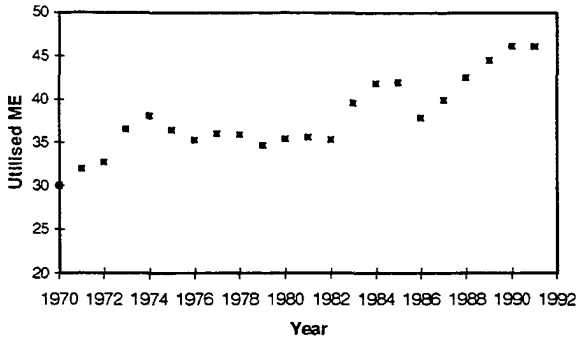


Fig. 3 Plot of utilised metabolisable energy for grazing livestock for Northern Ireland, 1971-91

The correlogram of the UME series indicated that the series was non-stationary. An AR(*0,1*) model was fitted to the data which is equivalent to first-order differencing of the series. None of the autocorrelation coefficients for the differenced series were statistically significantly different from 0.

The stationary series for all the meteorological time series were cross-correlated with the stationary time series constructed for the UME series. When significant cross-correlation coefficients were obtained, a dependency relationship was postulated and a regression analysis performed. The differenced UME time series was found to be most significantly correlated with the time series of annual mean soil temperatures recorded at Aldergrove, Co. Antrim. The regression equation was:

$$Y = -17.9 + 2.04\,X_1 \quad (R^2 = 0.30)$$

where Y is the differenced UME series and X_1 is the series of mean annual soil temperatures in deg. C. The residuals from this model were then correlated with the database of climatic variables and other relevant environmental variables. The time series of residuals were significantly correlated with the series of mean daily rainfall for the previous summer and a new regression model was postulated. The regression equation was:

$$Y = -15.3 + 2.2\,X_1 - 1.8\,X_2 \quad (R^2 = 0.53)$$

where Y and X_1 are the time series as defined above and X_2 is the time series of mean daily rainfall (mm) for the months June-September of the previous year.

This process was repeated and the time series of the residuals were found to be significantly correlated with the time series of silage dry matters for Northern Ireland. This latter series represents dry matter contents of silages taken from Northern Ireland farms and are assumed to be representative of silage made in Northern Ireland (Unsworth, 1981, 1992). These data have not been corrected for loss of volatiles. A new regression model was postulated and the regression coefficients of the three independent variables were all statistically significantly different from 0 ($R^2 = 0.66$).

The time series of residuals from this fitted model were then correlated with the database of environmental variables and found to be significantly associated with the time series of mean daily rainfall for the period February - May of the current year. A regression model was postulated and fitted to the data. The fitted regression model was:

$$Y = -9.9 + 2.8\,X_1 - 2.6\,X_2 - 0.58\,X_3 + 1.8\,X_4 \quad (R^2 = 0.75)$$

All regression coefficients were significantly different from 0 ($P<0.05$). The overall proportion of variation accounted for in the original time series of UME data was 95%. The model for the net UME from grass and forage was then formulated to be:

$$U_t = U_{t-1} - 9.9 + 2.8\,X_1 - 2.6\,X_2 - 0.58\,X_3 + 1.8X_4 + E_t$$

where U_t = net UME from grass and forage in year t; U_{t-1} = net UME from grass and forage in year $t-1$; X_1 = mean annual soil temperature in year t; X_2 = mean daily rainfall for the period June-September of year $t-1$; X_3 = mean silage dry matter for year t; X_4 = mean daily rainfall for the period February-May of year t. The fitted values from this model are plotted in Fig. 4 with the observed values of net UME for each year in the period 1970-91.

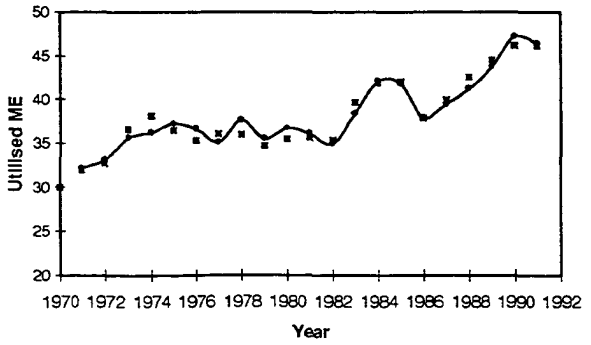


Fig. 4 The observed annual values of UME for grazing livestock and the predicted values.

DISCUSSION

The mathematical model formulated to predict the annual risk of fasciolosis in cattle would appear to offer potential as a tool for strategic planning regarding the use of flukicidal drugs. The formulation of the model facilitates a forecast of the level of risk in September of each year as the key components of the model are the August-July condemnation data for the previous annual cycle and the June-August mean air temperature. Forecasting the level of risk at this time of the year would facilitate the targeting of an effective veterinary campaign regarding the control and prevention of fasciolosis. Another advantage of the model is that it could be used in other regions of the world where information on both the previous year's disease level, as specified by specific abattoir condemnation data, and the relevant temporal meteorological conditions are available.

The model which predicts the level of UME on an annual basis highlights the variables which determine the UME from grass and forage. The inclusion of the positive variable for soil temperature represents the improved conditions for forage production. Rainfall is also an important contributor to this process and so would explain the inclusion of the positive variable for rainfall in the period February-May of the current year. This coincides with the main period in which fertiliser is applied to Northern Ireland grassland. High levels of rainfall over the summer months have a detrimental effect on the quality of the harvested forage. This would explain the inclusion of a negative variable representing rainfall in the previous summer indicating reduced feeding value of silage when the previous summer has high rainfall.

Finally, the inclusion of a negative variable for silage dry matter indicates the reduced feeding value of silage with a high dry matter content (Steen, 1984). Wilting of silage reduces dry matter content and has the potential to reduce the volume of silage effluent produced. Therefore, although wilting of silage may have potential environmental benefits, the agricultural disadvantages must also be considered.

REFERENCES

ARC, 1980, Nutrient requirements of ruminant livestock. Commonwealth Agricultural Bureau, Farnham Royal.

Box, G.E.P. and Jenkins, J.M., 1970. Time series analysis forecasting and control. Holden-Day, San Francisco.

Goodall, E.A., Menzies, F.D. and Taylor, S.M., 1993, A bivariate autoregressive model for estimation of prevalence of fasciolosis in cattle. Animal Production, 57: 221-226

HMSO, 1991, Statistical Review of Northern Ireland Agriculture 1990. Norwich: Her Majesty's Stationery Office.

McIlroy, S.G., Goodall, E.A., Stewart, D.A., Taylor, S.M. and McCracken, R.M., 1990. An integrated computerised data analysis system for the evaluation of diseases in production animal populations. Computers and Electronics in Agriculture, 3:147-156.

Ollerenshaw, C. and Rowlands, W.T., 1959, A method of forecasting the incidence of fasciolosis in Anglesey. Agricultural Meteorology, 3:35-53.

Smith, R.V., Lennox, S.D., Meek, R. and Smyth, D.R., 1995, The use of metabolisable energy for grazing livestock to model the flux of nitrogen through northern Ireland grassland. Journal of Environmental Management (In press).

Steen, R.W.J., 1984, The effects of wilting and mechanical treatment of grass prior to ensiling on the performance of beef cattle and beef output per hectare. 57th Annual Report of Agricultural Research Institute of Northern Ireland, pp. 21-32.

Unsworth, E.F., 1981, the composition and quality of grass silages made in Northern Ireland - An analysis of seven years results (1973-79). Record of Agricultural Research (DANI), 29: 91-97.

Unsworth, E.F., 1992, silage composition of northern Ireland farms. An analysis of twelve years results (1980-1991). In: 3rd BGS Research Conference, British Grassland Society, September 1992, pp. 127-128.

Urquhart, G.M., Armour, J., Duncan, J.L., Dunn, A.M. and Jennings, A.W., 1987, Veterinary Parasitology, pp. 103-108. Longman, London.

CORRESPONDING AUTHOR

Dr S.D. Lennox,
Biometrics Division,
Dept. of Agriculture (NI),
Newforge Lane,
Belfast, BT9 5PX
N. Ireland

SPECTRAL ESTIMATES OF THE SURFACE PRESSURE FLUCTUATIONS ASSOCIATED WITH THE "BORA" WIND RECORDED IN UDINE AND TRIESTE

Mario Ceschia and Gilberto Iob

University of Udine, Department of Physics, Udine, Italy

ABSTRACT

This paper concerns the estimate of power spectra determined through measurements of pressure fluctuations associated with some events of the "bora" wind, recorded in Udine and Trieste, using an absolute microbarograph. Since the pressure records are intrinsically nonstationary, the spectral analysis has been carried out in terms of evolutionary spectra by applying either the traditional FFT approach or other more sophisticated algorithms.

For both sites and regardless of synoptic weather conditions, we found a marked peak corresponding to a period of approximately 20-30 seconds, together with a time modulation with a period of about one hour in their evolutionary spectra.

1 INTRODUCTION

As is already well known, contributions to the atmospheric pressure fluctuations, extending over a large range of frequencies, come from many sources. At low frequencies the main contributors are the synoptic weather changes, the atmospheric tides, the diurnal solar heating and the sea-land breeze inversion. At higher frequencies the main contributors are internal gravity waves (IGW) or buoyancy waves (with periods ranging from a few seconds to some tens of minutes). Local convective activity and surface wind advected turbulence are strictly related to IGW. The strong wind shear near the jet streams in the upper troposphere generates "disturbances" travelling at their velocities, which can induce internal waves of periods from 10 to 20 min whose influence extends down to the earth's surface. Finally, let us recall pressure fluctuations associated with the lee waves, which are generated by stably stratified winds over hills or mountains with rather intense vertical gradient of their velocity. These are stationary gravity waves, provided that the flow conditions do not change.

A model of the atmospheric pressure spectrum, deduced from the wind spectra available in the literature, consists of an f^{-5} behaviour at very long periods and of an $f^{-7/3}$ in the mesoscale range as well as at lower periods where turbulence dominates. The gravity wave theory predicts an $f^{-5/3}$ behaviour for pressure spectra.

In this paper we deal with the estimate of power spectra determined through measurements of pressure fluctuations associated with some events of the "bora" wind. The "bora" is the name of the cold, dry and gusty winds that blow towards the Adriatic Sea over the Dalmatian Mountains of Croatia (ex Yugoslavia) reaching the Gulf of Trieste and inland of Udine with attenuated intensity. It is generally more intense in winter, with gusts in excess of 40 m s^{-1} frequently recorded at Trieste. Temperatures are around freezing on the coast and relative humidities may fall below 40% during anticyclonic bora situations.

The spectral analysis was carried out on some patterns of pressure fluctuations during bora events, recorded in Udine and Trieste, by using an absolute microbarograph. The pressure transducer adopted is the SETRA System model 270, which is a complete pressure transducer system for accurate pressure measurements in gaseous or liquid media.

Since the pressure records are intrinsically nonstationary, the analysis was carried out in terms of evolutionary spectra to take into account the time variations of the frequency components, i.e. partitioning the random process into time segments, and then by applying to each interval traditional techniques of analysis, which involve either a conventional approach (based on the Fast Fourier Transform, FFT) or other more sophisticated algorithms (such as the maximum entropy, autoregressive and maximum likelihood methods).

An interesting result, from the analysis of some microbarograms recorded under conditions of bora at Udine and Trieste, we found a marked peak corresponding to a period of approximately 20-30 seconds for both sites, together with a time modulation with a period of about one hour in their evolutionary spectra.

These very similar behaviours (in spite of the data recording taking place at different time period and in varied synoptic weather conditions) would suggest that these emerging features are pertaining to the origin of the bora and its generative mechanism, irrespective of particular synoptic weather.

2 THE DATA ACQUISITION SYSTEM

An appropriate multichannel acquisition system carries out the transfer of data from the pressure sensor to a static RAM memory-module, at pre-determined time intervals. It includes a pressure transducer and a signal conditioner together with a 13-bit data converter and an acquisition controller.

The pressure transducer is the SETRA System Model 270. This is a complete pressure transducer system for accurate pressure measurements in gaseous or liquid media. It is based on a new variable-capacitance ceramic sensor named SETRACERAM, combined with a particular electronic circuitry. The symmetric ceramic capsule deforms proportionally to the

applied pressure. As the pressure increases, the gold electrodes on the inside surface of the ceramic capsule are moved closer to each other, thereby increasing the capacitance. The capacitance is converted to a linear DC signal with a high degree of accuracy by Setra's unique custom-integrated circuit utilising the charge-balance principle. Absolute accuracy may be further enhanced by using the internal zero and sensitivity adjustments. Parameters pertaining to the scale and accuracy of the transducer are shown in *Table 1*.

Table 1. Scale and accuracy parameters of the pressure transducer

Non-linearity	< ± 0.05 % FS
Hysteresis	0.01 % FS
Non-repeatability	0.01 % FS
Time constant	< 50 ms to reach 63 % f.o.
Full scale output	0 to 5.00 V (± 5mV)
Barometric range	800 to 1100 mbar or hPa

To be able to detect fluctuations of the atmospheric pressure as small as a few μbar, a high quality differential amplifier with a variable reference voltage was used. At the beginning of the measurement, an input voltage (0 to 5 VDC), depending on the effective ambient pressure, is added to the negative reference voltage, so that only low-level signals have to be amplified. Indeed, the thermally compensated and adjustable voltage reference is inverted and added to the input signal. The balancing condition, corresponding to an output of zero volts from the amplifier, is monitored on a moving-coil instrument.

An adjustable timer allows for the sampling period to be pre-selected in a range from 1 to 999 seconds. To prevent aliasing from higher frequencies (greater than about 300 Hz), the pressure signal passed through a suitable low-pass filter.

The CMOS static RAM memory module contains up to 512K bytes of memory location with lithium battery backup. The standard serial RS-232C is a general-purpose interface for data handling in a computer-independent way.

3 EVOLUTIONARY SPECTRUM ANALYSIS

As it is well known, nonstationarity implies a variability of the spectral characteristics of the random process. Therefore, since a visual inspection of the pressure records particularly during bora events reveals the intermittent presence of random disturbances superimposed on longer lasting wavelike fluctuations, one has to perform the spectral analysis in terms of evolutionary spectra. An evolutionary spectrum $S(\omega,t)$ is an "instantaneous" spectrum which evolves in time t. The angular frequency ω is the only variable the spectral density S depends on when the process is stationary. The evolutionary spectrum can be estimated by partitioning the random process into time segments T_s in which the spectral characteristics vary slowly, and by applying traditional spectral analysis techniques to each interval.

When the original time series $x(t)$ is subdivided into time segments, each with N samples Δt apart, the discrete-time approximation of the spectral density $S(\omega,t)$ is the matrix

$$S_{jm} = (2\Delta t / N)|X_{jm}|^2$$

where j represents the segment number, m is a frequency label, and X_{jm} is the discrete Fourier transform of the zero-mean time segment.

Once the nonstationarity of the considered records was ascertained, an attempt was made to determine the time scale of stationarity. To this end we used a modified version of the method presented by Tsao (1984). The main assumption of Tsao's method is that the spectral estimate S_{jm} can be factorized into a term B_j depending only on the time subinterval, a term C_m depending on the frequency and an interaction term D_{jm} reflecting a nonseparable time-frequency behaviour:

$$S_{jm} = AB_j C_m D_{jm}, \qquad (1)$$

where A is a constant scale factor. To simplify the analysis scheme the test has been applied by grouping K frequencies together to form M/K bands. Thus, the new spectral quantities become

$$S'_{js} = (1/k) \sum_{k=(s-1)K}^{sK} S_{jk} \quad s = 1,2,\ldots,M/K, \qquad (2)$$

where s is the band index. Because of the Parseval theorem, the quantity S'_{js} represents the variance of the random process in the frequency band considered, and can be directly calculated from the filtered pressure records in the time domain, without the need for any Fourier transform calculations. Therefore, in the time domain, the quantities (2) can be rewritten as follows

$$\sigma^2_{js} = (1/N) \sum_{n=0}^{N-1} (\xi_{js}(n) - \bar{\xi}_{js})^2, \qquad (3)$$

where $\xi_{js}(n)$ represents the n-th sample of the j-th time segment for the s-th band, and it is the result of the band pass filtering applied to the original time series. The quantity $\bar{\xi}_{js}$ is the mean value of the filtered signal $\xi_{js}(n)$. As (2) and (3) are equivalent, any changes of the variance σ^2_{js} indicate nonstationarity.

Table 2. Bands utilised for the nonstationarity analysis

Band no.	Upper frequency cutoff (Hz)	Period of the upper frequency cutoff (Hz)	Lower frequency cutoff (Hz)	Decimation ratio in the window
I	$8.334*10^{-2}$	12	$4.167*10^{-2}$	1:1
II	$4.167*10^{-2}$	24	$2.083*10^{-2}$	1:1
III	$2.083*10^{-2}$	48	$1.041*10^{-2}$	1:2
IV	$1.041*10^{-2}$	96	$5.208*10^{-3}$	1:4
V	$5.208*10^{-3}$	192	$2.604*10^{-3}$	1:8
VI	$2.604*10^{-3}$	384	$1.302*10^{-3}$	1:16
VII	$1.302*10^{-3}$	768	$6.510*10^{-4}$	1:32
VIII	$6.510*10^{-4}$	1536	$3.255*10^{-4}$	1:64
IX	$3.255*10^{-4}$	3072	$1.628*10^{-4}$	1:128

For convenience in the variance analysis, the time T_s was chosen to be independent of s and equal to 12 h (certainly, it must be greater then the period of the lower cutoff of the s-th band). The characteristics of each frequency band are summarised in *Table 2*.

An analysis using this method was conducted over a sample ranging from 14 April to 20 April 1994, for Udine. A matrix Y_{js} was determined by taking the logarithm of the spectral density of each time interval, i.e.:

$$Y_{js} = 10\log_{10} S'_{js} = \alpha + \beta_j + \gamma_s + \delta_{js} \qquad (4)$$

The variance analysis tests the significance of the β_j, γ_s ,and δ_{js} terms. The effect of each term is evaluated by analysing the statistical distributions of rows and columns of the Y_{js} matrix. As an example, if we want to consider the effect of frequency, we must compare the distributions of the spectral values generated by grouping the matrix values by columns. If the histograms show almost equal means and variances, the frequency effect is said to be absent. Quantitatively, the comparison is done by calculating the F-ratio; large F values imply that the distribution of spectrum values varies from column to column (i.e. band by band) more than it does along any given column. The significance test for each term of the model (4) is done by comparing the F-value with the value that it is supposed to have for a matrix of Gaussian distributed numbers without column or row variability. If the former is larger than the latter, the hypotheses is rejected at a given percent significance level and the spectrum is interpreted as depending on such a variable.

Table 3. Results of the nonstationarity analysis. Significance of the time, frequency, and mixed terms in the model of the evolutionary spectrum

Analysis of Variance				
Source of variation	**Term in the model (4)**	**Degrees of freedom**	**F - value**	**P - value**
Model	Y_{js}	12	72.007	$<0.1*10^{-3}$
Time interval	β_j	4	3.149	$0.27*10^{-1}$
Frequency band	γ_s	8	106.43	$<0.1*10^{-3}$
Interaction term	δ_{js}	32		
TOTAL		44		

The results of nonstationarity analysis are reported in *Table 3*; the test indicate that the null hypothesis is significantly rejected for any single term of the model with a marginal probability less then 1%. Therefore, we can say that the pressure is nonstationary for all bands that were analysed; nevertheless, this technique does not provide any information on the characteristic nonstationarity time T_S.

The time scale (T_S) was determined using the test for stationarity proposed by Bendat and Piersol (1971). The method consists in generating a new time series from the original process by evaluating the quantity

$$\sigma^2{}_s(l) = (1/N_s) \sum_{n=(l-1)N_s}^{(l-1)N_s} (\xi_s(n) - \bar{\xi}_s)^2 \qquad (5)$$

which represents the variance of parts of the filtered process $\xi_s(n)$ for the s-th band. The quantity $\sigma^2{}_s(l)$ represents a good estimate of the variance of the process $\xi_s(n)$, while $T = N_s \Delta t$ must be larger than the lower cutoff period $(P_L)_s$ of the s-th band (we chose $T = 2(P_L)_s$). The "run test" was then applied to the new time series $\sigma^2{}_s(l)$. The time T_S was estimated by increasing the number of terms until the test indicated that the nonstationarity had emerged.

The difference between the current approach and Tsao's method resides in the avoidance of the use of the spectral analysis and so the estimate can be done directly in the time domain. Moreover, the band-pass filtering becomes unavoidable in order to reduce any possible contamination of the high frequencies by the large low-frequency amplitudes.

The test was repeated for the nine bands of *Table 2* and for various time segments during the same period, obtaining very similar values. The fluctuations are due in part to the primitiveness of the analysis and, in part, to the different meteorological situations corresponding to various time segments. The values reported in *Table 4* are such that 95% of the estimations for the time scale of stationarity are larger. Note that the "run test" applied to the process filtered in band *IX* (*Table 2*) did not put nonstationarity in evidence (probably because the sample is not statistically significant).

Table 4. Nonstationarity time scales

Band	**I**	**II**	**III**	**IV**	**V**	**VI**	**VII**	**VIII**
T (s)	24	48	96	192	384	768	1536	3072
T_s (h)	1.62	4.53	3.12	4.05	11.04	18.13	25.15	49.50

The nonstationariry analysis was used in designing the spectral analysis procedure, in order to accurately evaluate the spectral content of the pressure signals during bora, a typical nonstationary event. The choice of estimation techniques ranges from the conventional approach based on FFT to recent more sophisticated algorithms such as autoregressive and maximum likelihood methods. The conventional FFT spectral estimation has the advantage of computational efficiency and obtains reliable results for a wide range of processes, but shows two important limitations: one is the inability to resolve close peaks, the other is a possible distortion of the spectral shape due to leakage of energy from high density regions. The recent nonconventional techniques, in turn, suffer a lack of generality and assume different models for the input time process.

In relation to the evolutionary spectra, the FFT estimators are applied to the overlapped time-partition sequences to obtain consistent estimates near the boundaries, thus providing the time evolution of the frequency spectra. This overlap processing of course increases the work load to cover the total sequence length, but avoids the missing of events if they occurred near the boundaries.

4 RESULTS

The first analysis refers to a sample of bora with rainfall recorded in Udine on December 9th, 1987. This took place during December 5th - 10th, a period of synoptic weather characterised by Atlantic frontal disturbances moving across the entire Italian Peninsula.

Figure 1 shows the pressure fluctuations registered on the micro-barograph every 3 seconds. The estimate evolutionary spectrum is shown in *Figure 2*, while the characteristics of the spectral analysis are summarised in *Table 5*.

Table 5. Characteristics of the spectral analysis for the band relative to the bora event

Spectral characteristics	Udine	Trieste
Estimator	Daniell	Daniell
Sampling Interval (s)	3	3
Samples per segment	512	512
Lower frequency cutoff (Hz)	0.0833	0.0833
Upper frequency cutoff (Hz)	0.02083	0.02083
Nominal frequency resolution (Hz)	$0.32552*10^{-3}$	$0.32552*10^{-3}$
Effective bandwidth (Hz)	$0.10416*10^{-1}$	$0.10416*10^{-1}$

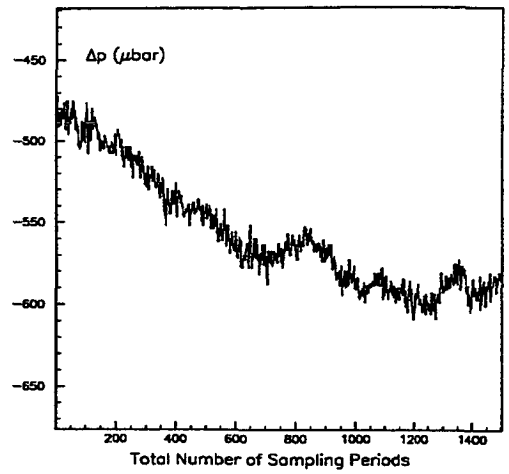


Figure 1. Pressure data-sample recorded in Udine

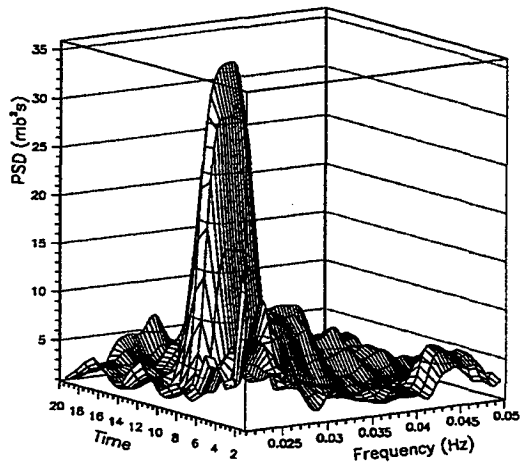


Figure 2. Estimated evolutionary spectra for the pressure record in Udine (time scale unit corresponds to approximately 150 s)

Subsequently, on the night of February 15th, 1988, a second bora case-study was carried out on the Cattinara hill, around Trieste, with readings taken every 3 seconds. This case was also characterised by strong gusts of wind, high pressure and a cloudy sky. A strong nucleus of high pressure (1036 mb) standing over Russia, influenced the weather in Italy during that time. The corresponding pressure fluctuations are shown in *Figure 3*. The spectrum analysis, performed with the Daniell's estimator, provides the results shown in *Figure 4*, whereas *Table 5* displays the characteristics of the spectral estimate in the band analysed.

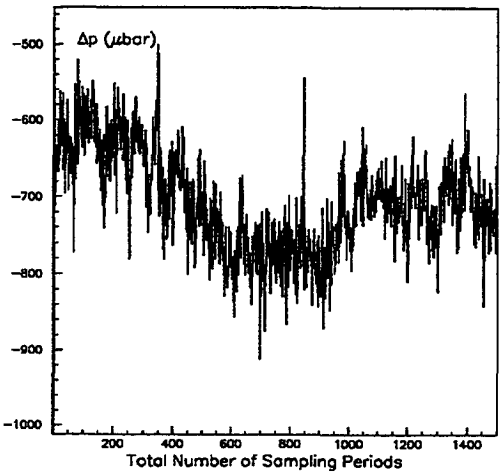


Figure 3. Pressure data-sample recorded in Trieste

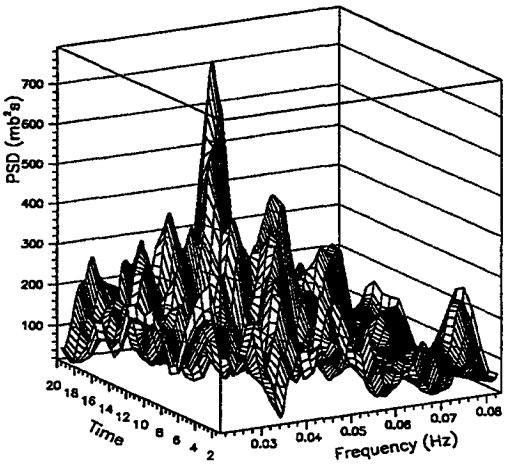


Figure 4. Estimated evolutionary spectra for the pressure record in Trieste (time scale unit corresponds to approximately 150 s)

The main result of the spectral analysis, shown in Figures 2 and 4, is the characteristic peak corresponding to a period of 20-30 seconds for pressure samples recorded in Udine and Trieste.

REFERENCES

Tsao, Y.H., 1984, " Tests for nonstationarity", J. Acoust. Soc. Am., Volume 75, pp. 486-498.

Bendat, J.S. and A.G. Piersol, 1971, "Random data: analysis and measurement procedures", Wiley-Interscience.

Canavero, F.G. and F. Einaudi, 1986, "Time and Space Variability of Spectral Estimates of Atmospheric Pressure", J. Atmos. Sci., Volume 44, No. 12, pp. 1589-1604.

CORRESPONDING AUTHOR

Professor Mario Ceschia,
Department of Physics,
University of Udine,
Udine, ITALY.

THE ASSESSMENT OF THE WATER REGIME FOR RAINFED AGRICULTURE IN AREAS OF SEASONAL RAINFALL IN VENEZUELA

M. T. Puche[1] and J. I. L. Morison[2]

1 Universidad Central De Venezuela, Maracay, Venezuela 2 University of Essex, Colchester, UK.

ABSTRACT

This work explored the assessment of the availability of water for crops and for the performance of mechanised operations using indices derived from rainfall and potential evapotranspiration (ET_o). Two places from the plains of Venezuela were taken as examples; Turén (West Plains) and Valle La Pascua (Central Plains). Both real and simulated daily rainfall data were used to derive characteristics of the rainy season and events associated with the availability of water and continuity of the water supply particularly at the beginning and the end of the rainy season.

1 INTRODUCTION

The assessment of water regime in regions with seasonal rainfall and rainfed agriculture must consider the availability of water as well as the continuity of the water supply; both aspects are particularly important at the beginning of the rainy season when the soil water reserves are scarce or nil. However, towards the end of the rainy season interruptions of the availability of water determine the start of the harvest and the performance of other mechanical operations. In the case of two crops growing sequentially in one rainy season this analysis of the water availability can help us to define the dates and conditions for a second sowing. This work explores different indices based on daily rainfall data and mean daily potential evapotranspiration (ET_o) for the assessment of the water regime.

2 METHODS

Two representative sites: Turén (9°16'N-69°05'W at 215 m.a.s.l.) in the West Plains and Valle La Pascua (9°15'N-66°01'W at 150 m.a.s.l) in the Central plains of Venezuela were used. The stations have good quality records and are located in agricultural areas within the regions of interest.

2.1 Weather data

Thirty years (1961-1990) of daily rainfall data for Turén and Sixteen years (1970-1985) for Valle La Pascua were used. Two approaches were followed: a direct analysis of the daily rainfall and a modelling approach where statistical models of daily rainfall were first derived following Stern and Coe (1984). Then these models were used in two ways: for generating long series (100 years) that were in turn analysed, and for deriving dry spell probabilities through recurrence relations.

In Turén, four years of daily input data were used to obtain ETo estimates from the Penman equation according to the FAO version (Gommes,1983). In Valle La Pascua, ETo estimates were obtained from Class A pan records multiplied by a pan factor of 0.8.

2.2 Evaluation using climatic indices

Using both original rainfall records and generated daily rainfall from the rainfall models. the following characteristics were obtained:

Dry Spell pattern:

A threshold (mm) for a dry day (rainfall on a dry day $<=0.9$) was set. The probability of a maximum dry spell (consecutive dry days) larger than 7, 10 or 15 days in the next 30 days starting on a particular date was derived in two ways: directly from the original data using a Pascal program, and from the statistical model of chance of rain through the recurrence relations using a FORTRAN program (Fernando, 1992). In either case the analysis were made either setting a condition of the starting day being rainy or unconditional to the state of the first day (Stern *et al.*, 1982)

A direct analysis of both the original and the generated rainfall data was performed in order to obtain

-**Characteristics describing the rainy season as a whole:** rainfall amounts and number of rainy days, dates for the start and end of the rainy season and maximum dry spells for each 30 day period within the rainy season.

-**Events in the climatic year:** Roughly two kinds of climatic events can be distinguished in a climatic year: events associated with the

availability of water and events associated with the continuity of the supply. In the first case the rainfall amounts as well as the ratio of rainfall to evaporative demand were chosen in this study. The length of the maximum dry spell was used in conjunction with the above in order to define a continuity of the supply (a similar approach has been used by Stern *et al.* 1982). The following events were considered:

a) The first rain (1stR);

b) The first time the accumulated 7 day rainfall was larger than half the cumulative ET_o for the same period. This event was defined as the start of the rainy season (Start);

c) Equal to b but with the condition that the maximum dry spell in the following 30 days is shorter than 15 days (St15).

d) Equal to b but with the condition that the a maximum dry spell in the following 30 days is shorter than 7 days (St7).

Interruptions of the rainy season were defined as:

e) The first time after St7 in which the accumulated 7 day rainfall was less than half the cumulative ET_o for the same period (D0.5);

f) The first time after St7 a dry spell longer than 7 days occurred (Mx7);

g) The first time after St7 a dry spell longer than 15 days occurred (Mx15);

h) The first time after St7 the accumulated 7 day rainfall was less than the cumulative 7 day ET_o and with a dry spell longer than 15 days occurring in the next 30 days (End).

i) The last time it rained (LstR).

The time difference "window" between some of these events as well as the relationship between these events and the characteristics of the rainy season was examined.

2.3 Software:

Statistical models of daily rainfall were derived using GLIM and FORTRAN programs (Fernando, 1992). Pascal programs were written to describe the characteristics and events in the rainy season. Most of the statistical description of the data was made in INSTAT (Stern *et al.*, 1990) and the results plotted with QPRO 4.0. All the analysis were performed in IBM compatible microcomputers with 80286 or 80386 microprocessors.

3. RESULTS AND DISCUSSION

i. General characteristics of the rainy season and dry spell pattern

The probability of weekly rainfall amounts (Turén, Figure 1a and Valle La Pascua, Figure 1b) as well as the dry spell pattern (Figures 2a and 2b) show the seasonality of the rainfall and the large interannual variability for both

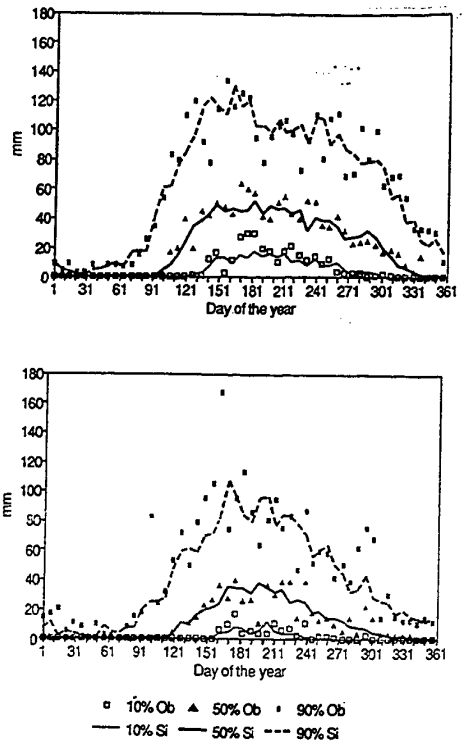


Figure 1. Simulated and observed percentage points for weekly rainfall amounts. a) Turen b) Valle La Pascua.

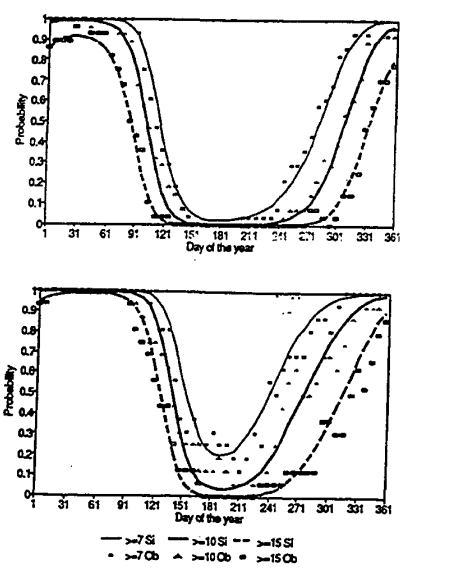


Figure 2. Probability of a dry spell of at least 7, 10 or 15 days. a) Turen b) Valle La Pascua.

stations. There is good agreement between simulated (Si) and Observed (Ob). In Turén (Figure 1a) there is a long period (June-middle of September) where each week has a 90% chance of at least 10 mm rainfall whereas the rainy season the rainfall pattern is more irregular in V. La Pascua (Figure 1b). Periods when there

is more than 90% chance of dry spells longer than 15 days can be identified at both stations. In Turén (Figure 2a) these periods occur from January to March and they extend towards the middle of April in V. La Pascua (Figure 2b). After this stage the curves are very steep indicating a rapid change in the probabilities. This time coincides with the start of the rainy season. In the middle of the rainy season the probability of a long (>10 days) dry spell is almost nil. In Turén this phase extends from June to the end of September whereas in V. La Pascua it extends from the middle of June towards the end of August. Dry spells of 7 days do occur in the rainy season but in Turén the probability is less than 10% between June and September. In V. La Pascua the chance of a dry spell of at least 7 days is more than 20% throughout the rainy season. From September onwards the dry spell probabilities increase but more gradually than at the start of the rainy season suggesting that the end of the season is not sharp. The pattern of dry spell probabilities conditional to the first rain being rainy was very similar to the unconditional ones (data not shown), the differences occur mainly at the beginning of the rainy season where, if it is already rainy, the probability of a long dry spell afterwards is much lower. Percentage points for general characteristics of the rainfall pattern and events are shown in table 1 and 2 respectively. Turén has larger amounts and a longer rainy season, however, large variability in the dates defining the rainy season can be observed in both stations. A common feature of the events (table 2) is their variability from year to year with interquartile values ranging from 20 to 60 days. Larger spread in these dates is observed in V. La Pascua than in Turén. Reductions of the supply (D0.5) occur earlier than a dry spell longer than 7 days (Mx7). These indexes show that even in a place like Turén where rainfall amounts seem plenty the irregularity of the supply may result in short periods of potential stress for crops or in problems for planning agricultural operations.

Table 2 also shows the total amounts (Sum) and Maximum dry spell (SpMx) in the first (Sum1, SpMx1) and second (Sum2, SpMx2) 30 day period (referred to as month) following the start of the rainy season. For Turén, the largest variability is observed in the first month and after that the total amounts should be large enough to satisfy crop requirements (assuming that all the rainfall is available for plants) as daily ET_o values are less than 5 mm.

Table 1. Cumulative percentages points for general rainfall characteristics in Turén and Valle La Pascua

	Turén			Valle La Pascua		
	25%	50%	75%	25%	50%	75%
Sum	1323	1443	1670	694	930	973
Nr	118	131	145	93	111	126
LenS	198	232	244	153	187	221

Sum: Annual rainfall amounts (mm); Nr: annual number of rainy days; LenS: length of the rainy season (days)

Table 2. Cumulative percentage points for: event dates in the climatic year, rainfall amounts and maximum dry spell on the the first and second month after the start of the rainy season in Turén and Valle La Pascua

Event	Turén			Valle La Pascua		
	25%	50%	75%	25%	50%	75%
1stR	67	83	92	81	99	112
Start	95	107	117	109	133	154
St15	105	113	125	123	137	154
St7	111	124	141	139	148	166
D0.5	124	139	160	151	167	199
Mx7	275	301	310	294	322	339
Mx15	346	359	4	242	266	284
End	318	331	349	318	342	362
LastR	366	29	54	347	32	42
Sum1	66	185	268	78	130	196
Sum2	146	221	294	112	148	176
SpMx1	4	8	13	4	8	14
SpMx2	3	5	9	4	5	10

DATES (day of the year): (1stR:First Rain; Start: Start of rainy season; St15: equal to Start but conditional on max dry spell<15 days in the following 30 days; St7:equal to Start but conditional on max dry spell<7 days in the following 30 days;d D0.5: 1st time after St7 that cumulative 7 day (rainfall/ET_o)<0.5;Mx7:1st time after St7 a dry spell longer than 7 days occurred;Mx15 1st time after St7 a dry spell longer than 15 days occurred; End: End of rainy season; LstR: Last rain)

Sum1 and Sum2: Rainfall amount (mm) in the first and second month of the rainy season respectively

SpMx1 and SpMx2: Maximum dry spell (number of days) in the first and second month of the rainy season respectively

In contrast, the amounts in V. La Pascua are more variable and in the first two months of the rainy season there is a risk of the rainfall supply being less than the ET_o. In both stations large dry spells can occur after the start of the rainy season. After the first two months dry spells longer than 7 days do not occur in the three following 30 day periods in Turén but in V. La Pascua a period completely free of risks of long dry spells does not occur.

Using the simulated data the following "windows" were analyzed at the beginning of the rainy season: (Start-1stR),(St15-Start) and (St7-Start) and after the start (D0.5-St15), (D0.5-St7), (End-St15), (Mx7-St7). In Turén, in only about 20% of the years were Start and 1stR the same and the difference between these dates could be up to 60 days. Nearly 80% of the years Start and St15 were the same indicating that dry spells longer than 15 days did not occur after the start but differences up to 60 days between Start and St15 are found in the remaining 20% of the years. Start and St7 were the same in only 25% of the years and, in 50% of the cases St7 occurred more than 30 days later and even up to 90 days.

In V. La Pascua, Start and St15 were the same in 70% of the years. However, risks of dry spells shorter than 15 days are high as in only 20% of the cases the Start was followed by dry spells shorter than 7 days. In 60% of the years differences between St7 and Start were larger than 30 days and windows up to 120 days long were found. D0.5-St15 and D0.5-St7 define the length of periods at the start of the rainy season when supply is adequate (interruptions of the rains are shorter than 15 days in the first case and shorter than 7 days in the second and rainfall amounts are larger than half the ET_o). There was more than a 50% probability for D0.5-St7 being shorter than 25 days in both stations. End-St15 define a period in the rainy season when long dry spells longer than 15 days did not occur, similarly Mx7-St7 define a period without dry spells longer than 7 days. In Turén (End-St15) extends from 150 towards more than 275 days. In V. La Pascua the range is even larger (from 75 to more than 250 days). In Turén the Mx7-St7 ranges from 25 to 250 days; "windows" longer than 130 days are found in 75% of the years. In V. La Pascua Mx7-St7 can be from less than 50 up to 175 days and in 75% of the years this "window" was shorter than 60 days.

Examining the correlation matrices between events and characteristics of the rainy season (data not shown) we can conclude that maximum dry spells in the first and second 30 day group (SpMx1 and SpMx2 respectively) show a high (>0,7) correlation value because often a long dry spell can extend from the first 30 day group to the second. Correlation values up to 0.6 are observed between the rainfall amounts of the first two 30 day periods of the rainy season. In Both stations 1stR showed no linear association with the characteristics analyzed and very small correlation values are also found between the start and the end of the rainy season. In Turén, there is also very little association between the start of the rainy season and characteristics of the season as a whole (Amount and number of rainy days). The date for the occurrence of dry spells towards the end of the rainy season (Mx7 and Mx15) do not seem to be associated with any event occurring earlier in the season. A modest ($r<-0.6$) negative linear association of NrS and the Start is observed in V. La Pascua. In both stations a negative correlation was observed between the date of the Start and the maximum dry spell occurring on the following 30 days (SpMx1). This association as well as the association observed between the characteristics in the first two months of the rainy season can be of practical importance and should be explored in more detail.

CONCLUSION

Events based on climatic indices can give an additional insight about the rainfall pattern showing that the start and the end of the rainy season is not smooth and intermittent situations of water supply occur. The events analyzed can be detected by the farmer and the relations with decision making should be investigated. It is expected that such a variability has direct effect on the growth of crop and also on management decisions. Particularly in Turén, where the rainy season is longer, variations in the continuity of the rainy season should result in a wide choice of possible growing strategies that should be investigated at field level

REFERENCES

FERNANDO, P. N. P. 1992. "Fitting and using stochastic models for rainfall data", MPhil Thesis. University of Colombo. 317 p.

GOMMES, R. A. 1983. "Pocket computers in agrometeorology", Plant Production and Protection Paper No. 45. FAO, Rome. 140 p.

STERN, R. D. and COE, R. 1984. "A model fitting analysis of daily rainfall data". Journal of the Royal Statistical Society, A, 147, Part 1, pp 1-34.

STERN, R. D., DENNETT, M. D. and DALE, I. C. 1982. "Analysing daily rainfall measurements to give agronomically useful results. I. Direct methods", Experimental Agriculture, 18:223-236.

CORRESPONDING AUTHOR

Dr. M. T. Puche. Universidad Central de Venezuela. Fac. Agronomía. Apdo 4579. Maracay. Aragua. Venezuela.

GENERAL PROBLEMS OF THE ESTIMATION OF INHOMOGENEITIES, OPTIMAL WEIGHTING OF THE REFERENCE STATIONS

T. Szentimrey

Hungarian Meteorological Service, Budapest, Hungary

ABSTRACT

Two of the general problems are treated in this paper. The first problem is connected with the break points detection of the examined time series, namely the formalization according to the statistical conventions (e. g. first kind error, second kind error etc.) otherwise the results of the decision methods can not be interpreted. The second problem is the way of defining the weighting factors of the applied homogeneous reference time series. In our opinion there exist optimal weighting factors and even optimal weighting is determined by the covariance structure unambiguously. Of course the mathematical solution is presented too.

1. INTRODUCTION

The homogeneous time series there are indispensable in respect of the statistical examination of climate change and climate variability. The aim of the homogenization is the estimation and correction of the inhomogeneities of the examined time series in climatic respect by comparing with certain homogeneous reference time series. In general the type of the inhomogeneity may be assumed to be a step function, so the essence of this problem is the detection of the break points on the basis of the weighted reference time series.

2. THE ADDITIVE STATISTICAL MODEL

The Examined Time Series

$$Y(t) = C(t) + IH(t) + \epsilon_0(t) \qquad t=1,2,...,n$$

where $C(t)$ is the trend function (signal) of the supposed climate change, $IH(t)$ is the possible inhomogeneity (step function), and $\epsilon_0(t)$ is a normal white noise. The aim of the examination is the estimation of the break points of the inhomogeneity $IH(t)$ and the correction of $Y(t)$.

The Reference Time Series

$$X(t) = [X_1(t),..,X_N(t)]^T$$

$$X_i(t) = C(t) + \epsilon_i(t) \qquad (i=1,2,..,N\,;\,t=1,2,...,n)$$

where $C(t)$ is the common trend function of the supposed climate change, and $\epsilon_i(t)$ ($i=0,1,2,..,N$) are normal white noise series. Furthermore let us assume that the joint distribution of the white noise series ϵ_i ($i=0,1,2,..,N$) is normal too.

The Difference Time Series

Let the vector of weighting factors

$$W = [W_1,..,W_N]^T \text{ and } W^T\mathbf{1} = 1 \quad (\mathbf{1} = [1,1,..,1]^T)$$

i. e. the sums of components is equal with 1.

Consequently the difference time series belonging to such a vector W are without the common climate change signal i. e.

$$Z_W(t) = Y(t) - W^TX(t) = IH(t) + \epsilon_W(t) \qquad (1)$$

$(t=1,2,...,n)$

where $\epsilon_W(t)$ is a normal white noise, and the statistical analysis of the difference time series $Z_W(t)$ makes possible the detection of the break points hopefully. Of course the result of the examination is depending on the chosen weighting factors therefore defining the optimal weighting vector W is one of the basic problems.

3. BREAK POINTS DETECTION

Let $Z_W(t)$ ($t=1,2,...,n$) be a given difference time series according to the formula (1) , where the weighting vector W is fixed, and the intention is to detect the break points of the inhomogeneity $IH(t)$. In this case the main difficulty is connected with the formalization of this problem according to the statistical conventions (e. g. first kind error, second kind error etc.) otherwise the results of the decision methods can not be interpreted. In our opinion the mentioned formalization can be solved by the outline as follows.

Representation of the Decision Method

Let us assume that the following points are the real break points of the inhomogeneity $IH(t)$ (to the right):

$$\Omega = \{\, 1<P_1<P_2<...<P_L\le n \,\}$$

Estimation of the number (L) of break points : L^*

Let us denote the Decision function in case of K estimated break points in interval $[i,j]$: $D_K([i,j])$

Our decision:

$$L^* \; ; \; D_{L^*}([1,n]) = \Omega^* = \{ 1<P^*1<P^*2<...<P^*L^*\leq n \}$$

Basic Postulates connected with the Decision Methods

(i) First kind error (significance)

There exists such a P^*l : $[P^*l\text{-}1, P^*l+1) \cap \Omega$ = empty set i. e. the interval $[P^*l\text{-}1, P^*l+1)$ does not include real break points but according to the decision method the P^*l is a break point in this one.

We have to intend to give the probability of the first kind error (q), or the significance level $(1\text{-}q)$ equivalently!

(ii) Logicality, coherency

$$D_K([P^*l\text{-}1, P^*l+K)) = \{ P^*l<P^*l+1<...<P^*l+K\text{-}1 \}$$

else the result of the decision method can not be interpreted unambiguously.

(iii) Second kind error (efficiency)

There exists such a real break point that we could not detect. As much as possible!

Significant Maximum Likelihood Method (SML)

Last year a significant maximum likelihood method was developed by us (Szentimrey, (1994)) fulfilling the above mentioned postulates such as "significance" and "logicality". In that paper the method was compared both with "Craddock test" (Craddock, (1979)) and with the Successive Use of SNHT (Alexandersson, (1986), (1993)) too.

4. WEIGHTING

In practice there are several ways of defining the weighting vector W (e. g. Steffensen et al. (1993)) but in spite of this fact in our opinion the problem of weighting can be solved by pure mathematical speculation. So that is the statement that there exist optimal weighting factors in statistical respect, i. e. weighting is not an empirical question and even optimal weighting is determined by the covariance structure unambiguously. Our belief is based on the undermentioned order of ideas.

According to the statistical model the difference time series $Z_W(t)$ (t=1,2,...,n) (formula (1)) are applied for break points detection. Taking into account that the efficiency of the break points detection depends on the "signal noise ratio" so minimizing of the variance of the noise term seems to be the natural postulate. Consequently the following minimum problem is obtained:

$$\text{Variance}(\epsilon_W) \approx \text{Variance}(Z_W) = \min$$

where the sums of the weighting factors is equal with 1. The solution of this minimum problem is presented by the following theorem.

Theorem

Let S the covariance matrix belonging to the variables $Y\text{-}X_i$ (i=1,2,..,N) and let us assume the existence of the inverse matrix S^{-1}. In this case the only solution of the minimum problem

$$\text{Var}(Z_W) = \text{Var}(\epsilon_W) = \min, \quad \text{if} \quad W^T\mathbf{1} = 1 , \qquad (2)$$

can be given in such a form:

$$W = (S^{-1}\mathbf{1}) / (\mathbf{1}^T S^{-1}\mathbf{1})$$

and the minimal variance:

$$\text{Var}(Z_W) = 1 / (\mathbf{1}^T S^{-1}\mathbf{1})$$

Proof

On the basis of the formula (1) the variance of the difference time series Z_W can be formed as:

$$\text{Var}(Z_W) = \text{Var}(Y - W^T X) = \text{Var}(W^T (Y - X)) = W^T S W$$

where the vector Y is equal with $Y\mathbf{1}$, and the matrix S is the covariance matrix of the variables $Y\text{-}X_i$ (i=1,2,..,N). So the minimum problem (2) can be written as follows:

$$W^T S W = \min, \quad \text{if} \quad W^T\mathbf{1} = 1 .$$

In consequence of the positive definiteness of the covariance matrix S there exists a symmetric matrix R that

$$R: \; S = RR, \; S^{-1} = R^{-1}R^{-1}$$

Applying the inequality Cauchy-Schwarz-Bunyakovszkij :

$$1 = (W^T\mathbf{1})^2 = (W^T R R^{-1}\mathbf{1})^2 \leq (W^T S W)(\mathbf{1}^T S^{-1}\mathbf{1})$$

that is if $W^T\mathbf{1} = 1$ then

$$W^T S W \geq 1 / (\mathbf{1}^T S^{-1}\mathbf{1})$$

and "equality" if and only if $W = (S^{-1}\mathbf{1}) / (\mathbf{1}^T S^{-1}\mathbf{1})$

Special case ($N = 2$)

Let us suppose having two reference time series: X_1, X_2

On the basis of the above theorem the "optimal" ratio of the weighting factors:

$$W_1 / W_2 = (V_2 - C_{1,2}) / (V_1 - C_{1,2})$$

where

$$V_1 = \text{Var}(Y - X_1), V_2 = \text{Var}(Y - X_2),$$

$$C_{1,2} = \text{Cov}(Y - X_1, Y - X_2)$$

The latter ratio can be expressed by the original covariance structure too of course, i. e.

$$W_1 / W_2 = (V(X_2) + C(Y,X_1) - C(Y,X_2) - C(X_1,X_2)) /$$

$$/ (V(X_1) + C(Y,X_2) - C(Y,X_1) - C(X_1,X_2))$$

where the notations: V=variance, C=covariance.

The above ratio can be compared with the usual methods applied in practice e. g.:

(i) $W_1 / W_2 = R(Y, X_1) / R(Y, X_2)$

where R is the correlation, or

(ii) $W_1 / W_2 = V(X_2) / V(X_1)$

So it can be seen that the "optimal" way of defining the weighting factors is much more difficult one than it seems at first sight.

5. EXAMINATION

(Example for "optimal" weighting)

Data: annual mean temperature time series (1881-1989).

Reference Stations

K: Kremsmünster (Austria)

H: Hurbanovo (Slovakia)]

The reference stations are homogeneous supposedly.

Examined Stations

W: Wien (Austria)

BP: Budapest (Hungary) (Distance W-BP: 250 km)

1-8: Hungarian Stations

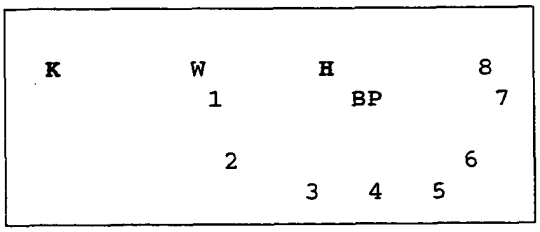


Figure 1. Illustration of the geographical situation of the stations

Table I. The weighting factors of the reference stations by the examined stations

St.	K	H
W	0.9	0.1
BP	0.2	0.8
1	0.7	0.3
2	0.4	0.6
3	0.4	0.6
4	0.1	0.9
5	0.2	0.8
6	0.1	0.9
7	-0.1	1.1
8	-0.1	1.1

On the basis of the comparison of the Figure 1. and Table 1. it can be seen a strong connection between the geographical situation and the weighting factors. In addition it is remarkable that the weighting factors are very "variable" similar to the partial correlation. It is not accidental because the weighting problem can be considered as being a special conditional multiple linear regression one, so the sensitivity is understandable.

References

Alexandersson, H., 1986, "A homogeneity test applied to precipitation data", J. of Climatology 6, pp. 661-675.

Alexandersson, H., 1993, "Urban effects on Nordic temperature data - a statistical test", Submitted to Journal of Climate.

Böhm, R., 1992, "Description of the procedure of homogenizing temperature time series in Austria", Middle European Research Initiative Project Group Meteorology, Working Paper 2, Vienna.

Craddock, J.M., 1979, "Methods for comparing annual rainfall records for climatic purposes", Weather 34, 332-346.

Steffensen, P., Lynge Larsen, F. and Cappelen, J., 1993, "Homogeneity test of climatological data", Danish Meteorological Institute, Technical Report 93-12.

Szentimrey, T., Faragó, T. and Szalai, S., 1992, "Window technique for climate trend analysis", Climate Dynamics 6, pp. 127-134.

Szentimrey, T., 1994, "Statistical problems connected with the homogenization of climatic time series", Proceedings of the European Workshop on Climate Variations, (Kirkkonummi, Finland), Publications of the Academy of Finland 3/94, pp. 330-339.

CORRESPONDING AUTHOR

Dr. T. Szentimrey

Hungarian Meteorological Service

H-1525, P.O. Box 38,

Budapest, Hungary

Response of the Intensity of Subtropical High in the Northern Hemisphere to Solar Activity

Xu Qun
Jiangsu Meteorological Institute, Nanjing 210008, China
Yang Qiuming
Jiangsu Meteorological Observatory, Nanjing 210008, China

ABSTRACT

Using the intensity data of each northern subtropical high measured by monthly 500 hPa height charts for the recent 38 years (1954-1991), we calculate their correlations with the monthly sunspot number and monthly solar radio flux at 10. 7cm wave length, respectively. Through strict test, we further confirm a series of high correlations. Next, using a method called the non-integer (year) wave, the significant response of each subtropical high' s intensity to solar activity at its main period of 10. 9-year length is found. Special attention is paid to that of the eastern Pacific high, the possible mechanism of such sensible response is also analysed.

I. INTRODUCTION

Xu Qun et al. (1984, 1986) have ever pointed out that significant positive correlations exist between solar activity and the strength of each subtropical high in the Northern Hemisphere (N. H.), but the data analysed were of 28 years only. In addition, the auto-correlation inhered in time series had not been removed when above-mentioned correlations were tested for statistical significance. Moreover, to detect the periods in time series only the power spectrum analysis was adopted, which now seems to be much limited in the calculation of real periods in low frequency. Hence, it is necessary to extend data and remove the effect of auto-correlations in time series in order to calculate the correlations with more strict test and obtain the real periods in time series by using a better method.

I. DATA

We use both the monthly mean area index (MAI) and monthly mean strength index (MSI) to measure the intensty of subtropical high. The MAI is the sum of grid points, of which heights (at the monthly 500 hPa height chart) exceeding 5880 GPM and the MSI is the sum of all larger heights ($>$ 5870 GPM) of grid points. We have sorted out the recent 38 year data (1954—1991) of MAI/MSI for the eastern Pacific high (EPH, 175°—115° W, $\geqslant$10°N), the western Pacific high (WPH, 110°—180°E, $\geqslant$10°N), the North Atlantic high (NAH, 0°—80°W, $\geqslant$ 20°N) and the Northern Hemispheric high (NH, $\geqslant$20°N), respectively, For removing the effects of seasonal change, all above MAIs and MSIs have been normalized one month by one month (Xu, 1986).

Solar data are the monthly Wolf' s number (W) and 10. 7 cm solar radio flux (SF).

II. CALCULATION OF CORRELATONS AND THE LENGTHS OF REAL PERIODS

We have calculated the cross correlations between the monthly W, SF and MAI, MSI of each subtropical high in the N. H. for 38 recent years (1954—1991) with the latters lagging 0—132 months respectively, In calculation, we have considered the auto-correlations (AC) of each time series, the test of significance for any correlation has considered the inherent persistence in time series, so we have estimated the number of indepedent sample of time series — the effective sample number (Chen, 1982). According to the AC of time series, the characteristical time scale (τ) between indepedent samples may be obtained as follows:

$\tau = \sum_{i=-\infty}^{\infty} C_{xx}(i\Delta t) \cdot C_{yy}(i\Delta t) \cdot \Delta t$. Hence, the effective number of indepedent samples: $N = n\Delta t/\tau$, where, n is the volume of original sample, Δt is the time lag of sample, C_{xx} and C_{yy} are the ACs of the time series X and Y respectively, both having a time lag of $i\Delta t$ (Chen, 1982).

In the tests of significance for all correlations in present work, we generally replace n by N. From calculated results we have:

1) Although the number of independent sample (N) has been reduced by an order of magnitude than original sample (n) under the consideration of AC in time series, the highly positive correlations (reaching 0. 05 to

0. 01 confidence) still exist between the W or SF and the MAI, MSI of each subtropical high in the N. H. during 38 recent years, especially the MSIs of the Northern Hemispheric high (NH_2), the eastern Pacific high (EPH_2) and North Atlantic high (NAH_2) are highly correlated ($\alpha \leqslant 0.05$) to the previous solar indices (W, SF) with the persistence of about 22, 32 and 21 months respectively.

2) Both the W and SF have significant positive correlation to the lagging MAI and MSI of EPH, coinciding well with the result of Xu (1986a). Special attention is paid to the significant positive correlations ($\alpha \leqslant 0.01$) of W and SF persisting in about one year with the EPH_2, which lags for 12-23 months with a correlative peak at the 16-17th month.

3) Though the correlations of the MAI and MSI of WPH with previous solar indices are lower than corresponding correlations of EPH, they are still sighificantly positive ($\alpha \leqslant 0.05$) when the WPH has a lag of about 16 month. In contrast, the maximal correlation between solar activity and the lagging indices of North Atlantic high (NAH_1, NAH_2) appears so late at the 27-29th month (lag of 2. 2—2. 4 years).

Next, it is essential to calculate all main periods of the solar activity and subtropical highs in order to find the possible relationship between them. Power spectrum and harmonical analysis are generally used to calculate the periods included in time series, but their sample points in the section of low frequencies are too few to define the real lengths of periods. As m is the maximum of the time lags, then we can obtain the spectrum estimation of the following period lengths only when $Tk = m/k$ ($0 \leqslant k \leqslant m/2$), here k is a positive integer. If the lengths of the real periods in data exist between the 11 and 22 years, then we have no hope to find out these real periods and their actual spectrum peaks by the method of spectrum analysis. Hence, now we use the non-integer wave method (the NI technique, Schickedanz et al. 1977) in present work.

The main characteristic of the NI technique is to transform both components ($\cos 2\pi kt/n$, $\sin 2\pi kt/n$) of a harmonical equation into two variable factors of a linear regression equation, the harmonical coefficients (a_0, a_k, b_k) then change into the regression coefficients of a new equation. First, we can calculate these regression coefficients from observed data, then obtain the corresponding complex regressive equation for any non-integer wave k ($1 \leqslant k \leqslant n/2$) and the square of complex correlation (R_k^2), which is positively proportional to the corresponding power spectrum value of the non-integer wave number k being able to reflect the magnitude of corresponding spectrum value. The F-test may be used to verify the significance of R_k^2. Now let us calculate the non-integer (year) wave of W and SF from their observed data of 456 months (1954-1991), i. e. , to calculate the squares of complex correlations (R_k^2) of all non-integer periods between 2. 0 and 38. 0 years with the sample interval of only one month. Each R_k^2 will be tested for significance by a statistic F.

Fig. 1 shows the distribution of R_k^2 (approximate value of spectrum) of each index in wave length of 40 — 160 months by the non-integer (year) wave method, which could find out all actual lengths of periods included in time series with any precision. Now we take the resolution as one month. From Fig. 1 we can see that periodical length of the maximal spectrum peak of EPH_2 (126 months-10. 5 year) approximates mostly to the periodical length of corresponding peak of W and SF (131 months-10. 9 years), other indices of subtropical highs also have significant spectrum values at the 131th month (all reaching the dotted line of 0. 01 level). The variations and phases of EPH_2 are much alike to W and SF (Fig. 2); though the index of WPH_1 contains a periodical effect of the 131 months from solar activity, it still includes some waves of short periods, which are the effects of the 3-5 year cycle of ENSO.

From calculated periods we have:

1) The variation of solar activity has three main periods, the most significant periods is 10. 9 years, then 7. 8 years and 37-38 years in sequence. Anyhow the R_k^2 and F_k of the 10. 9-year period are significantly larger than the corresponding values of other two periods. Moreover, no responses of the 7. 8-year period are found. Therefore, our analysis will concentrate on the effects of the 10. 9-year period in solar activity.

2) All indices of subtropical highs contain the significant influence from the main period (10. 9-year) of solar activity. Arranging the F_k by its magnitude, the most significant influences of the 131-month period occur successively at the following indices: EPH_2, EPH_1, NH_1, NH_2 and so on. Though the positive correlations between the indices of the western Pacific high (WPH_1, WPH_2) and preceding solar activity are not very significant, but the solar activity in main period (131-month) still has notable influence.

3) The 3. 5-4. 7 year short period is prevailing in the strength indices of the WPH, EPH and NH. This just reflects the significant influences of the Southern Oscillation.

Ⅳ. CONCLUSION AND DISCUSSION

1. Through a strict test with the consideration of autocorrelation in time series, both the sunspot number and 10.7 cm solar radio flux still show a series of significant positive correlations with the area/strength indices of subtropical highs in the N. H. with 1-2 years lag, especially the strength indices of the Northern Hemispheric high, the eastern Pacific high and North Atlantic high are significantly positively correlated to the intensity of preceding solar activity with the persistence of 22, 32 and 21 months, respectively.

2. The area/strength indices of the eastern Pacific high have the most sensitive positive response to the intensities of solar activity in preceding 1-2 years, especially in preceding 16-17 months. The intensity of the North Atlantic high also responds significantly positively to the preceding solar activity, but the time of largest response of the NAH delays to the 3-5th month of two years later.

3. The 10.7 cm solar radio flux has a higher relationship with the strength of each subtropical high in the N. H. than that of the sunspot number, also demonstrating that the former may be a better index for reflecting the intensity of solar activity.

4. Using an analytic technique of the non-integer (year) wave, we find that all indices of subtropical highs in the N. H. are significantly influenced by the main period (10.9-year) of solar activity.

5. A statistical analysis of the past 231-year data indicates that the summer floods in the mid-lower reaches of the Yangtze River occur at the peak years (0-+2 year) of the solar 11-year cycle (Xu, 1986b) usually, coincidly well with the present work, which means the strong solar activity will cause strong western Pacific high with its west ridge point stretching more westward, then the strong warm moist southwest wind from the Bay of Bengal will benefit plenty of rain in the mid-lower Yangtze basin during rainy season.

6. Above statistical results are highly supported by recent observations from satellite. Maxmum and minimum irradiances indeed occurred near the peak and low of the Sun's 11-year cycle respectively, as measured by the Earth Radiation Budget (ERB) cavity radiometer onboard the Nimbus-7 satellite through 15 recent years (1979-1993), see Fig. 2a of Lean & Rind (1994). According to the calculations by the GISS/GCM of the terrestrial temperature response to a reduction of 0.25% in total solar irradiance, annual surface air temperatures of most areas in tropical-subtropical regions are positively responded, especially in east Pacific, where the whole vast ocean are evenly responded by a decrease of 0.5-1.0℃ (Fig. 1 of Lean & Rind, 1994). Connected with the present result, following conclusion may be drawn:

Accompanying with an increase (decrease) in solar activity, the earth—atmosphere system will receive more (less) solar radiation. This difference exists clearly in the vast regions at low latitudes. Clear, dry atmosphere dominated by the subtropical high (especially of east Pacific) will benefit the mixed layer beneath ocean successively storing the anomaly of cumulative heat, which is produced by the changes of solar activity. Through affecting the sea surface temperature anomaly, above heat anomaly will modulate the anomaly fields both of atmospheric temperature and pressure aloft. Owing to more than a month is needed for the modulation of atmospheric T-P field to the change of heating field of underlying surface, it is reasonable that after a lag of only 1-4 month, the strength of EPH will begin closely to respond to the change of preceding solar activity, then their relation will rise to a peak, when the former has a lag of 16-17 months.

REFERENCES

Chen, W. Y., 1982, "Fluctuations in northern hemisphere 700 mb height field associated with the Southern Oscillation", Mon. Wea. Rev., Vol. 110, 808-824.

Lean, J. and D. Rind., 1994, "Solar variability: implications for global change", EOS, Vol. 75, No. 1, 1-7.

Schickedanz, P. T. and E. G. Bowen., 1977, "The computation of climatological power spectra", J. Appl. Met., Vol. 16, 359-367.

Xu Qun and Cao Hongxing, 1984, "Solar significant influence on the strength of summer subtropical high", Scientia Meteorologica, No. 1, 1-11 (in Chinese).

Xu Qun and Jing Long, 1986a, "Coupled oscillation of solar activity with the strength of subtropical high in northern hemisphere", Scientia Atmospherica Sinica, Vol. 10, 204-211 (in Chinese).

Xu Qun, 1986b, "Complex influences of solar activity and volcanic clouds on the abnormal climate of China for summer 1980", Scientia Meteorologica, No. 1, 17-26 (in Chinese).

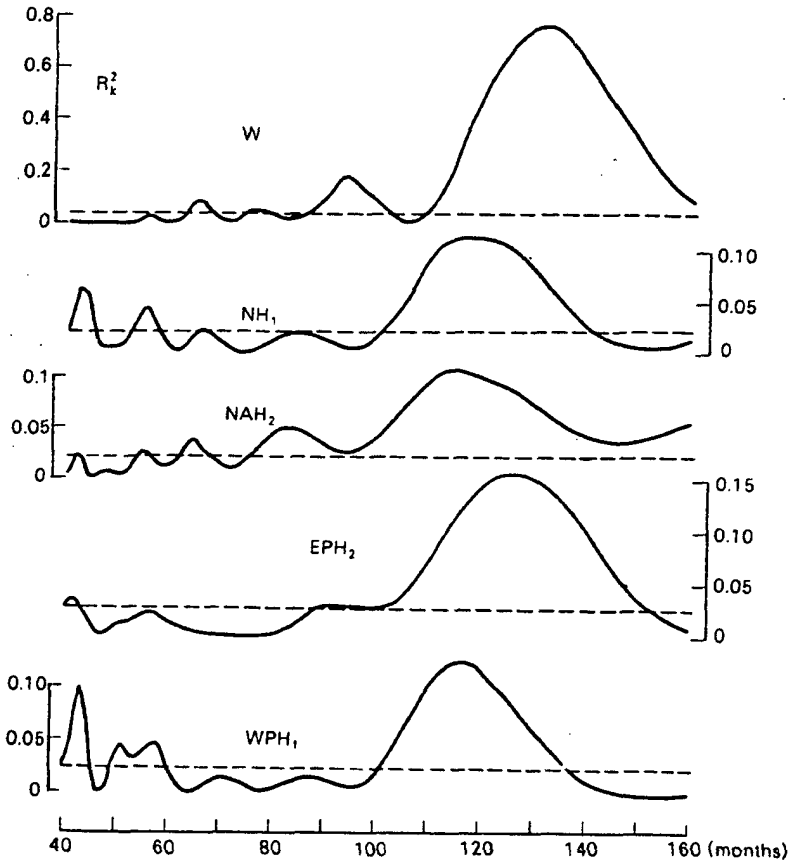


Fig. 1. Time distribution of R_k^2 between solar indices and the MAI, MSI of each subtropical high in wave section of 40–160 months ($k = 40, 41, \cdots, 160$). The coordinate denotes the magnitude of R_k^2. Dotted line means that the R_k^2 is significant at 0.01 confidence by the F–test.

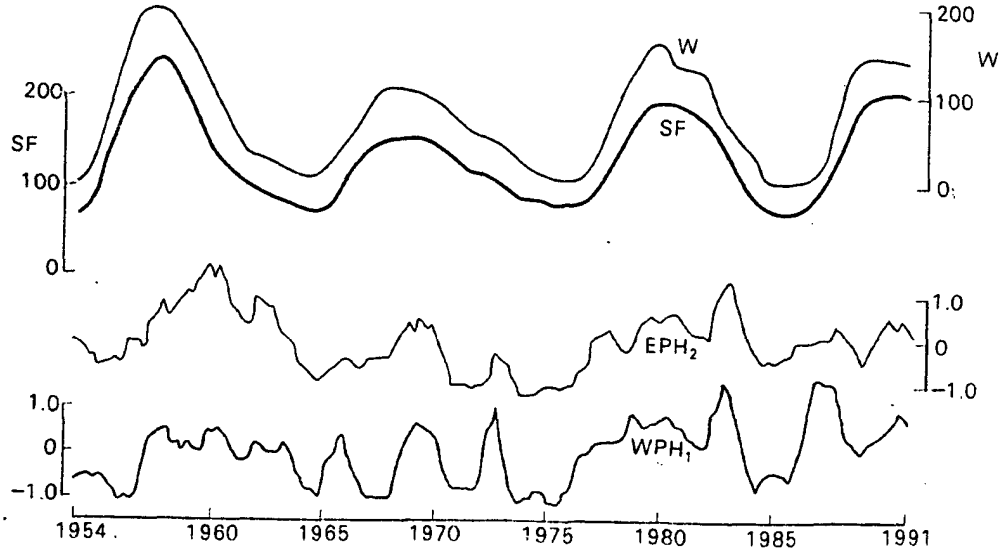


Fig. 2. The 12–month running average curves of W, SF, WPH$_1$ and EPH$_2$ in the past 38 years. The unit of SF is 10^{-22}Wm^{-2}Hz^{-1}. WPH$_1$ and EPH$_2$ are normalized anomaly (unit: 10GPM).

EFFECTS OF THE CONTINENTAL SHELF ON MONTHLY SPATIAL DIFFERENCES IN AIR AND SEA TEMPERATURES

S. A. Hsu

Louisiana State University, Baton Rouge, Louisiana, U.S.A.

ABSTRACT

On the basis of buoy records from the U.S. National Data Buoy Center, it is demonstrated that the difference in air temperature between the shelf and deep ocean in winter can be over 50% along the U.S. East Coast with the shelf water being colder. Along the northern Gulf it is over 30%. In the summer months, while the differences over the East and Gulf shelves are within 10%, the difference over the narrower shelf off California and Oregon is over 20%. The difference in water temperature follows similar characteristics along all three coasts. It is also found that the air temperatures over the coastal stations adjacent to the shelf cannot be used to represent the shelf situation. It is concluded that from statistical and dynamic climatological points of view, the continental shelf behaves differently from both nearby deep ocean and adjacent coasts and must be treated separately.

1 INTRODUCTION

The continental shelf is a mostly flat bottom underwater region surrounding continents or islands, extending from the shoreline outward to a comparatively abrupt steepening of slope, the shelf break. The depth of the continental shelf is normally about 200 m. From meteorological and climatological viewpoints, the continental shelf constitutes a transition zone if air and sea temperatures are not uniform between the shelf and deep water. In fact, during the winter season, polar fronts usually stall along the shelf break in the northwest Gulf of Mexico because a strong baroclinic zone exists there due to the warm-core Gulf eddies in the deeper water (shed previously from the Loop Current) and the cool continental shelf waters (due to active evaporation and Ekman pumping which can produce upwelling to further chill the waters). If an upper-level disturbance (e.g., subtropical jet) moves over this baroclinic zone, marine cyclogenesis can occur producing damaging winds and waves in the northwest Gulf. If these winter cyclones intensify further, blizzards will be the result which may bring devastating precipitation on the U.S. East Coast, e.g., the President's Day snowstorm of February 18-19, 1979 and more recently the "Blizzard of the Century" on March 12-14, 1993 (see Kocin et al., 1995).

The purpose of this study is to demonstrate that the continental shelf behaves differently in air and sea temperatures as compared to the situation both seaward in the deeper water and landward on the coast.

2 METHODS

In order to demonstrate that air and water temperatures for a shelf environment are different from the deeper ocean, climatic summaries for offshore buoys and stations available through the U.S. National Data Buoy Center (NDBC) (1990) are employed. Also, in order to show the effects of the size of a shelf on these two temperatures, three coasts around the contiguous U.S. are studied. In addition, buoy records around Hawaii are utilized to show there is no appreciable difference in these temperatures because there is no pronounced shelf around these islands.

3 RESULTS

The results are shown in Figs. 1 through 3. It can be seen that the difference in air temperature between the shelf and deep ocean in winter can be over 50% along the U.S. East Coast with the shelf water being colder (Fig. 1). Along the northern Gulf of Mexico it is over 30% (Fig. 2). In the summer months, while the differences over the East and Gulf shelves are within 10%, the difference over the narrower shelf off California and Oregon is over 20% (Fig. 3). Thus, the air temperature over the shelf waters is colder than that over the deep ocean all year round with larger (>30%) differences occurring mainly from December through March. Similar characteristics can be seen for the sea-surface temperatures for these three shelves.

In order to show the horizontal homogeneity in both air and sea temperatures over and in a deep ocean without the presence of a continental shelf, climatological data from four buoy stations around Hawaii were analyzed and shown to be within 10%. In addition, intra-shelf homogeneity of both air and sea temperatures for stations located in water depths less than 20 m exists, with variations within 10%.

A question arises that "can the air temperature over an adjacent coastal station be representative of the nearby continental shelf?" The answer is no. As shown in Fig. 1, the difference in air temperature between Atlantic City and a buoy on the nearby shelf can range from over positive 60% in January to over negative 60% in February. For narrower shelves shown in Fig. 2 (for the Gulf coast) and Fig. 3 (for the West coast) they are around 20% in November and January, respectively.

4 CONCLUSIONS

It is concluded that from statistical and dynamic climatological points of view, the continental shelf behaves differently from both the deep ocean and nearby coastal areas and must be treated separately. Therefore, in order to study the marine climatology over an ocean, one must first ask whether the study area is over the shelf or over the deep ocean away from the shelf break.

References

Kocin, P. J., Schumacker, P. N., Morales, R. F., Jr., and Uccellini, L. W., 1995, "Overview of the 12-14 March 1993 SuperStorm", Bulletin, American Meteorological Society, 76, 165-182.

National Data Buoy Center, 1990, "Climatic Summaries for NDBC Buoys and Stations, Update 1", available through NDBC at Stennis Space Center, MS, 39529, U.S.A.

CORRESPONDING AUTHOR

Prof. S. A. Hsu
Coastal Studies Institute
308 Howe/Russell Geoscience Complex
Louisiana State University
Baton Rouge, LA 70808 U.S.A.

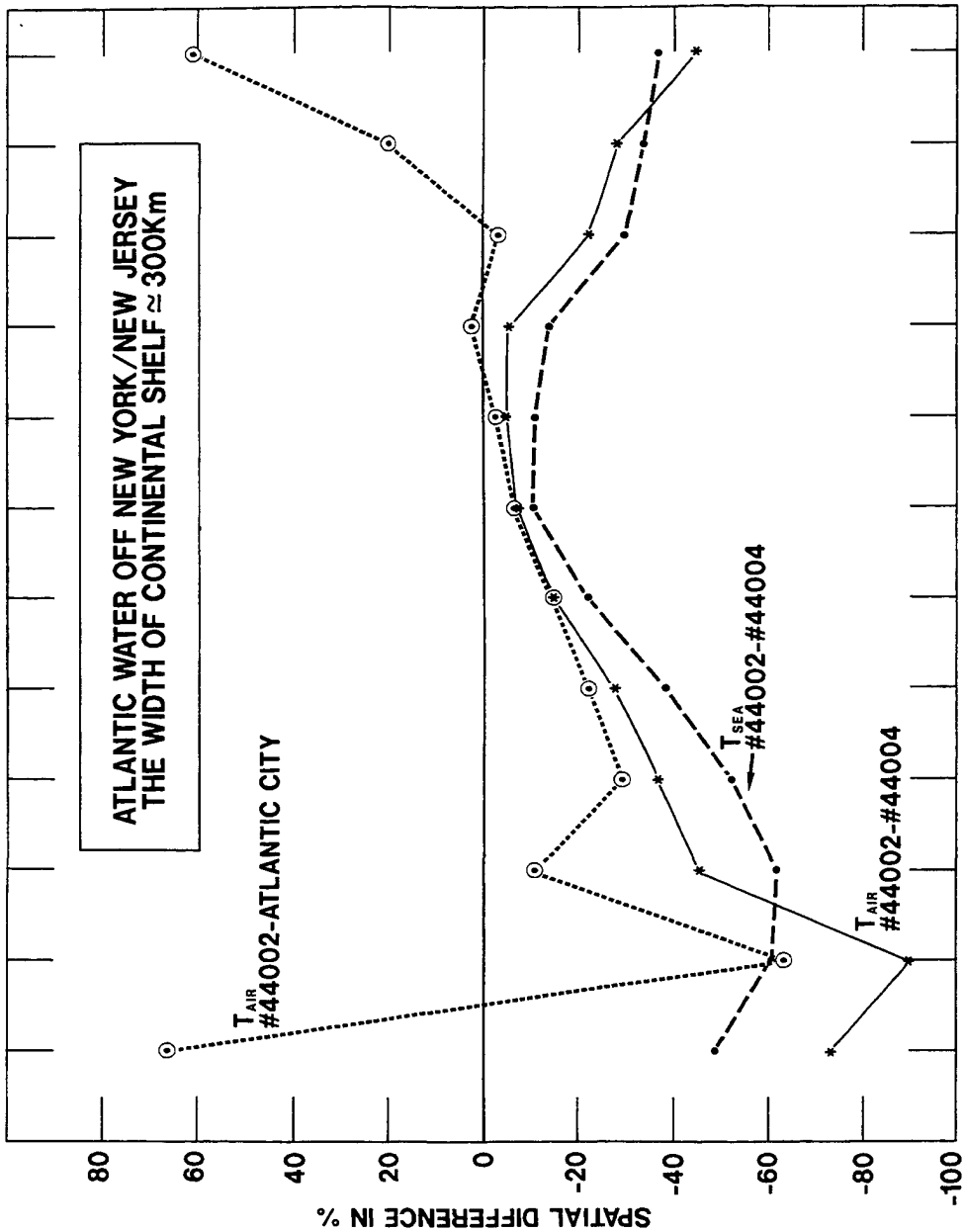


Figure 1. Examples of monthly spatial temperature differences off the U.S. East coast.

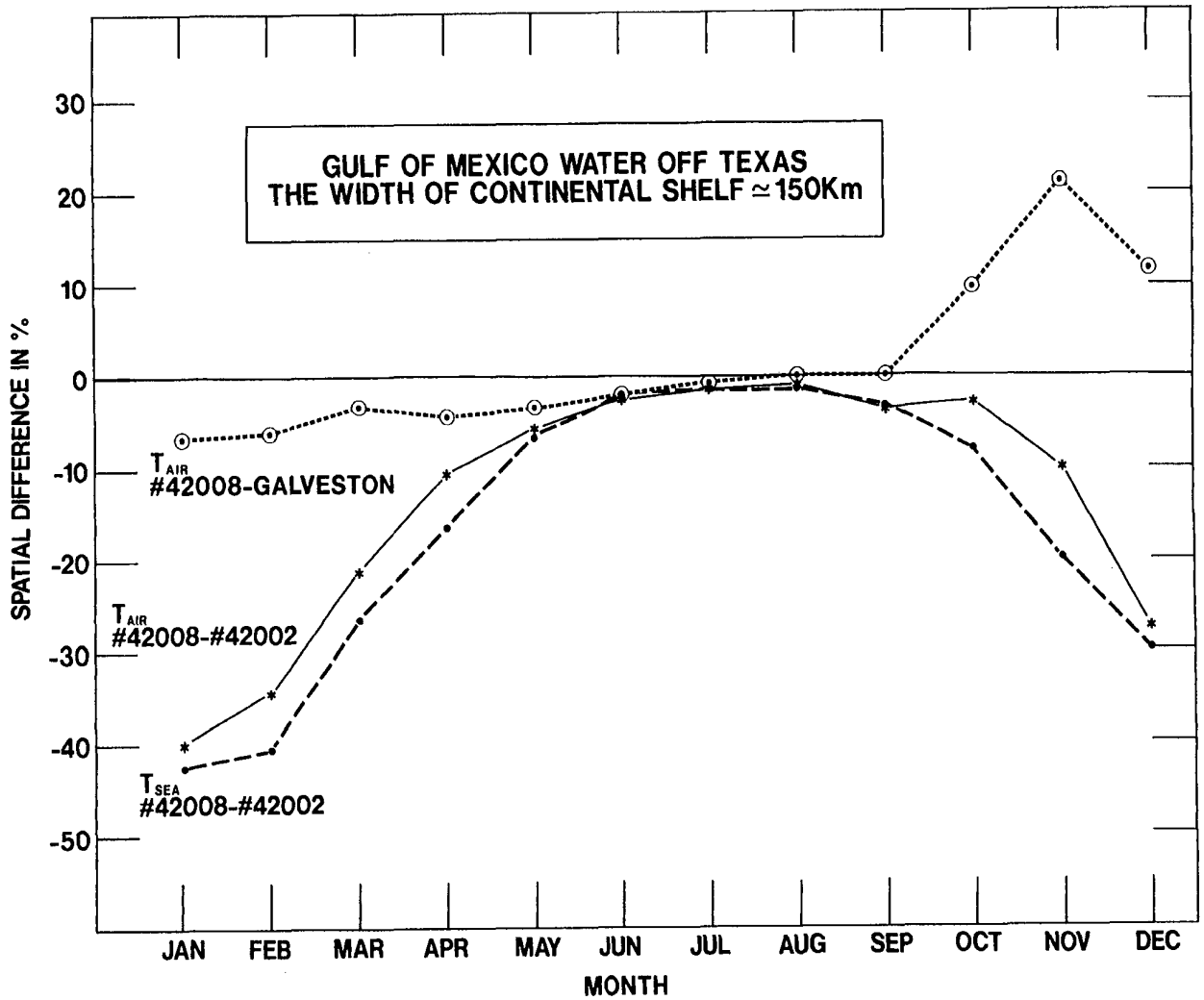


Figure 2. Examples of monthly spatial temperature differences off the U.S. Gulf coast.

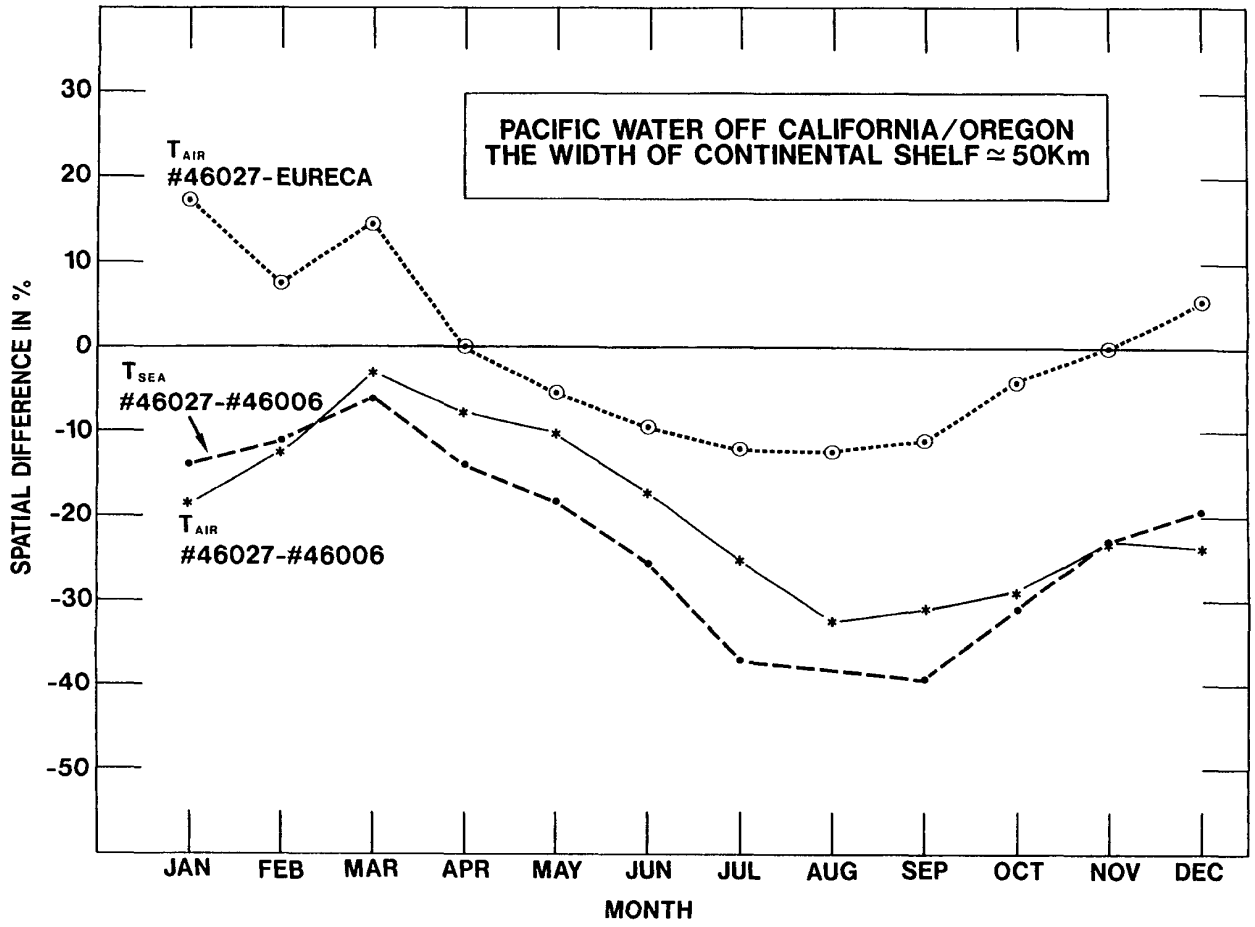


Figure 3. Examples of monthly spatial temperature differences off the U.S. West coast.

CHARACTERISTIC FREQUENCY DISTRIBUTIONS OF REMOTE-SENSED, GROUND-TRUTH, AND MODELED SURFACE WINDS

Eva Bauer

Institut für Meereskunde Universität Hamburg, Hamburg, Germany.

ABSTRACT

Statistical properties of near surface ocean wind speeds are intercompared. Wind speeds retrieved from the ERS-1 scatterometer, the ECMWF atmospheric model, the ocean weather station M in the North Atlantic and the TOGA buoys in the tropical Pacific are used. A direct comparison of these data sets is not possible because the sampling and the error characteristics are quite different. Despite these differences the wind speed distributions are shown to be reasonably simulated either by the Weibull distribution or by the generalized extreme value distribution.

1 INTRODUCTION

The distribution of the near surface ocean wind fields in space and time are routinely determined by atmospheric models for weather and climate predictions. The operational weather prediction is improved through the assimilation of conventional observations of the atmosphere which include wind measurements. Climate change studies look for possible wind field changes in the past and the future on time scales of decades. Thus modeled and measured winds of various scales are combined in different ways.

Recently global observations of near ocean surface wind fields from the first European Remote Sensing (ERS-1) scatterometer measurements enlarge the observational data base. The remote-sensed wind data have been compared with ground-truth data in dedicated campaigns. From the calibration and validation campaign in the North-East Atlantic in 1991, the accuracy of the remote-sensed wind vectors has been determined to be $\pm$ 2 m/s or 10% in the velocity range between 2 - 24 m/s (e.g. Stoffelen and Anderson, 1992). The number of data pairs which are collocated in space and time was limited and the actual dynamical range of wind velocities was only incompletely covered by the measurements.

Here, a frequency analysis is carried out to compare the dynamical range of wind velocities based on data sets as large as possible. The frequency distributions of the scatterometer wind speeds are compared with distributions inferred from two different in situ wind data sets. A 44-year time series of daily mean wind speeds measured at the ocean weather station M (OWS M) is typical for the conditions of the high latitudes of the North Atlantic (2°E, 66°N). The properties of tropical wind speeds are determined from daily mean values of a one-year period from the Tropical Ocean Global Atmosphere (TOGA) buoys in the Pacific. The global scatterometer winds of November 1992 are available with spatially and temporally collocated winds of the European Centre for Medium-Range Weather Forecasts (ECMWF). The scatterometer winds represent instantaneous values with an effective resolution of approximately 50 km $\times$ 50 km. Scatterometer measurements might detect tropical storms which are not resolved by the model calculations.

2 DISTRIBUTION OF EXTRATROPICAL WIND SPEEDS

The frequency density of the OWS M wind speeds taken over a long period is smoothly and unimodally distributed (Fig. 1). The wind speeds of the ECMWF model and the ERS-1 scatterometer from November 1992 which are collected in the vicinity of the OWS M show a multimodal frequency density. But wind speed ensembles of the model and the scatterometer from a sufficiently large area, e.g. the northern extratropical latitudes, are similarly distributed as the OWS M wind speeds (Fig. 2).

The frequency density of extratropical wind speeds is characterized by a positive skewness. The components of the wind velocities are not Gaussian distributed and consequently the wind speeds are not Rayleigh distributed.

The positive skewness is presumably generated by in homogeneous wind fields which are generated by frequently occurring strong wind events. The OWS M and the ECMWF data are well approximated by the Weibull function.

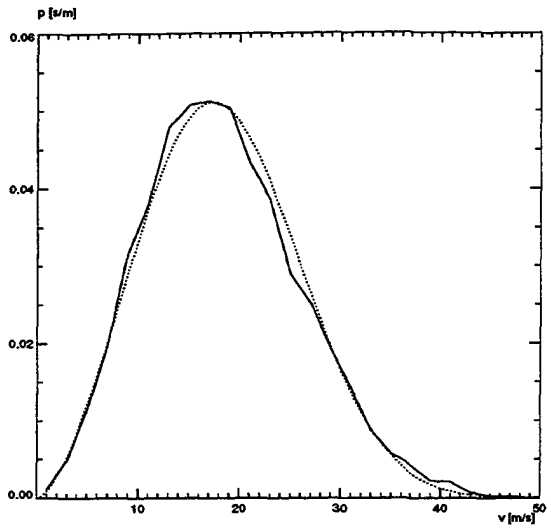


Figure 1: Frequency densities of daily mean wind speeds of OWS M (2°E, 66°N) from February 1949 until January 1993. The continuous and the dotted lines represent the measured wind speeds and the Weibull density distribution, respectively.

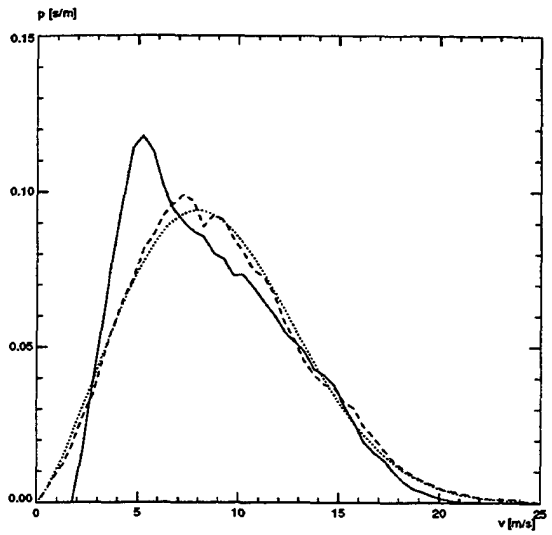


Figure 2: Frequency densities of wind speeds of the northern extratropical latitudes between 25°N and 60°N for November 1992 as obtained from the ERS-1 scatterometer measurements (continuous line), the ECMWF model calculations (dashed line) and the Weibull probability density fitted to the model wind speeds (dotted line).

The Weibull probability is defined

$$F(v) = 1 - exp[-(\frac{v}{c})^k], \qquad v \geq 0 \quad (1)$$

where v denotes the wind speed, c the scale factor and k the shape factor.

The shape and the scale parameter can be estimated directly from the first and the second moment, i.e. the mean and the standard deviation of the data (Justus et al., 1978, Stewart et al., 1978). The frequency density of the scatterometer wind speeds shows a more sharply peaked density with a lower value for the modus than obtained from the model wind speeds (Fig. 2). In part this may be attributed to the low cut-off at 2 m/s in the scatterometer wind speeds.

3 DISTRIBUTION OF TROPICAL WIND SPEEDS

Ground-truth of ocean wind speeds are provided by the TOGA buoy measurements in the tropical Pacific. Wind speeds of the entire year 1992 and also of November 1992 are unimodally distributed (Fig. 3). However, the frequency density of the tropical wind speeds is negatively skewed, i.e. the mean is lower than the modus. The histograms of neither the TOGA buoy nor the model wind speeds are reasonably simulated by the Weibull distribution.

The scatterometer wind speeds show again a lower modus than the modeled and the ground-truth wind speeds. The cut-off below 2 m/s presents the estimation of a theoretical distribution function.

4 FITTING OF THEORETICAL DISTRIBUTIONS

The frequency of the data distributions can often easily be adjusted to probability distributions using linear moments of order statistics (Hosking, 1990). The advantage of L-moments in comparison to conventional moments is that these are linearly depending on expectations of order statistics. Thus the determination of L-moments is relatively insensitive to spurious data in small data series. The L-moments λ_r can be inferred from the quantile function of the data $x(F)$ and the shifted Legendre Polynominals P_r^*

$$\lambda_r = \int_0^1 x(F)\, P_{r-1}^*(F)\, dF, \qquad r = 1, 2, \ldots \quad (2)$$

where

$$P_r^*(F) = \sum_{k=0}^{r} (-1)^{r-k} \binom{r}{k} \binom{r+k}{k} F^k (3)$$

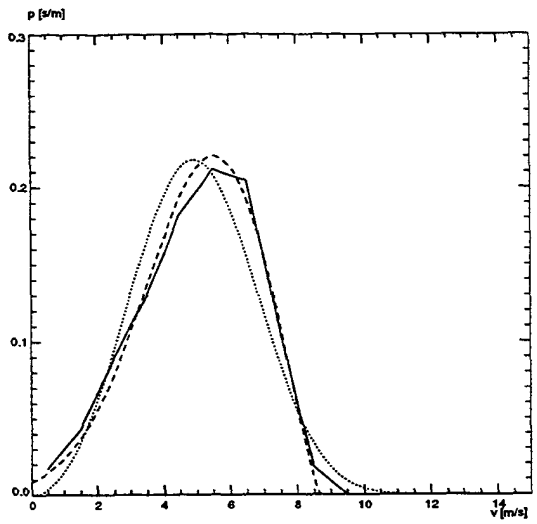


Figure 3: Frequency densities of wind speeds of the tropical Pacific between 8°S and 8°N and between 170°E and 265°E of November 1992 as obtained by the TOGA buoy measurements (continuous line), the Weibull density distribution (dotted line) and the GEV density distribution (dashed line).

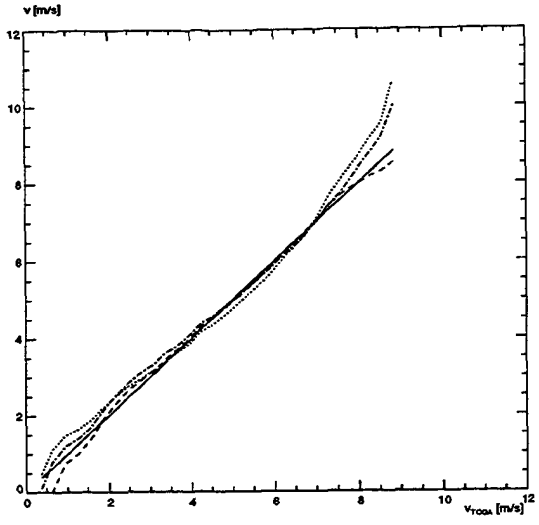


Figure 4: Quantile-quantile plot showing on the abscissa the wind speeds inferred from the TOGA buoy wind speed distribution of the tropical Pacific for November 1992 versus the wind speeds from the Weibull distribution (dotted line), the GEV distribution (dashed line) and the corresponding ECMWF model wind distribution (dashed-dotted line) in comparison with the optimum diagonal.

With the help of L-moments a parametric distribution function for tropical wind speeds is estimated. Tests have shown that the generalized extreme value (GEV) distribution simulates the bulk of the tropical wind speeds adequately. The GEV probability is defined as

$$F(x) = \exp[-(1 - \frac{\beta}{\alpha}(x - \xi))^{1/\beta}] \qquad (4)$$

However, for negatively skewed distribution densities the GEV may have a critical value beyond which the GEV is not defined. This limits the estimation of the probability of extreme wind speeds.

The frequency of the TOGA buoy wind speeds and of the model wind speeds in the tropical Pacific are appropriately described by the GEV though the parameters of the GEV are slightly different. The quantile-quantile plot for the wind speeds of the tropical Pacific depicts the good simulation by the GEV distribution (Fig. 4). The differences between the distributions of the ECMWF model and the TOGA buoy wind speeds are seen for wind speeds lower than 2 m/s or larger than 8 m/s.

5 CONCLUSIONS

The intercomparison of near surface ocean wind speeds from the ERS-1 scatterometer, the ECMWF model, the OWS M and the TOGA buoys is carried out by a frequency analysis. The various data sets have different sampling characteristics and are of different accuracy. A direct comparison of the statistical moments for the quality assessment of the data is not appropriate. However, it appears useful to characterize the wind speed distributions by theoretical distribution functions.

Modeled and ground-truth wind speeds are approximated reasonably by the Weibull and the generalized extreme value distribution for the extratropical and the tropical latitudes, respectively.

The corresponding frequency densities from the ERS-1 scatterometer measurements are more sharply peaked and have lower values for the modus. It cannot be decided yet whether this behaviour is due to the cut-off below 2 m/s, or the method of sampling instantaneous values, or probable insufficiencies in the retrieval algorithm of the scatterometer winds. Having solved this question the remote-sensed global wind data will certainly have positive impact through the assimilation in weather prediction models.

ACKNOWLEDGEMENTS

The provision of the ERS-1 scatterometer winds and the collocated ECMWF model winds by Ad Stoffelen is gratefully acknowledged. The TOGA wind data are obtained from the project office, Dr. Michael J. McPhaden via file-transfer-systems.

REFERENCES

Hosking, J.R.M., 1990, "L-moments: Analysis and Estimation of distributions using linear combinations of order statistics", J. R. Statist. Soc. B, 52, 105-124.

Justus, C.G., W.R. Hargraves, A. Mikhail and D. Graber, 1978, "Methods for estimating Wind speed frequency distributions", J. Appl. Meteor., 17, 350-353.

Stewart, D.A. and O.M. Essenwanger, 1978, "Frequency distribution of wind speed near the surface", J. Appl. Meteor., 17, 1633-1642.

Stoffelen, A. and D.L.T. Anderson, 1992, "ERS-1 scatterometer calibration and validation activities at ECMWF: a) The quality and the characteristics of the radar backscatter measurements, b) From radar backscatter characteristics to wind vector solutions" in Proc. Central Symposium of the International Space Year Conference, Munich, Germany, 30 March - 4 April; ESA SP-341, European Space Agency, Paris.

Weibull, W., 1939, "A statistical theory of strength of materials", Ing. Vet. Ak. Handl., 151, Stockholm.

CORRESPONDING AUTHOR

Dr. Eva Bauer,
Institut für Meereskunde,
Universität Hamburg,
Troplowitzstrasse 7,
D–22529 Hamburg, Germany,
e-mail: bauer@ifm.uni-hamburg.de

ROBUST ESTIMATES OF LOCATION AND SCALE PARAMETERS IN CLIMATOLOGICAL ANALYSIS OF RADIOSONDE DATA

Alexander M.Sterin

All-Russian Research Institute for Hydrometeorological Information - World Data Center

6, Korolyov str., Obninsk, Kaluga Region, RUSSIA 249020

ABSTRACT

Traditionally mean E and root mean square (rms) S are used for climatological processing of radiosonde data as measures of location and scale. The efficiency of estimates E and S is known to be maximal compared to other estimates, when the real distributions are close to hypothetical ones, but decreases rapidly as real distributions become different from hypothetical distributions.

Real archival radiosonde data, both raw and controlled, were used for calculations of traditional and resistant (robust) estimates of climate statistics. The behavior of various estimates, both traditional and resistant, is numerically estimated and analyzed for raw and controlled data of height H and temperature T.

INTRODUCTION

Mean E and rms S are known to be efficient nonbiased estimates for location and scale parameters respectively. But they are too sensitive to the situations when real data do not correspond the conditions and hypotheses which provide the optimality of these estimates. In other word, their efficiency drops rapidly as real data in archives do not correspond to hypotheses on their distributions. In particular, real data may be affected by changes in instrumentation and in processing techniques. They may be also affected by "noise", they may contain "outliers", such as rough errors of various nature.

Complex Quality Control (CQC) of radiosonde data (Alduchov, 1985) is a comprehensive method to detect errors in archival radiosonde data. The flags produced by CQC procedures are considered in calculating the statistics, and the influence of rough errors in data on the statistics is thus excluded.

The other way to exclude the effect of inhomogeneities and errors in data on the statistics calculated is to use methods of statistical estimation and hypotheses testing, which are robust in the situations when primary hypotheses on distributions are in practice violated as real data samples are considered, and which are resistant to "outliers", that may appear in data sets. A number of publications are devoted to using these methods for estimating characteristics of climate. In particular, in (Sterin, 1990, Lanzante, 1994), such estimates are used for processing radiosonde data and calculating upper-air climate characteristics.

This publication contains comparison of results of calculating simplest one-point statistics for the climatic system of free atmosphere - location and scale parameters, related to height H and temperature T on standard levels. Both traditional and robust estimates are studied, and results of CQC are considered.

In some publications on robust statistics, the errors are involved into data samples artificially, and thus various situations of appearing errors are simulated. For example, errors may be produced by random number generators, etc. It seems to be essential that the approach of this paper is based on the situations when the data samples contain the natural mixture of both correct values and erroneous values, and errors are of various origin as it happens in processing real data.

DATA

The upper-air data for H and T for various standard levels from 1000 to 10 hPa were used in this study. The data had passed through CQC procedures and contained data quality flags, which were considered in calculating the statistics. The results contained here are referred to data for the radiosounding station Gasan-Kuli (WMO number 38750) for the period of observations 1961-1978. This station was chosen because the preliminary analysis of quality flags in data after CQC for a group of station has shown that raw archival data from this station contained maximal fraction of values for H and T, flagged as errors.

PARAMETER ESTIMATES

Let x be the variable, used for climatological processing (H and T in this study). As the linear transformations are applied to x, the location G and scale ψ parameters are known to provide:

$G(ax+b)=aG(x)+b$, $\psi(ax+b)=abs(a)\psi(x)$.

As the data sample (X) of values x is considered, the following statistics for this ensemble will be calculated:

Location parameter:

E(X) -mean, $\mu(X)=Q_2$ - median, or second quartile, $W(X)=(Q_1+Q_3+2Q_2)/4$ - Tukey's trimmed mean.

Scale parameter:

S(X)-rms,

$A(X)=\mu(abs(x-\mu(X)))/.675$ - adjusted median of absolute deviations,

$D(X)=(Q_3-Q_1)/1.349$ - adjusted interquartile range.

Here Q_1, Q_2 and Q_3 are first, second (median) and third quartiles of the data sample respectively.

Comparison of estimates on "raw" and controlled data samples

Hereafter, two different samples of values x will be considered. The first sample X^R includes all the values of x as they are contained in the archives (raw data). The second sample X^C includes values of x flagged by CQC procedures as 'correct" values only. In other word, first sample X^R contains both values of x flagged as "correct", and erroneous values of x

We shall denote $(E_X)^{RC}=|E(X^R)-E(X^C)|$ - absolute value of difference between two values of mean E: the first one value of mean E is calculated on sample of "raw" data (X^R) and the second one value of mean E is calculated on sample of "correct" data (X^C). In a similar way we shall introduce such characteristics for other estimates of location parameter:

$(\mu_X)^{RC}=(\mu_X)^R-(\mu_X)^C$ - for medians,

$(W_X)^{RC}=(W_X)^R-(W_X)^C$ - for Tukey's trimmed mean.

The similar characteristics are also introduced for scale parameters:

$(S_X)^{RC}$ for rms S,

$(A_X)^{RC}$ - for adjusted median of absolute deviations A,

$(D_X)^{RC}$ - for adjusted interquartile range D.

The characteristics introduced above will be used to compare the differences in values of the same location and scale parameters, both traditional and robust, on two various sets of radiosonde data: "raw" data and controlled data.

Comparison between traditional and quantile-based estimates

To study how close are traditional location and scale estimates to their robust analogs based on sample quantiles, we shall consider the differences of the following kind, as the example explains:

$\gamma(E,\mu)=E(X^C)-\mu(X^R)$ - difference between the mean calculated on sample of CQC'd data and median calculated on the sample of "raw" data. Note that value of median, in practice, is the same both on samples of "raw" and CQC'd data. In a similar way, the differences $\gamma(E,W)$ for location parameter may be introduced. The differences $\gamma(S,A)$ and $\gamma(S,D)$ for scale parameters may be introduced in similar way.

The differences γ calculated for various pairs of samples, may be summarized in the following way:

$$\Gamma(E,W)=\{(1/N_{sum})\Sigma_{sum}\gamma^2(E,W)\}^{1/2}, \quad (1)$$

where the summarizing is performed upon the considered pairs of samples. For example, if the samples are values of temperature taken for each month of each year of some period, the summarizing in (1) may be done for all of 12 months and for all of years of the period. The summarizing estimates similar to (1) may be introduced for pairwise comparing various parameters, such as

$\Gamma(E,\mu)$, $\Gamma(E,W)$ - for location parameters,

$\Gamma(S,A)$, $\Gamma(S,D)$ - for scale parameters.

RESULTS AND DISCUSSION

Two groups of calculations were performed. The first group of experiments was devoted to estimates of how close are values of each of location or scale parameters, as calculations were done on two samples of data: sample of "raw" data and sample of data after CQC. In this group of experiments annual climatic parameters (location and scale), - were estimated for height H and temperature T on various standard levels for period 1961-1978. Table 1a contains absolute values of differences between values of location parameters for height H, as these parameters are estimated on samples of "raw" and CQC'd data. Table 1b contains absolute values of differences between values of scale parameters for height H, as samples of "raw" and CQC'd data are obtained in similar way.

Table 1a. Absolute values of differences between location parameters for height H, dam. Annual climatic parameters are estimated for period 1961-1978 both upon "raw" and CQC'd data

Level,hPa	$(E_H)^{RC}$	$(\mu_H)^{RC}$	$(W_H)^{RC}$
10	0.08	0.00	0.00
20	1.52	0.00	0.25
30	1.41	0.00	0.00
50	1.39	0.00	0.00
70	1.03	0.00	0.00
100	0.80	0.00	0.25
150	0.42	0.00	0.25
200	3.33	1.00	0.75
250	2.30	0.00	0.25
300	0.20	1.00	0.50
400	1.20	0.00	0.50
500	1.71	0.00	0.00
700	0.90	0.00	0.00
850	2.20	0.00	0.00
1000	1.27	0.00	0.00

Table 1b. As in Table 1a, but for scale parameters of H

Level,hPa	$(S_H)^{RC}$	$(A_H)^{RC}$	$(D_H)^{RC}$
10	183.36	0.00	0.00
20	134.59	1.48	0.74
30	39.64	0.00	0.00
50	.55.12	0.00	0.00
70	41.67	0.00	0.00
100	10.86	1.49	0.75
150	5.01	0.00	0.74
200	73.01	1.00	0.74
250	58.67	0.00	0.74
300	8.55	1.00	0.00
400	50.84	0.00	0.00
500	57.99	0.00	0.00
700	47.15	0.00	0.00
850	66.25	0.00	0.00
1000	21.22	0.00	0.00

For H, estimates of rms S are shown to be especially sensitive to mixture of various errors existing in the "raw" data sample. On upper levels, 20 and 10 hPa, values of H are large, and the variability of H is known to be bigger on upper levels than on the lower levels. On these upper levels possible distortions of values of H , due to losses or changes of figures, etc., are the most essential. Nevertheless,

even for these upper levels the presence of "outliers" in data is shown to affect miserably on scale quantile-based statistics.

Table 2a contains absolute values of differences between values of location parameters for temperature T as these parameters are estimated on samples of "raw" and CQC'd data. Table 2b contains absolute values of differences between values of scale parameters for temperature T as samples of "raw" and CQC'd data are obtained in similar way.

Table 2a. As in Table 1a, but for location parameters of temperature T, °C

Level,hPa	$(E_T)^{RC}$	$(\mu_T)^{RC}$	$(W_T)^{RC}$
10	0.05	0.00	0.02
20	0.03	0.00	0.00
30	0.03	0.00	0.00
50	0.01	0.00	0.00
70	0.05	0.10	0.05
100	0.05	0.00	0.00
150	0.00	0.00	0.00
200	0.09	0.00	0.00
250	0.02	0.10	0.05
300	0.02	0.00	0.00
400	0.02	0.00	0.00
500	0.04	0.00	0.00
700	0.01	0.00	0.00
850	0.08	0.10	0.05
1000	0.10	0.05	0.05

Table 2b. As in Table 2a, but for scale parameters of T

Level,hPa	$(S_T)^{RC}$	$(A_T)^{RC}$	$(D_T)^{RC}$
10	0.91	0.00	0.07
20	0.59	0.00	0.00
30	0.56	0.00	0.00
50	0.76	0.00	0.00
70	1.35	0.00	0.00
100	0.63	0.00	0.40
150	0.51	0.15	0.00
200	0.91	0.00	0.00
250	0.17	0.15	0.00
300	0.10	0.00	0.00
400	0.10	0.00	0.00
500	0.22	0.00	0.00
700	0.09	0.00	0.00
850	0.32	0.15	0.00
1000	0.22	0.23	0.08

As temperature T is considered, let us note that just differences between mean E estimates calculated on samples of "raw" and CQC'd data, are very small. For scale parameters of T, the differences between rms S estimates are a little bigger on upper levels than on lower levels. But this effect is not so impressive for T as for height H. As we believe, there are two possible explanations of this. First, the rough errors in values of temperature T, such as losses or changes of figure or changes or losses of sign, are identical upon the whole profile. Second, as the annual climatic statistics are estimated, the intraannual component of total variability is smaller in lower stratosphere than near the surface. At the same time, we must consider that volumes of samples on upper levels are smaller than those on lower levels.

The second group of experimental calculations was devoted to calculate how close are traditional estimates of location and scale parameters to corresponding resistant (robust) estimates of location and scale parameters. In this group of calculations, monthly statistics for height H on standard levels for each of 12 months and for each of the years of period 1961-1978 were considered. The differences between values of traditional location parameter E on samples of CQC'd data and robust location parameters μ and W on samples of "raw" data were calculated and then summarized according to (1). N_{sum} - the amount of statistics summarized by months and years, - is varying for different levels, because the minimal sample size for calculations was taken to be equal to five observations, and not all of the possible monthly statistics were calculated. The differences between values of scale parameters: rms S on samples of CQC'd data and robust location parameters A and D on samples of "raw" data, - were also calculated and summarized in similar way. The results are contained in Table 3.

Table 3. Summarized differences between traditional estimates of location and scale parameters and their robust analogs, for height H, dam.

Level, hPa	N_{sum}	$\Gamma(E,\mu)$	$\Gamma(E,W)$	$\Gamma(S,A)$	$\Gamma(S,D)$
10	185	3.83	14.96	4.61	43.29
20	325	2.66	5.43	3.16	13.80
30	363	2.04	1.37	2.55	2.62
50	391	2.76	6.48	3.95	12.25
70	405	1.56	0.99	1.93	1.95
100	412	1.71	4.56	2.09	12.35
150	413	1.87	1.04	2.08	2.10
200	414	2.06	5.74	2.61	15.08
250	410	1.87	5.12	2.39	13.69
300	414	1.55	0.90	1.66	1.81
400	414	1.28	3.69	1.32	10.13
500	414	0.97	3.28	1.18	9.28
700	414	0.63	0.37	0.81	0.74
850	414	1.78	4.12	4.32	12.23
1000	414	0.78	4.51	1.02	13.10

CONCLUSION

The calculations were made with real radiosonde data on temperature and height, containing rough errors. These calculations demonstrate that climatological estimates of location and scale parameters, based on order statistics, are very little sensitive to rough errors. Thus, the climatological calculations of resistant location and scale parameters could be performed even on samples of "raw" radiosonde data, which do not undergo just the simplest procedures of quality control.

On the other hand, as results of Table 3 demonstrate, the differences between traditional and resistant quantile-based statistics may be essential, and it may affect the results of further climatological

analysis. The climatology based on resistant estimates may be considered in parallel to the climatology based on traditional estimates, and it seems essential to discriminate these technics as different approaches.

REFERENCES

Alduchov, O.A., 1985, "Complex Quality Control of Geopotential and Temperature in Station Archives of Upper-Air Data". Proc. RIHMI-WDC, 115, pp. 34-63 (in Russian).

Lanzante, J.R., 1994, "Resistant, Robust and Nonparametric Techniques for the Analysis of Climate Data: Theory and Examples, Including Applications to Historical Radiosonde Station Data". Submitted to: "Journal of Climate".

Sterin, A.M., 1990, "Resistant Estimates of Location and Scale Parameters in Climatological Processing of Aerological Archival Data". Proc. RIHMI-WDC, 153, pp. 30-41 (in Russian).

ACKNOWLEDGMENTS

The study was partially supported by International Science Foundation (ISF, supplementary grant SC4000).

The efforts of Dr. Oleg Alduchov from RIHMI-WDC in assistance in understanding the results of Complex Quality Control are gratefully acknowledged. The manuscript of paper kindly submitted by Dr. J.Lanzante, was very useful for author of this paper.

CORRESPONDING AUTHOR

Dr. Alexander Sterin,
Head of Aerology Department,
RIHMI-WDC
6, Korolyov str., Obninsk, Kaluga region, Russia, 249020

PATTERNS AND CHANGES IN PRECIPITATION AND STREAMWATER CHEMISTRY OVER TEN YEARS FROM PLYNLIMON, WALES

T.H. Sparks[†] & B. Reynolds[§]

NERC Institute of Terrestrial Ecology, [†]Monks Wood & [§]Bangor, UK.

ABSTRACT

This paper examines precipitation and streamwater chemistry data recorded from an upland site in mid-Wales between 1979 and 1990. Changes in a number of chemical determinations were suggested; the most pronounced of these being a reduction in the acidity both of rainfall and of streamwater. An examination of changes in sulphate data suggested a reduction in the proportion from non-marine sources in line with a reduction in emissions of sulphur dioxide. However, observations of wind direction and strength indicate that these changes may be related to an increase of onshore winds.

1 INTRODUCTION

As part of a commitment to long term monitoring the Institute of Terrestrial Ecology has been recording water chemistry at two sub-catchments near Plynlimon since 1979. During this period UK emissions of sulphur dioxide have dropped from 4.9 million tonnes to 3.8 million tonnes (Gillham *et al.*, 1992). Acidification of freshwater is related to emissions of oxides of sulphur and nitrogen. Evidence of the reversibility of acidity in response to declining emissions have recently been reported for a Scottish loch (Allot *et al.*, 1992). The present paper examines trends and patterns in precipitation and streamwater chemistry from an area in mid-Wales to determine if reductions in acidity could also be determined.

2 DATA

Data were obtained from two catchments (Cyff and Gwy) near Plynlimon. Records involved sampling of bulk precipitation within the Cyff catchment and spot sampling of the Cyff and Gwy streams. Funding uncertainty led to sampling being carried out at various frequencies (weekly, fortnightly, four-weekly) during the monitoring period. Measurements of a number of chemical determinands and of pH were carried out on each sample. We have aggregated data into comparable 28-day periods (13 periods per year) for examination. This has some appeal over the inequality of calendar month recording, but leads to a slight registration problem of 1 day/annum. Precipitation data were also converted into volume weighted means, but this was not possible for stream sites because of the lack of an aggregated flow measurement.

Information from the Meteorological Office's MORECS database on soil moisture deficit (SMD), rainfall and temperature were abstracted for appropriate calendar months. These data were interpolated to the 28 day periods on which the rest of the data were accumulated.

The nearest met station to Plynlimon undertaking 6-hourly observations was Aberporth on the Welsh coast. Data on wind direction and wind speed were abstracted from published monthly summaries.

3 METHODS

Seasonal Box-Jenkins time series models (SARIMA; O'Donovan, 1983) were fitted to the data. For this paper the main interest was to examine the magnitude of the mean value of the seasonally differenced data (period 13) with its standard error. Values greater than twice their standard error give an indication of a significant annual trend in mean values.

Large and complex data sets of the type described here confound interpretation. Their multivariate nature often masks relationships or causations. The use of simple exploratory or graphical techniques can be of immense value in suggesting the pattern and nature of relationships, or the direction for further investigation. One of the simplest methods of representing multivariate data is the biplot display (Digby & Kempton, 1987). The biplot is simply a graphical or qualitative representation of the original data; whilst it can be used to suggest models, it is not suitable for formal statistical inferential analysis. Principal component biplots were carried out to examine the relationships amongst water chemistry variables and climatic data available from the MORECS database.

4 RESULTS

The mean value of the seasonal differences for precipitation and streamwater chemistry are given in Tables 1 & 2. Volume weighted means of the

precipitation data suggested possible increases over the monitoring period of calcium and marine sulphate. A decrease in non-marine (excess) sulphate (Figure 1) was only significant when considered as arithmetic means. Examination of pH suggested a reduction in acidity (an increase in pH) of 0.04 units/annum. Cyff streamwater data suggested a reduction in potassium and an increase in silicon. No chemical determinations reached significance from the Gwy site. There was strong indication from both stream sites of a decrease in acidity of a similar level of magnitude to that in precipitation (Figure 2).

Table 1. Mean Seasonal Differences ($mgl^{-1} \pm 1$ SE) of Arithmetic(A) and Volume Weighted(VW) Mean Precipitation Data.

	A	VW
Na	0.072±0.050	0.093±0.048
K	0.003±0.006	0.002±0.003
Ca	0.013±0.010	0.010±0.005
Mg	0.007±0.005	0.010±0.006
NO3-N	0.005±0.007	0.010±0.008
NH4-N	0.017±0.012	0.021±0.015
SO4-S total	-0.024±0.015	-0.014±0.014
SO4-S marine	0.006±0.004	0.008±0.004
SO4-S xs	-0.032±0.015	-0.022±0.014
Cl	0.147±0.094	0.136±0.072
Precipitation	-2.82±7.81	
pH	0.041±0.010	
Hydrogen ions	-2.10±0.92	

Table 2. Mean Seasonal Differences ($mgl^{-1} \pm 1$ SE) of Cyff(C) and Gwy(G) Mean Streamwater Data.

	C	G
Na	0.044±0.026	0.048±0.031
K	-0.005±0.002	-0.003±0.003
Ca	0.038±0.021	0.014±0.010
Mg	-0.001±0.007	-0.001±0.005
Si	0.019±0.007	0.012±0.010
NO3-N	0.006±0.005	-0.005±0.005
SO4-S total	-0.001±0.017	-0.023±0.021
Cl	0.087±0.058	0.068±0.062
DOC	-0.020±0.029	0.012±0.031
pH	0.059±0.009	0.052±0.012
Hydrogen ions	-0.144±0.031	-0.739±0.161

An examination of meteorological data from Aberporth suggested an increasing tendency for both onshore and stronger winds (Figure 3). Some of the changes in precipitation and streamwater chemistry may thus be partly attributed to an increase in the frequency of winds from a coastal direction, for example, the reduction in non-marine sulphate and increase in pH may be partly explained by this phenomenon. Additional evidence for an increase in onshore winds is given by an examination of sodium and chloride concentrations in precipitation. Whilst not significant (Table 1) these both suggest a large increase in these marine salts.

Comparisons of the three water sources using biplot presentations (Figure 4) showed very different relationships in precipitation chemistry compared to stream sites suggesting marked changes following percolation and run-off. Remarkable consistency was apparent between the two stream sites. A separation of the data by winter and summer seasons revealed different patterns for the two periods, but the level of agreement between streams and lack of agreement between streams and precipitation remained apparent. Many interesting patterns are revealed by these biplots, for instance it can be seen that high rainfall is associated with higher precipitation pH(lower acidity), but high rainfall leads to lower pH in streamwater as a consequence of run-off from acidic surface soils and high flow rates diluting baseflow alkalinity.

5 CONCLUSION

The data from Plynlimon are suggesting reversibility of acidification, possibly linked to changes in the nature of sulphate deposition, however caused. Changes to other aspects of water chemistry are less clear and further monitoring is continuing to assess these.

References

Allot, T.E.H., Harriman, R. & Battarbee, R.W. (1992). Reversibility of lake acidification at the Round Lock of Glenhead, Galloway, Scotland. *Environmental Pollution*, 77, 219-226.

Digby, P.G.N. & Kempton, R.A. (1987). *Multivariate analysis of ecological communities*. Chapman & Hall, London.

Gillham, C.A., Leech, P.K. & Egglestone, H.S. (1992). *UK emissions of air pollutants 1970-1990. Report LR 887 (AP).* Warren Spring Laboratory, UK.

O'Donovan, T.M (1983). *Short term forecasting. An introduction to the Box-Jenkins approach.* Wiley, Chichester.

ACKNOWLEDGEMENTS

This work was partly funded by the Department of the Environment. The authors thank their many colleagues at Bangor and Merlewood for data collection and chemical analysis.

CORRESPONDING AUTHOR

T H Sparks
ITE Monks Wood
Abbots Ripton
Huntingdon
Cambs PE17 2LS
UK

Figure 1. Non–marine SO4–S

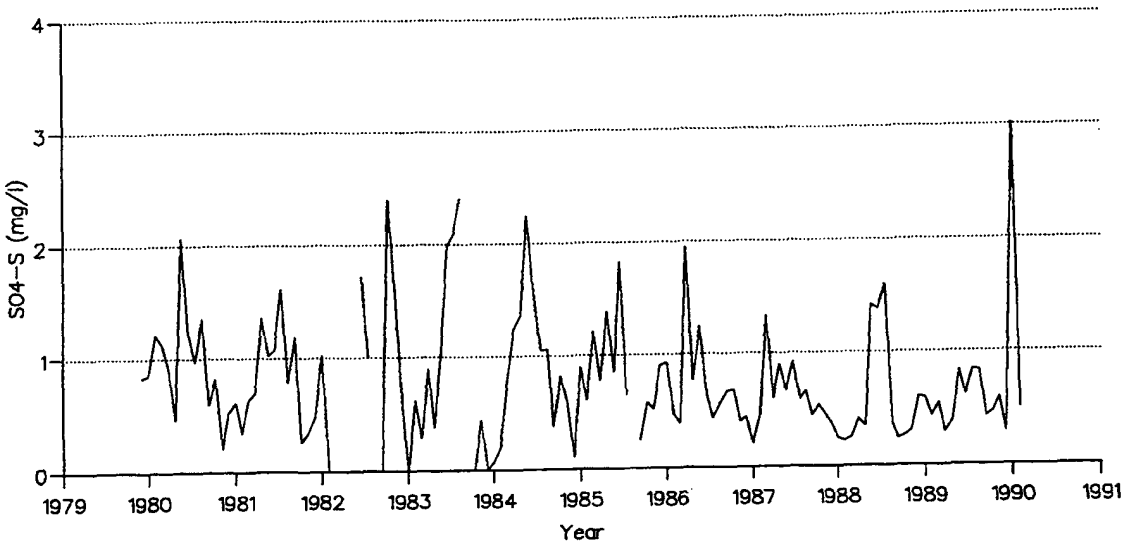


Figure 2. Annual mean pH

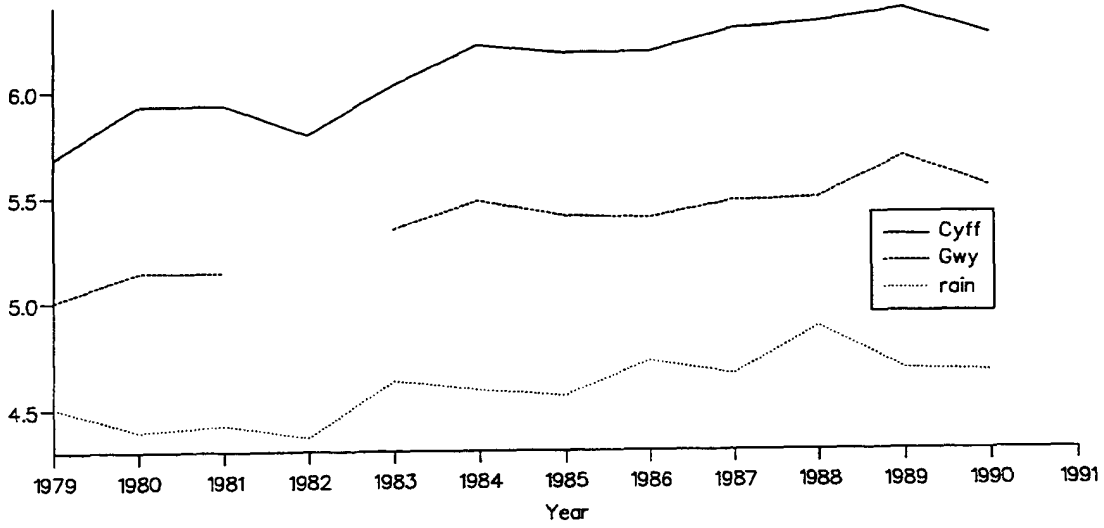


Figure 3. Aberporth 5 year moving average.
no. of obs sw/w winds

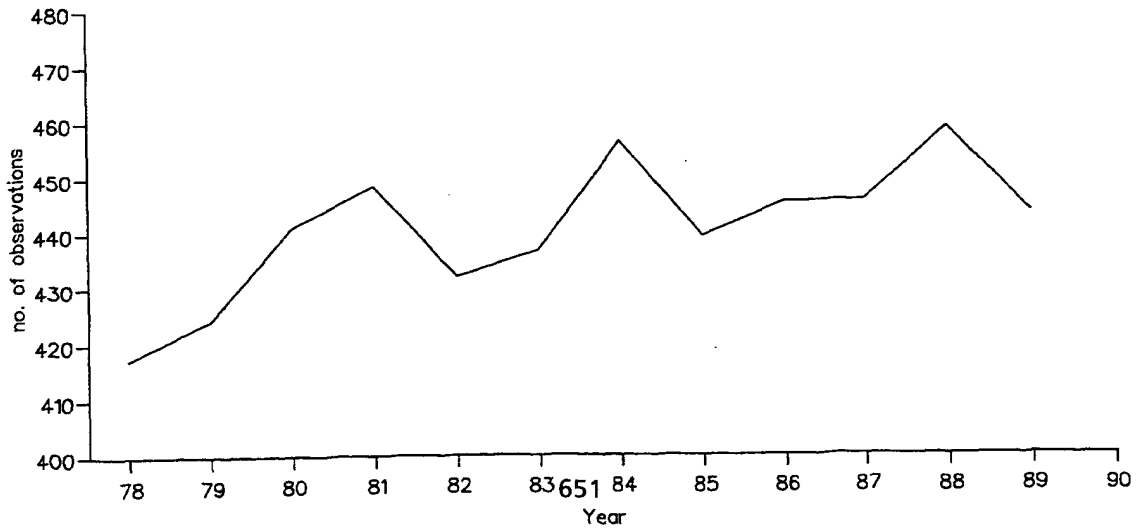


Figure 4. Biplots of precipitation, Cyff & Gwy streams

